

# Nonlinear Fiber Optics

*Fifth Edition*

# Nonlinear Fiber Optics

## *Fifth Edition*

**Govind P. Agrawal**

*The Institute of Optics  
University of Rochester  
Rochester, New York*



ELSEVIER

AMSTERDAM • BOSTON • HEIDELBERG • LONDON  
NEW YORK • OXFORD • PARIS • SAN DIEGO  
SAN FRANCISCO • SINGAPORE • SYDNEY • TOKYO

Academic Press is an Imprint of Elsevier



ACADEMIC  
PRESS

Academic Press is an imprint of Elsevier  
The Boulevard, Langford Lane, Kidlington, Oxford OX5 1GB, UK  
225 Wyman Street, Waltham, MA 02451, USA

Fourth edition 2007  
Fifth edition 2013

Copyright © 2013 Elsevier Inc. All rights reserved.

No part of this publication may be reproduced, stored in a retrieval system or transmitted in any form or by any means electronic, mechanical, photocopying, recording or otherwise without the prior written permission of the publisher

Permissions may be sought directly from Elsevier's Science & Technology Rights Department in Oxford, UK: phone (+44) (0) 1865 843830; fax (+44) (0) 1865 853333; email: [permissions@elsevier.com](mailto:permissions@elsevier.com). Alternatively you can submit your request online by visiting the Elsevier web site at <http://elsevier.com/locate/permissions>, and selecting Obtaining permission to use Elsevier material

#### **Notice**

No responsibility is assumed by the publisher for any injury and/or damage to persons or property as a matter of products liability, negligence or otherwise, or from any use or operation of any methods, products, instructions or ideas contained in the material herein. Because of rapid advances in the medical sciences, in particular, independent verification of diagnoses and drug dosages should be made

#### **British Library Cataloguing in Publication Data**

A catalogue record for this book is available from the British Library

#### **Library of Congress Cataloging-in-Publication Data**

A catalog record for this book is available from the Library of Congress

ISBN: 978-0-12397-023-7

For information on all Academic Press publications  
visit our web site at [books.elsevier.com](http://books.elsevier.com)

Printed and bound in Great Britain  
13 14 15 16 17 10 9 8 7 6 5 4 3 2 1

Working together to grow  
libraries in developing countries

[www.elsevier.com](http://www.elsevier.com) | [www.bookaid.org](http://www.bookaid.org) | [www.sabre.org](http://www.sabre.org)

ELSEVIER

BOOK AID  
International

Sabre Foundation

*In the memory of my mother and  
for Anne, Spira, Caroline, and Claire*

# Author Biography

**Govind Agrawal** holds positions of Professor of Optics and Professor of Physics at the University of Rochester, USA. His previous appointments were at Ecole Polytechnique, France, City University of New York, and AT & T Bell Laboratories. He is an author or coauthor of more than 400 research papers and eight books. He is also involved in planning of international conferences and is a frequent speaker at such meetings. Professor Agrawal is a Fellow of both the Optical society of America and IEEE. He served as an associate Editor of the Journal of the Optical Society of America from 1993 to 1998 and of Optics Express from 2001 to 2004. He is currently serving on the Editorial board of the OSA journal Advances in Optics and Photonics. Prof. Agrawal chaired the Publication Council of Optical society of America and was also a member of its Board of Directors during 2009 and He is also the recipient of the 2012 IEEE Photonics Society Quantum Electronics Award.

# Preface

Since the publication of the first edition of this book in 1989, the field of *nonlinear fiber optics* has remained an active area of research and has thus continued to grow at a rapid pace. During the 1990s, a major factor behind such a sustained growth was the advent of fiber amplifiers and lasers, made by doping silica fibers with rare-earth materials such as erbium and ytterbium. Erbium-doped fiber amplifiers revolutionized the design of fiber-optic communication systems, including those making use of optical solitons, whose very existence stems from the presence of nonlinear effects in optical fibers. Optical amplifiers permit propagation of lightwave signals over thousands of kilometers as they can compensate for all losses encountered by the signal in the optical domain. At the same time, fiber amplifiers enable the use of massive wavelength-division multiplexing, a technique that led, by 1999, to the development of lightwave systems with capacities exceeding 1~Tb/s. Nonlinear fiber optics plays an important role in the design of such high-capacity lightwave systems. In fact, an understanding of various nonlinear effects occurring inside optical fibers is almost a prerequisite for a lightwave-system designer.

Starting around 2000, a new development occurred in the field of *nonlinear fiber optics* that changed the focus of research and led to a number of advances and novel applications in recent years. Several kinds of new fibers, classified as highly nonlinear fibers, have been developed. They are referred to with names such as microstructured fibers, holey fibers, or photonic crystal fibers, and share the common property that a relatively narrow core is surrounded by a cladding containing a large number of air holes. The nonlinear effects are enhanced dramatically in such fibers to the extent that they can be observed even when the fiber is only a few centimeters long. Their dispersive properties are also quite different compared with those of conventional fibers developed for telecommunication applications. Because of these changes, microstructured fibers exhibit a variety of novel nonlinear effects that are finding applications in fields as diverse as optical coherence tomography and high-precision frequency metrology.

The fifth edition is intended to bring the book up-to-date so that it remains a unique source of comprehensive coverage on the subject of nonlinear fiber optics. It retains most of the material that appeared in the fourth edition. However, an attempt was made to include recent research results on most topics relevant to the field of nonlinear fiber optics, resulting in an increase in the size of the book. Major changes occur in Chapters 11 and 12. In particular Chapter 12 has been split into two chapters such that the new Chapter 13 is now wholly devoted to the phenomenon of supercontinuum generation. In the fifth edition, Chapters 11 and 12 have seen major additions because of recent advances in the design of photonic crystal and other microstructure fibers. All other chapters have also been updated, as found appropriate for improving the book. For example, a new subsection of Chapter 2 is now devoted to the nonlinear effects in multimode fibers. Polarization issues are discussed in detail in Chapters 6 to 10 because of their importance. Chapters 8 to

10 required major changes because of continuing advances in the research areas covered by them.

The potential readers of this book are likely to consist of senior undergraduate students, graduate students enrolled in the M.S. and Ph.D. degree programs, engineers and technicians involved with the fiber-optics industry, and scientists working in the fields of fiber optics and optical communications. This revised edition should continue to be a useful text for graduate and senior-level courses dealing with nonlinear optics, fiber optics, or optical communications that are designed to provide mastery of the fundamental aspects. Some universities may even opt to offer a high-level graduate course devoted to solely nonlinear fiber optics. The problems provided at the end of each chapter should be useful to instructors of such a course.

Many individuals have contributed, either directly or indirectly, to the completion of the fifth edition. I am thankful to all of them, especially to my graduate students whose curiosity and involvement led to several improvements. Several of my colleagues have helped me in preparing the fifth edition, and I thank them for reading drafts of selected chapters and for making helpful suggestions. I am grateful to many readers for their occasional feedback. Last, but not least, I thank my wife, Anne, and my daughters, Sipra, Caroline, and Claire, for their understanding and support for this project.

Govind P. Agrawal  
Rochester, New York

# Introduction

# 1

This introductory chapter is intended to provide an overview of the fiber characteristics that are important for understanding the nonlinear effects discussed in later chapters. Section 1.1 provides a historical perspective on the progress in the field of fiber optics. Section 1.2 discusses various fiber properties such as optical loss, chromatic dispersion, and birefringence. Particular attention is paid to chromatic dispersion because of its importance in the study of nonlinear effects probed by using ultrashort optical pulses. Section 1.3 introduces various nonlinear effects resulting from the intensity dependence of the refractive index and stimulated inelastic scattering. Among the nonlinear effects that have been studied extensively using optical fibers as a nonlinear medium are self-phase modulation (SPM), cross-phase modulation (XPM), four-wave mixing (FWM), stimulated Raman scattering (SRS), and stimulated Brillouin scattering (SBS). Each of these effects is considered in detail in separate chapters. Section 1.4 gives an overview of how this book is organized for discussing such a wide variety of nonlinear effects in optical fibers.

---

## 1.1 HISTORICAL PERSPECTIVE

Total internal reflection—the basic phenomenon responsible for guiding of light in optical fibers—is known from the 19th century. The reader is referred to a 1999 book for the interesting history behind the discovery of this phenomenon [1]. Although uncladded glass fibers were fabricated during the decade of the 1920s [2–4], the field of fiber optics was not born until the 1950s when the use of a cladding layer led to considerable improvement in the fiber characteristics [5–8]. The idea that optical fibers would benefit from a dielectric cladding was not obvious and has a remarkable history [1].

The field of fiber optics developed rapidly during the 1960s, mainly for the purpose of image transmission through a bundle of glass fibers [9]. These early fibers were extremely lossy ( $\text{loss} > 1000 \text{ dB/km}$ ) from the modern standard. However, the situation changed drastically in 1970 when, following an earlier suggestion [10], losses of silica fibers were reduced to below 20 dB/km [11]. Further progress in fabrication technology [12] resulted by 1979 in a loss of only 0.2 dB/km in the  $1.55\text{-}\mu\text{m}$

wavelength region [13], a loss level limited mainly by the fundamental process of Rayleigh scattering.

The availability of low-loss silica fibers led not only to a revolution in the field of optical fiber communications [14–16] but also to the advent of the new field of nonlinear fiber optics; see Refs. [17, 18] for a recent historical account. Raman and Brillouin scattering processes were studied as early as 1972 using optical fibers [19–21]. This work stimulated the study of other nonlinear phenomena such as optically induced birefringence, parametric four-wave mixing, and self-phase modulation [22–26]. An important contribution was made in 1973 when it was suggested that optical fibers can support soliton-like pulses as a result of an interplay between the dispersive and nonlinear effects [27]. Optical solitons were observed in a 1980 experiment [28] and led to a number of advances during the 1980s in the generation and control of ultrashort optical pulses [29–33]. The decade of the 1980s also saw the development of pulse-compression and optical-switching techniques that exploited the nonlinear effects in fibers [34–41]. Pulses as short as 6 fs were generated by 1987 [42]. Several reviews have covered the progress made during the 1980s [43–47].

The field of nonlinear fiber optics continued to grow during the decade of the 1990s. A new dimension was added when optical fibers were doped with rare-earth elements and used to make amplifiers and lasers. Erbium-doped fiber amplifiers attracted the most attention because they operate in the wavelength region near  $1.55\text{ }\mu\text{m}$  and are thus useful for fiber-optic telecommunication systems [48]. Their use led to a virtual revolution in the design of multichannel lightwave systems [14–16]. After 2000, two nonlinear effects occurring inside optical fibers, namely stimulated Raman scattering and four-wave mixing, were employed to develop new types of fiber-optic amplifiers. Such amplifiers do not require doped fibers and can operate in any spectral region. Indeed, the use of Raman amplification has become quite common in modern telecommunication systems [49]. Fiber-optic parametric amplifiers based on four-wave mixing are also attractive because of their potential for ultrafast signal processing [50].

The advent of fiber amplifiers also fueled research on optical solitons and led eventually to new types of solitons such as dispersion-managed solitons and dissipative solitons [51–54]. In another development, fiber gratings, first made in 1978 [55], were developed during the 1990s to the point that they became an integral part of lightwave technology [56]. Starting in 1996, new types of fibers, known under names such as photonic crystal fibers, holey fibers, and microstructure fibers were developed [57–61]; Chapter 11 is devoted to these new types of fibers. Structural changes in such fibers affect their dispersive as well as nonlinear properties. In particular, the wavelength at which the group-velocity dispersion (GVD) vanishes shifts toward the visible region, and some fibers exhibit two such wavelengths. At the same time, the nonlinear effects are enhanced considerably inside them because of a relatively small core size. This combination leads to a variety of novel nonlinear phenomena covered in Chapter 12. Supercontinuum generation [62–64], a phenomenon in which optical spectrum of incident light broadens by a factor of more than 100 over a relatively short length of fiber, is covered in Chapter 13. Because of these developments,

the field of nonlinear fiber optics has grown considerably over the last decade and is expected to continue to remain vibrant in the near future.

## 1.2 FIBER CHARACTERISTICS

In its simplest form, an optical fiber consists of a central glass core surrounded by a cladding layer whose refractive index  $n_c$  is slightly lower than the core index  $n_1$ . Such fibers are generally referred to as *step-index fibers* to distinguish them from *graded-index fibers* in which the refractive index of the core decreases gradually from center to core boundary [65–67]. Figure 1.1 shows schematically the cross-section and refractive-index profile of a step-index fiber. Two parameters that characterize an optical fiber are the relative core-cladding index difference:

$$\Delta = \frac{n_1 - n_c}{n_1} \quad (1.2.1)$$

and the so-called  $V$  parameter defined as

$$V = k_0 a (n_1^2 - n_c^2)^{1/2}, \quad (1.2.2)$$

where  $k_0 = 2\pi/\lambda$ ,  $a$  is the core radius, and  $\lambda$  is the wavelength of light.

The  $V$  parameter determines the number of modes supported by the fiber. Fiber modes are discussed in Section 2.2, where it is shown that a step-index fiber supports a single-mode if  $V < 2.405$ . Optical fibers designed to satisfy this condition are

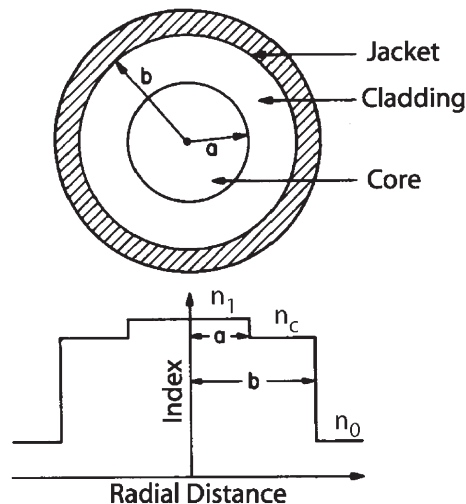


**Figure 1.1** Schematic illustration of the cross-section and the refractive-index profile of a step-index fiber.

called single-mode fibers. The main difference between the single-mode and multimode fiber is the core size. The core radius  $a$  is typically  $25\text{ }\mu\text{m}$  for multimode fibers. However, single-mode fibers with  $\Delta \approx 0.003$  require  $a$  to be  $<5\text{ }\mu\text{m}$ . The numerical value of the outer radius  $b$  is less critical as long as it is large enough to confine the fiber modes entirely. A standard value of  $b = 62.5\text{ }\mu\text{m}$  is commonly used for both single-mode and multimode fibers. Since nonlinear effects are mostly studied using single-mode fibers, the term optical fiber in this text refers to single-mode fibers (unless noted otherwise).

### 1.2.1 Material and Fabrication

The material of choice for low-loss optical fibers is pure silica glass synthesized by fusing  $\text{SiO}_2$  molecules. The refractive-index difference between the core and the cladding is realized by the selective use of dopants during the fabrication process. Dopants such as  $\text{GeO}_2$  and  $\text{P}_2\text{O}_5$  increase the refractive index of pure silica and are suitable for the core, while materials such as boron and fluorine are used for the cladding because they decrease the refractive index of silica. Additional dopants can be used depending on specific applications. For example, to make fiber amplifiers and lasers, the core of silica fibers is codoped with rare-earth ions using dopants such as  $\text{ErCl}_3$  and  $\text{Nd}_2\text{O}_3$ .

The fabrication of optical fibers involves two stages [68]. In the first stage, a vapor-deposition method is used to make a cylindrical preform with the desired refractive-index profile and the relative core–cladding dimensions. A typical preform is 1-m long with a 2-cm diameter. In the second stage, the preform is drawn into a fiber using a precision-feed mechanism that feeds it into a furnace at a proper speed. During this process, the relative core–cladding dimensions are preserved. Both stages, preform fabrication and fiber drawing, involve sophisticated technology to ensure the uniformity of the core size and the index profile [68–70].

Several methods can be used for making a preform. The three commonly used methods are modified chemical vapor deposition (MCVD), outside vapor deposition, and vapor-phase axial deposition. Figure 1.2 shows a schematic diagram of the MCVD process. In this process, successive layers of  $\text{SiO}_2$  are deposited on the

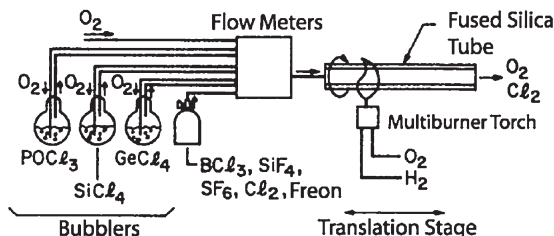


**Figure 1.2 Schematic diagram of the MCVD process commonly used for fiber fabrication.**  
(After Ref. [68]; © 1985 Elsevier.)

inside of a fused silica tube by mixing the vapors of  $\text{SiCl}_4$  and  $\text{O}_2$  at a temperature of  $\approx 1800^\circ\text{C}$ . To ensure uniformity, the multiburner torch is moved back and forth across the tube length. The refractive index of the cladding layers is controlled by adding fluorine to the tube. When a sufficient cladding thickness has been deposited with multiple passes of the torch, the vapors of  $\text{GeCl}_4$  or  $\text{POCl}_3$  are added to the vapor mixture to form the core. When all layers have been deposited, the torch temperature is raised to collapse the tube into a solid rod known as the preform.

This description is extremely brief and is intended to provide a general idea. The fabrication of optical fibers requires attention to a large number of technological details. The interested reader is referred to the extensive literature on this subject [68–70].

### 1.2.2 Fiber Losses

An important fiber parameter provides a measure of power loss during transmission of optical signals inside the fiber. If  $P_0$  is the power launched at the input of a fiber of length  $L$ , the transmitted power  $P_T$  is given by

$$P_T = P_0 \exp(-\alpha L), \quad (1.2.3)$$

where the *attenuation constant*  $\alpha$  is a measure of total fiber losses from all sources. It is customary to express  $\alpha$  in units of dB/km using the relation (see Appendix A for an explanation of decibel units)

$$\alpha_{\text{dB}} = -\frac{10}{L} \log \left( \frac{P_T}{P_0} \right) = 4.343\alpha, \quad (1.2.4)$$

where Eq. (1.2.3) was used to relate  $\alpha_{\text{dB}}$  and  $\alpha$ .

As one may expect, fiber losses depend on the wavelength of light. Figure 1.3 shows the loss spectrum of a silica fiber made by the MCVD process [68]. This fiber exhibits a minimum loss of about 0.2 dB/km near  $1.55\text{ }\mu\text{m}$ . Losses are considerably higher at shorter wavelengths, reaching a level of a few dB/km in the visible region.

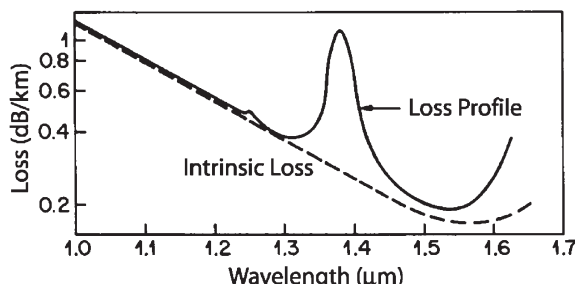


**Figure 1.3** Measured loss spectrum of a single-mode silica fiber. Dashed curve shows the contribution resulting from Rayleigh scattering. (After Ref. [68]; © 1985 Elsevier.)

Note, however, that even a 10-dB/km loss corresponds to an attenuation constant of only  $\alpha \approx 2 \times 10^{-5} \text{ cm}^{-1}$ , an incredibly low value compared to that of most other materials.

Several factors contribute to the loss spectrum of Figure 1.3, with material absorption and *Rayleigh scattering* contributing dominantly. Silica glass has electronic resonances in the ultraviolet region, and vibrational resonances in the far-infrared region beyond  $2 \mu\text{m}$ , but it absorbs little light in the wavelength region extending from 0.5 to  $2 \mu\text{m}$ . However, even a relatively small amount of impurities can lead to significant absorption in that wavelength window. From a practical point of view, the most important impurity affecting fiber loss is the OH ion, which has a fundamental vibrational absorption peak at  $\approx 2.73 \mu\text{m}$ . The overtones of this OH-absorption peak are responsible for the dominant peak seen in Figure 1.3 near  $1.4 \mu\text{m}$  and a smaller peak near  $1.23 \mu\text{m}$ . Special precautions are taken during the fiber-fabrication process to ensure an OH-ion level of less than one part in one hundred million [68]. In state-of-the-art fibers, the peak near  $1.4 \mu\text{m}$  can be reduced to below the 0.5-dB level. It virtually disappears in the so-called “dry” fibers [71]. Such fibers with low losses in the entire  $1.3\text{--}1.6 \mu\text{m}$  spectral region are useful for fiber-optic communications and were available commercially by the year 2000.

Rayleigh scattering is a fundamental loss mechanism arising from density fluctuations frozen into the fused silica during manufacture. Resulting local fluctuations in the refractive index scatter light in all directions. The Rayleigh-scattering loss varies as  $\lambda^{-4}$  and is dominant at short wavelengths. As this loss is intrinsic to the fiber, it sets the ultimate limit on fiber loss. The intrinsic loss level (shown by a dashed line in Figure 1.3) is estimated to be (dB/km)

$$\alpha_R = C_R / \lambda^4, \quad (1.2.5)$$

where the constant  $C_R$  is in the range  $0.7\text{--}0.9 \text{ dB}/(\text{km } \mu\text{m}^4)$  depending on the constituents of the fiber core. As  $\alpha_R$  is in the range of  $0.12\text{--}0.15 \text{ dB/km}$  near  $\lambda = 1.55 \mu\text{m}$ , losses in silica fibers are dominated by Rayleigh scattering. In some glasses,  $\alpha_R$  can be reduced to a level near  $0.05 \text{ dB/km}$  [72]. Such glasses may be useful for fabricating ultralow-loss fibers.

Among other factors that may contribute to losses are bending of the fiber and scattering of light at the core–cladding interface [65]. Modern fibers exhibit a loss of  $\approx 0.2 \text{ dB/km}$  near  $1.55 \mu\text{m}$ . Total loss of fiber cables used in optical communication systems is slightly larger because of splice and cabling losses.

### 1.2.3 Chromatic Dispersion

When an electromagnetic wave interacts with the bound electrons of a dielectric, the medium response, in general, depends on the optical frequency  $\omega$ . This property, referred to as chromatic dispersion, manifests through the frequency dependence of the refractive index  $n(\omega)$ . On a fundamental level, the origin of chromatic dispersion is related to the characteristic resonance frequencies at which the medium absorbs the electromagnetic radiation through oscillations of bound electrons. Far from the

medium resonances, the refractive index is well approximated by the *Sellmeier equation* [65]

$$n^2(\omega) = 1 + \sum_{j=1}^m \frac{B_j \omega_j^2}{\omega_j^2 - \omega^2}, \quad (1.2.6)$$

where  $\omega_j$  is the resonance frequency and  $B_j$  is the strength of  $j$ th resonance. The sum in Eq. (1.2.6) extends over all material resonances that contribute to the frequency range of interest. In the case of optical fibers, the parameters  $B_j$  and  $\omega_j$  are obtained experimentally by fitting the measured dispersion curves [73] to Eq. (1.2.6) with  $m = 3$  and they are dependant on the core constituents [67]. For bulk-fused silica, these parameters are found to be [74]  $B_1 = 0.6961663$ ,  $B_2 = 0.4079426$ ,  $B_3 = 0.8974794$ ,  $\lambda_1 = 0.0684043 \mu\text{m}$ ,  $\lambda_2 = 0.1162414 \mu\text{m}$ , and  $\lambda_3 = 9.896161 \mu\text{m}$ , where  $\lambda_j = 2\pi c/\omega_j$  and  $c$  is the speed of light in a vacuum. Figure 1.4 displays how  $n$  varies with wavelength for fused silica. As seen there,  $n$  has a value of about 1.46 in the visible region, and this value decreases by 1% in the wavelength region near  $1.5 \mu\text{m}$ .

Fiber dispersion plays a critical role in the propagation of short optical pulses because different spectral components associated with the pulse travel at different speeds given by  $c/n(\omega)$ . Even when the nonlinear effects are not important, dispersion-induced pulse broadening can be detrimental for optical communication systems. In the nonlinear regime, the combination of dispersion and nonlinearity can result in a qualitatively different behavior, as discussed in later chapters. Mathematically, the effects of fiber dispersion are accounted for by expanding the mode-propagation

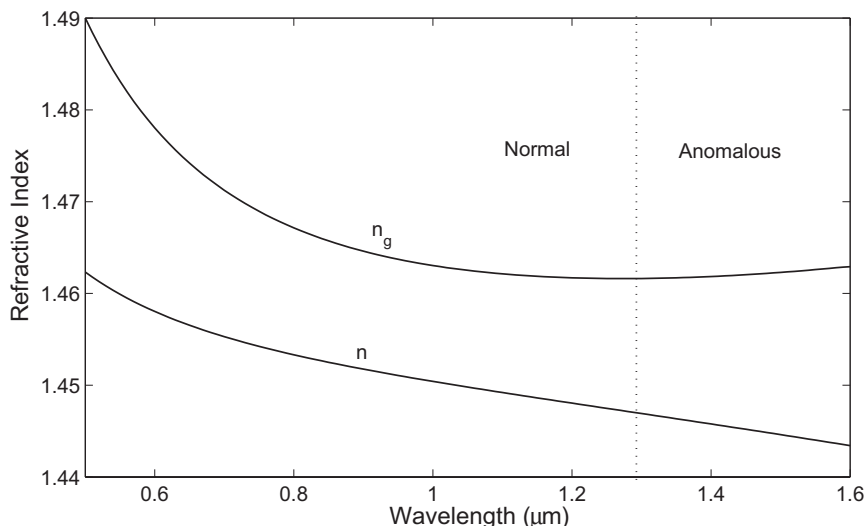


Figure 1.4 Variation of refractive index  $n$  and group index  $n_g$  with wavelength for fused silica.

constant  $\beta$  in a Taylor series about the frequency  $\omega_0$  at which the pulse spectrum is centered:

$$\beta(\omega) = n(\omega) \frac{\omega}{c} = \beta_0 + \beta_1(\omega - \omega_0) + \frac{1}{2}\beta_2(\omega - \omega_0)^2 + \dots, \quad (1.2.7)$$

where

$$\beta_m = \left( \frac{d^m \beta}{d\omega^m} \right)_{\omega=\omega_0} \quad (m = 0, 1, 2, \dots). \quad (1.2.8)$$

The parameters  $\beta_1$  and  $\beta_2$  are related to the refractive index  $n(\omega)$  and its derivatives through the relations

$$\beta_1 = \frac{1}{v_g} = \frac{n_g}{c} = \frac{1}{c} \left( n + \omega \frac{dn}{d\omega} \right), \quad (1.2.9)$$

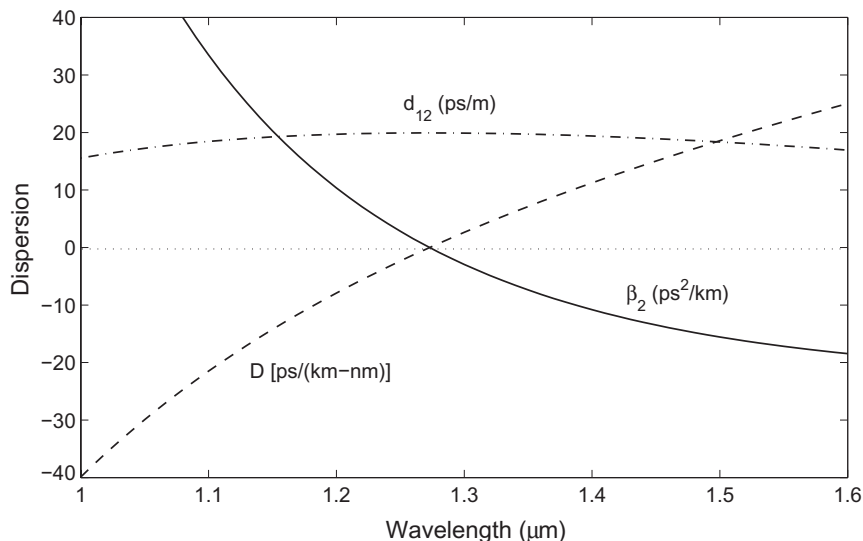
$$\beta_2 = \frac{1}{c} \left( 2 \frac{dn}{d\omega} + \omega \frac{d^2n}{d\omega^2} \right), \quad (1.2.10)$$

where  $n_g$  is the group index and  $v_g$  is the group velocity. Figure 1.4 shows the group index  $n_g$  changes with wavelength for fused silica. The group velocity can be found using  $v_g = c/n_g$ . Physically speaking, the envelope of an optical pulse moves at the group velocity, while the parameter  $\beta_2$  represents dispersion of the group velocity and is responsible for pulse broadening. This phenomenon is known as the *group-velocity dispersion* (GVD), and  $\beta_2$  is the GVD parameter. The dispersion parameter  $D$ , defined as  $d\beta_1/d\lambda$ , is also used in practice. It is related to  $\beta_2$  and  $n$  as

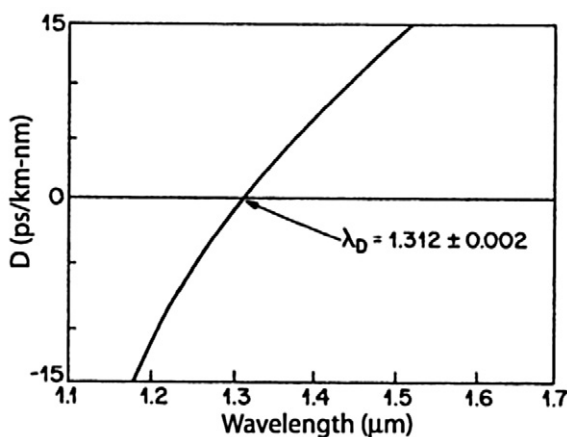
$$D = \frac{d\beta_1}{d\lambda} = -\frac{2\pi c}{\lambda^2} \beta_2 = -\frac{\lambda}{c} \frac{d^2n}{d\lambda^2}. \quad (1.2.11)$$

Figure 1.5 shows how  $\beta_2$  and  $D$  vary with wavelength  $\lambda$  for fused silica using Eqs (1.2.6) and (1.2.10). The most notable feature is that both  $\beta_2$  and  $D$  vanish at a wavelength of about  $1.27 \mu\text{m}$  and change sign for longer wavelengths. This wavelength is referred to as the *zero-dispersion wavelength* and is denoted as  $\lambda_D$ . However, the dispersive effects do not disappear completely at  $\lambda = \lambda_D$ . Pulse propagation near this wavelength requires the inclusion of the cubic term in Eq. (1.2.7). The coefficient  $\beta_3$  appearing in that term is called the *third-order dispersion* (TOD) parameter. Higher-order dispersive effects can distort ultrashort optical pulses both in the linear [65] and nonlinear regimes [75]. Their inclusion is necessary for ultrashort optical pulses, or when the input wavelength  $\lambda$  approaches  $\lambda_D$  to within a few nanometers.

The curves shown in Figures 1.4 and 1.5 are for bulk-fused silica. The dispersive behavior of actual glass fibers deviates from that shown in these figures for the following two reasons. First, the fiber core may have small amounts of dopants such as  $\text{GeO}_2$  and  $\text{P}_2\text{O}_5$ . Equation (1.2.6) in that case should be used with parameters appropriate to the amount of doping levels [67]. Second, because of dielectric waveguiding, the effective mode index is slightly lower than the material index  $n(\omega)$  of



**Figure 1.5** Variation of  $\beta_2$ ,  $D$ , and  $d_{12}$  with the wavelength for fused silica. Both  $\beta_2$  and  $D$  vanish at the zero-dispersion wavelength occurring near  $1.27\text{ }\mu\text{m}$ .



**Figure 1.6** Measured variation of the dispersion parameter  $D$  with the wavelength for a single-mode fiber. (After Ref. [68]; © 1985 Elsevier.)

the core, reduction itself being  $\omega$  dependent [65–67]. This results in a waveguide contribution that must be added to the material contribution to obtain the total dispersion. Generally, the waveguide contribution to  $\beta_2$  is relatively small except near the zero-dispersion wavelength  $\lambda_D$  where the two become comparable. The main effect

of the waveguide contribution is to shift  $\lambda_D$  slightly toward longer wavelengths;  $\lambda_D \approx 1.31 \mu\text{m}$  for standard fibers. Figure 1.6 shows the measured total dispersion of a single-mode fiber [68]. The quantity plotted is the dispersion parameter  $D$  related to  $\beta_2$  by the relationship given in Eq. (1.2.11).

An interesting feature of the waveguide dispersion is that its contribution to  $D$  (or  $\beta_2$ ) depends on fiber-design parameters such as core radius  $a$  and core-cladding index difference  $\Delta$ . This feature can be used to shift the zero-dispersion wavelength  $\lambda_D$  in to the vicinity of  $1.55 \mu\text{m}$  where the fiber loss is at a minimum. Such *dispersion-shifted* fibers [76] have found applications in optical communication systems. They are available commercially and are known by trade names such as TrueWave (OFS), LEAF (Corning), and TeraLight (Draka), depending on at what wavelength  $D$  becomes zero in the  $1.5 \mu\text{m}$  spectral region. The fibers in which GVD is shifted to the wavelength region beyond  $1.6 \mu\text{m}$  exhibit a large positive value of  $\beta_2$ . They are called *dispersion-compensating fibers* (DCFs). The slope of the curve in Figure 1.6 (called the *dispersion slope*) is related to the TOD parameter  $\beta_3$ . Fibers with reduced slope have been developed in recent years for wavelength-division-multiplexing (WDM) applications.

It is possible to design *dispersion-flattened* optical fibers having low dispersion over a relatively large wavelength range of  $1.3\text{--}1.6 \mu\text{m}$ . This is achieved by using multiple cladding layers. Figure 1.7 shows the measured dispersion spectra for two such multiple-clad fibers having two (double-clad) and four (quadruple-clad) cladding layers around the core applications. For comparison, dispersion of a single-clad fiber is also shown by a dashed line. The quadruply clad fiber has low dispersion ( $|D| \sim 1 \text{ ps/km-nm}$ ) over a wide wavelength range extending from  $1.25$  to  $1.65 \mu\text{m}$ . Waveguide dispersion can also be used to make fibers for which  $D$  varies along the fiber length. An example is provided by *dispersion-decreasing* fibers made by tapering the core diameter along the fiber length [78].

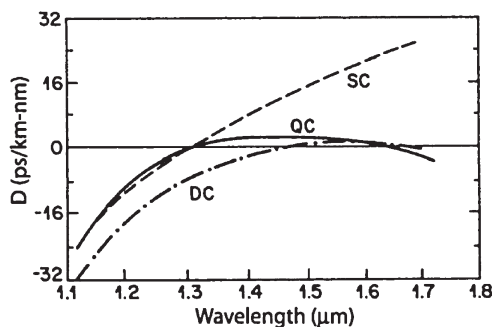


Figure 1.7 Variation of dispersion parameter  $D$  with wavelengths for three kinds of fibers. Labels SC, DC, and QC stand for single-clad, double-clad, and quadruple-clad fibers, respectively. (After Ref. [77]; © 1982 IEE.)

Nonlinear effects in optical fibers can manifest qualitatively different behaviors depending on the sign of the GVD parameter. For wavelengths such that  $\lambda < \lambda_D$ , the fiber is said to exhibit *normal dispersion* as  $\beta_2 > 0$  (see Figure 1.5). In the normal-dispersion regime, high-frequency (blue-shifted) components of an optical pulse travel slower than low-frequency (red-shifted) components of the same pulse. By contrast, the opposite occurs in the *anomalous-dispersion* regime in which  $\beta_2 < 0$ . As seen in Figure 1.5, silica fibers exhibit anomalous dispersion when the light wavelength exceeds the zero-dispersion wavelength ( $\lambda > \lambda_D$ ). The anomalous-dispersion regime is of considerable interest for the study of nonlinear effects because it is in this regime that optical fibers support solitons through a balance between the dispersive and nonlinear effects.

An important feature of chromatic dispersion is that pulses at different wavelengths propagate at different speeds inside a fiber because of a mismatch in their group velocities. This feature leads to a walk-off effect that plays an important role in the description of the nonlinear phenomena involving two or more closely spaced optical pulses. More specifically, the nonlinear interaction between two optical pulses ceases to occur when the faster moving pulse completely walks through the slower moving pulse. This feature is governed by the *walk-off parameter*  $d_{12}$  defined as

$$d_{12} = \beta_1(\lambda_1) - \beta_1(\lambda_2) = v_g^{-1}(\lambda_1) - v_g^{-1}(\lambda_2), \quad (1.2.12)$$

where  $\lambda_1$  and  $\lambda_2$  are the center wavelengths of two pulses and  $\beta_1$  at these wavelengths is evaluated using Eq. (1.2.9). For pulses of width  $T_0$ , one can define the walk-off length  $L_W$  by the relation

$$L_W = T_0 / |d_{12}|. \quad (1.2.13)$$

Figure 1.5 shows variation of  $d_{12}$  with  $\lambda_1$  for fused silica using Eq. (1.2.12) with  $\lambda_2 = 0.8 \mu\text{m}$ . In the normal-dispersion regime ( $\beta_2 > 0$ ), a longer-wavelength pulse travels faster, while the opposite occurs in the anomalous-dispersion region. For example, if a pulse at  $\lambda_1 = 1.3 \mu\text{m}$  copropagates with the pulse at  $\lambda_2 = 0.8 \mu\text{m}$ , it will separate from the shorter-wavelength pulse at a rate of about 20 ps/m. This corresponds to a walk-off length  $L_W$  of only 50 cm for  $T_0 = 10 \text{ ps}$ . The group-velocity mismatch plays an important role for nonlinear effects involving cross-phase modulation [47].

## 1.2.4 Polarization-Mode Dispersion

As discussed in Chapter 2, even a single-mode fiber is not truly single mode because it can support two degenerate modes that are polarized in two orthogonal directions. Under ideal conditions (perfect cylindrical symmetry and a stress-free fiber), a mode excited with its polarization in the  $x$ -direction would not couple to the mode with the orthogonal  $y$ -polarization state. In real fibers, small departures from cylindrical symmetry, occurring because of random variations in the core shape along

the fiber length, result in a mixing of the two polarization states by breaking the mode degeneracy. The stress-induced anisotropy can also break this degeneracy. Mathematically, the mode-propagation constant  $\beta$  becomes slightly different for the modes polarized in the  $x$ - and  $y$ -directions. This property is referred to as modal birefringence. The strength of modal birefringence is defined by a dimensionless parameter [79]

$$B_m = \frac{|\beta_x - \beta_y|}{k_0} = |n_x - n_y|, \quad (1.2.14)$$

where  $n_x$  and  $n_y$  are the modal refractive indices for the two orthogonally polarized states. For a given value of  $B_m$ , the two modes exchange their powers in a periodic fashion as they propagate inside the fiber with the period [79]

$$L_B = \frac{2\pi}{|\beta_x - \beta_y|} = \frac{\lambda}{B_m}. \quad (1.2.15)$$

The length  $L_B$  is called the *beat length*. The axis along which the mode index is smaller is called the *fast axis* because the group velocity is larger for light propagating in that direction. For the same reason, the axis with the larger mode index is called the *slow axis*.

In standard optical fibers,  $B_m$  is not constant along the fiber but changes randomly because of fluctuations in the core shape and anisotropic stress. As a result, light launched into the fiber with a fixed state of polarization changes its polarization in a random fashion. This change in polarization is typically harmless for continuous-wave (CW) light because most photodetectors do not respond to polarization changes of the incident light. It becomes an issue for optical communication systems when short pulses are transmitted over long lengths [16]. If an input pulse excites both polarization components, the two components travel along the fiber at different speeds because of their different group velocities. The pulse becomes broader at the output end because group velocities change randomly in response to random changes in fiber birefringence (analogous to a random-walk problem). This phenomenon, referred to as *polarization-mode dispersion* (PMD), has been studied extensively because of its importance for long-haul lightwave systems [80–82].

The extent of pulse broadening can be estimated from the time delay  $\Delta T$  occurring between the two polarization components during the propagation of an optical pulse. For a fiber of length  $L$  and constant birefringence  $B_m$ ,  $\Delta T$  is given by

$$\Delta T = \left| \frac{L}{v_{gx}} - \frac{L}{v_{gy}} \right| = L |\beta_{1x} - \beta_{1y}| = L (\Delta \beta_1), \quad (1.2.16)$$

where  $\Delta \beta_1$  is related to group-velocity mismatch. Eq. (1.2.16) cannot be used directly to estimate PMD for standard telecommunication fibers because of random changes in birefringence occurring along the fiber. These changes tend to equalize the propagation times for the two polarization components. In fact, PMD is characterized by

the root-mean-square (RMS) value of  $\Delta T$  obtained after averaging over random perturbations. The variance of  $\Delta T$  is found to be [81]

$$\sigma_T^2 = \langle (\Delta T)^2 \rangle = 2(\Delta\beta_1 l_c)^2 [\exp(-L/l_c) + L/l_c - 1], \quad (1.2.17)$$

where  $\Delta\beta_1 \equiv \Delta\tau/L$ ,  $\Delta\tau$  represents the differential group delay along the principal states of polarization [80], and the correlation length  $l_c$  is defined as the length over which two polarization components remain correlated; typical values of  $l_c$  are of the order of 10 m. For  $L > 0.1$  km, we can use  $l_c \ll L$  to find that

$$\sigma_T \approx \Delta\beta_1 \sqrt{2l_c L} \equiv D_p \sqrt{L}, \quad (1.2.18)$$

where  $D_p$  is the PMD parameter. For most fibers, values of  $D_p$  are in the range of 0.1–1 ps/ $\sqrt{\text{km}}$ . Because of its  $\sqrt{L}$  dependence, PMD-induced pulse broadening is relatively small compared with the GVD effects. However, PMD becomes a limiting factor for high-speed communication systems designed to operate over long distances near the zero-dispersion wavelength of the fiber [16].

For some applications it is desirable that fibers transmit light without changing their state of polarization. Such fibers are called *polarization-maintaining* or polarization-preserving fibers [83–88]. A large amount of birefringence is introduced intentionally in these fibers through design modifications so that relatively small birefringence fluctuations are masked by it and do not affect the state of polarization significantly. One scheme breaks the cylindrical symmetry by making the fiber core elliptical in shape [88]. The degree of birefringence achieved by this technique is typically  $\sim 10^{-6}$ . An alternative scheme makes use of stress-induced birefringence and permits  $B_m \sim 10^{-4}$ . In a widely adopted design, two rods of borosilicate glass are inserted on the opposite sides of the fiber core at the preform stage. The resulting birefringence depends on the location and the thickness of the stress-inducing elements. Figure 1.8 shows how  $B_m$  varies  $d$  for four shapes of stress-inducing elements located at a distance of five times the core radius [85]. Values of  $B_m \approx 2 \times 10^{-4}$  can be realized for  $d$  in the range of 50–60  $\mu\text{m}$ . Such fibers are often named after the shape of the stress-inducing element, resulting in whimsical names such as “panda” and “bow-tie” fibers.

The use of polarization-maintaining fibers requires identification of the slow and fast axes before an optical signal can be launched into the fiber. Structural changes are often made to the fiber for this purpose. In one scheme, cladding is flattened in such a way that the flat surface is parallel to the slow axis of the fiber. Such a fiber is called the “D fiber” after the shape of the cladding [88] and makes axes identification relatively easy. When the polarization direction of the linearly polarized light coincides with the slow or the fast axis, the state of polarization remains unchanged during propagation. In contrast, if the polarization direction makes an angle with these axes, polarization changes continuously along the fiber in a periodic manner with a period equal to the beat length [see Eq. (1.2.15)]. Figure 1.9 shows schematically the evolution of polarization over one beat length of a birefringent fiber. The state of polarization changes over one-half of the beat length from linear to elliptic,

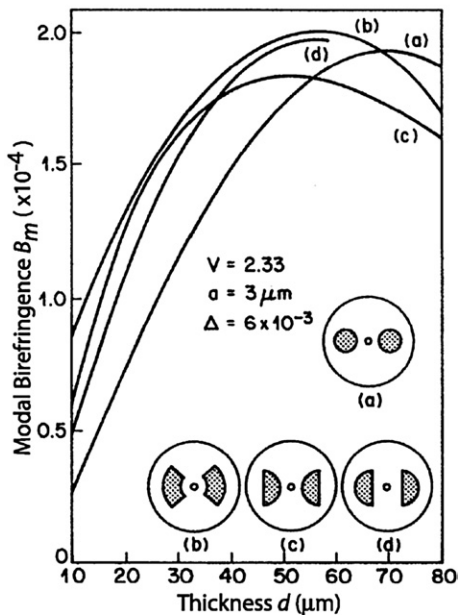


Figure 1.8 Variation of birefringence parameter  $B_m$  with thickness  $d$  of the stress-inducing element for four different polarization-maintaining fibers. Different shapes of the stress-applying elements (shaded region) are shown in the inset. (After Ref. [85]; © 1986 IEEE.)

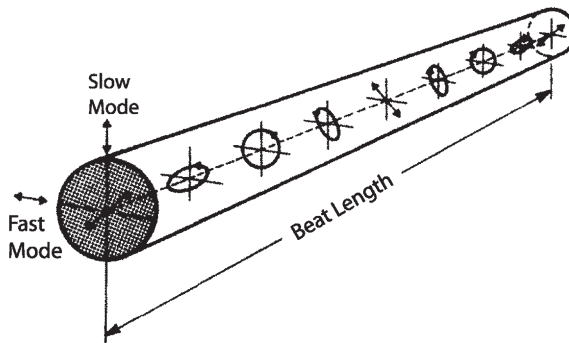


Figure 1.9 Evolution of the state of polarization along a polarization-maintaining fiber when the input signal is linearly polarized at  $45^\circ$  from the slow axis.

to circular, circular to elliptic, and then back to linear but is rotated by  $90^\circ$  from the incident linear polarization. The process is repeated over the remaining half of the beat length such that the initial state is recovered at  $z = L_B$  and its multiples. The beat length is typically  $\sim 1 \text{ m}$  but can be as small as  $1 \text{ cm}$  for a strongly birefringent fiber with  $B_m \sim 10^{-4}$ .

---

## 1.3 FIBER NONLINEARITIES

The response of any dielectric to light becomes nonlinear for intense electromagnetic fields, and optical fibers are no exception. On a fundamental level, the origin of nonlinear response is related to the anharmonic motion of bound electrons under the influence of an applied field. As a result, the total polarization  $\mathbf{P}$  induced by electric dipoles is not linear in the electric field  $\mathbf{E}$ , but satisfies the more general relation [89–92]

$$\mathbf{P} = \epsilon_0 \left( \chi^{(1)} \cdot \mathbf{E} + \chi^{(2)} : \mathbf{EE} + \chi^{(3)} : \mathbf{EEE} + \dots \right), \quad (1.3.1)$$

where  $\epsilon_0$  is the vacuum permittivity and  $\chi^{(j)}$  is  $j$ th order susceptibility. In general,  $\chi^{(j)}$  is a tensor of rank  $j + 1$ . The linear susceptibility  $\chi^{(1)}$  represents the dominant contribution to  $\mathbf{P}$ . Its effects are included through the refractive index  $n$  and the attenuation coefficient  $\alpha$  discussed in Section 1.2. The second-order susceptibility  $\chi^{(2)}$  is responsible for such nonlinear effects as second-harmonic generation and sum-frequency generation [90]. However, it is nonzero only for media that lack an inversion symmetry at the molecular level. As  $\text{SiO}_2$  is a symmetric molecule,  $\chi^{(2)}$  vanishes for silica glasses. As a result, optical fibers do not normally exhibit second-order nonlinear effects. Nonetheless, the electric-quadrupole and magnetic-dipole moments can generate weak second-order nonlinear effects. Defects or color centers inside the fiber core can also contribute to second-harmonic generation under certain conditions.

### 1.3.1 Nonlinear Refraction

The lowest-order nonlinear effects in optical fibers originate from the third-order susceptibility  $\chi^{(3)}$ , which is responsible for phenomena such as third-harmonic generation, four-wave mixing, and nonlinear refraction [90]. Unless special efforts are made to achieve phase matching, the nonlinear processes that involve the generation of new frequencies (e.g., third-harmonic generation and four-wave mixing) are not efficient in optical fibers. Most of the nonlinear effects in optical fibers therefore originate from nonlinear refraction, a phenomenon referring to the intensity dependence of the refractive index. In its simplest form, the refractive index can be written as

$$\tilde{n}(\omega, I) = n(\omega) + n_2 I = n + \bar{n}_2 |E|^2, \quad (1.3.2)$$

where  $n(\omega)$  is the linear part given by Eq. (1.2.6),  $I$  is the optical intensity associated with the electromagnetic field  $E$ , and  $\bar{n}_2$  is the *nonlinear-index coefficient* related to  $\chi^{(3)}$  by the relation (see Section 2.3.1 for its derivation)

$$\bar{n}_2 = \frac{3}{8n} \text{Re}(\chi_{xxxx}^{(3)}), \quad (1.3.3)$$

where  $\text{Re}$  stands for the real part and the optical field  $E$  is assumed to be linearly polarized so that only one component  $\chi_{xxxx}^{(3)}$  of the fourth-rank tensor contributes to

the refractive index. The tensorial nature of  $\chi^{(3)}$  can affect the polarization properties of optical beams through nonlinear birefringence. Such nonlinear effects are covered in Chapter 6.

The intensity dependence of the refractive index leads to a large number of interesting nonlinear effects; the two most widely studied are known as *self-phase modulation* (SPM) and *cross-phase modulation* (XPM). SPM refers to the self-induced phase shift experienced by an optical field during its propagation in optical fibers. Its magnitude can be obtained by noting that the phase of an optical field changes by

$$\phi = \tilde{n}k_0L = (n + \tilde{n}_2|E|^2)k_0L, \quad (1.3.4)$$

where  $k_0 = 2\pi/\lambda$  and  $L$  is the fiber length. The intensity-dependent nonlinear phase shift,  $\phi_{NL} = \tilde{n}_2k_0L|E|^2$ , is due to SPM. Among other things, SPM is responsible for spectral broadening of ultrashort pulses [26] and the formation of optical solitons in the anomalous-dispersion regime of fibers [27].

XPM refers to the nonlinear phase shift of an optical field induced by another field having a different wavelength, direction, or state of polarization. Its origin can be understood by noting that the total electric field  $\mathbf{E}$  in Eq. (1.3.1) is given by

$$\mathbf{E} = \frac{1}{2}\hat{x}[E_1 \exp(-i\omega_1 t) + E_2 \exp(-i\omega_2 t) + \text{c.c.}], \quad (1.3.5)$$

when two optical fields at frequencies  $\omega_1$  and  $\omega_2$ , polarized along the  $x$ -axis, propagate simultaneously inside the fiber. (The abbreviation c.c. stands for complex conjugate.) The nonlinear phase shift for the field at  $\omega_1$  is then given by

$$\phi_{NL} = \tilde{n}_2k_0L(|E_1|^2 + 2|E_2|^2), \quad (1.3.6)$$

where we have neglected all terms that generate polarization at frequencies other than  $\omega_1$  and  $\omega_2$  because of their non-phase-matched character. The two terms on the right-hand side of Eq. (1.3.6) are due to SPM and XPM, respectively. An important feature of XPM is that, for equally intense optical fields of different wavelengths, the contribution of XPM to the nonlinear phase shift is twice that of SPM. Among other things, XPM is responsible for asymmetric spectral broadening of copropagating optical pulses. Chapters 6 and 7 discuss the XPM-related nonlinear effects.

### 1.3.2 Stimulated Inelastic Scattering

The nonlinear effects governed by the third-order susceptibility  $\chi^{(3)}$  are elastic in the sense that no energy is exchanged between the electromagnetic field and the dielectric medium. A second class of nonlinear effects results from stimulated inelastic scattering in which the optical field transfers part of its energy to the nonlinear medium. Two important nonlinear effects in optical fibers fall in this category; both of them are related to vibrational excitation modes of silica. These phenomena, known as *stimulated Raman scattering* (SRS) and *stimulated Brillouin scattering* (SBS), were among the first nonlinear effects studied in optical fibers [19–21]. The

main difference between the two is that optical phonons participate in SRS while acoustic phonons participate in SBS.

In a simple quantum-mechanical picture applicable to both SRS and SBS, a photon of the incident field (called the pump) is annihilated to create a photon at a lower frequency (belonging to the Stokes wave) and a phonon with the right energy and momentum, to conserve the energy and the momentum. Of course, a higher-energy photon at the so-called anti-Stokes frequency can also be created if a phonon of right energy and momentum is available. Even though SRS and SBS are very similar in their origin, different dispersion relations for acoustic and optical phonons lead to some basic differences between the two. A fundamental difference is that SBS in single-mode fibers occurs only in the backward direction whereas SRS can occur in both directions.

Although a complete description of SRS and SBS in optical fibers is quite involved, the initial growth of the Stokes wave can be described by a simple relation. For SRS, this relation is given by

$$\frac{dI_s}{dz} = g_R I_p I_s, \quad (1.3.7)$$

where  $I_s$  is the Stokes intensity,  $I_p$  is the pump intensity, and  $g_R$  is the Raman-gain coefficient. A similar relation holds for SBS with  $g_R$  replaced by the Brillouin-gain coefficient  $g_B$ . Both  $g_R$  and  $g_B$  have been measured experimentally for silica fibers. The Raman-gain spectrum is found to be very broad, extending up to 40 THz [19]. The peak gain  $g_R \approx 6 \times 10^{-14}$  m/W at pump wavelengths is near 1.5 μm and occurs for a spectral shift of about 13.1 THz. In contrast, the Brillouin-gain spectrum is extremely narrow and has a bandwidth of <100 MHz. The peak value of Brillouin gain occurs, for the Stokes shift of ~10 GHz, for pump wavelengths near 1.5 μm. The peak gain is  $\approx 6 \times 10^{-11}$  m/W for a narrow-bandwidth pump [20] and decreases by a factor of  $\Delta\nu_p/\Delta\nu_B$  for a broad-bandwidth pump, where  $\Delta\nu_p$  is the pump bandwidth and  $\Delta\nu_B$  is the Brillouin-gain bandwidth.

An important feature of SRS and SBS is that they exhibit a threshold-like behavior, i.e., significant conversion of pump energy to Stokes energy occurs only when the pump intensity exceeds a certain threshold level. For SRS in a single-mode fiber with  $\alpha L \gg 1$ , the threshold pump intensity is given by [21]

$$I_p^{\text{th}} \approx 16(\alpha/g_R). \quad (1.3.8)$$

Typically  $I_p^{\text{th}} \sim 10$  MW/cm<sup>2</sup>, and SRS can be observed at a pump power ~1 W. A similar calculation for SBS shows that the threshold pump intensity is given by [21]

$$I_p^{\text{th}} \approx 21(\alpha/g_B). \quad (1.3.9)$$

As the Brillouin-gain coefficient  $g_B$  is larger by nearly three orders of magnitude compared with  $g_R$ , typical values of SBS threshold are ~1 mW. The nonlinear phenomena of SRS and SBS are discussed in Chapters 8 and 9, respectively.

### 1.3.3 Importance of Nonlinear Effects

Most measurements of the nonlinear-index coefficient  $n_2$  in silica fibers yield a value in the range  $2.2 - 3.4 \times 10^{-20} \text{ m}^2/\text{W}$  (see Chapter 11), depending on the core composition and whether the input polarization is preserved inside the fiber or not [93]. This value is small compared to most other nonlinear media by at least two orders of magnitude. Similarly, the measurements of Raman- and Brillouin-gain coefficients in silica fibers show that their values are smaller by two orders of magnitude or more compared with other common nonlinear media [47]. In spite of the intrinsically small values of the nonlinear coefficients in fused silica, the nonlinear effects in optical fibers can be observed at relatively low power levels. This is possible because of two important characteristics of single-mode fibers—a small spot size (mode diameter  $< 10 \mu\text{m}$ ) and extremely low loss ( $< 1 \text{ dB/km}$ ) in the wavelength range of  $1.0 - 1.6 \mu\text{m}$ .

A figure of merit for the efficiency of a nonlinear process in bulk media is the product  $I_0 L_{\text{eff}}$  where  $I_0$  is the optical intensity and  $L_{\text{eff}}$  is the effective length of the region where such a high intensity can be maintained [94]. If light is focused to a spot of radius  $w_0$ , then  $I_0 = P_0 / (\pi w_0^2)$ , where  $P_0$  is the incident optical power. Clearly,  $I_0$  can be increased by focusing the light tightly to reduce  $w_0$ . However, this results in a smaller  $L_{\text{eff}}$  because the length of the focal region decreases with tight focusing. For a Gaussian beam,  $L_{\text{eff}} \sim \pi w_0^2 / \lambda$ , and the product

$$(I_0 L_{\text{eff}})_{\text{bulk}} = \left( \frac{P_0}{\pi w_0^2} \right) \frac{\pi w_0^2}{\lambda} = \frac{P_0}{\lambda} \quad (1.3.10)$$

is independent of the spot size  $w_0$ .

In single-mode fibers, spot size  $w_0$  is determined by the core radius  $a$ . Furthermore, because of dielectric waveguiding, the same spot size can be maintained across the entire fiber length  $L$ . In this case, the interaction length  $L_{\text{eff}}$  is limited by the fiber loss  $\alpha$ . Using  $I(z) = I_0 \exp(-\alpha z)$ , where  $I_0 = P_0 / (\pi w_0^2)$  and  $P_0$  is the optical power coupled into the fiber, the product  $I_0 L_{\text{eff}}$  becomes

$$(I_0 L_{\text{eff}})_{\text{fiber}} = \int_0^L I_0 \exp(-\alpha z) dz = \frac{P_0}{\pi w_0^2 \alpha} [1 - \exp(-\alpha L)]. \quad (1.3.11)$$

A comparison of Eqs (1.3.10) and (1.3.11) shows that, for sufficiently long fibers, the efficiency of a nonlinear process in optical fibers can be improved by a factor [94]

$$\frac{(I_0 L_{\text{eff}})_{\text{fiber}}}{(I_0 L_{\text{eff}})_{\text{bulk}}} = \frac{\lambda}{\pi w_0^2 \alpha}, \quad (1.3.12)$$

where  $\alpha L \gg 1$  was assumed. In the visible region, the enhancement factor is  $\sim 10^7$  for  $\lambda = 0.53 \mu\text{m}$ ,  $w_0 = 2 \mu\text{m}$ , and  $\alpha = 2.5 \times 10^{-5} \text{ cm}^{-1}$  ( $10 \text{ dB/km}$ ). In the wavelength region near  $1.55 \mu\text{m}$  ( $\alpha = 0.2 \text{ dB/km}$ ), the enhancement factor can approach  $10^9$ . It is this tremendous enhancement in the efficiency of the nonlinear processes

that makes silica fibers a suitable nonlinear medium for the observation of a wide variety of nonlinear effects at relatively low power levels. The weak nonlinearity of silica fibers becomes an issue for applications in which it is desirable to use a short fiber length ( $<0.1$  km). This problem is solved in the so-called *highly nonlinear fibers* by reducing the core diameter so that  $w_0$  is reduced [95]. It is also possible to use nonlinear materials for which  $n_2$  is larger than silica. Optical fibers made with lead silicate glasses have  $n_2$  values larger by about a factor of 10 [96]. Even larger values ( $n_2 = 4.2 \times 10^{-18} \text{ m}^2/\text{W}$ ) have been measured in chalcogenide and other nonsilica fibers [97]. Such fibers are attracting attention and may become important for nonlinear fiber optics [98–102].

## 1.4 OVERVIEW

This book is intended to provide a comprehensive account of the nonlinear phenomena in optical fibers. Broadly speaking, Chapters 1–3 provide the background material and the mathematical tools needed for understanding the various nonlinear effects. Chapters 4–7 discuss the nonlinear effects that lead to spectral and temporal changes in an optical wave without changing its energy. Chapters 8–13 consider the nonlinear effects that generate new optical waves through an energy transfer from the incident waves. To keep the book size manageable, applications of nonlinear fiber optics are covered in a separate volume [103].

Chapter 2 provides the mathematical framework needed for a theoretical understanding of the nonlinear phenomena in optical fibers. Starting from Maxwell's equations, the wave equation in a nonlinear dispersive medium is used to discuss the fiber modes and to obtain a basic propagation equation satisfied by the amplitude of the pulse envelope. The procedure emphasizes the various approximations made in the derivation of this equation. The numerical methods used to solve the basic propagation equation are then discussed with emphasis on the split-step Fourier method, also known as the beam-propagation method.

Chapter 3 focuses on the dispersive effects that occur when the incident power and the fiber length are such that the nonlinear effects are negligible. The main effect of GVD is to broaden an optical pulse as it propagates through the fiber. Such dispersion-induced broadening is considered for several pulse shapes with particular attention paid to the effects of the frequency chirp imposed on the input pulse. The higher-order dispersive effects, important near the zero-dispersion wavelength of fibers, are also discussed.

Chapter 4 considers the nonlinear phenomenon of SPM occurring as a result of the intensity dependence of the refractive index. The main effect of SPM is to broaden the spectrum of optical pulses propagating through the fiber. The pulse shape is also affected if SPM and GVD act together to influence the optical pulse. The features of SPM-induced spectral broadening with and without the GVD effects are discussed in separate sections. The higher-order nonlinear and dispersive effects are also considered in this chapter.

Chapter 5 is devoted to the study of optical solitons, a topic that has drawn considerable attention because of its fundamental nature as well as potential applications for optical fiber communications. The modulation instability is considered first to emphasize the importance of the interplay between the dispersive and nonlinear effects that can occur in the anomalous-GVD regime of optical fibers. The fundamental and higher-order solitons are then introduced together with the inverse scattering method used to solve the nonlinear Schrödinger equation. Dark solitons are also discussed briefly. The last section considers higher-order nonlinear and dispersive effects with emphasis on the soliton decay.

Chapters 6 and 7 focus on the XPM effects occurring when two optical fields copropagate simultaneously and affect each other through the intensity dependence of the refractive index. The XPM-induced nonlinear coupling can occur not only when two beams of different wavelengths are incident on the fiber but also through the interaction between the orthogonally polarized components of a single beam in a birefringent fiber. The latter case is discussed first in Chapter 6 by considering the nonlinear phenomena such as the optical Kerr effect and birefringence-induced pulse shaping. Chapter 7 then focuses on the case in which two optical beams at different wavelengths are launched into the fiber. The XPM-induced coupling between the two beams can lead to modulation instability even in the normal-dispersion regime of the fiber. It can also lead to asymmetric spectral and temporal changes when the XPM effects are considered in combination with the SPM and GVD effects. The XPM-induced coupling between the counterpropagating waves is considered next with emphasis on its importance for fiber-optic gyroscopes.

Chapter 8 considers SRS, a nonlinear phenomenon in which the energy from a pump wave is transferred to a Stokes wave (downshifted by about 13 THz) as the pump wave propagates through the optical fiber. This happens only when the pump power exceeds a threshold level. The Raman gain and the Raman threshold in silica fibers are discussed first. Two separate sections then describe SRS for the case of a CW or quasi-CW pump and for the case of ultrashort pump pulses. In the latter case a combination of SPM, XPM, and GVD leads to new qualitative features. These features can be quite different depending on whether the pump and Raman pulses experience normal or anomalous GVD. The case of anomalous GVD is considered in Section 8.4 with emphasis on fiber-Raman soliton lasers. The last section focuses on the polarization effects that may occur during Raman amplification inside an optical fiber.

Chapter 9 is devoted to SBS, a nonlinear phenomenon that manifests in optical fibers in a way similar to SRS, but with important differences. Stimulated Brillouin scattering transfers a part of the pump energy to a counterpropagating Stokes wave, downshifted in frequency by only an amount  $\sim 10$  GHz. Because of the small bandwidth ( $\sim 10$  MHz) associated with the Brillouin gain, SBS occurs efficiently only for a CW pump or pump pulses whose spectral width is smaller than the gain bandwidth. The characteristics of the Brillouin gain in silica fibers are discussed first. Chapter 9 then describes the theory of SBS by considering important features such as the

Brillouin threshold, pump depletion, and gain saturation. The experimental results on SBS are described with emphasis on fiber-based Brillouin amplifiers. Section 9.4 focuses on the dynamic aspects that become important for nanosecond pulses. The last section is devoted to Brillouin fiber lasers.

Chapter 10 focuses on the phenomenon of four-wave mixing (FWM) in which four optical waves interact nonlinearly inside an optical fiber. This process can only occur efficiently when a phase-matching condition is satisfied. The parametric gain associated with the FWM process is obtained first. The phase-matching techniques used for realizing FWM are then discussed in detail. Parametric amplification is considered next. A separate section is devoted to the polarization effects because of their importance. The last section is devoted to FWM applications.

Chapter 11 is devoted to highly nonlinear fibers developed in recent years. Various techniques used to measure the nonlinear parameter are described first in Section 11.1. The next four section then focus on four types of highly nonlinear fibers and their properties with particular emphasis on the photonic crystal and other microstructured fibers. The last section provides details on a vectorial treatment of optical pulses that becomes necessary for such narrow-core fibers.

The focus of Chapters 12 and 13 is on the novel nonlinear effects that have become possible with the advent of highly nonlinear fibers. Chapter 12 describes the phenomena such as: soliton fission, dispersive-wave generation, and intrapulse Raman scattering that shifts the pulse spectrum toward longer wavelengths. It also describes a new type of FWM phase-matched through fourth-order dispersion. Chapter 13 is entirely devoted to the phenomenon of supercontinuum generation that attracted considerable attention after the year 2000 and continues to do so because of its applications in diverse fields such as biomedical imaging and metrology.

---

## PROBLEMS

- 1.1 Calculate the propagation distance over which the injected optical power is reduced by a factor of two for three fibers with losses of 0.2, 20, and 2000 dB/km. Also calculate the attenuation constant  $\alpha$  ( $\text{cm}^{-1}$ ) for the three fibers.
- 1.2 A single-mode fiber is measured to have  $\lambda^2(d^2n/d\lambda^2) = 0.02$  at  $0.8 \mu\text{m}$ . Calculate the dispersion parameters  $\beta_2$  and  $D$ .
- 1.3 Calculate the numerical values of  $\beta_2$  ( $\text{ps}^2/\text{km}$ ) and  $D$  [ $\text{ps}/(\text{km}\cdot\text{nm})$ ] at  $1.5 \mu\text{m}$  when the modal index varies with wavelength as  $n(\lambda) = 1.45 - s(\lambda - 1.3 \mu\text{m})^3$ , where  $s = 0.003 \mu\text{m}^{-3}$ .
- 1.4 For silica fiber doped with 7.9% of germania, parameters appearing in the Sellmeier equation have the following values [67]:  $B_1 = 0.7136824$ ,  $B_2 = 0.4254807$ ,  $B_3 = 0.8964226$ ,  $\lambda_1 = 0.0617167 \mu\text{m}$ ,  $\lambda_2 = 0.1270814 \mu\text{m}$ , and  $\lambda_3 = 0.896161 \mu\text{m}$ . Plot  $n$ ,  $n_g$ , and  $\beta_2$  in the wavelength range of 0.5–1.6  $\mu\text{m}$  and comment on changes from values shown in Figures 1.4 and 1.5.
- 1.5 Using the parameter values given in the preceding problem, calculate the values of third- and fourth-order dispersion parameters ( $\beta_3$  and  $\beta_4$ ) at the

zero-dispersion wavelength  $\lambda_D$  of the fiber. Calculate  $\beta_2$  and  $D$  when the input wavelength exceeds  $\lambda_D$  by 10 nm.

- 1.6 A 1-km-long single-mode fiber with the zero-dispersion wavelength at  $1.4 \mu\text{m}$  is measured to have  $D = 10 \text{ ps}/(\text{km}\cdot\text{nm})$  at  $1.5 \mu\text{m}$ . Two pulses from Nd:YAG lasers operating at 1.06 and  $1.32 \mu\text{m}$  are launched simultaneously into the fiber. Calculate the delay in the arrival time of the two pulses at the fiber output assuming that  $\beta_2$  varies linearly with wavelength over the range  $1.0\text{--}1.6 \mu\text{m}$ .
- 1.7 Define the dispersion parameters  $D$  and  $\beta_2$  and derive a relation between the two. Prove that  $D = -(\lambda/c)(d^2n/d\lambda^2)$ .
- 1.8 Explain the concepts of birefringence and beat length. Why does an optical fiber exhibit some residual birefringence that varies randomly along its length?
- 1.9 What is meant by polarization-mode dispersion in the context of optical fibers? What happens to optical pulses when a fiber exhibits randomly varying birefringence along its length?
- 1.10 Sketch a design for a polarization-maintaining fiber. Under what conditions do such fibers maintain polarization? What happens to the state of polarization when input light is polarized linearly at an angle of  $10^\circ$  from the slow axis of the fiber?
- 1.11 What is the relationship between  $n_2$  and  $\bar{n}_2$  in Eq. (1.3.2)? Use it to obtain the value of  $\bar{n}_2$  in units of  $\text{m}^2/\text{V}^2$  if  $n_2 = 2.6 \times 10^{-20} \text{ m}^2/\text{W}$ .

## REFERENCES

- [1] J. Hecht, *City of Light* (Oxford University Press, 1999).
- [2] J.L. Baird, British Patent 285,738 (1928).
- [3] C.W. Hansell, US Patent 1,751,584 (1930).
- [4] H. Lamm, *Z. Instrumenten.* **50**, 579 (1930).
- [5] A. C. S. van Heel, *Nature* **173**, 39 (1954).
- [6] H. H. Hopkins and N. S. Kapany, *Nature* **173**, 39 (1954); *Opt. Acta* **1**, 164 (1955).
- [7] B. O'Brian, US Patent 2,825,260 (1958).
- [8] B.I. Hirschowitz, US Patent 3,010,357 (1961).
- [9] N. S. Kapany, *Fiber Optics: Principles and Applications* (Academic Press, 1967).
- [10] K. C. Kao and G. A. Hockham, *IEE Proc.* **113**, 1151 (1966).
- [11] F. P. Kapron, D. B. Keck, and R. D. Maurer, *Appl. Phys. Lett.* **17**, 423 (1970).
- [12] W. G. French, J. B. MacChesney, P. B. O'Connor, and G. W. Tasker, *Bell Syst. Tech. J.* **53**, 951 (1974).
- [13] T. Miya, Y. Terunuma, T. Hosaka, and T. Miyashita, *Electron. Lett.* **15**, 106 (1979).
- [14] R. Ramaswami, K. Sivarajan, and G. Sasaki, *Optical Networks: A Practical Perspective*, 3rd ed. (Morgan Kaufman, 2009).
- [15] G. E. Keiser, *Optical Fiber Communications*, 4th ed. (McGraw-Hill, 2010).
- [16] G. P. Agrawal, *Fiber-Optic Communication Systems*, 4th ed. (Wiley, 2010).
- [17] R. H. Stolen, *J. Lightwave Technol.* **26**, 1021 (2008).
- [18] G. P. Agrawal, *J. Opt. Soc. Am. B* **28**, A1 (2011).

- [19] R. H. Stolen, E. P. Ippen, and A. R. Tynes, *Appl. Phys. Lett.* **20**, 62 (1972).
- [20] E. P. Ippen and R. H. Stolen, *Appl. Phys. Lett.* **21**, 539 (1972).
- [21] R. G. Smith, *Appl. Opt.* **11**, 2489 (1972).
- [22] R. H. Stolen and A. Ashkin, *Appl. Phys. Lett.* **22**, 294 (1973).
- [23] R. H. Stolen, J. E. Bjorkholm, and A. Ashkin, *Appl. Phys. Lett.* **24**, 308 (1974).
- [24] K. O. Hill, D. C. Johnson, B. S. Kawaski, and R. I. MacDonald, *J. Appl. Phys.* **49**, 5098 (1974).
- [25] R. H. Stolen, *IEEE J. Quantum Electron.* **11**, 100 (1975).
- [26] R. H. Stolen and C. Lin, *Phys. Rev. A* **17**, 1448 (1978).
- [27] A. Hasegawa and F. Tappert, *Appl. Phys. Lett.* **23**, 142 (1973).
- [28] L. F. Mollenauer, R. H. Stolen, and J. P. Gordon, *Phys. Rev. Lett.* **45**, 1095 (1980).
- [29] L. F. Mollenauer and R. H. Stolen, *Opt. Lett.* **9**, 13 (1984).
- [30] L. F. Mollenauer, J. P. Gordon, and M. N. Islam, *IEEE J. Quantum Electron.* **22**, 157 (1986).
- [31] J. D. Kafka and T. Baer, *Opt. Lett.* **12**, 181 (1987).
- [32] M. N. Islam, L. F. Mollenauer, R. H. Stolen, J. R. Simpson, and H. T. Shang, *Opt. Lett.* **12**, 814 (1987).
- [33] A. S. Gouveia-Neto, A. S. L. Gomes, and J. R. Taylor, *Opt. Quantum Electron.* **20**, 165 (1988).
- [34] H. Nakatsuka, D. Grischkowsky, and A. C. Balant, *Phys. Rev. Lett.* **47**, 910 (1981).
- [35] C. V. Shank, R. L. Fork, R. Yen, R. H. Stolen, and W. J. Tomlinson, *Appl. Phys. Lett.* **40**, 761 (1982).
- [36] (a) B. Nikolaus and D. Grischkowsky, *Appl. Phys. Lett.* **42**, 1 (1983); (b) *Appl. Phys. Lett.* **43**, 228 (1983).
- [37] A. S. L. Gomes, A. S. Gouveia-Neto, and J. R. Taylor, *Opt. Quantum Electron.* **20**, 95 (1988).
- [38] N. J. Doran and D. Wood, *Opt. Lett.* **13**, 56 (1988).
- [39] M. C. Farries and D. N. Payne, *Appl. Phys. Lett.* **55**, 25 (1989).
- [40] K. J. Blow, N. J. Doran, and B. K. Nayar, *Opt. Lett.* **14**, 754 (1989).
- [41] M. N. Islam, E. R. Sunderman, R. H. Stolen, W. Pleibel, and J. R. Simpson, *Opt. Lett.* **14**, 811 (1989).
- [42] R. L. Fork, C. H. Brito Cruz, P. C. Becker, and C. V. Shank, *Opt. Lett.* **12**, 483 (1987).
- [43] H. G. Winful, in *Optical-Fiber Transmission*, E. E. Basch, Ed. (SAMS Publishing, 1986).
- [44] S. A. Akhmanov, V. A. Vysloukh, and A. S. Chirkin, *Sov. Phys. Usp.* **29**, 642 (1986).
- [45] K. J. Blow and N. J. Doran, *IEE Proc.* **134** (Pt. J), 138 (1987).
- [46] E. M. Dianov, P. V. Mamyshev, and A. M. Prokhorov, *Sov. J. Quantum Electron.* **15**, 1 (1988).
- [47] R. R. Alfano, Ed., *The Supercontinuum Laser Source* (Springer, 1989).
- [48] E. Desurvire, D. Bayart, B. Desthieux, and S. Bigo, *Erbiump-Doped Fiber Amplifiers: Device and System Development* (Wiley, 2002).
- [49] C. Headley and G. P. Agrawal, Eds., *Raman Amplification in Fiber Optical Communication Systems* (Academic Press, 2005).
- [50] M. E. Marhic, *Fiber Optical Parametric Amplifiers, Oscillators and Related Devices* (Cambridge University Press, 2007).
- [51] A. Hasegawa and M. Matsumoto, *Optical Solitons in Fibers* (Springer, 2002).
- [52] Y. S. Kivshar and G. P. Agrawal, *Optical Solitons: From Fibers to Photonic Crystals* (Academic Press, 2003).

- [53] N. Akhmediev and A. Ankiewicz, Eds., *Dissipative Solitons* (Springer, 2005).
- [54] L. F. Mollenauer and J. P. Gordon, *Solitons in Optical Fibers: Fundamental and Applications* (Academic Press, 2006).
- [55] K. O. Hill, Y. Fujii, D. C. Johnson, and B. S. Kawasaki, *Appl. Phys. Lett.* **32**, 647 (1978).
- [56] R. Kashyap, *Fiber Bragg Gratings*, 2nd ed. (Academic Press, 2009).
- [57] J. C. Knight, T. A. Birks, P. St. J. Russell, and D. M. Atkin, *Opt. Lett.* **21**, 1547 (1996).
- [58] J. Broeng, D. Mogilevstev, S. B. Barkou, and A. Bjarklev, *Opt. Fiber Technol.* **5**, 305 (1999).
- [59] T. M. Monro, D. J. Richardson, N. G. R. Broderick, and P. J. Bennett, *J. Lightwave Technol.* **17**, 1093 (1999).
- [60] B. J. Eggleton, P. S. Westbrook, R. S. Windeler, S. Späler, and T. A. Sreasser, *Opt. Lett.* **24**, 1460 (1999).
- [61] M. Ibanescu, Y. Fink, S. Fan, E. L. Thomas, and J. D. Joannopoulos, *Science* **289**, 415 (2000).
- [62] J. K. Ranka, R. S. Windeler, and A. J. Stentz, *Opt. Lett.* **25**, 25 (2000).
- [63] T. A. Birks, W. J. Wadsworth, and P. St. J. Russell, *Opt. Lett.* **25**, 1415 (2000).
- [64] J. M. Dudley and J. R. Taylor, Eds., *Supercontinuum Generation in Optical Fibers* (Cambridge University Press, 2010).
- [65] D. Marcuse, *Light Transmission Optics* (Van Nostrand Reinhold, 1982), Chaps 8 and 12.
- [66] A. W. Snyder and J. D. Love, *Optical Waveguide Theory* (Chapman and Hall, 1983).
- [67] M. J. Adams, *An Introduction to Optical Waveguides* (Wiley, 1981).
- [68] T. Li, Ed., *Optical Fiber Communications: Fiber Fabrication*, Vol. 1 (Academic Press, 1985).
- [69] U. C. Paek, *J. Lightwave Technol.* **4**, 1048 (1986).
- [70] B. J. Ainslie, *J. Lightwave Technol.* **9**, 220 (1991).
- [71] G. A. Thomas, B. L. Shraiman, P. F. Glodis, and M. J. Stephan, *Nature* **404**, 262 (2000).
- [72] M. Ohashi and K. Tsujikawa, *Opt. Fiber Technol.* **6**, 74 (2000).
- [73] L. G. Cohen, *J. Lightwave Technol.* **3**, 958 (1985).
- [74] I. H. Malitson, *J. Opt. Soc. Am.* **55**, 1205 (1965).
- [75] G. P. Agrawal and M. J. Potasek, *Phys. Rev. A* **33**, 1765 (1986).
- [76] B. J. Ainslie and C. R. Day, *J. Lightwave Technol.* **4**, 967 (1986).
- [77] L. G. Cohen, W. L. Mammel, and S. J. Jang, *Electron. Lett.* **18**, 1023 (1982).
- [78] V. A. Bogatyryov, M. M. Bubnov, E. M. Dianov, and A. A. Sysoliatin, *Pure Appl. Opt.* **4**, 345 (1995).
- [79] I. P. Kaminow, *IEEE J. Quantum Electron.* **17**, 15 (1981).
- [80] C. D. Poole and J. Nagel, in *Optical Fiber Telecommunications III*, Vol. A, I. P. Kaminow and T. L. Koch, Eds. (Academic Press, 1997), Chap.6.
- [81] H. Kogelnik, R. M. Jopson, and L. E. Nelson, in *Optical Fiber Telecommunications*, Vol. 4A, I. P. Kaminow and T. Li, Eds. (Academic Press, 2002), Chap. 15.
- [82] J. N. Damask, *Polarization Optics in Telecommunications* (Springer, 2005).
- [83] D. N. Payne, A. J. Barlow, and J. J. R. Hansen, *IEEE J. Quantum Electron.* **18**, 477 (1982).
- [84] S. C. Rashleigh, *J. Lightwave Technol.* **1**, 312 (1983).
- [85] J. Noda, K. Okamoto, and Y. Sasaki, *J. Lightwave Technol.* **4**, 1071 (1986).
- [86] K. Tajima, M. Ohashi, and Y. Sasaki, *J. Lightwave Technol.* **7**, 1499 (1989).
- [87] M. J. Messerly, J. R. Onstott, and R. C. Mikkelsen, *J. Lightwave Technol.* **9**, 817 (1991).
- [88] R. B. Dyott, *Elliptical Fiber Waveguides* (Artec House, 1995).
- [89] N. Bloembergen, *Nonlinear Optics* (W.A. Benjamin, 1977), Chap. 1.

- [90] Y. R. Shen, *Principles of Nonlinear Optics* (Wiley, 1984).
- [91] P. N. Butcher and D. N. Cotter, *The Elements of Nonlinear Optics* (Cambridge University Press, 1990).
- [92] R. W. Boyd, *Nonlinear Optics*, 3rd ed. (Academic Press, 2008).
- [93] G. P. Agrawal, in *Properties of Glass and Rare-Earth Doped Glasses for Optical Fibers*, D. Hewak, Ed. (IEE, 1998), pp. 17–21.
- [94] E. P. Ippen, in *Laser Applications to Optics and Spectroscopy*, Vol. 2, , S. F. Jacobs et al., Ed. (Addison-Wesley, 1975), Chap. 6.
- [95] T. Okuno, M. Onishi, T. Kashiwada, S. Ishikawa, and M. Nichimura, *IEEE J. Sel. Topics Quantum Electron.* **5**, 1385 (1999).
- [96] M. A. Newhouse, D. L. Weidman, and D. W. Hall, *Opt. Lett.* **15**, 1185 (1990).
- [97] X. Feng, A. K. Mairaj, D. W. Hewak, and T. M. Monro, *J. Lightwave Technol.* **23**, 2046 (2005).
- [98] I. Kang, T. D. Krauss, F. W. Wise, B. G. Aitken, and N. F. Borrelli, *J. Opt. Soc. Am. B* **12**, 2053 (1995).
- [99] R. E. Slusher, G. Lenz, J. Hodelin, J. Sanghera, L. B. Shaw, and I. D. Aggarwal, *J. Opt. Soc. Am. B* **21**, 1146 (2004).
- [100] L. B. Fu, M. Rochette, V. G. Ta'eed, D. J. Moss, and B. J. Eggleton, *Opt. Express* **13**, 7637 (2005).
- [101] K. S. Abedin, *Opt. Express* **13**, 10266 (2005).
- [102] L. Brilland, F. Smektala, G. Renversez, T. Chartier, J. Troles, T. Nguyen, N. Traynor, and A. Monteville, *Opt. Express* **14**, 1280 (2006).
- [103] G. P. Agrawal, *Application of Nonlinear Fiber Optics*, 2nd ed. (Academic Press, 2008).

# Pulse Propagation in Fibers

# 2

For an understanding of the nonlinear phenomena in optical fibers, it is necessary to consider the theory of electromagnetic wave propagation in dispersive nonlinear media. The objective of this chapter is to obtain a basic equation that governs the propagation of optical pulses in single-mode fibers. Section 2.1 introduces Maxwell's equations and important concepts such as the linear and nonlinear parts of the induced polarization and the frequency-dependent dielectric constant. The concept of fiber modes is introduced in Section 2.2 where the single-mode condition is also discussed. Section 2.3 considers the theory of pulse propagation in nonlinear dispersive media in the slowly varying envelope approximation with the assumption that the spectral width of the pulse is much smaller than the frequency of the incident radiation. The numerical methods used to solve the resulting propagation equation are discussed in Section 2.4.

## 2.1 MAXWELL'S EQUATIONS

Like all electromagnetic phenomena, the propagation of optical fields in fibers is governed by Maxwell's equations. In the International System of Units (see Appendix A), these equations take the form [1]

$$\nabla \times \mathbf{E} = -\frac{\partial \mathbf{B}}{\partial t}, \quad (2.1.1)$$

$$\nabla \times \mathbf{H} = \mathbf{J} + \frac{\partial \mathbf{D}}{\partial t}, \quad (2.1.2)$$

$$\nabla \cdot \mathbf{D} = \rho_f, \quad (2.1.3)$$

$$\nabla \cdot \mathbf{B} = 0, \quad (2.1.4)$$

where  $\mathbf{E}$  and  $\mathbf{H}$  are electric and magnetic field vectors, respectively, and  $\mathbf{D}$  and  $\mathbf{B}$  are corresponding electric and magnetic flux densities. The current density vector  $\mathbf{J}$  and the charge density  $\rho_f$  represent the sources for the electromagnetic field. In the absence of free charges in a medium such as optical fibers,  $\mathbf{J} = 0$  and  $\rho_f = 0$ .

The flux densities  $\mathbf{D}$  and  $\mathbf{B}$  arise in response to the electric and magnetic fields  $\mathbf{E}$  and  $\mathbf{H}$  propagating inside the medium and are related to them through the constitutive relations given by [1]

$$\mathbf{D} = \epsilon_0 \mathbf{E} + \mathbf{P}, \quad (2.1.5)$$

$$\mathbf{B} = \mu_0 \mathbf{H} + \mathbf{M}, \quad (2.1.6)$$

where  $\epsilon_0$  is the vacuum permittivity,  $\mu_0$  is the vacuum permeability, and  $\mathbf{P}$  and  $\mathbf{M}$  are the induced electric and magnetic polarizations. For a nonmagnetic medium such as optical fibers,  $\mathbf{M} = 0$ .

Maxwell's equations can be used to obtain the wave equation that describes light propagation in optical fibers. By taking the curl of Eq. (2.1.1) and using Eqs (2.1.2), (2.1.5), and (2.1.6), one can eliminate  $\mathbf{B}$  and  $\mathbf{D}$  in favor of  $\mathbf{E}$  and  $\mathbf{P}$  and obtain

$$\nabla \times \nabla \times \mathbf{E} = -\frac{1}{c^2} \frac{\partial^2 \mathbf{E}}{\partial t^2} - \mu_0 \frac{\partial^2 \mathbf{P}}{\partial t^2}, \quad (2.1.7)$$

where  $c$  is the speed of light in vacuum and the relation  $\mu_0 \epsilon_0 = 1/c^2$  was used. To complete the description, a relation between the induced polarization  $\mathbf{P}$  and the electric field  $\mathbf{E}$  is needed. In general, the evaluation of  $\mathbf{P}$  requires a quantum-mechanical approach. Although such an approach is often necessary when the optical frequency is near a medium resonance, a phenomenological relation of the form (1.3.1) can be used to relate  $\mathbf{P}$  and  $\mathbf{E}$  far from medium resonances. This is the case for optical fibers in the wavelength range 0.5–2 μm that is of interest for the study of nonlinear effects. If we include only the third-order nonlinear effects governed by  $\chi^{(3)}$ , the induced polarization consists of two parts such that

$$\mathbf{P}(\mathbf{r}, t) = \mathbf{P}_L(\mathbf{r}, t) + \mathbf{P}_{NL}(\mathbf{r}, t), \quad (2.1.8)$$

where the linear part  $\mathbf{P}_L$  and the nonlinear part  $\mathbf{P}_{NL}$  are related to the electric field by the general relations [2–4]

$$\mathbf{P}_L(\mathbf{r}, t) = \epsilon_0 \int_{-\infty}^t \chi^{(1)}(t-t') \cdot \mathbf{E}(\mathbf{r}, t') dt', \quad (2.1.9)$$

$$\begin{aligned} \mathbf{P}_{NL}(\mathbf{r}, t) &= \epsilon_0 \int_{-\infty}^t dt_1 \int_{-\infty}^{t_1} dt_2 \int_{-\infty}^{t_2} dt_3 \\ &\quad \times \chi^{(3)}(t-t_1, t-t_2, t-t_3) : \mathbf{E}(\mathbf{r}, t_1) \mathbf{E}(\mathbf{r}, t_2) \mathbf{E}(\mathbf{r}, t_3). \end{aligned} \quad (2.1.10)$$

These relations are valid in the electric-dipole approximation and assume that the medium response is local.

Equations (2.1.7)–(2.1.10) provide a general formalism for studying the third-order nonlinear effects in optical fibers. Because of their complexity, it is necessary to make several simplifying approximations. In a major simplification, the nonlinear polarization  $\mathbf{P}_{NL}$  in Eq. (2.1.8) is treated as a small perturbation to the total induced polarization. This is justified because the nonlinear effects

are relatively weak in silica fibers. The first step therefore consists of solving Eq. (2.1.7) with  $\mathbf{P}_{NL} = 0$ . Because Eq. (2.1.7) is then linear in  $\mathbf{E}$ , it is useful to write it in the frequency domain as

$$\nabla \times \nabla \times \tilde{\mathbf{E}}(\mathbf{r}, \omega) = \epsilon(\omega) \frac{\omega^2}{c^2} \tilde{\mathbf{E}}(\mathbf{r}, \omega), \quad (2.1.11)$$

where  $\tilde{\mathbf{E}}(\mathbf{r}, \omega)$  is the Fourier transform of  $\mathbf{E}(\mathbf{r}, t)$  defined as

$$\tilde{\mathbf{E}}(\mathbf{r}, \omega) = \int_{-\infty}^{\infty} \mathbf{E}(\mathbf{r}, t) \exp(i\omega t) dt. \quad (2.1.12)$$

The frequency-dependent dielectric constant appearing in Eq. (2.1.11) is defined as

$$\epsilon(\omega) = 1 + \tilde{\chi}^{(1)}(\omega), \quad (2.1.13)$$

where  $\tilde{\chi}^{(1)}(\omega)$  is the Fourier transform of  $\chi^{(1)}(t)$ . As  $\tilde{\chi}^{(1)}(\omega)$  is in general complex, so is  $\epsilon(\omega)$ . Its real and imaginary parts can be related to the refractive index  $n(\omega)$  and the absorption coefficient  $\alpha(\omega)$  by using the definition

$$\epsilon = (n + i\alpha c/2\omega)^2. \quad (2.1.14)$$

From Eqs (2.1.13) and (2.1.14),  $n$  and  $\alpha$  are related to  $\chi^{(1)}$  by the relations

$$n(\omega) = 1 + \frac{1}{2} \operatorname{Re}[\tilde{\chi}^{(1)}(\omega)], \quad (2.1.15)$$

$$\alpha(\omega) = \frac{\omega}{nc} \operatorname{Im} [\tilde{\chi}^{(1)}(\omega)], \quad (2.1.16)$$

where  $\operatorname{Re}$  and  $\operatorname{Im}$  stand for the real and imaginary parts, respectively. The frequency dependence of  $n$  and  $\alpha$  has been discussed in Section 1.2.

Two further simplifications can be made before solving Eq. (2.1.11). First, because of low optical losses in fibers in the wavelength region of interest, the imaginary part of  $\epsilon(\omega)$  is small in comparison to the real part. Thus, we can replace  $\epsilon(\omega)$  by  $n^2(\omega)$  in the following discussion of fiber modes and include fiber loss later in a perturbative manner. Second, as  $n(\omega)$  is often independent of the spatial coordinates in both the core and the cladding of step-index fibers, one can use

$$\nabla \times \nabla \times \mathbf{E} \equiv \nabla(\nabla \cdot \mathbf{E}) - \nabla^2 \mathbf{E} = -\nabla^2 \mathbf{E}, \quad (2.1.17)$$

where the relation  $\nabla \cdot \mathbf{D} = \epsilon \nabla \cdot \mathbf{E} = 0$  was used from Eq. (2.1.3). With these simplifications, Eq. (2.1.11) takes the form of the Helmholtz equation:

$$\nabla^2 \tilde{\mathbf{E}} + n^2(\omega) \frac{\omega^2}{c^2} \tilde{\mathbf{E}} = 0. \quad (2.1.18)$$

This equation is solved in the next section on fiber modes.

---

## 2.2 FIBER MODES

At any frequency  $\omega$ , optical fibers can support a finite number of guided modes whose spatial distribution  $\tilde{\mathbf{E}}(\mathbf{r}, \omega)$  is a solution of the wave equation (2.1.18) and satisfies all appropriate boundary conditions. In addition, the fiber can support a continuum of unguided radiation modes. Although the inclusion of radiation modes is crucial in problems involving transfer of power between bounded and radiation modes [5], they do not play an important role in the discussion of nonlinear effects. As fiber modes are covered in many textbooks [5–7], they are discussed only briefly in this section.

### 2.2.1 Eigenvalue Equation

Because of the cylindrical symmetry of fibers, it is useful to express the wave equation (2.1.18) in cylindrical coordinates  $\rho$ ,  $\varphi$ , and  $z$ :

$$\frac{\partial^2 \tilde{\mathbf{E}}}{\partial \rho^2} + \frac{1}{\rho} \frac{\partial \tilde{\mathbf{E}}}{\partial \rho} + \frac{1}{\rho^2} \frac{\partial^2 \tilde{\mathbf{E}}}{\partial \varphi^2} + \frac{\partial^2 \tilde{\mathbf{E}}}{\partial z^2} + n^2 k_0^2 \tilde{\mathbf{E}} = 0, \quad (2.2.1)$$

where  $k_0 = \omega/c = 2\pi/\lambda$  and  $\tilde{\mathbf{E}}$  is the Fourier transform of the electric field  $\mathbf{E}$ , i.e.,

$$\mathbf{E}(\mathbf{r}, t) = \frac{1}{2\pi} \int_{-\infty}^{\infty} \tilde{\mathbf{E}}(\mathbf{r}, \omega) \exp(-i\omega t) d\omega. \quad (2.2.2)$$

Similar relations exist for the magnetic field  $\mathbf{H}(\mathbf{r}, t)$ . As  $\mathbf{E}$  and  $\mathbf{H}$  satisfy Maxwell's equations (2.1.1)–(2.1.4), only two components out of six are independent. It is customary to choose  $\tilde{E}_z$  and  $\tilde{H}_z$  as the independent components and express  $\tilde{E}_\rho$ ,  $\tilde{E}_\varphi$ ,  $\tilde{H}_\rho$ , and  $\tilde{H}_\varphi$  in terms of  $\tilde{E}_z$  and  $\tilde{H}_z$ . Both  $\tilde{E}_z$  and  $\tilde{H}_z$  satisfy Eq. (2.2.1). The wave equation for  $\tilde{E}_z$  is easily solved by using the method of separation of variables, resulting in the following general solution:

$$\tilde{E}_z(r, \omega) = A(\omega) F(\rho) \exp(im\phi) \exp(i\beta z), \quad (2.2.3)$$

where  $A$  depends only on the frequency  $\omega$ ,  $\beta$  is the propagation constant,  $m$  is an integer, and  $F(\rho)$  is the solution of

$$\frac{d^2 F}{d\rho^2} + \frac{1}{\rho} \frac{dF}{d\rho} + \left( n^2 k_0^2 - \beta^2 - \frac{m^2}{\rho^2} \right) F = 0, \quad (2.2.4)$$

where the refractive index  $n = n_1$  for  $\rho \leq a$  for a fiber of core radius  $a$  but takes the value  $n_c$  outside the core ( $\rho > a$ ).

Equation (2.2.4) is the well-known differential equation for Bessel functions. Its general solution inside the core can be written as

$$F(\rho) = C_1 J_m(p\rho) + C_2 N_m(p\rho), \quad (2.2.5)$$

where  $J_m(x)$  is the Bessel function,  $N_m(x)$  is the Neumann function, and  $p$  is defined as  $p = (n_1^2 k_0^2 - \beta^2)^{1/2}$ . The constants  $C_1$  and  $C_2$  are determined using the boundary

conditions. As  $N_m(p\rho)$  has a singularity at  $\rho = 0$ ,  $C_2 = 0$  for a physically meaningful solution. The constant  $C_1$  can be absorbed in  $A$  appearing in Eq. (2.2.3). Thus,

$$F(\rho) = J_m(p\rho), \quad \rho \leq a. \quad (2.2.6)$$

In the cladding region ( $\rho \geq a$ ), the solution  $F(\rho)$  should be such that it decays exponentially for large  $\rho$ . The modified Bessel function  $K_m$  represents such a solution. Therefore,

$$F(\rho) = K_m(q\rho), \quad \rho \geq a, \quad (2.2.7)$$

where  $q = (\beta^2 - n_c^2 k_0^2)^{1/2}$ .

The same procedure can be followed to obtain the magnetic field component  $\tilde{H}_z$ . The boundary condition that the tangential components of  $\mathbf{E}$  and  $\tilde{\mathbf{H}}$  be continuous across the core-cladding interface requires that  $E_z$ ,  $\tilde{H}_z$ ,  $E_\phi$ , and  $\tilde{H}_\phi$  be the same when  $\rho = a$  is approached from inside or outside the core. The equality of these field components at  $\rho = a$  leads to an eigenvalue equation whose solutions determine the propagation constant  $\beta$  for the fiber modes. Since the whole procedure is well known [5–7], we write the eigenvalue equation directly:

$$\left[ \frac{J'_m(p a)}{p J_m(p a)} + \frac{K'_m(q a)}{q K_m(q a)} \right] \left[ \frac{J'_m(p a)}{p J_m(p a)} + \frac{n_c^2}{n_1^2} \frac{K'_m(q a)}{q K_m(q a)} \right] = \left( \frac{m \beta k_0 (n_1^2 - n_c^2)}{a n_1 p^2 q^2} \right)^2, \quad (2.2.8)$$

where a “prime” denotes differentiation with respect to the argument and we used the important relation

$$p^2 + q^2 = (n_1^2 - n_c^2)k_0^2. \quad (2.2.9)$$

The eigenvalue equation (2.2.8) in general has several solutions for  $\beta$  for each integer value of  $m$ . It is customary to express these solutions by  $\beta_{mn}$ , where both  $m$  and  $n$  take integer values. Each eigenvalue  $\beta_{mn}$  corresponds to one specific mode supported by the fiber. The corresponding modal field distribution is obtained from Eq. (2.2.3). It turns out [5–7] that there are two types of fiber modes, designated as  $\text{HE}_{mn}$  and  $\text{EH}_{mn}$ . For  $m = 0$ , these modes are analogous to the transverse-electric (TE) and transverse-magnetic (TM) modes of a planar waveguide because the axial component of the electric field, or the magnetic field, vanishes. However, for  $m > 0$ , fiber modes become hybrid, i.e., all six components of the electromagnetic field are nonzero.

## 2.2.2 Single-Mode Condition

The number of modes supported by a specific fiber at a given wavelength depends on its design parameters, namely the core radius  $a$  and the core-cladding index difference  $n_1 - n_c$ . An important parameter for each mode is its cut-off frequency. This frequency is determined by the condition  $q = 0$ . The value of  $p$  when  $q = 0$  for a

given mode determines the cut-off frequency from Eq. (2.2.9). It is useful to define a normalized frequency  $V$  by the relation

$$V = p_c a = k_0 a (n_1^2 - n_c^2)^{1/2}, \quad (2.2.10)$$

where  $p_c$  is obtained from Eq. (2.2.9) by setting  $q = 0$ .

The eigenvalue equation (2.2.8) can be used to determine the values of  $V$  at which different modes reach cut-off. The procedure is complicated, but has been described in many texts [5–7]. Since we are interested mainly in single-mode fibers, we limit the discussion to the cut-off condition that allows the fiber to support only one mode. A single-mode fiber supports only the  $\text{HE}_{11}$  mode, also referred to as the fundamental mode. All other modes are beyond cut-off if the parameter  $V < V_c$ , where  $V_c$  is the smallest solution of  $J_0(V_c) = 0$  or  $V_c \approx 2.405$ . The actual value of  $V$  is a critical design parameter. Typically, microbending losses increase as  $V/V_c$  becomes small. In practice, therefore, fibers are designed such that  $V$  is close to  $V_c$ . The cut-off wavelength  $\lambda_c$  for single-mode fibers can be obtained by using  $k_0 = 2\pi/\lambda_c$  and  $V = 2.405$  in Eq. (2.2.10). For a typical value  $n_1 - n_c = 0.005$  for the index difference,  $\lambda_c = 1.2 \mu\text{m}$  for  $a = 4 \mu\text{m}$ , indicating that such a fiber supports a single mode only for  $\lambda > 1.2 \mu\text{m}$ . In practice, the core radius should be below  $2 \mu\text{m}$  for a fiber to support a single mode in the visible region.

### 2.2.3 Characteristics of the Fundamental Mode

The field distribution  $\mathbf{E}(\mathbf{r}, t)$  corresponding to the  $\text{HE}_{11}$  mode has three nonzero components:  $E_\rho$ ,  $E_\phi$ , and  $E_z$ , or in Cartesian coordinates:  $E_x$ ,  $E_y$ , and  $E_z$ . Among these, either  $E_x$  or  $E_y$  dominates. Thus, to a good degree of approximation, the fundamental fiber mode is linearly polarized in either the  $x$ - or  $y$ -direction depending on whether  $E_x$  or  $E_y$  dominates. In this respect, even a single-mode fiber is not truly single mode because it can support two modes of orthogonal polarizations. The notation  $\text{LP}_{mn}$  is sometimes used to denote the linearly polarized modes, which are approximate solutions of Eq. (2.2.1). The fundamental mode  $\text{HE}_{11}$  corresponds to  $\text{LP}_{01}$  in this notation [6].

The two orthogonally polarized modes of a single-mode fiber are degenerate (i.e., they have the same propagation constant) under ideal conditions. In practice, irregularities such as random variations in the core shape and size along the fiber length break this degeneracy slightly, mix the two polarization components randomly, and scramble the polarization of the incident light as it propagates down the fiber. As discussed in Section 1.2.4, polarization-preserving fibers can maintain the linear polarization if the light is launched with its polarization along one of the principal axes of the fiber. Assuming that the incident light is polarized along a principal axis (chosen to coincide with the  $x$ -axis), the electric field for the fundamental fiber mode  $\text{HE}_{11}$  is approximately given by

$$\tilde{\mathbf{E}}(\mathbf{r}, \omega) = \hat{x} \{A(\omega) F(x, y) \exp[i\beta(\omega)z]\}, \quad (2.2.11)$$

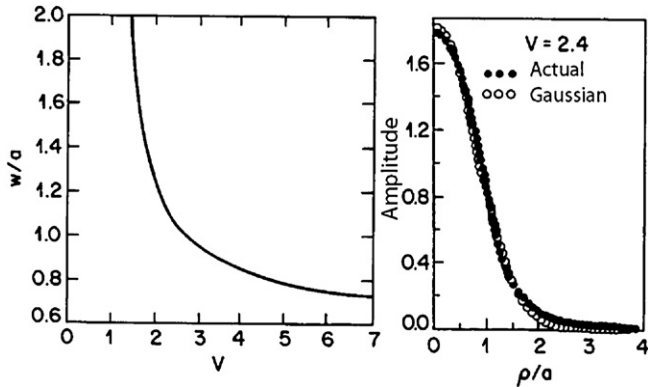


**Figure 2.1** Variation of mode-width parameter  $w$  with  $V$  obtained by fitting the fundamental fiber mode to a Gaussian distribution. Traces on the right show the quality of fit for  $V=2.4$ . (After Ref. [8]; © 1978 OSA.)

where  $A(\omega)$  is a normalization constant. The transverse distribution inside the core is found to be

$$F(x, y) = J_0(p\rho), \quad \rho \leq a, \quad (2.2.12)$$

where  $\rho = (x^2 + y^2)^{1/2}$  is the radial distance. Outside the fiber core, the field decays exponentially as [5]

$$F(x, y) = (a/\rho)^{1/2} J_0(p a) \exp[-q(\rho - a)], \quad \rho \geq a, \quad (2.2.13)$$

where  $K_m(q\rho)$  in Eq. (2.2.7) was approximated by the leading term in its asymptotic expansion and a constant factor was added to ensure the equality of  $F(x, y)$  at  $\rho = a$ . The propagation constant  $\beta(\omega)$  in Eq. (2.2.11) is obtained by solving the eigenvalue equation (2.2.8). Its frequency dependence results not only from the frequency dependence of  $n_1$  and  $n_c$  but also from the frequency dependence of  $p$ . The former is referred to as material dispersion while the latter is called waveguide dispersion. As discussed in Section 1.3, material dispersion generally dominates unless the light wavelength is close to the zero-dispersion wavelength. The evaluation of  $\beta(\omega)$  generally requires a numerical solution of Eq. (2.2.8) although approximate analytic expressions can be obtained in specific cases [5]. The effective mode index is related to  $\beta$  by  $n_{\text{eff}} = \beta/k_0$ .

As the use of modal distribution  $F(x, y)$  given by Eqs (2.2.12) and (2.2.13) is cumbersome in practice, the fundamental fiber mode is often approximated by a Gaussian distribution of the form

$$F(x, y) \approx \exp[-(x^2 + y^2)/w^2], \quad (2.2.14)$$

where the width parameter  $w$  is determined by a curve fitting or by following a variational procedure. Figure 2.1 shows the dependence of  $w/a$  on the fiber parameter  $V$

defined by Eq. (2.2.10). The comparison of the actual field distribution with the fitted Gaussian is also shown for a specific value  $V = 2.4$ . The quality of fit is generally quite good [8], particularly for  $V$  values in the neighborhood of 2. Figure 2.1 shows that  $w \approx a$  for  $V = 2$ , indicating that the core radius provides a good estimate of  $w$  for telecommunication fibers for which  $V \approx 2$ . However,  $w$  can be significantly larger than  $a$  for  $V < 1.8$ . An analytic approximation for  $w$  that is accurate to within 1% for  $1.2 < V < 2.4$  is given by [8]

$$w/a \approx 0.65 + 1.619V^{-3/2} + 2.879V^{-6}. \quad (2.2.15)$$

This expression is of considerable practical value as it expresses the mode width in terms of a single fiber parameter  $V$ .

## 2.3 PULSE-PROPAGATION EQUATION

The study of most nonlinear effects in optical fibers involves the use of short pulses with widths ranging from  $\sim 10\text{ ns}$  to  $10\text{ fs}$ . When such optical pulses propagate inside a fiber, both dispersive and nonlinear effects influence their shapes and spectra. In this section we derive a basic equation that governs propagation of optical pulses in nonlinear dispersive fibers. The starting point is the wave equation (2.1.7). By using Eqs (2.1.8) and (2.1.17), it can be written in the form

$$\nabla^2 \mathbf{E} - \frac{1}{c^2} \frac{\partial^2 \mathbf{E}}{\partial t^2} = \mu_0 \frac{\partial^2 \mathbf{P}_L}{\partial t^2} + \mu_0 \frac{\partial^2 \mathbf{P}_{NL}}{\partial t^2}, \quad (2.3.1)$$

where the linear and nonlinear parts of the induced polarization are related to the electric field  $\mathbf{E}(\mathbf{r}, t)$  through Eqs (2.1.9) and (2.1.10), respectively.

### 2.3.1 Nonlinear Pulse Propagation

It is necessary to make several simplifying assumptions before solving Eq. (2.3.1). First,  $\mathbf{P}_{NL}$  is treated as a small perturbation to  $\mathbf{P}_L$ . This is justified because nonlinear changes in the refractive index are  $< 10^{-6}$  in practice. Second, the optical field is assumed to maintain its polarization along the fiber length so that a scalar approach is valid. This is not really the case, unless polarization-maintaining fibers are used, but the approximation works quite well in practice; it will be relaxed later in Chapter 6. Third, the optical field is assumed to be quasi-monochromatic, i.e., the pulse spectrum, centered at  $\omega_0$ , is assumed to have a spectral width  $\Delta\omega$  such that  $\Delta\omega/\omega_0 \ll 1$ . Since  $\omega_0 \sim 10^{15} \text{ s}^{-1}$ , the last assumption is valid for pulses as short as 0.1 ps.

In the slowly varying envelope approximation adopted here, it is useful to separate the rapidly varying part of the electric field by writing it in the form:

$$\mathbf{E}(\mathbf{r}, t) = \frac{1}{2} \hat{x} [E(\mathbf{r}, t) \exp(-i\omega_0 t) + \text{c.c.}], \quad (2.3.2)$$

where  $\hat{x}$  is the polarization unit vector, and  $E(\mathbf{r}, t)$  is a slowly varying function of time (relative to the optical period). The polarization components  $\mathbf{P}_L$  and  $\mathbf{P}_{NL}$  can also be expressed in a similar way by writing

$$\mathbf{P}_L(\mathbf{r}, t) = \frac{1}{2} \hat{x} [P_L(\mathbf{r}, t) \exp(-i\omega_0 t) + \text{c.c.}], \quad (2.3.3)$$

$$\mathbf{P}_{NL}(\mathbf{r}, t) = \frac{1}{2} \hat{x} [P_{NL}(\mathbf{r}, t) \exp(-i\omega_0 t) + \text{c.c.}] \quad (2.3.4)$$

The linear component  $P_L$  can be obtained by substituting Eq. (2.3.3) in Eq. (2.1.9) and is given by

$$\begin{aligned} P_L(\mathbf{r}, t) &= \epsilon_0 \int_{-\infty}^{\infty} \chi_{xx}^{(1)}(t - t') E(\mathbf{r}, t') \exp[i\omega_0(t - t')] dt' \\ &= \frac{\epsilon_0}{2\pi} \int_{-\infty}^{\infty} \tilde{\chi}_{xx}^{(1)}(\omega) \tilde{E}(\mathbf{r}, \omega - \omega_0) \exp[-i(\omega - \omega_0)t] d\omega, \end{aligned} \quad (2.3.5)$$

where  $\tilde{E}(\mathbf{r}, \omega)$  is the Fourier transform of  $E(\mathbf{r}, t)$  and is defined as in Eq. (2.1.12).

The nonlinear component  $P_{NL}(\mathbf{r}, t)$  is obtained by substituting Eq. (2.3.4) in Eq. (2.1.10). Considerable simplification occurs if the nonlinear response is assumed to be instantaneous so that the time dependence of  $\chi^{(3)}$  in Eq. (2.1.10) is given by the product of three delta functions of the form  $\delta(t - t_1)$ . Equation (2.1.10) then reduces to

$$\mathbf{P}_{NL}(\mathbf{r}, t) = \epsilon_0 \chi^{(3)} : \mathbf{E}(\mathbf{r}, t) \mathbf{E}(\mathbf{r}, t) \mathbf{E}(\mathbf{r}, t). \quad (2.3.6)$$

The assumption of instantaneous nonlinear response amounts to neglecting the contribution of molecular vibrations to  $\chi^{(3)}$  (the Raman effect). In general, both electrons and nuclei respond to the optical field in a nonlinear manner. The nuclei response is inherently slower compared with the electronic response. For silica fibers the vibrational or Raman response occurs over a time scale 60–70 fs. Thus, Eq. (2.3.6) is approximately valid for pulse widths  $> 1$  ps. The Raman contribution is included later in this section.

When Eq. (2.3.2) is substituted in Eq. (2.3.6),  $\mathbf{P}_{NL}(\mathbf{r}, t)$  is found to have a term oscillating at  $\omega_0$  and another term oscillating at the third-harmonic frequency  $3\omega_0$ . The latter term requires phase matching and is generally negligible in optical fibers. By making use of Eq. (2.3.4),  $P_{NL}(\mathbf{r}, t)$  is given by

$$P_{NL}(\mathbf{r}, t) \approx \epsilon_0 \epsilon_{NL} E(\mathbf{r}, t), \quad (2.3.7)$$

where the nonlinear contribution to the dielectric constant is defined as

$$\epsilon_{NL}(\mathbf{r}, t) = \frac{3}{4} \chi_{xxxx}^{(3)} |E(\mathbf{r}, t)|^2. \quad (2.3.8)$$

To obtain the wave equation for the slowly varying amplitude  $E(\mathbf{r}, t)$ , it is more convenient to work in the Fourier domain. This is generally not possible as Eq. (2.3.1) is nonlinear because of the intensity dependence of  $\epsilon_{NL}$ . In one approach,

$\epsilon_{NL}$  is treated as a constant during the derivation of the propagation equation [9]. The approach is justified in view of the slowly varying envelope approximation and the perturbative nature of  $P_{NL}$ . Substituting Eqs (2.3.2)–(2.3.4) in Eq. (2.3.1), the Fourier transform  $\tilde{E}(\mathbf{r}, \omega - \omega_0)$ , defined as

$$\tilde{E}(\mathbf{r}, \omega - \omega_0) = \int_{-\infty}^{\infty} E(\mathbf{r}, t) \exp[i(\omega - \omega_0)t] dt, \quad (2.3.9)$$

is found to satisfy the Helmholtz equation

$$\nabla^2 \tilde{E} + \epsilon(\omega) k_0^2 \tilde{E} = 0, \quad (2.3.10)$$

where  $k_0 = \omega/c$  and

$$\epsilon(\omega) = 1 + \tilde{\chi}_{xx}^{(1)}(\omega) + \epsilon_{NL} \quad (2.3.11)$$

is the dielectric constant whose nonlinear part  $\epsilon_{NL}$  is given by Eq. (2.3.8). The presence of a time-dependent term may appear strange in a frequency-domain treatment. Its use can be justified for a pulse whose envelope varies relatively slowly compared to an optical cycle, i.e., whose spectral bandwidth is a small fraction of its carrier frequency.

Similar to Eq. (2.1.14), the dielectric constant can be used to define the refractive index  $\tilde{n}$  and the absorption coefficient  $\tilde{\alpha}$ . However, both  $\tilde{n}$  and  $\tilde{\alpha}$  become intensity dependent because of  $\epsilon_{NL}$ . It is customary to introduce

$$\tilde{n} = n + \bar{n}_2 |E|^2, \quad \tilde{\alpha} = \alpha + \alpha_2 |E|^2. \quad (2.3.12)$$

Using  $\epsilon = (\tilde{n} + i\tilde{\alpha}/2k_0)^2$  and Eqs (2.3.8) and (2.3.11), the nonlinear-index coefficient  $\bar{n}_2$  and the two-photon absorption coefficient  $\alpha_2$  are given by

$$\bar{n}_2 = \frac{3}{8n} \operatorname{Re} \left( \chi_{xxxx}^{(3)} \right), \quad \alpha_2 = \frac{3\omega_0}{4nc} \operatorname{Im} \left( \chi_{xxxx}^{(3)} \right). \quad (2.3.13)$$

The linear index  $n$  and the absorption coefficient  $\alpha$  are related to the real and imaginary parts of  $\tilde{\chi}_{xx}^{(1)}$  as in Eqs (2.1.15) and (2.1.16). As  $\alpha_2$  is relatively small for silica fibers, it is often ignored.

Equation (2.3.10) can be solved by using the method of separation of variables. If we assume a solution of the form

$$\tilde{E}(\mathbf{r}, \omega - \omega_0) = F(x, y) \tilde{A}(z, \omega - \omega_0) \exp(i\beta_0 z), \quad (2.3.14)$$

where  $\tilde{A}(z, \omega)$  is a slowly varying function of  $z$  and  $\beta_0$  is the wave number to be determined later, Eq. (2.3.10) leads to the following two equations for  $F(x, y)$  and  $\tilde{A}(z, \omega)$ :

$$\frac{\partial^2 F}{\partial x^2} + \frac{\partial^2 F}{\partial y^2} + \left[ \epsilon(\omega) k_0^2 - \tilde{\beta}^2 \right] F = 0, \quad (2.3.15)$$

$$2i\beta_0 \frac{\partial \tilde{A}}{\partial z} + \left( \tilde{\beta}^2 - \beta_0^2 \right) \tilde{A} = 0. \quad (2.3.16)$$

In obtaining Eq. (2.3.16), the second derivative  $\partial^2 \tilde{A} / \partial z^2$  was neglected since  $\tilde{A}(z, \omega)$  is assumed to be a slowly varying function of  $z$ . The wave number  $\tilde{\beta}$  is determined by solving the eigenvalue equation (2.3.15) for the fiber modes using a procedure similar to that used in Section 2.2. The dielectric constant  $\epsilon(\omega)$  in Eq. (2.3.15) can be approximated by

$$\epsilon = (n + \Delta n)^2 \approx n^2 + 2n\Delta n, \quad (2.3.17)$$

where  $\Delta n$  is a small perturbation given by

$$\Delta n = \bar{n}_2 |E|^2 + \frac{i\tilde{\alpha}}{2k_0}. \quad (2.3.18)$$

Equation (2.3.15) can be solved using first-order perturbation theory [10]. We first replace  $\epsilon$  with  $n^2$  and obtain the modal distribution  $F(x, y)$ , and the corresponding wave number  $\beta(\omega)$ . For a single-mode fiber,  $F(x, y)$  corresponds to the modal distribution of the fundamental fiber mode HE<sub>11</sub> given by Eqs (2.2.12) and (2.2.13), or by the Gaussian approximation (2.2.14). We then include the effect of  $\Delta n$  in Eq. (2.3.15). In the first-order perturbation theory,  $\Delta n$  does not affect the modal distribution  $F(x, y)$ . However, the eigenvalue  $\tilde{\beta}$  becomes

$$\tilde{\beta}(\omega) = \beta(\omega) + \Delta\beta(\omega), \quad (2.3.19)$$

where

$$\Delta\beta(\omega) = \frac{\omega^2 n(\omega)}{c^2 \beta(\omega)} \frac{\iint_{-\infty}^{\infty} \Delta n(\omega) |F(x, y)|^2 dx dy}{\iint_{-\infty}^{\infty} |F(x, y)|^2 dx dy}. \quad (2.3.20)$$

This step completes the formal solution of Eq. (2.3.1) to the first order in perturbation  $\mathbf{P}_{NL}$ . Using Eqs (2.3.2) and (2.3.14), the electric field  $\mathbf{E}(\mathbf{r}, t)$  can be written as

$$\mathbf{E}(\mathbf{r}, t) = \frac{1}{2} \hat{x} \{ F(x, y) A(z, t) \exp[i(\beta_0 z - \omega_0 t)] + c.c. \}, \quad (2.3.21)$$

where  $A(z, t)$  is the slowly varying pulse envelope. The Fourier transform  $\tilde{A}(z, \omega - \omega_0)$  of  $A(z, t)$  satisfies Eq. (2.3.16), which can be written as

$$\frac{\partial \tilde{A}}{\partial z} = i[\beta(\omega) + \Delta\beta(\omega) - \beta_0] \tilde{A}, \quad (2.3.22)$$

where we used Eq. (2.3.19) and approximated  $\tilde{\beta}^2 - \beta_0^2$  by  $2\beta_0(\tilde{\beta} - \beta_0)$ . The physical meaning of this equation is clear. Each spectral component within the pulse envelope acquires, as it propagates down the fiber, a phase shift whose magnitude is both frequency and intensity dependent.

At this point, we can go back to the time domain by taking the inverse Fourier transform of Eq. (2.3.22), and obtain the propagation equation for  $A(z, t)$ . However, as an exact functional form of  $\beta(\omega)$  is rarely known, it is useful to expand  $\beta(\omega)$  in a Taylor series around the carrier frequency  $\omega_0$  as

$$\beta(\omega) = \beta_0 + (\omega - \omega_0)\beta_1 + \frac{1}{2}(\omega - \omega_0)^2\beta_2 + \frac{1}{6}(\omega - \omega_0)^3\beta_3 + \dots, \quad (2.3.23)$$

where  $\beta_0 \equiv \beta(\omega_0)$  and other parameters are defined as

$$\beta_m = \left( \frac{d^m \beta}{d\omega^m} \right)_{\omega=\omega_0} \quad (m = 1, 2, \dots). \quad (2.3.24)$$

A similar expansion should be made for  $\Delta\beta(\omega)$ , i.e.,

$$\Delta\beta(\omega) = \Delta\beta_0 + (\omega - \omega_0)\Delta\beta_1 + \frac{1}{2}(\omega - \omega_0)^2\Delta\beta_2 + \dots, \quad (2.3.25)$$

where  $\Delta\beta_m$  is defined similar to Eq. (2.3.24).

The cubic and higher-order terms in the expansion (2.3.23) are negligible if the spectral width of the pulse satisfies the condition  $\Delta\omega \ll \omega_0$ . Their neglect is consistent with the quasi-monochromatic assumption used in the derivation of Eq. (2.3.22). If  $\beta_2 \approx 0$  for some specific values of  $\omega_0$ , it may be necessary to include the  $\beta_3$  term. Under the same conditions, we can use the approximation  $\Delta\beta \approx \Delta\beta_0$  in Eq. (2.3.25). After these simplifications in Eq. (2.3.22), we take the inverse Fourier transform using

$$A(z, t) = \frac{1}{2\pi} \int_{-\infty}^{\infty} \tilde{A}(z, \omega - \omega_0) \exp[-i(\omega - \omega_0)t] d\omega. \quad (2.3.26)$$

During the Fourier-transform operation,  $\omega - \omega_0$  is replaced by the differential operator  $i(\partial/\partial t)$ . The resulting equation for  $A(z, t)$  becomes

$$\frac{\partial A}{\partial z} + \beta_1 \frac{\partial A}{\partial t} + \frac{i\beta_2}{2} \frac{\partial^2 A}{\partial t^2} = i\Delta\beta_0 A. \quad (2.3.27)$$

The  $\Delta\beta_0$  term on the right side of Eq. (2.3.27) is obtained from Eq. (2.3.20) after setting  $\omega = \omega_0$ . Although, in general,  $\Delta n$  can be different inside the core and cladding regions of a fiber, it is nearly the same in both regions of most practical fibers and can be taken outside the integral. Using  $\beta(\omega) \approx n(\omega)\omega/c$  and assuming that  $F(x, y)$  in Eq. (2.3.20) does not vary much over the pulse bandwidth, Eq. (2.3.27) takes the form

$$\frac{\partial A}{\partial z} + \beta_1 \frac{\partial A}{\partial t} + \frac{i\beta_2}{2} \frac{\partial^2 A}{\partial t^2} + \frac{\alpha}{2} A = i\gamma(\omega_0)|A|^2 A, \quad (2.3.28)$$

where the nonlinear parameter  $\gamma$  is defined as

$$\gamma(\omega_0) = \frac{\omega_0 \bar{n}_2 \iint_{-\infty}^{\infty} |F(x, y)|^4 dx dy}{c \iint_{-\infty}^{\infty} |F(x, y)|^2 dx dy}. \quad (2.3.29)$$

The pulse amplitude  $A$  in Eq. (2.3.28) is in units of the electric field (V/m). For practical reasons, it is common to normalize  $A$  such that  $|A|^2$  represents the optical power. To do this, we introduce  $A'$  such that  $|A'|^2 = \frac{1}{2}\epsilon_0 n c A_m |A|^2$ , where  $A_m = \iint |F(x, y)|^2 dx dy$  is the mode area. It is easy to verify that  $A'$  also satisfies Eq. (2.3.28) provided the nonlinear parameter  $\gamma$  is redefined as

$$\gamma(\omega_0) = \frac{\omega_0 n_2}{c A_{\text{eff}}}, \quad n_2 = \frac{2\bar{n}_2}{\epsilon_0 n c}, \quad (2.3.30)$$

and the *effective mode area* of the fiber is introduced as

$$A_{\text{eff}} = \frac{\left(\iint_{-\infty}^{\infty} |F(x, y)|^2 dx dy\right)^2}{\iint_{-\infty}^{\infty} |F(x, y)|^4 dx dy}. \quad (2.3.31)$$

The quantity  $n_2$  is sometimes called the nonlinear Kerr parameter and has units of  $\text{m}^2/\text{W}$  (see Section 11.1.1). As a result,  $\gamma$  has units of  $\text{W}^{-1}/\text{m}$ .

The numerical value of the nonlinear parameter  $\gamma$  requires a knowledge of the modal distribution  $F(x, y)$  of the fundamental fiber mode. Clearly,  $A_{\text{eff}}$  depends on fiber parameters such as the core radius and the core–cladding index difference. If  $F(x, y)$  is approximated by a Gaussian function given in Eq. (2.2.14),  $A_{\text{eff}} = \pi w^2$ . The width parameter  $w$  depends on the  $V$  parameter of fiber and can be obtained from Figure 2.1 or Eq. (2.2.10). Typically,  $A_{\text{eff}}$  can vary in the range of  $1\text{--}100 \mu\text{m}^2$ , depending on the fiber design (see Chapter 11). As a result,  $\gamma$  takes values in the range  $1\text{--}100 \text{ W}^{-1}/\text{km}$ , if we use  $n_2 \approx 2.6 \times 10^{-20} \text{ m}^2/\text{W}$ . In the so-called highly nonlinear fibers covered in Chapter 11,  $A_{\text{eff}}$  is reduced intentionally to enhance the nonlinear effects inside such fibers.

Equation (2.3.28) describes the propagation of a picosecond optical pulse in single-mode fibers. It is related to the nonlinear Schrödinger (NLS) equation and it can be reduced to that form under certain conditions. It includes the effects of fiber losses through  $\alpha$ , of chromatic dispersion through  $\beta_1$  and  $\beta_2$ , and of fiber nonlinearity through  $\gamma$ . The physical significance of the parameters  $\beta_1$  and  $\beta_2$  was discussed in Section 1.2.3. Briefly, the pulse envelope moves at the group velocity  $v_g \equiv 1/\beta_1$ , while the effects of group-velocity dispersion (GVD) are governed by  $\beta_2$ . The GVD parameter  $\beta_2$  can be positive or negative depending on whether the wavelength  $\lambda$  is below or above the zero-dispersion wavelength  $\lambda_D$  of the fiber (see Figure 1.5). In the anomalous-dispersion regime ( $\lambda > \lambda_D$ ),  $\beta_2$  is negative, and the fiber can support optical solitons. In standard silica fibers,  $\beta_2 \sim 50 \text{ ps}^2/\text{km}$  in the visible region but becomes close to  $-20 \text{ ps}^2/\text{km}$  near  $1.5 \mu\text{m}$ , the change in sign occurring in the vicinity of  $1.3 \mu\text{m}$ . The term on the right side of Eq. (2.3.28) governs the nonlinear effects of self-phase modulation (SPM).

### 2.3.2 Higher-Order Nonlinear Effects

Although the propagation Equation (2.3.28) has been successful in explaining a large number of nonlinear effects, it may need to be modified depending on the experimental conditions. For example, Eq. (2.3.28) does not include the effects of stimulated inelastic scattering such as SRS and SBS (see Section 1.3.2). If peak power of the incident pulse is above a threshold level, SRS and SBS can transfer energy to a new pulse at a different wavelength, which may propagate in the same or the opposite direction. The two pulses also interact with each other through the phenomenon of cross-phase modulation (XPM). A similar situation occurs when two or more pulses at different wavelengths (separated by more than individual spectral widths) are incident on the fiber. Simultaneous propagation of multiple pulses is governed by a set

of equations similar to Eq. (2.3.28), modified suitably to include the contributions of XPM and the Raman or Brillouin gain.

Equation (2.3.28) should also be modified for ultrashort optical pulses whose widths are close to  $<1$  ps [11–26]. The spectral width of such pulses becomes large enough that several approximations made in the derivation of Eq. (2.3.28) become questionable. The most important limitation turns out to be the neglect of the Raman effect. For pulses with a wide spectrum ( $>0.1$  THz), the Raman-gain can amplify the low-frequency components of a pulse by transferring energy from the high-frequency components of the same pulse. This phenomenon is called *intrpulse Raman scattering*. As a result of it, the pulse spectrum shifts toward the low-frequency (red) side as the pulse propagates inside the fiber, a feature referred to as the *Raman-induced frequency shift* [11]. The physical origin of this effect is related to the delayed nature of the Raman (vibrational) response [12]. Mathematically, Eq. (2.3.6) cannot be used in the derivation of Eq. (2.3.28); one must use the general form of the nonlinear polarization given in Eq. (2.1.10).

In the case of a delayed Raman response governed by  $R(t)$ , the nonlinear response function in Eq. (2.1.10) is found to have following symmetrized form [27–29]:

$$\chi^{(3)}(\mathfrak{t}_1, \mathfrak{t}_2, \mathfrak{t}_3) = \chi^{(3)}[R(\mathfrak{t}_1)\delta(\mathfrak{t}_2)\delta(\mathfrak{t}_3 - \mathfrak{t}_1) + \delta(\mathfrak{t}_1 - \mathfrak{t}_2)R(\mathfrak{t}_2)\delta(\mathfrak{t}_3) + \delta(\mathfrak{t}_1)\delta(\mathfrak{t}_2 - \mathfrak{t}_3)R(\mathfrak{t}_3)], \quad (2.3.32)$$

where  $R(t)$  is normalized such that  $\int_{-\infty}^{\infty} R(t)dt = 1$ . We substitute Eq. (2.3.32) in Eq. (2.1.10) and introduce the slowly varying optical field through Eq. (2.3.2). As before, if we ignore third-harmonic terms requiring phase matching and retain only the terms oscillating at the frequency  $\omega_0$ , we can write the nonlinear polarization in the form of Eq. (2.3.4) with

$$P_{NL}(\mathbf{r}, t) = \frac{3\epsilon_0}{4}\chi_{xxxx}^{(3)}E(\mathbf{r}, t)\int_{-\infty}^t R(t - \tau)|E(\mathbf{r}, \tau)|^2d\tau, \quad (2.3.33)$$

where the upper limit of integration extends only up to  $t$  because the response function  $R(t - \tau)$  must be zero for  $\tau > t$  to ensure causality.

The analysis of Section 2.3.1 can still be used by working in the frequency domain, but the perturbation of the refractive index is now given by

$$\Delta n(\omega) = n_2(\omega)\int_0^{\infty} R(t')|E(\mathbf{r}, t - t')|^2dt' + \frac{i\alpha(\omega)}{2k_0}, \quad (2.3.34)$$

where we made a change of variable  $t' = t - \tau$  in Eq. (2.3.33) before using it. This form of  $\Delta n(\omega)$  leads to a different expression for  $\Delta\beta(\omega)$  appearing in Eq. (2.3.22). When converting back this equation from frequency to time domain, we expand  $\Delta\beta(\omega)$  in a Taylor series as indicated in Eq. (2.3.25) and truncate this series after two terms and retain both  $\Delta\beta_0$  and  $\Delta\beta_1$ . The frequency dependence of  $\alpha$  and  $n_2$  can be included by treating  $\gamma$  and  $\alpha$  as frequency dependent and writing them in the form

$$\gamma(\omega) = \gamma(\omega_0) + \gamma_1(\omega - \omega_0), \quad \alpha(\omega) = \alpha(\omega_0) + \alpha_1(\omega - \omega_0), \quad (2.3.35)$$

where  $\gamma_1 = d\gamma/d\omega$  and  $\alpha_1 = d\alpha/d\omega$ , both evaluated at  $\omega = \omega_0$ . For short pulses, it is also useful to retain multiple terms in the expansion (2.3.23). With these additions, we obtain the following generalized pulse-propagation equation [18]:

$$\begin{aligned} \frac{\partial A}{\partial z} + \frac{1}{2} \left( \alpha(\omega_0) + i\alpha_1 \frac{\partial}{\partial t} \right) A - i \sum_{n=1}^{\infty} \frac{i^n \beta_n}{n!} \frac{\partial^n A}{\partial t^n} \\ = i \left( \gamma(\omega_0) + i\gamma_1 \frac{\partial}{\partial t} \right) \left( A(z, t) \int_0^{\infty} R(t') |A(z, t-t')|^2 dt' \right). \end{aligned} \quad (2.3.36)$$

The integral in this equation accounts for the energy transfer resulting from intra-pulse Raman scattering. Equation (2.3.36) can be used for pulses as short as a few optical cycles if enough higher-order dispersive terms are included [22–26]. For example, dispersive terms up to the 12th order are sometimes included when dealing with supercontinuum generation in optical fibers, a phenomenon discussed in Chapter 13.

It is important to note that the use of  $\gamma_1$  in Eq. (2.3.36) automatically includes the frequency dependence of both  $n_2$  and  $A_{\text{eff}}$ . Noting that  $\gamma_1 = (d\gamma/d\omega)_{\omega=\omega_0}$ , the ratio  $\gamma_1/\gamma$  consists of the following three terms:

$$\frac{\gamma_1(\omega_0)}{\gamma(\omega_0)} = \frac{1}{\omega_0} + \frac{1}{n_2} \left( \frac{dn_2}{d\omega} \right)_{\omega=\omega_0} - \frac{1}{A_{\text{eff}}} \left( \frac{dA_{\text{eff}}}{d\omega} \right)_{\omega=\omega_0}. \quad (2.3.37)$$

The first term provides the dominant contribution, but the second and third terms become important in the case of a supercontinuum that may extend over 100 THz or more [26]. If spectral broadening is limited to 20 THz or so, one can employ  $\gamma_1 \approx \gamma/\omega_0$ . This approximation is often used in practice. If we combine the terms containing the derivative  $\partial A/\partial t$ , we find that the  $\gamma_1$  term forces the group velocity to depend on the optical intensity and leads to the phenomenon of self-steepening [33–37].

The nonlinear response function  $R(t)$  should include both the electronic and nuclear contributions. Assuming that the electronic contribution is nearly instantaneous, the functional form of  $R(t)$  can be written as [15–20]

$$R(t) = (1 - f_R)\delta(t) + f_R h_R(t), \quad (2.3.38)$$

where  $f_R$  represents the fractional contribution of the delayed Raman response to nonlinear polarization  $P_{\text{NL}}$ . The form of the Raman response function  $h_R(t)$  is set by vibrations of silica molecules induced by the optical field.

### 2.3.3 Raman Response Function and its Impact

It is not easy to calculate  $h_R(t)$  because of the amorphous nature of silica fibers. An indirect experimental approach is used in practice by noting that the Raman-gain spectrum is related to the imaginary part of the Fourier transform of  $h_R(t)$  as [15]

$$g_R(\Delta\omega) = \frac{f_R \omega_0}{cn(\omega_0)} \chi_{xxx}^{(3)} \text{Im} [\tilde{h}_R(\Delta\omega)], \quad (2.3.39)$$

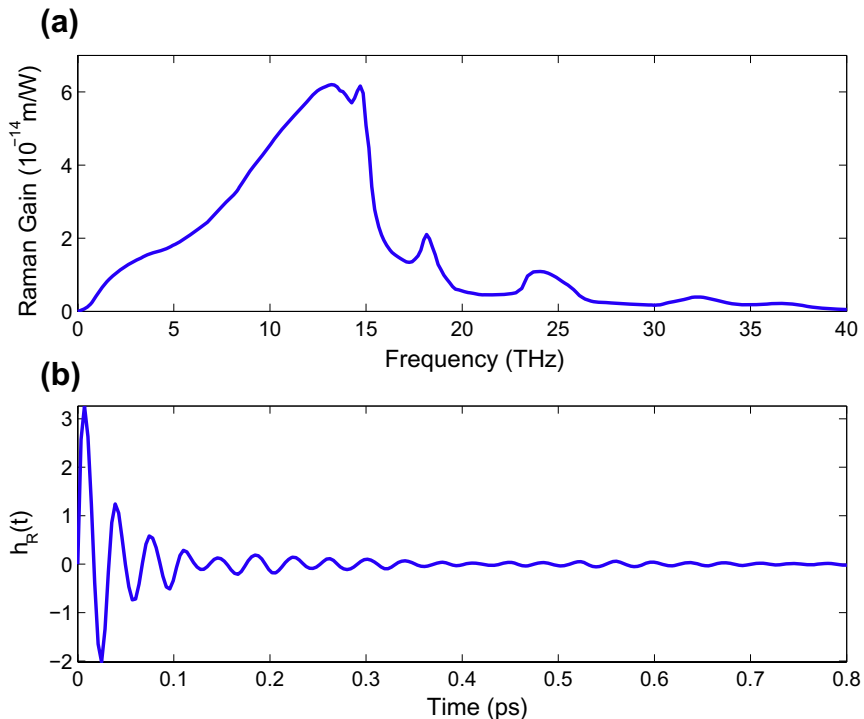


**Figure 2.2** (a) Measured Raman-gain spectrum of silica fibers; (b) temporal form of the Raman response function deduced from the gain data. (Based on the Raman-gain data provided by R.H. Stolen.)

where  $\Delta\omega = \omega - \omega_0$  and  $\text{Im}$  stands for the imaginary part. The real part of  $\tilde{h}_R(\Delta\omega)$  can be obtained from the imaginary part through the Kramers–Kronig relation [4]. The inverse Fourier transform of  $\tilde{h}_R(\Delta\omega)$  then provides the Raman response function  $h_R(t)$ . Figure 2.2 shows (a) the experimentally measured Raman-gain spectrum and (b) the temporal form of  $h_R(t)$  deduced from it [15].

Attempts have been made to determine an approximate analytic form of the Raman response function. If we assume that a single vibrational frequency  $\Omega_R$  of silica molecules is involved in the Raman process,  $h_R(t)$  can be written in the form [16]

$$h_R(t) = \left( \tau_1^{-2} + \tau_2^{-2} \right) \tau_1 \exp(-t/\tau_2) \sin(t/\tau_1), \quad (2.3.40)$$

where  $\tau_1 = 1/\Omega_R$  and  $\tau_2$  is the damping time of vibrations. In practice,  $\tau_1$  and  $\tau_2$  are two adjustable parameters and are chosen to provide a good fit to the actual Raman-gain spectrum. In a 1989 study, values of  $\tau_1 = 12.2$  fs and  $\tau_2 = 32$  fs were used [16]. The fraction  $f_R$  can also be estimated from Eq. (2.3.39). Using the known numerical value of peak Raman-gain,  $f_R$  is found to be about 0.18 [15–17].

One should be careful in using Eq. (2.3.40) for  $h_R(t)$  because it approximates the actual Raman-gain spectrum with a single Lorentzian profile, and thus fails to reproduce the hump seen in Figure 2.2 at frequencies below 5 THz. This hump is known as the *boson peak*, is a general feature of amorphous materials, and results from a vibrational instability of glasses [30]. A modified form of  $h_R(t)$  was proposed in 2006 to include this hump, and it is given by [31]

$$h_R^{\text{new}}(t) = (1 - f_b)h_R(t) + f_b \left[ (2\tau_b - t)/\tau_b^2 \right] \exp(-t/\tau_b), \quad (2.3.41)$$

where  $f_b = 0.21$  represents the relative contribution of the boson peak with  $\tau_b \approx 96$  fs; the value  $f_R = 0.245$  fits the Raman-gain spectrum reasonably well. The new form of the Raman response function provides a better fit to the experimental data on the Raman-induced frequency shifts of femtosecond pulses in optical fibers [32].

Equation (2.3.36) together with the response function  $R(t)$  given in Eq. (2.3.38) governs the evolution of ultrashort pulses in optical fibers. Its accuracy has been verified by showing that it preserves the number of photons during pulse evolution if fiber loss is ignored by setting  $\alpha = 0$  [17]. The pulse energy is not conserved in the presence of intrapulse Raman scattering because a part of the pulse energy is taken by silica molecules. Eq. (2.3.36) includes this source of nonlinear loss. It is easy to see that it reduces to the simpler Eq. (2.3.28) for optical pulses much longer than the time scale of the Raman response function  $h_R(t)$ . Noting that  $h_R(t)$  becomes nearly zero for  $t > 1$  ps (see Figure 2.2),  $R(t)$  for such pulses can be replaced by  $\delta(t)$ . As the higher-order dispersion term involving  $\beta_3$ , the loss term involving  $\alpha_1$ , and the nonlinear term involving  $\gamma_1$  are also negligible for such pulses, Eq. (2.3.36) reduces to Eq. (2.3.28).

For pulses wide enough to contain many optical cycles (pulse width > 100 fs), we can simplify Eq. (2.3.36) considerably by setting  $\alpha_1 = 0$ ,  $\gamma_1 = \gamma/\omega_0$ , and using the following Taylor-series expansion:

$$|A(z, t - t')|^2 \approx |A(z, t)|^2 - t' \frac{\partial}{\partial t} |A(z, t)|^2. \quad (2.3.42)$$

This approximation is reasonable if the pulse envelope evolves slowly along the fiber. Defining the first moment of the Raman response function as

$$T_R \equiv \int_0^\infty t R(t) dt \approx f_R \int_0^\infty t h_R(t) dt = f_R \frac{d(\text{Im } \tilde{h}_R)}{d(\Delta\omega)} \Bigg|_{\Delta\omega=0}, \quad (2.3.43)$$

and noting that  $\int_0^\infty R(t) dt = 1$ , Eq. (2.3.36) can be approximated by

$$\frac{\partial A}{\partial z} + \frac{\alpha}{2} A + \frac{i\beta_2}{2} \frac{\partial^2 A}{\partial T^2} - \frac{\beta_3}{6} \frac{\partial^3 A}{\partial T^3} = i\gamma \left( |A|^2 A + \frac{i}{\omega_0} \frac{\partial}{\partial T} (|A|^2 A) - T_R A \frac{\partial |A|^2}{\partial T} \right), \quad (2.3.44)$$

where a frame of reference moving with the pulse at the group velocity  $v_g$  (the so-called retarded frame) was used by making the transformation

$$T = t - z/v_g \equiv t - \beta_1 z. \quad (2.3.45)$$

A second-order term involving the ratio  $T_R/\omega_0$  was neglected in arriving at Eq. (2.3.44) because of its smallness.

It is easy to identify the origin of the three higher-order terms in Eq. (2.3.44). The term proportional to  $\beta_3$  results from including the cubic term in the expansion in Eq. (2.3.23). This term governs the effects of third-order dispersion and becomes important for ultrashort pulses because of their wide bandwidth. The term proportional to  $\omega_0^{-1}$  results from the frequency dependence of  $\Delta\beta$  in Eq. (2.3.20). It is responsible for the phenomenon of self-steepening [33–37]. The last term proportional to  $T_R$  in Eq. (2.3.44) has its origin in the delayed Raman response, and it is responsible for the Raman-induced frequency shift, also called a self-frequency shift [11] induced by intrapulse Raman scattering. By using Eqs (2.3.39) and (2.3.43),  $T_R$  can be related to the slope of the Raman-gain spectrum [12] in the vicinity of the carrier frequency  $\omega_0$ . Its numerical value has also been deduced experimentally [38] and is close to 3 fs at wavelengths near 1.5 μm. For pulses shorter than 0.5 ps, the Raman-gain may not vary linearly over the entire pulse bandwidth, and the use of Eq. (2.3.44) becomes questionable for such short pulses.

For pulses of width  $T_0 > 5$  ps, the parameters  $(\omega_0 T_0)^{-1}$  and  $T_R/T_0$  become so small (<0.001) that the last two terms in Eq. (2.3.44) can be neglected. As the contribution of the third-order dispersion term is also quite small for such pulses (as long as the carrier wavelength is not too close to the zero-dispersion wavelength), one can employ the simplified equation

$$i \frac{\partial A}{\partial z} + \frac{i\alpha}{2} A - \frac{\beta_2}{2} \frac{\partial^2 A}{\partial T^2} + \gamma |A|^2 A = 0. \quad (2.3.46)$$

This equation can also be obtained from Eq. (2.3.28) by using the transformation given in Eq. (2.3.45). In the special case of  $\alpha = 0$ , Eq. (2.3.46) is referred to as the NLS equation because it resembles the Schrödinger equation with a nonlinear potential term (variable  $z$  playing the role of time). To extend the analogy further, Eq. (2.3.44) is called the generalized (or extended) NLS equation. The NLS equation is a fundamental equation of nonlinear science and has been studied extensively in the context of solitons [39–45].

Equation (2.3.46) is the simplest nonlinear equation for studying third-order nonlinear effects in optical fibers. If the peak power associated with an optical pulse becomes so large that one needs to include the fifth and higher-order terms in Eq. (1.3.1), the NLS equation needs to be modified. A simple approach replaces the nonlinear parameter  $\gamma$  in Eq. (2.3.46) with  $\gamma = \gamma_0(1 - b_s|A|^2)$ , where  $b_s$  is a saturation parameter governing the power level at which the nonlinearity begins to saturate. For silica fibers,  $b_s|A|^2 \ll 1$  in most practical situations, and one can use Eq. (2.3.46). However, this term may become relevant when the peak intensity approaches 1 GW/cm<sup>2</sup>. The resulting equation is often called the cubic–quintic NLS equation [44] because it contains terms involving both the third and fifth powers of the amplitude  $A$ . For the same reason, Eq. (2.3.46) is referred to as the cubic NLS

equation. Fibers made by using materials with larger values of  $n_2$  (such as silicate and chalcogenide fibers) are likely to exhibit the saturation effects at a lower peak-power level. The cubic–quintic NLS equation may become relevant for them and for fibers whose core is doped with high-nonlinearity materials such as organic dyes [46] and semiconductors [47].

Equation (2.3.46) appears in optics in several different contexts [43]. For example, the same equation holds for propagation of CW beams in planar waveguides when the variable  $T$  is interpreted as a spatial coordinate. The  $\beta_2$  term in Eq. (2.3.46) then governs beam diffraction in the plane of the waveguide. This analogy between “diffraction in space” and “dispersion in time” is often exploited to advantage since the same equation governs the underlying physics.

### 2.3.4 Extension to Multimode Fibers

In deriving the NLS equation in Section 2.3.1 we implicitly assumed in Eq. (2.3.14) that the entire energy of the input pulse was carried by a single mode of the fiber with spatial distribution  $F(x, y)$ . In the case of a multimode fiber, pulse energy is likely to be distributed among several modes. In this case, the electric field at a distance  $z$  has the general form

$$\tilde{\mathbf{E}}(\mathbf{r}, \omega) = \sum_m \mathbf{F}_m(x, y, \omega) \tilde{A}_m(z, \omega) \exp[i\beta_m(\omega)z], \quad (2.3.47)$$

where  $\mathbf{F}_m(x, y, \omega)$  governs the shape of a specific mode,  $\beta_m$  is the propagation constant of this mode, and the sum extends over all guided modes of the waveguide. As a further generalization, we explicitly show the frequency dependence of mode profiles and account for the vectorial nature of fiber modes. This will allow us to discuss the polarization effects in Chapter 6. As discussed earlier, even a single-mode fiber waveguide supports two orthogonally polarized modes.

Since Eq. (2.3.7) cannot be used for arbitrarily polarized fields, we rewrite the Helmholtz equation (2.3.10) in the form

$$\nabla^2 \tilde{\mathbf{E}} + \frac{n^2 \omega^2}{c^2} \tilde{\mathbf{E}} = -\frac{\omega^2}{\epsilon_0 c^2} \tilde{\mathbf{P}}_{\text{NL}}(\mathbf{r}, \omega), \quad (2.3.48)$$

where  $n$  is the linear part of the refractive index. We substitute Eq. (2.3.47) into this equation and note that each fiber mode satisfies

$$\nabla_T^2 \mathbf{F}_m + n^2(\omega^2/c^2) \mathbf{F}_m = \beta_m^2 \mathbf{F}_m, \quad (2.3.49)$$

where the subscript T denotes the transverse part of the  $\nabla^2$  operator. Assuming that  $\tilde{A}_m$  varies slowly with  $z$  and neglecting its second derivative, we obtain

$$\sum_{m=1}^M 2i\beta_m \frac{\partial \tilde{A}_m}{\partial z} \mathbf{F}_m(x, y, \omega) e^{i\beta_m z} = -\frac{\omega^2}{\epsilon_0 c^2} \tilde{\mathbf{P}}_{\text{NL}}(\mathbf{r}, \omega). \quad (2.3.50)$$

Multiplying the preceding equation with  $\mathbf{F}_n^*$ , integrating over the transverse plane, and using the orthogonal nature of various modes, the mode amplitudes are found to satisfy

$$\frac{\partial \tilde{A}_m}{\partial z} = \frac{i\omega^2 e^{-i\beta_m z}}{2\epsilon_0 c^2 \beta_m} \frac{\iint \mathbf{F}_m^*(x, y, \omega) \cdot \tilde{\mathbf{P}}_{NL}(\mathbf{r}, \omega) dx dy}{\iint \mathbf{F}_m^*(x, y, \omega) \cdot \mathbf{F}_m(x, y, \omega) dx dy}, \quad (2.3.51)$$

where all integrations extend from  $-\infty$  to  $+\infty$ .

We need to convert this equation to the time domain by following the method outlined in Section 2.3.1. This is a difficult task without making some simplifications. As before, we assume that a linearly polarized input pulse with the carrier frequency  $\omega_0$  is launched into a multimode fiber and it maintains its linear polarization along the  $x$ -axis during propagation inside this fiber. Another simplifying approximation we make is that the mode distribution does not change significantly over the pulse bandwidth, and  $\mathbf{F}_m(x, y, \omega)$  can be replaced with its value at the carrier frequency  $\omega_0$ . As in Eq. (2.3.23), we expand  $\beta_m(\omega)$  in a Taylor series around the carrier frequency  $\omega_0$  in the exponential term  $e^{-i\beta_m z}$  in Eq. (2.3.51) but, in the denominator, we replace  $\beta_m(\omega)$  with  $\beta_m(\omega_0)$ . Noting that  $\omega - \omega_0$  is replaced with  $i\frac{\partial}{\partial t}$  during the integration, we obtain the following time-domain equation for  $A_m(z, t)$ :

$$\frac{\partial A_m}{\partial z} - i \sum_{n=1}^{\infty} \frac{i^n \beta_{mn}}{n!} \frac{\partial^n A_m}{\partial t^n} = \frac{i\omega_0}{2\epsilon_0 c \bar{n}_m} \frac{\iint F_m^*(x, y) \hat{x} \cdot \mathbf{P}_{NL}(\mathbf{r}, t) dx dy}{\iint |F(x, y)|^2 dx dy} e^{-i(\beta_{m0}z - \omega_0 t)}, \quad (2.3.52)$$

where  $\beta_{mn} = (d^n \beta_m / d\omega^n)_{\omega=\omega_0}$  is the  $n$ th-order dispersion parameter for the  $m$ th mode of the fiber with the effective mode index  $\bar{n}_m$ .

At this point we need to specify the nonlinear polarization  $\mathbf{P}_{NL}(\mathbf{r}, t)$ . To simplify the following discussion, we use its form given in Eq. (2.3.6) together with electric field,

$$\mathbf{E}(\mathbf{r}, t) = \hat{x} \sum_n F_n(x, y) A_n(z, t) \exp[i(\beta_{n0}z - \omega_0 t)], \quad (2.3.53)$$

and retain only the terms oscillating at the carrier frequency  $\omega_0$ . When the result is substituted in Eq. (2.3.52), we obtain

$$\frac{\partial A_m}{\partial z} - i \sum_{n=1}^{\infty} \frac{i^n \beta_{mn}}{n!} \frac{\partial^n A_m}{\partial t^n} = \sum_n \sum_p \sum_q i \gamma_{mnpq} A_n^* A_p A_q \exp(i\Delta\beta_{mnpq} z), \quad (2.3.54)$$

where  $\Delta\beta_{mnpq} = \beta_{p0} + \beta_{q0} - \beta_{m0} - \beta_{n0}$  is the phase mismatch and various nonlinear coefficients are defined as

$$\gamma_{mnpq} = \frac{\omega_0 \bar{n}_2 \iint F_m^*(x, y) F_n^*(x, y) F_p(x, y) F_q(x, y) dx dy}{c \iint F_m^*(x, y) F_m(x, y) dx dy}. \quad (2.3.55)$$

The triple sum appearing on the right side of Eq. (2.3.54) represents a nonlinear coupling among various fiber modes. The strength of this coupling depends on the

overlap among the four modes participating in the four-wave mixing responsible for the nonlinear coupling as well as on the extent of phase mismatch. It is easy to see that this equation takes the form of Eq. (2.3.28) when the optical fiber supports a single mode.

## 2.4 NUMERICAL METHODS

The NLS equation [Eq. (2.3.44) or (2.3.46)] is a nonlinear partial differential equation that does not generally lend itself to analytic solutions except for some specific cases in which the inverse scattering method [39] can be employed. A numerical approach is therefore often necessary for an understanding of the nonlinear effects in optical fibers. A large number of numerical methods have been developed for this purpose [48–76]. Most of them can be classified into two broad categories known as the finite-difference and pseudospectral methods. Generally speaking, pseudospectral methods are faster by up to an order of magnitude to achieve the same accuracy [56]. The one method that has been used extensively to solve the pulse-propagation problem in nonlinear dispersive media is the *split-step Fourier method* [50, 51]. The relative speed of this method compared with most finite-difference schemes can be attributed in part to the use of the finite-Fourier-transform (FFT) algorithm [77]. This section describes various numerical techniques used to study the pulse-propagation problem in optical fibers with emphasis on the split-step Fourier method and its modifications.

### 2.4.1 Split-Step Fourier Method

To understand the philosophy behind the split-step Fourier method, it is useful to write Eq. (2.3.44) formally in the form

$$\frac{\partial A}{\partial z} = (\widehat{D} + \widehat{N}) A, \quad (2.4.1)$$

where  $\widehat{D}$  is a differential operator that accounts for dispersion and losses within a linear medium and  $\widehat{N}$  is a nonlinear operator that governs the effect of fiber nonlinearities on pulse propagation. These operators are given by

$$\widehat{D} = -\frac{i\beta_2}{2} \frac{\partial^2}{\partial T^2} + \frac{\beta_3}{6} \frac{\partial^3}{\partial T^3} - \frac{\alpha}{2}, \quad (2.4.2)$$

$$\widehat{N} = i\gamma \left( |A|^2 + \frac{i}{\omega_0} \frac{1}{A} \frac{\partial}{\partial T} (|A|^2 A) - T_R \frac{\partial |A|^2}{\partial T} \right). \quad (2.4.3)$$

In general, dispersion and nonlinearity act together along the length of the fiber. The split-step Fourier method obtains an approximate solution by assuming that in propagating the optical field over a small distance  $h$ , the dispersive and nonlinear effects

can be assumed to act independently. More specifically, propagation from  $z$  to  $z + h$  is carried out in two steps. In the first step, the nonlinearity acts alone, and  $\widehat{D} = 0$  in Eq. (2.4.1). In the second step, dispersion acts alone, and  $\widehat{N} = 0$  in Eq. (2.4.1). Mathematically,

$$A(z + h, T) \approx \exp(h\widehat{D}) \exp(h\widehat{N}) A(z, T). \quad (2.4.4)$$

The exponential operator  $\exp(h\widehat{D})$  can be evaluated in the Fourier domain using the prescription

$$\exp(h\widehat{D})B(z, T) = F_T^{-1} \exp[h\widehat{D}(-i\omega)]F_T B(z, T), \quad (2.4.5)$$

where  $F_T$  denotes the Fourier-transform operation,  $\widehat{D}(-i\omega)$  is obtained from Eq. (2.4.2) by replacing the operator  $\partial/\partial T$  by  $-i\omega$ , and  $\omega$  is the frequency in the Fourier domain. As  $\widehat{D}(i\omega)$  is just a number in the Fourier space, the evaluation of Eq. (2.4.5) is straightforward. The use of the FFT algorithm [77] makes numerical evaluation of Eq. (2.4.5) relatively fast. It is for this reason that the split-step Fourier method can be faster by up to two orders of magnitude compared with most finite-difference schemes [56].

To estimate the accuracy of the split-step Fourier method, we note that a formally exact solution of Eq. (2.4.1) is given by

$$A(z + h, T) = \exp[h(\widehat{D} + \widehat{N})]A(z, T), \quad (2.4.6)$$

if  $\widehat{N}$  is assumed to be  $z$  independent. At this point, it is useful to recall the Baker–Hausdorff formula [78] for two noncommuting operators  $\hat{a}$  and  $\hat{b}$ ,

$$\exp(\hat{a}) \exp(\hat{b}) = \exp \left( \hat{a} + \hat{b} + \frac{1}{2}[\hat{a}, \hat{b}] + \frac{1}{12}[\hat{a} - \hat{b}, [\hat{a}, \hat{b}]] + \dots \right), \quad (2.4.7)$$

where  $[\hat{a}, \hat{b}] = \hat{a}\hat{b} - \hat{b}\hat{a}$ . A comparison of Eqs (2.4.4) and (2.4.6) shows that the split-step Fourier method ignores the noncommuting nature of the operators  $\widehat{D}$  and  $\widehat{N}$ . By using Eq. (2.4.7) with  $\hat{a} = h\widehat{D}$  and  $\hat{b} = h\widehat{N}$ , the dominant error term is found to result from the commutator  $\frac{1}{2}h^2[\widehat{D}, \widehat{N}]$ . Thus, the split-step Fourier method is accurate to second order in the step size  $h$ .

The accuracy of the split-step Fourier method can be improved by adopting a different procedure to propagate the optical pulse over one segment from  $z$  to  $z + h$ . In this procedure Eq. (2.4.4) is replaced by

$$A(z + h, T) \approx \exp \left( \frac{h}{2}\widehat{D} \right) \exp \left( \int_z^{z+h} \widehat{N}(z') dz' \right) \exp \left( \frac{h}{2}\widehat{D} \right) A(z, T). \quad (2.4.8)$$

The main difference is that the effect of nonlinearity is included in the middle of the segment rather than at the segment boundary. Because of the symmetric form of the exponential operators in Eq. (2.4.8), this scheme is known as the symmetrized

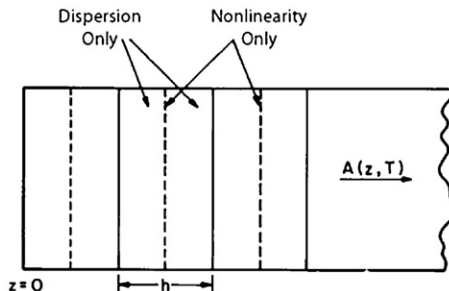


**Figure 2.3** Schematic illustration of the symmetrized split-step Fourier method used for numerical simulations. Fiber length is divided into a large number of segments of width  $h$ . Within a segment, the effect of nonlinearity is included at the midplane shown by a dashed line.

split-step Fourier method [79]. The integral in the middle exponential is useful to include the  $z$  dependence of the nonlinear operator  $\widehat{N}$ . If the step size  $h$  is small enough, it can be approximated by  $\exp(h\widehat{N})$ , similar to Eq. (2.4.4). The most important advantage of using the symmetrized form of Eq. (2.4.8) is that the leading error term results from the double commutator in Eq. (2.4.7) and is of third order in the step size  $h$ . This can be verified by applying Eq. (2.4.7) twice in Eq. (2.4.8).

The accuracy of the split-step Fourier method can be further improved by evaluating the integral in Eq. (2.4.8) more accurately than approximating it by  $h\widehat{N}(z)$ . A simple approach is to employ the trapezoidal rule and approximate the integral by [80]

$$\int_z^{z+h} \widehat{N}(z') dz' \approx \frac{h}{2} [\widehat{N}(z) + \widehat{N}(z+h)]. \quad (2.4.9)$$

However, the implementation of Eq. (2.4.9) is not simple because  $\widehat{N}(z+h)$  is unknown at the midsegment located at  $z+h/2$ . It is necessary to follow an iterative procedure that is initiated by replacing  $\widehat{N}(z+h)$  by  $\widehat{N}(z)$ . Equation (2.4.8) is then used to estimate  $A(z+h, T)$  which in turn is used to calculate the new value of  $\widehat{N}(z+h)$ . Although the iteration procedure is time-consuming, it can still reduce the overall computing time if the step size  $h$  can be increased because of the improved accuracy of the numerical algorithm. Two iterations are generally enough in practice.

The implementation of the split-step Fourier method is relatively straightforward. As shown in Figure 2.3, the fiber length is divided into a large number of segments that need not be spaced equally. The optical pulse is propagated from segment to segment using the prescription of Eq. (2.4.8). More specifically, the optical field  $A(z, T)$  is first propagated for a distance  $h/2$  with dispersion only using the FFT algorithm and Eq. (2.4.5). At the midplane  $z+h/2$ , the field is multiplied by a nonlinear term that represents the effect of nonlinearity over the whole segment length  $h$ . Finally, the field is propagated for the remaining distance  $h/2$  with dispersion only to obtain  $A(z+h, T)$ . In effect, the nonlinearity is assumed to be lumped at the midplane of each segment (dashed lines in Figure 2.3).

In practice, the split-step Fourier method can be made to run faster by noting that the application of Eq. (2.4.8) over  $M$  successive steps results in the following expression:

$$A(L, T) \approx e^{-\frac{1}{2}h\hat{D}} \left( \prod_{m=1}^M e^{h\hat{D}} e^{h\hat{N}} \right) e^{\frac{1}{2}h\hat{D}} A(0, T), \quad (2.4.10)$$

where  $L = Mh$  is the total fiber length and the integral in Eq. (2.4.9) was approximated with  $h\hat{N}$ . Thus, except for the first and last dispersive steps, all intermediate steps can be carried over the whole segment length  $h$ . This feature reduces the required number of FFTs roughly by a factor of 2 and speeds up the numerical code by the same factor. Note also that a different algorithm is obtained if we use Eq. (2.4.7) with  $\hat{a} = h\hat{N}$  and  $\hat{b} = h\hat{D}$ . In that case, Eq. (2.4.10) is replaced with

$$A(L, T) \approx e^{-\frac{1}{2}h\hat{N}} \left( \prod_{m=1}^M e^{h\hat{N}} e^{h\hat{D}} \right) e^{\frac{1}{2}h\hat{N}} A(0, T). \quad (2.4.11)$$

Both of these algorithms provide the same accuracy and are easy to implement in practice (see Appendix B). Higher-order versions of the split-step Fourier method can be used to improve the computational efficiency [74]. The use of an adaptive step size along  $z$  can also help in reducing the computational time for certain problems [75].

The split-step Fourier method has been applied to a wide variety of optical problems including wave propagation in atmosphere [80], graded-index fibers [81], semiconductor lasers [82], unstable resonators [83], and waveguide couplers [84]. It is referred to as the beam-propagation method when applied to the propagation of CW optical beams in nonlinear media when dispersion is replaced by diffraction [81–85].

For the specific case of pulse propagation in optical fibers, the split-step Fourier method was first applied in 1973 [40]. Since then, this method has been used extensively for studying various nonlinear effects in optical fibers [86–94], mainly because of its fast execution compared with most finite-difference schemes [50]. Although the method is relatively straightforward to implement, it requires that step sizes in  $z$  and  $T$  be selected carefully to maintain the required accuracy [75]. The optimum choice of step sizes depends on the complexity of the problem, and a few guidelines are available [95–98].

The use of FFT imposes periodic boundary conditions whenever the split-step Fourier method is employed. This is acceptable in practice if the temporal window used for simulations is made much wider than the pulse width. Typically, the window size is chosen to be 10–20 times the pulse width. In some problems, a part of the pulse energy may spread so rapidly that it may be difficult to prevent it from hitting the window boundary. This can lead to numerical instabilities as the energy reaching one edge of the window automatically re-enters from the other edge. It is common to use an “absorbing window” in which the radiation reaching window edges is artificially absorbed even though such an implementation does not

preserve the pulse energy. In general, the split-step Fourier method is a powerful tool provided care is taken to ensure that it is used properly. Several generalizations of this method have been developed that retain the basic idea behind the split-step technique but employ an expansion other than the Fourier series; examples include splines and wavelets [76].

### 2.4.2 Finite-Difference Methods

Although the split-step Fourier method is commonly used for analyzing nonlinear effects in optical fibers, its use becomes quite time-consuming when the NLS equation is solved for simulating the performance of wavelength-division-multiplexed (WDM) lightwave systems. In such systems, the temporal resolution should be a small fraction of the entire bandwidth of the WDM signal. For a 100-channel system, the bandwidth approaches 10 THz, requiring a temporal resolution of  $\sim 10$  fs. At the same time, the temporal window should be typically 1–10 ns wide, resulting in more than  $10^5$  mesh points in time domain. Even though each FFT operation is relatively fast, a large number of FFT operations on a large-size array leads to an overall computation time measured in hours (even days) on a state-of-the art computer. For this reason, finite-difference methods continue to attract attention.

Several finite-difference schemes have been used to solve the NLS equation (see Refs [56, 65]). Some of the common ones among them are: the Crank–Nicholson scheme and its variants, the hopscotch scheme and its variants, and the leap-frog method. A careful comparison of several finite-difference schemes with the split-step Fourier method shows that the latter is efficient only when the field amplitude varies slowly with time [65]. However, it is difficult to recommend a specific finite-difference scheme because the speed and accuracy depend to some extent on the number and form of the nonlinear terms included in the generalized NLS equation. A fourth-order Runge–Kutta scheme has been used with success for simulating supercontinuum generation inside optical fibers [99].

Another situation in which finite-difference schemes are useful corresponds to a propagation of optical pulses so short that one must employ the generalized NLS equation (2.3.36). The process of supercontinuum generation provides an example where it is often preferable to solve this equation in the frequency domain [100]. In this case we must solve Eq. (2.3.22) on a discrete frequency grid. The resulting set of coupled differential equation can be solved with any finite-difference scheme. We refer to Reference [100] for more details on the implementation of this approach. Its main advantage is that one can include the known frequency dependence of fiber loss  $\alpha(\omega)$ , propagation constant  $\beta(\omega)$ , and the nonlinear parameter  $n_2(\omega)$  through Eqs (2.3.20) and (2.3.34).

There are several limitations inherent in the use of the NLS equation for pulse propagation in optical fibers. The slowly varying envelope approximation may not always hold if pulse width becomes comparable to a single optical cycle. Another one is related to the total neglect of backward propagating waves. If the fiber has a built-in index grating, a part of the pulse energy will be reflected backward because

of Bragg diffraction. Such problems require simultaneous consideration of forward and backward propagating waves. The other major limitation is related to the neglect of the vector nature of the electromagnetic field. In essence, polarization effects are completely ignored. As was seen in Section 1.2.4, optical fibers exhibit birefringence. The inclusion of the birefringence effects requires consideration of all components of electric and magnetic field vectors.

In the case of a linear medium, the algorithms that solve Maxwell's equations, Eqs (2.1.1)–(2.1.4), directly in the time domain by using finite-difference methods have been developed for many years [101–103]. Such algorithms have been extended to the case of nonlinear media [104–108]. In a 1992 approach [104], the delayed nature of nonlinear response was incorporated by using Eqs (2.3.33) and (2.3.38) together with the functional form of the Raman response function given in Eq. (2.3.40). This work included the dispersive effects through a single resonance frequency. In an extension of this approach [108], dispersive effects were included through the Sellmeier equation given in Eq. (1.2.6) with three resonance frequencies ( $m = 3$ ). Conceptually, the main difference between the finite-difference time-domain (FDTD) method and the split-step Fourier method is that the former deals with all electromagnetic components without eliminating the carrier frequency  $\omega_0$ , in contrast with what was done in Section 2.3 in deriving the NLS equation. For this reason, the FDTD method can be used for pulses of arbitrary durations (as short as a single optical cycle).

The FDTD method is certainly more accurate because it solves Maxwell's equations directly with a minimum number of approximations. However, improvement in accuracy is achieved only at the expense of a vast increase in the computational effort. This can be understood by noting that the time step needed to resolve the optical carrier is by necessity a fraction of the optical period and should be  $<1$  fs. The step size along the fiber length is also required to be a fraction of the optical wavelength. Such a small step size forces one to limit the total fiber length to  $<1$  m. It may be necessary to use the FDTD method for ultrashort pulses ( $T_0 < 10$  fs) whose width is comparable to the optical period [108]. In most applications of nonlinear fiber optics, however, pulses are much wider than the optical period, and Eq. (2.3.36) and its approximate forms such as Eq. (2.3.46) provide a reasonably accurate solution to the underlying Maxwell's equations.

---

## PROBLEMS

- 2.1** Use Maxwell's equations to express the field components  $E_\rho$ ,  $E_\phi$ ,  $H_\rho$ , and  $H_\phi$  inside the fiber core in terms of  $E_z$  and  $H_z$ . Neglect the nonlinear part of the polarization in Eq. (2.1.8) for simplicity.
- 2.2** Derive eigenvalue equation (2.2.8) by matching the boundary conditions at the core–cladding interface of a step-index fiber. Consult References [5–7] if necessary.
- 2.3** Use the eigenvalue equation (2.2.8) to derive the single-mode condition in optical fibers.

- 2.4** A single-mode fiber has an index step of 0.005. Calculate the core radius if the fiber has a cut-off wavelength of  $1\text{ }\mu\text{m}$ . Assume a core index of 1.45.
- 2.5** Derive an expression for the confinement factor  $\Gamma$  of single-mode fibers defined as the fraction of the total mode power contained inside the fiber core. Use the Gaussian approximation made in Eq. (2.2.14) for the fundamental fiber mode.
- 2.6** Estimate the full width at half maximum (FWHM) of the spot size associated with the fiber mode and the fraction of the mode power inside the core when the fiber of Problem 2.4 is used to transmit  $1.3\text{-}\mu\text{m}$  light.
- 2.7** Derive Eq. (2.3.7) from Eq. (2.3.6). Explain the origin of the factor  $\frac{3}{4}$  in the definition of  $\epsilon_{NL}$ . Verify that Eq. (2.3.13) for  $\bar{n}_2$  follows from it.
- 2.8** Solve Eq. (2.3.15) by using perturbation theory to obtain the first-order correction for the propagation constant when  $\epsilon_{NL}$  is small. Show that this correction is given by Eq. (2.3.20).
- 2.9** Show that Eq. (2.3.28) can be obtained by taking the Fourier transform indicated in Eq. (2.3.26) together with Eq. (2.3.22). Fill in all the missing steps.
- 2.10** Calculate the effective mode area when the fiber of Problem 2.4 is used to transmit  $1.3\text{-}\mu\text{m}$  light.
- 2.11** Take the Fourier transform of the Raman response function given by Eq. (2.3.40) and plot the real and imaginary parts as a function of frequency. What is the physical meaning of the resulting curves?
- 2.12** The Raman-gain spectrum of a fiber is approximated by a Lorentzian profile whose FWHM is 5 THz. The gain peak is located at 15 THz from the carrier frequency of the pulse. Derive an expression for the Raman response function of this fiber.
- 2.13** Implement the split-step Fourier method of Section 2.4.1 using MATLAB software (see Appendix B) and solve the NLS equation (2.3.46) for a 10-ps Gaussian pulse propagating in a 100-km-long fiber using  $\alpha = 0.2\text{ dB/km}$ ,  $\beta_2 = -20\text{ ps}^2/\text{km}$  and  $\gamma = 10\text{ W}^{-1}/\text{km}$ .
- 2.14** Extend the numerical code developed in the preceding problem for solving the generalized NLS equation (2.3.44).

---

## REFERENCES

- [1] P. Diamant, *Wave Transmission and Fiber Optics* (Macmillan, 1990), Chap. 3.
- [2] Y. R. Shen, *Principles of Nonlinear Optics* (Wiley, 1984), Chap. 1.
- [3] P. N. Butcher and D. N. Cotter, *The Elements of Nonlinear Optics* (Cambridge University Press, 1990), Chap. 2.
- [4] R. W. Boyd, *Nonlinear Optics*, 3rd ed. (Academic Press, 2008), Chap. 1.
- [5] D. Marcuse, *Theory of Dielectric Optical Waveguides* (Academic Press, 1991), Chap. 2.
- [6] A. W. Snyder and J. D. Love, *Optical Waveguide Theory* (Chapman and Hall, 1983), Chaps. 12–15.

- [7] J. A. Buck, *Fundamentals of Optical Fibers*, 2nd ed. (Wiley, 2004), Chap. 3.
- [8] D. Marcuse, *J. Opt. Soc. Am.* **68**, 103 (1978).
- [9] H. A. Haus, *Waves and Fields in Optoelectronics* (Prentice-Hall, 1984), Chap. 10.
- [10] P. M. Morse and H. Feshbach, *Methods of Theoretical Physics* (McGraw-Hill, 1953), Chap. 9.
- [11] F. M. Mitschke and L. F. Mollenauer, *Opt. Lett.* **11**, 659 (1986).
- [12] J. P. Gordon, *Opt. Lett.* **11**, 662 (1986).
- [13] Y. Kodama and A. Hasegawa, *IEEE J. Quantum Electron.* **23**, 510 (1987).
- [14] E. A. Golovchenko, E. M. Dianov, A. N. Pilipetskii, A. M. Prokhorov, and V. N. Serkin, *Sov. Phys. JETP Lett.* **45**, 91 (1987).
- [15] R. H. Stolen, J. P. Gordon, W. J. Tomlinson, and H. A. Haus, *J. Opt. Soc. Am. B* **6**, 1159 (1989).
- [16] K. J. Blow and D. Wood, *IEEE J. Quantum Electron.* **25**, 2665 (1989).
- [17] P. V. Mamyshev and S. V. Chernikov, *Opt. Lett.* **15**, 1076 (1990).
- [18] S. V. Chernikov and P. V. Mamyshev, *J. Opt. Soc. Am. B* **8**, 1633 (1991).
- [19] P. V. Mamyshev and S. V. Chernikov, *Sov. Lightwave Commun.* **2**, 97 (1992).
- [20] R. H. Stolen and W. J. Tomlinson, *J. Opt. Soc. Am. B* **9**, 565 (1992).
- [21] S. Blair and K. Wagner, *Opt. Quantum Electron.* **30**, 697 (1998).
- [22] T. Brabec and F. Krausz, *Phys. Rev. Lett.* **78**, 3282 (1997).
- [23] N. Karasawa, S. Nakamura, N. Nakagawa, M. Shibata, R. Morita, H. Shigekawa, and M. Yamashita, *IEEE J. Quantum Electron.* **37**, 398 (2001).
- [24] A. Gaeta, *Phys. Rev. Lett.* **84**, 3582 (2000); *Opt. Lett.* **27**, 924 (2002).
- [25] G. Chang, T. B. Norris, and H. G. Winful, *Opt. Lett.* **28**, 546 (2003).
- [26] J. M. Dudley, G. Genty, and S. Coen, *Rev. Mod. Phys.* **78**, 1135 (2006).
- [27] R. W. Hellwarth, *Prog. Quantum Electron.* **5**, 1 (1977).
- [28] N. Tang and R. L. Sutherland, *J. Opt. Soc. Am. B* **14**, 3412 (1997).
- [29] A. Martínez-Rios, Andrey N. Starodumov, Yu. O. Barmenkov, V. N. Filippov, and I. Torres-Gomez, *J. Opt. Soc. Am. B* **18**, 794 (2001).
- [30] V. L. Gurevich, D. A. Parshin, and H. R. Schober, *Phys. Rev. B* **67**, 094203 (2003).
- [31] Q. Lin and G. P. Agrawal, *Opt. Lett.* **31**, 3086 (2006).
- [32] A. Podlipensky, P. Szarniak, N. Y. Joly, and P. St. J. Russell, *J. Opt. Soc. Am. B* **25**, 2049 (2008).
- [33] F. DeMartini, C. H. Townes, T. K. Gustafson, and P. L. Kelley, *Phys. Rev.* **164**, 312 (1967).
- [34] N. Tzoar and M. Jain, *Phys. Rev. A* **23**, 1266 (1981).
- [35] D. Anderson and M. Lisak, *Phys. Rev. A* **27**, 1393 (1983).
- [36] G. Yang and Y. R. Shen, *Opt. Lett.* **9**, 510 (1984).
- [37] E. Bourkoff, W. Zhao, R. I. Joseph, and D. N. Christodoulides, *Opt. Lett.* **12**, 272 (1987).
- [38] A. K. Atieh, P. Myslinski, J. Chrostowski, and P. Galko, *J. Lightwave Technol.* **17**, 216 (1999).
- [39] V. E. Zakharov and A. B. Shabat, *Sov. Phys. JETP* **34**, 62 (1972).
- [40] A. Hasegawa and F. Tappert, *Appl. Phys. Lett.* **23**, 142 (1973).
- [41] M. J. Ablowitz and P. A. Clarkson, *Solitons, Nonlinear Evolution Equations and Inverse Scattering* (Cambridge University Press, 1992).
- [42] C. Sulem and P.-L. Sulem, *Nonlinear Schrödinger Equations: Self-Focusing and Wave Collapse* (Springer, 1999).

- [43] Y. S. Kivshar and G. P. Agrawal, *Optical Solitons: From Fibers to Photonic Crystals* (Academic Press, 2003).
- [44] N. Akhmediev and A. Ankiewicz, Eds., *Dissipative Solitons* (Springer, 2005).
- [45] L. F. Mollenauer and J. P. Gordon, *Solitons in Optical Fibers: Fundamental and Applications* (Academic Press, 2006).
- [46] G. D. Peng, Z. Xiong, and P. L. Chu, *Opt. Fiber Technol.* **5**, 242 (1999).
- [47] B. J. Inslie, H. P. Girdlestone, and D. Cotter, *Electron. Lett.* **23**, 405 (1987).
- [48] V. I. Karpman and E. M. Krushkal, *Sov. Phys. JETP* **28**, 277 (1969).
- [49] N. Yajima and A. Outi, *Prog. Theor. Phys.* **45**, 1997 (1971).
- [50] R. H. Hardin and F. D. Tappert, *SIAM Rev. Chronicle* **15**, 423 (1973).
- [51] R. A. Fisher and W. K. Bischel, *Appl. Phys. Lett.* **23**, 661 (1973); *J. Appl. Phys.* **46**, 4921 (1975).
- [52] M. J. Ablowitz and J. F. Ladik, *Stud. Appl. Math.* **55**, 213 (1976).
- [53] I. S. Greig and J. L. Morris, *J. Comput. Phys.* **20**, 60 (1976).
- [54] B. Fornberg and G. B. Whitham, *Philos. Trans. Roy. Soc.* **289**, 373 (1978).
- [55] M. Delfour, M. Fortin, and G. Payre, *J. Comput. Phys.* **44**, 277 (1981).
- [56] T. R. Taha and M. J. Ablowitz, *J. Comput. Phys.* **55**, 203 (1984).
- [57] D. Pathria and J. L. Morris, *J. Comput. Phys.* **87**, 108 (1990).
- [58] L. R. Watkins and Y. R. Zhou, *J. Lightwave Technol.* **12**, 1536 (1994).
- [59] M. S. Ismail, *Int. J. Comput. Math.* **62**, 101 (1996).
- [60] K. V. Peddanarappagari and M. Brandt-Pearce, *J. Lightwave Technol.* **15**, 2232 (1997); *J. Lightwave Technol.* **16**, 2046 (1998).
- [61] E. H. Twizell, A. G. Bratsos, and J. C. Newby, *Math. Comput. Simul.* **43**, 67 (1997).
- [62] W. P. Zeng, *J. Comput. Math.* **17**, 133 (1999).
- [63] I. Daq, *Comput. Methods Appl. Mech. Eng.* **174**, 247 (1999).
- [64] A. G. Shagalov, *Int. J. Mod. Phys. C* **10**, 967 (1999).
- [65] Q. S. Chang, E. H. Jia, and W. Sun, *J. Comput. Phys.* **148**, 397 (1999).
- [66] W. Z. Dai and R. Nassar, *J. Comput. Math.* **18**, 123 (2000).
- [67] S. R. K. Iyengar, G. Jayaraman, and V. Balasubramanian, *Comput. Math. Appl.* **40**, 1375 (2000).
- [68] Q. Sheng, A. Q. M. Khaliq, and E. A. Al-Said, *J. Comput. Phys.* **166**, 400 (2001).
- [69] J. B. Chen, M. Z. Qin, and Y. F. Tang, *Comput. Math. Appl.* **43**, 1095 (2002).
- [70] J. I. Ramos, *Appl. Math. Comput.* **133**, 1 (2002).
- [71] X. M. Liu and B. Lee, *IEEE Photon. Technol. Lett.* **15**, 1549 (2003).
- [72] W. T. Ang and K. C. Ang, *Numer. Methods Partial Diff. Eqs.* **20**, 843 (2004).
- [73] M. Premaratne, *IEEE Photon. Technol. Lett.* **16**, 1304 (2004).
- [74] G. M. Muslu and H. A. Erbay, *Math. Comput. Simul.* **67**, 581 (2005).
- [75] O. V. Sinkin, R. Holzlöhner, J. Zweck, and C. R. Menyuk, *J. Lightwave Technol.* **21**, 61 (2003).
- [76] T. Kremp and W. Freude, *J. Lightwave Technol.* **23**, 1491 (2005).
- [77] J. W. Cooley and J. W. Tukey, *Math. Comput.* **19**, 297 (1965).
- [78] G. H. Weiss and A. A. Maradudin, *J. Math. Phys.* **3**, 771 (1962).
- [79] J. A. Fleck, J. R. Morris, and M. D. Feit, *Appl. Phys.* **10**, 129 (1976).
- [80] M. Lax, J. H. Batteh, and G. P. Agrawal, *J. Appl. Phys.* **52**, 109 (1981).
- [81] M. D. Feit and J. A. Fleck, *Appl. Opt.* **17**, 3990 (1978); *Appl. Opt.* **18**, 2843 (1979).
- [82] G. P. Agrawal, *J. Appl. Phys.* **56**, 3100 (1984); *J. Lightwave Technol.* **2**, 537 (1984).

- [83] M. Lax, G. P. Agrawal, M. Belic, B. J. Coffey, and W. H. Louisell, *J. Opt. Soc. Am. A* **2**, 732 (1985).
- [84] B. Hermansson, D. Yevick, and P. Danielsen, *IEEE J. Quantum Electron.* **19**, 1246 (1983).
- [85] L. Thylen, E. M. Wright, G. I. Stegeman, C. T. Seaton, and J. V. Moloney, *Opt. Lett.* **11**, 739 (1986).
- [86] G. P. Agrawal and M. J. Potasek, *Phys. Rev. A* **33**, 1765 (1986).
- [87] P. K. A. Wai, C. R. Menyuk, Y. C. Lee, and H. H. Chen, *Opt. Lett.* **11**, 464 (1986).
- [88] G. P. Agrawal, *Phys. Rev. A* **44**, 7493 (1991).
- [89] M. Margalit and M. Orenstein, *Opt. Commun.* **124**, 475 (1996).
- [90] J. R. Costa, C. R. Paiva, and A. M. Barbosa, *IEEE J. Quantum Electron.* **37**, 145 (2001).
- [91] B. R. Washburn, S. E. Ralph, and R. S. Windeler, *Opt. Express* **10**, 575 (2002).
- [92] J. M. Dudley and S. Coen, *IEEE J. Sel. Topics Quantum Electron.* **8**, 651 (2002).
- [93] G. Genty, M. Lehtonen, H. Ludvigsen, J. Broeng, and M. Kaivola, *Opt. Express* **10**, 1083 (2002).
- [94] T. Hori, N. Nishizawa, T. Goto, and M. Yoshida, *J. Opt. Soc. Am. B* **21**, 1969 (2004).
- [95] J. Van Roey, J. van der Donk, and P. E. Lagasse, *J. Opt. Soc. Am.* **71**, 803 (1981).
- [96] L. Thylen, *Opt. Quantum Electron.* **15**, 433 (1983).
- [97] J. Sajjonmaa and D. Yevick, *J. Opt. Soc. Am.* **73**, 1785 (1983).
- [98] D. Yevick and B. Hermansson, *J. Appl. Phys.* **59**, 1769 (1986); *IEEE J. Quantum Electron.* **25**, 221 (1989).
- [99] J. Hult, *J. Lightwave Technol.* **25**, 3770 (2007); *J. Lightwave Technol.* **27**, 3984 (2009).
- [100] J. M. Dudley and J. R. Taylor, *Supercontinuum Generation in Optical Fibers* (Cambridge University Press, 2010), Chap. 3.
- [101] K. S. Yee, *IEEE Trans. Antennas Propag.* **14**, 302 (1966).
- [102] A. Taflove and S. C. Hagness, *Computational Electrodynamics: The Finite-Difference Time-Domain Method*, 3rd ed. (Artech House, 2005).
- [103] U. S. Inan and R. A. Marshall, *Numerical Electromagnetics: The FDTD Method* (Cambridge University Press, 2011).
- [104] P. M. Goorjian, A. Taflove, R. M. Joseph, and S. C. Hagness, *IEEE J. Quantum Electron.* **28**, 2416 (1992).
- [105] R. M. Joseph, P. M. Goorjian, and A. Taflove, *Opt. Lett.* **18**, 491 (1993).
- [106] R. W. Ziolkowski and J. B. Judkins, *J. Opt. Soc. Am. B* **10**, 186 (1993).
- [107] P. M. Goorjian and Y. Silberberg, *J. Opt. Soc. Am. B* **14**, 3523 (1997).
- [108] S. Nakamura, N. Takasawa, and Y. Koyamada, *J. Lightwave Technol.* **23**, 855 (2005).

# Group-Velocity Dispersion

# 3

The preceding chapter showed how the combined effects of group-velocity dispersion (GVD) and self-phase modulation (SPM) on optical pulses propagating inside a fiber can be studied by solving a pulse-propagation equation. Before considering the general case, it is instructive to study the effects of GVD alone. This chapter considers the pulse-propagation problem by treating fibers as a linear optical medium. In Section 3.1 we discuss the conditions under which the GVD effects dominate over the nonlinear effects by introducing two length scales associated with GVD and SPM. Dispersion-induced broadening of optical pulses is considered in Section 3.2 for several specific pulse shapes, including Gaussian and “sech” pulses. The effects of initial frequency chirping are also discussed in this section. Section 3.3 is devoted to the effects of third-order dispersion (TOD) on pulse broadening. An analytic theory capable of predicting dispersive broadening for pulses of arbitrary shapes is also given in this section. Section 3.4 discusses how the GVD limits the performance of optical communication systems and how the technique of dispersion management can be used to combat them in practice.

---

## 3.1 DIFFERENT PROPAGATION REGIMES

In Section 2.3 we focused on the nonlinear Schrödinger (NLS) equation that governs the propagation of optical pulses inside single-mode fibers. For pulse widths  $>5$  ps, we can use Eq. (2.3.46) in the form

$$i\frac{\partial A}{\partial z} = -\frac{i\alpha}{2}A + \frac{\beta_2}{2}\frac{\partial^2 A}{\partial T^2} - \gamma|A|^2A, \quad (3.1.1)$$

where  $A$  is the slowly varying amplitude of the pulse envelope and  $T$  is measured in a frame of reference moving with the pulse at the group velocity  $v_g$  ( $T = t - z/v_g$ ). The three terms on the right-hand side of Eq. (3.1.1) govern, respectively, the effects of fiber losses, dispersion, and nonlinearity on pulses propagating inside optical fibers. Depending on the initial width  $T_0$  and the peak power  $P_0$  of the incident pulse, either dispersive or nonlinear effects may dominate along the fiber. It is useful to introduce two length scales, known as the *dispersion length*  $L_D$  and the *nonlinear*

length  $L_{\text{NL}}$  [1–3]. Depending on the relative magnitudes of  $L_{\text{D}}$ ,  $L_{\text{NL}}$ , and the fiber length  $L$ , pulses can evolve quite differently.

Let us introduce a time scale normalized to the input pulse width  $T_0$  as

$$\tau = \frac{T}{T_0} = \frac{t - z/v_g}{T_0}. \quad (3.1.2)$$

At the same time, we introduce a normalized amplitude  $U$  as

$$A(z, \tau) = \sqrt{P_0} \exp(-\alpha z/2) U(z, \tau), \quad (3.1.3)$$

where  $P_0$  is the peak power of the incident pulse. The exponential factor in Eq. (3.1.3) accounts for fiber losses. By using Eqs (3.1.1)–(3.1.3),  $U(z, \tau)$  is found to satisfy

$$i \frac{\partial U}{\partial z} = \frac{\text{sgn}(\beta_2)}{2L_{\text{D}}} \frac{\partial^2 U}{\partial \tau^2} - \frac{\exp(-\alpha z)}{L_{\text{NL}}} |U|^2 U, \quad (3.1.4)$$

where  $\text{sgn}(\beta_2) = \pm 1$  depending on the sign of the GVD parameter  $\beta_2$  and

$$L_{\text{D}} = \frac{T_0^2}{|\beta_2|}, \quad L_{\text{NL}} = \frac{1}{\gamma P_0}. \quad (3.1.5)$$

The dispersion length  $L_{\text{D}}$  and the nonlinear length  $L_{\text{NL}}$  provide the length scales over which dispersive or nonlinear effects become important for pulse evolution. Depending on the relative magnitudes of  $L$ ,  $L_{\text{D}}$ , and  $L_{\text{NL}}$ , the propagation behavior can be classified in the following four categories.

When fiber length  $L$  is such that  $L \ll L_{\text{NL}}$  and  $L \ll L_{\text{D}}$ , neither dispersive nor nonlinear effects play a significant role during pulse propagation. This can be seen by noting that both terms on the right-hand side of Eq. (3.1.4) can be neglected. (It is assumed that the pulse has a smooth temporal profile so that  $\partial^2 U / \partial \tau^2 \sim 1$ .) As a result,  $U(z, \tau) = U(0, \tau)$ , i.e., the pulse maintains its shape during propagation. The fiber plays a passive role in this regime and acts as a mere transporter of optical pulses (except for reducing the pulse energy because of fiber losses). This regime is useful for optical communication systems. For  $L \sim 50$  km,  $L_{\text{D}}$  and  $L_{\text{NL}}$  should be larger than 500 km for distortion-free transmission. One can estimate  $T_0$  and  $P_0$  from Eq. (3.1.5) for given values of the fiber parameters  $\beta_2$  and  $\gamma$ . At  $\lambda = 1.55$  μm,  $|\beta_2| \approx 20$  ps<sup>2</sup>/km, and  $\gamma \approx 2$  W<sup>-1</sup> km<sup>-1</sup> for standard telecommunication fibers. The use of these values in Eq. (3.1.5) shows that the dispersive and nonlinear effects are negligible for  $L < 50$  km if  $T_0 > 100$  ps and  $P_0 < 1$  mW. However,  $L_{\text{D}}$  and  $L_{\text{NL}}$  become smaller as pulses become shorter and more intense. For example,  $L_{\text{D}}$  and  $L_{\text{NL}}$  are  $\sim 0.1$  km for  $T_0 \sim 1$  ps and  $P_0 \sim 1$  W. For such optical pulses, both the dispersive and nonlinear effects need to be included if the fiber length exceeds 10 m.

When the fiber length is such that  $L \ll L_{\text{NL}}$  but  $L \sim L_{\text{D}}$ , the last term in Eq. (3.1.4) is negligible compared to the other two. The pulse evolution is then governed by GVD, and the nonlinear effects play a relatively minor role. The effect of GVD on

propagation of optical pulses is discussed in this chapter. The dispersion-dominant regime is applicable whenever the fiber and pulse parameters are such that

$$\frac{L_D}{L_{NL}} = \frac{\gamma P_0 T_0^2}{|\beta_2|} \ll 1. \quad (3.1.6)$$

As a rough estimate,  $P_0$  should be  $\ll 1$  W for 1-ps pulses, if we use typical values for the fiber parameters  $\gamma$  and  $|\beta_2|$  at  $\lambda = 1.55 \mu\text{m}$ .

When the fiber length  $L$  is such that  $L \ll L_D$  but  $L \sim L_{NL}$ , the dispersion term in Eq. (3.1.4) is negligible compared to the nonlinear term (as long as the pulse has a smooth temporal profile such that  $\partial^2 U / \partial T^2 \sim 1$ ). In that case, pulse evolution in the fiber is governed by SPM that produces changes in the pulse spectrum. This phenomenon is considered in Chapter 4. The nonlinearity-dominant regime is applicable whenever

$$\frac{L_D}{L_{NL}} = \frac{\gamma P_0 T_0^2}{|\beta_2|} \gg 1. \quad (3.1.7)$$

This condition is readily satisfied for relatively wide pulses ( $T_0 > 100$  ps) with a peak power  $P_0 \sim 1$  W. Note that SPM can lead to pulse shaping in the presence of weak GVD effects. If the pulse develops a sharp leading or trailing edge, the dispersion term may become important even when Eq. (3.1.7) is initially satisfied.

When the fiber length  $L$  is longer or comparable to both  $L_D$  and  $L_{NL}$ , dispersion and nonlinearity act together as the pulse propagates along the fiber. The interplay of the GVD and SPM effects can lead to a qualitatively different behavior compared with that expected from GVD or SPM alone. In the anomalous-dispersion regime ( $\beta_2 < 0$ ), the fiber can support solitons. In the normal-dispersion regime ( $\beta_2 > 0$ ), the GVD and SPM effects can be used for pulse compression. Equation (3.1.4) is extremely helpful in understanding pulse evolution in optical fibers when both dispersive and nonlinear effects should be taken into account. However, this chapter is devoted to the linear regime, and the following discussion is applicable to pulses whose parameters satisfy Eq. (3.1.6).

## 3.2 DISPERSION-INDUCED PULSE BROADENING

The effects of GVD on optical pulses propagating in a linear dispersive medium [4–17] are studied by setting  $\gamma = 0$  in Eq. (3.1.1). If we define the normalized amplitude  $U(z, T)$  according to Eq. (3.1.3),  $U(z, T)$  satisfies the following linear partial differential equation:

$$i \frac{\partial U}{\partial z} = \frac{\beta_2}{2} \frac{\partial^2 U}{\partial T^2}. \quad (3.2.1)$$

This equation is similar to the paraxial wave equation that governs diffraction of CW light and becomes identical to it when diffraction occurs in only one transverse

direction and  $\beta_2$  is replaced by  $-\lambda/(2\pi)$ , where  $\lambda$  is the wavelength of light. For this reason, the dispersion-induced temporal effects have a close analogy with the diffraction-induced spatial effects [2].

Equation (3.2.1) is readily solved by using the Fourier-transform method. If  $\tilde{U}(z, \omega)$  is the Fourier transform of  $U(z, T)$  such that

$$U(z, T) = \frac{1}{2\pi} \int_{-\infty}^{\infty} \tilde{U}(z, \omega) \exp(-i\omega T) d\omega, \quad (3.2.2)$$

then it satisfies an ordinary differential equation

$$i \frac{\partial \tilde{U}}{\partial z} = -\frac{1}{2} \beta_2 \omega^2 \tilde{U}, \quad (3.2.3)$$

whose solution is given by

$$\tilde{U}(z, \omega) = \tilde{U}(0, \omega) \exp\left(\frac{i}{2} \beta_2 \omega^2 z\right). \quad (3.2.4)$$

Equation (3.2.4) shows that the GVD changes the phase of each spectral component of the pulse by an amount that depends on both the frequency and the propagated distance. Even though such phase changes do not affect the pulse spectrum, they can modify the pulse shape. By substituting Eq. (3.2.4) in Eq. (3.2.2), the general solution of Eq. (3.2.1) is given by

$$U(z, T) = \frac{1}{2\pi} \int_{-\infty}^{\infty} \tilde{U}(0, \omega) \exp\left(\frac{i}{2} \beta_2 \omega^2 z - i\omega T\right) d\omega, \quad (3.2.5)$$

where  $\tilde{U}(0, \omega)$  is the Fourier transform of the incident field at  $z = 0$  and is obtained using

$$\tilde{U}(0, \omega) = \int_{-\infty}^{\infty} U(0, T) \exp(i\omega T) dT. \quad (3.2.6)$$

Equations (3.2.5) and (3.2.6) can be used for input pulses of arbitrary shapes.

### 3.2.1 Gaussian Pulses

As a simple example, consider the case of a Gaussian pulse for which the incident field is of the form [8]

$$U(0, T) = \exp\left(-\frac{T^2}{2T_0^2}\right), \quad (3.2.7)$$

where  $T_0$  is the half-width (at  $1/e$ -intensity point) introduced in Section 3.1. In practice, it is customary to use the full width at half maximum (FWHM) in place of  $T_0$ . For a Gaussian pulse, the two are related as

$$T_{\text{FWHM}} = 2(\ln 2)^{1/2} T_0 \approx 1.665 T_0. \quad (3.2.8)$$

If we use Eqs (3.2.5)–(3.2.7) and carry out the integration over  $\omega$  using the well-known identity [18]

$$\int_{-\infty}^{\infty} \exp(-ax^2 - bx) dx = \sqrt{\frac{\pi}{a}} \exp\left(\frac{b^2}{4a}\right), \quad (3.2.9)$$

the amplitude  $U(z, T)$  at any point  $z$  along the fiber is given by

$$U(z, T) = \frac{T_0}{(T_0^2 - i\beta_2 z)^{1/2}} \exp\left[-\frac{T^2}{2(T_0^2 - i\beta_2 z)}\right]. \quad (3.2.10)$$

Thus, a Gaussian pulse maintains its shape on propagation but its width  $T_1$  increases with  $z$  as

$$T_1(z) = T_0[1 + (z/L_D)^2]^{1/2}, \quad (3.2.11)$$

where the dispersion length  $L_D = T_0^2/|\beta_2|$ . Equation (3.2.11) shows how GVD broadens a Gaussian pulse. The extent of broadening is governed by the dispersion length  $L_D$ . For a given fiber length, short pulses broaden more because of a smaller dispersion length. At  $z = L_D$ , a Gaussian pulse broadens by a factor of  $\sqrt{2}$ . Figure 3.1a shows the extent of dispersion-induced broadening for a Gaussian pulse by plotting  $|U(z, T)|^2$  at  $z/L_D = 2$  and 4.

A comparison of Eqs (3.2.7) and (3.2.10) shows that although the incident pulse is unchirped (with no phase modulation), the transmitted pulse becomes chirped. This can be seen clearly by writing  $U(z, T)$  in the form

$$U(z, T) = |U(z, T)| \exp[i\phi(z, T)], \quad (3.2.12)$$

where

$$\phi(z, T) = -\frac{\text{sgn}(\beta_2)(z/L_D)}{1 + (z/L_D)^2} \frac{T^2}{2T_0^2} + \frac{1}{2} \tan^{-1}\left(\text{sgn}(\beta_2) \frac{z}{L_D}\right). \quad (3.2.13)$$

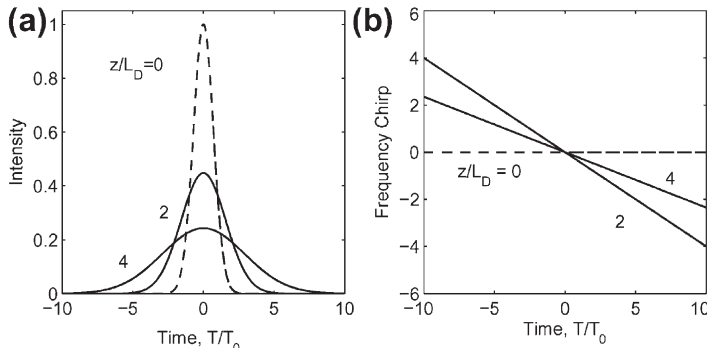


**Figure 3.1** Normalized (a) intensity  $|U|^2$  and (b) frequency chirp  $\delta\omega T_0$  as functions of  $T/T_0$  for a Gaussian pulse at  $z=2L_D$  and  $4L_D$ . Dashed lines show the input profiles at  $z=0$ .

The phase varies quadratically across the pulse at any distance  $z$ . It also depends on whether the pulse experiences normal or anomalous dispersion inside the fiber.

The time dependence of  $\phi(z, T)$  implies that the instantaneous frequency differs across the pulse from the central frequency  $\omega_0$ . The difference  $\delta\omega$  is just the time derivative  $-\partial\phi/\partial T$  [the minus sign is due to the choice  $\exp(-i\omega_0 t)$  in Eq. (2.3.2)] and is given by

$$\delta\omega(T) = -\frac{\partial\phi}{\partial T} = \frac{\text{sgn}(\beta_2)(z/L_D)}{1 + (z/L_D)^2} \frac{T}{T_0^2}. \quad (3.2.14)$$

Equation (3.2.14) shows that the frequency changes linearly across the pulse, i.e., a fiber imposes linear frequency chirp on the pulse. The chirp  $\delta\omega$  depends on the sign of  $\beta_2$ . In the normal-dispersion regime ( $\beta_2 > 0$ ),  $\delta\omega$  is negative at the leading edge ( $T < 0$ ) and increases linearly across the pulse. The opposite occurs in the anomalous-dispersion regime ( $\beta_2 < 0$ ); this case is shown in Figure 3.1b. As seen there, chirp imposed by GVD is perfectly linear for Gaussian pulses.

Dispersion-induced pulse broadening can be understood by recalling from Section 1.3 that different frequency components of a pulse travel at slightly different speeds along the fiber because of GVD. More specifically, red components travel faster than blue components in the normal-dispersion regime ( $\beta_2 > 0$ ), while the opposite occurs in the anomalous-dispersion regime ( $\beta_2 < 0$ ). The pulse can maintain its width only if all spectral components arrive together. Any time delay in the arrival of different spectral components leads to pulse broadening.

### 3.2.2 Chirped Gaussian Pulses

For an initially unchirped Gaussian pulse, Eq. (3.2.11) shows that dispersion-induced broadening of the pulse does not depend on the sign of the GVD parameter  $\beta_2$ . Thus, for a given value of the dispersion length  $L_D$ , the pulse broadens by the same amount in the normal- and anomalous-dispersion regimes of the fiber. This behavior changes if the Gaussian pulse has an initial frequency chirp [9]. In the case of linearly chirped Gaussian pulses, the incident field can be written as [compare with Eq. (3.2.7)]

$$U(0, T) = \exp \left[ -\frac{(1 + iC)}{2} \frac{T^2}{T_0^2} \right], \quad (3.2.15)$$

where  $C$  is a chirp parameter. By using Eq. (3.2.12) one finds that the instantaneous frequency increases linearly from the leading to the trailing edge (up-chirp) for  $C > 0$ , while the opposite occurs (down-chirp) for  $C < 0$ . It is common to refer to the chirp as being positive or negative, depending on whether  $C$  is positive or negative.

The numerical value of  $C$  can be estimated from the spectral width of the Gaussian pulse. By substituting Eq. (3.2.15) in Eq. (3.2.6) and using Eq. (3.2.9),  $\tilde{U}(0, \omega)$  is given by

$$\tilde{U}(0, \omega) = \left( \frac{2\pi T_0^2}{1 + iC} \right)^{1/2} \exp \left[ -\frac{\omega^2 T_0^2}{2(1 + iC)} \right]. \quad (3.2.16)$$

The spectral half-width (at  $1/e$ -intensity point) from Eq. (3.2.16) is given by

$$\Delta\omega = (1 + C^2)^{1/2} / T_0. \quad (3.2.17)$$

In the absence of frequency chirp ( $C = 0$ ), the spectral width is transformed, though limited, and satisfies the relation  $\Delta\omega T_0 = 1$ . Clearly, spectral width of a pulse is enhanced by a factor of  $(1 + C^2)^{1/2}$  in the presence of the linear chirp. Equation (3.2.17) can be used to estimate  $|C|$  from measurements of  $\Delta\omega$  and  $T_0$ .

To obtain the transmitted field,  $\tilde{U}(0, \omega)$  from Eq. (3.2.16) is substituted in Eq. (3.2.5). The integration can again be performed analytically using Eq. (3.2.9) with the result

$$U(z, T) = \frac{T_0}{[T_0^2 - i\beta_2 z(1 + iC)]^{1/2}} \exp \left( -\frac{(1 + iC)T^2}{2[T_0^2 - i\beta_2 z(1 + iC)]} \right). \quad (3.2.18)$$

Thus, even a chirped Gaussian pulse maintains its Gaussian shape on propagation. The width  $T_1$  after propagating a distance  $z$  is related to the initial width  $T_0$  by the relation [9]

$$\frac{T_1}{T_0} = \left[ \left( 1 + \frac{C\beta_2 z}{T_0^2} \right)^2 + \left( \frac{\beta_2 z}{T_0^2} \right)^2 \right]^{1/2}. \quad (3.2.19)$$

The chirp parameter of the pulse also changes from  $C$  to  $C_1$  such that

$$C_1(z) = C + (1 + C^2)(\beta_2 z / T_0^2). \quad (3.2.20)$$

It is useful to define a normalized distance  $\xi$  as  $\xi = z/L_D$ , where  $L_D \equiv T_0^2/|\beta_2|$  is the dispersion length introduced earlier. Figure 3.2 shows (a) the broadening factor  $T_1/T_0$  and (b) the chirp parameter  $C_1$  as a function of  $\xi$  in the case of anomalous dispersion ( $\beta_2 < 0$ ). An unchirped pulse ( $C = 0$ ) broadens monotonically by a factor of  $(1 + \xi^2)^{1/2}$  and develops a negative chirp such that  $C_1 = -\xi$  (the dotted curves). Chirped pulses, on the other hand, may broaden or compress depending on whether  $\beta_2$  and  $C$  have the same or opposite signs. When  $\beta_2 C > 0$ , a chirped Gaussian pulse broadens monotonically at a rate faster than that of the unchirped pulse (the dashed curves). The reason is related to the fact that the dispersion-induced chirp adds to the input chirp because the two contributions have the same sign.

The situation changes dramatically for  $\beta_2 C < 0$ . In this case, the contribution of the dispersion-induced chirp is of a kind opposite to that of the input chirp. As seen

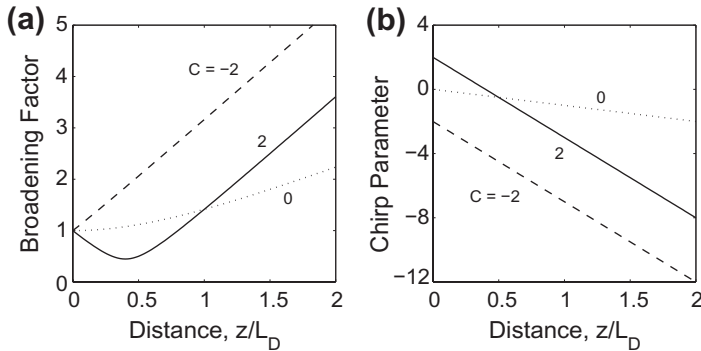


**Figure 3.2** Broadening factor (a) and the chirp parameter (b) as functions of distance for a chirped Gaussian pulse propagating in the anomalous-dispersion region of a fiber. Dashed curves correspond to the case of an unchirped Gaussian pulse. The same curves are obtained for normal dispersion ( $\beta_2 > 0$ ) if the sign of  $C$  is reversed.

from Figure 3.2b and Eq. (3.2.20),  $C_1$  becomes zero at a distance  $\xi = |C|/(1 + C^2)$ , and the pulse becomes unchirped. This is the reason why the pulse width initially decreases in Figure 3.2a and becomes minimum at that distance. The minimum value of the pulse width depends on the input chirp parameter as

$$T_1^{\min} = \frac{T_0}{(1 + C^2)^{1/2}}. \quad (3.2.21)$$

Since  $C_1 = 0$  when the pulse attains its minimum width, it becomes transformed, limited such that  $\Delta\omega_0 T_1^{\min} = 1$ , where  $\Delta\omega_0$  is the input spectral width of the pulse.

### 3.2.3 Hyperbolic-Secant Pulses

Although pulses emitted from many lasers can be approximated by a Gaussian shape, it is necessary to consider other pulse shapes. Of particular interest is the hyperbolic secant pulse shape that occurs naturally in the context of optical solitons and pulses emitted from some mode-locked lasers. The optical field associated with such pulses often takes the form

$$U(0, T) = \operatorname{sech}\left(\frac{T}{T_0}\right) \exp\left(-\frac{iCT^2}{2T_0^2}\right), \quad (3.2.22)$$

where the chirp parameter  $C$  controls the initial chirp similarly to that of Eq. (3.2.15).

The transmitted field  $U(z, T)$  is obtained by using Eqs (3.2.5), (3.2.6), and (3.2.22). Unfortunately, it is not easy to evaluate the integral in Eq. (3.2.5) in a closed form for non-Gaussian pulse shapes. Figure 3.3 shows the intensity and chirp profiles

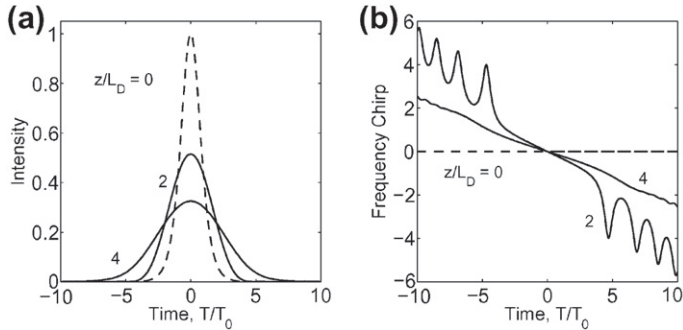


**Figure 3.3** Normalized (a) intensity  $|U|^2$  and (b) frequency chirp  $\delta\omega T_0$  as a function of  $T/T_0$  for a “sech” pulse at  $z=2L_D$  and  $4L_D$ . Dashed lines show the input profiles at  $z=0$ . Compare with [Figure 3.1](#) where the case of a Gaussian pulse is shown.

calculated numerically at  $z = 2L_D$  and  $z = 4L_D$  for initially unchirped pulses ( $C = 0$ ). A comparison of [Figures 3.1](#) and [3.3](#) shows that the qualitative features of dispersion-induced broadening are nearly identical for the Gaussian and “sech” pulses. The main difference is that the dispersion-induced chirp is no longer purely linear across the pulse. Note that  $T_0$  appearing in Eq. (3.2.22) is not the FWHM but is related to it by

$$T_{\text{FWHM}} = 2 \ln(1 + \sqrt{2}) T_0 \approx 1.763 T_0. \quad (3.2.23)$$

This relation should be used if the comparison is made on the basis of FWHM. The same relation for a Gaussian pulse is given in Eq. (3.2.8).

### 3.2.4 Super-Gaussian Pulses

So far we have considered pulse shapes with relatively broad leading and trailing edges. As one may expect, dispersion-induced broadening is sensitive to the steepness of pulse edges. In general, a pulse with steeper leading and trailing edges broadens more rapidly with propagation simply because such a pulse has a wider spectrum to start with. Pulses used as bits in certain lightwave systems fall in this category. A super-Gaussian shape can be used to model the effects of steep leading and trailing edges on dispersion-induced pulse broadening. For a super-Gaussian pulse, Eq. (3.2.15) is generalized to take the form [16]

$$U(0, T) = \exp \left[ -\frac{1+iC}{2} \left( \frac{T}{T_0} \right)^{2m} \right], \quad (3.2.24)$$

where the parameter  $m$  controls the degree of edge sharpness. For  $m = 1$  we recover the case of chirped Gaussian pulses. For a larger value of  $m$ , the pulse becomes square shaped with sharper leading and trailing edges. If the rise time  $T_r$  is defined as

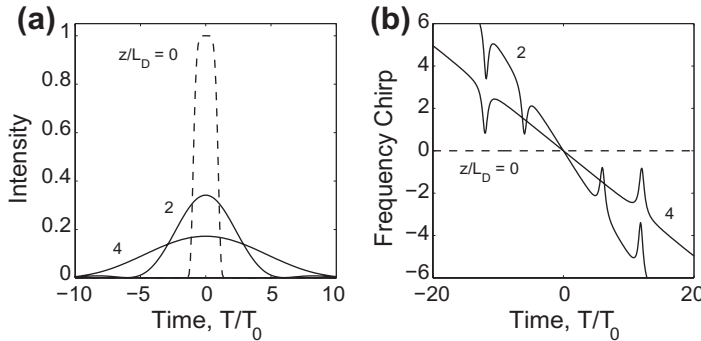


**Figure 3.4** Normalized (a) intensity  $|U|^2$  and (b) frequency chirp  $\delta\omega T_0$  as a function of  $T/T_0$  for a super-Gaussian pulse at  $z=2L_D$  and  $4L_D$ . Dashed lines show the input profiles at  $z=0$ . Compare with [Figure 3.1](#) where the case of a Gaussian pulse is shown.

the duration during which the intensity increases from 10% to 90% of its peak value, it is related to the parameter  $m$  as

$$T_r = (\ln 9) \frac{T_0}{2m} \approx \frac{T_0}{m}. \quad (3.2.25)$$

Thus the parameter  $m$  can be determined from the measurements of  $T_r$  and  $T_0$ .

[Figure 3.4](#) shows the intensity and chirp profiles at  $z = 2L_D$  and  $4L_D$  in the case of an initially unchirped super-Gaussian pulse ( $C = 0$ ) by using  $m = 3$ . It should be compared with [Figure 3.1](#) where the case of a Gaussian pulse ( $m = 1$ ) is shown. The differences between the two can be attributed to the steeper leading and trailing edges associated with a super-Gaussian pulse. Whereas the Gaussian pulse maintains its shape during propagation, the super-Gaussian pulse not only broadens at a faster rate but is also distorted in shape. The chirp profile is also far from being linear and exhibits high-frequency oscillations. Enhanced broadening of a super-Gaussian pulse can be understood by noting that its spectrum is wider than that of a Gaussian pulse because of steeper leading and trailing edges. As the GVD-induced delay of each frequency component is directly related to its separation from the central frequency  $\omega_0$ , a wider spectrum results in a faster rate of pulse broadening.

For complicated pulse shapes such as those seen in [Figure 3.4](#), the FWHM is not a true measure of the pulse width. The width of such pulses is more accurately described by the root-mean-square (RMS) width  $\sigma$  defined as [8]

$$\sigma = [\langle T^2 \rangle - \langle T \rangle^2]^{1/2}, \quad (3.2.26)$$

where the angle brackets denote averaging over the intensity profile as

$$\langle T^n \rangle = \frac{\int_{-\infty}^{\infty} T^n |U(z, T)|^2 dT}{\int_{-\infty}^{\infty} |U(z, T)|^2 dT}. \quad (3.2.27)$$

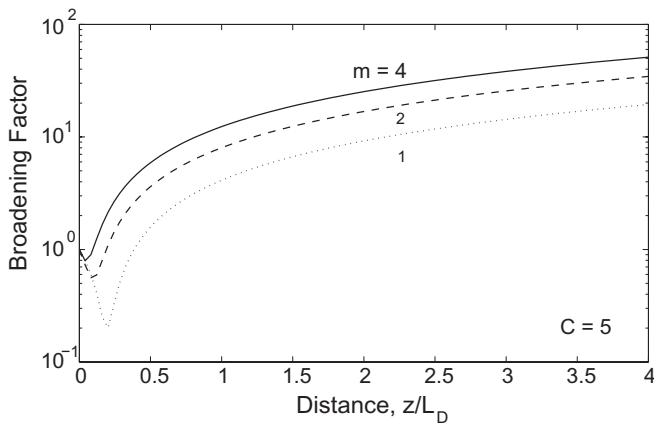


**Figure 3.5** Broadening factor  $\sigma/\sigma_0$  as a function of  $z/L_D$  in the anomalous-dispersion regime for chirped super-Gaussian pulses with  $C=5$ . The case  $m=1$  corresponds to a Gaussian pulse. Pulse edges become steeper with increasing values of  $m$ .

The moments  $\langle T \rangle$  and  $\langle T^2 \rangle$  can be calculated analytically for some specific cases. In particular, it is possible to evaluate the broadening factor  $\sigma/\sigma_0$  analytically for super-Gaussian pulses using Eqs (3.2.5) and (3.2.24)–(3.2.27) with the result [17]

$$\frac{\sigma}{\sigma_0} = \left[ 1 + \frac{\Gamma(1/2m)}{\Gamma(3/2m)} \frac{C\beta_2 z}{T_0^2} + m^2(1+C^2) \frac{\Gamma(2-1/2m)}{\Gamma(3/2m)} \left( \frac{\beta_2 z}{T_0^2} \right)^2 \right]^{1/2}, \quad (3.2.28)$$

where  $\Gamma(x)$  is the gamma function. For a Gaussian pulse ( $m = 1$ ) the broadening factor reduces to that given in Eq. (3.2.19).

To see how pulse broadening depends on the steepness of pulse edges, Figure 3.5 shows the broadening factor  $\sigma/\sigma_0$  of super-Gaussian pulses as a function of the propagation distance for values of  $m$  ranging from 1 to 4. The case  $m = 1$  corresponds to a Gaussian pulse; the pulse edges become increasingly steep for larger values of  $m$ . Noting from Eq. (3.2.25) that the rise time is inversely proportional to  $m$ , it is evident that a pulse with a shorter rise time broadens faster. The curves in Figure 3.5 are drawn for the case of initially chirped pulses with  $C = 5$ . When the pulses are initially chirped, the magnitude of pulse broadening depends on the sign of the product  $\beta_2 C$ . The qualitative behavior is similar to that shown in Figure 3.2 for the case of a Gaussian pulse ( $m = 1$ ), although pulse compression is reduced considerably for super-Gaussian pulses.

### 3.2.5 Experimental Results

The initial compression of chirped pulses has been observed experimentally using pulses emitted from a directly modulated semiconductor laser. In one experiment [10], the incident pulse at a wavelength of  $1.54 \mu\text{m}$  was positively chirped ( $C > 0$ ).

It compressed by about a factor of 5 after propagating 104 km in the anomalous-GVD regime of a fiber with  $\beta_2 \approx -20 \text{ ps}^2/\text{km}$ . In another experiment, the semiconductor laser emitted a negatively chirped pulse ( $C < 0$ ) at a wavelength of  $1.21 \mu\text{m}$  [11]. After propagating a distance of 1.5 km in the normal-dispersion regime ( $\beta_2 = 15 \text{ ps}^2/\text{km}$ ), the pulse width decreased from 190 to 150 ps. When the fiber length was increased to 6 km, the pulse width increased to 300 ps, in agreement with the qualitative behavior shown in Figure 3.2. In a different experiment much shorter optical pulses (initial FWHM  $\approx 26 \text{ ps}$ ) at  $1.3 \mu\text{m}$  were obtained from a distributed-feedback (DFB) semiconductor laser by using the gain-switching technique [15]. As the pulses were negatively chirped ( $C < 0$ ), a dispersion-shifted fiber was employed with a positive GVD at  $1.3 \mu\text{m}$  ( $\beta_2 \approx 12 \text{ ps}^2/\text{km}$ ). The pulse compressed by a factor of three after propagating inside a 4.8-km-long fiber and then started to broaden with a further increase in the fiber length.

Compression of chirped picosecond pulses through GVD in optical fibers has been used to advantage in some experiments in which a gain-switched DFB semiconductor laser was used as a source of solitons [19–22]. Even though a relatively broad optical pulse (duration 20–40 ps) emitted from such lasers is far from being transform limited, its passage through a fiber of optimized length with positive GVD produces compressed optical pulses that are nearly transform limited. In a 1989 demonstration of this technique [21], 14-ps pulses were obtained at the 3-GHz repetition rate by passing the gain-switched pulse through a polarization-preserving, dispersion-shifted, 3.7-km-long optical fiber with  $\beta_2 = 23 \text{ ps}^2/\text{km}$  at the  $1.55 \mu\text{m}$  operating wavelength. In another experiment, a narrowband optical filter was used to control the spectral width of the gain-switched pulse before its compression [22]. An erbium-doped fiber amplifier then amplified and compressed the pulse simultaneously. It was possible to generate nearly transform-limited 17-ps optical pulses at repetition rates of 6–24 GHz. Pulses as short as 3 ps were obtained by 1990 with this technique [23].

In a related method, amplification of picosecond pulses in a semiconductor laser amplifier produces optical pulses chirped such that they can be compressed by using optical fibers with anomalous GVD [24–26]. The method is useful in the wavelength region near  $1.5 \mu\text{m}$  because silica fibers commonly exhibit anomalous GVD in that spectral region. The technique was demonstrated in 1989 by using 40-ps input pulses obtained from a  $1.52 \mu\text{m}$  mode-locked semiconductor laser [24]. The pulse was first amplified in a semiconductor laser amplifier and then compressed by about a factor of two by propagating it through an 18-km-long fiber with  $\beta_2 = -18 \text{ ps}^2/\text{km}$ . Such a compression mechanism was useful for transmitting a 16-Gb/s signal over 70 km of standard telecommunication fiber [25].

### 3.3 THIRD-ORDER DISPERSION

The dispersion-induced pulse broadening discussed in Section 3.2 is due to the lowest-order GVD term proportional to  $\beta_2$  in Eq. (2.3.23). Although the contribution of this term dominates in most cases of practical interest, it is sometimes necessary

to include the third-order dispersion (TOD) governed by  $\beta_3$ . For example, if the pulse wavelength nearly coincides with the zero-dispersion wavelength  $\lambda_D$  and  $\beta_2 \approx 0$ , the  $\beta_3$  term provides the dominant contribution to the GVD effects [6]. For ultra-short pulses (with width  $T_0 < 1$  ps), it is necessary to include the  $\beta_3$  term even when  $\beta_2 \neq 0$  because the expansion parameter  $\Delta\omega/\omega_0$  is no longer small enough to justify the truncation of the expansion in Eq. (2.3.23) after the  $\beta_2$  term.

This section considers the dispersive effects by including both  $\beta_2$  and  $\beta_3$  terms while still neglecting the nonlinear effects. The appropriate propagation equation for the amplitude  $A(z, T)$  is obtained from Eq. (2.3.44) after setting  $\gamma = 0$ . Using Eq. (3.1.3),  $U(z, T)$  satisfies the following equation:

$$i \frac{\partial U}{\partial z} = \frac{\beta_2}{2} \frac{\partial^2 U}{\partial T^2} + \frac{i\beta_3}{6} \frac{\partial^3 U}{\partial T^3}. \quad (3.3.1)$$

This equation can also be solved by using the Fourier-transform technique of Section 3.2. In place of Eq. (3.2.5) the transmitted field is obtained from

$$U(z, T) = \frac{1}{2\pi} \int_{-\infty}^{\infty} \tilde{U}(0, \omega) \exp\left(\frac{i}{2}\beta_2\omega^2 z + \frac{i}{6}\beta_3\omega^3 z - i\omega T\right) d\omega, \quad (3.3.2)$$

where the Fourier transform  $\tilde{U}(0, \omega)$  of the incident field is given by Eq. (3.2.6). Equation (3.3.2) can be used to study the effect of higher-order dispersion if the incident field  $U(0, T)$  is specified. In particular, one can consider Gaussian, super-Gaussian, or hyperbolic-secant pulses in a manner analogous to Section 3.2. As an analytic solution in terms of the Airy functions can be obtained for Gaussian pulses [6], we consider this case first.

### 3.3.1 Evolution of Chirped Gaussian Pulses

In the case of a chirped Gaussian pulse, we use  $\tilde{A}(0, \omega)$  from Eq. (3.2.16) in Eq. (3.3.2) and introduce  $x = \omega p$  as a new integration variable, where

$$p^2 = \frac{T_0^2}{2} \left( \frac{1}{1+iC} - \frac{i\beta_2 z}{T_0^2} \right). \quad (3.3.3)$$

We then obtain the following expression:

$$U(z, T) = \frac{A_0}{\sqrt{\pi}} \int_{-\infty}^{\infty} \exp\left(-x^2 + \frac{ib}{3}x^3 - \frac{iT}{p}x\right) dx, \quad (3.3.4)$$

where  $b = \beta_3 z / (2p^3)$ . The  $x^2$  term can be eliminated with another transformation,  $x = b^{-1/3}u - i/b$ . The resulting integral can be written in terms of the Airy function  $\text{Ai}(x)$  as

$$U(z, T) = \frac{2A_0\sqrt{\pi}}{|b|^{1/3}} \exp\left(\frac{2p - 3bT}{3pb^2}\right) \text{Ai}\left(\frac{p - bT}{|b|^{4/3}}\right). \quad (3.3.5)$$

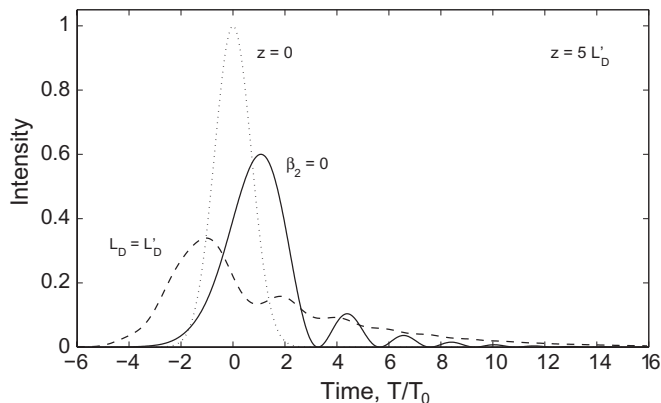


**Figure 3.6** Pulse shapes at  $z = 5L'_D$  of an initially Gaussian pulse at  $z=0$  (dotted curve) in the presence of higher-order dispersion. The solid curve is for the case of  $\lambda_0=\lambda_D$ . The dashed curve shows the effect of finite  $\beta_2$  in the case of  $L_D = L'_D$ .

where  $p$  depends on the fiber and pulse parameters as indicated in Eq. (3.3.3). For an unchirped pulse whose spectrum is centered exactly at the zero-dispersion wavelength of the fiber ( $\beta_2 = 0$ ),  $p = T_0/\sqrt{2}$ .

As one may expect, pulse evolution along the fiber depends on the relative magnitudes of  $\beta_2$  and  $\beta_3$ . To compare the relative importance of the  $\beta_2$  and  $\beta_3$  terms in Eq. (3.3.1), it is useful to introduce a dispersion length associated with the TOD as

$$L'_D = T_0^3/|\beta_3|. \quad (3.3.6)$$

The TOD effects play a significant role only if  $L'_D \leq L_D$  or  $T_0|\beta_2/\beta_3| \leq 1$ . For a 100-ps pulse, this condition implies that  $\beta_2 < 10^{-3} \text{ ps}^2/\text{km}$  when  $\beta_3 = 0.1 \text{ ps}^3/\text{km}$ . Such low values of  $\beta_2$  are realized only if  $\lambda_0$  and  $\lambda_D$  differ by  $<0.01 \text{ nm}$ . In practice, it is difficult to match  $\lambda_0$  and  $\lambda_D$  to such an accuracy, and the contribution of  $\beta_3$  is generally negligible compared with that of  $\beta_2$ . This was indeed the case in the experiments in which picosecond pulses were propagated near the zero-dispersion wavelength of a fiber [27]. The situation changes completely for ultrashort pulses with widths in the femtosecond range. For example,  $\beta_2$  can be as large as  $1 \text{ ps}^2/\text{km}$  for  $T_0 = 0.1 \text{ ps}$  before the contribution of  $\beta_3$  becomes negligible. As  $L'_D \sim 10 \text{ m}$  for such values of  $T_0$ , the effect of TOD can be studied experimentally by propagating 100-fs pulses across a few-meter-long fiber.

Figure 3.6 shows the pulse shapes at  $z = 5L'_D$  for an initially unchirped Gaussian pulse ( $C = 0$ ) for  $\beta_2 = 0$  (solid curve) and for a value of  $\beta_2$  such that  $L_D = L'_D$  (dashed curve). Whereas a Gaussian pulse remains Gaussian when only the  $\beta_2$  term in Eq. (3.3.1) contributes to GVD (Figure 3.1), the TOD distorts the pulse such that it becomes asymmetric with an oscillatory structure near one of its edges. In the case

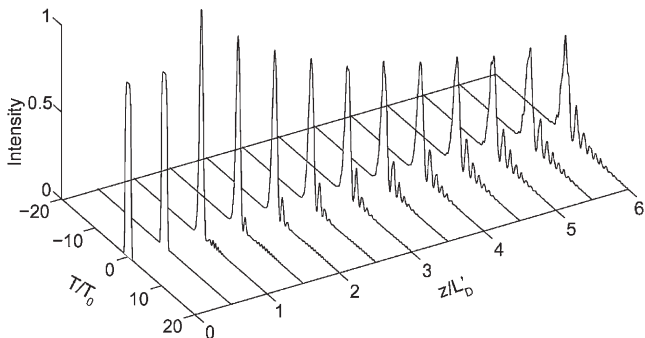


**Figure 3.7** Evolution of a super-Gaussian pulse with  $m=3$  along the fiber length for the case of  $\beta_2=0$  and  $\beta_3>0$ . Third-order dispersion is responsible for the oscillatory structure near the trailing edge of the pulse.

of positive  $\beta_3$  shown in Figure 3.6, oscillations appear near the trailing edge of the pulse. When  $\beta_3$  is negative, it is the leading edge of the pulse that develops oscillations. When  $\beta_2 = 0$ , oscillations are deep, with intensity dropping to zero between successive oscillations. However, these oscillations damp significantly even for relatively small values of  $\beta_2$ . For the case  $L_D = L'_D$  shown in Figure 3.6 ( $\beta_2 = \beta_3/T_0$ ), oscillations have nearly disappeared, and the pulse has a long tail on the trailing side. For larger values of  $\beta_2$  such that  $L_D \ll L'_D$ , the pulse shape becomes nearly Gaussian as the TOD plays a relatively minor role.

Equation (3.3.2) can be used to study pulse evolution for other pulse shapes although the Fourier transform must be performed numerically. As an example, Figure 3.7 shows evolution of an unchirped super-Gaussian pulse at the zero-dispersion wavelength ( $\beta_2 = 0$ ) with  $C = 0$  and  $m = 3$  in Eq. (3.2.24). It is clear that pulse shapes can vary widely depending on the initial conditions. In practice, one is often interested in the extent of dispersion-induced broadening rather than details of pulse shapes. As the FWHM is not a true measure of the width of pulses shown in Figures 3.6 and 3.7, we use the RMS width  $\sigma$  defined in Eq. (3.2.26). In the case of Gaussian pulses, it is possible to obtain a simple analytic expression of  $\sigma$  that includes the effects of  $\beta_2$ ,  $\beta_3$ , and the initial chirp  $C$  on dispersion broadening [9].

### 3.3.2 Broadening Factor

To calculate  $\sigma$  from Eq. (3.2.26), we need to find the  $n$ th moment  $\langle T^n \rangle$  of  $T$  using Eq. (3.2.27). As the Fourier transform  $\tilde{U}(z, \omega)$  of  $U(z, T)$  is known from Eq. (3.3.2), it is useful to evaluate  $\langle T^n \rangle$  in the frequency domain. By using the Fourier transform  $\tilde{I}(z, \omega)$  of the pulse intensity  $|U(z, T)|^2$ ,

$$\tilde{I}(z, \omega) = \int_{-\infty}^{\infty} |U(z, T)|^2 \exp(i\omega T) dT, \quad (3.3.7)$$

and differentiating it  $n$  times, we obtain

$$\lim_{\omega \rightarrow 0} \frac{\partial^n}{\partial \omega^n} \tilde{I}(z, \omega) = (\mathrm{i})^n \int_{-\infty}^{\infty} T^n |U(z, T)|^2 dT. \quad (3.3.8)$$

Using Eq. (3.3.8) in Eq. (3.2.27) we find that

$$\langle T^n \rangle = \frac{(-\mathrm{i})^n}{N_c} \lim_{\omega \rightarrow 0} \frac{\partial^n}{\partial \omega^n} \tilde{I}(z, \omega), \quad (3.3.9)$$

where the normalization constant

$$N_c = \int_{-\infty}^{\infty} |U(z, T)|^2 dT \equiv \int_{-\infty}^{\infty} |U(0, T)|^2 dT. \quad (3.3.10)$$

From the convolution theorem

$$\tilde{I}(z, \omega) = \int_{-\infty}^{\infty} \tilde{U}(z, \omega - \omega') \tilde{U}^*(z, \omega') d\omega'. \quad (3.3.11)$$

Performing the differentiation and limit operations indicated in Eq. (3.3.9), we obtain

$$\langle T^n \rangle = \frac{(\mathrm{i})^n}{N_c} \int_{-\infty}^{\infty} \tilde{U}^*(z, \omega) \frac{\partial^n}{\partial \omega^n} \tilde{U}(z, -\omega) d\omega. \quad (3.3.12)$$

In the case of a chirped Gaussian pulse,  $\tilde{U}(z, \omega)$  can be obtained from Eqs (3.2.16) and (3.3.2) and is given by

$$\tilde{U}(z, \omega) = \left( \frac{2\pi T_0^2}{1 + \mathrm{i}C} \right)^{1/2} \exp \left[ \frac{\mathrm{i}\omega^2}{2} \left( \beta_2 z + \frac{\mathrm{i}T_0^2}{1 + \mathrm{i}C} \right) + \frac{\mathrm{i}}{6} \beta_3 \omega^3 z \right]. \quad (3.3.13)$$

If we differentiate Eq. (3.3.13) two times and substitute the result in Eq. (3.3.12), we find that the integration over  $\omega$  can be performed analytically. Both  $\langle T \rangle$  and  $\langle T^2 \rangle$  can be obtained by this procedure. Using the resulting expressions in Eq. (3.2.26), we obtain [9]

$$\frac{\sigma}{\sigma_0} = \left[ \left( 1 + \frac{C\beta_2 z}{2\sigma_0^2} \right)^2 + \left( \frac{\beta_2 z}{2\sigma_0^2} \right)^2 + (1 + C^2)^2 \frac{1}{2} \left( \frac{\beta_3 z}{4\sigma_0^3} \right)^2 \right]^{1/2}, \quad (3.3.14)$$

where  $\sigma_0$  is the initial RMS width of the chirped Gaussian pulse ( $\sigma_0 = T_0/\sqrt{2}$ ). As expected, Eq. (3.3.14) reduces to Eq. (3.2.19) for  $\beta_3 = 0$ .

Equation (3.3.14) can be used to draw several interesting conclusions. In general, both  $\beta_2$  and  $\beta_3$  contribute to pulse broadening. However, the dependence of their contributions on the chirp parameter  $C$  is qualitatively different. Whereas the contribution of  $\beta_2$  depends on the sign of  $\beta_2 C$ , the contribution of  $\beta_3$  is independent of the sign of both  $\beta_3$  and  $C$ . Thus, in contrast to the behavior shown in Figure 3.2, a chirped pulse propagating exactly at the zero-dispersion wavelength never experiences width

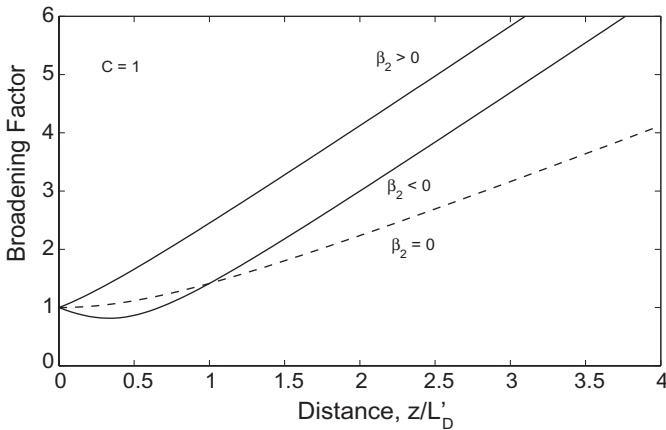


**Figure 3.8** Broadening factor as a function of  $z/L'_D$  for a chirped Gaussian pulse in the vicinity of  $\lambda_D$  such that  $L_D = L'_D$ . Dashed curve corresponds to the case of  $\lambda_0 = \lambda_D$  ( $\beta_2 = 0$ ).

contraction. However, even small departures from the exact zero-dispersion wavelength can lead to initial pulse contraction. This behavior is illustrated in Figure 3.8 where the broadening factor  $\sigma/\sigma_0$  is plotted as a function of  $z/L'_D$  for  $C = 1$  and  $L_D = L'_D$ . The dashed curve shows, for comparison, the broadening expected when  $\beta_2 = 0$ . In the anomalous-dispersion regime the contribution of  $\beta_2$  can counteract the  $\beta_3$  contribution in such a way that dispersive broadening is less than that expected when  $\beta_2 = 0$  for  $z \sim L'_D$ . For large values of  $z$  such that  $z \gg L_D/|C|$ , Eq. (3.3.14) can be approximated by

$$\sigma/\sigma_0 = (1 + C^2)^{1/2} [1 + (1 + C^2)(L_D/2L'_D)^2]^{1/2} (z/L_D), \quad (3.3.15)$$

where we have used Eqs (3.1.5) and (3.3.6). The linear dependence of the RMS pulse width on the propagation distance for large values of  $z$  is a general feature that holds for arbitrary pulse shapes, as discussed in the next section.

Equation (3.3.14) can be generalized to include the effects of a finite source bandwidth [9]. Spontaneous emission in any light source produces amplitude and phase fluctuations that manifest as a finite bandwidth  $\delta\omega$  of the source spectrum centered at  $\omega_0$  [28]. If the source bandwidth  $\delta\omega$  is much smaller than the pulse bandwidth  $\Delta\omega$ , its effect on the pulse broadening can be neglected. However, for many light sources such as light-emitting diodes (LEDs) this condition is not satisfied, and it becomes necessary to include the effects of a finite source bandwidth. In the case of a Gaussian pulse and a Gaussian source spectrum, the generalized form of Eq. (3.3.14) is given by [9]

$$\frac{\sigma^2}{\sigma_0^2} = \left(1 + \frac{C\beta_2 z}{2\sigma_0^2}\right)^2 + \left(1 + V_\omega^2\right) \left(\frac{\beta_2 z}{\sigma_0^2}\right)^2 + \left(1 + C^2 + V_\omega^2\right)^2 \frac{1}{2} \left(\frac{\beta_3 z}{4\sigma_0^3}\right)^2, \quad (3.3.16)$$

where  $V_\omega = 2\sigma_\omega\sigma_0$  and  $\sigma_\omega$  is the RMS width of the Gaussian source spectrum. This equation describes the broadening of chirped Gaussian pulses in a linear dispersive medium under quite general conditions. It can be used to discuss the effect of GVD on the performance of lightwave systems [29].

### 3.3.3 Arbitrary-Shape Pulses

The formal similarity of Eq. (3.2.1) with the Schrödinger equation can be exploited to obtain an analytic expression of the RMS width for pulses of arbitrary shape while including the third- and higher-order dispersive effects [30]. For this purpose, we write Eq. (3.3.1) in an operator form as

$$i \frac{\partial U}{\partial z} = \hat{H}U, \quad (3.3.17)$$

where the operator  $\hat{H}$  includes, in its general form, dispersive effects to all orders and is given by

$$\hat{H} = - \sum_{n=2}^{\infty} \frac{i^n}{n!} \left( \frac{\partial}{\partial T} \right)^n = \frac{\beta_2}{2} \frac{\partial^2}{\partial T^2} + \frac{i\beta_3}{6} \frac{\partial^3}{\partial T^3} + \dots \quad (3.3.18)$$

Using Eq. (3.2.27) and assuming that  $U(z, T)$  is normalized such that  $\int_{-\infty}^{\infty} |U|^2 dT = 1$ , the first and second moments of  $T$  are found to evolve with  $z$  as

$$\frac{d\langle T \rangle}{dz} = i \int_{-\infty}^{\infty} U^*(z, T) [\hat{H}, T] U(z, T) dT, \quad (3.3.19)$$

$$\frac{d\langle T^2 \rangle}{dz} = i^2 \int_{-\infty}^{\infty} U^*(z, T) [\hat{H}, [\hat{H}, T]] U(z, T) dT, \quad (3.3.20)$$

where  $[\hat{H}, T] \equiv \hat{H}T - T\hat{H}$  stands for the commutator.

Equations (3.3.19) and (3.3.20) can be integrated analytically and result in the following general expressions [30]:

$$\langle T \rangle = a_0 + a_1 z, \quad (3.3.21)$$

$$\langle T^2 \rangle = b_0 + b_1 z + b_2 z^2, \quad (3.3.22)$$

where the coefficients depend only on the incident field  $U_0(T) \equiv U(0, T)$  and are defined as

$$a_0 = \int_{-\infty}^{\infty} U_0^*(T) T U_0(T) dT, \quad (3.3.23)$$

$$a_1 = i \int_{-\infty}^{\infty} U_0^*(T) [\hat{H}, T] U_0(T) dT, \quad (3.3.24)$$

$$b_0 = \int_{-\infty}^{\infty} U_0^*(T) T^2 U_0(T) dT, \quad (3.3.25)$$

$$b_1 = i \int_{-\infty}^{\infty} U_0^*(T) [\hat{H}, T^2] U_0(T) dT, \quad (3.3.26)$$

$$b_2 = -\frac{1}{2} \int_{-\infty}^{\infty} U_0^*(T) [\hat{H}, [\hat{H}, T^2]] U_0(T) dT. \quad (3.3.27)$$

Physically,  $\langle T \rangle$  governs asymmetry of pulse shape while  $\langle T^2 \rangle$  is a measure of pulse broadening. Higher-order moments  $\langle T^3 \rangle$  and  $\langle T^4 \rangle$  can also be calculated by this technique and govern the skewness and kurtosis of the intensity profile, respectively. For initially symmetric pulses,  $a_0 = 0$ . If the effects of third- and higher-order dispersion are negligible it is easy to show that  $a_1$  is also zero. Since  $\langle T \rangle = 0$  in that case, the pulse retains its symmetric nature during its transmission through optical fibers. The variance  $\sigma^2 \equiv \langle T^2 \rangle - \langle T \rangle^2$  varies quadratically along the fiber length for pulses of arbitrary shape and chirp even when third- and higher-order dispersive effects are included.

As a simple example, consider the case of an unchirped “sech” pulse discussed in Section 3.2.3 numerically and retain only the effects of GVD ( $\beta_m = 0$  for  $m > 2$ ). Using  $U_0(T) = (2T_0)^{-1/2} \text{sech}(T/T_0)$  in Eqs (3.3.23)–(3.3.27) one can show that  $a_0 = a_1 = b_1 = 0$ , while

$$b_0 = (\pi^2/12)T_0^2, \quad b_2 = \beta_2^2/(3T_0^2). \quad (3.3.28)$$

Noting that  $\sigma_0^2 = b_0$  and  $\sigma^2 = b_0 + b_2 z^2$ , the broadening factor becomes

$$\frac{\sigma}{\sigma_0} = \left[ 1 + \left( \frac{\pi \beta_2 z}{6\sigma_0^2} \right)^2 \right]^{1/2}, \quad (3.3.29)$$

where  $\sigma_0 = (\pi/\sqrt{12})T_0$  is the RMS width of the input pulse. This result should be compared with Eq. (3.3.14) obtained for a Gaussian pulse after setting  $C = 0$  and  $\beta_3 = 0$ . Noting that  $\pi/6 \approx 0.52$ , one can conclude that a “sech” pulse broadens at almost the same rate and exhibits the same qualitative behavior as a Gaussian pulse when the comparison is made on the basis of their RMS widths.

The preceding analysis can readily be extended to chirped pulses. For a chirped Gaussian pulse, all integrals in Eqs (3.3.23)–(3.3.27) can be evaluated in a closed form, and one recovers Eq. (3.3.14) for the broadening factor. For a super-Gaussian pulse, Eq. (3.2.28) is obtained when TOD is neglected. It is possible to obtain  $\sigma/\sigma_0$  in a closed form for a super-Gaussian pulse even when both  $\beta_2$  and  $\beta_3$  are finite but the resulting expression is quite complex [17].

The effect of TOD is to make the intensity profile asymmetric and introduce a long oscillating tail similar to that seen in Figure 3.6. The quantity  $\langle T \rangle$  provides a simple measure of this asymmetry. If we consider again the example of a “sech” pulse, we find that  $\langle T \rangle$  is zero initially but changes linearly with  $z$  at a rate given by  $a_1 = \beta_3/(6T_0^2)$ . The same behavior occurs for a Gaussian pulse but  $\langle T \rangle$  changes at a different rate. These results are in agreement with the numerically calculated pulse

shapes in Figure 3.6. As seen there, pulse develops a long tail on the trailing edge for positive values of  $\beta_3$ , resulting in  $\langle T \rangle > 0$ .

The most important conclusion that one can draw from Eqs (3.3.22) and (3.3.29) is that, for a long fiber whose length  $L \gg L_D$ , the GVD-induced pulse broadening scales as  $L/L_D$  irrespective of the pulse shape. As the dispersion length  $L_D \equiv T_0^2/|\beta_2|$  scales as  $T_0^2$ , it decreases rapidly as pulses become shorter. As an example,  $L_D = 100$  km for pulses with  $T_0 = 10$  ps launched into a dispersion-shifted fiber having  $|\beta_2| = 1$  ps<sup>2</sup>/km but becomes only 1 km if pulse width is reduced to  $T_0 = 1$  ps. Such a pulse will broaden by a factor  $\sim 100$  in a 100-km-long fiber. Because  $L$  can exceed thousands of kilometers for fiber-optic communication systems designed to transmit information over transoceanic distances, it is evident that GVD-induced pulse broadening may limit the performance of most lightwave systems unless a suitable dispersion-management scheme is employed.

### 3.3.4 Ultrashort-Pulse Measurements

As the GVD and TOD effects can change the shape and width of ultrashort pulses considerably, one should consider how such pulses can be measured experimentally. For pulses broader than 100 ps, pulse characteristics can be measured directly by using a high-speed photodetector. Streak cameras can be used for pulses as short as 0.5 ps. However, most of them operate in the visible spectral region, although infrared operation (up to 1.6 μm) has become possible in recent years.

A common technique for characterizing ultrashort optical pulses is based on the nonlinear phenomenon of second-harmonic generation. In this method, known as the *autocorrelation technique*, the pulse is sent through a nonlinear crystal together with a delayed replica of its own [31]. A second-harmonic signal is generated inside the crystal only when two pulses overlap in time. Measuring the second-harmonic power as a function of the delay time produces an autocorrelation trace. The width of this trace is related to the width of the original pulse. The exact relationship between the two widths depends on the pulse shape. If pulse shape is known *a priori*, or it can be inferred indirectly, the autocorrelation trace provides an accurate measurement of the pulse width. This technique can measure widths down to a few femtoseconds but provides little information on details of the pulse shape. In fact, an autocorrelation trace is always symmetric even when the pulse shape is known to be asymmetric. The use of cross-correlation, a technique in which an ultrashort pulse of known shape and width is combined with the original pulse inside a second-harmonic crystal, solves this problem to some extent. The auto- and cross-correlation techniques can also make use of other nonlinear effects such as third-harmonic generation [32] and two-photon absorption [33]. All such methods, however, record intensity correlation and cannot provide any information on the phase or chirp variations across the pulse.

An interesting technique, called frequency-resolved optical gating (FROG) and developed during the 1990s, solves this problem quite nicely [34–36]. It can not only measure the pulse shape but can also provide information on how the optical phase and the frequency chirp vary across the pulse. The technique works by recording a

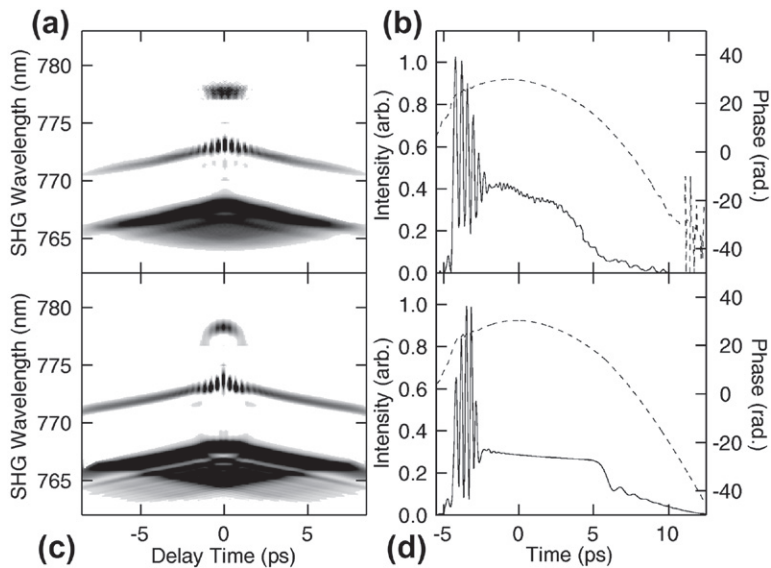


**Figure 3.9** (a) Measured FROG spectrogram and (b) retrieved intensity (solid curve) and phase profiles (dashed curve) at the output of a 700-m-long fiber; parts (c) and (d) show corresponding numerical results. (After Ref. [37]; © 1997 OSA.)

series of spectrally resolved autocorrelation traces and uses them to deduce the intensity and phase profiles associated with the pulse. Mathematically, the FROG output is described by

$$S(\tau, \omega) = \left| \int_{-\infty}^{\infty} A(L, t) A(L, t - \tau) \exp(i\omega t) dt \right|^2, \quad (3.3.30)$$

where  $\tau$  is an adjustable delay and  $L$  is the fiber length. Experimentally, the output pulse is split into two parts that are combined inside a nonlinear crystal after introducing the delay  $\tau$  in one path. A series of the second-harmonic spectra is recorded as  $\tau$  is varied from negative to positive values.

The FROG technique has been used to characterize pulse propagation in optical fibers with considerable success [37–42]. As an example, Figure 3.9 shows the measured FROG traces and the retrieved intensity and phase profiles at the output of a 700-m-long fiber when 2.2-ps pulses with a peak power of 22 W are launched into it [37]. Parts (c) and (d) show the results of numerical simulations using the NLS equation with the nonlinear terms included. Such complicated pulse shapes cannot be deduced from the autocorrelation and spectral measurements alone.

A related technique, known as the cross-correlation FROG, can also be used for measuring the intensity and phase profiles of ultrashort pulses [40]. It makes use of a reference pulse and is discussed in Section 12.2.2. Another technique, known as

time-resolved optical gating, can also be employed [43]. In this method, the pulse is passed through a dispersive medium (e.g., an optical fiber) whose GVD is varied over a certain range, and a number of autocorrelation traces are recorded for different GVD values. Both the intensity and phase profiles can be deduced from such autocorrelation traces.

## 3.4 DISPERSION MANAGEMENT

In a fiber-optic communication system, information is transmitted over a fiber by using a coded sequence of optical pulses whose width is set by the bit rate  $B$  of the system. Dispersion-induced broadening of pulses is undesirable as it interferes with the detection process and leads to errors if the pulse spreads outside its allocated bit slot ( $T_B = 1/B$ ). Clearly, GVD limits the bit rate  $B$  for a fixed transmission distance  $L$  [44]. The dispersion problem becomes quite serious when optical amplifiers are used to compensate for fiber losses because  $L$  can exceed thousands of kilometers for long-haul systems. A useful measure of the information-transmission capacity is the bit rate-distance product  $BL$ . This section shows how the  $BL$  product is limited by fiber dispersion and how it can be improved by using the technique of dispersion management.

### 3.4.1 GVD-Induced Limitations

Consider first the case in which pulse broadening is dominated by the large spectral width  $\sigma_\omega$  of the source. For a Gaussian pulse, the broadening factor can be obtained from Eq. (3.3.16). Assuming that the contribution of the  $\beta_3$  term is negligible together with  $C = 0$  and  $V_\omega \gg 1$ , the RMS pulse width  $\sigma$  is given by

$$\sigma = \left[ \sigma_0^2 + (\beta_2 L \sigma_\omega)^2 \right]^{1/2} = \left[ \sigma_0^2 + (DL\sigma_\lambda)^2 \right]^{1/2}, \quad (3.4.1)$$

where  $L$  is the fiber-link length and  $\sigma_\lambda$  is the RMS spectral width of the source in wavelength units. The dispersion parameter  $D$  is related to the GVD parameter  $\beta_2$  as indicated in Eq. (1.2.11).

One can relate  $\sigma$  to the bit rate  $B$  by using the criterion that the broadened pulse should remain confined to its own bit slot ( $T_B = 1/B$ ). A commonly used criterion is  $4\sigma < T_B$  [44]; for a Gaussian pulse, at least 95% of the pulse energy remains within the bit slot when this condition is satisfied. The limiting bit rate is obtained using  $4B\sigma < 1$ . Assuming  $\sigma_0 \ll \sigma$ , this condition becomes

$$4BL|D|\sigma_\lambda < 1. \quad (3.4.2)$$

As an illustration, consider the case of multimode semiconductor lasers [28] for which  $\sigma_\lambda \approx 2 \text{ nm}$ . If the system is operating near  $\lambda = 1.55 \mu\text{m}$  using standard fibers,  $D \approx 16 \text{ ps}/(\text{km}\cdot\text{nm})$ . With these parameter values, Eq. (3.4.2) requires  $BL < 8 \text{ (Gb/s)}\cdot\text{km}$ . For a 100-km-long fiber, GVD restricts the bit rate to relatively low values of

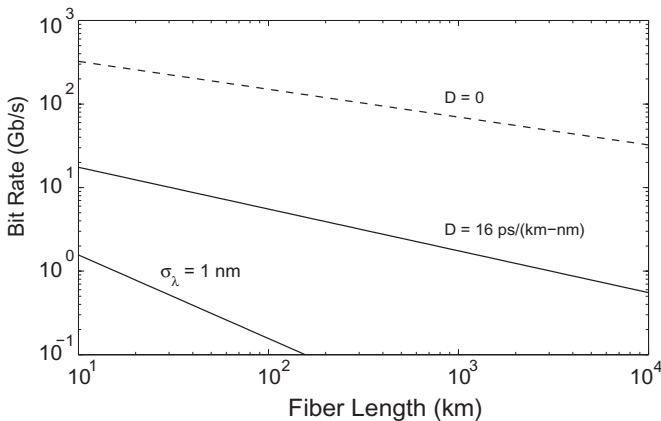


**Figure 3.10** Limiting bit rate as a function of the fiber length for  $\sigma_\lambda = 1 \text{ nm}$  and negligible  $\sigma_\lambda$ . The standard fiber is assumed to have a dispersion of  $16 \text{ ps}/(\text{km-nm})$  in both cases. The dashed line shows the case in which the system operates exactly at the zero-dispersion wavelength using  $\beta_3 = 0.1 \text{ ps}^3/\text{km}$ .

only 80 Mb/s. However, if the system is designed to operate near the zero-dispersion wavelength (occurring near  $1.3 \mu\text{m}$ ) such that  $|D| < 1 \text{ ps}/(\text{km-nm})$ , the  $BL$  product increases to beyond 100 (Gb/s)-km.

Modern fiber-optic communication systems operating near  $1.55 \mu\text{m}$  reduce the GVD effects using dispersion-shifted fibers designed such that the minimum-loss wavelength and the zero-dispersion wavelengths nearly coincide. At the same time, they use lasers designed to operate in a single longitudinal mode such that the source spectral width is well below 100 MHz [28]. Under such conditions,  $V_\omega \ll 1$  in Eq. (3.3.16). If we neglect the  $\beta_3$  term and set  $C = 0$ , Eq. (3.3.16) can be approximated by

$$\sigma = \left[ \sigma_0^2 + (\beta_2 L / 2\sigma_0)^2 \right]^{1/2}. \quad (3.4.3)$$

A comparison with Eq. (3.4.1) reveals a major difference: dispersion-induced broadening now depends on the initial width  $\sigma_0$ . In fact,  $\sigma$  can be minimized by choosing an optimum value of  $\sigma_0$ . The minimum value of  $\sigma$  is found to occur for  $\sigma_0 = (|\beta_2|L/2)^{1/2}$  and is given by  $\sigma = (|\beta_2|L)^{1/2}$ . The limiting bit rate is obtained by using  $4B\sigma < 1$  or the condition

$$4B(|\beta_2|L)^{1/2} < 1. \quad (3.4.4)$$

The main difference from Eq. (3.4.2) is that  $B$  scales as  $L^{-1/2}$  rather than  $L^{-1}$ . Figure 3.10 compares the decrease in the bit rate with increasing  $L$  by choosing  $D = 16 \text{ ps}/(\text{km-nm})$  and  $\sigma_\lambda = 0$  and  $1 \text{ nm}$ . Equation (3.4.4) was used in the case  $\sigma_\lambda = 0$ .

For a lightwave system operating exactly at the zero-dispersion wavelength,  $\beta_2 = 0$  in Eq. (3.3.16). Assuming  $V_\omega \ll 1$  and  $C = 0$ , the pulse width is given by

$$\sigma = \left[ \sigma_0^2 + \frac{1}{2} \left( \beta_3 L / 4\sigma_0^2 \right)^2 \right]^{1/2}. \quad (3.4.5)$$

Similar to the case of Eq. (3.4.3),  $\sigma$  can be minimized by optimizing the input pulse width  $\sigma_0$ . The minimum value of  $\sigma_0$  is found to occur for  $\sigma_0 = (|\beta_3|L/4)^{1/3}$ . The limiting bit rate is obtained by using the condition  $4B\sigma < 1$  and is given by [44]

$$B(|\beta_3|L)^{1/3} < 0.324. \quad (3.4.6)$$

The dispersive effects are most forgiving in this case. For a typical value  $\beta_3 = 0.1 \text{ ps}^3/\text{km}$ , the bit rate can be as large as 150 Gb/s for  $L = 100 \text{ km}$ . It decreases to only 70 Gb/s even when  $L$  increases by a factor of 10 because of the  $L^{-1/3}$  dependence of the bit rate on the fiber length. The dashed line in Figure 3.10 shows this dependence using Eq. (3.4.6) with  $\beta_3 = 0.1 \text{ ps}^3/\text{km}$ . Clearly, the performance of a lightwave system can be considerably improved by operating it close to the zero-dispersion wavelength of the fiber.

### 3.4.2 Dispersion Compensation

Even though operation at the zero-dispersion wavelength is most desirable from the standpoint of pulse broadening, other considerations may preclude such a design. For example, one channel at most can be located at the zero-dispersion wavelength in a wavelength-division multiplexed (WDM) system. Moreover, as discussed in Chapter 10, four-wave mixing occurring when GVD is relatively low forces one to operate WDM systems away from the zero-dispersion wavelength. Of course, GVD-induced pulse broadening then becomes of serious concern. The technique of dispersion management provides a solution to this dilemma. It consists of combining fibers with different characteristics such that the average GVD of the entire fiber link is quite low, while the GVD of each fiber section is chosen to be large enough to make the four-wave-mixing effects negligible [45]. In practice, a periodic dispersion map is used with a period equal to the amplifier spacing (typically 50–100 km). Amplifiers compensate for accumulated fiber losses in each section. Between each pair of amplifiers, just two kinds of fibers, with opposite signs of  $\beta_2$ , are combined to reduce the average dispersion to a small value. When the average GVD is set to zero, dispersion is totally compensated.

Such a dispersion-compensation technique takes advantage of the linear nature of Eq. (3.2.1). The basic idea can be understood from Eq. (3.2.5) representing the general solution of Eq. (3.2.1). For a dispersion map consisting of two fiber segments, Eq. (3.2.5) becomes

$$U(L_m, t) = \frac{1}{2\pi} \int_{-\infty}^{\infty} \tilde{U}(0, \omega) \exp \left[ \frac{i}{2} \omega^2 (\beta_{21} L_1 + \beta_{22} L_2) - i\omega t \right] d\omega, \quad (3.4.7)$$

where  $L_m = L_1 + L_2$  is the dispersion-map period, and  $\beta_{2j}$  is the GVD parameter of the fiber segment of length  $L_j$  ( $j = 1, 2$ ). By using  $D_j = -(2\pi c/\lambda^2)\beta_{2j}$ , the condition for dispersion compensation can be written as

$$D_1L_1 + D_2L_2 = 0. \quad (3.4.8)$$

As  $A(L_m, t) = A(0, t)$  when Eq. (3.4.8) is satisfied, the pulse recovers its initial width after each map period even though pulse width can change significantly within each period.

Equation (3.4.8) can be satisfied in several different ways. If two segments are of equal lengths ( $L_1 = L_2$ ), the two fibers should have  $D_1 = -D_2$ . Fibers with equal and opposite values of GVD can be made by shifting the zero-dispersion wavelength appropriately during the manufacturing stage. Alternatively, if standard fibers with large anomalous GVD [ $D \approx 16 \text{ ps}/(\text{km-nm})$ ] are employed, dispersion can be compensated by using a relatively short segment of dispersion-compensating fiber (DCF) designed to have “normal” GVD with values of  $D < -100 \text{ ps}/(\text{km-nm})$ . Several other devices (such as fiber gratings) can also be used for dispersion management [29].

### 3.4.3 Compensation of Third-Order Dispersion

When the bit rate of a single channel exceeds 100Gb/s, one must use ultrashort pulses (width  $\sim 1 \text{ ps}$ ) in each bit slot. For such short optical pulses, the pulse spectrum becomes broad enough that it is difficult to compensate GVD over the entire bandwidth of the pulse (because of the frequency dependence of  $\beta_2$ ). The simplest solution to this problem is provided by fibers, or other devices, designed such that both  $\beta_2$  and  $\beta_3$  are compensated simultaneously.

The dispersion-management conditions can be obtained from Eq. (3.3.2). For a fiber link containing two different fibers of lengths  $L_1$  and  $L_2$ , the conditions for broadband dispersion compensation are given by

$$\beta_{21}L_1 + \beta_{22}L_2 = 0 \quad \text{and} \quad \beta_{31}L_1 + \beta_{32}L_2 = 0, \quad (3.4.9)$$

where  $\beta_{2j}$  and  $\beta_{3j}$  are the GVD and TOD parameters for fiber of length  $L_j$  ( $j = 1, 2$ ). It is generally difficult to satisfy both conditions simultaneously over a wide wavelength range. However, for a 1-ps pulse, it is sufficient to satisfy Eq. (3.4.9) over a 4–5 nm bandwidth. This requirement is easily met by especially designed DCFs [46] and other devices such as fiber gratings and liquid-crystal modulators.

Several experiments have demonstrated signal transmission at relatively high bit rates ( $>100 \text{ Gb/s}$ ) over distances  $\sim 100 \text{ km}$  with simultaneous compensation of both GVD and TOD [47–53]. In a 1996 experiment, a 100-Gb/s signal was transmitted over 560 km with 80-km amplifier spacing [47]. In a later experiment, bit rate was extended to 400 Gb/s by using 0.98-ps optical pulses within the 2.5-ps time slot [48]. Without compensation of the TOD, the pulse broadened to 2.3 ps after 40 km and exhibited a long oscillatory tail extending over 5–6 ps (see Figure 3.6). With partial compensation of TOD, the oscillatory tail disappeared and the pulse

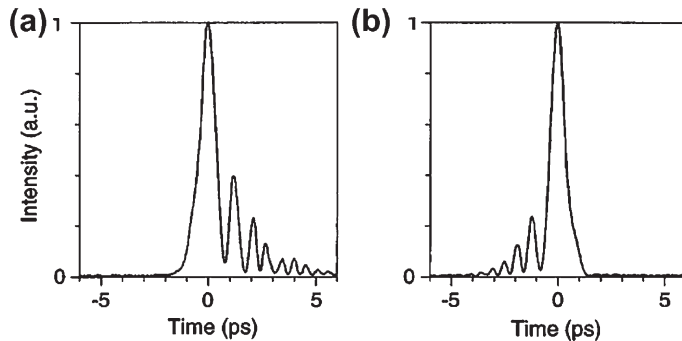


**Figure 3.11** Experimentally observed shapes of a 0.5-ps input pulse at the output of a 2.5-km GVD-compensated fiber link. The value of  $\beta_3$  was changed from 0.124 (left) to  $-0.076 \text{ ps}^3/\text{km}$  (right) using a liquid-crystal modulator. (After Ref. [51]; © 1998 OSA.)

width reduced to 1.6 ps. In another experiment [49], a planar lightwave circuit was designed to have a dispersion slope of  $-15.8 \text{ ps/nm}^2$  over a 170-GHz bandwidth. It was used to compensate the TOD over 300 km of a dispersion-shifted fiber for which  $\beta_3 \approx 0.05 \text{ ps}/(\text{km}\cdot\text{nm}^2)$  at the operating wavelength. The dispersion compensator eliminated the long oscillatory tail and reduced the width of the main peak from 4.6 to 3.8 ps. The increase in pulse width from its input value of 2.6 ps can be attributed to the PMD effects.

The dispersion-compensation technique has also been used for femtosecond optical pulses. For a pulse with  $T_0 = 0.1$  ps, the TOD length  $L'_D$  is only 10 m for a typical value  $\beta_3 = 0.1 \text{ ps}^3/\text{km}$ . Such pulses cannot propagate more than a few meters before becoming severely distorted even when  $\beta_2$  is compensated fully so that its average value is zero. Nonetheless, a 0.5-ps pulse ( $T_0 \approx 0.3$  ps) was transmitted over 2.5 km of fiber using a 445-m-long DCF with  $\beta_2 \approx 98 \text{ ps}^2/\text{km}$  and  $\beta_3 \approx -0.5 \text{ ps}^3/\text{km}$  [50]. The output pulse was slightly distorted because  $\beta_3$  could not be fully compensated. In a later experiment, a liquid-crystal modulator was used to compensate for the residual  $\beta_3$  [51], and the pulse remained nearly unchanged after propagating over 2.5 km of the dispersion-compensated fiber link. In a 1999 experiment [52], the use of the same technique with a different DCF (length 1.5 km) permitted transmission of a 0.4-ps pulse ( $T_0 \approx 0.25$  ps) over 10.6 km of fiber with little distortion in the pulse shape. The main advantage of a liquid-crystal modulator is that it acts as a programmable pulse shaper. It can even be used to enhance the TOD effects artificially. As an example, Figure 3.11 shows the pulse shapes at the output of a 2.5-km GVD-compensated fiber link when the effective value of  $\beta_3$  changes from 0.124 to  $-0.076 \text{ ps}^3/\text{km}$  [51]. The observed pulse shapes are in agreement with those predicted by Eq. (3.3.2) as long as the nonlinear effects remain negligible. On the system level, a single high-speed channel at 640 Gb/s (generated through time-division multiplexing) has been transmitted over 92 km by compensating  $\beta_2$  and  $\beta_3$  over the entire link [53].

When both  $\beta_2$  and  $\beta_3$  are nearly compensated, propagation of femtosecond optical pulses is limited by the fourth-order dispersive effects governed by the parameter  $\beta_4$  [54–56]. In a 1999 experiment, the combination of a DCF and a programmable dispersion compensator compensated  $\beta_2$ ,  $\beta_3$ , and  $\beta_4$  simultaneously over a 30-nm-wide wavelength range [54]. This scheme allowed transmission of a 0.2-ps pulse train with 22-nm bandwidth over a distance of 85 km. In a later experiment, 0.25-ps pulses could be transmitted over 139 km when dispersion up to the fourth order was compensated using a DCF with a negative slope [55]. Input pulses were prechirped appropriately with a phase modulator. In a 2001 experiment, the bit rate was extended to 1.28 Tb/s by transmitting 380-fs pulses over 70 km of fiber, while compensating its dispersion up to fourth order [56].

---

## PROBLEMS

- 3.1 A dispersion-shifted fiber is measured to have  $D = 2 \text{ ps}/(\text{km}\cdot\text{nm})$  at  $1.55 \mu\text{m}$ . It has an effective core area of  $40 \mu\text{m}^2$ . Calculate the dispersion and nonlinear lengths when (i) 10-ps pulses with 100-mW peak power and (ii) 1-ps pulses with 1-W peak power are launched into the fiber. Are nonlinear effects important in both cases?
- 3.2 A chirped Gaussian pulse is well described by Eq. (3.2.15) with  $C=5$  and  $T_0 = 50 \text{ ps}$ . Determine the temporal and spectral widths (FWHM) of this pulse.
- 3.3 Prove that for an unchirped Gaussian pulse of arbitrary width, the product  $\Delta\nu\Delta t$  approximately equals 0.44, where  $\Delta t$  and  $\Delta\nu$  are the temporal and spectral widths (both measured as FWHM), respectively.
- 3.4 Repeat Problem 3.3 for an unchirped “sech” pulse and prove that  $\Delta\nu\Delta t$  approximately equals 0.315.
- 3.5 Starting with Eq. (3.2.24), derive an expression for the RMS width of a super-Gaussian pulse.
- 3.6 Show that a chirped Gaussian pulse is compressed initially inside a single-mode fiber when  $\beta_2 C < 0$ . Derive expressions for the minimum width and the fiber length at which the minimum occurs.
- 3.7 Evaluate the integral in Eq. (3.3.2) numerically for an unchirped Gaussian pulse with 1-ps width (FWHM) assuming  $\beta_2 = 0$  and  $\beta_3 = 0.1 \text{ ps}^3/\text{km}$ . Plot the pulse shapes for  $L=2$  and  $4 \text{ km}$ . What happens to the pulse shape if the sign of  $\beta_3$  is reversed?
- 3.8 Repeat Problem 3.7 for an unchirped “sech” pulse and compare the pulse shapes for  $L=2$  and  $4 \text{ km}$  with the Gaussian case. What happens to the pulse shape if the sign of  $\beta_3$  is reversed?
- 3.9 Calculate the RMS width of an unchirped Gaussian pulse using Eqs (3.3.21)–(3.3.27). Retain the  $\beta_2$  and  $\beta_3$  terms in Eq. (3.3.18) but neglect all others.
- 3.10 Evaluate the integral in Eq. (3.3.30) analytically for an unchirped Gaussian pulse and plot  $S(\tau, \omega)$  as a surface plot in the case of 1-ps width (FWHM) of the Gaussian pulse.

- 3.11** Estimate the limiting bit rate for a 60-km single-mode fiber link at 1.3- and  $1.55\text{-}\mu\text{m}$  wavelengths assuming transform-limited 50-ps (FWHM) input pulses. Assume  $\beta_2 = 0$  and  $-20 \text{ ps}^2/\text{km}$  and  $\beta_3 = 0.1$  and  $0 \text{ ps}^3/\text{km}$  at 1.3 and  $1.55\text{-}\mu\text{m}$  wavelengths, respectively.
- 3.12** An optical communication system is operating with chirped Gaussian input pulses. Assume  $\beta_3 = 0$  and  $V_\omega \ll 1$  in Eq. (3.3.16) and obtain a condition on the bit rate in terms of the parameters  $C$ ,  $\beta_2$ , and  $L$ .

## REFERENCES

- [1] I. N. Sisakyan and A. B. Shvartsburg, *Sov. J. Quantum Electron.* **14**, 1146 (1984).
- [2] S. A. Akhmanov, V. A. Vysloukh, and A. S. Chirkin, *Optics of Femtosecond Laser Pulses* (American Institute of Physics, 1992), Chap. 1.
- [3] G. P. Agrawal, in *Supercontinuum Laser Source*, R. R. Alfano, Ed. (Springer, 1989), Chap. 3.
- [4] C. G. B. Garrett and D. E. McCumber, *Phys. Rev. A* **1**, 305 (1970).
- [5] H. G. Unger, *Arch. Elektron. Uebertragungstech.* **31**, 518 (1977).
- [6] M. Miyagi and S. Nishida, *Appl. Opt.* **18**, 678 (1979).
- [7] D. Glogé, *Electron. Lett.* **15**, 686 (1979).
- [8] D. Marcuse, *Appl. Opt.* **19**, 1653 (1980).
- [9] D. Marcuse, *Appl. Opt.* **20**, 3573 (1981).
- [10] K. Iwashita, K. Nakagawa, Y. Nakano, and Y. Suzuki, *Electron. Lett.* **18**, 873 (1982).
- [11] C. Lin and A. Tomita, *Electron. Lett.* **19**, 837 (1983).
- [12] D. Anderson, M. Lisak, and P. Anderson, *Opt. Lett.* **10**, 134 (1985).
- [13] F. Koyama and Y. Suematsu, *IEEE J. Quantum Electron.* **21**, 292 (1985).
- [14] K. Tajima and K. Washio, *Opt. Lett.* **10**, 460 (1985).
- [15] A. Takada, T. Sugie, and M. Saruwatari, *Electron. Lett.* **21**, 969 (1985).
- [16] G. P. Agrawal and M. J. Potasek, *Opt. Lett.* **11**, 318 (1986).
- [17] D. Anderson and M. Lisak, *Opt. Lett.* **11**, 569 (1986).
- [18] A. Jeffrey and D. Zwillinger, Eds., *Table of Integrals, Series, and Products*, 6th Ed. (Academic Press, 2003).
- [19] A. Takada, T. Sugie, and M. Saruwatari, *J. Lightwave Technol.* **5**, 1525 (1987).
- [20] K. Iwatsuki, A. Takada, and M. Saruwatari, *Electron. Lett.* **24**, 1572 (1988).
- [21] K. Iwatsuki, A. Takada, S. Nishi, and M. Saruwatari, *Electron. Lett.* **25**, 1003 (1989).
- [22] M. Nakazawa, K. Suzuki, and Y. Kimura, *Opt. Lett.* **15**, 588 (1990).
- [23] R. T. Hawkins, *Electron. Lett.* **26**, 292 (1990).
- [24] G. P. Agrawal and N. A. Olsson, *Opt. Lett.* **14**, 500 (1989).
- [25] N. A. Olsson, G. P. Agrawal, and K. W. Wecht, *Electron. Lett.* **25**, 603 (1989).
- [26] G. P. Agrawal and N. A. Olsson, *IEEE J. Quantum Electron.* **25**, 2297 (1989).
- [27] D. M. Bloom, L. F. Mollenauer, C. Lin, D. W. Taylor, and A. M. DelGaudio, *Opt. Lett.* **4**, 297 (1979).
- [28] G. P. Agrawal and N. K. Dutta, *Semiconductor Lasers*, 2nd ed. (Van Nostrand Reinhold, 1993), Chap. 6.
- [29] G. P. Agrawal, *Lightwave Technology: Telecommunication Systems* (Wiley, 2005).
- [30] D. Anderson and M. Lisak, *Phys. Rev. A* **35**, 184 (1987).
- [31] J. C. Diels, *Ultrashort Laser Pulse Phenomena* (Academic Press, 1996).

- [32] D. Meshulach, Y. Barad, and Y. Silberberg, *J. Opt. Soc. Am. B* **14**, 2122 (1997).
- [33] D. T. Reid, W. Sibbett, J. M. Dudley, L. P. Barry, B. C. Thomsen, and J. D. Harvey, *Appl. Opt.* **37**, 8142 (1998).
- [34] K. W. DeLong, D. N. Fittinghoff, and R. Trebino, *IEEE J. Quantum Electron.* **32**, 1253 (1996).
- [35] D. J. Kane, *IEEE J. Quantum Electron.* **35**, 421 (1999).
- [36] X. Gu, S. Akturk, A. Shreenath, Q. Cao, and R. Trebino, *Opt. Rev.* **11**, 141 (2004).
- [37] J. M. Dudley, L. P. Barry, P. G. Bollond, J. D. Harvey, R. Leonhardt, and P. D. Drummond, *Opt. Lett.* **22**, 457 (1997).
- [38] J. M. Dudley, L. P. Barry, P. G. Bollond, J. D. Harvey, and R. Leonhardt, *Opt. Fiber Technol.* **4**, 237 (1998).
- [39] F. G. Omenetto, B. P. Luce, D. Yarotski, and A. J. Taylor, *Opt. Lett.* **24**, 1392 (1999).
- [40] N. Nishizawa and T. Goto, *Opt. Express* **8**, 328 (2001).
- [41] J. M. Dudley, F. Gutty, S. Pitois, and G. Millot, *IEEE J. Quantum Electron.* **37**, 587 (2001).
- [42] C. Finot, G. Millot, S. Pitois, C. Bille, and J. M. Dudley, *IEEE J. Sel. Topics Quantum Electron.* **10**, 1211 (2004).
- [43] R. G. M. P. Koumans and A. Yariv, *IEEE J. Quantum Electron.* **36**, 137 (2000); *IEEE Photon. Technol. Lett.* **12**, 666 (2000).
- [44] G. P. Agrawal, *Fiber-Optic Communication Systems*, 4th ed. (Wiley, 2010).
- [45] A. H. Gnauck and R. M. Jopson, in *Optical Fiber Telecommunications III*, I. P. Kaminow and T. L. Koch, Eds. (Academic Press, 1997), Chap. 7.
- [46] C. C. Chang, A. M. Weiner, A. M. Vengsarkar, and D. W. Peckham, *Opt. Lett.* **21**, 1141 (1996).
- [47] S. Kawanishi, H. Takara, O. Kamatani, T. Morioka, and M. Saruwatari, *Electron. Lett.* **32**, 470 (1996).
- [48] S. Kawanishi, H. Takara, T. Morioka, O. Kamatani, K. Takiguchi, T. Kitoh, and M. Saruwatari, *Electron. Lett.* **32**, 916 (1996).
- [49] K. Takiguchi, S. Kawanishi, H. Takara, K. Okamoto, and Y. Ohmori, *Electron. Lett.* **32**, 755 (1996).
- [50] C. C. Chang and A. M. Weiner, *IEEE J. Quantum Electron.* **33**, 1455 (1997).
- [51] C. C. Chang, H. P. Sardesai, and A. M. Weiner, *Opt. Lett.* **23**, 283 (1998).
- [52] S. Shen and A. M. Weiner, *IEEE Photon. Technol. Lett.* **11**, 827 (1999).
- [53] T. Yamamoto, E. Yoshida, K. R. Tamura, K. Yonenaga, and M. Nakazawa, *IEEE Photon. Technol. Lett.* **12**, 353 (2000).
- [54] F. Futami, K. Taira, K. Kikuchi, and A. Suzuki, *Electron. Lett.* **35**, 2221 (1999).
- [55] M. D. Pelusi, F. Futami, K. Kikuchi, and A. Suzuki, *IEEE Photon. Technol. Lett.* **12**, 795 (2000).
- [56] T. Yamamoto and M. Nakazawa, *Opt. Lett.* **26**, 647 (2001).

# Self-Phase Modulation

# 4

An interesting manifestation of the intensity dependence of the refractive index in nonlinear optical media occurs through self-phase modulation (SPM), a phenomenon that leads to spectral broadening of optical pulses [1–9]. SPM is the temporal analog of self-focusing that manifests as a narrowing of the spot size of CW beams in a nonlinear medium with  $n_2 > 0$ . SPM was first observed in 1967 in the context of transient self-focusing of optical pulses propagating in a  $\text{CS}_2$ -filled cell [1]. By 1970, SPM had been observed in solids and glasses by using picosecond pulses. The earliest observation of SPM in optical fibers was made with a fiber whose core was filled with  $\text{CS}_2$  liquid [7]. This work led by 1978 to a systematic study of SPM in a silica-core fiber [9]. This chapter considers SPM as a simple example of the nonlinear optical effects that can occur in optical fibers. Section 4.1 is devoted to the case of pure SPM as it neglects the GVD effects and focuses on spectral changes induced by SPM. The combined effects of GVD and SPM are discussed in Section 4.2 with emphasis on the SPM-induced frequency chirp. Section 4.3 presents two analytic techniques and uses them to solve the NLS equation approximately. Section 4.4 extends the analysis to include the higher-order nonlinear effects such as self-steepening.

---

## 4.1 SPM-INDUCED SPECTRAL CHANGES

A general description of SPM in optical fibers requires numerical solutions of the pulse-propagation equation (2.3.44) obtained in Section 2.3. The simpler equation (2.3.46) can be used for pulse widths  $T_0 < 5 \text{ ps}$ . A further simplification occurs if the effect of GVD on SPM is negligible so that the  $\beta_2$  term in Eq. (2.3.36) can be set to zero. The conditions under which GVD can be ignored were discussed in Section 3.1 by introducing the length scales  $L_D$  and  $L_{\text{NL}}$  [see Eq. (3.1.5)]. In general, the pulse width and the peak power should be such that  $L_D \gg L > L_{\text{NL}}$  for a fiber of length  $L$ . Equation (3.1.7) shows that the GVD effects are negligible for relatively wide pulses ( $T_0 > 50 \text{ ps}$ ) launched into an optical fiber with a large peak power ( $P_0 > 1 \text{ W}$ ).

### 4.1.1 Nonlinear Phase Shift

In terms of the normalized amplitude  $U(z, T)$  defined in Eq. (3.1.3), the pulse-propagation equation (3.1.4) in the limit  $\beta_2 = 0$  becomes

$$\frac{\partial U}{\partial z} = \frac{i e^{-\alpha z}}{L_{NL}} |U|^2 U, \quad (4.1.1)$$

where  $\alpha$  accounts for fiber losses. The nonlinear length is defined as

$$L_{NL} = (\gamma P_0)^{-1}, \quad (4.1.2)$$

where  $P_0$  is the peak power and  $\gamma$  is related to the nonlinear Kerr coefficient  $n_2$  as in Eq. (2.3.29).

Equation (4.1.1) can be solved by using  $U = V \exp(i\phi_{NL})$  and equating the real and imaginary parts so that

$$\frac{\partial V}{\partial z} = 0; \quad \frac{\partial \phi_{NL}}{\partial z} = \frac{e^{-\alpha z}}{L_{NL}} V^2. \quad (4.1.3)$$

As the amplitude  $V$  does not change along the fiber length  $L$ , the phase equation can be integrated analytically to obtain the general solution

$$U(L, T) = U(0, T) \exp[i\phi_{NL}(L, T)], \quad (4.1.4)$$

where  $U(0, T)$  is the field amplitude at  $z = 0$  and

$$\phi_{NL}(L, T) = |U(0, T)|^2 (L_{eff}/L_{NL}). \quad (4.1.5)$$

The effective length  $L_{eff}$  for a fiber of length  $L$  is defined as

$$L_{eff} = [1 - \exp(-\alpha L)]/\alpha. \quad (4.1.6)$$

Equation (4.1.4) shows that SPM gives rise to an intensity-dependent phase shift but the pulse shape remains unaffected. The nonlinear phase shift  $\phi_{NL}$  in Eq. (4.1.5) increases with fiber length  $L$ . The quantity  $L_{eff}$  plays the role of an effective length that is smaller than  $L$  because of fiber losses. In the absence of fiber losses,  $\alpha = 0$ , and  $L_{eff} = L$ . The maximum phase shift  $\phi_{max}$  occurs at the pulse center located at  $T = 0$ . With  $U$  normalized such that  $|U(0, 0)| = 1$ , it is given by

$$\phi_{max} = L_{eff}/L_{NL} = \gamma P_0 L_{eff}. \quad (4.1.7)$$

The physical meaning of the nonlinear length  $L_{NL}$  is clear from Equation (4.1.7): it is the effective propagation distance at which  $\phi_{max} = 1$ . If we use a typical value  $\gamma = 2 \text{ W}^{-1}/\text{km}$  in the  $1.55\text{-}\mu\text{m}$  wavelength region,  $L_{NL} = 50 \text{ km}$  at a power level  $P_0 = 10 \text{ mW}$  and it decreases inversely with an increase in  $P_0$ .

Spectral changes induced by SPM are a direct consequence of the time dependence of  $\phi_{NL}$ . This can be understood by recalling from Section 3.2 that a temporally

varying phase implies that the instantaneous optical frequency differs across the pulse from its central value  $\omega_0$ . The difference  $\delta\omega$  is given by

$$\delta\omega(T) = -\frac{\partial\phi_{NL}}{\partial T} = -\left(\frac{L_{eff}}{L_{NL}}\right)\frac{\partial}{\partial T}|U(0, T)|^2, \quad (4.1.8)$$

where the minus sign is due to the choice of the factor  $\exp(-i\omega_0 t)$  in Eq. (2.3.2). The time dependence of  $\delta\omega$  is referred to as *frequency chirping*. The chirp induced by SPM increases in magnitude with the propagated distance. In other words, new frequency components are generated continuously as the pulse propagates down the fiber. These SPM-generated frequency components broaden the spectrum over its initial width at  $z = 0$  for initially unchirped pulses.

The qualitative features of frequency chirp depend on the pulse shape. Consider, for example, the case of a super-Gaussian pulse with the incident field  $U(0, T)$  given in Eq. (3.2.24). The SPM-induced chirp  $\delta\omega(T)$  for such a pulse is

$$\delta\omega(T) = \frac{2m}{T_0} \frac{L_{eff}}{L_{NL}} \left(\frac{T}{T_0}\right)^{2m-1} \exp\left[-\left(\frac{T}{T_0}\right)^{2m}\right], \quad (4.1.9)$$

where  $m = 1$  for a Gaussian pulse. For larger values of  $m$ , the incident pulse becomes nearly rectangular with increasingly steeper leading and trailing edges. Figure 4.1 shows the variation of (a) the nonlinear phase shift  $\phi_{NL}$  and (b) the induced frequency chirp  $\delta\omega$  across the pulse at  $L_{eff} = L_{NL}$  in the cases of a Gaussian pulse ( $m = 1$ ) and a super-Gaussian pulse ( $m = 3$ ). As  $\phi_{NL}$  is directly proportional to  $|U(0, T)|^2$  in Eq. (4.1.5), its temporal variation is identical to that of the pulse intensity.

The temporal profile of the SPM-induced frequency chirp  $\delta\omega$  shown in Figure 4.1b has several interesting features. First,  $\delta\omega$  is negative near the leading edge (a red shift) and becomes positive near the trailing edge (a blue shift) of the

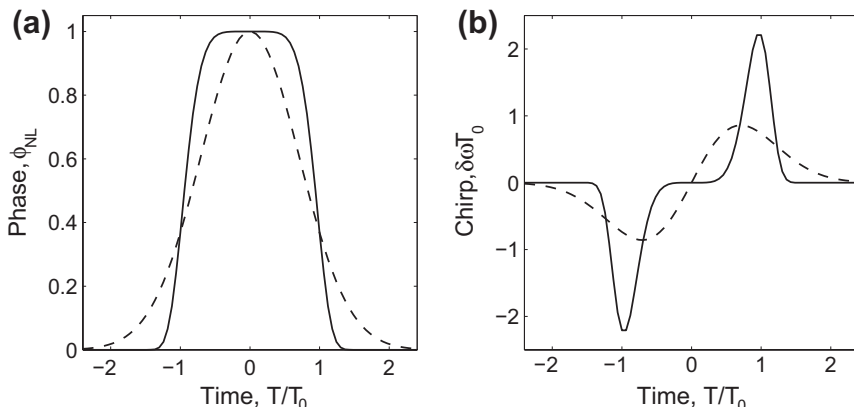


**Figure 4.1** Temporal variation of SPM-induced (a) phase shift  $\phi_{NL}$  and (b) frequency chirp  $\delta\omega$  for Gaussian (dashed curve) and super-Gaussian (solid curve) pulses.

pulse. Second, the chirp is linear and positive (up-chirp) over a large central region of the Gaussian pulse. Third, the chirp is considerably larger for pulses with steeper leading and trailing edges. Fourth, super-Gaussian pulses behave differently than Gaussian pulses because the chirp occurs only near pulse edges and does not vary in a linear fashion. The main point is that chirp variations across an optical pulse depend considerably on the exact pulse shape.

### 4.1.2 Changes in Pulse Spectra

The SPM-induced chirp can produce spectral broadening or narrowing depending on how the input pulse is chirped. In the case of unchirped input pulses, SPM always leads to spectral broadening, and we focus on this case first. An estimate of the magnitude of SPM-induced spectral broadening can be obtained from the peak value of  $\delta\omega$  in Figure 4.1. More quantitatively, we can calculate the peak value by maximizing  $\delta\omega(T)$  from Eq. (4.1.9). By setting its time derivative to zero, the maximum value of  $\delta\omega$  is given by

$$\delta\omega_{\max} = \frac{m f(m)}{T_0} \phi_{\max}, \quad (4.1.10)$$

where  $\phi_{\max}$  is given in Eq. (4.1.7) and  $f(m)$  is defined as

$$f(m) = 2 \left(1 - \frac{1}{2m}\right)^{1-1/2m} \exp\left[-\left(1 - \frac{1}{2m}\right)\right]. \quad (4.1.11)$$

The numerical value of  $f$  depends on  $m$  only slightly;  $f = 0.86$  for  $m = 1$  and tends toward 0.74 for large values of  $m$ . To obtain the spectral broadening factor, the width parameter  $T_0$  should be related to the initial spectral width  $\Delta\omega_0$  of the pulse. For an unchirped Gaussian pulse,  $\Delta\omega_0 = T_0^{-1}$  from Eq. (3.2.17), where  $\Delta\omega_0$  is the 1/e half-width. Equation (4.1.10) then becomes (with  $m = 1$ )

$$\delta\omega_{\max} = 0.86 \Delta\omega_0 \phi_{\max}, \quad (4.1.12)$$

showing that the spectral broadening factor is approximately given by the numerical value of the maximum phase shift  $\phi_{\max}$ .

In the case of a super-Gaussian pulse, it is difficult to estimate  $\Delta\omega_0$  because its spectrum is not Gaussian. However, if we use Eq. (3.2.24) to obtain the rise time,  $T_r = T_0/m$ , and assume that  $\Delta\omega_0$  approximately equals  $T_r^{-1}$ , Eq. (4.1.10) shows that the broadening factor of a super-Gaussian pulse is also approximately given by  $\phi_{\max}$ . As  $\phi_{\max} \sim 100$  is possible for intense pulses or long fibers, SPM can broaden the spectrum considerably. In the case of intense ultrashort pulses, the broadened spectrum can extend over 100 THz or more, especially when SPM is accompanied by other nonlinear processes such as stimulated Raman scattering and four-wave mixing. Such an extreme spectral broadening is referred to as *supercontinuum generation* [4].

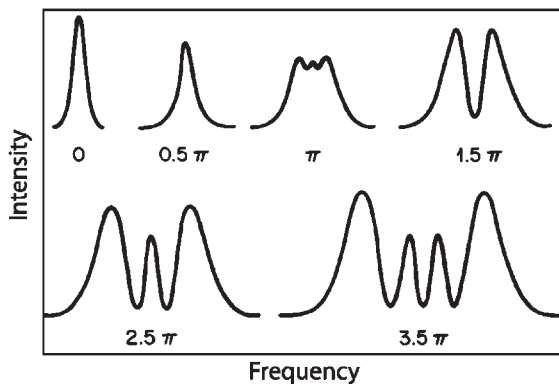


**Figure 4.2** SPM-broadened spectra for an unchirped Gaussian pulse. Spectra are labeled by the maximum nonlinear phase shift  $\phi_{\max}$ . (After Ref. [9]; © 1978 American Physical Society.)

The actual shape of the pulse spectrum  $S(\omega)$  is found by taking the Fourier transform of Eq. (4.1.4). Using  $S(\omega) = |\tilde{U}(L, \omega)|^2$ , we obtain

$$S(\omega) = \left| \int_{-\infty}^{\infty} U(0, T) \exp[i\phi_{NL}(L, T) + i(\omega - \omega_0)T] dT \right|^2. \quad (4.1.13)$$

In general, the spectrum depends not only on the pulse shape but also on the initial chirp imposed on the pulse. Figure 4.2 shows the spectra of an unchirped Gaussian pulse for several values of the maximum phase shift  $\phi_{\max}$ . For a given fiber length,  $\phi_{\max}$  increases linearly with peak power  $P_0$  according to Eq. (4.1.7). Thus, spectral evolution seen in Figure 4.2 can be observed experimentally by increasing the peak power. Figure 4.3 shows the experimentally recorded spectra [9] of nearly Gaussian pulses ( $T_0 \approx 90$  ps), obtained from an argon-ion laser, at the output of a 99-m-long fiber with 3.35-μm core diameter (parameter  $V = 2.53$ ). The experimental spectra are also labeled with  $\phi_{\max}$  and should be compared with the calculated spectra of Figure 4.2. The asymmetry seen in the experimental traces can be attributed to the asymmetric shape of the incident pulse [9]. The overall agreement between theory and the experiment is remarkably good.

The most notable feature of Figures 4.2 and 4.3 is that SPM-induced spectral broadening is accompanied by an oscillatory structure covering the entire frequency range. In general, the spectrum consists of many peaks, and the outermost peaks are the most intense. The number of peaks depends on  $\phi_{\max}$  and increases linearly with it. The origin of the oscillatory structure can be understood by referring to Figure 4.1 where the time dependence of the SPM-induced frequency chirp is shown. In general, the same chirp occurs at two values of  $T$ , showing that the pulse has the same instantaneous frequency at two distinct points. Qualitatively speaking, these two points represent two waves of the same frequency but at different phases that can interfere constructively or destructively depending on their relative phase difference.

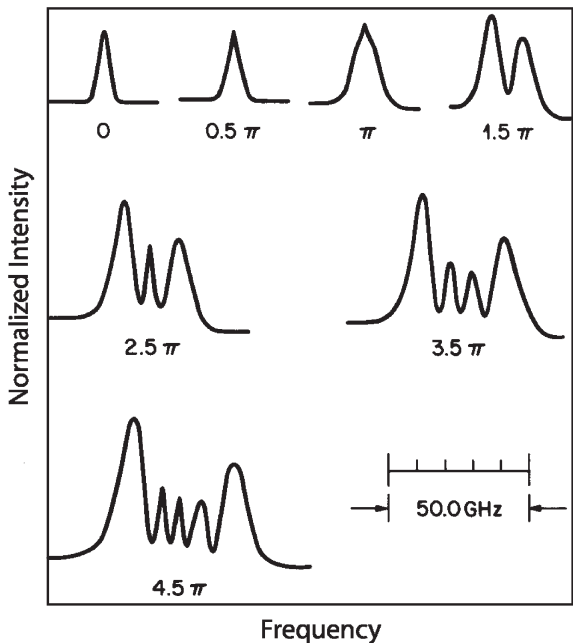


**Figure 4.3** Experimentally observed spectra for a nearly Gaussian pulse at the output of a 99-m-long fiber. Spectra are labeled by  $\phi_{\max}$  related linearly to the peak power. (After Ref. [9]; © 1978 American Physical Society.)

The multipeak structure in the pulse spectrum is a result of such interference [1]. Mathematically, the Fourier integral in Eq. (4.1.13) gets dominant contributions at the two values of  $T$  at which the chirp is the same. These contributions, being complex quantities, may add up in phase or out of phase. Indeed, one can use the method of stationary phase to obtain an analytic expression of  $S(\omega)$  that is valid for large values of  $\phi_{\max}$ . This expression shows that the number of peaks  $M$  in the SPM-broadened spectrum is given approximately by the relation [3]

$$\phi_{\max} \approx \left( M - \frac{1}{2} \right) \pi. \quad (4.1.14)$$

Equation (4.1.12) together with Eq. (4.1.14) can be used to estimate the extent of SPM-induced spectral broadening [6]. To obtain a more accurate measure of spectral broadening, one should use the RMS spectral width  $\Delta\omega_{\text{rms}}$  defined as

$$\Delta\omega_{\text{rms}}^2 = \langle (\omega - \omega_0)^2 \rangle - \langle (\omega - \omega_0) \rangle^2, \quad (4.1.15)$$

where the angle brackets denote an average over the SPM-broadened spectrum given in Eq. (4.1.13). More specifically,

$$\langle (\omega - \omega_0)^n \rangle = \frac{\int_{-\infty}^{\infty} (\omega - \omega_0)^n S(\omega) d\omega}{\int_{-\infty}^{\infty} S(\omega) d\omega}. \quad (4.1.16)$$

Using a procedure similar to that of Section 3.3, the spectral broadening factor for a Gaussian pulse is found to be [10]

$$\frac{\Delta\omega_{\text{rms}}}{\Delta\omega_0} = \left(1 + \frac{4}{3\sqrt{3}}\phi_{\max}^2\right)^{1/2}, \quad (4.1.17)$$

where  $\Delta\omega_0$  is the initial RMS spectral width of the pulse.

### 4.1.3 Effect of Pulse Shape and Initial Chirp

As mentioned earlier, the shape of the SPM-broadened spectrum depends on the pulse shape, and on the initial chirp if the input pulse is chirped [11–13]. Figure 4.4 compares the evolution of pulse spectra for Gaussian ( $m = 1$ ) and super-Gaussian ( $m = 2$ ) pulses over  $50L_{\text{NL}}$  using Eq. (3.2.24) in Eq. (4.1.13) and performing the integration numerically. In both cases, input pulses are assumed to be unchirped ( $C = 0$ ) and fiber losses are ignored ( $\alpha = 0$ ). The qualitative differences between the two spectra can be understood by referring to Figure 4.1, where the SPM-induced chirp is shown for the Gaussian and super-Gaussian pulses. The spectral range is larger for the super-Gaussian pulse because the maximum chirp from Eq. (4.1.10)

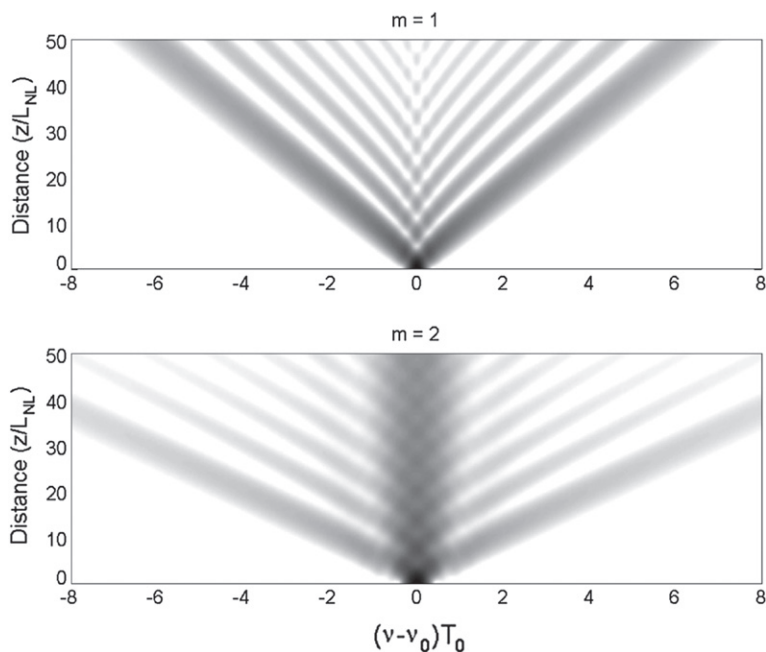


**Figure 4.4 Evolution of SPM-broadened spectra for fiber lengths in the range 0 to  $50L_{\text{NL}}$  for unchirped ( $C=0$ ) Gaussian ( $m=1$ ) and super-Gaussian ( $m=2$ ) pulses. A gray scale with a 20-dB range is used for the spectral density.**

is larger in that case. Even though both spectra in Figure 4.4 exhibit multiple peaks, most of the energy remains in the central peak for the super-Gaussian pulse. This is so because the chirp is nearly zero over the central region in Figure 4.1 for such a pulse, a consequence of the nearly uniform intensity of super-Gaussian pulses for  $|T| < T_0$ . A triangular shape of the spectral evolution in Figure 4.4 indicates that the SPM-induced spectral broadening increases linearly with distance.

An initial frequency chirp can also lead to drastic changes in the SPM-broadened pulse spectrum. This is illustrated in Figure 4.5, which shows the spectra of a Gaussian pulse for both positive and negative chirps using  $\phi_{\max} = 4.5\pi$ . It is evident that the sign of the chirp parameter  $C$  plays a critical role. For  $C > 0$ , spectral broadening increases and the oscillatory structure becomes less pronounced, as seen in Figure 4.5b. However, a negatively chirped pulse undergoes *spectral narrowing* through SPM, as seen clearly in parts (c) and (d) of Figure 4.5. The spectrum contains a central dominant peak for  $C = -20$  and narrows further as  $C$  decreases. This behavior can be understood from Eq. (4.1.10) by noting that the SPM-induced chirp is linear and positive (frequency increases

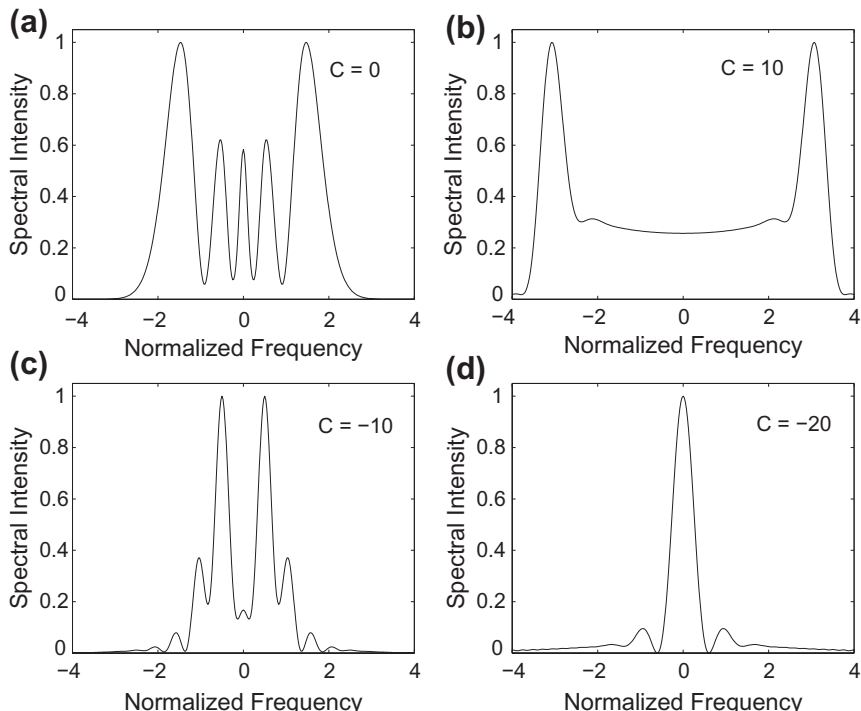


**Figure 4.5 Comparison of output spectra for Gaussian pulses for four values of chirp parameter  $C$  when fiber length and peak powers are chosen such that  $\phi_{\max} = 4.5\pi$ . The spectrum broadens for  $C > 0$  but becomes narrower for  $C < 0$  when compared with that of the input pulse.**

with increasing  $T$ ) over the central portion of a Gaussian pulse (see Figure 4.1). Thus, it adds to the initial chirp for  $C > 0$ , resulting in a broader spectrum. In the case of  $C < 0$ , the two chirp contributions are of opposite signs (except near the pulse edges), and the pulse becomes less chirped. If we employ the approximation that  $\phi_{NL}(t) \approx \phi_{\max}(1 - t^2/T_0^2)$  near the pulse center for Gaussian pulses, the SPM-induced chirp is nearly cancelled for  $C = -2\phi_{\max}$ . This relation provides a rough estimate of the value of  $C$  for which the narrowest spectrum occurs for a given value of  $\phi_{\max}$ .

The SPM-induced spectral narrowing has been observed in several experiments [11–13]. In a 1993 experiment, 100-fs pulses, obtained from a Ti:sapphire laser operating near 800 nm, were first chirped with a prism pair before launching them into a 48-cm-long fiber [11]. The 10.6 nm spectral width of the input pulses was nearly unchanged at low peak powers but became progressively smaller as the peak power was increased: it was reduced to 3.1 nm at a 1.6 kW peak power. The output spectral width also changed with the fiber length at a given peak power and exhibited a minimum value of 2.7 nm for a fiber length of 28 cm at the 1 kW peak power. The spectrum rebroadened for longer fibers. In a 2000 experiment, spectral compression from 8.4 to 2.4 nm was observed when a negatively chirped 110-fs pulse was transmitted through a 50-cm-long fiber. Figure 4.6 shows the measured pulse spectra for several values of the average power [12]. The FROG technique was used to verify that the phase of the spectrally compressed pulse was indeed constant over the pulse envelope. This feature resulted in a transform-limited pulse when peak power was suitably adjusted. For a quantitative modeling of the experimental data it was necessary to include the effects of GVD on the optical pulse. This issue is covered in Section 4.2.

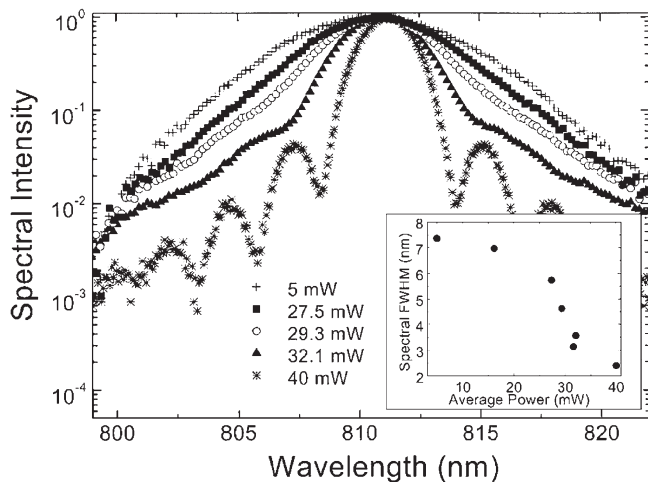


**Figure 4.6** Observed output spectra at several average power levels when a negatively chirped 110-fs pulse was transmitted through a 50-cm-long fiber. The inset shows the spectral FWHM as a function of average power. (After Ref. [12]; © 2000 OSA.)

#### 4.1.4 Effect of Partial Coherence

In the preceding discussion, SPM-induced spectral changes occur only for optical pulses because, as seen in Eq. (4.1.5), the nonlinear phase shift mimics temporal variations of the pulse shape. Indeed, the SPM-induced chirp in Eq. (4.1.8) vanishes for continuous-wave (CW) radiation, implying that a CW beam would not experience any spectral broadening in optical fibers. This conclusion, however, is a consequence of an implicit assumption that the input optical field is perfectly coherent. In practice, all optical beams are only partially coherent. The degree of coherence for laser beams is large enough that the effects of partial coherence are negligible in most cases of practical interest. For example, SPM-induced spectral broadening of optical pulses is relatively unaffected by the partial temporal coherence of the laser source as long as the coherence time  $T_c$  of the laser beam is much larger than the pulse width  $T_0$ .

When the coherence time becomes shorter than the pulse width, effects of partial coherence must be included [14–21]. In the case of a CW beam, SPM can lead to spectral broadening during its propagation inside an optical fiber. The physical reason behind such broadening can be understood by noting that partially coherent light exhibits both intensity and phase fluctuations. The SPM converts intensity fluctuations into additional phase fluctuations [see Eq. (4.1.5)] and broadens the optical spectrum. Alternatively, SPM reduces the coherence time  $T_c$  as the CW beam propagates inside the fiber, making it less and less coherent.

The optical spectrum of partially coherent light at the fiber output is obtained using the Wiener–Khintchine theorem [22]:

$$S(\omega) = \int_{-\infty}^{\infty} \Gamma(z, \tau) \exp(i\omega\tau) d\tau, \quad (4.1.18)$$

where the coherence function  $\Gamma(z, \tau)$  is defined as

$$\Gamma(z, \tau) = \langle U^*(z, T) U(z, T + \tau) \rangle. \quad (4.1.19)$$

The optical field  $U(z, T)$  inside the fiber at a distance  $z$  is known from Eq. (4.1.4). The angle brackets denote an ensemble average over fluctuations in the input field  $U(0, T)$ . The statistical properties of  $U(0, T)$  depend on the optical source and are generally quite different for laser and nonlaser sources.

The average in Eq. (4.1.19) can be performed analytically for thermal sources because both the real and imaginary parts of  $U(0, T)$  follow a Gaussian distribution for such a source. Even though the laser light used commonly in nonlinear-optics experiments is far from being thermal, it is instructive to consider the case of a thermal field. The coherence function of Eq. (4.1.19) in that specific case is found to evolve as [15]

$$\Gamma(Z, \tau) = \Gamma(0, \tau) [1 + Z^2 (1 - |\Gamma(0, \tau)|^2)]^{-2}, \quad (4.1.20)$$

where  $Z = L_{\text{eff}}/L_{\text{NL}}$  is the normalized propagation distance. For a perfectly coherent field,  $\Gamma(0, \tau) = 1$ . Equation (4.1.20) shows that such a field remains perfectly

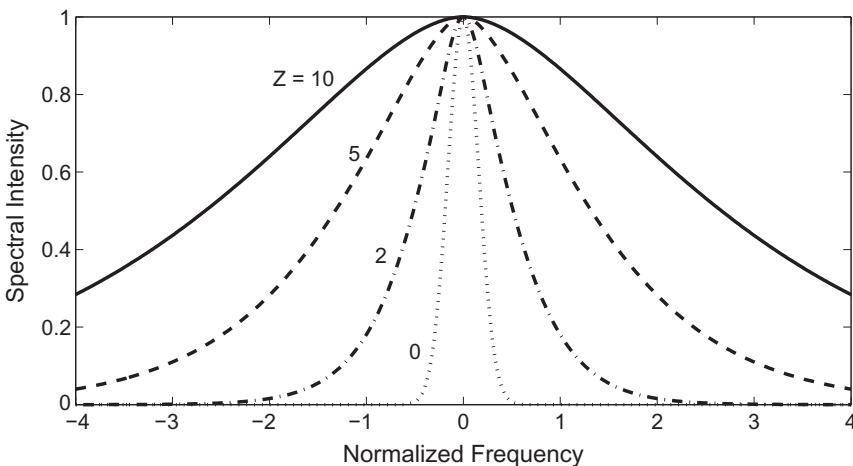


**Figure 4.7 SPM-induced spectral broadening of a partially coherent CW beam for several values of  $Z$ . The curve marked  $Z=0$  shows the input Gaussian spectrum.**

coherent on propagation. In contrast, partially coherent light becomes progressively less coherent as it travels inside the fiber.

The spectrum is obtained by substituting Eq. (4.1.20) in Eq. (4.1.18). The integral can be performed analytically in some specific cases [14], but in general requires numerical evaluation (through the FFT algorithm, for example). As an example, Figure 4.7 shows the optical spectra at several propagation distances assuming a Gaussian form for the input coherence function,

$$\Gamma(0, \tau) = \exp[-\tau^2/(2T_c^2)], \quad (4.1.21)$$

where  $T_c$  is the coherence time of the input field. As expected, shortening of the coherence time is accompanied with SPM-induced spectral broadening. Little broadening occurs until light has propagated a distance equal to the nonlinear length  $L_{NL}$ , but the spectrum broadens by a large factor at a distance of  $10L_{NL}$ . The spectral shape is quite different qualitatively compared with those seen in Figure 4.2 for the case of a completely coherent pulse. In particular, note the absence of a multipeak structure.

One may ask how the SPM-broadened spectrum of an optical pulse is affected by the partial coherence of the optical source. Numerical simulations show that each peak of the multipeak structure seen in Figure 4.2 begins to broaden when the coherence time becomes comparable to or shorter than the pulse width. As a result, individual peaks begin to merge together. In the limit of very short coherence time, the multipeak structure disappears altogether, and spectral broadening has features similar to those seen in Figure 4.7. The SPM-induced coherence degradation and the associated spectral broadening were first observed in a 1991 experiment by using stimulated Raman scattering (see Chapter 8) as a source of partially coherent light [16]. The coherence time of output pulses was reduced by a factor of  $>2.5$  in this experiment.

---

## 4.2 EFFECT OF GROUP-VELOCITY DISPERSION

The SPM effects discussed in Section 4.1 describe the propagation behavior realistically for only relatively long pulses ( $T_0 < 50$  ps) for which the dispersion length  $L_D$  is much larger compared with both the fiber length  $L$  and the nonlinear length  $L_{NL}$ . As pulses become shorter and the dispersion length becomes comparable to the fiber length, it becomes necessary to consider the combined effects of GVD and SPM [8]. New qualitative features arise from an interplay between GVD and SPM. In the anomalous-dispersion regime of an optical fiber, the two phenomena can cooperate in such a way that the pulse propagates as an optical soliton (see Chapter 5). In the normal-dispersion regime, the combined effects of GVD and SPM can be used for pulse compression. This section considers the temporal and spectral changes that occur when the effects of GVD are included in the description of SPM [23–34].

### 4.2.1 Pulse Evolution

The starting point is the NLS equation (2.3.46) or its form given in Eq. (3.1.4). The later equation can be written in a normalized form as

$$i \frac{\partial U}{\partial \xi} = \text{sgn}(\beta_2) \frac{1}{2} \frac{\partial^2 U}{\partial \tau^2} - N^2 e^{-\alpha z} |U|^2 U, \quad (4.2.1)$$

where  $\xi$  and  $\tau$  represent the normalized distance and time variables defined as

$$\xi = z/L_D, \quad \tau = T/T_0, \quad (4.2.2)$$

and the parameter  $N$  is introduced by using

$$N^2 = \frac{L_D}{L_{NL}} \equiv \frac{\gamma P_0 T_0^2}{|\beta_2|}. \quad (4.2.3)$$

The physical significance of  $N$  will become clear in Chapter 5. The practical significance of this dimensionless parameter is that solutions of Eq. (4.2.1) obtained for a specific  $N$  value are applicable to multiple practical situations through the scaling relation in Eq. (4.2.3). For example, if  $N = 1$  for  $T_0 = 1$  ps and  $P_0 = 1$  W, the calculated results apply equally well for  $T_0 = 10$  ps and  $P_0 = 10$  mW, or for  $T_0 = 0.1$  ps and  $P_0 = 100$  W. As evident from Eq. (4.2.3),  $N$  governs the relative importance of the SPM and GVD effects on pulse evolution along the fiber. Dispersion dominates for  $N \ll 1$ , while SPM dominates for  $N \gg 1$ . For values of  $N \sim 1$ , both SPM and GVD play an equally important role during pulse evolution. In Eq. (4.2.1),  $\text{sgn}(\beta_2) = \pm 1$  depending on whether GVD is normal ( $\beta_2 > 0$ ) or anomalous ( $\beta_2 < 0$ ). The split-step Fourier method of Section 2.4.1 can be used to solve Eq. (4.2.1) numerically.

Figure 4.8 shows evolution of the shape and the spectrum of an initially unchirped Gaussian pulse in the normal-dispersion regime of a fiber using  $N = 1$  and  $\alpha = 0$ . The qualitative behavior is quite different from that expected when either GVD or

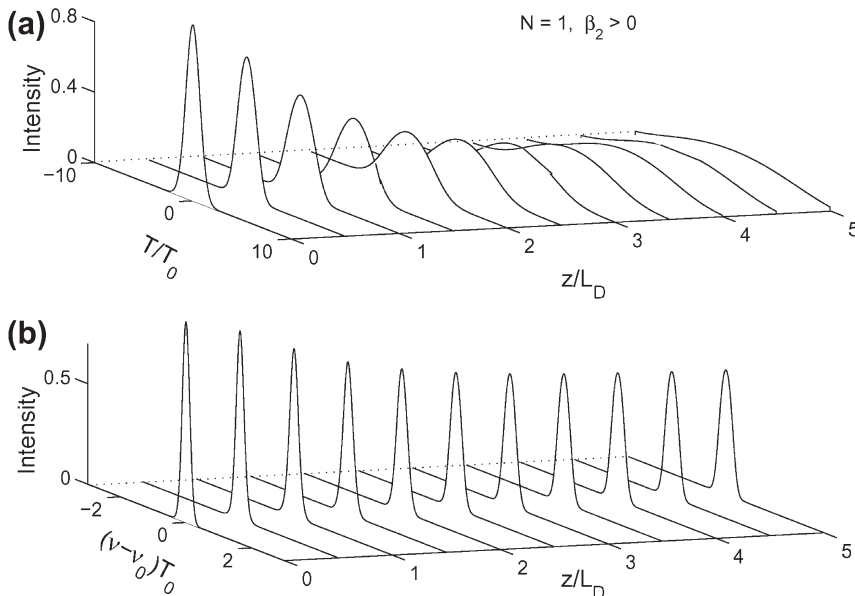


**Figure 4.8** Evolution of (a) pulse shapes and (b) optical spectra over a distance of  $5L_D$  for an initially unchirped Gaussian pulse propagating in the normal-dispersion regime of the fiber ( $\beta_2 > 0$ ) with parameters such that  $N = 1$ .

SPM dominates. In particular, the pulse broadens much more rapidly compared with the  $N = 0$  case (no SPM). This can be understood by noting that SPM generates new frequency components that are red-shifted near the leading edge and blue-shifted near the trailing edge of the pulse. As the red components travel faster than the blue components in the normal-dispersion regime, SPM leads to an enhanced rate of pulse broadening compared with that expected from GVD alone. This in turn affects spectral broadening as the SPM-induced phase shift  $\phi_{NL}$  becomes less than that occurring if the pulse shape were to remain unchanged. Indeed,  $\phi_{max} = 5$  at  $z = 5L_D$ , and a two-peak spectrum is expected in the absence of GVD. The single-peak spectrum for  $z/L_D = 5$  in Figure 4.8 implies that the effective  $\phi_{max}$  is below  $\pi$  because of pulse broadening.

The situation is different for pulses propagating in the anomalous dispersion regime of the fiber. Figure 4.9 shows the pulse shapes and spectra under conditions identical to those of Figure 4.8 except that the sign of the GVD parameter has been reversed ( $\beta_2 < 0$ ). The pulse broadens initially at a rate much lower than that expected in the absence of SPM and then appears to reach a steady state for  $z > 4L_D$ . At the same time, the spectrum narrows rather than exhibiting broadening expected by SPM in the absence of GVD. This behavior can be understood by noting that the SPM-induced chirp given by Eq. (4.1.9) is positive while the dispersion-induced chirp given in Eq. (3.2.14) is negative for  $\beta_2 < 0$ . The two chirp contributions nearly cancel

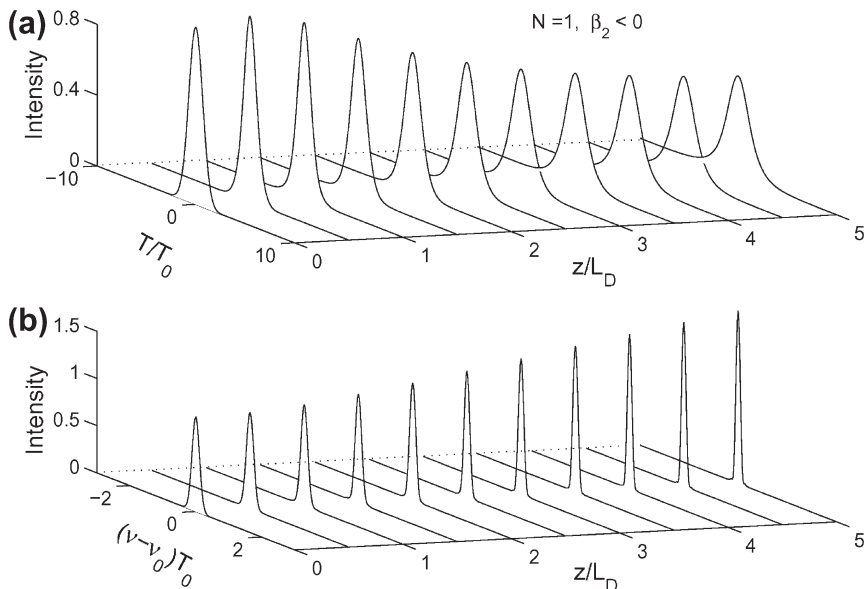


**Figure 4.9** Evolution of (a) pulse shapes and (b) optical spectra under conditions identical to those of [Figure 4.8](#) except that the Gaussian pulse propagates in the anomalous-dispersion regime ( $\beta_2 < 0$ ) of the fiber.

each other along the center portion of the Gaussian pulse when  $L_D = L_{NL}$  ( $N = 1$ ). Pulse shape adjusts itself during propagation to make such cancelation as complete as possible. Thus, GVD and SPM cooperate with each other to maintain a chirp-free pulse. The preceding scenario corresponds to soliton evolution; initial broadening of the Gaussian pulse occurs because the Gaussian profile is not the characteristic shape associated with a fundamental soliton. Indeed, if the input pulse is chosen to be a “sech” pulse [Eq. (3.2.22) with  $C = 0$ ], both its shape and spectrum remain unchanged during propagation. When the input pulse deviates from a “sech” shape, the combination of GVD and SPM affects the pulse in such a way that it evolves to become a “sech” pulse, as seen in [Figure 4.9](#). This aspect is discussed in detail in Chapter 5.

#### 4.2.2 Broadening Factor

[Figures 4.8](#) and [4.9](#) show that the main effect of SPM is to alter the broadening rate imposed on the pulse by the GVD alone. [Figure 4.10](#) shows the broadening factor  $\sigma_p/\sigma_0$  as a function of  $z/L_D$  for  $N = 1$  when unchirped Gaussian pulses are launched into the fiber. Here  $\sigma$  is the RMS width defined in Eq. (3.2.26) and  $\sigma_0$  is its initial value. The dashed line shows, for comparison, the broadening factor in the absence of SPM ( $N = 0$ ). The SPM enhances the broadening rate in the normal-dispersion regime and decreases it in the anomalous-dispersion regime. The slower

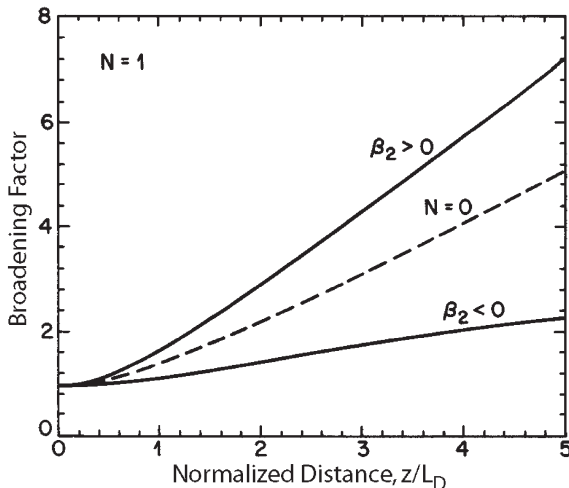


**Figure 4.10** The broadening factor of a Gaussian pulses in the cases of normal ( $\beta_2 > 0$ ) and anomalous ( $\beta_2 < 0$ ) GVD. The parameter  $N=1$  in both cases. The dashed curve shows, for comparison, the broadening expected in the absence of SPM ( $N=0$ ).

broadening rate for  $\beta_2 < 0$  is useful for  $1.55 \mu\text{m}$  optical communication systems for which  $\beta_2 \approx -20 \text{ ps}^2/\text{km}$  when standard fibers with their zero-dispersion wavelength near  $1.3 \mu\text{m}$  are used. The performance of such systems is limited by dispersion to the extent that the bit rate–distance product is typically below  $100 (\text{Gb/s})\text{-km}$  for chirped pulses with  $C = -5$ . It turns out that this product can be nearly doubled by increasing the peak power of input pulses in the range of  $20\text{--}30 \text{ mW}$  [29]. This enhancement is due to the SPM-induced pulse narrowing seen in Figure 4.9 in the case of  $\beta_2 < 0$ .

To study the combined effects of GVD and SPM, it is generally necessary to solve Eq. (4.2.1) numerically. However, even an approximate analytic expression for the pulse width would be useful to see the functional dependence of the broadening rate on various physical parameters. Several approaches have been used to solve the NLS equation approximately [35–42]. A variational approach was used as early as 1983 [35]. Another technique known as the *moment method* has also been used with success [40–42]. Both of these techniques are discussed in Section 4.3; they assume that the pulse maintains a certain shape during propagation inside the fiber, even though its amplitude, phase, width, and chirp change with  $z$ . A variant of the moment method has been used to include the effects of fiber losses and to predict not only the pulse width but also the spectral width and the frequency chirp [41].

In a different approach [38], the NLS equation is first solved by neglecting the GVD effects. The result is used as the initial condition, and Eq. (4.2.1) is solved again by neglecting the SPM effects. The approach is similar to the split-step Fourier method of Section 2.4, except that the step size is equal to the fiber length. The RMS

pulse width can be calculated analytically by following the method discussed in Section 3.3. When an unchirped Gaussian pulse is incident at the input end of a fiber of length  $L$ , the broadening factor is given by [38]

$$\frac{\sigma}{\sigma_0} = \left[ 1 + \sqrt{2}\phi_{\max} \frac{L}{L_D} + \left( 1 + \frac{4}{3\sqrt{3}}\phi_{\max}^2 \right) \frac{L^2}{L_D^2} \right]^{1/2}, \quad (4.2.4)$$

where  $\phi_{\max}$  is the SPM-induced maximum phase shift given in Eq. (4.1.7). This expression is fairly accurate for  $\phi_{\max} < 1$ .

In another approach, Eq. (4.2.1) is solved in the frequency domain [39]. Such a spectral approach shows that SPM can be viewed as a four-wave mixing process [25] in which two photons at pump frequencies are annihilated to create two photons at frequencies shifted toward the blue and red sides. These newly created spectral components result in SPM-induced spectral broadening of the pulse. The oscillatory structure of the SPM spectra is due to the phase-matching requirement of four-wave mixing (see Chapter 10). Although in general the equation describing the evolution of the spectral components should be solved numerically, it can be solved analytically in some cases if the pulse shape is assumed not to change significantly.

### 4.2.3 Optical Wave Breaking

Equation (4.2.1) suggests that the effects of SPM should dominate over those of GVD for values of  $N \gg 1$ , at least during the initial stages of pulse evolution. In fact, by introducing a new distance variable as  $Z = N^2\xi = z/L_{NL}$ , Eq. (4.2.1) can be written as

$$i \frac{\partial U}{\partial Z} - \frac{d}{2} \frac{\partial^2 U}{\partial \tau^2} + |U|^2 U = 0, \quad (4.2.5)$$

where fiber losses are neglected and  $d = \beta_2/(\gamma P_0 T_0^2)$  is a small parameter. If we use the transformation

$$U(z, T) = \sqrt{\rho(z, T)} \exp \left( i \int_0^T v(z, T) dT \right) \quad (4.2.6)$$

in Eq. (4.2.5), we find that the pulse-propagation problem reduces approximately to a fluid-dynamics problem in which the variables  $\rho$  and  $v$  play, respectively, the role of density and velocity of a fluid [43]. In the optical case, these variables represent the power and chirp profiles of the pulse. For a square-shape pulse, the pulse-propagation problem becomes identical to the one related to “breaking of a dam” and can be solved analytically. This solution is useful for lightwave systems employing the NRZ format and provides considerable physical insight [44–46].

The approximate solution, although useful, does not account for a phenomenon termed *optical wave breaking* [47–53]. It turns out that GVD cannot be treated as a small perturbation even when  $N$  is large. The reason is that, because of a large

amount of the SPM-induced frequency chirp imposed on the pulse, even weak dispersive effects lead to significant pulse shaping. In the case of normal dispersion ( $\beta_2 > 0$ ), the pulse becomes nearly rectangular with relatively sharp leading and trailing edges and is accompanied by a linear chirp across its entire width [23]. It is this linear chirp that can be used to compress the pulse by passing it through a dispersive delay line.

The GVD-induced pulse shaping has another effect on pulse evolution. It increases the importance of GVD because the second derivative in Eq. (4.2.1) becomes large near the pulse edges. As a consequence, the pulse develops a fine structure near its edges. Figure 4.11 shows the temporal and spectral evolution for  $N = 30$  in the case of an initially unchirped Gaussian pulse. The oscillatory structure near pulse edges is present already at  $z/L_D = 0.06$ . Further increase in  $z$  leads to broadening of the pulse tails. The oscillatory structure depends considerably on the pulse shape. Figure 4.12 shows the pulse shape and the spectrum at  $z/L_D = 0.08$  for an unchirped “sech” pulse. A noteworthy feature is that rapid oscillations near pulse edges are always accompanied by the sidelobes in the spectrum. The central multipeak part of the spectrum is also considerably modified by the GVD. In particular, the minima are not as deep as expected from SPM alone.

The physical origin of temporal oscillations near the pulse edges is related to optical wave breaking [47]. Both GVD and SPM impose frequency chirp on the pulse as it travels down the fiber. However, as seen from Eqs (3.2.14) and (4.1.9),

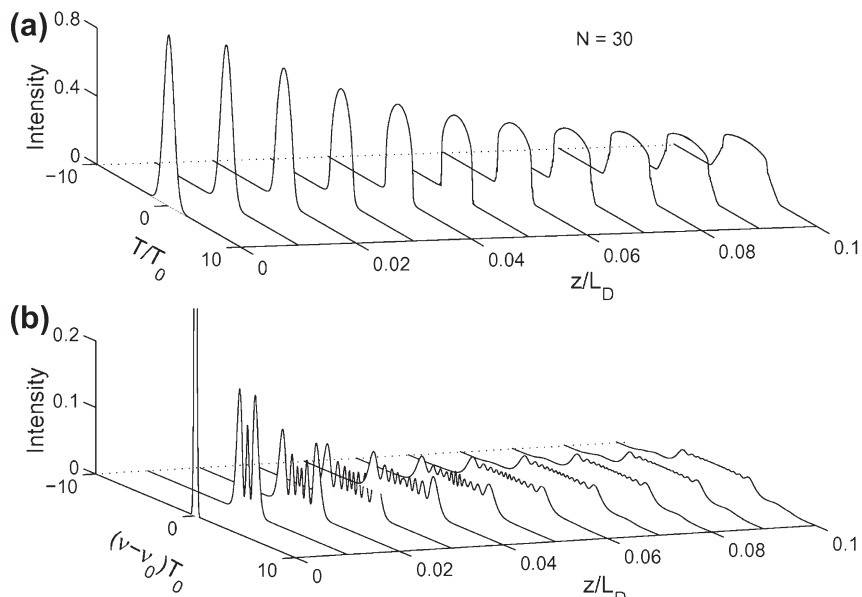


**Figure 4.11** (a) Temporal and (b) spectral evolution of an initially unchirped Gaussian pulse with  $N=30$  at a distance  $z=0.1L_D$  in the normal-dispersion regime of an optical fiber.

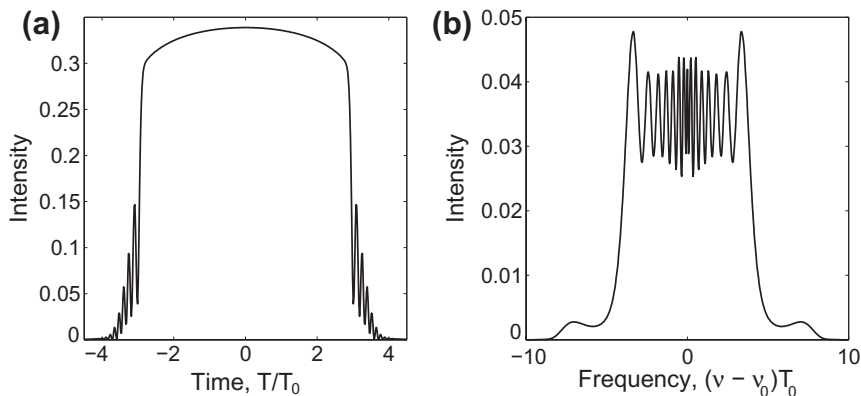


**Figure 4.12** (a) Shape and (b) spectrum of an initially unchirped secant hyperbolic pulse with  $N=30$  at a distance  $z=0.08L_0$ . Spectral sidelobes and temporal structure near pulse edges are due to optical wave breaking.

although the GVD-induced chirp is linear in time, the SPM-induced chirp is far from being linear across the entire pulse. Because of the nonlinear nature of the composite chirp, different parts of the pulse propagate at different speeds [52]. In particular, in the case of normal GVD ( $\beta_2 > 0$ ), the red-shifted light near the leading edge travels faster and overtakes the unshifted light in the forward tail of the pulse. The opposite occurs for the blue-shifted light near the trailing edge. In both cases, the leading and trailing regions of the pulse contain light at two different frequencies that interfere. Oscillations near the pulse edges in Figure 4.11 are a result of such interference.

The phenomenon of optical wave breaking can also be understood as a four-wave mixing process (see Chapter 10). Nonlinear mixing of two different frequencies  $\omega_1$  and  $\omega_2$  in the pulse tails creates new frequencies at  $2\omega_1 - \omega_2$  and  $2\omega_2 - \omega_1$ . The spectral sidelobes in Figure 4.12 represent these new frequency components. Temporal oscillations near pulse edges and the spectral sidelobes are manifestations of the same phenomenon. It is interesting to note that optical wave breaking does not occur in the case of anomalous GVD. The reason is that the red-shifted part of the pulse cannot take over the fast-moving forward tail. Instead, the energy in the pulse tail spreads out, and the pulse acquires a pedestal [52].

The results shown in Figures 4.11 and 4.12 are obtained for an unchirped pulse ( $C = 0$ ). Pulses emitted from practical laser sources are often chirped and may follow quite a different evolution pattern depending on the sign and magnitude of the chirp parameter  $C$  [49]. Figure 4.13 shows the pulse shape and the spectrum for a chirped Gaussian pulse using  $C = -20$  and  $N = 30$ . The dramatic changes in the pulse shape and spectrum compared with Figure 4.12 illustrate how much an initial chirp can modify the propagation behavior. For an initially chirped pulse, the shape becomes nearly triangular rather than rectangular. At the same time, the spectrum exhibits an oscillatory structure in the wings while the central SPM-like structure (seen in Figure 4.12 in the case of an unchirped pulse) has almost disappeared. These changes

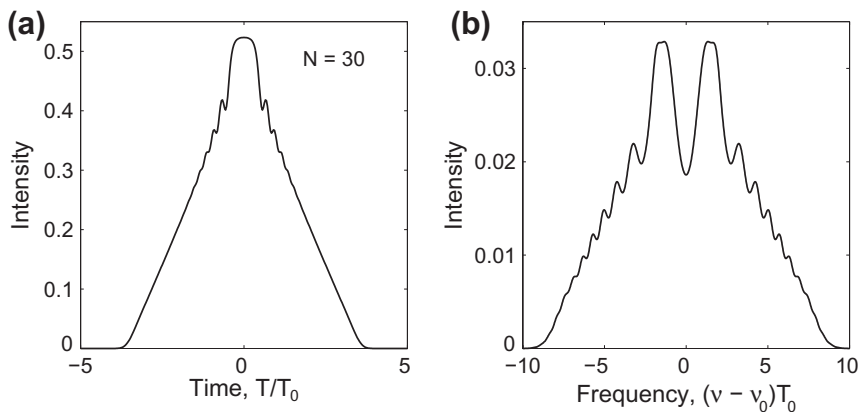


**Figure 4.13** (a) Shape and (b) spectrum at a distance  $z=0.08 L_0$  for an input Gaussian pulse chirped such that  $C=-20$ . The input peak power corresponds to  $N=30$ .

in the pulse shape and spectrum can be understood qualitatively by recalling that a positive initial chirp adds to the SPM-induced chirp. As a result, optical wave breaking sets in earlier for chirped pulses. Pulse evolution is also sensitive to fiber losses. For an actual comparison between theory and experiment, it is necessary to include both the chirp and losses in numerical simulations.

#### 4.2.4 Experimental Results

The combined effects of GVD and SPM in optical fibers were first observed in an experiment in which 5.5-ps (FWHM) pulses from a mode-locked dye laser (at 587 nm) were propagated through a 70-m fiber [23]. For an input peak power of 10 W ( $N \approx 7$ ), output pulses were nearly rectangular and had a positive linear chirp. The pulse shape was deduced from autocorrelation measurements as pulses were too short to be measured directly (see Section 3.3.4). In a later experiment, much wider pulses (FWHM  $\approx 150$  ps) from a Nd:YAG laser operating at 1.06  $\mu\text{m}$  were transmitted through a 20-km-long fiber [26]. As the peak power of the input pulses was increased from 1 to 40 W (corresponding to  $N$  in the range 20–150), the output pulses broadened, became nearly rectangular and then developed substructure near its edges, resulting in an evolution pattern similar to that shown in Figure 4.11. For such long fibers, it is necessary to include fiber losses. The experimental results were indeed in good agreement with the predictions of Eq. (4.2.1).

The evidence of optical wave breaking was seen in an experiment in which 35-ps (FWHM) pulses at 532 nm (from a frequency-doubled Nd:YAG laser) with peak powers of 235 W were propagated through a 93.5-m-long polarization-maintaining fiber [47]. Figure 4.14 shows the experimentally observed spectrum of the output pulses. Even though  $N \approx 173$  in this experiment, the formal similarity with the spectrum shown in Figure 4.12 is evident. In fact, the phenomenon of optical wave breaking was discovered in an attempt to explain the presence of the sidelobes in Figure 4.14. In a 1988

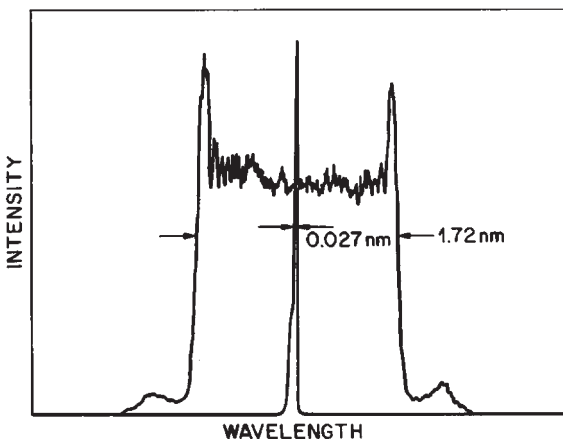


**Figure 4.14** Output spectrum of 35-ps input pulses showing SPM-induced spectral broadening. Initial pulse spectrum is also shown for comparison. (After Ref. [47]; © 1985 OSA.)

experiment [50], the frequency chirp across the pulse was directly measured by using a combination of a streak camera and a spectrograph. The spectral sidelobes associated with the optical wave breaking were indeed found to be correlated with the generation of new frequencies near the pulse edges. In a later experiment [51], rapid oscillations across the leading and trailing edges of the optical pulse were observed directly by using a cross-correlation technique that permitted subpicosecond resolution. The experimental results were in excellent agreement with the predictions of Eq. (4.2.1).

#### 4.2.5 Effect of Third-Order Dispersion

If the optical wavelength  $\lambda_0$  nearly coincides with the zero-dispersion wavelength  $\lambda_D$  so that  $\beta_2 \approx 0$ , it is necessary to include the effects of third-order dispersion (TOD) on SPM-induced spectral broadening [54–63]. The pulse-propagation equation is obtained from Eq. (2.3.44) by setting  $\beta_2 = 0$  and neglecting the higher-order nonlinear terms. If we introduce the dispersion length  $L'_D$  from Eq. (3.3.6) and define  $\xi' = z/L'_D$  as the normalized distance, we obtain

$$i\frac{\partial U}{\partial \xi'} = \text{sgn}(\beta_3) \frac{i}{6} \frac{\partial^3 U}{\partial \tau^3} - \bar{N}^2 e^{-\alpha z} |U|^2 U, \quad (4.2.7)$$

where

$$\bar{N}^2 = \frac{L'_D}{L_{NL}} = \frac{\gamma P_0 T_0^3}{|\beta_3|}. \quad (4.2.8)$$

Similar to Eq. (4.2.1), the parameter  $\bar{N}$  governs the relative importance of the TOD and SPM effects during pulse evolution; TOD dominates for  $\bar{N} \ll 1$  while SPM

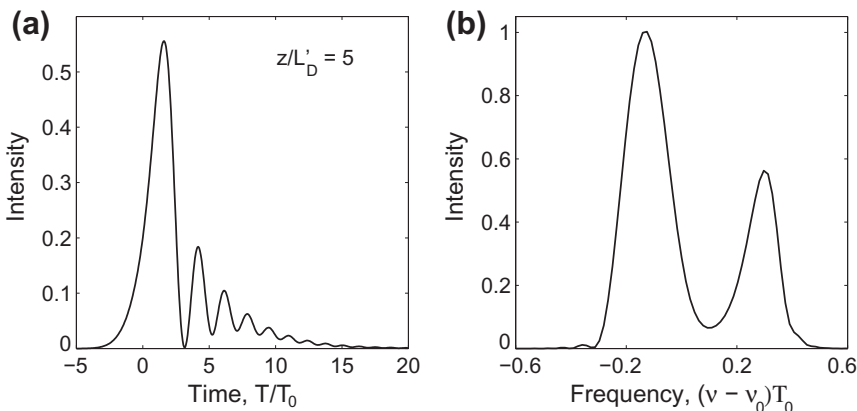


**Figure 4.15 (a)** Shape and **(b)** spectrum of an unchirped Gaussian pulse propagating exactly at the zero-dispersion wavelength with  $\bar{N} = 1$  and  $z = 5L'_D$ .

dominates for  $\bar{N} \gg 1$ . Equation (4.2.7) can be solved numerically with the split-step Fourier method of Section 2.4.1. In the following discussion, we assume  $\beta_3 > 0$  and neglect fiber losses by setting  $\alpha = 0$ .

Figure 4.15 shows the shape and the spectrum of an initially unchirped Gaussian pulse at  $\xi' = 5$  for the case  $\bar{N} = 1$ . The pulse shape should be compared with that shown in Figure 3.6 where SPM effects were absent ( $\bar{N} = 0$ ). The effect of SPM is to increase the number of oscillations seen near the trailing edge of the pulse. At the same time, the intensity does not become zero at the oscillation minima. The effect of TOD on the spectrum is also evident in Figure 4.15. In the absence of TOD, a symmetric two-peak spectrum is expected (similar to the one shown in Figure 4.2 for the case  $\phi_{\max} = 1.5\pi$ ) since  $\phi_{\max} = 5$  for the parameter values used in Figure 4.15. The effect of TOD is to introduce spectral asymmetry without affecting the two-peak structure. This behavior is in sharp contrast with the one shown in Figure 4.8 for the normal-dispersion case where GVD hindered splitting of the spectrum.

Pulse evolution exhibits qualitatively different features for large values of  $N$ . As an example, Figure 4.16 shows the evolution of the shape and spectrum of an initially unchirped Gaussian pulse in the range of  $\xi' = 0-0.2$  for  $\bar{N} = 10$ . The pulse develops an oscillatory structure with deep modulations. Because of rapid temporal variations, the third derivative in Eq. (4.2.7) becomes large locally, and the TOD effects become more important as the pulse propagates inside the fiber. The most noteworthy feature of the spectrum is that the pulse energy is distributed in multiple spectral bands, a feature common to all values of  $\bar{N} \geq 1$ . As one of the spectral bands lies in the anomalous-dispersion regime, pulse energy in that band can form a soliton [62]. The energy in other spectral bands, lying in the normal-GVD regime of the fiber, disperses with propagation. The soliton-related features are discussed later in Chapter 5. The important point to note is that, because of SPM-induced spectral broadening, the pulse does not

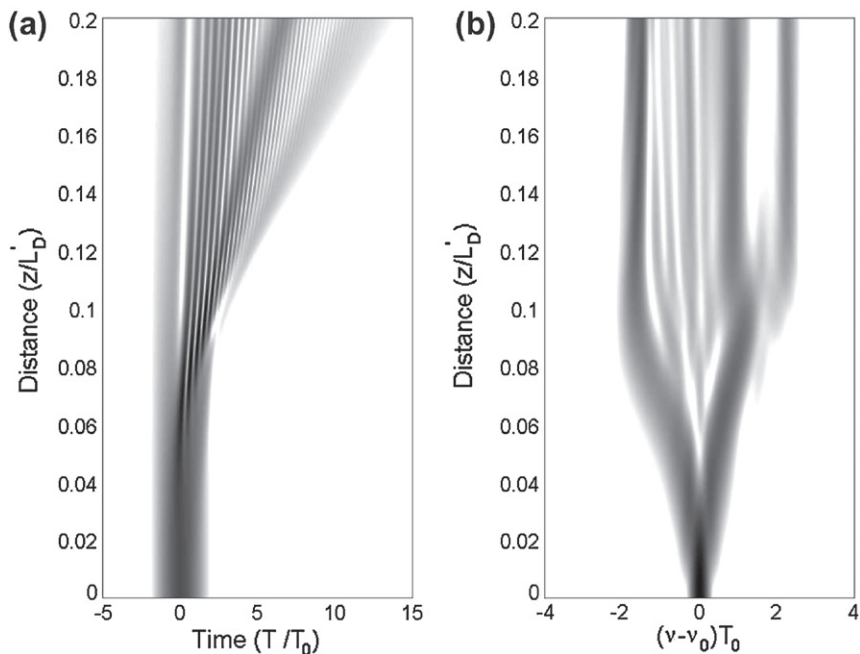


**Figure 4.16 Evolution of the (a) shape and (b) spectrum of an initially Gaussian pulse over  $0.2L_D'$  for  $\bar{N} = 10$ . The gray intensity scale is over a 20-dB range.**

really propagate at the zero-dispersion wavelength even if  $\beta_2 \approx 0$  initially. In effect, the pulse creates its own  $\beta_2$  through SPM. Roughly speaking, the effective value of  $\beta_2$  is given by

$$|\beta_2| \approx \beta_3 |\delta\omega_{\max}| / 2\pi, \quad (4.2.9)$$

where  $\delta\omega_{\max}$  is the maximum chirp given in Eq. (4.1.10). Physically,  $\beta_2$  is set by the dominant outermost spectral peak in the SPM-broadened spectrum.

In dispersion-managed fiber links,  $\beta_2$  is large locally but nearly vanishes on average. The effects of TOD play an important role in such links, especially for short optical pulses [64]. The spectral or temporal evolution depends on whether a dispersion-compensating fiber is placed before or after the standard fiber. In the case of post-compensation, the pulse develops an oscillating tail because of TOD and exhibits spectral narrowing. These features have been seen experimentally by transmitting 0.4-ps pulses over a 2.5-km-long dispersion-compensated fiber link.

#### 4.2.6 SPM Effects in Fiber Amplifiers

In a fiber amplifier, the input field is amplified as it propagates down the fiber. In the case of a CW beam, the input power increases exponentially by a factor  $G = \exp(gL)$

for an amplifier of length  $L$ , where  $g$  is the gain coefficient, provided the gain remains unsaturated. In the case of optical pulses, as the pulse energy grows exponentially, the impact of SPM becomes stronger. This is evident from Eq. (4.2.1) if we replace the loss parameter  $\alpha$  with  $-g$ . In the absence of dispersion, the results of Section 4.1 still hold, but the effective length appearing in Eq. (4.1.7) is defined as  $L_{\text{eff}} = [\exp(gL) - 1]/g$ , and it may become much larger than the actual amplifier length  $L$ , depending on the value of  $gL$ . As a result, spectral broadening depends on the amplifier gain and is enhanced considerably.

When dispersive effects are included, the impact of amplification depends on the nature of GVD (normal versus anomalous). In the case of anomalous GVD and for values of  $N$  close to 1, the pulse begins to compress as it is amplified [65]. The reason is related to the soliton nature of pulse propagation (see Chapter 5). As the pulse is amplified,  $N$  can be maintained close to 1 only if its width  $T_0$  is reduced simultaneously. In the case of normal GVD, pulse broadens rapidly when  $g = 0$ . However, it turns out that when  $g > 0$ , the pulse evolves asymptotically to become nearly parabolic, while maintaining a linear chirp across its temporal profile [66–72]. In fact, the asymptotic solution of the NLS equation (3.1.1) with  $\alpha = -g$  can be obtained analytically in the form [66]

$$A(z, T) = A_p(z)[1 - T^2/T_p^2(z)] \exp[i\phi_p(z, T)] \quad (4.2.10)$$

for  $|T| \leq T_p(z)$  with  $A(z, T) = 0$  for  $|T| < T_p(z)$ . The amplitude  $A_p$ , width  $T_p$ , and phase  $\phi_p$  of the pulse depend on various fiber parameters as

$$A_p(z) = \frac{1}{2}(gE_0)^{1/3}(\gamma\beta_2/2)^{-1/6} \exp(gz/3), \quad (4.2.11)$$

$$T_p(z) = 6g^{-1}(\gamma\beta_2/2)^{1/2} A_p(z), \quad (4.2.12)$$

$$\phi_p(z, T) = \phi_0 + (3\gamma/2g)A_p^2(z) - (g/6\beta_2)T^2, \quad (4.2.13)$$

where  $E_0$  is the input pulse energy. An important feature of this solution is that the pulse width  $T_p(z)$  scales linearly with the amplitude  $A_p(z)$ , which is evident from Eq. (4.2.12). Such a solution is referred to as being self-similar [73]. Because of self-similarity, the pulse maintains its parabolic shape even though its width and amplitude increase with  $z$  in an exponential fashion.

The most noteworthy feature of the preceding self-similar solution is that the time-dependence of the phase is quadratic in Eq. (4.2.13), indicating that the amplified pulses are linearly chirped across their entire temporal profile. It follows from the discussion in Section 4.1 that a purely linear chirp is possible through SPM only when pulse shape is parabolic. A somewhat surprising feature of the solution in Eq. (4.2.10) is the total absence of optical wave breaking in the normal-GVD regime. It was discovered in a 1993 study that a parabolic shape represent the only shape for which optical wave breaking can be suppressed [53]. Optical amplifiers facilitate the production of a parabolic shape since new frequency components are generated continuously through SPM in such a way that the pulse maintains a linear chirp as it is amplified and its width increases through dispersion.

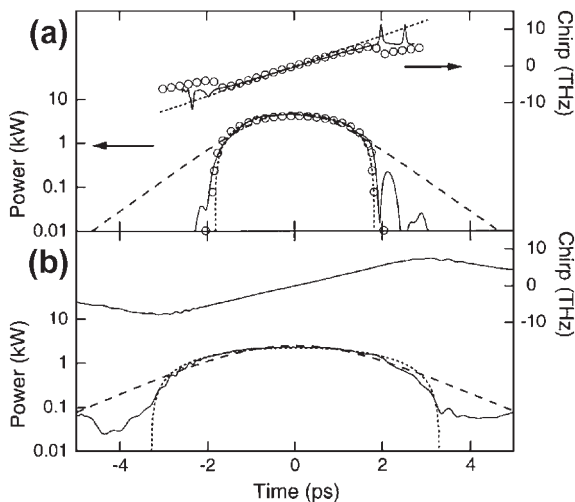


**Figure 4.17** Measured (solid lines) intensity and chirp profiles (a) at the output of a Yb-doped fiber amplifier with 30-dB gain and (b) after propagation in a 2-m-long passive fiber. The circles show numerical results based on the NLS equation, dotted lines show the asymptotic solution, and dashed lines show the intensity profile of a sech pulse. (After Ref. [66]; © 2000 American Physical Society.)

An important property of the self-similar solution given in Eqs (4.2.10–4.2.13) is that the amplified pulse depends on the energy of the input pulse, but not on its other properties such as its shape and width. Parabolic pulses have been observed in several experiments in which picosecond or femtosecond pulses were amplified in the normal-dispersion regime of a fiber amplifier. Figure 4.17a shows the intensity and phase profiles (deduced from FROG traces) observed at the output end of a 3.6-m-long Yb-doped fiber amplifier with 30-dB gain when a 200-fs pulse with 12-pJ energy was launched into it [66]. Part (b) shows the two profiles after further propagation in a 2-m-long passive fiber. The experimental results agree well with both the numerical results obtained by solving the NLS equation (circles) and the asymptotic solution corresponding to a parabolic pulse (dotted lines). As shown by the dashed lines in Figure 4.17, the observed intensity profile is far from that of a “sech” pulse.

Self-similar evolution toward a parabolic pulse has also been observed in fiber-based Raman amplifiers [69]. In such amplifiers the nonlinear phenomenon of stimulated Raman scattering is used to amplify the input pulse (see Section 8.3.6). Mode-locked Yb-doped fiber lasers can also emit parabolic-shape pulses under suitable conditions [70]. The self-similar nature of parabolic pulses is helpful for generating high-energy pulses from lasers and amplifiers based on Yb-doped fibers [74–77]. It was found in a 2011 experiment that a parabolic shape is optimum for SPM-induced spectral compression [78]. Indeed, the spectrum of negatively chirped parabolic pulses could be compressed through SPM within 20% of the Fourier-transform limit.

---

## 4.3 SEMIANALYTIC TECHNIQUES

The results of the preceding section are based on the numerical solutions of the NLS equation with the split-step Fourier method of Section 2.4.1. Although a numerical solution is necessary for accuracy, considerable physical insight is gained if the NLS equation can be solved approximately in a semianalytic fashion. In this section we employ two such techniques for solving the NLS equation (2.3.46). Using  $A = \sqrt{P_0}e^{-\alpha z}U$ , this equation can be written in the form

$$i\frac{\partial U}{\partial z} - \frac{\beta_2}{2}\frac{\partial^2 U}{\partial T^2} + \gamma P_0 e^{-\alpha z}|U|^2 U = 0. \quad (4.3.1)$$

### 4.3.1 Moment Method

The moment method was used as early as 1971 in the context of nonlinear optics [79]. It can be used to solve Eq. (4.3.1) approximately, provided one can assume that the pulse maintains a specific shape as it propagates down a fiber even though its amplitude, width, and chirp change in a continuous fashion [80–82]. This assumption may hold in some cases. For example, it was seen in Section 3.2 that a Gaussian pulse maintains its shape in a linear dispersive medium even though its amplitude, width, and chirp change during propagation. If the nonlinear effects are relatively weak ( $L_{NL} \gg L_D$ ), a Gaussian shape may remain approximately valid. Similarly, it was seen in Section 4.1 that a pulse maintains its shape even when nonlinear effects are strong provided dispersive effect are negligible ( $L_{NL} \ll L_D$ ). It will be seen in Chapter 5 in the context of solitons that, even when  $L_{NL}$  and  $L_D$  are comparable, a pulse may maintain its shape under certain conditions.

The basic idea behind the moment method is to treat the optical pulse like a particle whose energy  $E_p$ , RMS width  $\sigma_p$ , and chirp  $C_p$  are related to  $U(z, T)$  as

$$E_p = \int_{-\infty}^{\infty} |U|^2 dT, \quad \sigma_p^2 = \frac{1}{E_p} \int_{-\infty}^{\infty} T^2 |U|^2 dT, \quad (4.3.2)$$

$$C_p = \frac{i}{E_p} \int_{-\infty}^{\infty} T \left( U^* \frac{\partial U}{\partial T} - U \frac{\partial U^*}{\partial T} \right) dT. \quad (4.3.3)$$

As the pulse propagates inside the fiber, these three moments change. To find how they evolve with  $z$ , we differentiate Eqs (4.3.2) and (4.3.3) with respect to  $z$  and use Eq. (4.3.1). After some algebra, we find that  $dE_p/dz = 0$  but  $\sigma_p^2$  and  $C_p$  satisfy

$$\frac{d\sigma_p^2}{dz} = \frac{\beta_2}{E_p} \int_{-\infty}^{\infty} T^2 \text{Im} \left( U^* \frac{\partial^2 U}{\partial T^2} \right) dT, \quad (4.3.4)$$

$$\frac{dC_p}{dz} = \frac{2\beta_2}{E_p} \int_{-\infty}^{\infty} \left| \frac{\partial U}{\partial T} \right|^2 dT + e^{-\alpha z} \frac{\gamma P_0}{E_p} \int_{-\infty}^{\infty} |U|^4 dT. \quad (4.3.5)$$

In the case of a chirped Gaussian pulse, the field  $U(z, T)$  at any distance  $z$  has the form

$$U(z, T) = a_p \exp \left[ -\frac{1}{2}(1 + iC_p)(T/T_p)^2 + i\phi_p \right], \quad (4.3.6)$$

where all four pulse parameters,  $a_p$ ,  $C_p$ ,  $T_p$ , and  $\phi_p$ , are functions of  $z$ . The phase  $\phi_p$  does not appear in Eqs (4.3.4) and (4.3.5). Even though  $\phi_p$  changes with  $z$ , it does not affect other pulse parameters and can be ignored. The peak amplitude  $a_p$  is related to the energy as  $E_p = \sqrt{\pi}a_p^2 T_p$ . Since  $E_p$  does not change with  $z$ , we can replace it with its initial value  $E_0 = \sqrt{\pi}T_0$ . The width parameter  $T_p$  is related to the RMS width  $\sigma_p$  of the pulse as  $T_p = \sqrt{2}\sigma_p$ . Using Eq. (4.3.6) and performing integrals in Eqs (4.3.4) and (4.3.5), the width  $T_p$  and chirp  $C_p$  are found to change with  $z$  as

$$\frac{dT_p}{dz} = \frac{\beta_2 C_p}{T_p}, \quad (4.3.7)$$

$$\frac{dC_p}{dz} = (1 + C_p^2) \frac{\beta_2}{T_p^2} + \frac{\gamma P_0 T_0}{\sqrt{2} T_p} e^{-\alpha z}. \quad (4.3.8)$$

This set of two first-order differential equations can be used to find how the nonlinear effects modify the width and chirp of the pulse.

Considerable physical insight can be gained from Eqs (4.3.7) and (4.3.8). The SPM phenomenon does not affect the pulse width directly as the nonlinear parameter  $\gamma$  appears only in the chirp equation (4.3.8). The two terms on the right side of this equation originate from dispersive and nonlinear effects, respectively. They have the same sign for normal GVD ( $\beta_2 > 0$ ). Since SPM-induced chirp in this case adds to the GVD-induced chirp, we expect SPM to increase the rate of pulse broadening. In contrast, when GVD is anomalous ( $\beta_2 < 0$ ), the two terms on the right side of Eq. (4.3.8) have opposite signs, and the pulse broadening should be reduced in the presence of SPM because of the smaller values of  $C_p$  in Eq. (4.3.7). In fact, this equation can be integrated to obtain the following general relation between pulse width and chirp:

$$T_p^2(z) = T_0^2 + 2 \int_0^z \beta_2(z) C_p(z) dz. \quad (4.3.9)$$

The equation shows explicitly that the pulse compresses whenever the quantity  $\beta_2 C_p < 0$ , a result obtained earlier in Section 3.2.

### 4.3.2 Variational Method

The variational method is well known from classical mechanics and is used in many different contexts [83–85]. It was applied as early as 1983 to the problem of pulse propagation inside optical fibers [35]. Mathematically, it makes use of the Lagrangian  $\mathcal{L}$  defined as

$$\mathcal{L} = \int_{-\infty}^{\infty} \mathcal{L}_d(q, q^*) dT, \quad (4.3.10)$$

where the Lagrangian density  $\mathcal{L}_d$  is a function of the generalized coordinate  $q(z)$  and  $q^*(z)$ , both of which evolve with  $z$ . Minimization of the “action” functional,  $\mathcal{S} = \int \mathcal{L} dz$ , requires that  $\mathcal{L}_d$  satisfy the Euler–Lagrange equation

$$\frac{\partial}{\partial T} \left( \frac{\partial \mathcal{L}_d}{\partial q_t} \right) + \frac{\partial}{\partial z} \left( \frac{\partial \mathcal{L}_d}{\partial q_z} \right) - \frac{\partial \mathcal{L}_d}{\partial q} = 0, \quad (4.3.11)$$

where  $q_t$  and  $q_z$  denote the derivative of  $q$  with respect to  $T$  and  $z$ , respectively.

The variational method makes use of the fact that the NLS equation (4.3.1) can be derived from the Lagrangian density

$$\mathcal{L}_d = \frac{i}{2} \left( U^* \frac{\partial U}{\partial z} - U \frac{\partial U^*}{\partial z} \right) + \frac{\beta_2}{2} \left| \frac{\partial U}{\partial T} \right|^2 + \frac{1}{2} \gamma P_0 e^{-\alpha z} |U|^4, \quad (4.3.12)$$

with  $U^*$  acting as the generalized coordinate  $q$  in Eq. (4.3.11). If we assume that the pulse shape is known in advance in terms of a few parameters, the time integration in Eq. (4.3.10) can be performed analytically to obtain the Lagrangian  $\mathcal{L}$  in terms of these pulse parameters. In the case of a chirped Gaussian pulse of the form given in Eq. (4.3.6), we obtain

$$\mathcal{L} = \frac{\beta_2 E_p}{4T_p^2} (1 + C_p^2) + \frac{\gamma e^{-\alpha z} E_p^2}{\sqrt{8\pi} T_p} + \frac{E_p}{4} \left( \frac{dC_p}{dz} - \frac{2C_p}{T_p} \frac{dT_p}{dz} \right) - E_p \frac{d\phi_p}{dz}, \quad (4.3.13)$$

where  $E_p = \sqrt{\pi} a_p^2 T_p$  is the pulse energy.

The final step is to minimize the action  $\mathcal{S} = \int \mathcal{L}(z) dz$  with respect to the four pulse parameters. This step results in the reduced Euler–Lagrange equation

$$\frac{d}{dz} \left( \frac{\partial \mathcal{L}}{\partial q_z} \right) - \frac{\partial \mathcal{L}}{\partial q} = 0, \quad (4.3.14)$$

where  $q_z = dq/dz$  and  $q$  represents one of the pulse parameters. If we use  $q = \phi_p$  in Eq. (4.3.14), we obtain  $dE_p/dz = 0$ . This equation indicates that the energy  $E_p$  remains constant, as expected. Using  $q = E_p$  in Eq. (4.3.14), we obtain the following equation for the phase  $\phi_p$ :

$$\frac{d\phi_p}{dz} = \frac{\beta_2}{2T_p^2} + \frac{5\gamma e^{-\alpha z} E_p}{4\sqrt{2\pi} T_p}. \quad (4.3.15)$$

We can follow the same procedure to obtain equations for  $T_p$  and  $C_p$ . In fact, using  $q = C_p$  and  $T_p$  in Eq. (4.3.14), we find that pulse width and chirp satisfy the same two equations, namely Eqs (4.3.7) and (4.3.8), obtained earlier with the moment method. Thus, the two approximate methods lead to identical results in the case of the NLS equation.

### 4.3.3 Specific Analytic Solutions

As a simple application of the moment or variational method, consider first the case of a low-energy pulse propagating in a constant-dispersion fiber with negligible nonlinear effects. Recalling that  $(1 + C_p^2)/T_p^2$  is related to the spectral width of the pulse that does not change in a linear medium, we can replace this quantity with its initial value  $(1 + C_0^2)/T_0^2$ , where  $T_0$  and  $C_0$  are input values at  $z = 0$ . Since the second term is negligible in Eq. (4.3.8), it can be integrated easily and provides the solution

$$C_p(z) = C_0 + \text{sgn}(\beta_2)(1 + C_0^2)z/L_D, \quad (4.3.16)$$

where  $L_D$  is the dispersion length. Using this solution in Eq. (4.3.9), we find that the pulse width changes as

$$T_p^2(z) = T_0^2[1 + 2\text{sgn}(\beta_2)C_0(z/L_D) + (1 + C_0^2)(z/L_D)^2]. \quad (4.3.17)$$

It is easy to verify that these expressions agree with those obtained in Section 3.2 by solving the pulse-propagation equation directly.

In the absence of dispersive effects, Eqs (4.3.7) and (4.3.8) are easily solved by setting  $\beta_2 = 0$ . The pulse width  $T_p$  remains fixed at its input value  $T_0$ , as expected. However, the chirp parameter changes because of SPM and is given by

$$C_p(z) = C_0 + \gamma P_0(1 - e^{-\alpha z})/(\sqrt{2}\alpha), \quad (4.3.18)$$

If the input pulse is unchirped ( $C_0 = 0$ ), SPM chirps the pulse such that  $C_p(L) = \phi_{\max}/\sqrt{2}$ , where  $\phi_{\max}$  is given in Eq. (4.1.8). Equation (4.3.18) shows that the SPM-induced chirp is always positive. As a result, when the input pulse is negatively chirped, SPM can reduce the net chirp and produce spectral narrowing, as found earlier in Section 4.1.

To solve Eqs (4.3.7) and (4.3.8) in the weakly nonlinear case, we make two approximations. First, we assume that fiber losses are negligible and set  $\alpha = 0$ . Second, the nonlinear effects are weak enough that the chirp at any distance  $z$  can be written as  $C_p = C_L + C'$ , where the nonlinear part  $C' \ll C_L$ . It is easy to see that the linear part is given by Eq. (4.3.16), while the nonlinear part satisfies

$$\frac{dC'}{dz} = \frac{\gamma P_0}{\sqrt{2}} \frac{T_0}{T_p}. \quad (4.3.19)$$

Dividing Eqs (4.3.7) and (4.3.19), we obtain

$$\frac{dC'}{dT_p} = \frac{\gamma P_0 T_0}{\sqrt{2} \beta_2 C_p} \approx \frac{\gamma P_0 T_0}{\sqrt{2} \beta_2 C_L}, \quad (4.3.20)$$

where we replaced  $C$  with  $C_L$  as  $C' \ll C_L$ . This equation is now easy to solve, and the result can be written as

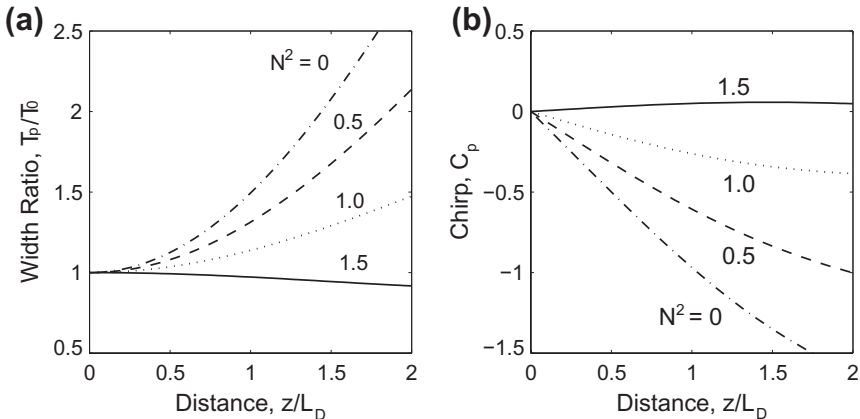


**Figure 4.18** Evolution of pulse width  $T_p$  and chirp parameter  $C_p$  as a function of  $z/L_D$  for several values of  $N$  for an unchirped Gaussian pulse propagating with  $\beta_2 < 0$ .

$$C'(z) = \frac{\gamma P_0 T_0}{\sqrt{2} \beta_2 C_L} (T - T_0). \quad (4.3.21)$$

Once  $C = C_L + C'$  is known, the pulse width can be found from Eq. (4.3.9).

The preceding analytic solution can only be used when the parameter  $N^2 = L_D/L_{NL}$  is less than 0.3 or so. However, one can easily solve Eqs (4.3.7) and (4.3.8) numerically for any value of  $N$ . Figure 4.18 shows changes in  $T_p/T_0$  and  $C_p$  as a function of  $z/L_D$  for several values of  $N$  assuming that input pulses are unchirped ( $C_0 = 0$ ) and propagate in the region of anomalous regime ( $\beta_2 < 0$ ). In the linear case ( $N = 0$ ), pulse broadens rapidly and develops considerable chirp. However, as the nonlinear effects increase and  $N$  becomes larger, pulse broadens less and less. Eventually, it even begins to compress, as seen in Figure 4.18 for  $N^2 = 1.5$ .

The behavior seen in Figure 4.18 can be understood in terms of the SPM-induced chirp as follows. As seen from Eq. (4.3.8), the two terms on its right side have opposite signs when  $\beta_2 < 0$ . As a result, SPM tends to cancel the dispersion-induced chirp, and reduces pulse broadening. For a certain value of the nonlinear parameter  $N$ , the two terms nearly cancel, and pulse width does not change much with propagation. As discussed in Section 5.2, this feature points to the possibility of soliton formation. For even larger values of  $N$ , pulse may even compress, at least initially. In the case of normal dispersion, the two terms on the right side have the same sign. Since SPM enhances the dispersion-induced chirp, the pulse broadens even faster than that expected in the absence of SPM.

## 4.4 HIGHER-ORDER NONLINEAR EFFECTS

The discussion of SPM so far is based on the simplified propagation equation (2.3.46). For ultrashort optical pulses ( $T_0 < 1$  ps), it is necessary to include the higher-order

nonlinear effects through Eq. (2.3.44). If Eq. (3.1.3) is used to define the normalized amplitude  $U$ , this equation takes the form

$$\begin{aligned} \frac{\partial U}{\partial z} + i \frac{\operatorname{sgn}(\beta_2)}{2L_D} \frac{\partial^2 U}{\partial \tau^2} - \frac{\operatorname{sgn}(\beta_3)}{6L'_D} \frac{\partial^3 U}{\partial \tau^3} \\ = i \frac{e^{-\alpha z}}{L_{NL}} \left( |U|^2 U + i s \frac{\partial}{\partial \tau} (|U|^2 U) - \tau_R U \frac{\partial |U|^2}{\partial \tau} \right), \end{aligned} \quad (4.4.1)$$

where  $L_D$ ,  $L'_D$ , and  $L_{NL}$  are the three length scales defined as

$$L_D = \frac{T_0^2}{|\beta_2|}, \quad L'_D = \frac{T_0^3}{|\beta_3|}, \quad L_{NL} = \frac{1}{\gamma P_0}. \quad (4.4.2)$$

The parameters  $s$  and  $\tau_R$  govern the effects of self-steepening and intrapulse Raman scattering, respectively, and are defined as

$$s = \frac{1}{\omega_0 T_0}, \quad \tau_R = \frac{T_R}{T_0}. \quad (4.4.3)$$

Both of these effects are quite small for picosecond pulses but must be considered for ultrashort pulses with  $T_0 < 1$  ps.

#### 4.4.1 Self-Steepening

Self-steepening results from the intensity dependence of the group velocity [86–89]. Its effects on SPM were first considered in liquid nonlinear media [2] and later extended to optical fibers [90–94]. Self-steepening leads to an asymmetry in the SPM-broadened spectra of ultrashort pulses [95–101].

Before solving Eq. (4.4.1) numerically, it is instructive to consider the dispersionless case by setting  $\beta_2 = \beta_3 = 0$ . Equation (4.4.1) can be solved analytically in this specific case if we also set  $\tau_R = 0$  [88]. Defining a normalized distance as  $Z = z/L_{NL}$  and neglecting fiber losses ( $\alpha = 0$ ), Eq. (4.4.1) becomes

$$\frac{\partial U}{\partial Z} + s \frac{\partial}{\partial \tau} (|U|^2 U) = i |U|^2 U. \quad (4.4.4)$$

Using  $U = \sqrt{I} \exp(i\phi)$  in Eq. (4.4.4) and separating the real and imaginary parts, we obtain the following two equations:

$$\frac{\partial I}{\partial Z} + 3sI \frac{\partial I}{\partial \tau} = 0, \quad (4.4.5)$$

$$\frac{\partial \phi}{\partial Z} + sI \frac{\partial \phi}{\partial \tau} = I. \quad (4.4.6)$$

Since the intensity Eq. (4.4.5) is decoupled from the phase equation (4.4.6), it can be solved easily using the method of characteristics. Its general solution is given by [90]

$$I(Z, \tau) = f(\tau - 3sIZ), \quad (4.4.7)$$

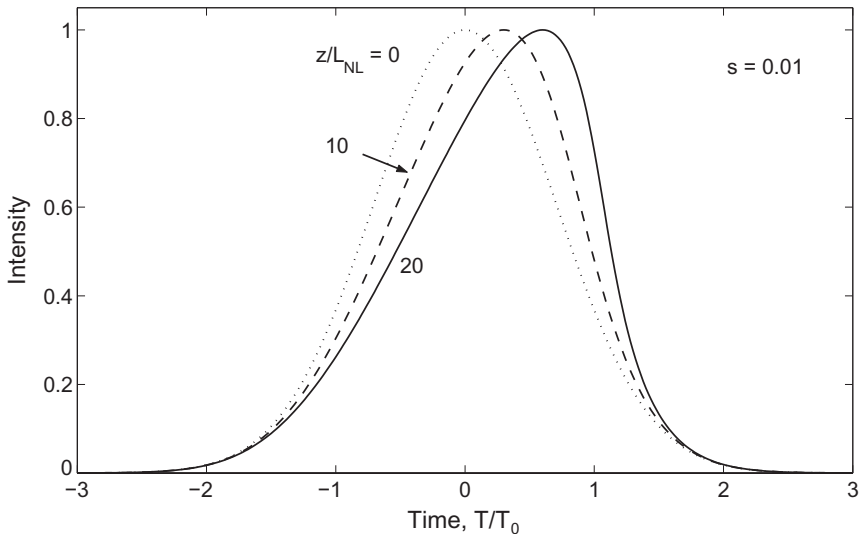


**Figure 4.19 Self-steepening of a Gaussian pulse in the dispersionless case. The dashed curve shows the input pulse shape at  $z=0$ .**

where we used the initial condition  $I(0, \tau) = f(\tau)$  and  $f(\tau)$  describes the pulse shape at  $z = 0$ . Equation (4.4.7) shows that each point  $\tau$  moves along a straight line from its initial value, and the slope of the line is intensity dependent. This feature leads to pulse distortion. As an example, consider the case of a Gaussian pulse for which

$$I(0, \tau) \equiv f(\tau) = \exp(-\tau^2). \quad (4.4.8)$$

From Eq. (4.4.7), the pulse shape at a distance  $Z$  is obtained by using

$$I(Z, \tau) = \exp[-(\tau - 3sIZ)^2]. \quad (4.4.9)$$

The implicit relation for  $I(Z, \tau)$  should be solved for each  $\tau$  to obtain the pulse shape at a given value of  $Z$ . Figure 4.19 shows the calculated pulse shapes at  $Z = 10$  and  $20$  for  $s = 0.01$ . As the pulse propagates inside the fiber, it becomes asymmetric, with its peak shifting toward the trailing edge. As a result, the trailing edge becomes steeper and steeper with increasing  $Z$ . Physically, the group velocity of the pulse is intensity dependent such that the peak moves at a lower speed than the wings.

Self-steepening of the pulse eventually creates an optical shock, analogous to the development of an acoustic shock on the leading edge of a sound wave [88]. The distance at which the shock is formed is obtained from Eq. (4.4.9) by requiring that  $\partial I / \partial \tau$  be infinite at the shock location. It is given by [91]

$$z_s = \left(\frac{e}{2}\right)^{1/2} \frac{L_{NL}}{3s} \approx 0.39(L_{NL}/s). \quad (4.4.10)$$

A similar relation holds for a “sech” pulse with only a slight change in the numerical coefficient (0.43 in place of 0.39). For picosecond pulses with  $T_0 = 1$  ps and  $P_0 \sim 1$  W, the shock occurs at a distance  $z_s \sim 100$  km. However, for femtosecond pulses with  $T_0 < 100$  fs and  $P_0 > 1$  kW,  $z_s$  becomes  $< 1$  m. As a result, significant self-steepening of the pulse can occur in a few-centimeter-long fiber. Optical shocks with an infinitely sharp trailing edge never occur in practice because of the GVD; as the pulse edge becomes steeper, the dispersive terms in Eq. (4.4.1) become increasingly more important and cannot be ignored. The shock distance  $z_s$  is also affected by fiber losses  $\alpha$ . In the dispersionless case, fiber losses delay the formation of optical shocks; if  $\alpha z_s > 1$ , the shock does not develop at all [91].

Self-steepening also affects SPM-induced spectral broadening. In the dispersionless case,  $\phi(z, \tau)$  is obtained by solving Eq. (4.4.6). It can then be used to calculate the spectrum using

$$S(\omega) = \left| \int_{-\infty}^{\infty} [I(z, \tau)]^{1/2} \exp[i\phi(z, \tau) + i(\omega - \omega_0)\tau] d\tau \right|^2. \quad (4.4.11)$$

Figure 4.20 shows the calculated spectrum at  $sz/L_{NL} = 0.2$  for  $s = 0.01$ . The most notable feature is spectral asymmetry—the red-shifted peaks are more intense than blue-shifted peaks. The other notable feature is that SPM-induced spectral broadening is larger on the blue side (called the anti-Stokes side in the terminology used for stimulated Raman scattering) than the red side (or the Stokes side). Both of these features can be understood qualitatively from the changes in the pulse shape induced by self-steepening. The spectrum is asymmetric simply because the pulse shape is

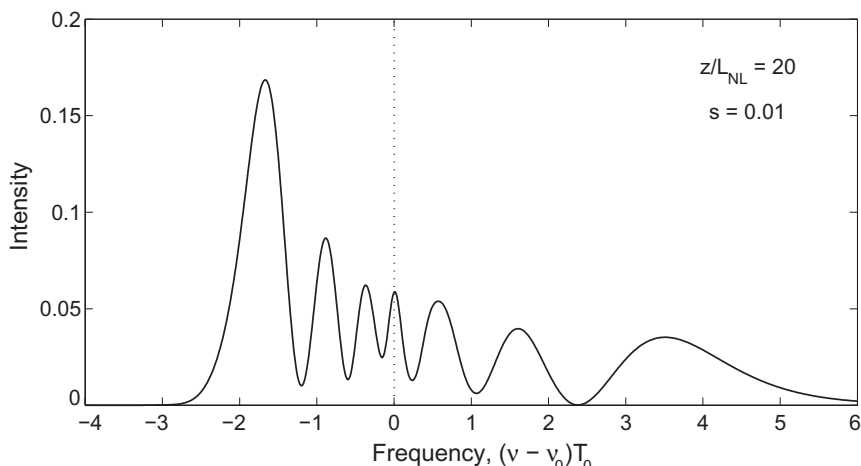


**Figure 4.20 Spectrum of a Gaussian pulse at a distance  $z=0.2L_{NL}/s$ , where  $s=0.01$  and  $L_{NL}$  is the nonlinear length. Self-steepening is responsible for the asymmetry in the SPM-broadened spectrum. The effects of GVD are neglected.**

asymmetric. A steeper trailing edge of the pulse implies larger spectral broadening on the blue side as SPM generates blue components near the trailing edge (see Figure 4.1). In the absence of self-steepening ( $s = 0$ ), a symmetric six-peak spectrum is expected because  $\phi_{\max} \approx 6.4\pi$  for the parameter values used in Figure 4.20. Self-steepening stretches the blue portion. The amplitude of the high-frequency peaks decreases because the same energy is distributed over a wider spectral range.

#### 4.4.2 Effect of GVD on Optical Shocks

The spectral features seen in Figure 4.20 are considerably affected by GVD, which cannot be ignored when short optical pulses propagate inside silica fibers [102–109]. The pulse evolution in this case is studied by solving Eq. (4.4.1) numerically. Figure 4.21 shows the pulse shapes and the spectra at  $z/L_D = 0.2$  and  $0.4$  in the case of an initially unchirped Gaussian pulse propagating with normal dispersion ( $\beta_2 > 0$ ) and  $\beta_3 = 0$ . The parameter  $N$ , defined in Eq. (4.2.3), is taken to be 10 and corresponds to  $L_D = 100L_{NL}$ . In the absence of GVD ( $\beta_2 = 0$ ), the pulse shape and the spectrum

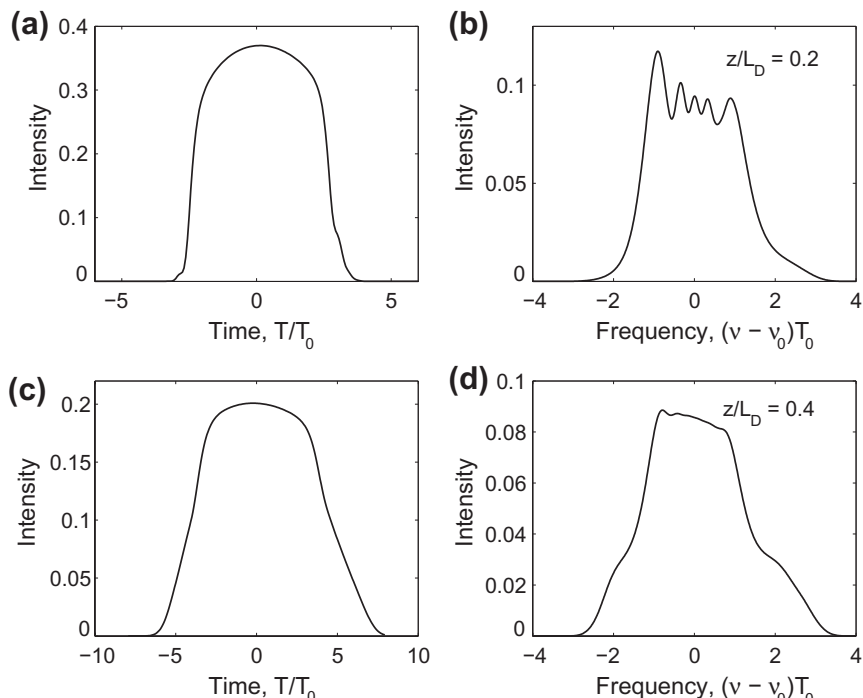


**Figure 4.21** Pulse shapes and spectra at  $z/L_D = 0.2$  (upper row) and  $0.4$  (lower row) for a Gaussian pulse propagating in the normal-dispersion regime of the fiber. The other parameters are  $\alpha = 0$ ,  $\beta_3 = 0$ ,  $s = 0.01$ , and  $N = 10$ .

shown in the upper row of Figure 4.21 reduce to those shown in Figures 4.19 and 4.20 in the case of  $sz/L_{NL} = 0.2$ . A direct comparison shows that both the shape and spectrum are significantly affected by GVD even though the propagation distance is only a fraction of the dispersion length ( $z/L_D = 0.2$ ). The lower row of Figure 4.21 shows the pulse shape and spectrum at  $z/L_D = 0.4$ ; the qualitative changes induced by GVD are self-evident. For this value of  $z/L_D$ , the propagation distance  $z$  exceeds the shock distance  $z_s$  given by Eq. (4.4.10). It is the GVD that dissipates the shock by broadening the steepened trailing edge, a feature clearly seen in the asymmetric pulse shapes of Figure 4.21. Although the pulse spectra do not exhibit deep oscillations (seen in Figure 4.20 for the dispersionless case), the longer tail on the blue side is a manifestation of self-steepening. With a further increase in the propagation distance  $z$ , the pulse continues to broaden while the spectrum remains nearly unchanged.

The effect of self-steepening on pulse evolution has been seen experimentally in liquids and solids as a larger spectral broadening on the blue side compared with that on the red side [4]. In these early experiments, GVD played a relatively minor role, and the spectral structure similar to that of Figure 4.20 was observed. In the case of optical fibers, the GVD effects are strong enough that the spectra similar to those of Figure 4.21 are expected to occur in practice. In an experiment on pulse compression [102], 40-fs optical pulses at 620 nm were propagated over a 7-mm-long fiber. Figure 4.22 shows the experimentally observed spectra at the fiber output

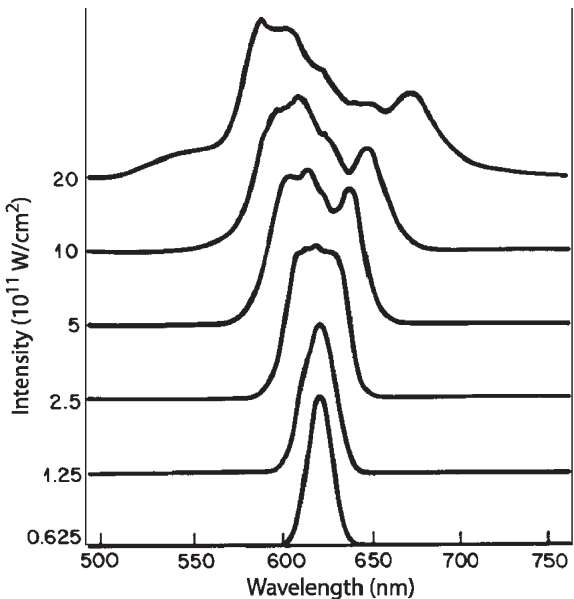


**Figure 4.22** Experimentally observed spectra of 40-fs input pulses at the output of a 7-mm-long fiber. Spectra are labeled by the peak intensity of input pulses. The top spectrum corresponds to  $N \approx 7.7$ . (After Ref. [102]; © 1985 American Institute of Physics.)

for several values of peak intensities. The spectrum broadens asymmetrically with a longer tail on the blue side than on the red side. This feature is due to self-steepening. In this experiment, the self-steepening parameter  $s \approx 0.026$ , and the dispersion length  $L_D \approx 1$  cm if we use  $T_0 = 24$  fs (corresponding to a FWHM of 40 fs for a Gaussian pulse). Assuming an effective mode area of  $10 \mu\text{m}^2$ , the peak power for the top trace in Figure 4.22 is about 200 kW. This value results in a nonlinear length  $L_{NL} \approx 0.16$  mm and  $N \approx 7.7$ . Equation (4.4.1) can be used to simulate the experiment by using these parameter values. Inclusion of the  $\beta_3$  term is generally necessary to reproduce the detailed features seen in the experimental spectra of Figure 4.22 [93]. Similar conclusions were reached in another experiment in which asymmetric spectral broadening of 55-fs pulses from a 620 nm dye laser was observed in a 11-mm-long optical fiber [103].

#### 4.4.3 Intrapulse Raman Scattering

The discussion so far has neglected the last term in Eq. (4.4.1) that is responsible for intrapulse Raman scattering. In the case of optical fibers, this term becomes quite important for ultrashort optical pulses ( $T_0 < 1$  ps) and should be included in modeling pulse evolution of such short pulses in optical fibers [105–111]. Equation (4.4.1) is solved numerically, typically with the split-step Fourier method, to study the impact of intrapulse Raman scattering on ultrashort pulses.

Figure 4.23 shows the temporal and spectral evolution of an unchirped Gaussian pulse over 8 dispersion lengths in the cases of normal (left) and anomalous (right) dispersion by solving Eq. (4.4.1) with  $N = 2$ ,  $\tau_R = 0.03$ ,  $s = 0$ , and  $\beta_3 = 0$ . One can see immediately the dramatic effect of the nature of the fiber dispersion. In the case of normal dispersion, the pulse broadens rapidly while its spectrum is broadened

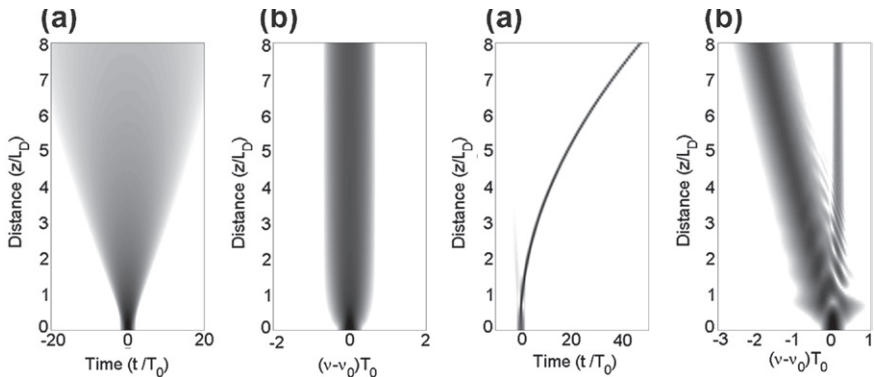


**Figure 4.23 (a)** Temporal and (b) spectral evolution of an unchirped Gaussian pulse over 8 dispersion lengths in the cases of normal (left) and anomalous (right) dispersion. Parameters used were  $N=2$ ,  $\tau_R=0.03$ ,  $s=0$ , and  $\beta_3=0$ . The gray intensity scale is over a 20-dB range.

through SPM by a factor of 2 or so. In contrast, in the case of anomalous dispersion, the optical pulse undergoes an initial narrowing stage and then slows down, as is apparent from its bent trajectory. The most noteworthy features of Figure 4.23 is a Raman-induced frequency shift (RIFS) in the pulse spectrum toward longer wavelengths. This is a direct consequence of intrapulse Raman scattering. As discussed in Section 2.3.2, when the input pulse is relatively short, its high-frequency components can pump the low-frequency components of the same pulse through stimulated Raman scattering, thereby transferring energy to the red side. As the pulse spectrum shifts through the RIFS, the pulse slows down because the group velocity of a pulse is lower at longer wavelengths in the  $\beta_2 < 0$  case. This deacceleration is responsible for the bent trajectory of the pulse seen in Figure 4.23.

The RIFS occurs in the case of normal dispersion also, but its magnitude depends on the pulse width and is reduced drastically because of a rapid dispersion-induced broadening of the input pulse. It is possible to extend the moment method of Section 4.3 to obtain an approximate semianalytic expression of the spectral shift induced by intrapulse Raman scattering [111]. Its use requires the introduction of two new moments, representing a temporal shift  $q_p(z)$  and a spectral shift  $\Omega_p(z)$ , and defined as

$$q_p(z) = \frac{1}{E_p} \int_{-\infty}^{\infty} T |U(z, T)|^2 dT, \quad (4.4.12)$$

$$\Omega_p(z) = \frac{i}{2E_p} \int_{-\infty}^{\infty} \left( U^* \frac{\partial U}{\partial T} - U \frac{\partial U^*}{\partial T} \right) dT. \quad (4.4.13)$$

Following the technique described in Section 4.3.1, these two moments are found to satisfy

$$\frac{dq_p}{dz} = \beta_2 \Omega_p, \quad \frac{d\Omega_p}{dz} = -T_R e^{-\alpha z} \frac{\gamma P_0 T_0}{\sqrt{2} T_p^3}. \quad (4.4.14)$$

Physically speaking, the Raman term shifts the carrier frequency at which pulse spectrum is centered. This spectral shift  $\Omega_p$  in turn shifts the pulse position  $q_p$  in the time domain because of changes in the group velocity through fiber dispersion.

Equation (4.4.14) should be solved together with Eqs (4.3.7) and (4.3.8) to study how  $\Omega_p$  evolves along the fiber length. Figure 4.24 shows the evolution of the RIFS,  $\Delta\nu_R \equiv \Omega_p/2\pi$ , when a chirped Gaussian pulse with  $T_0 = 50$  fs is launched into a fiber exhibiting normal dispersion [ $D = -4$  ps/(km nm)]. In the case of unchirped pulses,  $\Delta\nu_R$  saturates at a value of about 0.5 THz. This saturation is related to pulse broadening. Indeed, the spectral shift can be increased by chirping Gaussian pulses such that  $\beta_2 C < 0$ . The reason is related to the discussion in Section 3.2.2, where it was shown that such chirped Gaussian pulses go through an initial compression phase before they broaden rapidly.

Figure 4.25a shows the experimentally recorded pulse spectrum when 109-fs pulses ( $T_0 \approx 60$  fs) with 7.4 kW peak power were sent through a 6-m-long fiber

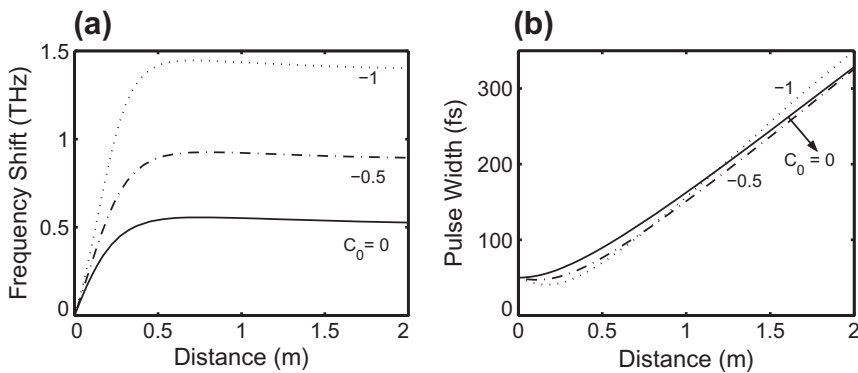


**Figure 4.24** Evolution of (a) Raman-induced frequency shift and (b) pulse width when an unchirped Gaussian pulse with  $T_0=50\text{fs}$  propagates in the normal-dispersion region of a fiber.

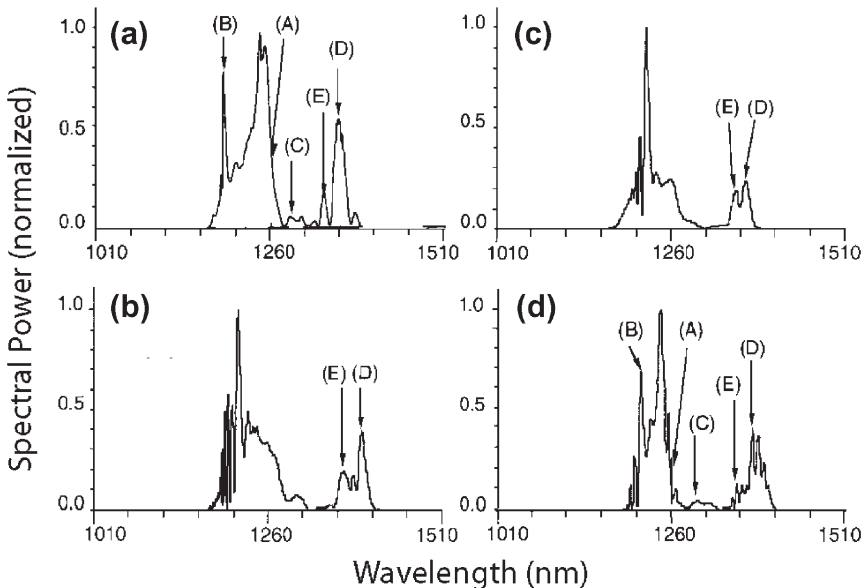


**Figure 4.25** (a) Experimental spectrum of 109-fs input pulses at the output of a 6-m-long fiber and predictions of the generalized NLS equation with (b)  $s = \tau_R = 0$ , (c)  $s = 0$ , and (d) both  $s$  and  $\tau_R$  nonzero. Letters (A–E) mark different spectral features observed experimentally. (After Ref. [109]; © 1999 OSA.)

[109]. The fiber had  $\beta_2 \approx 4 \text{ ps}^2/\text{km}$  and  $\beta_3 \approx 0.06 \text{ ps}^3/\text{km}$  at the 1260 nm wavelength used in this experiment. The traces (b)–(d) show the prediction of Eq. (4.4.1) under three different conditions. Both self-steepening and intrapulse Raman scattering were neglected in the trace (b) and included in the trace (d), while only the

latter was included in the trace (c). All experimental features, marked as (A)–(E), were reproduced only when both higher-order nonlinear effects were included in the numerical model. Inclusion of the fourth-order dispersion was also necessary for a good agreement. Even the predicted pulse shapes were in agreement with the cross-correlation traces obtained experimentally.

The SPM and other nonlinear effects such as stimulated Raman scattering and four-wave mixing, occurring simultaneously inside optical fibers, can broaden the spectrum of an ultrashort pulse so much that it may extend over more than 100 THz. Such extreme spectral broadening is called supercontinuum generation, a phenomenon that has attracted considerable attention in recent years because of its applications in diverse areas [112–114]. Pulse spectra extending over 1000 nm or more have been generated using the so-called highly nonlinear fibers (see Chapter 11). Chapter 13 is devoted to the phenomenon of supercontinuum generation.

## PROBLEMS

- 4.1** A 1.06-μm Q-switched Nd:YAG laser emits unchirped Gaussian pulse with 1-nJ energy and 100-ps width (FWHM). Pulses are transmitted through a 1-km-long fiber having a loss of 3 dB/km and an effective mode area of 20 μm<sup>2</sup>. Calculate the maximum values of the nonlinear phase shift and the frequency chirp at the fiber output.
- 4.2** Plot the spectrum of the chirped output pulse obtained in the preceding by using Eq. (4.1.13). Does the number of spectral peaks agree with the prediction of Eq. (4.1.14)?
- 4.3** Repeat Problem 4.1 for a hyperbolic-secant pulse. Plot the spectrum of the chirped output pulse using Eq. (4.1.13). Comment on the impact of the pulse shape on SPM-induced spectral broadening.
- 4.4** Determine the shape, width, and peak power of the optical pulse that will produce a linear chirp at the rate of 1 GHz/ps over a 100-ps region when transmitted through a 1-km-long fiber with a loss of 1 dB/km and an effective mode area of 50 μm<sup>2</sup>.
- 4.5** Calculate numerically the SPM-broadened spectra of a super-Gaussian pulse ( $m = 3$ ) for  $C = -15, 0$ , and  $15$ . Assume a peak power such that  $\phi_{\max} = 4.5\pi$ . Compare your spectra with those shown in Figure 4.5 and comment on the main qualitative differences.
- 4.6** Perform the ensemble average in Eq. (4.1.19) for a thermal field with Gaussian statistics and prove that the coherence function is indeed given by Eq. (4.1.20).
- 4.7** Solve Eq. (4.2.1) numerically using the split-step Fourier method of Section 2.4. Generate curves similar to those shown in Figures 4.8 and 4.9 for an input pulse with  $U(0, \tau) = \text{sech}(\tau)$  using  $N = 1$  and  $\alpha = 0$ . Compare your results with the Gaussian-pulse case and discuss the differences qualitatively.

- 4.8** Use the computer program developed for the preceding problem to study numerically optical wave breaking for an unchirped super-Gaussian pulse with  $m = 3$  by using  $N = 30$  and  $\alpha = 0$ . Compare your results with those shown in Figures 4.11 and 4.12.
- 4.9** Perform the integrals appearing in Eqs (4.3.4) and (4.3.5) using  $U(z, T)$  from Eq. (4.3.6) and reproduce Eqs (4.3.7) and (4.3.8).
- 4.10** Perform the integrals appearing in Eqs (4.3.4) and (4.3.5) using the field amplitude in the form  $U(z, T) = a_p \operatorname{sech}(T/T_p) \exp(-iC_p T^2/2T_p^2)$  and derive equations for  $T_p$  and  $C_p$ .
- 4.11** Prove that the Euler–Lagrange Eq. (4.3.11) with  $\mathcal{L}_d$  given in Eq. (4.3.12) reproduces the NLS Eq. (4.3.1).
- 4.12** Perform the integral appearing in Eqs (4.3.10) using  $\mathcal{L}_d$  from Eq. (4.3.12) and  $U(z, T)$  from Eq. (4.3.6) and reproduce Eq. (4.3.13).
- 4.13** Show that the solution given in Eq. (4.4.9) is indeed the solution of Eq. (4.4.4) for a Gaussian pulse. Calculate the phase profile  $\phi(Z, \tau)$  at  $sZ = 0.2$  analytically (if possible) or numerically.
- 4.14** Use the moment method and Ref. [111] to derive equations for the derivatives  $dq/dz$  and  $d\Omega_p/dz$  for a Gaussian pulse. Use them to find an approximate expression for the Raman-induced frequency shift  $\Omega_p$ .

## REFERENCES

- [1] F. Shimizu, *Phys. Rev. Lett.* **19**, 1097 (1967).
- [2] T. K. Gustafson, J. P. Taran, H. A. Haus, J. R. Lifsitz, and P. L. Kelley, *Phys. Rev.* **177**, 306 (1969).
- [3] R. Cubeddu, R. Polloni, C. A. Sacchi, and O. Svelto, *Phys. Rev. A* **2**, 1955 (1970).
- [4] R. R. Alfano and S. L. Shapiro, *Phys. Rev. Lett.* **24**, 592 (1970); *Phys. Rev. Lett.* **24**, 1217 (1970).
- [5] Y. R. Shen and M. M. T. Loy, *Phys. Rev. A* **3**, 2099 (1971).
- [6] C. H. Lin and T. K. Gustafson, *J. Quantum Electron.* **8**, 429 (1972).
- [7] E. P. Ippen, C. V. Shank, and T. K. Gustafson, *Appl. Phys. Lett.* **24**, 190 (1974).
- [8] R. A. Fisher and W. K. Bischel, *J. Appl. Phys.* **46**, 4921 (1975).
- [9] R. H. Stolen and C. Lin, *Phys. Rev. A* **17**, 1448 (1978).
- [10] S. C. Pinault and M. J. Potasek, *J. Opt. Soc. Am. B* **2**, 1318 (1985).
- [11] M. Oberthaler and R. A. Höpfel, *Appl. Phys. Lett.* **63**, 1017 (1993).
- [12] B. R. Washburn, J. A. Buck, and S. E. Ralph, *Opt. Lett.* **25**, 445 (2000).
- [13] M. T. Myaing, J. Urayama, A. Braun, and T. Norris, *Opt. Express* **7**, 210 (2000).
- [14] J. T. Manassah, *Opt. Lett.* **15**, 329 (1990); *Opt. Lett.* **16**, 1638 (1991).
- [15] B. Gross and J. T. Manassah, *Opt. Lett.* **16**, 1835 (1991).
- [16] M. T. de Araujo, H. R. da Cruz, and A. S. Gouveia-Neto, *J. Opt. Soc. Am. B* **8**, 2094 (1991).
- [17] H. R. da Cruz, J. M. Hickmann, and A. S. Gouveia-Neto, *Phys. Rev. A* **45**, 8268 (1992).
- [18] J. N. Elgin, *Opt. Lett.* **18**, 10 (1993); *Phys. Rev. A* **47**, 4331 (1993).
- [19] S. Cavalcanti, G. P. Agrawal, and M. Yu, *Phys. Rev. A* **51**, 4086 (1995).
- [20] J. Garnier, L. Videau, C. Gouédard, and A. Migus, *J. Opt. Soc. Am. B* **15**, 2773 (1998).

- [21] S. M. Pietralunga, P. Martelli, M. Ferrario, and M. Martinelli, *IEEE Photon. Technol. Lett.* **13**, 1179 (2001).
- [22] L. Mandel and E. Wolf, *Optical Coherence and Quantum Optics* (Cambridge University Press, 1995).
- [23] H. Nakatsuka, D. Grischkowsky, and A. C. Balant, *Phys. Rev. Lett.* **47**, 910 (1981).
- [24] D. Grischkowsky and A. C. Balant, *Appl. Phys. Lett.* **41**, 1 (1982).
- [25] J. Botineau and R. H. Stolen, *J. Opt. Soc. Am.* **72**, 1592 (1982).
- [26] B. P. Nelson, D. Cotter, K. J. Blow, and N. J. Doran, *Opt. Commun.* **48**, 292 (1983).
- [27] W. J. Tomlinson, R. H. Stolen, and C. V. Shank, *J. Opt. Soc. Am. B* **1**, 139 (1984).
- [28] I. N. Sisakyan and A. B. Shvartsburg, *Sov. J. Quantum Electron.* **14**, 1146 (1984).
- [29] M. J. Potasek and G. P. Agrawal, *Electron. Lett.* **22**, 759 (1986).
- [30] A. Kumar and M. S. Sodha, *Electron. Lett.* **23**, 275 (1987).
- [31] M. J. Potasek and G. P. Agrawal, *Phys. Rev. A* **36**, 3862 (1987).
- [32] J. M. Hickmann, J. F. Martino-Filho, and A. S. L. Gomes, *Opt. Commun.* **84**, 327 (1991).
- [33] A. Kumar, *Phys. Rev. A* **44**, 2130 (1991).
- [34] P. Weidner and A. Penzkofer, *Opt. Quantum Electron.* **25**, 1 (1993).
- [35] D. Anderson, *Phys. Rev. A* **27**, 3135 (1983).
- [36] A. M. Fattakhov and A. S. Chirkin, *Sov. J. Quantum Electron.* **14**, 1556 (1984).
- [37] D. Anderson, *IEE Proc.* **132** (Pt. J), 122 (1985).
- [38] M. J. Potasek, G. P. Agrawal, and S. C. Pinault, *J. Opt. Soc. Am. B* **3**, 205 (1986).
- [39] C. Pask and A. Vatarescu, *J. Opt. Soc. Am. B* **3**, 1018 (1986).
- [40] D. Marcuse, *J. Lightwave Technol.* **10**, 17 (1992).
- [41] P. A. Bélanger and N. Bélanger, *Opt. Commun.* **117**, 56 (1995).
- [42] Q. Yu and C. Fan, *J. Quantum Electron.* **15**, 444 (1997).
- [43] Y. Kodama and S. Wabnitz, *Opt. Lett.* **20**, 2291 (1995).
- [44] Y. Kodama and S. Wabnitz, *Electron. Lett.* **31**, 1761 (1995).
- [45] Y. Kodama, S. Wabnitz, and K. Tanaka, *Opt. Lett.* **21**, 719 (1996).
- [46] A. M. Kamchatnov and H. Steudel, *Opt. Commun.* **162**, 162 (1999).
- [47] W. J. Tomlinson, R. H. Stolen, and A. M. Johnson, *Opt. Lett.* **10**, 457 (1985).
- [48] A. M. Johnson and W. M. Simpson, *J. Opt. Soc. Am. B* **2**, 619 (1985).
- [49] H. E. Lassen, F. Mengel, B. Tromborg, N. C. Albertsen, and P. L. Christiansen, *Opt. Lett.* **10**, 34 (1985).
- [50] J.-P. Hamaide and P. Emplit, *Electron. Lett.* **24**, 818 (1988).
- [51] J. E. Rothenbeg, *J. Opt. Soc. Am. B* **6**, 2392 (1989); *J. Opt. Lett.* **16**, 18 (1991).
- [52] D. Anderson, M. Desaix, M. Lisak, and M. L. Quiroga-Teixeiro, *J. Opt. Soc. Am. B* **9**, 1358 (1992).
- [53] D. Anderson, M. Desaix, M. Karlsson, M. Lisak, and M. L. Quiroga-Teixeiro, *J. Opt. Soc. Am. B* **10**, 1185 (1993).
- [54] K. J. Blow, N. J. Doran, and E. Cummins, *Opt. Commun.* **48**, 181 (1983).
- [55] V. A. Vysloukh, *Sov. J. Quantum Electron.* **13**, 1113 (1983).
- [56] G. P. Agrawal and M. J. Potasek, *Phys. Rev. A* **33**, 1765 (1986).
- [57] P. K. A. Wai, C. R. Menyuk, Y. C. Lee, and H. H. Chen, *Opt. Lett.* **11**, 464 (1986).
- [58] G. R. Boyer and X. F. Carlotti, *Opt. Commun.* **60**, 18 (1986); *Phys. Rev. A* **38**, 5140 (1988).
- [59] P. K. A. Wai, C. R. Menyuk, H. H. Chen, and Y. C. Lee, *Opt. Lett.* **12**, 628 (1987).
- [60] A. S. Gouveia-Neto, M. E. Faldon, and J. R. Taylor, *Opt. Lett.* **13**, 770 (1988).
- [61] S. Wen and S. Chi, *Opt. Quantum Electron.* **21**, 335 (1989).

- [62] P. K. A. Wai, H. H. Chen, and Y. C. Lee, *Phys. Rev. A* **41**, 426 (1990).
- [63] J. N. Elgin, *Opt. Lett.* **15**, 1409 (1992).
- [64] S. Shen, C. C. Chang, H. P. Sardesai, V. Binjrajka, and A. M. Weiner, *J. Quantum Electron.* **17**, 452 (1999).
- [65] G. P. Agrawal, *Phys. Rev. A* **44**, 7493 (1991).
- [66] M. E. Fermann, V. I. Kruglov, B. C. Thomsen, J. M. Dudley, and J. D. Harvey, *Phys. Rev. Lett.* **84**, 6010 (2000).
- [67] V. I. Kruglov, A. C. Peacock, J. D. Harvey, and J. M. Dudley, *J. Opt. Soc. Am. B* **19**, 461 (2002).
- [68] S. Boscolo, S. K. Turitsyn, V. Y. Novokshenov, and J. H. B. Nijhof, *Theor. Math. Phys.* **133**, 1647 (2002).
- [69] C. Finot, G. Millot, S. Pitois, C. Billet, and J. M. Dudley, *J. Sel. Topics Quantum Electron.* **10**, 1211 (2004).
- [70] F. Ö. Ilday, J. R. Buckley, W. G. Clark, and F. W. Wise, *Phys. Rev. Lett.* **92**, 213902 (2004).
- [71] C. Billet, J. M. Dudley, N. Joly, and J. C. Knight, *Opt. Express* **13**, 323 (2005).
- [72] C. Finot, G. Millot, and J. M. Dudley, *Fiber Integ. Opt.* **27**, 505 (2008).
- [73] G. I. Barenblatt, *Scaling* (Cambridge University Press, 2003).
- [74] J. Limpert, T. Schreiber, T. Clausnitzer, et al., *Opt. Express* **10**, 628 (2002).
- [75] J. Buckley, F. Ö. Ilday, F. W. Wise, and T. Sosnowski, *Opt. Lett.* **30**, 1888 (2005).
- [76] C. K. Nielsen, B. Ortac, T. Schreiber, J. Limpert, R. Hohmuth, W. Richter, and A. Tünnermann, *Opt. Express* **13**, 9346 (2005).
- [77] T. Schreiber, C. K. Nielsen, B. Ortac, J. Limpert, and A. Tünnermann, *Opt. Lett.* **31**, 574 (2006).
- [78] E. R. Andresen, J. M. Dudley, D. Oron, C. Finot, and H. Rigneault, *Opt. Lett.* **36**, 707 (2011).
- [79] S. N. Vlasov, V. A. Petrishchev, and V. I. Talanov, *Radiophys. Quantum Electron.* **14**, 1062 (1971).
- [80] V. S. Grigoryan, C. R. Menyuk, and R. M. Mu, *J. Lightwave Technol.* **17**, 1347 (1999).
- [81] C. J. McKinstry, J. Santhanam, and G. P. Agrawal, *J. Opt. Soc. Am. B* **19**, 640 (2002).
- [82] J. Santhanam and G. P. Agrawal, *J. Sel. Topics Quantum Electron.* **8**, 632 (2002).
- [83] M. Struwe, *Variational Methods* (Springer, 1990).
- [84] B. Malomed, in *Progress in Optics*, Vol. 43, E. Wolf, Ed. (North-Holland, 2002), Chap. 2.
- [85] R. K. Nesbet, *Variational Principles and Methods in Theoretical Physics and Chemistry* (Cambridge University Press, 2003).
- [86] L. A. Ostrovskii, *Sov. Phys. JETP* **24**, 797 (1967).
- [87] R. J. Jonek and R. Landauer, *Phys. Lett.* **24A**, 228 (1967).
- [88] F. DeMartini, C. H. Townes, T. K. Gustafson, and P. L. Kelley, *Phys. Rev.* **164**, 312 (1967).
- [89] D. Grischkowsky, E. Courtens, and J. A. Armstrong, *Phys. Rev. Lett.* **31**, 422 (1973).
- [90] N. Tzoar and M. Jain, *Phys. Rev. A* **23**, 1266 (1981).
- [91] D. Anderson and M. Lisak, *Phys. Rev. A* **27**, 1393 (1983).
- [92] E. A. Golovchenko, E. M. Dianov, A. M. Prokhorov, and V. N. Serkin, *JETP Lett.* **42**, 87 (1985); *Sov. Phys. Dokl.* **31**, 494 (1986).
- [93] E. Bourkoff, W. Zhao, R. L. Joseph, and D. N. Christoulides, *Opt. Lett.* **12**, 272 (1987); *Opt. Commun.* **62**, 284 (1987).
- [94] W. Zhao and E. Bourkoff, *J. Quantum Electron.* **24**, 365 (1988).

- [95] R. L. Fork, C. V. Shank, C. Herlimann, R. Yen, and W. J. Tomlinson, *Opt. Lett.* **8**, 1 (1983).
- [96] G. Yang and Y. R. Shen, *Opt. Lett.* **9**, 510 (1984).
- [97] J. T. Manassah, M. A. Mustafa, R. R. Alfano, and P. P. Ho, *Phys. Lett.* **113A**, 242 (1985); *IEEE J. Quantum Electron.* **22**, 197 (1986).
- [98] D. Mestdagh and M. Haelterman, *Opt. Commun.* **61**, 291 (1987).
- [99] B. R. Suydam, in *Supercontinuum Laser Source*, R. R. Alfano, Ed, 2nd ed. (Springer, 2006), Chap. 6.
- [100] X. Fang, N. Karasawa, R. Morita, R. S. Windeler, and M. Yamashita, *IEEE Photon. Technol. Lett.* **15**, 33 (2003).
- [101] S. Nakamura, N. Takasawa, and Y. Koyamada, *J. Lightwave Technol.* **23**, 855 (2005).
- [102] W. H. Knox, R. L. Fork, M. C. Downer, R. H. Stolen, and C. V. Shank, *Appl. Phys. Lett.* **46**, 1120 (1985).
- [103] G. R. Boyer and M. Franco, *Opt. Lett.* **14**, 465 (1989).
- [104] J. R. de Oliveira, M. A. de Moura, J. M. Hickmann, and A. S. L. Gomes, *J. Opt. Soc. Am. B* **9**, 2025 (1992).
- [105] A. B. Grudinin, E. M. Dianov, D. V. Korobkin, A. M. Prokhorov, V. N. Serkin, and D. V. Khaidarov, *JETP Lett.* **46**, 221 (1987).
- [106] W. Hodel and H. P. Weber, *Opt. Lett.* **12**, 924 (1987).
- [107] V. Yanovsky and F. Wise, *Opt. Lett.* **19**, 1547 (1994).
- [108] C. Headley and G. P. Agrawal, *J. Opt. Soc. Am. B* **13**, 2170 (1996).
- [109] G. Boyer, *Opt. Lett.* **24**, 945 (1999).
- [110] B. R. Washburn, S. E. Ralph, and R. S. Windeler, *Opt. Express* **10**, 475 (2002).
- [111] J. Santhanam and G. P. Agrawal, *Opt. Commun.* **222**, 413 (2003).
- [112] R. R. Alfano, Ed., *Supercontinuum Laser Source*, 2nd ed. (Springer, 2006).
- [113] J. M. Dudley, G. Genty, and S. Coen, *Rev. Mod. Phys.* **78**, 1135 (2006).
- [114] J. M. Dudley and J. R. Taylor, *Supercontinuum Generation in Optical Fibers* (Cambridge University Press, 2010).

# Optical Solitons

# 5

A fascinating manifestation of the fiber nonlinearity occurs through optical solitons, formed as a result of the interplay between the dispersive and nonlinear effects. The word *soliton* refers to special kinds of wave packets that can propagate undistorted over long distances. Solitons have been discovered in many branches of physics. In the context of optical fibers, not only are solitons of fundamental interest but they have also found practical applications in the field of fiber-optic communications. This chapter is devoted to the study of pulse propagation in optical fibers in the regime in which both the group-velocity dispersion (GVD) and self-phase modulation (SPM) are equally important and must be considered simultaneously.

The chapter is organized as follows. Section 5.1 considers the phenomenon of modulation instability and shows that propagation of a continuous-wave (CW) beam inside optical fibers is inherently unstable because of the nonlinear phenomenon of SPM and leads to the formation of a pulse train in the anomalous-dispersion regime of optical fibers. Section 5.2 discusses the inverse-scattering method and uses it to obtain soliton solutions of the underlying wave-propagation equation. The properties of the fundamental and higher-order solitons are considered in this section. Section 5.3 is devoted to other kinds of solitons forming in optical fibers, with an emphasis on dark solitons. Section 5.4 considers the effects of external perturbations on solitons. Perturbations discussed include fiber losses, amplification of solitons, and noise introduced by optical amplifiers. Higher-order nonlinear effects such as self-steepening and intrapulse Raman scattering are the focus of Section 5.5.

---

## 5.1 MODULATION INSTABILITY

Many nonlinear systems exhibit an instability that leads to modulation of the steady state as a result of an interplay between the nonlinear and dispersive effects. This phenomenon is referred to as the *modulation instability* and it was studied during the 1960s in such diverse fields as fluid dynamics [1], nonlinear optics [2–4] and plasma physics [5–7]. In the context of optical fibers, modulation instability requires anomalous dispersion and manifests itself as breakup of the CW or quasi-CW radiation into a train of ultrashort pulses [8–27]. This section discusses modulation instability in optical fibers as an introduction to soliton theory.

### 5.1.1 Linear Stability Analysis

Consider propagation of CW light inside an optical fiber. The starting point is the simplified propagation equation (2.3.46). If fiber losses are ignored, this equation takes the form

$$i \frac{\partial A}{\partial z} = \frac{\beta_2}{2} \frac{\partial^2 A}{\partial T^2} - \gamma |A|^2 A, \quad (5.1.1)$$

and is referred to as the nonlinear Schrödinger (NLS) equation in the soliton literature. As discussed in Section 2.3,  $A(z, T)$  represents the amplitude of the field envelope,  $\beta_2$  is the GVD parameter, and the nonlinear parameter  $\gamma$  is responsible for SPM. In the case of CW radiation, the amplitude  $A$  is independent of  $T$  at the input end of the fiber at  $z = 0$ . Assuming that  $A(z, T)$  remains time independent during propagation inside the fiber, Eq. (5.1.1) is readily solved to obtain the steady-state solution

$$\bar{A} = \sqrt{P_0} \exp(i\phi_{NL}), \quad (5.1.2)$$

where  $P_0$  is the incident power and  $\phi_{NL} = \gamma P_0 z$  is the nonlinear phase shift induced by SPM. Equation (5.1.2) implies that CW light should propagate through the fiber unchanged except for acquiring a power-dependent phase shift (and for reduction in power in the presence of fiber losses).

Before reaching this conclusion, however, we must ask whether the steady-state solution (5.1.2) is stable against small perturbations. To answer this question, we perturb the steady state slightly such that

$$A = (\sqrt{P_0} + a) \exp(i\phi_{NL}) \quad (5.1.3)$$

and examine evolution of the perturbation  $a(z, T)$  using a linear stability analysis. Substituting Eq. (5.1.3) in Eq. (5.1.1) and linearizing in  $a$ , we obtain

$$i \frac{\partial a}{\partial z} = \frac{\beta_2}{2} \frac{\partial^2 a}{\partial T^2} - \gamma P_0(a + a^*). \quad (5.1.4)$$

This linear equation can be solved easily in the frequency domain. However, because of the  $a^*$  term, the Fourier components at frequencies  $\Omega$  and  $-\Omega$  are coupled. Thus, we should consider its solution in the form

$$a(z, T) = a_1 \exp[i(Kz - \Omega T)] + a_2 \exp[-i(Kz - \Omega T)], \quad (5.1.5)$$

where  $K$  and  $\Omega$  are the wave number and the frequency of perturbation, respectively. Equations (5.1.4) and (5.1.5) provide a set of two homogeneous equations for  $a_1$  and  $a_2$ . This set has a nontrivial solution only when  $K$  and  $\Omega$  satisfy the following dispersion relation

$$K = \pm \frac{1}{2} |\beta_2 \Omega| [\Omega^2 + \text{sgn}(\beta_2) \Omega_c^2]^{1/2}, \quad (5.1.6)$$

where  $\text{sgn}(\beta_2) = \pm 1$  depending on the sign of  $\beta_2$ ,

$$\Omega_c^2 = \frac{4\gamma P_0}{|\beta_2|} = \frac{4}{|\beta_2| L_{\text{NL}}}, \quad (5.1.7)$$

and the nonlinear length  $L_{\text{NL}}$  is defined in Eq. (3.1.5). Because of the factor  $\exp[i(\beta_0 z - \omega_0 t)]$  that has been factored out in Eq. (2.3.21), the actual wave number and the frequency of perturbation are  $\beta_0 \pm K$  and  $\omega_0 \pm \Omega$ , respectively. With this factor in mind, the two terms in Eq. (5.1.5) represent two different frequency components,  $\omega_0 + \Omega$  and  $\omega_0 - \Omega$ , that are present simultaneously. It will be seen later that these frequency components correspond to the two spectral sidebands that are generated when modulation instability occurs.

The dispersion relation (5.1.6) shows that steady-state stability depends critically on whether light experiences normal or anomalous GVD inside the fiber. In the case of normal GVD ( $\beta_2 > 0$ ), the wave number  $K$  is real for all  $\Omega$ , and the steady state is stable against small perturbations. By contrast, in the case of anomalous GVD ( $\beta_2 < 0$ ),  $K$  becomes imaginary for  $|\Omega| < \Omega_c$ , and the perturbation  $a(z, T)$  grows exponentially with  $z$  as seen from Eq. (5.1.5). As a result, the CW solution (5.1.2) is inherently unstable for  $\beta_2 < 0$ . This instability is referred to as modulation instability because it leads to a spontaneous temporal modulation of the CW beam and transforms it into a pulse train. Similar instabilities occur in many other nonlinear systems and are often called self-pulsing instabilities [28–31].

### 5.1.2 Gain Spectrum

The gain spectrum of modulation instability is obtained from Eq. (5.1.6) by setting  $\text{sgn}(\beta_2) = -1$  and  $g(\Omega) = 2\text{Im}(K)$ , where the factor of 2 converts  $g$  to power gain. The gain exists only if  $|\Omega| < \Omega_c$  and is given by

$$g(\Omega) = |\beta_2 \Omega| (\Omega_c^2 - \Omega^2)^{1/2}. \quad (5.1.8)$$

Figure 5.1 shows the gain spectra for three values of the nonlinear length ( $L_{\text{NL}} = 1, 2$ , and  $5 \text{ km}$ ) for an optical fiber with  $\beta_2 = -5 \text{ ps}^2/\text{km}$ . As an example,  $L_{\text{NL}} = 5 \text{ km}$  at a power level of  $100 \text{ mW}$  if we use  $\gamma = 2 \text{ W}^{-1}/\text{km}$  in the wavelength region near  $1.55 \mu\text{m}$ . The gain spectrum is symmetric with respect to  $\Omega = 0$  such that  $g(\Omega)$  vanishes at  $\Omega = 0$ . The gain becomes maximum at two frequencies given by

$$\Omega_{\text{max}} = \pm \frac{\Omega_c}{\sqrt{2}} = \pm \left( \frac{2\gamma P_0}{|\beta_2|} \right)^{1/2}, \quad (5.1.9)$$

with a peak value

$$g_{\text{max}} \equiv g(\Omega_{\text{max}}) = \frac{1}{2} |\beta_2| \Omega_c^2 = 2\gamma P_0, \quad (5.1.10)$$

where Eq. (5.1.7) was used to relate  $\Omega_c$  to  $P_0$ . The peak gain does not depend on  $\beta_2$ , but it increases linearly with the incident power such that  $g_{\text{max}} L_{\text{NL}} = 2$ .

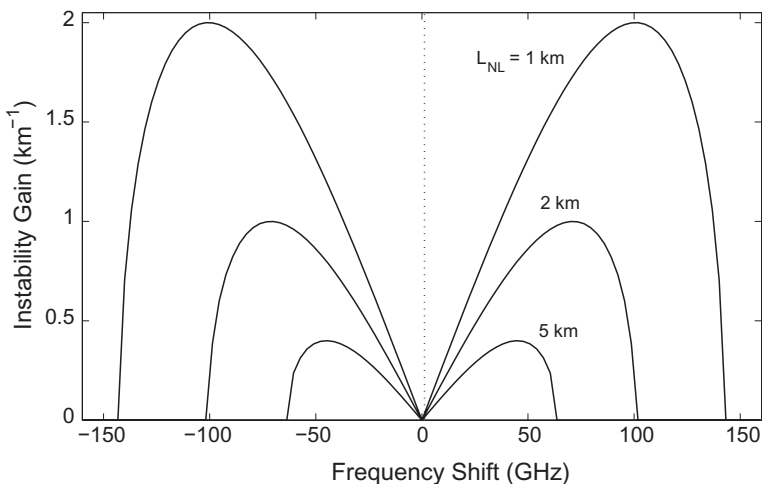


**Figure 5.1** Gain spectra of modulation instability for three values of the nonlinear length,  $L_{NL} = (\gamma P_0)^{-1}$  when a CW beam with power  $P_0$  is launched into a fiber with  $\beta_2 = -5 \text{ ps}^2/\text{km}$ .

The modulation-instability gain is affected by the loss parameter  $\alpha$  that has been neglected in the derivation of Eq. (5.1.8). The main effect of fiber losses is to decrease the gain along the fiber length because of reduced power [9–11]. In effect,  $\Omega_c$  in Eq. (5.1.8) is replaced by  $\Omega_c \exp(-\alpha z/2)$ . Modulation instability still occurs as long as  $\alpha L_{NL} < 1$ . The effect of higher-order dispersive and nonlinear effects such as self-steepening and intrapulse Raman scattering can also be included using Eq. (2.3.44) in place of Eq. (5.1.1) as the starting point [14–16]. The third-order dispersion  $\beta_3$  (or any odd-order dispersive term) does not affect the gain spectrum of modulation instability. The main effect of self-steepening is to reduce the growth rate and the frequency range over which gain occurs from the values seen in Figure 5.1.

As discussed in Chapter 10, modulation instability can be interpreted in terms of a four-wave-mixing process that is phase-matched by SPM. If a probe wave at a frequency  $\omega_1 = \omega_0 + \Omega$  were to copropagate with the CW beam at  $\omega_0$ , it would experience a net power gain given by Eq. (5.1.8) as long as  $|\Omega| < \Omega_c$ . Physically, the energy of two photons from the intense pump beam is used to create two different photons, one at the probe frequency  $\omega_1$  and the other at the idler frequency  $2\omega_0 - \omega_1$ . The case in which a probe is launched together with the intense pump wave is referred to as *induced* modulation instability.

Even when the pump wave propagates by itself, modulation instability can lead to a spontaneous breakup of the CW beam into a periodic pulse train. Noise photons (vacuum fluctuations) act as a probe in this situation and are amplified by the gain provided by modulation instability [27]. As the largest gain occurs for frequencies  $\omega_0 \pm \Omega_{\max}$ , where  $\Omega_{\max}$  is given by Eq. (5.1.9), these frequency components are amplified most. Thus, a clear-cut evidence of *spontaneous* modulation instability

is provided by the appearance of two spectral sidebands at the fiber output, located symmetrically at  $\pm\Omega_{\max}$  on each side of the central line at  $\omega_0$ . In the time domain, the CW beam is converted into a periodic pulse train with a period  $T_m = 2\pi/\Omega_{\max}$ .

One may wonder whether modulation instability can occur in the normal-dispersion region of optical fibers under certain conditions. It turns out that cross-phase modulation, occurring when two optical beams at different wavelengths or with orthogonal polarizations propagate simultaneously, can lead to modulation instability even in normally dispersive fibers. This case is discussed in Chapters 6 and 7. Even a single CW beam can become unstable in a normally dispersive medium that responds slowly to the optical field [24]. Modulation instability can also occur for  $\beta_2 > 0$  if the fiber has two zero-dispersion wavelengths. This is the case for dispersion-flattened fibers [25]. This is also the case for tapered and other microstructured fibers in which a narrow core changes dispersive properties of the fiber considerably [26]. In such fibers, the gain spectrum of modulation instability exhibits a second peak even in the case of anomalous dispersion.

### 5.1.3 Experimental Results

Modulation instability in the anomalous-dispersion regime of optical fibers was first observed in an experiment in which 100-ps (FWHM) pulses from a Nd:YAG laser operating at  $1.319 \mu\text{m}$  were transmitted through a 1-km-long fiber having  $\beta_2 \approx -3 \text{ ps}^2/\text{km}$  [12]. Figure 5.2 shows the autocorrelation trace and the optical spectrum measured at the fiber output for a peak power  $P_0 = 7.1 \text{ W}$ . The location of spectral sidebands is in agreement with the prediction of Eq. (5.1.9). Furthermore, the interval between the oscillation peaks in the autocorrelation trace is inversely related to  $\Omega_{\max}$  as predicted by theory. The secondary sidebands seen in Figure 5.2 are also expected when pump depletion is included. In this experiment, it was necessary to use 100-ps pulses rather than CW radiation to avoid stimulated Brillouin scattering (see Chapter 9). However, as the modulation period is  $\sim 1 \text{ ps}$ , the relatively broad 100-ps pulses provide a quasi-CW environment for the observation of modulation instability.

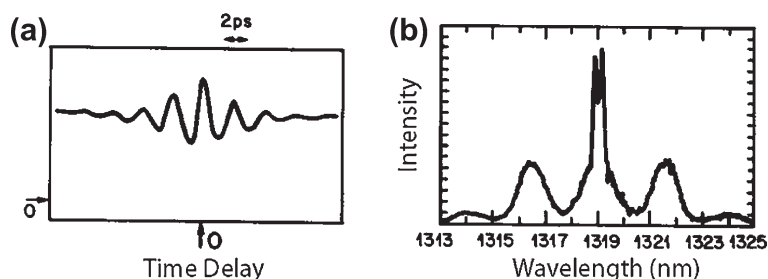


**Figure 5.2** Autocorrelation trace and optical spectrum of 100-ps input pulses showing evidence of modulation instability at a peak power of 7.1 W. (After Ref. [12]; © 1986 American Physical Society.)

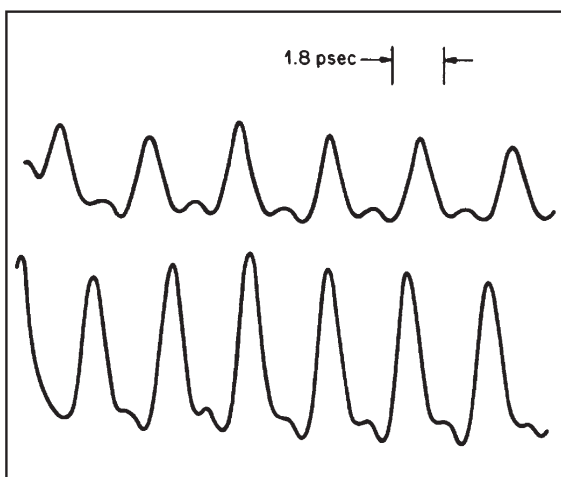


**Figure 5.3** Autocorrelation traces showing induced modulation instability at two different probe wavelengths. The modulation period can be adjusted by tuning the semiconductor laser acting as a probe. (After Ref. [13]; © 1986 American Institute of Physics.)

In a related experiment, modulation instability was induced by sending a weak CW probe wave together with the intense pump pulses [13]. The probe was obtained from a single-mode semiconductor laser whose wavelength could be tuned over a few nanometers in the vicinity of the pump wavelength. The CW probe power of 0.5 mW was much smaller compared with the pump-pulse peak power of  $P_0 = 3$  W. However, its presence led to the breakup of each pump pulse into a periodic pulse train whose period was inversely related to the frequency difference between the pump and probe waves. Moreover, the period could be adjusted by tuning the wavelength of the probe laser. Figure 5.3 shows the autocorrelation traces for two different probe wavelengths. As the observed pulse width is  $<1$  ps, this technique is useful for generating subpicosecond pulses whose repetition rate can be controlled by tuning the probe wavelength.

When optical pulses with widths  $<100$  ps are used, modulation instability can be initiated by SPM. If spectral broadening induced by SPM is large enough to exceed  $\Omega_{\max}$ , the SPM-generated frequency components near  $\Omega_{\max}$  can act as a probe and get amplified by modulation instability. This phenomenon is called SPM-induced modulation instability. One can estimate the fiber length  $L$  at which the spectral width approaches  $\Omega_{\max}$  by using  $\delta\omega_{\max}$  from Eq. (4.1.9) and requiring that  $\Omega_{\max} \approx \delta\omega_{\max}$ . In the case of a Gaussian pulse this condition is satisfied when

$$L \approx (2L_DL_{NL})^{1/2}, \quad (5.1.11)$$

where  $L_D = T_0^2/|\beta_2|$  is the dispersion length introduced in Section 3.1. Numerical solutions of Eq. (5.1.1) confirm the occurrence of SPM-induced modulation instability [17]. In particular, the input pulse develops deep modulations at the frequency

$\Omega_{\max}/2\pi$  and the spectrum exhibits sidelobes at that frequency. The SPM-induced modulation instability has also been observed experimentally [17].

### 5.1.4 Ultrashort Pulse Generation

The linear stability analysis of the steady-state solution of Eq. (5.1.1) provides only the initial exponential growth of weak perturbations with the power gain given by Eq. (5.1.8). Clearly, an exponential growth cannot be sustained indefinitely because the frequency components at  $\omega_0 \pm \Omega$  grow at the expense of the pump wave at  $\omega_0$ , and pump depletion slows down the growth rate. Moreover, the sidebands at  $\omega_0 \pm \Omega$  eventually become strong enough, and the perturbation becomes large enough, that the linear stability analysis breaks down. Evolution of the modulated state is then governed by the NLS equation (5.1.1). A simple approach solves this equation in the frequency domain as a four-wave mixing problem [23]; it is discussed in detail in Chapter 10. The main disadvantage of this approach is that it cannot treat the generation of higher-order sidebands located at  $\omega_0 \pm m\Omega$  ( $m = 2, 3, \dots$ ) that are invariably created when the first-order sidebands ( $m = 1$ ) become strong.

The time-domain approach solves the NLS equation directly. Numerical solutions of Eq. (5.1.1) obtained with the input corresponding to a CW beam with weak sinusoidal modulation imposed on it show that the nearly CW beam evolves into a train of narrow pulses, separated by the period of initial modulation [8]. The fiber length required to realize such a train of narrow pulses depends on the initial modulation depth and is typically  $\sim 5L_D$ . With further propagation, the multipeak structure deforms and eventually returns to the initial input form. This behavior is found to be generic when Eq. (5.1.1) is solved by considering arbitrary periodic modulation of the steady state. The foregoing scenario suggests that the NLS equation should have periodic solutions whose forms change with propagation. Indeed, it turns out that the NLS equation has a multiparameter family of periodic solutions [32–40]. In their most general form, these solutions are expressed in the form of Jacobian elliptic functions. In some specific cases, the solution can be written in terms of trigonometric and hyperbolic functions [37]. A specific family of periodic solutions of the NLS equation is referred to as the Akhmediev breather [32], and it has attracted attention recently in the context of optical rogue waves and supercontinuum generation [41–43]. See Section 13.7.3 for further details.

From a practical standpoint, modulation instability is useful for generating a train of short optical pulses whose repetition rate can be externally controlled. As early as 1989, 130-fs pulses at a 2-THz repetition rate were generated through induced modulation instability [44]. Since then, this technique has been used to create optical sources capable of producing periodic trains of ultrashort pulses at repetition rates higher than those attainable from mode-locked lasers. Several experiments have used dispersion-decreasing fibers for this purpose [45–47]. Initial sinusoidal modulation in these experiments was imposed by beating two optical signals. In a 1992 experiment [46], the outputs of two distributed feedback (DFB) semiconductor lasers, operating continuously at slightly different wavelengths near 1.55  $\mu\text{m}$ ,

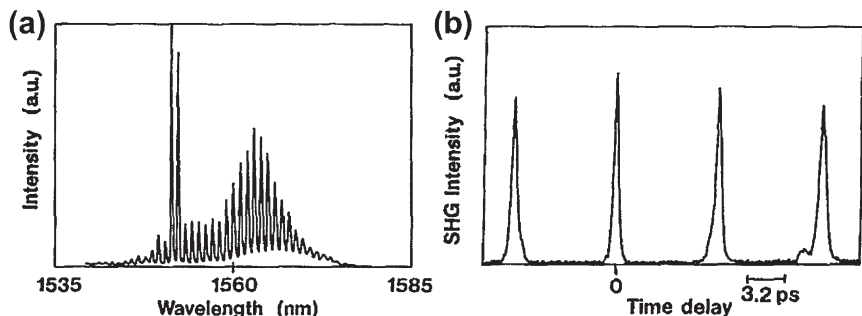


**Figure 5.4** Measured (a) optical spectrum and (b) autocorrelation trace for a 114-GHz pulse train generated through modulation instability. Two dominant spectral peaks correspond to the two input CW beams launched into a 1.6-km-long dispersion-decreasing fiber. (After Ref. [47]; © 1993 American Institute of Physics.)

were combined in a fiber coupler to produce a sinusoidally modulated signal at a beat frequency that could be varied in the 70–90 GHz range by controlling the laser temperature. In a later experiment [47], 250-fs pulses at a tunable repetition rate of 80–120 GHz were generated. The beat signal from two DFB lasers was amplified to power levels  $\sim 0.8$  W by using a fiber amplifier and then propagated through a 1.6-km-long dispersion-decreasing fiber, whose GVD decreased from 10 to 0.5 ps/(km nm) over its length. Figure 5.4 shows the output pulse train (width 250 fs) at a 114-GHz repetition rate and the corresponding optical spectrum. The spectrum was shifted toward red because of intrapulse Raman scattering that becomes important for such short pulses (see Section 5.5.4).

The use of a dispersion-decreasing fiber is not essential for producing pulse trains through modulation instability. In an interesting experiment, a comb-like dispersion profile was produced by splicing pieces of low- and high-dispersion fibers [48]. A dual-frequency fiber laser was used to generate the high-power signal modulated at a frequency equal to the longitudinal-mode spacing (59 GHz). When such a modulated signal was launched into the fiber, the output consisted of a 2.2-ps pulse train at the 59-GHz repetition rate. In another experiment [49], a periodic train of 1.3-ps pulses at the 123-GHz repetition rate was generated by launching the high-power beat signal into a 5-km-long dispersion-shifted fiber. The experimental results were in good agreement with the numerical simulations based on the NLS equation.

The main problem with the preceding technique is that its use requires a relatively long fiber ( $\sim 5$  km) and relatively high input powers ( $\sim 100$  mW) for the pulse train to build up. This problem can be solved by enclosing the fiber within a cavity. The gain provided by modulation instability converts such a device into a self-pulsing laser. As early as 1988, a ring-cavity configuration was used to generate a pulse train through modulation instability [50]. Since then, modulation instability occurring inside an optical resonator has attracted considerable attention [51–55].

Mathematical treatment is cumbersome in the case of a Fabry–Perot resonator because one must use a set of two coupled NLS equations for the counterpropagating optical fields. It turns out that modulation instability can occur even in the normal-dispersion regime of the fiber because of the feedback provided by cavity mirrors [52]. Moreover, a relatively small feedback occurring at the fiber–air interface (about 4%) is enough for this fundamental change to occur [53]. As a result, a self-pulsing fiber laser can be made without actually using any mirrors. Numerical and analytical results show that such a laser can generate ultrashort pulse trains with repetition rates in the terahertz range by using CW pump beams with power levels  $\sim 10$  mW [54].

### 5.1.5 Impact on Lightwave Systems

Modulation instability affects the performance of optical communication systems in which fiber losses are compensated periodically using optical amplifiers [56–67]. Computer simulations showed, as early as 1990, that it can be a limiting factor for systems employing the nonreturn-to-zero (NRZ) format for data transmission [56]. Since then, the impact of modulation instability has been studied both numerically and experimentally [63]. Physically, spontaneous emission of amplifiers can provide a seed for the growth of sidebands through induced modulation instability. As a result, signal spectrum broadens substantially. Since GVD-induced broadening of optical pulses depends on their bandwidth, this effect degrades system performance. Experimental results on a lightwave system operating at 10 Gb/s showed considerable degradation for a transmission distance of only 455 km [62]. As expected, system performance improved when GVD was compensated partially using a dispersion-compensating fiber.

The periodic use of optical amplifiers in a lightwave system can induce modulation instability through another mechanism and generate additional sidebands in which noise can be amplified in both the normal and anomalous GVD regimes of optical fibers [57]. The new mechanism has its origin in the periodic sawtooth-like variation of the average power  $P_0$  occurring along the link length. To understand the physics more clearly, note that a periodic variation of  $P_0$  in  $z$  is equivalent to the creation of a nonlinear index grating because the term  $\gamma P_0$  in Eq. (5.1.4) becomes a periodic function of  $z$ . The period of this grating is equal to the amplifier spacing and is typically in the range 50–100 km. Such a long-period grating provides a new coupling mechanism between the spectral sidebands located at  $\omega_0 + \Omega$  and  $\omega_0 - \Omega$  and allows them to grow when the perturbation frequency  $\Omega$  satisfies the Bragg condition.

The analysis of Section 5.1.1 can be extended to include periodic variations of  $P_0$ . If we replace  $P_0$  in Eq. (5.1.4) by  $P_0 f(z)$ , where  $f(z)$  is a periodic function, expand  $f(z)$  in a Fourier series as  $f(z) = \sum c_m \exp(2\pi i mz/L_A)$ , the frequencies at which the gain peaks are found to be [57]

$$\Omega_m = \pm \left( \frac{2\pi m}{\beta_2 L_A} - \frac{2\gamma P_0 C_0}{\beta_2} \right)^{1/2}, \quad (5.1.12)$$

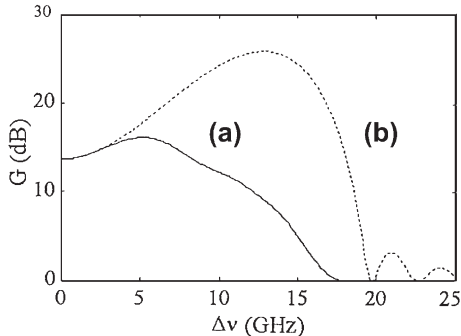


**Figure 5.5** Predicted gain spectrum (a) for a 1000-km-long fiber link when 95% of dispersion is compensated after each 100-km-long span such that the average dispersion  $D = 0.8 \text{ ps}/(\text{km nm})$ . The curve (b) shows the gain spectrum for a constant-dispersion fiber link with the same net dispersion. (After Ref. [65]; © 1999 IEEE.)

where the integer  $m$  represents the order of Bragg diffraction,  $L_A$  is the spacing between amplifiers (grating period), and the Fourier coefficient  $c_m$  is related to the fiber loss  $\alpha$  as

$$c_m = \frac{1 - \exp(-\alpha L_A)}{\alpha L_A + 2im\pi}. \quad (5.1.13)$$

In the absence of grating, or when  $m = 0$ ,  $\Omega_0$  exists only for anomalous dispersion, in agreement with Eq. (5.1.9). However, when  $m \neq 0$ , modulation-instability sidebands can occur even for normal dispersion ( $\beta_2 > 0$ ). Physically, this behavior can be understood by noting that the nonlinear index grating helps to satisfy the phase-matching condition necessary for four-wave mixing to occur when  $m \neq 0$ .

With the advent of wavelength-division multiplexing (WDM), it has become common to employ the technique of dispersion management to reduce the GVD globally, while keeping it high locally by using a periodic dispersion map. The periodic variation of  $\beta_2$  creates another grating that affects modulation instability considerably. Mathematically, the situation is similar to the preceding case except that  $\beta_2$  rather than  $P_0$  in Eq. (5.1.4) is a periodic function of  $z$ . The gain spectrum of modulation instability is obtained following a similar technique [61]. The  $\beta_2$  grating not only generates new sidebands but also affects the gain spectrum seen in Figure 5.1. In the case of strong dispersion management (relatively large GVD variations), both the peak value and the bandwidth of the modulation-instability gain are reduced, indicating that such systems should not suffer much from amplification of noise induced by modulation instability.

Figure 5.5 shows the impact of dispersion compensation on the gain spectrum of modulation instability for a 1000-km lightwave system consisting of 100-km spans of standard fiber with a loss of 0.22 dB/km, dispersion  $D = 16 \text{ ps}/(\text{km nm})$ , and  $\gamma = 1.7 \text{ W}^{-1}/\text{km}$ . An amplifier at the end of each span compensates the total losses incurred in that span [65]. When dispersion is not compensated, the spectrum exhibits its many sidebands. These sidebands are suppressed and the peak gain is reduced

considerably when 95% of dispersion is compensated after each span (curve a) such that the average dispersion is 0.8 ps/(km nm). As shown by curve (b), the gain is much higher if the lightwave system is designed using a uniform-dispersion fiber with  $D = 0.8$  ps/(km nm).

Modulation instability affects WDM systems in several other ways. It has been shown that WDM systems suffer from a resonant enhancement of four-wave mixing that degrades the system performance considerably when channel spacing is close to the frequency at which the modulation-instability gain is strongest [64]. On the positive side, this enhancement can be used for low-power, high-efficiency, wavelength conversion [68]. Modulation instability has been used for measuring the distribution of zero-dispersion wavelength along a fiber by noting that the instability gain becomes quite small in the vicinity of  $|\beta_2| = 0$  [69]. As discussed in Chapter 11, it can also be used to deduce the value of the nonlinear parameter  $\gamma$  [70].

## 5.2 FIBER SOLITONS

The occurrence of modulation instability in the anomalous-GVD regime of optical fibers is an indication of a fundamentally different character of Eq. (5.1.1) when  $\beta_2 < 0$ . It turns out that this equation has specific pulselike solutions that either do not change along fiber length or follow a periodic evolution pattern—such solutions are known as optical solitons. The history of solitons, in fact, dates back to 1834, the year in which Scott Russell observed a heap of water in a canal that propagated undistorted over several kilometers. Here is a quote from his report published in 1844 [71]:

*I was observing the motion of a boat which was rapidly drawn along a narrow channel by a pair of horses, when the boat suddenly stopped—not so the mass of water in the channel which it had put in motion; it accumulated round the prow of the vessel in a state of violent agitation, then suddenly leaving it behind, rolled forward with great velocity, assuming the form of a large solitary elevation, a rounded, smooth and well-defined heap of water, which continued its course along the channel apparently without change of form or diminution of speed. I followed it on horseback, and overtook it still rolling on at a rate of some eight or nine miles an hour, preserving its original figure some thirty feet long and a foot to a foot and a half in height. Its height gradually diminished, and after a chase of one or two miles I lost it in the windings of the channel. Such, in the month of August 1834, was my first chance interview with that singular and beautiful phenomenon which I have called the Wave of Translation.*

Such waves were later called solitary waves. However, their properties were not understood completely until the inverse scattering method was developed [72]. The term *soliton* was coined in 1965 to reflect the particlelike nature of those solitary waves that remained intact even after mutual collisions [73]. Since then, solitons have been discovered and studied in many branches of physics including optics [74–79]. In the context of optical fibers, the use of solitons for optical

communications was first suggested in 1973 [80]. By the year 1999, several field trials making use of fiber solitons had been completed [81]. The word “soliton” has become so popular in recent years that a search on the Internet returns thousands of hits. Similarly, scientific databases reveal that hundreds of research papers are published every year with the word “soliton” in their title. It should be stressed that the distinction between a soliton and a solitary wave is not always made in modern optics literature, and it is quite common to refer to all solitary waves as solitons.

### 5.2.1 Inverse Scattering Method

Only certain nonlinear wave equations can be solved with the inverse scattering method [74]. The NLS equation (5.1.1) belongs to this special class of equations. Zakharov and Shabat used the inverse scattering method in 1971 to solve the NLS equation [82]. This method is similar in spirit to the Fourier-transform method used commonly for solving linear partial differential equations. The approach consists of identifying a suitable scattering problem whose potential is the solution sought. The incident field at  $z = 0$  is used to find the initial scattering data, whose evolution along  $z$  is then determined by solving the linear scattering problem. The propagated field is reconstructed from the evolved scattering data. Since details of the inverse scattering method are available in many texts [74–79], only a brief description is given here.

Similar to Chapter 4, it is useful to normalize Eq. (5.1.1) by introducing three dimensionless variables

$$U = \frac{A}{\sqrt{P_0}}, \quad \xi = \frac{z}{L_D}, \quad \tau = \frac{T}{T_0}, \quad (5.2.1)$$

and write it in the form

$$i \frac{\partial U}{\partial \xi} = \text{sgn}(\beta_2) \frac{1}{2} \frac{\partial^2 U}{\partial \tau^2} - N^2 |U|^2 U, \quad (5.2.2)$$

where  $P_0$  is the peak power,  $T_0$  is the width of the incident pulse, and the parameter  $N$  is introduced as

$$N^2 = \frac{L_D}{L_{NL}} = \frac{\gamma P_0 T_0^2}{|\beta_2|}. \quad (5.2.3)$$

The dispersion length  $L_D$  and the nonlinear length  $L_{NL}$  are defined as in Eq. (3.1.5). Fiber losses are neglected in this section but will be included later.

The parameter  $N$  can be eliminated from Eq. (5.2.2) by introducing

$$u = NU = \sqrt{\gamma L_D} A. \quad (5.2.4)$$

Equation (5.2.2) then takes the standard form of the NLS equation:

$$i \frac{\partial u}{\partial \xi} + \frac{1}{2} \frac{\partial^2 u}{\partial \tau^2} + |u|^2 u = 0, \quad (5.2.5)$$

where the choice  $\text{sgn}(\beta_2) = -1$  has been made to focus on the case of anomalous GVD. Note that an important scaling relation holds for Eq. (5.2.5). If  $u(\xi, \tau)$  is a solution of this equation, then  $\epsilon u(\epsilon^2 \xi, \epsilon \tau)$  is also a solution, where  $\epsilon$  is an arbitrary scaling factor. The importance of this scaling will become clear later.

In the inverse scattering method, the scattering problem associated with Eq. (5.2.5) is found to be [75]

$$i \frac{\partial v_1}{\partial \tau} + u v_2 = \zeta v_1, \quad (5.2.6)$$

$$i \frac{\partial v_2}{\partial \tau} + u^* v_1 = -\zeta v_2, \quad (5.2.7)$$

where  $v_1$  and  $v_2$  are the amplitudes of the two waves scattered by the potential  $u(\xi, \tau)$ . The eigenvalue  $\zeta$  plays a role similar to that played by the frequency in the standard Fourier analysis except that  $\zeta$  can take complex values when  $u \neq 0$ . This feature can be identified by noting that, in the absence of potential ( $u = 0$ ),  $v_1$  and  $v_2$  vary as  $\exp(\pm i\zeta \tau)$ .

Equations (5.2.6) and (5.2.7) apply for all values of  $\xi$ . In the inverse scattering method, they are first solved at  $\xi = 0$ . For a given initial form of  $u(0, \tau)$ , Eqs (5.2.6) and (5.2.7) are solved to obtain the initial scattering data. The direct scattering problem is characterized by a reflection coefficient  $r(\zeta)$  that plays a role analogous to the Fourier coefficient. Formation of the bound states (solitons) corresponds to the poles of  $r(\zeta)$  in the complex  $\zeta$  plane. Thus, the initial scattering data consist of the reflection coefficient  $r(\zeta)$ , the complex poles  $\zeta_j$ , and their residues  $c_j$ , where  $j = 1$  to  $N$  if  $N$  such poles exist. Although the parameter  $N$  of Eq. (5.2.3) is not necessarily an integer, the same notation is used for the number of poles to stress that its integer values determine the number of poles.

Evolution of the scattering data along the fiber length is determined by using well-known techniques [74]. The desired solution  $u(\xi, \tau)$  is reconstructed from the evolved scattering data using the inverse scattering method. This step is quite cumbersome mathematically because it requires the solution of a complicated linear integral equation. However, in the specific case in which  $r(\zeta)$  vanishes for the initial potential  $u(0, \tau)$ , the solution  $u(\xi, \tau)$  can be determined by solving a set of algebraic equations. This case corresponds to solitons. The soliton order is characterized by the number  $N$  of poles, or eigenvalues  $\zeta_j$  ( $j = 1$  to  $N$ ). The general solution can be written as [82]

$$u(\xi, \tau) = -2 \sum_{j=1}^N \lambda_j^* \psi_{2j}^*, \quad (5.2.8)$$

where

$$\lambda_j = \sqrt{c_j} \exp(i\zeta_j \tau + i\zeta_j^2 \xi), \quad (5.2.9)$$

and  $\psi_{2j}^*$  is obtained by solving the following set of algebraic linear equations:

$$\psi_{1j} + \sum_{k=1}^N \frac{\lambda_j \lambda_k^*}{\zeta_j - \zeta_k^*} \psi_{2k}^* = 0, \quad (5.2.10)$$

$$\psi_{2j}^* - \sum_{k=1}^N \frac{\lambda_j^* \lambda_k}{\zeta_j^* - \zeta_k} \psi_{1k} = \lambda_j^*. \quad (5.2.11)$$

The eigenvalues  $\zeta_j$  are generally complex ( $2\zeta_j = \delta_j + i\eta_j$ ). Physically, the real part  $\delta_j$  produces a change in the group velocity associated with the  $j$ th component of the soliton. For the  $N$ th-order soliton to remain bound, it is necessary that all of its components travel at the same speed. Thus, all eigenvalues  $\zeta_j$  should lie on a line parallel to the imaginary axis, i.e.,  $\delta_j = \delta$  for all  $j$ . This feature simplifies the general solution in Eq. (5.2.9) considerably. It will be seen later that the parameter  $\delta$  represents a frequency shift of the soliton from the carrier frequency  $\omega_0$ .

## 5.2.2 Fundamental Soliton

The first-order soliton ( $N = 1$ ) corresponds to the case of a single eigenvalue. It is referred to as the fundamental soliton because its shape does not change on propagation. Its field distribution is obtained from Eqs (5.2.8)–(5.2.11) after setting  $j = k = 1$ . Noting that  $\psi_{21} = \lambda_1(1 + |\lambda_1|^4/\eta^2)^{-1}$  and substituting it in Eq. (5.2.8), we obtain

$$u(\xi, \tau) = -2(\lambda_1^*)^2(1 + |\lambda_1|^4/\eta^2)^{-1}. \quad (5.2.12)$$

After using Eq. (5.2.9) for  $\lambda_1$  together with  $\zeta_1 = (\delta + i\eta)/2$  and introducing the parameters  $\tau_s$  and  $\phi_s$  through  $-c_1/\eta = \exp(\eta\tau_s - i\phi_s)$ , we obtain the following general form of the fundamental soliton:

$$u(\xi, \tau) = \eta \operatorname{sech}[\eta(\tau - \tau_s + \delta\xi)] \exp[i(\eta^2 - \delta^2)\xi/2 - i\delta\tau + i\phi_s], \quad (5.2.13)$$

where  $\eta$ ,  $\delta$ ,  $\tau_s$ , and  $\phi_s$  are four arbitrary parameters that characterize the soliton. Thus, an optical fiber supports a four-parameter family of fundamental solitons, all sharing the condition  $N = 1$ .

Physically, the four parameters  $\eta$ ,  $\delta$ ,  $\tau_s$ , and  $\phi_s$  represent amplitude, frequency, position, and phase of the soliton, respectively. The phase  $\phi_s$  can be dropped from the discussion because a constant absolute phase has no physical significance. It will become relevant later when nonlinear interaction between a pair of solitons is considered. The parameter  $\tau_s$  can also be dropped because it denotes the position of the soliton peak: if the origin of time is chosen such that the peak occurs at  $\tau = 0$  at  $\xi = 0$ , one can set  $\tau_s = 0$ . It is clear from the phase factor in Eq. (5.2.13) that the parameter  $\delta$  represents a frequency shift of the soliton from the carrier frequency  $\omega_0$ . Using the

carrier part,  $\exp(-i\omega_0 t)$ , the new frequency becomes  $\omega'_0 = \omega_0 + \delta/T_0$ . Note that a frequency shift also changes the soliton speed from its original value  $v_g$ . This can be seen more clearly by using  $\tau = (t - \beta_1 z)/T_0$  in Eq. (5.2.13) and writing it as

$$|u(\xi, \tau)| = \eta \operatorname{sech}[\eta(t - \beta'_1 z)/T_0], \quad (5.2.14)$$

where  $\beta'_1 = \beta_1 + \delta|\beta_2|/T_0$ . As expected on physical grounds, the change in group velocity ( $v_g = 1/\beta_1$ ) is a consequence of fiber dispersion.

The frequency shift  $\delta$  can also be removed from Eq. (5.2.13) by choosing the carrier frequency appropriately. Fundamental solitons then form a single-parameter family described by

$$u(\xi, \tau) = \eta \operatorname{sech}(\eta\tau) \exp(i\eta^2\xi/2). \quad (5.2.15)$$

The parameter  $\eta$  determines not only the soliton amplitude but also its width. In real units, the soliton width changes with  $\eta$  as  $T_0/\eta$ , i.e., it scales inversely with the soliton amplitude. This inverse relationship between the amplitude and the width of a soliton is the most crucial property of solitons. Its relevance will become clear later. The canonical form of the fundamental soliton is obtained by choosing  $u(0, 0) = 1$  so that  $\eta = 1$ . With this choice, Eq. (5.2.15) becomes

$$u(\xi, \tau) = \operatorname{sech}(\tau) \exp(i\xi/2). \quad (5.2.16)$$

One can verify by direct substitution in Eq. (5.2.5) that this solution is indeed a solution of the NLS equation.

The solution in Eq. (5.2.16) can also be obtained by solving the NLS equation directly, without using the inverse scattering method. The approach consists of assuming that a shape-preserving solution of the NLS equation exists and has the form

$$u(\xi, \tau) = V(\tau) \exp[i\phi(\xi, \tau)], \quad (5.2.17)$$

where  $V$  is independent of  $\xi$  for Eq. (5.2.17) to represent a fundamental soliton that maintains its shape during propagation. The phase  $\phi$  can depend on both  $\xi$  and  $\tau$ . If Eq. (5.2.17) is substituted in Eq. (5.2.5) and the real and imaginary parts are separated, one obtains two equations for  $V$  and  $\phi$ . The phase equation shows that  $\phi$  should be of the form  $\phi(\xi, \tau) = K\xi - \delta\tau$ , where  $K$  and  $\delta$  are constants. Choosing  $\delta = 0$  (no frequency shift),  $V(\tau)$  is found to satisfy

$$\frac{d^2V}{d\tau^2} = 2V(K - V^2). \quad (5.2.18)$$

This nonlinear equation can be solved by multiplying it by  $2(dV/d\tau)$  and integrating over  $\tau$ . The result is

$$(dV/d\tau)^2 = 2KV^2 - V^4 + C, \quad (5.2.19)$$

where  $C$  is a constant of integration. Using the boundary condition that both  $V$  and  $dV/d\tau$  vanish as  $|\tau| \rightarrow \infty$ ,  $C$  is found to be 0. The constant  $K$  is determined from the condition that  $V = 1$  and  $dV/d\tau = 0$  at the soliton peak, assumed to occur at  $\tau = 0$

. Its use provides  $K = \frac{1}{2}$ , and hence  $\phi = \xi/2$ . Equation (5.2.19) is easily integrated to obtain  $V(\tau) = \text{sech}(\tau)$ . We have thus recovered the solution in Eq. (5.2.16) using a simple technique.

In the context of optical fibers, the solution (5.2.16) indicates that if a hyperbolic-secant pulse, whose width  $T_0$  and the peak power  $P_0$  are chosen such that  $N = 1$  in Eq. (5.2.3), is launched inside an ideal lossless fiber, the pulse will propagate undistorted without change in shape for arbitrarily long distances. It is this feature of the solitons that makes them attractive for optical communication systems [80]. The peak power  $P_0$  required to support the fundamental soliton is obtained from Eq. (5.2.3) by setting  $N = 1$  and is given by

$$P_0 = \frac{|\beta_2|}{\gamma T_0^2} \approx \frac{3.11|\beta_2|}{\gamma T_{\text{FWHM}}^2}, \quad (5.2.20)$$

where the FWHM of the soliton is defined using  $T_{\text{FWHM}} \approx 1.76 T_0$  from Eq. (3.2.22). Using typical parameter values,  $\beta_2 = -1 \text{ ps}^2/\text{km}$  and  $\gamma = 3 \text{ W}^{-1}/\text{km}$ , for dispersion-shifted fibers, the required  $P_0$  is  $\sim 1 \text{ W}$  for  $T_0 = 1 \text{ ps}$  but reduces to only  $10 \text{ mW}$  when  $T_0 = 10 \text{ ps}$ . Thus, fundamental solitons can form in optical fibers at power levels available from semiconductor lasers even for 10-ps-wide input pulses.

### 5.2.3 Second and Higher-Order Solitons

Higher-order solitons are also described by the general solution in Eq. (5.2.8). Various combinations of the eigenvalues  $\eta_j$  and the residues  $c_j$  generally lead to an infinite variety of soliton forms. If the soliton is assumed to be symmetric about  $\tau = 0$ , the residues are related to the eigenvalues by the relation [83]

$$c_j = \frac{\prod_{k=1}^N (\eta_j + \eta_k)}{\prod_{k \neq j} |\eta_j - \eta_k|}. \quad (5.2.21)$$

This condition selects a subset of all possible solitons. Among this subset, a special role is played by solitons whose initial shape at  $\xi = 0$  is given by

$$u(0, \tau) = N \text{sech}(\tau), \quad (5.2.22)$$

where the soliton order  $N$  is an integer. The peak power necessary to launch the  $N$ th-order soliton is obtained from Eq. (5.2.3) and is  $N^2$  times that required for the fundamental soliton. For the second-order soliton ( $N = 2$ ), the field distribution is obtained from Eqs (5.2.8)–(5.2.11). Using  $\zeta_1 = i/2$  and  $\zeta_2 = 3i/2$  for the two eigenvalues, the field associated with the second-order soliton is given by [84]

$$u(\xi, \tau) = \frac{4[\cosh(3\tau) + 3 \exp(4i\xi) \cosh(\tau)] \exp(i\xi/2)}{[\cosh(4\tau) + 4 \cosh(2\tau) + 3 \cos(4\xi)]}. \quad (5.2.23)$$

An interesting property of the solution (5.2.23) is that  $|u(\xi, \tau)|^2$  is periodic in  $\xi$  with the period  $\xi_0 = \pi/2$ . In fact, this periodicity occurs for all solitons with  $N \geq 2$ .

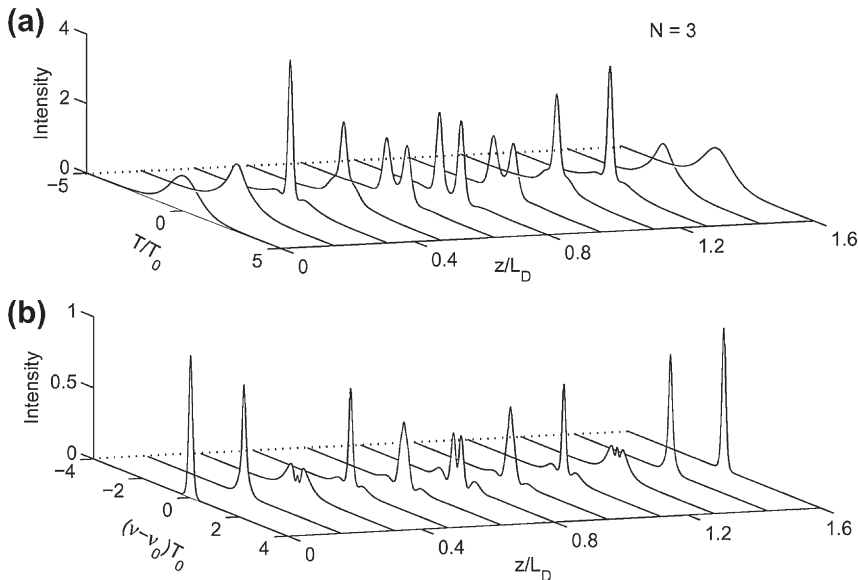


**Figure 5.6 (a)** Temporal and (b) spectral evolution of the third-order soliton over one soliton period. Note splitting of the pulse near  $z/L_D=0.5$  and its recovery beyond that.

Using the definition  $\xi = z/L_D$  from Eq. (5.2.1), the soliton period  $z_0$  in real units becomes

$$z_0 = \frac{\pi}{2} L_D = \frac{\pi}{2} \frac{T_0^2}{|\beta_2|} \approx \frac{T_{\text{FWHM}}^2}{2|\beta_2|}. \quad (5.2.24)$$

Periodic evolution of a third-order soliton over one soliton period is shown in Figure 5.6a. As the pulse propagates along the fiber, it first contracts to a fraction of its initial width, splits into two distinct pulses at  $z_0/2$ , and then merges again to recover the original shape at the end of the soliton period at  $z = z_0$ . This pattern is repeated over each section of length  $z_0$ .

To understand the origin of periodic evolution for higher-order solitons, it is helpful to look at changes in the pulse spectra shown in Figure 5.6b for the  $N = 3$  soliton. The temporal and spectral changes result from an interplay between the SPM and GVD effects. Initially, SPM generates a frequency chirp and broadens the pulse spectrum. This spectral broadening is clearly seen in Figure 5.6b near  $z/L_D = 0.3$  with its typical oscillatory structure. In the absence of GVD, the pulse shape would have remained unchanged. However, anomalous GVD contracts the pulse as the pulse is positively chirped (see Section 3.2). Only the central portion of the pulse contracts because the chirp is nearly linear only over that part. However, as a result of a substantial increase in the pulse intensity near the central part of the pulse, the spectrum changes significantly as seen in Figure 5.6b near  $z/L_D = 0.5$ . It is this

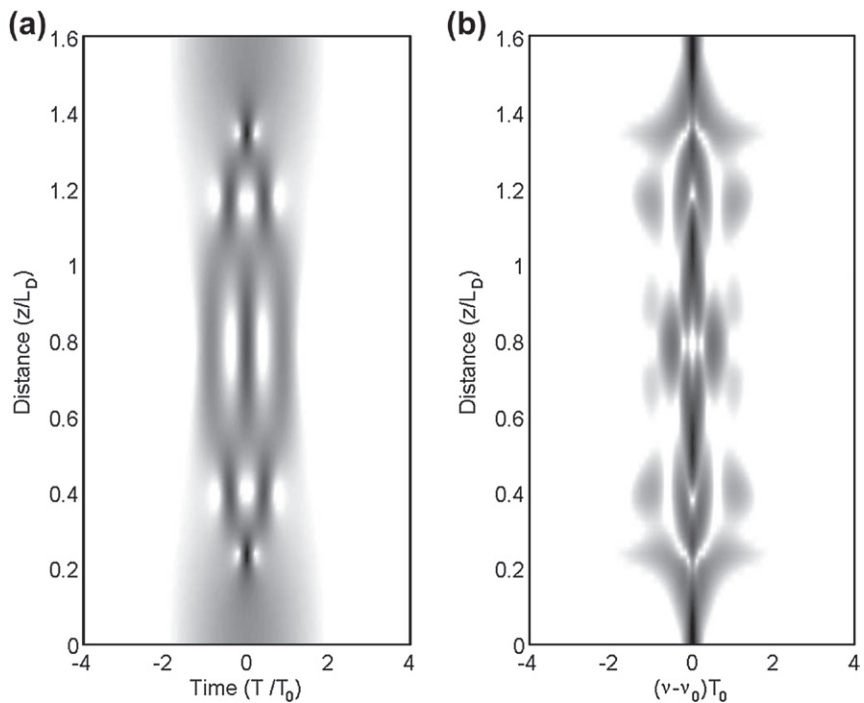


**Figure 5.7** (a) Temporal and (b) spectral evolution of a fourth-order soliton over one soliton period. The gray intensity scale is over a 20-dB range.

mutual interaction between the GVD and SPM effects that is responsible for the periodic evolution pattern seen in Figure 5.6. Evolution becomes more complicated for larger soliton orders. As an example, Figure 5.7 shows the evolution of a fourth-order ( $N = 4$ ) soliton as a surface plot. One can see in part (a), an initial narrowing of the pulse near  $\xi = 0.2$ , followed by a splitting into two and three pulses, and then a subsequent reversal to the original pulse shape at  $\xi = \pi/2$ . The spectrum in part (b) also exhibits a complicated evolutionary pattern.

In the case of a fundamental soliton ( $N = 1$ ), GVD and SPM balance each other in such a way that neither the pulse shape nor the pulse spectrum changes along the fiber length. In the case of higher-order solitons, SPM dominates initially but GVD soon catches up and leads to pulse contraction seen in Figures 5.6 and 5.7. Soliton theory shows that for pulses with a hyperbolic-secant shape and with peak powers determined from Eq. (5.2.3), the two effects can cooperate in such a way that the pulse follows a periodic evolution pattern with original shape recurring at multiples of the soliton period  $z_0$  given by Eq. (5.2.24). Near the 1.55- $\mu\text{m}$  wavelength, if we use  $\beta_2 = -20 \text{ ps}^2/\text{km}$  for standard silica fibers, the soliton period is  $\sim 80 \text{ m}$  for  $T_0 = 1 \text{ ps}$  and scales as  $T_0^2$ , becoming 8 km when  $T_0 = 10 \text{ ps}$ . For dispersion-shifted fibers  $\beta_2$  is smaller by a factor of 10 or so, and  $z_0$  increases by the same factor for a given value of  $T_0$ .

### 5.2.4 Experimental Confirmation

The possibility of soliton formation in optical fibers was suggested as early as 1973 [80]. However, the lack of a suitable source of picosecond optical pulses at wavelengths  $> 1.3 \mu\text{m}$  delayed their experimental observation until 1980. Solitons in optical fibers were first observed in an experiment [85] that used a mode-locked color-center laser capable of emitting short optical pulses ( $T_{\text{FWHM}} \approx 7 \text{ ps}$ ) near  $1.55 \mu\text{m}$ , a wavelength near which optical fibers exhibit anomalous GVD together with minimum losses. The pulses were propagated inside a 700-m-long single-mode fiber with a core diameter of  $9.3 \mu\text{m}$ . The fiber parameters for this experiment were estimated to be  $\beta_2 \approx -20 \text{ ps}^2/\text{km}$  and  $\gamma \approx 1.3 \text{ W}^{-1}/\text{km}$ . Using  $T_0 = 4 \text{ ps}$  in Eq. (5.2.20), the peak power for exciting a fundamental soliton is  $\sim 1 \text{ W}$ .

In the experiment, the peak power of optical pulses was varied over a range  $0.3\text{--}25 \text{ W}$ , and their pulse shapes and spectra were monitored at the fiber output. Figure 5.8 shows autocorrelation traces and pulse spectra at several power levels and compares them with those of the input pulse. The measured spectral width of  $25 \text{ GHz}$  of the input pulse is nearly transform limited, indicating that mode-locked pulses used in the experiment were unchirped. At a low power level of  $0.3 \text{ W}$ , optical pulses experienced dispersion-induced broadening inside the fiber, as expected from Section 3.2. However, as the power was increased, output pulses steadily narrowed, and their width became the same as the input width at  $P_0 = 1.2 \text{ W}$ . This power level corresponds to the formation of a fundamental soliton and should be compared with the theoretical value of  $1 \text{ W}$  obtained from Eq. (5.2.20). The agreement is quite good in spite of many uncertainties inherent in the experiment.

At higher power levels, output pulses exhibited dramatic changes in their shape and developed a multipeak structure. For example, the autocorrelation trace for  $11.4 \text{ W}$  exhibits three peaks. Such a three-peak structure corresponds to twofold splitting

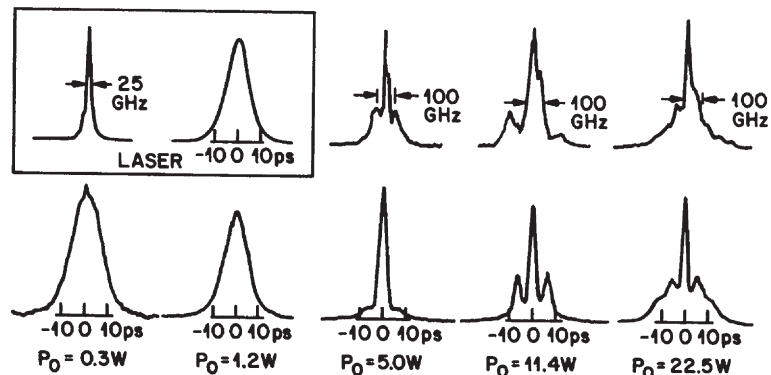


**Figure 5.8** Autocorrelation traces (lower row) and pulse spectra (upper row) for several values of input peak power  $P_0$ . The corresponding traces for the input pulse are shown inside the rectangular box. (After Ref. [85]; © 1980 American Physical Society.)

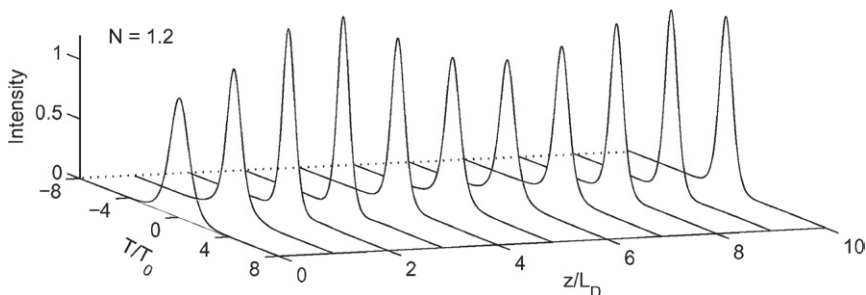


**Figure 5.9** Temporal evolution over 10 dispersion lengths when  $N=1.2$  at  $z=0$ . The pulse evolves into a fundamental soliton of narrower width for which  $N$  approaches 1 asymptotically.

of the pulse, similar to that seen in Figure 5.6 near  $z/z_0 = 0.5$  for the third-order soliton. The observed spectrum also shows characteristic features seen in Figure 5.9 near  $z/z_0 = 0.5$ . The estimated soliton period for this experiment is 1.26 km. Thus, at the fiber output  $z/z_0 = 0.55$  for the 700-m-long fiber used in the experiment. As the power level of 11.4 W is also nearly nine times the fundamental soliton power, the data of Figure 5.8 indeed correspond to the  $N = 3$  soliton. This conclusion is further corroborated by the autocorrelation trace for  $P_0 = 22.5$  W. The observed five-peak structure corresponds to threefold splitting of the laser pulse, in agreement with the prediction of soliton theory for the fourth-order soliton (see Figure 5.7).

The periodic nature of a high-order soliton implies that the pulse should restore its original shape and spectrum at distances that are multiples of the soliton period. This feature was observed for second- and third-order solitons in a 1983 experiment in which the fiber length of 1.3 km corresponded to nearly one soliton period [86]. In a different experiment, initial narrowing of high-order solitons, seen in Figure 5.6 for  $N = 3$ , was observed for values of  $N$  up to 13 [87]. High-order solitons were also found to form inside the cavity of a mode-locked dye laser operating in the visible region near 620 nm by incorporating an optical element with negative GVD inside the laser cavity [88]. Such a laser emitted asymmetric second-order solitons, under certain operating conditions, as predicted by the inverse scattering theory.

### 5.2.5 Soliton Stability

A natural question is: what happens if the initial pulse shape or the peak power is not matched to that required by Eq. (5.2.22) so that the input pulse does not correspond to an optical soliton? Similarly, one may ask how the soliton is affected if it is perturbed during its propagation inside the fiber. Such questions are answered by using perturbation methods developed for solitons and are discussed later in Section 5.4. In general, one must solve the NLS equation (5.2.2) numerically to study the pulse evolution inside optical fibers (see Appendix B for a sample numerical code).

Consider first the case when the peak power is not exactly matched and the value of  $N$  obtained from Eq. (5.2.3) is not an integer. Figure 5.9 shows the evolution of a “sech” pulse launched with  $N = 1.2$  by solving the NLS equation numerically. Even though pulse width and peak power change initially, the pulse eventually evolves toward a fundamental soliton of narrower width for which  $N = 1$  asymptotically. Perturbation theory has been used to study this behavior analytically [84]. Because details are cumbersome, only results are summarized here. In physical terms, the pulse adjusts its shape and width as it propagates along the fiber and evolves into a soliton. A part of the pulse energy is dispersed away in the process. This part is known as the continuum radiation. It separates from the soliton as  $\xi$  increases and its amplitude decays as  $\xi^{-1/2}$ . For  $\xi \gg 1$ , the pulse evolves asymptotically into a soliton whose order is an integer  $\tilde{N}$  closest to the launched value of  $N$ . Mathematically, if  $N = N + \epsilon$ , where  $|\epsilon| < 1/2$ , the soliton part corresponds to an initial pulse shape of the form

$$u(0, \tau) = (\tilde{N} + 2\epsilon) \operatorname{sech}[(1 + 2\epsilon/\tilde{N})\tau]. \quad (5.2.25)$$

The pulse broadens if  $\epsilon < 0$  and narrows if  $\epsilon > 0$ . No soliton is formed when  $N \leq \frac{1}{2}$ .

The effect of pulse shape on soliton formation can also be investigated solving Eq. (5.2.5) numerically. Figure 4.8 of Chapter 4 shows the evolution of a Gaussian pulse using the initial field  $u(0, \tau) = \exp(-\tau^2/2)$ . Even though  $N = 1$ , pulse shape changes along the fiber because of deviations from the “sech” shape required for a fundamental soliton. The interesting feature of Figure 4.8 is that the pulse adjusts its width and evolves asymptotically into a fundamental soliton. In fact, the evolution appears to be complete by  $z/L_D = 5$ , a distance that corresponds to about three soliton periods. An essentially similar evolution pattern occurs for other pulse shapes such as a super-Gaussian shape. The final width of the soliton and the distance needed to evolve into a fundamental soliton depend on the exact shape but the qualitative behavior remains the same.

As pulses emitted from laser sources are often chirped, we should also consider the effect of initial frequency chirp on soliton formation [89–94]. The chirp can be detrimental simply because it superimposes on the SPM-induced chirp and disturbs the exact balance between the GVD and SPM effects necessary for solitons. Its effect on soliton formation can be studied by solving Eq. (5.2.5) numerically with an input amplitude

$$u(0, \tau) = N \operatorname{sech}(\tau) \exp(-iC\tau^2/2), \quad (5.2.26)$$

where  $C$  is the chirp parameter introduced in Section 3.2. The quadratic form of phase variation corresponds to a linear chirp such that the optical frequency increases with time (up-chirp) for positive values of  $C$ .

Figure 5.10 shows the evolution of a fundamental soliton ( $N = 1$ ) in the case of a relatively low chirp ( $C = 0.5$ ). The pulse compresses initially mainly because of the positive chirp; initial compression occurs even in the absence of nonlinear effects. The pulse then broadens but is eventually compressed a second time with the tail separating from the main peak gradually. The main peak evolves into a soliton over

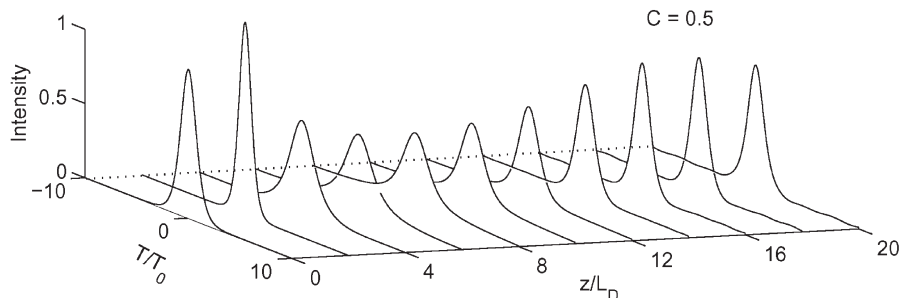


**Figure 5.10 Soliton formation in the presence of an initial linear chirp for the case  $N=1$  and  $C=0.5$ .**

a propagation distance  $\xi > 15$ . A similar behavior occurs for negative values of  $C$ . Formation of a soliton is expected for small values of  $|C|$  because solitons are generally stable under weak perturbations. However, a soliton is destroyed if  $|C|$  exceeds a critical value  $C_{\text{cr}}$ . For  $N = 1$ , a soliton does not form if  $C$  is increased from 0.5 to 2.

The critical value of the chirp parameter can be obtained with the inverse scattering method [91–93]. More specifically, Eqs (5.2.6) and (5.2.7) are solved to obtain the eigenvalue  $\zeta$  using  $u$  from Eq. (5.2.26). Solitons exist as long as the imaginary part of  $\zeta$  is positive. The critical value depends on  $N$  and is found to be about 1.64 for  $N = 1$ . It also depends on the form of the phase factor in Eq. (5.2.26). From a practical standpoint, initial chirp should be minimized as much as possible. This is necessary because, even if the chirp is not detrimental for  $|C| < C_{\text{cr}}$ , a part of the pulse energy is shed as dispersive waves (also called continuum radiation) during the process of soliton formation [91]. For example, only 83% of the input energy is converted into a soliton in the case of  $C = 0.5$  shown in Figure 5.10, and this fraction reduces to 62% for  $C = 0.8$ .

It is clear from the preceding discussion that the exact shape of the input pulse used to launch a fundamental ( $N = 1$ ) soliton is not critical. Moreover, as solitons can form for values of  $N$  in the range  $0.5 < N < 1.5$ , even the width and peak power of the input pulse can vary over a wide range [see Eq. (5.2.3)] without hindering soliton formation. It is this relative insensitivity to the exact values of input parameters that makes the use of solitons feasible in practical applications [95–97]. However, it is important to realize that, when input parameters deviate substantially from their ideal values, a part of the pulse energy is invariably shed away in the form of dispersive waves as the pulse evolves to form a fundamental soliton [98]. Such dispersive waves can interfere with the soliton itself and modify its characteristics [99]. In a practical situation, solitons can be subjected to many types of perturbations as they propagate inside an optical fiber. Examples of perturbations include fiber losses, amplifier noise (if amplifiers are used to compensate fiber losses), third-order dispersion, and intrapulse Raman scattering. Such perturbations are discussed in Sections 5.4 and 5.5.

## 5.3 OTHER TYPES OF SOLITONS

The soliton solution given in Eq. (5.2.8) is not the only possible solution of the NLS equation. Many other kinds of solitons have been discovered depending on the dispersive and nonlinear properties of fibers. This section describes several of them, focusing mainly on dark and bistable solitons.

### 5.3.1 Dark Solitons

Dark solitons correspond to the solutions of Eq. (5.2.2) with  $\text{sgn}(\beta_2) = 1$  and occur in the normal-GVD region of fibers. They were discovered in 1973 and have attracted considerable attention since then [100–118]. The intensity profile associated with such solitons exhibits a dip in a uniform background, hence the name *dark* soliton. Pulse-like solutions obtained in Section 5.2 are called *bright* solitons to make the distinction clear. The NLS equation describing dark solitons is obtained from Eq. (5.2.5) by changing the sign of the second-derivative term and is given by

$$i \frac{\partial u}{\partial \xi} - \frac{1}{2} \frac{\partial^2 u}{\partial \tau^2} + |u|^2 u = 0. \quad (5.3.1)$$

Similar to the case of bright solitons, the inverse scattering method can be used [101] to find dark-soliton solutions of Eq. (5.3.1) by imposing the boundary condition that  $|u(\xi, \tau)|$  tends toward a constant nonzero value for large values of  $|\tau|$ . Dark solitons can also be obtained by assuming a solution of the form  $u(\xi, \tau) = V(\tau) \exp[i\phi(\xi, \tau)]$ , and then solving the ordinary differential equations satisfied by  $V$  and  $\phi$ . The main difference compared with the case of bright solitons is that  $V(\tau)$  becomes a constant (rather than being zero) as  $|\tau| \rightarrow \infty$ . The general solution can be written as [118]

$$u(\xi, \tau) = \eta [B \tanh(\zeta) - i\sqrt{1 - B^2}] \exp(i\eta^2 \xi), \quad (5.3.2)$$

where  $\zeta = \eta B (\tau - \tau_s - \eta B \sqrt{1 - B^2})$ . The parameters  $\eta$  and  $\tau_s$  represent the background amplitude and the dip location, respectively. Similar to the bright-soliton case,  $\tau_s$  can be chosen to be zero without loss of generality. In contrast with the bright-soliton case, the dark soliton has a new parameter  $B$ . Physically,  $B$  governs the depth of the dip ( $|B| \leq 1$ ). For  $|B| = 1$ , the intensity at the dip center falls to zero. For other values of  $B$ , the dip does not go to zero. Dark solitons for which  $|B| < 1$  are called *gray* solitons to emphasize this feature. The  $|B| = 1$  case corresponds to a *black* soliton.

For a given value of  $\eta$ , Eq. (5.3.2) describes a family of dark solitons whose width increases inversely with  $B$ . Figure 5.11 shows the intensity and phase profiles of such dark solitons for three values of  $B$ . Whereas the phase of bright solitons [Eq. (5.2.15)] remains constant across the entire pulse, the phase of dark soliton changes with a total phase shift of  $2 \sin^{-1} B$ , i.e., dark solitons are chirped. For the black soliton ( $|B| = 1$ ), the chirp is such that the phase changes abruptly by  $\pi$  in the center. This phase change becomes more gradual and smaller for smaller values of  $|B|$ . The

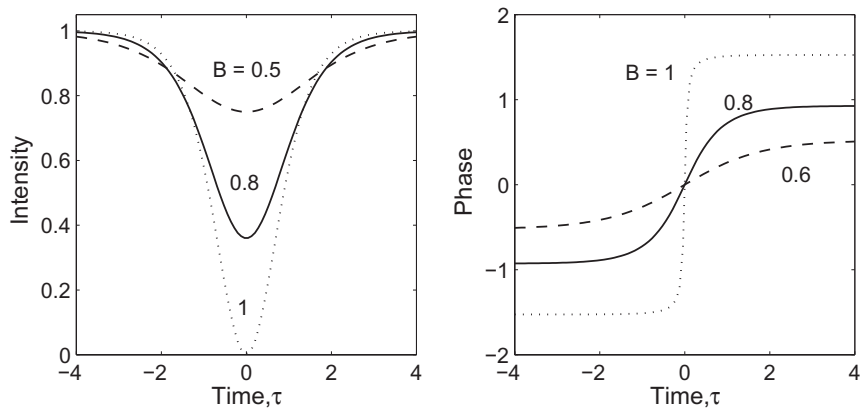


**Figure 5.11** Intensity and phase profiles of dark solitons for several values of the blackness parameter  $B$ .

time-dependent phase or frequency chirp of dark solitons represents a major difference between the bright and dark solitons. One consequence of this difference is that higher-order dark solitons neither form a bound state nor follow a periodic evolution pattern discussed in Section 5.2.3 in the case of bright solitons.

Dark solitons exhibit several interesting features [118]. Consider a black soliton whose canonical form, obtained from Eq. (5.3.2) after choosing  $\eta = 1$  and  $B = 1$ , is given by

$$u(\xi, \tau) = \tanh(\tau) \exp(i\xi), \quad (5.3.3)$$

where the phase jump of  $\pi$  at  $\tau = 0$  is included in the amplitude part. Thus, an input pulse with “tanh” amplitude, exhibiting an intensity “hole” at the center, would propagate unchanged in the normal-dispersion region of optical fibers. One may ask, in analogy with the case of bright solitons, what happens when the input power exceeds the  $N = 1$  limit. This question can be answered by solving Eq. (5.3.1) numerically with an input of the form  $u(0, \tau) = N \tanh(\tau)$ . Figure 5.12 shows the evolution pattern for  $N = 3$ ; it should be compared with Figure 5.6 where the evolution of a third-order bright soliton is shown. Two pairs of gray solitons appear and move away from the central black soliton as the propagation distance increases. At the same time, the width of the black soliton decreases [106]. This behavior can be understood by noting that an input pulse of the form  $N \tanh(N\tau)$  can form a fundamental black soliton of amplitude  $N \tanh(N\tau)$  provided its width decreases by a factor of  $N$ . It sheds part of its energy in the process; that appears in the form of gray solitons. These gray solitons move away from the central black soliton because of their different group velocities. The number of pairs of gray solitons is  $N' - 1$ , where  $N'$  is the next integer closest to  $N$  when  $N$  is not an integer. The important feature is that a fundamental dark soliton always forms for  $N > 1$ .

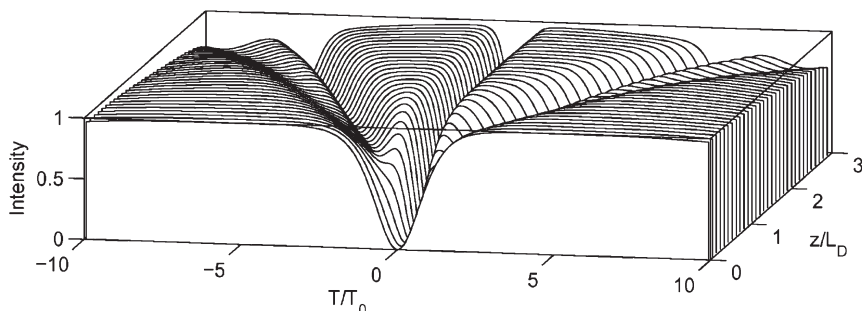


**Figure 5.12 Evolution of a third-order dark soliton showing narrowing of the central dip and the creation of two pairs of gray solitons.**

Experimental realization of dark solitons is possible only with a finite background instead of the infinite background associated with ideal dark solitons. In practice, a pulse with a narrow dip at its center is used to excite a dark soliton. Numerical calculations show that dark solitons with a finite background pulse exhibit propagation properties nearly identical to those with infinite background if the background pulse is wider by a factor of 10 or more compared with the soliton width [105]. Several techniques have been used to generate optical pulses with a narrow dip in the center [102–104]. Such pulses have been used for observing dark solitons in optical fibers. In one experiment [102], 26-ps input pulses (at 595 nm) with a 5-ps-wide central hole were launched along a 52-m fiber. In another experiment [103], the input to a 10-m fiber was a relatively wide 100-ps pulse (at 532 nm) with a 0.3-ps-wide hole that served as a dark pulse. However, as the phase was relatively constant over the hole width, such even-symmetry input pulses did not have the chirp appropriate for a dark soliton. Nonetheless, output pulses exhibited features that were in agreement with the predictions of Eq. (5.3.1).

The odd-symmetry input pulses appropriate for launching a dark soliton were used in a 1988 experiment [104]. A spatial mask, in combination with a grating pair, was used to modify the pulse spectrum such that the input pulse had a phase profile appropriate for forming the dark soliton represented by Eq. (5.3.3). The input pulses obtained from a 620-nm dye laser were  $\approx$ 2-ps wide with a 185-fs hole in their center. The central hole widened at low powers but narrowed down to its original width when the peak power was high enough to sustain a dark soliton of that width. The experimental results agreed with the theoretical predictions of Eq. (5.3.1) quite well. In this experiment, the optical fiber was only 1.2 m long. In a 1993 experiment [110], 5.3-ps dark solitons, formed on a 36-ps wide pulse obtained from a 850-nm Ti:sapphire laser, were propagated over 1 km of fiber. The same technique was later extended to transmit dark-soliton pulse trains at a repetition rate of up to 60 GHz over 2 km of fiber. These results show that dark solitons can be generated and maintained over considerable fiber lengths.

During the 1990s, several practical techniques were introduced for generating dark solitons. In one method, a Mach–Zehnder modulator, driven by nearly rectangular electrical pulses, modulates the CW output of a semiconductor laser [108]. In an extension of this method, electric modulation is performed in one of the two arms of a Mach–Zehnder interferometer. A simple all-optical technique consists of propagating two optical pulses, with a relative time delay between them, in the normal-GVD region of the fiber [109]. The two pulse broaden, become chirped, and acquire a nearly rectangular shape as they propagate inside the fiber. As these chirped pulses merge into each other, they interfere. The result at the fiber output is a train of isolated dark solitons. In another all-optical technique, the nonlinear conversion of a beat signal in a dispersion-decreasing fiber is used to generate a train of dark solitons [111]. The technique is similar to that discussed in Section 5.1 for generating a regular pulse train except that fiber GVD is chosen to be in the normal-dispersion regime everywhere along the fiber length. A 100-GHz train of 1.6-ps dark solitons was generated by using this technique and propagated over 2.2 km (two soliton periods) of a dispersion-shifted fiber. Optical switching using a fiber-loop mirror, in which a phase modulator is placed asymmetrically, can also be used to generate dark solitons [112]. In another variation, a fiber with comblike dispersion profile was used to generate dark soliton pulses with a width of 3.8 ps at the 48-GHz repetition rate [115].

An interesting scheme uses electronic circuitry to generate a coded train of dark solitons directly from the NRZ data in electric form [113]. First, the NRZ data and its clock at the bit rate are passed through an AND gate. The resulting signal is then sent to a flip-flop circuit in which all rising slopes flip the signal. The resulting electrical signal drives a Mach–Zehnder LiNbO<sub>3</sub> modulator and converts the CW output from a semiconductor laser into a coded train of dark solitons. This technique was used for data transmission, and a 10-Gb/s signal was transmitted over 1200 km by using dark solitons [114]. Another relatively simple method uses spectral filtering of a mode-locked pulse train by using a fiber grating [116]. This scheme has also been used to generate a 6.1-GHz train and propagate it over a 7-km-long fiber [117].

Dark solitons remain a subject of continuing interest. Numerical simulations show that they are more stable in the presence of noise and spread more slowly in the presence of fiber loss compared with bright solitons. They are also relatively less affected by many other factors that have an impact on the use of bright solitons (amplifier-induced timing jitter, intrapulse Raman scattering, etc.). These properties point to potential application of dark solitons for optical communication systems [76].

### 5.3.2 Bistable Solitons

The discussion in this chapter is based on a specific form of the nonlinear polarization in Eq. (2.3.6), resulting in a refractive index that increases linearly with the mode intensity  $I$ , i.e.,  $\tilde{n}(I) = n + n_2 I$ . Such intensity dependence is referred to as the Kerr nonlinearity. The nonlinear response of any material begins to saturate at

high intensity levels, and it becomes necessary to modify the form of  $n(I)$ . For silica fibers, saturation of the Kerr nonlinearity occurs at quite high intensity levels. However, if fibers are made with other materials (such as chalcogenide glasses) or if a silica fiber is doped with other nonlinear materials (such as an organic dye), the nonlinear response can saturate at practical intensity levels. In that case, the refractive index changes with intensity as

$$\tilde{n}(I) = n + n_2 f(I), \quad (5.3.4)$$

where  $f(I)$  is some known function of the mode intensity  $I$ .

The NLS equation (5.2.5) can be generalized to accommodate Eq. (5.3.4) and takes the form [119]

$$i\frac{\partial u}{\partial \xi} + \frac{1}{2}\frac{\partial^2 u}{\partial \tau^2} + f(|u|^2)u = 0. \quad (5.3.5)$$

This equation is not generally integrable by the inverse scattering method. However, it can be solved to find shape-preserving solutions by the method outlined in Section 5.2. The approach consists of assuming a solution of the form  $u(\xi, \tau) = V(\tau) \exp(iK\xi)$ , where  $K$  is a constant and  $V$  is independent of  $\xi$ . Using this form in Eq. (5.3.5),  $V(\tau)$  is found to satisfy

$$\frac{d^2V}{d\tau^2} = 2V[K - f(V^2)]. \quad (5.3.6)$$

This equation can be solved by multiplying it by  $2(dV/d\tau)$  and integrating over  $\tau$ . Using the boundary condition  $V = 0$  as  $|\tau| \rightarrow \infty$ , we obtain

$$(dV/d\tau)^2 = 4 \int_0^V [K - f(V^2)]V dV. \quad (5.3.7)$$

The preceding equation can be integrated to yield

$$2\tau = \int_0^V \left( \int_0^{V^2} [K - f(P)]dP \right)^{-1/2} dV. \quad (5.3.8)$$

where  $P = V^2$ . For a given functional form of  $f(P)$ , we can determine the soliton shape  $V(\tau)$  from Eq. (5.3.8) if  $K$  is known. The parameter  $K$  can be related to the soliton energy defined as  $E_s = \int_{-\infty}^{\infty} V^2 d\tau$ . Using Eq. (5.3.7),  $E_s$  depends on the wave number  $K$  as [119]

$$E_s(K) = \frac{1}{2} \int_0^{P_m} [K - F(P)]^{-1/2} dP, \quad F(P) = \frac{1}{P} \int_0^P f(P)dP, \quad (5.3.9)$$

where  $F(0) = 0$  and  $P_m$  is the smallest positive root of  $F(P) = K$ . Depending on the function  $f(P)$ , this relation can have more than one solution, each having the same energy  $E_s$  but different values of  $K$  and  $P_m$ . Typically, only two solutions correspond

to stable solitons. Such solitons are called bistable solitons and have been studied extensively since their discovery in 1985 [119–125]. For a given amount of pulse energy, bistable solitons propagate in two different stable states and can be made to switch from one state to another [120]. An analytic form of the bistable soliton has also been found for a specific form of the saturable nonlinearity [123]. Bistable behavior has not yet been observed in optical fibers as the peak-power requirements are extremely high. Other nonlinear media with easily saturable nonlinearity may be more suitable for this purpose.

### 5.3.3 Dispersion-Managed Solitons

The NLS equation (5.2.5) and its soliton solutions assume that the GVD parameter  $\beta_2$  is constant along the fiber. As discussed in Section 3.5, the technique of dispersion management is often used in the design of modern fiber-optic communication systems. This technique consists of using a periodic dispersion map by combining fibers with different characteristics such that the average GVD in each period is quite low while the local GVD at every point along the fiber link is relatively large. In practice, just two kinds of fibers with opposite signs of  $\beta_2$  are combined to reduce the average dispersion to a small value. Mathematically, Eq. (5.2.5) is replaced with

$$i \frac{\partial u}{\partial \xi} + \frac{d(\xi)}{2} \frac{\partial^2 u}{\partial \tau^2} + |u|^2 u = 0, \quad (5.3.10)$$

where  $d(\xi)$  is a periodic function of  $\xi$  with the period  $\xi_{\text{map}} = L_{\text{map}}/L_D$ . Here  $L_{\text{map}}$  is the length associated with the dispersion map and is typically in the range of 50–100 km.

Equation (5.3.10) does not appear to be integrable with the inverse scattering method. However, it has been found to have pulselike, periodic solutions. These solutions are referred to as *dispersion-managed* solitons [126–129]. It should be stressed that the term soliton is used loosely in this context because the properties of dispersion-managed solitons are quite different from those of the bright solitons discussed in Section 5.2. Not only the amplitude and the width of dispersion-managed solitons oscillate in a periodic manner, but their frequency also varies across the pulse, i.e., such solitons are chirped. Pulse shape is also close to being Gaussian, although it contains considerable oscillatory structure in the pulse wings. Even more surprisingly, such solitons can exist even when average dispersion along the fiber link is normal. Dispersion-managed solitons continue to be of interest because of their potential applications in lightwave systems [130–132].

### 5.3.4 Optical Similaritons

Equation (5.3.10) corresponds to the situation in which the dispersion parameter  $\beta_2$  changes along the fiber length but the nonlinear parameter  $\gamma$  remains constant. In the

most general case, one may allow all fiber parameters in Eq. (2.3.46), to vary with  $z$ , resulting in the so-called *inhomogeneous* NLS equation,

$$i \frac{\partial A}{\partial z} - \frac{\beta_2(z)}{2} \frac{\partial^2 A}{\partial T^2} + \gamma(z) |A|^2 A = \frac{i g(z)}{2} A, \quad (5.3.11)$$

where the loss parameter  $\alpha$  has been replaced with  $-g(z)$  to allow for distributed amplification. The solutions of this equation have attracted considerable attention in recent years [133–139]. Some of these solutions describe pulses that evolve in a self-similar fashion and are known as optical similaritons. The situation is similar to that encountered in Section 4.2.5, in the context of pulse propagation in fiber amplifiers, with the difference that those similaritons form only in an asymptotic limit.

Similariton solutions of Eq. (5.3.11) do not require the asymptotic limit and thus are exact solutions. It turns out that a self-similar transformation reduces Eq. (5.3.11) to the standard homogeneous NLS equation, provided a certain relation exists among  $g(z)$ ,  $\beta(z)$ , and  $\gamma(z)$ . Thus, any soliton solution of the NLS equation can be mapped to a similariton using this transformation. More specifically, the transformation has the form [138]

$$A(z, T) = a(z) U(\xi, \chi) \exp[i\phi(z, T)], \quad (5.3.12)$$

where the similarity variable  $\chi$  depends on both  $z$  and  $T$  as

$$\chi(z, T) = [T - T_c(z)]/T_p(z), \quad (5.3.13)$$

and the quantities  $a(z)$ ,  $T_p(z)$ , and  $T_c(z)$  represent the amplitude, width, and position of the similariton, respectively. Here,  $\xi(z)$  is an effective propagation distance, yet to be determined. The phase in Eq. (5.3.12) is assumed to vary quadratically with time and has the general form

$$\phi(z, T) = C(z) T^2 / (2T_0^2) + b(z) T + d(z). \quad (5.3.14)$$

This phase dependence corresponds to a pulse that is linearly chirped with the  $z$ -dependent chirp parameter  $C(z)$ . The linear term with  $b(z)$  allows for a frequency shift. The input pulse width  $T_0 = T_p(0)$  has been introduced to make the chirp parameter  $C(z)$  dimensionless.

The use of Eqs (5.3.12) and (5.3.14) into Eq. (5.3.11) results in a set of differential equations for the parameters describing the evolution of the pulse. These equations can be solved if the the pulse and fiber parameters satisfy a compatibility condition [133–138]

$$g(z) = C(z) \frac{\beta_2(z)}{T_0^2} + \frac{d}{dz} \ln \left[ \frac{\beta_2(z)}{\gamma(z)} \right], \quad (5.3.15)$$

and  $U(\xi, \chi)$  obeys the standard NLS equation

$$i \frac{\partial U}{\partial \xi} - \text{sgn}(\beta_2) \frac{1}{2} \frac{\partial^2 U}{\partial \chi^2} + |U|^2 U = 0. \quad (5.3.16)$$

As long as the compatibility condition (5.3.15) is satisfied, the effective propagation distance and the amplitude, width, and position of the pulse are given by

$$\zeta(z) = D(z)[1 - C_0D(z)]^{-1}, \quad A(z) = \sqrt{|\beta_2(z)|/[T_p^2(z)\gamma(z)]}, \quad (5.3.17)$$

$$T_p(z) = T_0[1 - C_0D(z)], \quad T_c(z) = T_{c0} - (C_0T_{c0} + b_0)D(z), \quad (5.3.18)$$

where the dimensionless parameter  $D(z) = T_0^{-2} \int_0^z \beta_2(z) dz$  represents the total dispersion accumulated over the distance  $z$ . The parameters related to the phase evolve with  $z$  as

$$C(z) = \frac{C_0}{1 - C_0D(z)}, \quad b(z) = \frac{b_0}{1 - C_0D(z)}, \quad d(z) = \frac{(b_0^2/2)D(z)}{1 - C_0D(z)}, \quad (5.3.19)$$

where  $C_0$  is the input chirp parameter.

Equations (5.3.16)–(5.3.19) show that any soliton of the standards NLS equation can be mapped into to a similariton obeying the inhomogeneous NLS equation with the compatibility condition given in Eq. (5.3.15). It follows from the integrability of the NLS equation [74] that all such similaritons must be stable, even though their width, amplitude, and chirp change continuously as the pulse propagates down the fiber.

As a simple example, consider a fiber with  $z$ -dependent gain but constant values of  $\beta_2$  and  $\gamma$ . This case was first studied in 1996 [140], and it leads to a simple compatibility condition  $g(z) = \beta_2C(z)/T_0^2$ . If the initial chirp  $C_0 = 0$ , the fiber should exhibit no gain or loss to satisfy this condition. Since all pulse parameters then become independent of  $z$ , we recover the standard solitons. On the other hand, if  $C_0 \neq 0$ , the compatibility condition is satisfied if the gain (or loss) of the fiber varies with  $z$  as [140]

$$g(z) = (C_0\beta_2/T_0^2)[1 - C_0D(z)]^{-1}, \quad (5.3.20)$$

where  $D(z) = (\beta_2/T_0^2)z$  varies linearly with  $z$ . The gain is needed when  $C_0\beta_2 > 0$ . Thus, a fiber amplifier whose gain increases along the fiber length, as indicated in Eq. (5.3.20), supports bright similaritons when  $\beta_2 < 0$ , and dark similaritons when  $\beta_2 > 0$ , with the opposite types of chirps. In both cases, the temporal width decreases with  $z$  as indicated in Eq. (5.3.18). It is important to stress that the limit  $C_0D(z) \rightarrow 1$  cannot be attained in practice not only because it requires infinite gain but also because the higher-order effects not included in Eq. (5.3.11) would stop the compression process well before this limit is reached.

The opposite case of  $C_0\beta_2 < 0$  in Eq. (5.3.20) is even more interesting because in this case similaritons form in a lossy fiber ( $g < 0$ ). However, fiber losses must decrease with  $z$ . Figure 5.13 shows the evolution of a bright similariton over 8 dispersion lengths for two values of initial chirp  $C_0$  after choosing  $b_0 = 0$ , and  $T_{c0} = 0$ . As the pulse is propagating as a similariton in the anomalous-dispersion region of a lossy fiber, its width and chirp increase continuously. It is remarkable that stable similaritons can form in a lossy, constant-dispersion fiber. In practice, fiber losses can be made  $z$ -dependent by pumping the fiber suitably so that the gain compensates for a part of the total loss.

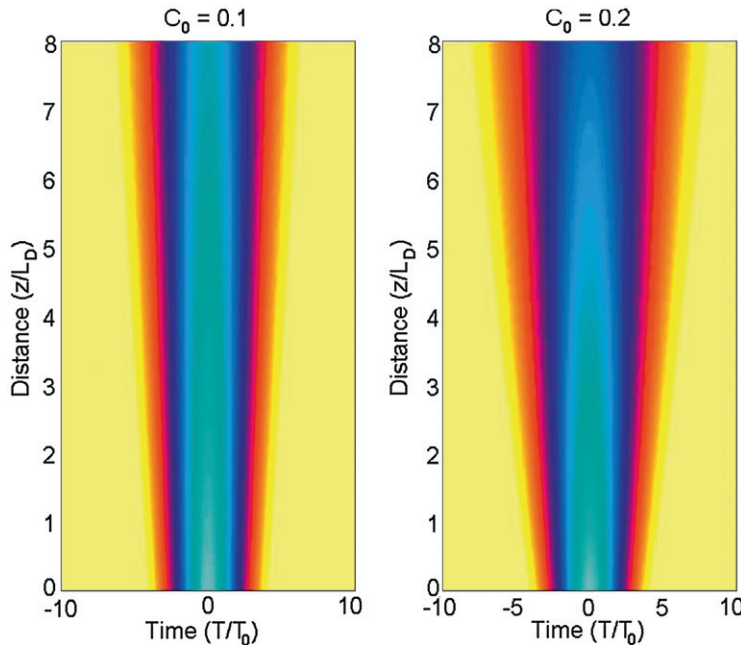


**Figure 5.13** Evolution of a bright similariton over 8 dispersion lengths in the anomalous-dispersion region of a lossy fiber for when the input pulse has an initial chirp with (a)  $C_0=0.1$  and (b)  $C_0=0.2$ .

## 5.4 PERTURBATION OF SOLITONS

As we saw in Section 5.2, an optical soliton can form inside optical fibers provided the input pulse has the right shape and the peak power such that the condition  $N = 1$  is satisfied in Eq. (5.2.3). However, in practice, pulses do not propagate as an ideal soliton because they are perturbed by a variety of effects that are not included in the standard NLS equation (5.2.2). The impact of such perturbations on a soliton is studied using a suitable perturbation technique [141–148]. In this section, we first discuss the technique and then apply it to perturbations resulting from fiber losses, periodic amplification, amplifier noise, and soliton interaction.

### 5.4.1 Perturbation Methods

Consider the perturbed NLS equation written in the form

$$i\frac{\partial u}{\partial \xi} + \frac{1}{2}\frac{\partial^2 u}{\partial \tau^2} + |u|^2 u = ie(u), \quad (5.4.1)$$

where  $\epsilon(u)$  is a small perturbation that can depend on  $u$ ,  $u^*$ , and their derivatives. In the absence of perturbation ( $\epsilon = 0$ ), the soliton solution of the NLS equation is known and is given by Eq. (5.2.13). The question then becomes what happens to the soliton when  $\epsilon \neq 0$ . Several perturbation techniques have been developed for answering this question [149–156]. They all assume that the functional form of the soliton remains intact in the presence of a small perturbation but the four soliton parameters change with  $\xi$  as the soliton propagates down the fiber, i.e., the solution of the perturbed NLS equation can be written as

$$u(\xi, \tau) = \eta(\xi) \operatorname{sech}[\eta(\xi)(\tau - q(\xi))] \exp[i\phi(\xi) - i\delta(\xi)\tau]. \quad (5.4.2)$$

The  $\xi$  dependence of  $\eta$ ,  $\delta$ ,  $q$ , and  $\phi$  is yet to be determined.

The perturbation techniques developed for solitons include the adiabatic perturbation method, the perturbed inverse scattering method, the Lie-transform method, and the variational method [75]. All of them attempt to obtain a set of four ordinary differential equations for the four soliton parameters. As an example, consider the variational method discussed in Section 4.3.2; it was applied to solitons as early as 1979 [157]. In this approach, Eq. (5.4.1) is obtained from the Euler–Lagrange equation using the Lagrangian density [158]

$$\mathcal{L}_d = \frac{i}{2} \left( u^* \frac{du}{d\xi} - u \frac{du^*}{d\xi} \right) + \frac{1}{2} \left( |u|^4 - \left| \frac{du}{d\tau} \right|^2 \right) + i(\epsilon^* u - \epsilon u^*). \quad (5.4.3)$$

This Lagrangian density has the same form as Eq. (4.3.12) except for the last two terms resulting from the perturbation.

As in Section 4.3.2, we integrate the Lagrangian density over  $\tau$  and then use the reduced Euler–Lagrange equation to determine how the four soliton parameters evolve with  $\xi$ . This procedure leads to the following set of four ordinary differential equations [75]:

$$\frac{d\eta}{d\xi} = \operatorname{Re} \int_{-\infty}^{\infty} \epsilon(u) u^*(\tau) d\tau, \quad (5.4.4)$$

$$\frac{d\delta}{d\xi} = -\operatorname{Im} \int_{-\infty}^{\infty} \epsilon(u) \tanh[\eta(\tau - q)] u^*(\tau) d\tau, \quad (5.4.5)$$

$$\frac{dq}{d\xi} = -\delta + \frac{1}{\eta^2} \operatorname{Re} \int_{-\infty}^{\infty} \epsilon(u) (\tau - q) u^*(\tau) d\tau, \quad (5.4.6)$$

$$\begin{aligned} \frac{d\phi}{d\xi} = & \operatorname{Im} \int_{-\infty}^{\infty} \epsilon(u) \{1/\eta - (\tau - q) \tanh[\eta(\tau - q)]\} u^*(\tau) d\tau \\ & + \frac{1}{2} (\eta^2 - \delta^2) + q(d\delta/d\xi), \end{aligned} \quad (5.4.7)$$

where  $\operatorname{Re}$  and  $\operatorname{Im}$  stand for the real and imaginary parts, respectively. This set of four equations can also be obtained by using the adiabatic perturbation theory or the perturbation theory based on the inverse scattering method [149–156].

### 5.4.2 Fiber Losses

Because solitons result from a balance between the nonlinear and dispersive effects, the pulse must maintain its peak power if it has to preserve its soliton character. Fiber losses are detrimental simply because they reduce the peak power of solitons along the fiber length. As a result, the width of a fundamental soliton also increases with propagation because of power loss. Mathematically, fiber losses are accounted for by adding a loss term to Eq. (5.1.1) so that it takes the form of Eq. (2.3.46). In terms of the soliton units used in Section 5.2, the NLS equation becomes

$$i\frac{\partial u}{\partial \xi} + \frac{1}{2}\frac{\partial^2 u}{\partial \tau^2} + |u|^2 u = -\frac{i}{2}\Gamma u, \quad (5.4.8)$$

where

$$\Gamma = \alpha L_D = \alpha T_0^2 / |\beta_2|. \quad (5.4.9)$$

Equation (5.4.8) can be solved by using the variational method if  $\Gamma \ll 1$  so that the loss term can be treated as a weak perturbation. Using  $\epsilon(u) = -\Gamma u/2$  in Eqs (5.4.4)–(5.4.7) and performing the integrations, we find that only soliton amplitude  $\eta$  and phase  $\phi$  are affected by fiber losses, and they vary along the fiber length as [141]

$$\eta(\xi) = \exp(-\Gamma\xi), \quad \phi(\xi) = \phi(0) + [1 - \exp(-2\Gamma\xi)]/(4\Gamma), \quad (5.4.10)$$

where we assumed that  $\eta(0) = 1$ ,  $\delta(0) = 0$ , and  $q(0) = 0$ . Both  $\delta$  and  $q$  remain zero along the fiber.

Recalling that the amplitude and width of a soliton are related inversely, a decrease in soliton amplitude leads to a broadening of the soliton. Indeed, if we write  $\eta(\tau - q)$  in Eq. (5.4.2) as  $T/T_1$  and use  $\tau = T/T_0$ ,  $T_1$  increases along the fiber exponentially as

$$T_1(z) = T_0 \exp(\Gamma\xi) \equiv T_0 \exp(\alpha z). \quad (5.4.11)$$

An exponential increase in the soliton width with  $z$  cannot be expected to continue for arbitrarily large distances. This can be seen from Eq. (3.3.29), which predicts a linear increase in the limit of large  $z$  when the nonlinear effects become negligible. Numerical solutions of Eq. (5.4.8) show that the perturbative solution is accurate only for values of  $z$  such that  $\alpha z \ll 1$  [159]. Figure 5.14 shows the broadening factor  $T_1/T_0$  as a function of  $\xi$  when a fundamental soliton is launched into a fiber with  $\Gamma = 0.07$ . The perturbative result is acceptable for up to  $\Gamma\xi \approx 1$ . In the regime ( $\xi \gg 1$ ), pulse width increases linearly with a rate slower than that of a linear medium [160]. Higher-order solitons show a qualitatively similar asymptotic behavior. However, their pulse width oscillates a few times before increasing monotonically [159]. The origin of such oscillations lies in the periodic evolution of higher-order solitons.

How can a soliton survive inside lossy optical fibers? An interesting scheme restores the balance between GVD and SPM in a lossy fiber by changing dispersive properties of the fiber [161]. Such fibers are called *dispersion-decreasing* fibers (DDFs) because their GVD must decrease in such a way that it compensates for the

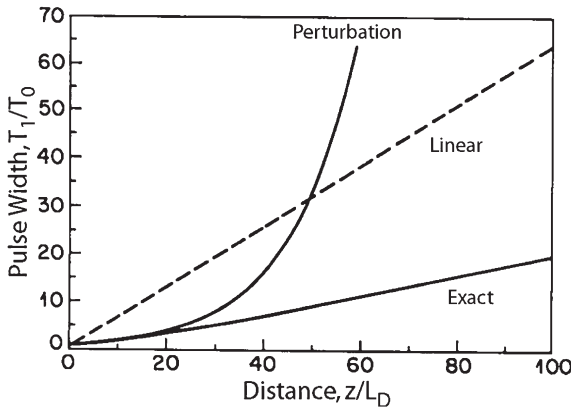


**Figure 5.14** Variation of pulse width with distance in a lossy fiber for the fundamental soliton. The prediction of perturbation theory is also shown. Dashed curve shows the behavior expected in the absence of nonlinear effects. (After Ref. [159]; © 1985 Elsevier.)

reduced SPM experienced by the soliton, as its energy is reduced by fiber loss. To see which GVD profile is needed, we modify Eq. (5.4.8) to allow for GVD variations along the fiber length and eliminate the loss term using  $u = v \exp(-\Gamma\xi/2)$ , resulting in the following equation:

$$i \frac{\partial v}{\partial \xi} + \frac{d(\xi)}{2} \frac{\partial^2 v}{\partial \tau^2} + e^{-\Gamma\xi} |v|^2 v = 0, \quad (5.4.12)$$

where  $d(\xi) = |\beta_2(\xi)/\beta_2(0)|$  is the normalized local GVD. The distance  $\xi$  is normalized to the dispersion length  $L_D = T_0^2/|\beta_2(0)|$ , defined using the GVD value at the input end of the fiber.

If we rescale  $\xi$  using the transformation  $\xi' = \int_0^\xi d(\xi) d\xi$ , Eq. (5.4.12) becomes

$$i \frac{\partial v}{\partial \xi'} + \frac{1}{2} \frac{\partial^2 v}{\partial \tau^2} + \frac{e^{-\Gamma\xi}}{d(\xi)} |v|^2 v = 0, \quad (5.4.13)$$

If the GVD profile is chosen such that  $d(\xi) = \exp(-\Gamma\xi)$ , Eq. (5.4.13) reduces to the standard NLS equation. Thus, fiber losses have no effect on soliton propagation if the GVD of a fiber decreases exponentially along its length as

$$|\beta_2(z)| = |\beta_2(0)| \exp(-\alpha z). \quad (5.4.14)$$

This result can be easily understood from Eq. (5.2.3). If the soliton peak power  $P_0$  decreases exponentially with  $z$ , the requirement  $N = 1$  can still be maintained at every point along the fiber if  $|\beta_2|$  were also to reduce exponentially. Fibers with a nearly exponential GVD profile have been fabricated [162].

A practical technique for making DDFs consists of reducing the core diameter along fiber length in a controlled manner during the fiber-drawing process. Variations

in the core diameter change the waveguide contribution to  $\beta_2$  and reduce its magnitude. Typically, GVD can be changed by a factor of 10 over a length of 20–40 km. The accuracy realized by the use of this technique is estimated to be better than  $0.1 \text{ ps}^2/\text{km}$  [163]. Among other applications, DDFs can produce parabolic-shape pulses when the input pulse propagates in the normal-dispersion region and  $\beta_2$  decreases with  $z$  as  $(1 + az)^{-1}$ , where  $a$  is a constant [164].

### 5.4.3 Soliton Amplification

As already discussed, fiber losses lead to the broadening of solitons. Such loss-induced broadening is unacceptable for many applications, especially when solitons are used for optical communications. To overcome the effect of fiber losses, a soliton needs to be amplified periodically so that its energy is restored to its initial value. Two different approaches have been used for this purpose [141–148], known as lumped and distributed amplification schemes and shown in Figure 5.15 schematically.

In the lumped scheme [142], an optical amplifier boosts the soliton's energy to its input level after it has propagated a certain distance. The soliton then readjusts its parameters to their input values. However, it also sheds a part of its energy as dispersive waves (continuum radiation) during this adjustment phase. The dispersive part is undesirable and can accumulate to significant levels over a large number of amplification stages. This problem can be solved by reducing the spacing  $L_A$  between neighboring amplifiers such that  $L_A \ll L_D$ . The reason is that the dispersion length  $L_D$  sets the scale over which a soliton responds to external perturbations. If the amplifier spacing is much smaller than this length scale, soliton width is hardly affected over one amplifier spacing in spite of energy variations. In practice, the condition  $L_A \ll L_D$  restricts  $L_A$  typically in the range of 20–40 km even when the dispersion length is close to 100 km [142]. Moreover, the lumped-amplification scheme

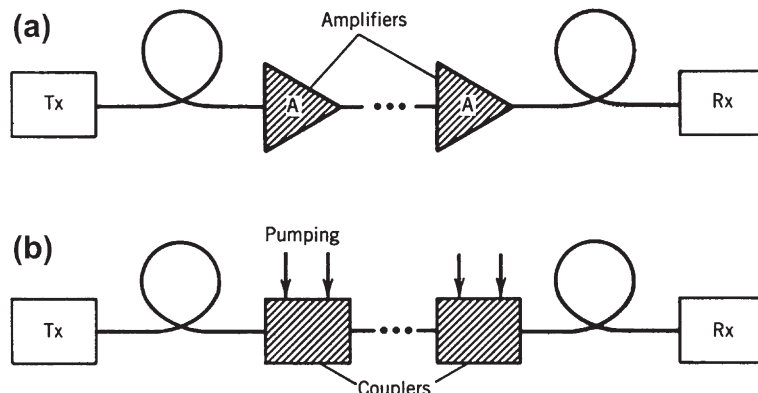


Figure 5.15 (a) Lumped and (b) distributed amplification schemes used for compensating for fiber losses. Tx and Rx stand for transmitters and receivers, respectively.

becomes impractical at high bit rates requiring short solitons ( $T_0 < 0$  ps) because dispersion length can then become quite short.

The distributed-amplification scheme often employs stimulated Raman scattering [143–146] to provide gain (see Chapter 8). In this approach, a pump beam (up-shifted in frequency from the soliton carrier frequency by nearly 13 THz) is injected periodically into the fiber. For solitons propagating in the 1.55- $\mu\text{m}$  wavelength region, one needs a high-power pump laser operating near 1.45  $\mu\text{m}$  and emitting power levels in excess of 100 mW. Since the optical gain is distributed over the entire fiber length, solitons can be amplified adiabatically while maintaining  $N$  close to 1, a feature that reduces the dispersive part almost entirely [145].

Feasibility of the Raman-amplification scheme was first demonstrated in 1985 in an experiment in which soliton pulses of 10-ps width were propagated over a 10-km-long fiber [144]. In the absence of Raman gain, the width of solitons increased by  $\approx 50\%$  because of loss-induced broadening. This is in agreement with Eq. (5.4.11), which predicts  $T_1/T_0 = 1.51$  for  $z = 10$  km and  $\alpha = 0.18$  dB/km, the values relevant for the experiment. The Raman gain was obtained by injecting a CW pump beam at 1.46  $\mu\text{m}$  from a color-center laser in the direction opposite to that of soliton propagation. The pump power was adjusted close to 125 mW such that the total fiber loss of 1.8 dB was exactly balanced by the Raman gain. In a 1988 experiment [146], 55-ps solitons could be circulated up to 96 times inside a 42-km fiber loop without significant increase in their width, resulting in an effective transmission distance of  $>4000$  km. The lumped-amplification scheme was used starting in 1989 [147]. With the advent of erbium-doped fiber amplifiers in around 1990, they were used almost exclusively until 2002, in spite of the lumped nature of amplification provided by them. After 2002, the use of distributed Raman amplification has become more prevalent for long-haul lightwave systems.

The main shortcoming of lumped amplifiers is that soliton energy can vary by as much as a factor of 100 between two neighboring amplifiers. To understand how solitons can survive in spite of such large energy variations, we include the gain provided by lumped amplifiers in Eq. (5.4.8) by replacing  $\Gamma$  with a periodic function  $\tilde{\Gamma}(\xi)$  such that  $\tilde{\Gamma}(\xi) = \Gamma$  everywhere except at the location of amplifiers where it changes abruptly. If we make the transformation

$$u(\xi, \tau) = \exp\left(-\frac{1}{2}\int_0^\xi \tilde{\Gamma}(\xi)d\xi\right)v(\xi, \tau) \equiv a(\xi)v(\xi, \tau), \quad (5.4.15)$$

where  $a(\xi)$  contains rapid variations and  $v(\xi, \tau)$  is a slowly varying function of  $\xi$ , and use it in Eq. (5.4.8),  $v(\xi, \tau)$  is found to satisfy

$$i\frac{\partial v}{\partial \xi} + \frac{1}{2}\frac{\partial^2 v}{\partial \tau^2} + a^2(\xi)|v|^2v = 0. \quad (5.4.16)$$

In this equation,  $a(\xi)$  is a periodic function of  $\xi$  with the period  $\xi_A = L_A/L_D$ , where  $L_A$  is the amplifier spacing. In each period,  $a(\xi) \equiv a_0 \exp(-\Gamma\xi/2)$  decreases exponentially and jumps to its initial value  $a_0$  at the end of the period.

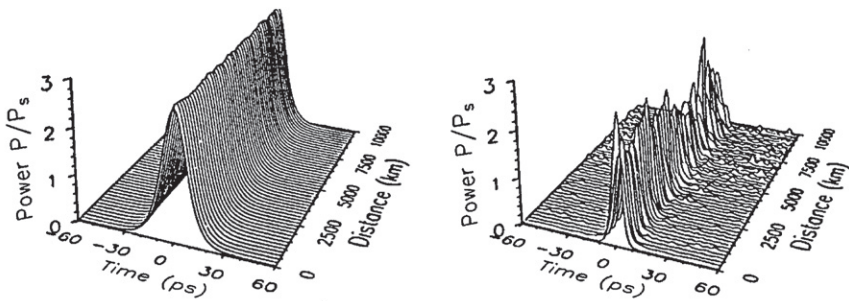


**Figure 5.16** Evolution of loss-managed solitons over 10,000 km for  $L_D = 200$  (left) and  $L_D = 25$  km (right) when  $L_A = 50$  km,  $\alpha = 0.22$  dB/km, and  $\beta_2 = 0.5$  ps $^2$ /km.

The concept of the *guiding-center* or *path-averaged* soliton [165] makes use of the fact that  $a^2(\xi)$  in Eq. (5.4.16) varies rapidly in a periodic fashion. If the period  $\xi_A \ll 1$ , solitons evolve little over a distance short compared with the dispersion length  $L_D$ . Over one period,  $a^2(\xi)$  varies so rapidly that its effects are averaged out, and we can replace  $a^2(\xi)$  by its average value. With this approximation, Eq. (5.4.16) reduces to the standard NLS equation:

$$i\frac{\partial v}{\partial \xi} + \frac{1}{2}\frac{\partial^2 v}{\partial \tau^2} + \langle a^2(\xi) \rangle |v|^2 v = 0. \quad (5.4.17)$$

The practical importance of the averaging concept stems from the fact that Eq. (5.4.17) describes soliton propagation quite accurately when  $\xi_A \ll 1$  [75]. In practice, this approximation works reasonably well for values up to  $\xi_A$  as large as 0.25.

From a practical viewpoint, the input peak power  $P_s$  of the path-averaged soliton should be chosen such that  $\langle a^2(\xi) \rangle = 1$  in Eq. (5.4.17). Introducing the amplifier gain  $G = \exp(\Gamma \xi_A)$ , the peak power is given by

$$P_s = \frac{\Gamma \xi_A P_0}{1 - \exp(-\Gamma \xi_A)} = \frac{G \ln G}{G - 1} P_0, \quad (5.4.18)$$

where  $P_0$  is the peak power in lossless fibers. Thus, soliton evolution in lossy fibers with periodic lumped amplification is identical to that in lossless fibers provided: (1) amplifiers are spaced such that  $L_A \ll L_D$ ; and (2) the launched peak power is larger by a factor  $G \ln G / (G - 1)$ . As an example,  $G = 10$  and  $P_{in} \approx 2.56 P_0$  for 50-km amplifier spacing and a fiber loss of 0.2 dB/km.

Figure 5.16 shows pulse evolution in the average-soliton regime over a distance of 10,000 km, assuming solitons are amplified every 50 km. When the soliton width corresponds to a dispersion length of 200 km, the soliton is well preserved even after 200 lumped amplifiers because the condition  $\xi_A \ll 1$  is reasonably well satisfied. However, if the dispersion length reduces to 25 km, the soliton is destroyed because of relatively large loss-induced perturbations.

The condition  $L_A \ll L_D$  required for the average-soliton regime can be related to the soliton width  $T_0$  by using  $L_D = T_0^2/|\beta_2|$ . The resulting condition is

$$T_0 \gg \sqrt{|\beta_2|L_A}. \quad (5.4.19)$$

The bit rate  $B$  of an optical communication system can be related to  $T_0$  through  $T_B = 1/B = 2q_0 T_0$ , where  $T_B$  is the bit duration and  $q_0$  is the factor by which  $T_B$  is larger than the soliton width. Thus, the condition (5.4.19) can be written in the form of a design criterion:

$$B^2 L_A \ll (4q_0^2 |\beta_2|)^{-1}. \quad (5.4.20)$$

For typical values  $\beta_2 = -0.5 \text{ ps}^2/\text{km}$ ,  $L_A = 50 \text{ km}$ , and  $q_0 = 5$ , we obtain  $T_0 \gg 5 \text{ ps}$  and  $B \ll 20 \text{ GHz}$ . Clearly, the use of amplifiers for soliton amplification imposes a severe limitation on both the bit rate and the amplifier spacing in practice.

Optical amplifiers, needed to restore the soliton energy, also add noise originating from spontaneous emission. The effect of spontaneous emission is to change randomly the four soliton parameters,  $\eta$ ,  $\delta$ ,  $q$ , and  $\phi$  in Eq. (5.4.2), at the output of each amplifier [153]. Amplitude fluctuations, as one might expect, degrade the signal-to-noise ratio. However, for applications of solitons in optical communications, frequency fluctuations are of much more concern. The reason can be understood from Eq. (5.4.2), and noting that a change in the soliton frequency by  $\delta$  affects the speed at which the soliton propagates through the fiber. If  $\delta$  fluctuates because of amplifier noise, soliton's transit time through the fiber also becomes random. Fluctuations in the arrival time of a soliton are referred to as the Gordon–Haus timing jitter [166]. Such a timing jitter limits the performance of long-haul systems, but it can be reduced in practice by using a variety of techniques [95–97].

#### 5.4.4 Soliton Interaction

The time interval  $T_B$  between two neighboring pulses sets the bit rate of a communication system as  $B = 1/T_B$ . It is thus important to determine how close two solitons can come without affecting each other. Interaction between two solitons has been studied both analytically and numerically [167–179]. This section focuses the origin of this interaction and its affect on individual solitons.

It is clear on physical grounds that two solitons would begin to affect each other only when they are close enough that their tails overlap. Mathematically, the total field is  $u = u_1 + u_2$ , where

$$u_j(\xi, \tau) = \eta_j \operatorname{sech}[\eta_j(\tau - q_j)] \exp(i\phi_j - i\delta_j \tau), \quad (5.4.21)$$

with  $j = 1, 2$ . It is  $u$  that satisfies the NLS equation, rather than  $u_1$  and  $u_2$  individually. In fact, by substituting  $u = u_1 + u_2$  in Eq. (5.2.5), we can obtain the following perturbed NLS equation satisfied by the  $u_1$  soliton:

$$i \frac{\partial u_1}{\partial \xi} + \frac{1}{2} \frac{\partial^2 u_1}{\partial \tau^2} + |u_1|^2 u_1 = -2|u_1|^2 u_2 - u_1^2 u_2^*. \quad (5.4.22)$$

The NLS equation for  $u_2$  is obtained by interchanging  $u_1$  and  $u_2$ . The two terms on the right-hand side act as a perturbation and are responsible for nonlinear interaction between two neighboring solitons.

Equations (5.4.4)–(5.4.7) can now be used to study how the four soliton parameters,  $\eta_j$ ,  $q_j$ ,  $\delta_j$ , and  $\phi_j$ , are affected by the perturbation. Introducing new variables as

$$\eta_{\pm} = \eta_1 \pm \eta_2, \quad q_{\pm} = q_1 \pm q_2, \quad (5.4.23)$$

$$\delta_{\pm} = \delta_1 \pm \delta_2, \quad \phi_{\pm} = \phi_1 \pm \phi_2, \quad (5.4.24)$$

we obtain, after some algebra, the following set of equations [155]:

$$\frac{d\eta_+}{d\xi} = 0, \quad \frac{d\eta_-}{d\xi} = \eta_+^3 \exp(-q_-) \sin \phi_-, \quad (5.4.25)$$

$$\frac{d\delta_+}{d\xi} = 0, \quad \frac{d\delta_-}{d\xi} = \eta_+^3 \exp(-q_-) \cos \phi_-, \quad (5.4.26)$$

$$\frac{dq_-}{d\xi} = -\delta_-, \quad \frac{d\phi_-}{d\xi} = \frac{1}{2}\eta_+\eta_-. \quad (5.4.27)$$

Equations for  $q_+$  and  $\phi_+$  are omitted since their dynamics do not affect soliton interaction. Further,  $\eta_+$  and  $\delta_+$  remain constant during interaction. Using  $\eta_+ = 2$  for two interacting fundamental solitons, the remaining four equations can be combined to yield:

$$\frac{d^2q}{d\xi^2} = -4e^{-2q} \cos(2\psi), \quad \frac{d^2\psi}{d\xi^2} = 4e^{-2q} \sin(2\psi), \quad (5.4.28)$$

where we introduced two new variables as  $q = q_-/2$  and  $\psi = \phi_-/2$ . The same equations are obtained with the inverse scattering method [168]. They show that the relative separation  $q$  between two solitons depends only on their relative phase. Two solitons may attract (come closer) or repel (move apart) each other depending on the initial value of  $\psi$ .

Equation (5.4.28) can be solved analytically under quite general conditions [172]. In the case in which two solitons initially have the same amplitudes and frequencies, the solution becomes [75]

$$q(\xi) = q_0 + \frac{1}{2} \ln[\cosh^2(2\xi e^{-q_0} \sin \psi_0) + \cos^2(2\xi e^{-q_0} \cos \psi_0) - 1]. \quad (5.4.29)$$

where  $q_0$  and  $\psi_0$  are the initial values of  $q$  and  $\psi$ , respectively. Figure 5.17 shows how the relative separation  $q(\xi)$  changes along the fiber length for two solitons with different phases. For  $\psi_0$  below a certain value,  $q$  becomes zero periodically. This is referred to as a “collision” resulting from an attractive force between the two solitons. For values of  $\psi_0 > \pi/8$ ,  $q$  increases monotonically with  $\xi$ . This is interpreted in terms of a repulsive force between the two solitons. The specific cases  $\psi_0 = 0$  and  $\pi/2$  correspond, respectively, to two solitons that are initially in phase or out of phase.

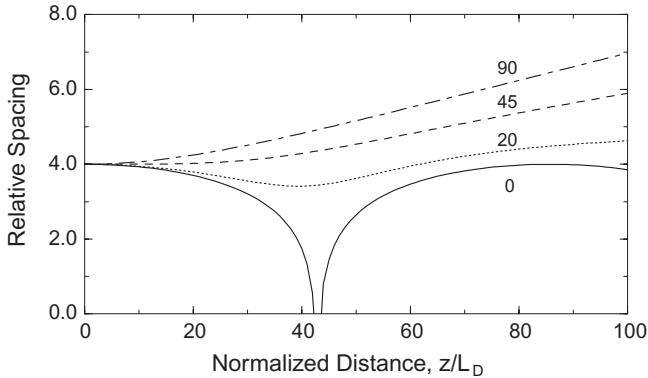


**Figure 5.17** Relative spacing  $q$  between two interacting solitons as a function of fiber length for several values of initial phase difference  $\Psi_0$  (in degrees) when  $q_0=4$ .

In the case of two in-phase solitons ( $\psi_0 = 0$ ), their separation  $q$  changes with propagation periodically as

$$q(\xi) = q_0 + \ln |\cos(2\xi e^{-q_0})|. \quad (5.4.30)$$

Because  $q(\xi) \leq q_0$  for all values of  $\xi$ , two in-phase solitons attract each other. In fact,  $q$  becomes zero after a distance

$$\xi = \frac{1}{2} e^{q_0} \cos^{-1}(e^{-q_0}) \approx \frac{\pi}{4} \exp(q_0), \quad (5.4.31)$$

where the approximate form is valid for  $q_0 > 5$ . At this distance, two solitons collide for the first time. Because of the periodic nature of the  $q(\xi)$  in Eq. (5.4.30) the two solitons separate from each other and collide periodically. The oscillation period is called the collision length. In real units, the collision length is given by

$$L_{\text{col}} = \frac{\pi}{2} L_D \exp(q_0) \equiv z_0 \exp(q_0), \quad (5.4.32)$$

where  $z_0$  is the soliton period given in Eq. (5.2.24). This expression is quite accurate for  $q_0 > 3$ , as also found numerically [169]. A more accurate expression, valid for arbitrary values of  $q_0$ , is obtained using inverse scattering theory and is given by [175]

$$\frac{L_{\text{col}}}{L_D} = \frac{\pi \sinh(2q_0) \cosh(q_0)}{2q_0 + \sinh(2q_0)}. \quad (5.4.33)$$

In the case of two out-of-phase solitons ( $\psi_0 = \pi/2$ ), the relative separation  $q$  changes with propagation as

$$q(\xi) = q_0 + \ln[\cosh(2\xi e^{-q_0})]. \quad (5.4.34)$$

As  $\cosh(x) > 1$  for all values of  $x$ ,  $q$  increases monotonically with  $\xi$ .

Numerical solutions of the NLS equation are quite instructive and allow exploration of different amplitudes and different phases associated with a soliton pair by using the following form at the input end of the fiber:

$$u(0, \tau) = \operatorname{sech}(\tau + q_0) + r \operatorname{sech}[r(\tau - q_0)] e^{i\theta}, \quad (5.4.35)$$

where  $r$  is relative amplitude,  $\theta = 2\psi_0$  is the initial phase difference, and  $2q_0$  is the initial separation between the two solitons. Figure 5.18 shows the evolution of a soliton pair with an initial separation  $q_0 = 3.5$  for several values of parameters  $r$  and  $\theta$ . In the case of equal-amplitude solitons ( $r = 1$ ), the two solitons attract each other in the in-phase case ( $\theta = 0$ ) and collide periodically along the fiber length, just as predicted by perturbation theory. For  $\theta = \pi/4$ , the solitons separate from each other after an initial attraction stage in agreement with the results shown in Figure 5.17. For  $\theta = \pi/2$ , the solitons repel each other even more strongly, and their spacing increases with distance monotonically. The last case shows the effect of slightly different soliton amplitudes by choosing  $r = 1.1$ . Two in-phase solitons oscillate periodically but never collide or move far away from each other.

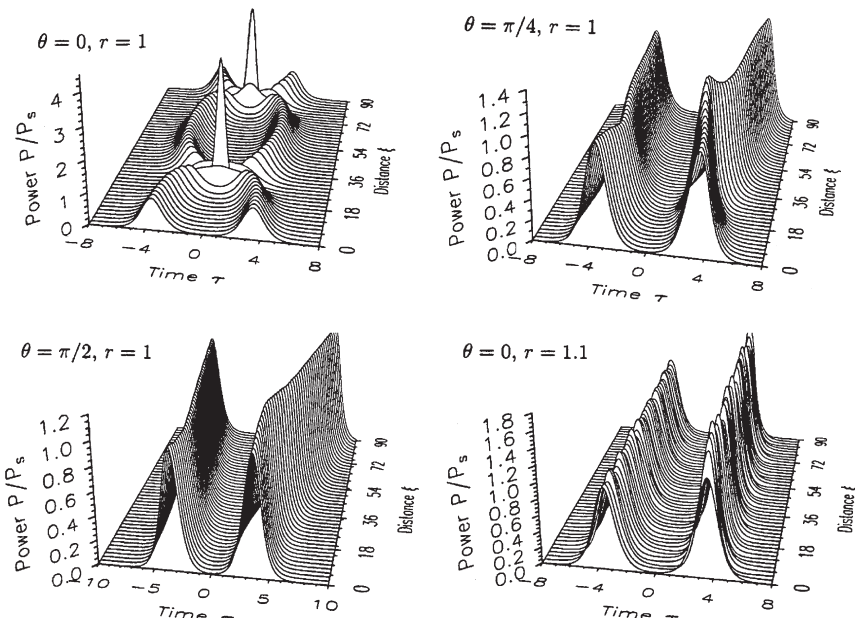


**Figure 5.18** Evolution of a soliton pair over 90 dispersion lengths showing the effects of soliton interaction for four different choices of amplitude ratio  $r$  and relative phase  $\theta$ . Initial separation  $q_0 = 3.5$  in all four cases.

The periodic collapse of neighboring solitons is undesirable from a practical standpoint. One way to avoid the collapse is to increase soliton separation such that  $L_{\text{col}} \gg L_T$ , where  $L_T$  is the transmission distance. Because  $L_{\text{col}} \approx 3000 z_0$  for  $q_0 = 8$ , and  $z_0 \sim 100$  km typically, a value of  $q_0 = 8$  is large enough for any communication system. Several schemes can be used to reduce the soliton separation further without inducing the collapse. The interaction between two solitons is quite sensitive to their relative phase  $\theta$  and the relative amplitude  $r$ . If the two solitons have the same phase ( $\theta = 0$ ) but different amplitudes, the interaction is still periodic but without collapse [175]. Even for  $r = 1.1$ , the separation does not change by more than 10% during each period if  $q_0 > 4$ . Soliton interaction can also be modified by other factors such as higher-order effects [177], bandwidth-limited amplification [178], and timing jitter [179].

## 5.5 HIGHER-ORDER EFFECTS

The properties of optical solitons considered so far are based on the NLS equation (5.1.1). As discussed in Section 2.3, when input pulses are so short that  $T_0 < 5$  ps, it is necessary to include higher-order nonlinear and dispersive effects through the generalized NLS equation (2.3.44). If Eq. (3.1.3) is used to define the normalized amplitude  $U$ , this equation takes the form

$$\frac{\partial U}{\partial z} + \frac{i\beta_2}{2} \frac{\partial^2 U}{\partial T^2} - \frac{\beta_3}{6} \frac{\partial^3 U}{\partial T^3} = i\gamma P_0 e^{-\alpha z} \left( |U|^2 U + \frac{i}{\omega_0} \frac{\partial}{\partial T} (|U|^2 U) - T_R U \frac{\partial |U|^2}{\partial T} \right). \quad (5.5.1)$$

### 5.5.1 Moment Equations for Pulse Parameters

In general, Eq. (5.5.1) equation should be solved numerically. However, if we assume that higher-order effects are weak enough that the pulse maintains its shape, even though its parameters change, we can employ the moment method of Section 4.3.1 to gain some physical insight. In the anomalous-GVD regime, we employ the following form for  $U(z, T)$

$$U(z, T) = a_p \operatorname{sech} \left( \frac{T - q_p}{T_p} \right) \exp \left[ -i\Omega_p(T - q_p) - iC_p \frac{(T - q_p)^2}{2T_p^2} + i\phi_p \right], \quad (5.5.2)$$

where  $a_p$ ,  $T_p$ ,  $C_p$ , and  $\phi_p$  represent the amplitude, width, chirp, and phase of the pulse. We also allow for the temporal shift  $q_p$  of the pulse envelope and the frequency shift  $\Omega_p$  of the pulse spectrum. All six parameters may change with  $z$  as the pulse propagates through the fiber.

Using the definitions of moments in Sections 4.3.1 and 4.4.2 and the moment method, we obtain the following set of equations for the evolution of pulse parameters [180, 181].

$$\frac{dT_p}{dz} = (\beta_2 + \beta_3 \Omega_p) \frac{C_p}{T_p}, \quad (5.5.3)$$

$$\frac{dC_p}{dz} = \left( \frac{4}{\pi^2} + C_p^2 \right) \frac{(\beta_2 + \beta_3 \Omega_p)}{T_p^2} + \frac{4T_0}{\pi^2 T_p} (\bar{\gamma} + \Omega_p/\omega_0) P_0, \quad (5.5.4)$$

$$\frac{dq_p}{dz} = \beta_2 \Omega_p + \frac{\beta_3}{2} \Omega_p^2 + \frac{\beta_3}{6T_p^2} \left( 1 + \frac{\pi^2}{4} C_p^2 \right) + \frac{\bar{\gamma} P_0}{\omega_0} \frac{T_0}{T_p}, \quad (5.5.5)$$

$$\frac{d\Omega_p}{dz} = -\frac{8T_R \bar{\gamma} P_0}{15} \frac{T_0}{T_p^3} + \frac{2\bar{\gamma} P_0}{3\omega_0} \frac{T_0 C_p}{T_p^3}, \quad (5.5.6)$$

where  $\bar{\gamma} = \gamma \exp(-\alpha z)$ . As in Section 4.3.1, we have ignored the phase equation. The amplitude  $a_p$  can be determined from the relation  $E_0 = 2P_0 T_0 = 2a_p^2(z) T_p(z)$ , where  $E_0$  is the input pulse energy.

It is evident from Eqs (5.5.3)–(5.5.6) that the pulse parameters are affected considerably by the three higher-order terms in Eq. (5.5.1). Before considering their impact, we use these equations to determine the conditions under which a fundamental soliton can form. Equation (5.5.3) shows that pulse width will not change if the chirp  $C_p$  remains zero for all  $z$ . The chirp Eq. (5.5.4) is quite complicated. However, if we neglect the higher-order terms and fiber losses ( $\alpha = 0$ ), this equation reduces to

$$\frac{dC_p}{dz} = \left( \frac{4}{\pi^2} + C_p^2 \right) \frac{\beta_2}{T_p^2} + \frac{4\gamma P_0}{\pi^2} \frac{T_0}{T_p}. \quad (5.5.7)$$

It is clear that if  $\beta_2 > 0$ , both terms on the right side are positive, and  $C_p$  cannot remain zero even if  $C_p = 0$  initially. However, in the case of anomalous dispersion ( $\beta_2 < 0$ ), the two terms cancel precisely when pulse parameters initially satisfy the condition  $\gamma P_0 T_0^2 = |\beta_2|$ . It follows from Eq. (5.2.3) that this condition is equivalent to setting  $N = 1$ .

It is useful in the following discussion to normalize Eq. (5.5.1) using dimensionless variables  $\xi$  and  $\tau$  defined in Eq. (5.2.1). The normalized NLS equation takes the form

$$i \frac{\partial u}{\partial \xi} + \frac{1}{2} \frac{\partial^2 u}{\partial \tau^2} + |u|^2 u = i\delta_3 \frac{\partial^3 u}{\partial \tau^3} - is \frac{\partial}{\partial \tau} (|u|^2 u) + \tau_R u \frac{\partial |u|^2}{\partial \tau}, \quad (5.5.8)$$

where the pulse is assumed to propagate in the region of anomalous GVD ( $\beta_2 < 0$ ) and fiber losses are neglected ( $\alpha = 0$ ). The parameters  $\delta_3$ ,  $s$ , and  $\tau_R$  govern, respectively, the effects of third-order dispersion (TOD), self-steepening, and intrapulse Raman scattering. Their explicit expressions are

$$\delta_3 = \frac{\beta_3}{6|\beta_2|T_0}, \quad s = \frac{1}{\omega_0 T_0}, \quad \tau_R = \frac{T_R}{T_0}. \quad (5.5.9)$$

All three parameters vary inversely with pulse width and are negligible for  $T_0 \gg 1$  ps. They become appreciable for femtosecond pulses. As an example,  $\delta_3 \approx 0.03$ ,  $s \approx 0.03$ , and  $\tau_R \approx 0.1$  for a 50-fs pulse ( $T_0 \approx 30$  fs) propagating at 1.55  $\mu\text{m}$  in a standard silica fiber if we take  $T_R = 3$  fs.

### 5.5.2 Third-Order Dispersion

When optical pulses propagate relatively far from the zero-dispersion wavelength of an optical fiber, the TOD effects on solitons are small and can be treated perturbatively. To study such effects as simply as possible, let us set  $s = 0$  and  $\tau_R = 0$  in Eq. (5.5.8) and treat the  $\delta_3$  term as a small perturbation. It follows from Eqs (5.5.3)–(5.5.6) that, since  $\Omega_p = 0$  under such conditions,  $C_p = 0$ , and  $T_p = T_0$ . However, the temporal position of the pulse changes linearly with  $z$  as

$$q_p(z) = (\beta_3/6T_0^2)z \equiv \delta_3(z/L_D). \quad (5.5.10)$$

Thus the main effect of TOD is to shift the soliton peak from its original position. Whether the peak is delayed or advanced depends on the sign of  $\beta_3$ . When  $\beta_3 > 0$ , the TOD slows down the soliton, and the soliton peak is delayed by an amount that increases linearly with distance. This TOD-induced delay is negligible in practice for picosecond pulses. If we use a typical value of  $\beta_3 = 0.1 \text{ ps}^3/\text{km}$ , the temporal shift is only 17 fs for  $T_0 = 10$  ps even after a distance of 100 km. However, the shift becomes relatively large for femtosecond pulses. For example, the peak shifts at a rate of 1.7 ps/km for  $T_0 = 100$  fs.

What happens if an optical pulse propagates at or near the zero-dispersion wavelength of an optical fiber such that  $\beta_2$  is nearly zero. Considerable work has been done to understand propagation behavior in this regime [182–191]. The case  $\beta_2 = 0$  has been discussed in Section 4.2.5 for Gaussian pulses by solving Eq. (4.2.7) numerically. We can use the same equation for a soliton by using  $U(0, \xi') = \text{sech}(\tau)$  as the input at  $z = 0$ . Figure 5.19 shows the temporal and spectral evolution of a “sech” pulse with  $N = 2$  for  $z/L'_D$  in the range of 0–4.

The most striking feature of Figure 5.19 is the splitting of the spectrum into two well-resolved spectral peaks [182]. These peaks correspond to the outermost peaks of the SPM-broadened spectrum (see Figure 4.2). As the red-shifted peak lies in the anomalous-GVD regime, pulse energy in that spectral band can form a soliton. The energy in the other spectral band disperses away simply because that part of the pulse experiences normal GVD. It is the trailing part of the pulse that disperses away with propagation because SPM generates blue-shifted components near the trailing edge. The pulse shapes in Figure 5.19 show a long trailing edge with oscillations that continues to separate away from the leading part with increasing  $\xi'$ . The important point to note is that, because of SPM-induced spectral broadening, the input pulse does not really propagate at the zero-dispersion wavelength even if  $\beta_2 = 0$  initially. In effect, the pulse creates its own  $|\beta_2|$  through SPM. The effective value of  $|\beta_2|$  is given by Eq. (4.2.9) and is larger for pulses with higher peak powers.

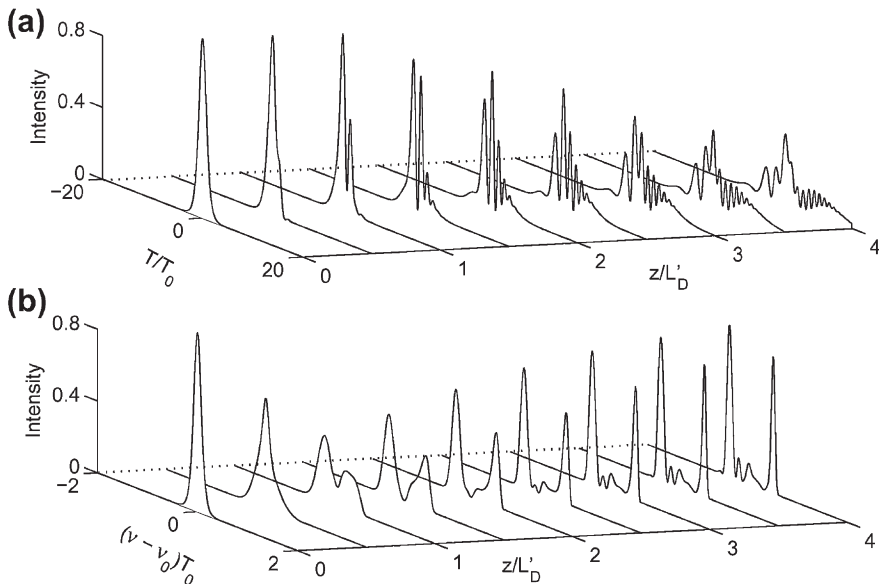


**Figure 5.19 (a)** Temporal and (b) spectral evolutions of a “sech” pulse propagating at the zero-dispersion wavelength with a peak power such that  $\tilde{N} = 2$ .

An interesting question is whether soliton-like solutions exist at the zero-dispersion wavelength of an optical fiber. Equation (5.5.8) does not appear to be integrable by the inverse scattering method even when  $s = \tau_R = 0$ . Numerical solutions show [184] that for  $\tilde{N} > 1$ , a “sech” pulse evolves over a length  $\xi' \sim 10/\tilde{N}^2$  into a soliton that contains about half of the pulse energy. The remaining energy is carried by an oscillatory structure near the trailing edge that disperses away with propagation. These features of solitons have also been quantified by solving Eq. (5.5.8) approximately [184–188]. In general, solitons at the zero-dispersion wavelength require less power than those occurring in the anomalous-GVD regime. This can be seen by comparing Eqs (5.2.3) and (4.2.8). To achieve the same values of  $N$  and  $\tilde{N}$ , the required power is smaller by a factor of  $T_0|\beta_2/\beta_3|$  for pulses propagating at the zero-dispersion wavelength.

With the advent of WDM technique, special fibers have been developed in which  $\beta_3$  is nearly zero over a certain wavelength range, while  $|\beta_2|$  remains finite. Such fibers are called dispersion-flattened fibers. Their use requires consideration of the effects of fourth-order dispersion on solitons. The NLS equation in this case takes the form

$$i \frac{\partial u}{\partial \xi} + \frac{1}{2} \frac{\partial^2 u}{\partial \tau^2} + |u|^2 u = -\delta_4 \frac{\partial^4 u}{\partial \tau^4}, \quad (5.5.11)$$

where  $\delta_4 = \beta_4/(24|\beta_2|T_0^2)$ .

The parameter  $\delta_4$  is relatively small for  $T_0 > 1$  ps, and its effect can be treated perturbatively. However,  $\delta_4$  may become large enough for ultrashort pulses that a perturbative solution is not appropriate. A shape-preserving, solitary-wave solution of Eq. (5.5.11) can be found by assuming  $u(\xi, \tau) = V(\tau) \exp(iK\xi)$  and solving the resulting ordinary differential equation for  $V(\tau)$ . This solution is given by [192]

$$u(\xi, \tau) = 3b^2 \operatorname{sech}^2(b\tau) \exp(8ib^2\xi/5), \quad (5.5.12)$$

where  $b = (40\delta_4)^{-1/2}$ . Note the  $\operatorname{sech}^2$ -type form of the pulse amplitude rather than the usual “ $\operatorname{sech}$ ” form required for standard bright solitons. It should be stressed that both the amplitude and the width of the soliton are determined uniquely by the fiber parameters. Such fixed-parameter solitons are sometimes called *autosolitons*.

The effect of TOD on the second and higher-order solitons is remarkable in the sense that it leads to breakup of such solitons into multiple fundamental solitons of different widths, a phenomenon referred to as *soliton fission* [184]. It is discussed in Section 12.1 in detail. Soliton fission can also be initiated by higher-order nonlinear effects as will become clear later.

### 5.5.3 Self-Steepening

The phenomenon of self-steepening has already been discussed in Section 4.4.1. It introduces several new features for solitons forming in the anomalous-dispersion regime [193–197]. The effects of self-steepening appear in Eqs (5.5.3)–(5.5.6) through the terms containing  $\omega_0$ . The most important feature is that self-steepening can produce spectral and temporal shifts of the soliton even when  $T_R = 0$ . In fact, we can integrate Eq. (5.5.6) to obtain the spectral shift in the form

$$\Omega_p(z) = \frac{\gamma E_0}{3\omega_0} \int_0^z \frac{C_p(z)}{T_p^3(z)} e^{-\alpha z} dz, \quad (5.5.13)$$

where  $E_0 = 2P_0 T_0$  is the input pulse energy. As soon as the pulse becomes chirped, its spectrum shifts because of self-steepening. If the chirp is negligible, spectral shift is relatively small. Even when  $\Omega_p = 0$ , self-steepening produces a temporal shift because of the last term in Eq. (5.5.5). If we assume that soliton maintains its width to the first order, the temporal shift of the soliton peak for a fiber of length  $L$  given by

$$q_p(L) = \gamma P_0 L_{\text{eff}} / \omega_0 = \phi_{\max} / \omega_0, \quad (5.5.14)$$

where  $L_{\text{eff}}$  is the effective length and  $\phi_{\max}$  is the maximum SPM-induced phase shift introduced in Section 4.1.1. Noting that  $\omega_0 = 2\pi/T_{\text{opt}}$ , where  $T_{\text{opt}}$  is the optical period, the shift is relatively small even when  $\phi_{\max}$  exceeds  $10\pi$ . However, when  $\Omega_p \neq 0$ , the temporal shift is enhanced considerably.

The preceding analysis is valid for relatively small values of the parameter  $s$ . When pulses are so short that  $s$  exceeds 0.1, one must use a numerical approach. To

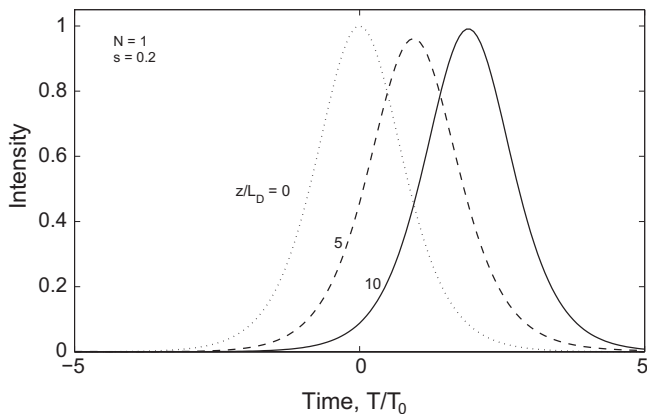


**Figure 5.20** Pulse shapes at  $z/L_D = 5$  and  $10$  for a fundamental soliton in the presence of self-steepening ( $s=0.2$ ). The dotted curve shows the initial pulse shape at  $z=0$  for comparison. The solid and dashed curves coincide with the dotted curve when  $s=0$ .

isolate the effects of self-steepening governed by the parameter  $s$ , it is useful to set  $\delta_3 = 0$  and  $\tau_R = 0$  in Eq. (5.5.8). Pulse evolution inside fibers is then governed by

$$i \frac{\partial u}{\partial \xi} + \frac{1}{2} \frac{\partial^2 u}{\partial \tau^2} + |u|^2 u + is \frac{\partial}{\partial \tau} (|u|^2 u) = 0. \quad (5.5.15)$$

The self-steepening-induced temporal shift is shown in Figure 5.20 where pulse shapes at  $\xi = 0, 5$ , and  $10$  are plotted for  $s = 0.2$  and  $N = 1$  by solving Eq. (5.5.15) numerically with the input  $u(0, \tau) = \text{sech}(\tau)$ . As the peak moves slower than the wings for  $s \neq 0$ , it is delayed and appears shifted toward the trailing side. Although the pulse broadens slightly with propagation (by about 20% at  $\xi = 10$ ), it nonetheless maintains its soliton nature. This feature suggests that Eq. (5.5.15) has a soliton solution toward which the input pulse is evolving asymptotically. Such a solution indeed exists and has the form [158]

$$u(\xi, \tau) = V(\tau + M\xi) \exp[i(K\xi - M\tau)], \quad (5.5.16)$$

where  $M$  is related to the shift  $\Omega_p$  of the carrier frequency. The group velocity changes as a result of this shift. The delay of the peak seen in Figure 5.20 is due to this change in the group velocity. The explicit form of  $V(\tau)$  depends on  $M$  and  $s$  [197]. In the limit  $s = 0$ , it reduces to the hyperbolic secant form given in Eq. (5.2.16). Note also that Eq. (5.5.15) can be transformed into a so-called derivative NLS equation that is integrable by the inverse scattering method and whose solutions have been studied extensively in plasma physics [198–201].

Self-steepening also leads to breakup of higher-order solitons through the phenomenon of soliton fission if the parameter  $s$  is relatively large [194]. Figure 5.21 shows this behavior for a second-order soliton ( $N = 2$ ) by displaying the temporal

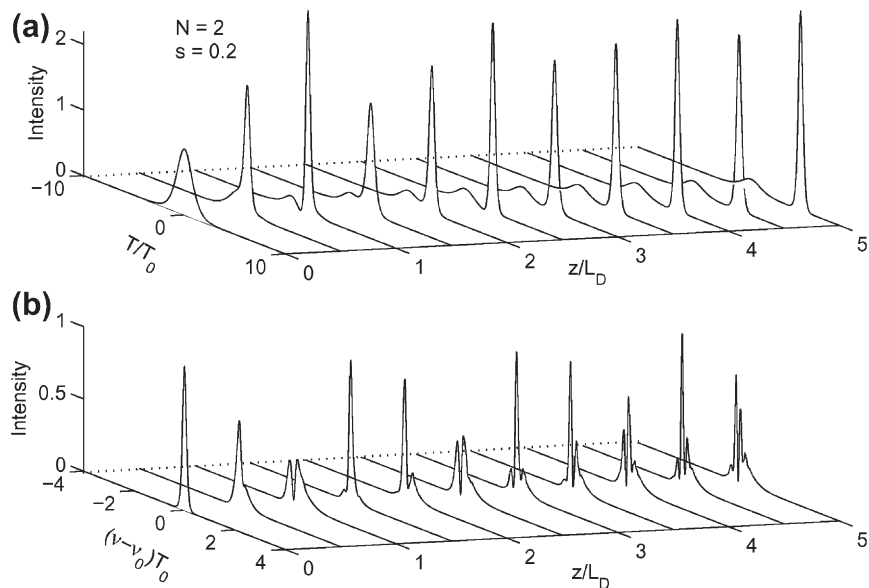


**Figure 5.21** (a) Temporal and (b) spectral evolutions of a second-order soliton ( $N=2$ ) over five dispersion lengths for  $s=0.2$ .

and spectral evolutions for  $s = 0.2$ . For this value of  $s$ , the two solitons separate from each other within a distance of  $2L_D$  and continue to move apart with further propagation inside the fiber. The soliton fission can be understood from the inverse scattering method, with the self-steepening term acting as a perturbation. In the absence of self-steepening ( $s = 0$ ), the two solitons form a bound state because both of them propagate at the same speed (the eigenvalues  $\zeta_j$  in Section 5.2.1 have the same real part). The effect of self-steepening is to break the degeneracy so that the two solitons propagate at different speeds. As a result, they separate from each other, and the separation increases almost linearly with the distance [195]. The ratio of the peak heights in Figure 5.21 is about 9 and is in agreement with the expected ratio  $(\eta_2/\eta_1)^2$ , where  $\eta_1$  and  $\eta_2$  are the imaginary parts of the eigenvalues introduced in Section 5.2.1. The third- and higher-order solitons follow a similar fission pattern. In particular, the third-order soliton ( $N = 3$ ) decays into three solitons whose peak heights are again in agreement with inverse scattering theory.

#### 5.5.4 Intrapulse Raman Scattering

Intrapulse Raman scattering plays the most important role among the higher-order nonlinear effects. Its effects on solitons are governed by the last term in Eq. (5.5.8) and were observed experimentally as early as 1985 [202]. The need to include this term became apparent when a new phenomenon, called the *soliton self-frequency*

*shift*, was observed in 1986 [203] and explained using the delayed nature of the Raman response [204]. Since then, this higher-order nonlinear effect has been studied extensively [205–223].

Let us focus first on a fundamental soliton and consider the prediction of the moment method. We isolate the effects of intrapulse Raman scattering by using  $\beta_3 = 0$  and  $\omega_0 \rightarrow \infty$  in Eqs (5.5.3)–(5.5.6). The main effect of the Raman term is to shift the soliton frequency  $\Omega_p$  that changes along the fiber length through Eq. (5.5.6). Integrating this equation, we obtain [180]

$$\Omega_p(z) = -\frac{8T_R}{15}\gamma P_0 T_0 \int_0^z \frac{e^{-\alpha z}}{T_p^3(z)} dz. \quad (5.5.17)$$

The evolution of the pulse width  $T_p(z)$  along the fiber is governed by Eq. (5.5.3).

If fiber length is short enough that losses are negligible, and  $\Omega_p$  remains small enough that the  $\Omega_p$  terms in Eq. (5.5.4) remain negligible, the soliton can maintain ( $C_p \approx 0$ ) with its width fixed at its input value  $T_0$ . Only under such restrictive conditions, we can replace the integral in Eq. (5.5.17) with  $z/T_0^3$  (assuming negligible losses) and find that the Raman-induced frequency shift (RIFS) grows linearly with distance as

$$\Omega_p(z) = -\frac{8T_R\gamma P_0}{15T_0^2}z \equiv -\frac{8T_R|\beta_2|}{15T_0^4}z, \quad (5.5.18)$$

where we used the condition  $N = \gamma P_0 T_0^2 / |\beta_2| = 1$ . The negative sign shows that the carrier frequency is reduced, i.e., the soliton spectrum shifts toward longer wavelengths (the “red” side). The scaling of  $\Omega_p$  with pulse width as  $T_0^{-4}$  was first found in 1986 using soliton perturbation theory [204]. It shows why the RIFS becomes important for only ultrashort pulses with widths  $\sim 1$  ps or less. However, one should keep in mind that such a dependence holds only over relatively short fiber lengths over which the soliton remains unchirped.

Physically, the red shift of fundamental solitons can be understood in terms of stimulated Raman scattering (see Chapter 8). For pulse widths  $\sim 1$  ps or shorter, the spectral width of the pulse is large enough that the Raman gain can amplify the low-frequency (red) spectral components of the pulse, with high-frequency (blue) components of the same pulse acting as a pump. The process continues along the fiber, and the energy from blue components is continuously transferred to red components. Such an energy transfer appears as a red shift of the soliton spectrum, with shift increasing with distance. As seen from Eq. (5.5.18), the frequency shift increases linearly along the fiber. However, as it scales with the pulse width as  $T_0^{-4}$ , it can become quite large for short pulses. As an example, soliton frequency shifts at a rate of 51 GHz/m for  $T_0 = 0.1$  ps (FWHM of about 175 fs) if we use  $\beta_2 = -20$  ps<sup>2</sup>/km and  $T_R = 3$  fs in Eq. (5.5.18). The spectrum of such pulses will shift by 5.1 THz after only 100 m of propagation. This is a large shift if we note that the initial spectral width (FWHM) of such a soliton is <2 THz. In general, the RIFS cannot be neglected for pulses shorter than 1 ps.

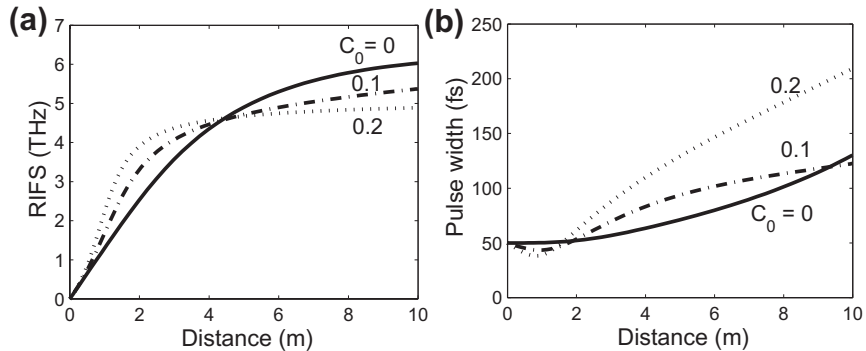


**Figure 5.22** Evolution of (a) Raman-induced frequency shift and (b) pulse width when a fundamental soliton with  $T_0 = 50$  fs propagates inside a 10-m-long fiber. The input chirp parameter  $C_0$  is varied in the range of 0–0.2.

To see how  $\Omega_p$  evolves in the general case, one must use Eq. (5.5.17). As a numerical example, consider the propagation of solitons with an initial width  $T_0 = 50$  fs (FWHM about 88 fs) in a 10-m-long, dispersion-shifted fiber with  $D = 4$  ps/(km nm). Figure 5.22 shows the evolution of RIFS  $\Omega_p$  and pulse width  $T_p$  along the fiber length for  $\gamma = 2$  W $^{-1}$ /km [180]. The effects of TOD were included using  $\beta_3 = 0.1$  ps $^3$ /km because they cannot be ignored for such short pulses. Fiber losses were included using  $\alpha = 0.2$  dB/km, but their impact is small for a 10-m-long fiber. The solid curve in Figure 5.22 shows the case  $C_0 = 0$  that corresponds to standard solitons. The pulse width is indeed maintained in the beginning, as expected, but begins to increase after 2 m because of the RIFS and TOD effects.

The most important feature seen in Figure 5.22 is that the RIFS grows linearly with  $z$  at the early stages of pulse evolution and then becomes saturated. The physical reason behind this saturation is related to the chirping of solitons. For an unchirped soliton ( $C_0 = 0$ ), the magnitude of RIFS becomes comparable to the spectral width of the pulse (about 2 THz) at a distance of about 2 m, and it begins to affect the soliton by chirping it, as evident from Eq. (5.5.4). The use of Eq. (5.5.18) becomes inappropriate under such conditions. The dashed and dash-dotted lines show that even a relatively small chirp affects the RIFS considerably. For positive values of  $C_p$ , the pulse is initially compressed, as expected for  $\beta_2 C_p < 0$ , and then broadens after attaining its minimum width at a distance of about 1 m. For this reason,  $\Omega_p$  initially increases faster than the unchirped case, but also saturates at a lower value because of pulse broadening. The main point to note is that the chirp can increase the RIFS when  $C_p > 0$ . For  $C_p < 0$ , pulse begins to broaden immediately, and RIFS is reduced considerably.

The RIFS of solitons was observed in 1986 using 0.5-ps pulses obtained from a color-center laser [203]. The pulse spectrum was found to shift as much as 8 THz for a fiber length under 0.4 km. The observed spectral shift was called the soliton

self-frequency shift because it was induced by the soliton itself [204]. However, as discussed in Section 4.4.3, RIFS is a general phenomenon and occurs for all short pulses, irrespective of whether they propagate as a soliton or not [180]. The shift is relatively large if a pulse maintains its width along the fiber. In recent years, RIFS has attracted considerable attention for producing femtosecond pulses whose wavelength can be tuned over a wide range by simply propagating them through tapered or other microstructured fibers [224–227]. This scheme is discussed in more detail in Section 12.2.

In the case of higher-order solitons, one must solve the generalized NLS equation (5.5.8) numerically. To focus on the effects of intrapulse Raman scattering, we set  $\delta_3 = 0$  and  $s = 0$  in this equation. Pulse evolution inside fibers is then governed by

$$i \frac{\partial u}{\partial \xi} + \frac{1}{2} \frac{\partial^2 u}{\partial \tau^2} + |u|^2 u = \tau_R u \frac{\partial |u|^2}{\partial \tau}. \quad (5.5.19)$$

Figure 5.23 shows the spectral and temporal evolution of a second-order soliton ( $N = 2$ ) by solving Eq. (5.5.19) numerically with  $\tau_R = 0.01$ . The effect of intrapulse Raman scattering on higher-order solitons is similar to the case of self-steepening. In particular, even relatively small values of  $\tau_R$  lead to the fission of higher-order solitons into its constituents [211].

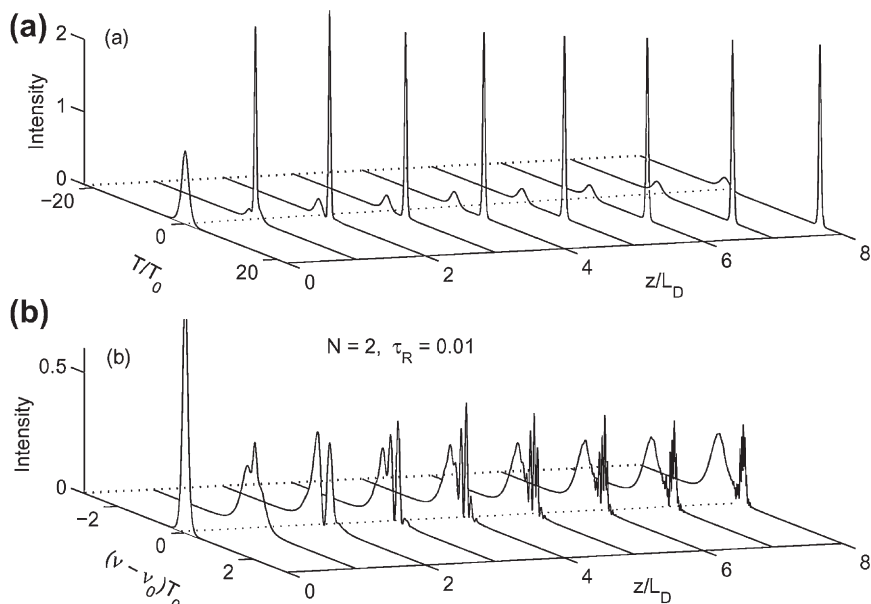


Figure 5.23 (a) Temporal and (b) spectral evolutions of a second-order ( $N=2$ ) soliton when  $\tau_R=0.01$ , depicting soliton's fission induced by intrapulse Raman scattering.

A comparison of Figures 5.21 and 5.23 shows the similarity and the differences for two different higher-order nonlinear mechanisms. An important difference is that relatively smaller values of  $\tau_R$  compared with  $s$  can induce soliton fission over a given distance. For example, if  $s = 0.01$  is chosen in Figure 5.21, the soliton does not split over the distance of  $5L_D$ . This feature indicates that the effects of  $\tau_R$  are likely to dominate in practice over those of self-steepening. Another difference is that both solitons are delayed in the case of self-steepening, while in the Raman case the low-intensity soliton appears not to have shifted in both the spectral and temporal domains. This feature is related to the  $T_0^{-4}$  dependence of the RIFS on the soliton width in Eq. (5.5.18). The second soliton is much wider than the first one, and thus its spectrum shifts at a much smaller rate.

A question one may ask is whether Eq. (5.5.19) has soliton solutions. A bright soliton does not form when the Raman term is included because the resulting perturbation is of non-Hamiltonian type [154]. This feature of the Raman term can be understood by noting that the Raman-induced spectral red shift does not preserve pulse energy because a part of the energy is dissipated through the excitation of molecular vibrations. However, a kink-type topological soliton (with infinite energy) has been found and is given by [220]

$$u(\xi, \tau) = [e^{-b\tau} \operatorname{sech}(b\tau)]^{1/2} \exp(ib^2\xi/2) \quad (5.5.20)$$

where  $b = 3/(2\tau_R)$ . Figure 5.24 shows the intensity profiles by plotting  $|u(\xi, \tau)|^2$  for several values of  $\tau_R$ . Steepness of the shock depends on  $\tau_R$  such that the shock front becomes increasingly steeper as  $\tau_R$  is reduced. It is difficult to observe such optical shocks experimentally because of large power requirements.

An approximate soliton-like solution of Eq. (5.5.19) was found in 1990 using a group-theory approach [228]. It exhibits both the RIFS in the spectrum and the

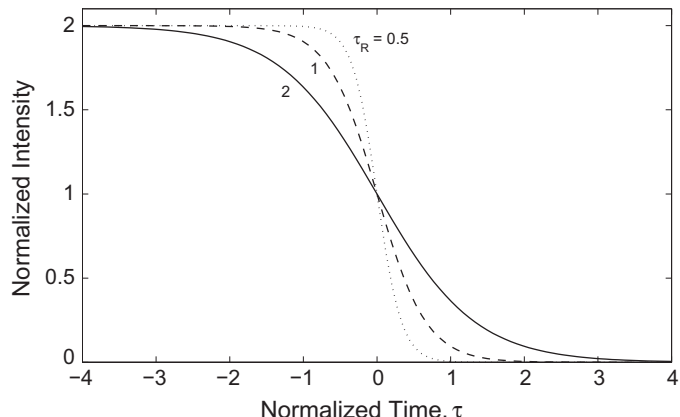


**Figure 5.24** Temporal intensity profiles of kink solitons in the form of an optical shock for several values of  $\tau_R$ . (After Ref. [220]; © 1992 American Physical Society.)

corresponding temporal delay seen in [Figure 5.23](#) for the fundamental soliton formed after the fission of a second-order soliton. This solution has the form

$$u(\xi, \tau) \approx [1 + \epsilon(\tau')] \operatorname{sech}(\tau') \exp[i\xi(\frac{1}{2} + b\tau - b^2\xi^2/3)]. \quad (5.5.21)$$

where the parameter  $b$  depends on the Raman parameter as  $b = 8\tau_R/15$  and  $\epsilon$  represents a small correction to the amplitude. The new temporal variable is in a reference frame moving with the soliton and is defined as  $\tau' = \tau - b\xi^2/2$ . In terms of the original variables,  $z$  and  $T$ , this solution can be written as (neglecting the small  $\epsilon$  term)

$$u(z, T) \approx \operatorname{sech}\left(\frac{T - T_d(z)}{T_0}\right) \exp[i\phi(z) - i\Delta\Omega_p(z)T], \quad (5.5.22)$$

where  $\Delta\Omega_p(z)$  is the RIFS given in Eq. [\(5.5.18\)](#) and  $T_d(z)$  is the delay experienced by the soliton:

$$T_d(z) = \frac{b}{2}\xi^2 T_0 = \frac{4T_R}{15} \left(\frac{z}{L_D}\right)^2. \quad (5.5.23)$$

In the case of a second- or higher-order soliton, this solution applies to each fundamental soliton created after the soliton fission, and  $T_0$  is the width of this soliton (and not the input pulse width).

### 5.5.5 Propagation of Femtosecond Pulses

For femtosecond pulses ( $T_0 < 1$  ps), it becomes necessary to include all the higher-order terms in Eq. [\(5.5.8\)](#) because all three parameters  $\delta_3$ ,  $s$ , and  $\tau_R$  become non-negligible. Evolution of such ultrashort pulses in optical fibers can be studied by solving Eq. [\(5.5.8\)](#) numerically [\[229\]](#). As an example, [Figure 5.25](#) shows the evolutions of pulse shape and spectrum (parts a and b) when a fourth-order soliton is launched at the input end of a fiber, after choosing  $\delta_3 = 0.03$ ,  $s = 0.03$ , and  $\tau_R = 0.1$ . These values are appropriate for a 50-fs pulse ( $T_0 \approx 28$  fs) propagating in the  $1.55\text{-}\mu\text{m}$  region of a standard silica fiber ( $L_D \approx 4$  cm). Soliton fission occurs within  $0.4L_D$ , and the shortest fundamental soliton shifts toward the trailing side at a rapid rate with increasing distance as it slows down. This deacceleration is due to a decrease in the group velocity occurring because of a red shift of soliton's spectrum. In physical units, the 50-fs pulse has shifted by almost 40 THz, or 20% of its carrier frequency after propagating a distance of only 8 cm. We also see evidence of dispersive waves at a blue-shifted frequency (vertical line in part b) that spread rapidly in the time domain.

Equation [\(5.5.8\)](#) should be used with care because of its approximate nature [\[230\]](#). As discussed in Section 2.3, an accurate approach employs Eq. [\(2.3.36\)](#), where  $R(t)$  takes into account the time-dependent response of the fiber nonlinearity. The form of  $R(t)$  given in Eq. [\(2.3.38\)](#) includes both the electronic and molecular (the Raman

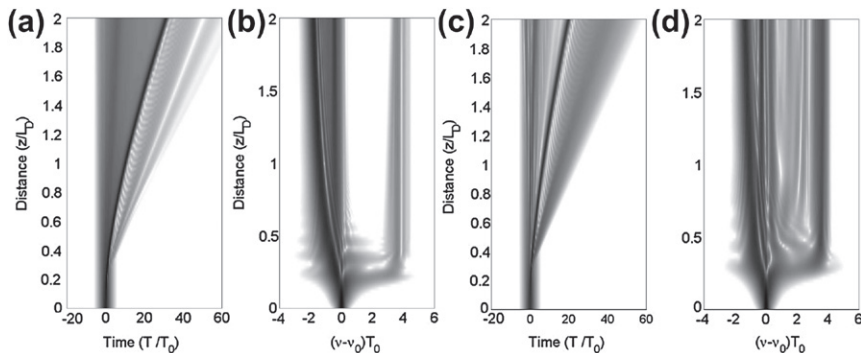


**Figure 5.25** Temporal and spectral evolution over a distance of  $2L_D$  when a 50-fs input pulse propagates as a fourth-order soliton ( $N=4$ ) inside a standard fiber. These numerical results were obtained using the approximate (a and b) and more accurate (c and d) generalized NLS equations.

effect) contributions [212–215]. Eq. (2.3.36) was used as early as 1992 to study how intrapulse Raman scattering affects the evolution of femtosecond optical pulses in optical fibers [217–219]. As an example, parts (c) and (d) of Figure 5.25 show the evolution of the 50-fs pulse using this more accurate equation, with the form of Raman Response given in Eq. (2.3.41). A comparison of the temporal and spectral evolutions in the two cases reveals the similarities and the differences between the predictions of Eq. (2.3.36) and Eq. (5.5.8). More specifically, although qualitative features are produced by both equations, there are major quantitative differences, and one must use Eq. (2.3.36) for such short optical pulse to get accurate results.

As seen in Figure 5.25, when the input peak power is large enough to excite a high-order soliton ( $N > 1$ ), the pulse spectrum evolves into several bands, each corresponding to fundamental solitons of different widths produced after the fission process. Such an evolution pattern was observed in 1987 when 830-fs pulses with peak powers up to 530 W were propagated in fibers up to 1 km long [229]. The spectral peak at the extreme red end was associated with a soliton whose width was the shortest ( $\approx 55$  fs) after 12 m and then increased with a further increase in the fiber length. These experimental results are discussed further in Section 12.1. In microstructured fibers with a relatively large value of the nonlinear parameter  $\gamma$ , the value of  $N$  can exceed 10, and pulse spectrum may extend over more than 100 THz. Such an extreme spectral broadening is referred to as supercontinuum and is the topic of Chapter 13.

An interesting question is whether Eq. (5.5.8) permits solitary-wave solutions under certain conditions. Several such solutions have been found using a variety of techniques [231–244]. In most cases, the solution exists only for a specific choice of parameter combinations. For example, fundamental and higher-order solitons have been found when  $\tau_R = 0$  with  $s = -2\delta_3$  or  $s = -6\delta_3$  [237]. From a practical standpoint, such solutions of Eq. (5.5.8) are rarely useful because it is hard to find fibers whose parameters satisfy the required constraints.

For pulses shorter than 20 fs, even the use of Eq. (2.3.36) becomes questionable because of the slowly varying envelope approximation made in its derivation (see Section 2.3). Because such short pulses can be generated from modern mode-locked lasers, attempts have been made to improve upon this approximation, while still working with the pulse envelope [245–247]. For supershort pulses containing only a few optical cycles, it eventually becomes necessary to abandon the concept of the pulse envelope and solve Maxwell's equations directly with a finite-difference time-domain (FDTD) algorithm [248–250]. However, because of a subwavelength resolution required by the FDTD algorithm, this technique is limited in practice to relatively short fiber lengths (<1 cm).

## PROBLEMS

- 5.1** Solve Eq. (5.1.4) and derive an expression for the gain of modulation instability. What is the peak value of the gain and at what frequency does this gain occur?
- 5.2** Extend Eq. (5.1.4) such that it includes dispersive effects up to fourth-order. Derive an expression for the gain produced by modulation instability. Comment on the new features associated with this instability.
- 5.3** Consider a lightwave system in which fiber losses are compensated periodically using optical amplifiers. Solve Eq. (5.1.4) for this case and derive an expression for the gain produced by modulation instability. Prove that the gain peaks at frequencies given in Eq. (5.1.12).
- 5.4** Consider a dispersion-managed fiber link for which  $\beta_2$  in Eq. (5.1.4) is a periodic function. Derive an expression for the gain produced by modulation instability for such a link. You are allowed to consult Ref. [61].
- 5.5** A 1.55-μm soliton communication system is operating at 10 Gb/s using dispersion-shifted fibers with  $D = 2 \text{ ps}/(\text{km nm})$ . The effective core area of the fiber is  $50 \mu\text{m}^2$ . Calculate the peak power and the pulse energy required for launching fundamental solitons of 30-ps width (FWHM) into the fiber.
- 5.6** Verify by direct substitution that the soliton solution given in Eq. (5.2.16) that satisfies Eq. (5.2.5).
- 5.7** Develop a numerical code using Matlab software for solving Eq. (5.2.5) with the split-step Fourier method of Section 2.4.1. Test it by comparing its output with the analytical solution in Eq. (5.2.16) when a fundamental soliton is launched into the fiber.
- 5.8** Use the computer code developed in the preceding problem to study the case of an input pulse of the form given in Eq. (5.2.22) for  $N=0.2, 0.6, 1.0$ , and 1.4. Explain the different behavior occurring in each case.
- 5.9** Solve numerically the NLS equation (5.2.5) for an input pulse with  $u(0, \tau) = 4\text{sech}(\tau)$ . Plot the pulse shapes and spectra over one soliton period and compare your results with those shown in Figure 5.6. Comment on new qualitative features of the fourth-order bright soliton.

- 5.10** Repeat the preceding problem for a fourth-order dark soliton by solving Eq. (5.2.5) with the input  $u(0, \tau) = 4 \tanh(\tau)$ . Plot the pulse shapes and spectra over three dispersion lengths and compare your results with those shown in Figure 5.12. Comment on new qualitative features.
- 5.11** A soliton communication system is designed with an amplifier spacing of 50 km. What should the input value of the soliton parameter  $N$  be to ensure that a fundamental soliton is maintained in spite of 0.2-dB/km fiber losses? What should the amplifier gain be? Is there any limit on the bit rate of such a system?
- 5.12** Study the soliton interaction numerically using an input pulse profile given in Eq. (5.4.35). Choose  $r = 1$ ,  $q_0 = 3$ , and four values of  $\theta = 0, \pi/4, \pi/2$ , and  $\pi$ . Compare your results with those shown in Figure 5.18.
- 5.13** A soliton system is designed to transmit a signal over 5000 km at  $B = 5$  Gb/s. What should the pulse width (FWHM) be to ensure that the neighboring solitons do not interact during transmission? The dispersion parameter  $D = 2$  ps/(km nm) at the operating wavelength.
- 5.14** Follow Ref. [180] and derive the moment equations for the pulse parameters given as Eqs (5.5.3)–(5.5.6).
- 5.15** Verify by direct substitution that the solution given in Eq. (5.5.12) is indeed the solution of Eq. (5.5.11) with  $(b = 40\delta_4)^{-1/2}$ .
- 5.16** What is intrapulse Raman scattering? Why does it lead to a shift in the carrier frequency of solitons? Derive an expression for the frequency shift of a fundamental from Eqs (5.5.3)–(5.5.6) assuming that  $\alpha = 0$ ,  $\beta_3 = 0$  and  $C_p = 0$ . Neglect also the self-steepening terms containing  $\omega_0$ .
- 5.17** Verify by direct substitution that the solution given in Eq. (5.5.20), is indeed the solution of Eq. (5.5.8), when  $\delta_3 = 0$ ,  $s = 0$ , and  $N = 3/(4\tau_R)$ .

## REFERENCES

- [1] G. B. Whitham, *Proc. Roy. Soc.* **283**, 238 (1965); T. B. Benjamin and J. E. Feir *J. Fluid Mech.* **27**, 417 (1967).
- [2] L. A. Ostrovskii, *Sov. Phys. Tech. Phys.* **8**, 679 (1964); *Sov. Phys. JETP* **24**, 797 (1967).
- [3] V. I. Bespalov and V. I. Talanov, *JETP Lett.* **3**, 307 (1966).
- [4] V. I. Karpman, *JETP Lett.* **6**, 277 (1967).
- [5] T. Taniuti and H. Washimi, *Phys. Rev. Lett.* **21**, 209 (1968).
- [6] C. K. W. Tam, *Phys. Fluids* **12**, 1028 (1969).
- [7] A. Hasegawa, *Phys. Rev. Lett.* **24**, 1165 (1970); *Phys. Fluids* **15**, 870 (1971).
- [8] A. Hasegawa, *Opt. Lett.* **9**, 288 (1984).
- [9] D. Anderson and M. Lisak, *Opt. Lett.* **9**, 468 (1984).
- [10] B. Hermansson and D. Yevick, *Opt. Commun.* **52**, 99 (1984).
- [11] K. Tajima, *J. Lightwave Technol.* **4**, 900 (1986).
- [12] K. Tai, A. Hasegawa, and A. Tomita, *Phys. Rev. Lett.* **56**, 135 (1986).
- [13] K. Tai, A. Tomita, J. L. Jewell, and A. Hasegawa, *Appl. Phys. Lett.* **49**, 236 (1986).
- [14] P. K. Shukla and J. J. Rasmussen, *Opt. Lett.* **11**, 171 (1986).
- [15] M. J. Potasek, *Opt. Lett.* **12**, 921 (1987).

- [16] I. M. Uzunov, *Opt. Quantum Electron.* **22**, 529 (1990).
- [17] M. J. Potasek and G. P. Agrawal, *Phys. Rev. A* **36**, 3862 (1987).
- [18] V. A. Vysloukh and N. A. Sukhotskova, *Sov. J. Quantum Electron.* **17**, 1509 (1987).
- [19] M. N. Islam, S. P. Dijaili, and J. P. Gordon, *Opt. Lett.* **13**, 518 (1988).
- [20] F. Ito, K. Kitayama, and H. Yoshinaga, *Appl. Phys. Lett.* **54**, 2503 (1989).
- [21] C. J. McKinstrie and G. G. Luther, *Physica Scripta* **30**, 31 (1990).
- [22] G. Cappellini and S. Trillo, *J. Opt. Soc. Am. B* **8**, 824 (1991).
- [23] S. Trillo and S. Wabnitz, *Opt. Lett.* **16**, 986 (1991).
- [24] J. M. Soto-Crespo and E. M. Wright, *Appl. Phys. Lett.* **59**, 2489 (1991).
- [25] M. Yu, C. J. McKinstrie, and G. P. Agrawal, *Phys. Rev. E* **52**, 1072 (1995).
- [26] F. Biancalana, D. V. Skryabin, and P. St. J. Russell, *Phys. Rev. E* **68**, 046003 (2003).
- [27] E. Brainis, D. Amans, and S. Massar, *Phys. Rev. A* **71**, 023808 (2005).
- [28] R. W. Boyd, M. G. Raymer, and L. M. Narducci, Eds., *Optical Instabilities* (Cambridge University Press, 1986).
- [29] F. T. Arecchi and R. G. Harrison, Eds., *Instabilities and Chaos in Quantum Optics* (Springer-Verlag, 1987).
- [30] C. O. Weiss and R. Vilaseca, *Dynamics of Lasers* (Weinheim, 1991).
- [31] G. H. M. van Tartwijk and G. P. Agrawal, *Prog. Quantum Electron.* **22**, 43 (1998).
- [32] N. Akhmediev and V. I. Korneev, *Theor. Math. Phys.* **69**, 1089 (1986).
- [33] N. N. Akhmediev, V. M. Eleonskii, and N. E. Kulagin, *Theor. Math. Phys.* **72**, 809 (1987).
- [34] H. Hadachira, D. W. McLaughlin, J. V. Moloney, and A. C. Newell, *J. Math. Phys.* **29**, 63 (1988).
- [35] L. Gagnon, *J. Opt. Soc. Am. B* **7**, 1098 (1990).
- [36] D. Mihalache and N. C. Panoiu, *Phys. Rev. A* **45**, 673 (1992); *J. Math. Phys.* **33**, 2323 (1992).
- [37] D. Mihalache, F. Lederer, and D. M. Baboiu, *Phys. Rev. A* **47**, 3285 (1993).
- [38] S. Kumar, G. V. Anand, and A. Selvarajan, *J. Opt. Soc. Am. B* **10**, 697 (1993).
- [39] N. N. Akhmediev, *Phys. Rev. A* **47**, 3213 (1993).
- [40] A. M. Kamchatnov, *Phys. Rep.* **286**, 200 (1997).
- [41] J. M. Dudley, G. Genty, F. Dias, B. Kibler, and N. Akhmediev, *Opt. Express* **17**, 21497 (2009).
- [42] B. Kibler, J. Fatome, , C. Finot, et al., *Nature Phys.* **6**, 790 (2010).
- [43] K. Hammani, B. Wetzel, , B. Kibler, et al., *Opt. Lett.* **36**, 2140 (2011).
- [44] E. J. Greer, D. M. Patrick, and P. G. J. Wigley, *Electron. Lett.* **25**, 1246 (1989).
- [45] P. V. Mamyshev, S. V. Chernikov, and E. M. Dianov, *IEEE J. Quantum Electron.* **27**, 2347 (1991).
- [46] S. V. Chernikov, J. R. Taylor, P. V. Mamyshev, and E. M. Dianov, *Electron. Lett.* **28**, 931 (1992).
- [47] S. V. Chernikov, E. M. Dianov, D. J. Richardson, R. I. Laming, and D. N. Payne, *Appl. Phys. Lett.* **63**, 293 (1993).
- [48] S. V. Chernikov, J. R. Taylor, and R. Kashyap, *Electron. Lett.* **29**, 1788 (1993); *Electron. Lett.* **30**, 433 (1994);(c) *Opt. Lett.* **19**, 539 (1994).
- [49] E. A. Swanson and S. R. Chinn, *IEEE Photon. Technol. Lett.* **6**, 796 (1994).
- [50] M. Nakazawa, K. Suzuki, and H. A. Haus, *Phys. Rev. A* **38**, 5193 (1988).
- [51] M. Nakazawa, K. Suzuki, H. Kubota, and H. A. Haus, *Phys. Rev. A* **39**, 5768 (1989).
- [52] S. Coen and M. Haelterman, *Phys. Rev. Lett.* **79**, 4139 (1997).

- [53] M. Yu, C. J. McKinistrie, and G. P. Agrawal, *J. Opt. Soc. Am. B* **15**, 607 (1998); *J. Opt. Soc. Am. B* **15**, 617 (1998).
- [54] S. Coen and M. Haelterman, *Opt. Commun.* **146**, 339 (1998); *Opt. Lett.* **24**, 80 (1999).
- [55] S. Coen, M. Haelterman, P. Emplit, L. Delage, L. M. Simohamed, and F. Reynaud, *J. Opt. Soc. Am. B* **15**, 2283 (1998); *J. Opt. B* **1**, 36 (1999).
- [56] J. P. Hamide, P. Emplit, and J. M. Gabriagues, *Electron. Lett.* **26**, 1452 (1990).
- [57] F. Matera, A. Mecozzi, M. Romagnoli, and M. Settembre, *Opt. Lett.* **18**, 1499 (1993); *Microwave Opt. Tech. Lett.* **7**, 537 (1994).
- [58] M. Yu, G. P. Agrawal, and C. J. McKinistrie, *J. Opt. Soc. Am. B* **12**, 1126 (1995).
- [59] M. Karlsson, *J. Opt. Soc. Am. B* **12**, 2071 (1995).
- [60] N. Kikuchi and S. Sasaki, *Electron. Lett.* **32**, 570 (1996).
- [61] N. J. Smith and N. J. Doran, *Opt. Lett.* **21**, 570 (1996).
- [62] R. A. Saunders, B. A. Patel, and D. Garthe, *IEEE Photon. Technol. Lett.* **9**, 699 (1997).
- [63] R. Q. Hui, M. O'Sullivan, A. Robinson, and M. Taylor, *J. Lightwave Technol.* **15**, 1071 (1997).
- [64] D. F. Grosz, C. Mazzali, S. Celaschi, A. Paradisi, and H. L. Fragnito, *IEEE Photon. Technol. Lett.* **11**, 379 (1999).
- [65] E. Ciaramella and M. Tamburini, *IEEE Photon. Technol. Lett.* **11**, 1608 (1999).
- [66] A. Kumar, A. Labruyere, and P. T. Dinda, *Opt. Commun.* **219**, 221 (2003).
- [67] X. Tang and Z. Wu, *IEEE Photon. Technol. Lett.* **17**, 926 (2005).
- [68] G. A. Nowak, Y. H. Kao, T. J. Xia, M. N. Islam, and D. Nolan, *Opt. Lett.* **23**, 936 (1998).
- [69] S. Nishi and M. Saruwatari, *Electron. Lett.* **31**, 225 (1995).
- [70] C. Mazzali, D. F. Grosz, and H. L. Fragnito, *IEEE Photon. Technol. Lett.* **11**, 251 (1999).
- [71] J. Scott Russell, Report of 14th Meeting of the British Association for Advancement of Science (York, September 1844), pp. 311–390.
- [72] C. S. Gardner, J. M. Green, M. D. Kruskal, and R. M. Miura, *Phys. Rev. Lett.* **19**, 1095 (1967); *Commun. Pure Appl. Math.* **27**, 97 (1974).
- [73] N. J. Zabusky and M. D. Kruskal, *Phys. Rev. Lett.* **15**, 240 (1965).
- [74] M. J. Ablowitz and P. A. Clarkson, *Solitons, Nonlinear Evolution Equations, and Inverse Scattering* (Cambridge University Press, 1991).
- [75] H. Hasegawa and Y. Kodama, *Solitons in Optical Communications* (Oxford University Press, 1995).
- [76] Y. S. Kivshar and G. P. Agrawal, *Optical Solitons: From Fibers to Photonic Crystals* (Academic Press, 2003).
- [77] J. T. Taylor, P. L. Knight, and A. Miller, Eds., *Optical Solitons—Theory and Experiment* (Cambridge University Press, 2005).
- [78] N. N. Akhmediev and A. A. Ankiewicz, Eds., *Dissipative Solitons* (Springer, 2005).
- [79] L. F. Mollenauer and J. P. Gordon, *Solitons in Optical Fibers: Fundamental and Applications* (Academic Press, 2006).
- [80] A. Hasegawa and F. Tappert, *Appl. Phys. Lett.* **23**, 142 (1973).
- [81] P. Andrekson, *Laser Focus World* **35** (5), 145 (1999).
- [82] V. E. Zakharov and A. B. Shabat, *Sov. Phys. JETP* **34**, 62 (1972).
- [83] H. A. Haus and M. N. Islam, *IEEE J. Quantum Electron.* **21**, 1172 (1985).
- [84] J. Satsuma and N. Yajima, *Prog. Theor. Phys. Suppl.* **55**, 284 (1974).
- [85] L. F. Mollenauer, R. H. Stolen, and J. P. Gordon, *Phys. Rev. Lett.* **45**, 1095 (1980).
- [86] R. H. Stolen, L. F. Mollenauer, and W. J. Tomlinson, *Opt. Lett.* **8**, 186 (1983).
- [87] L. F. Mollenauer, R. H. Stolen, J. P. Gordon, and W. J. Tomlinson, *Opt. Lett.* **8**, 289 (1983).

- [88] F. Salin, P. Grangier, G. Roger, and A. Brun, *Phys. Rev. Lett.* **56**, 1132 (1986); *Phys. Rev. Lett.* **6**, 569 (1988).
- [89] R. Meinel, *Opt. Commun.* **47**, 343 (1983).
- [90] E. M. Dianov, A. M. Prokhorov, and V. N. Serkin, *Sov. Phys. Dokl.* **28**, 1036 (1983).
- [91] C. Desem and P. L. Chu, *Opt. Lett.* **11**, 248 (1986).
- [92] K. J. Blow and D. Wood, *Opt. Commun.* **58**, 349 (1986).
- [93] A. I. Maimistov and Y. M. Sklyarov, *Sov. J. Quantum Electron.* **17**, 500 (1987).
- [94] A. S. Gouveia-Neto, A. S. L. Gomes, and J. R. Taylor, *Opt. Commun.* **64**, 383 (1987).
- [95] L. F. Mollenauer, J. P. Gordon, and P. V. Mamyshev, *Optical Fiber Telecommunications III*, in I. P. Kaminow and T. L. Koch, Eds. (Academic Press, 1997), Chap. 12.
- [96] E. Iannone, F. Matera, A. Mecozzi, and M. Settembre, *Nonlinear Optical Communication Networks* (Wiley, 1998).
- [97] G. P. Agrawal, *Fiber-Optic Communication Systems*, 4th ed. (Wiley, 2010).
- [98] J. P. Gordon, *J. Opt. Soc. Am. B* **9**, 91 (1992).
- [99] M. W. Chbat, P. R. Prucnal, M. N. Islam, C. E. Soccilich, and J. P. Gordon, *J. Opt. Soc. Am. B* **10**, 1386 (1993).
- [100] A. Hasegawa and F. Tappert, *Appl. Phys. Lett.* **23**, 171 (1973).
- [101] V. E. Zakharov and A. B. Shabat, *Sov. Phys. JETP* **37**, 823 (1973).
- [102] P. Emplit, J. P. Hamaide, F. Reynaud, C. Froehly, and A. Barthelemy, *Opt. Commun.* **62**, 374 (1987).
- [103] D. Krökel, N. J. Halas, G. Giuliani, and D. Grischkowsky, *Phys. Rev. Lett.* **60**, 29 (1988).
- [104] A. M. Weiner, J. P. Heritage, R. J. Hawkins, R. N. Thurston, E. M. Krischner, D. E. Leaird, and W. J. Tomlinson, *Phys. Rev. Lett.* **61**, 2445 (1988).
- [105] W. J. Tomlinson, R. J. Hawkins, A. M. Weiner, J. P. Heritage, and R. N. Thurston, *J. Opt. Soc. Am. B* **6**, 329 (1989).
- [106] W. Zhao and E. Bourkoff, *Opt. Lett.* **14**, 703 (1989); *Opt. Lett.* **14**, 808 (1989).
- [107] R. N. Thurston and A. M. Weiner, *J. Opt. Soc. Am. B* **8**, 471 (1991).
- [108] W. Zhao and E. Bourkoff, *Opt. Lett.* **15**, 405 (1990); *J. Opt. Soc. Am. B* **9**, 1134 (1992).
- [109] J. E. Rothenberg and H. K. Heinrich, *Opt. Lett.* **17**, 261 (1992).
- [110] P. Emplit, M. Haelterman, and J. P. Hamaide, *Opt. Lett.* **18**, 1047 (1993).
- [111] D. J. Richardson, R. P. Chamberlain, L. Dong, and D. N. Payne, *Electron. Lett.* **30**, 1326 (1994).
- [112] O. G. Okhotnikov and F. M. Araujo, *Electron. Lett.* **31**, 2187 (1995).
- [113] M. Nakazawa and K. Suzuki, *Electron. Lett.* **31**, 1084 (1995).
- [114] M. Nakazawa and K. Suzuki, *Electron. Lett.* **31**, 1076 (1995).
- [115] A. K. Atieh, P. Myslinski, J. Chrostowski, and P. Galko, *Opt. Commun.* **133**, 541 (1997).
- [116] P. Emplit, M. Haelterman, R. Kashyap, and M. DeLathouwer, *IEEE Photon. Technol. Lett.* **9**, 1122 (1997).
- [117] R. Leners, P. Emplit, D. Foursa, M. Haelterman, and R. Kashyap, *J. Opt. Soc. Am. B* **14**, 2339 (1997).
- [118] Y. S. Kivshar and B. Luther-Davies, *Phys. Rep.* **298**, 81 (1998).
- [119] A. E. Kaplan, *Phys. Rev. Lett.* **55**, 1291 (1985); *IEEE J. Quantum Electron.* **QE-21**, 1538 (1985).
- [120] R. H. Enns and S. S. Rangnekar, *IEEE J. Quantum Electron.* **23**, 1199 (1987); *Phys. Rev. A* **43**, 4047 (1991); (c) *Phys. Rev. A* **44**, 3373 (1991).
- [121] R. H. Enns, S. S. Rangnekar, and A. E. Kaplan, *Phys. Rev. A* **35**, 446 (1987); *Phys. Rev. A* **36**, 1270 (1987).

- [122] S. Gatz and J. Hermann, *J. Opt. Soc. Am. B* **8**, 2296 (1991); *Opt. Lett.* **17**, 484 (1992).
- [123] W. Krolikowski and B. Luther-Davies, *Opt. Lett.* **17**, 1414 (1992).
- [124] C. Deangelis, *IEEE J. Quantum Electron.* **30**, 818 (1994).
- [125] A. Kumar, *Phys. Rev. E* **58**, 5021 (1998).
- [126] N. J. Smith, N. J. Doran, W. Forysiak, and F. M. Knox, *J. Lightwave Technol.* **15**, 1808 (1997).
- [127] L. F. Mollenauer and P. V. Mamyshev, *IEEE J. Quantum Electron.* **34**, 2089 (1998).
- [128] R. M. Mu, C. R. Menyuk, G. M. Carter, and J. M. Jacob, *IEEE J. Sel. Topics Quantum Electron.* **6**, 248 (2000).
- [129] S. K. Turitsyn, M. P. Fedourk, E. G. Shapiro, V. K. Mezentsev, and E. G. Turitsyna, *IEEE J. Sel. Topics Quantum Electron.* **6**, 263 (2000).
- [130] M. Suzuki and N. Edagawa, *J. Lightwave Technol.* **21**, 916 (2003).
- [131] E. Poutrina and G. P. Agrawal, *J. Lightwave Technol.* **20**, 790 (2002); *J. Lightwave Technol.* **21**, 990 (2003).
- [132] A. Del Duce, R. I. Killey, and P. Bayvel, *J. Lightwave Technol.* **22**, 1263 (2004).
- [133] V. N. Serkin and A. Hasegawa, *Phys. Rev. Lett.* **85**, 4502 (2000); *IEEE J. Sel. Topics Quantum Electron.* **8**, 418 (2002).
- [134] V. I. Kruglov, A. C. Peacock, and J. D. Harvey, *Phys. Rev. Lett.* **90**, 113902 (2003); *Phys. Rev. E* **71**, 056619 (2005).
- [135] B. Tian, W. R. Shan, C. Y. Zhang, G. M. Wei, and Y. T. Gao, *Eur. Phys. J. B* **47**, 329 (2005).
- [136] S. A. Ponomarenko and G. P. Agrawal, *Phys. Rev. Lett.* **97**, 013901 (2006).
- [137] V. I. Kruglov and J. D. Harvey, *J. Opt. Soc. Am. B* **23**, 2541 (2006).
- [138] S. A. Ponomarenko and G. P. Agrawal, *Opt. Express* **15**, 2963 (2007).
- [139] S. A. Ponomarenko and G. P. Agrawal, *J. Opt. Soc. Am. B* **29**, 983 (2008).
- [140] J. D. Moores, *Opt. Lett.* **21**, 555 (1996).
- [141] A. Hasegawa and Y. Kodama, *Proc. IEEE* **69**, 145 (1981); *Opt. Lett.* **7**, 285 (1982).
- [142] Y. Kodama and A. Hasegawa, *Opt. Lett.* **7**, 339 (1982); *Opt. Lett.* **8**, 342 (1983).
- [143] A. Hasegawa, *Opt. Lett.* **8**, 650 (1983); *Appl. Opt.* **23**, 3302 (1984).
- [144] L. F. Mollenauer, R. H. Stolen, and M. N. Islam, *Opt. Lett.* **10**, 229 (1985).
- [145] L. F. Mollenauer, J. P. Gordon, and M. N. Islam, *IEEE J. Quantum Electron.* **QE-22**, 157 (1986).
- [146] L. F. Mollenauer and K. Smith, *Opt. Lett.* **13**, 675 (1988).
- [147] M. Nakazawa, Y. Kimura, and K. Suzuki, *Electron. Lett.* **25**, 199 (1989).
- [148] M. Nakazawa, K. Suzuki, and Y. Kimura, *IEEE Photon. Technol. Lett.* **2**, 216 (1990).
- [149] V. I. Karpman and E. M. Maslov, *Sov. Phys. JETP* **46**, 281 (1977).
- [150] D. J. Kaup and A. C. Newell, *Proc. R. Soc. London, Ser. A* **361**, 413 (1978).
- [151] V. I. Karpman, *Sov. Phys. JETP* **50**, 58 (1979); *Physica Scripta* **20**, 462 (1979).
- [152] Y. S. Kivshar and B. A. Malomed, *Rev. Mod. Phys.* **61**, 761 (1989).
- [153] H. Haus, *J. Opt. Soc. Am. B* **8**, 1122 (1991).
- [154] C. R. Menyuk, *J. Opt. Soc. Am. B* **10**, 1585 (1993).
- [155] T. Georges and F. Favre, *J. Opt. Soc. Am. B* **10**, 1880 (1993).
- [156] T. Georges, *Opt. Fiber Technol.* **1**, 97 (1995).
- [157] A. Bonderson, M. Lisak, and D. Anderson, *Physica Scripta* **20**, 479 (1979).
- [158] D. Anderson and M. Lisak, *Phys. Rev. A* **27**, 1393 (1983).
- [159] K. J. Blow and N. J. Doran, *Opt. Commun.* **52**, 367 (1985).
- [160] D. Anderson and M. Lisak, *Opt. Lett.* **10**, 390 (1985).
- [161] K. Tajima, *Opt. Lett.* **12**, 54 (1987).

- [162] V. A. Bogatyrov, M. M. Bubnov, E. M. Dianov, and A. A. Sysoliatin, *Pure Appl. Opt.* **4**, 345 (1995).
- [163] D. J. Richardson, R. P. Chamberlin, L. Dong, and D. N. Payne, *Electron. Lett.* **31**, 1681 (1995).
- [164] T. Hirooka and M. Nakazawa, *Opt. Lett.* **29**, 498 (2004).
- [165] A. Hasegawa and Y. Kodama, *Phys. Rev. Lett.* **66**, 161 (1991).
- [166] J. P. Gordon and H. A. Haus, *Opt. Lett.* **11**, 665 (1986).
- [167] V. I. Karpman and V. V. Solov'ev, *physica* **3D**, 487 (1981).
- [168] J. P. Gordon, *Opt. Lett.* **8**, 596 (1983).
- [169] K. J. Blow and N. J. Doran, *Electron. Lett.* **19**, 429 (1983).
- [170] B. Hermansson and D. Yevick, *Electron. Lett.* **19**, 570 (1983).
- [171] P. L. Chu and C. Desem, *Electron. Lett.* **19**, 956 (1983); *Electron. Lett.* **21**, 228 (1985).
- [172] D. Anderson and M. Lisak, *Phys. Rev. A* **32**, 2270 (1985); *Opt. Lett.* **11**, 174 (1986).
- [173] E. M. Dianov, Z. S. Nikonova, and V. N. Serkin, *Sov. J. Quantum Electron.* **16**, 1148 (1986).
- [174] F. M. Mitschke and L. F. Mollenauer, *Opt. Lett.* **12**, 355 (1987).
- [175] C. Desem and P. L. Chu, *Opt. Lett.* **12**, 349 (1987); *Electron. Lett.* **23**, 260 (1987).
- [176] C. Desem and P. L. Chu, *IEE Proc.* **134** (Pt. J), 145 (1987).
- [177] Y. Kodama and K. Nozaki, *Opt. Lett.* **12**, 1038 (1987).
- [178] V. V. Afanasjev, *Opt. Lett.* **18**, 790 (1993).
- [179] A. N. Pinto, G. P. Agrawal, and J. F. da Rocha, *J. Lightwave Technol.* **18**, 515 (1998).
- [180] J. Santhanam and G. P. Agrawal, *Opt. Commun.* **222**, 413 (2003).
- [181] Z. Chen, A. J. Taylor, and A. Efimov, *J. Opt. Soc. Am. B* **27**, 1022 (2010).
- [182] G. P. Agrawal and M. J. Potasek, *Phys. Rev. A* **33**, 1765 (1986).
- [183] G. R. Boyer and X. F. Carlotti, *Opt. Commun.* **60**, 18 (1986).
- [184] P. K. Wai, C. R. Menyuk, H. H. Chen, and Y. C. Lee, *Opt. Lett.* **11**, 464 (1987); *Opt. Lett.* **12**, 628 (1987).
- [185] M. Desaix, D. Anderson, and M. Lisak, *Opt. Lett.* **15**, 18 (1990).
- [186] V. K. Mezentsev and S. K. Turitsyn, *Sov. Lightwave Commun.* **1**, 263 (1991).
- [187] Y. S. Kivshar, *Phys. Rev. A* **43**, 1677 (1981); *Opt. Lett.* **16**, 892 (1991).
- [188] V. I. Karpman, *Phys. Rev. E* **47**, 2073 (1993); *Phys. Lett. A* **181**, 211 (1993).
- [189] Y. Kodama, M. Romagnoli, S. Wabnitz, and M. Midrio, *Opt. Lett.* **19**, 165 (1994).
- [190] T. I. Lakoba and G. P. Agrawal, *J. Opt. Soc. Am. B* **16**, 1332 (1999).
- [191] A. Peleg and Y. Chung, *J. Phys. A* **26**, 10029 (2003).
- [192] M. Karlsson and A. Höök, *Opt. Commun.* **104**, 303 (1994).
- [193] N. Tzoar and M. Jain, *Phys. Rev. A* **23**, 1266 (1981).
- [194] E. A. Golovchenko, E. M. Dianov, A. M. Prokhorov, and V. N. Serkin, *JETP Lett.* **42**, 87 (1985); *Sov. Phys. Dokl.* **31**, 494 (1986).
- [195] K. Ohkuma, Y. H. Ichikawa, and Y. Abe, *Opt. Lett.* **12**, 516 (1987).
- [196] A. M. Kamchatnov, S. A. Darmanyan, and F. Lederer, *Phys. Lett. A* **245**, 259 (1998).
- [197] W. P. Zhong and H. J. Luo, *Chinese Phys. Lett.* **17**, 577 (2000).
- [198] E. Mjølhus, *J. Plasma Phys.* **16**, 321 (1976); *J. Plasma Phys.* **19**, 437 (1978).
- [199] K. Mio, T. Ogino, K. Minami, and S. Takeda, *J. Phys. Soc. Jpn.* **41**, 265 (1976).
- [200] M. Wadati, K. Konno, and Y. H. Ichikawa, *J. Phys. Soc. Jpn.* **46**, 1965 (1979).
- [201] Y. H. Ichikawa, K. Konno, M. Wadati, and H. Sanuki, *J. Phys. Soc. Jpn.* **48**, 279 (1980).
- [202] E. M. Dianov, A. Y. Karasik, , P. V. Mamyshev, et al., *JETP Lett.* **41**, 294 (1985).
- [203] F. M. Mitschke and L. F. Mollenauer, *Opt. Lett.* **11**, 659 (1986).
- [204] J. P. Gordon, *Opt. Lett.* **11**, 662 (1986).

- [205] Y. Kodama and A. Hasegawa, *IEEE J. Quantum Electron.* **23**, 510 (1987).
- [206] B. Zysset, P. Beaud, and W. Hodel, *Appl. Phys. Lett.* **50**, 1027 (1987).
- [207] V. A. Vysloukh and T. A. Matveeva, *Sov. J. Quantum Electron.* **17**, 498 (1987).
- [208] V. N. Serkin, *Sov. Tech. Phys. Lett.* **13**, 320 (1987); *Sov. Tech. Phys. Lett.* **13**, 366 (1987).
- [209] A. B. Grudinin, E. M. Dianov, D. V. Korobkin, et al., *JETP Lett.* **46**, 221 (1987).
- [210] A. S. Gouveia-Neto, A. S. L. Gomes, and J. R. Taylor, *IEEE J. Quantum Electron.* **24**, 332 (1988).
- [211] K. Tai, A. Hasegawa, and N. Bekki, *Opt. Lett.* **13**, 392 (1988).
- [212] R. H. Stolen, J. P. Gordon, W. J. Tomlinson, and H. A. Haus, *J. Opt. Soc. Am. B* **6**, 1159 (1989).
- [213] K. J. Blow and D. Wood, *IEEE J. Quantum Electron.* **25**, 2665 (1989).
- [214] V. V. Afansasyev, V. A. Vysloukh, and V. N. Serkin, *Opt. Lett.* **15**, 489 (1990).
- [215] P. V. Mamyshev and S. V. Chernikov, *Opt. Lett.* **15**, 1076 (1990).
- [216] B. J. Hong and C. C. Yang, *J. Opt. Soc. Am. B* **8**, 1114 (1991).
- [217] P. V. Mamyshev and S. V. Chernikov, *Sov. Lightwave Commun.* **2**, 97 (1992).
- [218] R. H. Stolen and W. J. Tomlinson, *J. Opt. Soc. Am. B* **9**, 565 (1992).
- [219] K. Kurokawa, H. Kubota, and M. Nakazawa, *Electron. Lett.* **28**, 2050 (1992).
- [220] G. P. Agrawal and C. Headley III, *Phys. Rev. A* **46**, 1573 (1992).
- [221] Y. S. Kivshar and B. A. Malomed, *Opt. Lett.* **18**, 485 (1993).
- [222] V. N. Serkin, V. A. Vysloukh, and J. R. Taylor, *Electron. Lett.* **29**, 12 (1993).
- [223] N. Nishizawa and T. Goto, *IEEE Photon. Technol. Lett.* **11**, 325 (1999); *IEEE J. Sel. Topics Quantum Electron.* **7**, 518 (2001).
- [224] M. E. Fermann, A. Galvanauskas, M. L. Stock, K. K. Wong, D. Harter, and L. Goldberg, *Opt. Lett.* **24**, 1428 (1999).
- [225] X. Liu, C. Xu, W. H. Knox, J. K. Chandalia, B. J. Eggleton, S. G. Kosinski, and R. S. Windeler, *Opt. Lett.* **26**, 358 (2001).
- [226] R. Washburn, S. E. Ralph, P. A. Lacourt, J. M. Dudley, W. T. Rhodes, R. S. Windeler, and S. Coen, *Electron. Lett.* **37**, 1510 (2001).
- [227] K. S. Abedin and F. Kubota, *IEEE J. Sel. Topics Quantum Electron.* **10**, 1203 (2004).
- [228] L. Gagnon and P. A. Bélanger, *Opt. Lett.* **9**, 466 (1990).
- [229] P. Beaud, W. Hodel, B. Zysset, and H. P. Weber, *IEEE J. Quantum Electron.* **23**, 1938 (1987).
- [230] M. Erkintalo, G. Genty, B. Wetzel, and J. M. Dudley, *Opt. Express* **18**, 25449 (2010).
- [231] D. N. Christodoulides and R. I. Joseph, *Appl. Phys. Lett.* **47**, 76 (1985).
- [232] L. Gagnon, *J. Opt. Soc. Am. B* **9**, 1477 (1989).
- [233] A. B. Grudinin, V. N. Men'shov, and T. N. Fursa, *Sov. Phys. JETP* **70**, 249 (1990).
- [234] M. J. Potasek and M. Tabor, *Phys. Lett. A* **154**, 449 (1991).
- [235] M. Florjanczyk and L. Gagnon, *Phys. Rev. A* **41**, 4478 (1990); *Phys. Rev. A* **45**, 6881 (1992).
- [236] M. J. Potasek, *J. Appl. Phys.* **65**, 941 (1989); *IEEE J. Quantum Electron.* **29**, 281 (1993).
- [237] S. Liu and W. Wang, *Phys. Rev. E* **49**, 5726 (1994).
- [238] D. J. Frantzeskakis, K. Hizanidis, G. S. Tombras, and I. Belia, *IEEE J. Quantum Electron.* **31**, 183 (1995).
- [239] K. Porsezian and K. Nakkeeran, *Phys. Rev. Lett.* **76**, 3955 (1996).
- [240] G. J. Dong and Z. Z. Liu, *Opt. Commun.* **128**, 8 (1996).
- [241] M. Gedalin, T. C. Scott, and Y. B. Band, *Phys. Rev. Lett.* **78**, 448 (1997).
- [242] D. Mihalache, N. Truta, and L. C. Crasovan, *Phys. Rev. E* **56**, 1064 (1997).

- [243] C. E. Zaspel, *Phys. Rev. Lett.* **82**, 723 (1999).
- [244] Z. Li, L. Li, H. Tian, and G. Zhou, *Phys. Rev. Lett.* **84**, 4096 (2000).
- [245] T. Brabec and F. Krausz, *Phys. Rev. Lett.* **78**, 3282 (1997).
- [246] J. K. Ranka and A. L. Gaeta, *Opt. Lett.* **23**, 534 (1998).
- [247] A. V. Husakou and J. Herrmann, *J. Opt. Soc. Am. B* **19**, 2171 (2002).
- [248] S. Nakamura, N. Takasawa, and Y. Koyamada, *J. Lightwave Technol.* **23**, 855 (2005).
- [249] J. J. Hu, P. Shum, C. Lu, and G. Ren, *IEEE Photon. Technol. Lett.* **24**, 1970 (2007).
- [250] I. Udagedara, M. Premaratne, I. D. Rukhlenko, H. T. Hattori, and G. P. Agrawal, *Opt. Express* **17**, 22124 (2009).

# Polarization Effects

# 6

A major simplification was made in Section 2.3 while deriving the nonlinear Schrödinger (NLS) equation. It consisted of assuming that the polarization state of the incident light is preserved during its propagating inside an optical fiber. This is not really the case in practice. In this chapter we focus on the polarization effects and consider the coupling between the two orthogonally polarized components of an optical field induced by the nonlinear phenomenon known as cross-phase modulation (XPM). The XPM phenomenon is always accompanied with self-phase modulation (SPM) and can also occur between two optical fields of different wavelengths. The nondegenerate case involving different wavelengths is discussed in Chapter 7.

The chapter is organized as follows. The origin of nonlinear birefringence is discussed first in Section 6.1. It is followed with the derivation of a set of two coupled NLS equations that describes the evolution of the two orthogonally polarized components of an optical pulse inside a fiber. The XPM-induced nonlinear birefringence has several practical applications discussed in Section 6.2. The next section considers nonlinear polarization changes with focus on polarization instability. Section 6.4 is devoted to the vector modulation instability occurring in birefringent fibers. In contrast with the scalar case discussed in Section 5.1, the vector modulation instability can occur even in the normal-dispersion regime of a birefringent fiber. Section 6.5 considers the effects of birefringence on solitons. The last section focuses on polarization-mode dispersion (PMD) in fibers with randomly varying birefringence along their length and its implications for lightwave systems.

---

## 6.1 NONLINEAR BIREFRINGENCE

As mentioned in Section 2.2, even a single-mode fiber, in fact, supports two orthogonally polarized modes with the same spatial distribution. The two modes are degenerate in an ideal fiber (maintaining perfect cylindrical symmetry along its entire length) in the sense that their effective refractive indices,  $n_x$  and  $n_y$ , are identical. In practice, all fibers exhibit some modal birefringence ( $n_x \neq n_y$ ) because of unintentional variations in the core shape and anisotropic stresses along the fiber length. Moreover, the degree of modal birefringence,  $B_m = |n_x - n_y|$ , and the orientation of  $x$ - and  $y$ -axes change randomly over a length scale  $\sim 10\text{ m}$  unless special precautions are taken.

In polarization-maintaining fibers, the built-in birefringence is made much larger than random changes occurring due to stress and core-shape variations. As a result, such fibers exhibit nearly constant birefringence along their entire length. This kind of birefringence is called *linear* birefringence. When the nonlinear effects in optical fibers become important, a sufficiently intense optical field can induce *nonlinear* birefringence whose magnitude is intensity dependent. Such self-induced polarization effects were observed as early as 1964 in bulk nonlinear media [1] and have been studied extensively since then [2–10]. In this section, we discuss the origin of nonlinear birefringence and develop mathematical tools that are needed for studying the polarization effects in optical fibers, assuming a constant modal birefringence. Fibers in which linear birefringence change randomly over their length are considered in Section 6.6.

### 6.1.1 Origin of Nonlinear Birefringence

A fiber with constant modal birefringence has two principal axes along which the fiber is capable of maintaining the state of linear polarization of the incident light. These axes are called the slow and fast axes based on the speed at which light polarized along them travels inside the fiber. Assuming  $n_x > n_y$ ,  $n_x$ , and  $n_y$  are the mode indices along the *slow* and *fast* axes, respectively. When low-power, continuous-wave (CW) light is launched with its polarization direction oriented at an angle with respect to the slow axis, the polarization state of the CW light changes along the fiber from linear to elliptic, and then back to linear, in a periodic manner (see Figure 1.9) over a distance known as the *beat length*. The beat length is defined as  $L_B = \lambda/B_m$  and it can be as small as 1 cm in high-birefringence fibers with  $B_m \sim 10^{-4}$ . In low-birefringence fibers, typically  $B_m$  is less than  $10^{-6}$ , and the beat length exceeds 1 m.

If we assume that the longitudinal (or axial) component  $E_z$  of the electromagnetic field remains small enough that it can be ignored in comparison with the transverse components, the electric field associated with an arbitrarily polarized optical wave can be written as

$$\mathbf{E}(\mathbf{r}, t) = \frac{1}{2}(\hat{x}E_x + \hat{y}E_y)\exp(-i\omega_0t) + \text{c.c.}, \quad (6.1.1)$$

where  $\hat{x}$  and  $\hat{y}$  stand for unit vectors,  $E_x$  and  $E_y$  are the complex amplitudes of the polarization components of the field oscillating at the carrier frequency  $\omega_0$ , and c.c. stands for the complex conjugate of the preceding terms.

The nonlinear part of the induced polarization<sup>1</sup>  $\mathbf{P}_{NL}$  is obtained by substituting Eq. (6.1.1) in Eq. (2.3.6). In general, the third-order susceptibility is a fourth-rank tensor with 81 elements. In an isotropic medium, such as silica glass, only three elements are independent of one another, and the third-order susceptibility can be written in terms of them as [10]

$$\chi_{ijkl}^{(3)} = \chi_{xxyy}^{(3)}\delta_{ij}\delta_{kl} + \chi_{xyxy}^{(3)}\delta_{ik}\delta_{jl} + \chi_{xyyx}^{(3)}\delta_{il}\delta_{jk}, \quad (6.1.2)$$

---

<sup>1</sup> Polarization induced inside a dielectric medium by an electromagnetic field should not be confused with the state of polarization of that field. The terminology is certainly confusing but is accepted for historical reasons.

where  $\delta_{ij}$  is the Kronecker delta function defined such that  $\delta_{ij} = 1$  when  $i = j$  and zero otherwise. Using this result in Eq. (2.3.6),  $\mathbf{P}_{\text{NL}}$  can be written as

$$\mathbf{P}_{\text{NL}}(\mathbf{r}, t) = \frac{1}{2}(\hat{x}P_x + \hat{y}P_y)\exp(-i\omega_0 t) + \text{c.c.}, \quad (6.1.3)$$

with  $P_x$  and  $P_y$  given by

$$P_i = \frac{3\epsilon_0}{4} \sum_j \left( \chi_{xxyy}^{(3)} E_i E_j E_j^* + \chi_{xyxy}^{(3)} E_j E_i E_j^* + \chi_{xyyx}^{(3)} E_j E_j E_i^* \right), \quad (6.1.4)$$

where  $i, j = x$  or  $y$ . From the rotational symmetry of an isotropic medium, we also have the relation [10]

$$\chi_{xxxx}^{(3)} = \chi_{xxyy}^{(3)} + \chi_{xyxy}^{(3)} + \chi_{xyyx}^{(3)}, \quad (6.1.5)$$

where  $\chi_{xxxx}^{(3)}$  is the element appearing in the scalar theory of Section 2.3, and used in Eq. (2.3.13) to define the nonlinear-index coefficient  $n_2$ .

The relative magnitudes of the three components in Eq. (6.1.5) depend on the physical mechanisms that contribute to  $\chi^{(3)}$ . In the case of silica fibers, the dominant contribution is of electronic origin [4], and the three components have nearly the same magnitude. If they are assumed to be identical, the polarization components  $P_x$  and  $P_y$  in Eq. (6.1.4) take the form

$$P_x = \frac{3\epsilon_0}{4} \chi_{xxxx}^{(3)} \left[ \left( |E_x|^2 + \frac{2}{3}|E_y|^2 \right) E_x + \frac{1}{3}(E_x^* E_y) E_y \right], \quad (6.1.6)$$

$$P_y = \frac{3\epsilon_0}{4} \chi_{xxxx}^{(3)} \left[ \left( |E_y|^2 + \frac{2}{3}|E_x|^2 \right) E_y + \frac{1}{3}(E_y^* E_x) E_x \right]. \quad (6.1.7)$$

The last term in Eqs (6.1.6) and (6.1.7) leads to degenerate four-wave mixing. Its importance will be discussed later.

The nonlinear contribution  $\Delta n_x$  to the refractive index is governed by the term proportional to  $E_x$  in Eq. (6.1.6). Writing  $P_j = \epsilon_0 \epsilon_j^{\text{NL}} E_j$  and using

$$\epsilon_j = \epsilon_j^L + \epsilon_j^{\text{NL}} = \left( n_j^L + \Delta n_j \right)^2, \quad (6.1.8)$$

where  $n_j^L$  is the linear part of the refractive index ( $j = x, y$ ), the nonlinear contributions  $\Delta n_x$  and  $\Delta n_y$  are given by

$$\Delta n_x = \bar{n}_2 \left( |E_x|^2 + \frac{2}{3}|E_y|^2 \right), \quad \Delta n_y = \bar{n}_2 \left( |E_y|^2 + \frac{2}{3}|E_x|^2 \right), \quad (6.1.9)$$

where  $\bar{n}_2$  is the nonlinear-index coefficient defined in Eq. (2.3.13). The physical meaning of the two terms on the right-hand side of these equations is quite clear. The first term is responsible for SPM. The second term results in XPM because the nonlinear phase shift acquired by one polarization component depends on the intensity

of the other polarization component. The presence of this term induces a nonlinear coupling between the field components  $E_x$  and  $E_y$ . The nonlinear contributions  $\Delta n_x$  and  $\Delta n_y$  are in general unequal and thus create nonlinear birefringence whose magnitude depends on the intensity and the polarization state of the incident light. In practice, nonlinear birefringence manifests as a rotation of the polarization ellipse [1], a phenomenon referred to as *nonlinear polarization rotation*.

### 6.1.2 Coupled-Mode Equations

The propagation equations governing the evolution of the two polarization components along a fiber can be obtained following the method of Section 2.3. Assuming that the nonlinear effects do not affect the fiber mode significantly, the transverse dependence of  $E_x$  and  $E_y$  can be factored out using

$$E_j(\mathbf{r}, t) = F(x, y)A_j(z, t)\exp(i\beta_{0j}z), \quad (6.1.10)$$

where  $F(x, y)$  is the spatial distribution of the single mode supported by the fiber,  $A_j(z, t)$  is the slowly varying amplitude, and  $\beta_{0j}$  is the corresponding propagation constant ( $j = x, y$ ). The dispersive effects are included by expanding the frequency-dependent propagation constant in a manner similar to Eq. (2.3.23). The slowly varying amplitudes,  $A_x$  and  $A_y$ , are found to satisfy the following set of two coupled-mode equations:

$$\begin{aligned} \frac{\partial A_x}{\partial z} + \beta_{1x} \frac{\partial A_x}{\partial t} + \frac{i\beta_2}{2} \frac{\partial^2 A_x}{\partial t^2} + \frac{\alpha}{2} A_x \\ = i\gamma \left( |A_x|^2 + \frac{2}{3} |A_y|^2 \right) A_x + \frac{i\gamma}{3} A_x^* A_y^2 \exp(-2i\Delta\beta z), \end{aligned} \quad (6.1.11)$$

$$\begin{aligned} \frac{\partial A_y}{\partial z} + \beta_{1y} \frac{\partial A_y}{\partial t} + \frac{i\beta_2}{2} \frac{\partial^2 A_y}{\partial t^2} + \frac{\alpha}{2} A_y \\ = i\gamma \left( |A_y|^2 + \frac{2}{3} |A_x|^2 \right) A_y + \frac{i\gamma}{3} A_y^* A_x^2 \exp(2i\Delta\beta z), \end{aligned} \quad (6.1.12)$$

where

$$\Delta\beta = \beta_{0x} - \beta_{0y} = (2\pi/\lambda)B_m = 2\pi/L_B \quad (6.1.13)$$

is related to the linear birefringence of the fiber. The linear or modal birefringence leads to different group velocities for the two polarization components because  $\beta_{1x} \neq \beta_{1y}$  in general. In contrast, the parameters  $\beta_2$  and  $\gamma$  are the same for both polarization components because they have the same wavelength  $\lambda$ .

The last term in Eqs (6.1.11) and (6.1.12) is due to coherent coupling between the two polarization components and leads to degenerate four-wave mixing. Its importance to the process of polarization evolution depends on the extent to which the phase-matching condition is satisfied (see Chapter 10). If the fiber length  $L$  is much larger than the beat length  $L_B$ , the last term in Eqs (6.1.11) and (6.1.12) changes sign often and its contribution averages out to zero. In highly

birefringent fibers ( $L_B \sim 1$  cm typically), the four-wave-mixing term can often be neglected for this reason. In contrast, this term should be retained for weakly birefringent fibers, especially those with short lengths. In that case, it is often convenient to rewrite Eqs (6.1.11) and (6.1.12) using circularly polarized components defined as

$$A_+ = (\bar{A}_x + i\bar{A}_y)/\sqrt{2}, \quad A_- = (\bar{A}_x - i\bar{A}_y)/\sqrt{2}, \quad (6.1.14)$$

where  $\bar{A}_x = A_x \exp(i\Delta\beta z/2)$  and  $\bar{A}_y = A_y \exp(-i\Delta\beta z/2)$ . The variables  $A_+$  and  $A_-$  represent right- and left-handed circularly polarized (often denoted as  $\sigma_+$  and  $\sigma_-$ ) states, respectively, and satisfy somewhat simpler equations:

$$\frac{\partial A_+}{\partial z} + \beta_1 \frac{\partial A_+}{\partial t} + \frac{i\beta_2}{2} \frac{\partial^2 A_+}{\partial t^2} + \frac{\alpha}{2} A_+ = \frac{i\Delta\beta}{2} A_- + \frac{2i\gamma}{3} (|A_+|^2 + 2|A_-|^2) A_+, \quad (6.1.15)$$

$$\frac{\partial A_-}{\partial z} + \beta_1 \frac{\partial A_-}{\partial t} + \frac{i\beta_2}{2} \frac{\partial^2 A_-}{\partial t^2} + \frac{\alpha}{2} A_- = \frac{i\Delta\beta}{2} A_+ + \frac{2i\gamma}{3} (|A_-|^2 + 2|A_+|^2) A_-, \quad (6.1.16)$$

where we assumed that  $\beta_{1x} \approx \beta_{1y} = \beta_1$  for fibers with relatively low birefringence. Notice that the four-wave-mixing terms appearing in Eqs (6.1.11) and (6.1.12) are replaced with a linear coupling term containing  $\Delta\beta$ . At the same time, the relative strength of XPM changes from  $\frac{2}{3}$  to 2 when circularly polarized components are used to describe wave propagation.

### 6.1.3 Elliptically Birefringent Fibers

The derivation of Eqs (6.1.11) and (6.1.12) assumes that the fiber is linearly birefringent, i.e., it has two principal axes along which linearly polarized light remains linearly polarized in the absence of nonlinear effects. Although this is ideally the case for polarization-maintaining fibers, *elliptically* birefringent fibers can be made by twisting a fiber preform during the draw stage [11].

The coupled-mode equations are modified considerably for elliptically birefringent fibers. This case can be treated by replacing Eq. (6.1.1) with

$$\mathbf{E}(\mathbf{r}, t) = \frac{1}{2}(\hat{e}_x E_x + \hat{e}_y E_y) \exp(-i\omega_0 t) + \text{c.c.}, \quad (6.1.17)$$

where  $\hat{e}_x$  and  $\hat{e}_y$  are orthonormal polarization eigenvectors related to the unit vectors  $\hat{x}$  and  $\hat{y}$  used before as [12]

$$\hat{e}_x = \frac{\hat{x} + ir\hat{y}}{\sqrt{1+r^2}}, \quad \hat{e}_y = \frac{r\hat{x} - i\hat{y}}{\sqrt{1+r^2}}. \quad (6.1.18)$$

The parameter  $r$  represents the ellipticity introduced by twisting the preform. It is common to introduce the ellipticity angle  $\theta$  as  $r = \tan(\theta/2)$ . The cases  $\theta = 0$  and  $\pi/2$  correspond to linearly and circularly birefringent fibers, respectively.

Following a procedure similar to that outlined earlier for linearly birefringent fibers, the slowly varying amplitudes  $A_x$  and  $A_y$  are found to satisfy the following set of coupled-mode equations [12]:

$$\begin{aligned} \frac{\partial A_x}{\partial z} + \beta_{1x} \frac{\partial A_x}{\partial t} + \frac{i\beta_2}{2} \frac{\partial^2 A_x}{\partial t^2} + \frac{\alpha}{2} A_x &= i\gamma \left[ (|A_x|^2 + B|A_y|^2)A_x + CA_x^* A_y^2 e^{-2i\Delta\beta z} \right] \\ &\quad + i\gamma D \left[ A_y^* A_x^2 e^{i\Delta\beta z} + (|A_y|^2 + 2|A_x|^2)A_y e^{-i\Delta\beta z} \right], \end{aligned} \quad (6.1.19)$$

$$\begin{aligned} \frac{\partial A_y}{\partial z} + \beta_{1y} \frac{\partial A_y}{\partial t} + \frac{i\beta_2}{2} \frac{\partial^2 A_y}{\partial t^2} + \frac{\alpha}{2} A_y &= i\gamma \left[ (|A_y|^2 + B|A_x|^2)A_y + CA_y^* A_x^2 e^{2i\Delta\beta z} \right] \\ &\quad + i\gamma D \left[ A_x^* A_y^2 e^{-i\Delta\beta z} + (|A_x|^2 + 2|A_y|^2)A_x e^{i\Delta\beta z} \right], \end{aligned} \quad (6.1.20)$$

where the parameters  $B$ ,  $C$ , and  $D$  are related to the ellipticity angle  $\theta$  as

$$B = \frac{2 + 2 \sin^2 \theta}{2 + \cos^2 \theta}, \quad C = \frac{\cos^2 \theta}{2 + \cos^2 \theta}, \quad D = \frac{\sin \theta \cos \theta}{2 + \cos^2 \theta}. \quad (6.1.21)$$

For a linearly birefringent fiber ( $\theta = 0$ ),  $B = \frac{2}{3}$ ,  $C = \frac{1}{3}$ ,  $D = 0$ , and Eqs (6.1.19) and (6.1.20) reduce to Eqs (6.1.11) and (6.1.12), respectively.

Equations (6.1.19) and (6.1.20) can be simplified considerably for optical fibers with large birefringence. For such fibers, the beat length  $L_B$  is much smaller than typical propagation distances. As a result, the exponential factors in the last three terms of Eqs (6.1.19) and (6.1.20) oscillate rapidly, contributing little to the pulse evolution process on average. If these terms are neglected, propagation of optical pulses in an elliptically birefringent fiber is governed by the following set of coupled-mode equations:

$$\frac{\partial A_x}{\partial z} + \beta_{1x} \frac{\partial A_x}{\partial t} + \frac{i\beta_2}{2} \frac{\partial^2 A_x}{\partial t^2} + \frac{\alpha}{2} A_x = i\gamma(|A_x|^2 + B|A_y|^2)A_x, \quad (6.1.22)$$

$$\frac{\partial A_y}{\partial z} + \beta_{1y} \frac{\partial A_y}{\partial t} + \frac{i\beta_2}{2} \frac{\partial^2 A_y}{\partial t^2} + \frac{\alpha}{2} A_y = i\gamma(|A_y|^2 + B|A_x|^2)A_y. \quad (6.1.23)$$

These equations represent an extension of the scalar NLS equation, derived in Section 2.3, without the polarization effects [see Eq. (2.3.27)], to the vector case and are referred to as the coupled NLS equations. The coupling parameter  $B$  depends on the ellipticity angle  $\theta$  [see Eq. (6.1.21)] and can vary from  $\frac{2}{3}$  to 2 for values of  $\theta$  in the range 0 to  $\pi/2$ . For a linearly birefringent fiber,  $\theta = 0$ , and  $B = \frac{2}{3}$ . In contrast,  $B = 2$  for a circularly birefringent fiber ( $\theta = \pi/2$ ). Note also that  $B = 1$  when  $\theta \approx 35^\circ$ . As discussed later, this case is of particular interest because Eqs (6.1.22) and (6.1.23) can be solved with the inverse scattering method only when  $B = 1$  and  $\alpha = 0$ .

## 6.2 NONLINEAR PHASE SHIFT

As seen in Section 6.1, a nonlinear coupling between the two orthogonally polarized components of an optical wave changes the modal refractive index by different amounts for the two components. As a result, the nonlinear effects in birefringent fibers are polarization dependent. In this section we use the coupled NLS equations obtained in the case of high-birefringence fibers to study the XPM-induced nonlinear phase shift and its device applications.

### 6.2.1 Nondispersive XPM

Equations (6.1.22) and (6.1.23) need to be solved numerically when ultrashort optical pulses propagate inside birefringent fibers. However, they can be solved analytically in the case of CW radiation. The CW solution is also applicable for pulses whenever the fiber length  $L$  is much shorter than both the dispersion length  $L_D = T_0^2/|\beta_2|$  and the walk-off length  $L_W = T_0/|\Delta\beta|$ , where  $T_0$  is a measure of the pulse width. As this case can be applicable to pulses as short as 100 ps and sheds considerable physical insight, we discuss it first.

Neglecting the terms with time derivatives in Eqs (6.1.22) and (6.1.23), we obtain the following two ordinary differential equations:

$$\frac{dA_x}{dz} + \frac{\alpha}{2}A_x = i\gamma(|A_x|^2 + B|A_y|^2)A_x, \quad (6.2.1)$$

$$\frac{dA_y}{dz} + \frac{\alpha}{2}A_y = i\gamma(|A_y|^2 + B|A_x|^2)A_y. \quad (6.2.2)$$

These equations describe nondispersive XPM in birefringent fibers and extend the scalar theory of SPM in Section 4.1, to the vector case. They can be solved by using

$$A_x = \sqrt{P_x} e^{-\alpha z/2} e^{i\phi_x}, \quad A_y = \sqrt{P_y} e^{-\alpha z/2} e^{i\phi_y}, \quad (6.2.3)$$

where  $P_x$  and  $P_y$  are the powers and  $\phi_x$  and  $\phi_y$  are the phases associated with the two polarization components. It is easy to deduce that  $P_x$  and  $P_y$  do not change with  $z$ . However, the phases  $\phi_x$  and  $\phi_y$  do change and evolve as

$$\frac{d\phi_x}{dz} = \gamma e^{-\alpha z}(P_x + BP_y), \quad \frac{d\phi_y}{dz} = \gamma e^{-\alpha z}(P_y + BP_x). \quad (6.2.4)$$

Since  $P_x$  and  $P_y$  are constants, the phase equations can be solved easily with the result

$$\phi_x = \gamma(P_x + BP_y)L_{\text{eff}}, \quad \phi_y = \gamma(P_y + BP_x)L_{\text{eff}}, \quad (6.2.5)$$

where the effective fiber length  $L_{\text{eff}} = [1 - \exp(-\alpha L)]/\alpha$  is defined in the same way as in the SPM case [see Eq. (4.1.6)].

It is clear from Eq. (6.2.5) that both polarization components develop a nonlinear phase shift whose magnitude is the sum of the SPM and XPM contributions. In practice, the quantity of practical interest is the relative phase difference given by

$$\Delta\phi_{\text{NL}} \equiv \phi_x - \phi_y = \gamma L_{\text{eff}}(1 - B)(P_x - P_y). \quad (6.2.6)$$

No relative phase shift occurs when  $B = 1$ . However, when  $B \neq 1$ , a relative nonlinear phase shift between the two polarization components occurs if input light is launched such that  $P_x \neq P_y$ . As an example, consider a linearly birefringent fiber for which  $B = \frac{2}{3}$ . If CW light with power  $P_0$  is launched such that it is linearly polarized at an angle  $\theta$  from the slow axis,  $P_x = P_0 \cos^2 \theta$ ,  $P_y = P_0 \sin^2 \theta$ , and the relative phase shift becomes

$$\Delta\phi_{\text{NL}} = (\gamma P_0 L_{\text{eff}}/3) \cos(2\theta). \quad (6.2.7)$$

This  $\theta$ -dependent phase shift has several applications discussed next.

### 6.2.2 Optical Kerr Effect

In the optical Kerr effect, the nonlinear phase shift induced by an intense, high-power, pump beam is used to change the transmission of a weak probe through a nonlinear medium [4]. This effect can be used to make an optical shutter with picosecond response times [6]. It was first observed in optical fibers in 1973 [13] and has attracted considerable attention since then [14–25].

The operating principle of a Kerr shutter can be understood from Figure 6.1. The pump and probe beams are linearly polarized at the fiber input with a  $45^\circ$  angle between their directions of polarization. A crossed polarizer at the fiber output blocks probe transmission in the absence of the pump beam. When the pump is turned on, the refractive indices for the parallel and perpendicular components of the probe (with respect to the direction of pump polarization) become slightly different because of pump-induced birefringence. The phase difference between the two components at the fiber output manifests as a change in the probe polarization, and a portion of the probe intensity is transmitted through the polarizer. The probe transmissivity depends on the pump intensity and can be controlled simply by changing it. In particular, a pulse at the pump wavelength opens the Kerr shutter only during its passage through the fiber. As the probe output at one wavelength can be

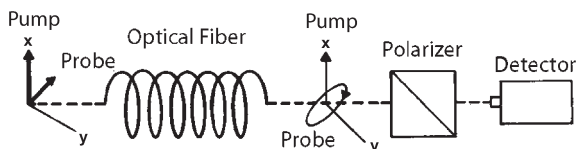


**Figure 6.1** Schematic illustration of a Kerr shutter. Pump and probe beams are linearly polarized at  $45^\circ$  to each other at the input end. Polarizer blocks probe transmission in the absence of pump.

modulated through a pump at a different wavelength, this device is also referred to as the Kerr modulator. It has potential applications in fiber-optical networks requiring all-optical switching.

Equation (6.2.6) cannot be used to calculate the phase difference between the  $x$  and  $y$  components of the probe because the pump and probe beams have different wavelengths in Kerr shutters. We follow a slightly different approach and neglect fiber losses for the moment; they can be included later by replacing  $L$  with  $L_{\text{eff}}$ . The relative phase difference for the probe at the output of a fiber of length  $L$  can always be written as

$$\Delta\phi = (2\pi/\lambda)(\tilde{n}_x - \tilde{n}_y)L, \quad (6.2.8)$$

where  $\lambda$  is the probe wavelength and

$$\tilde{n}_x = n_x + \Delta n_x, \quad \tilde{n}_y = n_y + \Delta n_y. \quad (6.2.9)$$

As discussed earlier, the linear parts  $n_x$  and  $n_y$  of the refractive indices are different because of modal birefringence. The nonlinear parts  $\Delta n_x$  and  $\Delta n_y$  are different because of pump-induced birefringence.

Consider the case of a pump polarized linearly along the  $x$ -axis. The  $x$  component of the probe is polarized parallel to the pump but its wavelength is different. For this reason, the corresponding index change  $\Delta n_x$  must be obtained by using the theory of Section 7.1. If the SPM contribution is neglected,

$$\Delta n_x = 2n_2|E_p|^2, \quad (6.2.10)$$

where  $|E_p|^2$  is the pump intensity? When the pump and probe are orthogonally polarized, only the first term in Eq. (6.1.4) contributes to  $\Delta n_y$  because of different wavelengths of the pump and probe beams [9]. Again neglecting the SPM term,  $\Delta n_y$  becomes

$$\Delta n_y = 2n_2|E_p|^2, \quad b = \chi_{xyy}^{(3)}/\chi_{xxx}^{(3)}. \quad (6.2.11)$$

If the origin of  $\chi^{(3)}$  is purely electronic,  $b = \frac{1}{3}$ . Combining, Eqs (6.2.8)–(6.2.11) the phase difference becomes

$$\Delta\phi \equiv \Delta\phi_L + \Delta\phi_{NL} = (2\pi L/\lambda)(\Delta n_L + n_{2B}|E_p|^2), \quad (6.2.12)$$

where  $\Delta n_L = n_x - n_y$  accounts for linear birefringence, and the Kerr coefficient  $n_{2B}$  is given by

$$n_{2B} = 2n_2(1 - b). \quad (6.2.13)$$

The probe transmittivity  $T_p$  can now be obtained noting that probe light is blocked by the polarizer when  $\Delta\phi = 0$  (see Figure 6.1). When  $\Delta\phi \neq 0$ , fiber acts as a birefringent phase plate, and some probe light passes through the polarizer. The probe transmittivity is related to  $\Delta\phi$  by the simple relation

$$T_p = \frac{1}{4}|1 - \exp(i\Delta\phi)|^2 = \sin^2(\Delta\phi/2). \quad (6.2.14)$$

It becomes 100% when  $\Delta\phi = \pi$  or an odd multiple of  $\pi$ . On the other hand, a phase shift by an even multiple of  $\pi$  blocks the probe completely.

To observe the optical Kerr effect, a polarization-maintaining fiber is generally used to ensure that the pump maintains its state of polarization. The constant phase shift  $\Delta\phi_L$  resulting from linear birefringence, can be compensated by inserting a quarter-wave plate before the polarizer in Figure 6.1. However, in practice,  $\Delta\phi_L$  fluctuates because of temperature and pressure variations, making it necessary to adjust the wave plate continuously. An alternative approach is to use two identical pieces of polarization-maintaining fibers, spliced together such that their fast (or slow) axes are at right angles to each other [18]. As  $\Delta n_L$  changes sign in the second fiber, the net phase shift resulting from linear birefringence is canceled.

Under ideal conditions, the response time of a Kerr shutter would be limited only by the response time of the Kerr nonlinearity (<10 fs for optical fibers). In practice, however, fiber dispersion limits the response time to values that can range from 1 ps to 1 ns depending on the operating parameters [14]. A major limiting factor is the group-velocity mismatch between the pump and the probe. The relative group delay is given by

$$\Delta t_g = |L/v_{g1} - L/v_{g2}|. \quad (6.2.15)$$

It can easily exceed 1 ns for a 100-m-long fiber unless special precautions are taken to reduce the group-velocity mismatch. One possibility is to choose the pump and probe wavelengths on opposite sides of the zero-dispersion wavelength.

Modal birefringence of the fiber sets another limit on the response time. Because of the index difference  $\Delta n_L$ , the orthogonally polarized components of the probe travel at different speeds and develop a relative delay  $\Delta t_p = L \Delta n_L / c$ . For a 100-m-long fiber with  $\Delta n_L = 5 \times 10^{-5}$ ,  $\Delta t_p \approx 17$  ps. It can be reduced by using fibers with smaller birefringence. The use of two fibers spliced together with their fast axes at right angles to each other can nearly eliminate  $\Delta t_p$ . The fundamental limit on the response time is then set by group velocity dispersion (GVD) that broadens the pump pulse during its propagation inside the fiber. It can be reduced to 1 ps or less either by reducing the fiber length or by bringing the pump wavelength closer to the zero-dispersion wavelength.

The minimum pump power required for 100% probe transmission can be estimated by setting  $\Delta\phi_L = 0$  (complete compensation) and  $\Delta\phi_{NL} = \pi$  in Eq. (6.2.12). It is given by

$$P_p = |E_p|^2 A_{\text{eff}} = \lambda A_{\text{eff}} / (2n_{2B}L), \quad (6.2.16)$$

where  $A_{\text{eff}}$  is the effective mode area. The effect of fiber loss can be included by replacing  $L$  with the effective length  $L_{\text{eff}}$  introduced earlier. Using  $n_{2B} = 4 \times 10^{-16} \text{ cm}^2/\text{W}$ ,  $A_{\text{eff}} = 10 \mu\text{m}^2$ , and  $\lambda = 1.06 \mu\text{m}$ , the pump power  $P_p$  is  $\approx 1 \text{ W}$  for a 130-m-long fiber. The power can be reduced by increasing the fiber length, but only at the expense of a slower response time limited by Eq. (6.2.15). In one experiment [15],  $P_p = 0.39 \text{ W}$  was measured for  $L = 580 \text{ m}$  and  $A_{\text{eff}} = 22 \mu\text{m}^2$ . In another experiment [21], the

effective mode area was reduced to  $2 \mu\text{m}^2$ , and a semiconductor laser operating at  $1.3 \mu\text{m}$  was used as a pump. A phase shift of  $17^\circ$  was realized at a pump power of only  $27 \text{ mW}$ . The estimated value of  $P_p L = 11 \text{ W m}$  for this experiment indicates that pump powers  $\sim 50 \text{ mW}$  may be sufficient for 100% probe transmission if 200-m-long fibers were used in each arm of a Mach-Zehnder interferometer.

Equation (6.2.16) can be used to estimate the Kerr coefficient  $n_{2B}$ . Most measurements indicate that  $n_{2B} \approx 4 \times 10^{-16} \text{ cm}^2/\text{W}$  with an experimental uncertainty of  $\sim 20\%$  [13–21]. This value is in agreement with Eq. (6.2.13) if we use  $n_2 \approx 3 \times 10^{-16} \text{ cm}^2/\text{W}$  and  $b = \frac{1}{3}$ . The parameter  $b$  has been measured in an experiment [18] designed to allow an independent measurement of the susceptibility ratio indicated in Eq. (6.2.11). The measured value  $b = 0.34$  suggests that the electronic contribution to  $\chi^{(3)}$  dominates in silica fibers. This conclusion is in agreement with the measurements made using bulk glasses [5].

On the practical side, an all-fiber Kerr shutter has been used for optical sampling [16]. Figure 6.2 shows the experimental set up schematically. A Babinet-Soleil compensator was used to compensate for modal birefringence of the fiber. A highly birefringent piece of fiber was used as a polarizer with about 20-dB extinction ratio. It also served as a filter because fiber losses were quite high at the  $1.06-\mu\text{m}$  pump wavelength. A laser diode at  $0.84 \mu\text{m}$  served as the probe. The sampled probe output was in the form of a sequence of pulses whose separation and width were determined by pump pulses. In this experiment, pump pulses were fairly long ( $\sim 300 \text{ ps}$ ). In a different experiment, 30-ps probe pulses at a repetition rate of  $1.97 \text{ GHz}$  (obtained from a  $1.3-\mu\text{m}$ , gain-switched, distributed feedback semiconductor laser) were demultiplexed using 85-ps pump pulses from a mode-locked Nd:YAG laser [18].

In most experiments on Kerr shutters, it is generally necessary to use bulky high-power lasers to realize optical switching in silica fibers, making practical use of such devices difficult. As evident from Eq. (6.2.16), the product  $P_p L$  can be reduced considerably if optical fibers made with a high-nonlinearity material are used in place of silica fibers. Chalcogenide glasses offer such an opportunity because their nonlinear parameter  $n_2$  is larger by a factor  $\sim 100$  compared with silica. Several experiments have shown that chalcogenide glass fibers offer a solution to making practical nonlinear Kerr shutters operating at high speeds [22–24]. In a 1992 experiment,

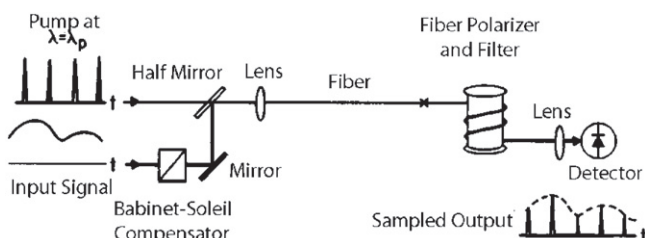


**Figure 6.2 Schematic diagram of an all-optical Kerr shutter used for optical sampling. (After Ref. [16]; © 1985 American Institute of Physics.)**

a 1.319- $\mu\text{m}$  mode-locked Nd:YAG laser in combination with a pulse compressor provided pump pulses of widths in the range 2.5–40 ps at the 100-MHz repetition rate [22]. The fiber length was kept <1 m to avoid large losses associated with the As<sub>2</sub>S<sub>3</sub>-based chalcogenide fiber. In spite of such a small interaction length, the required pump power for optical switching was only  $\sim 5\text{ W}$ .

In a later experiment, all-optical switching was realized using a semiconductor laser as a pump source [23]. Gain switching of a distributed feedback semiconductor laser, in combination with pulse compression, provided 8.2-ps pump pulses at the 100-MHz repetition rate. The peak power of pump pulses was increased to 13.9 W using an erbium-doped fiber amplifier. For a 1-m-long fiber the switched signal pulse had nearly the same width as the pump pulse, demonstrating ultrafast switching on a picosecond time scale. Signal pulses could be switched through the Kerr effect even when the signal was in the form of a 100-GHz pulse train, indicating the potential of a Kerr shutter for demultiplexing a 100-Gb/s communication channel.

A Kerr shutter can also be used for converting the wavelength of a communication channel. Optical pulses representing bits of the channel act as the pump and open the Kerr shutter, but only over their temporal duration. The resulting probe output has the same bit pattern as the pump channel and becomes the wavelength-converted channel at the probe wavelength. In a 2005 experiment [25], a new kind of fiber made with Bi<sub>2</sub>O<sub>3</sub> was used to realize wavelength conversion at 80 Gb/s. The nonlinear parameter was so large for this fiber ( $\gamma = 1100 \text{ W}^{-1}/\text{km}$ ) that the fiber length could be reduced to 1 m. Such a short length helps in mitigating the degradations induced by temperature-dependent fluctuations in local linear birefringence and results in a stable compact device.

### 6.2.3 Pulse Shaping

Nonlinear birefringence induced by an intense pulse can be used to modify the shape of the same pulse, even in the absence of a pump pulse, because its transmission through a combination of fiber and polarizer is generally intensity dependent. As a result, such a device can block low-intensity tails of a pulse while passing the central intense part of the same pulse. This phenomenon of nonlinear polarization rotation can be used to remove a low-intensity pedestal associated with some compressed pulses [26–28]. It can also be used for making fiber-optic logic gates [29] and for the passive mode-locking of fiber lasers [30].

The operating principle of an intensity discriminator is similar to that of the Kerr shutter shown in Figure 6.1. The main difference is that instead of a pump, the signal pulse itself produces nonlinear birefringence and modifies its own state of polarization. To understand the physics behind such a device as simply as possible, let us neglect the GVD effects and use the nondispersive XPM theory of Section 6.2.1. Consider the case of an input beam linearly polarized at an angle  $\theta$  with respect to one of the principal axes ( $x$ -axis) of the fiber. The relative phase shift introduced between the two polarization components is then given by Eq. (6.2.7). This phase

shift allows some power to be transmitted through the polarizer when  $\theta \neq 0$ . The transmittivity  $T_p$  is obtained by noting that

$$A_x = \sqrt{P_0} \cos \theta \exp(i\Delta\phi_{NL}), \quad A_y = \sqrt{P_0} \sin \theta, \quad (6.2.17)$$

where  $\Delta\phi_{NL}$  is the nonlinear phase shift. Because the cross polarizer makes an angle  $\pi/2 + \theta$  from the  $x$ -axis, the total transmitted field becomes  $A_t = \sqrt{P_0} \sin \theta \cos \theta [1 - \exp(i\Delta\phi_{NL})]$ . As a result,  $T_p$  is given by [26]

$$T_p(\theta) = |A_t|^2/P_0 = \sin^2[(\gamma P_0 L/6) \cos(2\theta)] \sin^2(2\theta), \quad (6.2.18)$$

where Eq. (6.2.7) was used. In the case of optical pulses propagating through the fiber, the product  $\gamma P_0 L$  is related to the maximum phase shift  $\phi_{max}$  induced by SPM [see Eq. (4.1.6)] and can also be related to the nonlinear length scale  $L_{NL}$  through the relation

$$\phi_{max} = \gamma P_0 L = L/L_{NL}. \quad (6.2.19)$$

Pulse shaping occurs because  $T_p$  is power dependent at a given angle  $\theta$ . If the angle  $\theta$  is set to maximize the transmission at the pulse peak, the wings are removed because of their relatively low power levels. As a result, the output pulse becomes narrower than the input pulse. This behavior has been observed experimentally [27]. The optimum value of  $\theta$  depends on the peak power  $P_0$ . Figure 6.3 shows  $T_p$

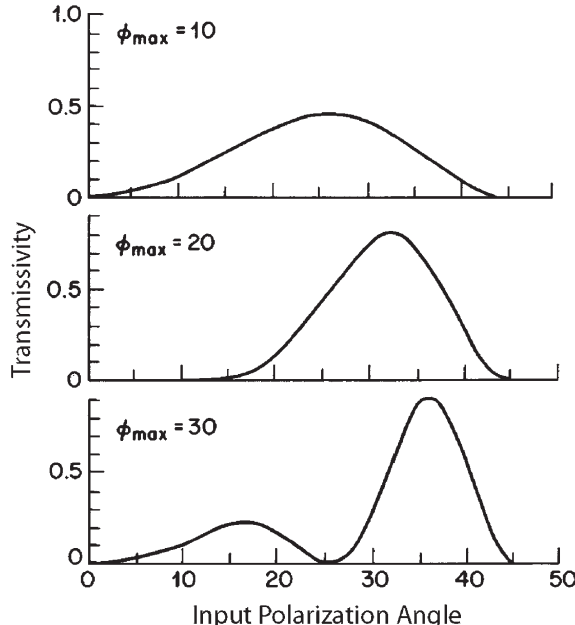


**Figure 6.3** Transmittivity  $T_p$  as a function of input polarization angle  $\theta$  for three different peak powers corresponding to  $\phi_{max} = 10, 20$ , and  $30$ . (After Ref. [26]; © 1982 OSA.)

as a function of  $\theta$  for three values of  $\phi_{\max}$ . The transmission can approach 90% at  $\theta = 36.2^\circ$  for  $\phi_{\max} = 30$ .

Experimental results on pulse shaping indicate that the observed behavior does not always agree with Eq. (6.2.18). In particular, this equation predicts that  $T_p = 0$  for  $\theta = 45^\circ$ , i.e., the input light is blocked by the polarizer when the two polarization components are excited with equal amplitudes. In practice, this is not the case. The reason for this discrepancy can be traced back to the neglect of the last term in Eqs (6.1.11) and (6.1.12). A more accurate theory should include this term. In the CW or the quasi-CW case for which the dispersive effects are negligible, Eqs (6.1.11) and (6.1.12) can be solved analytically by neglecting the time derivatives and the loss terms. The analytic solution is given in the next section. Its use shows that Eq. (6.2.18) is quite accurate in the case of highly birefringent fibers ( $\Delta\beta L \gg 1$ ) except near  $\theta = 45^\circ$ . In low-birefringence fibers, transmissivity can be quite different from that given in Eq. (6.2.18). Figure 6.4 shows  $T_p$  as a function of  $\theta$  for  $\Delta\beta L = 2\pi$  and  $\phi_{\max} = 6.5\pi$ . A comparison with the prediction of Eq. (6.2.18) reveals the importance of including linear birefringence. Physically, the linear and nonlinear birefringence contributions to the refractive index compete with each other, and both should be included.

### 6.3 EVOLUTION OF POLARIZATION STATE

An accurate description of the nonlinear polarization effects in birefringent fibers requires simultaneous consideration of both the modal birefringence and self-induced nonlinear birefringence [31–47]. Evolution of the two polarization components along such fibers is governed by Eqs (6.1.11) and (6.1.12) or their variants. However, before turning to the case of pulse propagation, it is useful to consider how

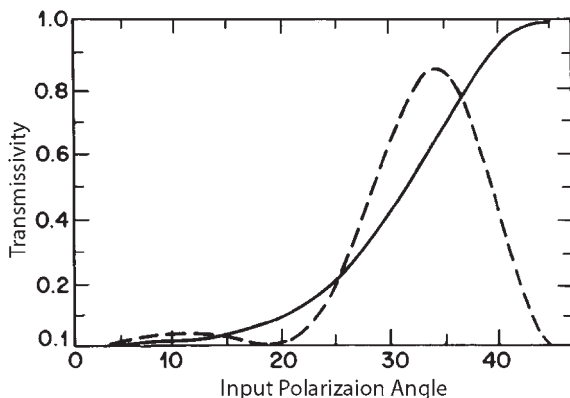


**Figure 6.4** Transmittivity  $T_p$  as a function of the input polarization angle  $\theta$  when the effect of linear birefringence is included for  $\Delta\beta L = 2\pi$  and  $\phi_{\max} = 6.5\pi$ . The dashed line shows the behavior when  $\Delta\beta = 0$ . (After Ref. [31]; © 1985 American Institute of Physics.)

the state of polarization evolves within the fiber when a CW (or quasi-CW) beam is launched at the input end.

### 6.3.1 Analytic Solution

In place of Eqs (6.1.11) and (6.1.12), it is more convenient to use Eqs (6.1.15) and (6.1.16) written in terms of the circularly polarized components. The terms containing time derivatives can be set to zero in the quasi-CW case. If we also neglect fiber losses, Eqs (6.1.15) and (6.1.16) reduce to

$$\frac{dA_+}{dz} = \frac{i\Delta\beta}{2} A_- + \frac{2i\gamma}{3} (|A_+|^2 + 2|A_-|^2) A_+, \quad (6.3.1)$$

$$\frac{dA_-}{dz} = \frac{i\Delta\beta}{2} A_+ + \frac{2i\gamma}{3} (|A_-|^2 + 2|A_+|^2) A_-. \quad (6.3.2)$$

Consider first the low-power case and neglect the nonlinear effects ( $\gamma = 0$ ). The resulting linear equations are easily solved. As an example, when the input beam with power  $P_0$  is  $\sigma_+$ -polarized, the solution is given by

$$A_+(z) = \sqrt{P_0} \cos(\pi z/L_B), \quad A_-(z) = i\sqrt{P_0} \sin(\pi z/L_B), \quad (6.3.3)$$

where the beat length  $L_B = 2\pi/(\Delta\beta)$ . The state of polarization is generally elliptical and evolves periodically with a period equal to the beat length. The ellipticity and the azimuth of the polarization ellipse at any point along the fiber can be obtained using

$$e_p = \frac{|A_+| - |A_-|}{|A_+| + |A_-|}, \quad \theta = \frac{1}{2} \tan^{-1} \left( \frac{A_+}{A_-} \right). \quad (6.3.4)$$

Equations (6.3.1) and (6.3.2) can be solved analytically even when nonlinear effects become important. For this purpose, we introduce four real variables using

$$A_{\pm} = \left( \frac{3\Delta\beta}{2\gamma} \right)^{1/2} \sqrt{p_{\pm}} \exp(i\phi_{\pm}), \quad (6.3.5)$$

and obtain the following three equations satisfied by the normalized powers  $p_+$  and  $p_-$  and the phase difference  $\psi \equiv \phi_+ - \phi_-$ :

$$\frac{dp_+}{dz} = 2\sqrt{p_+ p_-} \sin \psi, \quad (6.3.6)$$

$$\frac{dp_-}{dz} = -2\sqrt{p_+ p_-} \sin \psi, \quad (6.3.7)$$

$$\frac{d\psi}{dz} = \frac{p_- - p_+}{\sqrt{p_+ p_-}} \cos \psi + 2(p_- - p_+), \quad (6.3.8)$$

where  $Z = (\Delta\beta)z/2$ . These equations have the following two quantities that remain constant along the fiber [44]:

$$p = p_+ + p_-, \quad \Gamma = \sqrt{p_+ p_-} \cos \psi + p_+ p_-. \quad (6.3.9)$$

Note that  $p$  is related to the total power  $P_0$  launched into the fiber through  $p = P_0/P_{\text{cr}}$ , where  $P_{\text{cr}}$  is obtained from Eq. (6.3.5) and is given by

$$P_{\text{cr}} = 3|\Delta\beta|/(2\gamma). \quad (6.3.10)$$

Because of the two constants of motion, Eqs (6.3.6)–(6.3.8) can be solved analytically in terms of the elliptic functions. The solution for  $p_+$  is [34]

$$p_+(z) = \frac{1}{2}p - \sqrt{m|q|}\text{cn}(x), \quad (6.3.11)$$

where  $\text{cn}(x)$  is a Jacobian elliptic function with the argument

$$x = \sqrt{|q|}(\Delta\beta)z + K(m), \quad (6.3.12)$$

$K(m)$  is the quarter-period, and  $m$  and  $q$  are defined as

$$m = \frac{1}{2}[1 - \text{Re}(q)/|q|], \quad q = 1 + p \exp(i\psi_0). \quad (6.3.13)$$

Here  $\psi_0$  is the value of  $\psi$  at  $z = 0$ . Both  $p_-(z)$  and  $\psi(z)$  can be obtained in terms of  $p_+(z)$  using Eq. (6.3.9). The ellipticity and the azimuth of the polarization ellipse at any point along the fiber are then obtained from Eq. (6.3.4) after noting that  $\theta = \psi/2$ .

It is useful to show the evolution of the polarization state as trajectories in an ellipticity–azimuth phase plane. Figure 6.5 shows such phase-space trajectories in the cases of (a) low input power ( $p \ll 1$ ) and (b) high input power ( $p = 3$ ). In the low-power case, all trajectories close, indicating the oscillatory evolution of the polarization state [see Eq. (6.3.3)]. However, at power levels such that  $p > 1$ , a “seperatrix” divides the phase space into two distinct regions. In the region near  $e_p = 0$  and  $\theta = 0$

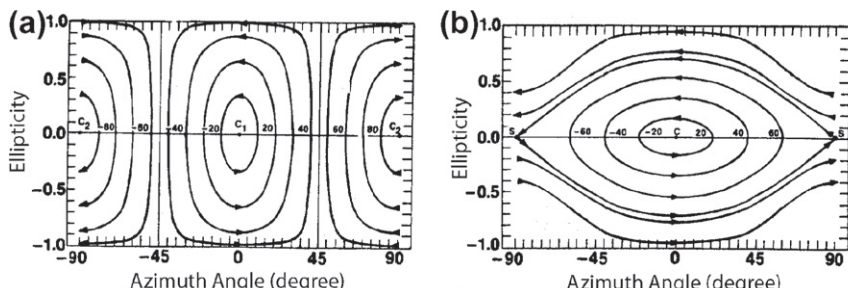


Figure 6.5 Phase-space trajectories representing the evolution of the polarization state along the fiber for (a)  $p \ll 1$  and (b)  $p = 3$ . (After Ref. [34]; © 1986 OSA.)

(light polarized close to the slow axis), trajectories form closed orbits, and the polarization evolution is qualitatively similar to the low-power case. However, when light is polarized close to the fast axis, nonlinear rotation of the polarization ellipse leads to qualitatively different behavior because the fast axis corresponds to an unstable saddle point.

One can use the analytic solution to find the “fixed points” in the phase space. A fixed point represents a polarization state that does not change as light propagates inside the fiber. Below the critical power ( $p < 1$ ), light polarized linearly ( $e_p = 0$ ) along the slow and fast axes ( $\theta = 0$  and  $\pi/2$ ) represents two stable fixed points. At the critical power ( $p = 1$ ), the fast-axis fixed point exhibits a pitchfork bifurcation. Beyond this power level, the linear-polarization state along the fast axis becomes unstable, but two new elliptically polarized states emerge as fixed points. These new polarization eigenstates are discussed next using the Poincaré-sphere representation.

### 6.3.2 Poincaré-Sphere Representation

An alternative approach to describing the evolution of the polarization state in optical fibers is based on the rotation of the Stokes vector on the Poincaré sphere [33]. In this case, it is useful to write Eqs (6.3.1) and (6.3.2) in terms of linearly polarized components using Eq. (6.1.14). The resulting equations are

$$\frac{d\bar{A}_x}{dz} - \frac{i}{2}(\Delta\beta)\bar{A}_x = \frac{2i\gamma}{3} \left( |\bar{A}_x|^2 + \frac{2}{3}|\bar{A}_y|^2 \right) \bar{A}_x + \frac{i\gamma}{3}\bar{A}_x^*\bar{A}_y, \quad (6.3.14)$$

$$\frac{d\bar{A}_y}{dz} + \frac{i}{2}(\Delta\beta)\bar{A}_y = \frac{2i\gamma}{3} \left( |\bar{A}_y|^2 + \frac{2}{3}|\bar{A}_x|^2 \right) \bar{A}_y + \frac{i\gamma}{3}\bar{A}_y^*\bar{A}_x. \quad (6.3.15)$$

These equations can also be obtained from Eqs (6.1.11) and (6.1.12).

At this point, we introduce the four real variables known as the *Stokes parameters* and defined as

$$\begin{aligned} S_0 &= |\bar{A}_x|^2 + |\bar{A}_y|^2, & S_1 &= |\bar{A}_x|^2 - |\bar{A}_y|^2, \\ S_2 &= 2\operatorname{Re}(\bar{A}_x^*\bar{A}_y), & S_3 &= 2\operatorname{Im}(\bar{A}_x^*\bar{A}_y), \end{aligned} \quad (6.3.16)$$

and rewrite Eqs (6.3.14) and (6.3.15) in terms of them. After considerable algebra, we obtain

$$\frac{dS_0}{dz} = 0, \quad \frac{dS_1}{dz} = \frac{2\gamma}{3}S_2S_3, \quad (6.3.17)$$

$$\frac{dS_2}{dz} = -(\Delta\beta)S_3 - \frac{2\gamma}{3}S_1S_3, \quad \frac{dS_3}{dz} = (\Delta\beta)S_2. \quad (6.3.18)$$

It can be easily verified from Eq. (6.3.16) that  $S_0^2 = S_1^2 + S_2^2 + S_3^2$ . As  $S_0$  is independent of  $z$  from Eq. (6.3.17), the Stokes vector  $\mathbf{S}$  with components  $S_1$ ,  $S_2$ , and  $S_3$

moves on the surface of a sphere of radius  $S_0$  as the CW light propagates inside the fiber. This sphere is known as the Poincaré sphere and provides a visual description of the polarization state. In fact, Eqs (6.3.17) and (6.3.18) can be written in the form of a single vector equation as [33]

$$\frac{d\mathbf{S}}{dz} = \mathbf{W} \times \mathbf{S}, \quad (6.3.19)$$

where the vector  $\mathbf{W} = \mathbf{W}_L + \mathbf{W}_{NL}$  such that

$$\mathbf{W}_L = (\Delta\beta, 0, 0), \quad \mathbf{W}_{NL} = (0, 0, -2\gamma S_3/3). \quad (6.3.20)$$

Equation (6.3.19) includes linear as well as nonlinear birefringence. It describes the evolution of the polarization state of a CW optical field within the fiber under quite general conditions.

Figure 6.6 shows motion of the Stokes vector on the Poincaré sphere in several different cases. In the low-power case, nonlinear effects can be neglected by setting  $\gamma = 0$ . As  $\mathbf{W}_{NL} = 0$  in that case, the Stokes vector rotates around the  $S_1$ -axis with an angular velocity  $\Delta\beta$  (upper left sphere in Figure 6.6). This rotation is equivalent to the periodic solution given in Eq. (6.3.3) obtained earlier. If the Stokes vector

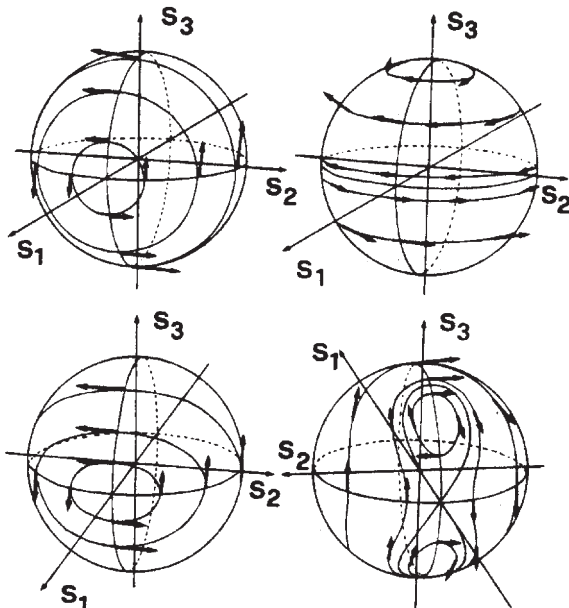


**Figure 6.6** Trajectories showing the motion of the Stokes vector on the Poincaré sphere.  
 (a) Linear birefringence case (upper left); (b) nonlinear case with  $\Delta\beta=0$  (upper right);  
 (c) mixed case with  $\Delta\beta>0$  and  $P_0>P_{cr}$  (lower row). Left and right spheres in the bottom row  
 show the front and back of the Poincaré sphere. (After Ref. [33]; © 1986 OSA.)

is initially oriented along the  $S_1$ -axis, it remains fixed. This can also be seen from the steady-state ( $z$ -invariant) solution of Eqs (6.3.17) and (6.3.18) because  $(S_0, 0, 0)$  and  $(-S_0, 0, 0)$  represent their fixed points. These two locations of the Stokes vector correspond to the linearly polarized incident light oriented along the slow and fast axes, respectively.

In the purely nonlinear case of isotropic fibers ( $\Delta\beta = 0$ ),  $\mathbf{W}_L = 0$ . The Stokes vector now rotates around the  $S_3$ -axis with an angular velocity  $2\gamma S_3/3$  (upper right sphere in Figure 6.6). This rotation is referred to as self-induced ellipse rotation, or as nonlinear polarization rotation, because it has its origin in the nonlinear birefringence. Two fixed points in this case correspond to the north and south poles of the Poincaré sphere and represent right and left circular polarizations, respectively.

In the mixed case, the behavior depends on the power of incident light. As long as  $P_0 < P_{\text{cr}}$ , nonlinear effects play a minor role, and the situation is similar to the linear case. At higher power levels, the motion of the Stokes vector on the Poincaré sphere becomes quite complicated because  $\mathbf{W}_L$  is oriented along the  $S_1$ -axis while  $\mathbf{W}_{\text{NL}}$  is oriented along the  $S_3$ -axis. Moreover, the nonlinear rotation of the Stokes vector along the  $S_3$ -axis depends on the magnitude of  $S_3$  itself. The bottom row in Figure 6.6 shows motion of the Stokes vector on the front and back of the Poincaré sphere in the case  $P_0 > P_{\text{cr}}$ . When input light is polarized close to the slow axis (left sphere), the situation is similar to the linear case. However, the behavior is qualitatively different when input light is polarized close to the fast axis (right sphere).

To understand this asymmetry, let us find the fixed points of Eqs (6.3.17) and (6.3.18) by setting the  $z$  derivatives to zero. The location and number of fixed points depend on the beam power  $P_0$  launched inside the fiber. More specifically, the number of fixed points changes from two to four at a critical power level  $P_{\text{cr}}$  defined in Eq. (6.3.10). For  $P_0 < P_{\text{cr}}$ , only two fixed points,  $(S_0, 0, 0)$  and  $(-S_0, 0, 0)$ , occur; these are identical to the low-power case. In contrast, when  $P_0 > P_{\text{cr}}$ , two new fixed points emerge. The components of the Stokes vector at the location of the new fixed points on the Poincaré sphere are given by [46]

$$S_1 = -P_{\text{cr}}, \quad S_2 = 0, \quad S_3 = \pm\sqrt{P_0^2 - P_{\text{cr}}^2}. \quad (6.3.21)$$

These two fixed points correspond to elliptically polarized light and occur on the back of the Poincaré sphere in Figure 6.6 (lower right). At the same time, the fixed point  $(-S_0, 0, 0)$ , corresponding to light polarized linearly along the fast axis, becomes unstable. This is equivalent to the pitchfork bifurcation discussed earlier. If the input beam is polarized elliptically with its Stokes vector oriented as indicated in Eq. (6.3.21), the polarization state will not change inside the fiber. When the polarization state is close to the new fixed points, the Stokes vector forms a close loop around the elliptically polarized fixed point. This behavior corresponds to the analytic solution discussed earlier. However, if the polarization state is close to the unstable fixed point  $(-S_0, 0, 0)$ , small changes in input polarization can induce large changes at the output. This issue is discussed next.

### 6.3.3 Polarization Instability

The polarization instability manifests as large changes in the output state of polarization when the input power or the polarization state of a CW beam is changed slightly [33–35]. The presence of polarization instability shows that slow and fast axes of a polarization-preserving fiber are not entirely equivalent.

The origin of polarization instability can be understood from the following qualitative argument [34]. When the input beam is polarized close to the slow axis ( $x$ -axis if  $n_x > n_y$ ), nonlinear birefringence adds to intrinsic linear birefringence, making the fiber more birefringent. By contrast, when the input beam is polarized close to the fast axis, nonlinear effects decrease total birefringence by an amount that depends on the input power. As a result, the fiber becomes less birefringent, and the effective beat length  $L_B^{\text{eff}}$  increases. At a critical value of the input power nonlinear birefringence can cancel intrinsic birefringence completely, and  $L_B^{\text{eff}}$  becomes infinite. With a further increase in the input power, the fiber again becomes birefringent but the roles of the slow and fast axes are reversed. Clearly large changes in the output polarization state can occur when the input power is close to the critical power necessary to balance the linear and nonlinear birefringences. Roughly speaking, the polarization instability occurs when the input peak power is large enough to make the nonlinear length  $L_{\text{NL}}$  comparable to the intrinsic beat length  $L_B$ .

The period of the elliptic function in Eq. (6.3.11) determines the effective beat length as [34]

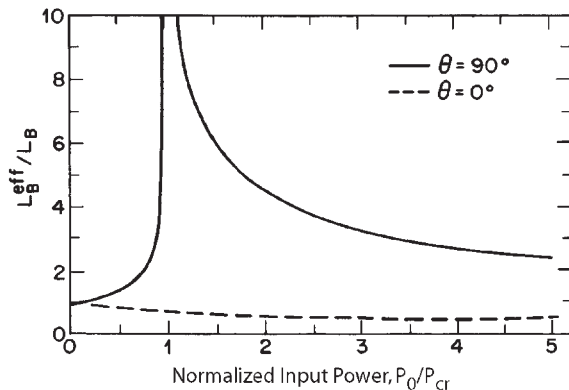
$$L_B^{\text{eff}} = \frac{2K(m)}{\pi\sqrt{|q|}} L_B, \quad (6.3.22)$$

where  $L_B$  is the low-power beat length,  $K(m)$  is the quarter-period of the elliptic function, and  $m$  and  $q$  are given by Eq. (6.3.13) in terms of the normalized input power defined as  $p = P_0/P_{\text{cr}}$ . In the absence of nonlinear effects,  $p = 0$ ,  $q = 1$ , and we recover

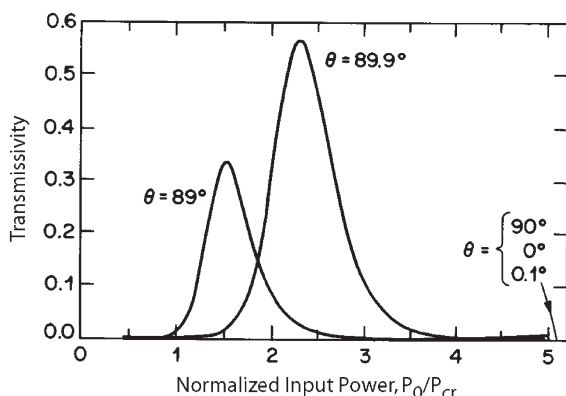
$$L_B^{\text{eff}} = L_B = 2\pi/|\Delta\beta|. \quad (6.3.23)$$

Figure 6.7 shows how  $L_B^{\text{eff}}$  varies with  $p$  for  $\theta = 0^\circ$  and  $\theta = 90^\circ$ . The effective beat length becomes infinite when  $P_0 = P_{\text{cr}}$  and  $\theta = 90^\circ$  because of complete cancellation between the linear and nonlinear birefringences [35]. This is the origin of polarization instability. The critical power level  $P_{\text{cr}}$  at which  $L_B^{\text{eff}}$  becomes infinite is the same at which the number of fixed points on the Poincaré sphere changes from 2 to 4. Thus, polarization instability can be interpreted in terms of the emergence of elliptically polarized fixed points on the Poincaré sphere. The two viewpoints are identical.

As a result of large changes in  $L_B^{\text{eff}}$ , the output polarization state can change drastically when  $P_0$  is close to  $P_{\text{cr}}$  and the input beam is polarized close to the fast axis. Figure 6.8 shows the transmittivity  $T_p$  as a function of the input power for several values of  $\theta$  after assuming that a crossed polarizer at the fiber output blocks the light at low intensities (see Figure 6.1). When  $\theta = 0^\circ$  or  $90^\circ$ ,  $T_p$  remains zero at all power



**Figure 6.7** Effective beat length as a function of the input power for beams polarized along the fast (solid line) and slow (dashed line) axes. (After Ref. [34]; © 1986 OSA.)



**Figure 6.8** Transmittivity of a birefringent fiber of length  $L = L_B$  as a function of the input power for different input angles. (After Ref. [34]; © 1986 OSA.)

levels. Small changes in  $\theta$  near the slow axis still keep  $T_p$  near zero. However,  $T_p$  changes dramatically when  $\theta$  is changed slightly near the fast axis. Note the extreme sensitivity of  $T_p$  to the input polarization angle as  $\theta$  is varied from  $89^\circ$  to  $90^\circ$ . Figure 6.8 is drawn for the case  $(\Delta\beta)L = 2\pi$  or  $L = L_B$ . However, the qualitative behavior remains the same for other fiber lengths as well.

Polarization instability was first observed in 1986 by transmitting 80-ps pulses (at 532 nm) through a 53-cm-long fiber with a measured intrinsic beat length  $L_B \approx 50$  cm [37]. The input pulses were right-circularly polarized and passed through a circular analyzer at the fiber output that transmitted only left-circularly polarized light. The shape of output pulses was found to change dramatically when the peak power exceeded a critical value. The measured critical power and the output pulse shapes

were in agreement with the theoretical predictions. In a later experiment, polarization instability led to significant enhancement of weak intensity modulations when the input signal was polarized near the fast axis of a low-birefringence fiber [44]. The 200-ns input pulses were obtained from a Q-switched Nd:YAG laser operating at 1.06  $\mu\text{m}$ . The intensity of these pulses exhibited 76-MHz modulation because of longitudinal-mode beating inside the laser. These small-amplitude modulations were unaffected when the signal was polarized near the slow axis of the fiber, but became amplified by as much as a factor of 6 when input pulses were polarized near the fast axis. The experimental results were in good qualitative agreement with theory, especially when the theory was generalized to include twisting of the fiber that resulted in elliptical birefringence [44].

The power-dependent transmissivity seen in Figure 6.8 can be useful for optical switching. Self switching of linearly polarized beams induced by polarization instability has been demonstrated in silica fibers [45]. It can also be used to switch the polarization state of an intense beam through a weak pulse. Polarization switching can also occur for solitons [47]. In all cases, the input power required for switching is quite large unless fibers with low modal birefringence are used. A fiber with a beat length  $L_B = 1 \text{ m}$  requires  $P_0 \sim 1 \text{ kW}$  if we use  $\gamma = 10 \text{ W}^{-1}/\text{km}$  in Eq. (6.3.10). This value becomes larger by a factor of 100 or more when high-birefringence fibers are used. For this reason, polarization instability is not of concern when highly birefringent fibers are used because  $P_0$  remains  $<1 \text{ kW}$  in most experiments.

### 6.3.4 Polarization Chaos

Polarization instability can lead to chaos in the output polarization state if linear birefringence of a fiber is modulated along its length. This can occur if the fiber is uniformly twisted while being wound onto a drum. Modulated birefringence can also be introduced during fiber fabrication through periodic rocking of the preform or by means of a periodic distribution of stress. The effects of modulated linear birefringence on evolution of the polarization state have been studied [39–42]. This section considers twisted fibers briefly.

Twisting of birefringent fibers produces two effects simultaneously. First, the principal axes are no longer fixed but rotate in a periodic manner along the fiber length. Second, shear strain induces circular birefringence in proportion to the twist rate. When both of these effects are included, Eqs (6.3.1) and (6.3.2) take the following form [44]:

$$\frac{dA_+}{dz} = ib_c A_+ + \frac{i\Delta\beta}{2} e^{2ir_t z} A_- + \frac{2i\gamma}{3} (|A_+|^2 + 2|A_-|^2) A_+, \quad (6.3.24)$$

$$\frac{dA_-}{dz} = ib_c A_- + \frac{i\Delta\beta}{2} e^{-2ir_t z} A_+ + \frac{2i\gamma}{3} (|A_-|^2 + 2|A_+|^2) A_-, \quad (6.3.25)$$

where  $b_c = hr_t/2\bar{n}$  is related to circular birefringence,  $r_t$  is the twist rate per unit length, and  $\bar{n}$  is the average mode index. The parameter  $h$  has a value of  $\sim 0.15$  for

silica fibers. The preceding equations can be used to find the fixed points, as done in Section 6.3.1 for an untwisted fiber. Above a critical power level, we again find four fixed points. As a result, polarization instability still occurs along the fast axis but the critical power becomes larger.

Birefringence modulation can also be included by making the parameter  $\Delta\beta$  in Eqs (6.3.1) and (6.3.2) a periodic function of  $z$  such that  $\Delta\beta = \Delta\beta_0[1 - i\epsilon \cos(b_m z)]$ , where  $\epsilon$  is the amplitude and  $b_m$  is the spatial frequency of modulation [42]. The resulting equations can not be solved analytically but one can use the phase-space or the Poincaré-sphere approach to study evolution of the polarization state approximately [39–42]. This approach shows that the motion of the Stokes vector on the Poincaré sphere becomes chaotic in the sense that polarization does not return to its original state after each successive period of modal birefringence  $\Delta\beta$ . Such studies are useful for estimating the range of parameter values that must be maintained to avoid chaotic switching if the fiber was to be used as an optical switch.

## 6.4 VECTOR MODULATION INSTABILITY

This section extends the scalar analysis of Section 5.1, to the vector case in which a CW beam, when launched into a birefringent fiber, excites both polarization components simultaneously. Similar to the scalar case, modulation instability is expected to occur in the anomalous-GVD region of the fiber. The main issue is whether the XPM-induced coupling can destabilize the CW state even when the wavelength of the CW beam is in the normal-GVD regime of the fiber. Vector modulation instability in an isotropic nonlinear medium (no birefringence) was predicted as early as 1970 using the coupled NLS equations [48]. In the context of birefringent fibers, it has been studied extensively since 1988, both theoretically and experimentally [49–68]. Since the qualitative behavior is different for weakly and strongly birefringent fibers, we consider the two cases separately.

### 6.4.1 Low-Birefringence Fibers

In the case of low-birefringence fibers, one must retain the coherent-coupling term in Eqs (6.1.11) and (6.1.12) in a study of modulation instability [49]. As before, it is easier to use Eqs (6.1.15) and (6.1.16), written in terms of the circularly polarized components of the optical field. The steady-state or CW solution of these equations is given in Section 6.3 but is quite complicated to use for the analysis of modulation instability as it involves elliptic functions. The problem becomes tractable when the polarization state of the incident CW beam is oriented along a principal axis of the fiber.

Consider first the case in which the polarization state is oriented along the fast axis ( $A_x = 0$ ). This case is especially interesting because the polarization instability discussed in Section 6.3 can also occur. If fiber losses are neglected by setting  $\alpha = 0$ , the steady-state solution becomes

$$\bar{A}_\pm(z) = \pm i\sqrt{P_0/2} \exp(i\gamma P_0 z), \quad (6.4.1)$$

where  $P_0$  is the input power. Following the procedure of Section 5.1, the stability of the steady state is examined by assuming a solution in the form

$$A_{\pm}(z, t) = \pm[i\sqrt{P_0/2} + a_{\pm}(z, t)] \exp(i\gamma P_0 z), \quad (6.4.2)$$

where  $a_{\pm}(z, t)$  is a small perturbation. Using Eq. (6.4.2) in Eqs (6.1.15) and (6.1.16) and linearizing in  $a_+$  and  $a_-$ , we obtain a set of two coupled linear equations. These equations can be solved by assuming a solution of the form

$$a_{\pm} = u_{\pm} \exp[i(Kz - \Omega t)] + iv_{\pm} \exp[-i(Kz - \Omega t)], \quad (6.4.3)$$

where  $K$  is the wave number and  $\Omega$  is the frequency of perturbation. We then obtain a set of four algebraic equations for  $u_{\pm}$  and  $v_{\pm}$ . This set has a nontrivial solution only when the perturbation satisfies the following dispersion relation [49]:

$$[(K - \beta_1 \Omega)^2 - C_1][(K - \beta_1 \Omega)^2 - C_2] = 0, \quad (6.4.4)$$

where

$$C_1 = \frac{1}{2}\beta_2\Omega^2 \left( \frac{1}{2}\beta_2\Omega^2 + 2\gamma P_0 \right), \quad (6.4.5)$$

$$C_2 = \left( \frac{1}{2}\beta_2\Omega^2 + \Delta\beta - 2\gamma P_0/3 \right) \left( \frac{1}{2}\beta_2\Omega^2 + \Delta\beta \right). \quad (6.4.6)$$

As discussed in Section 5.1, the steady-state solution becomes unstable if the wave number  $K$  has an imaginary part for some values of  $\Omega$ , indicating that a perturbation at that frequency would grow exponentially along the fiber with the power gain  $g = 2 \operatorname{Im}(K)$ . The nature of modulation instability depends strongly on whether the input power  $P_0$  is below or above the polarization-instability threshold  $P_{\text{cr}}$  given in Eq. (6.3.10). For  $P_0 < P_{\text{cr}}$ , modulation instability occurs only in the case of anomalous dispersion, and the results are similar to those of Section 5.1. The effect of XPM is to reduce the gain from that of Eq. (5.1.9), but the maximum gain occurs at the same value of  $\Omega$  (see Figure 5.1).

It is easy to deduce from Eq. (6.4.4) that modulation instability can occur even in the normal-dispersion regime of the fiber ( $\beta_2 > 0$ ) provided  $C_2 < 0$ . This condition is satisfied for frequencies in the range  $0 < |\Omega| < \Omega_{\text{c1}}$ , where

$$\Omega_{\text{c1}} = (4\gamma/3\beta_2)^{1/2} \sqrt{P_0 - P_{\text{cr}}}. \quad (6.4.7)$$

Thus,  $P_0 > P_{\text{cr}}$  is required for modulation instability to occur in the normal-dispersion regime of the fiber. When this condition is satisfied, the gain is given by

$$g(\Omega) = |\beta_2| \sqrt{(\Omega^2 + \Omega_{\text{c2}}^2)(\Omega_{\text{c1}}^2 - \Omega^2)}, \quad (6.4.8)$$

with

$$\Omega_{\text{c2}} = (2\Delta\beta/\beta_2)^{1/2}. \quad (6.4.9)$$

Consider now the case in which the CW beam is polarized along the slow axis ( $A_y = 0$ ). We can follow essentially the same steps to find the dispersion relation  $K(\Omega)$ . In fact, Eqs (6.4.4)–(6.4.6) remain applicable if we change the sign of  $\Delta\beta$ . Modulation instability can still occur in the normal-dispersion regime of the fiber but the gain exists only for frequencies in the range  $\Omega_{c2} < |\Omega| < \Omega_{c3}$ , where

$$\Omega_{c3} = (4\gamma/3\beta_2)^{1/2} \sqrt{P_0 + P_{cr}}. \quad (6.4.10)$$

The instability gain is now given by

$$g(\Omega) = |\beta_2| \sqrt{(\Omega^2 - \Omega_{c2}^2)(\Omega_{c3}^2 - \Omega^2)}. \quad (6.4.11)$$

**Figure 6.9** compares the gain spectra for light polarized along the slow and fast axes using  $\beta_2 = 60 \text{ ps}^2/\text{km}$  and  $\gamma = 25 \text{ W}^{-1}/\text{km}$  for a fiber with a beat length  $L_B = 5 \text{ m}$ . For these parameter values,  $p = 1$  at an input power of 75.4 W. At a power level of 100 W,  $p = 1.33$  (left part) while  $p > 2$  at 200 W (right part). The most noteworthy feature of **Figure 6.9** is that, in contrast with the gain spectra of Figure 5.1, the gain does not vanish near  $\Omega = 0$  when light is polarized along the fast axis such that  $p > 1$ . This is a manifestation of the polarization instability discussed in Section 6.3, occurring only when the input beam is polarized along the fast axis. When  $p < 2$ , the gain is larger for CW light polarized along the slow axis. However, the three peaks become comparable as  $p$  approaches 2. When  $p$  exceeds 2, the fast-axis gain spectrum develops a dip at  $\Omega = 0$ , and the gain peak occurs for a finite value of  $\Omega$ . In that case, the CW beam would develop spectral sidebands irrespective of whether it is polarized along the slow or fast axis. This situation is similar to the scalar case of Section 5.1. The new feature is that the sidebands can develop even in the

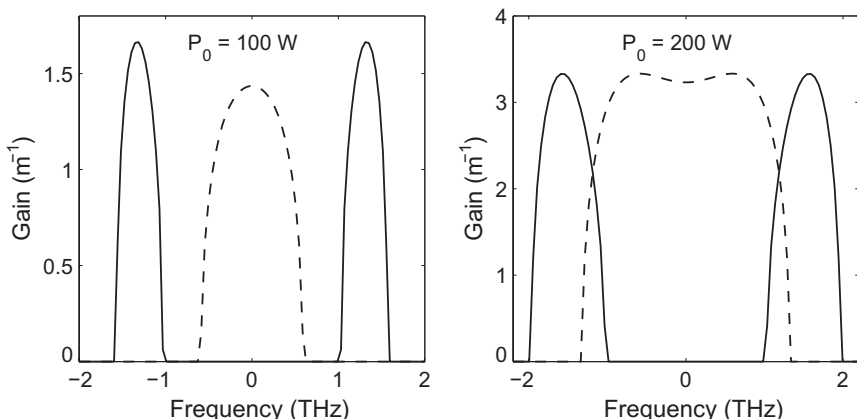


**Figure 6.9** Gain spectra of modulation instability in the case of normal dispersion at power levels of 100 W (left) and 200 W (right) for a CW beam polarized along the slow (solid curves) or fast (dashed curves) axis of a low-birefringence fiber ( $L_B = 5 \text{ m}$ ).

normal-GVD regime of a birefringent fiber. All of these features have been observed experimentally [58].

### 6.4.2 High-Birefringence Fibers

For high-birefringence fibers, the last term representing coherent coupling (or four-wave mixing) can be neglected in Eqs (6.1.11) and (6.1.12). These equations then reduce to Eqs (6.1.22) and (6.1.23) with  $B = \frac{2}{3}$  and exhibit a different kind of modulation instability [51–54]. This case is mathematically similar to the two-wavelength case discussed in Chapter 7.

To obtain the steady-state solution, the time derivatives in Eqs (6.1.22) and (6.1.23) can be set to zero. If fiber losses are neglected by setting  $\alpha = 0$ , the steady-state solution is given by (see Section 6.2.1)

$$A_x(z) = \sqrt{P_x} \exp[i\phi_x(z)], \quad A_y(z) = \sqrt{P_y} \exp[i\phi_y(z)], \quad (6.4.12)$$

where  $P_x$  and  $P_y$  are the constant mode powers and

$$\phi_x(z) = \gamma(P_x + BP_y)z, \quad \phi_y(z) = \gamma(P_y + BP_x)z. \quad (6.4.13)$$

The phase shifts depend on the powers of both polarization components. In contrast with the case of weakly birefringent fibers, this solution is valid for a CW beam polarized at an arbitrary angle with respect to the slow axis.

Stability of the steady state is examined assuming a time-dependent solution of the form

$$A_j = \left( \sqrt{P_j} + a_j \right) \exp(i\phi_j), \quad (6.4.14)$$

where  $a_j(z, t)$  is a weak perturbation with  $j = x, y$ . We substitute Eq. (6.4.14) in Eqs (6.1.22) and (6.1.23) and linearize them with respect to  $a_x$  and  $a_y$ . The resulting linear equations can again be solved in the form

$$a_j = u_j \exp[i(Kz - \Omega t)] + iv_j \exp[-i(Kz - \Omega t)], \quad (6.4.15)$$

where  $j = x, y$ ,  $K$  is the wave number, and  $\Omega$  is the frequency of perturbation.

To simplify the algebra, let us focus on the case in which the input CW beam is polarized at  $45^\circ$  from the slow axis. As a result, both polarization modes have equal powers ( $P_x = P_y = P$ ). The dispersion relation in this case can be written as [51]

$$[(K - b)^2 - H][(K + b)^2 - H] = C_X^2, \quad (6.4.16)$$

where  $b = (\beta_{1x} - \beta_{1y})\Omega/2$  takes into account the group-velocity mismatch,

$$H = \beta_2 \Omega^2 (\beta_2 \Omega^2 / 4 + \gamma P), \quad (6.4.17)$$

and the XPM coupling parameter  $C_X$  is defined as  $C_X = B\beta_2\gamma P\Omega^2$ . As before, modulation instability occurs when  $K$  becomes complex for some values of  $\Omega$ . Its gain is obtained from  $g = 2 \operatorname{Im}(K)$ .

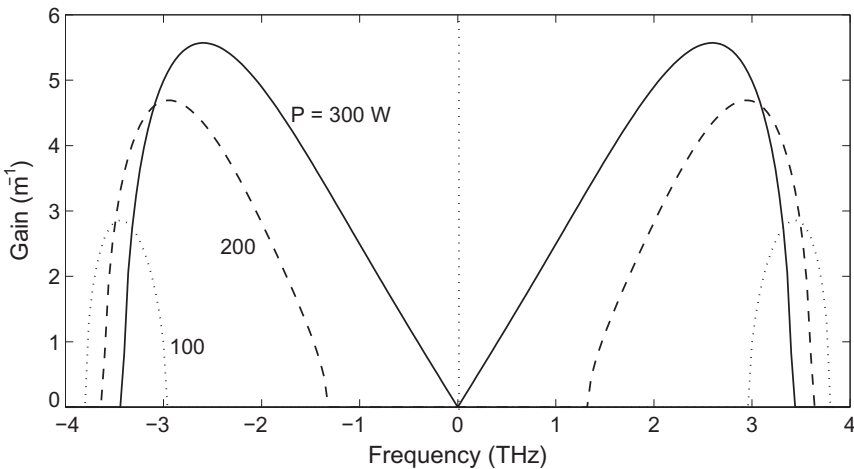


**Figure 6.10** Gain spectra of modulation instability in the normal-GVD region of a high-birefringence fiber when the input beam is linearly polarized at  $45^\circ$  from the slow axis.

The most important conclusion drawn from Eq. (6.4.16) is that modulation instability can occur irrespective of the sign of the GVD parameter [51]. In the case of normal GVD ( $\beta_2 > 0$ ), the gain exists only if  $C_X > |H - b|^2$ . Figure 6.10 shows the gain spectra at three power levels using parameter values  $\beta_2 = 60 \text{ ps}^2/\text{km}$ ,  $\gamma = 25 \text{ W}^{-1}/\text{km}$ , and a group-velocity mismatch of  $1.5 \text{ ps/m}$ . At low power levels, the gain spectrum is relatively narrow and its peak is located near  $\Omega_m = |\beta_{1x} - \beta_{1y}|/\beta_2$ . As input power increases, gain spectrum widens and its peak shifts to lower frequencies. In all three cases shown in Figure 6.10, the CW beam develops temporal modulations at frequencies  $> 2.5 \text{ THz}$  as it propagates through the fiber. As  $\Omega_m$  depends on birefringence of the fiber, it can be changed easily and provides a tuning mechanism for the modulation frequency. An unexpected feature is that modulation instability ceases to occur when the input power exceeds a critical value

$$P_c = 3(\beta_{1x} - \beta_{1y})^2 / (4\beta_2\gamma). \quad (6.4.18)$$

Another surprising feature is that modulation instability ceases to occur when the input light is polarized close to a principal axis of the fiber [52].

Both of these features can be understood qualitatively if we interpret modulation instability in terms of a four-wave-mixing process that is phase matched by the modal birefringence of the fiber (see Chapter 10). In the case of normal GVD, the SPM- and XPM-induced phase shifts actually add to the GVD-induced phase mismatch. It is the fiber birefringence that cancels the phase mismatch. Thus, for a given value of birefringence, the phase-matching condition can only be satisfied if the nonlinear phase shifts remain below a certain level. This is the origin of the critical power level in Eq. (6.4.18). An interesting feature of the four-wave-mixing

process is that spectral sidebands are generated such that the low-frequency sideband at  $\omega_0 - \Omega$  appears along the slow axis whereas the sideband at  $\omega_0 + \Omega$  is polarized along the fast axis. This can also be understood in terms of the phase-matching condition of Section 10.3.3.

### 6.4.3 Isotropic Fibers

It is clear that modal birefringence of fibers plays an important role for modulation instability to occur. A natural question is whether modulation instability can occur in isotropic fibers with no birefringence ( $n_x = n_y$ ). Even though such fibers are hard to fabricate, fibers with extremely low birefringence ( $|n_x - n_y| < 10^{-8}$ ) can be made by spinning the preform during the drawing stage. The question is also interesting from a fundamental standpoint and was discussed as early as 1970 [48].

The theory developed for high-birefringence fibers cannot be used in the limit  $\Delta\beta = 0$  because the coherent-coupling term has been neglected. In contrast, theory developed for low-birefringence fibers remains valid in that limit. The main difference is that  $P_{cr} = 0$  as polarization instability does not occur for isotropic fibers. As a result,  $\Omega_{c2} = 0$  while  $\Omega_{c1} = \Omega_{c3} \equiv \Omega_c$ . The gain spectrum of modulation instability in Eq. (6.4.8) reduces to

$$g(\Omega) = |\beta_2\Omega|\sqrt{\Omega_c^2 - \Omega^2}, \quad (6.4.19)$$

irrespective of whether the input beam is polarized along the slow or fast axis. This is the same result obtained in Section 5.1, for the scalar case. It shows that the temporal and spectral features of modulation instability should not depend on the direction in which the input beam is linearly polarized. This is expected for any isotropic nonlinear medium on physical grounds.

The situation changes when the input beam is circularly or elliptically polarized. We can consider this case by setting  $\Delta\beta = 0$  in Eqs (6.1.15) and (6.1.16). Using  $\alpha = 0$  for simplicity, these equations reduce to the following set of two coupled NLS equations [48]:

$$\frac{\partial A_+}{\partial z} + \frac{i\beta_2}{2} \frac{\partial^2 A_+}{\partial T^2} + i\gamma' \left( |A_+|^2 + 2|A_-|^2 \right) A_+ = 0, \quad (6.4.20)$$

$$\frac{\partial A_-}{\partial z} + \frac{i\beta_2}{2} \frac{\partial^2 A_-}{\partial T^2} + i\gamma' \left( |A_-|^2 + 2|A_+|^2 \right) A_- = 0, \quad (6.4.21)$$

where  $T = t - \beta_1 z$  is the reduced time and  $\gamma' = 2\gamma/3$ . The steady-state solution of these equations is obtained easily and is given by

$$\bar{A}_\pm(z) = \sqrt{P_\pm} \exp(i\phi_\pm), \quad (6.4.22)$$

where  $P_\pm$  is the input power in the two circularly polarized components and  $\phi_\pm(z) = \gamma'(P_\mp + 2P_\pm)z$  is the nonlinear phase shift.

As before, we perturb the steady-state solution using

$$A_{\pm}(z, t) = [\sqrt{P_{\pm}} + a_{\pm}(z, t)] \exp(i\phi_{\pm}), \quad (6.4.23)$$

where  $a_{\pm}(z, t)$  is a small perturbation. By using Eq. (6.4.23) in Eqs (6.4.20) and (6.4.21) and linearizing in  $a_+$  and  $a_-$ , we obtain a set of two coupled linear equations. These equations can be solved assuming a solution in the form of Eq. (6.4.3). We then obtain a set of four algebraic equations for  $u_{\pm}$  and  $v_{\pm}$ . This set has a nontrivial solution only when the perturbation satisfies the following dispersion relation [48]:

$$(K - H_+)(K - H_-) = C_X^2, \quad (6.4.24)$$

where

$$H_{\pm} = \frac{1}{2}\beta_2\Omega^2 \left( \frac{1}{2}\beta_2\Omega^2 + \gamma P_{\pm} \right), \quad (6.4.25)$$

and the XPM coupling parameter  $C_X$  is now defined as

$$C_X = 2\beta_2\gamma\Omega^2\sqrt{P_+P_-}. \quad (6.4.26)$$

A necessary condition for modulation instability to occur is  $C_X^2 > H_+H_-$ . As  $C_X$  depends on  $\sqrt{P_+P_-}$  and vanishes for a circularly polarized beam, we can conclude that no instability occurs in that case. For an elliptically polarized beam, the instability gain depends on the ellipticity  $e_p$  defined in Eq. (6.3.4).

#### 6.4.4 Experimental Results

The vector modulation instability was first observed in the normal-dispersion region of a high-birefringence fiber [51–53]. In one experiment, 30-ps pulses at the 514-nm wavelength with 250-W peak power were launched into a 10-m fiber with a 45° polarization angle [52]. At the fiber output, the pulse spectrum exhibited modulation sidebands with a 2.1-THz spacing, and the autocorrelation trace showed 480-fs intensity modulation. The observed sideband spacing was in good agreement with the value calculated theoretically. In another experiment, 600-nm input pulses were of only 9-ps duration [51]. As the 18-m-long fiber had a group-velocity mismatch of  $\approx 1.6 \text{ ps/m}$ , the two polarization components would separate from each other after only 6 m of fiber. The walk-off problem was solved by delaying the faster-moving polarization component by 25 ps at the fiber input. The temporal and spectral measurements indicated that both polarization components developed high-frequency ( $\sim 3 \text{ THz}$ ) modulations, as expected from theory. Moreover, the modulation frequency decreased with an increase in the peak power. This experiment also revealed that each polarization component of the beam develops only one sideband, in agreement with theory. In a later experiment [53], modulation instability developed from temporal oscillations induced by optical wave breaking (see Section 4.2.3). This behavior can be understood from Figure 4.13, noting that optical wave breaking manifests as

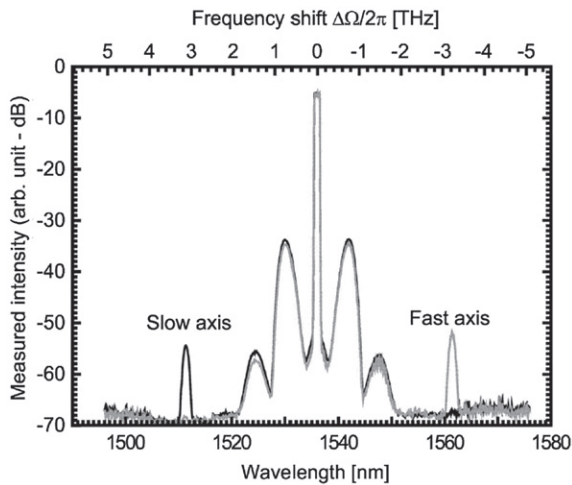


**Figure 6.11 Spectral sidebands observed at the output of a 51-m-long high-birefringence fiber when the pump is polarized at  $45^\circ$  from the principal axes. Black and gray traces correspond to light polarized along the fast and slow axes, respectively. The central multiplet structure results from the scalar modulation instability.** (After Ref. [66]; © 2005 OSA.)

spectral sidebands. If these sidebands fall within the bandwidth of the modulation-instability gain curve, their energy can seed the instability process.

Although vector modulation instability is predicted to occur even in the anomalous-GVD regime of a high-birefringence fiber, its experimental observation turned out to be more difficult [64]. The reason is that the scalar modulation instability (discussed in Section 5.1) also occurs in this regime. If the input field is polarized along a principal axis, the scalar one dominates. In a 2005 experiment, clear-cut evidence of vector modulation instability was seen when the input field was polarized at a  $45^\circ$  angle from a principal axis [66]. Figure 6.11 shows the observed spectrum at the output of a 51-m-long fiber, with a birefringence-induced differential group delay (DGD) of 286 fs/m, when 3.55-ns pulses at a 2.5-kHz repetition rate (with an average power of about 1 mW) were launched into it. The central multipeak structure is due to scalar modulation instability, but the two extreme peaks result from vector modulation instability. These two peaks are orthogonally polarized along the fast and slow axes, a feature unique to the vector modulation instability.

Modulation instability in low-birefringence fibers was observed in 1995 using 60-ps pulses (peak power  $> 1\text{ kW}$ ) obtained from a krypton-ion laser operating at 647 nm [55]. Fibers used in the experiment were a few meters long, and their birefringence was controlled through stress induced by winding the fiber on a spool with a relatively small diameter. When input pulses were polarized along the slow axis, the two sidebands indicative of modulation instability had the same polarization and were polarized along the fast axis. Their spacing could be varied over a range of 20 nm or so by simply changing the spool size (a smaller spool diameter produces

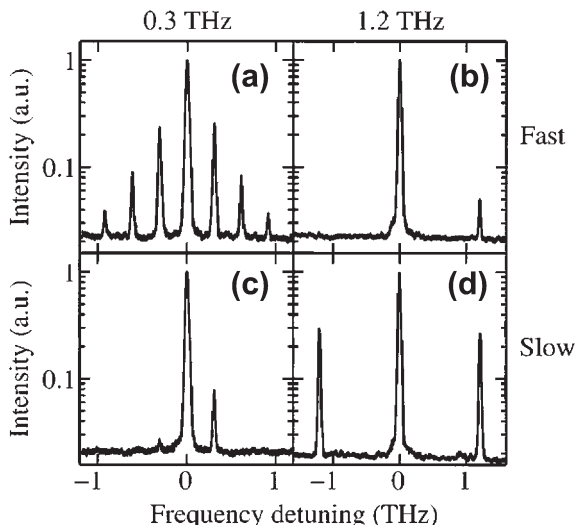


**Figure 6.12 Modulation-instability sidebands observed in a low-birefringence fiber. The pump is polarized along the fast (top row) or slow axis (bottom row). Pump–probe detuning is 0.3 THz for left and 1.2 THz for right columns. (After Ref. [58]; © 1998 OSA.)**

more stress-induced birefringence), resulting in larger sideband spacing. In a variation of this idea, fibers with periodically varying birefringence along their length were produced by wrapping the fiber around two spools [56]. Such a periodic variation can create new sidebands through quasi-phase matching, similar to the periodic variation of dispersion and nonlinearity discussed in Section 5.1.

A systematic study of induced modulation instability in low-birefringence fibers was performed in 1998 using a pump–probe configuration [58]. The probe beam was used to seed the process. In a series of experiments, the pump beam was obtained from a dye laser operating near 575 nm and consisted of 4-ns pulses that were wide enough to realize quasi-CW operation. The pump–probe wavelength separation was tunable; tuning allowed different regimes of modulation instability to be investigated. The fiber was drawn using a rapidly rotating preform so that its intrinsic birefringence averaged out to zero. A controlled amount of weak birefringence was introduced by winding the fiber onto a 14.5-cm-diameter spool. The measured beat length of 5.8 m for the fiber corresponded to a modal birefringence of only  $10^{-7}$ . The critical power  $P_{\text{cr}}$  required for the onset of polarization instability [see Eq. (6.3.10)] was estimated to be 70 W for this fiber.

Figure 6.12 shows the pump spectra measured under several different experimental conditions. In all cases, the pump power was 112 W ( $1.6P_{\text{cr}}$ ) while the probe power was kept low ( $\sim 1$  W). Consider first the case of a pump polarized along the fast axis (top row). For a pump–probe detuning of 0.3 THz, the probe frequency falls within the gain spectrum of modulation instability (see Figure 6.9). As a result, the

pump spectrum develops a series of sidebands spaced apart by 0.3 THz. In contrast, the probe frequency falls outside the gain spectrum for a detuning of 1.2 THz, and modulation instability does not occur. When the pump is polarized along the slow axis (bottom row), the situation is reversed. Now the 0.3-THz detuning falls outside the gain spectrum, and modulation-instability sidebands form only when the detuning is 1.2 THz. These experimental results are in agreement with the theory given earlier. In the time domain, the pump pulse develops deep modulations that correspond to a train of dark solitons with repetition rates in the terahertz regime [58]. A dark soliton is also formed when modulation instability occurs in high-birefringence fibers [59]. The formation of dark solitons is not surprising if we recall from Chapter 5 that optical fibers support only dark solitons in their normal-GVD regime.

In all of these experiments, fiber birefringence plays an important role. As discussed before, vector modulation instability can occur in isotropic fibers ( $n_x = n_y$ ) such that the gain spectrum depends on the polarization state of the input CW beam. Unfortunately, it is difficult to make birefringence-free fibers. As an alternative, modulation instability was observed in a bimodal fiber in which the input beam excited two fiber modes (the LP<sub>01</sub> and LP<sub>11</sub> modes) with nearly equal power levels, and the two modes had the same group velocity [57]. In a 1999 experiment [60], a nearly isotropic fiber was realized by winding 50 m of “spun” fiber with a large radius of curvature of 25 cm. The beat length for this fiber was  $\sim 1$  km, indicating a birefringence level  $< 10^{-8}$ . Over the 50-m length used in the experiment, the fiber was nearly isotropic. Modulation-instability sidebands were observed when 230-ps pulses ( $\lambda = 1.06 \mu\text{m}$ ) with a peak power of 120 W were launched into the fiber. The recorded spectra were almost identical when the polarization angle of linearly polarized light was changed over a 90° range. Sidebands disappeared for circularly polarized light. This behavior is expected since isotropic fibers have no preferred direction. When input light was elliptically polarized, the amplitude of spectral sidebands varied with the ellipticity, again in agreement with theory.

## 6.5 BIREFRINGENCE AND SOLITONS

The discussion of optical solitons in Chapter 5 neglected polarization effects and assumed implicitly that the fiber had no birefringence. The results presented there also apply for high-birefringence fibers when the input pulse is linearly polarized along one of the principal axes of a polarization-maintaining fiber. This section focuses on solitons forming when the input pulse is polarized at a finite angle from the slow axis [69–83]. There are two important issues. First, in a weakly birefringent fiber, the peak power of the soliton may exceed the critical power [see Eq. (6.3.10)] at which polarization instability occurs. This instability is likely to affect the solitons launched with their linear-polarization state aligned along the fast axis. Second, in a strongly birefringent fiber, the group-velocity mismatch between the two orthogonally polarized components can lead to their physical separation within the fiber. Both of these issues are discussed in this section.

### 6.5.1 Low-Birefringence Fibers

Consider first the case of low-birefringence fibers. As the group-velocity mismatch is relatively small in such fibers, we can set  $\beta_{1x} \approx \beta_{1y}$  in Eqs (6.1.11) and (6.1.12) and use Eqs (6.1.15) and (6.1.16) when circularly polarized components of the field are used in place of the linear ones. These equations can be scaled using the soliton units introduced in Section 5.2. The resulting coupled NLS equations take the form [69]

$$i\frac{\partial u_+}{\partial \xi} + \frac{i}{2}\frac{\partial^2 u_+}{\partial \tau^2} + bu_- + \frac{2}{3}(|u_+|^2 + 2|u_-|^2)u_+ = 0, \quad (6.5.1)$$

$$i\frac{\partial u_-}{\partial \xi} + \frac{i}{2}\frac{\partial^2 u_-}{\partial \tau^2} + bu_+ + \frac{2}{3}(|u_-|^2 + 2|u_+|^2)u_- = 0, \quad (6.5.2)$$

where  $b = (\Delta\beta)L_D/2$  and fiber losses are neglected. The normalized variables  $\xi$ ,  $\tau$ , and  $u_\pm$  are defined as

$$\xi = z/L_D, \quad \tau = (t - \beta_1 z)/T_0, \quad u_\pm = (\gamma L_D)^{1/2} A_\pm, \quad (6.5.3)$$

where  $L_D = T_0^2/|\beta_2|$  is the dispersion length and  $T_0$  is a measure of the pulse width. These equations generalize the scalar NLS equation of Section 5.2 to the vector case for low-birefringence fibers. They can be solved numerically using the split-step Fourier method of Section 2.4.

The numerical results show that the polarization instability affects solitons in a manner analogous to the CW case discussed in Section 6.2.3. If the nonlinear length  $L_{NL}$  is larger than the beat length  $L_B = 2\pi/\Delta\beta$ , solitons remain stable even if they are polarized close to the fast axis. By contrast, if  $L_{NL} \ll L_B$ , solitons polarized along the slow axis remain stable but become unstable if polarized along the fast axis. A linearly polarized fundamental soliton ( $N = 1$ ), launched with its polarization close to the fast axis with  $L_{NL} \ll L_B$ , follows adheres to the following evolution scenario [69]. Because of the onset of polarization instability, most of the pulse energy is transferred from the fast mode to the slow mode within a few soliton periods while a part of it is dispersed away. The pulse energy switches back and forth between the two modes a few times, a process similar to relaxation oscillations. Most of the input energy, however, appears eventually in a soliton-like pulse propagating along the slow axis. Higher-order solitons follow a somewhat different scenario. After going through an initial narrowing stage, they split into individual components, a behavior similar to that discussed in Section 5.5. A part of the energy is then transferred to the slow mode. A fundamental soliton eventually appears along the slow axis with a width narrower than the input width.

The CW instability condition can be used to obtain a condition on the soliton period. If we use Eq. (6.3.10), the condition  $P_0 > P_{cr}$  becomes  $(\Delta\beta)L_{NL} < \frac{2}{3}$ , where  $L_{NL} = (\gamma P_0)^{-1}$  is the nonlinear length. By using  $\Delta\beta = 2\pi/L_B$ ,  $N^2 = L_D/L_{NL}$  and  $z_0 = (\pi/2)L_D$ , the condition can be written as  $z_0 < N^2 L_B/6$ . The numerical results agree with this condition [69]. Typically,  $L_B \sim 1$  m for weakly birefringent fibers. Thus, polarization instability affects a fundamental soliton ( $N = 1$ ) only if  $z_0 \ll 1$  m. Such values of  $z_0$  are realized in practice only for femtosecond pulses ( $T_0 < 100$  fs).

### 6.5.2 High-Birefringence Fibers

In high-birefringence fibers, the group-velocity mismatch between the fast and slow components of the input pulse cannot be neglected. Such a mismatch would normally split a pulse into its two components polarized along the two principal axes if the input polarization angle  $\theta$  deviates from  $0^\circ$  or  $90^\circ$ . The interesting question is whether such a splitting also occurs for solitons.

The effects of group-velocity mismatch are studied by solving Eqs (6.1.22) and (6.1.23) numerically. If we assume anomalous dispersion ( $\beta_2 < 0$ ) and use the soliton units of Section 5.2, these equations become

$$i \left( \frac{\partial u}{\partial \xi} + \delta \frac{\partial u}{\partial \tau} \right) + \frac{1}{2} \frac{\partial^2 u}{\partial \tau^2} + (|u|^2 + B|v|^2)u = 0, \quad (6.5.4)$$

$$i \left( \frac{\partial v}{\partial \xi} - \delta \frac{\partial v}{\partial \tau} \right) + \frac{1}{2} \frac{\partial^2 v}{\partial \tau^2} + (|v|^2 + B|u|^2)v = 0, \quad (6.5.5)$$

where  $u$  and  $v$  are the normalized amplitudes of the field components polarized linearly along the  $x$ - and  $y$ -axes, respectively, and

$$\delta = (\beta_{1x} - \beta_{1y})T_0/(2|\beta_2|) \quad (6.5.6)$$

governs the group-velocity mismatch between the two polarization components. The normalized time  $\tau = (t - \bar{\beta}_1 z)/T_0$ , where  $\bar{\beta}_1 = \frac{1}{2}(\beta_{1x} + \beta_{1y})$  is inversely related to the average group velocity. Fiber losses are ignored for simplicity but can be included easily. The XPM coupling parameter  $B = \frac{2}{3}$  is for linearly birefringent fibers.

When an input pulse is launched with a polarization angle  $\theta$  (measured from the slow axis), Eqs (6.5.4) and (6.5.5) should be solved with the input

$$u(0, \tau) = N \cos \theta \operatorname{sech}(\tau), \quad v(0, \tau) = N \sin \theta \operatorname{sech}(\tau), \quad (6.5.7)$$

where  $N$  is the soliton order. In the absence of XPM-induced coupling, the two polarization components evolve independently and separate from each other because of their different group velocities. The central question is how this behavior is affected by the XPM. This question is answered by solving Eqs (6.5.4) and (6.5.5) numerically with  $B = 2/3$  for various values of  $N$ ,  $\theta$ , and  $\delta$  [70–72]. The numerical results can be summarized as follows.

When the two modes are equally excited ( $\theta = 45^\circ$ ), the two components remain bound together if  $N$  exceeds a critical value  $N_{\text{th}}$  that depends on  $\delta$ ;  $N_{\text{th}} \approx 0.7$  for  $\delta = 0.15$ , but  $N_{\text{th}} \approx 1$  for  $\delta = 0.5$ . As an example, Figure 6.13 shows the temporal and spectral evolution of the slow and fast components of the pulse over 10 dispersion lengths by choosing  $N = 1$  and  $\delta = 0.2$ . The two polarization components move initially at different speeds but they trap each other soon after and move at a common speed. This trapping is a consequence of spectral shifts occurring in opposite directions for the two components. This trapping behavior is clearly evident in Figure 6.14 where the shapes and spectra of the two components are compared at a distance of  $z = 10L_D$ . As seen there, the temporal profiles almost overlap, but the spectra are

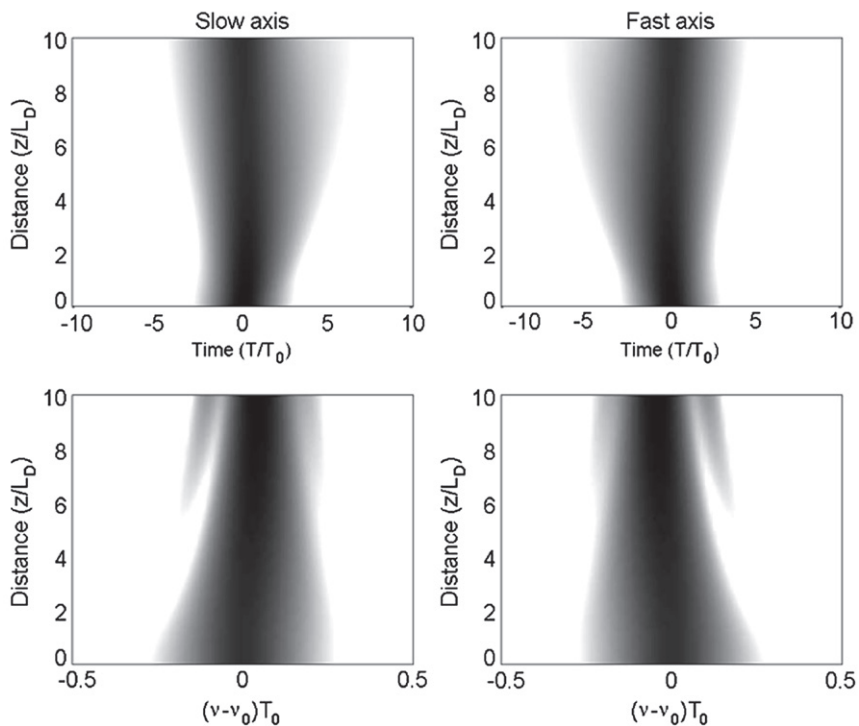


**Figure 6.13** Temporal and spectral evolution of the two components of a vector soliton over 10 dispersion lengths for  $N=1$ ,  $\theta=45^\circ$ , and  $\delta=0.2$ . The gray scale is over a 20-dB intensity range.

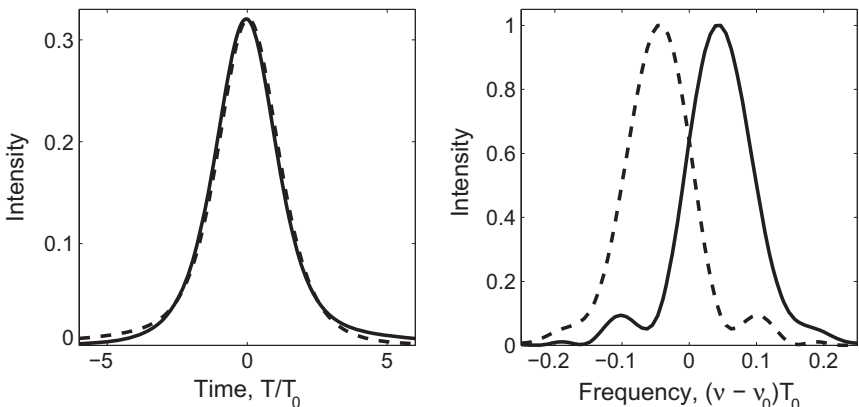


**Figure 6.14** Comparison of the temporal and spectral profiles at  $z=10L_D$  for the slow (solid line) and fast (dashed line) components for  $N=1$ ,  $\theta=45^\circ$ , and  $\delta=0.2$ .

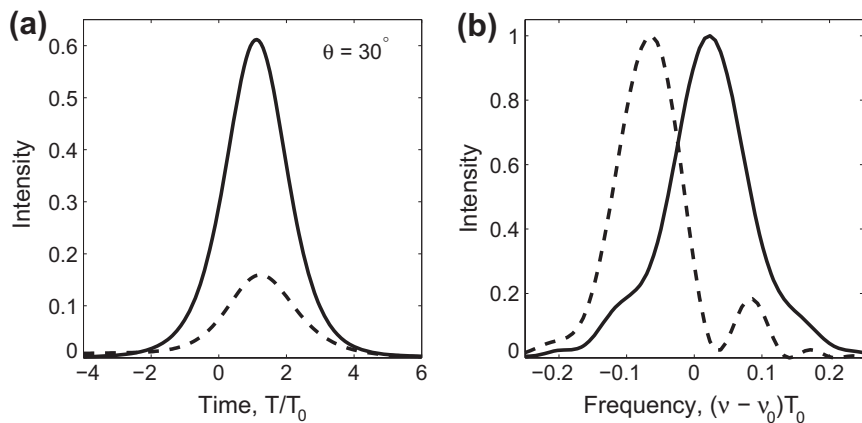


**Figure 6.15 Comparison of the temporal and spectral profiles at  $z=10L_0$  for the slow (solid line) and fast (dashed line) components for  $N=1$ ,  $\theta=30^\circ$ , and  $\delta=0.2$ .**

shifted in opposite directions. A similar behavior is observed for larger values of  $\delta$  as long as  $N > N_{\text{th}}$ . Solitons can form even when  $N < N_{\text{th}}$ , but the two components travel at their own group velocities and become widely separated.

When  $\theta \neq 45^\circ$ , the two modes have unequal amplitudes initially. In this case, if  $N$  exceeds  $N_{\text{th}}$ , a qualitatively different evolution scenario occurs depending on the value of  $\delta$ . Figure 6.15 is obtained under conditions identical to those of Figure 6.14 except that  $\theta$  is reduced to  $30^\circ$  so that the slow-axis component of the vector soliton dominates. As seen there, the weaker pulse (polarized along the fast axis) is still captured by the stronger one polarized along the fast axis, and the two move together. However, the trapped pulses are shifted from the center because the stronger pulse moves slower initially and has shifted toward the right before it captures the fast-axis component. Notice also how the pulse spectra in Figure 6.15b are affected differently for the two pulse components because of the asymmetric nature of the XPM-induced coupling.

The numerical results shown in Figures 6.13–6.15 clearly indicate that, under certain conditions, the two orthogonally polarized components of a pulse move with a common group velocity in spite of their different speeds in the absence of XPM-induced coupling ( $B = 0$ ). This phenomenon is called *soliton trapping* and, as discussed later, it can be used for optical switching. It owes its existence solely to XPM. It is the XPM-induced nonlinear coupling between them that allows the two solitons to propagate at a common group velocity. Physically, the two solitons shift their carrier frequencies in the opposite directions to realize such a temporal synchronization. Specifically, the soliton along the fast axis slows down while the one along the slow axis speeds up.

Because soliton trapping requires a balance between XPM and linear birefringence, it can occur only when the peak power of the input pulse, or equivalently the

soliton order  $N$ , exceeds a threshold value  $N_{\text{th}}$ . As  $N_{\text{th}}$  depends on both the polarization angle  $\theta$  and  $\delta$ , attempts have been made to estimate  $N_{\text{th}}$  analytically by solving Eqs (6.5.4) and (6.5.5) approximately [74–82]. In a simple approach, the XPM term is treated as a perturbation within the Lagrangian formulation. In the case of equal amplitudes, realized by choosing  $\theta = 45^\circ$  in Eq. (6.5.7), the threshold value for soliton trapping is found to be [74]

$$N_{\text{th}} = [2(1 + B)]^{-1/2} + (3/8B)^{1/2}\delta. \quad (6.5.8)$$

For  $B = \frac{2}{3}$ , the predictions of Eq. (6.5.8) are in good agreement with the numerical results for small values of  $\delta$  (up to 0.5). For large values of  $\delta$ , the threshold value is well approximated by [82]  $N_{\text{th}} = [(1 + 3\delta^2)/(1 + B)]^{1/2}$ .

Soliton trapping was first observed [84] in 1989 by launching 300-fs pulses (obtained from a color-center laser) into a 20-m single-mode fiber with modal birefringence  $\Delta n \approx 2.4 \times 10^{-5}$ , a value leading to polarization dispersion of 80 ps/km. In this experiment, the soliton period  $z_0$  was 3.45 m with  $\delta = 0.517$ . The measured pulse spectra for the orthogonally polarized components were found to be separated by about 1 THz when the polarization angle was  $45^\circ$ . The autocorrelation trace indicated that the two pulses at the fiber output were synchronized temporally as expected for soliton trapping. In a 2007 experiment, collisions of two solitons were observed inside a birefringent fiber by launching optical pulses at two different wavelengths [85].

### 6.5.3 Soliton-Dragging Logic Gates

An important application of XPM interaction in birefringent fibers has led to the realization of all-optical, cascadable, ultrafast, logic gates, first demonstrated in 1989 [86]. Since then the performance of such logic gates has been studied extensively, both theoretically and experimentally [87–96].

The basic idea behind the operation of fiber-optic logic gates has its origin in the nonlinear phenomenon of soliton trapping discussed earlier. It can be understood as follows. In digital logic, each optical pulse is assigned a time slot whose duration is determined by the clock speed. If a signal pulse is launched together with an orthogonally polarized control pulse, and the control pulse is intense enough to trap the signal pulse during a collision, then both pulses can be dragged out of their assigned time slot because of the XPM-induced change in their group velocity. In other words, the absence or presence of a signal pulse at the fiber input dictates whether the control pulse ends up arriving within the assigned time slot or not. This temporal shift forms the basic logic element and can be used to perform more complex logic operations. Because the control pulse propagating as a soliton is dragged out of its time slot through the XPM interaction, such devices are referred to as soliton-dragging logic gates. In a network configuration, the output signal pulse can be discarded while the control pulse becomes the signal pulse for the next gate. This strategy makes the switching operation cascadable. In effect, each control pulse is used for switching only once irrespective of the number of gates in the network.

The experimental demonstration of various logic gates (such as exclusive OR, AND, and NOR gates), based on the concept of soliton trapping, used femtosecond optical pulses (pulse width  $\sim 300$  fs) from a mode-locked color-center laser operating at  $1.685 \mu\text{m}$  [86–90]. In these experiments, orthogonally polarized signal and control pulses were launched into a highly birefringent fiber. In the implementation of a NOR gate, the experimental conditions were arranged such that the control pulse arrived in its assigned time slot of 1-ps duration in the absence of signal pulses (logical “1” state). In the presence of one or both signal pulses, the control pulse shifted by 2–4 ps because of soliton dragging and missed the assigned time slot (logical “0” state). The energy of each signal pulse was 5.8 pJ. The energy of the control pulse was 54 pJ at the fiber input but reduced to 35 pJ at the output, resulting in an energy gain by a factor of 6. The experimental results can be explained quite well by solving Eqs (6.5.4) and (6.5.5) numerically [95]. Since the first demonstration of such logic gates in 1989, considerable progress has been made. The use of soliton-dragging logic gates for soliton ring networks has also been proposed [96].

#### 6.5.4 Vector Solitons

The phenomenon of soliton trapping suggests that the coupled NLS equations may possess exact solitary-wave solutions with the property that the orthogonally polarized components propagate in a birefringent fiber without a change in shape. Such solitary waves are referred to as *vector solitons* to emphasize the fact that an input pulse maintains not only its intensity profile but also its state of polarization even when it is not launched along one of the principal axes of the fiber [97]. A more general question one may ask is whether conditions exist under which two orthogonally polarized pulses of different widths and different peak powers propagate undistorted in spite of the XPM-induced nonlinear coupling between them.

Consider the case of high-birefringence fibers. To obtain soliton solutions of Eqs (6.5.4) and (6.5.5), it is useful to simplify them using the transformation

$$u = \tilde{u} \exp(i\delta^2\xi/2 - i\delta\tau), \quad v = \tilde{v} \exp(i\delta^2\xi/2 + i\delta\tau). \quad (6.5.9)$$

The resulting equations are independent of  $\delta$  and take the form

$$i\frac{\partial\tilde{u}}{\partial\xi} + \frac{1}{2}\frac{\partial^2\tilde{u}}{\partial\tau^2} + (|\tilde{u}|^2 + B|\tilde{v}|^2)\tilde{u} = 0, \quad (6.5.10)$$

$$i\frac{\partial\tilde{v}}{\partial\xi} + \frac{1}{2}\frac{\partial^2\tilde{v}}{\partial\tau^2} + (|\tilde{v}|^2 + B|\tilde{u}|^2)\tilde{v} = 0. \quad (6.5.11)$$

In the absence of XPM-induced coupling ( $B = 0$ ), the two NLS equations become decoupled and have independent soliton solutions of the form discussed in Section 5.2. When  $B \neq 0$ , Eqs (6.5.10) and (6.5.11) can be solved by the inverse scattering

method only for a specific value of parameter  $B$ , namely  $B = 1$ . Manakov obtained such a solution in 1973 [98]. In its simplest form, the solution can be written as

$$\tilde{u}(\xi, \tau) = \cos \theta \operatorname{sech}(\tau) \exp(i\xi/2), \quad (6.5.12)$$

$$\tilde{v}(\xi, \tau) = \sin \theta \operatorname{sech}(\tau) \exp(i\xi/2), \quad (6.5.13)$$

where  $\theta$  is an arbitrary angle. A comparison with Eq. (5.2.15) shows that this solution corresponds to a vector soliton that is identical with the fundamental soliton ( $N = 1$ ) of Section 5.2 in all respects. The angle  $\theta$  can be identified as the polarization angle. More complex forms of vector solitons have also been found in the  $B = 1$  case [99].

The preceding solution predicts that a “sech” pulse, launched with  $N = 1$  and linearly polarized at an arbitrary angle from a principal axis, can maintain both its shape and polarization provided the fiber is birefringent such that the XPM parameter  $B = 1$ . However, as discussed in Section 6.1, unless the fiber is especially designed,  $B \neq 1$  in practice. In particular,  $B = \frac{2}{3}$  for linearly birefringent fibers. For this reason, solitary-wave solutions of Eqs (6.5.10) and (6.5.11) for  $B \neq 1$  have been studied in many different contexts [100–125]. Such solutions are not solitons in a strict mathematical sense but, nevertheless, exhibit the shape-preserving property of solitons.

In the specific case of equal amplitudes ( $\theta = 45^\circ$ ), a solitary-wave solution of Eqs (6.5.10) and (6.5.11) is given by [106]

$$\tilde{u} = \tilde{v} = \eta \operatorname{sech}[(1 + B)^{1/2} \eta \tau] \exp[i(1 + B)\eta^2 \xi/2], \quad (6.5.14)$$

where  $\eta$  represents the soliton amplitude. For  $B = 0$ , this solution reduces to the scalar soliton of Section 5.2. For  $B \neq 0$ , it represents a vector soliton polarized at  $45^\circ$  with respect to the principal axes of the fiber. Because of the XPM interaction, the vector soliton is narrower by a factor of  $(1 + B)^{1/2}$  compared with the scalar soliton. For such a soliton, the combination of SPM and XPM compensates for the GVD. At the same time, the carrier frequencies of two polarization components must be different for compensating the PMD. This can be seen by substituting Eq. (6.5.14) in Eq. (6.5.9). The canonical form of the vector soliton, obtained by setting  $\eta = 1$  is then given by

$$u(\xi, \tau) = \operatorname{sech}[(1 + B)^{1/2} \tau] \exp[i(1 + B + \delta^2)\xi/2 - i\delta\tau], \quad (6.5.15)$$

$$v(\xi, \tau) = \operatorname{sech}[(1 + B)^{1/2} \tau] \exp[i(1 + B + \delta^2)\xi/2 + i\delta\tau]. \quad (6.5.16)$$

The only difference between  $u(\xi, \tau)$  and  $v(\xi, \tau)$  is the sign of the last phase term involving the product  $\delta\tau$ . This sign change reflects the shift of the carrier frequency of the soliton components in the opposite directions.

The solution given by Eq. (6.5.14) represents only one of the several solitary-wave solutions that have been discovered in birefringent fibers by solving Eqs (6.1.19) and (6.1.20) under various approximations. In one case, the two components not only have an asymmetric shape but they can also have a double-peak structure [103]. In another interesting class of solutions, two solitary waves form bound states such that

the state of polarization is not constant over the entire pulse but changes with time [104]. In some cases the state of polarization can even evolve periodically along the fiber length [118]. Several other solitary-wave solutions were found during the 1990s [114–125]. We refer the reader to Reference [97] for further details.

Similar to the case of modulation instability, we should ask whether vector solitons exist in isotropic fibers with no birefringence. In this case, we should use Eqs (6.5.1) and (6.5.2), written in terms of the circularly polarized components defined in Eq. (6.5.3), and set  $b = 0$ . The solitary-wave solutions of these equations are found assuming  $u_+ = U \exp(ip\xi)$  and  $u_- = V \exp(iq\xi)$ , where  $U$  and  $V$  do not vary with  $\xi$  and satisfy

$$\frac{d^2U}{d\tau^2} = 2pU - \frac{2}{3}(U^2 + 2V^2)U, \quad (6.5.17)$$

$$\frac{d^2V}{d\tau^2} = 2qV - \frac{2}{3}(V^2 + 2U^2)V. \quad (6.5.18)$$

These equations have a variety of solutions representing vector solitary waves with different polarization properties that can exist in isotropic fibers [121–124]. The simplest solution corresponds to a circularly polarized vector soliton of the form

$$U(\tau) = \sqrt{6p} \operatorname{sech}(\sqrt{2p}\tau), \quad V(\tau) = 0. \quad (6.5.19)$$

A linearly polarized vector soliton is obtained when  $q = p$  and has the form

$$U(\tau) = V(\tau) = \sqrt{2p} \operatorname{sech}(\sqrt{2p}\tau). \quad (6.5.20)$$

It corresponds to a linearly polarized pulse whose electric field vector may be oriented at any angle in the plane transverse to the fiber axis. It should be emphasized that, strictly speaking, these solutions only represent solitary waves and their stability under collisions is not guaranteed. However, it is common to call them vector solitons.

Elliptically polarized vector solitons with  $U(\tau) > V(\tau) > 0$  can also form in isotropic fibers [121]. However, it is not possible to write an analytic form for them. Their origin is related to the phenomenon of soliton trapping and can be understood as follows. In the case of  $V \ll U$ , the solution of  $U(\tau)$  given in Eq. (6.5.19) can be used in Eq. (6.5.18). The resulting linear equation for  $V(\tau)$  has two types of bound solutions. These symmetric and asymmetric solution are given by [123]

$$V_s(\tau) = V_0 \operatorname{sech}^s(\sqrt{2p}\tau), \quad q_s = (4 - s)p, \quad (6.5.21)$$

$$V_a(\tau) = V_0 \operatorname{sech}^{s-1}(\sqrt{2p}\tau) \tanh(\sqrt{2p}\tau), \quad q_a = (5 - 3s)p, \quad (6.5.22)$$

where  $s = \frac{1}{2}(\sqrt{17} - 1) \approx 1.562$ . These solutions are valid as long as  $V_0^2 \ll 2p$ . As long as this condition is satisfied, the fast-axis component is trapped by the much stronger slow-axis component of the same pulse, and the two form a bound vector soliton. Notice that  $q_s$  exceeds  $p$  for the symmetric branch but  $q_a < p$  for the asymmetric branch. Also, the state of polarization is not uniform across the pulse for such

vector solitons and has an ellipticity that varies with  $\tau$ . Moreover, the axes of the ellipse rotate at a fixed rate  $q - p$  as the pulse propagates down the fiber.

Numerically, simulations show that elliptically polarized vector solitons with comparable magnitudes of  $U$  and  $V$  also exist [121]. Although their stability over long distances is not guaranteed, such solitons can propagate stably over hundreds of dispersion lengths when they correspond to the symmetric branch. In contrast, the double-hump vector solitons on the asymmetric branch are much less stable and they loose their stability over distances  $z < 100L_D$  [123]. In addition to these pulse-like solitons, dark vector solitons also form in the case of normal dispersion [122]. Vector solitons in isotropic Kerr media have continued to attract attention in recent years [126–130].

---

## 6.6 RANDOM BIREFRINGENCE

As mentioned in Section 6.1, modal birefringence in optical fibers changes randomly over a length scale  $\sim 10\text{ m}$  unless polarization-maintaining fibers are used. Because lightwave systems commonly use fibers with randomly varying birefringence, it is important to study how optical pulses are affected by random birefringence changes. Indeed, this issue has been investigated extensively since 1986, when the so-called PMD problem was identified [131–137]. In this section we focus on the effects of random birefringence.

### 6.6.1 Polarization-Mode Dispersion

It is intuitively clear that the polarization state of CW light propagating in fibers with randomly varying birefringence will generally be elliptical and would change randomly along the fiber during propagation. In the case of optical pulses, the polarization state can also be different for different parts of the pulse unless the pulse propagates as a soliton. Such random polarization changes are not typically of concern for lightwave systems because photodetectors used inside optical receivers are insensitive to the state of polarization of the incident light (unless a coherent-detection scheme is employed). What affects such systems is not the random polarization state but pulse broadening induced by random changes in the birefringence. This is referred to as PMD-induced pulse broadening.

The analytical treatment of PMD is quite complex in general because of its statistical nature. A simple model, first introduced in 1986 [131], divides the fiber into a large number of sections. Both the degree of birefringence and the orientation of the principal axes remain constant in each section but change randomly from section to section. In effect, each fiber section can be treated as a phase plate and a Jones matrix can be used for it [136]. Propagation of each frequency component associated with an optical pulse through the entire fiber length is then governed by a composite Jones matrix obtained by multiplying individual Jones matrices for each fiber section. The composite Jones matrix shows that two principal states of polarization exist

for any fiber such that, when a pulse is polarized along them, the polarization state at fiber output is frequency independent to first order, in spite of random changes in fiber birefringence. These states are analogs of the slow and fast axes associated with polarization-maintaining fibers. Indeed, the differential group delay  $\Delta T$  (relative time delay in the arrival time of the two polarization components) is largest for the principal states of polarization [133].

The principal states of polarization provide a convenient basis for calculating the moments of  $\Delta T$  [138]. The PMD-induced pulse broadening is characterized by the root-mean-square (RMS) value of  $\Delta T$ , obtained after averaging over random birefringence changes. Several approaches have been used to calculate this average using different models [139–142]. The variance  $\sigma_T^2 \equiv \langle (\Delta T)^2 \rangle$  turns out to be the same in all cases and is given by [143]

$$\sigma_T^2(z) = 2(\Delta\beta_1)^2 l_c^2 [\exp(-z/l_c) + z/l_c - 1], \quad (6.6.1)$$

where the intrinsic modal dispersion  $\Delta\beta_1 = d(\Delta\beta)/d\omega$  is related to the difference in group velocities along the two principal states of polarization. The parameter  $l_c$  is the correlation length, defined as the length over which two polarization components remain correlated; its typical values are  $\sim 10\text{ m}$ .

For short distances such that  $z \ll l_c$ ,  $\sigma_T = (\Delta\beta_1)z$  from Eq. (6.6.1), as expected for a polarization-maintaining fiber. For distances  $z > 1\text{ km}$ , a good estimate of pulse broadening is obtained using  $z \gg l_c$ . For a fiber of length  $L$ ,  $\sigma_T$  in this approximation becomes

$$\sigma_T \approx \Delta\beta_1 \sqrt{2l_c L} \equiv D_p \sqrt{L}, \quad (6.6.2)$$

where  $D_p$  is the PMD parameter. Measured values of  $D_p$  vary from fiber to fiber, typically in the range  $D_p = 0.1 - 2\text{ ps}/\sqrt{\text{km}}$  [144]. Modern fibers are designed to have low PMD, with values of  $D_p$  as low as  $0.05\text{ ps}/\sqrt{\text{km}}$  [132]. Because of the  $\sqrt{L}$  dependence, PMD-induced pulse broadening is relatively small compared with the GVD effects. If we use  $D_p = 0.1\text{ ps}/\sqrt{\text{km}}$  as a typical value,  $\sigma_T \sim 1\text{ ps}$  for fiber lengths  $\sim 100\text{ m}$  and can be ignored for pulse widths  $> 10\text{ ps}$ . However, PMD becomes a limiting factor for lightwave systems designed to operate over long distances at high bit rates.

Several other factors need to be considered in practice. The derivation of Eq. (6.6.1) assumes that the fiber link has no elements exhibiting polarization-dependent loss or gain. The presence of polarization-dependent losses along a fiber link can modify the PMD effects considerably [145–152]. Similarly, the effects of second-order PMD should be considered for fibers with relatively low values of  $D_p$ . Such effects have been studied and lead to additional distortion of optical pulses [135].

## 6.6.2 Vector Form of the NLS Equation

As mentioned earlier, the polarization state of a pulse in general becomes nonuniform across the pulse because of random changes in fiber birefringence. At the same

time, PMD leads to pulse broadening. Such effects can be studied by generalizing the coupled NLS equations derived in Section 6.1, namely Eqs (6.1.11) and (6.1.12) to the case in which a fiber exhibits random birefringence changes along its length. It is more convenient to write these equations in terms of the normalized amplitudes  $u$  and  $v$  defined as

$$u = A_x \sqrt{\gamma L_D} e^{i\Delta\beta z/2}, \quad v = A_y \sqrt{\gamma L_D} e^{-i\Delta\beta z/2}. \quad (6.6.3)$$

If we also use soliton units and introduce normalized distance and time as

$$\xi = z/L_D, \quad \tau = (t - \bar{\beta}_1 z)/T_0, \quad (6.6.4)$$

where  $\bar{\beta}_1 = \frac{1}{2}(\beta_{1x} + \beta_{1y})$ , Eqs (6.1.11) and (6.1.12) take the form

$$i \left( \frac{\partial u}{\partial \xi} + \delta \frac{\partial u}{\partial \tau} \right) + bu + \frac{1}{2} \frac{\partial^2 u}{\partial \tau^2} + \left( |u|^2 + \frac{2}{3} |v|^2 \right) u + \frac{1}{3} v^2 u^* = 0, \quad (6.6.5)$$

$$i \left( \frac{\partial v}{\partial \xi} - \delta \frac{\partial v}{\partial \tau} \right) - bv + \frac{1}{2} \frac{\partial^2 v}{\partial \tau^2} + \left( |v|^2 + \frac{2}{3} |u|^2 \right) v + \frac{1}{3} u^2 v^* = 0, \quad (6.6.6)$$

where

$$b = \frac{T_0^2(\Delta\beta)}{2|\beta_2|}, \quad \delta = \frac{T_0}{2|\beta_2|} \frac{d(\Delta\beta)}{d\omega}. \quad (6.6.7)$$

Equations (6.6.5) and (6.6.6) can be written in a compact form using the Jones-matrix formalism. We introduce the Jones vector  $|U\rangle$  and the Pauli matrices as [136]

$$|U\rangle = \begin{pmatrix} u \\ v \end{pmatrix}, \quad \sigma_1 = \begin{pmatrix} 1 & 0 \\ 0 & -1 \end{pmatrix}, \quad \sigma_2 = \begin{pmatrix} 0 & 1 \\ 1 & 0 \end{pmatrix}, \quad \sigma_3 = \begin{pmatrix} 0 & -i \\ i & 0 \end{pmatrix}. \quad (6.6.8)$$

In terms of the Jones vector  $|U\rangle$ , the coupled NLS equations become [154]

$$i \frac{\partial |U\rangle}{\partial \xi} + \sigma_1 \left( b|U\rangle + i\delta \frac{\partial |U\rangle}{\partial \tau} \right) + \frac{1}{2} \frac{\partial^2 |U\rangle}{\partial \tau^2} + s_0|U\rangle - \frac{1}{3} s_3 \sigma_3 |U\rangle = 0, \quad (6.6.9)$$

where the Stokes parameters are defined in terms of  $|U\rangle$  as [136]

$$s_0 = \langle U|U\rangle = |u|^2 + |v|^2, \quad s_1 = \langle U|\sigma_1|U\rangle = |u|^2 - |v|^2, \quad (6.6.10)$$

$$s_2 = \langle U|\sigma_2|U\rangle = 2 \operatorname{Re}(u^*v), \quad s_3 = \langle U|\sigma_3|U\rangle = 2 \operatorname{Im}(u^*v). \quad (6.6.11)$$

These Stokes parameters are analogous to those introduced in Section 6.3.2 for describing the polarization state of CW light on the Poincaré sphere. The main difference is that they are time dependent and describe the polarization state of a pulse. They can be reduced to those of Section 6.3.2 by integrating over time such that  $S_j = \int_{-\infty}^{\infty} s_j(t) dt$  for  $j=0-3$ .

Fiber birefringence is assumed to be constant in deriving Eq. (6.6.9). It is not enough to treat the parameters  $\delta$  and  $b$  appearing in this equation as random variables because the principal axes themselves rotate along the fiber in a random fashion. To include such random rotations, it is common in numerical simulations to divide the fiber into many sections of length  $l_c$  or shorter and rotate the Jones vector at the end of each section through the transformation  $|U'\rangle = \mathcal{R}|U\rangle$ , where  $\mathcal{R}$  is a random rotation matrix of the form

$$\mathcal{R} = \begin{pmatrix} \cos \theta & \sin \theta e^{i\phi} \\ -\sin \theta e^{-i\phi} & \cos \theta \end{pmatrix}, \quad (6.6.12)$$

and the two random variables  $\theta$  and  $\phi$  are distributed uniformly in the range  $[-\pi, \pi]$  and  $[-\pi/2, \pi/2]$ , respectively. Of course,  $b$  and  $\delta$  also vary randomly from section to section because of the randomness of  $\Delta\beta$ . In a simple but reasonably accurate model,  $\Delta\beta$  is treated as a Gaussian stochastic process whose first two moments are given by

$$\overline{\Delta\beta(z)} = 0, \quad \overline{\Delta\beta(z)\Delta\beta(z')} = \sigma_\beta^2 \exp(-|z - z'|/l_c), \quad (6.6.13)$$

where  $\sigma_\beta^2$  is the variance and  $l_c$  is the correlation length of birefringence fluctuations.

### 6.6.3 Effects of PMD on Solitons

In the absence of nonlinear effects or low-energy pulses, one can neglect the last two terms in Eq. (6.6.9). The resulting linear equation is often solved in the frequency domain to study how PMD affects an optical pulse [133–137]. The Fourier-domain approach cannot be used for pulses that propagate as solitons in the anomalous-GVD regime of the fiber because the nonlinear effects play an essential role for solitons. An interesting question is how the XPM-induced coupling modifies the birefringence-induced PMD effects. This issue has been investigated extensively, mainly in the context of long-haul lightwave systems [153–171].

In the case of constant birefringence, it was seen in Section 6.5 that the orthogonally polarized components of a soliton can travel at the same speed, in spite of different group velocities associated with them at low powers. Solitons realize this synchronization by shifting their frequencies appropriately. It is thus not hard to imagine that solitons may avoid splitting and PMD-induced pulse broadening through the same mechanism. Indeed, numerical simulations based on Eqs (6.1.11) and (6.1.12) indicate this to be the case [153] as long as the PMD parameter is small enough to satisfy the condition  $D_p < 0.3\sqrt{|\beta_2|}$ . It thus appears that solitons are relatively immune to random changes because of their particle-like nature.

As in the CW case, the Stokes vector with components  $s_1$ ,  $s_2$ , and  $s_3$  moves on the surface of the Poincaré sphere of radius  $s_0$ . When birefringence of the fiber varies randomly along the fiber, the tip of the Stokes vector moves randomly over the

Poincaré sphere. The important question is the length scale over which such motion covers the entire surface of the Poincaré sphere and how this length compares with the dispersion length. To answer this question, one should consider on what length scale random variations in  $b$  occur compared with the soliton period (or the dispersion length).

For most fibers, random changes in  $b$  occur on a length scale  $\sim 10$  m. As they only affect the phases of  $u$  and  $v$ , it is clear that such changes leave  $s_1$  unchanged. As a result, the Stokes vector rotates rapidly around the  $s_1$ -axis. In contrast, changes in the orientation of the birefringence axes leave  $s_3$  unchanged and thus rotate the Stokes vector around that axis. The combination of these two types of rotations forces the Stokes vector to fill the entire surface of the Poincaré sphere over a length scale  $\sim 1$  km. As this distance is typically much shorter than the dispersion length, soliton parameters are not much affected by random changes in birefringence. The situation is similar to the case of energy variations occurring when fiber losses are compensated periodically using optical amplifiers (see Section 5.4). We can thus follow a similar approach and average Eq. (6.6.9) over random birefringence changes. The last term in this equation requires the average of  $s_3\sigma_3|U\rangle$ . This average turns out to be  $s_0|U\rangle/3$  if we make use of the identity  $|U\rangle\langle U| = s_1\sigma_1 + s_2\sigma_2 + s_3\sigma_3$  [136].

As  $\bar{b} = 0$  from Eq. (6.6.13), the two terms containing  $\sigma_1$  change sign often along the fiber length. If we ignore them to the first order and average over birefringence fluctuations, Eq. (6.6.9) reduces to

$$i \frac{\partial|U\rangle}{\partial\xi} + \frac{1}{2} \frac{\partial^2|U\rangle}{\partial\tau^2} + \frac{8}{9}s_0|U\rangle = 0. \quad (6.6.14)$$

The factor of  $\frac{8}{9}$  can be absorbed in the normalization used for  $|U\rangle$  and amounts to reducing the nonlinear parameter  $\gamma$ , or increasing the input peak power  $P_0$ , by this factor. Recalling from Eq. (6.6.11) that  $s_0 = |u|^2 + |v|^2$ , Eq. (6.6.14) can be written in terms of the components  $u$  and  $v$  as

$$i \frac{\partial u}{\partial\xi} + \frac{1}{2} \frac{\partial^2 u}{\partial\tau^2} + (|u|^2 + |v|^2)u = 0, \quad (6.6.15)$$

$$i \frac{\partial v}{\partial\xi} + \frac{1}{2} \frac{\partial^2 v}{\partial\tau^2} + (|v|^2 + |u|^2)v = 0. \quad (6.6.16)$$

As discussed in Section 6.5.3, this set of two coupled NLS equations is integrable by the inverse scattering method [98] and has the solution in the form of a fundamental vector soliton given in Eqs (6.5.12) and (6.5.13). This solution shows that a fundamental soliton maintains the same polarization across the entire pulse “on average” in spite of random birefringence changes along the fiber. This is an extraordinary result and is indicative of the particle-like nature of solitons. In effect, solitons maintain uniform polarization across the entire pulse and resist small random changes in fiber birefringence [153]. Extensive numerical simulations based on Eqs (6.6.5)

and (6.6.6) confirm that solitons can maintain an approximately uniform polarization state over long fiber lengths even when optical amplifiers are used periodically for compensating fiber losses [154].

It is important to note that the vector soliton associated with Eqs (6.6.15) and (6.6.16) represents the average behavior. The five parameters associated with this soliton (amplitude, frequency, position, phase, and polarization angle) will generally fluctuate along fiber length in response to random birefringence changes. Perturbation theory, similar to that used for scalar solitons in Section 5.4, can be used to study birefringence-induced changes in soliton parameters [155–159]. For example, the amplitude of the soliton decreases and its width increases because of perturbations produced by random birefringence. The reason behind soliton broadening is related to the generation of dispersive waves (continuum radiation) and the resulting energy loss. The perturbation technique can also be used to study interaction between orthogonally polarized solitons [160] and timing jitter induced by amplifier-induced fluctuations in the polarization state of the soliton [162].

From a practical standpoint, uniformity of soliton polarization can be useful for polarization-division multiplexing. In this scheme, two orthogonally polarized bit streams are interleaved in the time domain. As a result, alternate pulses have orthogonal polarization states initially and are able to maintain their orthogonality if they propagate as solitons. This allows much tighter packing of solitons (resulting in a higher bit rate) because the interaction between two neighboring solitons is reduced when they are orthogonally polarized. However, extensive numerical simulations show that the technique of polarization-division multiplexing is useful in practice only when the PMD parameter  $D_p$  is relatively small [161]. When  $D_p$  is large, copolarized solitons provide a better overall system performance.

To quantify the robustness of copolarized solitons to PMD, one must retain the birefringence terms in Eq. (6.6.9) while averaging over the last nonlinear term. Thus, one must solve the perturbed vector NLS equation

$$i\frac{\partial|U\rangle}{\partial\xi} + \frac{1}{2}\frac{\partial^2|U\rangle}{\partial\tau^2} + \frac{8}{9}s_0|U\rangle = -\sigma_1\left(b|U\rangle + i\delta\frac{\partial|U\rangle}{\partial\tau}\right), \quad (6.6.17)$$

where the random variables  $b$  and  $\delta$  take into account the birefringence-induced phase shift and differential group delay (DGD), respectively, experienced by a soliton inside the fiber. This equation is solved either numerically or approximately using a perturbative approach [164–171]. The results can be summarized as follows. As the vector soliton propagates through the fiber, it sheds a part of its energy in the form of dispersive waves and its position shifts in a random fashion. The energy loss and peak-position jitter manifest as a broadening of the soliton on average.

As one may expect, pulse width at any point within the fiber depends on the statistical distribution of birefringence along the fiber. In practice, it fluctuates with time because birefringence distribution in a realistic fiber is not static but changes with environmental factors such as stress and temperature. For this reason, the PMD effects are often quantified through the average RMS width of the pulse.

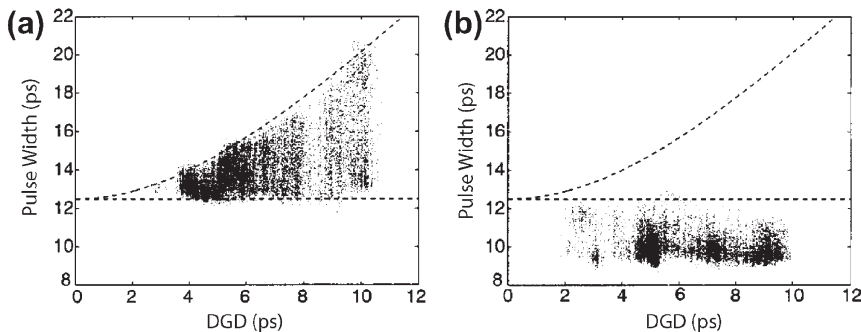


**Figure 6.16** PMD-induced pulse-width fluctuations as a function of DGD in the (a) linear and (b) nonlinear propagation regimes. The dotted curves show the range of fluctuations in the linear case. (After Ref. [167]; © 2001 IEEE.)

Perturbation theory shows that the RMS width of the soliton for a fiber of length  $L$  is given by [168]

$$\sigma_s^2 = \sigma_0^2 + (\pi^2/108)\sigma_T^2, \quad (6.6.18)$$

where  $\sigma_T$  is defined as in Eq. (6.6.4). A comparison with the linear case ( $\gamma = 0$ ) shows that pulse broadening is reduced considerably in the case of solitons. Numerical simulations based on Eq. (6.6.17) confirm this prediction [168].

The effects of PMD on solitons has been observed in several experiments for both the conventional and dispersion-managed solitons [167]. The results show that the pulse width at the output end of the fiber fluctuates with time, in both the linear and nonlinear propagation regimes, but the range over which pulse width fluctuates is reduced considerably for solitons. As seen in Figure 6.16, this range depends on the instantaneous value of DGD. Whereas the range of width fluctuations increases with DGD for linear pulses, it remains relatively constant for solitons. It is this feature that indicates the robustness of solitons to birefringence fluctuations. It should be stressed that the average and RMS values of pulse-width fluctuations are not sufficient to quantify the data in Figure 6.16 because their statistical distribution is far from being Gaussian. A collective-variable approach has been used to find an analytic expression for the probability density function of width fluctuations [169]. It shows that the XPM-induced coupling between the orthogonally polarized components of a soliton narrows down the width distribution considerably.

## PROBLEMS

- 6.1 Derive an expression for the nonlinear part of the refractive index when an optical beam propagates inside a high-birefringence optical fiber.
- 6.2 Prove that Eqs (6.1.15) and (6.1.16) indeed follow from Eqs (6.1.11) and (6.1.12).

- 6.3** Prove that a high-birefringence fiber of length  $L$  introduces a relative phase shift of  $\Delta\phi_{NL} = (\gamma P_0 L / 3) \cos(2\theta)$  between the two linearly polarized components when a CW beam with peak power  $P_0$  and polarization angle  $\theta$  propagates through it. Neglect fiber losses.
- 6.4** Explain the operation of a Kerr shutter. What factors limit the response time of such a shutter when optical fibers are used as the Kerr medium?
- 6.5** How can fiber birefringence be used to remove the low-intensity pedestal associated with an optical pulse?
- 6.6** Solve Eqs (6.3.1) and (6.3.2) in terms of the elliptic functions. You can consult Reference [44].
- 6.7** Prove that Eqs (6.3.14) and (6.3.15) can be written in the form of Eq. (6.3.19) after introducing the Stokes parameters through Eq. (6.3.16).
- 6.8** What is meant by polarization instability in birefringent optical fibers? Explain the origin of this instability.
- 6.9** Derive the dispersion relation  $K(\Omega)$  for modulation instability to occur in low-birefringence fibers starting from Eqs (6.1.15) and (6.1.16). Discuss the frequency range over which the gain exists when  $\beta_2 > 0$ .
- 6.10** Derive the dispersion relation  $K(\Omega)$  for modulation instability to occur in high-birefringence fibers starting from Eqs (6.1.22) and (6.1.23). Discuss the frequency range over which the gain exists when  $\beta_2 > 0$ .
- 6.11** Solve Eqs (6.5.4) and (6.5.5) numerically by using the split-step Fourier method. Reproduce the results shown in Figures 6.14 and 6.15. Check the accuracy of Eq. (6.5.8) for  $\delta = 0.2$  and  $B = \frac{2}{3}$ .
- 6.12** Verify by direct substitution that the solution given by Eq. (6.5.14) satisfies Eqs (6.5.4) and (6.5.5).
- 6.13** Explain the operation of soliton-dragging logic gates. How would you design a NOR gate by using such a technique?
- 6.14** Explain the origin of PMD in optical fibers. Why does PMD lead to pulse broadening. Do you expect PMD-induced broadening to occur for solitons?

---

## REFERENCES

- [1] P. D. Maker, R. W. Terhune, and C. M. Savage, *Phys. Rev. Lett.* **12**, 507 (1964).
- [2] G. Mayer and F. Gires, *Compt. Rend. Acad. Sci.* **258**, 2039 (1964).
- [3] P. D. Maker and R. W. Terhune, *Phys. Rev. A* **137**, A801 (1965).
- [4] M. A. Duguay and J. W. Hansen, *Appl. Phys. Lett.* **15**, 192 (1969).
- [5] A. Owyoung, R. W. Hellwarth, and N. George, *Phys. Rev. B* **5**, 628 (1972).
- [6] M. A. Duguay, in *Progress in Optics*, Vol. 14, E. Wolf, Ed. (North-Holland, 1976), Chap. 4.
- [7] R. W. Hellwarth, *Prog. Quantum Electron.* **5**, 1 (1977).
- [8] N. G. Phu-Xuan and G. Rivoire, *Opt. Acta* **25**, 233 (1978).
- [9] Y. R. Shen, *The Principles of Nonlinear Optics* (Wiley, 1984).
- [10] R. W. Boyd, *Nonlinear Optics*, 3rd ed. (Academic Press, 2008).
- [11] R. Ulrich and A. Simon, *Appl. Opt.* **18**, 2241 (1979).

- [12] C. R. Menyuk, *IEEE J. Quantum Electron.* **25**, 2674 (1989).
- [13] R. H. Stolen and A. Ashkin, *Appl. Phys. Lett.* **22**, 294 (1973).
- [14] J. M. Dziedzic, R. H. Stolen, and A. Ashkin, *Appl. Opt.* **20**, 1403 (1981).
- [15] J. L. Aryal, J. P. Pocholle, J. Raffy, and M. Papuchon, *Opt. Commun.* **49**, 405 (1984).
- [16] K. Kitayama, Y. Kimura, and S. Sakai, *Appl. Phys. Lett.* **46**, 623 (1985).
- [17] E. M. Dianov, E. A. Zakhidov, A. Y. Karasik, M. A. Kasymdzhanov, F. M. Mirtadzhiev, A. M. Prokhorov, and P. K. Khabibullaev, *Sov. J. Quantum Electron.* **17**, 517 (1987).
- [18] T. Morioka, M. Saruwatari, and A. Takada, *Electron. Lett.* **23**, 453 (1987).
- [19] K. C. Byron, *Electron. Lett.* **23**, 1324 (1987).
- [20] T. Morioka and M. Saruwatari, *IEEE J. Sel. Areas Commun.* **6**, 1186 (1988).
- [21] I. H. White, R. V. Penty, and R. E. Epworth, *Electron. Lett.* **24**, 340 (1988).
- [22] M. Asobe, T. Kanamori, and K. Kubodera, *IEEE Photon. Technol. Lett.* **4**, 362 (1992); *IEEE J. Quantum Electron.* **29**, 2325 (1993).
- [23] M. Asobe, H. Kobayashi, H. Itoh, and T. Kanamori, *Opt. Lett.* **18**, 1056 (1993).
- [24] M. Asobe, *Opt. Fiber Technol.* **3**, 142 (1997).
- [25] J. H. Lee, K. Kikuchi, T. Nagashima, T. Hasegawa, S. Ohara, and N. Sugimoto, *Opt. Express* **13**, 3144 (2005).
- [26] R. H. Stolen, J. Botineau, and A. Ashkin, *Opt. Lett.* **7**, 512 (1982).
- [27] B. Nikolaus, D. Grischkowsky, and A. C. Balant, *Opt. Lett.* **8**, 189 (1983).
- [28] N. J. Halas and D. Grischkowsky, *Appl. Phys. Lett.* **48**, 823 (1986).
- [29] K. Kitayama, Y. Kimura, and S. Seikai, *Appl. Phys. Lett.* **46**, 317 (1985); *Appl. Phys. Lett.* **46**, 623 (1985).
- [30] K. Tamura, E. P. Ippen, H. A. Haus, and L. E. Nelson, *Opt. Lett.* **18**, 1080 (1993).
- [31] H. G. Winful, *Appl. Phys. Lett.* **47**, 213 (1985).
- [32] B. Crosignani and P. Di Porto, *Opt. Acta* **32**, 1251 (1985).
- [33] B. Daino, G. Gregori, and S. Wabnitz, *Opt. Lett.* **11**, 42 (1986).
- [34] H. G. Winful, *Opt. Lett.* **11**, 33 (1986).
- [35] G. Gregori and S. Wabnitz, *Phys. Rev. Lett.* **56**, 600 (1986).
- [36] F. Matera and S. Wabnitz, *Opt. Lett.* **11**, 467 (1986).
- [37] S. Trillo, S. Wabnitz, R. H. Stolen, G. Assanto, C. T. Seaton, and G. I. Stegeman, *Appl. Phys. Lett.* **49**, 1224 (1986).
- [38] A. Vatarescu, *Appl. Phys. Lett.* **49**, 61 (1986).
- [39] S. Wabnitz, *Phys. Rev. Lett.* **58**, 1415 (1987).
- [40] A. Mecozzi, S. Trillo, S. Wabnitz, and B. Daino, *Opt. Lett.* **12**, 275 (1987).
- [41] Y. Kimura and M. Nakazawa, *Jpn. J. Appl. Phys.* **2**, 1503 (1987).
- [42] E. Caglioti, S. Trillo, and S. Wabnitz, *Opt. Lett.* **12**, 1044 (1987).
- [43] S. Trillo, S. Wabnitz, E. M. Wright, and G. I. Stegeman, *Opt. Commun.* **70**, 166 (1989).
- [44] S. F. Feldman, D. A. Weinberger, and H. G. Winful, *Opt. Lett.* **15**, 311 (1990);(b) *J. Opt. Soc. Am. B* **10**, 1191 (1993).
- [45] P. Ferro, S. Trillo, and S. Wabnitz, *Appl. Phys. Lett.* **64**, 2782 (1994).
- [46] N. N. Akhmediev and J. M. Soto-Crespo, *Phys. Rev. E* **49**, 5742 (1994).
- [47] Y. Barad and Y. Silberberg, *Phys. Rev. Lett.* **78**, 3290 (1997).
- [48] A. L. Berkhoer and V. E. Zakharov, *Sov. Phys. JETP* **31**, 486 (1970).
- [49] S. Wabnitz, *Phys. Rev. A* **38**, 2018 (1988).
- [50] S. Trillo and S. Wabnitz, *J. Opt. Soc. Am. B* **6**, 238 (1989).
- [51] J. E. Rothenberg, *Phys. Rev. A* **42**, 682 (1990).
- [52] P. D. Drummond, T. A. B. Kennedy, J. M. Dudley, R. Leonhardt, and J. D. Harvey, *Opt. Commun.* **78**, 137 (1990).

- [53] J. E. Rothenberg, *Opt. Lett.* **16**, 18 (1991).
- [54] W. Huang and J. Hong, *J. Lightwave Technol.* **10**, 156 (1992).
- [55] S. G. Murdoch, R. Leonhardt, and J. D. Harvey, *Opt. Lett.* **20**, 866 (1995).
- [56] S. G. Murdoch, M. D. Thomson, R. Leonhardt, and J. D. Harvey, *Opt. Lett.* **22**, 682 (1997).
- [57] G. Millot, S. Pitois, P. Tchofo Dinda, and M. Haelterman, *Opt. Lett.* **22**, 1686 (1997).
- [58] G. Millot, E. Seve, S. Wabnitz, and M. Haelterman, *J. Opt. Soc. Am. B* **15**, 1266 (1998).
- [59] E. Seve, G. Millot, and S. Wabnitz, *Opt. Lett.* **23**, 1829 (1998).
- [60] P. Kockaert, M. Haelterman, S. Pitois, and G. Millot, *Appl. Phys. Lett.* **75**, 2873 (1999).
- [61] E. Seve, G. Millot, and S. Trillo, *Phys. Rev. E* **61**, 3139 (2000).
- [62] T. Tanemura and K. Kikuchi, *J. Opt. Soc. Am. B* **20**, 2502 (2003).
- [63] F. Biancalana and D. V. Skryabin, *J. Opt. A* **6**, 301 (2004).
- [64] B. Kibler, C. Billet, J. M. Dudley, R. S. Windeler, and G. Millot, *Opt. Lett.* **29**, 1903 (2004).
- [65] E. Brainis, D. Amans, and S. Massar, *Phys. Rev. A* **71**, 023808 (2005).
- [66] D. Amans, E. Brainis, M. Haelterman, P. Emplit, and S. Massar, *Opt. Lett.* **30**, 1051 (2005).
- [67] R. J. Kruhlak, G. K. Wong, , J. S. Chen, et al., *Opt. Lett.* **31**, 1379 (2006).
- [68] H. S. Chiu and K. W. Chow, *Phys. Rev. A* **79**, 065803 (2009).
- [69] K. J. Blow, N. J. Doran, and D. Wood, *Opt. Lett.* **12**, 202 (1987).
- [70] C. R. Menyuk, *IEEE J. Quantum Electron.* **23**, 174 (1987).
- [71] C. R. Menyuk, *Opt. Lett.* **12**, 614 (1987).
- [72] C. R. Menyuk, *J. Opt. Soc. Am. B* **5**, 392 (1988).
- [73] A. D. Boardman and G. S. Cooper, *J. Opt. Soc. Am. B* **5**, 403 (1988); *J. Mod. Opt.* **35**, 407 (1988).
- [74] Y. S. Kivshar, *J. Opt. Soc. Am. B* **7**, 2204 (1990).
- [75] R. J. Dowling, *Phys. Rev. A* **42**, 5553 (1990).
- [76] B. A. Malomed, *Phys. Rev. A* **43**, 410 (1991).
- [77] D. Anderson, Y. S. Kivshar, and M. Lisak, *Phys. Scripta* **43**, 273 (1991).
- [78] B. A. Malomed and S. Wabnitz, *Opt. Lett.* **16**, 1388 (1991).
- [79] N. A. Kostov and I. M. Uzunov, *Opt. Commun.* **89**, 389 (1991).
- [80] V. K. Mesentsev and S. K. Turitsyn, *Opt. Lett.* **17**, 1497 (1992).
- [81] B. A. Malomed, *Phys. Rev. A* **43**, 410 (1991); *J. Opt. Soc. Am. B* **9**, 2075 (1992).
- [82] X. D. Cao and C. J. McKinstry, *J. Opt. Soc. Am. B* **10**, 1202 (1993).
- [83] D. J. Kaup and B. A. Malomed, *Phys. Rev. A* **48**, 599 (1993).
- [84] M. N. Islam, C. D. Poole, and J. P. Gordon, *Opt. Lett.* **14**, 1011 (1989).
- [85] D. Rand, I. Glesk, , C.-S. Brés, et al., *Phys. Rev. Lett.* **98**, 053902 (2007).
- [86] M. N. Islam, *Opt. Lett.* **14**, 1257 (1989); *Opt. Lett.* **15**, 417 (1990).
- [87] M. N. Islam, C. E. Soccilich, and D. A. B. Miller, *Opt. Lett.* **15**, 909 (1990).
- [88] M. N. Islam and J. R. Sauer, *IEEE J. Quantum Electron.* **27**, 843 (1991).
- [89] M. N. Islam, C. R. Menyuk, C.-J. Chen, and C. E. Soccilich, *Opt. Lett.* **16**, 214 (1991).
- [90] M. N. Islam, *Ultrafast Fiber Switching Devices and Systems* (Cambridge University Press, 2006).
- [91] C.-J. Chen, P. K. A. Wai, and C. R. Menyuk, *Opt. Lett.* **15**, 477 (1990).
- [92] C. R. Menyuk, M. N. Islam, and J. P. Gordon, *Opt. Lett.* **16**, 566 (1991).
- [93] C.-J. Chen, C. R. Menyuk, M. N. Islam, and R. H. Stolen, *Opt. Lett.* **16**, 1647 (1991).
- [94] M. W. Chbat, B. Hong, M. N. Islam, C. E. Soccilich, and P. R. Prucnal, *J. Lightwave Technol.* **12**, 2011 (1992).

- [95] Q. Wang, P. K. A. Wai, C.-J. Chen, and C. R. Menyuk, *Opt. Lett.* **17**, 1265 (1992); *J. Opt. Soc. Am. B* **10**, 2030 (1993).
- [96] J. R. Sauer, M. N. Islam, and S. P. Dijali, *J. Lightwave Technol.* **11**, 2182 (1994).
- [97] Y. S. Kivshar and G. P. Agrawal, *Optical Solitons: From Fibers to Photonic Crystals* (Academic Press, 2003), Chap. 9.
- [98] S. V. Manakov, *Sov. Phys. JETP* **38**, 248 (1974).
- [99] Z.-Y. Sun, Y.-T. Gao, X. Yu, W.-J. Liu, and Y. Liu, *Phys. Rev. E* **80**, 066608 (2009).
- [100] Y. Inoue, *J. Plasma Phys.* **16**, 439 (1976); *J. Phys. Soc. Jpn.* **43**, 243 (1977).
- [101] M. R. Gupta, B. K. Som, and B. Dasgupta, *J. Plasma Phys.* **25**, 499 (1981).
- [102] V. E. Zakharov and E. I. Schulman, *Physica D* **4**, 270 (1982).
- [103] D. N. Christoulides and R. I. Joseph, *Opt. Lett.* **13**, 53 (1988).
- [104] M. V. Tratnik and J. E. Sipe, *Phys. Rev. A* **38**, 2011 (1988).
- [105] N. N. Akhmediev, V. M. Elonskii, N. E. Kulagin, and L. P. Shilnikov, *Sov. Tech. Phys. Lett.* **15**, 587 (1989).
- [106] T. Ueda and W. L. Kath, *Phys. Rev. A* **42**, 563 (1990).
- [107] D. David and M. V. Tratnik, *Physica D* **51**, 308 (1991).
- [108] S. Trillo and S. Wabnitz, *Phys. Lett.* **159**, 252 (1991).
- [109] L. Gagnon, *J. Phys. A* **25**, 2649 (1992).
- [110] B. A. Malomed, *Phys. Rev. A* **45**, R8821 (1992).
- [111] M. V. Tratnik, *Opt. Lett.* **17**, 917 (1992).
- [112] D. Kapor, M. Skrinjar, and S. Stojanovic, *J. Phys. A* **25**, 2419 (1992).
- [113] R. S. Tasgal and M. J. Potasek, *J. Math. Phys.* **33**, 1280 (1992).
- [114] M. Wadati, T. Iizuka, and M. Hisakado, *J. Phys. Soc. Jpn.* **61**, 2241 (1992).
- [115] Y. S. Kivshar, *Opt. Lett.* **17**, 1322 (1992).
- [116] Y. S. Kivshar and S. K. Turitsyn, *Opt. Lett.* **18**, 337 (1993).
- [117] V. V. Afanasjev and A. B. Grudinin, *Sov. Lightwave Commun.* **3**, 77 (1993).
- [118] M. Haelterman, A. P. Sheppard, and A. W. Snyder, *Opt. Lett.* **18**, 1406 (1993).
- [119] D. J. Kaup, B. A. Malomed, and R. S. Tasgal, *Phys. Rev. E* **48**, 3049 (1993).
- [120] J. C. Bhakta, *Phys. Rev. E* **49**, 5731 (1994).
- [121] M. Haelterman and A. P. Sheppard, *Phys. Lett. A* **194**, 191 (1994).
- [122] M. Haelterman and A. P. Sheppard, *Phys. Rev. E* **49**, 3389 (1994).
- [123] Y. Silberberg and Y. Barad, *Opt. Lett.* **20**, 246 (1995).
- [124] N. N. Akhmediev, A. V. Buryak, J. M. Soto-Crespo, and D. R. Andersen, *J. Opt. Soc. Am. B* **12**, 434 (1995).
- [125] Y. Chen and J. Atai, *Phys. Rev. E* **55**, 3652 (1997).
- [126] F. Lu, Q. Lin, W. H. Knox, and G. P. Agrawal, *Phys. Rev. Lett.* **93**, 183901 (2004).
- [127] M. Delqué, T. Sylvestre, , H. Maillotte, et al., *Opt. Lett.* **30**, 3383 (2005).
- [128] M. Delqué, G. Fanjoux, and T. Sylvestre, *Phys. Rev. E* **75**, 016611 (2007).
- [129] Z.-B. Liu, X.-Q. Yan, W.-Y. Zhou, and J.-G. Tian, *Opt. Express* **16**, 8144 (2008).
- [130] A. V. Kim and S. A. Skobelev, *Phys. Rev. A* **83**, 063832 (2011).
- [131] C. D. Poole and R. E. Wagner, *Electron. Lett.* **22**, 1029 (1986).
- [132] F. Bruyère, *Opt. Fiber Technol.* **2**, 269 (1996).
- [133] C. D. Poole and J. Nagel, in *Optical Fiber Telecommunications*, Vol. 3A, I. P. Kaminow and T. L. Koch, Eds. (Academic Press, 1997), Chap. 6.
- [134] J. P. Gordon and H. Kogelnik, *Proc. Natl. Acad. Sci. USA* **97**, 4541 (2000).
- [135] H. Kogelnik, R. M. Jopson, and L. E. Nelson, in *Optical Fiber Telecommunications*, Vol. 4A, I. P. Kaminow and T. Li, Eds. (Academic Press, 2002), Chap. 15.
- [136] J. N. Damask, *Polarization Optics in Telecommunications* (Springer, 2005).

- [137] G. P. Agrawal, *Lightwave Technology: Telecommunication Systems* (Wiley, 2005), Chap. 3.
- [138] C. D. Poole, *Opt. Lett.* **13**, 687 (1988).
- [139] F. Curti, B. Diano, G. De Marchis, and F. Matera, *J. Lightwave Technol.* **8**, 1162 (1990).
- [140] C. D. Poole, J. H. Winters, and J. A. Nagel, *Opt. Lett.* **16**, 372 (1991).
- [141] N. Gisin, J. P. von der Weid, and J.-P. Pellaux, *J. Lightwave Technol.* **9**, 821 (1991).
- [142] G. J. Foschini and C. D. Poole, *J. Lightwave Technol.* **9**, 1439 (1991).
- [143] P. K. A. Wai and C. R. Menyuk, *J. Lightwave Technol.* **14**, 148 (1996).
- [144] M. C. de Lignie, H. G. Nagel, and M. O. van Deventer, *J. Lightwave Technol.* **12**, 1325 (1994).
- [145] B. Huttner and N. Gisin, *Opt. Lett.* **22**, 504 (1997).
- [146] A. El Amari, N. Gisin, B. Perny, H. Zbinden, and C. W. Zimmer, *J. Lightwave Technol.* **16**, 332 (1998).
- [147] B. Huttner, C. Geiser, and N. Gisin, *IEEE J. Sel. Topics Quantum Electron.* **6**, 317 (2000).
- [148] Y. Li and A. Yariv, *J. Opt. Soc. Am. B* **17**, 1821 (2000).
- [149] D. Wang and C. R. Menyuk, *J. Lightwave Technol.* **19**, 487 (2001).
- [150] R. M. Craig, *J. Lightwave Technol.* **21**, 432 (2003).
- [151] C. Xie and L. F. Mollenauer, *J. Lightwave Technol.* **21**, 1953 (2003).
- [152] M. Shtaif and A. Mecozzi, *IEEE Photon. Technol. Lett.* **16**, 671 (2004).
- [153] L. F. Mollenauer, K. Smith, J. P. Gordon, and C. R. Menyuk, *Opt. Lett.* **14**, 1219 (1989).
- [154] S. G. Evangelides, L. F. Mollenauer, J. P. Gordon, and N. S. Bergano, *J. Lightwave Technol.* **10**, 28 (1992).
- [155] T. Ueda and W. L. Kath, *Physica D* **55**, 166 (1992).
- [156] C. de Angelis, S. Wabnitz, and M. Haelterman, *Electron. Lett.* **29**, 1568 (1993).
- [157] M. Matsumoto, Y. Akagi, and A. Hasegawa, *J. Lightwave Technol.* **15**, 584 (1997).
- [158] D. Marcuse, C. R. Menyuk, and P. K. A. Wai, *J. Lightwave Technol.* **15**, 1735 (1997).
- [159] T. L. Lakoba and D. J. Kaup, *Phys. Rev. E* **56**, 6147 (1997).
- [160] C. de Angelis, P. Franco, and M. Romagnoli, *Opt. Commun.* **157**, 161 (1998).
- [161] X. Zhang, M. Karlsson, P. A. Andrekson, and E. Kolltveit, *IEEE Photon. Technol. Lett.* **10**, 1742 (1998).
- [162] S. M. Baker, J. N. Elgin, and H. J. Harvey, *Opt. Commun.* **165**, 27 (1999).
- [163] C. Xie, M. Karlsson, and P. A. Andrekson, *IEEE Photon. Technol. Lett.* **12**, 801 (2000).
- [164] Y. Chen and H. Haus, *Chaos* **10**, 529 (2000); *Opt. Lett.* **25**, 290 (2000).
- [165] I. Nishioka, T. Hirooka, and A. Hasegawa, *IEEE Photon. Technol. Lett.* **12**, 1480 (2000).
- [166] C. Xie, M. Karlsson, P. A. Andrekson, and H. Sunnerud, *IEEE Photon. Technol. Lett.* **13**, 121 (2001).
- [167] H. Sunnerud, J. Li, C. Xie, and P. A. Andrekson, *J. Lightwave Technol.* **19**, 1453 (2001).
- [168] C. Xie, M. Karlsson, P. A. Andrekson, H. Sunnerud, and J. Li, *IEEE J. Sel. Topics Quantum Electron.* **8**, 575 (2002).
- [169] A. Levent, S. G. Rajeev, F. Yaman, and G. P. Agrawal, *Phys. Rev. Lett.* **90**, 013902 (2003).
- [170] P. Kylemark, H. Sunnerud, M. Karlsson, and P. A. Andrekson, *IEEE Photon. Technol. Lett.* **15**, 1372 (2003).
- [171] A. Hasegawa, *Physica D* **188**, 241 (2004).

# Cross-Phase Modulation

# 7

So far in this book, only a single electromagnetic wave is assumed to propagate inside optical fibers. When two or more optical fields having different wavelengths propagate simultaneously inside a fiber, they interact with each other through the fiber nonlinearity. In general, such an interaction can generate new waves under appropriate conditions through a variety of nonlinear phenomena such as stimulated Raman or Brillouin scattering, harmonic generation, and four-wave mixing; these topics are covered in Chapters 8–12. The Kerr-type nonlinearity can also couple two optical fields through cross-phase modulation (XPM) without inducing any energy transfer between them. In practice, the phenomenon of XPM always accompanies self-phase modulation (SPM) when two or more optical fields are launched simultaneously into an optical fiber. From a physical perspective, XPM occurs because the effective refractive index seen by an optical beam in a nonlinear medium depends not only on the intensity of that beam but also on the intensity of other copropagating beams [1].

The XPM-induced coupling among multiple optical fields gives rise to a number of interesting nonlinear effects in optical fibers. The coupling between two fields of different wavelengths is considered in Section 7.1, where a set of two coupled nonlinear Schrödinger (NLS) equations is derived, assuming that each wave maintains its state of polarization. These equations are used in Section 7.2 to discuss how the XPM affects the phenomenon of modulation instability. Similar to the analysis in Section 6.4, this instability can occur even in the normal-dispersion regime of an optical fiber. Section 7.3 focuses on soliton pairs whose members support each other through XPM. The effects of XPM on the shape and the spectrum of copropagating ultrashort pulses are described in Section 7.4. Several applications of XPM-induced coupling in optical fibers are discussed in Section 7.5. A vector theory of XPM is developed in Section 7.6 and is used to discuss several new effects such as polarization-dependent spectral broadening, pulse trapping, and optical wave breaking. Section 7.7 extends this theory to the case of birefringent fibers. A pump–probe configuration is used to reveal that random changes in the birefringence of a fiber along its length lead to the phenomenon of intrapulse depolarization.

## 7.1 XPM-INDUCED NONLINEAR COUPLING

This section extends the theory of Section 2.3 to the case of two optical pulses of different wavelengths copropagating inside a single-mode fiber. In general, the two optical fields can differ not only in their wavelengths but also in their states of polarization. To simplify the presentation, we first focus on the case in which the two optical fields at different wavelengths are linearly polarized and they maintain their state of polarization inside the fiber. The case of arbitrarily polarized beams is discussed in Sections 7.6 and 7.7.

### 7.1.1 Nonlinear Refractive Index

In the quasi-monochromatic approximation, it is useful to separate the rapidly varying part of the electric field by writing it in the form

$$\mathbf{E}(\mathbf{r}, t) = \frac{1}{2} \hat{x} [E_1 \exp(-i\omega_1 t) + E_2 \exp(-i\omega_2 t)] + \text{c.c.}, \quad (7.1.1)$$

where  $\hat{x}$  is the polarization unit vector,  $\omega_1$  and  $\omega_2$  are the carrier frequencies of the two pulses, and the corresponding amplitudes  $E_1$  and  $E_2$  are slowly varying functions of time compared with an optical period. This requirement is equivalent to assuming that the spectral width of each pulse satisfies the condition  $\Delta\omega_j \ll \omega_j$  ( $j = 1, 2$ ), and it holds quite well for pulse widths  $> 0.1$  ps. Evolution of the slowly varying amplitudes  $E_1$  and  $E_2$  is governed by the wave Eq. (2.3.1) with the linear and nonlinear parts of the induced polarization given by Eqs (2.3.5) and (2.3.6).

To see the origin of XPM, we substitute Eq. (7.1.1) in Eq. (2.3.6) and find that the nonlinear polarization can be written as

$$\begin{aligned} \mathbf{P}_{\text{NL}}(\mathbf{r}, t) = & \frac{1}{2} \hat{x} [P_{\text{NL}}(\omega_1) e^{-i\omega_1 t} + P_{\text{NL}}(\omega_2) e^{-i\omega_2 t} + P_{\text{NL}}(2\omega_1 - \omega_2) e^{-i(2\omega_1 - \omega_2)t} \\ & + P_{\text{NL}}(2\omega_2 - \omega_1) e^{-i(2\omega_2 - \omega_1)t}] + \text{c.c.}, \end{aligned} \quad (7.1.2)$$

where the four terms depend on  $E_1$  and  $E_2$  as

$$P_{\text{NL}}(\omega_1) = \chi_{\text{eff}}(|E_1|^2 + 2|E_2|^2)E_1, \quad (7.1.3)$$

$$P_{\text{NL}}(\omega_2) = \chi_{\text{eff}}(|E_2|^2 + 2|E_1|^2)E_2, \quad (7.1.4)$$

$$P_{\text{NL}}(2\omega_1 - \omega_2) = \chi_{\text{eff}} E_1^2 E_2^*, \quad (7.1.5)$$

$$P_{\text{NL}}(2\omega_2 - \omega_1) = \chi_{\text{eff}} E_2^2 E_1^*, \quad (7.1.6)$$

with  $\chi_{\text{eff}} = (3\epsilon_0/4)\chi_{xxxx}^{(3)}$  acting as an effective nonlinear parameter.

The induced nonlinear polarization in Eq. (7.1.2) has terms oscillating at the new frequencies  $2\omega_1 - \omega_2$  and  $2\omega_2 - \omega_1$ . These terms result from the phenomenon of four-wave mixing discussed in Chapter 10. It is necessary to satisfy a phase-matching condition for the new frequency components to build up significantly. The four-wave

mixing terms are neglected in this chapter after assuming that phase matching does not occur. The remaining two terms provide a nonlinear contribution to the refractive index. This can be seen writing  $P_{\text{NL}}(\omega_j)$  in the form  $P_{\text{NL}}(\omega_j) = \epsilon_0 \epsilon_j^{\text{NL}} E_j$  and combining it with the linear part so that the total induced polarization is given by ,  $P(\omega_j) = \epsilon_0 \epsilon_j E_j$  where  $j = 1$  or  $2$ ,

$$\epsilon_j = \epsilon_j^{\text{L}} + \epsilon_j^{\text{NL}} = (n_j^{\text{L}} + \Delta n_j)^2, \quad (7.1.7)$$

$n_j^{\text{L}}$  is the linear part of the refractive index, and  $\Delta n_j$  is the change induced by the third-order nonlinear effects. With the approximation  $\Delta n_j \ll n_j^{\text{L}}$ , the nonlinear part of the refractive index is given by ( $j = 1, 2$ )

$$\Delta n_j \approx \epsilon_j^{\text{NL}} / 2n_j^{\text{L}} \approx \bar{n}_2 (|E_j|^2 + 2|E_{3-j}|^2), \quad (7.1.8)$$

where the nonlinear parameter  $\bar{n}_2$  is defined in Eq. (2.3.13).

Equation (7.1.8) shows that the refractive index seen by an optical field inside an optical fiber depends not only on the intensity of that field but also on the intensity of other copropagating fields [2–4]. As the optical field propagates inside the fiber, it acquires an intensity-dependent nonlinear phase shift

$$\phi_j^{\text{NL}}(z) = (\omega_j/c) \Delta n_j z = n_2(\omega_j/c) (|E_j|^2 + 2|E_{3-j}|^2) z, \quad (7.1.9)$$

where  $j = 1$  or  $2$ . The first term is responsible for SPM discussed in Chapter 4. The second term results from phase modulation of one wave by the copropagating wave and is responsible for XPM. The factor of 2 on the right-hand side of Eq. (7.1.9) shows that XPM is twice as effective as SPM for the same intensity [1]. Its origin can be traced back to the number of terms that contribute to the triple sum implied in Eq. (2.3.6). Qualitatively speaking, the number of terms doubles when the two optical frequencies are distinct compared with that when the frequencies are degenerate. The XPM-induced phase shift in optical fibers was measured as early as 1984 by injecting two continuous-wave (CW) beams into a 15-km-long fiber [3]. Soon after, picosecond pulses were used to observe the XPM-induced spectral changes [4–6].

### 7.1.2 Coupled NLS Equations

The pulse-propagation equations for the two optical fields can be obtained by following the procedure of Section 2.3. Assuming that the nonlinear effects do not significantly affect the fiber modes, the transverse dependence can be factored out writing  $E_j(\mathbf{r}, t)$  in the form

$$E_j(\mathbf{r}, t) = F_j(x, y) A_j(z, t) \exp(i\beta_{0j} z), \quad (7.1.10)$$

where  $F_j(x, y)$  is the transverse distribution of the fiber mode for the  $j$ th field ( $j = 1, 2$ ),  $A_j(z, t)$  is the slowly varying amplitude, and  $\beta_{0j}$  is the corresponding propagation constant at the carrier frequency  $\omega_j$ . The dispersive effects are included by expanding the frequency-dependent propagation constant  $\beta_j(\omega)$  for each wave in a way similar

to Eq. (2.3.23) and retaining only up to the quadratic term. The resulting propagation equation for  $A_j(z, t)$  becomes

$$\frac{\partial A_j}{\partial z} + \beta_{1j} \frac{\partial A_j}{\partial t} + \frac{i\beta_{2j}}{2} \frac{\partial^2 A_j}{\partial t^2} + \frac{\alpha_j}{2} A_j = \frac{in_2\omega_j}{c} \left( f_{jj}|A_j|^2 + 2f_{jk}|A_k|^2 \right), \quad (7.1.11)$$

where  $k \neq j$ ,  $\beta_{1j} = 1/v_{gj}$ ,  $v_{gj}$  is the group velocity,  $\beta_{2j}$  is the GVD parameter, and  $\alpha_j$  is the loss coefficient. The overlap integral  $f_{jk}$  is defined as

$$f_{jk} = \frac{\iint_{-\infty}^{\infty} |F_j(x, y)|^2 |F_k(x, y)|^2 dx dy}{(\iint_{-\infty}^{\infty} |F_j(x, y)|^2 dx dy)(\iint_{-\infty}^{\infty} |F_k(x, y)|^2 dx dy)}. \quad (7.1.12)$$

The differences among the overlap integrals can be significant in multimode fibers if the two waves propagate in different fiber modes. Even in single-mode fibers,  $f_{11}$ ,  $f_{22}$ , and  $f_{12}$  differ from each other because of the frequency dependence of the modal distribution  $F_j(x, y)$ . The difference is small, however, and can be neglected in practice. In that case, Eq. (7.1.11) can be written as the following set of two coupled NLS equations [7–10]

$$\frac{\partial A_1}{\partial z} + \frac{1}{v_{g1}} \frac{\partial A_1}{\partial t} + \frac{i\beta_{21}}{2} \frac{\partial^2 A_1}{\partial t^2} + \frac{\alpha_1}{2} A_1 = i\gamma_1(|A_1|^2 + 2|A_2|^2)A_1, \quad (7.1.13)$$

$$\frac{\partial A_2}{\partial z} + \frac{1}{v_{g2}} \frac{\partial A_2}{\partial t} + \frac{i\beta_{22}}{2} \frac{\partial^2 A_2}{\partial t^2} + \frac{\alpha_2}{2} A_2 = i\gamma_2(|A_2|^2 + 2|A_1|^2)A_2, \quad (7.1.14)$$

where the nonlinear parameter  $\gamma_j$  is defined similar to Eq. (2.3.28) as

$$\gamma_j = n_2\omega_j/(cA_{\text{eff}}), \quad (j = 1, 2), \quad (7.1.15)$$

and  $A_{\text{eff}}$  is the effective mode area ( $A_{\text{eff}} = 1/f_{11}$ ), assumed to be the same for both optical waves. In the case of conventional single-mode fibers,  $\gamma_1$  and  $\gamma_2$  are  $\sim 1 \text{ W}^{-1}/\text{km}$  in the  $1.55\text{-}\mu\text{m}$  wavelength region but their values increase considerably for highly nonlinear fibers designed with smaller values of  $A_{\text{eff}}$  (see Chapter 11). Generally, the two pulses propagate at different speeds because of the difference in their group velocities. The group-velocity mismatch plays an important role because it separates pulses from each other and limits their XPM interaction. One can define the walk-off length  $L_w$  using Eq. (1.2.13). Physically, it is a measure of the fiber length over which two overlapping pulses separate from each other as a result of the group-velocity mismatch.

## 7.2 XPM-INDUCED MODULATION INSTABILITY

This section extends the analysis of Section 5.1 to the case in which two CW beams of different wavelengths propagate inside a fiber simultaneously. Similar to the single beam case, modulation instability is expected to occur in the anomalous-GVD region

of the fiber. The main issue is whether XPM-induced coupling can destabilize the CW state even when one or both beams experience normal GVD [11–20].

### 7.2.1 Linear Stability Analysis

The following analysis is similar to that of Section 6.4.2. The main difference is that XPM-induced coupling is stronger and the parameters  $\beta_2$  and  $\gamma$  are different for the two beams because of their different wavelengths. As usual, the steady-state solution is obtained by setting the time derivatives in Eqs (7.1.13) and (7.1.14) to zero. If fiber losses are neglected, the solution is of the form

$$\bar{A}_j(z) = \sqrt{P_j} \exp[i\phi_j(z)], \quad \phi_j(z) = \gamma_j(P_j + 2P_{3-j})z. \quad (7.2.1)$$

where  $j = 1$  or  $2$ ,  $P_j$  is the incident optical power, and  $\phi_j$  is the nonlinear phase shift acquired by the  $j$ th field.

Following the procedure of Section 5.1, stability of the steady state is examined assuming a time-dependent solution of the form

$$A_j = \left( \sqrt{P_j} + a_j \right) \exp(i\phi_j), \quad (7.2.2)$$

where  $a_j(z, t)$  is a small perturbation. By using Eq. (7.2.2) in Eqs (7.1.13) and (7.1.14) and linearizing in  $a_1$  and  $a_2$ , the perturbations  $a_1$  and  $a_2$  satisfy the following set of two coupled linear equations:

$$\frac{\partial a_1}{\partial z} + \frac{1}{v_{g1}} \frac{\partial a_1}{\partial t} + \frac{i\beta_{21}}{2} \frac{\partial^2 a_1}{\partial t^2} = i\gamma_1 P_1(a_1 + a_1^*) + 2i\gamma_1 \sqrt{P_1 P_2}(a_2 + a_2^*), \quad (7.2.3)$$

$$\frac{\partial a_2}{\partial z} + \frac{1}{v_{g2}} \frac{\partial a_2}{\partial t} + \frac{i\beta_{22}}{2} \frac{\partial^2 a_2}{\partial t^2} = i\gamma_2 P_2(a_2 + a_2^*) + 2i\gamma_2 \sqrt{P_1 P_2}(a_1 + a_1^*), \quad (7.2.4)$$

where the last term is due to XPM.

The preceding set of linear equations has the following general solution:

$$a_j = u_j \exp[i(Kz - \Omega t)] + iv_j \exp[-i(Kz - \Omega t)], \quad (7.2.5)$$

where  $\Omega$  is the frequency of perturbation, and  $K$  is its wave number. Equations (7.2.3) to (7.2.5) provide a set of four homogeneous equations for  $u_1$ ,  $u_2$ ,  $v_1$ , and  $v_2$ . This set has a nontrivial solution only when the perturbation satisfies the dispersion relation

$$[(K - \Omega/v_{g1})^2 - f_1][(K - \Omega/v_{g2})^2 - f_2] = C_{\text{XPM}}, \quad (7.2.6)$$

where

$$f_j = \frac{1}{2}\beta_{2j}\Omega^2(\frac{1}{2}\beta_{2j}\Omega^2 + 2\gamma_j P_j) \quad (7.2.7)$$

for  $j = 1$  or  $2$ . The coupling parameter  $C_{\text{XPM}}$  is defined as

$$C_{\text{XPM}} = 4\beta_{21}\beta_{22}\gamma_1\gamma_2 P_1 P_2 \Omega^4. \quad (7.2.8)$$

The steady-state solution becomes unstable if the wave number  $K$  has an imaginary part for some values of  $\Omega$ . The perturbations  $a_1$  and  $a_2$  then experience an exponential growth along the fiber length. In the absence of XPM coupling ( $C_{\text{XPM}} = 0$ ), Eq. (7.2.6) shows that the analysis of Section 5.1 applies to each wave independently.

In the presence of XPM coupling, Eq. (7.2.6) provides a fourth-degree polynomial in  $K$  whose roots determine the conditions under which  $K$  becomes complex. In general, these roots are obtained numerically. If the wavelengths of the two optical beams are close to each other or they are located on opposite sides of the zero-dispersion wavelength such that  $v_{g1} \approx v_{g2}$ , the four roots are given by [11]

$$K = \Omega/v_{g1} \pm \left\{ \frac{1}{2}(f_1 + f_2) \pm [(f_1 - f_2)^2/4 + C_{\text{XPM}}]^{1/2} \right\}^{1/2}. \quad (7.2.9)$$

It is easy to verify that  $K$  can become complex only if  $C_{\text{XPM}} > f_1 f_2$ . Using Eqs (7.2.7) and (7.2.8), the condition for modulation instability to occur can be written as

$$[\Omega^2/\Omega_{c1}^2 + \text{sgn}(\beta_{21})][\Omega^2/\Omega_{c2}^2 + \text{sgn}(\beta_{22})] < 4, \quad (7.2.10)$$

where  $\Omega_{cj} = (4\gamma_j P_j / |\beta_{2j}|)^{1/2}$  with  $j = 1$  or  $2$ . When the condition (7.2.10) is satisfied, the gain spectrum of modulation instability is obtained using  $g(\Omega) = 2 \text{Im}(K)$ .

The modulation-instability condition (7.2.10) shows that there is a range of  $\Omega$  over which the gain  $g(\Omega)$  exists. The steady-state solution (7.2.2) is unstable to perturbations at those frequencies. The most important conclusion drawn from Eq. (7.2.10) is that modulation instability can occur irrespective of the signs of the GVD coefficients. Thus, whereas modulation instability requires anomalous GVD in the case of a single beam (see Section 5.1), it can occur in the two-beam case even if both beams experience normal GVD. The frequency range over which  $g(\Omega) > 0$  depends on whether  $\beta_{21}$  and  $\beta_{22}$  are both positive, both negative, or one positive and the other negative. The smallest frequency range corresponds to the case in which both beams are in the normal-dispersion regime of the fiber. Because modulation instability in that case is due solely to XPM, only this case is discussed further.

Figure 7.1 shows the gain spectra of XPM-induced modulation instability for silica fibers in the visible region near  $0.53 \mu\text{m}$  choosing  $\beta_{2j} = 60 \text{ ps}^2/\text{km}$  and  $\gamma_j = 15 \text{ W}^{-1}/\text{km}$  in Eq. (7.2.7). The group-velocity mismatch is neglected in the left graph where different curves correspond to values of the power ratio  $P_2/P_1$  in the range  $0\text{--}2$ . The right graph shows the effect of group-velocity mismatch for equal beam powers by varying the parameter  $\delta = |v_{g1}^{-1} - v_{g2}^{-1}|$  in the range  $0\text{--}3 \text{ ps/m}$ . These results show that XPM-induced modulation instability can occur in the normal-GVD regime for relatively small values of  $\delta$ . The peak gain of about  $5 \text{ m}^{-1}$  at the  $100\text{-W}$  power level implies that the instability can develop in fibers a few meters long.

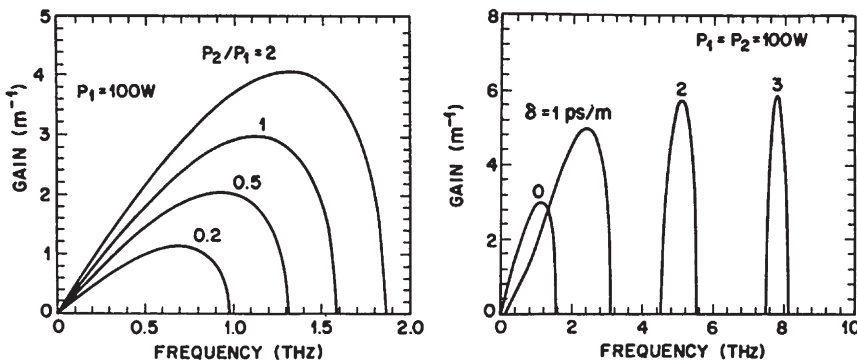


**Figure 7.1** Gain spectra of XPM-induced modulation instability in the normal-dispersion regime of a fiber for (i) different power ratios with  $\delta=0$  and (ii) different values of  $\delta$  with equal beam powers. (After Ref. [11]; © 1987 American Physical Society.)

## 7.2.2 Experimental Results

The experimental attempts to observe the XPM-induced modulation instability in the normal-dispersion region of an optical fiber have focused mostly on the case of two polarization components of a single beam (see Section 6.4). It appears that this instability is difficult to observe in the case of two beams of different wavelengths. The reason is related to the fact that Eqs (7.1.13) and (7.1.14) neglect four-wave mixing. The neglect of the four-wave-mixing terms can be justified when the wavelength difference is so large that phase matching cannot occur [16–18]. However, to observe modulation instability, the wavelength difference needs to be reduced to  $\sim 1 \text{ nm}$  or less. Four-wave mixing then becomes nearly phase matched and cannot be ignored. Indeed, a careful analysis that includes dispersion to all orders shows that XPM-induced modulation instability is not likely to occur in the normal-dispersion region of conventional silica fibers [18]. It can occur in especially designed, dispersion-flattened fibers in which two normal-dispersion regions are separated by an intermediate wavelength region of anomalous dispersion. In such fibers, it is possible to match the group velocities even when the wavelengths of two beams differ by 100 nm or more.

The XPM-induced modulation instability has been observed when one of the beams propagates in the normal-dispersion region while the other beam experiences anomalous dispersion. In a 1988 experiment [21], a pump–probe configuration was used such that the  $1.06\text{-}\mu\text{m}$  pump pulses experienced normal dispersion, while  $1.32\text{-}\mu\text{m}$  probe pulses propagated in the anomalous-dispersion regime of the fiber. When the pump and probe pulses were launched simultaneously, the probe developed modulation sidebands, with a spacing of 260 GHz at the 0.4-W peak-power level of pump pulses, as a result of the XPM-induced modulation instability. This configuration can be used to advantage if the pump beam is in the form of intense pulses whereas the other beam forms a weak CW signal. The weak CW beam can be converted into a

train of ultrashort pulses because it is amplified through the XPM-induced modulation instability only when the two waves are present simultaneously [8].

In an experimental realization of the preceding idea [22], 100-ps pump pulses were obtained from a 1.06- $\mu\text{m}$ , mode-locked, Nd:YAG laser while an external-cavity semiconductor laser provided the weak CW signal (power  $< 0.5 \text{ mW}$ ) whose wavelength was tunable over 1.43–1.56  $\mu\text{m}$ . The zero-dispersion wavelength of the 1.2-km-long optical fiber was near 1.273  $\mu\text{m}$  such that the group velocities were nearly equal at 1.06 and 1.51  $\mu\text{m}$ . When 60- $\mu\text{W}$  signal power was coupled into the fiber together with the pump pulses (peak power  $< 500 \text{ W}$ ), the signal spectrum developed sidebands indicative of the XPM-induced modulation instability. The experimental results were in qualitative agreement with the numerical solutions of Eqs (7.1.13) and (7.1.14) and indicated that the CW signal was converted into a train of picosecond pulses.

This technique has been used to generate a 10-GHz pulse train by launching the CW signal from a 1543-nm semiconductor laser into a fiber together with 13.7-ps pump pulses (10-GHz repetition rate) obtained from a 1558-nm, mode-locked semiconductor laser [23]. The 11-km-long dispersion-shifted fiber had its zero-dispersion wavelength at 1550 nm, resulting in nearly equal group velocities at the pump and signal wavelengths. The streak-camera measurements indicated that XPM-induced modulation instability converted the CW signal into a train of 7.4-ps pulses. If pump pulses were coded to carry digital information, signal pulses will reproduce the information faithfully because the XPM interaction requires the presence of a pump pulse. Such a device is useful for wavelength conversion of signals in optical communication systems.

## 7.3 XPM-PAIRED SOLITONS

Similar to the case of vector solitons discussed in Section 6.5.3, the XPM-induced modulation instability indicates that the coupled NLS equations may have solitary-wave solutions in the form of two paired solitons that preserve their shape through the XPM interaction. In fact, solitonic and periodic solutions of the coupled NLS equations have been studied since 1977 [24–49]. Because such solutions specify intensity profiles of both pulses and always occur in pairs, they are referred to as XPM-paired solitons (also called symbiotic solitons). Some of such paired solutions have been discussed in Section 6.5.3 in the context of vector solitons. However, in that case the two polarization components of a single beam experience the same GVD (either normal or anomalous). In the general case discussed here, the carrier frequencies of two solitons can be different enough that the two members of the soliton pair can have different signs for the GVD parameter.

### 7.3.1 Bright–Dark Soliton Pair

Solitons paired by XPM represent the specific solutions of Eqs (7.1.13) and (7.1.14) for which the pulse shape does not change with  $z$  although the phase may vary along

the fiber. Such solutions are not solitons in a strict mathematical sense and should be referred to more accurately as solitary waves. The group-velocity mismatch represents the biggest hurdle for the existence of XPM-paired solitons. It is possible to realize equal group velocities ( $v_{g1} = v_{g2}$ ) if the wavelengths of two optical waves are chosen appropriately on opposite sides of the zero-dispersion wavelength such that one wave experiences normal GVD while the other wave lies in the anomalous-GVD region. Indeed, several examples of XPM-paired solitons were discovered exactly under such operating conditions [26–28].

An interesting example is provided by the bright–dark soliton pair formed when  $\beta_{21} < 0$  and  $\beta_{22} > 0$ . If fiber losses are ignored ( $\alpha_1 = \alpha_2 = 0$ ) and group velocities are assumed to be equal by setting  $v_{g1} = v_{g2} = v_g$  in Eqs (7.1.13) and (7.1.14), a bright–dark soliton pair is given by [26]

$$A_1(z, t) = B_1 \tanh[W(t - z/V)] \exp[i(K_1 z - \Omega_1 t)], \quad (7.3.1)$$

$$A_2(z, t) = B_2 \operatorname{sech}[W(t - z/V)] \exp[i(K_2 z - \Omega_2 t)], \quad (7.3.2)$$

where the soliton amplitudes are determined from

$$B_1^2 = (2\gamma_1\beta_{22} + \gamma_2|\beta_{21}|)W^2/(3\gamma_1\gamma_2), \quad (7.3.3)$$

$$B_2^2 = (2\gamma_2|\beta_{21}| + \gamma_1\beta_{22})W^2/(3\gamma_1\gamma_2), \quad (7.3.4)$$

the wave numbers  $K_1$  and  $K_2$  are given by

$$K_1 = \gamma_1 B_1^2 - |\beta_{21}| \Omega_1^2/2, \quad K_2 = \beta_{22}(\Omega_2^2 - W^2)/2, \quad (7.3.5)$$

and the effective group velocity of the soliton pair is obtained from

$$V^{-1} = v_g^{-1} - |\beta_{21}| \Omega_1 = v_g^{-1} + \beta_{22} \Omega_2. \quad (7.3.6)$$

As seen from Eq. (7.3.6), the frequency shifts  $\Omega_1$  and  $\Omega_2$  must have opposite signs and cannot be chosen independently. The parameter  $W$  governs the pulse width and determines the soliton amplitudes through Eqs (7.3.3) and (7.3.4). Thus, two members of the soliton pair have the same width, the same group velocity, but different shapes and amplitudes such that they support each other through the XPM coupling. In fact, their shapes correspond to bright and dark solitons discussed in Chapter 5. The most striking feature of this soliton pair is that the dark soliton propagates in the anomalous-dispersion regime whereas the bright soliton propagates in the normal-dispersion regime, exactly opposite of the behavior expected in the absence of XPM. The physical mechanism behind such an unusual pairing can be understood as follows. Because XPM is twice as strong as SPM, it can counteract the temporal spreading of an optical pulse induced by the combination of SPM and normal dispersion, provided the XPM-induced chirp is of the opposite kind than that produced by SPM. A dark soliton can generate this kind of chirp. At the same time, the XPM-induced chirp on the dark soliton is such that the pair of bright and dark solitons can support each other in a symbiotic manner.

### 7.3.2 Bright–Gray Soliton Pair

A more general form of an XPM-coupled soliton pair can be obtained by solving Eqs (7.1.13) and (7.1.14) with the postulate

$$A_j(z, t) = Q_j(t - z/V) \exp[i(K_j z - \Omega_j t + \phi_j)], \quad (7.3.7)$$

where  $V$  is the common velocity of the soliton pair,  $Q_j$  governs the soliton shape,  $K_j$  and  $\Omega_j$  represent changes in the propagation constant and the frequency of two solitons, and  $\phi_j$  is the phase ( $j = 1, 2$ ). The resulting solution has the form [33]

$$Q_1(\tau) = B_1[1 - b^2 \operatorname{sech}^2(W\tau)], \quad Q_2(\tau) = B_2 \operatorname{sech}(W\tau), \quad (7.3.8)$$

where  $\tau = t - z/V$ . The parameters  $W$  and  $b$  depend on the soliton amplitudes,  $B_1$  and  $B_2$ , and on fiber parameters through the relations

$$W = \left( \frac{3\gamma_1\gamma_2}{2\gamma_1\beta_{22} - 4\gamma_2\beta_{21}} \right)^{1/2} B_2, \quad b = \left( \frac{2\gamma_1\beta_{22} - \gamma_2\beta_{21}}{\gamma_1\beta_{22} - 2\gamma_2\beta_{21}} \right)^{1/2} \frac{B_2}{B_1}. \quad (7.3.9)$$

The constants  $K_1$  and  $K_2$  are also fixed by various fiber parameters and soliton amplitudes. The phase of the bright soliton is constant but the dark-soliton phase  $\phi_1$  is time-dependent. The frequency shifts  $\Omega_1$  and  $\Omega_2$  are related to the soliton-pair speed as in Eq. (7.3.6).

The new feature of the XPM-coupled soliton pair in Eq. (7.3.8) is that the dark soliton is of “gray” type. The parameter  $b$  controls the depth of the intensity dip associated with a gray soliton. Both solitons have the same width  $W$  but different amplitudes. A new feature is that the two GVD parameters can be positive or negative. However, the soliton pair exists only under certain conditions. The solution is always possible if  $\beta_{21} < 0$  and  $\beta_{22} > 0$  and does not exist when  $\beta_{21} > 0$  and  $\beta_{22} < 0$ . As discussed before, this behavior is opposite to what would normally be expected and is due solely to XPM. If both solitons experience normal GVD, the bright–gray soliton pair can exist if  $\gamma_1\beta_{22} > 2\gamma_2\beta_{21}$ . Similarly, if both solitons experience anomalous GVD, the soliton pair can exist if  $2\gamma_1|\beta_{22}| < \gamma_2|\beta_{21}|$ .

The preceding soliton-pair solutions are not the only possible solutions of Eqs (7.1.13) and (7.1.14). These equations also support pairs with two bright or two dark solitons depending on various parameter values [28]. Moreover, the XPM-supported soliton pairs can exist even when group velocities are not equal because, similar to soliton trapping in birefringent fibers (see Section 6.5), two pulses can shift their carrier frequencies to equalize their group velocities. A simple way to find the conditions under which XPM-paired solitons can exist is to postulate an appropriate solution, substitute it in Eqs (7.1.13) and (7.1.14), and then investigate whether soliton parameters (amplitude, width, group velocity, frequency shift, and wave number) can be determined with physically possible values [33–35]. As an example, consider the case when Eqs (7.3.1) and (7.3.2) describe the postulated solution. Assume also that  $K_1 = K_2$  and  $\Omega_1 = \Omega_2$  so that the frequency shifts are equal. It turns out that the postulated solution is always possible if  $\beta_{21} < 0$  and  $\beta_{22} > 0$ , but exists only under

certain conditions if  $\beta_{21}$  and  $\beta_{22}$  have the same sign [35]. Further, the assumption  $\Omega_1 = \Omega_2$  can be relaxed to obtain another set of solitary-wave solutions. Stability of the XPM-paired solitons is not always guaranteed and should be checked through numerical simulations.

### 7.3.3 Periodic Solutions

The coupled NLS equations, (7.1.13) and (7.1.14) also have periodic solutions that represent two pulse trains that propagate undistorted through an optical fiber because of the XPM-induced coupling between them. One such periodic solution in terms of the elliptic functions was found in 1989 in the specific case in which both pulse trains have the same group velocity and experienced anomalous GVD inside the fiber [30]. By 1998, nine periodic solutions, written as different combinations of the elliptic functions, have been found [44]. All of these solutions assume equal group velocities and anomalous GVD for the two pulse trains.

The case in which one wave experiences anomalous GVD, while the other propagates in the normal-dispersion region, is of practical interest because the group velocities for the two waves can then be matched with a proper choice of the zero-dispersion wavelength of the fiber. If we assume this to be the case, neglect fiber losses, and introduce normalized variables using

$$\xi = z/L_D, \quad \tau = (t - z/v_{g1})/T_0, \quad A_j = \gamma_1 L_D u_j, \quad (7.3.10)$$

Equations (7.1.13) and (7.1.14) can be written in the form

$$i \frac{\partial u_1}{\partial \xi} - \frac{d_1}{2} \frac{\partial^2 u_1}{\partial \tau^2} + (|u_1|^2 + \sigma |u_2|^2) u_1 = 0, \quad (7.3.11)$$

$$i \frac{\partial u_2}{\partial \xi} + \frac{d_2}{2} \frac{\partial^2 u_2}{\partial \tau^2} + (|u_2|^2 + \sigma |u_1|^2) u_2 = 0, \quad (7.3.12)$$

where  $d_j = |\beta_{2j}/\beta_{20}|$ ,  $\beta_{20}$  is a reference value used to define the dispersion length, and  $u_1$  is assumed to propagate in the normal-dispersion region. We have also assumed  $\gamma_2 \approx \gamma_1$ . The parameter  $\sigma$  has a value of 2 when all waves are linearly polarized but becomes  $< 1$  for orthogonally polarized waves.

The coupled NLS Equations (7.3.11) and (7.3.12) have been solved with the Hirota method to obtain several families of periodic solutions in terms of elliptic functions [49]. For  $\sigma > 1$ , the solution has the following form:

$$u_1(\xi, \tau) = r \sqrt{\frac{\sigma d_2 + d_1}{\sigma^2 - 1}} \operatorname{dn}(r\tau, p) [q \operatorname{dn}^{-2}(r\tau, p) \mp 1] \exp(iQ_1^\pm \xi), \quad (7.3.13)$$

$$u_2(\xi, \tau) = r \sqrt{\frac{d_2 + \sigma d_1}{\sigma^2 - 1}} \frac{p^2 \operatorname{sn}(r\tau, p) \operatorname{cn}(r\tau, p)}{\operatorname{dn}(r\tau, p)} \exp(iQ_2^\pm \xi), \quad (7.3.14)$$

where the propagation constants  $Q_1$  and  $Q_2$  are given by

$$Q_1^\pm = \frac{r^2}{\sigma^2 - 1} [\sigma(d_2 + \sigma d_1)(1 + q^2) \mp 2q(\sigma d_2 + d_1)] - \frac{r^2 d_1}{2} (1 \mp q)^2, \quad (7.3.15)$$

$$Q_2^\pm = \frac{r^2}{\sigma^2 - 1} [(d_2 + \sigma d_1)(1 + q^2) \mp 2q\sigma(\sigma d_2 + d_1)]. \quad (7.3.16)$$

In these equations, sn, cn, and dn are the standard Jacobi elliptic functions [50] with the modulus  $p$  ( $0 < p < 1$ ) and the period  $2K(p)/r$ , where  $K(p)$  is the complete elliptic integral of the first kind,  $q = (1 - p^2)^{1/2}$ , and  $r$  is an arbitrary scaling constant. Two families of periodic solutions correspond to the choice of upper and lower signs. For each family,  $p$  can take any value in the range of 0–1.

The preceding solution exists only for  $\sigma > 1$ . When  $\sigma < 1$ , the following single family of periodic solutions is found [49]:

$$u_1(\xi, \tau) = r \sqrt{\frac{\sigma d_2 + d_1}{1 - \sigma^2}} p \operatorname{sn}(r\tau, p) \exp(iQ_1\xi), \quad (7.3.17)$$

$$u_2(\xi, \tau) = r \sqrt{\frac{d_2 + \sigma d_1}{1 - \sigma^2}} p \operatorname{dn}(r\tau, p) \exp(iQ_2\xi), \quad (7.3.18)$$

where the propagation constants  $Q_1$  and  $Q_2$  are given by

$$Q_1 = -\frac{1}{2} r^2 d_1 q^2 + r^2 (d_1 + \sigma d_2)/(1 - \sigma^2), \quad (7.3.19)$$

$$Q_2 = \frac{1}{2} r^2 d_2 (1 + q^2) + r^2 \sigma (d_1 + \sigma d_2)/(1 - \sigma^2). \quad (7.3.20)$$

It is well known that period of any Jacobi elliptic function becomes infinite in the limit  $p = 1$ . In this limit, the preceding periodic solutions reduce to the bright–dark soliton pairs discussed earlier in this section. We should stress that the mere existence of a periodic or solitary-wave solution does not guarantee that it can be observed experimentally. The stability of such solutions must be studied by perturbing them and then propagating the perturbed field over long distances. Numerical simulations show that all periodic solutions are unstable in principle, but the distance after which instability sets in depends on the strength of perturbation [49]. In particular, a periodic solution can survive over tens of dispersion lengths for relatively weak perturbations.

### 7.3.4 Multiple Coupled NLS Equations

The concept of XPM-paired solitons can be easily generalized to multicomponent solitons in which multiple pulses at different carrier frequencies are transmitted

over the same fiber. In practice, such a situation occurs naturally in wavelength-division-multiplexed (WDM) lightwave systems [51]. In this case, in place of Eqs (7.1.13) and (7.1.14), one needs to solve a set of multiple coupled NLS equations of the form

$$\frac{\partial A_j}{\partial z} + \frac{1}{v_{gj}} \frac{\partial A_j}{\partial t} + \frac{i\beta_{2j}}{2} \frac{\partial^2 A_j}{\partial t^2} = i \left( \gamma_j |A_j|^2 + \sigma \sum_{k \neq j} \gamma_k |A_k|^2 \right) A_j, \quad (7.3.21)$$

where  $j = -M$  to  $M$  and  $2M + 1$  is the total number of components. The dimensionless parameter  $\sigma$  indicates the XPM strength and has a value of 2 when all waves are linearly polarized. These equations have periodic as well as soliton solutions for certain combinations of parameter values [45–48]. In this section, we focus on the soliton solutions with multiple components. Such solitons are often referred to as multicomponent vector solitons [52].

We normalize Eq. (7.3.21) using the central  $j = 0$  component as a reference and introduce the normalized variables  $\xi$ ,  $\tau$ , and  $u_j$  as indicated in Eq. (7.3.10), where the dispersion length  $L_D = T_0^2/|\beta_{20}|$  and  $\beta_{20}$  is taken to be negative. The set (7.3.21) can then be written as

$$i \left( \frac{\partial u_j}{\partial \xi} + \delta_j \frac{\partial u_j}{\partial \tau} \right) + \frac{d_j}{2} \frac{\partial^2 u_j}{\partial \tau^2} + \left( \gamma_j |A_j|^2 + \sigma \sum_{k \neq j} \gamma_k |A_k|^2 \right) A_j = 0, \quad (7.3.22)$$

where  $\delta_j = v_{gj}^{-1} - v_{g0}^{-1}$  represents group-velocity mismatch with respect to the central component,  $d_j = \beta_{2j}/\beta_{20}$ , and the parameter  $\gamma_j$  is now dimensionless as it has been normalized with  $\gamma_0$ .

The solitary-wave solution of Eq. (7.3.22) is found by seeking a solution in the form

$$u_j(\xi, \tau) = U_j(\tau) \exp[i(K_j \xi - \Omega_j \tau)], \quad (7.3.23)$$

where  $K_j$  is the propagation constant and  $\Omega_j$  represents a frequency shift from the carrier frequency. It is easy to show that  $U_j$  satisfies the ordinary differential equation

$$\frac{d_j}{2} \frac{d^2 U_j}{d\tau^2} + \left( \gamma_j |U_j|^2 + \sigma \sum_{k \neq j} \gamma_k |U_k|^2 \right) U_j = \lambda_j U_j (K_j - \frac{1}{2} \beta_{2j} \Omega_j^2) U_j, \quad (7.3.24)$$

provided frequency shifts are such that  $\Omega_j = (\beta_{2j} v_{gj})^{-1}$  and  $\lambda_j = K_j - \delta_j^2/(2d_j)$ .

For the central  $j = 0$  component,  $d_0 = \gamma_0 = 1$ . In the absence of XPM terms, this component has the standard soliton solution  $U_0(x) = \operatorname{sech}(x)$ . We assume that, in the presence of XPM, all components have the same “sech” shape but different

amplitudes, i.e.,  $U_n(\tau) = a_n \operatorname{sech}(\tau)$ . Substituting this solution in Eq. (7.3.24), the amplitudes  $a_n$  are found to satisfy the following set of algebraic equations:

$$a_0^2 + \sigma \sum_{n \neq 0} \gamma_n a_n^2 = 1, \quad \gamma_n a_n^2 + \sigma \sum_{m \neq n} \gamma_m a_m^2 = d_n. \quad (7.3.25)$$

As long as parameters  $d_n$  and  $\gamma_n$  are close to 1 for all components, this solution describes a vector soliton with  $N$  components of nearly equal intensity. In the degenerate case,  $d_n = \gamma_n = 1$ , the amplitudes can be found analytically [45] in the form  $U_n = [1 + \sigma(N - 1)]^{-1/2}$ , where  $N$  is the total number of components. The stability of any multicomponent vector soliton is not guaranteed and should be studied carefully. We refer to Ref. [52] for a detailed discussion of the stability issue.

## 7.4 SPECTRAL AND TEMPORAL EFFECTS

This section considers the spectral and temporal changes occurring as a result of XPM interaction between two copropagating pulses with nonoverlapping spectra [53–59]. For simplicity, the polarization effects are ignored assuming that the input beams preserve their polarization during propagation. Equations (7.1.13) and (7.1.14) then govern the evolution of the two pulses along the fiber length and include the effects of group-velocity mismatch, GVD, SPM, and XPM. If fiber losses are neglected for simplicity, these equations become

$$\frac{\partial A_1}{\partial z} + \frac{i\beta_{21}}{2} \frac{\partial^2 A_1}{\partial T^2} = i\gamma_1(|A_1|^2 + 2|A_2|^2)A_1, \quad (7.4.1)$$

$$\frac{\partial A_2}{\partial z} + d \frac{\partial A_2}{\partial T} + \frac{i\beta_{22}}{2} \frac{\partial^2 A_2}{\partial T^2} = i\gamma_2(|A_2|^2 + 2|A_1|^2)A_2, \quad (7.4.2)$$

where

$$T = t - \frac{z}{v_{g1}}, \quad d = \frac{v_{g1} - v_{g2}}{v_{g1}v_{g2}}. \quad (7.4.3)$$

Time  $T$  is measured in a reference frame moving with the pulse traveling at speed  $v_{g1}$ . The parameter  $d$  is a measure of group-velocity mismatch between the two pulses.

In general, two pulses can have different widths. Using the width  $T_0$  of the first pulse at the wavelength  $\lambda_1$  as a reference, we introduce the walk-off length  $L_W$  and the dispersion length  $L_D$  as

$$L_W = T_0/|d|, \quad L_D = T_0^2/|\beta_{21}|. \quad (7.4.4)$$

Depending on the relative magnitudes of  $L_W$ ,  $L_D$ , and the fiber length  $L$ , the two pulses can evolve very differently. If  $L$  is small compared to both  $L_W$  and  $L_D$ , the dispersive effects do not play a significant role and can be neglected. For example,

this can occur for  $T_0 < 100$  ps and  $L < 10$  m if the center wavelengths of the two pulses are within 10 nm of each other ( $|d| < 1$  ps/m). In this quasi-CW situation, the steady-state solution of Section 7.3 is applicable. If  $L_W < L$  but  $L_D \gg L$ , the second derivatives in Eqs (7.4.1) and (7.4.2) can be neglected, but the first derivatives must be retained. Even though the pulse shape does not change under such conditions, the combination of group-velocity mismatch and the nonlinearity-induced frequency chirp can affect the spectrum drastically. This is generally the case for  $T_0 \sim 100$  ps,  $L \sim 10$  m, and  $|d| < 10$  ps/m. Finally, for ultrashort pulses ( $T_0 < 10$  ps), the GVD terms should also be included; XPM then affects both the pulse shape and the spectrum. Both of these cases are discussed in what follows.

### 7.4.1 Asymmetric Spectral Broadening

Consider first the simple case  $L \ll L_D$  for which the second-derivative terms in Eqs (7.4.1) and (7.4.2) can be neglected. The group-velocity mismatch is included through the parameter  $d$  assuming  $L_W < L$ . As the pulse shapes do not change in the absence of GVD, Eqs (7.4.1) and (7.4.2) can be solved analytically. The general solution at  $z = L$  is given by [55]

$$A_1(L, T) = A_1(0, T)e^{i\phi_1}, \quad A_2(L, T) = A_2(0, T - dL)e^{i\phi_2}, \quad (7.4.5)$$

where the time-dependent nonlinear phase shifts are obtained from

$$\phi_1(T) = \gamma_1 \left( L|A_1(0, T)|^2 + 2 \int_0^L |A_2(0, T - zd)|^2 dz \right), \quad (7.4.6)$$

$$\phi_2(T) = \gamma_2 \left( L|A_2(0, T)|^2 + 2 \int_0^L |A_1(0, T + zd)|^2 dz \right). \quad (7.4.7)$$

The physical interpretation of Eqs (7.4.5) through (7.4.7) is clear. As the pulse propagates through the fiber, its phase is modulated because of the intensity dependence of the refractive index. The modulated phase has two contributions. The first term in Eqs (7.4.6) and (7.4.7) is due to SPM (see Section 4.1) but the second term has its origin in XPM. The XPM contribution changes along the fiber length because of the group-velocity mismatch. The total XPM contribution to the phase is obtained by integrating over the fiber length.

The integration in Eqs (7.4.6) and (7.4.7) can be performed analytically for some specific pulse shapes. As an illustration, consider the case of two unchirped Gaussian pulses of the same width  $T_0$  with the initial amplitudes

$$A_1(0, T) = \sqrt{P_1} \exp\left(-\frac{T^2}{2T_0^2}\right), \quad A_2(0, T) = \sqrt{P_2} \exp\left(-\frac{(T - T_d)^2}{2T_0^2}\right), \quad (7.4.8)$$

where  $P_1$  and  $P_2$  are the peak powers and  $T_d$  is the initial time delay between the two pulses. Substituting Eq. (7.4.8) in Eq. (7.4.6),  $\phi_1$  is given by

$$\phi_1(\tau) = \gamma_1 L \left( P_1 e^{-\tau^2} + P_2 \frac{\sqrt{\pi}}{\delta} [\operatorname{erf}(\tau - \tau_d) - \operatorname{erf}(\tau - \tau_d - \delta)] \right), \quad (7.4.9)$$

where  $\operatorname{erf}(x)$  stands for the error function and

$$\tau = T/T_0, \quad \tau_d = T_d/T_0, \quad \delta = dL/T_0. \quad (7.4.10)$$

A similar expression can be obtained for  $\phi_2(T)$  using Eq. (7.4.7).

As discussed in Section 4.1, the time dependence of the phase manifests as spectral broadening. Similar to the case of pure SPM, the spectrum of each pulse is expected to broaden and develop a multipeak structure. However, the spectral shape is now governed by the combined contributions of SPM and XPM to the pulse phase. Figure 7.2 shows the spectra of two pulses using  $\gamma_1 P_1 L = 40$ ,  $P_2/P_1 = 0.5$ ,  $\gamma_2/\gamma_1 = 1.2$ ,  $\tau_d = 0$ , and  $\delta = 5$ . These parameters correspond to an experimental situation in which a pulse at 630 nm, with 100-W peak power, is launched inside a fiber together with another pulse at 530 nm with 50-W peak power such that  $T_d = 0$ ,  $T_0 = 10$  ps, and  $L = 5$  m. The most noteworthy feature of Figure 7.2 is spectral asymmetry that is due solely to XPM. In the absence of XPM interaction the two spectra would be symmetric and would exhibit less broadening. The spectrum of pulse 2 is more asymmetric because the XPM contribution is larger for this pulse ( $P_1 = 2P_2$ ).

A qualitative understanding of the spectral features seen in Figure 7.2 can be developed from the XPM-induced frequency chirp using

$$\Delta\nu_1(\tau) = -\frac{1}{2\pi} \frac{\partial\phi_1}{\partial T} = \frac{\gamma_1 L}{\pi T_0} \left[ P_1 \tau e^{-\tau^2} - \frac{P_2}{\delta} (e^{-(\tau-\tau_d)^2} - e^{-(\tau-\tau_d-\delta)^2}) \right], \quad (7.4.11)$$

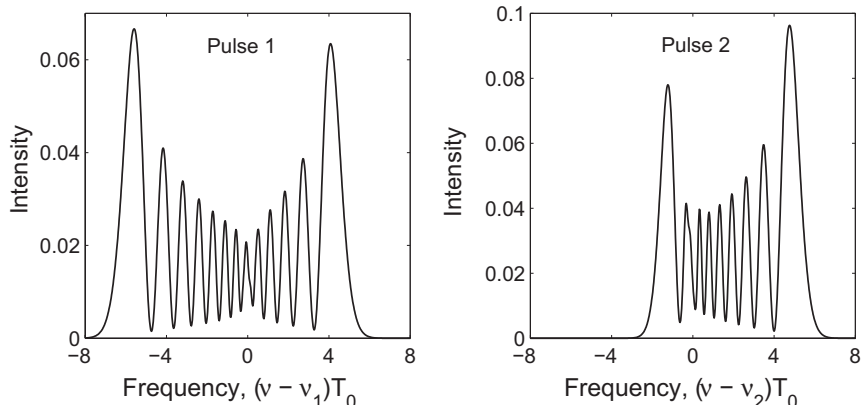


**Figure 7.2 Spectra of two pulses exhibiting XPM-induced asymmetric spectral broadening.** The parameters are  $\gamma_1 P_1 L = 40$ ,  $P_2/P_1 = 0.5$ ,  $\gamma_2/\gamma_1 = 1.2$ ,  $\tau_d = 0$ , and  $L/L_W = 5$ .

where Eq. (7.4.9) was used. For  $\tau_d = 0$  and  $|\delta| \ll 1$  ( $L \ll L_w$ ), the chirp is given by the simple relation

$$\Delta\nu_1(\tau) \approx \frac{\gamma_1 L}{\pi T_0} e^{-\tau^2} [P_1\tau + P_2(2\tau - \delta)]. \quad (7.4.12)$$

The chirp for pulse 2 is obtained following the same procedure and is given by

$$\Delta\nu_2(\tau) \approx \frac{\gamma_2 L}{\pi T_0} e^{-\tau^2} [P_2\tau + P_1(2\tau + \delta)]. \quad (7.4.13)$$

For positive values of  $\delta$ , the chirp is larger near the leading edge for pulse 1 while the opposite occurs for pulse 2. Because the leading and trailing edges carry red- and blue-shifted components, respectively, the spectrum of pulse 1 is shifted toward red while that of pulse 2 is shifted toward blue. This is precisely what occurs in Figure 7.2. The spectrum of pulse 2 shifts less on the red side because the SPM contribution is much smaller for it. When  $P_1 = P_2$  and  $\gamma_1 \approx \gamma_2$ , the spectra of two pulses would be the mirror images of each other.

The qualitative features of spectral broadening can be quite different if the two pulses do not overlap initially but have a relative time delay [55]. To isolate the effects of XPM, it is useful to consider the pump–probe configuration assuming  $P_1 \ll P_2$ . The pump-induced chirp imposed on the probe pulse is obtained from Eq. (7.4.11) by neglecting the SPM contribution and is of the form

$$\Delta\nu_1(\tau) = \text{sgn}(\delta)\Delta\nu_{\max} \exp[-(\tau - \tau_d)^2] - \exp[-(\tau - \tau_d - \delta)^2], \quad (7.4.14)$$

where  $\Delta\nu_{\max}$  is the maximum XPM-induced chirp given by

$$\Delta\nu_{\max} = \frac{\gamma_1 P_2 L}{\pi T_0 |\delta|} = \frac{\gamma_1 P_2 L_w}{\pi T_0}. \quad (7.4.15)$$

Note that  $\Delta\nu_{\max}$  is set by the walk-off length  $L_w$  rather than the actual fiber length  $L$ . This is expected because the XPM interaction occurs as long as the two pulses overlap.

Equation (7.4.14) shows that the XPM-induced chirp can vary significantly along the probe pulse if  $\tau_d$  and  $\delta$  are of opposite signs. As a result, the probe spectrum can have qualitatively different features depending on the relative values of  $\tau_d$  and  $\delta$ . Consider, for example, the case in which the pump pulse travels faster than the probe pulse ( $\delta < 0$ ) and is delayed initially ( $\tau_d \geq 0$ ). Figure 7.3 shows the probe spectrum together with the phase  $\phi_1$  and the chirp  $\Delta\nu_1$  for  $\delta = -4$  and  $\tau_d = 0, 2$ , and 4. The fiber length  $L$  and the pump peak power  $P_2$  are chosen such that  $\gamma_1 P_2 L = 40$  and  $L/L_w = 4$ . For reference, a 10-ps pump pulse with a group-velocity mismatch  $d = 10$  ps/m has  $L_w = 1$  m. The probe spectrum in Figure 7.3 is shifted toward blue with strong asymmetry for  $\tau_d = 0$ . For  $\tau_d = 2$ , it becomes symmetric while for  $\tau_d = 4$  it is again asymmetric with a shift toward red. In fact, the spectra for  $\tau_d = 0$  and  $\tau_d = 4$  are mirror images of each other about the central frequency  $\nu_1 = \omega_1/(2\pi)$ .

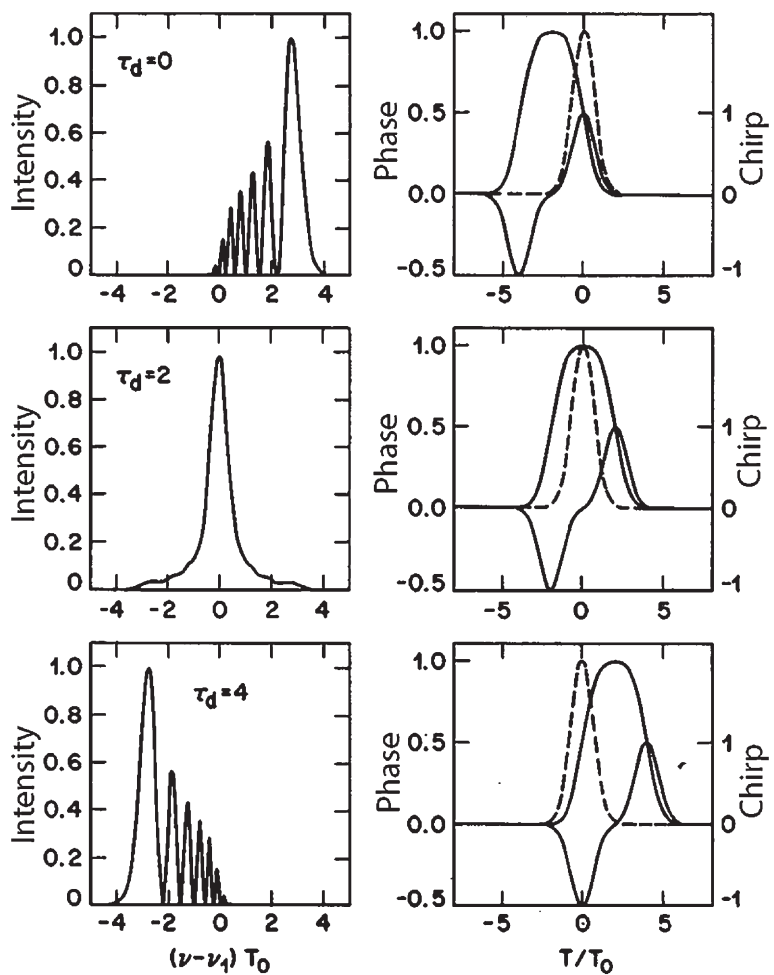


Figure 7.3 Optical spectra (left column) and XPM-induced phase and chirp (right column) for a probe pulse copropagating with a faster-moving pump pulse. The shape of probe pulse is shown by a dashed line. Three rows correspond to  $\tau_d=0, 2$ , and  $4$ , respectively. (After Ref. [55]; © 1989 American Physical Society.)

The probe spectra can be understood physically by considering the XPM-induced chirp shown in the right column of Figure 7.3. For  $\tau_d = 0$ , the chirp is positive across the entire probe pulse, and the maximum chirp occurs at the pulse center. This is in contrast to the SPM case (shown in Figure 4.1) where the chirp is negative near the leading edge, zero at the pulse center, and positive near the trailing edge. The differences in the SPM and XPM cases are due to group-velocity mismatch. When  $\tau_d = 0$ , the slow-moving probe pulse interacts mainly with the trailing edge of the pump pulse. As a result, the XPM-induced chirp is positive and the probe spectrum has

only blue-shifted components. When  $\tau_d = 4$ , the pump pulse just catches up with the probe pulse at the fiber output. Its leading edge interacts with the probe; the chirp is therefore negative and the spectrum is shifted toward red. When  $\tau_d = 2$ , the pump pulse has time not only to catch up but pass through the probe pulse in a symmetric manner. The chirp is zero at the pulse center similar to the case of SPM. However, its magnitude is considerably smaller across the entire pulse. As a result, the probe spectrum is symmetrically broadened but its tails carry a relatively small amount of pulse energy. The probe spectrum in this symmetric case depends quite strongly on the ratio  $L/L_w$ . If  $L/L_w = 2$  with  $\tau_d = 1$ , the spectrum is broader with considerably more structure. By contrast, if  $L \gg L_w$ , the probe spectrum remains virtually unchanged.

The XPM-induced spectral broadening has been observed experimentally in the pump–probe configuration. In one experiment [5], the 10-ps pump pulses were obtained from a color-center laser operating at  $1.51\text{ }\mu\text{m}$  while the probe pulses at  $1.61\text{ }\mu\text{m}$  were generated using a fiber-Raman laser (see Section 8.2). The walk-off length was about  $80\text{ m}$  while the dispersion length exceeded  $10\text{ km}$ . Both the symmetric and asymmetric probe spectra were observed as the fiber length was increased from  $50$  to  $400\text{ m}$  and the effective delay between the pulses was varied using time-dispersion tuning.

In a different experiment, a Nd:YAG laser was used to provide 33-ps pump pulses at  $1.06\text{ }\mu\text{m}$  and 25-ps probe pulses at  $0.53\text{ }\mu\text{m}$  [54]. The delay between two pulses was adjusted using a Mach–Zehnder interferometer. Because of a relatively large group-velocity mismatch ( $d \approx 80\text{ ps/m}$ ), the walk-off length was only about  $25\text{ cm}$ . For a 1-m-long fiber used in the experiment,  $L/L_w = 4$ . The probe spectra were recorded by varying the delay  $T_d$  and the peak power of the pump pulse. The spectra exhibited a shift toward the red or the blue side with some broadening as the multiple peaks could not be resolved. Such a XPM-induced shift is referred to as the induced frequency shift [54].

Figure 7.4 shows the induced shift as a function of the time delay  $T_d$ . The solid curve is the theoretical prediction of Eq. (7.4.14). The frequency shift for a given time delay is obtained by maximizing  $\Delta\nu_1(\tau)$ . The maximum occurs near  $\tau = 0$ , and the frequency shift is given by

$$\Delta\nu_1 = \Delta\nu_{\max} \{ \exp(-\tau_d^2) - \exp[-(\tau_d + \delta)^2] \}, \quad (7.4.16)$$

where  $\delta \approx -4$  for the experimental values of the parameters and  $\tau_d = T_d/T_0$  with  $T_0 \approx 20\text{ ps}$ . Equation (7.4.16) shows that the maximum shift  $\Delta\nu_{\max}$  occurs for  $\tau_d = 0$  and  $\tau_d = 4$ , but the shift vanishes for  $\tau_d = 2$ . These features are in agreement with the experiment. According to Eq. (7.4.15) the maximum shift should increase linearly with the peak power of the pump pulse. This behavior is indeed observed experimentally, as seen in Figure 7.4. The XPM-induced shift of the probe wavelength is about  $0.1\text{ nm/kW}$ . It is limited by the walk-off length and can be increased by an order of magnitude or more if the wavelength difference between the pump and probe is reduced to a few nanometers. The XPM-induced frequency shift may be useful for optical communication applications.

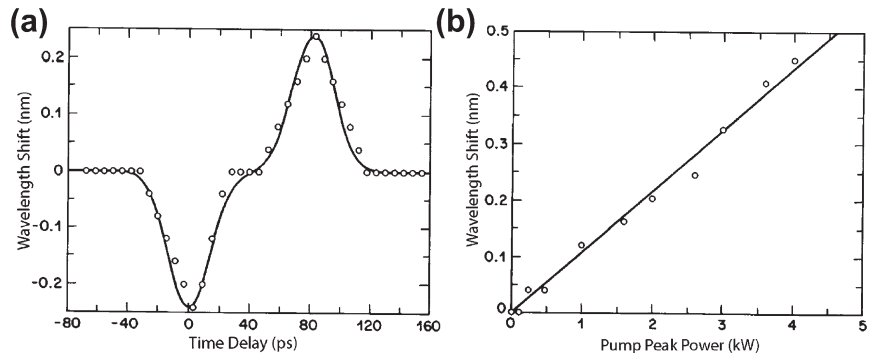


**Figure 7.4** XPM-induced wavelength shift of a  $0.53\text{-}\mu\text{m}$  probe pulse as a function of (a) the time delay  $T_d$  and (b) peak power of the  $1.06\text{-}\mu\text{m}$  pump pulse for  $T_d=0$ . Open circles show the experimental data and the solid lines show theoretical predictions. (After Ref. [54]; © 1988 American Institute of Physics.)

### 7.4.2 Asymmetric Temporal Changes

In the preceding discussion, the dispersion length  $L_D$  was assumed to be much larger than the fiber length  $L$ . As a result, both pulses maintained their shape during propagation through the fiber. If  $L_D$  becomes comparable to  $L$  or the walk-off length  $L_W$ , the combined effects of XPM, SPM, and GVD can lead to qualitatively new temporal changes that accompany the spectral changes discussed earlier. These temporal changes can be studied by solving Eqs (7.1.13) and (7.1.14) numerically. It is useful to introduce the normalization scheme of Section 4.2 by defining

$$\xi = \frac{z}{L_D}, \quad \tau = \frac{t - z/v_{g1}}{T_0}, \quad U_j = \frac{A_j}{\sqrt{P_1}}, \quad (7.4.17)$$

and write the coupled amplitude equations in the form [55]

$$\frac{\partial U_1}{\partial \xi} + \text{sgn}(\beta_{21}) \frac{i}{2} \frac{\partial^2 U_1}{\partial \tau^2} = iN^2 (|U_1|^2 + 2|U_2|^2) U_1, \quad (7.4.18)$$

$$\frac{\partial U_2}{\partial \xi} \pm \frac{L_D}{L_W} \frac{\partial U_2}{\partial \tau} + \frac{i}{2} \frac{\beta_{22}}{\beta_{21}} \frac{\partial^2 U_2}{\partial \tau^2} = iN^2 \frac{\omega_2}{\omega_1} (|U_2|^2 + 2|U_1|^2) U_2, \quad (7.4.19)$$

where the parameter  $N$  is introduced as

$$N^2 = \frac{L_D}{L_{NL}} = \frac{\gamma_1 P_1 T_0^2}{|\beta_{21}|}. \quad (7.4.20)$$

Fiber losses have been neglected assuming that  $\alpha_j L \ll 1$  for  $j=1$  and 2. The second term in Eq. (7.4.19) accounts for the group-velocity mismatch between the two

pulses. The choice of plus or minus depends on the sign of the parameter  $d$  defined in Eq. (7.4.3).

To isolate the XPM effects, it is useful to consider a pump–probe configuration. If we assume  $|U_2|^2 \ll |U_1|^2$ , we can neglect the term containing  $|U_2|^2$  in Eqs (7.4.18) and (7.4.19). Evolution of the pump pulse, governed by Eq. (7.4.18), is then unaffected by the probe pulse. Evolution of the probe pulse is, however, affected considerably by the presence of the pump pulse because of XPM. Equation (7.4.19) governs the combined effects of XPM and GVD on the shape and the spectrum of the probe pulse. These equations can be solved numerically using the split-step Fourier method discussed in Section 2.4.

Figure 7.5 shows the shapes and the spectra of the pump and probe pulses at  $\xi = 0.4$  for the case  $N = 10$ ,  $L_D/L_w = 10$ ,  $\omega_2/\omega_1 = 1.2$ , and  $\beta_{22} \approx \beta_{21} > 0$ . Both pulses at the fiber input are taken to be Gaussian of the same width with no initial time delay between them. The pump pulse is assumed to travel faster than the probe pulse ( $d > 0$ ). The shape and the spectrum of the pump pulse have features resulting from the combined effects of SPM and GVD (see Section 4.2). In contrast, the shape and the spectrum of the probe pulse are governed by the combined effects of

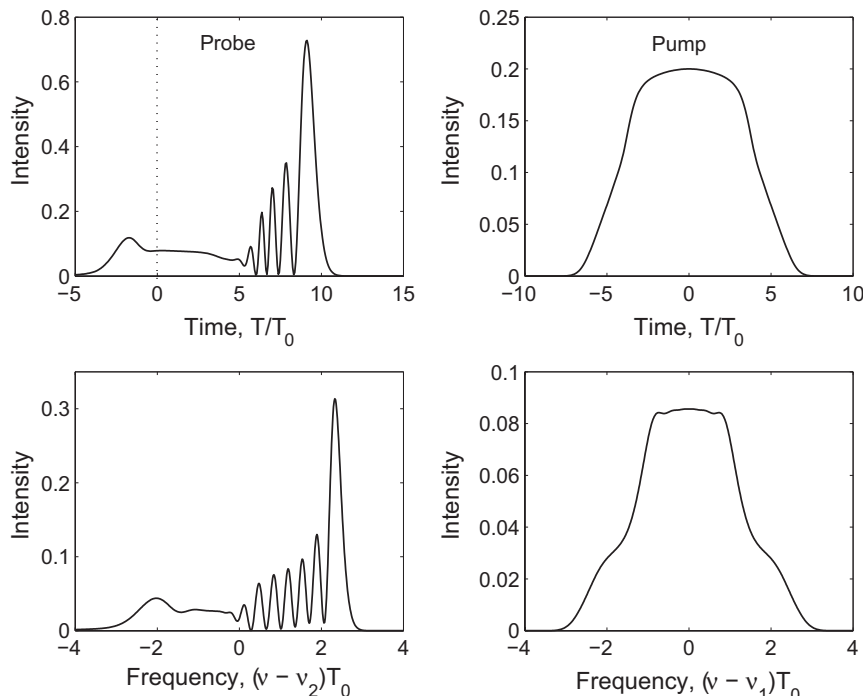


**Figure 7.5 Shapes (upper row) and spectra (lower row) of probe and pump pulses at  $\xi=0.4$ . Dashed line shows location of input pulses. Both pulses are Gaussian with the same width and overlap entirely at  $\xi=0$ .** (After Ref. [55]; © 1989 American Physical Society.)

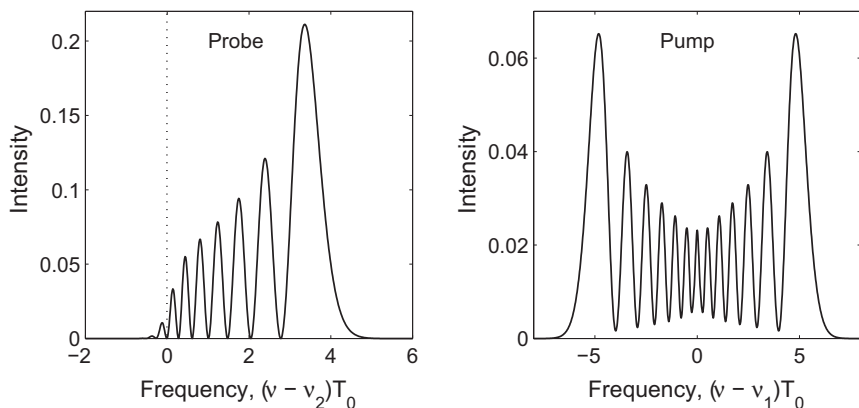


**Figure 7.6 Spectra of probe and pump pulses under conditions identical to those of Figure 7.5 except that the GVD effects are ignored. Pulse shapes are not shown as they remain unchanged.**

XPM and GVD. For comparison, Figure 7.6 shows the probe and pump spectra in the absence of GVD; asymmetric spectral broadening of the probe spectrum toward the blue side in the absence of GVD is discussed in Section 7.4.1. The effect of GVD is to reduce the extent of asymmetry; a part of the pulse energy is now carried by the red-shifted spectral components (see Figure 7.5).

The most notable effect of GVD is seen in the shape of the probe pulse in Figure 7.5. In the absence of GVD, the pulse shape remains unchanged as XPM only affects the optical phase. However, when GVD is present, different parts of the probe pulse propagate at different speeds because of the XPM-induced chirp imposed on the probe pulse. This results in an asymmetric shape with considerable structure [55]. The probe pulse develops rapid oscillations near the trailing edge while the leading edge is largely unaffected. These oscillations are related to the phenomenon of optical wave breaking discussed in Section 4.2.3. There, the combination of SPM and GVD led to oscillations in the pulse wings (see Figure 4.12). Here, it is the combination of XPM and GVD that results in oscillations over the entire trailing half of the probe pulse.

The features seen in Figure 7.5 can be understood qualitatively noting that the XPM-induced chirp is maximum at the pulse center (as seen in the top row of Figure 7.3). The combined effect of frequency chirp and positive GVD is to slow down the peak of the probe pulse with respect to its tails. The XPM-induced optical wave breaking occurs because the peak lags behind and interferes with the trailing edge. This can also be understood by noting that the faster moving pump pulse interacts mainly with the trailing edge of the probe pulse. In fact, if the probe and pump wavelengths were reversed so that the slower moving pump pulse interacts mainly with the leading edge, oscillations would develop near the leading edge because the XPM-induced chirp would speed up the peak of the probe pulse with

respect to its tails. The effect of initial delay between the pump and probe pulses can lead to qualitative features quite different for the dispersive XPM compared with those shown in Figure 7.3. For example, even if the pump pulse walks through the probe pulse in an asymmetric manner, the probe spectrum is no longer symmetric when the GVD effects are included.

The experimental observation of the XPM-induced asymmetric temporal effects requires the use of femtosecond pulses. This is so because  $L_D > 1$  km for  $T_0 > 5$  ps while  $L_w \sim 1$  m for typical values of  $|d| \sim 10$  ps/m. Because XPM occurs only during a few walk-off lengths, the interplay between the XPM and GVD effects can occur only if  $L_D$  and  $L_w$  become comparable. For example, if  $T_0 = 100$  fs,  $L_D$  and  $L_w$  both become  $\sim 10$  cm, and the temporal effects discussed earlier can occur in a fiber less than one meter long. For such short pulses, however, it becomes necessary to include the higher-order nonlinear effects.

### 7.4.3 Higher-Order Nonlinear Effects

As discussed in Sections 2.3 and 5.5, several higher-order nonlinear effects should be considered for femtosecond optical pulses. The most important among them in practice is the Raman effect. In the case of a single pulse, its inclusion leads to intrapulse Raman scattering that manifests through a Raman-induced frequency shift. In the case of two pulses at different wavelengths, energy transfer between them can also occur during the XPM interaction [60–62].

When the Raman contribution to the nonlinear polarization  $P_{NL}$  is included, one must use Eq. (2.3.38) in place of Eq. (2.3.6). The coupled NLS equations can still be obtained by following the procedure of Section 7.1 but mathematical details become quite cumbersome. By using Eq. (2.3.41) for the functional form of the Raman response function, the resulting equations can be written as [61]

$$\begin{aligned} \frac{\partial A_j}{\partial z} + \frac{1}{v_{gj}} \frac{\partial A_j}{\partial t} + \frac{i\beta_{2j}}{2} \frac{\partial^2 A_j}{\partial t^2} + \frac{\alpha_j}{2} A_j &= i\gamma_j (1 - f_R) (|A_j|^2 + 2|A_m|^2) A_j \\ &+ i\gamma_j f_R \int_0^\infty ds h_R(s) \{[|A_j(z, t-s)|^2 + |A_m(z, t-s)|^2] A_j(z, t) \\ &+ A_j(z, t-s) A_m^*(z, t-s) \exp[i(\omega_j - \omega_m)s] A_m(z, t)\}, \end{aligned} \quad (7.4.21)$$

where  $j = 1$  or  $2$  and  $m = 3 - j$ . The Raman response function  $h_R(t)$  and the parameter  $f_R$  appeared first in Eq. (2.3.41) of Section 2.3.

In spite of the complexity of Eq. (7.4.21), the physical meaning of various nonlinear terms is quite clear. On the right side of Eq. (7.4.21), the first two terms represent the SPM and XPM contributions from the electronic response, the next two terms provide the SPM and XPM contributions from molecular vibrations, and the last term governs the energy transfer between the two pulses due to Raman amplification (see Chapter 8). When the Raman contribution is neglected by setting  $f_R = 0$ , Eq. (7.4.21) reduces to Eqs (7.1.13) and (7.1.14). Similarly, if the two pulses are assumed to be much wider than the Raman response time ( $\sim 50$  fs) and  $h_R(t)$  is

replaced by a delta function, Eqs (7.1.13) and (7.1.14) are again recovered, provided the Raman amplification term is neglected.

Equation (7.4.21) shows that the XPM-induced coupling affects ultrashort optical pulses in several different ways when the Raman contribution is included. Energy transfer represented by the last term is discussed in Chapter 8 in the context of stimulated Raman scattering. The novel aspect of Eq. (7.4.21) is the SPM and XPM contributions from molecular vibrations. Similar to the single-pulse case, these contributions lead to a shift of the carrier frequency. The most interesting feature is that such a shift results from both *intrpulse* and *interpulse* Raman scattering. In the context of solitons, the self-frequency shift is accompanied by a cross-frequency shift [61], occurring because of the overlapping of two copropagating pulses. The self- and cross-frequency shifts may have the same or the opposite signs depending on whether the difference  $\omega_1 - \omega_2$  in the carrier frequencies is smaller or larger than the frequency at which the Raman gain is maximum (see Chapter 8). As a result, the XPM interaction between two pulses of different carrier frequencies can either enhance or suppress the self-frequency shift expected when each pulse propagates alone [7].

## 7.5 APPLICATIONS OF XPM

The nonlinear phenomenon of XPM can be both beneficial and harmful. Its most direct impact is related to multichannel lightwave systems whose performance is invariably limited by the XPM interaction among neighboring channels. Such systems are also affected by the so-called intrachannel XPM, resulting from overlapping of neighboring pulses belonging to the same channel [51]. This section is devoted to the beneficial applications of XPM such as pulse compression and optical switching.

### 7.5.1 XPM-Induced Pulse Compression

It is well known that the SPM-induced chirp can be used to compress optical pulses [63]. Because XPM also imposes a frequency chirp on an optical pulse, it can be used for pulse compression as well [64–70]. An obvious advantage of XPM-induced pulse compression is that, in contrast to the SPM technique requiring the input pulse to be intense and energetic, XPM can compress weak input pulses because the frequency chirp is produced by a copropagating intense pump pulse. However, the XPM-induced chirp is affected by the walk-off effects and depends critically on the initial relative pump–probe delay. As a result, the practical use of XPM-induced pulse compression requires a careful control of the pump-pulse parameters such as its width, peak power, wavelength, and initial delay relative to the probe pulse.

Two cases must be distinguished depending on the relative magnitudes of the walk-off length  $L_w$  and the dispersion length  $L_D$ . If  $L_D \gg L_w$  throughout the fiber, the GVD effects are negligible. In that case, an optical fiber generates the chirp through XPM, and a grating pair is needed to compress the chirped pulse.

Equation (7.4.11) can be used to analyze the magnitude and the form of the chirp. A nearly linear chirp can be imposed across the signal pulse when the pump pulse is much wider compared with it [66]. The compression factor depends on the pump-pulse energy and can easily exceed 10.

Another pulse-compression mechanism can be used when  $L_D$  and  $L_W$  are comparable. In this case, the same piece of fiber that is used to impose the XPM-induced chirp also compresses the pulse through the GVD. Interestingly, in contrast to the SPM case where such compression can occur only in the anomalous-GVD region, the XPM offers the possibility of pulse compression even in the visible region (normal GVD) without the need of a grating pair. The performance of such a compressor can be studied by solving Eqs (7.4.18) and (7.4.19) numerically for a given set of pump and signal pulses [55]. It is generally necessary to introduce a relative time delay  $T_d$  between the pump and probe pulses such that the faster moving pulse overtakes the slower pulse and passes through it. The maximum compression occurs at a distance  $|\tau_d|L_W$  although the pulse quality is not necessarily the best at the point of maximum compression.

In general, a trade-off exists between the magnitude and the quality of compression. As an example, Figure 7.7 compares the pulse shapes for both the pump and probe at a distance of  $z/L_D = 0.2$  (solid curves). Both pulses are initially Gaussian of the same width (dashed curves) but have different wavelengths such that  $\lambda_1/\lambda_2 = 1.2$ . However, the probe is advanced by  $\tau_d = -2.5$ . Other parameters are  $N = 10$  and  $L_D/L_W = 10$ . As expected, the pump pulse broadens considerably in the normal-dispersion regime of the fiber. However, the probe pulse is compressed by about a factor of 4 and, except for some ringing on the leading edge, is pedestal-free. Even this ringing can be suppressed if the pump pulse is initially made wider than the signal pulse, although only at the expense of reduction in the amount of compression

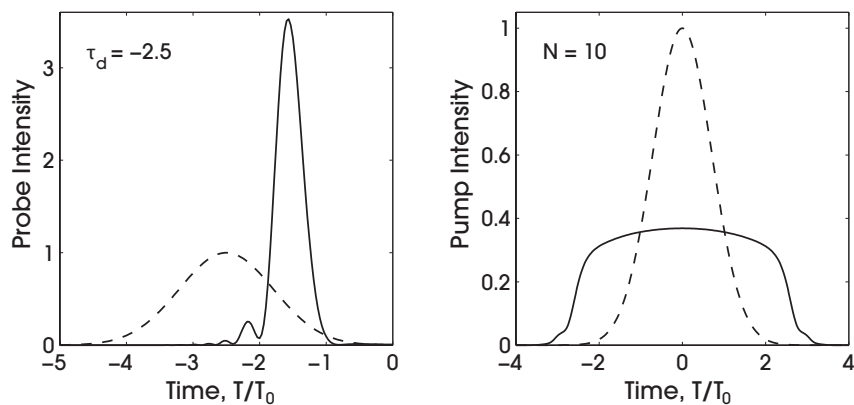


**Figure 7.7** Pulse shapes for the pump and probe at a distance  $z/L_D = 0.2$ . The dashed curves show for comparison input pulse shapes at  $z=0$ . XPM-induced pulse compression is realized using pump pulses of peak power such that  $N=10$ .

achievable at a given pump power. Of course, larger compression factors can be realized by increasing the pump power.

XPM-induced pulse compression in the normal-GVD region of a fiber can also occur when the XPM coupling is due to interaction between two orthogonally polarized components of a single beam [68]. An experiment in 1990 demonstrated pulse compression using just such a technique [67]. A polarizing Michelson interferometer was used to launch 2-ps pulses in a 1.4-m fiber (with a 2.1-mm beat length) such that the peak power and the relative delay of the two polarization components were adjustable. For a relative delay of 1.2 ps, the weak component was compressed by a factor of about 6.7 when the peak power of the other polarization component was 1.5 kW.

When both the pump and signal pulses propagate in the normal-GVD region of the fiber, the compressed pulse is necessarily asymmetric because of the group-velocity mismatch and the associated walk-off effects. The group velocities can be made nearly equal when wavelengths of the two pulses lie on opposite sides of the zero-dispersion wavelength. One possibility consists of compressing 1.55- $\mu\text{m}$  pulses by using 1.06- $\mu\text{m}$  pump pulses. The signal pulse by itself is too weak to form an optical soliton. However, the XPM-induced chirp imposed on it by a copropagating pump pulse can be made strong enough that the signal pulse goes through an initial compression phase associated with higher-order solitons [8].

Figure 7.8 shows the evolution of signal and pump pulses when the pump pulse has the same width as the signal pulse but is intense enough that  $N = 30$  in Eq. (7.4.18). Because of the XPM-induced chirp, the signal pulse compresses by about a factor of 10 before its quality degrades. Both the compression factor and the pulse quality depend on the width and the energy of the pump pulse and can be controlled by optimizing pump-pulse parameters. This method of pulse compression is similar to that provided by higher-order solitons even though, strictly speaking, the signal pulse never forms a soliton. With the use of dispersion-shifted fibers, the technique can be used even when both pump and signal wavelengths are in the 1.55- $\mu\text{m}$  region as long as the zero-dispersion wavelength of the fiber lies in the middle. In a 1993 experiment, 10.6-ps signal pulses were compressed to 4.6 ps by using 12-ps pump pulses [69]. Pump and signal pulses were obtained from mode-locked semiconductor lasers operating at 1.56 and 1.54  $\mu\text{m}$ , respectively, but pump pulses were amplified using a fiber amplifier. This experiment demonstrated that XPM-induced pulse compression can occur at power levels achievable with semiconductor lasers.

### 7.5.2 XPM-Induced Optical Switching

The XPM-induced phase shift can also be used for optical switching [63]. Several interferometric schemes have been used to take advantage of XPM for ultrafast optical switching [71–83]. The physics behind XPM-induced switching can be understood by considering a generic interferometer designed such that a weak signal pulse, divided equally between its two arms, experiences identical phase shifts in each arm and is transmitted through constructive interference. If a pump pulse at a different

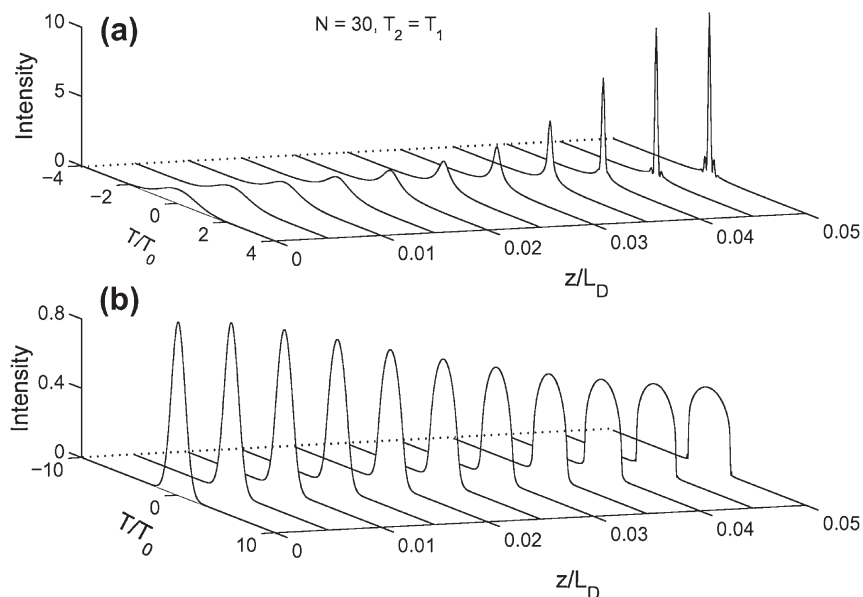


**Figure 7.8** Temporal evolution of (a) signal and (b) pump pulses when the pump pulse propagates in the normal-dispersion regime with the same group velocity and has a peak power such that  $N$  equals 30. (After Ref. [55]; © 1989 American Physical Society.)

wavelength is injected into one of the arms of the interferometer, it would change the signal phase through XPM in that arm. If the XPM-induced phase shift is large enough (close to  $\pi$ ), the signal pulse will not be transmitted because of the destructive interference occurring at the output. Thus, an intense pump pulse can switch the signal pulse through the XPM-induced phase shift.

XPM-induced optical switching was demonstrated in 1990 using a fiber-loop mirror acting as a Sagnac interferometer [73]. A dichroic fiber coupler, with 50:50 splitting ratio at  $1.53\text{ }\mu\text{m}$  and 100:0 splitting ratio at  $1.3\text{ }\mu\text{m}$ , was used to allow for dual-wavelength operation. A  $1.53\text{-}\mu\text{m}$  color-center laser provided a low-power ( $\sim 5\text{ mW}$ ) CW signal. As expected, the counterpropagating signal beams experienced identical phase shifts, and the 500-m-long fiber loop acted as a perfect mirror, in the absence of a pump beam. When 130-ps pump pulses, obtained from a  $1.3\text{-}\mu\text{m}$  Nd:YAG laser, were injected into the clockwise direction, the XPM interaction between the pump and the signal introduced a phase difference between the counterpropagating signal beams. Most of the signal power was transmitted when the peak power of the pump pulse was large enough to introduce a  $\pi$  phase shift.

The XPM-induced phase shift depends not only on the width and the shape of the pump pulse but also on the group-velocity mismatch. In the case in which both the pump and signal beams are pulsed, the phase shift also depends on the initial relative time delay between the pump and signal pulses. In fact, the magnitude and

the duration of the XPM-induced phase shift can be controlled through the initial delay (see Figure 7.3). The main point to note is that phase shift can be quite uniform over most of the signal pulse when the two pulses are allowed to completely pass through each other, resulting in complete switching of the signal pulse. The pump power required to produce  $\pi$  phase shift is generally quite large because of the group-velocity mismatch.

The group-velocity mismatch can be reduced significantly if the pump and signal pulses are orthogonally polarized but have the same wavelength. Moreover, even if the XPM-induced phase shift is less than  $\pi$  because of the birefringence-related pulse walk-off, the technique of cross-splicing can be used to accumulate it over long lengths [76]. In this technique, the fiber loop consists of multiple sections of polarization-maintaining fibers that are spliced together in such a way that the fast and slow axes are rotated by  $90^\circ$  in successive sections. As a result, the pump and signal pulses are forced to pass through each other in each section of the fiber loop, and the XPM-induced phase shift is enhanced by a factor equal to the number of sections.

### 7.5.3 XPM-Induced Nonreciprocity

XPM also occurs when two beams having the same (or different) wavelengths are propagated in opposite directions inside a fiber such that the counterpropagating waves interact with each other through XPM. Such an interaction can lead to new qualitative features, manifested through optical bistability and other instabilities when the fiber is used to construct a nonlinear ring resonator [84–95]. Of particular interest is the XPM-induced nonreciprocity that can affect the performance of fiber gyroscopes [96–101].

The origin of nonreciprocity between two counterpropagating waves can be understood by following the analysis of Section 7.1. If  $A_1$  and  $A_2$  are the amplitudes of the forward and backward propagating waves, they satisfy the coupled amplitude equations similar to Eqs (7.1.13) and (7.1.14),

$$\pm \frac{\partial A_j}{\partial z} + \frac{1}{v_g} \frac{\partial A_j}{\partial t} + \frac{i\beta_2}{2} \frac{\partial^2 A_j}{\partial t^2} + \frac{\alpha}{2} A_j = i\gamma(|A_j|^2 + 2|A_{3-j}|^2)A_j, \quad (7.5.1)$$

where the plus or minus sign corresponds to  $j = 1$  or  $2$ , respectively. In the case of CW beams, this set of two equations is readily solved. If fiber losses are neglected for simplicity, the solution is given as

$$A_j(z) = \sqrt{P_j} \exp(\pm i\phi_j), \quad (7.5.2)$$

where  $P_j$  is the peak power and the nonlinear phase shift is given by  $\phi_j = \gamma z(P_j + 2P_{3-j})$  with  $j = 1, 2$ . If  $P_1 \neq P_2$ , the phase shifts  $\phi_1$  and  $\phi_2$  are not the same for the two counterpropagating waves. This nonreciprocity is due to the presence of the factor of two in the XPM term in Eq. (7.5.1).

XPM-induced nonreciprocity can be detrimental for high-precision fiber gyroscopes used to measure rotation rates as small as  $0.01^\circ$  per hour [102]. Figure 7.9

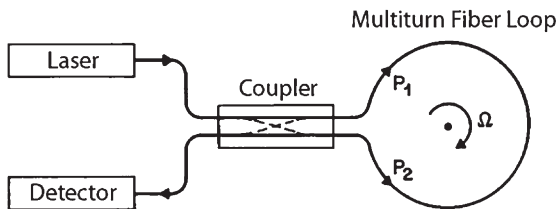


**Figure 7.9 Schematic of a fiber gyroscope.** Light from a laser is coupled through a 50% coupler to launch a counterpropagating waves in a multturn fiber loop. The rotation-induced phase difference is measured through a phase-sensitive detector.

shows the design of a fiber gyroscope schematically. Its operation is based on the Sagnac effect, known to introduce a rotation-dependent relative phase shift between the counterpropagating waves [103]. This phase difference is given by

$$\Delta\phi = \phi_1 - \phi_2 = \gamma L(P_2 - P_1) + S\Omega, \quad (7.5.3)$$

where  $L$  is the total fiber length,  $\Omega$  is the rotation rate, and  $S$  is a scale factor that depends on the fiber length  $L$  as well as on the radius of the fiber loop [102]. If the powers  $P_1$  and  $P_2$  were constant, the XPM term in Eq. (7.5.3) would be of little concern. However, the power levels can fluctuate in practice. Even a power difference of  $1 \mu\text{W}$  between the counterpropagating waves can change  $\Delta\phi$  by  $\sim 1 \times 10^{-6} \text{ rad}$  if we use  $\gamma \approx 10 \text{ W}^{-1}/\text{km}$  and  $L \sim 100 \text{ m}$ . This value typically corresponds to an equivalent rotation rate of  $0.1^\circ$  per hour. For this reason, XPM severely limits the sensitivity of fiber gyroscopes unless the power levels are controlled to within  $10 \text{ nW}$ .

Several schemes can be used to mitigate the XPM problem and improve the gyroscope performance. In one scheme, the laser power is modulated before the counterpropagating waves are launched inside a fiber loop [97]. Because of the time dependence of optical fields, this case is analyzed by solving Eq. (7.5.1) with the appropriate boundary conditions [101]. The results show that the effect of nonreciprocity is reduced drastically if the modulation frequency is chosen suitably. This can be understood physically by noting that XPM occurs only if the two pulses overlap temporally. On a more fundamental level, XPM-induced nonreciprocity results from interference between the counterpropagating waves. Modulation reduces the coherence between the counterpropagating waves, thereby reducing the effectiveness of such an interference. Indeed, the same result can also be obtained by using broadband sources with a limited coherence time [98–100]. Thermal sources or light-emitting diodes have been used for this purpose [102].

Let us consider briefly the effect of XPM on optical bistability. Any nonlinear medium placed inside a cavity can exhibit bistability [104], and optical fibers are no exception. If a fiber-ring cavity is used for this purpose, optical bistability can occur irrespective of whether the beam propagates in the clockwise or counterclockwise direction. An interesting situation occurs when the optical beams are launched in both directions. Because of the XPM-induced coupling between the counterpropagating

beams, the device acts as two coupled bistable systems and can exhibit many new qualitative features [85–87]. Although optical bistability has been observed in the case of unidirectional propagation in a fiber-ring cavity [88], the bidirectional case has not attracted much attention.

The XPM interaction between two counterpropagating optical pulses is generally quite weak and can be neglected in the case of ultrashort pulses. The reason can be understood by noting that the XPM-induced phase shift decreases even for copropagating pulses as the relative group-velocity difference increases [see Eq. (7.4.9)]. For counterpropagating pulses the group-velocity mismatch is so large that the two pulses have little time to interact with each other. Nonetheless, measurable effects can occur for very intense pulses. For example, the spectral shift of a probe pulse observed in an experiment in which 0.7-ps pump pulses with peak intensities  $\sim 10 \text{ TW/cm}^2$  were propagated through a 1-mm-thick glass plate could be accounted for only when the XPM interaction between the counterpropagating pump and probe pulses was included [105]. In the case of optical fibers, XPM interaction between counterpropagating waves becomes important for fiber Bragg gratings.

## 7.6 POLARIZATION EFFECTS

So far in this chapter, all optical fields that are coupled through XPM are assumed to maintain their initial linear state of polarization. This assumption holds only for isotropic fibers and should be relaxed for fibers exhibiting birefringence. Even in an isotropic fiber, XPM-induced nonlinear birefringence leads to changes in the state of polarization (SOP) when the input field is not linearly polarized [106–108]. In this section we develop a vector theory of XPM that applies to optical fields launched and propagating with different states of polarization (SOPs) inside an optical fiber [107].

### 7.6.1 Vector Theory of XPM

As in Section 6.6, it is useful to employ the Jones-matrix formalism to account for the polarization effects in a succinct fashion. The form of the third-order nonlinear polarization is given in Eq. (2.3.6). In the case of two distinct optical fields propagating simultaneously inside an optical fiber, the total electric field can be written as

$$\mathbf{E}(\mathbf{r}, t) = \frac{1}{2} [\mathbf{E}_1 \exp(-i\omega_1 t) + \mathbf{E}_2 \exp(-i\omega_2 t)] + \text{c.c.}, \quad (7.6.1)$$

where  $\mathbf{E}_j$  is the slowly varying amplitude of the optical field oscillating at frequency  $\omega_j$  ( $j = 1, 2$ ). If we follow the method described in Section 6.1.1 and use Eq. (6.1.2) for the third-order susceptibility,  $\mathbf{P}_{\text{NL}}$  can be written in the form

$$\mathbf{P}_{\text{NL}} = \frac{1}{2} [\mathbf{P}_1 \exp(-i\omega_1 t) + \mathbf{P}_2 \exp(-i\omega_2 t)] + \text{c.c.}, \quad (7.6.2)$$

where  $\mathbf{P}_1$  and  $\mathbf{P}_2$  are given by

$$\begin{aligned} \mathbf{P}_j = & \frac{\epsilon_0}{4} \chi_{xxxx}^{(3)} [(\mathbf{E}_j \cdot \mathbf{E}_j) \mathbf{E}_j^* + 2(\mathbf{E}_j^* \cdot \mathbf{E}_j) \mathbf{E}_j + 2(\mathbf{E}_m^* \cdot \mathbf{E}_m) \mathbf{E}_j \\ & + 2(\mathbf{E}_m \cdot \mathbf{E}_j) \mathbf{E}_m^* + 2(\mathbf{E}_m^* \cdot \mathbf{E}_j) \mathbf{E}_m], \end{aligned} \quad (7.6.3)$$

with  $j \neq m$ . In obtaining this expression, we used the relation (6.1.5) among the components of  $\chi^{(3)}$  and assumed that the three components on its right side have the same magnitude.

To a good approximation, one can neglect the longitudinal component of the two field vectors  $\mathbf{E}_1$  and  $\mathbf{E}_2$  and assume that they lie in the  $x$ - $y$  plane. It is also useful to employ the ket notation for a Jones vector representing light polarized in the  $x$ - $y$  plane [109] and write the two fields at any point  $\mathbf{r}$  inside the fiber in the form

$$\mathbf{E}_j(\mathbf{r}, t) = F_j(x, y) |A_j(z, t) \exp(i\beta_j z), \quad (7.6.4)$$

where  $F_j(x, y)$  represents the fiber-mode profile and  $\beta_j$  is the propagation constant at the carrier frequency  $\omega_j$ . The Jones vector  $|A_j\rangle$  is a two-dimensional column vector representing the two components of the electric field in the  $x$ - $y$  plane. In this notation,  $\mathbf{E}_j^* \cdot \mathbf{E}_j$  and  $\mathbf{E}_j \cdot \mathbf{E}_j$  are related to  $\langle A_j | A_j \rangle$  and  $\langle A_j^* | A_j \rangle$ , respectively.

We can now follow the method of Section 7.1.2 and obtain the following vector form of the coupled NLS equations [107]:

$$\begin{aligned} \frac{\partial |A_1\rangle}{\partial z} + \frac{1}{v_{g1}} \frac{\partial |A_1\rangle}{\partial t} + \frac{i\beta_{21}}{2} \frac{\partial^2 |A_1\rangle}{\partial t^2} + \frac{\alpha_1}{2} |A_1\rangle = & \frac{i\gamma_1}{3} (2\langle A_1 | A_1 \rangle + |A_1^* \rangle \langle A_1^*| \\ & + 2\langle A_2 | A_2 \rangle + 2|A_2\rangle \langle A_2| + 2|A_2^*\rangle \langle A_2^*|) |A_1\rangle, \end{aligned} \quad (7.6.5)$$

$$\begin{aligned} \frac{\partial |A_2\rangle}{\partial z} + \frac{1}{v_{g2}} \frac{\partial |A_2\rangle}{\partial t} + \frac{i\beta_{22}}{2} \frac{\partial^2 |A_2\rangle}{\partial t^2} + \frac{\alpha_2}{2} |A_2\rangle = & \frac{i\gamma_2}{3} (2\langle A_2 | A_2 \rangle + |A_2^* \rangle \langle A_2^*| \\ & + 2\langle A_1 | A_1 \rangle + 2|A_1\rangle \langle A_1| + 2|A_1^*\rangle \langle A_1^*|) |A_2\rangle, \end{aligned} \quad (7.6.6)$$

where  $\gamma_j$  is defined in Eq. (7.1.15). As usual,  $\langle A |$  represents the Hermitian conjugate of  $|A\rangle$ , i.e., it is a row vector whose elements have been complex-conjugated. The inner product  $\langle A | A \rangle$  is related to the power associated with the optical field  $|A\rangle$ . In deriving the coupled NLS equations, the fiber is assumed to be without any birefringence. As shown in Section 7.7, the residual birefringence of realistic fibers can be included in a simple fashion.

## 7.6.2 Polarization Evolution

In general, Eqs (7.6.5) and (7.6.6) are quite complicated and their solution requires a numerical approach. To study the XPM-induced polarization effects as simply as possible, we make two simplifications in this section. First, we assume that the fiber length  $L$  is much shorter than the dispersion lengths associated with the two waves and neglect the effects of GVD. Second, we adopt a pump-probe configuration and assume that the probe power  $\langle A_2 | A_2 \rangle$  is much smaller than the pump power  $\langle A_1 | A_1 \rangle$ . This allows us to neglect the nonlinear effects induced by the probe and to simplify the right side of Eqs (7.6.5) and (7.6.6) considerably. If we work in a frame moving

with the probe pulse and introduce a normalized time as  $\tau = (t - z/v_{g2})/T_0$ , where  $T_0$  is the width of input pump pulse, Eqs (7.6.5) and (7.6.6) reduce to

$$\frac{\partial|A_1\rangle}{\partial z} + \frac{1}{L_W} \frac{\partial|A_1\rangle}{\partial \tau} = \frac{i\gamma_1}{3} (2\langle A_1|A_1\rangle + |A_1^*\rangle\langle A_1^*|) |A_1\rangle, \quad (7.6.7)$$

$$\frac{\partial|A_2\rangle}{\partial z} = \frac{2i\gamma_2}{3} (\langle A_1|A_1\rangle + |A_1\rangle\langle A_1| + |A_1^*\rangle\langle A_1^*|) |A_2\rangle, \quad (7.6.8)$$

where  $L_W = |v_{g1} - v_{g2}|/(T_0 v_{g1} v_{g2})$  is the walk-off length and fiber losses have been neglected.

As was seen in Chapter 6, the evolution of the SOP of an optical field is easier to visualize through the rotation of the Stokes vector on the Poincaré sphere. We thus introduce the normalized Stokes vectors for the pump and probe fields as [109]

$$\mathbf{p} = \langle A_1|\boldsymbol{\sigma}|A_1\rangle/P_0, \quad \mathbf{s} = \langle A_2|\boldsymbol{\sigma}|A_2\rangle/P_{20}, \quad (7.6.9)$$

where  $P_0$  and  $P_{20}$  represent the peak powers of the pump and probe pulses at  $z = 0$ . The Pauli spin vector  $\boldsymbol{\sigma}$  is defined using the unit vectors  $\hat{e}_j$  in the Stokes space as  $\boldsymbol{\sigma} = \sigma_1\hat{e}_1 + \sigma_2\hat{e}_2 + \sigma_3\hat{e}_3$ , where the three Pauli matrices are given in Eq. (6.6.8). Using Eqs (7.6.7) through (7.6.9), the two Stokes vectors are found to satisfy [107]

$$\frac{\partial \mathbf{p}}{\partial \xi} + \mu \frac{\partial \mathbf{p}}{\partial \tau} = \frac{2}{3} \mathbf{p}_3 \times \mathbf{p}, \quad (7.6.10)$$

$$\frac{\partial \mathbf{s}}{\partial \xi} = -\frac{4\omega_2}{3\omega_1} (\mathbf{p} - \mathbf{p}_3) \times \mathbf{s}, \quad (7.6.11)$$

where  $\xi = z/L_{NL}$  is the distance normalized to the nonlinear length  $L_{NL} = (\gamma_1 P_0)^{-1}$ ,  $\mu = L_{NL}/L_W$ , and  $\mathbf{p}_3 = (\mathbf{p} \cdot \hat{e}_3)\hat{e}_3$  is the third component of the Stokes vector  $\mathbf{p}$ . Whenever  $p_3 = 0$ ,  $\mathbf{p}$  lies entirely in the equatorial plane of the Poincaré sphere, and the pump field is linearly polarized. In deriving Eqs (7.6.10) and (7.6.11), we made use of the following identities [109]

$$|A\rangle\langle A| = \frac{1}{2} [\mathcal{I} + \langle A|\boldsymbol{\sigma}|A\rangle \cdot \boldsymbol{\sigma}], \quad (7.6.12)$$

$$|A^*\rangle\langle A^*| = |A\rangle\langle A| - \langle A|\sigma_3|A\rangle\sigma_3, \quad (7.6.13)$$

$$\boldsymbol{\sigma}(\mathbf{a} \cdot \boldsymbol{\sigma}) = \mathbf{a}\mathcal{I} + \mathbf{i}\mathbf{a} \times \boldsymbol{\sigma}, \quad (7.6.14)$$

where  $\mathcal{I}$  is an identity matrix and  $\mathbf{a}$  is an arbitrary Stokes vector.

The pump Eq. (7.6.10) is relatively easy to solve and has the solution

$$\mathbf{p}(\xi, \tau) = \exp[(2\xi/3)\mathbf{p}_3(0, \tau - \mu\xi) \times] \mathbf{p}(0, \tau - \mu\xi), \quad (7.6.15)$$

where  $\exp(\mathbf{a} \times)$  is an operator interpreted in terms of a series expansion [109]. Physically speaking, the Stokes vector  $\mathbf{p}$  rotates on the Poincaré sphere along the vertical axis at a rate  $2p_3/3$ . As discussed in Section 6.3, this rotation is due to XPM-induced nonlinear birefringence and is known as the nonlinear polarization rotation. If the pump is linearly or circularly polarized initially, its SOP does not change along the

fiber. For an elliptically polarized pump, the SOP changes as the pump pulse propagates through the fiber. Moreover, as the rotation rate depends on the optical power, different parts of the pump pulse acquire different SOPs. Such *intrapulse* polarization effects have a profound effect on the probe evolution.

The probe Eq. (7.6.11) shows that the pump rotates the probe's Stokes vector around  $\mathbf{p} - \mathbf{p}_3$ , a vector that lies in the equatorial plane of the Poincaré sphere. As a result, if the pump is circularly polarized initially, XPM effect becomes polarization independent since  $\mathbf{p} - \mathbf{p}_3 = 0$ . On the other hand, if the pump is linearly polarized,  $\mathbf{p}_3 = 0$ , and  $\mathbf{p}$  remains fixed in the Stokes space. However, even though the pump SOP does not change in this case, the probe SOP can still change through XPM. Moreover, XPM produces different SOPs for different parts of the probe pulse depending on the local pump power, resulting in nonuniform polarization along the probe pulse profile. The XPM-induced polarization effects become quite complicated when the pump is elliptically polarized because the pump SOP itself changes along the fiber.

As an example, consider the case in which the pump pulse is elliptically polarized but the probe pulse is linearly polarized at the input end. Assuming a Gaussian shape for both pulses, the Jones vectors for the two input pulses have the form

$$|A_1(0, \tau)\rangle = \begin{pmatrix} \cos \phi \\ i \sin \phi \end{pmatrix} P_0^{1/2} \exp\left(-\frac{\tau^2}{2}\right), |A_2(0, \tau)\rangle = \begin{pmatrix} \cos \theta \\ \sin \theta \end{pmatrix} P_{20}^{1/2} \exp\left(-\frac{\tau^2}{2r^2}\right), \quad (7.6.16)$$

where  $\phi$  is the ellipticity angle for the pump,  $\theta$  is the angle at which probe is linearly polarized from the  $x$  axis, and  $r = T_2/T_0$  is the relative width of the probe compared to the pump. Figure 7.10 shows how the pump SOP (solid curve) and the probe SOP (dashed curve) change on the Poincaré sphere with  $\tau$  at a distance of  $\xi = 20$ , assuming  $\phi = 20^\circ$ ,  $\theta = 45^\circ$ ,  $r = 1$ , and  $\mu = 0.1$  ( $L_W = L/2$ ). The pump SOP varies

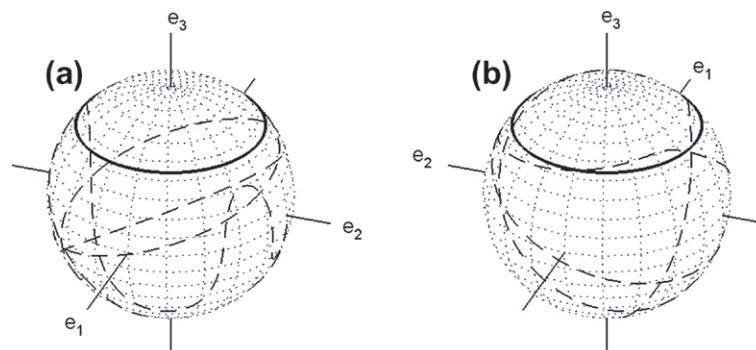


**Figure 7.10** Evolution of a pump SOP (solid curve) and a probe SOP (dashed curve) on the Poincaré sphere as a function of  $\tau$  at a distance of  $\xi = 20$ . Parts (a) and (b) show the front and back faces of the Poincaré sphere, respectively. Both pulses are assumed to be Gaussian of the same width but are launched with different SOPs.

in a simple manner as it rotates around  $\hat{e}_3$  and traces a circle on the Poincaré sphere. In contrast, the probe SOP traces a complicated pattern, indicating that the SOP of the probe is quite different across different parts of the probe pulse. Such polarization changes impact the XPM-induced chirp. As a result, the spectral profile of the probe develops a much more complicated structure compared with the scalar case. We focus next on such spectral effects.

### 7.6.3 Polarization-Dependent Spectral Broadening

In general, Eq. (7.6.8) should be solved numerically except when the pump maintains its SOP. As discussed earlier, this happens if the pump pulse is linearly or circularly polarized when it is launched into the fiber. To gain some physical insight, we first consider the case in which both the pump and probe fields are linearly polarized at the input end, but the probe is oriented at an angle  $\theta$  with respect to the pump. The Jones vectors for the two input fields are then obtained from Eq. (7.6.16) after setting  $\phi = 0$ .

As the SPM does not affect the pump SOP in this case, the analytical solution of Eq. (7.6.8) is found to be

$$|A_2(z, \tau)\rangle = \begin{bmatrix} \cos \theta \exp(i\phi_n) \\ \sin \theta \exp(i\phi_n/3) \end{bmatrix} \sqrt{P_{20}} \exp\left(-\frac{\tau^2}{2r^2}\right), \quad (7.6.17)$$

where  $\phi_n(z, \tau) = 2\gamma_2 \int_0^z P_0(z', \tau - z/L_w) dz'$  is the XPM-induced nonlinear phase shift. The shape of probe pulse does not change in the absence of GVD, as expected. However, its SOP changes and it acquires a nonlinear time-dependent phase shift that is different for the two polarization components. More specifically, the XPM-induced phase shift for the orthogonally polarized component is one third of the copolarized one because of a reduced XPM coupling efficiency. Clearly spectral broadening for the two components would be different under such conditions.

Figure 7.11 shows the (a) probe shapes and (b) spectra for the  $x$  (dashed curve) and  $y$  (dotted curve) components for a fiber of length  $L = 20L_{NL}$ , assuming  $\phi = 0$ ,  $\theta = 45^\circ$ ,  $r = 1$ , and  $\mu = 0.1$  ( $L_w = L/2$ ). The copolarized component has a broader spectrum and exhibits more oscillations compared with the orthogonally polarized one. If the spectrum is measured without placing a polarizer in front of the photodetector, one would record the total spectral intensity shown by a solid line in Figure 7.11b. However, it is important to realize that the SOP is not the same for all spectral peaks. For example, the leftmost peak is  $x$ -polarized, whereas the dominant peak in the center is mostly  $y$ -polarized. This spectral nonuniformity of the SOP is a direct consequence of the XPM-induced polarization effects.

Consider next the case when the pump is elliptically polarized initially with  $\phi = 20^\circ$  but the probe remains linearly polarized. The Jones vectors for these two pulses at  $\xi = 0$  are given in Eq. (7.6.16). Using this form, we solve Eqs (7.6.7) and (7.6.8) numerically to obtain the probe's Jones vector  $|A_2(z, \tau)\rangle$  at a distance  $\xi = 20$ . The spectrum for the two orthogonally polarized components of the probe is then

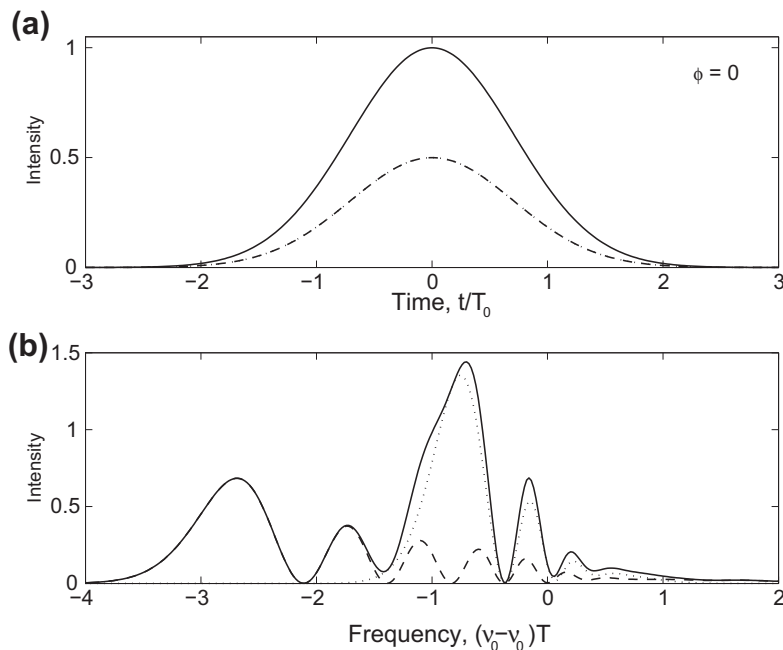


**Figure 7.11** (a) Shapes and (b) spectra at  $\xi = 20$  for the  $x$  (dashed curve) and  $y$  (dotted curve) components of the probe pulse, linearly polarized with  $\theta = 45^\circ$ , when the pump pulse is polarized along the  $x$  axis ( $\phi = 0$ ). Total intensity is shown by the solid line.

obtained by taking the Fourier transform. Figure 7.12 shows the (a) probe shapes and (b) spectra for the  $x$  (solid curve) and  $y$  (dashed curve) components under conditions identical to those of Figure 7.11 except that the pump pulse is polarized elliptically rather than linearly. A comparison of Figures 7.11b and 7.12b gives an idea how much probe spectrum can change with a relatively small change in the pump SOP. The spectral asymmetry seen in these figures is a direct consequence of the walk-off effects resulting from the group-velocity mismatch.

The most dramatic changes occur in the temporal shape of the probe when the pump is elliptically polarized. In contrast with the case of a linearly polarized pump pulse, the temporal profiles for the  $x$ - and  $y$ -polarized probe components become different and develop considerable internal structure, even though the total power remains unchanged as long as GVD effects are negligible. In Figure 7.12a pulse shapes for the two polarization components exhibit a multipeak structure such that the total power at any time adds up to the input value. The physical origin of this behavior is related to the XPM-induced changes in the SOP of the pump pulse. As the pump SOP evolves, the probe SOP changes in a complex manner, as seen in Figure 7.10. The temporal structure seen in Figure 7.12a stems from this complex polarization behavior.

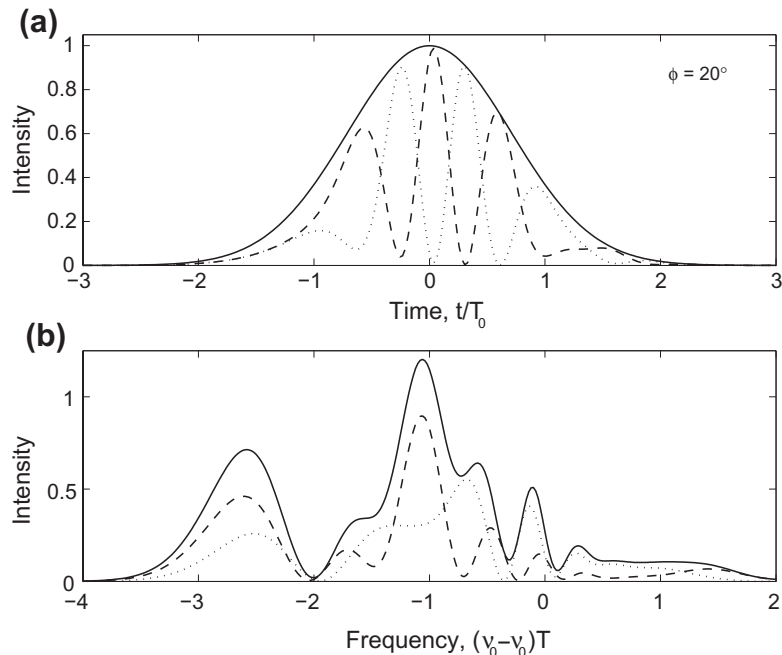


Figure 7.12 (a) Shapes and (b) spectra at  $\xi=20$  for the  $x$  (dashed curve) and  $y$  (dotted curve) components of the probe pulse, linearly polarized with  $\theta=45^\circ$ , when the pump pulse is elliptically polarized ( $\phi=20^\circ$ ). Total intensity is shown by the solid line.

#### 7.6.4 Pulse Trapping and Compression

The preceding discussion of the polarization effects ignores the GVD effects and is valid if the fiber is much shorter than the dispersion length. In this section we relax this restriction and focus on the polarization-dependent temporal effects. In the presence of GVD, we should retain the second-derivative term in Eqs (7.6.5) and (7.6.6). If we consider again the pump–probe configuration and ignore the nonlinear effects induced by the weak probe, Eqs (7.6.7) and (7.6.8) contain an extra term and take the form [107]

$$\frac{\partial|A_1\rangle}{\partial\xi} + \mu\frac{\partial|A_1\rangle}{\partial\tau} + \frac{i\beta_{21}L_{\text{NL}}}{2T_0^2}\frac{\partial^2|A_1\rangle}{\partial\tau^2} = \frac{i}{3}(3h_p - \mathbf{p}_3 \cdot \boldsymbol{\sigma})|A_1\rangle, \quad (7.6.18)$$

$$\frac{\partial|A_2\rangle}{\partial\xi} + \frac{i\beta_{22}L_{\text{NL}}}{2T_0^2}\frac{\partial^2|A_1\rangle}{\partial\tau^2} = \frac{2i\omega_2}{3\omega_1}[2h_p + (\mathbf{p} - \mathbf{p}_3) \cdot \boldsymbol{\sigma}]|A_2\rangle, \quad (7.6.19)$$

where  $h_p(\xi, \tau) = \langle A_1(\xi, \tau)|A_1(\xi, \tau)\rangle/P_0$  is the temporal profile of the pump pulse normalized to 1 at the pulse center at  $\xi = 0$ . One can introduce two dispersion lengths as  $L_{dj} = T_0^2/|\beta_{2j}|(j = 1, 2)$ . In the following discussion, we assume for simplicity that  $L_{d1} = L_{d2} \equiv L_d$ . This may be the case for a dispersion-flattened fiber, or

when the pump and probe wavelengths do not differ by more than a few nanometers. The two vector NLS equations can be solved numerically with the split-step Fourier method. Note that this amounts to solving four coupled NLS equations.

Similar to the scalar case studied in Section 7.4, three length scales—nonlinear length  $L_{NL}$ , walk-off length  $L_w$ , and dispersion length  $L_D$ —govern the interplay between the dispersive and nonlinear effects. The temporal evolution of the probe pulse depends considerably on whether the GVD is normal or anomalous. Consider first the anomalous-dispersion case. [Figure 7.13](#) shows an example of probe evolution over a length  $L = 50L_{NL}$  when both the pump and probe pulses are initially Gaussian, have the same width, and are linearly polarized at a  $45^\circ$  angle. The dispersion and walk-off lengths are chosen such that  $L_D = 5L_{NL}$  and  $L_w = 10L_{NL}$ , respectively. Since  $N^2 = L_D/L_{NL} = 5$ , the pump pulse evolves toward a second-order soliton. As seen in [Figure 7.14](#), the pump pulse is compressed considerably at  $\xi = 50$  and has a shape expected for a second-order soliton. It also shifts toward right because of the group-velocity mismatch between the pump and probe.

The probe pulse would disperse completely in the absence of the XPM effects because of its low peak power. However, as seen in [Figure 7.13](#), its  $x$  component, which is copolarized with the pump pulse and experiences XPM-induced chirp, shifts with the pump pulse and travels at the same speed as the pump pulse. This feature is similar to the phenomenon of soliton trapping discussed in Section 6.5.2 in

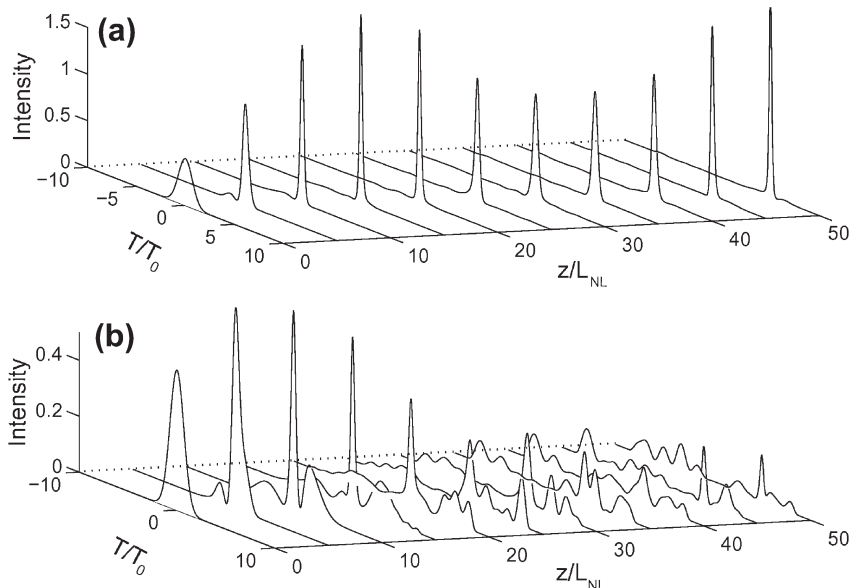


**Figure 7.13 Evolution of (a) copolarized and (b) orthogonally polarized components of a probe pulse polarized at  $45^\circ$  with respect to a pump pulse polarized linearly along the  $x$  axis.**

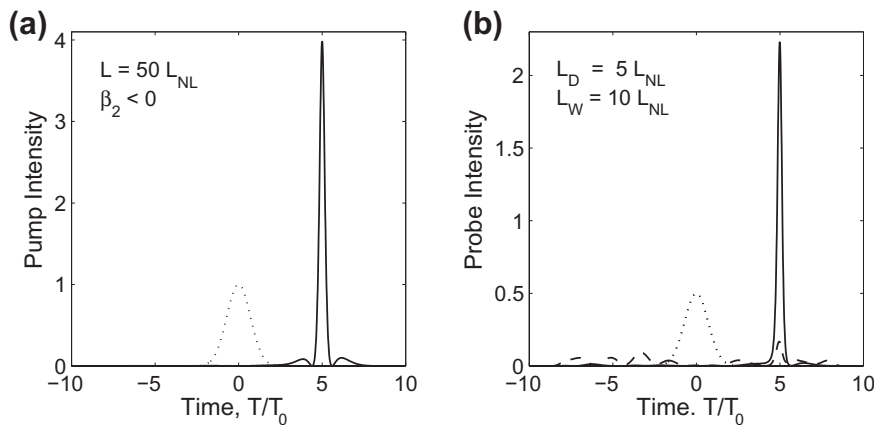


**Figure 7.14** Temporal shapes of (a) pump and (b) probe pulses at  $\xi=0$  (dotted curves) and  $\xi=50$  for the  $x$  (solid curves) and  $y$  (dashed curve) components. The pump pulse is linearly polarized along the  $x$  axis ( $\phi=0$ ) while the probe is oriented at  $45^\circ$  with respect to it.

the context of high-birefringence fibers. The pump pulse traps the copolarized component and the two move together because of XPM coupling between the two. The XPM also compresses the probe pulse. This feature is seen more clearly in Figure 7.14, where the copolarized component of the probe appears to be compressed even more than the pump pulse, and the two occupy nearly the same position because of soliton trapping. The enhanced compression of the probe is related to the fact that the XPM-induced chirp is larger by a factor of two when the pump and probe are copolarized. The  $y$  component of the probe pulse (dashed curve), in contrast, disperses completely as it is not trapped by the orthogonally polarized pump pulse.

If the pump pulse is elliptically polarized, both the  $x$  and  $y$  components of the probe would experience XPM-induced chirp, but the amount of this chirp would depend on the ellipticity angle. Figure 7.15 shows, as an example, the case in which the pump pulse is elliptically polarized with  $\phi = 20^\circ$ . All other parameters remain identical to those used for Figure 7.13. As expected, both components of the probe pulse are now trapped by the pump pulse, and both of them move with the pump pulse, while also getting compressed. The two probe components also exhibit a kind of periodic power transfer between them. This behavior is related to the complicated polarization evolution of the probe pulse occurring when the pump pulse is elliptically polarized (see Figure 7.10).

### 7.6.5 XPM-Induced Wave Breaking

The situation is quite different in the case of normal dispersion because the pump pulse then cannot evolve toward a soliton. However, interesting temporal effects still occur if the three length scales are chosen such that  $L_{NL} \ll L_W \ll L_D$ . Under such conditions, a relatively weak dispersion can lead to XPM-induced optical wave

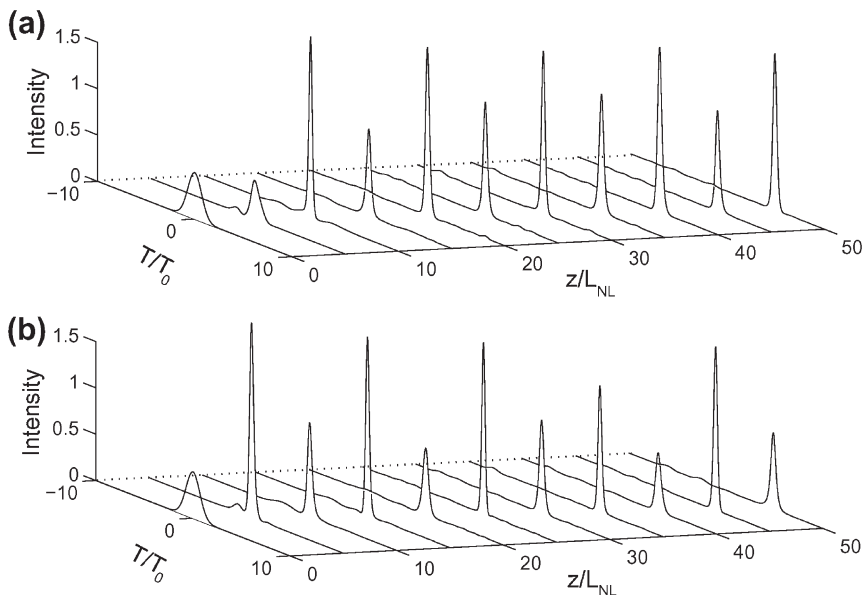


**Figure 7.15** Temporal evolution of (a) copolarized and (b) orthogonally polarized components of the probe pulse when the pump pulse is elliptically polarized with  $\phi = 20^\circ$ . All other parameters are identical to those used for Figure 7.13.

breaking, a phenomenon discussed in Section 4.2.3 in the context of self-phase modulation (SPM). Similar to the XPM case, XPM-induced wave breaking forces the probe pulse to break up into multiple parts, but in an asymmetric fashion.

Figure 7.16 shows XPM-induced wave breaking when under conditions identical to those used for Figure 7.13 except that the GVD is normal and its strength is reduced such that  $L_D = 100L_{NL}$ . As a result, the parameter  $N \equiv (L_D/L_{NL})^{1/2}$  is larger and has a value of 10. The temporal evolution of the  $x$  and  $y$  component of the probe pulse seen in Figure 7.16 exhibits different features, and both pulses evolve in an asymmetric fashion. The asymmetry is related to the walk-off effects governed by the walk-off length ( $L_w = 10L_{NL}$ ). Physically speaking, the leading edge of the probe pulse experiences the maximum XPM-induced chirp because the pump and probe pulses overlap initially. As the pump pulse walks off and separates from the probe pulse, it is also considerably broadened. As a result, the XPM-induced chirp is much reduced near the trailing edge. For this reason, an oscillatory structure only develops near the leading or trailing edge of the probe pulse, depending on how the pump walks away from the probe pulse.

The details of wave breaking are quite different for the two polarization components of the probe in Figure 7.16. In the case of a linearly polarized pump, the copolarized component of the probe develops much more oscillatory structure than the orthogonally polarized one because the XPM-induced chirp and spectral broadening

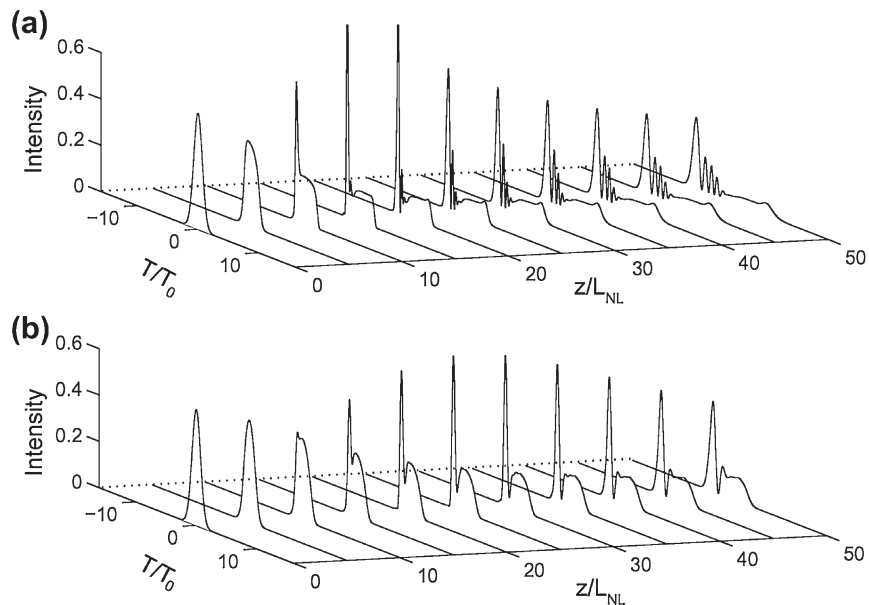


**Figure 7.16** Temporal evolution of (a) copolarized and (b) orthogonally polarized components of the probe pulse polarized at  $45^\circ$  with respect to a pump pulse that is linearly polarized along the  $x$  axis. Both pulses propagate in the normal-dispersion regime.

is larger for the former. This feature can be verified experimentally by placing a polarizer before the photodetector and noticing that the oscillatory structure changes as the polarizer is rotated. When the pump pulse is elliptically polarized, the polarization dependence of the probe is reduced as both components have some pump power in the same state of polarization. In particular, when  $\phi = 45^\circ$ , the two probe components would evolve in a nearly identical fashion.

## 7.7 XPM EFFECTS IN BIREFRINGENT FIBERS

In a birefringent fiber, the orthogonally polarized components of each wave propagate with different propagation constants because of a slight difference in their effective mode indices. In addition, these two components are coupled through XPM, resulting in nonlinear birefringence [106–114]. In this section we incorporate the effects of linear birefringence in the Jones-matrix formalism developed in the preceding section.

### 7.7.1 Fibers with Low Birefringence

The induced nonlinear polarization can still be written in the form of Eq. (7.6.3) but Eq. (7.6.4) for the optical field  $\mathbf{E}_j$  should be modified as

$$\mathbf{E}_j(\mathbf{r}, t) = F_j(x, y)[\hat{x}A_{jx}\exp(i\beta_{jx}z) + \hat{y}A_{jy}\exp(i\beta_{jy}z)], \quad (7.7.1)$$

where  $\beta_{jx}$  and  $\beta_{jy}$  are the propagation constants for the two orthogonally polarized components of the optical field with the carrier frequency  $\omega_j$ . It is useful to write Eq. (7.7.1) in the form

$$\mathbf{E}_j(\mathbf{r}, t) = F_j(x, y)[\hat{x}A_{jx} \exp(i\delta\beta_j z/2) + \hat{y}A_{jy} \exp(-i\delta\beta_j z/2)] \exp(i\bar{\beta}_j z), \quad (7.7.2)$$

where  $\bar{\beta}_j = \frac{1}{2}(\beta_{jx} + \beta_{jy})$  is the average value of the propagation constants and  $\delta\beta_j$  is their difference. One can now introduce the Jones vector  $|A_j\rangle$  and write Eq. (7.7.2) in the form of Eq. (7.6.4), provided  $|A_j\rangle$  is defined as

$$|A_j\rangle = \begin{pmatrix} A_{jx} \exp(i\delta\beta_j z/2) \\ A_{jy} \exp(-i\delta\beta_j z/2) \end{pmatrix}. \quad (7.7.3)$$

At this point, we can follow the method outlined in Section 7.1.2 to obtain the coupled vector NLS equations. It is important to keep in mind that  $\delta\beta_j(\omega)$  itself is frequency dependent and it should be expanded in a Taylor series together with  $\bar{\beta}_j(\omega)$ . However, it is sufficient in practice to approximate it as

$$\delta\beta_j(\omega) \approx \delta\beta_{j0} + \delta\beta_{j1}(\omega - \omega_j), \quad (7.7.4)$$

where  $\delta\beta_{j1}$  is evaluated at the carrier frequency  $\omega_j$ . The  $\delta\beta_{j1}$  term is responsible for different group velocities of the orthogonally polarized components. It should be retained for fibers with high birefringence but can be neglected when linear birefringence is relatively small. We assume that to be the case in this subsection.

The final set of coupled NLS equations for low-birefringence fibers is identical to those given in Eqs (7.6.5) and (7.6.6) but contains an additional birefringence term on the right side of the form  $B_j = \frac{1}{2}\delta\beta_{j0}\sigma_1|A_j\rangle$ , where  $j = 1$  or 2. The Pauli matrix  $\sigma_1$  takes into account the different phase shifts acquired by the  $x$  and  $y$  components of an optical field in a birefringent fiber. It is useful to write the birefringence term as

$$B_j = \frac{1}{2}i\omega_j b\sigma_1|A_j\rangle, \quad (7.7.5)$$

where  $b = (\bar{n}_x - \bar{n}_y)/c$  is a measure of the modal birefringence of the fiber. As discussed in Section 6.6,  $b$  varies randomly in most fibers because of unintentional random variations in the core shape and size along the fiber length. Moreover, the principal axes of the fiber also rotate in a random fashion on a length scale  $\sim 10$  m. Such random variations can be included by replacing the matrix  $b\sigma_1$  in Eq. (7.7.5) with  $\mathbf{b} \cdot \boldsymbol{\sigma}$ , where  $\boldsymbol{\sigma}$  is the Pauli spin vector and  $\mathbf{b}$  is a random vector in the Stokes space. It is common to model  $\mathbf{b}$  as a three-dimensional Markovian process whose first and second-order moments are given by

$$\overline{\mathbf{b}(z)} = 0, \quad \overline{\mathbf{b}(z)\mathbf{b}(z')} = \frac{1}{3}D_p^2\mathcal{I}\delta(z - z'), \quad (7.7.6)$$

where  $D_p$  is the PMD parameter of the fiber and  $\mathcal{I}$  is the identity matrix.

An important question is how the PMD affects the XPM coupling between two waves copropagating simultaneously inside a fiber. To answer this question, it is

useful to consider a pump–probe configuration and neglect the nonlinear effects induced by the probe but retain those induced by the pump. Working in a reference frame in which the probe pulse is stationary, and neglecting the  $\beta_2$  terms, Eqs (7.6.5) and (7.6.6) lead to Eqs (7.6.7) and (7.6.8) but with an additional birefringence term on the right side. These modified equations can be written as [108]

$$\frac{\partial|A_1\rangle}{\partial z} + \frac{1}{L_W} \frac{\partial|A_1\rangle}{\partial \tau} = \frac{i\omega_1}{2} \mathbf{b} \cdot \boldsymbol{\sigma}|A_1\rangle + \frac{i\gamma_1}{3} (2\langle A_1|A_1\rangle + |A_1^*\rangle\langle A_1^*|)|A_1\rangle \quad (7.7.7)$$

$$\frac{\partial|A_2\rangle}{\partial z} = \frac{i\omega_2}{2} \mathbf{b} \cdot \boldsymbol{\sigma}|A_2\rangle + \frac{2i\gamma_2}{3} (\langle A_1|A_1\rangle + |A_1\rangle\langle A_1 + |A_1^*\rangle\langle A_1^*|)|A_2\rangle. \quad (7.7.8)$$

The preceding coupled NLS equations are stochastic in nature because of the random nature of the birefringence vector  $\mathbf{b}$ . To simplify them, we note that, even though fluctuating residual birefringence of the fiber randomizes the SOP of both the pump and probe, it is only their relative orientation that affects the XPM process. Since randomization of the pump and probe SOPs occurs over a length scale (related to the birefringence correlation length) much shorter than a typical nonlinear length, one can average over rapid random SOP variations by adopting a rotating frame in which the pump SOP remains fixed. Following the averaging procedure discussed in Section 6.6.2 and Ref. [110], we obtain

$$\frac{\partial|A_1\rangle}{\partial z} + \frac{1}{L_W} \frac{\partial|A_1\rangle}{\partial \tau} = i\gamma_e P_1|A_1\rangle, \quad (7.7.9)$$

$$\frac{\partial|A_2\rangle}{\partial z} + \frac{i}{2}\Omega \mathbf{b}' \cdot \boldsymbol{\sigma}|A_2\rangle = \frac{i\omega_2}{2\omega_1} \gamma_e P_1 (3 + \hat{p} \cdot \boldsymbol{\sigma})|A_2\rangle, \quad (7.7.10)$$

where  $\Omega = \omega_1 - \omega_2$  is the pump–probe frequency difference,  $P_1 = \langle A_1|A_1\rangle$  is the pump power and  $\hat{p} = \langle A_1|\boldsymbol{\sigma}|A_1\rangle/P_1$  is the Stokes vector representing the pump SOP on the Poincaré sphere. The effective nonlinear parameter,  $\gamma_e = 8\gamma/9$ , is reduced by a factor of 8/9 because of the averaging over rapid variations of the pump SOP. Residual birefringence enters through the vector  $\mathbf{b}'$  that is related to  $\mathbf{b}$  by a random rotation on the Poincaré sphere. Since such rotations leave the statistics of  $\mathbf{b}$  unchanged, we drop the prime over  $\mathbf{b}'$  in what follows.

The pump Eq. (7.7.9) can be easily solved. The solution shows that the pump pulse shifts in time as its walks away from the probe pulse but its shape does not change, i.e.,  $P_1(z, \tau) = P_1(0, \tau - z/L_W)$ . The total probe power also does not change as it is easy to show from Eq. (7.7.10) that the probe power  $P_2 = \langle A_2|A_2\rangle$  satisfies  $\partial P_2/\partial z = 0$ . However, the orthogonally polarized components of the probe pulse can exhibit complicated dynamics as its state of polarization evolves because of XPM. It is useful to introduce the normalized Stokes vectors for the pump and probe as

$$\hat{p} = \langle A_1|\boldsymbol{\sigma}|A_1\rangle/P_1, \quad \hat{s} = \langle A_2|\boldsymbol{\sigma}|A_2\rangle/P_2, \quad (7.7.11)$$

and write Eq. (7.7.10) in the Stokes space as [108]

$$\frac{\partial \hat{s}}{\partial z} = (\Omega \mathbf{b} - \gamma_e P_1 \hat{p}) \times \hat{s}. \quad (7.7.12)$$

The two terms on the right side of this equation show that the SOP of the probe rotates on the Poincaré sphere along an axis whose direction changes in a random fashion as dictated by  $\mathbf{b}$ . Moreover, the speed of rotation also changes with  $z$  randomly.

It is useful to note that Eq. (7.7.12) is isomorphic to the Bloch equation governing the motion of spin density in a solid [108]. In that context,  $P_1$  corresponds to a static magnetic field and  $\mathbf{b}$  has its origin in small magnetic fields associated with nuclei [111]. In a fashion similar to the phenomenon of spin decoherence, the probe SOP evolves along the fiber in a random fashion and leads to intrapulse depolarization, a phenomenon produced by the combination of XPM and PMD. Physically speaking, the XPM interaction between the pump and probe makes the probe SOP vary across the temporal profile of the pump. Fluctuating residual birefringence of the fiber then transfers this spatial randomness into temporal randomness of the signal polarization. The distance over which the SOPs of the pump and probe become decorrelated because of PMD is governed by the PMD diffusion length defined as  $L_{\text{diff}} = 3/(D_p \Omega)^2$ . This distance is  $< 1$  km when pump and probe are separated by 1 THz, if we use a typical value of  $D_p = 0.1 \text{ ps}/\sqrt{\text{km}}$  for the PMD parameter of the fiber.

The extent of intrapulse depolarization can be quantified by the relative orientation of the probe SOPs at two different times, or by  $\cos \psi = \hat{s}(z, \tau_1) \cdot \hat{s}(z, \tau_2)$ . As  $\cos \psi$  fluctuates along the fiber length, its average value,  $d_i$ , serves as a measure of intrapulse depolarization. In the absence of XPM and PMD,  $d_i = 1$  because  $\psi$  equals 0, and it does not fluctuate. As PMD effects begin to dominate,  $d_i$  tends toward zero. Clearly, depolarization would occur only over the region in which pump and probe overlap. As an example, Figure 7.17 shows how  $d_i$  changes across a broad probe pulse when it is launched with a Gaussian pump pulse,  $P_1(0, \tau) = P_0 \exp(-\tau^2)$ , such that  $\gamma P_0 L = \pi$ , where  $L$  is the fiber length. The PMD parameter of the fiber is such that  $L_{\text{diff}} = L_{\text{NL}}$ .

Several features of Figure 7.17 are noteworthy. In the absence of the walk-off effects,  $d_i$  decreases only in the temporal region over which probe and pump pulses overlap. As the walk-off effects increase, this region widens but, at the same time, the magnitude of  $d_i$  increases. This behavior is related to the discussion in Section 7.4.1, where the XPM-induced chirp was found to be affected by the group-velocity mismatch between the pump and probe. As the pump pulse walks away because of its different speed, it interacts with different parts of the probe, thereby enlarging the region over which  $d_i$  is reduced. However, at the same time the magnitude of the XPM-induced phase shift is reduced so that the impact of XPM is lower and  $d_i$  decreases less compared with its value realized in the absence of a walk-off.

### 7.7.2 Fibers with High Birefringence

In a high-birefringence fiber, the difference in the modal indices of the orthogonally polarized components is large enough that it becomes important to include the different group velocities associated with them. Mathematically, the  $\delta\beta_{j1}$  term appearing in Eq. (7.7.4) cannot be ignored. If we retain both terms in this equation, two additional

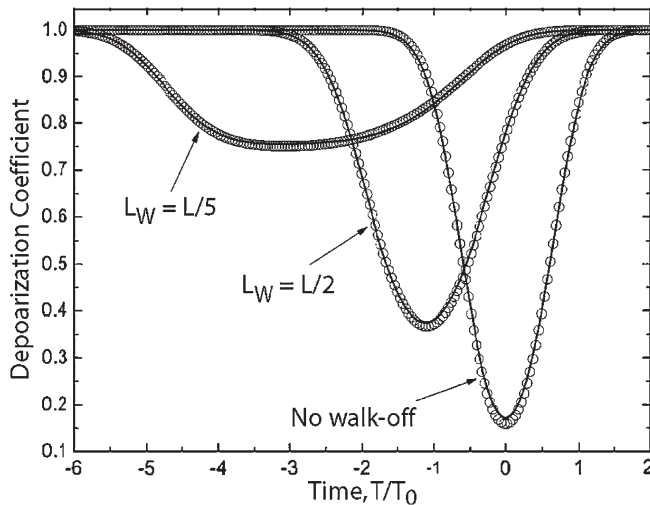


**Figure 7.17** Intrapulse depolarization  $d_i$  across the probe profile for three walk-off lengths when the probe is launched with a copolarized Gaussian pump pulse. Fiber length is such that  $\gamma P_0 L = \pi$ . (After Ref. [108]; © 2005 OSA.)

terms appear in Eqs (7.6.5) and (7.6.6). The final set of coupled vector NLS equations can be written as

$$\begin{aligned} \frac{\partial|A_1\rangle}{\partial z} + \left( \frac{1}{v_{g1}} + \frac{1}{2}\delta\beta_{11}\sigma_1 \right) \frac{\partial|A_1\rangle}{\partial t} + \frac{i\beta_{21}}{2} \frac{\partial^2|A_1\rangle}{\partial t^2} + \frac{\alpha_1}{2}|A_1\rangle &= \frac{i}{2}\delta\beta_{10}\sigma_1|A_1\rangle + \frac{i\gamma_1}{3} \\ \times (2\langle A_1|A_1\rangle + |A_1^*\rangle\langle A_1^*| + 2\langle A_2|A_2\rangle + 2|A_2\rangle\langle A_2| + 2\langle A_2^*\rangle\langle A_2^*|) &|A_1\rangle, \end{aligned} \quad (7.7.13)$$

$$\begin{aligned} \frac{\partial|A_2\rangle}{\partial z} + \left( \frac{1}{v_{g2}} + \frac{1}{2}\delta\beta_{21}\sigma_1 \right) \frac{\partial|A_2\rangle}{\partial t} + \frac{i\beta_{22}}{2} \frac{\partial^2|A_2\rangle}{\partial t^2} + \frac{\alpha_2}{2}|A_2\rangle &= \frac{i}{2}\delta\beta_{20}\sigma_1|A_2\rangle + \frac{i\gamma_2}{3} \\ \times (2\langle A_2|A_2\rangle + |A_2^*\rangle\langle A_2^*| + 2\langle A_1|A_1\rangle + 2|A_1\rangle\langle A_1| + 2|A_1^*\rangle\langle A_1^*|) &|A_2\rangle. \end{aligned} \quad (7.7.14)$$

The preceding equations are quite complicated as they include all nonlinear terms (both coherent and incoherent). However, they are considerably simplified in the case of high-birefringence fibers for which coherent-coupling terms can then be neglected as they are rarely phase-matched. If we further write Eqs (7.7.13) and (7.7.14) in terms of linearly polarized components  $A_{1x}$ ,  $A_{1y}$ ,  $A_{2x}$ , and  $A_{2y}$ , we obtain the following set of four coupled NLS equations [106]:

$$\begin{aligned} \frac{\partial A_{1p}}{\partial z} + \frac{1}{v_{g1p}} \frac{\partial A_{1p}}{\partial t} + \frac{i\beta_{21}}{2} \frac{\partial^2 A_{1p}}{\partial t^2} + \frac{\alpha_1}{2} A_{1p} &= i\gamma_1(|A_{1p}|^2 + 2|A_{2p}|^2 + B|A_{1q}|^2 + B|A_{2q}|^2) A_{1p}, \end{aligned} \quad (7.7.15)$$

$$\begin{aligned} \frac{\partial A_{2p}}{\partial z} + \frac{1}{v_{g2p}} \frac{\partial A_{2p}}{\partial t} + \frac{i\beta_{22}}{2} \frac{\partial^2 A_{2p}}{\partial t^2} + \frac{\alpha_2}{2} A_{2p} \\ = i\gamma_2 (|A_{2p}|^2 + 2|A_{1p}|^2 + B|A_{1q}|^2 + B|A_{2q}|^2) A_{2p}, \end{aligned} \quad (7.7.16)$$

where  $p = x, y$  and  $q = x, y$  such that  $p \neq q$  and  $v_{gjp}^{-1} = v_{gj}^{-1} \pm \frac{1}{2}\delta\beta_{j1}$  for  $j = 1, 2$ . The parameter  $B$  is given in Eq. (6.1.34) and equals  $2/3$  for linearly birefringent fibers. These equations reduce to Eqs (7.1.13) and (7.1.14) when both waves are polarized along a principal axis ( $A_{1y} = A_{2y} = 0$ ).

The preceding set of four coupled equations should be used to investigate the XPM-induced modulation instability when two elliptically polarized CW beams are launched into a high-birefringence fiber. The new feature is that the dispersion relation given in Eq. (7.2.6) for the scalar case becomes an eighth-degree polynomial in  $K$ . If one of the beams is polarized along a principal axis of the fiber, the dispersion relation reduces to a sixth-degree polynomial in  $K$  [106]. The gain spectrum of XPM-induced modulation instability in this case depends on the polarization angle of the other beam. In general, the bandwidth and the peak value of the gain are reduced when the two beams are not polarized along the same axis.

Equations (7.7.15) and (7.7.16) can also be used to study whether the XPM-paired vector solitons exist in birefringent fibers. By following the method discussed in Section 7.3, one finds that such soliton solutions indeed exist [106]. Depending on the parameter values, birefringent fibers can support a pair of bright vector solitons or a pair composed of one dark and one bright vector soliton. The XPM interaction of two elliptically polarized beams appears to have a rich variety of interesting features.

Practical applications of fibers for optical signal processing often require that the device operation be insensitive to the SOP of the incoming signal [112–114]. In one approach, twisted fibers with circular birefringence are employed [112]. In another, polarization independence is realized even in a linearly birefringent fiber using a suitable design [113]. In highly birefringent fibers, polarization-independent XPM can also be realized by optimizing the wavelength separation between the pump and the signal [114].

## PROBLEMS

- 7.1 Derive an expression for the nonlinear part of the refractive index when two optical beams of different wavelengths but identical polarizations are propagating inside an optical fiber.
- 7.2 Derive the dispersion relation (7.2.6) for XPM-induced modulation instability starting from Eqs (7.1.13) and (7.1.14). Under what conditions can modulation instability occur in the normal-GVD regime of a fiber?
- 7.3 Write a computer program in MATLAB (or any other programming language) and reproduce the gain curves shown in Figure 7.1.
- 7.4 Verify that the pair of bright and dark solitons given by Eqs (7.3.1) and (7.3.2) indeed satisfies the coupled NLS equations.

- 7.5** Solve Eqs (7.4.1) and (7.4.2) analytically after neglecting the GVD terms with second derivatives.
- 7.6** Starting from the solution given in Eq. (7.4.5), derive an expression for the XPM-induced phase shift imposed on a probe pulse by a copropagating pump pulse. Assume that the two pulses have “sech” shape, the same width, and are launched simultaneously.
- 7.7** Use the result obtained in the preceding problem to calculate the frequency chirp imposed on the probe pulse. Plot the chirp profile when the pump pulse is 10 ps wide and is launched into a 1-km-long fiber with 10-W peak power. Assume  $\gamma = 2 \text{ W}^{-1}/\text{km}$  for the probe and  $d = 0.1 \text{ ps/m}$ .
- 7.8** Make a figure similar to Figure 7.3 using the same parameter values but assume that both pulses have “sech” shapes.
- 7.9** Explain why XPM produces a shift in the wavelength of a  $0.53\text{-}\mu\text{m}$  probe pulse when a  $1.06\text{-}\mu\text{m}$  pump pulse is launched with it simultaneously (no initial time delay). Can you predict the sign of a wavelength shift for standard optical fibers?
- 7.10** Write a computer program using the split-step Fourier method and solve Eqs (7.4.18) and (7.4.19) numerically. Reproduce the results shown in Figure 7.5.
- 7.11** Use the program developed for the preceding problem to study XPM-induced pulse compression. Reproduce the results shown in Figure 7.8.
- 7.12** Use the third-order instantaneous nonlinear response of silica fibers and derive Eq. (7.6.3) when the total optical field is of the form given in Eq. (7.6.1).
- 7.13** Derive the vector form of the nonlinear coupled equations given in Eqs (7.6.5) and (7.6.6) using Eqs (7.6.3) and (7.6.4).
- 7.14** Write a computer program (using MATLAB or other software) and solve Eqs (7.6.7) and (7.6.8) numerically. Use it to reproduce the results shown in Figures 7.10 and 7.11.
- 7.15** Write a computer program (using MATLAB or other software) and solve Eqs (7.6.18) and (7.6.19) numerically. Use it to reproduce the results shown in Figs. 7.13 and 7.14.
- 7.16** Derive the dispersion relation for XPM-induced modulation instability starting from Eqs (7.7.15) and (7.7.16). Assume that one of the CW beams is polarized along the slow axis while the other beam is linearly polarization at an angle  $\theta$  from that axis.
- 7.17** Use the dispersion relation obtained in the preceding problem to plot the gain spectra of modulation instability for several values of the polarization angle ( $\theta$  equals 0, 20, 45, 70, and  $90^\circ$ ). Discuss your results physically.

---

## REFERENCES

- [1] S. A. Akhmanov, R. V. Khokhlov, and A. P. Sukhorukov, in *Laser Handbook*, Vol. 2, F. T. Arecchi and E. O. Schulz-Dubois, Eds. (North-Holland, 1972), Chaps. E3.
- [2] J. I. Gersten, R. R. Alfano, and M. Belic, *Phys. Rev. A* **21**, 1222 (1980).

- [3] A. R. Chraplyvy and J. Stone, *Electron. Lett.* **20**, 996 (1984).
- [4] R. R. Alfano, Q. X. Li, T. Jimbo, J. T. Manassah, and P. P. Ho, *Opt. Lett.* **14**, 626 (1986).
- [5] M. N. Islam, L. F. Mollenauer, R. H. Stolen, J. R. Simpson, and H. T. Shang, *Opt. Lett.* **12**, 625 (1987).
- [6] R. R. Alfano, P. L. Baldeck, F. Raccah, and P. P. Ho, *Appl. Opt.* **26**, 3491 (1987).
- [7] D. Schadt and B. Jaskorzynska, *Electron. Lett.* **23**, 1090 (1987); *J. Opt. Soc. Am. B* **4**, 856 (1987); *J. Opt. Soc. Am. B* **5**, 2374 (1988).
- [8] B. Jaskorzynska and D. Schadt, *IEEE J. Quantum Electron.* **24**, 2117 (1988).
- [9] R. R. Alfano and P. P. Ho, *IEEE J. Quantum Electron.* **24**, 351 (1988).
- [10] R. R. Alfano, Ed., *The Supercontinuum Laser Source*, 2nd ed. (Springer, 2006).
- [11] G. P. Agrawal, *Phys. Rev. Lett.* **59**, 880 (1987).
- [12] G. P. Agrawal, P. L. Baldeck, and R. R. Alfano, *Phys. Rev. A* **39**, 3406 (1989).
- [13] C. J. McKinstry and R. Bingham, *Phys. Fluids B* **1**, 230 (1989).
- [14] C. J. McKinstry and G. G. Luther, *Physica Scripta* **30**, 31 (1990).
- [15] W. Huang and J. Hong, *J. Lightwave Technol.* **10**, 156 (1992).
- [16] J. E. Rothenberg, *Phys. Rev. Lett.* **64**, 813 (1990).
- [17] G. P. Agrawal, *Phys. Rev. Lett.* **64**, 814 (1990).
- [18] M. Yu, C. J. McKinstry, and G. P. Agrawal, *Phys. Rev. E* **48**, 2178 (1993).
- [19] I. O. Zolotovskii and D. I. Sementsov, *Opt. Spectroscopy* **96**, 789 (2004).
- [20] S. M. Zhang, F. Y. Lu, W. C. Xu, and J. Wang, *Opt. Fiber Technol.* **11**, 193 (2005).
- [21] A. S. Gouveia-Neto, M. E. Faldon, A. S. B. Sombra, P. G. J. Wigley, and J. R. Taylor, *Opt. Lett.* **13**, 901 (1988).
- [22] E. J. Greer, D. M. Patrick, P. G. J. Wigley, and J. R. Taylor, *Electron. Lett.* **18**, 1246 (1989); *Opt. Lett.* **15**, 851 (1990).
- [23] D. M. Patrick and A. D. Ellis, *Electron. Lett.* **29**, 1391 (1993).
- [24] Y. Inoue, *J. Phys. Soc. Jpn.* **43**, 243 (1977).
- [25] M. R. Gupta, B. K. Som, and B. Dasgupta, *J. Plasma Phys.* **25**, 499 (1981).
- [26] S. Trillo, S. Wabnitz, E. M. Wright, and G. I. Stegeman, *Opt. Lett.* **13**, 871 (1988).
- [27] V. V. Afanasjev, E. M. Dianov, A. M. Prokhorov, and V. N. Serkin, *JETP Lett.* **48**, 638 (1988).
- [28] V. V. Afanasjev, Y. S. Kivshar, V. V. Konotop, and V. N. Serkin, *Opt. Lett.* **14**, 805 (1989).
- [29] V. V. Afanasjev, E. M. Dianov, and V. N. Serkin, *IEEE J. Quantum Electron.* **25**, 2656 (1989).
- [30] M. Florjanczyk and R. Tremblay, *Phys. Lett.* **141**, 34 (1989).
- [31] L. Wang and C. C. Yang, *Opt. Lett.* **15**, 474 (1990).
- [32] V. V. Afanasjev, L. M. Kovachev, and V. N. Serkin, *Sov. Tech. Phys. Lett.* **16**, 524 (1990).
- [33] M. Lisak, A. Höök, and D. Anderson, *J. Opt. Soc. Am. B* **7**, 810 (1990).
- [34] J. T. Manassah, *Opt. Lett.* **15**, 670 (1990).
- [35] P. C. Subramaniam, *Opt. Lett.* **16**, 1560 (1991).
- [36] Y. S. Kivshar, D. Anderson, M. Lisak, and V. V. Afanasjev, *Physica Scripta* **44**, 195 (1991).
- [37] V. Y. Khasilev, *JETP Lett.* **56**, 194 (1992).
- [38] M. Wadati, T. Iizuka, and M. Hisakado, *J. Phys. Soc. Jpn.* **61**, 2241 (1992).
- [39] D. Anderson, A. Höök, M. Lisak, V. N. Serkin, and V. V. Afanasjev, *Electron. Lett.* **28**, 1797 (1992).
- [40] S. G. Dinev, A. A. Dreischuh, and S. Balushev, *Physica Scripta* **47**, 792 (1993).

- [41] A. Höök, D. Anderson, M. Lisak, V. N. Serkin, and V. V. Afanasjev, *J. Opt. Soc. Am. B* **10**, 2313 (1993).
- [42] A. Höök and V. N. Serkin, *IEEE J. Quantum Electron.* **30**, 148 (1994).
- [43] J. C. Bhakta, *Phys. Rev. E* **49**, 5731 (1994).
- [44] F. T. Hioe, *Phys. Lett. A* **234**, 351 (1997); *Phys. Rev. E* **56**, 2373 (1997); *Phys. Rev. E* **58**, 6700 (1998).
- [45] C. Yeh and L. Bergman, *Phys. Rev. E* **60**, 2306 (1999).
- [46] F. T. Hioe, *Phys. Rev. Lett.* **82**, 1152 (1999); *J. Phys. A* **36**, 7307 (2003).
- [47] K. Nakkeeran, *Phys. Rev. E* **62**, 1313 (2000).
- [48] E. A. Ostrovskaya, Y. S. Kivshar, D. Mihalache, and L. C. Crasovan, *IEEE J. Sel. Topics Quantum Electron.* **8**, 591 (2002).
- [49] S. C. Tsang, K. Nakkeeran, B. A. Malomed, and K. W. Chow, *Opt. Commun.* **249**, 117 (2005).
- [50] M. Abramowitz and I. A. Stegun, *Handbook of Mathematical Functions* (Dover, 1972), Chap. 16.
- [51] G. P. Agrawal, *Lightwave Technology: Telecommunication Systems* (Wiley, 2005), Chap. 9.
- [52] Y. S. Kivshar and G. P. Agrawal, *Optical Solitons: From Fibers to Photonic Crystals* (Academic Press, 2003), Chap. 9.
- [53] J. T. Manassah, *Appl. Opt.* **26**, 3747 (1987).
- [54] P. L. Baldeck, R. R. Alfano, and G. P. Agrawal, *Appl. Phys. Lett.* **52**, 1939 (1988).
- [55] G. P. Agrawal, P. L. Baldeck, and R. R. Alfano, *Phys. Rev. A* **39**, 5063 (1989).
- [56] T. Morioka and M. Saruwatari, *Electron. Lett.* **25**, 646 (1989).
- [57] R. R. Alfano, P. L. Baldeck, P. P. Ho, and G. P. Agrawal, *J. Opt. Soc. Am. B* **6**, 824 (1989).
- [58] M. Yamashita, K. Torizuka, T. Shiota, and T. Sato, *Jpn. J. Appl. Phys.* **29**, 294 (1990).
- [59] D. M. Patrick and A. D. Ellis, *Electron. Lett.* **29**, 1391 (1993).
- [60] A. Höök, *Opt. Lett.* **17**, 115 (1992).
- [61] S. Kumar, A. Selvarajan, and G. V. Anand, *Opt. Commun.* **102**, 329 (1993).
- [62] C. S. Aparna, S. Kumar, and A. Selvarajan, *Opt. Commun.* **131**, 267 (1996).
- [63] G. P. Agrawal, *Applications of Nonlinear Fiber Optics* (Academic Press, 2008), Chap. 6.
- [64] E. M. Dianov, P. V. Mamyshev, A. M. Prokhorov, and S. V. Chernikov, *Sov. J. Quantum Electron.* **18**, 1211 (1988).
- [65] J. T. Manassah, *Opt. Lett.* **13**, 755 (1988).
- [66] G. P. Agrawal, P. L. Baldeck, and R. R. Alfano, *Opt. Lett.* **14**, 137 (1989).
- [67] J. E. Rothenberg, *Opt. Lett.* **15**, 495 (1990).
- [68] Q. Z. Wang, P. P. Ho, and R. R. Alfano, *Opt. Lett.* **15**, 1023 (1990); *Opt. Lett.* **16**, 496 (1991).
- [69] A. D. Ellis and D. M. Patrick, *Electron. Lett.* **29**, 149 (1993).
- [70] M. Scalfardi, A. Bogoni, F. Ponzini, and L. Poti, *Opt. Commun.* **239**, 199 (2004).
- [71] M. J. La Gasse, D. Liu-Wong, J. G. Fujimoto, and H. A. Haus, *Opt. Lett.* **14**, 311 (1989).
- [72] T. Morioka and M. Saruwatari, *Opt. Eng.* **29**, 200 (1990).
- [73] K. J. Blow, N. J. Doran, B. K. Nayar, and B. P. Nelson, *Opt. Lett.* **15**, 248 (1990).
- [74] H. Vanherzeele and B. K. Nayar, *IEEE Photon. Technol. Lett.* **2**, 603 (1990).
- [75] M. Jinno and T. Matsumoto, *IEEE Photon. Technol. Lett.* **2**, 349 (1990); *Opt. Lett.* **16**, 220 (1991).
- [76] J. D. Moores, K. Bergman, H. A. Haus, and E. P. Ippen, *Opt. Lett.* **16**, 138 (1991); *J. Opt. Soc. Am. B* **8**, 594 (1991).
- [77] H. Avramopoulos, P. M. W. French, M. C. Gabriel, H. H. Houh, N. A. Whitaker, and T. Morse, *IEEE Photon. Technol. Lett.* **3**, 235 (1991).

- [78] H. Vanherzele and B. K. Nayar, *Int. J. Nonlinear Opt. Phys.* **1**, 119 (1992).
- [79] M. Jinno, *Opt. Lett.* **18**, 726 (1993).
- [80] J. E. Rothenberg, *Opt. Lett.* **18**, 796 (1993).
- [81] M. A. Franco, A. Alexandrou, and G. R. Boyer, *Pure Appl. Opt.* **4**, 451 (1995).
- [82] P. M. Ramos and C. R. Pavia, *IEEE J. Sel. Topics Quantum Electron.* **3**, 1224 (1997).
- [83] N. G. R. Broderick, D. Taverner, D. J. Richardson, and M. Ibsen, *J. Opt. Soc. Am. B* **17**, 345 (2000).
- [84] G. P. Agrawal, *Appl. Phys. Lett.* **38**, 505 (1981).
- [85] A. E. Kaplan, *Opt. Lett.* **6**, 360 (1981).
- [86] A. E. Kaplan and P. Meystre, *Opt. Commun.* **40**, 229 (1982).
- [87] G. P. Agrawal, *IEEE J. Quantum Electron.* **18**, 214 (1982).
- [88] H. Nakatsuka, S. Asaka, H. Itoh, K. Ikeda, and M. Matsuoka, *Phys. Rev. Lett.* **50**, 109 (1983).
- [89] K. Ikeda, *J. Phys.* **44**, C2-183 (1983).
- [90] K. Otsuka, *Opt. Lett.* **8**, 471 (1983).
- [91] Y. Silberberg and I. Bar-Joseph, *J. Opt. Soc. Am. B* **1**, 662 (1984).
- [92] W. J. Firth, A. Fitzgerald, and C. Paré, *J. Opt. Soc. Am. B* **7**, 1087 (1990).
- [93] C. T. Law and A. E. Kaplan, *J. Opt. Soc. Am. B* **8**, 58 (1991).
- [94] R. Vallé, *Opt. Commun.* (81), 419 (1991); *Opt. Commun.* **93**, 389 (1992).
- [95] M. Yu, C. J. McKinstry, and G. P. Agrawal, *J. Opt. Soc. Am. B* **15**, 607 (1998).
- [96] S. Ezekiel, J. L. Davis, and R. W. Hellwarth, *Opt. Lett.* **7**, 457 (1982).
- [97] R. A. Bergh, H. C. Lefevre, and H. J. Shaw, *Opt. Lett.* **7**, 282 (1982).
- [98] R. A. Bergh, B. Culshaw, C. C. Cutler, H. C. Lefevre, and H. J. Shaw, *Opt. Lett.* **7**, 563 (1982).
- [99] K. Petermann, *Opt. Lett.* **7**, 623 (1982).
- [100] N. J. Frigo, H. F. Taylor, L. Goldberg, J. F. Weller, and S. C. Rasleigh, *Opt. Lett.* **8**, 119 (1983).
- [101] B. Crosignani and A. Yariv, *J. Lightwave Technol.* **LT-3**, 914 (1985).
- [102] R. A. Bergh, H. C. Lefevre, and H. J. Shaw, *J. Lightwave Technol.* **LT-2**, 91 (1984).
- [103] G. Sagnac, *Compt. Rend. Acad. Sci.* **95**, 708 (1913).
- [104] H. M. Gibbs, *Optical Bistability: Controlling Light with Light* (Academic Press, 1985).
- [105] B. V. Vu, A. Szoke, and O. L. Landen, *Opt. Lett.* **18**, 723 (1993).
- [106] S. Kumar, A. Selvarajan, and G. V. Anand, *J. Opt. Soc. Am. B* **11**, 810 (1994).
- [107] Q. Lin and G. P. Agrawal, *IEEE J. Quantum Electron.* **40**, 958 (2004).
- [108] Q. Lin and G. P. Agrawal, *Opt. Lett.* **30**, 921 (2005).
- [109] J. N. Damask, *Polarization Optics in Telecommunications* (Springer, 2005), Chap. 2.
- [110] Q. Lin and G. P. Agrawal, *J. Opt. Soc. Am. B* **20**, 1616 (2003).
- [111] D. Awschalom, D. Loss, and N. Samarth, Eds., *Semiconductor Spintronics and Quantum Computation* (Springer, 2002).
- [112] T. Tanemura and K. Kikuchi, *J. Lightwave Technol.* **24**, 4108 (2006).
- [113] F. Yaman, Q. Lin, and G. P. Agrawal, *IEEE Photon. Technol. Lett.* **18**, 2335 (2006).
- [114] R. Salem, A. S. Lenihan, G. M. Carter, and T. E. Murphy, *IEEE J. Sel. Topics Quantum Electron.* **14**, 540 (2008).

# Stimulated Raman Scattering

# 8

Stimulated Raman scattering (SRS) is an important nonlinear process that can turn optical fibers into broadband Raman amplifiers and tunable Raman lasers. It can also severely limit the performance of multichannel lightwave systems by transferring energy from one channel to the neighboring channels. This chapter is devoted to a thorough study of SRS phenomenon in optical fibers. Section 8.1 presents the basic theory behind SRS with emphasis on the pump power required to reach the Raman threshold. SRS under continuous-wave (CW) and quasi-CW conditions is considered in Section 8.2, where we also discuss the performance of fiber-based Raman lasers and amplifiers. Ultrafast SRS occurring for pulses of 100-ps width or less is considered in Sections 8.3 and 8.4 for normal and anomalous group-velocity dispersion (GVD), respectively. In both cases, attention is paid to the walk-off effects together with those resulting from self-phase modulation (SPM) and cross-phase modulation (XPM). Section 8.5 focuses on the polarization effects.

---

## 8.1 BASIC CONCEPTS

In any molecular medium, spontaneous Raman scattering can transfer a small fraction (typically  $\sim 10^{-6}$ ) of power from one optical field to another field, whose frequency is downshifted by an amount determined by the vibrational modes of the medium. This process was discovered by Raman in 1928 and is known as the *Raman effect* [1]. It can be described quantum mechanically as conversion of a photon of energy  $\hbar\omega_p$  by a molecule to a lower-frequency photon with energy  $\hbar\omega_s$ , as the molecule makes transition to a vibrational excited state (see Figure 8.1). From a practical perspective, incident light acts as a pump and generates the frequency-shifted radiation, the so-called *Stokes wave*, that serves as a spectroscopic tool. It was observed in 1962 that, for intense pump fields, the nonlinear phenomenon of SRS can occur in which the Stokes wave grows rapidly inside the medium such that most of the pump energy is transferred to it [2]. Since then, SRS has been studied extensively in a variety of molecular media [3–7]. This section introduces the basic concepts, such as the Raman gain and the Raman threshold, and provides a theoretical framework for describing SRS in optical fibers.

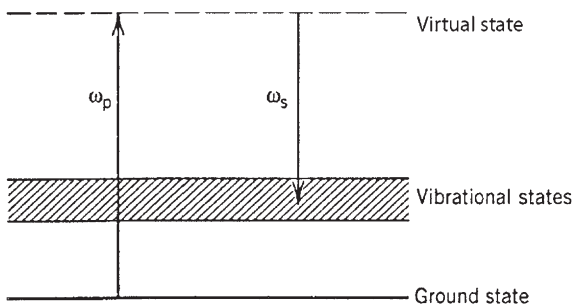


**Figure 8.1** Schematic illustration of spontaneous Raman scattering from a quantum-mechanical viewpoint. A photon of reduced energy  $\hbar\omega_s$  is created spontaneously after a pump photon of energy  $\hbar\omega_p$  excites the molecule to a virtual state (shown by a dashed line).

### 8.1.1 Raman-Gain Spectrum

In a simple approach valid under the CW and quasi-CW conditions, the initial growth of the Stokes wave is described by [7]

$$\frac{dI_s}{dz} = g_R I_p I_s, \quad (8.1.1)$$

where  $I_s$  is the Stokes intensity,  $I_p$  is the pump intensity, and the Raman-gain coefficient  $g_R$  is related to the cross section of spontaneous Raman scattering [6]. On a more fundamental level,  $g_R$  is related to the imaginary part of the third-order nonlinear susceptibility.

The Raman-gain coefficient  $g_R(\Omega)$ , where  $\Omega \equiv \omega_p - \omega_s$  represents the frequency difference between the pump and Stokes waves, is the most important quantity for describing SRS. It was measured for silica fibers in the early experiments on SRS, with refinements continuing in later years [8–14]. In general,  $g_R$  depends on the composition of the fiber core and can vary significantly with the use of different dopants. It also depends on whether the pump and Stokes are copolarized or orthogonally polarized. Figure 8.2 shows  $g_R$  for fused silica as a function of the frequency shift [12], normalized such that  $g_R \approx 1 \times 10^{-13} \text{ m/W}$  at a pump wavelength  $\lambda_p = 1 \mu\text{m}$ . For other pump wavelengths  $g_R$  scales inversely with  $\lambda_p$ . The most significant feature of the Raman gain in silica fibers is that  $g_R(\Omega)$  extends over a large frequency range (up to 40 THz) with a broad peak located near 13 THz. This behavior is due to the noncrystalline nature of silica glass. In amorphous materials such as fused silica, molecular vibrational frequencies spread out into bands that overlap and create a continuum [15]. As a result, in contrast to most molecular media for which the Raman gain occurs at specific well-defined frequencies, it extends continuously over a broad range of frequencies in the case of silica fibers. As will be seen later, optical fibers can act as broadband amplifiers because of this feature.

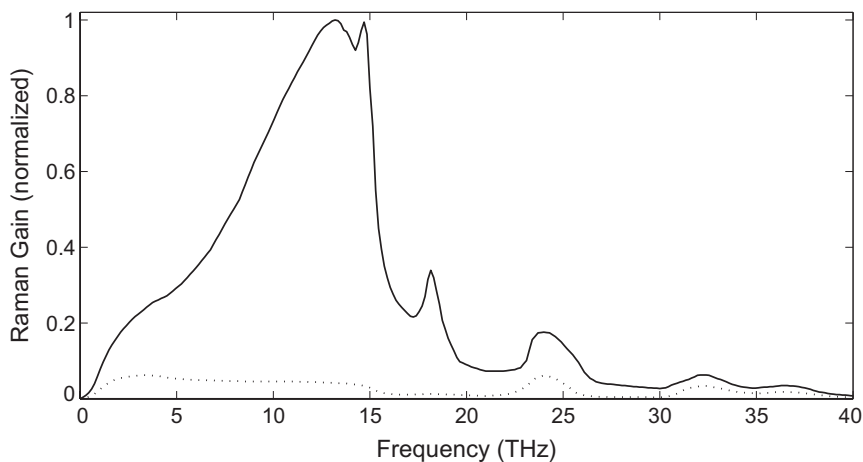


**Figure 8.2** Normalized Raman gain for fused silica when the pump and Stokes waves are copolarized (solid curve). The dotted curve shows the situation in which the pump and Stokes waves are orthogonally polarized. (Courtesy of R.H. Stolen.)

To see how the process of SRS develops, consider a CW pump beam propagating inside a fiber. If a probe beam is launched with the pump at the fiber input, it will be amplified because of the Raman gain, as long as the frequency difference  $\Omega \equiv \omega_p - \omega_s$  lies within the bandwidth of the Raman-gain spectrum. If only the pump beam is launched at the input end, spontaneous Raman scattering acts as a probe and is amplified with propagation. Because spontaneous Raman scattering generates photons within the entire bandwidth of the Raman-gain spectrum, all frequency components are amplified. However, the frequency component for which  $g_R$  is maximum builds up most rapidly. In the case of fused silica,  $g_R$  is maximum for the frequency component that is downshifted from the pump frequency by about 13.2 THz. When the pump power exceeds a threshold value, this component builds up almost exponentially [16]. As a result, SRS leads to generation of the Stokes wave whose frequency is determined by the peak of the Raman gain. The corresponding frequency shift is called the Raman shift (or the Stokes shift). The Stokes radiation is also copolarized with the pump because the Raman gain is relatively small when the two are orthogonally polarized (see Figure 8.2). For this reason, we first focus on the copolarized case.

### 8.1.2 Raman Threshold

Consider the simplest situation in which a single CW pump beam is launched into an optical fiber. Even in this case, Eq. (8.1.1) should be modified to include fiber losses before it can be used. Moreover, the pump power does not remain constant along the fiber, and we must consider the nonlinear interaction between the pump and Stokes

waves. When these effects are included, the SRS process is governed by the following set of two coupled equations:

$$\frac{dI_s}{dz} = g_R I_p I_s - \alpha_s I_s, \quad (8.1.2)$$

$$\frac{dI_p}{dz} = -\frac{\omega_p}{\omega_s} g_R I_p I_s - \alpha_p I_p, \quad (8.1.3)$$

where  $\alpha_s$  and  $\alpha_p$  account for fiber losses at the Stokes and pump frequencies, respectively. As seen in Section 8.1.3, these equations can be derived rigorously. They can also be written phenomenologically by considering the processes through which photons appear in or disappear from each beam. One can readily verify that in the absence of losses,

$$\frac{d}{dz} \left( \frac{I_s}{\omega_s} + \frac{I_p}{\omega_p} \right) = 0. \quad (8.1.4)$$

This equation merely states that the total number of photons in the pump and Stokes beams remains constant during SRS.

Although pump depletion must be included for a complete description of SRS, it can be neglected for the purpose of estimating the Raman threshold [16]. Equation (8.1.3) is readily solved if we neglect the first term on its right side that is responsible for pump depletion. If we substitute this solution in Eq. (8.1.2), we obtain

$$dI_s/dz = g_R I_0 \exp(-\alpha_p z) I_s - \alpha_s I_s, \quad (8.1.5)$$

where  $I_0$  is the incident pump intensity at  $z = 0$ . Equation (8.1.5) can be easily solved, and the result is

$$I_s(L) = I_s(0) \exp(g_R I_0 L_{\text{eff}} - \alpha_s L), \quad (8.1.6)$$

where  $L$  is the fiber length with the effective length

$$L_{\text{eff}} = [1 - \exp(-\alpha_p L)]/\alpha_p. \quad (8.1.7)$$

The solution (8.1.6) shows that, because of fiber losses, the effective fiber length is reduced from  $L$  to  $L_{\text{eff}}$ .

The use of Eq. (8.1.6) requires an input intensity  $I_s(0)$  at  $z = 0$ . In practice, SRS builds up from spontaneous Raman scattering occurring throughout the fiber length. It has been shown that this process is equivalent to injecting one fictitious photon per mode at the input end of the fiber [16]. Thus, we can calculate the Stokes power by considering amplification of each frequency component of energy  $\hbar\omega$  according to Eq. (8.1.6) and then integrating over the whole range of the Raman-gain spectrum. The result is given by

$$P_s(L) = \int_{-\infty}^{\infty} \hbar\omega \exp[g_R(\omega_p - \omega) I_0 L_{\text{eff}} - \alpha_s L] d\omega, \quad (8.1.8)$$

where the fiber is assumed to support a single mode. The frequency dependence of  $g_R$  is shown in Figure 8.2. Even though the functional form of  $g_R(\Omega)$  is not known,

the integral in Eq. (8.1.8) can be evaluated approximately using the method of steepest descent because the main contribution to the integral comes from a narrow region around the gain peak. Using  $\omega = \omega_s$ , we obtain

$$P_s(L) = P_{s0}^{\text{eff}} \exp[g_R(\Omega_R)I_0L_{\text{eff}} - \alpha_s L], \quad (8.1.9)$$

where the effective input power at  $z = 0$  is given by

$$P_{s0}^{\text{eff}} = \hbar\omega_s B_{\text{eff}}, \quad B_{\text{eff}} = \left( \frac{2\pi}{I_0 L_{\text{eff}}} \right)^{1/2} \left| \frac{\partial^2 g_R}{\partial \omega^2} \right|_{\omega=\omega_s}^{-1/2}. \quad (8.1.10)$$

Physically,  $B_{\text{eff}}$  is the effective bandwidth of the Stokes radiation centered near the gain peak at  $\Omega_R = \omega_p - \omega_s$ . Although  $B_{\text{eff}}$  depends on the pump intensity and the fiber length, the spectral width of the dominant peak in Figure 8.2 provides an order-of-magnitude estimate for it.

The Raman threshold is defined as the input pump power at which the Stokes power becomes equal to the pump power at the fiber output [16] or

$$P_s(L) = P_p(L) \equiv P_0 \exp(-\alpha_p L), \quad (8.1.11)$$

where  $P_0 = I_0 A_{\text{eff}}$  is the input pump power and  $A_{\text{eff}}$  is the effective core area as defined in Section 2.3. Using Eq. (8.1.9) in Eq. (8.1.11) and assuming  $\alpha_s \approx \alpha_p$ , the threshold condition becomes

$$P_{s0}^{\text{eff}} \exp(g_R P_0 L_{\text{eff}} / A_{\text{eff}}) = P_0, \quad (8.1.12)$$

where  $P_{s0}^{\text{eff}}$  also depends on  $P_0$  through Eq. (8.1.10). The solution of Eq. (8.1.12) provides the critical pump power required to reach the Raman threshold. Assuming a Lorentzian shape for the Raman-gain spectrum, the critical pump power, to a good approximation, is given by Smith [16]

$$\frac{g_R P_0^{\text{cr}} L_{\text{eff}}}{A_{\text{eff}}} \approx 16. \quad (8.1.13)$$

A similar analysis can be carried out for the backward SRS. The threshold condition in that case is still given by Eq. (8.1.13) but the numerical factor 16 is replaced with 20. As the threshold for forward SRS is reached first at a given pump power, backward SRS is generally not observed in optical fibers. Of course, the Raman gain can be used to amplify a backward propagating signal. Note also that the derivation of Eq. (8.1.13) assumes that the polarization of the pump and Stokes waves is maintained along the fiber. If polarization is not preserved, the Raman threshold is increased by a factor whose value lies between 1 and 2. In particular, if the polarization is completely scrambled, it increases by a factor of two.

In spite of various approximations made in the derivation of Eq. (8.1.13), it is able to predict the Raman threshold of lossy fibers quite accurately. For long fibers such that  $\alpha_p L \gg 1$ ,  $L_{\text{eff}} \approx 1/\alpha_p$ . At  $\lambda_p = 1.55 \mu\text{m}$ , a wavelength near which the fiber loss is minimum (about 0.2 dB/km),  $L_{\text{eff}} \approx 20 \text{ km}$ . If we use a typical value

$A_{\text{eff}} = 50 \mu\text{m}^2$ , the predicted Raman threshold is  $P_0^{\text{cr}} \approx 600 \text{ mW}$ . Clearly, SRS is not likely to occur in an isolated channel of an optical communication system because power levels are typically below 10 mW. However, SRS becomes a limiting factor for multichannel systems because of the Raman-induced power transfer among channels.

In practice, SRS is observed using high-power lasers. Typically,  $A_{\text{eff}}$  is in the range of  $20\text{--}80 \mu\text{m}^2$  in single-mode fibers depending on the operating wavelength. If we use  $A_{\text{eff}} = 50 \mu\text{m}^2$  as a representative value, Eq. (8.1.13) yields  $P_0^{\text{cr}} \approx 8 \text{ W}$  for a 1-km-long fiber at a pump wavelength near  $1 \mu\text{m}$ . As such power levels are readily available (from Nd:YAG lasers, for example), SRS can be easily observed using CW or pulsed lasers.

The simple theory of this section cannot explain the growth of the Stokes wave beyond the Raman threshold as it neglects pump depletion. Equations (8.1.2) and (8.1.3) should be solved to include the effect of pump depletion. As discussed later in Section 8.2.3, these equations can be solved analytically in the specific case  $\alpha_s = \alpha_p$  [17]. The results show that the threshold condition (8.1.13) remains fairly accurate. Once the Raman threshold is reached, the power is transferred from the pump to the Stokes rapidly. The theory predicts a complete transfer of pump power to the Stokes (except for fiber losses). In practice, however, the Stokes wave serves as a pump to generate a second-order Stokes wave if its power becomes large enough to satisfy Eq. (8.1.13). This process of cascaded SRS can generate multiple Stokes bands whose numbers depend on the input pump power.

### 8.1.3 Coupled Amplitude Equations

The CW theory of SRS needs modification when optical pulses are used for pumping. This is often the case for optical fibers. In fact, in the case of CW pumping, stimulated Brillouin scattering (SBS) dominates and inhibits SRS because of its lower threshold (see Chapter 9). However, SBS can be nearly suppressed by using pump pulses of widths  $< 1 \text{ ns}$ . Each pump pulse then generates a Stokes (or Raman) pulse if the SRS threshold is reached. Similar to the CW case, the carrier frequency  $\omega_s$  of the Raman pulse is downshifted from that of the pump by the Stokes shift of about  $13 \text{ THz}$ .

A full dynamical description of SRS generally requires an equation of motion describing molecular vibrations [7]. However, it is considerably simplified if the medium can be assumed to respond instantaneously [18]. This assumption is justified for optical fibers because the broad gain spectrum of Figure 8.2 implies a Raman response time of well below  $100 \text{ fs}$ . Except for ultrashort pump pulses (widths  $\sim 10 \text{ fs}$ ), the Raman response time is generally much smaller than typical pulse widths. The mutual interaction between the Raman and pump pulses is then governed by a set of two coupled amplitude equations obtained such that they include the effects of Raman gain, pump depletion, SPM, XPM, and GVD. These equations can be derived following the approach discussed in Section 2.3.

A unified description should include nonlinear response function  $R(t)$  given in Eq. (2.3.38) so that both the Kerr and Raman effects are included simultaneously

[19–23]. The analysis is somewhat complicated because the electrical field  $\mathbf{E}(\mathbf{r}, t)$  in Eq. (2.3.33) is of the form

$$\mathbf{E}(\mathbf{r}, t) = \frac{1}{2} \hat{x} \left\{ A_p \exp[i(\beta_{0p} z - \omega_p t)] + A_s \exp[i(\beta_{0s} z - \omega_s t)] \right\} + \text{c. c.}, \quad (8.1.14)$$

where  $\beta_{0p}$  and  $\beta_{0s}$  are the propagation constants at the pump and Stokes frequencies, respectively, and  $A_p$  and  $A_s$  are the slowly varying envelopes associated with the pump and Raman pulses. After considerable algebra, one can derive the following set of two equations [23]:

$$\frac{\partial A_p}{\partial z} + \frac{1}{v_{gp}} \frac{\partial A_p}{\partial t} + \frac{i\beta_{2p}}{2} \frac{\partial^2 A_p}{\partial t^2} + \frac{\alpha_p}{2} A_p = i\gamma_p (1 - f_R) (|A_p|^2 + 2|A_s|^2) A_p + R_p(z, t), \quad (8.1.15)$$

$$\frac{\partial A_s}{\partial z} + \frac{1}{v_{gs}} \frac{\partial A_s}{\partial t} + \frac{i\beta_{2s}}{2} \frac{\partial^2 A_s}{\partial t^2} + \frac{\alpha_s}{2} A_s = i\gamma_s (1 - f_R) (|A_s|^2 + 2|A_p|^2) A_s + R_s(z, t), \quad (8.1.16)$$

where  $v_{gj}$  is the group velocity,  $\beta_{2j}$  is the GVD coefficient, and  $\gamma_j$  is the nonlinear parameter as defined in Eq. (7.1.15) with  $j=p$  or  $s$ . Further, the Raman contributions,  $R_p$  and  $R_s$ , have the form

$$R_j(z, t) = i\gamma_j f_R A_j \int_{-\infty}^t h_R(t-t') \left[ |A_j(z, t')|^2 + |A_k(z, t')|^2 \right] dt' + i\gamma_j f_R A_k \times \int_{-\infty}^t h_R(t-t') A_j(z, t') A_k^*(z, t') \exp[\pm i\Omega(t-t')] dt', \quad (8.1.17)$$

where  $j, k = p$  or  $s$  such that  $j \neq k$ ,  $\Omega = \omega_p - \omega_s$  is the Stokes shift, and  $f_R$  represents the fractional Raman contribution (see Section 2.3.2). The Raman response function  $h_R(t)$  is responsible for SRS. The effects of third-order dispersion can be included adding a third-derivative term proportional to  $\beta_3$ . Spontaneous Raman scattering can also be included by adding a noise term to the preceding set of two equations [22].

In the picosecond regime in which pulse widths exceed 1 ps, Eqs (8.1.15) and (8.1.16) can be simplified considerably [23]. The reason is that  $A_p$  and  $A_s$  vary little over the time scale over which the Raman response function  $h_R(t)$  changes. Treating  $A_p$  and  $A_s$  as constants, the integrals in Eq. (8.1.17) can be performed analytically to obtain

$$R_j = i\gamma_j f_R [(|A_j|^2 + |A_k|^2) A_j + \tilde{h}_R(\pm\Omega) |A_k|^2 A_j], \quad (8.1.18)$$

where  $\tilde{h}_R$  is the Fourier transform of the  $h_R(t)$  and the negative sign is chosen for  $j = s$ . Figure 8.3 shows the real (curves symmetric around  $\Omega = 0$ ) and imaginary (asymmetric curves) parts of  $\tilde{h}_R(\Omega)$  when the pump and Stokes are polarized parallel or perpendicular to each other using the same data plotted in Figure 8.2.

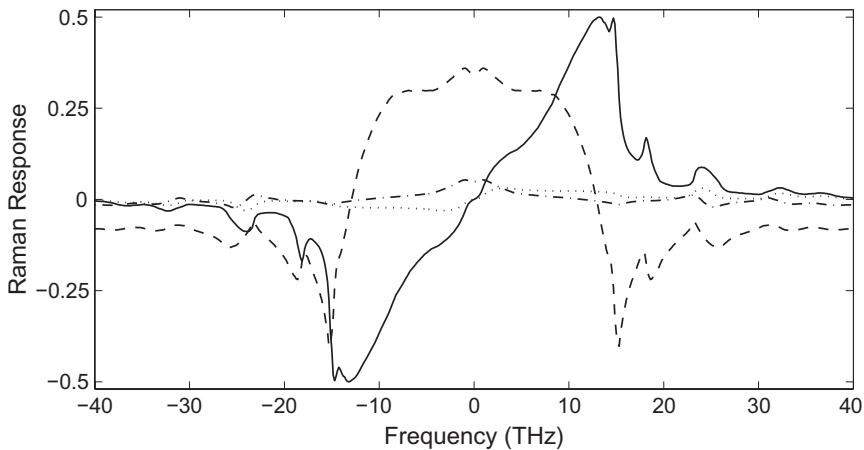


**Figure 8.3** Imaginary and real parts of  $\tilde{h}_R(\Omega)$  when the pump and Stokes are polarized parallel (solid and dashed curves) or perpendicular (dotted and dot-dashed curves) to each other.

Physically, the real part of  $\tilde{h}_R$  leads to Raman-induced index changes, while its imaginary part is related to the Raman gain. Introducing the index and gain coefficients as

$$\delta_R = f_R \operatorname{Re}[\tilde{h}_R(\Omega)], \quad g_j = 2\gamma_j f_R \operatorname{Im}[\tilde{h}_R(\Omega)], \quad (8.1.19)$$

the coupled amplitude equations become

$$\begin{aligned} \frac{\partial A_p}{\partial z} + \frac{1}{v_{gp}} \frac{\partial A_p}{\partial t} + \frac{i\beta_{2p}}{2} \frac{\partial^2 A_p}{\partial t^2} + \frac{\alpha_p}{2} A_p \\ = i\gamma_p \left[ |A_p|^2 + (2 + \delta_R - f_R) |A_s|^2 \right] A_p - \frac{g_p}{2} |A_s|^2 A_p, \end{aligned} \quad (8.1.20)$$

$$\begin{aligned} \frac{\partial A_s}{\partial z} + \frac{1}{v_{gs}} \frac{\partial A_s}{\partial t} + \frac{i\beta_{2s}}{2} \frac{\partial^2 A_s}{\partial t^2} + \frac{\alpha_s}{2} A_s \\ = i\gamma_s \left[ |A_s|^2 + (2 + \delta_R - f_R) |A_p|^2 \right] A_s + \frac{g_s}{2} |A_p|^2 A_s. \end{aligned} \quad (8.1.21)$$

Note that the XPM factor is  $2 + \delta_R - f_R$ , rather than being 2, when the Raman-induced index changes are included [20]. The parameter  $f_R$  has a value of about 0.18 [10]. Even though  $\delta_R$  is relatively small in magnitude, its frequency dependence can affect the group velocity of Stokes pulses.

Equations (8.1.20) and (8.1.21) are solved in Section 8.3 where we consider SRS with picosecond pump pulses. The most important new feature is the group-velocity mismatch that limits the SRS process to a duration during which the pump

and Raman pulses overlap. The walk-off length can be introduced as in Section 7.4 using

$$L_W = T_0 / |v_{gp}^{-1} - v_{gs}^{-1}|, \quad (8.1.22)$$

where  $T_0$  represents duration of the pump pulse. Typically  $L_W \sim 1$  m in the visible region for  $T_0 \sim 5$  ps. For pump pulses of width  $T_0 > 1$  ns,  $L_W$  exceeds 200 m and is larger than fiber lengths commonly used to observe SRS. The GVD effects are negligible for such pulses and the CW theory is approximately valid in this quasi-CW regime. In fact, Eqs (8.1.2) and (8.1.3) can be obtained from Eqs (8.1.20) and (8.1.21) if the time derivatives are neglected and  $I_j = |A_j|^2/A_{\text{eff}}$  is used ( $j = p$  or  $s$ ). Note that Eqs (8.1.20) and (8.1.21) are not valid for femtosecond pump pulses whose spectral widths exceed the Raman shift. This case is considered in Section 8.4.

### 8.1.4 Effect of Four-Wave Mixing

Four-wave mixing, a nonlinear phenomenon discussed in Chapter 10, is known to affect the SRS in any medium [6]. Its impact on the SRS process in optical fibers has been studied extensively [24–32]. This subsection describes the relevant features qualitatively.

To understand how four-wave mixing can influence SRS, it is useful to reconsider the physics behind the SRS process. As shown in Figure 8.1, Raman scattering can be thought of as down-conversion of a pump photon into a lower-frequency photon and a phonon associated with a vibrational mode of molecules. An up-conversion process in which a phonon combines with the pump photon to generate a higher-frequency photon is also possible, but occurs rarely because it requires the presence of a phonon of the right energy and momentum. The optical wave associated with higher-frequency photons is called the anti-Stokes and is generated at a frequency  $\omega_a = \omega_p + \Omega$  together with the Stokes wave of frequency  $\omega_s = \omega_p - \Omega$ , where  $\omega_p$  is the pump frequency. Because  $2\omega_p = \omega_a + \omega_s$ , four-wave mixing, a process where two pump photons annihilate themselves to produce Stokes and anti-Stokes photons, can occur provided the total momentum is conserved. The momentum-conservation requirement leads to the phase-matching condition,  $\Delta k = 2k(\omega_p) - k(\omega_a) - k(\omega_s) = 0$ , where  $k(\omega)$  is the propagation constant, that must be satisfied for FWM to occur (see Section 10.1).

The phase-matching condition is not easily satisfied in single-mode fibers for  $\Omega \sim 10$  THz. For this reason, the anti-Stokes wave is rarely observed during SRS. As discussed in Section 10.3, the phase-matching condition may be nearly satisfied when GVD is not too large. In that case, Eqs (8.1.20) and (8.1.21) should be supplemented with a third equation that describes propagation of the anti-Stokes wave and its coupling to the Stokes wave through four-wave mixing. The set of three equations can be solved approximately when pump depletion is neglected [25]. The results show that the Raman gain  $g_R$  depends on the mismatch  $\Delta k$ , and may increase or decrease from its value in Figure 8.2 depending on the value of  $\Delta k$ . In particular

$g_R$  becomes small near  $\Delta k = 0$ , indicating that four-wave mixing can suppress SRS under appropriate conditions. Partial suppression of SRS was indeed observed in an experiment [25] in which the Raman gain was reduced by a factor of 2 when the pump power  $P_0$  was large enough to make  $|\Delta k| < 3g_R P_0$ . A spectral component at the anti-Stokes frequency was also observed in the experiment. Such a FWM process is called coherent anti-Stokes Raman scattering (CARS) and is used extensively for biomedical imaging.

The effects of four-wave mixing on SRS were also observed in another experiment [27] in which the spectrum of Raman pulses was found to exhibit a double-peak structure corresponding to two peaks at 13.2 and 14.7 THz in Figure 8.2. At low pump powers, the 13.2-THz peak dominated as the Raman gain was slightly larger (by about 1%) for this peak. However, as pump power was increased, the 14.7-THz peak began to dominate the Raman-pulse spectrum. These results can be understood by noting that the Raman-gain reduction induced by four-wave mixing is frequency dependent such that the effective Raman gain becomes larger for the 14.7-THz peak for pump intensities in excess of 1 GW/cm<sup>2</sup>.

The effects of fiber birefringence have been ignored in writing Eqs (8.1.20) and (8.1.21). Their inclusion complicates the SRS analysis considerably [28]. For example, if a pump pulse is polarized at an angle with respect to a principal axis of the fiber so that it excites both the slow and fast polarization modes of the fiber, each of them can generate a Stokes pulse if its intensity exceeds the Raman threshold. These Stokes waves interact with the two pump-pulse components and with each other through XPM. To describe such an interaction, Eqs (8.1.20) and (8.1.21) must be replaced by a set of four equations that includes all nonlinear terms appropriately, as discussed in Section 7.1. The situation is even more complicated if the anti-Stokes wave is included: one must then solve a set of six coupled equations. Polarization effects are discussed later in Section 8.5.

For pump pulses propagating in the anomalous-GVD regime of optical fibers, one should consider how modulation instability and SRS influence each other. As discussed in Section 5.1, modulation instability can be thought of as a four-wave mixing process phase-matched by SPM (see Section 10.3). It generates new waves at frequencies  $\omega_p + \Omega_m$  and  $\omega_p - \Omega_m$ , where  $\Omega_m$  depends on the pump power and is generally different than the Raman shift  $\Omega$ . Thus, a unified analysis should consider five waves at frequencies  $\omega_p$ ,  $\omega_p \pm \Omega_m$ , and  $\omega_p \pm \Omega$ . Each of these five waves can have two orthogonally polarized components, resulting in a set of ten coupled-amplitude equations. The analysis becomes simpler for ultrashort pump pulses whose spectrum is so broad that the frequencies  $\Omega_m$  and  $\Omega$  fall within its bandwidth. The propagation of such pump pulses is described by a set of two coupled equations that include the effects of GVD, SPM, XPM, fiber birefringence, four-wave mixing, and intrapulse SRS. A linear stability analysis of such equations can be performed to obtain the effective gain spectrum when a CW pump beam enters an optical fiber [30].

## 8.2 QUASI-CONTINUOUS SRS

Since the initial observation of SRS in optical fibers [9], SRS has been studied extensively using pump pulses of widths in the range 1–100 ns, a situation that corresponds to the quasi-CW regime [33–49]. In the single-pass geometry, each pump pulse launched at one end of the fiber generates a Stokes pulse at the other end. In the multipass geometry, the fiber is placed inside a cavity, resulting in a tunable Raman laser. Another application consists of using SRS for signal amplification. This section discusses all three aspects of SRS in optical fibers.

### 8.2.1 Single-Pass Raman Generation

The 1972 demonstration of SRS in silica fibers was carried out in the visible region using 532-nm pulses from a frequency-doubled Nd:YAG laser [8]. About 75 W of pump power was required to generate the Stokes radiation at 545 nm in a single-mode fiber of 9-m length and 4- $\mu\text{m}$  core diameter. In later experiments, 150-ns infrared pump pulses, from a Nd:YAG laser operating at 1.06  $\mu\text{m}$ , were used to initiate SRS [34]. In one experiment, the first-order Stokes line at 1.12  $\mu\text{m}$  was observed at a pump power of 70 W [36]. Higher-order Stokes lines appeared at higher pump powers when the Stokes power became large enough to pump the next-order Stokes line. Figure 8.4 shows the optical spectrum at a pump power of about 1 kW with five Stokes lines clearly seen. Each successive Stokes line is broader than the preceding one. This broadening is due to several competing nonlinear processes and limits the total number of Stokes lines. Stokes line of up to the 15th order have been generated in the visible region [39].

In these experiments no attempt was made to resolve spectral details of each Stokes line. In a subsequent experiment [44], the resolution was fine enough to resolve the line shape of the first-order Stokes line, generated by launching in a 100-m-long fiber pump pulses of about 1-ns duration, obtained from a mode-locked argon laser ( $\lambda_p = 514.5 \text{ nm}$ ). Figure 8.5 shows the observed spectra at three pump powers. The spectra exhibit a broad peak at  $440 \text{ cm}^{-1}$  (13.2 THz) and a narrow peak at  $490 \text{ cm}^{-1}$  (14.7 THz). As pump power is increased, the peak power of the broad peak saturates while that of the narrow peak keeps increasing.

The appearance of the double-peak Stokes spectrum can be understood by noting from Figure 8.2 that the dominant peak in the Raman-gain spectrum actually consists of two peaks whose locations exactly coincide with the two peaks in the Stokes spectra of Figure 8.5. A detailed numerical model, in which the shape of the Raman-gain spectrum is included and each spectral component of the Stokes line is propagated along the fiber including both the Raman gain and spontaneous Raman scattering, predicts line shapes in agreement with the experimentally observed spectra [44].

The features seen in Figure 8.5 can be understood qualitatively as follows: spontaneous Raman scattering generates Stokes light across the entire frequency range of the Raman-gain spectrum. After a short length of fiber, these weak signals are amplified with the appropriate gain coefficients while more spontaneous light is added. At low pump powers, the observed Stokes spectrum looks like  $\exp[g_R(\Omega)]$  because

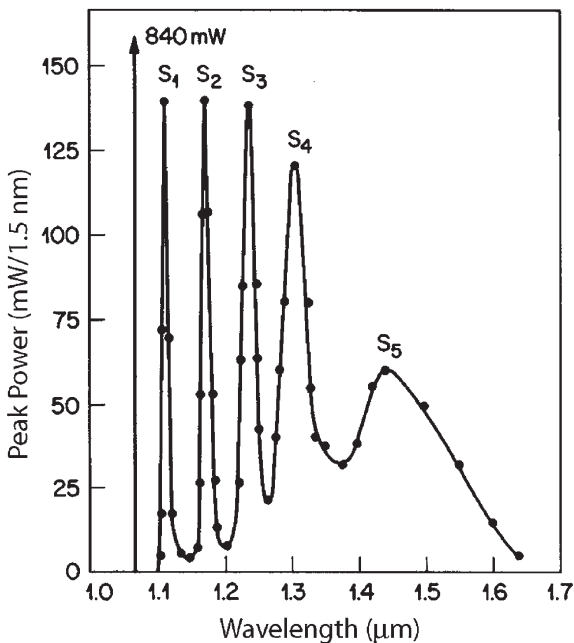


**Figure 8.4** Five Stokes lines  $S_1$  to  $S_5$  generated simultaneously using 1.06- $\mu\text{m}$  pump pulses. Vertical line corresponds to the residual pump. Powers were measured through a monochromator with 1.5-nm resolution. (After Ref. [36]; © 1978 IEEE.)

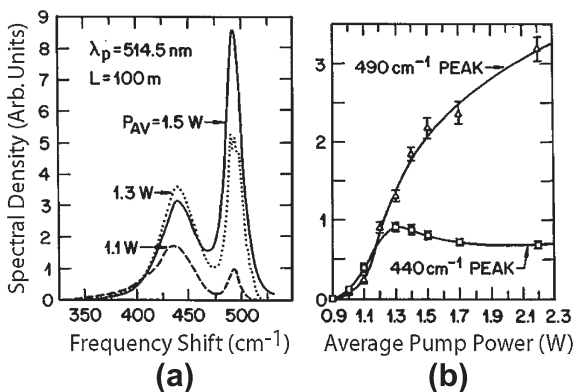


**Figure 8.5** (a) Stokes spectra at three pump powers and (b) variations of peak powers with a pump power. (After Ref. [44]; © 1984 IEEE.)

of the exponential amplification process. As pump power is increased, the high-frequency peak at  $440 \text{ cm}^{-1}$  can pump the low-frequency peak at  $490 \text{ cm}^{-1}$  through the Raman-amplification process. This is precisely what is seen in Figure 8.5.

Eventually, the Stokes power becomes high enough to generate a second-order Stokes line. Even though this model is based on the CW theory of SRS, it is able to explain the qualitative features of Figure 8.5 because the GVD effects are of minor importance for pulse widths  $\sim 1$  ns. When the pump pulses become shorter than 1 ns, it becomes increasingly more important to include the GVD effects, especially the group-velocity mismatch that leads to pulse walk-off. These effects are considered in Section 8.3.

The Stokes radiation generated through SRS is generally noisy because it builds up from spontaneous Raman scattering. As a result, both the width and the energy of Stokes pulses exhibit shot-to-shot fluctuations even when pump pulses have constant width and energy. The statistics associated with such fluctuations have been quantified by using Q-switched pulses emitted from a Nd:YAG laser at a repetition rate of 1 kHz [48]. The relative noise level of pulse energy decreases rapidly as the peak power of pump pulses is increased beyond the Raman threshold. Close to the threshold, the distribution of pulse energies is nearly exponential, as expected from quantum-noise theory [50]. However, just before the onset of the second-order Stokes line, the energy distribution of the first-order Stokes pulse becomes considerably narrower with a nearly Gaussian shape. The experimental results can be simulated solving Eqs (8.1.2) and (8.1.3) with a random Stokes seed [49].

### 8.2.2 Raman Fiber Lasers

An important application of the SRS phenomenon in optical fibers has resulted in the development of fiber-based Raman lasers [51–68]. Such lasers can be tuned over a wide frequency range ( $\sim 10$  THz). Figure 8.6 shows a schematic of a Raman laser. A piece of single-mode fiber is placed inside a Fabry–Perot cavity formed by two partially reflecting mirrors  $M_1$  and  $M_2$ . The cavity provides wavelength-selective feedback for the Stokes light generated inside the fiber through SRS. An intracavity prism allows tuning of the laser wavelength by dispersing various Stokes wavelengths spatially, each of which can be selected by turning the mirror  $M_2$ . The laser threshold corresponds to the pump power at which Raman amplification during a round trip is large enough to balance cavity losses consisting mainly of the transmission loss at the mirrors and coupling losses at the two ends of the fiber. If we assume a typical value of 10 dB for the round-trip loss, the threshold condition is

$$G = \exp(2g_R P_0 L_{\text{eff}} / A_{\text{eff}}) = 10, \quad (8.2.1)$$

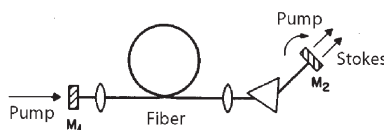


**Figure 8.6** Schematic illustration of a tunable Raman laser. Mirrors  $M_1$  and  $M_2$  form a Fabry–Perot cavity. (After Ref. [54]; © 1977 American Institute of Physics.)

where  $L_{\text{eff}}$  is given by Eq. (8.1.7) for a fiber of length  $L$ . If optical fiber does not preserve polarization,  $g_R$  in Eq. (8.2.1) is reduced by a factor of two because of scrambling of the relative polarization between the pump and the Stokes waves [58]. A comparison of Eqs (8.1.13) and (8.2.1) shows that the threshold pump power for a Raman laser is lower by at least one order of magnitude than that of single-pass SRS.

In the 1972 demonstration of a Raman laser [8], the threshold power was relatively large (about 500W) because of a short fiber length ( $L = 1.9$  m) used in the experiment. In subsequent experiments [51–53], the threshold was reduced to a level  $\sim 1$  W by using longer fibers ( $L \sim 10$  m). This feature permitted CW operation of a Raman laser at wavelengths in the range 0.50–0.53  $\mu\text{m}$  using an argon-ion laser as the pump. Stimulated Brillouin scattering was suppressed by ensuring that the spectral width of the multimode pump was much larger than the Brillouin-gain bandwidth (see Section 9.1). The use of an intracavity prism allowed tuning of the laser wavelength over a range of about 10 nm.

At high pump powers, higher-order Stokes wavelengths are generated inside the fiber. These wavelengths are dispersed spatially by the intracavity prism. By adding separate mirrors for each Stokes beam, such a Raman laser can be operated at several wavelengths simultaneously, each of which can be independently tuned by turning a cavity mirror [52]. In one experiment, a ring-cavity configuration was used to generate five orders of tunable Stokes bands [56]. Raman lasers have been operated in the infrared region extending from 1.1 to 1.6  $\mu\text{m}$ , a region useful for optical fiber communications, using a Nd:YAG laser as a pump [57].

When a Raman laser is pumped by a train of pump pulses, each Raman pulse after one round trip should be properly synchronized with one of the succeeding pump pulses. It is relatively easy to achieve synchronization in Raman lasers. The reason is that the laser can select a particular wavelength that fulfills the synchronous-pumping requirement among the wide range of possible wavelengths near the peak of the Raman-gain spectrum (see Figure 8.2). Moreover, the laser wavelength can be tuned by simply changing the cavity length. This technique is referred to as time-dispersion tuning [54] to distinguish it from prism tuning (see Figure 8.6) that works because of spatial dispersion provided by the prism. The technique is very effective in tuning pulsed Raman lasers over a wide wavelength range. The tuning rate can be obtained as follows. If the cavity length is changed by  $\Delta L$ , the time delay  $\Delta t$  should be exactly compensated by a wavelength change  $\Delta\lambda$  such that

$$\Delta t \equiv \Delta L/c = |D(\lambda)|L\Delta\lambda, \quad (8.2.2)$$

where  $L$  is the fiber length and  $D$  is the dispersion parameter introduced in Section 1.2.3. The tuning rate is therefore given by

$$\frac{\Delta\lambda}{\Delta L} = \frac{1}{cL|D(\lambda)|} = \frac{\lambda^2}{2\pi c^2 L |\beta_2|}, \quad (8.2.3)$$

where Eq. (1.2.11) was used to relate  $D$  to the GVD coefficient  $\beta_2$ . The tuning rate depends on the fiber length  $L$  and the wavelength  $\lambda$ , and is typically  $\sim 1$  nm/cm.

In one experiment, a tuning rate of  $1.8 \text{ nm/cm}$  with a tuning range of  $24 \text{ nm}$  was obtained for  $L = 600 \text{ m}$  and  $\lambda = 1.12 \mu\text{m}$  [55].

Synchronously pumped Raman lasers have attracted attention for generating ultrashort optical pulses [60]. In general, it becomes necessary to take into account the effects of GVD, group-velocity mismatch, SPM, and XPM when such lasers are pulsed using pump pulses of widths below  $100 \text{ ps}$ . These effects are discussed in Section 8.3. If the Raman pulse falls in the anomalous-GVD regime of the fiber, the soliton effects can create pulses of widths  $\sim 100 \text{ fs}$  or less. Such lasers are called Raman soliton lasers and are covered in Section 8.4.

The development of Raman lasers advanced considerably during the 1990s. A new feature was the integration of cavity mirrors within the fiber to make a compact device. In an early approach, a ring-cavity configuration was used to make a low-threshold, all-fiber Raman laser using a fiber loop and a fiber coupler [61]. With the advent of fiber Bragg gratings, it has become possible to replace cavity mirrors with such gratings [62]. Fused fiber couplers can also be used for this purpose. In an interesting approach, three pairs of fiber gratings or couplers are arranged such that they form three cavities for the three Raman lasers operating at wavelengths  $1.117$ ,  $1.175$ , and  $1.24 \mu\text{m}$ , corresponding to the first-, second-, and third-order Stokes lines of a  $1.06-\mu\text{m}$  pump [63]. The resulting  $1.24-\mu\text{m}$  Raman laser is useful for amplifying  $1.31-\mu\text{m}$  signals [64].

The same approach can be used for making a  $1.48-\mu\text{m}$  Raman laser if a phosphosilicate fiber is used [65]. Such a fiber provides a Stokes shift of nearly  $40 \text{ THz}$  and can convert  $1.06-\mu\text{m}$  pump to  $1.48-\mu\text{m}$  radiation through the second-order Stokes line. Output powers of more than  $1 \text{ W}$  were generated by this technique using  $3.3 \text{-W}$  pump power at  $1.06 \mu\text{m}$  from a double-clad Yb-doped fiber laser laser. Much higher pump powers became available after 2000 with advances in the technology behind Yb-doped fiber lasers [66–68]. In a 2009 experiment,  $150 \text{ W}$  of linearly polarized CW power was produced at  $1120 \text{ nm}$  with an optical efficiency of  $85\%$  [68]. A  $30 \text{-m}$  long standard single-mode fiber was used as a gain medium. Figure 8.7 shows the experimental setup schematically. Two fiber gratings act as mirrors to form the laser cavity. Two fiber Bragg gratings (FBG) act as mirrors and form a Fabry-Perot cavity. Two WDM couplers are used to inject the pump power and a third one is used to separate the residual pump power from output.

Raman lasers, operating in the visible and ultraviolet regions and tunable over a wide range, have been made using a double-pass scheme with multimode fibers [69].

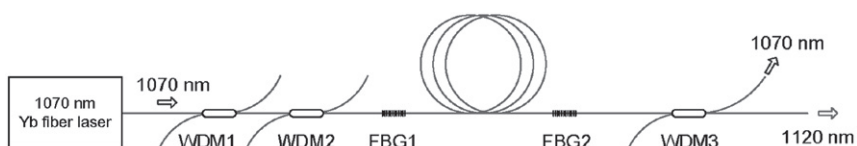


**Figure 8.7 Schematic of a high-power all-fiber Raman laser.** Two fiber Bragg gratings (FBG) act as mirrors and form a Fabry-Perot cavity. Two WDM couplers are used to inject the pump power and a third one is used to separate the residual pump power from output. (After Ref. [68]; © 2009 OSA.)

Tuning over a wide wavelength range (540–970 nm) with high peak-power levels (>12 kW) was realized when a 50-m-long multimode fiber (core diameter 200  $\mu\text{m}$ ) was pumped at 532 nm using second-harmonic pulses from a Q-switched Nd:YAG laser having peak powers of more than 400 kW. The same technique provided tuning over the wavelength range 360–527 nm when Q-switched pulses at 335 nm were used using third-harmonic generation. As the broadband light generated by SRS passes through the fiber only twice, such cavityless lasers are not real lasers in the usual sense. They are nonetheless useful as a tunable source.

### 8.2.3 Raman Fiber Amplifiers

Optical fibers can be used to amplify a weak signal if that signal is launched together with a strong pump wave such that their frequency difference lies within the bandwidth of the Raman-gain spectrum. Because SRS is the physical mechanism behind amplification, such amplifiers are called Raman fiber amplifiers. They were made as early as 1976 [70] and studied during the 1980s [71–85], but their development matured only after 2000 when their use in fiber-optic communication systems became prevalent. The experimental setup is similar to that of Figure 8.6 except that mirrors are not needed. In the forward-pumping configuration, the pump propagates with the signal in the same direction whereas the two counterpropagate in the backward-pumping configuration.

The gain provided by Raman amplifiers under CW or quasi-CW operation can be obtained from Eqs (8.1.2) and (8.1.3). If the signal intensity  $I_s(z)$  remains much smaller than the pump intensity, pump depletion can be ignored. The signal intensity at the amplifier output at  $z = L$  is then given by Eq. (8.1.6). Because  $I_s(L) = I_s(0) \exp(-\alpha_s L)$  in the absence of pump, the amplification factor is given by

$$G_A = \exp(g_R P_0 L_{\text{eff}} / A_{\text{eff}}), \quad (8.2.4)$$

where  $P_0 = I_0 A_{\text{eff}}$  is the pump power at the amplifier input and  $L_{\text{eff}}$  is given by Eq. (8.1.7). If we use typical parameter values,  $g_R = 1 \times 10^{-13} \text{ m/W}$ ,  $L_{\text{eff}} = 100 \text{ m}$ , and  $A_{\text{eff}} = 10 \mu\text{m}^2$ , the signal is amplified considerably for  $P_0 > 1 \text{ W}$ . Figure 8.8 shows the observed variation of  $G_A$  with  $P_0$  when a 1.3-km-long fiber was used to amplify a 1.064- $\mu\text{m}$  signal by using a 1.017- $\mu\text{m}$  pump [71]. The amplification factor  $G_A$  increases exponentially with  $P_0$  initially but starts to deviate for  $P_0 > 1 \text{ W}$ . This is due to gain saturation occurring because of pump depletion. The solid lines in Figure 8.8 are obtained by solving Eqs (8.1.2) and (8.1.3) numerically to include pump depletion. The numerical results are in excellent agreement with the data.

An approximate expression for the saturated gain  $G_s$  in Raman amplifiers can be obtained by solving Eqs (8.1.2) and (8.1.3) analytically [17] with the assumption  $\alpha_s = \alpha_p \equiv \alpha$ . Making the transformation  $I_j = \omega_j F_j \exp(-\alpha z)$  with  $j = s$  or  $p$ , we obtain two simple equations:

$$\frac{dF_s}{dz} = \omega_p g_R F_p F_s e^{-\alpha z}, \quad \frac{dF_p}{dz} = -\omega_p g_R F_p F_s e^{-\alpha z}. \quad (8.2.5)$$

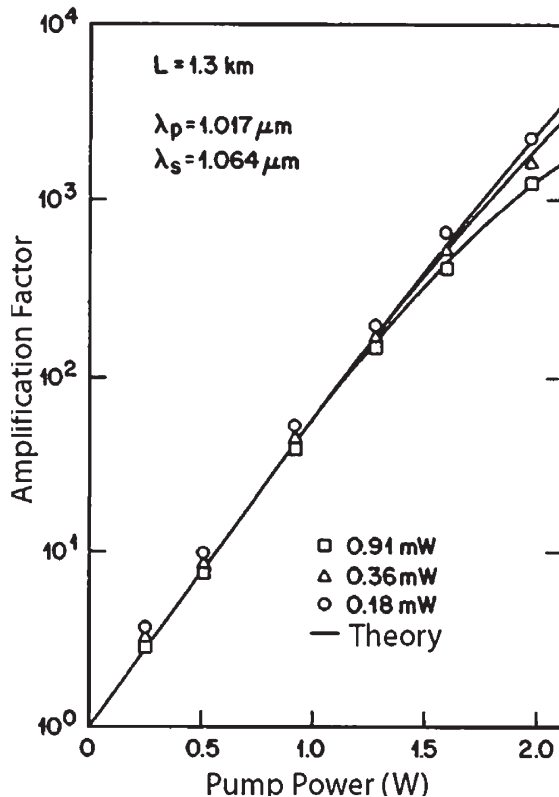


**Figure 8.8** Variation of amplifier gain  $G_A$  with pump power  $P_0$ . Different symbols show the experimental data for three values of input signal power. Solid curves show the theoretical prediction using  $g_R = 9.2 \times 10^{-14} \text{ m/W}$ . (After Ref. [71]; © 1981 Elsevier.)

Noting that  $F_p(z) + F_s(z) = C$ , where  $C$  is a constant, the differential equation for  $F_s$  can be integrated over the amplifier length, and the result is

$$G_s = \frac{F_s(L)}{F_s(0)} = \left( \frac{C - F_s(L)}{C - F_s(0)} \right) \exp(\omega_p g_R C L_{\text{eff}} - \alpha L). \quad (8.2.6)$$

Using  $C = F_p(0) + F_s(0)$  in this equation the saturated gain of the amplifier is given by

$$G_s = \frac{(1 + r_0)e^{-\alpha L}}{r_0 + G_A^{-(1+r_0)}}, \quad (8.2.7)$$

where  $r_0$  is related to the signal-to-pump power ratio at the fiber input as

$$r_0 = \frac{F_s(0)}{F_p(0)} = \frac{\omega_p}{\omega_s} \frac{P_s(0)}{P_0}, \quad (8.2.8)$$

and  $G_A = \exp(g_R P_0 L_{\text{eff}} / A_{\text{eff}})$  is the small-signal (unsaturated) gain.

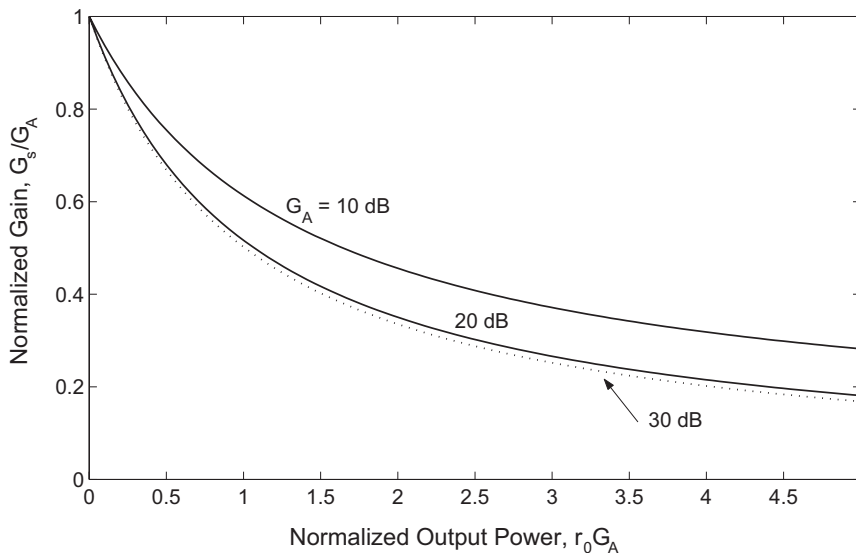


**Figure 8.9 Gain-saturation characteristics of Raman amplifiers for several values of the unsaturated amplifier gain  $G_A$ .**

Figure 8.9 shows the saturation characteristics by plotting  $G_s/G_A$  as a function of  $G_A r_0$  for several values of  $G_A$  with  $\alpha=0$ . The saturated gain is reduced by a factor of 2 when  $G_A r_0 \approx 1$ . This condition is satisfied when the power in the amplified signal starts to approach the input pump power  $P_0$  that is a good measure of the saturation power of Raman amplifiers. As typically  $P_0 \sim 1\text{ W}$ , the saturation power of Raman amplifiers is much larger compared with that of doped-fiber amplifiers or semiconductor optical amplifiers [79].

As seen in Figure 8.8, Raman amplifiers can easily amplify an input signal by a factor of 1000 (30-dB gain) at a pump power of about 1W [71]. In a 1983 experiment, a  $1.24\text{-}\mu\text{m}$  signal from a semiconductor laser was amplified by 45dB using a 2.4-km-long fiber [73]. This experiment used the forward-pumping configuration. In a different experiment [72], a  $1.4\text{-}\mu\text{m}$  signal was amplified using both the forward- and backward-pumping configurations. The CW light from a Nd:YAG laser operating at  $1.32\text{ }\mu\text{m}$  acted as the pump. Gain levels of up to 21dB were obtained at a pump power of 1W. The amplifier gain was nearly the same in both pumping configurations.

For optimum performance of Raman amplifiers, the frequency difference between the pump and signal beams should correspond to the peak of the Raman gain in Figure 8.2. In the near-infrared region, the most practical pump source is the Nd:YAG laser operating at  $1.06$  or  $1.32\text{ }\mu\text{m}$ . For this laser, the maximum gain occurs for signal wavelengths near  $1.12$  and  $1.40\text{ }\mu\text{m}$ , respectively. However, the signal wavelengths of most interest from the standpoint of optical fiber communications are near  $1.3$  and  $1.5\text{ }\mu\text{m}$ . A Nd:YAG laser can still be used if a higher-order Stokes line is used as a pump.

For example, the third-order Stokes line at  $1.24\text{ }\mu\text{m}$  from a  $1.06\text{-}\mu\text{m}$  laser can act as a pump to amplify the signals at  $1.3\text{ }\mu\text{m}$ . Similarly, the first-order Stokes line at  $1.4\text{ }\mu\text{m}$  from a  $1.32\text{-}\mu\text{m}$  laser can act as a pump to amplify the signals near  $1.5\text{ }\mu\text{m}$ . As early as 1984, amplification factors of more than 20 dB were realized by using such schemes [74]. These experiments also indicated the importance of matching the polarization directions of the pump and probe waves as SRS nearly ceases to occur in the case of orthogonal polarizations. The use of a polarization-preserving fiber with a high-germania core has resulted in 20-dB gain at  $1.52\text{ }\mu\text{m}$  by using only 3.7 W of input power from a Q-switched  $1.34\text{-}\mu\text{m}$  laser [75].

From a practical standpoint, the quantity of interest is the so-called on–off ratio, defined as the ratio of the signal power with the pump onto that with the pump off. This ratio can be measured experimentally. The experimental results for a  $1.34\text{-}\mu\text{m}$  pump show that the on–off ratio is about 24 dB for the first-order Stokes line at  $1.42\text{ }\mu\text{m}$  but degrades to 8 dB when the first-order Stokes line is used to amplify a  $1.52\text{-}\mu\text{m}$  signal. The on–off ratio is also found to be smaller in the backward-pumping configuration [78]. It can be improved if the output is passed through an optical filter that passes the amplified signal but reduces the bandwidth of the spontaneous noise.

An attractive feature of Raman amplifiers is related to their broad bandwidth. They can be used to amplify several channels simultaneously in a WDM lightwave system. This feature was demonstrated in a 1987 experiment [80] in which signals from three distributed feedback semiconductor lasers operating in the range  $1.57\text{--}1.58\text{ }\mu\text{m}$  were amplified simultaneously using a  $1.47\text{-}\mu\text{m}$  pump. The gain of 5 dB was obtained at a pump power of only 60 mW. A theoretical analysis shows that a trade-off exists between the on–off ratio and channel gains [81]. During the 1980s, several experiments used the Raman gain for improving the performance of optical communication systems [82–85]. This scheme is called distributed amplification as fiber losses accumulated over 100 km or so are compensated in a distributed manner. It was used in 1988 to demonstrate soliton transmission over 4000 km [85].

The main drawback of Raman amplifiers from the standpoint of lightwave system applications is that a high-power laser is required for pumping. Early experiments employed tunable color-center lasers that were too bulky for practical applications. Indeed, with the advent of erbium-doped fiber amplifiers in 1989, Raman amplifiers were rarely used for  $1.55\text{-}\mu\text{m}$  lightwave systems. The situation changed with the availability of compact high-power semiconductor lasers in the 1990s. As early as 1992, a Raman amplifier was pumped using a  $1.55\text{-}\mu\text{m}$  semiconductor laser [86]. The 140-ns pump pulses had a 1.4-W peak-power level at the 1-kHz repetition rate and were capable of amplifying  $1.66\text{-}\mu\text{m}$  signal pulses by more than 23 dB in a 20-km-long dispersion-shifted fiber. The resulting 200-mW peak power of  $1.66\text{-}\mu\text{m}$  pulses was large enough for their use for optical time-domain reflection measurements, a technique commonly used for supervising and maintaining fiber-optic networks [87].

The use of Raman amplifiers in the  $1.3\text{-}\mu\text{m}$  region has attracted considerable attention [88–93]. In one approach, three pairs of fiber gratings are inserted within the fiber used for Raman amplification [88]. The Bragg wavelengths of these gratings are chosen such that they form three cavities for three Raman lasers operating

at wavelengths 1.117, 1.175, and 1.24 μm that correspond to the first-, second-, and third-order Stokes lines of a 1.06-μm pump. All three lasers are pumped using a diode-pumped Nd-fiber laser through cascaded SRS. The 1.24-μm laser then pumps the Raman amplifier to provide signal amplification in the 1.3-μm region. The same idea of cascaded SRS was used to obtain a 39-dB gain at 1.3 μm by using WDM couplers in place of fiber gratings [89]. In a different approach, the core of silica fiber is doped heavily with germania. Such a fiber can be pumped to provide 30-dB gain at a pump power of only 350 mW [90]. Such pump powers can be obtained by using two or more semiconductor lasers. A dual-stage configuration has also been used in which a 2-km-long germania-doped fiber is placed in series with a 6-km-long dispersion-shifted fiber in a ring geometry [93]. Such a Raman amplifier, when pumped by a 1.24-μm Raman laser, provided a 22-dB gain in the 1.3-μm wavelength region with a noise figure of about 4 dB.

Raman amplifiers can be used to extend the bandwidth of WDM systems operating in the 1.55-μm region [94–96]. Erbium-doped fiber amplifiers used commonly in this wavelength regime, have a bandwidth of under 40 nm. Moreover, a gain-flattening technique is needed to use the entire 40-nm bandwidth. Massive WDM systems typically require optical amplifiers capable of providing uniform gain over a 70–80-nm wavelength range. Hybrid amplifiers made by combining erbium doping with Raman gain have been developed for this purpose. In one implementation of this idea [96], a nearly 80-nm bandwidth was realized by combining an erbium-doped fiber amplifier with two Raman amplifiers, pumped simultaneously at three different wavelengths (1471, 1495, and 1503 nm) using four pump modules, each module launching more than 150 mW of power into the fiber. The combined gain of 30 dB was nearly uniform over a wavelength range of 1.53–1.61 μm.

Starting around 2000, distributed Raman amplification was used for compensation of fiber losses in long-haul WDM systems [97–102]. In this configuration, in place of using erbium-doped fiber amplifiers, relatively long spans (80–100 km) of the transmission fiber are pumped bidirectionally to provide Raman amplification. In a 2000 demonstration of this technique, 100 WDM channels with 25-GHz channel spacing, each operating at a bit rate of 10 Gb/s, were transmitted over 320 km [97]. All channels were amplified simultaneously by pumping each 80-km fiber span in the backward direction using four semiconductor lasers. By 2004, 128 channels, each operating at 10 Gb/s, could be transmitted over 4000 km with the use of distributed Raman amplification [101].

With the advent of high-power Yb-doped fiber lasers, high-power Raman amplifiers have been made in recent years by using such lasers as a pumping source. In a 2008 experiment, 4.8 W of CW power was produced at 1178 nm by pumping a 150-m long single-mode fiber with a Yb-doped fiber laser operating at 1120 nm. The 1178-nm signal obtained from a DFB laser could be amplified by 27 dB while maintaining a 10-MHz linewidth [103]. By 2010, the output power could be increased to above 60 W, while maintaining a narrow linewidth, by combining coherently the output of three such Raman amplifiers [104]. Moreover, frequency doubling of this output beam inside an external cavity provided 50 W of CW power at a wavelength of 589 nm.

### 8.2.4 Raman-Induced Crosstalk

The same Raman gain that is beneficial for making fiber amplifiers and lasers is also detrimental to WDM systems. The reason is that a short-wavelength channel can act as a pump for longer-wavelength channels and thus transfer part of the pulse energy to neighboring channels. This leads to Raman-induced crosstalk among channels that can affect the system performance considerably [105–115].

Consider first a two-channel system with the short-wavelength channel acting as a pump. The power transfer between the two channels is governed by Eqs (8.1.2) and (8.1.3). These equations can be solved analytically if the fiber loss is assumed to be the same for both channels ( $\alpha_s = \alpha_p$ ), an assumption easily justified for typical channel spacings near  $1.55\text{ }\mu\text{m}$ . The amplification factor  $G_s$  for the longer-wavelength channel is given by Eq. (8.2.7). The associated reduction in the short-wavelength channel power is obtained from the pump-depletion factor

$$D_p = \frac{I_p(L)}{I_p(0) \exp(-\alpha_p L)} = \frac{1 + r_0}{1 + r_0 G_A^{1+r_0}}, \quad (8.2.9)$$

where  $G_A$  and  $r_0$  are defined by Eqs (8.2.4) and (8.2.8), respectively. Figure 8.10 shows the pump-depletion characteristics by plotting  $D_p$  as a function of  $G_A$  for several values of  $r_0$ . These curves can be used to obtain the Raman-induced power penalty defined as the relative increase in the pump power necessary to maintain the

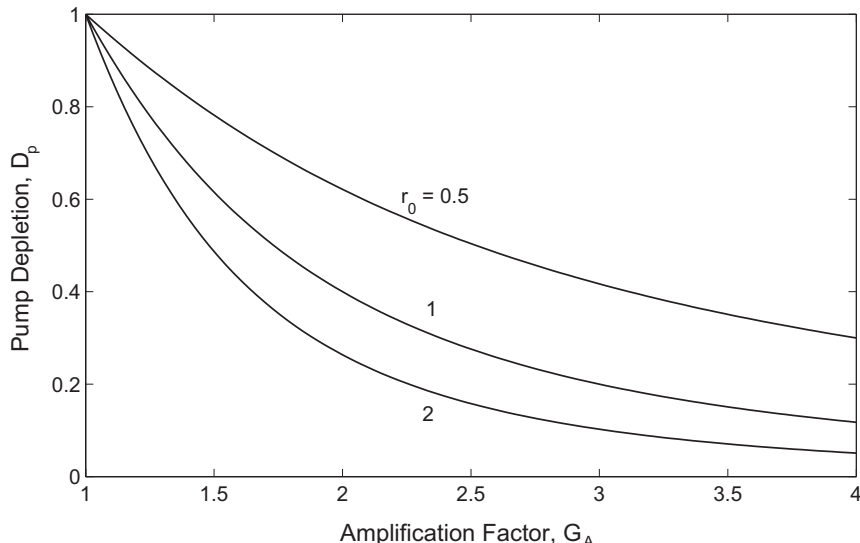


Figure 8.10 Pump-depletion characteristics showing variation of  $D_p$  with  $G_A$  for three values of  $r_0$ .

same level of output power as that in the absence of Raman crosstalk. The power penalty can be written as (in decibels)

$$\Delta_R = 10 \log(1/D_p). \quad (8.2.10)$$

A 1-dB penalty corresponds to  $D_p \approx 0.8$ . If we assume equal channel powers at the fiber input ( $r_0 \approx 1$ ),  $D_p = 0.8$  corresponds to  $G_A \approx 1.22$ . The input channel powers corresponding to 1-dB penalty can be obtained from Eq. (8.2.4). If we use the typical values for 1.55-μm optical communication systems,  $g_R = 7 \times 10^{-14} \text{ m/W}$ ,  $A_{\text{eff}} = 50 \mu\text{m}^2$ , and  $L_{\text{eff}} = 1\alpha_p \approx 20 \text{ km}$ ,  $G_A = 1.22$  corresponds to  $P_0 = 7 \text{ mW}$ . If the Raman gain is reduced by a factor of 2 to account for polarization scrambling, this value increases to  $P_0 = 14 \text{ mW}$ . The experimental measurements of the power penalty are in agreement with the predictions of Eqs (8.2.9) and (8.2.10).

The situation is more complicated for multichannel WDM systems. The intermediate channels not only transfer energy to the longer-wavelength channels but, at the same time, also receive energy from the shorter-wavelength channels. For an  $M$ -channel system one can obtain the output powers for each channel by solving a set of  $M$  coupled equations [108] similar to Eqs (8.1.2) and (8.1.3). The shortest-wavelength channel is most affected by Raman-induced crosstalk because it transfers a part of its energy to all channels lying within the Raman-gain bandwidth. The transferred amount, however, is different for each channel as it is determined by the amount of the Raman gain corresponding to the relative wavelength spacing. In one approach, the Raman-gain spectrum of Figure 8.2 is approximated by a triangular profile [105]. The results show that for a 10-channel system with 10-nm separation, the input power of each channel should not exceed 3 mW to keep the power penalty below 0.5 dB. In a 10-channel experiment with 3-nm channel spacing, no power penalty related to Raman crosstalk was observed when the input channel power was kept below 1 mW [106].

The foregoing discussion provides only a rough estimate of the Raman crosstalk as it neglects the fact that signals in different channels consist of different random sequences of 0 and 1 bits. It is intuitively clear that such pattern effects will reduce the level of Raman crosstalk. The GVD effects that were neglected in the preceding analysis also reduce the Raman crosstalk since pulses in different channels travel at different speeds because of the group-velocity mismatch [109]. For a realistic WDM system, one must also consider dispersion management and add the contributions of multiple fiber segments separated by optical amplifiers [115].

### 8.3 SRS WITH SHORT PUMP PULSES

The quasi-CW regime of SRS considered in Section 8.2 applies for pump pulses of widths  $> 1 \text{ ns}$  because the walk-off length  $L_w$ , defined in Eq. (8.1.22), generally exceeds the fiber length  $L$  for such pulses. However, for ultrashort pulses of widths below 100 ps, typically  $L_w < L$ . SRS is then limited by the group-velocity mismatch

and occurs only over distances  $z \sim L_W$  even if the actual fiber length  $L$  is considerable larger than  $L_W$ . At the same time, the nonlinear effects such as SPM and XPM become important because of relatively large peak powers and affect considerably the evolution of both pump and Raman pulses [116–138]. This section discusses the experimental and theoretical aspects of SRS in the normal-GVD regime of optical fibers. Section 8.4 is devoted to the case of anomalous GVD where the role of soliton effects becomes important. In both cases, pulse widths are assumed to be larger than the Raman response time ( $\sim 50$  fs) so that transient effects are negligible.

### 8.3.1 Pulse-Propagation Equations

In the general case in which GVD, SPM, XPM, pulse walk-off, and pump depletion all play an important role, Eqs (8.1.20) and (8.1.21) should be solved numerically. If we neglect fiber losses because of relatively small fiber lengths used in most experiments, set  $\delta_R = 0$  assuming  $\Omega = \Omega_R$ , and measure time in a frame of reference moving with the pump pulse, these equations take the form

$$\frac{\partial A_p}{\partial z} + \frac{i\beta_{2p}}{2} \frac{\partial^2 A_p}{\partial T^2} = i\gamma_p \left[ |A_p|^2 + (2 - f_R)|A_s|^2 \right] A_p - \frac{g_p}{2} |A_s|^2 A_p, \quad (8.3.1)$$

$$\frac{\partial A_s}{\partial z} - d \frac{\partial A_s}{\partial T} + \frac{i\beta_{2s}}{2} \frac{\partial^2 A_s}{\partial T^2} = i\gamma_s \left[ |A_s|^2 + (2 - f_R)|A_p|^2 \right] A_p + \frac{g_s}{2} |A_p|^2 A_s, \quad (8.3.2)$$

where

$$T = t - z/v_{gp}, \quad d = v_{gp}^{-1} - v_{gs}^{-1}. \quad (8.3.3)$$

The walk-off parameter  $d$  accounts for the group-velocity mismatch between the pump and Raman pulses and is typically 2–6 ps/m. The GVD parameter  $\beta_{2j}$ , the nonlinearity parameter  $\gamma_j$ , and the Raman-gain coefficient  $g_j$  ( $j = p$  or  $s$ ) are slightly different for the pump and Raman pulses because of the Raman shift of about 13 THz between their carrier frequencies. In terms of the wavelength ratio  $\lambda_p/\lambda_s$ , these parameters for pump and Raman pulses are related as

$$\beta_{2s} = \frac{\lambda_p}{\lambda_s} \beta_{2p}, \quad \gamma_s = \frac{\lambda_p}{\lambda_s} \gamma_p, \quad g_s = \frac{\lambda_p}{\lambda_s} g_p. \quad (8.3.4)$$

Four length scales can be introduced to determine the relative importance of various terms in Eqs (8.3.1) and (8.3.2). For pump pulses of duration  $T_0$  and peak power  $P_0$ , these are defined as

$$L_D = \frac{T_0^2}{|\beta_{2p}|}, \quad L_W = \frac{T_0}{|d|}, \quad L_{NL} = \frac{1}{\gamma_p P_0}, \quad L_G = \frac{1}{g_p P_0}. \quad (8.3.5)$$

The dispersion length  $L_D$ , the walk-off length  $L_W$ , the nonlinear length  $L_{NL}$ , and the Raman-gain length  $L_G$  provide, respectively, the length scales over which the effects

of GVD, pulse walk-off, nonlinearity (both SPM and XPM), and Raman gain become important. The shortest length among them plays the dominant role. Typically,  $L_W \sim 1$  m (for  $T_0 < 10$  ps) while  $L_{NL}$  and  $L_G$  become smaller or comparable to it for  $P_0 > 100$  W. In contrast,  $L_D \sim 1$  km for  $T_0 = 10$  ps. Thus, the GVD effects are generally negligible for pulses as short as 10 ps. The situation changes for pulse widths  $\sim 1$  ps or less because  $L_D$  decreases faster than  $L_W$  with a decrease in the pulse width. The GVD effects can then affect SRS evolution significantly, especially in the anomalous-dispersion regime.

### 8.3.2 Nondispersive Case

When the second-derivative term in Eqs (8.3.1) and (8.3.2) is neglected, these equations can be solved analytically [135–138]. The analytic solution takes a simple form if pump depletion during SRS is neglected. As this assumption is justified for the initial stages of SRS and permits us to gain physical insight, let us consider it in some detail. The resulting analytic solution includes the effects of both XPM and pulse walk-off. The XPM effects without walk-off effects were considered relatively early [117]. Both of them can be included by solving Eqs (8.3.1) and (8.3.2) with  $\beta_{2p} = \beta_{2s} = 0$  and  $g_p = 0$ . Equation (8.3.1) for the pump pulse then yields the solution

$$A_p(z, T) = A_p(0, T) \exp[i\gamma_p |A_p(0, T)|^2 z], \quad (8.3.6)$$

where the XPM term has been neglected assuming  $|A_s|^2 \ll |A_p|^2$ . For the same reason, the SPM term in Eq. (8.3.2) can be neglected. The solution of Eq. (8.3.2) is then given by [126]

$$A_s(z, T) = A_s(0, T + zd) \exp\{[g_s/2 + i\gamma_s(2 - f_R)]\psi(z, T)\}, \quad (8.3.7)$$

where

$$\psi(z, T) = \int_0^z |A_p(0, T + zd - z'd)|^2 dz'. \quad (8.3.8)$$

Equation (8.3.6) shows that the pump pulse of initial amplitude  $A_p(0, T)$  propagates without change in its shape. The SPM-induced phase shift imposes a frequency chirp on the pump pulse that broadens its spectrum (see Section 4.1). The Raman pulse, by contrast, changes both its shape and spectrum as it propagates through the fiber. Temporal changes occur owing to Raman gain while spectral changes have their origin in XPM. Because of pulse walk-off, both kinds of changes are governed by an overlap factor  $\psi(z, T)$  that takes into account the relative separation between the two pulses along the fiber. This factor depends on the pulse shape. For a Gaussian pump pulse with the input amplitude

$$A_p(0, T) = \sqrt{P_0} \exp(-T^2/2T_0^2), \quad (8.3.9)$$

the integral in Eq. (8.3.8) can be performed in terms of error functions with the result

$$\psi(z, \tau) = [\text{erf}(\tau + \delta) - \text{erf}(\tau)](\sqrt{\pi} P_0 z / \delta), \quad (8.3.10)$$

where  $\tau = T/T_0$  and  $\delta$  is the distance in units of the walk-off length, that is,

$$\delta = zd/T_0 = z/L_W. \quad (8.3.11)$$

An analytic expression for  $\psi(z, \tau)$  can also be obtained for pump pulses having “sech” shape [135]. In both cases, the Raman pulse compresses initially, reaches a minimum width, and then begins to rebroaden as it is amplified through SRS. It also acquires a frequency chirp through XPM. This qualitative behavior persists even when pump depletion is included [135–137].

Equation (8.3.7) describes Raman amplification when a weak signal pulse is injected together with the pump pulse. The case in which the Raman pulse builds from noise is much more involved from a theoretical viewpoint. A general approach should use a quantum-mechanical treatment, similar to that employed for describing SRS in molecular gases [50]. It can be considerably simplified for optical fibers if transient effects are ignored by assuming that pump pulses are much wider than the Raman response time. In that case, Eqs (8.3.1) and (8.3.2) can be used, provided a noise term (often called the Langevin force) is added to the right-hand side of these equations. The noise term leads to pulse-to-pulse fluctuations in the amplitude, width, and energy of the Raman pulse, similar to those observed for SRS in molecular gases [22]. Its inclusion is essential if the objective is to quantify such fluctuations.

The *average* features of noise-seeded Raman pulses can be described with the theory of Section 8.1.2, where the effective Stokes power at the fiber input is obtained by using one photon per mode at all frequencies within the Raman-gain spectrum. Equation (8.1.10) then provides the input peak power of the Raman pulse, while its shape remains undetermined. Numerical solutions of Eqs (8.3.1) and (8.3.2) show that the *average* pulse shapes and spectra at the fiber output are not dramatically affected by different choices of the shape of the seed pulse. A simple approximation consists of assuming

$$A_s(0, T) = (P_{s0}^{\text{eff}})^{1/2}, \quad (8.3.12)$$

where  $P_{s0}^{\text{eff}}$  is given by Eq. (8.1.10). Alternatively, one may take the seed pulse to be Gaussian with a peak power  $P_{s0}^{\text{eff}}$ .

As a simple application of the analytic solution (8.3.7), consider the Raman threshold for SRS induced by short pump pulses of width  $T_0$  and peak power  $P_0$  [121]. The peak power of the Raman pulse at the fiber output ( $z = L$ ) is given by

$$P_s(L) = |A_s(L, 0)|^2 = P_{s0}^{\text{eff}} \exp(\sqrt{\pi} g_s P_0 L_W), \quad (8.3.13)$$

where Eq. (8.3.10) was used with  $\tau = 0$  and  $L/L_W \gg 1$ . If we define the Raman threshold in the same way as for the CW case, the threshold is achieved when  $P_s(L) = P_0$ . The comparison of Eqs (8.1.12) and (8.3.13) shows that one can use the CW criterion provided the effective length is taken to be

$$L_{\text{eff}} = \sqrt{\pi} L_W \approx T_{\text{FWHM}}/|d|. \quad (8.3.14)$$

In particular, Eq. (8.1.13) can be used to obtain the critical peak power of the pump pulse if  $L_{\text{eff}}$  is obtained from Eq. (8.3.14). This change is expected because the effective interaction length between the pump and Raman pulses is determined by the length  $L_w$ —SRS ceases to occur when the two pulses move apart enough that they stop overlapping significantly. Equations (8.1.13) and (8.3.14) show that the Raman threshold depends on the width of the pump pulse and increases inversely with  $T_{\text{FWHM}}$ . For pulse widths  $\sim 10 \text{ ps}$  ( $L_w \sim 1 \text{ m}$ ), the threshold pump powers are  $\sim 100 \text{ W}$ .

The analytic solution (8.3.7) can be used to obtain both the shape and the spectrum of the Raman pulse during the initial stages of SRS [126]. The spectral evolution is governed by the XPM-induced frequency chirp. The chirp behavior has been discussed in Section 7.4 in the context of XPM-induced asymmetric spectral broadening (see Figure 7.3). The qualitative features of the XPM-induced chirp are identical to those shown there as long as the pump remains undepleted. Note, however, that the Raman pulse travels faster than the pump pulse in the normal-GVD regime. As a result, chirp is induced mainly near the trailing edge. It should be stressed that both pulse shapes and spectra are considerably modified when pump depletion is included [123]. As the energy of the Raman pulse grows, it affects itself through SPM and the pump pulse through XPM.

### 8.3.3 Effects of GVD

When the fiber length is comparable to the dispersion length  $L_D$ , it is important to include the GVD effects. Such effects cannot be described analytically, and a numerical solution of Eqs (8.3.1) and (8.3.2) is necessary to understand the SRS evolution. A generalization of the split-step Fourier method of Section 2.4 can be used for this purpose. The method requires specification of the Raman pulse at the fiber input by using Eq. (8.1.10).

For numerical purposes, it is useful to introduce the normalized variables. A relevant length scale along the fiber length is provided by the walk-off length  $L_w$ . By defining

$$z' = \frac{z}{L_w}, \quad \tau = \frac{T}{T_0}, \quad U_j = \frac{A_j}{\sqrt{P_0}}, \quad (8.3.15)$$

and using Eq. (8.3.4), Eqs (8.3.1) and (8.3.2) become

$$\frac{\partial U_p}{\partial z'} + \frac{iL_w}{2L_D} \frac{\partial^2 U_p}{\partial \tau^2} = \frac{iL_w}{L_{\text{NL}}} \left[ |U_p|^2 + (2 - f_R) |U_s|^2 \right] U_p - \frac{L_w}{2L_G} |U_s|^2 U_p, \quad (8.3.16)$$

$$\frac{\partial U_s}{\partial z'} - \frac{\partial U_s}{\partial \tau} + \frac{irL_w}{2L_D} \frac{\partial^2 U_s}{\partial \tau^2} = \frac{irL_w}{L_{\text{NL}}} \left[ |U_s|^2 + (2 - f_R) |U_p|^2 \right] U_s + \frac{rL_w}{2L_G} |U_p|^2 U_s, \quad (8.3.17)$$

where the lengths  $L_D$ ,  $L_w$ ,  $L_{\text{NL}}$ , and  $L_G$  are given by Eq. (8.3.5). The parameter  $r = \lambda_p/\lambda_s$  and is about 0.95 at  $\lambda_p = 1.06 \mu\text{m}$ .

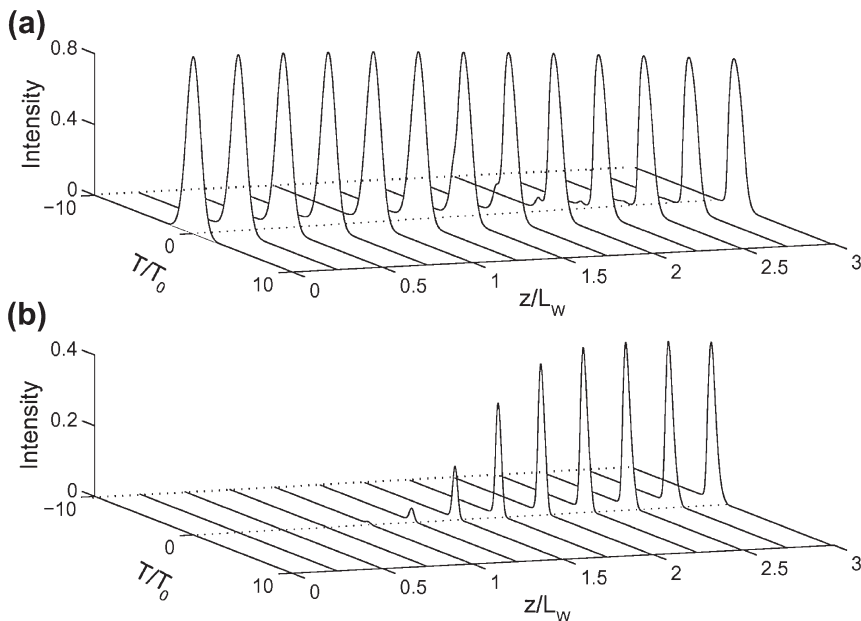


**Figure 8.11** Evolution of (a) pump and (b) Raman pulses over three walk-off lengths in the specific case for which  $L_D/L_W = 1000$ ,  $L_W/L_{NL} = 24$ , and  $L_W/L_G = 12$ .

Figure 8.11 shows the evolution of the pump and Raman pulses over three walk-off lengths using  $L_D/L_W = 1000$ ,  $L_W/L_{NL} = 24$ , and  $L_W/L_G = 12$ . The pump pulse is taken to be a Gaussian. The Stokes pulse is seeded at  $z = 0$  as indicated in Eq. (8.3.12) such that its power is initially smaller by a factor of  $2 \times 10^{-7}$  compared with the pump pulse. The results shown in Figure 8.11 are applicable to a wide variety of input pulse widths and pump wavelengths by using the scaling of Eqs (8.3.5) and (8.3.15). The choice  $L_W/L_G = 12$  implies that

$$\sqrt{\pi} g_s P_0 L_W \approx 21, \quad (8.3.18)$$

and corresponds to a peak power 30% above the Raman threshold.

Several features of Figure 8.11 are noteworthy. The Raman pulse starts to build up after one walk-off length. Energy transfer to the Raman pulse from the pump pulse is nearly complete by  $z = 3L_W$  because the two pulses are then physically separated owing to the group-velocity mismatch. As the Raman pulse moves faster than the pump pulse in the normal-GVD regime, the energy for SRS comes from the leading edge of the pump pulse. This is clearly apparent at  $z = 2L_W$  where energy transfer has led to a two-peak structure in the pump pulse as a result of pump depletion—the hole near the leading edge corresponds exactly to the location of the Raman pulse. The small peak near the leading edge disappears with further propagation as the Raman pulse walks through it. The pump pulse

at  $z = 3L_W$  is asymmetric in shape and appears narrower than the input pulse as it consists of the trailing portion of the input pulse. The Raman pulse is also narrower than the input pulse and is asymmetric with a sharp leading edge.

The spectra of pump and Raman pulses display many interesting features resulting from the combination of SPM, XPM, group-velocity mismatch, and pump depletion. Figure 8.12 shows the pump and Raman spectra at  $z = 2L_W$  (top row) and  $3L_W$  (bottom row). The asymmetric nature of these spectra is due to XPM-induced chirp. The high-frequency side of the pump spectra exhibits an oscillatory structure that is characteristic of SPM (see Section 4.1). In the absence of SRS, the spectrum would be symmetric with the same structure appearing on the low-frequency side. As the low-frequency components occur near the leading edge of the pump pulse and because the pump is depleted on the leading side, the energy is transferred mainly from the low-frequency components of the pump pulse. This is clearly seen in the pump spectra of Figure 8.12. The long tail on the low-frequency side of the Raman spectra is also partly for the same reason. The Raman spectrum is nearly featureless at  $z = 2L_W$  but develops considerable internal structure at  $z = 3L_W$ . This is due to the combination of XPM and pump depletion; the frequency chirp across the Raman pulse induced by these effects

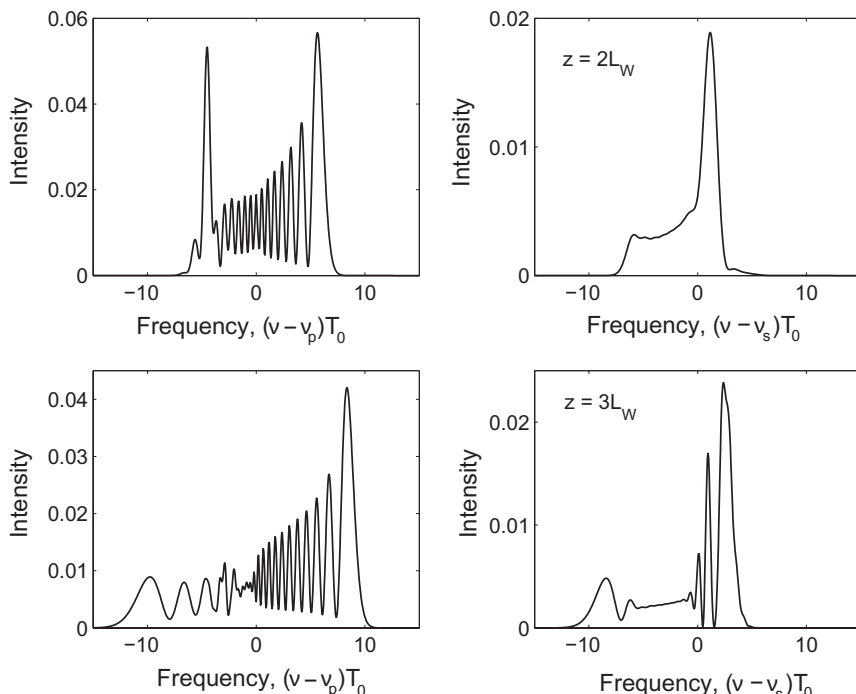


**Figure 8.12 Spectra of pump (left column) and Raman (right column) pulses at  $z = 2L_W$  and  $3L_W$  under the conditions of Figure 8.11.**

can vary rapidly both in magnitude and sign and leads to a complicated spectral shape [123].

The temporal and spectral features seen in Figures 8.11 and 8.12 depend on the peak power of input pulses through the lengths  $L_G$  and  $L_{NL}$  in Eqs (8.3.16) and (8.3.17). When peak power is increased, both  $L_G$  and  $L_{NL}$  decrease by the same factor. Numerical results show that because of a larger Raman gain, the Raman pulse grows faster and carries more energy than that shown in Figure 8.11. More importantly, because of a decrease in  $L_{NL}$ , both the SPM and XPM contributions to the frequency chirp are enhanced, and the pulse spectra are wider than those shown in Figure 8.12. An interesting feature is that the Raman-pulse spectrum becomes considerably wider than the pump spectrum. This is due to the stronger effect of XPM on the Raman pulse compared with that of the pump pulse. The XPM-enhanced frequency chirp for the Raman pulse was predicted as early as 1976 [116]. In a theoretical study that included XPM but neglected group-velocity mismatch and pump depletion, the spectrum of the Raman pulse was shown to be wider by a factor of two [117]. Numerical results that include all of these effects show an enhanced broadening by up to a factor of three, in agreement with experiments discussed later. Direct measurements of the frequency chirp also show an enhanced chirp for the Raman pulse compared with that of the pump pulse [132].

### 8.3.4 Raman-Induced Index Changes

So far we have ignored the impact of the Raman-induced changes in the refractive index of the fiber mode. As seen from Eq. (8.1.19) and Figure 8.3, the parameter  $\delta_R$  should not be ignored because it produces a change in the refractive index seen by the Stokes pulse as it propagates down the fiber. From Eqs. (8.1.19) and (8.1.21), the Raman-induced index change  $\Delta n_R$  can be written in the form

$$\Delta n_R = (c/\omega_s) \gamma_s \delta_R |A_p|^2 = \frac{\text{Re}[\tilde{h}_R(\Omega)]}{\text{Im}[\tilde{h}_R(\Omega)]} \frac{c}{2\omega_s} g_s(\Omega) |A_p|^2. \quad (8.3.19)$$

This equation shows that Raman-induced index changes scale linearly with the pump power and depend strongly on the frequency dependence of the Raman response.

The usefulness of Eq. (8.3.19) is limited because an analytic form of  $\tilde{h}_R(\Omega)$  is not known for silica fibers. Considerable physical insight can be gained by using the approximate form of the Raman response function  $h_R(t)$  given in Eq. (2.3.40). By taking its Fourier transform, we obtain

$$\tilde{h}_R(\Omega) = \frac{\Omega_R^2 + \Gamma_R^2/4}{\Omega_R^2 - (\Omega + i\Gamma_R/2)^2} \approx \frac{\Omega_R/2}{(\Omega_R - \Omega) - i\Gamma_R/2}, \quad (8.3.20)$$

where  $\Omega_R = 1/\tau_1$  is the vibrational resonance frequency (the Raman shift) and  $\Gamma_R = 2/\tau_2$  is the damping rate of molecular vibrations. The approximate form is

obtained by using  $\Gamma_R/2 \ll \Omega_R$  and assuming that  $\Omega$  is close to  $\Omega_R$ . Using this functional form of  $\tilde{h}_R(\Omega)$  in Eq. (8.3.19) and taking into account of the frequency dependence of  $g_s(\Omega)$ , the Raman-induced index change is found to be

$$\Delta n_R = \frac{c}{2\omega_s} \left( \frac{\delta}{1 + \delta^2} \right) g_s(\Omega_R) |A_p|^2, \quad (8.3.21)$$

where  $\delta = 2(\Omega_R - \Omega)/\Gamma_R$  is a normalized detuning parameter and  $g_s(\Omega_R)$  is the peak value of the Raman gain at  $\delta = 0$ .

Even though  $\Delta n_R$  itself is relatively small, it varies rapidly with  $\Omega$  near the Raman-gain peak. The group velocity of a pulse is related inversely to the group index as  $v_g = c/n_g$  with  $n_g = n_t + \omega(dn_t/d\omega)$ , where the total refractive index  $n_t$  includes  $\Delta n_R$ . For this reason, rapid changes in  $\Delta n_R$  with  $\delta$  can change  $n_g$  considerably and affect the group velocity of a pulse. Including the contribution of fiber dispersion as well, the group index is given by

$$n_g = n_{g0} + \left( \frac{c g_R P_0}{\Gamma_R A_{\text{eff}}} \right) \frac{1 - \delta^2}{(1 + \delta^2)^2}, \quad (8.3.22)$$

where  $n_{g0}$  is the group index in the absence of SRS and we used  $g_s(\Omega_R) = g_R/A_{\text{eff}}$  together with  $P_0 = |A_p|^2$ . The contribution of the last term peaks at the Raman-gain peak ( $\delta=0$ ). Thus, when the Stokes frequency is tuned to match the Raman shift ( $\Omega = \Omega_R$ ), one can expect the Stokes pulse to travel considerably slower because of Raman-induced changes in the refractive index of the fiber mode.

The slowing down of optical pulses in the vicinity of an optical resonance (the so-called slow light) has attracted considerable attention in recent years. This phenomenon is discussed in Section 9.4.3 in the context of SBS because Brillouin gain is exploited more often than the Raman gain for this purpose. In a 2005 experiment, Raman amplification of 430-fs pulses inside a 1-km-long fiber resulted in their relative delay of up to 370 fs [139]. Since the use of the Raman gain for slowing down of optical pulses requires high pump powers together with femtosecond pulses, it is unlikely to be employed in practice.

As we saw in Section 8.3.3, any group-velocity mismatch between the pump and Stokes pulses is undesirable for the Raman-amplification process because it leads to the separation of two pulses and hinders transfer of energy from the pump to the Stokes pulse. An interesting question is whether the walk-off effects can be reduced, or even eliminated, by using the slow-light effect. The answer is affirmative when both pulses experience normal GVD inside the fiber providing the Raman gain, because the Stokes pulse travels faster than the pump pulse in that situation [140]. It is evident that any amount of slowing down of the Stokes pulse will reduce the impact of group-velocity mismatch. However, a complete cancellation can occur only for a specific input pump power because it requires the Raman-induced reduction in the Stokes speed to match the speed of the pump pulse. In the case of  $\delta = 0$  corresponding to  $\Omega = \Omega_R$ , the relative slowing down of the Stokes pulse over a fiber of length  $L$  is found from Eq. (8.3.22) to be  $\Delta T = g_R P_0 L / (\Gamma_R A_{\text{eff}})$ . This should

match the relative delay of  $Ld = L\beta_2\Omega_R$  resulting from the group-velocity mismatch, where the parameter  $d$  is taken from Eq. (8.3.3) and  $\beta_2$  is the GVD parameter at the pump wavelength. Equating the two delays, the pump power required for a complete elimination of the walk-off effects is found to be

$$P_0 = \beta_2\Omega_R\Gamma_R A_{\text{eff}}/g_R. \quad (8.3.23)$$

Numerical simulations validate this analytical reasoning [140], although a complete elimination of the walk-off effects is difficult to realize in practice because of the pump-depletion effects. As another application of the slow-light effect, it was found that the XPM-induced frequency chirp can also be tuned optically through Raman-induced changes in the group velocity of the Stokes pulse [141].

### 8.3.5 Experimental Results

The spectral and temporal features of ultrafast SRS have been studied in many experiments performed in the visible as well as in the near-infrared region. In one experiment, 60-ps pulses from a mode-locked Nd:YAG laser operating at  $1.06\mu\text{m}$  were propagated through a 10-m-long fiber [118]. When the pump power exceeded the Raman threshold ( $\sim 1\text{ kW}$ ), a Raman pulse was generated. Both the pump and Raman pulses were narrower than the input pulse as expected from the results shown in Figure 8.11. The spectrum of the Raman pulse was much broader (spectral width  $\approx 2\text{ THz}$ ) than that of the pump pulse. The XPM-enhanced spectral broadening of the Raman pulse was quantified in an experiment in which 25-ps pulses at 532 nm were propagated through a 10-m-long fiber [125]. Figure 8.13 shows the observed spectra at four values of pump-pulse energies. The Raman spectral band located at 544.5 mm has a width about three times that of the pump. This is expected from theory and is due to the XPM-induced frequency chirp [117].

In the spectra of Figure 8.13 the fine structure could not be resolved because of a limited spectrometer resolution. Details of the pump spectrum were resolved in another experiment in which 140-ps input pulses at  $1.06\mu\text{m}$  were propagated through a 150-m-long fiber [124]. Figure 8.14 shows the observed pump spectra at several values of input peak powers. The Raman threshold is about 100 W in this experiment. For  $P_0 < 100\text{ W}$ , the spectrum exhibits a multipeak structure, typical of SPM (see Section 4.1). However, the pump spectrum broadens and becomes highly asymmetric for  $P_0 > 100\text{ W}$ . In fact, the two spectra corresponding to peak powers beyond the Raman threshold show features that are qualitatively similar to those of Figure 8.12 (left column). The spectral asymmetry is due to the combined effects of XPM and pump depletion.

Another phenomenon that can lead to new qualitative features in the pump spectrum is the XPM-induced modulation instability. It has been discussed in Section 7.2 for the case in which two pulses at different wavelengths are launched at the fiber input. However, the same phenomenon should occur even if the second pulse is internally generated through SRS. Similar to the case of modulation instability occurring in the anomalous-dispersion regime (see Section 5.1), XPM-induced modulation instability manifests through the appearance of spectral sidelobes in the pulse spectra.

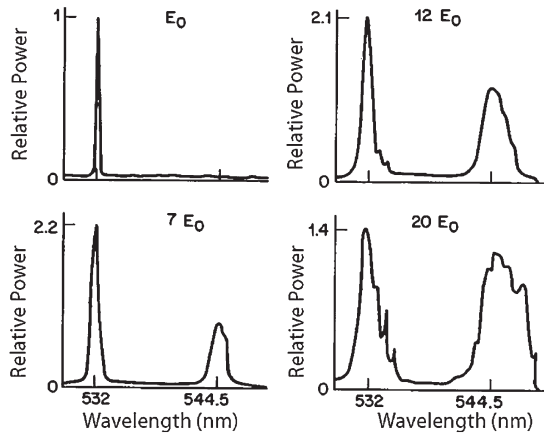


**Figure 8.13** Experimental spectra observed when 25-ps pump pulses at 532 nm were propagated through a 10-m-long fiber. Four spectra correspond to different input pulse energies normalized to  $E_0$ . (After Ref. [125]; ©1987 OSA.)

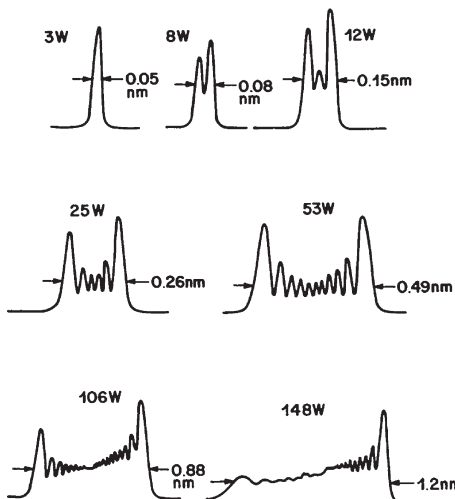


**Figure 8.14** Experimental spectra of pump pulses at different input peak powers after 140-ps pump pulses have propagated through a 150-m-long fiber. The Raman threshold is reached near 100 W. (After Ref. [124]; ©1987 IEE.)

Figure 8.15 shows the observed spectra of the pump and Raman pulses in an experiment in which 25-ps pulses at 532 nm were propagated through a 3-m-long fiber [133]. The fiber-core diameter was only  $3\ \mu\text{m}$  to rule out the possibility of multimode four-wave mixing (see Chapter 10). The central peak in the pump spectrum contains considerable internal structure (Figure 8.14) that remained unresolved in

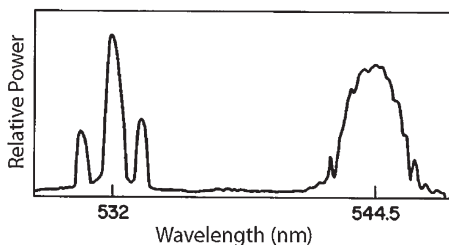


**Figure 8.15 Spectra of pump and Raman pulses showing spectral sidelobes as a result of XPM-induced modulation instability. (After Ref. [133]; © 1988 Springer.)**

this experiment. The two sidebands provide clear evidence of XPM-induced modulation instability. The position of sidebands changes with the fiber length and with the peak power of pump pulses. The Stokes spectrum also shows sidelobes, as expected from the theory of Section 7.2, although they are barely resolved because of XPM-induced broadening of the spectrum.

The temporal measurements of ultrafast SRS show features that are similar to those shown in Figure 8.11 [119–122]. In one experiment, 5-ps pulses from a dye laser operating at 615 nm were propagated through a 12-m-long fiber with a core diameter of  $3.3\text{ }\mu\text{m}$  [120]. Figure 8.16 shows the cross-correlation traces of the pump and Raman pulses at the fiber output. The Raman pulse arrives about 55 ps earlier than the pump pulse; this is consistent with the group-velocity mismatch at 620 nm. More importantly, the Raman pulse is asymmetric with a sharp leading edge and a long trailing edge, features qualitatively similar to those shown in Figure 8.11. Similar results have been obtained in other experiments where the pulse shapes are directly recorded using a streak camera [124] or a high-speed photodetector [131].

The effects of pulse walk-off on SRS were studied by varying the peak power of 35-ps pump pulses (at 532 nm) over a range of 140–210 W while fiber length was varied over a range of 20–100 m [121]. Temporal measurements of the pump and Raman pulses were made with a high-speed CdTe photodetector and a sampling oscilloscope. The results show that the Raman pulse is produced within the first three to four

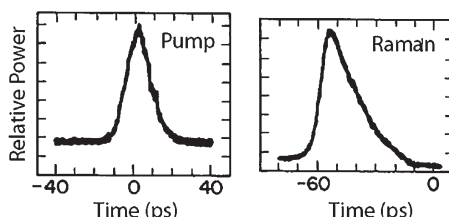


**Figure 8.16 Cross-correlation traces of a pump and Raman pulses at the output of a 12-m-long fiber. The intensity scale is arbitrary. (After Ref. [120]; © 1985 Elsevier.)**

walk-off lengths. The peak appears after about two walk-off lengths into the fiber for 20% energy conversion and moves closer to the input for higher peak powers. These conclusions are in agreement with the numerical results shown in Figure 8.11.

So far, only first-order SRS has been considered. When the input peak power of pump pulses exceeds the Raman threshold considerably, the Raman pulse may become intense enough to act as a pump to generate the second-order Stokes pulse. Such a cascaded SRS was seen in a 615-nm experiment using 5-ps pump pulses with a peak power of 1.5 kW [120]. In the near-infrared region multiple orders of Stokes can be generated using 1.06- $\mu\text{m}$  pump pulses. The efficiency of the SRS process can be improved considerably by using silica fibers whose core has been doped with  $\text{P}_2\text{O}_5$  because of a relatively large Raman gain associated with  $\text{P}_2\text{O}_5$  glasses [142–144].

From a practical standpoint ultrafast SRS limits the performance of fiber-grating compressors [145]; the peak power of input pulses must be kept below the Raman threshold to ensure optimum performance. In this case SRS not only acts as a loss mechanism but also limits the quality of pulse compression by distorting the linear nature of the frequency chirp resulting from the XPM interaction between pump and Raman pulses [146]. A spectral-filtering technique had been used to improve the quality of compressed pulses even in the presence of SRS [131]. In this approach a portion of the pulse spectrum is selected by using an asymmetric spectral window so that the filtered pulse has nearly linear chirp across its entire width. Good-quality compressed pulses can be obtained in the strong-SRS regime but only at the expense of substantial energy loss [135].

### 8.3.6 Synchronously Pumped Raman Lasers

The preceding section has focused on single-pass SRS. By placing the fiber inside a cavity (see Figure 8.6), a single-pass SRS configuration can be turned into a Raman laser. Such lasers were discussed in Section 8.2.2 in the case of CW or quasi-CW operation ( $T_0 \sim 1$  ns). This section considers Raman lasers pumped synchronously to emit short optical pulses with widths <100 ps. In a commonly used scheme, pump pulses are typically 100 ps wide and are obtained from a mode-locked Nd:YAG laser operating at 1.06  $\mu\text{m}$ .

Figure 8.17 compares the temporal and spectral features at the output under single-pass (solid curve) and multipass (dashed curve) operations, the latter case corresponding to a Raman laser. In this experiment, the fiber was 150-m long and the pump-pulse width was about 120 ps [128]. In the single-pass case, the spectrum shows a SRS peak near 1.12  $\mu\text{m}$ . The corresponding Raman pulse appears 300 ps earlier than the pump pulse, as expected from the walk-off effects. In the case of resonant operation of a Raman laser, the dominant spectral peak occurs at a wavelength of 1.093  $\mu\text{m}$  when the laser is synchronously pumped at 1.06  $\mu\text{m}$ . Furthermore, this wavelength could be tuned over 50 nm through the time-dispersion technique by changing the fiber-cavity length by 10 cm [see Eq. (8.2.3)]. The second spectral peak in Figure 8.17 corresponds to a nonresonant second-order Stokes line. In the

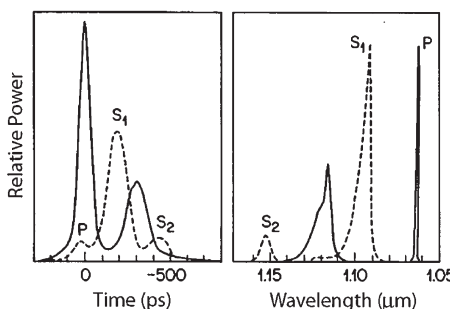


**Figure 8.17 Temporal and spectral output of a Raman laser in the case of resonant (dashed curve) and single-pass (full curve) operation. (After Ref. [128]; © 1987 Taylor & Francis.)**

time domain, the three-peak structure results from a superposition of the pump pulse and the two Raman pulses corresponding to the two spectral peaks. The first-Stokes Raman pulse dominates because of its resonant nature.

Pulse widths generated from Raman lasers are about the same as those of pump pulses ( $\sim 100$  ps). However, because of the SPM and XPM effects, output pulses are chirped and, if the chirp is linear over a significant portion of the pulse, a fiber-grating compressor can be used to compress them. In an important development, pulses as short as 0.8 ps were obtained by placing a fiber-grating compressor inside the cavity of a Raman laser [60]. The grating separation was adjusted to provide a slightly anomalous GVD over a complete round trip inside the ring cavity, that is, the grating pair not only compensated the normal GVD of the fiber but also provided a net anomalous-GVD environment to the pulses circulating inside the cavity. Pulses as short as 0.4 ps have been obtained by using this technique [127]. Furthermore, the Raman laser was tunable from 1.07 to 1.12  $\mu\text{m}$  with pulse widths in the range 0.4–0.5 ps over the entire tuning interval. Such a performance was achieved with the use of spectral filtering by placing an aperture inside the fiber-grating compressor.

A tunable Raman laser has been used to demonstrate amplification of femtosecond optical pulses in a Raman amplifier in both forward and backward-pumping configurations [127]. In the forward-pumping configuration, the 500-fs pulses are first passed through a 100-m-long fiber, where they broaden to about 23 ps as a result of SPM and GVD. The broadened pulses then enter a Raman amplifier, consisting of only a 1-m-long fiber and pumped by 50-ps pulses at 1.06  $\mu\text{m}$ . The amplified pulses are compressed in a fiber-grating compressor. The compressed pulse was slightly broader (about 0.7 ps) than the input pulse but had its energy amplified by up to a factor of 15,000 when pumped by 150-kW pulses. The experiment demonstrated that the frequency chirp of the 23-ps input pulses was nearly unaffected by the process of Raman amplification. Such features indicate that ultrafast SRS in optical fibers not only is capable of generating femtosecond pulses but can also provide high peak powers.

### 8.3.7 Short-Pulse Raman Amplification

In this section we discuss what happens to a short pulse being amplified inside a Raman amplifier while experiencing normal dispersion. It turns out that the pulse acquires a parabolic shape whose width does not depend on the shape and width of input pulses. As found in Section 4.2.6, parabolic pulses constitute an example of self-similar solutions in the sense that the pulse maintains its parabolic shape but its width and peak power scale with distance by a factor that depends on the amplifier gain. The parabolic pulses are expected to form in the normal-GVD region of any fiber-based amplifier. They were first observed in Yb-doped fiber amplifiers [147–150].

There is no fundamental reason why parabolic pulses should not form in a distributed Raman amplifier, provided the dispersion is normal for the signal pulse. Indeed, by 2003, parabolic pulses had been predicted and observed in Raman amplifiers [151–154]. In the 2003 experiment, the Raman amplifier was pumped using a CW laser operating at 1455 nm that was capable of delivering up to 2 W of power [152]. Signal pulses of 10-ps width were obtained from a mode-locked fiber laser. The pump and signal were launched inside a 5.3-km-long fiber, whose GVD parameter was about  $5 \text{ ps}^2/\text{km}$  (normal GVD) at the signal wavelength. The amplified pulses were characterized using the frequency-resolved optical gating (FROG) technique, and the pulse shape and frequency chirp were deduced from it when a pulse with 0.75 pJ energy was amplified by 17 dB. The pulse shape was found to be approximately parabolic together with a nearly linear chirp across its entire temporal profile.

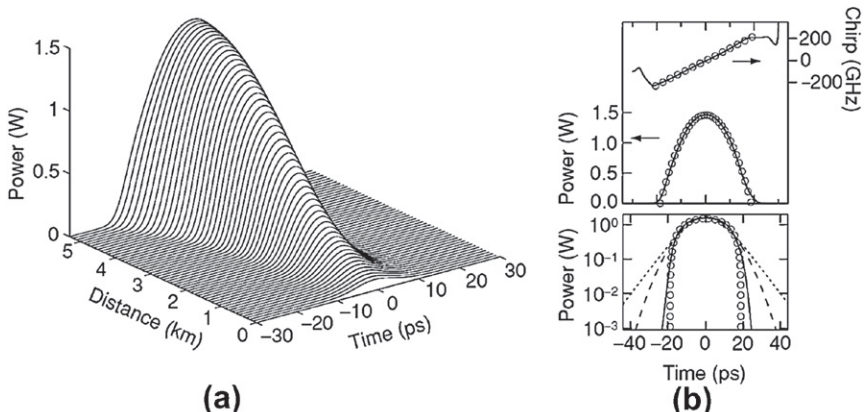


**Figure 8.18** (a) Evolution toward a parabolic shape of a “sech” input pulse over the 5.3-km length of the Raman amplifier. (b) Intensity and chirp (solid lines) profiles of the output pulse together with parabolic and linear fits, respectively (circles). The bottom part shows the same results on a logarithmic scale together with the Gaussian (dashed curve) and “sech” (dotted curve) fits. (After Ref. [152]; © 2003 OSA.)

One can predict the pulse shape and chirp profiles by solving Eqs (8.1.15) and (8.1.16) numerically. For a CW pump, the dispersive effects can be neglected, but the nonlinear effects should be included. Figure 8.18 shows the evolution toward a parabolic shape when a “sech” input pulse is amplified over the 5.3-km length of the Raman amplifier [152]. The shape of the output pulse can be fitted quite well with a parabola but the fit is relatively poor when the shape is assumed to be either Gaussian (dashed curve) or hyperbolic secant (dotted curve). The chirp is approximately linear. Both the predicted pulse shape and the chirp profile agree well with the experimental data. It was also confirmed experimentally that the final pulse characteristics were independent of the input pulse parameters and were determined solely by the Raman amplifier. Both the width and the chirp changed when the gain of the amplifier was changed, but the pulse shape remained parabolic, and the frequency chirped across the pulse remained nearly linear.

## 8.4 SOLITON EFFECTS

When wavelengths of the pump and Raman pulses lie in the anomalous-GVD region of a fiber, the soliton effects become important (see Section 5.2.1). Such effects have attracted considerable attention, both theoretically and experimentally [155–171]. When the Raman pulse propagates as a soliton, it is common to refer to it as a Raman soliton [170]. These solitons must be distinguished from the pair of bright and dark solitons formed during transient SRS in molecular gases. In that case, it is necessary to include the dynamics of the vibrational mode participating in the process of transient SRS [172–174]. In contrast, Raman solitons discussed here occur in the stationary SRS regime.

### 8.4.1 Raman Solitons

In the anomalous-dispersion region of an optical fiber, under suitable conditions, almost all of the pump-pulse energy can be transferred to a Raman pulse that propagates undistorted as a fundamental soliton. Numerical results show that this is possible if the Raman pulse is formed at a distance at which the pump pulse, propagating as a higher-order soliton, achieves its minimum width [155]. By contrast, if energy transfer to the Raman pulse is delayed and occurs at a distance where the pump pulse has split into its components (see Figure 5.6 for  $N = 3$ ), the Raman pulse does not form a fundamental soliton, and its energy rapidly disperses.

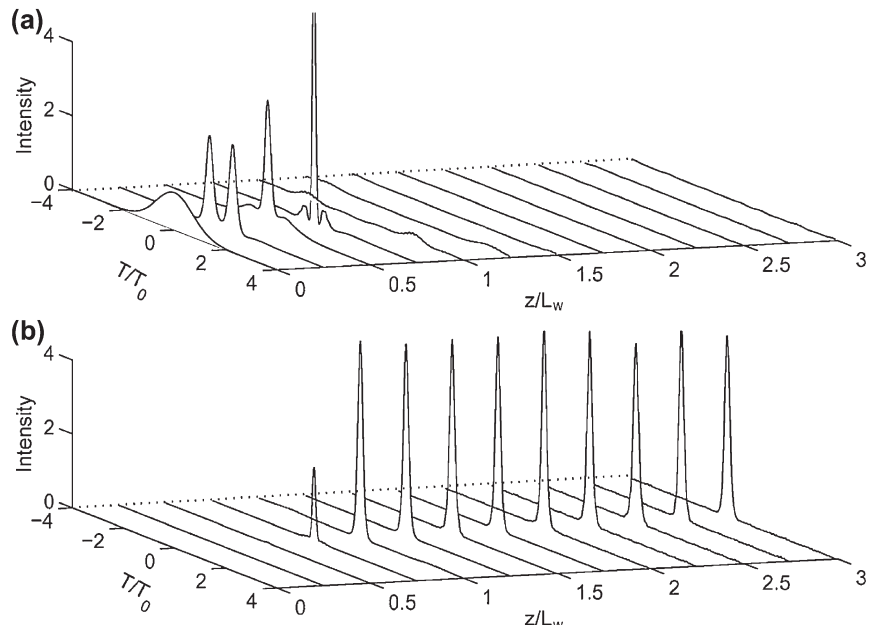
Equations (8.3.16) and (8.3.17) can be used to study ultrafast SRS in the anomalous-GVD regime by simply changing the sign of the second-derivative terms.

Figure 8.19 shows the evolution of the pump and Raman pulses under conditions identical to those used for Figure 8.11 except that  $L_w/L_D = 2$ . The pump pulse travels as a higher-order soliton and is compressed as it propagates down the fiber, while also amplifying the Raman seed. As in the case of normal GVD, energy transfer to the Raman pulse occurs near  $z \approx L_w$ . If the pump pulse is shortest close to this distance, most of its energy is transferred to the Raman pulse, which forms a soliton whose width is only a fraction of the input pump pulse.

For the Raman soliton to form,  $L_w$  should be comparable to the dispersion length  $L_D$ . In silica fibers  $L_w$  and  $L_D$  become comparable only for femtosecond pulses of width  $\sim 100$  fs. For such ultrashort pump pulses, the distinction between pump and Raman pulses gets blurred, as their spectra begin to overlap considerably. This can be seen by noting that the Raman-gain peak in Figure 8.2 corresponds to a spectral separation of about 13 THz, while the spectral width of a 100-fs pulse is  $\sim 10$  THz. Equations (8.3.16) and (8.3.17) do not provide a realistic description of ultrafast SRS with femtosecond pump pulses, particularly in the case of anomalous GVD where the input pulse may shorten considerably during early stages of propagation.

An alternative approach is provided by the generalized propagation equation of Section 2.3. Equation (2.3.44) includes the effect of Raman gain through the last term proportional to the parameter  $T_R$ . As discussed there,  $T_R$  is related to the slope of the Raman gain near origin in Figure 8.2. Effects of this Raman-gain term on the evolution of femtosecond pulses have been discussed in Section 5.5.4. Figure 5.23 shows the pulse shapes and spectra for a pump pulse whose peak power corresponds to a second-order soliton ( $N = 2$ ). As seen there, the input pulse splits into two pulses within one soliton period.

The same behavior can also be interpreted in terms of intrapulse Raman scattering [156], a phenomenon that can occur even before the threshold of noise-induced SRS is reached. The basic idea is the following. The input pulse, propagating as a higher-order soliton, narrows its width and broadens its spectrum during the initial



**Figure 8.19 Evolution of (a) pump and (b) Raman pulses over three walk-off lengths when both pulses propagate in the anomalous-GVD regime of the fiber.**

contraction phase. Spectral broadening on the red side provides a seed for Raman amplification, that is, the blue components of the pulse pump; the red components through self-induced SRS. This is clearly seen in Figure 5.23 where the dominant spectral peak moves continuously toward the red side because of such a Raman-induced frequency shift [158]. In the time domain, energy in the red-shifted components appears in the form of a Raman pulse that lags behind the input pulse because the red-shifted components travel slowly in the anomalous-GVD regime. The use of Eq. (2.3.44) becomes questionable for pulses of widths 100 fs or less because it does not take into account the shape of the Raman-gain spectrum shown in Figure 8.2. Equation (2.3.36) should be used for such ultrashort pulses. This equation is used in Chapter 12 in the context of supercontinuum generation.

Intrapulse Raman scattering can occur even for picosecond input pulses as long as the soliton order  $N$  is large enough to broaden the input spectrum (through SPM) to widths  $\sim 1$  THz. Indeed, in the first experimental demonstration of this phenomenon, 30-ps pulses at  $1.54\text{ }\mu\text{m}$  were propagated through a 250-m-long fiber [156]. Figure 8.20 shows the observed pulse spectra for four input peak powers  $P_0$  in the range of 50–900 W. For  $P_0 = 80$  W, a long tail toward the red side appears. This value of  $P_0$  corresponds to  $N = 30$  in this experiment. A soliton of such a high order is compressed by a factor of about 120 at a distance of 300 m, if we use  $z_0 = 27$  km for the soliton period ( $T_0 \approx 17$  ps). The spectral width of such a compressed pulse is close to 2 THz. The autocorrelation trace of the energy in the Stokes tail of the topmost spectrum (downshifted 1.6 THz from the pump frequency) is also shown in Figure 8.20. It corresponds to a pedestal-free Raman soliton of 200-fs width.

Intrapulse Raman scattering has attracted considerable attention as it provides a convenient way of generating Raman solitons whose carrier wavelength can be tuned by changing fiber length or input peak power [156–163]. In one experiment [160], the use of a dye laser permitted the tuning of the input wavelength over a range of 1.25 to  $1.35\text{ }\mu\text{m}$  as 0.83-ps input pulses with a peak power of 530 W were propagated over a 150-m-long fiber. In this experiment, the input pulse could be launched in the

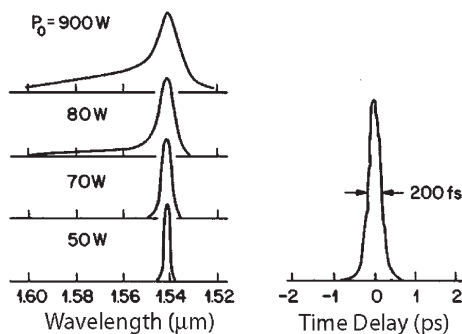


**Figure 8.20** Pulse spectra of 30-ps input pulses at the output of a 250-m-long fiber for peak powers in the range of 50–900 W. The autocorrelation trace on the right side corresponds to the Stokes tail in the topmost spectrum. (After Ref. [156]; © 1985 Nauka.)

normal or the anomalous-GVD regime of the fiber whose zero-dispersion wavelength was near  $1.317\text{ }\mu\text{m}$ . Figure 8.21 shows the pulse spectra as the input wavelength  $\lambda_p$  is varied from  $1.28$  to  $1.317\text{ }\mu\text{m}$ . No Stokes band was generated for  $\lambda_p = 1.28\text{ }\mu\text{m}$  because of the normal GVD of the fiber, although SPM-induced spectral broadening is clearly seen. Two Stokes bands formed for  $\lambda_p = 1.3\text{ }\mu\text{m}$ , even though the input wavelength is below the zero-dispersion wavelength, because a substantial part of the pulse energy appeared in the negative-GVD region after SPM-induced spectral broadening. For  $\lambda_p = 1.317\text{ }\mu\text{m}$ , the Stokes bands are more intense because SRS is more effective in transferring pulse energy toward low frequencies.

Spectral changes for input pulses launched well into the anomalous-GVD regime are also shown in Figure 8.21 for  $\lambda_p = 1.341\text{ }\mu\text{m}$  and a fiber length of  $1\text{ km}$ . Pulse spectra change considerably with an increase in the input peak power. Three Stokes bands appear for  $P_0 = 530\text{ W}$  (topmost curve). An anti-Stokes band carrying 5–10% of the input energy also appears. In the time domain, a separate Raman pulse is associated with each of the Stokes bands. The autocorrelation measurements show that the widths of these Raman solitons are  $\sim 300\text{ fs}$  [160]. The width depends considerably on the fiber length; the smallest width was  $55\text{ fs}$  for  $150\text{-ps}$  wide input pulses. When input peak power was increased to  $5\text{ kW}$ , multiple Stokes bands could be generated in a  $20\text{-m}$ -long fiber. The fourth-order Stokes band near  $1.3\text{ }\mu\text{m}$  served as a pump to generate a continuum that extended up to  $1.7\text{ }\mu\text{m}$ . Using a two-stage compression configuration, the pulse width could be reduced to  $18\text{ fs}$ , a pulse consisting of only three optical cycles. This 1987 experiment constitutes an early example of the formation of Raman solitons and supercontinuum

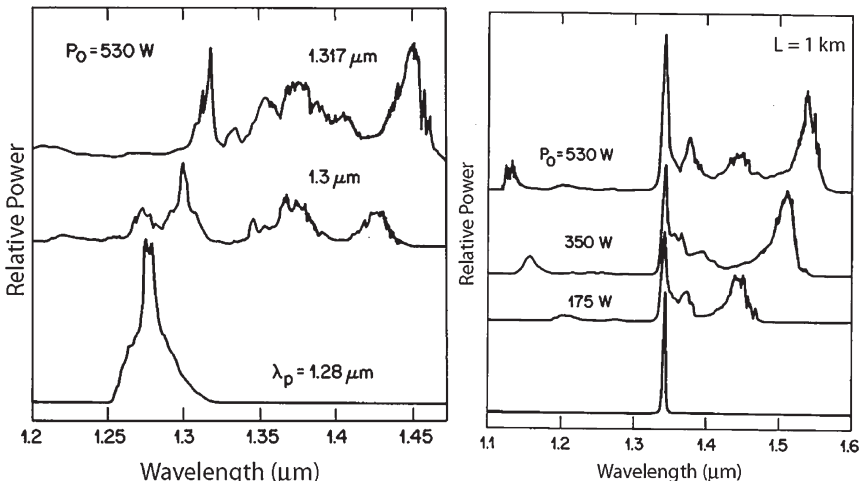


**Figure 8.21** Pulse spectra at the output of (a) a  $150\text{-m}$ -long fiber for pulses with  $530\text{-W}$  peak power at three input wavelengths and (b) a  $1\text{-km}$ -long fiber for pulses with different peak powers at the wavelength of  $1.341\text{ }\mu\text{m}$  when  $0.83\text{-ps}$  pulses are launched at the input end. The zero-dispersion wavelength of the fiber is  $1.317\text{ }\mu\text{m}$ . (After Ref. [160]; © 1987 IEEE.)

generation. This phenomenon has attracted considerable attention in recent years [175–177] with the advent of highly nonlinear fibers and is discussed in detail in Chapter 13.

Raman solitons have also been generated using 100-ps pump pulses from a mode-locked Nd:YAG laser operating at  $1.32\text{ }\mu\text{m}$ . In one experiment, the use of a conventional fiber with the zero-dispersion wavelength near  $1.3\text{ }\mu\text{m}$  led to 100-fs Raman pulses near  $1.4\text{ }\mu\text{m}$  [162]. In another experiment, a dispersion-shifted fiber, having its zero-dispersion wavelength at  $1.46\text{ }\mu\text{m}$ , was used with the same laser. The first-order Stokes at  $1.407\text{ }\mu\text{m}$  served as a pump to generate the second-order Stokes (at  $1.516\text{ }\mu\text{m}$ ) in the anomalous-dispersion regime of the fiber [161]. The Raman pulse associated with the second-order Stokes band was 130-fs wide. The pulse had a broad pedestal and carried only about 30% of its energy in the form of a soliton.

Modulation instability plays an important role in the formation of Raman solitons when pump wavelength lies in the anomalous-GVD regime of an optical fiber [170]. The role of modulation instability can be understood as follows. When the pump pulse experiences anomalous GVD, it develops sidebands because of modulation instability. The low-frequency sideband (typical spacing  $\sim 1\text{ THz}$ ) falls within the bandwidth of the Raman-gain spectrum and seeds the formation of the Raman pulse. At high pump powers, the spectrum of the Raman pulse becomes so broad ( $\sim 10\text{ THz}$ ) that the fiber can support a Raman soliton of width  $\sim 100\text{ fs}$  even when injected pump pulses are more than 100-ps wide. In one experiment, Raman solitons of 60-fs duration were observed by pumping a 25-m-long,  $\text{P}_2\text{O}_5$ -doped, silica fiber with 150-ps pump pulses obtained from a  $1.319\text{-}\mu\text{m}$  Nd:YAG laser [169]. The zero-dispersion wavelength of the fiber was chosen to be close to the pump wavelength to enhance the modulation frequency.

Before closing this section, let us consider whether Eqs (8.3.1) and (8.3.2) have solitary-wave solutions that can be interpreted as Raman solitons. As early as 1988, it was found that soliton-like Raman pulses with a “sech” profile can form under certain conditions provided the pump remains largely undepleted [166]. When pump depletion is included, pulselike solutions of Eqs (8.3.1) and (8.3.2), similar to the XPM-paired solitons discussed in Section 7.3.3, have not been found. However, as discussed in Section 5.5, these equations permit shocklike solutions in the form of a sharp front [178].

### 8.4.2 Raman Soliton Lasers

An interesting application of the soliton effects has led to the development of a new kind of laser known as the Raman soliton laser [179–188]. Such lasers provide their output in the form of solitons of widths  $\sim 100\text{ fs}$ , but at a wavelength corresponding to the first-order Stokes wavelength. Furthermore, the wavelength can be tuned over a considerable range ( $\sim 10\text{ nm}$ ) by using the time-dispersion technique discussed in Section 8.2.2. A ring-cavity configuration, shown schematically in Figure 8.22, is commonly employed. A dichroic beam splitter, highly reflective at

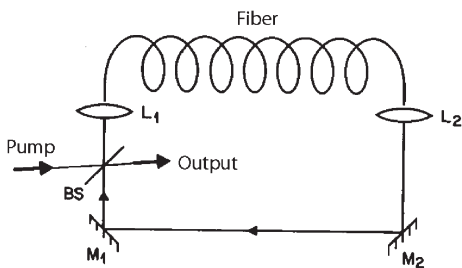


**Figure 8.22 Schematic illustration of the ring-cavity geometry used for Raman soliton lasers. BS is a dichroic beam splitter,  $M_1$  and  $M_2$  are mirrors of 100% reflectivity, and  $L_1$  and  $L_2$  are microscope objective lenses.**

the pump wavelength and partially reflective at the Stokes wavelength  $\lambda_s$ , is used to couple pump pulses into the ring cavity and to provide the laser output.

In a 1987 experimental demonstration of the Raman soliton laser [179], 10-ps pulses from a mode-locked color-center laser operating near  $1.48\text{ }\mu\text{m}$  were used to pump the Raman laser synchronously. The ring cavity had a 500-m-long, polarization-preserving, dispersion-shifted fiber having its zero-dispersion wavelength  $\lambda_D$  near  $1.536\text{ }\mu\text{m}$ . Such a fiber permitted the pump and Raman pulses to overlap over a considerable portion of the fiber as the pump and Raman wavelengths were on opposite sides of  $\lambda_D$  by nearly the same amount ( $\lambda_s \approx 1.58\text{ }\mu\text{m}$ ). Output pulses with widths  $\sim 300\text{ fs}$  were produced with a low but broad pedestal. In an attempt to remove the pedestal, the ring cavity of Figure 8.22 was modified by replacing the fiber with two fiber pieces with variable coupling between them. A 100-m-long section provided the Raman gain while another 500-m-long section was used for pulse shaping. The SRS did not occur in the second section because the coupler reduced pump power levels below the Raman threshold. It was possible to obtain pedestal-free pulses of 284-fs width when wavelength separation corresponded to 11.4 THz (about 90 nm). However, when the wavelengths were 13.2 THz apart (corresponding to maximum Raman gain), considerable pulse energy appeared in the form of a broad pedestal. This complex behavior can be attributed to the XPM effects.

In later experiments, 100-ps pulses from a mode-locked Nd:YAG laser operating at  $1.32\text{ }\mu\text{m}$  were used to synchronously pump a Raman soliton laser [180–182]. This wavelength regime is of interest because conventional fibers with  $\lambda_D \sim 1.3\text{ }\mu\text{m}$  can be used. Furthermore, both the pump and Raman pulses are close to the zero-dispersion wavelength of the fiber so that they can overlap for long enough to provide the required Raman gain (the walk-off length  $\approx 300\text{ m}$ ). Pulse widths as short as 160 fs were obtained in an experiment that employed a 1.1-km fiber that did not even preserve wave polarization [180]. Output pulses contained a broad pedestal with only 20% of the energy appearing in the form of a Raman soliton. In another experiment, a dispersion-shifted fiber with  $\lambda_D = 1.46\text{ }\mu\text{m}$  was used [181]. Raman solitons of

about 200-fs width were then observed through the second- and third-order Stokes lines, generated near 1.5 and 1.6 μm, respectively. This process of cascaded SRS has also been used to generate Raman solitons near 1.5 μm by pumping the laser with 1.06-μm pump pulses [183]. The first three Stokes bands then lie in the normal-GVD regime of a conventional fiber ( $\lambda_D > 1.3 \mu\text{m}$ ). The fourth and fifth Stokes bands form a broad spectral band encompassing the range 1.3–1.5 μm that contains about half of the input energy. Autocorrelation traces of output pulses in the spectral region near 1.35, 1.4, 1.45, and 1.5 μm showed that the energy in the pedestal decreased as the wavelength increased. In fact, output pulses near 1.5 μm were nearly pedestal free.

Even though Raman soliton lasers are capable of generating femtosecond pulses that are useful for many applications, they suffer from a noise problem that limits their usefulness. Measurements of intensity noise for a synchronously pumped Raman soliton laser indicated that the noise was more than 50 dB above the shot-noise level [184]. Pulse-to-pulse timing jitter was also found to be quite large, exceeding 5 ps at 1.6-W pump power. Such large noise levels can be understood if one considers the impact of the Raman-induced frequency shift (see Section 5.5) on the performance of such lasers. For synchronous pumping to be effective, the round-trip time of the Raman soliton inside the laser cavity must be an integer multiple of the spacing between pump pulses. However, the Raman-induced frequency shift changes the group velocity and slows down the pulse in such an unpredictable manner that synchronization is quite difficult to achieve in practice. As a result, Raman soliton lasers generate pulses in a way similar to single-pass Raman amplifiers and suffer from the noise problems associated with such amplifiers.

The performance of Raman soliton lasers can be significantly improved if the Raman-induced frequency shift can be eliminated. It turns out that such frequency shifts can be suppressed with a proper choice of pump power and laser wavelength. In a 1992 experiment, a Raman soliton laser was synchronously pumped by using 200-ps pump pulses from a 1.32-μm Nd:YAG laser. This laser was tunable over a wavelength range of 1.37–1.44 μm [185]. The Raman-induced frequency shift was suppressed in the wavelength range of 1.41–1.44 μm for which the Raman-gain spectrum in Figure 8.2 had a positive slope. Measurements of noise indicated significant reduction in both intensity noise and timing jitter [186]. Physically, Raman-gain dispersion is used to cancel the effects of the last term in Eq. (2.3.44) that is responsible for the Raman-induced frequency shift.

It is difficult to operate a soliton laser at wavelengths below 1.3 μm because most fibers exhibit normal GVD for  $\lambda < 1.3 \mu\text{m}$ . A grating pair is often employed to solve this problem, but its use makes the device bulky. A compact, all-fiber, laser can be built if a suitable fiber exists that can provide anomalous dispersion at the Raman-laser wavelength. Such fibers have become available in recent years in the form of the so-called microstructured or holey fibers. In a 2003 experiment [187], a 23-m-long holey fiber was employed within the cavity of an all-fiber Raman laser to generate 2-ps output pulses at the 1.14-μm wavelength. The laser was pumped synchronously with 17-ps pulses from a Yb-doped fiber laser. The Raman gain was provided by 15 m of standard silica fiber with 3% Ge doping.

In the wavelength region near  $1.6\text{ }\mu\text{m}$ , one can employ dispersion-shifted fibers that permit the control of cavity dispersion while also acting as a Raman-gain medium. Such a fiber was used in a 2004 experiment to realize a compact, synchronously pumped, Raman laser that was also tunable from 1620 to 1660 nm [188]. The 2.1-km-long fiber loop inside a ring cavity had its zero-dispersion wavelength at 1571 nm with a dispersion slope of about  $0.1\text{ ps}^3/\text{km}$ . This laser also employed, as a pump, a gain-switched DFB semiconductor laser emitting 110-ps pulses at a 54.5 MHz repetition rate that were amplified to an average power level of up to 200 mW. Such a Raman laser produced pulses shorter than 0.5 ps over its entire 40-nm tuning range.

### 8.4.3 Soliton-Effect Pulse Compression

In some sense, Raman solitons formed in Raman amplifiers or lasers take advantage of the pulse compression occurring for higher-order solitons (see Section 5.2). Generally speaking, Raman amplification can be used for simultaneous amplification and compression of picosecond optical pulses by taking advantage of the anomalous GVD in optical fibers. In a 1991 experiment 5.8-ps pulses, obtained from a gain-switched semiconductor laser and amplified using an erbium-doped fiber amplifier to an energy level appropriate for forming a fundamental soliton, were compressed to 3.6-ps through Raman amplification in a 23-km-long dispersion-shifted fiber [189]. The physical mechanism behind simultaneous amplification and compression can be understood from Eq. (5.2.3) for the soliton order  $N$ . If a fundamental soliton is amplified adiabatically, the condition  $N = 1$  can be maintained during amplification, provided the soliton width changes as  $P_0^{-1/2}$  as its peak power  $P_0$  increases.

In many practical situations, the input signal pulse is not intense enough to sustain a soliton inside the fiber during Raman amplification. It is possible to realize pulse compression even for such weak pulses through the XPM effects that invariably occur during SRS [190]. In essence, the pump and signal pulses are injected simultaneously into the fiber. The signal pulse extracts energy from the pump pulse through SRS and is amplified. At the same time, it interacts with the pump pulse through XPM that imposes a nearly linear frequency chirp on it and compresses it in the presence of anomalous GVD. As discussed in Section 7.5 in the context of XPM-induced pulse compression, the effectiveness of such a scheme depends critically on the relative group-velocity mismatch between the pump and signal pulses. A simple way to minimize the group-velocity mismatch and maximize the XPM-induced frequency chirp is to choose the zero-dispersion wavelength of the fiber in the middle of the pump and signal wavelengths.

Numerical simulations based on Eqs (8.3.1) and (8.3.2) show that compression factors as large as 15 can be realized while the signal-pulse energy is amplified a millionfold [190]. Figure 8.23 shows (a) the compression factor and (b) the amplification factor as a function of the propagation distance ( $\xi = z/L_D$ ) for several values of the parameter  $N$ , related to the peak power  $P_0$  of pump pulses through  $N = (\gamma_p P_0 L_D)^{1/2}$ , where  $L_D$  is defined in Eq. (8.3.5). The pump and signal pulses are assumed to be Gaussian, have the same width, and propagate at the same speed. Pulse compression is maximum for an optimum fiber length, a feature similar to that of compressors based on

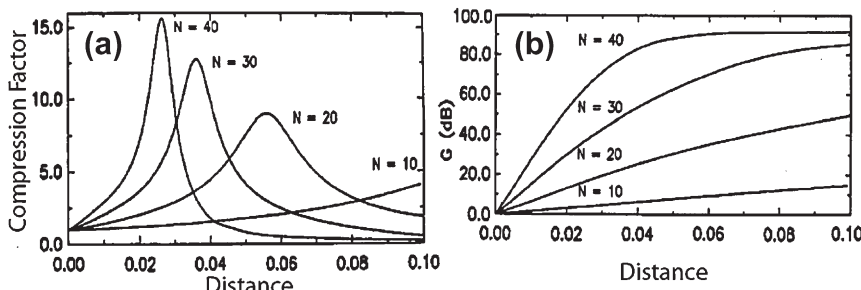


**Figure 8.23** (a) Compression factor and (b) amplification factor as a function of normalized distance for several values of  $N$  in the case of a Gaussian-shape pump and signal pulses.  
(After Ref. [190]; © 1993 OSA.)

higher-order solitons. This behavior is easily understood by noting that GVD reduces the XPM-induced chirp to nearly zero at the point of maximum compression (see Section 3.2). The main point to note from Figure 8.23 is that weak input pulses can be amplified by 50–60 dB while getting compressed simultaneously by a factor of 10 or more. The quality of compressed pulses is also quite good with no pedestal and little ringing. The qualitative features of pulse compression remain nearly the same when pulse widths or group velocities of the pump and signal pulses are not the same, making this technique quite attractive from a practical standpoint. Simultaneous amplification and compression of picosecond optical pulses were indeed observed in a 1996 experiment [191].

## 8.5 POLARIZATION EFFECTS

In the scalar approach used so far, it has been implicitly assumed that both pump and signal are copolarized and maintain their state of polarization (SOP) inside the fiber. However, unless a special kind of polarization-maintaining fiber is used for making Raman amplifiers, residual fluctuating birefringence of most fibers changes the SOP of any optical field in a random fashion and leads to polarization-mode dispersion (PMD), a phenomenon discussed in Section 7.7.1. In this section we develop a vector theory of SRS. It turns out that the amplified signal fluctuates over a wide range if PMD changes with time, and the average gain is significantly lower than that expected in the absence of PMD [192–195]. Such features have also been observed experimentally [196–198].

### 8.5.1 Vector Theory of Raman Amplification

The starting point is Eq. (2.1.10) for the third-order nonlinear polarization induced inside the fiber material (silica glass) in response to an optical field  $\mathbf{E}(\mathbf{r}, t)$ . In the scalar case, this equation leads to Eq. (2.3.33) as only the component  $\chi_{xxxx}^{(3)}$  is relevant for

the nonlinear response. In the vector case, the situation is much more complicated. Using Eq. (2.3.32) together with  $\mathbf{E}(t) = \frac{1}{2}[\mathbf{E}(t) \exp(-i\omega_0 t) + \text{c.c.}]$ , the slowly varying part of polarization can be written in the form

$$P_i^{\text{NL}}(t) = \frac{\epsilon_0}{4} \sum_j \sum_k \sum_l \chi_{ijkl}^{(3)} E_j(t) \int_{-\infty}^t R(t-t_1) E_k^*(t_1) E_l(t_1) dt_1, \quad (8.5.1)$$

where  $E_j$  is the  $j$ th component of the slowly varying field  $\mathbf{E}$  and the spatial coordinate  $\mathbf{r}$  has been suppressed to simplify the notation.

The functional form of the nonlinear response function  $R(t)$  is similar to that given in Eq. (2.3.38) and is given by [5]

$$R(t) = (1 - f_R) \delta(t) + f_a h_a(t) + f_b h_b(t), \quad (8.5.2)$$

where  $f_R \equiv f_a + f_b$  is the fractional contribution added by silica nuclei through the Raman response functions  $h_a(t)$  and  $h_b(t)$ , normalized such that  $\int_0^\infty h_j(t) dt = 1$  for  $j = a$  and  $b$ . Physically,  $h_a$  and  $h_b$  represent the isotropic and anisotropic parts of the nuclear response with the relative strengths  $f_a$  and  $f_b$ , respectively.

The tensor nature of  $\chi^{(3)}$  plays an important role in Eq. (8.5.1). For silica fibers, the third-order susceptibility has the form given in Eq. (6.1.2). Using it in Eq. (8.5.1) together with Eq. (8.5.2), the product  $\chi_{ijkl}^{(3)} R(t)$  can be written as [5]:

$$\begin{aligned} \chi_{ijkl}^{(3)} R(t) &= \chi_{xxx}^{(3)} \left[ \frac{1-f_R}{3} (\delta_{ij} \delta_{kl} + \delta_{ik} \delta_{jl} + \delta_{il} \delta_{jk}) \right. \\ &\quad \left. + f_a h_a(t) \delta_{ij} \delta_{kl} + \frac{1}{2} f_b h_b(t) (\delta_{ik} \delta_{jl} + \delta_{il} \delta_{jk}) \right], \end{aligned} \quad (8.5.3)$$

where the three components of  $\chi_{ijkl}^{(3)}$  appearing in Eq. (6.1.2) were taken to be equal in magnitude.

In the case of SRS, we should consider the pump and Stokes fields separately. We follow the treatment of Section 7.6.1 and write the total electric field  $\mathbf{E}$  and induced polarization  $\mathbf{P}^{\text{NL}}$  in the form

$$\mathbf{E}(t) = \text{Re}[\mathbf{E}_p \exp(-i\omega_p t) + \mathbf{E}_s \exp(-i\omega_s t)], \quad (8.5.4)$$

$$\mathbf{P}_{\text{NL}}(t) = \text{Re}[\mathbf{P}_p \exp(-i\omega_p t) + \mathbf{P}_s \exp(-i\omega_s t)]. \quad (8.5.5)$$

The dependence of  $\mathbf{P}_p$  and  $\mathbf{P}_s$  on the pump and Stokes fields is found by substituting Eq. (8.5.4) in Eq. (8.5.1). The result is given by

$$\begin{aligned} \mathbf{P}_j &= \frac{3\epsilon_0}{4} \chi_{xxx}^{(3)} \left[ c_0 (\mathbf{E}_j \cdot \mathbf{E}_j) \mathbf{E}_j^* + c_1 (\mathbf{E}_j^* \cdot \mathbf{E}_j) \mathbf{E}_j \right. \\ &\quad \left. + c_2 (\mathbf{E}_m^* \cdot \mathbf{E}_m) \mathbf{E}_j + c_3 (\mathbf{E}_m \cdot \mathbf{E}_j) \mathbf{E}_m^* + c_4 (\mathbf{E}_m^* \cdot \mathbf{E}_j) \mathbf{E}_m \right], \end{aligned} \quad (8.5.6)$$

where  $j \neq m$  and  $c_0 = \frac{1}{3}(1 - f_R) + \frac{1}{2} f_b$ . The remaining coefficients are defined as

$$c_1 = \frac{2}{3}(1 - f_R) + f_a + \frac{1}{2} f_b, \quad c_2 = \frac{2}{3}(1 - f_R) + f_a + \frac{1}{2} f_b \tilde{h}_b(\Omega), \quad (8.5.7)$$

$$c_3 = \frac{2}{3}(1 - f_R) + \frac{1}{2} f_b + f_a \tilde{h}_a(\Omega), \quad c_4 = \frac{2}{3}(1 - f_R) + \frac{1}{2} f_b + \frac{1}{2} f_b \tilde{h}_b(\Omega), \quad (8.5.8)$$

with  $\Omega = \omega_p - \omega_s$ . In arriving at Eq. (8.5.6), we made use of the relation  $\tilde{h}_a(0) = \tilde{h}_b(0) = 1$ .

We can now introduce the Jones vectors  $|A_p\rangle$  and  $|A_s\rangle$  as in Section 7.6.1. To keep the following analysis relatively simple, we assume that both the pump and Stokes are in the form of CW or quasi-CW waves and neglect the dispersive effects. With this simplification, we obtain the following set of two coupled vector equations [193]:

$$\frac{d|A_p\rangle}{dz} + \frac{\alpha_p}{2}|A_p\rangle + \frac{i}{2}\omega_p \mathbf{b}_l \cdot \boldsymbol{\sigma}|A_p\rangle = i\gamma_p \left( c_1 \langle A_p | A_p \rangle + c_0 |A_p^*\rangle \langle A_p^*| \right. \\ \left. + c_2 \langle A_s | A_s \rangle + c_3 |A_s\rangle \langle A_s| + c_4 |A_s^*\rangle \langle A_s^*| \right) |A_p\rangle, \quad (8.5.9)$$

$$\frac{d|A_s\rangle}{dz} + \frac{\alpha_s}{2}|A_s\rangle + \frac{i}{2}\omega_s \mathbf{b}_l \cdot \boldsymbol{\sigma}|A_s\rangle = i\gamma_s \left( c_1 \langle A_s | A_s \rangle + c_0 |A_s^*\rangle \langle A_s^*| \right. \\ \left. + c_2 \langle A_p | A_p \rangle + c_3 |A_p\rangle \langle A_p| + c_4 |A_p^*\rangle \langle A_p^*| \right) |A_s\rangle, \quad (8.5.10)$$

where the effects of linear birefringence are included through the birefringence vector  $\mathbf{b}_l$ .

The coefficients  $c_2$ ,  $c_3$ , and  $c_4$  contain the Fourier transforms,  $\tilde{h}_a(\Omega)$  and  $\tilde{h}_b(\Omega)$  of the two Raman response functions  $h_a(t)$  and  $h_b(t)$  appearing in Eq. (8.5.2). Their imaginary parts can be used to define the corresponding Raman gains,  $g_a$  and  $g_b$  for the Stokes field as [5]

$$g_j = \gamma_s f_j \text{Im}[\tilde{h}_j(\Omega)]; \quad (j = a, b), \quad (8.5.11)$$

where  $\Omega = \omega_p - \omega_s$  is the Raman shift. For silica fibers,  $g_b/g_a$  is much smaller than 1. In the case of pump equation (8.5.9), we should replace  $\Omega$  with  $-\Omega$ ; this change sign makes  $g_j$  negative in Eq. (8.5.11). This is expected since the gain for Stokes results in a power loss for the pump. The real parts of  $\tilde{h}_a(\Omega)$  and  $\tilde{h}_b(\Omega)$  lead to small changes in the refractive index. Such changes invariably occur and are governed by the Kramers–Kronig relation. It is useful to introduce two dimensionless parameters  $\delta_a$  and  $\delta_b$  which are defined as

$$\delta_j = (f_j/c_1) \text{Re}[\tilde{h}_j(\Omega) - 1]; \quad (j = a, b). \quad (8.5.12)$$

Equations (8.5.9) and (8.5.10) appear quite complicated in the Jones-matrix formalism. They can be simplified considerably if we write them in the Stokes space using the Pauli spin vector  $\boldsymbol{\sigma}$ . After introducing the Stokes vectors for the pump and Stokes fields as

$$\mathbf{P} = \langle A_p | \boldsymbol{\sigma} | A_p \rangle, \quad \mathbf{S} = \langle A_s | \boldsymbol{\sigma} | A_s \rangle, \quad (8.5.13)$$

and making use of the identities in Eqs (7.6.12)–(7.6.14) we obtain the following two vector equations that govern the dynamics of  $\mathbf{P}$  and  $\mathbf{S}$  on the Poincaré sphere:

$$\frac{d\mathbf{P}}{dz} + \alpha_p \mathbf{P} = -\frac{\omega_p}{2\omega_s} [(g_a + 3g_b) P_s \mathbf{P} + (g_a + g_b) P_p \mathbf{S} - 2g_b P_p \mathbf{S}_3] \\ + (\omega_p \mathbf{b}_l + \mathbf{W}_p) \times \mathbf{P}, \quad (8.5.14)$$

$$\frac{d\mathbf{S}}{dz} + \alpha_s \mathbf{S} = \frac{1}{2} [(g_a + 3g_b) P_p \mathbf{S} + (g_a + g_b) P_s \mathbf{P} - 2g_b P_s \mathbf{P}_3] \\ + (\omega_s \mathbf{b}_l + \mathbf{W}_s) \times \mathbf{S}, \quad (8.5.15)$$

where  $P_p = |\mathbf{P}|$  is the pump power,  $P_s = |\mathbf{S}|$  is the Stokes power, and

$$\mathbf{W}_p = \frac{2\gamma_p}{3} [\mathbf{P}_3 + 2(1 + \delta_b)\mathbf{S}_3 - (2 + \delta_a + \delta_b)\mathbf{S}], \quad (8.5.16)$$

$$\mathbf{W}_s = \frac{2\gamma_s}{3} [\mathbf{S}_3 + 2(1 + \delta_b)\mathbf{P}_3 - (2 + \delta_a + \delta_b)\mathbf{P}]. \quad (8.5.17)$$

The vectors  $\mathbf{W}_p$  and  $\mathbf{W}_s$  account for the nonlinear polarization rotation on the Poincaré sphere through the SPM and XPM effects.

Equations (8.5.14) and (8.5.15) simplify considerably when both the pump and signal are linearly polarized, as  $\mathbf{P}$  and  $\mathbf{S}$  then lie in the equatorial plane of the Poincaré sphere with  $P_3 = S_3 = 0$ . In the absence of birefringence ( $\mathbf{b}_l = 0$ ),  $\mathbf{P}$  and  $\mathbf{S}$  maintain their initial SOPs with propagation. When the pump and signal are copolarized, the two gain terms add in phase, and Raman gain is maximum with a value  $g_{\parallel} = g_a + 2g_b$ . In contrast, when the two are orthogonally polarized, the two gain terms add out of phase, and the Raman gain becomes minimum with the value  $g_{\perp} = g_b$ . These two gains correspond to the solid and dashed curves of Figure 8.2, respectively, which can be used to deduce the depolarization ratio  $g_{\perp}/g_{\parallel}$ . This ratio is measured to be about 1/3 near  $\Omega/(2\pi) = 1$  THz, but it drops to below 0.05 near the gain peak located at  $\Omega = \Omega_R$  [14]. If we use the value  $g_{\perp}/g_{\parallel} = 1/3$  together with the relation  $g_{\parallel}/g_{\perp} = 2 + g_a/g_b$ , we deduce that  $g_b = g_a$  for small values of  $\Omega$ . However, close to the Raman gain peak, the contribution of  $g_b(t)$  becomes relatively minor.

In the case of circular polarization, the vectors  $\mathbf{P}$  and  $\mathbf{S}$  point toward the north or south pole on the Poincaré sphere. It is easy to deduce from Eqs (8.5.14) and (8.5.15) that  $g_{\parallel} = g_a + g_b$  and  $g_{\perp} = 2g_b$  under such conditions. The depolarization ratio  $g_{\parallel}/g_{\perp}$  for circular polarization is thus expected to be quite different compared to the case of linear polarization. In particular, it should be close to 1 for small values of  $\Omega$  for which  $g_b \approx g_a$ .

We now solve Eqs (8.5.14) and (8.5.15) in the presence of fluctuating residual birefringence. Such fluctuations occur on a length scale ( $\sim 10$  m) much smaller than a typical nonlinear length ( $> 1$  km). As a result, the tips of  $\mathbf{P}$  and  $\mathbf{S}$  move on the Poincaré sphere randomly at high rates proportional to  $\omega_p$  and  $\omega_s$ , respectively. However, the SRS process depends only on the relative orientation of  $\mathbf{P}$  and  $\mathbf{S}$ . To simplify the following analysis, we adopt a rotating frame in which  $\mathbf{P}$  remains stationary and focus on the changes in the relative angle between  $\mathbf{P}$  and  $\mathbf{S}$ . Equations (8.5.18) and (8.5.19) then become [193]

$$\frac{d\mathbf{P}}{dz} + \alpha_p \mathbf{P} = -\frac{\omega_p}{2\omega_s} [(g_a + 3g_b)P_s \mathbf{P} + (g_a + g_b/3)P_p \mathbf{S}] - \bar{\gamma}_p \mathbf{S} \times \mathbf{P}, \quad (8.5.18)$$

$$\frac{d\mathbf{S}}{dz} + \alpha_s \mathbf{S} = \frac{1}{2} [(g_a + 3g_b)P_p \mathbf{S} + (g_a + g_b/3)P_s \mathbf{P}] - (\Omega \mathbf{b}' + \bar{\gamma}_s \mathbf{P}) \times \mathbf{S}, \quad (8.5.19)$$

where  $\mathbf{b}'$  is related to  $\mathbf{b}_l$  through a rotation on the Poincaré sphere and

$$\bar{\gamma}_j = (2\gamma_j/9)(4 + 3\delta_a + \delta_b), \quad \Omega = \omega_p - \omega_s. \quad (8.5.20)$$

To simplify Eqs (8.5.18) and (8.5.19) further, we neglect the pump depletion as well as signal-induced XPM assuming that  $P_s \ll P_p$ , a condition often valid in practice. The pump equation (8.5.18) then contains only the loss term and can be easily integrated to yield

$$\mathbf{P}(z) = \hat{\mathbf{p}} P_{\text{in}} \exp(-\alpha_p z) \equiv \hat{\mathbf{p}} P_p(z), \quad (8.5.21)$$

where  $\hat{\mathbf{p}}$  is the SOP of the pump at the input end. The term  $\tilde{\gamma}_s \mathbf{P} \times \mathbf{S}$  in Eq. (8.5.19) represents the pump-induced nonlinear polarization rotation of the signal being amplified. Such rotations of the Stokes vector do not affect the Raman gain. We can eliminate this term with a simple transformation to obtain [193]

$$\frac{d\mathbf{S}}{dz} + \alpha_s \mathbf{S} = \frac{1}{2} [(g_a + 3g_b) P_p \mathbf{S} + (g_a + g_b/3) P_s \mathbf{P}] - \Omega \mathbf{b} \times \mathbf{S}, \quad (8.5.22)$$

where  $\mathbf{b}$  is related to  $\mathbf{b}'$  by a deterministic rotation that does not affect its statistical properties. It is modeled as a three-dimensional Gaussian process whose first-order and second-order moments are given in Eq. (7.7.6) in terms of the PMD parameter  $D_p$  of the fiber. The stochastic differential Eq. (8.5.22) should be treated on physical ground in the Stratonovich sense [199].

Equation (8.5.22) can be solved by noting that the terms that do not change the direction of  $\mathbf{S}$  can be removed with the transformation

$$\mathbf{S} = \mathbf{s} \exp \left\{ \int_0^z \left[ \frac{1}{2} (g_a + 3g_b) P_p(z) - \alpha_s \right] dz \right\}. \quad (8.5.23)$$

The new Stokes vector  $\mathbf{s}$  then satisfies

$$\frac{ds}{dz} = \frac{1}{2} (g_a + g_b/3) P_p(z) s_0(z) \hat{\mathbf{p}} - \Omega \mathbf{b} \times \mathbf{s}, \quad (8.5.24)$$

where  $s_0 = |\mathbf{s}|$  is the magnitude of vector  $\mathbf{s}$ . The equation governing evolution of  $s_0$  along the fiber length is obtained by using the relation  $s_0^2 = \mathbf{s} \cdot \mathbf{s}$  and is given by

$$\frac{ds_0}{dz} = \frac{\mathbf{s}}{s_0} \cdot \frac{ds}{dz} = (g_a + g_b/3) P_p(z) \hat{\mathbf{p}} \cdot \mathbf{s}. \quad (8.5.25)$$

Equation (8.5.24) is derived assuming that both the pump and signal travel in the same direction (the so-called forward pumping scheme). In the case of backward pumping, the derivative  $d\mathbf{P}/dz$  in Eq. (8.5.14) becomes negative. Following the preceding procedure, the Stokes equation can still be written in the form of Eq. (8.5.14) provided  $\Omega$  is redefined as  $\Omega = -(\omega_p + \omega_s)$ . Such a large value of  $\Omega$  enhances the contribution of the birefringence term in Eq. (8.5.24). It will be seen later that backward pumping improves the performance of Raman amplifiers because of this feature.

## 8.5.2 PMD Effects on Raman Amplification

The residual birefringence of fibers, responsible for PMD, affects the performance of Raman amplifiers considerably because of its statistical nature. Equation (8.5.24) can be used to calculate the power  $P_s$  of the amplified signal as well its SOP at any

distance within the amplifier. In practice,  $\mathbf{b}(z)$  fluctuates along the fiber in a dynamic fashion as it depends on environmental factors such as stress and temperature. As a result, the amplified signal  $P_s(L)$  at the output of an amplifier also fluctuates. Such fluctuations affect the performance of any Raman amplifier. In this section we calculate the average and the variance of the amplified signal fluctuating because of PMD.

The signal gain is defined as  $G(L) = P_s(L)/P_s(0)$ . Its average value,  $G_{av}$ , and variance of signal power fluctuations,  $\sigma_s^2$ , can be calculated using

$$G_{av} = \overline{P_s(L)} / P_s(0), \quad \sigma_s^2 = \overline{P_s^2(L)} / [\overline{P_s(L)}]^2 - 1. \quad (8.5.26)$$

To find the average signal power  $\overline{P_s(L)}$  at the end of a Raman amplifier of length  $L$ , we calculate  $\overline{s_0}$  by taking an average over  $\mathbf{b}$  in Eq. (8.5.25). However, this average depends on  $\rho = s_0 \cos \theta$ , where  $\theta$  represents an angle in the Stokes space between the pump and signal SOPs. Using a well-known technique [199], we obtain the following two coupled but deterministic equations [193]:

$$\frac{ds_0}{dz} = \frac{1}{2}(g_a + g_b/3)P_p(z)\rho, \quad (8.5.27)$$

$$\frac{d\rho}{dz} = \frac{1}{2}(g_a + g_b/3)P_p(z)\overline{s_0} - \eta\rho, \quad (8.5.28)$$

where  $\eta = 1/L_d = D_p^2\Omega^2/3$ . The diffusion length  $L_d$  is a measure of the distance after which the SOPs of the two optical fields, separated in frequency by  $\Omega$ , become decorrelated.

Equations (8.5.27) and (8.5.28) are two linear first-order differential equations that can be easily integrated. When PMD effects are large and  $L_d \ll L$ ,  $\rho$  reduces to zero over a short fiber section. The average gain in this case is given by

$$G_{av} = \exp \left[ \frac{1}{2}(g_a + g_b/3)P_{in}L_{eff} - \alpha_s L \right]. \quad (8.5.29)$$

Compared to the ideal copolarized case (no birefringence) for which  $g_{||} = g_a + 2g_b$ , PMD reduces the Raman gain by a factor of about 2 [58]. This is expected on physical grounds. However, it should be stressed that the amplification factor  $G_A$  is reduced by a large factor because of its exponential dependence on  $g_a$  and  $g_b$ .

The variance of signal fluctuations requires the second-order moment  $\overline{P_s^2(L)}$  of the amplified signal. Following a similar averaging procedure [193], Eq. (8.5.24) leads to the following set of three linear equations:

$$\frac{ds_0^2}{dz} = (g_a + g_b/3)P_p(z)\rho_1, \quad (8.5.30)$$

$$\frac{d\rho_1}{dz} = -\eta\rho_2 + \frac{1}{2}(g_a + g_b/3)P_p(z)[\overline{s_0^2} + \rho_2], \quad (8.5.31)$$

$$\frac{d\rho_2}{dz} = -3\eta\rho_2 + \eta\overline{s_0^2} + (g_a + g_b/3)P_p(z)\rho_2, \quad (8.5.32)$$

where  $\rho_1 = \overline{s_0^2 \cos \theta}$  and  $\rho_2 = \overline{s_0^2 \cos^2 \theta}$ . These equations show that signal fluctuations have their origin in fluctuations of the relative angle  $\theta$  between the Stokes vectors associated with the pump and signal.

To illustrate the impact of PMD on the performance of Raman amplifiers, we consider a 10-km-long Raman amplifier pumped with 1 W of power using a single 1.45- $\mu\text{m}$  laser and use  $g_a = 0.6 \text{ W}^{-1}/\text{km}$  with  $g_b/g_a = 0.012$  near the signal wavelength 1.55  $\mu\text{m}$ . Fiber losses are taken to be 0.273 dB/km and 0.2 dB/km at the pump and signal wavelengths, respectively. Figure 8.24 shows how  $G_{av}$  and  $\sigma_s$  change with the PMD parameter  $D_p$  when the input signal is copolarized (solid curves) or orthogonally polarized (dashed curves) with respect to the pump. The curves are shown for both the forward and backward pumping schemes. When  $D_p$  is zero, the two beams maintain their SOP, and the copolarized signal experiences a maximum gain of 17.6 dB. In contrast, an orthogonally polarized signal exhibits a 1.7-dB loss, irrespective of the pumping configuration. The loss is not exactly 2 dB because of a finite value of  $g_b$ . As the PMD parameter increases, the gain difference between the copolarized and orthogonally polarized cases decreases and disappears eventually.

The level of signal fluctuations in Figure 8.24 increases quickly with the PMD parameter, reaches a peak value, and then decreases slowly toward zero with a further increase in  $D_p$  because of an averaging effect produced by the PMD. The location of the peak depends on the pumping scheme as well as on the initial polarization of the pump; the noise level near this peak exceeds 40%. If a fiber with low PMD is used, the noise level can exceed 70% under some operating conditions. The behavior for backward pumping is similar to those for forward pumping but the peak shifts to smaller  $D_p$  values. This shift is due to a much larger value of  $|\Omega| = \omega_p + \omega_s$ . Since the diffusion length scales as  $|\Omega|^{-2}$ , it is smaller by about a factor of  $(\omega_p + \omega_s)/(\omega_p - \omega_s) \approx 30$

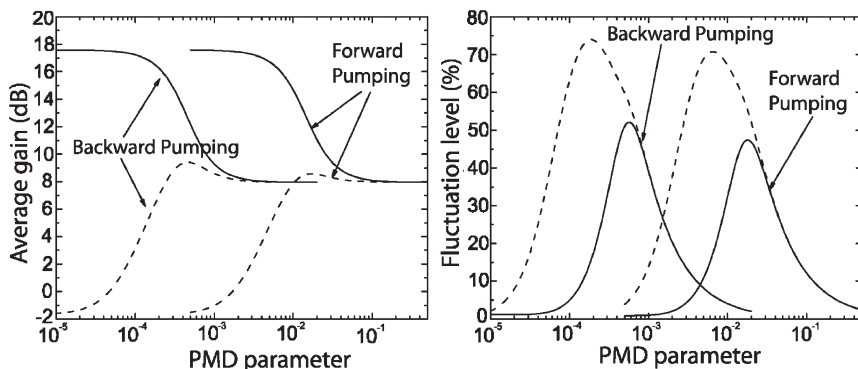


**Figure 8.24** (a) Average gain and (b) standard deviation of signal fluctuations at the output of a Raman amplifier as a function of PMD parameter in the cases of forward and backward pumping. The solid and dashed curves correspond to the cases of copolarized and orthogonally polarized signals, respectively. (After Ref. [193]; © 2003 OSA.)

in the backward-pumping case. A smaller diffusion length results in rapid averaging over birefringence fluctuations and reduces the noise level.

An important question is which pumping configuration is better from a practical viewpoint. The answer depends on the value of  $D_p$ . For fibers with values of  $D_p < 0.001 \text{ ps}/\sqrt{\text{km}}$ , forward pumping is the appropriate choice. However,  $D_p$  exceeds  $0.01 \text{ ps}/\sqrt{\text{km}}$  for most fibers. In this situation, backward pumping produces the least signal degradation in practice. It also reduces the polarization dependence of the Raman gain in optical communication systems where the SOP of the input signal itself may change with time in a random fashion.

## PROBLEMS

- 8.1** What is meant by Raman scattering? Explain its origin. What is the difference between spontaneous and stimulated Raman scattering?
- 8.2** Solve Eqs (8.1.2) and (8.1.3) neglecting pump deletion. Calculate the Stokes power at the output of a 1-km-long fiber when  $1\text{-}\mu\text{W}$  power is injected together with an intense pump beam. Assume  $g_R I_p(0) = 2 \text{ km}^{-1}$  and  $\alpha_p = \alpha_s = 0.2 \text{ dB/km}$ .
- 8.3** Perform the integration in Eq. (8.1.9) using the method of steepest descent and derive Eq. (8.1.9).
- 8.4** Use Eq. (8.1.9) to derive the Raman-threshold condition given in Eq. (8.1.13).
- 8.5** Solve Eqs (8.1.2) and (8.1.3) analytically after assuming  $\alpha_p = \alpha_s$ .
- 8.6** Calculate the threshold pump power of a  $1.55\text{-}\mu\text{m}$  Raman laser whose cavity includes a 1-km-long fiber with  $40\text{-}\mu\text{m}^2$  effective core area. Use  $\alpha_p = 0.3 \text{ dB/km}$  and total cavity losses of 6 dB. Use the Raman gain from Figure 8.2.
- 8.7** Explain the technique of time-dispersion tuning used commonly for synchronously pumped Raman lasers. Estimate the tuning range for the laser of Problem 8.7.
- 8.8** Solve Eqs (8.3.1) and (8.3.2) analytically after setting  $\beta_{2p} = \beta_{2s} = 0$ .
- 8.9** Use the results of the preceding problem to plot the output pulse shapes for Raman amplification in a 1-km-long fiber. Assume  $\lambda_p = 1.06 \mu\text{m}$ ,  $\lambda_s = 1.12 \mu\text{m}$ ,  $\gamma_p = 10 \text{ W}^{-1} \text{ km}$ ,  $g_R = 1 \times 10^{-3} \text{ m/W}$ ,  $d = 5 \text{ ps/m}$ , and  $A_{\text{eff}} = 40 \mu\text{m}^2$ . Input pump and Stokes pulses are Gaussian with the same 100-ps width (FWHM) and with 1 kW and 10 mW peak powers, respectively.
- 8.10** Solve Eqs (8.3.16) and (8.3.17) numerically using the split-step Fourier method and reproduce the results shown in Figures 8.11 and 8.12.
- 8.11** Solve Eqs (8.3.16) and (8.3.17) in the case of anomalous dispersion and reproduce the results shown in Figure 8.19. Explain why the Raman pulse forms a soliton when the walk-off length and the dispersion length have comparable magnitudes.
- 8.12** Design an experiment for amplifying 50-ps (FWHM) Gaussian pulses through SRS by at least 30 dB such that they are also compressed by a factor of 10. Use numerical simulations to verify your design.

- 8.13** Derive Eq. (8.5.3) by using Eq. (8.5.1) and taking into account the properties of the  $\chi^{(3)}$  tensor discussed in Section 6.1.
- 8.14** Derive the set of two coupled vector equations given as Eqs (8.5.9) and (8.5.10) starting from the nonlinear polarization given in Eq. (8.5.1).
- 8.15** Convert Eqs (8.5.9) and (8.5.10) to the Stokes space and prove that the Stokes vectors for the pump and signal indeed satisfy Eqs (8.5.14) and (8.5.15).

## REFERENCES

- [1] C. V. Raman, *Indian J. Phys.* **2**, 387 (1928).
- [2] E. J. Woodbury and W. K. Ng, *Proc. IRE* **50**, 2347 (1962).
- [3] G. Eckhardt, R. W. Hellwarth, F. J. McClung, S. E. Schwarz, and D. Weiner, *Phys. Rev. Lett.* **9**, 455 (1962).
- [4] W. Kaiser and M. Maier, in *Laser Handbook*, Vol. 2, F. T. Arecchi and E. O. Schulz-Dubois, Eds. (North-Holland, 1972), Chap. E2.
- [5] R. W. Hellwarth, *Prog. Quantum Electron.* **5**, 1 (1977).
- [6] Y. R. Shen, *The Principles of Nonlinear Optics* (Wiley, New York, 1984), Chap. 10.
- [7] R. W. Boyd, *Nonlinear Optics*, 3rd ed. (Academic Press, Boston, 2008), Chap. 10.
- [8] R. H. Stolen, E. P. Ippen, and A. R. Tynes, *Appl. Phys. Lett.* **20**, 62 (1972).
- [9] R. H. Stolen and E. P. Ippen, *Appl. Phys. Lett.* **22**, 276 (1973).
- [10] R. H. Stolen, J. P. Gordon, W. J. Tomlinson, and H. A. Haus, *J. Opt. Soc. Am. B* **6**, 1159 (1989).
- [11] D. J. Dougherty, F. X. Kärtner, H. A. Haus, and E. P. Ippen, *Opt. Lett.* **20**, 13 (1995).
- [12] R. H. Stolen, in *Raman Amplifiers for Telecommunications, Part 1*, M. N. Islam, Ed. (Springer, 2004), (Chap. 2.).
- [13] X. Li, P. L. Voss, J. Chen, K. F. Lee, and P. Kumar, *Opt. Express* **13**, 2236 (2005).
- [14] I. Mandelbaum, M. Bolshtyansky, T. F. Heinz, and A. R. Hight Walker, *J. Opt. Soc. Am. B* **23**, 621 (2006).
- [15] R. Shuker and R. W. Gammon, *Phys. Rev. Lett.* **25**, 222 (1970).
- [16] R. G. Smith, *Appl. Opt.* **11**, 2489 (1972).
- [17] J. AuYeung and A. Yariv, *IEEE J. Quantum Electron.* **14**, 347 (1978).
- [18] A. Picozzi, C. Montes, J. Botineau, and E. Picholle, *J. Opt. Soc. Am. B* **15**, 1309 (1998).
- [19] C. R. Menyuk, M. N. Islam, and J. P. Gordon, *Opt. Lett.* **16**, 566 (1991).
- [20] A. Höök, *Opt. Lett.* **17**, 115 (1992).
- [21] S. Kumar, A. Selvarajan, and G. V. Anand, *Opt. Commun.* **102**, 329 (1993); *J. Opt. Soc. Am. B* **11**, 810 (1994).
- [22] C. Headley and G. P. Agrawal, *IEEE J. Quantum Electron.* **31**, 2058 (1995).
- [23] C. Headley and G. P. Agrawal, *J. Opt. Soc. Am. B* **13**, 2170 (1996).
- [24] K. J. Blow and D. Wood, *IEEE J. Quantum Electron.* **25**, 2656 (1989).
- [25] E. Golovchenko, P. V. Mamyshev, A. N. Pilipetskii, and E. M. Dianov, *IEEE J. Quantum Electron.* **26**, 1815 (1990); *J. Opt. Soc. Am. B* **8**, 1626 (1991).
- [26] P. N. Morgan and J. M. Liu, *IEEE J. Quantum Electron.* **27**, 1011 (1991).
- [27] P. V. Mamyshev, A. M. Vertikov, and A. M. Prokhorov, *Sov. Lightwave Commun.* **2**, 73 (1992).
- [28] A. M. Vertikov and P. V. Mamyshev, *Sov. Lightwave Commun.* **2**, 119 (1992).
- [29] S. Trillo and S. Wabnitz, *J. Opt. Soc. Am. B* **9**, 1061 (1992).

- [30] E. Golovchenko and A. N. Pilipetskii, *J. Opt. Soc. Am. B* **11**, 92 (1994).
- [31] R. Schulz and H. Harde, *J. Opt. Soc. Am. B* **12**, 1279 (1995).
- [32] P. T. Dinda, G. Millot, and S. Wabnitz, *J. Opt. Soc. Am. B* **15**, 1433 (1998).
- [33] C. Lin and R. H. Stolen, *Appl. Phys. Lett.* **28**, 216 (1976).
- [34] C. Lin, L. G. Cohen, R. H. Stolen, G. W. Tasker, and W. G. French, *Opt. Commun.* **20**, 426 (1977).
- [35] V. V. Grigoryants, B. L. Davydov, M. E. Zhabotinsky, V. F. Zolin, G. A. Ivanov, V. I. Smirnov, and Y. K. Chamorovski, *Opt. Quantum Electron.* **9**, 351 (1977).
- [36] L. G. Cohen and C. Lin, *IEEE J. Quantum Electron.* **QE-14**, 855 (1978).
- [37] V. S. Butylkin, V. V. Grigoryants, and V. I. Smirnov, *Opt. Quantum Electron.* **11**, 141 (1979).
- [38] P.-J. Gao, C.-J. Nie, T.-L. Yang, and H.-Z. Su, *Appl. Phys.* **24**, 303 (1981).
- [39] G. Rosman, *Opt. Quantum Electron.* **14**, 92 (1982).
- [40] Y. Ohmori, Y. Sesaki, and T. Edahiro, *Trans. IECE Japan* **E66**, 146 (1983).
- [41] R. Pini, M. Mazzoni, R. Salimbeni, M. Matera, and C. Lin, *Appl. Phys. Lett.* **43**, 6 (1983).
- [42] M. Rothschild and H. Abad, *Opt. Lett.* **8**, 653 (1983).
- [43] F. R. Barbosa, *Appl. Opt.* **22**, 3859 (1983).
- [44] R. H. Stolen, C. Lee, and R. K. Jain, *J. Opt. Soc. Am. B* **1**, 652 (1984).
- [45] C. Lin, *J. Lightwave Technol.* **LT-4**, 1103 (1986).
- [46] A. S. L. Gomes, V. L. DaSilva, J. R. Taylor, B. J. Ainslie, and S. P. Craig, *Opt. Commun.* **64**, 373 (1987).
- [47] K. X. Liu and E. Garmire, *IEEE J. Quantum Electron.* **27**, 1022 (1991).
- [48] J. Chang, D. Baiocchi, J. Vas, and J. R. Thompson, *Opt. Commun.* **139**, 227 (1997).
- [49] E. Landahl, D. Baiocchi, and J. R. Thompson, *Opt. Commun.* **150**, 339 (1998).
- [50] M. G. Raymer and I. A. Walmsley, in *Progress in Optics*, Vol. 30, E. Wolf, Ed. (Elsevier, 1990), (Chap. 3).
- [51] K. O. Hill, B. S. Kawasaki, and D. C. Johnson, *Appl. Phys. Lett.* **28**, 608 (1976); *Appl. Phys. Lett.* **29**, 181 (1976).
- [52] R. K. Jain, C. Lin, R. H. Stolen, W. Pleibel, and P. Kaiser, *Appl. Phys. Lett.* **30**, 162 (1977).
- [53] D. C. Johnson, K. O. Hill, B. S. Kawasaki, and D. Kato, *Electron. Lett.* **13**, 53 (1977).
- [54] R. H. Stolen, C. Lin, and R. K. Jain, *Appl. Phys. Lett.* **30**, 340 (1977).
- [55] C. Lin, R. H. Stolen, and L. G. Cohen, *Appl. Phys. Lett.* **31**, 97 (1977).
- [56] R. H. Stolen, C. Lin, J. Shah, and R. F. Leheny, *IEEE J. Quantum Electron.* **14**, 860 (1978).
- [57] C. Lin and W. G. French, *Appl. Phys. Lett.* **34**, 10 (1979).
- [58] R. H. Stolen, *IEEE J. Quantum Electron.* **15**, 1157 (1979).
- [59] M. Nakazawa, T. Masamitsu, and N. Ichida, *J. Opt. Soc. Am. B* **1**, 86 (1984).
- [60] J. D. Kafka, D. F. Head, and T. Baer, in *Ultrafast Phenomena V*, G. R. Fleming and A. E. Siegman, Eds. (Springer, 1986), p. 51.
- [61] E. Desurvire, A. Imamoglu, and H. J. Shaw, *J. Lightwave Technol.* **5**, 89 (1987).
- [62] P. N. Kean, K. Smith, B. D. Sinclair, and W. Sibbett, *J. Mod. Opt.* **35**, 397 (1988).
- [63] A. J. Stentz, *Proc. SPIE* **3263**, 91 (1998).
- [64] S. V. Chernikov, N. S. Platonov, D. V. Gapontsev, D. I. Chang, M. J. Guy, and J. R. Taylor, *Electron. Lett.* **34**, 680 (1998).
- [65] E. M. Dianov and A. M. Prokhorov, *IEEE J. Sel. Topics Quantum Electron.* **6**, 1022 (2000).

- [66] S. A. Skubchenko, M. Y. Vyatkin, and D. V. Gapontsev, *IEEE Photon. Technol. Lett.* **16**, 1014 (2004).
- [67] E. Bélanger, M. Bernier, D. Faucher, D. Cote, and R. Vallée, *J. Lightwave Technol.* **26**, 1696 (2008).
- [68] Y. Feng, L. R. Taylor, and D. B. Calia, *Opt. Express* **17**, 23678 (2009).
- [69] I. K. Ilev, H. Kumagai, and H. Toyoda, *Appl. Phys. Lett.* **69**, 1846 (1996); *Appl. Phys. Lett.* **70**, 3200 (1997).
- [70] C. Lin and R. H. Stolen, *Appl. Phys. Lett.* **29**, 428 (1976).
- [71] M. Ikeda, *Opt. Commun.* **39**, 148 (1981).
- [72] Y. Aoki, S. Kishida, H. Honmou, K. Washio, and M. Sugimoto, *Electron. Lett.* **19**, 620 (1983).
- [73] E. Desurvire, M. Papuchon, J. P. Pocholle, J. Raffy, and D. B. Ostrowsky, *Electron. Lett.* **19**, 751 (1983).
- [74] M. Nakazawa, M. Tokuda, Y. Negishi, and N. Uchida, *J. Opt. Soc. Am. B* **1**, 80 (1984).
- [75] M. Nakazawa, T. Nakashima, and S. Seikai, *J. Opt. Soc. Am. B* **2**, 215 (1985).
- [76] N. A. Olsson and J. Hegarty, *J. Lightwave Technol.* **4**, 391 (1986).
- [77] S. Seikai, T. Nakashima, and N. Shibata, *J. Lightwave Technol.* **4**, 583 (1986).
- [78] K. Mochizuki, N. Edagawa, and Y. Iwamoto, *J. Lightwave Technol.* **4**, 1328 (1986).
- [79] M. J. O'Mahony, *J. Lightwave Technol.* **6**, 531 (1988).
- [80] N. Edagawa, K. Mochizuki, and Y. Iwamoto, *Electron. Lett.* **23**, 196 (1987).
- [81] M. L. Dakss and P. Melman, *IEE Proc.* **135** (Pt. J), 96 (1988).
- [82] K. Mochizuki, *J. Lightwave Technol.* **3**, 688 (1985).
- [83] L. F. Mollenauer, R. H. Stolen, and M. N. Islam, *Opt. Lett.* **10**, 229 (1985).
- [84] L. F. Mollenauer, J. P. Gordon, and M. N. Islam, *IEEE J. Quantum Electron.* **22**, 157 (1986).
- [85] L. F. Mollenauer and K. Smith, *Opt. Lett.* **13**, 675 (1988).
- [86] T. Horiguchi, T. Sato, and Y. Koyamada, *IEEE Photon. Technol. Lett.* **4**, 64 (1992).
- [87] T. Sato, T. Horiguchi, Y. Koyamada, and I. Sankawa, *IEEE Photon. Technol. Lett.* **4**, 923 (1992).
- [88] S. G. Grubb, *Proc. Conf. on Optical Amplifiers and Applications* (Optical Society of America, 1995).
- [89] S. V. Chernikov, Y. Zhu, R. Kashyap, and J. R. Taylor, *Electron. Lett.* **31**, 472 (1995).
- [90] E. M. Dianov, *Laser Phys.* **6**, 579 (1996).
- [91] D. I. Chang, S. V. Chernikov, M. J. Guy, J. R. Taylor, and H. J. Kong, *Opt. Commun.* **142**, 289 (1997).
- [92] A. Bertoni and G. C. Reali, *Appl. Phys. B* **67**, 5 (1998).
- [93] D. V. Gapontsev, S. V. Chernikov, and J. R. Taylor, *Opt. Commun.* **166**, 85 (1999).
- [94] H. Masuda, S. Kawai, K. Suzuki, and K. Aida, *IEEE Photon. Technol. Lett.* **10**, 516 (1998).
- [95] H. Kidorf, K. Rottwitt, M. Nissov, M. Ma, and E. Rabariaona, *IEEE Photon. Technol. Lett.* **11**, 530 (1999).
- [96] H. Masuda and S. Kawai, *IEEE Photon. Technol. Lett.* **11**, 647 (1999).
- [97] H. Suzuki, J. Kani, H. Masuda, N. Takachio, K. Iwatsuki, Y. Tada, and M. Sumida, *IEEE Photon. Technol. Lett.* **12**, 903 (2000).
- [98] S. Namiki and Y. Emori, *IEEE J. Sel. Topics Quantum Electron.* **7**, 3 (2001).
- [99] M. N. Islam, Ed., *Raman Amplifiers for Telecommunications*, Vol. 1 and 2 (Springer, 2004).
- [100] J. Bromage, *J. Lightwave Technol.* **22**, 79 (2004).

- [101] D. F. Grosz, A. Agarwal, S. Banerjee, D. N. Maywar, and A. P. Künig, *J. Lightwave Technol.* **22**, 423 (2004).
- [102] C. Headley and G. P. Agrawal, Eds., *Raman Amplification in Fiber Optical Communication Systems* (Academic Press, 2005).
- [103] Y. Feng, L. R. Taylor, and D. Bonaccini Calia, *Opt. Express* **16**, 10927 (2008).
- [104] L. R. Taylor, Y. Feng, and D. B. Calia, *Opt. Express* **18**, 8540 (2010).
- [105] A. R. Chraplyvy, *Electron. Lett.* **20**, 58 (1984).
- [106] N. A. Olsson, J. Hegarty, R. A. Logan, L. F. Johnson, K. L. Walker, L. G. Cohen, B. L. Kasper, and J. C. Campbell, *Electron. Lett.* **21**, 105 (1985).
- [107] A. R. Chraplyvy, *J. Lightwave Technol.* **8**, 1548 (1990).
- [108] D. N. Christodoulides and R. B. Jander, *IEEE Photon. Technol. Lett.* **8**, 1722 (1996).
- [109] J. Wang, X. Sun, and M. Zhang, *IEEE Photon. Technol. Lett.* **10**, 540 (1998).
- [110] M. E. Marhic, F. S. Yang, and L. G. Kazovsky, *J. Opt. Soc. Am. B* **15**, 957 (1998).
- [111] S. Bigo, S. Gauchard, A. Bertaina, and J. P. Hamaide, *IEEE Photon. Technol. Lett.* **11**, 671 (1999).
- [112] A. G. Grandpierre, D. N. Christodoulides, and J. Toulouse, *IEEE Photon. Technol. Lett.* **11**, 1271 (1999).
- [113] K.-P. Ho, *J. Lightwave Technol.* **18**, 915 (2000).
- [114] X. Zhou and M. Birk, *J. Lightwave Technol.* **21**, 2194 (2003).
- [115] T. Yamamoto and S. Norimatsu, *J. Lightwave Technol.* **21**, 2229 (2003).
- [116] V. N. Lugovoi, *Sov. Phys. JETP* **44**, 683 (1976).
- [117] J. I. Gersten, R. R. Alfano, and M. Belic, *Phys. Rev. A* **21**, 1222 (1980).
- [118] E. M. Dianov, A. Y. Karasik, P. V. Mamyshev, G. I. Onishchukov, A. M. Prokhorov, M. F. Stel'makh, and A. A. Fomichev, *JETP Lett.* **39**, 691 (1984).
- [119] E. M. Dianov, A. Y. Karasik, P. V. Mamyshev, A. M. Prokhorov, and V. N. Serkin, *Sov. Phys. JETP* **62**, 448 (1985).
- [120] B. Valk, W. Hodel, and H. P. Weber, *Opt. Commun.* **54**, 363 (1985).
- [121] R. H. Stolen and A. M. Johnson, *IEEE J. Quantum Electron.* **QE-22**, 2154 (1986).
- [122] P. M. W. French, A. S. L. Gomes, A. S. Gouveia-Neto, and J. R. Taylor, *IEEE J. Quantum Electron.* **QE-22**, 2230 (1986).
- [123] D. Schadt and B. Jaskorzynska, *J. Opt. Soc. Am. B* **4**, 856 (1987).
- [124] P. N. Kean, K. Smith, and W. Sibbett, *IEE Proc. Pt. J.* **134**, 163 (1987).
- [125] R. R. Alfano, P. L. Baldeck, F. Raccah, and P. P. Ho, *Appl. Opt.* **26**, 3492 (1987).
- [126] J. T. Manassah, *Appl. Opt.* **26**, 3747 (1987); J. T. Manassah and O. Cockings, *Appl. Opt.* **26**, 3749 (1987).
- [127] E. M. Dianov, P. V. Mamyshev, A. M. Prokhorov, and D. G. Fursa, *JETP Lett.* **45**, 599 (1987); *JETP Lett.* **46**, 482 (1987).
- [128] K. Smith, P. N. Kean, D. W. Crust, and W. Sibbett, *J. Mod. Opt.* **34**, 1227 (1987).
- [129] M. Nakazawa, M. S. Stix, E. P. Ippen, and H. A. Haus, *J. Opt. Soc. Am. B* **4**, 1412 (1987).
- [130] R. R. Alfano and P. P. Ho, *IEEE J. Quantum Electron.* **24**, 351 (1988).
- [131] A. M. Weiner, J. P. Heritage, and R. H. Stolen, *J. Opt. Soc. Am. B* **5**, 364 (1988).
- [132] A. S. L. Gomes, V. L. da Silva, and J. R. Taylor, *J. Opt. Soc. Am. B* **5**, 373 (1988).
- [133] P. L. Baldeck, R. R. Alfano, and G. P. Agrawal, in *Ultrafast Phenomena VI*, T. Yajima et al., Eds. (Springer, 1988), p. 53.
- [134] M. Kuckartz, R. Schultz, and A. Harde, *Opt. Quantum Electron.* **19**, 237 (1987); *J. Opt. Soc. Am. B* **5**, 1353 (1988).
- [135] J. Hermann and J. Mondry, *J. Mod. Opt.* **35**, 1919 (1988).

- [136] R. Osborne, *J. Opt. Soc. Am. B* **6**, 1726 (1989).
- [137] D. N. Cristodoulides and R. I. Joseph, *IEEE J. Quantum Electron.* **25**, 273 (1989).
- [138] Y. B. Band, J. R. Ackerhalt, and D. F. Heller, *IEEE J. Quantum Electron.* **26**, 1259 (1990).
- [139] J. E. Sharping, Y. Okawachi, and A. L. Gaeta, *Opt. Express* **13**, 6092 (2005).
- [140] G. Fanjoux and T. Sylvestre, *Opt. Lett.* **33**, 2506 (2008).
- [141] G. Fanjoux and T. Sylvestre, *Opt. Lett.* **34**, 3824 (2009).
- [142] K. Suzuki, K. Noguchi, and N. Uesugi, *Opt. Lett.* **11**, 656 (1986); *J. Lightwave Technol.* **6**, 94 (1988).
- [143] A. S. L. Gomes, V. L. da Silva, J. R. Taylor, B. J. Ainslie, and S. P. Craig, *Opt. Commun.* **64**, 373 (1987).
- [144] E. M. Dianov, L. A. Bufetov, M. M. Bubnov, M. V. Grekov, S. A. Vasiliev, and O. I. Medvedkov, *Opt. Lett.* **25**, 402 (2000).
- [145] T. Nakashima, M. Nakazawa, K. Nishi, and H. Kubota, *Opt. Lett.* **12**, 404 (1987).
- [146] A. S. L. Gomes, A. S. Gouveia-Neto, and J. R. Taylor, *Opt. Quantum Electron.* **20**, 95 (1988).
- [147] K. Tamura and M. Nakazawa, *Opt. Lett.* **21**, 68 (1996).
- [148] M. E. Fermann, V. I. Kruglov, B. C. Thomsen, J. M. Dudley, and J. D. Harvey, *Phys. Rev. Lett.* **26**, 6010 (2000).
- [149] V. I. Kruglov, A. C. Peacock, J. D. Harvey, and J. M. Dudley, *J. Opt. Soc. Am. B* **19**, 461 (2002).
- [150] J. Limpert, T. Schreiber, T. Clausnitzer, K. Zollner, H. J. Fuchs, E. B. Kley, H. Zellmer, and A. Tunnermann, *Opt. Express* **10**, 628 (2002).
- [151] A. C. Peacock, N. G. R. Broderick, and T. M. Monro, *Opt. Commun.* **218**, 167 (2003).
- [152] C. Finot, G. Millot, C. Billet, and J. M. Dudley, *Opt. Express* **11**, 1547 (2003).
- [153] C. Finot, G. Millot, S. Pitois, C. Billet, and J. M. Dudley, *IEEE J. Sel. Topics Quantum Electron.* **10**, 1211 (2004).
- [154] G. Q. Chang, A. Galvanauskas, H. G. Winful, and T. B. Norris, *Opt. Lett.* **29**, 2647 (2004).
- [155] V. A. Vysloukh and V. N. Serkin, *JETP Lett.* **38**, 199 (1983).
- [156] E. M. Dianov, A. Y. Karasik, P. V. Mamyshev, A. M. Prokhorov, V. N. Serkin, M. F. Stel'makh, and A. A. Fomichev, *JETP Lett.* **41**, 294 (1985).
- [157] E. M. Dianov, A. M. Prokhorov, and V. N. Serkin, *Opt. Lett.* **11**, 168 (1986).
- [158] F. M. Mitschke and L. F. Mollenauer, *Opt. Lett.* **11**, 659 (1986).
- [159] V. N. Serkin, *Sov. Tech. Phys. Lett.* **13**, 366 (1987).
- [160] P. Beaud, W. Hodel, B. Zyss, and H. P. Weber, *IEEE J. Quantum Electron.* **23**, 1938 (1987).
- [161] A. S. Gouveia-Neto, A. S. L. Gomes, J. R. Taylor, B. J. Ainslie, and S. P. Craig, *Electron. Lett.* **23**, 1034 (1987).
- [162] A. S. Gouveia-Neto, A. S. L. Gomes, and J. R. Taylor, *Opt. Lett.* **12**, 1035 (1987); *IEEE J. Quantum Electron.* **24**, 332 (1988).
- [163] K. J. Blow, N. J. Doran, and D. Wood, *J. Opt. Soc. Am. B* **5**, 381 (1988).
- [164] A. S. Gouveia-Neto, A. S. L. Gomes, J. R. Taylor, and K. J. Blow, *J. Opt. Soc. Am. B* **5**, 799 (1988).
- [165] A. S. Gouveia-Neto, M. E. Faldon, and J. R. Taylor, *Opt. Lett.* **13**, 1029 (1988); *Opt. Commun.* **69**, 325 (1989).
- [166] A. Höök, D. Anderson, and M. Lisak, *Opt. Lett.* **13**, 1114 (1988); *J. Opt. Soc. Am. B* **6**, 1851 (1989).

- [167] E. A. Golovchenko, E. M. Dianov, P. V. Mamyshev, A. M. Prokhorov, and D. G. Fursa, *J. Opt. Soc. Am. B* **7**, 172 (1990).
- [168] E. J. Greer, D. M. Patrick, P. G. J. Wigley, J. I. Vukusic, and J. R. Taylor, *Opt. Lett.* **15**, 133 (1990).
- [169] A. S. Gouveia-Neto, *J. Lightwave Technol.* **10**, 1536 (1992).
- [170] E. M. Dianov, A. B. Grudinin, A. M. Prokhorov, and V. N. Serkin, in *Optical Solitons—Theory and Experiment*, J. R. Taylor, Ed. (Cambridge University Press, 1992), (Chap. 7).
- [171] K. Chan and W. Cao, *Opt. Commun.* **158**, 159 (1998).
- [172] K. Drühl, R. G. Wenzel, and J. L. Carlsten, *Phys. Rev. Lett.* **51**, 1171 (1983); *J. Stat. Phys.* **39**, 615 (1985).
- [173] C. R. Menyuk, *Phys. Rev. Lett.* **62**, 2937 (1989).
- [174] J. C. Englund and C. M. Bowden, *Phys. Rev. Lett.* **57**, 2661 (1986); *Phys. Rev. A* **42**, 2870 (1990); *Phys. Rev. A* **46**, 578 (1992).
- [175] N. Nishizawa, Y. Ito, and N. Goto, *IEEE Photon. Technol. Lett.* **14**, 896 (2002).
- [176] A. V. Husakou and J. Herrmann, *J. Opt. Soc. Am. B* **19**, 2171 (2002).
- [177] K. S. Abedin and F. Kubota, *IEEE J. Sel. Topics Quantum Electron.* **10**, 1203 (2004).
- [178] D. N. Christodoulides, *Opt. Commun.* **86**, 431 (1991).
- [179] M. N. Islam, L. F. Mollenauer, R. H. Stolen, J. R. Simpson, and H. T. Shang, *Opt. Lett.* **12**, 814 (1987).
- [180] J. D. Kafka and T. Baer, *Opt. Lett.* **12**, 181 (1987).
- [181] A. S. Gouveia-Neto, A. S. L. Gomes, and J. R. Taylor, *Electron. Lett.* **23**, 537 (1987); *Opt. Quantum Electron.* **20**, 165 (1988).
- [182] H. A. Haus and M. Nakazawa, *J. Opt. Soc. Am. B* **4**, 652 (1987).
- [183] V. L. da Silva, A. S. L. Gomes, and J. R. Taylor, *Opt. Commun.* **66**, 231 (1988).
- [184] U. Keller, K. D. Li, M. Rodwell, and D. M. Bloom, *IEEE J. Quantum Electron.* **25**, 280 (1989).
- [185] M. Ding and K. Kikuchi, *IEEE Photon. Technol. Lett.* **4**, 927 (1992); *IEEE Photon. Technol. Lett.* **4**, 1109 (1992).
- [186] M. Ding and K. Kikuchi, *Fiber Integ. Opt.* **13**, 337 (1994).
- [187] C. J. S. de Matos, S. V. Popov, and J. R. Taylor, *Opt. Lett.* **28**, 1891 (2003).
- [188] D. A. Chestnut and J. R. Taylor, *Opt. Lett.* **29**, 262 (2004).
- [189] K. Iwaisuki, K. Suzuki, and S. Nishi, *IEEE Photon. Technol. Lett.* **3**, 1074 (1991).
- [190] C. Headley III and G. P. Agrawal, *J. Opt. Soc. Am. B* **10**, 2383 (1993).
- [191] R. F. de Souza, E. J. S. Fonseca, M. J. Hickmann, and A. S. Gouveia-Neto, *Opt. Commun.* **124**, 79 (1996).
- [192] Q. Lin and G. P. Agrawal, *Opt. Lett.* **27**, 2194 (2002); *Opt. Lett.* **28**, 227 (2003).
- [193] Q. Lin and G. P. Agrawal, *J. Opt. Soc. Am. B* **20**, 1616 (2003).
- [194] E. S. Son, J. H. Lee, and Y. C. Chung, *J. Lightwave Technol.* **23**, 1219 (2005).
- [195] S. Sergeev, S. Popov, and A. T. Friberg, *Opt. Commun.* **262**, 114 (2006); *J. Opt. A: Pure Appl. Opt.* **9**, 1119 (2007).
- [196] P. Ebrahimi, M. C. Hauer, Q. Yu, et al., *Proc. Conf. on Lasers and Electro-optics* (Optical Society of America, 2001), p. 143.
- [197] S. Popov, E. Vanin, and G. Jacobsen, *Opt. Lett.* **27**, 848 (2002).
- [198] A. B. dos Santos and J. P. von der Weid, *Opt. Lett.* **29**, 1324 (2004).
- [199] C. W. Gardiner, *Handbook of Stochastic Methods*, 2nd ed. (Springer, 1985).

# Stimulated Brillouin Scattering 9

Stimulated Brillouin scattering (SBS) is a nonlinear process that can occur in optical fibers at input power levels much lower than those needed for stimulated Raman scattering (SRS). It manifests through the generation of a backward-propagating Stokes wave that carries most of the input power, once the Brillouin threshold is reached. For this reason, SBS limits the channel power in optical communication systems. At the same time, it can be useful for making fiber-based Brillouin lasers and amplifiers. This chapter is devoted to the SBS phenomenon in optical fibers. Section 9.1 presents the basic concepts behind SBS with emphasis on the spectrum of Brillouin gain. Section 9.2 focuses on the Brillouin threshold in the case of a continuous-wave (CW) pump and the techniques used to control it. Fiber-Brillouin amplifiers and their properties are discussed in Section 9.3. The dynamic aspects of SBS are the focus of Section 9.4, where we discuss SBS for a pulsed pump together with phenomena such as SBS-induced modulation instability and optical chaos. Section 9.5 is devoted to Brillouin lasers operating continuously or pulsed.

---

## 9.1 BASIC CONCEPTS

The nonlinear phenomenon of SBS, first observed in 1964, has been studied extensively [1–10]. SBS is similar to SRS inasmuch as it manifests through the generation of a Stokes wave whose frequency is downshifted from that of the incident light by an amount set by the nonlinear medium. However, several major differences exist between the two. For example, the Stokes wave propagates backward when SBS occurs in a single-mode optical fiber, in contrast to SRS that can occur in both directions. The Stokes shift ( $\sim 10$  GHz) is smaller by three orders of magnitude for SBS compared with that of SRS. The threshold pump power for SBS depends on the spectral width associated with the pump wave. It can be as low as 1 mW for a CW pump, or when the pumping is in the form of relatively wide pulses (width  $> 1 \mu\text{s}$ ). In contrast, SBS nearly ceases to occur for short pump pulses (width  $< 1 \text{ ns}$ ). All of these differences stem from a single fundamental change—acoustical phonons participate in SBS whereas optical phonons are involved in the case of SRS.

### 9.1.1 Physical Process

The process of SBS can be described classically as a nonlinear interaction among the pump and Stokes fields and an acoustic wave (initially generated thermally) through the process of *electrostriction* [10]. The acoustic wave produces density modulations that in turn modulate the refractive index of the medium. This pump-induced index grating scatters the pump light through Bragg diffraction. Scattered light is downshifted in frequency because of the Doppler shift associated with a grating moving at the acoustic velocity  $v_A$ . The same scattering process can be viewed quantum mechanically as if annihilation of a pump photon creates a Stokes photon and an acoustic phonon simultaneously. As both the energy and the momentum must be conserved during each scattering event, the frequencies and the wave vectors of the three waves are related by

$$\Omega_B = \omega_p - \omega_s, \quad \mathbf{k}_A = \mathbf{k}_p - \mathbf{k}_s, \quad (9.1.1)$$

where  $\omega_p$  and  $\omega_s$  are the frequencies, and  $\mathbf{k}_p$  and  $\mathbf{k}_s$  are the wave vectors, of the pump and Stokes waves, respectively.

The frequency  $\Omega_B$  and the wave vector  $\mathbf{k}_A$  of the acoustic wave satisfy the standard dispersion relation

$$\Omega_B = v_A |\mathbf{k}_A| \approx 2v_A |\mathbf{k}_p| \sin(\theta/2), \quad (9.1.2)$$

where  $\theta$  is the angle between the pump and Stokes fields, and we used  $|\mathbf{k}_p| \approx |\mathbf{k}_s|$  in Eq. (9.1.1). Equation (9.1.2) shows that the frequency shift of the Stokes wave depends on the scattering angle. In particular,  $\Omega_B$  is the maximum in the backward direction ( $\theta = \pi$ ) and vanishes in the forward direction ( $\theta = 0$ ). In a single-mode optical fiber, the only relevant directions are the forward and backward directions. For this reason, SBS occurs only in the backward direction with the Brillouin shift given by

$$v_B = \Omega_B / 2\pi = 2n_p v_A / \lambda_p, \quad (9.1.3)$$

where Eq. (9.1.2) was used with  $|\mathbf{k}_p| = 2\pi n_p / \lambda_p$  and  $n_p$  is the effective mode index at the pump wavelength  $\lambda_p$ . If we use  $v_A = 5.96$  km/s and  $n_p = 1.45$ , the values appropriate for silica fibers,  $v_B \approx 11.1$  GHz at  $\lambda_p = 1.55$  μm.

Even though Eq. (9.1.2) predicts correctly that SBS should occur only in the backward direction in single-mode fibers (SMFs), spontaneous Brillouin scattering can occur in the forward direction. This happens because the guided nature of acoustic waves leads to a relaxation of the wave-vector selection rule. As a result, a small amount of Stokes light is generated in the forward direction. This phenomenon is referred to as guided-acoustic-wave Brillouin scattering [11]. In practice, the Stokes spectrum shows multiple lines with frequency shifts ranging from 10 to 1000 MHz. Because of its extremely weak character, this phenomenon is not considered further in this chapter.

### 9.1.2 Brillouin-Gain Spectrum

Similar to the case of SRS, the growth of the Stokes wave is characterized by the Brillouin-gain spectrum  $g_B(\Omega)$  peaking at  $\Omega = \Omega_B$ . However, in contrast to the SRS case, the spectral width of the gain spectrum is very small (~10 MHz in lieu

of  $\sim 10$  THz) because it is related to the damping time of acoustic waves related to the phonon lifetime. As shown later in Section 9.4.1, when acoustic waves decay as  $\exp(-\Gamma_B t)$ , the Brillouin gain has a Lorentzian spectrum of the form [10]

$$g_B(\Omega) = \frac{g_p(\Gamma_B/2)^2}{(\Omega - \Omega_B)^2 + (\Gamma_B/2)^2}, \quad (9.1.4)$$

where the peak value of the Brillouin gain at  $\Omega = \Omega_B$  is given by

$$g_p \equiv g_B(\Omega_B) = \frac{4\pi^2 \gamma_e^2 f_A}{n_p c \lambda_p^2 \rho_0 v_A \Gamma_B}. \quad (9.1.5)$$

Here,  $\rho_0 \approx 2210$  kg/m<sup>3</sup> is material density,  $\gamma_e \approx 0.902$  is the electrostrictive constant of silica [12], and  $f_A$  is the fraction (defined later in Section 9.4.1) by which the SBS gain is reduced if the acoustic and optical modes do not fully overlap inside the fiber. The full width at half maximum (FWHM) of the gain spectrum is related to  $\Gamma_B$  as  $\Delta\nu_B = \Gamma_B/(2\pi)$ . The phonon lifetime,  $T_B = \Gamma_B^{-1}$ , is typically  $< 10$  ns.

Measurements of the Brillouin gain in bulk silica were carried out as early as 1950 [13]. Measurements performed in 1979 with an argon-ion laser show that  $v_B = 34.7$  GHz, and  $\Delta\nu_B = 54$  MHz, and  $\lambda_p = 486$  nm [14]. These experiments also indicate that  $\Delta\nu_B$  depends on the Brillouin shift and varies slightly faster than  $v_B^2$ ; a quadratic dependence is expected from the theory. Noting from Eq. (9.1.3) that  $v_B$  varies inversely with  $\lambda_p$ ,  $\Delta\nu_B$  follows a  $\lambda_p^{-2}$  dependence on the pump wavelength. This narrowing of the Brillouin-gain profile with an increase in  $\lambda_p$  cancels the decrease in gain apparent from Eq. (9.1.5). As a result, the peak value  $g_p$  is nearly independent of the pump wavelength. If parameter values typical of silica fibers are used in Eq. (9.1.5),  $g_p$  is in the range  $3 - 5 \times 10^{-11}$  m/W. This value is larger by nearly three orders of magnitude compared with that of the Raman-gain coefficient (see Section 8.1).

The Brillouin-gain spectrum for silica fibers can differ significantly from that of bulk silica because of the guided nature of optical modes and the presence of dopants in the fiber core [15–24]. Figure 9.1 shows the gain spectra measured

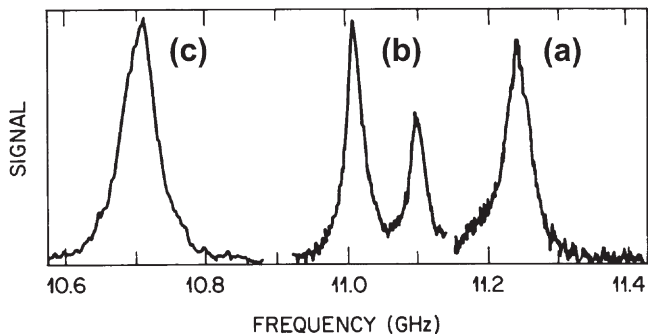


**Figure 9.1** Brillouin-gain spectra of three fibers for  $\lambda_p = 1.525$  μm: (a) silica-core fiber, (b) depressed-cladding fiber, and (c) dispersion-shifted fiber. (After Ref. [17]; © 1986 IEE.)

for three different fibers having different structures and different doping levels of germania ( $\text{GeO}_2$ ) in their cores. The measurements were made by using an external-cavity semiconductor laser operating at  $1.525 \mu\text{m}$  and employed a heterodyne-detection technique with 3-MHz resolution [17]. The fiber (a) has a core of nearly pure silica ( $\text{GeO}_2$  concentration of about 0.3%/mole). The measured Brillouin shift  $v_B \approx 11.25 \text{ GHz}$  is in agreement with Eq. (9.1.3) for this fiber if we use the acoustic velocity of bulk silica. The Brillouin shift is reduced for fibers (b) and (c) with nearly inverse dependence on  $\text{GeO}_2$  concentration. The fiber (b) has a double-peak structure that results from an inhomogeneous distribution of  $\text{GeO}_2$  within the core [17].

More recent measurements indicate that the Brillouin-gain spectrum depends considerably on details of the fiber design and may contain multiple peaks that have their origin in different acoustic modes supported by the fiber [22–24]. A three-peak gain spectrum was observed as early as 1988 and interpreted to result from different acoustic velocities in the core and cladding regions of the fiber [19]. In a 2002 experiment [22], gain spectra were recorded for four kinds of fibers differing not only in core sizes but also in doping levels of  $\text{GeO}_2$  within the core (varying from 3.6% to 20%). The gain spectra exhibited as many as five peaks, depending on the fiber design. The Brillouin shift associated with the dominant peak also varied from 9 to 11 GHz, smaller values occurring for fiber cores with larger  $\text{GeO}_2$  concentration. As an example, Figure 9.2 shows the gain spectra measured for a dispersion-compensating fiber (DCF) with 18%  $\text{GeO}_2$  at several pump-power levels. The dominant peak occurs at 9.77 GHz but four smaller peaks are clearly seen. These peaks correspond to different acoustic modes of the fiber [23]. Since each mode has a different acoustic velocity  $v_A$ , it also has a different Brillouin shift, as indicated in Eq. (9.1.3). Changes in gain spectra at high pump powers are related to the onset of SBS.

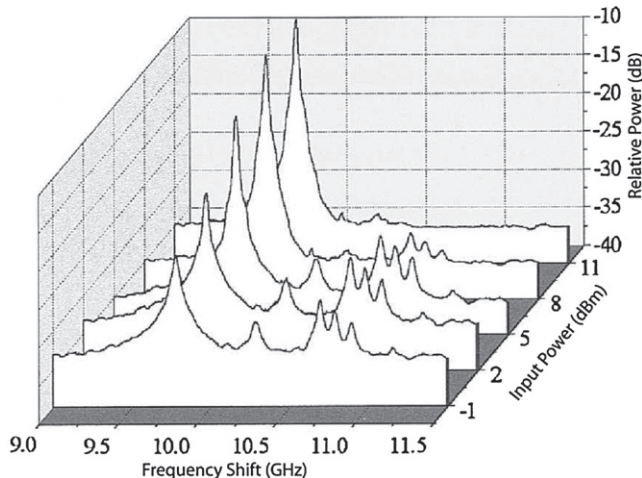


**Figure 9.2** Brillouin-gain spectra of a dispersion-compensating fiber recorded at five input power levels at 1552 nm. (After Ref. [22]; © 2002 IEEE.)

The bandwidth of the dominant gain peak in Figures 9.1 and 9.2 corresponds to the Brillouin-gain bandwidth  $\Delta\nu_B$  and is related to the phonon lifetime. It is much larger than that expected for bulk silica ( $\Delta\nu_B \approx 17$  MHz at  $\lambda_p = 1.525$  μm). Other experiments have also shown similarly large bandwidths for silica-based fibers [18–20]. A part of the increase is due to the guided nature of acoustic modes in optical fibers [15]. Most of the increase, however, can be attributed to inhomogeneities in the fiber-core cross section along the fiber length. The numerical aperture of the fiber also plays a role in broadening the SBS gain spectrum [25]. Because such factors are specific to each fiber,  $\Delta\nu_B$  is generally different for different fibers and can exceed 100 MHz in the 1.55-μm spectral region.

Equation (9.1.4) for the Brillouin gain is obtained under steady-state conditions and is valid for a CW or quasi-CW pump (pulse width  $T_0 \gg T_B$ ), whose spectral width  $\Delta\nu_p$  is much smaller than  $\Delta\nu_B$ . For pump pulses of width  $T_0 < T_B$ , the Brillouin gain is substantially reduced [5] compared with that obtained from Eq. (9.1.5). Indeed, if the pulse width becomes much smaller than the phonon lifetime ( $T_0 < 1$  ns), the Brillouin gain is reduced below the Raman gain; such a pump pulse generates a forward-propagating Raman pulse through SRS, as discussed in Section 8.3.

Even for a CW pump, the Brillouin-gain spectrum is broadened considerably if the spectral width  $\Delta\nu_p$  of the pump exceeds  $\Delta\nu_B$ . This can happen when a multimode laser is used for pumping. It can also happen for a single-mode pump laser whose phase varies rapidly on a time scale shorter than the phonon lifetime  $T_B$ . Detailed calculations show that the Brillouin gain, under broadband pumping conditions, depends on the relative magnitudes of the pump-coherence length [26–28], defined by  $L_{coh} = c / (n_p \Delta\nu_p)$ , and the SBS-interaction length  $L_{int}$ , defined as the distance over which the Stokes amplitude varies appreciably. If  $L_{coh} \gg L_{int}$ , the SBS process is independent of the mode structure of the pump laser provided the mode spacing exceeds  $\Delta\nu_B$ , and the Brillouin gain is nearly the same as for a single-mode laser after a few interaction lengths [26]. In contrast, the Brillouin gain is reduced significantly if  $L_{coh} \ll L_{int}$ . The latter situation is generally applicable to optical fibers, where interaction length is comparable to the fiber length  $L$  whenever fiber losses are not too large.

The effective Brillouin gain  $g_B^{\text{eff}}(\omega_s)$  for a broadband CW pump can be obtained by convolving the Brillouin gain with the pump spectrum  $S_p(\omega_p)$ . However, as discussed later in Section 9.4.3, the SBS gain is accompanied with changes in the refractive index, and we must use a complex form  $g_c$  of the gain spectrum whose real part provides the SBS gain:

$$g_c(\omega_s) = \int_{-\infty}^{\infty} \frac{g_p \Gamma_B / 2}{\Gamma_B / 2 + i(\omega - \omega_s - \Omega_B)} S_p(\omega - \omega_p) d\omega, \quad (9.1.6)$$

where  $S_p(\omega - \omega_p)$  is normalized such that  $\int_{-\infty}^{\infty} S_p(\omega - \omega_p) d\omega = 1$ . In the case of a pump laser with a Gaussian spectrum of width  $\Delta\omega_p$ , the pump spectrum has the form

$$S_p(\omega - \omega_p) = \frac{1}{\sqrt{\pi} \Delta\omega_p} \exp \left[ -\frac{(\omega - \omega_p)^2}{(\Delta\omega_p)^2} \right]. \quad (9.1.7)$$

Using it in Eq. (9.1.6) and performing the integral in terms of a complimentary error function [29], we obtain

$$g_c(\omega_s) = g_p \sqrt{\pi} q e^{-(p+iq)^2} \operatorname{erfc}(q - ip), \quad (9.1.8)$$

where  $p = (\Omega_B + \omega_s - \omega_p)/\Delta\omega_p$  and  $q = \Gamma_B/(2\Delta\omega_p)$  are two dimensionless numbers. Noting that  $g_B = \operatorname{Im}(g_c)$ , we obtain

$$g_B^{\text{eff}}(\omega_s) = g_p \sqrt{\pi} q \exp(q^2 - p^2) \operatorname{Im}[\operatorname{erfc}(q - ip)e^{-2ipq}]. \quad (9.1.9)$$

In the limit  $q \ll 1$ , the Brillouin-gain spectrum becomes nearly Gaussian and has the same width as the pump spectrum, i.e., it is broadened by a factor of  $(2\Delta\omega_p)/\Gamma_B$ . At the same time, the peak value of the gain is reduced by the same factor. This is the reason why the SBS threshold increases by a large factor when  $\Delta\omega_p \gg \Gamma_B$ .

## 9.2 QUASI-CW SBS

Similar to the SRS case, the development of SBS in optical fibers requires consideration of mutual interaction between the pump and Stokes waves. In this section we develop a simple theory valid under CW or quasi-CW conditions and use it to discuss the concept of Brillouin threshold.

### 9.2.1 Brillouin Threshold

Under steady-state conditions, applicable for a CW or quasi-CW pump, SBS is governed by the two coupled equations similar to Eqs (8.1.2) and (8.1.3). The only difference is that the sign of  $dI_s/dz$  should be changed to account for the counterpropagating nature of the Stokes wave with respect to the pump wave. Two simplifications can be made; the first  $\omega_p \approx \omega_s$  owing to a relatively small value of the Brillouin shift and the second, for the same reason,  $\alpha_p \approx \alpha_s \equiv \alpha$ , i.e., fiber losses are nearly the same for the pump and Stokes waves. With these changes, Eqs (8.1.2) and (8.1.3) become

$$\frac{dI_p}{dz} = -g_B I_p I_s - \alpha I_p, \quad (9.2.1)$$

$$-\frac{dI_s}{dz} = +g_B I_p I_s - \alpha I_s. \quad (9.2.2)$$

One can readily verify that in the absence of fiber losses ( $\alpha=0$ ),  $d(I_p - I_s)/dz = 0$ , and  $I_p - I_s$  remains constant along the fiber.

Equations (9.2.1) and (9.2.2) assume implicitly that the counterpropagating pump and Stokes waves are linearly polarized along the same direction and maintain their states of polarization (SOP) along the fiber. This is the case when the two waves are polarized along a principal axis of a polarization-maintaining fiber (PMF).

For the purpose of estimating the Brillouin threshold, pump depletion can be neglected. Using  $I_p(z) = I_p(0)e^{-\alpha z}$  in Eq. (9.2.2) and integrating it over the fiber length  $L$ , the Stokes intensity is found to grow exponentially in the backward direction as

$$I_s(0) = I_s(L) \exp(g_B P_0 L_{\text{eff}} / A_{\text{eff}} - \alpha L), \quad (9.2.3)$$

where  $P_0 = I_p(0)A_{\text{eff}}$  is the input pump power,  $A_{\text{eff}}$  is the effective mode area, and  $L_{\text{eff}}$  is the effective fiber length as defined in Eq. (4.1.6).

Equation (9.2.3) shows how a Stokes signal incident at  $z = L$  grows in the backward direction because of Brillouin amplification occurring as a result of SBS. In practice, no such signal is generally fed (unless the fiber is used as a Brillouin amplifier), and the Stokes wave grows from noise provided by spontaneous Brillouin scattering occurring throughout the fiber. Similar to the SRS case, the noise power is equivalent to injecting a fictitious photon per mode at a distance where the gain exactly equals the fiber loss. Following the method of Section 8.1.2, the Brillouin threshold is found to occur at a critical pump power  $P_{\text{cr}}$  such that [7]

$$g_B(\Omega_B)P_{\text{cr}}L_{\text{eff}}/A_{\text{eff}} \approx 21, \quad (9.2.4)$$

where the peak value of the Brillouin gain is given in Eq. (9.1.5). It should be stressed that the factor of 21 in Eq. (9.2.4) is based on an approximate analysis [7]. More accurate results have been obtained in recent years by taking into account the distributed nature of spontaneous Brillouin scattering [30–32]. They indicate that 21 in (9.2.4) should be reduced to nearer 16 for long fibers.

To estimate the SBS threshold power, consider first a long fiber section ( $L > 50$  km) likely to be encountered in a typical optical communication system operating near 1.55  $\mu\text{m}$ . Since  $\alpha L \gg 1$  under such conditions,  $L_{\text{eff}} = 1/\alpha$ , and  $P_{\text{cr}} = 21\alpha A_{\text{eff}}/g_B$ . If we use typical values for fiber parameters,  $A_{\text{eff}} = 80 \mu\text{m}^2$ ,  $\alpha = 0.2 \text{ dB/km}$ , and  $g_B = 5 \times 10^{-11} \text{ m/W}$ , Eq. (9.2.4) leads to  $P_{\text{cr}} \approx 2 \text{ mW}$ . Such a low Brillouin threshold is a consequence of the long fiber length. If the fiber section is relatively short, say  $L = 1 \text{ m}$ , the threshold power increases to 20 W. It can be increased even more by using fibers with wider cores for which the effective mode area is larger.

### 9.2.2 Polarization Effects

The threshold level predicted by Eq. (9.2.4) is also approximate because it assumes that the Stokes and pump fields remain copolarized along the entire fiber length. This is not the case in practice, and an important role is played by the polarization properties of the Brillouin gain. In contrast with the case of the Raman gain (see Figure 8.2), the Brillouin gain vanishes when the pump and Stokes are linearly and orthogonally polarized [33]. As a result, if the pump and Stokes are linearly polarized at  $45^\circ$  when they are launched into a polarization-maintaining fiber, the effective SBS gain is reduced by a factor of 2.

The situation is more complicated in fibers exhibiting some residual fluctuating birefringence. When only the pump is launched into such a fiber, the Stokes wave

is seeded through spontaneous Brillouin scattering occurring at the back end of the fiber. However, as this seed is amplified by the pump, residual birefringence of the fiber changes the states of polarization (SOP) of both the pump and Stokes in a random fashion. The effective Brillouin gain is reduced because of such polarization changes. The threshold pump power for the onset of SBS is thus expected to be higher for most fibers whose residual birefringence fluctuates along its length. However, the enhancement factor is not 2 because, in general, the pump and Stokes do not remain linearly polarized.

Although a complete analysis is complicated, one can estimate the gain-reduction factor using simple physical arguments [34]. First, note that the Stokes wave is generated in the backward direction through reflection from a grating moving at the acoustic speed. Second, even if the Stokes has the same SOP as the pump, the handedness of the SOP is altered on reflection. Mathematically, the vertical component  $s_3$  of the Stokes vector changes sign if the direction of an optical wave is reversed. Thus, the SBS efficiency for an arbitrarily polarized pump and Stokes is governed by

$$\eta_B = \frac{1}{2}(1 + \hat{s} \cdot \hat{p}) = \frac{1}{2}(1 + s_1 p_1 + s_2 p_2 - s_3 p_3), \quad (9.2.5)$$

where  $\hat{s} = (s_1, s_2, s_3)$  and  $\hat{p} = (p_1, p_2, p_3)$  are unit vectors representing SOPs of the Stokes and pump on the Poincaré sphere. It follows from this equation that the SBS efficiency for the copolarized and orthogonally polarized pump and Stokes is  $1 - s_3^2$  and  $s_3^2$ , respectively. Only in the specific case in which the pump and Stokes are linearly and orthogonally polarized ( $s_3 = 0$ ) does the SBS efficiency drop to zero [33].

If the SOP changes in response to birefringence fluctuations,  $s_3$  would vary randomly taking all its possible values in the range of  $-1$  to  $1$ . The average value of  $s_3^2$  is  $1/3$ , if we note that  $s_1^2 + s_2^2 + s_3^2 = 1$  is always maintained and the three components have the same average value. Thus, the average SBS efficiency for the copolarized case is  $2/3$ , and we should reduce the SBS gain  $g_B$  by this factor in Eqs (9.2.1) and (9.2.2). Since the threshold power from Eq. (9.2.4) scales inversely with the Brillouin gain, it increases by a factor of  $3/2$ , that is, the SBS threshold increases by 50% when the state of polarization of the pump field becomes completely scrambled on the Poincaré sphere because of birefringence fluctuations [34].

### 9.2.3 Techniques for Controlling the SBS Threshold

The derivation of Eq. (9.2.4) for the SBS threshold power assumes that the fiber core is perfectly circular and homogeneous across its entire length. This is rarely the case in practice. Radial inhomogeneities occur when the fiber core is doped to enhance its refractive index in such a fashion that its concentration varies along the radial direction. Variations in the doping level along the radial direction lead to slight changes in the acoustic velocity in that direction. As a result, the SBS threshold depends, to some extent, on various dopants used to make the fiber [35]. A common core dopant for silica fibers is germania. The acoustic velocity in such fibers is reduced near the center of the core as  $v_A = 5.944(1 - b_x x)$  km/s, where  $b_x = 0.0072$  and  $x$  represents

the fraction of germania concentration [23]. A 10% doping of germania (by weight) reduces the acoustic velocity by 7.2% at the core center. Because of such radial effects, it is possible to design a refractive-index profile such that the SBS threshold is doubled compared with a standard step-index design [36].

Variations in fiber parameters along the fiber length are even more helpful in controlling the SBS threshold. The reason is that the backward-propagating Stokes wave grows exponentially along the fiber length. If this exponential growth is interrupted by some mechanism, the SBS threshold can be forced to increase significantly. For example, if the Brillouin shift  $v_B$  along the fiber length is made inhomogeneous such that it shifts by more than the SBS gain bandwidth, the Stokes will cease to grow after the shift because of a substantial reduction in the Brillouin gain. As seen from Eq. (9.1.3),  $v_B$  depends on both the acoustic velocity  $v_A$  and the mode index  $n_p$  at the pump wavelength, and it can be shifted if one of these parameters changes along the fiber length.

The mode index  $n_p$  depends not only on fiber parameters, such as the core diameter and doping levels, but also on environmental factors such as temperature and stress. Several techniques developed for SBS suppression make use of this feature [37–44]. For example, the SBS threshold could be increased by more than a factor of 2 by intentionally changing the core diameter along the length of a fiber [39]. In a variation of this idea,  $v_B$  was changed along the fiber length with nonuniform doping levels [40]. The SBS threshold for such a fiber exceeded 30 mW in the wavelength region near 1.55 μm. In another approach, a sinusoidal strain was applied along the fiber by twisting it during the cabling process [38]. Such a twist shifted  $v_B$  periodically in a distributed fashion and expanded the Brillouin-gain bandwidth from 50 to 400 MHz. Since the peak value of the gain  $g_B$  was reduced, the threshold power was found to increase from 5 mW to more than 30 mW. A temperature gradient along the fiber length also increases the SBS threshold by shifting  $v_B$  in a distributed fashion. In a 1993 experiment, the threshold power increased from 4.5 to 10 mW with a 37 °C temperature difference across a 1.6-km-long fiber [37]. A threefold increase in the SBS threshold was observed in a 2001 experiment with a 140 °C temperature difference across a 100-m-long fiber [42].

The preceding techniques either require especially designed fibers or are cumbersome to implement in practice. For this reason, a common technique for SBS suppression consists of modulating the phase of the pump beam before it is launched into the fiber. It turns out that a phase modulation is equivalent to changing  $\Omega_B$  along the fiber length [45]. In practice, the pump phase is modulated sinusoidally using an electro-optic phase modulator. Typically, modulation frequency  $\Delta\nu_m$  is chosen in the range of 200–400 MHz. Because the effective Brillouin gain is reduced by a factor of  $(1 + \Delta\nu_m/\Delta\nu_B)$ , the SBS threshold increases by the same factor. A variant of the phase-modulation technique, known as the frequency-sweeping spread spectrum technique [46], was implemented as early as 1994 in a four-wave mixing experiment [47]. The launched power can be increased by a factor of 10 or more with the phase-modulation technique. Even larger enhancement factors are possible by using multiple modulation frequencies, a pseudorandom bit pattern at a high bit rate, or

frequency-hopped chirping [48–50]. A microwave noise source has also been used for this purpose [51].

The phase-modulation idea has been extended in several directions. In one scheme, a polarization-maintaining fiber is used in combination with a phase modulator to produce a periodically varying differential phase shift between the two orthogonally polarized components of the pump. With a proper choice of the modulator parameters, the degree of polarization can be reduced to zero, resulting in depolarized light and a considerable enhancement in the SBS threshold [52]. In another scheme, the nonlinear phenomenon of cross-phase modulation (XPM) is used to chirp a CW pump inside the fiber [53]. In this case, a second beam in the form of a regular or pseudorandom pulse train at a different wavelength is launched with the CW pump. The XPM-induced phase shift modulates the phase of the CW beam because this shift occurs only during time intervals in which the secondary channel contains a pulse.

Fiber gratings can also be used to increase the SBS threshold. The Bragg grating is designed such that it is transparent to the forward-propagating pump beam, but the spectrum of the Stokes wave generated through SBS falls entirely within its stop band [54]. As a result, the exponential buildup of the Stokes is perturbed by the grating. A new Stokes wave can still build up in the front section of the fiber, but its power is reduced considerably. Multiple gratings may be used for long fibers to interrupt the coherent buildup of the Stokes wave over the entire fiber length. The same idea can be implemented by combining multiple fiber sections with different Brillouin shifts [32].

Recently, ytterbium-doped fiber lasers and amplifiers have been used to produce high-power CW output ( $> 1 \text{ kW}$ ) as well as Q-switched pulses with energies exceeding  $1 \mu\text{J}$  [55–58]. SBS is often the limiting factor and its control is essential in such devices. As SBS threshold scales linearly with fiber length, a short fiber with high Yb-doping levels is employed. A considerable increase in the SBS threshold occurs for large-core fibers because the effective mode area  $A_{\text{eff}}$  in Eq. (9.2.4) scales quadratically with the core diameter. This is the approach adopted for modern Yb-doped fiber lasers. In a 2004 experiment [56],  $1.36 \text{ kW}$  of CW power was produced directly from such a laser by employing a  $40\text{-}\mu\text{m}$ -core fiber with  $A_{\text{eff}} \approx 900 \mu\text{m}^2$ . Even larger powers have been realized since then. A variety of schemes are used for SBS suppression in such high-power lasers and amplifiers. In addition to using a relatively large core, fiber structure is modified to decrease the overlap between the optical and acoustic modes either through different core dopants [59] or through air holes in the cladding [60]. Such modifications reduce the overlap factor  $f_A$  in Eq. (9.1.5) below 1 and can increase the SBS threshold by as much as a factor of 20.

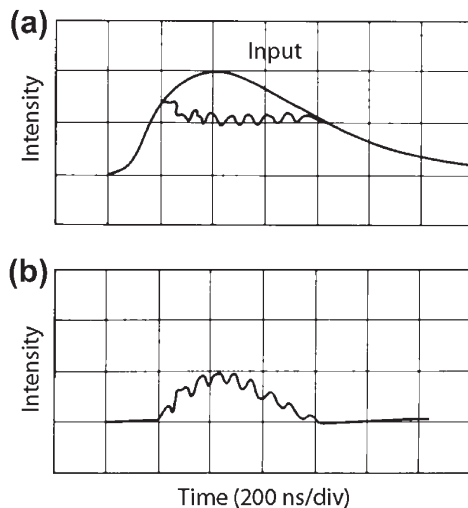
The SBS threshold predicted by Eq. (9.2.4) is only approximate for large-core fibers because its derivation assumes a single-mode fiber. A fiber with core diameter of  $> 25 \mu\text{m}$  may support hundreds of modes. Not only is the input pump power distributed among many fiber modes, but each pump mode can also contribute to multiple Stokes modes. For this reason, it is not easy to estimate the SBS threshold for a multimode fiber [61–64]. A detailed analysis shows that the threshold pump

power increases from the prediction of Eq. (9.2.4) by a factor that depends on the numerical aperture of the fiber, in addition to the core diameter [62]. An increase by a factor of 2 is expected for fibers with a numerical aperture of 0.2 at wavelengths near  $1.06 \mu\text{m}$ .

### 9.2.4 Experimental Results

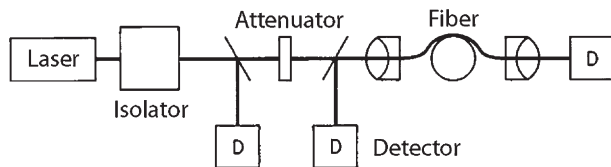
In the 1972 demonstration of SBS in optical fibers, a xenon laser operating at  $535.5 \text{ nm}$  was used as a source of relatively wide (width  $\sim 1 \mu\text{s}$ ) pump pulses [6]. Because of large fiber losses (about  $1300 \text{ dB/km}$ ), only small sections of fibers ( $L = 5\text{--}20 \text{ m}$ ) were used in the experiment. The measured Brillouin threshold was  $2.3 \text{ W}$  for a  $5.8\text{-m-long}$  fiber and reduced to below  $1 \text{ W}$  for  $L = 20 \text{ m}$ , in good agreement with Eq. (9.2.4) if we use the estimated value  $A_{\text{eff}} = 13.5 \mu\text{m}^2$  for the effective mode area. The Brillouin shift of  $v_B = 32.2 \text{ GHz}$  also agreed with Eq. (9.1.3).

Figure 9.3 shows the oscilloscope traces of incident and transmitted pump pulses, as well as the corresponding Stokes pulse, for SBS occurring in a  $5.8\text{-m-long}$  fiber. The oscillatory structure is due to relaxation oscillations whose origin is discussed in Section 9.4.4. The oscillation period of  $60 \text{ ns}$  corresponds to the round-trip time within the fiber. The Stokes pulse is narrower than the pump pulse because SBS transfers energy only from the central part of the pump pulse where power is large enough to exceed the Brillouin threshold. As a result, the peak power of the Stokes pulse can exceed the input peak power of the pump pulse. Indeed, SBS can damage the fiber permanently because of such an increase in the Stokes intensity [6].



**Figure 9.3** Oscilloscope traces of (a) input and transmitted pump pulses and (b) the Stokes pulse for SBS occurring inside a  $5.8\text{-m-long}$  fiber. (After Ref. [6]; © 1972 American Institute of Physics.)

In most of the early experiments, the SBS threshold was relatively high ( $> 100$  mW) because of extremely large fiber losses. As mentioned earlier, it can become as low as 1 mW if long lengths of low-loss fiber are employed. A threshold of 30 mW was measured when a ring dye laser, operating in a single-longitudinal mode at  $0.71\text{ }\mu\text{m}$ , was used to couple CW light into a 4-km-long fiber having a loss of about 4 dB/km [65]. In a later experiment, the threshold power was reduced to only 5 mW [66] by using a Nd:YAG laser operating at  $1.32\text{ }\mu\text{m}$ . Figure 9.4 shows a schematic of this experiment. The 1.6-MHz spectral width of the CW pump was considerably smaller than the Brillouin-gain bandwidth. The experiment employed a 13.6-km-long fiber with losses of only 0.41 dB/km, resulting in an effective length of 7.66 km. The isolator served to block the Stokes light from entering the laser. The transmitted and reflected powers were measured as a function of input power launched into the fiber. Figure 9.5 shows the experimental data. At low input powers, the reflected signal is due to 4% reflection at the air–fiber interface. The Brillouin threshold is reached at an input power of about 5 mW as manifested through a substantial increase in the reflected



**Figure 9.4** Schematic of the experimental setup used to observe SBS in optical fibers. (After Ref. [66]; © 1982 IEE.)

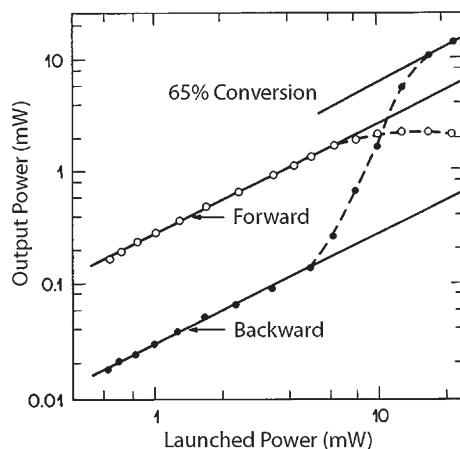


**Figure 9.5** Transmitted (forward) and reflected (backward) powers as a function of the input power launched into a 13.6-km-long single-mode fiber. (After Ref. [66]; © 1982 IEE.)

power through SBS. At the same time, the transmitted power decreases because of pump depletion, and reaches a saturation level of about 2 mW for input powers in excess of 10 mW. The SBS conversion efficiency is nearly 65% at that level.

In a 1987 experiment, SBS was observed by using a 1.3- $\mu\text{m}$  semiconductor laser, which utilized the distributed-feedback mechanism to emit light in a single-longitudinal mode with a spectral width  $\sim 10$  MHz [67]. The CW pump light was coupled into a 30-km-long fiber with a loss of 0.46 dB/km, resulting in an effective fiber length of about 9 km. The Brillouin threshold was reached at a pump power of 9 mW. To check if the bandwidth of the pump laser affected the SBS threshold, the measurements were also performed using a Nd:YAG laser having a bandwidth of only 20 kHz. The results were virtually identical with those obtained with the semiconductor laser, indicating that the Brillouin-gain bandwidth  $\Delta\nu_B$  was considerably larger than 15 MHz. As mentioned in Section 9.1.2,  $\Delta\nu_B$  is considerably enhanced for optical fibers from its value in bulk silica ( $\approx 22$  MHz at 1.3  $\mu\text{m}$ ) because of fiber inhomogeneities. The threshold power is smaller ( $\sim 1$  mW) near 1.55  $\mu\text{m}$  because of relatively low losses of optical fibers (0.2 dB/km) at that wavelength.

In most experiments on SBS, it is essential to use an optical isolator between the laser and the fiber to prevent the Stokes signal from reentering into the fiber after reflection at the laser-cavity mirror. In the absence of an isolator, a significant portion of the Stokes power can be fed back into the fiber. In one experiment, about 30% of the Stokes power was reflected back and appeared in the forward direction [68]. It was observed that several orders of Stokes and anti-Stokes lines were generated in the spectrum as a result of the feedback. Figure 9.6 shows the output spectra in the forward and backward directions for SBS occurring in a 53-m-long fiber. The 34-GHz spacing between adjacent spectral lines corresponds exactly to the Brillouin shift at  $\lambda_p = 514.5$  nm. The anti-Stokes components are generated as a result of four-wave mixing between the copropagating pump and Stokes waves (see Section 10.1). The higher-order Stokes lines are generated when power in the lower-order Stokes

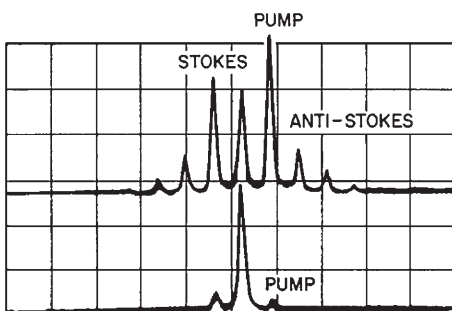


**Figure 9.6** Output spectra in the forward (upper trace) and backward (lower trace) directions showing multiple orders of Stokes and anti-Stokes waves generated without isolation between laser and fiber. (After Ref. [68]; © 1980 Elsevier.)

wave becomes large enough to satisfy the threshold condition given in Eq. (9.2.4). Even when optical isolators are used to prevent external feedback, Rayleigh back-scattering, occurring within the fiber, can provide feedback to the SBS process. In a 1998 experiment, this internal feedback process in a high-loss fiber (length 300 m) was strong enough to produce lasing when the fiber was pumped using 1.06- $\mu\text{m}$  CW radiation [69].

## 9.3 BRILLOUIN-FIBER AMPLIFIERS

Similar to the case of SRS, the SBS-produced gain in an optical fiber can be used to amplify a weak signal whose frequency is shifted from the pump frequency by an amount equal to the Brillouin shift. Of course, the pump and injected signal must propagate in opposite directions in the case of single-mode fibers if SBS were to transfer pump power to the signal. Such amplifiers were first studied during the 1980s [70–81] and are useful for sensing and other applications.

### 9.3.1 Gain Saturation

When the pump and signal waves counterpropagate inside an optical fiber, a large part of the pump power can be transferred to the Stokes wave when their frequencies differ by the Brillouin shift (about 10 GHz). Initially, the signal power increases exponentially, as indicated in Eq. (9.2.3). However, this growth is reduced when the Brillouin gain begins to saturate. To account for pump depletion, it is necessary to solve Eqs (9.2.1) and (9.2.2). Their general solution is somewhat complicated [82]. However, if fiber losses are neglected by setting  $\alpha = 0$ , we can make use of the fact that  $d(I_p - I_s)/dz = 0$ . If we use  $I_p - I_s = C$ , where  $C$  is a constant, Eq. (9.2.2) can be integrated along the fiber length to yield

$$\frac{I_s(z)}{I_s(0)} = \left( \frac{C + I_s(z)}{C + I_s(0)} \right) \exp(g_B C z). \quad (9.3.1)$$

Using  $C = I_p(0) - I_s(0)$ , the Stokes intensity  $I_s(z)$  is given by [4]

$$I_s(z) = \frac{b_0(1 - b_0)}{G(z) - b_0} I_p(0), \quad (9.3.2)$$

where  $G(z) = \exp[(1 - b_0)g_0 z]$  with

$$b_0 = I_s(0)/I_p(0), \quad g_0 = g_B I_p(0). \quad (9.3.3)$$

The parameter  $b_0$  is a measure of the SBS efficiency as it shows what fraction of the input pump power is converted to the Stokes power. The quantity  $g_0$  is the small-signal gain associated with the SBS process.

Equation (9.3.2) shows how the Stokes intensity varies in a Brillouin amplifier along the fiber length when the input signal is launched at  $z = L$  and the pump is

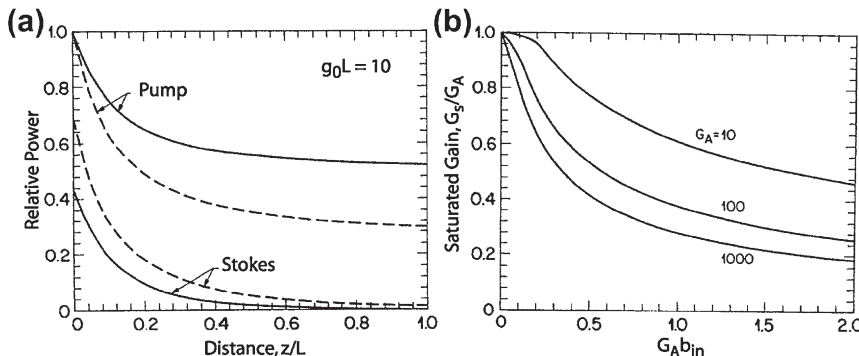


**Figure 9.7** (a) Evolution of pump and Stokes powers (normalized to the input pump power) along a fiber length for  $b_{\text{in}} = 0.001$  (solid lines) and  $0.01$  (dashed lines). (b) Saturated gain as a function of Stokes output for several values of  $G_A$ .

incident at  $z = 0$ . Figure 9.7 shows this variation for two input signals such that  $b_{\text{in}} = I_s(L)/I_p(0) = 0.001$  and  $0.01$ . The value of  $g_0 L = 10$  corresponds to unsaturated amplifier gain of  $e^{10}$  or  $43 \text{ dB}$ . Because of pump depletion, the net gain is considerably smaller. Nonetheless, about 50% and 70% of the pump power is transferred to the Stokes for  $b_{\text{in}} = 0.001$  and  $0.01$ , respectively. Note also that most of the power transfer occurs within the first 20% of the fiber length.

The saturation characteristics of Brillouin amplifiers can be obtained from Eq. (9.3.2) if we define the saturated gain using

$$G_s = I_s(0)/I_s(L) = b_0/b_{\text{in}}, \quad (9.3.4)$$

and introduce the unsaturated gain as  $G_A = \exp(g_0 L)$ . Figure 9.7 shows gain saturation by plotting  $G_s/G_A$  as a function of  $G_A b_{\text{in}}$  for several values of  $G_A$ . It should be compared with Figure 8.9 where the saturation characteristics of Raman amplifiers are shown. The saturated gain is reduced by a factor of 2 (by  $3 \text{ dB}$ ) when  $G_A b_{\text{in}} \approx 0.5$  for  $G_A$  in the range of  $20\text{--}30 \text{ dB}$ . This condition is satisfied when the amplified signal power becomes about 50% of the input pump power. As typical pump powers are  $\sim 1 \text{ mW}$ , the saturation power of Brillouin amplifiers is also  $\sim 1 \text{ mW}$ .

### 9.3.2 Amplifier Design and Applications

A semiconductor laser can be used to pump Brillouin amplifiers provided it operates in a single-longitudinal mode whose spectral width is considerably less than the Brillouin-gain bandwidth. Distributed-feedback or external-cavity semiconductor lasers [83] are most appropriate for pumping Brillouin amplifiers. In a 1986 experiment, two external-cavity semiconductor lasers, with line widths below  $0.1 \text{ MHz}$ , were used as pump and probe lasers [70]. Both lasers operated continuously and were tunable in the spectral region near  $1.5 \mu\text{m}$ . Figure 9.8 shows the experimental

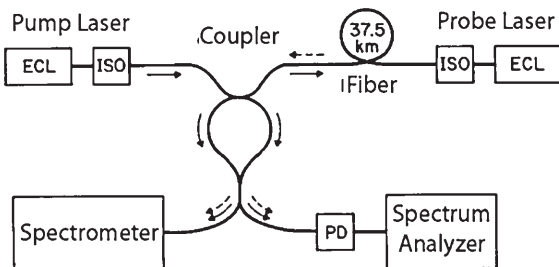


**Figure 9.8 Schematic illustration of a Brillouin amplifier; ECL, ISO, and PD stand for external-cavity laser, isolator, and photodetector, respectively. Solid and dashed arrows show the path of pump and probe lasers. (After Ref. [70]; © 1986 American Institute of Physics.)**

setup schematically. Radiation from the pump laser was coupled into a 37.5-km-long fiber through a 3-dB coupler. The probe laser provided a weak input signal ( $\sim 10 \mu\text{W}$ ) at the other end of the fiber. Its wavelength was tuned in the vicinity of the Brillouin shift ( $\nu_B = 11.3 \text{ GHz}$ ) to maximize the Brillouin gain. The measured amplification factor increased exponentially with the pump power. This is expected from Eq. (9.3.4). If gain saturation is neglected, the amplification factor can be written as

$$G_A = I_s(0)/I_s(L) = \exp(g_B P_0 L_{\text{eff}}/A_{\text{eff}} - \alpha L). \quad (9.3.5)$$

The amplifier gain was 16 dB ( $G_A = 40$ ) at a pump power of only 3.7 mW because of a long fiber length used in the experiment.

An exponential increase in the signal power with increasing pump powers occurs only if the amplified signal remains below the saturation level. The saturated gain  $G_A$  is reduced by 3 dB when

$$G_A(P_{\text{in}}/P_0) \approx 0.5, \quad (9.3.6)$$

for  $G_A$  in the range 20–30 dB, where  $P_{\text{in}}$  is the incident power of the signal being amplified. As discussed in Section 9.3.1, the saturation power of Brillouin amplifiers is  $\sim 1 \text{ mW}$ . In spite of gain saturation, Brillouin amplifiers are capable of providing 30 dB gain at a pump power under 10 mW. However, because  $\Delta\nu_B < 100 \text{ MHz}$ , the bandwidth of such amplifiers is also less than 100 MHz, in sharp contrast with Raman amplifiers whose bandwidth exceeds 5 THz. In fact, the difference between the signal and pump frequencies should be matched to the Brillouin shift  $\nu_B$  (about 11 GHz in the 1.55- $\mu\text{m}$  region) with an accuracy to better than 10 MHz. For this reason, Brillouin amplifiers are not suitable for amplifying signals in fiber-optic communication systems.

Brillouin amplifiers may be useful in practice for applications requiring selective amplification [71–73]. One such application consists of amplifying the carrier of a modulated signal selectively, while leaving its modulation sidebands unamplified [84]. The underlying principle is similar to that of homodyne detection, except that

the amplified carrier acts as a reference signal. This feature eliminates the need of a local oscillator that must be phase locked to the transmitter—a difficult task in general. In a demonstration of this scheme, the carrier was amplified by 30 dB more than the modulation sidebands even at a modulation frequency as low as 80 MHz [71]. With a proper design, sensitivity improvements of up to 15 dB or more are possible at bit rates in excess of 100 Mb/s. The limiting factor is the nonlinear phase shift induced by the pump (a kind of cross-phase modulation), if the difference between the pump and carrier frequencies does not match the Brillouin shift exactly. The calculations show [72] that deviations from the Brillouin shift should be within 100 kHz for a phase stability of 0.1 rad. Nonlinear phase shifts can also lead to undesirable amplitude modulation of a frequency-modulated signal [75].

Another application of narrowband Brillouin amplifiers consists of using them as a tunable narrowband optical filter for channel selection in a densely packed multichannel communication system [73]. If channel spacing exceeds but the bit rate is smaller than the bandwidth  $\Delta\nu_B$ , the pump laser can be tuned to amplify a particular channel selectively. This scheme was demonstrated in 1986 using a tunable color-center laser as a pump [73]. Two 45-Mb/s channels were transmitted through a 10-km-long fiber. Each channel could be amplified by 20–25 dB by using 14 mW of pump power when pump frequency was tuned in the vicinity of the Brillouin shift associated with each channel. More importantly, each channel could be detected with a low bit-error rate ( $<10^{-8}$ ) when channel spacing exceeded 140 MHz. Because  $\Delta\nu_B < 100$  MHz typically, channels can be packed as close as  $1.5\Delta\nu_B$  without introducing crosstalk from neighboring channels. Brillouin gain has been used as a narrowband amplifier at bit rates of up to 250 Mb/s with pumping from semiconductor lasers [76].

SBS can also be used for making distributed fiber sensors capable of sensing temperature and strain changes over relatively long distances [85–94]. The basic idea behind the use of SBS for fiber sensors can be understood from Eq. (9.1.3). As the Brillouin shift depends on the effective index of the fiber mode, it changes whenever the refractive index changes in response to local environmental variations. Both temperature and strain can change the refractive index of silica. By monitoring changes in the Brillouin shift along the fiber length, it is possible to map out the distribution of temperature or strain over long distances over which the SBS signal can be detected with a good signal-to-noise ratio.

The basic idea has been implemented in several experiments to demonstrate distributed sensing. A tunable CW probe laser and a pulsed pump laser inject light at the opposite ends of a fiber. The CW signal is amplified through SBS only when the pump–probe frequency difference coincides exactly with the Brillouin shift. The time delay between the launch of the pump pulse and increase in the received probe signal indicates the exact location where Brillouin amplification occurs. By tuning the probe frequency and measuring time delays, one can map the distribution of temperature or strain over the entire fiber length. In one experiment [87], two diode-pumped, 1.319- $\mu\text{m}$ , Nd:YAG lasers were used as the pump and probe. Frequency difference between the two lasers was adjusted by temperature tuning the probe-laser

cavity. A Bragg cell was used as an optical switch to generate pump pulses of widths in the range of 0.1–1 μs. A temperature resolution of 1 °C and a spatial resolution of 10 m were realized for a 22-km-long fiber. In a later experiment [88], spatial resolution was improved to 5 m, and fiber length was increased to 32 km. Similar performance is achieved for sensing of distributed strain. A resolution of 20 microstrain with a spatial resolution of 5 m has been demonstrated by using Brillouin loss [88]. It is even possible to combine the temperature and strain measurements in a single fiber sensor [89].

## 9.4 SBS DYNAMICS

The dynamic aspects of SBS are more important than SRS because the medium response in the SBS case is governed by the phonon lifetime with a typical value of <10 ns in silica fibers. The quasi-CW regime is thus valid only for pump pulses of widths 100 ns or more. When pulse width is ~10 ns, it becomes necessary to consider the dynamics of the acoustic mode participating in the SBS process. This section focuses on such time-dependent effects.

### 9.4.1 Coupled Amplitude Equations

The coupled intensity Eqs (9.2.1) and (9.2.2) are valid only under steady-state conditions. To include the transient effects, we need to solve the Maxwell wave equation (2.3.1) with the following material equation [10]:

$$\frac{\partial^2 \rho'}{\partial t^2} - \Gamma_A \nabla^2 \frac{\partial \rho'}{\partial t} - v_A^2 \nabla^2 \rho' = -\epsilon_0 \gamma_e \nabla^2 (\mathbf{E} \cdot \mathbf{E}), \quad (9.4.1)$$

where  $\rho' = \rho - \rho_0$  is a change in the local density from its average value  $\rho_0$ ,  $\Gamma_A$  is the damping coefficient, and  $\gamma_e = \rho_0 (\partial \epsilon / \partial \rho)_{\rho=\rho_0}$  is the electrostrictive constant introduced earlier in Section 9.1. The nonlinear polarization  $\mathbf{P}_{NL}$  appearing in Eq. (2.3.1) also has an additional term that depends on  $\rho'$  as

$$\mathbf{P}_{NL} = \epsilon_0 [\chi^{(3)} : \mathbf{E} \mathbf{E} \mathbf{E} + (\gamma_e / \rho_0) \rho' \mathbf{E}]. \quad (9.4.2)$$

Its origin lies in a change in material's dielectric constant,  $\Delta \epsilon = (\partial \epsilon / \partial \rho)_{\rho=\rho_0} \rho'$ , in response to acoustically induced density variations.

To simplify the following analysis, we assume that all fields remain linearly polarized along the  $x$  axis and introduce the slowly varying fields,  $A_p$  and  $A_s$ , as

$$\begin{aligned} \mathbf{E}(r,t) = & \hat{x} \operatorname{Re}[F_p(x,y)A_p(z,t)\exp(i k_p z - i \omega_p t) \\ & + F_s(x,y)A_s(z,t)\exp(-i k_s z - i \omega_s t)], \end{aligned} \quad (9.4.3)$$

where  $F_j(x,y)$  is the mode profile for the pump ( $j = p$ ) or Stokes wave ( $j = s$ ). The density  $\rho'$  is expanded in a similar fashion as

$$\rho'(\mathbf{r},t) = \operatorname{Re}[F_A(x,y)Q(z,t)\exp(i k_A z - i \Omega t)], \quad (9.4.4)$$

where  $\Omega = \omega_p - \omega_s$  and  $F_A(x, y)$  is the spatial distribution of the acoustic mode with the amplitude  $Q(z, t)$ . If several acoustic modes participate in the SBS process [32], a sum over all modes should be used in Eq. (9.4.4). In the following we consider a single acoustic mode responsible for the dominant peak in the Brillouin-gain spectrum.

By using Eqs (9.4.1)–(9.4.4) and (2.3.1) with the slowly varying envelope approximation, we obtain the following set of three coupled amplitude equations:

$$\frac{\partial A_p}{\partial z} + \frac{1}{v_g} \frac{\partial A_p}{\partial t} = -\frac{\alpha}{2} A_p + i\gamma(|A_p|^2 + 2|A_s|^2)A_p + i\kappa_1 A_s Q, \quad (9.4.5)$$

$$-\frac{\partial A_s}{\partial z} + \frac{1}{v_g} \frac{\partial A_s}{\partial t} = -\frac{\alpha}{2} A_s + i\gamma(|A_s|^2 + 2|A_p|^2)A_s + i\kappa_1 A_p Q^*, \quad (9.4.6)$$

$$\frac{\partial Q}{\partial t} + v_A \frac{\partial Q}{\partial z} = -\left[\frac{1}{2}\Gamma_B + i(\Omega_B - \Omega)\right]Q + i\kappa_2 A_p A_s^*, \quad (9.4.7)$$

where  $\Gamma_B = k_A^2 \Gamma_A$  is the acoustic damping rate and  $A_p$  is normalized such that  $|A_p|^2$  represents optical power. The two coupling coefficients are defined as

$$\kappa_1 = \frac{\omega_p \gamma_e \langle F_p^2 F_A \rangle}{2n_p c \rho_0 \langle F_p^2 \rangle}, \quad \kappa_2 = \frac{\omega_p \gamma_e \langle F_p^2 F_A \rangle}{2c^2 v_A \langle F_A^2 \rangle A_{\text{eff}}}, \quad (9.4.8)$$

where the angle brackets denote integration over the entire  $x$ - $y$  domain and we used  $F_s \approx F_p$ ,  $\omega_s \approx \omega_p$ , and  $n_s \approx n_p$  in view of a relatively small Brillouin shift.

Equations (9.4.5)–(9.4.7) govern the SBS dynamics under quite general conditions [95–103]. They include the nonlinear phenomena of SPM and XPM, but the effects of GVD are ignored. This is justified by noting that pulse widths typically exceed 1 ns, and the dispersion length is so large that GVD plays little role in the SBS process. In view of a small frequency difference between the pump and Stokes waves (about 10 GHz), we assumed that  $\gamma$  and  $\alpha$  are nearly the same for both waves.

For pump pulses of widths  $T_0 \gg T_B = \Gamma_B^{-1}$ , Eqs (9.4.5)–(9.4.7) can be simplified considerably because the acoustic amplitude  $Q$  decays so rapidly to its steady-state value that we can neglect both derivatives in Eq. (9.4.7). If we introduce the optical power as  $P_j = |A_j|^2$  where  $j=p$  or  $s$ , the SBS process is governed by the following two simple equations:

$$\frac{\partial P_p}{\partial z} + \frac{1}{v_g} \frac{\partial P_p}{\partial t} = -\frac{g_B(\Omega)}{A_{\text{eff}}} P_p P_s - \alpha P_p, \quad (9.4.9)$$

$$-\frac{\partial P_s}{\partial z} + \frac{1}{v_g} \frac{\partial P_s}{\partial t} = \frac{g_B(\Omega)}{A_{\text{eff}}} P_p P_s - \alpha P_s, \quad (9.4.10)$$

where  $g_B(\Omega)$  is the SBS gain given in Eq. (9.1.4). Its peak value  $g_B(\Omega_B)$  takes the form in Eq. (9.1.5) if we define the acoustic overlap factor as [32]

$$f_A = \frac{\left(\langle F_p^2 F_A \rangle\right)^2}{\langle F_p^2 \rangle \langle F_A^2 \rangle} = \frac{\left(\iint F_p^2(x, y) F_A(x, y) dx dy\right)^2}{\left(\iint F_p^2(x, y) dx dy\right) \left(\iint F_A^2(x, y) dx dy\right)}. \quad (9.4.11)$$

Thus, the SBS gain is reduced by a fraction  $f_A$  whose numerical value depends on the extent of overlap between the optical and acoustic modes supported by the fiber. When the spatial profiles associated with the optical and acoustic modes occupy a comparable area within the fiber, the numerical value of  $f_A$  is close to 1. However, it can be reduced considerably if the fiber is designed to reduce the overlap between the optical and acoustic modes participating in the SBS process [36]. In a 2009 study, aluminum doping was used to reduce this overlap, resulting in a 4.3 dB increase in the pump power at which the SBS threshold was reached [59].

### 9.4.2 SBS with Q-Switched Pulses

Equations (9.4.5)–(9.4.7) can be used to study SBS in the transient regime applicable for pump pulses shorter than 100 ns. From a practical standpoint, two cases are of interest depending on the repetition rate of pump pulses. Both cases are discussed here.

In the case relevant for optical communication systems, the repetition rate of pump pulses is  $>1$  GHz, while the width of each pulse is  $<100$  ps. The pulse train is not uniform for lightwave signals as “1” and “0” bits form a pseudorandom sequence. Nevertheless, the effect of such a pulse train is similar to the quasi-CW case discussed earlier because of its high repetition rate. The time interval between pump pulses is short enough that successive pulses can pump the same acoustic wave in a coherent manner (except in rare instances of a long sequence of “0” bits). The main effect of a pseudorandom pulse train is that the Brillouin threshold is increased by a factor of 2 or so compared with the CW case; the exact factor depends on the bit rate as well as modulation format. The SBS threshold can be increased even more by modulating the phase of the CW beam at the optical transmitter (before information is encoded on it) at frequencies in excess of 100 MHz [45]. Such phase modulations reduce the effective Brillouin gain by increasing spectral bandwidth of the optical source. Phase modulations can also be used to convert the CW beam into a train of optical pulses whose width ( $\sim 0.5$  ns) is a small fraction of the phonon lifetime [98–100].

The second case corresponds to the propagation of high-energy Q-switched pulses in a relatively short fiber ( $\sim 10$  m) at relatively low repetition rates (10 MHz or less). In this situation, the acoustic wave created by each pump pulse decays almost completely before the next pump pulse arrives. This case has become relevant with the advent of Yb-doped fiber lasers that can generate pulses with high peak powers. When a Yb-doped amplifier is used to increase the pulse energy further, SBS is often a limiting factor. As pulse widths are typically  $\sim 10$  ns, the dynamic nature of SBS plays an important role, and one must solve Eqs (9.4.5)–(9.4.7) numerically.

To illustrate the transient features, we assume that Gaussian-shape pump pulses of 15-ns width (FWHM) are launched into a 1-m-long fiber. Figure 9.9 shows (a) transmitted pump pulses and (b) reflected Stokes pulse for three values of peak powers in the range of 0.2–1 kW using  $\lambda_p = 1.06 \mu\text{m}$ ,  $A_{\text{eff}} = 50 \mu\text{m}^2$ ,  $T_B = 5$  ns,  $v_A = 5.96 \text{ km/s}$ , and other parameter values such that the Brillouin gain  $g_B = 5 \times 10^{-11} \text{ m/W}$  under steady-state conditions [102]. The SBS threshold

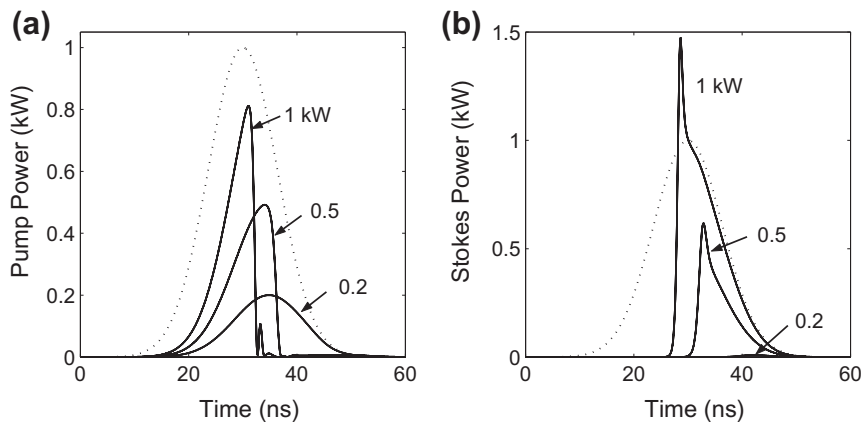


**Figure 9.9** (a) Transmitted pump pulses and (b) reflected Stokes pulses for three values of peak powers in the range of 0.2–1 kW when 15-ns Gaussian-shape pump pulses are launched into a 1-m-long fiber. Dashed curves show the input pump pulse with 1-kW peak power.

predicted from Eq. (9.2.4) for a CW pump beam is 21 W under such conditions. However, the Stokes pulse is barely visible for  $P_0 = 0.2$  kW, indicating that the SBS threshold for 15-ns pulses is more than 10 times higher. In terms of pulse energy, the SBS threshold exceeds 5  $\mu\text{J}$ . For  $P_0=0.5$  and 1 kW, the Stokes pulse is well formed and has a peak power larger than that of the input pump pulse.

Several other features of Figure 9.9 are noteworthy. The Stokes pulse is far from being Gaussian and exhibits a sharp leading edge, followed by a much shallower trailing edge. The width of the Stokes pulse is also shorter than the 15-ns width of input pump pulses. Transmitted pump pulses exhibit a sharp trailing edge and are also reduced in width. In the case of 1-kW peak power, the sharp trailing edge is followed by several secondary peaks of much reduced amplitude. All of these features can be understood by recalling that (a) the Stokes pulse builds up in the backward direction and is thus amplified mainly by the trailing edge of the pump pulse; (b) the round-trip time for a 1-m-long fiber is about 10 ns; and (c) the length of a 15-ps pump input pulse is about 3 m.

The width of the pump pulse also plays a critical role. Figure 9.10 compares (a) transmitted pump pulses and (b) reflected Stokes pulse for Gaussian-shape pump pulse with 1-kW peak power as the pump width is reduced from 20 to 10 ns. Transmitted pump pulses have similar shapes in both cases, although Stokes pulses exhibit different features. The important point is that, as the pump pulse becomes shorter, less and less energy is transferred to the Stokes pulse. SBS eventually ceases to occur for pump pulse widths smaller than the phonon lifetime.

The experiments performed using a Q-switched Nd:YAG laser exhibit features similar to those seen in Figures 9.9–9.11 showing the reflected Stokes pulse

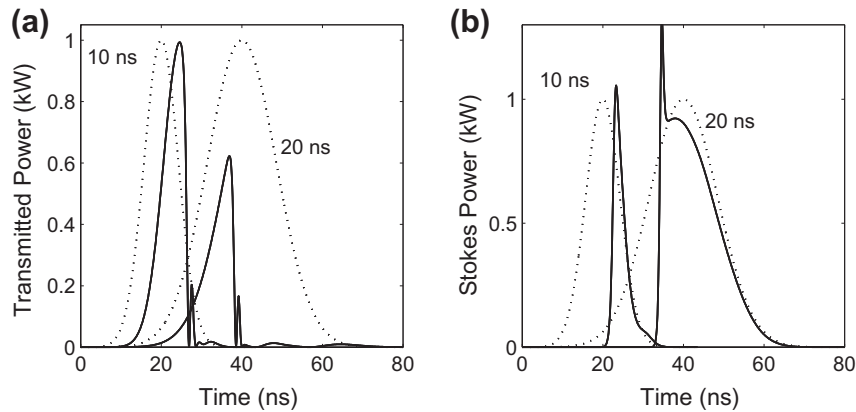


**Figure 9.10** (a) Transmitted pump pulses and (b) reflected Stokes pulses when Gaussian-shape pump pulses with 10 or 20 ns width are launched into a 1-m-long fiber. Dashed curves show, for comparison, the input pump pulse in each case.

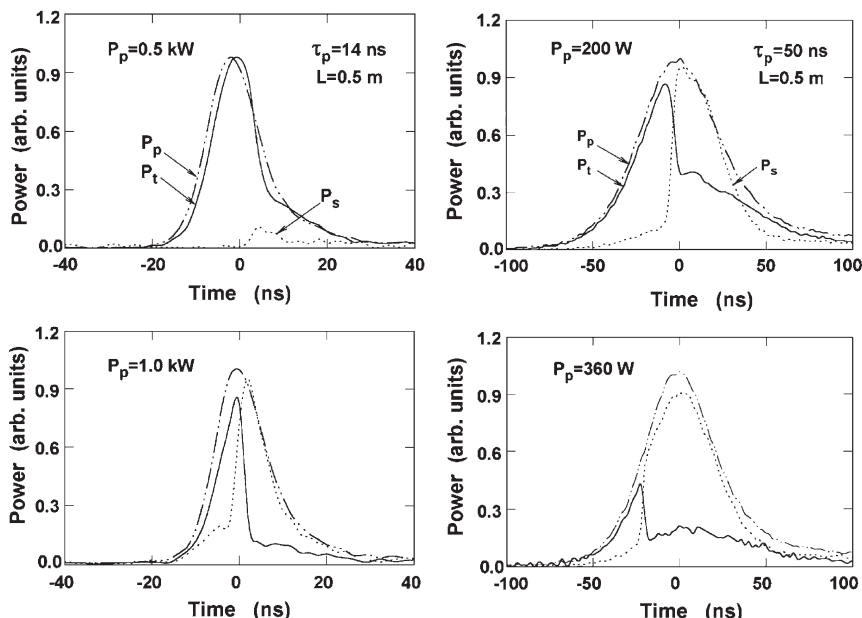


**Figure 9.11** Stokes (dotted) and transmitted pump (solid) pulses observed for several peak powers when 14-ns (left column) and 50-ns (right column) input pump pulses (dot-dashed curve) were transmitted through a 0.5-m-long fiber. (After Ref. [102]; © 1999 JSAP.)

(dotted curve) and the transmitted pump pulse (solid curve) for several peak powers when 14- and 50-ns pump pulses at the 10-Hz repetition rate were transmitted through a 0.5-m-long optical fiber [102]. The experimental results agree reasonably well with the numerical predictions based on Eqs (9.4.5)–(9.4.7).

An interesting question is whether Eqs (9.4.5)–(9.4.7) permit solitary-wave solutions such that each pump pulse generates the Stokes field  $A_s$  in the form of a backward-propagating soliton. It turns out that, under certain conditions, the pump and Stokes waves can support each other as a coupled bright–dark soliton pair [104–106], similar to the XPM-paired solitons discussed in Section 7.3. If we neglect the SPM and XPM terms by setting  $\gamma = 0$ , assume  $\Omega = \Omega_B$ , and introduce new variables as

$$Z = z/v_g, \quad B_a = -iv_g\kappa_1 Q, \quad B_j = (\kappa_1\kappa_2 v_g)^{1/2} A_j, \quad (9.4.12)$$

where  $j = p, s$ , we can write Eqs (9.4.5)–(9.4.7) in the form

$$\frac{\partial B_p}{\partial t} + \frac{\partial B_p}{\partial Z} + \frac{\alpha v_g}{2} B_p = -B_s B_a, \quad (9.4.13)$$

$$\frac{\partial B_s}{\partial t} + \frac{\partial B_s}{\partial Z} - \frac{\alpha v_g}{2} B_p = B_p B_a^*, \quad (9.4.14)$$

$$\frac{\partial B_a}{\partial t} + \frac{\Gamma_B}{2} B_a = B_p B_s^*. \quad (9.4.15)$$

It turns out that these equations have the following solution in the form of three coupled solitons [104]:

$$B_p(Z, t) = C_p[1 - b \tanh[p(Z + Vt)]], \quad (9.4.16)$$

$$B_s(Z, t) = C_s \operatorname{sech}[p(Z + Vt)], \quad B_a(Z, t) = C_a \operatorname{sech}[p(Z + Vt)], \quad (9.4.17)$$

where  $b$  is an arbitrary constant and other parameters are defined as

$$C_p = \frac{1}{2}\Gamma_B\sqrt{\mu}, \quad C_s = b\sqrt{2/\mu - 1}C_p, \quad C_a = \sqrt{2 - \mu}, \quad (9.4.18)$$

$$V = (1 - \mu)^{-1}, \quad p = (b\Gamma_B/2)(1 - \mu), \quad \mu = \alpha v_g / \Gamma_B. \quad (9.4.19)$$

Figure 9.12 shows an example of the SBS-coupled solitons for  $\mu = 0.1$  and  $b = 0.95$ . In this case, the Stokes wave travels backward in the form of a bright soliton at a velocity larger than  $v_g$  by a factor of  $V$ . At the same time, the pump travels forward as a dark soliton. Another solution of Eqs (9.4.13)–(9.4.15) shows that Stokes can also form a dark soliton, while the pump propagates as a bright soliton [105]. Such solitons exist even in the absence of GVD ( $\beta_2 = 0$ ) and XPM ( $\gamma = 0$ ) because they rely on the presence of a solitary acoustic wave. They are referred to as the *Brillouin solitons* and constitute an example of the so-called dissipative solitons because they can exist in spite of losses. Such solitons have been observed in a Brillouin-fiber ring laser [104].

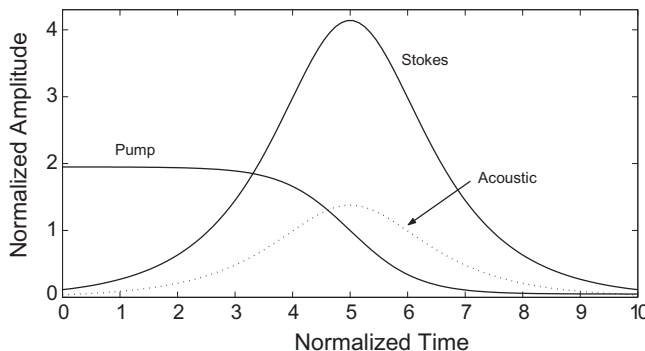


**Figure 9.12** Temporal profiles associated with the pump, Stokes, and acoustic waves when the three form a Brillouin soliton for  $\mu = 0.1$  and  $b = 0.95$ .

### 9.4.3 SBS-Induced Index Changes

When the pump and Stokes pulses differ in their carrier frequencies by the Brillouin shift exactly ( $\Omega = \Omega_B$ ), the Stokes falls on the Brillouin-gain peak and experiences the most gain. However, if  $\Omega = \omega_p - \omega_s$  differs from  $\Omega_B$  by even a few MHz, the gain is reduced but, at the same time, the refractive index changes by a small amount because of the SBS-induced amplification. This can be seen from Eqs (9.4.5)–(9.4.7) as follows. If we use the steady-state solution of Eq. (9.4.7) in Eq. (9.4.6), the Stokes wave satisfies

$$-\frac{\partial A_s}{\partial z} + \frac{1}{v_g} \frac{\partial A_s}{\partial t} + \frac{\alpha}{2} A_s = i\gamma(|A_s|^2 + 2|A_p|^2)A_s + \frac{\kappa_1 \kappa_2}{1 + i\delta} |A_p|^2 A_s, \quad (9.4.20)$$

where  $\delta = 2(\Omega - \Omega_B)/\Gamma_B$  is a normalized detuning parameter.

The last term in this equation represents the contribution of SBS to the total susceptibility of the medium. We can write it in the form  $(g_c/2)A_s$  and introduce the complex gain  $g_c$  as

$$g_c(\delta) = \frac{g_p |A_p|^2}{A_{\text{eff}}} \left( \frac{1}{1 + i\delta} \right), \quad (9.4.21)$$

where  $g_p \equiv g_B(\Omega_B)$  is the peak value of the Brillouin gain given in Eq. (9.1.5). The real part of  $g_c$  is related to the SBS gain as  $g_B = \text{Re}(g_c)$ , while the imaginary part provides the SBS-induced index change  $\Delta n_B = (c/2\omega_s)\text{Im}(g_c)$ . From Eq. (9.4.21) this index change is given by

$$\Delta n_B = \frac{cg_p |A_p|^2}{2\omega_s A_{\text{eff}}} \left( \frac{\delta}{1 + \delta^2} \right). \quad (9.4.22)$$

The physical origin of the SBS-induced index change lies in the requirement of causality that leads to a so-called Kramers–Kronig relation. According to this

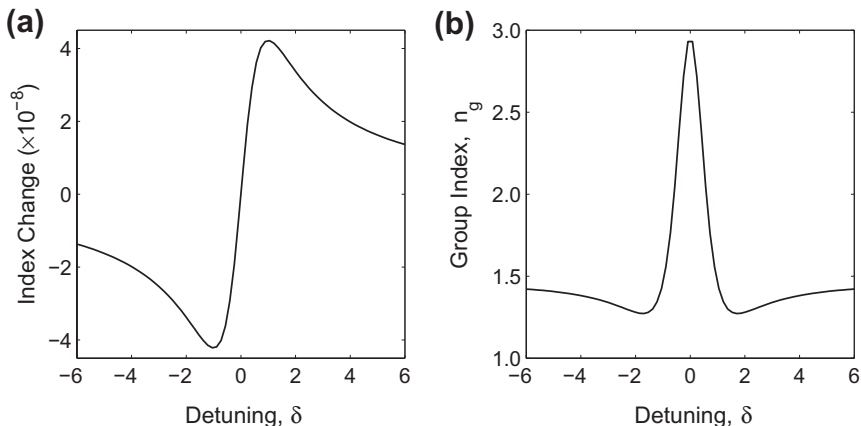


**Figure 9.13 (a) SBS-induced index change and (b) the resulting group index at a pump power of 1 W.**

relation, changes in the gain (or loss) of a medium are always accompanied with changes in the refractive index. The magnitude of such changes may be relatively small. For example, the maximum index change from Eq. (9.4.22) occurs for  $\delta = 1$  and has a value of  $< 10^{-7}$  even at a peak power level of 1 W, if we use typical parameter values  $g_p \approx 5 \times 10^{-11} \text{ m/W}$ ,  $A_{\text{eff}} = 50 \mu\text{m}^2$ , and  $\lambda_s = 1.06 \mu\text{m}$ .

Even though  $\Delta n_B$  itself is relatively small, it varies rapidly with  $\Omega$  near the Brillouin-gain peak. As seen from Eq. (1.2.9), the group velocity of a pulse is related inversely to  $\beta_1 = d\beta/d\omega = n_g/c$  with the group index  $n_g = n_t + \omega(dn_t/d\omega)$ . The total refractive index  $n_t$  should include  $\Delta n_B$ . For this reason, rapid changes in  $\Delta n_B$  with  $\omega$  can change  $n_g$  considerably and affect the group velocity of a pulse. If we include the contribution of fiber dispersion as well, the group index is given by

$$n_g = n_{g0} + \left( \frac{cg_p P_p}{\Gamma_B A_{\text{eff}}} \right) \frac{1 - \delta^2}{(1 + \delta^2)^2}, \quad (9.4.23)$$

where  $P_p = |A_p|^2$  is the pump power and  $n_{g0}$  is the group index in the absence of SBS gain. Figure 9.13 shows how  $\Delta n_B$  and  $n_g$  vary in the vicinity of the Brillouin-gain peak using parameter values quoted earlier with  $n_{g0} = 1.47$ ,  $\Gamma_B = 2 \times 10^8$  ( $T_B = 5 \text{ ns}$ ), and  $P_p = 1 \text{ W}$ . At this power level, index changes are  $\sim 10^{-8}$  but the group index is doubled near the gain peak from its original value of 1.47. Thus, the Stokes pulse should propagate at only 50% of the speed expected in the absence of SBS gain. Even a larger reduction is possible by increasing the peak power of the pump. As seen clearly from Eq. (9.4.23), the Stokes can also be forced to propagate faster than its nominal speed by detuning it such that  $\delta$  is close to 2.

Because of SBS-induced modification of the group velocity, the time  $T_r$  taken by the Stokes pulse to propagate through a fiber of length  $L$  also changes. The transit time is obtained from Eq. (9.4.23) using  $T_r = L/v_g$  and is given by

$$T_r = T_f + \left( \frac{g_p P_p L}{\Gamma_B A_{\text{eff}}} \right) \frac{1 - \delta^2}{(1 + \delta^2)^2}, \quad (9.4.24)$$

where  $T_f = n_{g0}L/c$  is the normal transit time through the fiber in the absence of SBS gain. The second term in this expression represents the SBS-induced temporal shift of the Stokes pulse, which is delayed for  $\delta < 1$  but speeds up when  $\delta \approx 2$ . Since the maximum delay occurs for  $\delta = 0$ , it is common to define the maximum SBS-induced pulse delay as

$$T_d = T_r - T_f = \frac{g_p P_p L}{\Gamma_B A_{\text{eff}}} = \frac{\ln G_A}{\Gamma_B}, \quad (9.4.25)$$

where  $G_A$  is the factor by which the signal is amplified. As this delay scales linearly with pump power, tunable delays are easily realized by adjusting the pump power.

The slowing down or speedup of optical pulses in the vicinity of an optical resonance (often called slow or fast light) has attracted considerable attention in recent years [107–109]. Early experiments made use of atomic vapors that are not suitable for a practical device. The use of SBS in optical fibers has the potential of realizing a compact device in which pulses can be delayed by an amount that is externally controllable. For this reason, starting in 2005, SBS was exploited for realizing tunable optical delays [110–119]. In a 2005 experiment, the output of a DFB laser, operating continuously at 1552 nm, was modulated using an electro-optic modulator to create two spectral sidebands separated by 11 GHz or so [110]. The upper sideband was used as a CW pump, while the lower one was used to create 100-ns Stokes pulses. The observed temporal delay was about 30 ns for a 11.8-km-long standard fiber when the pump power was large enough to provide a 30-dB gain.

A figure of merit used often to characterize the effectiveness of a slow-light technique is the fractional delay  $\tau_d = T_d/T_0$  experienced by a pulse of width  $T_0$  inside the medium [109]. This fractional delay could be increased considerably in a 2005 experiment [111] in which 15-ns Stokes pulses were delayed by 20 ns when they were amplified by 40 dB inside a 0.5-km-long fiber, but delayed pulses were also broadened noticeably. In another 2005 experiment [112] 40-ns Stokes pulses were delayed by up to 1500 ns by using four cascaded fiber segments, each 1.1 km long. Again, delayed pulses were considerably broader compared to input pulses. In both experiments, observed changes in the group velocity were relatively small because the transit time (about 500 ns for a 1-km-long fiber) of the pulse changed by <10%.

A problem with the use of SBS for slow-light applications is related to a relatively narrow bandwidth of the Brillouin-gain spectrum (typically <50 MHz). This problem was solved in a 2006 experiment by modulating the current of the semiconductor laser used as a pump with a pseudorandom bit pattern at 38 Mb/s [113].

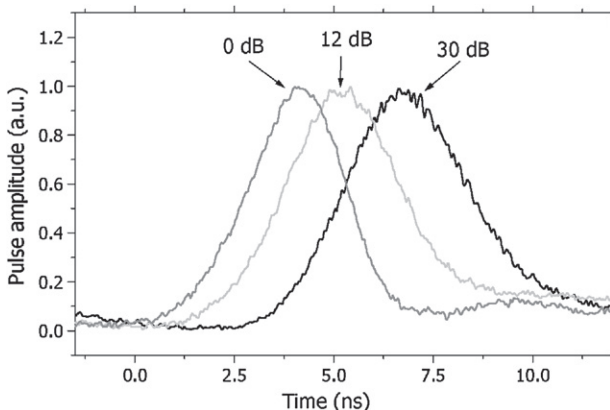


**Figure 9.14** Measured shapes of output Stokes pulses at three pump powers resulting in the amplification factors of 0, 12, and 30 dB (After Ref. [113]; © 2006 OSA.)

Small changes in the laser current manifested as random changes in the pump frequency, such that the effective gain bandwidth, increased to about 325 MHz. As a result, 2.7-ns pulses could be delayed by up to 3 ns inside a 6.7-km-long dispersion-shifted fiber. Figure 9.14 shows the measured pulse shapes at three values of the amplification factor defined as  $G_A = \exp(g_p P_p L / A_{\text{eff}})$ . The Stokes pulse shifts by about 3 ns for  $G_A = 30$  dB. The same technique was employed in a 2007 experiment to create a 12-GHz-wide SBS gain spectrum that was used to delay 75-ps pulses by up to 47 ps [114]. Although such a device could, in principle, be used for 10-Gb/s telecommunication channels, it was found to suffer from pattern dependence. Spectral broadening of the SBS gain suffers from two additional problems. Such a technique requires higher pump powers because of a considerable reduction in the peak Brillouin gain appearing in Eq. (9.4.25). At the same time, realizable pulse delays are smaller because the effective value of  $\Gamma_B$  in this equation is larger.

The simultaneous use of two pumps has led to further progress in this field. In one approach [115], pump frequencies lie on opposite sides of the signal frequency  $\omega_s$  and have values  $\omega_1 = \omega_s + \Omega_B$  and  $\omega_2 = \omega_s - \Omega_B$ . The first pump amplifies the signal through SBS gain, while the second pump deamplifies it. The reason behind this loss is that the signal is located on the anti-Stokes side of the second pump. From Eq. (9.4.25) the combined pulse delay provided by the two pumps is given by

$$T_d = \ln(G_1)/\Gamma_1 - \ln(G_2)/\Gamma_2, \quad (9.4.26)$$

where  $G_j$  and  $\Gamma_j$  are the peak value and effective bandwidth of the SBS gain induced by the two pumps ( $j = 1, 2$ ). If the pump powers are chosen such that  $G_1 = G_2$ , the signal experiences no net gain (or loss) but it can still be delayed considerably by making  $\Gamma_2 \gg \Gamma_1$ .

In a 2007 experiment [116], two pumps were used to realize an effective 25-GHz bandwidth for the SBS gain spectrum. In this case, the spectra of both pumps were broadened by more than the Brillouin shift (about 11 GHz). Although the second pump still provided a loss to the signal, the overlapping of the gain and loss spectra resulted in a net signal gain over a wide bandwidth. The resulting delays of 37-ps pulses were limited to below 11 ps because of a large increase in the value of  $\Gamma_B$  in Eq. (9.4.25). In another 2007 experiment, three pumps were employed to delay 30-ns pulses by as much as 120 ns [117]. One of these pumps, at frequency  $\omega_p$ , provided a gain to the signal, while the other two at frequencies  $\omega_p \pm \delta$  were used to induce losses in the wings of the SBS gain spectrum. The main point to note is that the SBS gain spectrum can be tailored by using multiple pumps. Therefore, resulting changes in the refractive index can be optimized to enhance the temporal delay of a signal pulse.

In all of these experiments, observed changes in the group velocity were a small fraction of the transit time because of long fiber lengths employed, indicating that the group velocity of the pulse changed by <10%. It is possible to reduce the group velocity by more than a factor of 2 by using short highly nonlinear fibers (see Chapter 11). In a 2007 experiment, a 2-m-long BiO<sub>2</sub> fiber was used for this purpose [118]. Because of a relatively small core diameter, the effective mode area  $A_{\text{eff}}$  was only 3  $\mu\text{m}^2$  for this fiber. At a pump power of about 400 mW, 200-ns pulses were delayed by about 55 ns. Noting that the transit time for this fiber is only 14 ns, this delay corresponds to a five-fold reduction in the group velocity of the pulse.

#### 9.4.4 Relaxation Oscillations

The dynamic response of SBS has many interesting features even for pump pulses that are much wider than  $T_B$  so that the acoustic dynamics plays little role. It turns out that the Stokes power does not approach its steady-state value monotonically but exhibits relaxation oscillations with a period  $2T_r$ , where  $T_r = L/v_g$  is the transit time for a fiber of length  $L$  [120]. An example of such oscillations is seen in Figure 9.3 for 1- $\mu\text{s}$ -wide pump pulses. In the presence of external feedback, relaxation oscillations can turn into stable oscillations [121], i.e., both the pump and Stokes waves can develop self-induced intensity modulation.

Even though the group velocity  $v_g$  is nearly the same for the pump and the Stokes waves, their relative speed is  $2v_g$  because of their counterpropagating nature. Relaxation oscillations occur as a result of this effective group-velocity mismatch. A simple way to obtain the frequency and the decay time of relaxation oscillations is to perform a linear stability analysis of the steady-state solution (9.3.2) of Eqs (9.4.9) and (9.4.10), following a procedure similar to that used in Section 5.1 in the context of modulation instability. The effect of external feedback can be included by assuming that optical fiber is enclosed within a cavity and by applying the appropriate boundary conditions at fiber ends [121]. Such a linear stability analysis also provides the conditions under which the steady state becomes unstable.

Assuming that small perturbations from the steady state decay as  $\exp(-ht)$ , the complex parameter  $h$  can be determined by linearizing Eqs (9.4.9) and (9.4.10). If the

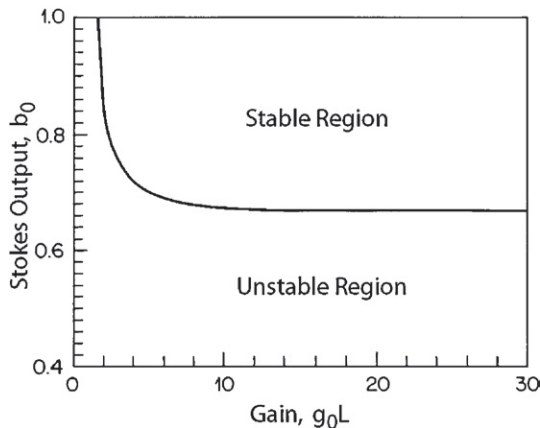


**Figure 9.15 Stable and unstable regions of SBS in the presence of feedback.** The solid line shows the critical value of the relative Stokes intensity [ $b_0 = I_s(0)/I_p(0)$ ] below which the steady state is unstable. (After Ref. [121]; © 1985 OSA.)

real part of  $h$  is positive, perturbations decay exponentially with time through relaxation oscillations whose frequency is given by  $\nu_r = \text{Im}(h)/2\pi$ . By contrast, if the real part of  $h$  becomes negative, perturbations grow with time, and the steady state is unstable. In that case, SBS leads to temporal modulation of the pump and Stokes intensities even for a CW pump. Figure 9.15 shows the stable and unstable regions in the case of feedback as a function of the gain factor  $g_0L$  that is related to the pump power  $P_p$  as  $g_0 = g_B P_p / A_{\text{eff}}$ . The parameter  $b_0$  represents the fraction of the pump power converted to the Stokes power.

Figure 9.16 shows the temporal evolution of the Stokes and pump intensities obtained by solving Eqs (9.4.9) and (9.4.10) numerically. The top row for  $g_0L = 30$  shows relaxation oscillations occurring in the absence of feedback. The oscillation period is  $2T_r$ , where  $T_r$  is the transit time. Physically, the origin of relaxation oscillations can be understood as follows [120]. Rapid growth of the Stokes power near the input end of the fiber depletes the pump. This reduces the gain until the depleted portion of the pump passes out of the fiber. The gain then builds up, and the process repeats itself.

The bottom row in Figure 9.16 corresponds to the case of weak feedback such that  $R_1 R_2 = 5 \times 10^{-5}$ , where  $R_1$  and  $R_2$  are the reflectivities at the fiber ends. The gain factor of  $g_0L = 13$  is below the Brillouin threshold. The Stokes wave is nonetheless generated because of the reduction in Brillouin threshold as a result of the feedback. However, a steady state is not reached because of the instability indicated in Figure 9.15. Instead, both the pump output at  $z = L$  and the Stokes output at  $z = 0$  exhibit steady oscillations. Interestingly enough, a steady state is reached if the feedback is increased such that  $R_1 R_2 \geq 2 \times 10^{-2}$ . This happens because  $b_0$  for this amount of feedback lies in the stable regime of Figure 9.15. All such dynamic features have been observed experimentally [121].

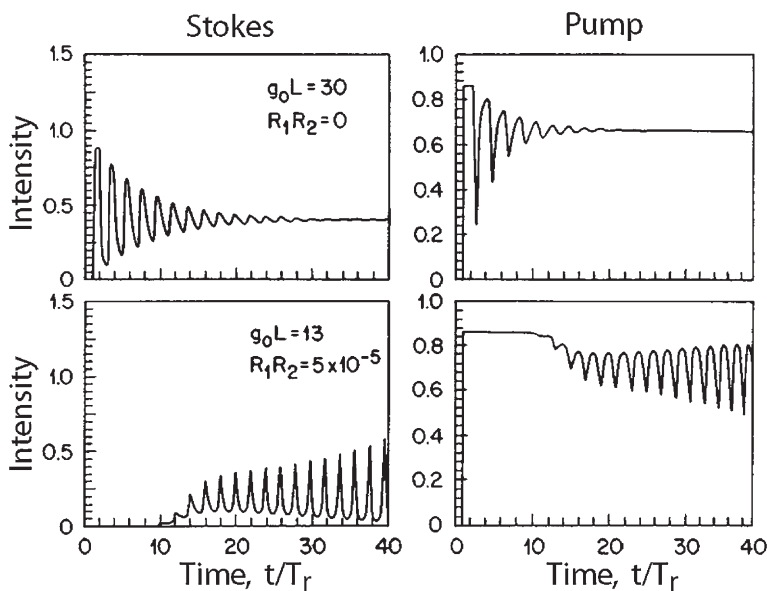


**Figure 9.16** Temporal evolution of the Stokes (left column) and pump (right column) intensities without (top row) and with (bottom row) feedback. Fiber losses correspond to  $\alpha L = 0.15$ . (After Ref. [121]; © 1985 OSA.)

#### 9.4.5 Modulation Instability and Chaos

Another instability can occur when two counterpropagating pump waves are present simultaneously, even though none of them is intense enough to reach the Brillouin threshold [122–127]. The origin of this instability lies in the SBS-induced coupling between the counterpropagating pump waves through an acoustic wave at the frequency  $\nu_B$ . The instability manifests as the spontaneous growth of side modes in the pump spectrum at  $\nu_p \pm \nu_B$  around the pump frequency  $\nu_p$  [123]. In the time domain, both pump waves develop modulations at the frequency  $\nu_B$ . The SBS-induced modulation instability is analogous to the XPM-induced modulation instability discussed in Section 7.3 except that it occurs for waves propagating in the opposite directions. The instability threshold depends on the forward and backward input pump intensities  $I_f$  and  $I_b$ , fiber length  $L$ , and parameters  $g_B$ ,  $\nu_B$ , and  $\Delta\nu_B$ .

Figure 9.17 shows the forward pump intensity  $I_f$  (in the normalized form) needed to reach the instability threshold as a function of the intensity ratio  $I_b/I_f$  for  $\Delta\nu_B/\nu_B = 0.06$  and several values of the normalized fiber length  $4\pi n \nu_B L/c$ . The instability threshold is significantly smaller than the Brillouin threshold ( $g_B I_f L = 21$ ) and can be as small as  $g_B I_f L = 3$  for specific values of the parameters. Numerical results show that temporal evolution of pump intensities at the fiber output may become chaotic [126], following a period-doubling route, if the Brillouin-gain bandwidth  $\Delta\nu_B$  is comparable to the Brillouin shift  $\nu_B$ . Subharmonics

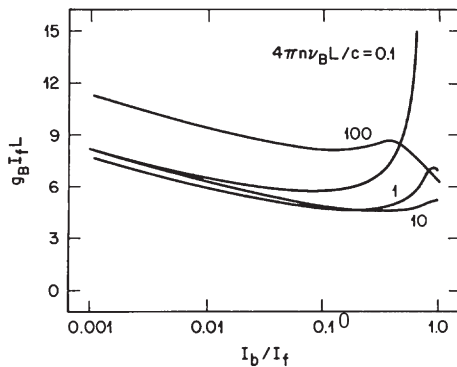


**Figure 9.17 Threshold of SBS-induced modulation instability for counterpropagating pump waves of input intensities  $I_f$  and  $I_b$ . Normalized forward intensity is plotted as a function of  $I_b/I_f$  for  $\Delta\nu_B/\nu_B=0.06$  for several fiber lengths. (After Ref. [126]; © 1988 OSA.)**

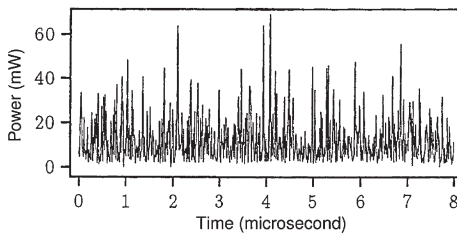


**Figure 9.18 Fluctuations observed in Stokes power at a pump power  $P_0=1.5P_{\text{cr}}$  when SBS occurred inside a 166-m-long fiber. (After Ref. [137]; © 1993 American Physical Society.)**

of  $\nu_B$  appear in the spectrum of the scattered light with successive period-doubling bifurcations. The chaotic evolution is also predicted when the backward pump is not launched externally but is produced by the feedback of the forward pump at a reflector [124].

Considerable effort was devoted during the 1990s to observe and characterize SBS-induced chaos in optical fibers [128–140]. Irregular fluctuations in the Stokes intensity, occurring at a time scale  $\sim 0.1 \mu\text{s}$ , were observed in several experiments [128–130]. Figure 9.18 shows an example of fluctuations in the Stokes power observed for SBS occurring inside a 166-m-long fiber when the CW pump power was 50% above the SBS threshold ( $P_0 = 1.5P_{\text{cr}}$ ). Whether such fluctuations are stochastic or chaotic in nature is an issue that is not easy to resolve. Interpretation of the experimental results requires a careful consideration of both spontaneous Brillouin scattering and the effects of optical feedback. It was established by 1993 that fluctuations in the Stokes power, observed when care was taken to suppress optical feedback, were due to stochastic noise arising from spontaneous Brillouin scattering [137].

The mathematical description of such fluctuations requires inclusion of spontaneous Brillouin scattering through a Langevin noise source in Eq. (9.4.7) governing changes in the material density [134]. Such a stochastic model is able to explain most of the experimentally observed features [141].

The SBS dynamics change drastically in the presence of optical feedback introduced either by using an external mirror or occurring naturally at the fiber ends because of a refractive-index discontinuity at the glass-air interface. As discussed earlier in this section, feedback destabilizes relaxation oscillations and leads to periodic output at a repetition rate  $(2T_r)^{-1}$ , where  $T_r$  is the transit time. Under certain conditions, the envelope of the pulse train exhibits irregular fluctuations occurring at a time scale much longer than  $T_r$ . In one experiment, such fluctuations were found to be stochastic in nature and were attributed to fluctuations of the relative phase between the pump light and the fiber resonator [137]. In another experiment, a quasi-periodic route to chaos was observed in a limited range of pump powers [138]. Fiber nonlinearity may have played a role in this experiment because chaos was observed at pump powers close to 0.8 W. Numerical simulations based on Eqs (9.4.5)–(9.4.7) predict that inclusion of SPM and XPM can lead to optical chaos, even in the absence of feedback, if the nonlinearity is large enough [131–133]. In the presence of feedback, chaos is predicted to occur even at low pump powers for which the contribution of SPM and XPM is negligible [140]. Numerical simulations show that the Stokes power may exhibit periodic or quasi-periodic oscillations that ultimately become chaotic, depending on the pumping level.

## 9.5 BRILLOUIN-FIBER LASERS

Similar to the SRS case considered in Section 8.2, the Brillouin gain in optical fibers can be used to make lasers by placing the fiber inside a cavity. Such lasers were made as early as 1976 and have remained an active topic of study since then [142–154]. Both the ring-cavity and the Fabry–Perot geometries have been used for making Brillouin lasers, each having its own advantages. As seen in Figure 9.19, no mirrors are needed in the case of a ring cavity if a directional fiber coupler is employed.

### 9.5.1 CW Operation

The threshold pump power required for laser oscillations is reduced considerably from that given in Eq. (9.2.4) because of the feedback provided by the cavity. In the case of a ring cavity, using the boundary condition  $P_s(L) = R_m P_s(0)$ , the threshold condition can be written as

$$R_m \exp(g_B P_{th} L_{eff}/A_{eff} - \alpha L) = 1, \quad (9.5.1)$$

where  $L$  is the ring-cavity length,  $R_m$  is the fraction of Stokes power fed back after each round trip, and  $P_{th}$  is the threshold value of the pump power. Fiber losses can be neglected in most cases of practical interest because  $L$  is typically 100 m

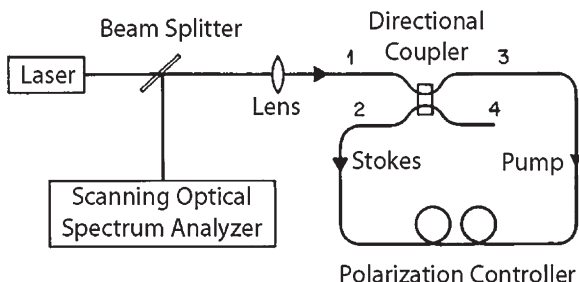


**Figure 9.19** Schematic illustration of a Brillouin ring laser. A directional coupler is used to inject the pump beam into the ring cavity. (After Ref. [146]; © 1982 OSA.)

or less. A comparison with Eq. (9.2.4) shows that, for the same fiber length, the factor of 21 is typically replaced by a number in the range of 0.1–1 depending on the value of  $R_m$ .

In a 1976 demonstration of a CW Brillouin laser, a 9.5-m-long ring cavity was pumped using an argon-ion laser [142]. The length of fiber was chosen to be relatively small in view of its large losses (about 100 dB/km) at the pump wavelength of 514.5 nm. The round-trip losses (about 70%) were still so large that the threshold power was more than 100 mW for this laser. By 1982, the threshold pump power was reduced to a mere 0.56 mW [146] by using an all-fiber ring resonator shown schematically in Figure 9.19. The round-trip cavity losses were only 3.5% for this ring cavity. Such a low loss resulted in an enhancement of the input pump power by a factor of 30 inside the ring cavity. A He–Ne laser operating at 633 nm could be used as a pump source because of such a low laser threshold. Semiconductor lasers were used for pumping of Brillouin lasers soon after, resulting in a compact device [147]. Such lasers are routinely used in high-performance laser gyroscopes for inertial rotation sensing.

Brillouin-fiber lasers consisting of a Fabry–Perot cavity exhibit features that are qualitatively different from those making use of a ring cavity. The difference arises from the simultaneous presence of the forward and backward propagating components associated with the pump and Stokes waves. Higher-order Stokes waves are generated through cascaded SBS, a process in which each successive Stokes component pumps the next-order Stokes component after its power becomes large enough to reach the Brillouin threshold. At the same time, anti-Stokes components are generated through four-wave mixing between copropagating pump and Stokes waves. The frequency spectrum of the laser output appears similar to that shown in Figure 9.6. The number of Stokes and anti-Stokes lines depends on the pump power. In one experiment [142], up to 14 spectral lines were observed, with 10 lines appearing on the Stokes side, when a 20-m-long fiber was used inside a Fabry–Perot cavity, which was pumped with a CW argon-ion laser operating at 514.5 nm. The 34-GHz frequency spacing between adjacent lines corresponded to the expected Brillouin shift.

Most Brillouin-fiber lasers use a ring cavity to avoid generation of multiple Stokes lines through cascaded SBS. The performance of a Brillouin ring laser depends on the fiber length  $L$  used to make the cavity (see Figure 9.19), as it determines the longitudinal-modespacing through  $\Delta\nu_L = c/(\bar{n}L)$ , where  $\bar{n}$  is the effective mode index. For short fibers such that  $\Delta\nu_L > \Delta\nu_B$ , where  $\Delta\nu_B$  is the Brillouin-gain bandwidth (typically 20 MHz), the ring laser operates stably in a single-longitudinal mode. Such lasers can be designed to have low threshold [146] and to emit CW light with a narrow spectrum [149]. In contrast, a Brillouin ring laser operates in multiple longitudinal modes when  $\Delta\nu_L \ll \Delta\nu_B$ , and the number of modes increases with fiber length. As early as 1981, it was noted that such lasers required active intracavity stabilization to operate continuously [145]. In fact, their output can become periodic, and even chaotic, under some conditions. This issue is discussed in Section 9.5.2.

An important application of CW Brillouin lasers consists of using them as a sensitive laser gyroscope [150–152]. Laser gyroscopes differ from fiber gyroscopes, both conceptually and operationally. Whereas passive fiber gyroscopes use a fiber ring as an interferometer, active laser gyroscopes use the fiber ring as a laser cavity. The rotation rate is determined by measuring the frequency difference between the counterpropagating laser beams. Similarly to the case of passive fiber gyroscopes, fiber nonlinearity affects the performance of a Brillouin-laser fiber gyroscope through XPM-induced nonreciprocity and constitutes a major source of error [151].

Considerable attention was paid during the 1990s to developing hybrid Brillouin-erbium fiber lasers capable of operating either at several wavelengths simultaneously or in a single mode, whose wavelength is tunable over a wide range [155–164]. The basic idea is to incorporate an erbium-doped fiber amplifier (EDFA) within the Brillouin-laser cavity [155] that provides gain over its entire bandwidth of 40 nm or so. The EDFA is pumped such that its gain is below the threshold gain of the cavity. The addition of Brillouin gain allows the laser to reach the threshold over the narrow Brillouin bandwidth (30 MHz or so) and to generate the first-order Stokes line. However, this line acts as a pump to create the second-order Stokes line, and the process repeats again and again, generating multiple wavelengths spaced apart exactly by the Brillouin shift  $\nu_B$  of about 11 GHz. Since the pump and its corresponding Stokes must propagate in the opposite direction, even and odd order Stokes travel in opposite directions when a ring cavity is used. As a result, output in any direction consists of laser modes spaced apart by  $2\nu_B$ . This problem can be solved if a Fabry–Perot cavity is employed because all waves then propagate in both directions.

As early as 1998, the use of a fiber-loop Sagnac interferometer, acting as one of the mirrors of a Fabry–Perot cavity, resulted in generation of up to 34 spectral lines through cascaded SBS [156]. The other mirror was made 100% reflecting to ensure that all laser modes exit through the Sagnac loop. This configuration has an added benefit. Even though SBS generates only Stokes lines that are shifted toward the red side of the injected pump, multiple anti-Stokes lines are also produced within

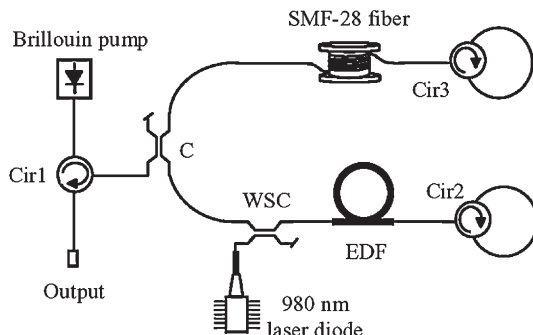


**Figure 9.20** Schematic of a Brillouin-fiber laser with two fiber loops containing optical circulators (Cir2 and Cir3) and acting as two mirrors of a Fabry–Perot cavity. WSC stands for a wavelength-selective coupler. (After Ref. [161]; © 2005 OSA.)

the Sagnac loop through four-wave mixing. As a result, the laser output has modes whose wavelengths lie on both sides of the pump wavelength.

For some applications, tuning of the frequency comb generated inside a Brillouin-fiber laser is desirable. Several techniques can be used for this purpose. A Sagnac loop made with 18 cm of polarization-maintaining fiber was used as an optical filter in a 2004 experiment for tuning the laser output [159]. Such a tunable filter selects different spectral windows of the amplified spontaneous emission produced by the EDFA, while SBS gain generates a frequency comb within this window. The laser produced its output at 12 wavelengths that was tunable over 14.5 nm. A tuning range of up to 60 nm was realized in a 2005 experiment [161]. Figure 9.20 shows the schematic cavity design for this laser. Two fiber loops act as mirrors because of the embedded optical circulators. The SBS gain is provided by 8.8 km of single-mode fiber (SMF-28), pumped with an external-cavity semiconductor laser tunable from 1520 to 1620 nm. The 10-m-long EDFA is pumped at 980 nm using another semiconductor laser. The tuning range and the number of Stokes lines produced by such a laser varied with the relative power levels of two pump lasers.

In an interesting configuration, the SBS pump is generated internally through self-seeding, and only one laser is needed for pumping the EDFA [160]. Figure 9.21 shows the laser design schematically. The ring cavity contains a 16-m-long EDFA and 5-km of standard fiber to produce SBS gain. A Sagnac loop, built using a polarization-maintaining fiber (PMF), is used as a mirror. This mirror doubles the SBS gain as light passes through the 5-km fiber twice during each round trip. The Brillouin pump is first generated with self-seeding provided by the amplified spontaneous emission of EDFA. This pump then creates multiple Stokes lines through SBS gain. Such a laser produced as many as 120 Stokes lines with nearly equal power levels that were separated by the Brillouin shift of 11 GHz and occupied a 12-nm spectral window within the EDFA gain bandwidth.

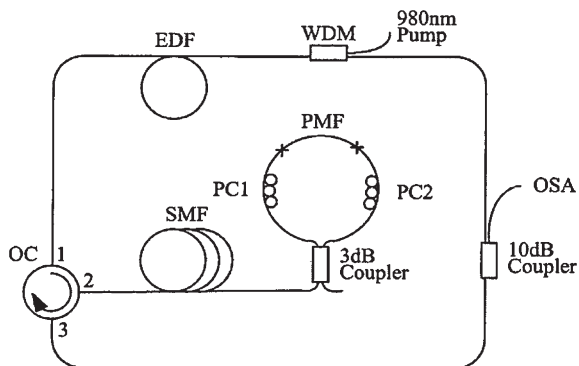


**Figure 9.21** Schematic of a self-seeded Brillouin-fiber laser: OC, PC, PMF, and OSA stand for optical circulator, polarization controller, polarization-maintaining fiber, and optical spectrum analyzer, respectively. (After Ref. [160]; © 2005 OSA.)

### 9.5.2 Pulsed Operation

Brillouin-fiber lasers with long cavity lengths can be forced to emit a pulse train using several different methods. The technique of active mode locking was used in a 1978 experiment by placing an amplitude modulator inside the laser cavity [144]. Laser output consisted of a train of pulses (width about 8 ns) at a repetition rate of 8 MHz, determined by the cavity length. These pulses result from the locking of multiple longitudinal modes of the cavity.

Another type of mode locking can occur in Fabry–Perot cavities in which multiple Stokes lines are generated through cascaded SBS. Relaxation oscillations can seed the mode-locking process because their period is equal to the round-trip time in the cavity. Indeed, partial mode locking of such a Brillouin laser by itself was observed [144], but the process was not very stable. The reason can be understood from Eq. (9.1.3) showing that the Brillouin shift depends on pump wavelength. In cascaded SBS, different Stokes waves act as pumps for the successive Stokes. As a result, multiple Stokes lines are not spaced equally but differ in frequencies by a small amount  $\sim 1$  MHz. In a 1989 experiment, mode locking was achieved by using a multimode fiber [148]. As different modes have slightly different effective indexes (modal dispersion), equally spaced Stokes lines can be generated by using different fiber modes.

An interesting technique for generating short Stokes pulses from a Brillouin laser makes use of synchronous pumping using a mode-locked train of pump pulses [153]. The idea is quite simple. The length of a ring cavity is adjusted such that the round-trip time exactly equals the spacing between pump pulses. Each pump wave is so short that it is unable to excite the acoustic wave significantly. However, if the next pump pulse arrives before the acoustic wave has decayed, the cumulative effect of multiple pump pulses can build up the acoustic wave to a large amplitude. After the

build-up process is complete, a short Stokes pulse will be generated through transient SBS with the passage of each pump pulse. This technique has produced Stokes pulses of 200-ps duration when 300-ps pulses from a mode-locked Nd:YAG laser were used for pumping a Brillouin ring laser.

Brillouin ring lasers with long cavity lengths can produce pulse trains, even when pumped continuously, through a nonlinear self-pulsing mechanism based on an inherent instability of such lasers. The origin of this instability lies in the relaxation oscillations discussed earlier in Section 9.4.4. Typically, pulses have widths in the range of 20–30 ns and are emitted with a repetition rate nearly equal to the longitudinal-mode spacing  $\Delta\nu_L \equiv 1/t_r$ , where  $t_r$  is the round-trip time.

Physics behind such lasers attracted considerable attention during the 1990s [165–169]. Equations (9.4.5)–(9.4.7) describe the nonlinear dynamics in Brillouin ring lasers when supplemented with the boundary conditions

$$A_s(L, t) = \sqrt{R} A_s(0, t), \quad A_p(0, t) = \sqrt{P_0} + \sqrt{R_p} A_p(L, t), \quad (9.5.2)$$

where  $R$  and  $R_p$  are the feedback levels for the Stokes and pump fields after one round-trip inside the ring cavity. In modern Brillouin lasers, feedback of the pump on each round trip is avoided using either an optical isolator or an optical circulator in place of the directional coupler (see Figure 9.18) so that  $R_p = 0$ .

Neither dispersive nor nonlinear effects play an important role in determining the self-pulsing threshold in Brillouin lasers. Thus, we can set  $\Omega = \Omega_B$  and  $\gamma = 0$  in Eqs (9.4.5)–(9.4.7), and also neglect the  $z$  derivative in Eq. (9.4.7). A linear stability analysis, similar to that used for modulation instability, of the resulting set of three equations predicts that the stability of the CW state depends on the pumping parameter  $g_0 \equiv g_B P_0 / A_{\text{eff}}$ , defined as the small-signal gain at the pump power  $P_0$ . The linear stability analysis is quite complicated when the nonlinear effects and the finite medium response time  $T_B$  are taken into account. However, a simplified approach shows that the CW state is unstable whenever the pump power  $P_0$  satisfies the inequality [168]

$$\ln\left(\frac{1}{R}\right) < g_0 L < 3 \ln\left(\frac{1+2R}{3R}\right). \quad (9.5.3)$$

The laser threshold is reached when  $g_0 L = \ln(1/R)$ . However, the laser does not emit CW light until  $g_0 L$  is large enough to be outside the instability domain predicted by Eq. (9.5.3). Noting that the instability domain shrinks as  $R$  approaches 1, it is easy to conclude that stable CW operation with a low threshold can be realized in low-loss ring cavities [146]. On the other hand, the pump-power level at which CW operation is possible becomes quite high when  $R \ll 1$  (high-loss cavity). As an example, the laser threshold is reached at  $g_0 L = 4.6$  when  $R = 0.01$  but CW operation is possible only for  $g_0 L > 10.6$ .

Numerical solutions based on Eqs (9.4.5)–(9.4.7) show that the laser emits a pulse train in the unstable region except close to the instability boundary where the laser output exhibits periodic oscillations whose frequency depends on the number of

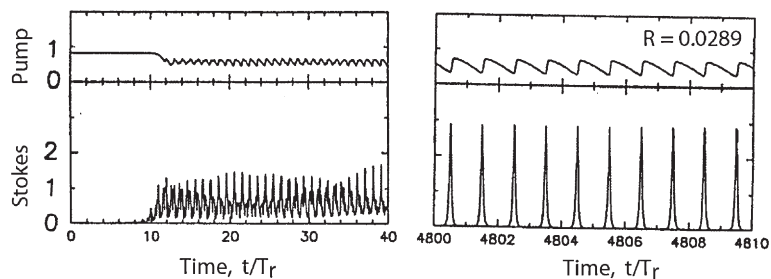


**Figure 9.22** Evolution of Stokes (lower trace) and pump (upper trace) amplitudes over multiple round trips in the self-pulsing regime: (left) initial build-up from noise; (right) fully formed pulse train after 4800 round trips. (After Ref. [168]; © 1999 OSA.)

longitudinal modes supported by the laser [168]. Moreover, in this transition region, the laser exhibits bistable behavior in the sense that the transition between the CW and periodic states occurs at different pump levels depending on whether  $P_0$  is increasing or decreasing. The width of the hysteresis loop depends on the nonlinear parameter  $\gamma$  responsible for SPM and XPM, and bistability ceases to occur when  $\gamma = 0$ .

In the self-pulsing regime, the laser emits a train of optical pulses. As an example, Figure 9.22 shows evolution of the Stokes and pump amplitudes over multiple round trips. The laser output exhibits transients (Stokes traces) that last over hundreds of round trips. A regular pulse train is eventually formed (right traces) such that a pulse is emitted nearly once per round-trip time. The emitted pulse can be characterized as a Brillouin soliton. All of these features have been seen experimentally using two Brillouin lasers, one pumped at 514.5 nm by an argon-ion laser and another at 1319 nm by a Nd:YAG laser [168]. The observed behavior was in agreement with the numerical solutions of Eqs (9.4.5)–(9.4.7). Specifically, both lasers emitted a pulse train when the pumping level satisfied the inequality in Eq. (9.5.3). A Brillouin ring laser can thus be designed to emit a soliton train, with a pulse width  $\sim 10$  ns and a repetition rate ( $\sim 1$  MHz) determined by the round-trip time of the ring cavity.

In a 2002 study, the origin of self-pulsing was attributed to the phenomenon of spectral hole burning [169]. This phenomenon is well known for lasers and occurs when the gain spectrum exhibits inhomogeneous broadening [170]. The SBS gain spectrum, resulting from Eqs (9.4.5)–(9.4.7) under steady-state conditions, is homogeneously broadened and has a Lorentzian line shape with width  $\Gamma_B$ , as shown in Eq. (9.1.3). However, small variations in the Brillouin shift  $\Omega_B$  along the radial direction, resulting from a finite numerical aperture of the fiber, can lead to inhomogeneous broadening of the SBS gain spectrum [25]. This interpretation of self-pulsing phenomenon in Brillouin lasers is debatable as the onset of spectral hole burning does not always require inhomogeneous broadening [171].

The self-pulsing instability is also affected by the linear birefringence of the fiber when the pump beam is not linearly polarized along one of the principal axes of a polarization-maintaining fiber. In this case, the two orthogonally polarized

components of the pump generate their own Stokes waves, and Eqs (9.4.5)–(9.4.7) should be generalized to a set of five equations. The situation is even more complicated if the fiber within the laser cavity is rotated so that its principal axes do not coincide at the input and output ends. A detailed linear stability analysis has been performed for this general situation, and it reveals the complicated dynamic behavior of such Brillouin lasers [167]. Experimental results agree well with the theoretical predictions.

## PROBLEMS

- 9.1** What is meant by Brillouin scattering? Explain its origin. What is the difference between spontaneous and stimulated Brillouin scattering?
- 9.2** Use the phase-matching condition to derive an expression for the Brillouin shift. Why does SBS occur only in the backward direction in single-mode fibers?
- 9.3** What are the main differences between SBS and SRS? What is the origin of these differences and how do they manifest in practice?
- 9.4** Estimate SBS threshold at  $1.55 \mu\text{m}$  for a 40-km-long fiber with  $8\text{-}\mu\text{m}$  core diameter. How much does it change at  $1.3 \mu\text{m}$ ? Use  $g_B = 5 \times 10^{-11} \text{ m/W}$  and loss values of 0.5 and 0.2 dB/km at 1.3 and  $1.55 \mu\text{m}$ , respectively.
- 9.5** Solve Eqs (9.2.1) and (9.2.2) after neglecting pump deletion. Use the solution to derive the threshold condition for SBS.
- 9.6** Explain how a Bragg grating can be used to increase the pump power at which SBS reaches its threshold. What other techniques can be used for this purpose?
- 9.7** Solve Eqs (9.2.1) and (9.2.2) including pump deletion. Neglect fiber losses by setting  $\alpha = 0$ . Plot  $I_p$  and  $I_s$  as a function of  $z/L$  when  $g_0 L = 12$ . Assume that the injected Stokes power at  $z = L$  is 0.1%, 1%, and 10% of the input pump power.
- 9.8** Solve Eqs (9.2.1) and (9.2.2) numerically for a 20-km-long fiber using  $g_B I_p(0) = 1 \text{ km}^{-1}$  and  $\alpha = 0.2 \text{ dB/km}$ . Plot  $I_p$  and  $I_s$  along the fiber length assuming  $I_p(0) = 2 \text{ MW/cm}^2$  and  $I_s(L) = 1 \text{ kW/cm}^2$ .
- 9.9** Solve Eqs (9.4.9) and (9.4.10) numerically assuming that both pump and Stokes pulses are Gaussian in shape initially with a FWHM of  $1 \mu\text{s}$ . Plot output pulse shapes when SBS occurs in a 10-m-long fiber assuming  $g_B I_p(0) = 1 \text{ m}^{-1}$ .
- 9.10** Write a computer code for solving Eqs (9.4.5)–(9.4.7). You can neglect the  $z$  derivative in Eq. (9.4.7). Use the parameters from Reference [102] and reproduce the curves given in Figures 9.9 and 9.10.
- 9.11** Verify by direct substitution that the soliton solution given in Eqs (9.4.16) and (9.4.17) indeed satisfies Eqs (9.4.13)–(9.4.15).
- 9.12** Use Eqs (9.4.5)–(9.4.7) to show that the SBS gain modifies the effective refractive index seen by the Stokes wave. Derive an expression for the transit

time through a fiber of length  $L$  in terms of the detuning parameter defined as  $\delta = 2(\Omega - \Omega_B)/\Gamma_B$ , where  $\Omega = \omega_p - \omega_s$ .

- 9.13** Follow the analysis of Reference [168] and derive the inequality given in Eq. (9.5.3).

## REFERENCES

- [1] R. Y. Chiao, C. H. Townes, and B. P. Stoicheff, *Phys. Rev. Lett.* **12**, 592 (1964).
- [2] E. Garmire and C. H. Townes, *Appl. Phys. Lett.* **5**, 84 (1964).
- [3] N. M. Kroll, *J. Appl. Phys.* **36**, 34 (1965).
- [4] C. L. Tang, *J. Appl. Phys.* **37**, 2945 (1966).
- [5] W. Kaiser and M. Maier, in *Laser Handbook*, Vol. 2, F. T. Arecchi and E. O. Schulz-Dubois, Eds. (North-Holland, 1972), Chap. E2.
- [6] E. P. Ippen and R. H. Stolen, *Appl. Phys. Lett.* **21**, 539 (1972).
- [7] R. G. Smith, *Appl. Opt.* **11**, 2489 (1972).
- [8] D. Cotter, *J. Opt. Commun.* **4**, 10 (1983).
- [9] Y. R. Shen, *The Principles of Nonlinear Optics* (Wiley, 1984), Chap. 11.
- [10] R. W. Boyd, *Nonlinear Optics*, 3rd ed. (Academic Press, 2008), Chap. 9.
- [11] R. M. Shelby, M. D. Levenson, and P. W. Bayer, *Phys. Rev. Lett.* **54**, 939 (1985); *Phys. Rev. B* **31**, 5244 (1985).
- [12] A. Melloni, M. Frasca, A. Garavaglia, A. Tonini, and M. Martinelli, *Opt. Lett.* **23**, 691 (1998).
- [13] R. S. Krishnan, *Nature* **165**, 933 (1950).
- [14] D. Heiman, D. S. Hamilton, and R. W. Hellwarth, *Phys. Rev. B* **19**, 6583 (1979).
- [15] P. J. Thomas, N. L. Rowell, H. M. van Driel, and G. I. Stegeman, *Phys. Rev. B* **19**, 4986 (1979).
- [16] J. Stone and A. R. Chraplyvy, *Electron. Lett.* **19**, 275 (1983).
- [17] R. W. Tkach, A. R. Chraplyvy, and R. M. Derosier, *Electron. Lett.* **22**, 1011 (1986).
- [18] N. Shibata, R. G. Waarts, and R. P. Braun, *Opt. Lett.* **12**, 269 (1987).
- [19] Y. Azuma, N. Shibata, T. Horiguchi, and M. Tateda, *Electron. Lett.* **24**, 250 (1988).
- [20] N. Shibata, K. Okamoto, and Y. Azuma, *J. Opt. Soc. Am. B* **6**, 1167 (1989).
- [21] T.-O. Sun, A. Wada, T. Sakai, and R. Yamuchi, *Electron. Lett.* **28**, 247 (1992).
- [22] A. Yeniay, J.-M. Delavaux, and J. Toulouse, *J. Lightwave Technol.* **20**, 1425 (2002).
- [23] Y. Koyamada, S. Sato, S. Nakamura, H. Sotobayashi, and W. Chujo, *J. Lightwave Technol.* **22**, 631 (2004).
- [24] J. H. Lee, T. Tanemura, K. Kikuchi, T. Nagashima, T. Hasegawa, S. Ohara, and N. Sugimoto, *Opt. Lett.* **30**, 1698 (2005).
- [25] V. I. Kovalev and R. G. Harrison, *Opt. Lett.* **27**, 2022 (2002).
- [26] G. C. Valley, *IEEE J. Quantum Electron.* **22**, 704 (1986).
- [27] P. Narum, M. D. Skeldon, and R. W. Boyd, *IEEE J. Quantum Electron.* **22**, 2161 (1986).
- [28] E. Lichtman, A. A. Friesem, R. G. Waarts, and H. H. Yaffe, *J. Opt. Soc. Am. B* **4**, 1397 (1987).
- [29] M. Abramowitz and I. A. Stegun, Eds., *Handbook of Mathematical Functions* (Dover, 1974), Chap. 7.
- [30] S. Le Floch and P. Cambon, *J. Opt. Soc. Am. A* **20**, 1132 (2003).
- [31] A. Kobyakov, S. A. Darmanyan, and D. Chowdhury, *Opt. Commun.* **260**, 46 (2006).

- [32] A. Kobyakov, M. Sauer, and D. Chowdhury, *Adv. Opt. Photon.* **2**, 1 (2010).
- [33] R. H. Stolen, *IEEE J. Quantum Electron.* **15**, 1157 (1979).
- [34] M. O. van Deventer and A. J. Boot, *J. Lightwave Technol.* **12**, 585 (1994).
- [35] J. Botineau, E. Picholle, and D. Bahloul, *Electron. Lett.* **31**, 2032 (1995).
- [36] A. Kobyakov, S. Kumar, D. Q. Chowdhury, A. B. Ruffin, M. Sauer, S. R. Bickham, and R. Mishra, *Opt. Express* **13**, 5338 (2005).
- [37] Y. Imai and N. Shimada, *IEEE Photon. Technol. Lett.* **5**, 1335 (1993).
- [38] N. Yoshizawa and T. Imai, *J. Lightwave Technol.* **11**, 1518 (1993).
- [39] K. Shiraki, M. Ohashi, and M. Tateda, *Electron. Lett.* **31**, 668 (1995).
- [40] K. Shiraki, M. Ohashi, and M. Tateda, *J. Lightwave Technol.* **14**, 50 (1996); *J. Lightwave Technol.* **14**, 549 (1996).
- [41] K. Tsujikawa, K. Nakajima, Y. Miyajima, and M. Ohashi, *IEEE Photon. Technol. Lett.* **10**, 1139 (1998).
- [42] J. Hansryd, F. Dross, M. Westlund, P. A. Andrekson, and S. N. Knudsen, *J. Lightwave Technol.* **19**, 1691 (2001).
- [43] J. M. Chavez Boggio, J. D. Marconi, and H. L. Fragnito, *J. Lightwave Technol.* **23**, 3808 (2005).
- [44] V. I. Kovalev and R. G. Harrison, *Opt. Lett.* **31**, 161 (2006).
- [45] E. M. Dianov, B. Y. Zeldovich, A. Y. Karasik, and A. N. Pilipetskii, *Sov. J. Quantum Electron.* **19**, 1051 (1989).
- [46] A. Hirose, Y. Takushima, and T. Okoshi, *J. Opt. Commun.* **12**, 82 (1991).
- [47] K. Kikuchi and C. Lorattanasane, *IEEE Photon. Technol. Lett.* **6**, 992 (1994).
- [48] M. E. Marhic, F. S. Yang, and L. G. Kazovsky, *Electron. Lett.* **32**, 2336 (1994).
- [49] J. Hansryd, P. A. Andrekson, M. Westlund, J. Li, and P. O. Hedekvist, *IEEE J. Sel. Topics Quantum Electron.* **8**, 506 (2002).
- [50] J. B. Coles, B.-P.-P. Kuo, N. Alic, et al., *Opt. Express* **18**, 18138 (2010).
- [51] A. Mussot, M. Le Parquier, and P. Sriftgiser, *Opt. Commun.* **283**, 2607 (2010).
- [52] M. M. Howerton, W. K. Burns, and G. K. Gopalakrishnan, *J. Lightwave Technol.* **14**, 417 (1996).
- [53] S. S. Lee, H. J. Lee, W. Seo, and S. G. Lee, *IEEE Photon. Technol. Lett.* **13**, 741 (2001).
- [54] H. Lee and G. P. Agrawal, *Opt. Express* **11**, 3467 (2003).
- [55] V. Philippov, C. Codemard, Y. Jeong, et al., *Opt. Lett.* **29**, 2590 (2004).
- [56] Y. Jeong, J. K. Sahu, D. N. Payne, and J. Nilsson, *Opt. Express* **12**, 6088 (2004).
- [57] Y. M. Huo, P. K. Cheo, and G. G. King, *Opt. Express* **12**, 6230 (2004).
- [58] J. Limpert, F. Röser, S. Klingebiel, et al., *IEEE J. Sel. Topics Quantum Electron.* **13**, 537 (2007).
- [59] M. D. Mermelstein, *Opt. Express* **17**, 16225 (2009).
- [60] T. Sakamoto, T. Matsui, K. Shiraki, and T. Kurashima, *J. Lightwave Technol.* **27**, 4401 (2009).
- [61] V. Pashinina, V. Sturmb, V. Tumorina, and R. Nollb, *Opt. Laser Technol.* **33**, 617 (2001).
- [62] K. Tei, Y. Tsuruoka, T. Uchiyama, and T. Fujioka, *Jpn. J. Appl. Phys.* **40**, 3191 (2001).
- [63] M. Sjöberg, M. L. Quiroga-Teixeiro, S. Galt, and S. Hård, *J. Opt. Soc. Am. B* **20**, 434 (2003).
- [64] A. Mocafanescu, L. Wang, R. Jain, K. D. Shaw, A. Gavrielides, P. Peterson, and M. P. Sharma, *Opt. Express* **13**, 2019 (2005).
- [65] N. Uesugi, M. Ikeda, and Y. Sasaki, *Electron. Lett.* **17**, 379 (1981).
- [66] D. Cotter, *Electron. Lett.* **18**, 495 (1982).

- [67] Y. Aoki, K. Tajima, and I. Mito, *Opt. Quantum Electron.* **19**, 141 (1987).
- [68] P. Labudde, P. Anliker, and H. P. Weber, *Opt. Commun.* **32**, 385 (1980).
- [69] A. A. Fotiadi and R. V. Kiyan, *Opt. Lett.* **23**, 1805 (1998).
- [70] N. A. Olsson and J. P. van der Ziel, *Appl. Phys. Lett.* **48**, 1329 (1986).
- [71] C. G. Atkins, D. Cotter, D. W. Smith, and R. Wyatt, *Electron. Lett.* **22**, 556 (1986).
- [72] D. Cotter, D. W. Smith, C. G. Atkins, and R. Wyatt, *Electron. Lett.* **22**, 671 (1986).
- [73] A. R. Chraplyvy and R. W. Tkach, *Electron. Lett.* **22**, 1084 (1986).
- [74] N. A. Olsson and J. P. van der Ziel, *J. Lightwave Technol.* **5**, 147 (1987).
- [75] R. G. Waarts, A. A. Friesem, and Y. Hefetz, *Opt. Lett.* **13**, 152 (1988).
- [76] R. W. Tkach, A. R. Chraplyvy, R. M. Derosier, and H. T. Shang, *Electron. Lett.* **24**, 260 (1988); *IEEE Photon. Technol. Lett.* **1**, 111 (1989).
- [77] A. A. Fotiadi, E. A. Kuzin, M. P. Petrov, and A. A. Ganichev, *Sov. Tech. Phys. Lett.* **15**, 434 (1989).
- [78] R. W. Tkach and A. R. Chraplyvy, *Opt. Quantum Electron.* **21**, S105 (1989).
- [79] A. S. Siddiqui and G. G. Vienne, *J. Opt. Commun.* **13**, 33 (1992).
- [80] Y. Takushima and K. Kikuchi, *Opt. Lett.* **20**, 34 (1995).
- [81] S. J. Strutz, K. J. Williams, and R. D. Esman, *IEEE Photon. Technol. Lett.* **13**, 936 (2001).
- [82] L. Chen and X. Bao, *Opt. Commun.* **152**, 65 (1998).
- [83] G. P. Agrawal and N. K. Dutta, *Semiconductor Lasers*, 2nd ed. (Van Nostrand Reinhold, 1993).
- [84] J. A. Arnaud, *IEEE J. Quantum Electron.* **4**, 893 (1968).
- [85] C. Culverhouse, F. Farahi, C. N. Pannell, and D. A. Jackson, *Electron. Lett.* **25**, 913 (1989).
- [86] T. Kurashima, T. Horiguchi, and M. Tateda, *Opt. Lett.* **15**, 1038 (1990).
- [87] X. Bao, D. J. Webb, and D. A. Jackson, *Opt. Lett.* **18**, 1561 (1993).
- [88] X. Bao, D. J. Webb, and D. A. Jackson, *Opt. Commun.* **104**, 298 (1994); *Opt. Lett.* **19**, 141 (1994).
- [89] T. R. Parker, M. Farhadiroushan, R. Feced, V. A. Handerek, and A. J. Rogers, *IEEE J. Quantum Electron.* **34**, 645 (1998).
- [90] H. H. Kee, G. P. Lees, and T. P. Newson, *Opt. Lett.* **25**, 695 (2000).
- [91] X. Bao, M. DeMerchant, A. Brown, and T. Bremner, *J. Lightwave Technol.* **19**, 1698 (2001).
- [92] K. Hotate and M. Tanaka, *IEEE Photon. Technol. Lett.* **14**, 179 (2002).
- [93] Y. T. Cho, M. N. Alahbabi, G. Brambilla, and T. P. Newson, *IEEE Photon. Technol. Lett.* **17**, 1256 (2005).
- [94] W. Zou, Z. He, and K. Hotate, *J. Lightwave Technol.* **28**, 2736 (2010).
- [95] G. N. Burlak, V. V. Grimal'skii, and Y. N. Taranenko, *Sov. Tech. Phys. Lett.* **32**, 259 (1986).
- [96] J. Costes and C. Montes, *Phys. Rev. A* **34**, 3940 (1986).
- [97] E. Lichtman, R. G. Waarts, and A. A. Friesem, *J. Lightwave Technol.* **7**, 171 (1989).
- [98] A. Höök, *J. Opt. Soc. Am. B* **8**, 1284 (1991).
- [99] A. Höök and A. Bolle, *J. Lightwave Technol.* **10**, 493 (1992).
- [100] G. Grossio and A. Höök, *J. Opt. Soc. Am. B* **10**, 946 (1993).
- [101] S. Rae, I. Bennion, and M. J. Carswell, *Opt. Commun.* **123**, 611 (1996).
- [102] H. Li and K. Oguisu, *Jpn. J. Appl. Phys.* **38**, 6309 (1999); *J. Opt. Soc. Am. B* **18**, 93 (2002).
- [103] K. Oguisu, *J. Opt. Soc. Am. B* **17**, 769 (2001); *Opt. Rev.* **8**, 358 (2001).

- [104] E. Picholle, C. Montes, C. Leycuras, O. Legrand, and J. Botineau, *Phys. Rev. Lett.* **66**, 1454 (1991).
- [105] Y. N. Taranenko and L. G. Kazovsky, *IEEE Photon. Technol. Lett.* **4**, 494 (1992).
- [106] C. Montes, A. Mikhailov, A. Picozzi, and F. Ginovart, *Phys. Rev. E* **55**, 1086 (1997).
- [107] R. W. Boyd and D. J. Gauthier, in *Progress in Optics*, Vol. 43, E. Wolf, Ed. (Elsevier, 2002), Chap. 6.
- [108] L. Thévenaz, *Nature Photon.* **2**, 474 (2008).
- [109] G. M. Gehring, R. W. Boyd, Al. L. Gaeta, D. J. Gauthier, and A. E. Willner, *J. Lightwave Technol.* **26**, 3752 (2008).
- [110] K. Y. Song, M. G. Herráez, and L. Thévenaz, *Opt. Express* **13**, 82 (2005).
- [111] Y. Okawachi, M. S. Bigelow, J. E. Sharping, et al., *Phys. Rev. Lett.* **94**, 153902 (2005).
- [112] K. Y. Song, M. G. Herráez, and L. Thévenaz, *Opt. Lett.* **30**, 1782 (2005).
- [113] M. G. Herráez, K. Y. Song, and L. Thévenaz, *Opt. Express* **14**, 1395 (2006).
- [114] Z. Zhu, A. M. C. Dawes, D. J. Gauthier, L. Zhang, and A. E. Willner, *J. Lightwave Technol.* **25**, 201 (2007).
- [115] S. Chin, M. G. Herráez, and L. Thévenaz, *Opt. Express* **14**, 10684 (2006).
- [116] K. Y. Song and K. Hotate, *Opt. Lett.* **32**, 217 (2007).
- [117] T. Schneider, R. Henker, K.-U. Lauterbach, and M. Junker, *Opt. Express* **15**, 9606 (2007).
- [118] C. J. Misas, P. Petropoulos, and D. J. Richardson, *J. Lightwave Technol.* **25**, 216 (2007).
- [119] Y. Zhu, M. Lee, M. A. Neifeld, and D. J. Gauthier, *Opt. Express* **19**, 687 (2011).
- [120] R. V. Johnson and J. H. Marburger, *Phys. Rev. A* **4**, 1175 (1971).
- [121] I. Bar-Joseph, A. A. Friesem, E. Lichtman, and R. G. Waarts, *J. Opt. Soc. Am. B* **2**, 1606 (1985).
- [122] B. Y. Zeldovich and V. V. Shkunov, *Sov. J. Quantum Electron.* **12**, 223 (1982).
- [123] N. F. Andreev, V. I. Bespalov, A. M. Kiselev, G. A. Pasmanik, and A. A. Shilov, *Sov. Phys. JETP* **55**, 612 (1982).
- [124] C. J. Randall and J. R. Albritton, *Phys. Rev. Lett.* **52**, 1887 (1984).
- [125] P. Narum and R. W. Boyd, *IEEE J. Quantum Electron.* **23**, 1216 (1987).
- [126] P. Narum, A. L. Gaeta, M. D. Skeldon, and R. W. Boyd, *J. Opt. Soc. Am. B* **5**, 623 (1988).
- [127] K. Oogusu, *J. Opt. Soc. Am. B* **17**, 769 (2000).
- [128] R. G. Harrison, J. S. Uppal, A. Johnstone, and J. V. Moloney, *Phys. Rev. Lett.* **65**, 167 (1990).
- [129] A. L. Gaeta and R. W. Boyd, *Phys. Rev. A* **44**, 3205 (1991).
- [130] M. Dämmig, C. Boden, and F. Mitschke, *Appl. Phys. B* **55**, 121 (1992).
- [131] A. Johnstone, W. Lu, J. S. Uppal, and R. G. Harrison, *Opt. Commun.* **81**, 122 (1991).
- [132] W. Lu and R. G. Harrison, *Europhys. Lett.* **16**, 655 (1991).
- [133] W. Lu, A. Johnstone, and R. G. Harrison, *Phys. Rev. A* **46**, 4114 (1992).
- [134] A. L. Gaeta and R. W. Boyd, *Int. J. Nonlinear Opt. Phys.* **1**, 581 (1992).
- [135] C. Chow and A. Bers, *Phys. Rev. A* **47**, 5144 (1993).
- [136] R. G. Harrison, W. Lu, D. S. Lim, D. Yu, and P. M. Ripley, *Proc. SPIE* **2039**, 91 (1993).
- [137] M. Dämmig, G. Zimmer, F. Mitschke, and H. Welling, *Phys. Rev. A* **48**, 3301 (1993).
- [138] R. G. Harrison, P. M. Ripley, and W. Lu, *Phys. Rev. A* **49**, R24 (1994).
- [139] Y. Imai and H. Aso, *Opt. Rev.* **4**, 476 (1997).
- [140] V. Leceeuche, B. Ségarde, and J. Zemmouri, *Opt. Commun.* **172**, 335 (1999).
- [141] A. A. Fotiadi, R. Kiyan, O. Deparis, P. Mégrét, and M. Blondel, *Opt. Lett.* **27**, 83 (2002).
- [142] K. O. Hill, B. S. Kawasaki, and D. C. Johnson, *Appl. Phys. Lett.* **28**, 608 (1976).

- [143] K. O. Hill, D. C. Johnson, and B. S. Kawasaki, *Appl. Phys. Lett.* **29**, 185 (1976).
- [144] B. S. Kawasaki, D. C. Johnson, Y. Fujii, and K. O. Hill, *Appl. Phys. Lett.* **32**, 429 (1978).
- [145] D. R. Ponikvar and S. Ezekiel, *Opt. Lett.* **6**, 398 (1981).
- [146] L. F. Stokes, M. Chodorow, and H. J. Shaw, *Opt. Lett.* **7**, 509 (1982).
- [147] P. Bayvel and I. P. Giles, *Opt. Lett.* **14**, 581 (1989).
- [148] E. M. Dianov, S. K. Isaev, L. S. Kornienko, V. V. Firsov, and Y. P. Yatsenko, *Sov. J. Quantum Electron.* **19**, 1 (1989).
- [149] S. P. Smith, F. Zarinetchi, and S. Ezekiel, *Opt. Lett.* **16**, 393 (1991).
- [150] F. Zarinetchi, S. P. Smith, and S. Ezekiel, *Opt. Lett.* **16**, 229 (1991).
- [151] S. Huang, K. Toyama, P.-A. Nicati, L. Thévenaz, B. Y. Kim, and H. J. Shaw, *Proc. SPIE* **1795**, 48 (1993).
- [152] S. Huang, L. Thévenaz, K. Toyama, B. Y. Kim, and H. J. Shaw, *IEEE Photon. Technol. Lett.* **5**, 365 (1993).
- [153] T. P. Mirtchev and N. I. Minkovski, *IEEE Photon. Technol. Lett.* **5**, 158 (1993).
- [154] P.-A. Nicati, K. Toyama, S. Huang, and H. J. Shaw, *Opt. Lett.* **18**, 2123 (1993); *IEEE Photon. Technol. Lett.* **6**, 801 (1994).
- [155] D. Y. Stepanov and G. J. Cowle, *IEEE J. Sel. Topics Quantum Electron.* **3**, 1049 (1997).
- [156] D. S. Lim, H. K. Lee, K. H. Kim, S. B. Kang, J. T. Ahn, and M. Y. Jeon, *Opt. Lett.* **23**, 1671 (1998).
- [157] W. Y. Oh, J. S. Ko, D. S. Lim, and W. Seo, *Opt. Commun.* **201**, 399 (2002).
- [158] J. C. Yong, L. Thévenaz, and B. Y. Kim, *J. Lightwave Technol.* **21**, 546 (2003).
- [159] Y. J. Song, L. Zhan, S. Hu, Q. H. Ye, and Y. X. Xia, *IEEE Photon. Technol. Lett.* **16**, 2015 (2004).
- [160] Y. J. Song, L. Zhan, J. H. Ji, Y. Su, Q. H. Ye, and Y. X. Xia, *Opt. Lett.* **30**, 486 (2005).
- [161] M. H. Al-Mansoori, M. K. Abd-Rahman, F. R. M. Adikan, and M. A. Mahdi, *Opt. Express* **13**, 3471 (2005).
- [162] M. H. Al-Mansoori, M. A. Mahdi, and M. Premaratne, *IEEE J. Sel. Topics Quantum Electron.* **15**, 415 (2009).
- [163] M. H. Al-Mansoori and M. A. Mahdi, *J. Lightwave Technol.* **27**, 5038 (2009).
- [164] Y. G. Shee, M. H. Al-Mansoori, A. Ismail, S. Hitam, and M. A. Mahdi, *Opt. Express* **19**, 1699 (2011).
- [165] C. Montes, A. Mahmhoud, and E. Picholle, *Phys. Rev. A* **49**, 1344 (1994).
- [166] S. Randoux, V. Lecoueche, B. Ségrad, and J. Zemmouri, *Phys. Rev. A* **51**, R4345 (1995); *Phys. Rev. A* **52**, 221 (1995).
- [167] S. Randoux and J. Zemmouri, *Phys. Rev. A* **59**, 1644 (1999).
- [168] C. Montes, D. Bahloul, I. Bongrand, J. Botineau, G. Cheval, A. Mahmhoud, E. Picholle, and A. Picozzi, *J. Opt. Soc. Am. B* **16**, 932 (1999).
- [169] V. I. Kovalev and R. G. Harrison, *Opt. Commun.* **204**, 349 (2002).
- [170] A. E. Siegman, *Lasers* (University Science Books, 1986).
- [171] L. Stepien, S. Randoux, and J. Zemmouri, *Phys. Rev. A* **65**, 053812 (2002).

# Four-Wave Mixing

# 10

In the stimulated scattering processes covered in Chapters 8 and 9, optical fibers play an active role in the sense that the process depends on molecular vibrations or density variations of silica. In a separate class of nonlinear phenomena, optical fibers play a passive role except for mediating interaction among several optical waves. Such nonlinear processes are referred to as parametric processes, because they involve modulation of a medium parameter, such as the refractive index, and require phase-matching before they can build up along the fiber. Among these, four-wave mixing (FWM) plays the dominant role. Although FWM can be detrimental for WDM systems that must be designed to reduce its impact, it is also useful for a variety of applications. The origin of FWM is discussed in Section 10.1 before developing in Section 10.2 a simple scalar theory of this process. The techniques used for phase-matching are covered in Section 10.3. The focus of Section 10.4 is on parametric amplification, and the polarization effects related to this process are discussed in Section 10.5. Some applications of FWM are covered in Section 10.6.

---

## 10.1 ORIGIN OF FOUR-WAVE MIXING

The origin of FWM lies in the nonlinear response of bound electrons of a material to an electromagnetic field. As discussed in Section 2.3, the polarization induced in the medium contains terms whose magnitude is governed by their nonlinear susceptibilities [1–5]. The resulting nonlinear effects can be classified as second- or third-order parametric processes, depending on whether the second-order susceptibility  $\chi^{(2)}$ , or the third-order susceptibility  $\chi^{(3)}$ , is responsible for them. Because  $\chi^{(2)}$  vanishes for an isotropic medium (in the dipole approximation), the second-order processes such as second-harmonic generation should not occur in silica fibers. In practice, they do occur because of quadrupole and magnetic-dipole effects but with a relatively low conversion efficiency.

The third-order parametric processes involve nonlinear interaction among four optical waves and include the phenomena such as FWM and third-harmonic generation [1–5]. Indeed, FWM in optical fibers was studied soon after low-loss fibers first

became available [6–26]. The main features of FWM can be understood from the third-order polarization term in Eq. (1.3.1),

$$\mathbf{P}_{\text{NL}} = \epsilon_0 \chi^{(3)} : \mathbf{E} \mathbf{E} \mathbf{E}, \quad (10.1.1)$$

where  $\mathbf{E}$  is the electric field and  $\mathbf{P}_{\text{NL}}$  is the induced nonlinear polarization.

In general, FWM is polarization-dependent and one must develop a full vector theory for it (presented in Section 10.5). However, considerable physical insight is gained by first considering the scalar case in which all four fields are linearly polarized along a principal axis of a birefringent fiber such that they maintain their state of polarization. Consider four CW waves oscillating at frequencies  $\omega_1, \omega_2, \omega_3$ , and  $\omega_4$  and linearly polarized along the same axis  $x$ . The total electric field can be written as

$$\mathbf{E} = \frac{1}{2} \hat{x} \sum_{j=1}^4 E_j \exp[i(\beta_j z - \omega_j t)] + \text{c.c.}, \quad (10.1.2)$$

where the propagation constant  $\beta_j = \tilde{n}_j \omega_j / c$ ,  $\tilde{n}_j$  being the mode index. If we substitute Eq. (10.1.2) in Eq. (10.1.1) and express  $\mathbf{P}_{\text{NL}}$  in the same form as  $\mathbf{E}$  using

$$\mathbf{P}_{\text{NL}} = \frac{1}{2} \hat{x} \sum_{j=1}^4 P_j \exp[i(\beta_j z - \omega_j t)] + \text{c.c.}, \quad (10.1.3)$$

we find that  $P_j$  ( $j = 1\text{--}4$ ) consists of a large number of terms involving the products of three electric fields. For example,  $P_4$  can be expressed as

$$\begin{aligned} P_4 = \frac{3\epsilon_0}{4} \chi_{xxx}^{(3)} & \left[ |E_4|^2 E_4 + 2(|E_1|^2 + |E_2|^2 + |E_3|^2) E_4 \right. \\ & \left. + 2E_1 E_2 E_3 \exp(i\theta_+) + 2E_1 E_2 E_3^* \exp(i\theta_-) + \dots \right], \end{aligned} \quad (10.1.4)$$

where  $\theta_+$  and  $\theta_-$  are defined as

$$\theta_+ = (\beta_1 + \beta_2 + \beta_3 - \beta_4)z - (\omega_1 + \omega_2 + \omega_3 - \omega_4)t, \quad (10.1.5)$$

$$\theta_- = (\beta_1 + \beta_2 - \beta_3 - \beta_4)z - (\omega_1 + \omega_2 - \omega_3 - \omega_4)t. \quad (10.1.6)$$

The first four terms containing  $E_4$  in Eq. (10.1.4) are responsible for the SPM and XPM effects, but the remaining terms result from the frequency combinations (sum or difference) of all four waves. How many of these are effective during a FWM process depends on the phase mismatch between  $E_4$  and  $P_4$  governed by  $\theta_+$ ,  $\theta_-$ , or a similar quantity.

Significant FWM occurs only if the phase mismatch nearly vanishes. This requires the matching of frequencies as well as of the wave vectors. The latter requirement is often referred to as phase matching. In quantum-mechanical terms, FWM occurs when photons from one or more waves are annihilated and new photons are created at different frequencies such that the net energy and momentum are conserved during the parametric interaction. The main difference between a FWM process

and a stimulated scattering process discussed in Chapters 8 and 9 is that the phase-matching condition is automatically satisfied in the case of Raman or Brillouin scattering as a result of the active participation of the nonlinear medium. In contrast, the phase-matching condition requires a specific choice of input wavelengths and fiber parameters before FWM can occur with high efficiency.

There are two types of FWM terms in Eq. (10.1.4). The term containing  $\theta_+$  corresponds to the case in which three photons transfer their energy to a single photon at the frequency  $\omega_4 = \omega_1 + \omega_2 + \omega_3$ . This term is responsible for the phenomena such as third-harmonic generation ( $\omega_1 = \omega_2 = \omega_3$ ). In general, it is difficult to satisfy the phase-matching condition for such processes to occur in optical fibers with high efficiencies. The term containing  $\theta_-$  in Eq. (10.1.4) corresponds to the case in which two photons at frequencies  $\omega_1$  and  $\omega_2$  are annihilated, while two photons at frequencies  $\omega_3$  and  $\omega_4$  are created simultaneously such that

$$\omega_3 + \omega_4 = \omega_1 + \omega_2. \quad (10.1.7)$$

The phase-matching requirement for this process is  $\Delta k = 0$ , where

$$\Delta k = \beta_3 + \beta_4 - \beta_1 - \beta_2 = (\tilde{n}_3\omega_3 + \tilde{n}_4\omega_4 - \tilde{n}_1\omega_1 - \tilde{n}_2\omega_2)/c, \quad (10.1.8)$$

and  $\tilde{n}_j$  is the effective mode index at the frequency  $\omega_j$ .

In the general case in which  $\omega_1 \neq \omega_2$ , one must launch two pump beams for FWM to occur. The special case, in which  $\omega_1 = \omega_2$ , is interesting because FWM can be initiated with a single pump beam. This degenerate case is often useful for optical fibers. Physically, it manifests in a way similar to SRS. A strong pump wave at  $\omega_1$  creates two sidebands located symmetrically at frequencies  $\omega_3$  and  $\omega_4$  with a frequency shift

$$\Omega_s = \omega_1 - \omega_3 = \omega_4 - \omega_1, \quad (10.1.9)$$

where we assumed for definiteness  $\omega_3 < \omega_4$ . The low-frequency sideband at  $\omega_3$  and the high-frequency sideband at  $\omega_4$  are referred to as the Stokes and anti-Stokes bands in direct analogy with SRS. The degenerate FWM was originally called three-wave mixing as only three distinct frequencies are involved in the nonlinear process [6]. However, the term three-wave mixing should be reserved for the processes mediated by  $\chi^{(2)}$ . The name four-photon mixing is also used for FWM [7]. The Stokes and anti-Stokes bands are often called the signal and idler waves, borrowing the terminology from the field of microwaves.

## 10.2 THEORY OF FOUR-WAVE MIXING

Degenerate FWM transfers energy from a strong pump wave to two waves, upshifted and downshifted in frequency from the pump frequency  $\omega_1$  by an amount  $\Omega_s$  given in Eq. (10.1.9). If only the pump wave is incident at the fiber, and the phase-matching condition is satisfied, the Stokes and anti-Stokes waves at the frequencies  $\omega_3$  and  $\omega_4$

can be generated from noise, similar to the stimulated scattering processes discussed in Chapters 8 and 9. On the other hand, if a weak signal at  $\omega_3$  is also launched into the fiber together with the pump, the signal is amplified while a new idler wave at  $\omega_4$  is generated simultaneously. The gain responsible for such amplification is called the parametric gain. In this section, we consider the FWM mixing process in detail and derive an expression for the parametric gain. The nondegenerate case ( $\omega_1 \neq \omega_2$ ) is considered for generality.

### 10.2.1 Coupled Amplitude Equations

The starting point is, as usual, the wave equation (2.31) for the total electric field  $\mathbf{E}(\mathbf{r}, t)$  with  $\mathbf{P}_{\text{NL}}$  given in Eq. (10.1.1). We substitute Eqs (10.1.2) and (10.1.3) in the wave equation, together with a similar expression for the linear part of the polarization, and neglect the time dependence of the field components  $E_j$  ( $j = 1-4$ ) assuming quasi-CW conditions. Their spatial dependence is, however, included using  $E_j(\mathbf{r}) = F_j(x, y)A_j(z)$ , where  $F_j(x, y)$  is the spatial distribution of the fiber mode in which the  $j$ th field propagates inside the fiber [12]. Integrating over the spatial mode profiles, the evolution of the amplitude  $A_j(z)$  inside an optical fiber is governed by the following set of four coupled equations:

$$\frac{dA_1}{dz} = \frac{in_2\omega_1}{c} \left[ \left( f_{11}|A_1|^2 + 2 \sum_{k \neq 1} f_{1k}|A_k|^2 \right) A_1 + 2f_{1234}A_2^*A_3A_4 e^{i\Delta kz} \right], \quad (10.2.1)$$

$$\frac{dA_2}{dz} = \frac{in_2\omega_2}{c} \left[ \left( f_{22}|A_2|^2 + 2 \sum_{k \neq 2} f_{2k}|A_k|^2 \right) A_2 + 2f_{2134}A_1^*A_3A_4 e^{i\Delta kz} \right], \quad (10.2.2)$$

$$\frac{dA_3}{dz} = \frac{in_2\omega_3}{c} \left[ \left( f_{33}|A_3|^2 + 2 \sum_{k \neq 3} f_{3k}|A_k|^2 \right) A_3 + 2f_{3412}A_1A_2A_4^* e^{-i\Delta kz} \right], \quad (10.2.3)$$

$$\frac{dA_4}{dz} = \frac{in_2\omega_4}{c} \left[ \left( f_{44}|A_4|^2 + 2 \sum_{k \neq 4} f_{4k}|A_k|^2 \right) A_4 + 2f_{4312}A_1A_2A_3^* e^{-i\Delta kz} \right], \quad (10.2.4)$$

where the wave-vector mismatch  $\Delta k$  is given in Eq. (10.1.8). The overlap integral  $f_{jk}$  is defined in Eq. (7.1.12) of Section 7.1. The new overlap integral  $f_{ijkl}$  is given by [12]

$$f_{ijkl} = \frac{\langle F_i^* F_j^* F_k F_l \rangle}{[\langle |F_i|^2 \rangle \langle |F_j|^2 \rangle \langle |F_k|^2 \rangle \langle |F_l|^2 \rangle]^{1/2}}, \quad (10.2.5)$$

where angle brackets denote integration over the transverse coordinates  $x$  and  $y$ . In deriving Eqs (10.2.1–10.2.4), we kept only nearly phase-matched terms and neglected frequency dependence of  $\chi^{(3)}$ . The parameter  $n_2$  is the nonlinear-index coefficient defined first in Section 2.3.

### 10.2.2 Approximate Solution

Equations (10.2.1–10.2.4) are quite general in the sense that they include the effects of SPM, XPM, and pump depletion on the FWM process; a numerical approach is necessary to solve them exactly. Considerable physical insight is gained if the pump waves are assumed to be much more intense than the other waves and to remain undepleted during the FWM process. As a further simplification, we assume that all overlap integrals are nearly the same, that is,

$$f_{ijkl} \approx f_{ij} \approx 1/A_{\text{eff}} \quad (i, j, k, l = 1, 2, 3, 4), \quad (10.2.6)$$

where  $A_{\text{eff}}$  is the effective mode area introduced in Section 2.3. This assumption is valid for single-mode fibers. The following analysis can easily be extended to include differences in the overlap integrals [12].

We can now introduce the nonlinear parameter using the definition

$$\gamma_j = n_2 \omega_j / (c A_{\text{eff}}) \approx \gamma, \quad (10.2.7)$$

where  $\gamma$  is an average value if we ignore the relatively small differences in optical frequencies of the four waves. Equations (10.2.1) and (10.2.2) for the pump fields are easily solved to obtain

$$A_1(z) = A_1(0) \exp[i\gamma(P_1 + 2P_2)z], \quad (10.2.8)$$

$$A_2(z) = A_2(0) \exp[i\gamma(P_2 + 2P_1)z], \quad (10.2.9)$$

where  $P_j = |A_j(0)|^2$ , and  $P_1$  and  $P_2$  are the incident pump powers at  $z = 0$ . This solution shows that, in the undepleted-pump approximation, the pump waves only acquire a phase shift occurring as a result of SPM and XPM.

Substituting Eqs (10.2.8) and (10.2.9) in Eqs (10.2.3) and (10.2.4), we obtain two linear coupled equations for the signal and idler fields:

$$\frac{dA_3}{dz} = 2i\gamma[(P_1 + P_2)A_3 + A_1(0)A_2(0)e^{-i\theta}A_4^*], \quad (10.2.10)$$

$$\frac{dA_4^*}{dz} = -2i\gamma[(P_1 + P_2)A_4^* + A_1^*(0)A_2^*(0)e^{i\theta}A_3], \quad (10.2.11)$$

where  $\theta = [\Delta k - 3\gamma(P_1 + P_2)]z$ . To solve these equations, we introduce

$$B_j = A_j \exp[-2i\gamma(P_1 + P_2)z], \quad (j = 3, 4). \quad (10.2.12)$$

Using Eqs (10.2.10) through (10.2.12), we then obtain

$$\frac{dB_3}{dz} = 2i\gamma A_1(0)A_2(0)e^{-i\kappa z}B_4^*, \quad (10.2.13)$$

$$\frac{dB_4^*}{dz} = -2i\gamma A_1^*(0)^*A_2(0)e^{i\kappa z}B_3, \quad (10.2.14)$$

where the *effective* phase mismatch is given by

$$\kappa = \Delta k + \gamma(P_1 + P_2). \quad (10.2.15)$$

Equations (10.2.13) and (10.2.14) can be solved readily. If we differentiate  $B_3$  a second time, and eliminate  $B_4^*$ , we obtain the following equation for  $B_3$ :

$$\frac{d^2 B_3}{dz^2} + i\kappa \frac{dB_3}{dz} - (4\gamma^2 P_1 P_2) B_3 = 0. \quad (10.2.16)$$

The same equation is obtained for  $B_4^*$ . Thus, the general solution of the form [12]

$$B_3(z) = (a_3 e^{gz} + b_3 e^{-gz}) \exp(-i\kappa z/2), \quad (10.2.17)$$

$$B_4^*(z) = (a_4 e^{gz} + b_4 e^{-gz}) \exp(i\kappa z/2), \quad (10.2.18)$$

where  $a_3$ ,  $b_3$ ,  $a_4$ , and  $b_4$  are determined from the boundary conditions. The *parametric gain*  $g$  depends on the pump power and is defined as

$$g = \sqrt{(\gamma P_0 r)^2 - (\kappa/2)^2}, \quad (10.2.19)$$

where we have introduced the parameters  $r$  and  $P_0$  as

$$r = 2(P_1 P_2)^{1/2}/P_0, \quad P_0 = P_1 + P_2. \quad (10.2.20)$$

The solution given in Eqs (10.2.17) and (10.2.18) is valid only when the pump waves remain largely undepleted. Pump depletion is included by solving the complete set of four equations, Eqs (10.2.1–10.2.4). Such a solution can be written in terms of elliptic functions [27, 28] but is not discussed here because of its complexity.

### 10.2.3 Effect of Phase Matching

The preceding derivation of the parametric gain has assumed that the two pumps are distinct. If the pump fields cannot be distinguished on the basis of their frequency, polarization, or spatial mode, the entire procedure should be carried out with only three terms in Eq. (10.1.2). The parametric gain is still given by Eq. (10.2.19) if we choose  $P_1 = P_2 = P_0/2$  ( $r = 1$ ) and use

$$\kappa = \Delta k + 2\gamma P_0. \quad (10.2.21)$$

**Figure 10.1** shows variations of  $g$  with  $\Delta k$  in this specific case for several values of  $\gamma P_0$ . The maximum gain ( $g_{\max} = \gamma P_0$ ) occurs at  $\kappa = 0$ , or at  $\Delta k = -2\gamma P_0$ . The range over which the gain exists is given by  $0 > \Delta k > -4\gamma P_0$ , as dictated by Eqs (10.2.19) and (10.2.21). The shift of the gain peak from  $\Delta k = 0$  is due to the contribution of SPM and XPM to the phase mismatch as apparent from Eq. (10.2.21).

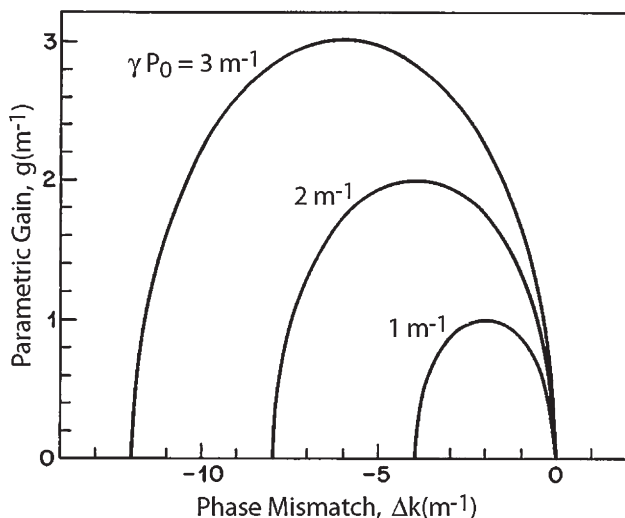


**Figure 10.1** Variation of parametric gain with phase mismatch  $\Delta k$  for several pump powers  $P_0$ . The shift of the gain peak from  $\Delta k=0$  is due to a combination of the SPM and XPM effects.

It is useful to compare the peak value of the parametric gain with that of the Raman gain [7]. From Eq. (10.2.19) the maximum gain is given by (using  $r = 1$ )

$$g_{\max} = \gamma P_0 = g_P(P_0/A_{\text{eff}}), \quad (10.2.22)$$

where  $\gamma$  is used from Eq. (10.2.7) and  $g_P$  is defined as  $g_P = 2\pi n_2/\lambda_1$  at the pump wavelength  $\lambda_1$ . Using  $\lambda_1 = 1 \mu\text{m}$  and  $n_2 \approx 2.7 \times 10^{-20} \text{ m}^2/\text{W}$ , we obtain  $g_P \approx 1.7 \times 10^{-13} \text{ m/W}$ . This value should be compared with the peak value of the Raman gain  $g_R$  in Figure 8.1. The parametric gain is larger by about 70% compared with  $g_R$ . As a result, the pump power for the FWM gain is expected to be lower than that required for Raman amplification, if phase matching can be realized. In practice, SRS dominates for long fibers because it is difficult to maintain phase matching over long fiber lengths.

We can define a length scale, known as the *coherence length*, using  $L_{\text{coh}} = 2\pi/|\Delta\kappa|$ , where  $\Delta\kappa$  is the maximum value of the wave-vector mismatch that can be tolerated. Significant FWM occurs if  $L < L_{\text{coh}}$ . Even when this condition is satisfied, SRS can influence the FWM process significantly when the frequency shift  $\Omega_s$  lies within the Raman-gain bandwidth. The interplay between SRS and FWM has been studied extensively [29–36]. The main effect in practice is that the Stokes component gets amplified through SRS, resulting in an asymmetric sideband spectrum. This feature is discussed further in the next section where experimental results are presented.

### 10.2.4 Ultrafast Four-Wave Mixing

The simplified analysis of this section is based on Eqs (10.2.10) and (10.2.11) that assume, among other things, a CW or quasi-CW regime so that group-velocity dispersion (GVD) can be neglected. The effects of GVD can be included by allowing  $A_j(z)$  to be a slowly varying function of time and following the analysis of Section 2.3. If polarization effects are neglected, assuming that all four waves are polarized along a principal axis of a birefringent fiber, the inclusion of GVD effects and fiber losses in Eqs (10.2.1–10.2.4) amounts to replacing the derivative  $dA_j/dz$  with

$$\frac{dA_j}{dz} \rightarrow \frac{\partial A_j}{\partial z} + \beta_{1j} \frac{\partial A_j}{\partial t} + \frac{i}{2} \beta_{2j} \frac{\partial^2 A_j}{\partial t^2} + \frac{1}{2} \alpha_j A_j \quad (10.2.23)$$

for all four waves ( $j = 1–4$ ) in analogy with Eq. (2.3.28). The resulting four coupled NLS equations describe FWM of picosecond optical pulses and include the effects of GVD, SPM, and XPM. It is difficult to solve the four coupled NLS equations analytically, and a numerical approach is used in practice. The group velocity of four pulses participating in the FWM process can be quite different. As a result, efficient FWM requires not only phase matching but also matching of the group velocities.

A natural question is whether the four coupled NLS equations have solutions in the form of optical solitons that support each other in the same way as the nonlinear phenomenon of XPM allows pairing of two solitons. Such solitons do exist for specific combination of parameters and are sometimes called parametric or FWM solitons. They have been investigated for both three- and four-wave interactions [37–43]. As an example, if we assume that the four waves satisfy both the phase-matching and group-velocity-matching conditions and, at the same time  $|\beta_2|$  is the same for all waves, a solitary-wave solution in the form of two bright and two dark solitons has been found for a specific choice of the signs of GVD parameters [39].

In the case of intense CW pumping, such that the pump remains nearly undepleted, the pump equations can be solved analytically. When a single pump beam of power  $P_0$  is incident at  $z = 0$ , the signal and idler fields are found to satisfy the following set of two coupled NLS equations:

$$\begin{aligned} \frac{\partial A_3}{\partial z} + \beta_{13} \frac{\partial A_3}{\partial t} + \frac{i}{2} \beta_{23} \frac{\partial^2 A_3}{\partial t^2} + \frac{1}{2} \alpha_3 A_3 \\ = i\gamma(|A_3|^2 + 2|A_4|^2 + 2P_0)A_3 + i\gamma P_0 A_4^* e^{-i\theta}, \end{aligned} \quad (10.2.24)$$

$$\begin{aligned} \frac{\partial A_4}{\partial z} + \beta_{14} \frac{\partial A_4}{\partial t} + \frac{i}{2} \beta_{24} \frac{\partial^2 A_4}{\partial t^2} + \frac{1}{2} \alpha_4 A_4 \\ = i\gamma(|A_4|^2 + 2|A_3|^2 + 2P_0)A_4 + i\gamma P_0 A_3^* e^{-i\theta}, \end{aligned} \quad (10.2.25)$$

where the net phase mismatch  $\theta = (\Delta k + 2\gamma P_0)z$  takes into account the SPM-induced phase shift of the pump. Numerical results show that these equations can support “symbiotic” soliton pairs [44], similar to those discussed in Section 7.3, if the

pump wavelength nearly coincides with the zero-dispersion wavelength of the fiber and the signal and idler wavelengths are equally spaced from it such that  $\beta_{13} = \beta_{14}$  and  $\beta_{23} = -\beta_{24}$  (opposite GVD but same group velocities). Such solitons require a balance between the parametric gain and fiber losses, similar to the case of Brillouin solitons, and are referred to as dissipative solitons. Both members of the soliton pair are bright solitons even though one pulse travels in the normal-GVD region of the fiber.

The use of multiple NLS equations is necessary when carrier frequencies of four pulses are widely separated ( $>5$  THz). In the case of smaller frequency spacings ( $<1$  THz), it is more practical to use a single NLS equation of the form given in Eq. (2.3.36) or (2.3.44) and solve it with an initial amplitude of the form

$$A(0, t) = A_1(0, t) + A_3(0, t) \exp(-i\Omega_s t) + A_4(0, t) \exp(i\Omega_s t), \quad (10.2.26)$$

where two pump waves are assumed to be degenerate in frequency and  $\Omega_s$  is the frequency shift given in Eq. (10.1.9). Such an approach includes SPM, XPM and FWM effects automatically and is routinely used for modeling of WDM lightwave systems. The only requirement is that the time step used in numerical simulations should be much shorter than  $2\pi/\Omega_s$ . This approach also permits inclusion of the Raman and birefringence effects and provides a unified treatment of various nonlinear phenomena for pulses propagating inside optical fibers [34–36].

## 10.3 PHASE-MATCHING TECHNIQUES

As seen from the solution given in Section 10.2.2, the parametric gain  $g$  in Eq. (10.2.19) is maximum when the phase mismatch  $\kappa = 0$  for the underlying FWM process, where  $\kappa$  is given by Eq. (10.2.15). This section discusses several different methods used for realizing phase matching in practice.

### 10.3.1 Physical Mechanisms

The phase-matching condition  $\kappa = 0$  can be written in the form

$$\kappa = \Delta k_M + \Delta k_W + \Delta k_{NL} = 0, \quad (10.3.1)$$

where  $\Delta k_M$ ,  $\Delta k_W$ , and  $\Delta k_{NL}$  represent the mismatch occurring as a result of material dispersion, waveguide dispersion, and the nonlinear effects, respectively. The contributions  $\Delta k_M$  and  $\Delta k_W$  can be obtained from Eq. (10.1.8) if the effective indices are written as

$$\tilde{n}_j = n_j + \Delta n_j, \quad (10.3.2)$$

where  $\Delta n_j$  is the change in the material index  $n_j \equiv n_M(\omega_j)$  due to waveguiding. In the case of degenerate FWM ( $\omega_1 = \omega_2$ ), the three contributions in Eq. (10.3.1) are

$$\Delta k_M = [n_3\omega_3 + n_4\omega_4 - 2n_1\omega_1]/c, \quad (10.3.3)$$

$$\Delta k_W = [\Delta n_3 \omega_3 + \Delta n_4 \omega_4 - (\Delta n_1 + \Delta n_2) \omega_1] / c, \quad (10.3.4)$$

$$\Delta k_{NL} = \gamma(P_1 + P_2). \quad (10.3.5)$$

To realize phase matching, at least one of them should be negative.

The material contribution  $\Delta k_M$  can be expressed in terms of the frequency shift  $\Omega_s$  [see Eq. (10.1.9)] if we use the expansion (2.3.23) and note that  $\beta_j = n_j \omega_j / c$  ( $j = 1-4$ ). Retaining up to fourth-order terms in  $\Omega_s$  in this expansion,

$$\Delta k_M \approx \beta_2 \Omega_s^2 + (\beta_4 / 12) \Omega_s^4, \quad (10.3.6)$$

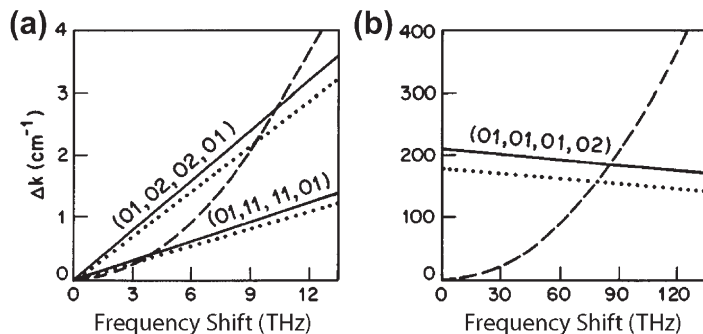
where  $\beta_2$  and  $\beta_4$  are the dispersion parameters at the pump frequency  $\omega_1$ . If the pump wavelength ( $\lambda_1 = 2\pi c / \omega_1$ ) is not too close to the zero-dispersion wavelength  $\lambda_0$  of the fiber, we can use  $\Delta k_M \approx \beta_2 \Omega_s^2$ . As  $\beta_2 > 0$  for  $\lambda_1 < \lambda_0$ ,  $\Delta k_M$  is positive in the visible or near-infrared region. Phase matching for  $\lambda_1 < \lambda_0$  can be realized if we make  $\Delta k_W$  negative by propagating different waves in different modes of a multimode fiber. Most of the early experiments used this method of phase matching [6–11].

In the case of a single-mode fiber,  $\Delta k_W = 0$  because  $\Delta n$  is nearly the same for all waves. Three techniques can be used to realize phase matching in single-mode fibers. (1) If the pump wavelength exceeds  $\lambda_0$ ,  $\Delta k_M$  becomes negative. This allows one to achieve phase matching for  $\lambda_1$  in the vicinity of  $\lambda_0$ . (2) For  $\lambda_1 > \lambda_0$ , phase matching can be realized by adjusting  $\Delta k_{NL}$  through the pump power. (3) For  $\lambda_1 < \lambda_0$ , modal birefringence in polarization-preserving fibers makes it possible to achieve phase matching by polarizing different waves differently with respect to a principal axis of the fiber. All three techniques are discussed in this section.

### 10.3.2 Phase Matching in Multimode Fibers

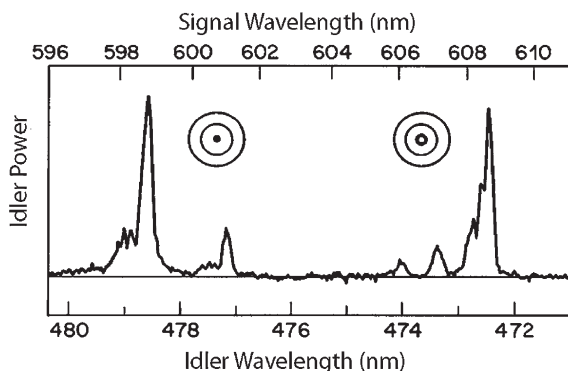
Multimode fibers allow phase matching when the waveguide contribution  $\Delta k_W$  is negative and exactly compensates the positive contribution  $\Delta k_M + \Delta k_{NL}$  in Eq. (10.3.1). The magnitude of  $\Delta k_W$  depends on the choice of fiber modes in which four waves participating in the FWM process propagate. The eigenvalue equation (2.2.8) of Section 2.2 can be used to calculate  $\Delta n_j$  ( $j = 1-4$ ) for each mode. Equation (10.3.4) is then used to calculate  $\Delta k_W$ .

Figure 10.2 shows the calculated value of  $\Delta k_W$  as a function of the frequency shift ( $\nu_s = \Omega_s / 2\pi$ ) for a fiber with 5-μm-core radius and a core-cladding index difference of 0.006. The dashed line shows the quadratic variation of  $\Delta k_M$  from Eq. (10.3.6). The frequency shift  $\nu_s$  is determined by the intersection of the solid and dashed curves (assuming that  $\Delta k_{NL}$  is negligible). Two cases are shown in Figure 10.2 corresponding to whether the pump wave propagates with its power divided in two different fiber modes or whether it propagates in a single fiber mode. In the former case, frequency shifts are in the range 1–10 THz, while in the latter case  $\nu_s \sim 100$  THz. The exact value of frequency shifts is sensitive to several fiber parameters. The dotted lines in Figure 10.2 show how  $\nu_s$  changes with a 10% increase in the core radius. In general, the phase-matching condition can be satisfied for several combinations of the fiber modes.



**Figure 10.2** Phase-matching diagrams for (a) mixed-mode and (b) single-mode pump propagation. Solid and dashed lines show variations of  $\Delta k_M$  with frequency shift. Dotted lines illustrate the effect of increasing the core radius by 10%. Fiber modes are indicated using the  $LP_{mn}$  terminology. (After Ref. [7]; © 1975 IEEE.)

In the 1974 demonstration of phase-matched FWM in silica fibers, pump pulses at 532 nm with peak powers  $\sim 100$  W were launched in a 9-cm-long fiber, together with a CW signal (power  $\sim 10$  mW) obtained from a dye laser tunable in the range of 565–640 nm [6]. FWM generated a new wave in the blue region ( $\omega_4 = 2\omega_1 - \omega_3$ ), called the idler wave in the parametric-amplifier configuration used for the experiment. Figure 10.3 shows the observed idler spectrum obtained by varying the signal frequency  $\omega_3$ . The five different peaks correspond to different combinations of fiber modes for which phase matching is achieved. Different far-field patterns for the two dominant peaks clearly indicate that the idler wave is generated in different fiber modes. In this experiment, the pump propagated in a single fiber mode. As expected



**Figure 10.3** Idler power as a function of a wavelength generated by tuning the signal wavelength (upper scale). Far-field patterns corresponding to the two dominant peaks are shown as insets. (After Ref. [6]; © 1974 American Institute of Physics.)

from Figure 10.2, phase-matching occurred for relatively large frequency shifts in the range of 50–60 THz. In another experiment, the frequency shift was as large as 130 THz, a value that corresponds to a 23% change in the pump frequency [11].

FWM with much smaller frequency shifts ( $\nu_s = 1 - 10$  THz) can occur if the pump power is divided between two different fiber modes (see Figure 10.2). This configuration is also relatively insensitive to variations in the core diameter [7] and results in coherence lengths  $\sim 10$  m. When  $\nu_s$  is close to 10 THz, the Raman process can interfere with the FWM process as the generated Stokes line falls near the Raman-gain peak and can be amplified by SRS. In an experiment in which 532-nm pump pulses with peak powers  $\sim 100$  W were transmitted through a multimode fiber, the Stokes line was always more intense than the anti-Stokes line as a result of Raman amplification [7].

When picosecond pump pulses are propagated through a multimode fiber, the FWM process is affected not only by SRS but also by SPM, XPM, and GVD. In a 1987 experiment [26], 25-ps pump pulses were transmitted through a 15-m-long fiber, supporting four modes at the pump wavelength of 532 nm. Figure 10.4 shows the observed spectra at the fiber output as the pump peak intensity is increased above the FWM threshold occurring near 500 MW/cm<sup>2</sup>. Only the pump line is observed below threshold (trace a). Three pairs of Stokes and anti-Stokes lines with frequency shifts in the range 1–8 THz are observed just above threshold (trace b). All of these lines have nearly the same amplitude, indicating that SRS does not play a significant role at this pump power.

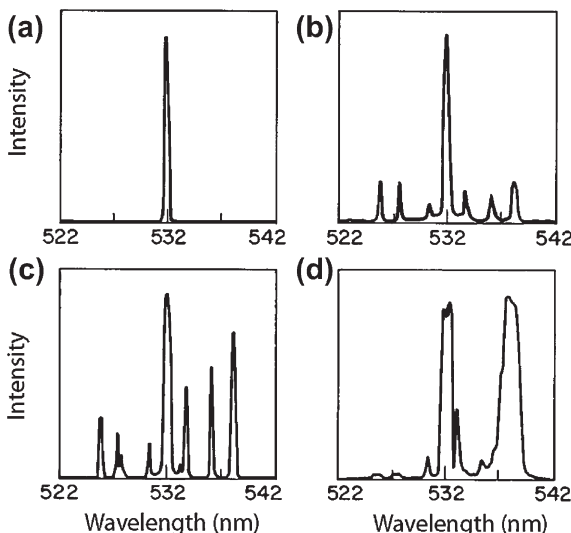


**Figure 10.4** Output spectra of 25-ps pump pulses when their peak intensity is increased progressively beyond the FWM threshold in going from (a) to (d). (After Ref. [26]; © 1987 IEEE.)

As pump power is slightly increased, the Stokes lines become much more intense than the anti-Stokes lines as a result of Raman amplification (trace c). With a further increase in pump power, the Stokes line closest to the Raman-gain peak becomes as intense as the pump line itself whereas the anti-Stokes lines are nearly depleted (trace d). At the same time, the pump and the dominant Stokes line exhibit spectral broadening and splitting that are characteristic of SPM and XPM (see Section 7.4). As the pump power is increased further, higher-order Stokes lines are generated through cascaded SRS. At a pump intensity of  $1.5 \text{ GW/cm}^2$ , the broadened multiple Stokes lines merge, and a supercontinuum extending from 530 to 580 nm is generated as a result of the combined effects of SPM, XPM, SRS, and FWM. Figure 10.5 shows the spectra observed at the fiber output under such conditions. Under certain conditions, supercontinuum can extend over a wide range ( $>100 \text{ nm}$ ). Supercontinuum generation in single-mode fibers is discussed in Chapter 12.

### 10.3.3 Phase Matching in Single-Mode Fibers

In single-mode fibers the waveguide contribution  $\Delta k_w$  in Eq. (10.3.1) is very small compared with the material contribution  $\Delta k_M$  for identically polarized waves, except near the zero-dispersion wavelength  $\lambda_0$  where the two become comparable. The three possibilities for approximate phase matching consist of: (i) reducing  $\Delta k_M$  and  $\Delta k_{NL}$  by using small frequency shifts and low pump powers; (ii) operating near the zero-dispersion wavelength so that  $\Delta k_w$  nearly cancels  $\Delta k_M + \Delta k_{NL}$ ; and (iii) working in the anomalous GVD regime so that  $\Delta k_M$  is negative and can be cancelled by  $\Delta k_{NL} + \Delta k_w$ .

#### 10.3.3.1 Nearly Phase-Matched Four-Wave Mixing

The gain spectrum shown in Figure 10.1 indicates that significant FWM can occur even if phase matching is not perfect to yield  $\kappa = 0$  in Eq. (10.3.1). The amount of tolerable wave-vector mismatch depends on how long the fiber is compared with the coherence length  $L_{coh}$ . Assuming that the contribution  $\Delta k_M$  dominates in

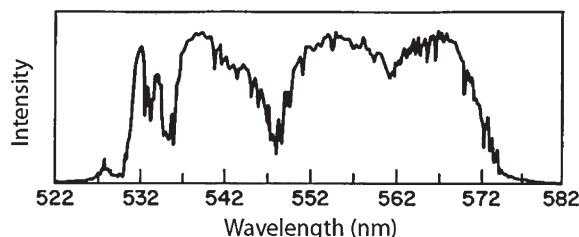


**Figure 10.5** Supercontinuum observed when the pump intensity is increased to  $1.5 \text{ GW/cm}^2$ . (After Ref. [26]; © 1987 IEEE.)

Eq. (10.3.1), the coherence length can be related to the frequency shift  $\Omega_s$  by using  $L_{coh} = 2\pi/|\Delta\kappa|$  with Eq. (10.3.6) and is given by

$$L_{coh} = \frac{2\pi}{|\Delta k_M|} = \frac{2\pi}{|\beta_2|\Omega_s^2}. \quad (10.3.7)$$

In the visible region,  $\beta_2 \sim 50 \text{ ps}^2/\text{km}$ , resulting in  $L_{coh} \sim 1 \text{ km}$  for frequency shifts  $\nu_s = \Omega_s/2\pi \sim 100 \text{ GHz}$ . Such large coherence lengths indicate that significant FWM can occur when the fiber length satisfies the condition  $L < L_{coh}$ .

In an early experiment, three CW waves with a frequency separation in the range 1–10 GHz were propagated through a 150-m-long fiber, whose 4-μm core diameter ensured single-mode operation near the argon-ion laser wavelength of 514.5 nm [8]. The FWM generated nine new frequencies such that  $\omega_4 = \omega_i + \omega_j - \omega_k$ , where  $i, j, k$  equal 1, 2, or 3 with  $j \neq k$ . The experiment also showed that FWM can lead to spectral broadening whose magnitude increases with an increase in the incident power. The 3.9-GHz linewidth of the CW input from a multimode argon laser increased to 15.8 GHz at an input power of 1.63 W after passing through the fiber. The spectral components within the incident light generate new frequency components through FWM as the light propagates through the fiber. In fact, SPM-induced spectral broadening discussed in Section 4.1 can be interpreted in terms of such a FWM process [45].

From a practical standpoint FWM can lead to crosstalk in multichannel (WDM) communication systems, where the channel spacing is typically in the range of 10–100 GHz. This issue attracted considerable attention during the 1990s with the advent of WDM systems [46–52]. In an early experiment [25], three CW waves with a frequency separation  $\sim 10 \text{ GHz}$  were propagated through a 3.5-km-long fiber and the amount of power generated in the nine frequency components was measured by varying the frequency separation and the input power levels. Figure 10.6 shows measured variations for two frequency components  $f_{332}$  and  $f_{231}$  using the notation

$$f_{ijk} = f_i + f_j - f_k, \quad f_j = \omega_j/(2\pi). \quad (10.3.8)$$

In part (a),  $f_3 - f_1 = 11 \text{ GHz}$ ,  $f_2 - f_1 = 17.2 \text{ GHz}$ ,  $P_1 = 0.43 \text{ mW}$ ,  $P_2 = 0.14 \text{ mW}$ , and  $P_3$  is varied from 0.15 to 0.60 mW. In part (b),  $f_3 - f_2$  is varied from 10 to 25 GHz for  $P_3 = 0.55 \text{ mW}$ , while keeping all other parameters the same.

The generated power  $P_4$  varies with  $P_3$  linearly for the frequency component  $f_{231}$  but quadratically for the frequency component  $f_{332}$ . This is expected from the theory of Section 10.2 by noting that  $f_{231}$  results from nondegenerate pump waves but the pump waves are degenerate in frequency for  $f_{332}$ . More power is generated in the frequency component  $f_{231}$  because  $f_{231}$  and  $f_{321}$  are degenerate, and the measured power is the sum of powers generated through two FWM processes. Finally,  $P_4$  decreases with increasing frequency separation because of a larger phase mismatch. A noteworthy feature of Figure 10.6 is that up to 0.5 nW of power is generated for input powers  $< 1 \text{ mW}$ . In practice, input channel powers should typically be kept below 1 mW to avoid degradation induced by FWM [53].

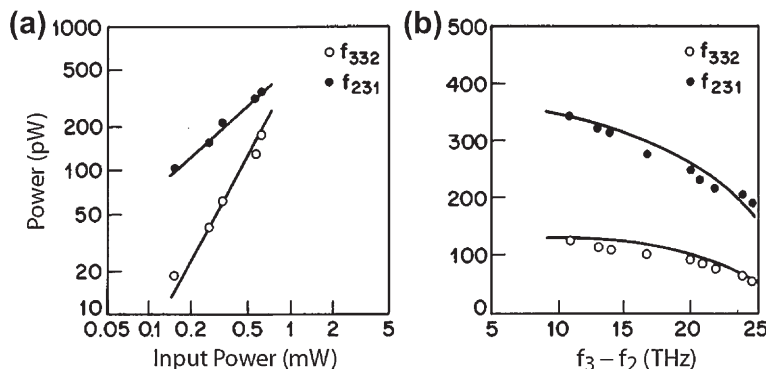


Figure 10.6 Variation of FWM-generated power at the output of a 3.5-km-long fiber with (a) input power  $P_3$  and (b) frequency separation. (After Ref. [25]; © 1987 IEEE.)

### 10.3.3.2 Phase Matching Near the Zero-Dispersion Wavelength

The material contribution  $\Delta k_M$  to the phase mismatch becomes quite small near the zero-dispersion wavelength of the fiber before it changes from positive to negative values around  $1.28 \mu\text{m}$ . The waveguide contribution  $\Delta k_W$  depends on the fiber design, but is generally positive near  $1.3 \mu\text{m}$ . In a limited range of pump wavelengths  $\Delta k_M$  can cancel  $\Delta k_W + \Delta k_{NL}$  for specific values of frequency shifts  $v_s$ . Figure 10.7 shows such cancellation, assuming  $\Delta k_{NL}$  to be negligible, for a fiber of  $7-\mu\text{m}$  core diameter and a core-cladding index difference of 0.006. The frequency shift depends on the pump wavelength  $\lambda_1$  and can vary over a wide range of  $1\text{--}100\text{ THz}$ . It is also sensitive to the values of core diameter and index difference. These two parameters can be used to tailor the frequency shift at a given pump wavelength [16].

In a 1980 experiment on FWM near  $1.3 \mu\text{m}$ , a 30-m-long standard fiber ( $\lambda_0 \approx 1.3 \mu\text{m}$ ) was used as a parametric amplifier that was pumped by  $1.319\text{-}\mu\text{m}$

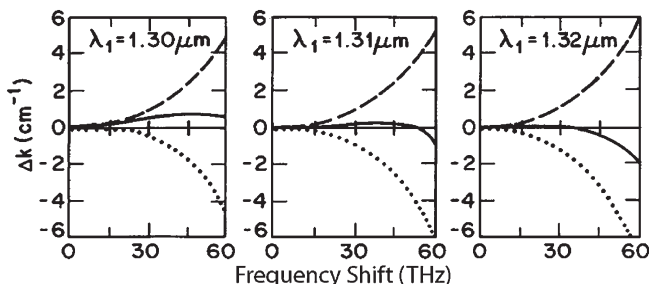


Figure 10.7 Phase-matching diagrams near the zero-dispersion wavelength for three values of the pump wavelength  $\lambda_1$ . Dotted, dashed, and solid lines show respectively  $\Delta k_M$ ,  $\Delta k_W$ , and their sum. (After Ref. [15]; © 1981 OSA.)

pulses from a Q-switched Nd:YAG laser [14]. A signal at  $1.338\text{ }\mu\text{m}$  ( $\nu_s = 3.3\text{ THz}$ ) was amplified by up to 46 dB while, at the same time, three pairs of Stokes and anti-Stokes lines were observed at the fiber output. These equally spaced lines (spacing 3.3 THz) originate from a cascade of FWM processes in which successive lines interact with each other to generate new frequencies. In a later experiment, FWM occurred spontaneously without an input signal [15]. Mode-locked input pulses at  $1.319\text{ }\mu\text{m}$ , with peak powers  $\sim 1\text{ kW}$ , were propagated through a 50-m-long fiber. Their peak power was large enough to exceed the Raman threshold. Figure 10.8 shows the spectrum observed at the fiber output. The Stokes and anti-Stokes lines at  $1.67$  and  $1.09\text{ }\mu\text{m}$ , respectively, originate from FWM. The huge frequency shift ( $\nu_s \approx 48\text{ THz}$ ) is comparable to that achieved in multimode fibers. Similar experiments show that  $\nu_s$  can be varied in the range 3–50 THz by changing the core diameter from  $7.2$  to  $8.2\text{ }\mu\text{m}$  [16]. This scheme is useful for realizing new optical sources pumped by a  $1.319\text{-}\mu\text{m}$  Nd:YAG laser.

### 10.3.3.3 Phase Matching Due to Self-Phase Modulation

When the pump wavelength lies in the anomalous-GVD regime and deviates considerably from  $\lambda_0$ ,  $\Delta k_M$  exceeds significantly from  $\Delta k_W$  and it becomes difficult to achieve phase matching (see Figure 10.7). However, because  $\Delta k_M + \Delta k_W$  is negative, it is possible to compensate it by the nonlinear contribution  $\Delta k_{NL}$  in Eq. (10.3.1). The frequency shift  $\Omega_s$  in that case depends on the input pump power. In fact, if we use Eq. (10.2.21) with  $\Delta k \approx \Delta k_M \approx \beta_2 \Omega_s^2$  from Eq. (10.3.6), phase-matching occurs ( $\kappa = 0$ ) when

$$\Omega_s = (2\gamma P_0 / |\beta_2|)^{1/2}, \quad (10.3.9)$$

where  $P_0$  is the input pump power. Thus, a pump wave propagating in the anomalous-GVD regime would develop sidebands located at  $\omega_1 \pm \Omega_s$  as a result of FWM that is phase-matched by the nonlinear process of self-phase modulation. This case has been discussed in Section 5.1 in the context of modulation instability. As was indicated there, modulation instability can be interpreted in terms of FWM in the frequency domain, whereas in the time domain it results from an unstable growth of weak perturbations from the steady state. In fact, the modulation frequency given in Eq. (5.1.9) is identical to  $\Omega_s$  of Eq. (10.3.9). The output spectrum shown in Figure

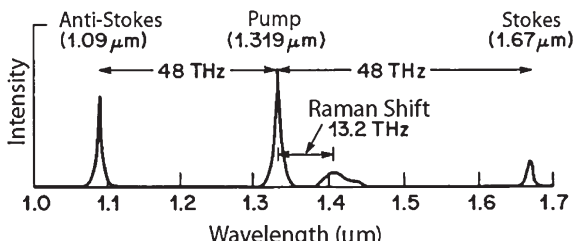


**Figure 10.8** Output spectra showing Stokes and anti-Stokes bands generated through FWM. The Raman band near  $1.4\text{ }\mu\text{m}$  is also evident. (After Ref. [15]; © 1981 OSA.)

5.2 provides an experimental evidence of phase matching occurring as a result of self-phase modulation. The frequency shifts are in the range 1–10 THz for pump powers  $P_0$  ranging from 1 to 100 W. This phenomenon has been used to convert the wavelength of femtosecond pulses from the 1.5- to the 1.3- $\mu\text{m}$  spectral region [54].

The derivation of Eq. (10.3.9) is based on the assumption that the linear phase mismatch  $\Delta k$  is dominated by the  $\beta_2$  term in Eq. (10.3.6). When  $|\beta_2|$  is relatively small, one should include the  $\beta_4$  term as well. The frequency shift  $\Omega_s$  is then obtained by solving the fourth-order polynomial

$$(\beta_4/12)\Omega_s^4 + \beta_2\Omega_s^2 + 2\gamma P_0 = 0. \quad (10.3.10)$$

Depending on the relative signs and magnitudes of  $\beta_2$  and  $\beta_4$ ,  $\Omega_s$  can vary over a large range. In particular, as mentioned in Section 5.1.2, modulation instability can also occur for  $\beta_2 > 0$  provided  $\beta_4 < 0$ . This situation can occur for dispersion-flattened fibers [55]. In practice, it is easily realized in tapered or microstructured fibers [56–59]. In a fiber exhibiting normal dispersion with  $\beta_4 < 0$ , Eq. (10.3.9) leads to the following expression for  $\Omega_s$ :

$$\Omega_s^2 = \frac{6}{|\beta_4|} \left( \sqrt{\beta_2^2 + 2|\beta_4|\gamma P_0/3} + \beta_2 \right). \quad (10.3.11)$$

Figure 10.9 shows how the frequency shift,  $v_s = \Omega_s/(2\pi)$ , varies with  $\beta_2$  and  $|\beta_4|$  for  $\gamma P_0 = 10 \text{ km}^{-1}$ . In the limit  $|\beta_4|\gamma P_0 \ll \beta_2^2$ , this shift is given by the simple expression  $\Omega_s = (12\beta_2/|\beta_4|)^{1/2}$ . For typical values of  $\beta_2$  and  $\beta_4$ , the frequency shift can exceed 25 THz, indicating that FWM can amplify a signal that is more than 200 nm away from the pump wavelength. Such FWM is discussed in more detail in Chapter 12 in the context of microstructured and photonic-crystal fibers.

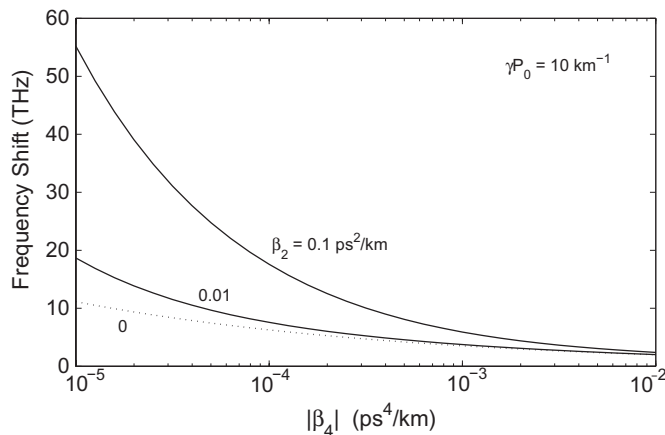


**Figure 10.9** Frequency shift between the pump and signal waves plotted as a function of  $|\beta_4|$  for several values of  $\beta_2$  when the FWM-process is phase-matched by SPM in a dispersion-flattened fiber.

### 10.3.4 Phase Matching in Birefringent Fibers

An important phase-matching technique in single-mode fibers takes advantage of the modal birefringence, resulting from different effective mode indices for optical waves propagating with orthogonal polarizations. The index difference

$$\delta n = \Delta n_x - \Delta n_y, \quad (10.3.12)$$

where  $\Delta n_x$  and  $\Delta n_y$  represent changes in the refractive indices (from the material value) for the optical fields polarized along the slow and fast axes of the fiber, respectively. A complete description of the parametric gain in birefringent fibers should generalize the formalism of Section 10.2 by following an approach similar to that used in Section 6.1. Such a vector theory of FWM is discussed in Section 10.5. However, this theory is not needed for the following discussion of phase matching.

If we assume that each of the four waves is polarized either along the slow or along the fast axis of a polarization-maintaining fiber, we can use the scalar theory of Section 10.2. The parametric gain is then given by Eq. (10.2.19) with only minor changes in the definitions of the parameters  $\gamma$  and  $\kappa$ . In particular,  $\gamma$  is reduced by a factor of 3 whenever the pump and signal are polarized orthogonally. The wavevector mismatch  $\kappa$  still has three contributions as in Eq. (10.3.1). However, the waveguide contribution  $\Delta k_w$  is now dominated by  $\delta n$ . The nonlinear contribution  $\Delta k_{NL}$  is also different than that given by Eq. (10.3.5). In the following discussion  $\Delta k_{NL}$  is assumed to be negligible compared with  $\Delta k_M$  and  $\Delta k_w$ .

As before, phase matching occurs when  $\Delta k_M$  and  $\Delta k_w$  cancel each other out. Both of them can be positive or negative. For  $\lambda_1 < \lambda_0$ , a range that covers the visible region,  $\Delta k_M$  is positive because  $\beta_2$  is positive in Eq. (10.3.6). The waveguide contribution  $\Delta k_w$  can be made negative if the pump is polarized along the slow axis, while the signal and idler are polarized along the fast axis. This can be seen from Eq. (10.3.4). As  $\Delta n_3 = \Delta n_4 = \Delta n_y$  and  $\Delta n_1 = \Delta n_2 = \Delta n_x$ , the waveguide contribution becomes

$$\Delta k_w = [\Delta n_y(\omega_3 + \omega_4) - 2\Delta n_x\omega_1]/c = -2\omega_1(\delta n)/c, \quad (10.3.13)$$

where Eq. (10.3.12) was used together with  $\omega_3 + \omega_4 = 2\omega_1$ . From Eqs (10.3.6) and (10.3.13),  $\Delta k_M$  and  $\Delta k_w$  compensate each other for a frequency shift  $\Omega_s$  given by [17]

$$\Omega_s = [4\pi\delta n/(\beta_2\lambda_1)]^{1/2}, \quad (10.3.14)$$

where  $\lambda_1 = 2\pi c/\omega_1$ . At a pump wavelength  $\lambda_1 = 0.532 \mu\text{m}$ ,  $\beta_2 \approx 60 \text{ ps}^2/\text{km}$ . If we use a typical value  $\delta n = 1 \times 10^{-5}$  for the fiber birefringence, the frequency shift  $\nu_s$  is  $\sim 10 \text{ THz}$ . In a 1981 experiment on FWM in birefringent fibers, the frequency shift was in the range of 10–30 THz [17]. Furthermore, the measured values of  $\nu_s$  agreed well with those estimated from Eq. (10.3.14).

Equation (10.3.14) for the frequency shift is derived for a specific choice of field polarizations, namely, that the pump fields  $A_1$  and  $A_2$  are polarized along the slow axis while  $A_3$  and  $A_4$  are polarized along the fast axis. Several other combinations can be used for phase matching depending on whether  $\beta_2$  is positive or negative. The

**Table 1** Phase-matched FWM processes in birefringent fibers<sup>a</sup>

Process	$A_1$	$A_2$	$A_3$	$A_4$	Frequency shift $\Omega_s$	Condition
I	s	f	s	f	$\delta n / ( \beta_2 c)$	$\beta_2 > 0$
II	s	f	f	s	$\delta n / ( \beta_2 c)$	$\beta_2 < 0$
III	s	s	f	f	$(4\pi\delta n /  \beta_2 \lambda_1)^{1/2}$	$\beta_2 > 0$
IV	f	f	s	s	$(4\pi\delta n /  \beta_2 \lambda_1)^{1/2}$	$\beta_2 < 0$

<sup>a</sup>The symbols s and f denote the direction of polarization along the slow and fast axes of the birefringent fiber, respectively.

corresponding frequency shifts  $\Omega_s$  are obtained by evaluating  $\Delta k_w$  from Eq. (10.3.4) with  $\Delta n_j$  ( $j = 1-4$ ) replaced by  $\Delta n_x$  or  $\Delta n_y$ , depending on the wave polarization, and by using Eq. (10.3.6). Table 1 lists the four phase-matching processes that can occur in birefringent fibers together with the corresponding frequency shifts [31]. The frequency shifts of the first two processes are smaller by more than one order of magnitude compared with the other two processes. All frequency shifts in Table 1 are approximate because frequency dependence of  $\delta n$  has been ignored; its inclusion can reduce them by about 10%. Several other phase-matched processes have been identified [20] but are not generally observed in a silica fiber because of its predominantly isotropic nature.

From a practical standpoint, the four processes shown in Table 1 can be divided into two categories. The first two correspond to the case in which pump power is divided between the slow and fast modes. In contrast, the pump field is polarized along a principal axis for the remaining two processes. In the first category, the parametric gain is maximum when the pump power is divided equally by choosing  $\theta = 45^\circ$ , where  $\theta$  is the polarization angle measured from the slow axis. Even then, different processes compete with each other because the parametric gain is nearly the same for all of them. In one experiment, FWM occurring as a result of Process I was observed by using 15-ps pump pulses from a mode-locked dye laser operating at 585.3 nm [21]. Because of a relatively small group-velocity mismatch among the four waves in this case, Process I became dominant compared with the others.

Figure 10.10 shows the spectrum observed at the output of a 20-m-long fiber for an input peak power  $\sim 1$  kW and a pump-polarization angle  $\theta = 44^\circ$ . The Stokes and anti-Stokes bands located near  $\pm 4$  THz are due to FWM phase-matched by Process I. As expected, the Stokes band is polarized along the slow axis, while the anti-Stokes band is polarized along the fast axis. Asymmetric broadening of the pump and Stokes bands results from the combined effects of SPM and XPM (see Section 7.4). Selective enhancement of the Stokes band is due to the Raman gain. The peak near 13 THz is also due to SRS. It is polarized along the slow axis because the pump component along that axis is slightly more intense for  $\theta = 44^\circ$ . An increase in  $\theta$  by  $2^\circ$  flips the polarization of the Raman peak along the fast axis. The small peak near 10 THz results from a nondegenerate FWM process in which both the pump and the

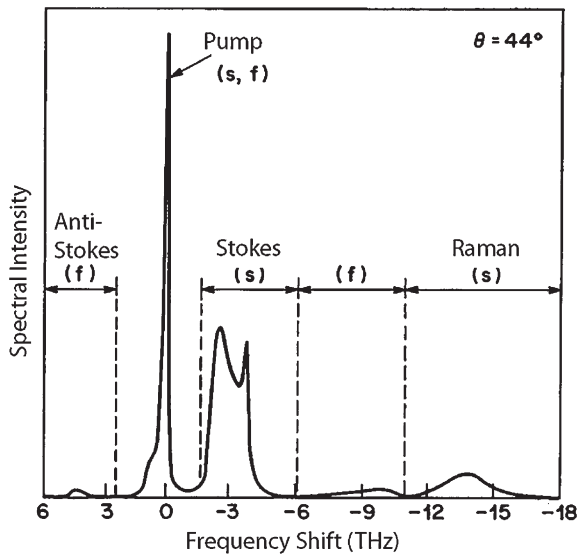


**Figure 10.10** Output spectra showing Stokes and anti-Stokes bands generated in a 20-m-long birefringent fiber when 15-ps pump pulses with a peak power  $\sim 1$  kW are incident at the fiber. The pump is polarized at  $44^\circ$  from the slow axis. (After Ref. [21]; © 1984 OSA.)

Stokes bands act as pump waves ( $\omega_1 \neq \omega_2$ ) and the Raman band provides a weak signal for the parametric process to occur. Phase matching can occur only if the Raman band is polarized along the slow axis. Indeed, the peak near 10 THz disappeared when  $\theta$  was increased beyond  $45^\circ$  to flip the polarization of the Raman band.

The use of birefringence for phase matching in single-mode fibers has an added advantage in that the frequency shift  $v_s$  can be tuned over a considerable range ( $\sim 4$  THz). Such a tuning is possible because birefringence can be changed through external factors such as stress and temperature. In one experiment, the fiber was pressed with a flat plate to apply the stress [18]. The frequency shift  $v_s$  could be tuned over 4 THz for a stress of 0.3 kg/cm. In a similar experiment, stress was applied by wrapping the fiber around a cylindrical rod [19]. The frequency shift  $v_s$  was tuned over 3 THz by changing the rod diameter. Tuning is also possible by varying the temperature as the built-in stress in birefringent fibers is temperature dependent. A tuning range of 2.4 THz was demonstrated by heating the fiber up to  $700^\circ\text{C}$  [22]. In general, FWM provides a convenient way of measuring the net birefringence of a fiber because the frequency shift depends on  $\delta n$  [23].

The frequency shift associated with the FWM process depends on the pump power through the nonlinear contribution  $\Delta k_{\text{NL}}$  in Eq. (10.3.1). This contribution has been neglected in obtaining Eq. (10.3.14) and other expressions of  $\Omega_s$  in Table 1, but can be included in a straightforward manner. In general  $\Omega_s$  decreases with increasing pump power. In one experiment,  $\Omega_s$  decreased with pump power at a rate

of  $1.4\% \text{ W}^{-1}$  [24]. The nonlinear contribution  $\Delta k_{\text{NL}}$  can also be used to satisfy the phase-matching condition. This feature is related to modulation instability in birefringent fibers (see Section 6.4).

## 10.4 PARAMETRIC AMPLIFICATION

Similar to the case of the Raman gain, the parametric gain in optical fibers can be used for making an optical amplifier. Such FWM-based devices are known as fiber-optic parametric amplifiers (FOPAs), or parametric oscillators if a FOPA is placed within an optical cavity providing feedback periodically. Although FOPAs were studied during the 1980s [60–62], they attracted considerably more attention after 1995 because of their potential applications in fiber-optic communication systems [63–69]. In this section we first review the early work and then focus on the single- and dual-pump configurations used for modern FOPAs.

### 10.4.1 Review of Early Work

Phase-matching techniques discussed in Section 10.3 were used for making FOPAs soon after low-loss silica fibers became available. Most experiments until 2000 employed a single pump and made use of the degenerate FWM configuration. In the original 1974 experiment, phase matching was achieved by using a multimode fiber [6]. The peak power of 532-nm pump pulses used in this experiment was  $\sim 100 \text{ W}$ , whereas the CW signal with a power  $\sim 10 \text{ mW}$  was tunable near 600 nm. The amplifier gain was quite small because of a short fiber length (9 cm) used in the experiment. In a 1980 experiment [14], phase matching was realized using a pump at  $1.319 \mu\text{m}$ , a wavelength close to the zero-dispersion wavelength of the fiber employed (see Figure 10.7). The peak power of the pump pulses was varied in the range of 30–70 W. A CW beam at the  $1.338\text{-}\mu\text{m}$  wavelength acted as the signal and propagated with the pump pulses in a 30-m-long fiber. The power of the amplified signal was measured to determine the amplification factor.

Figure 10.11 shows the signal gain  $G_s$  as a function of pump power  $P_0$  for three values of the input signal power  $P_3$ . Departure from the exponential increase in  $G_s$  with  $P_0$  is due to gain saturation occurring as a result of pump depletion. Note also that  $G_s$  reduces considerably as  $P_3$  increases from 0.26 to 6.2 mW. For the 0.26-mW input signal, the amplifier gain was as large as 46 dB for  $P_0 = 70 \text{ W}$ . Such large values indicated the potential of FWM for constructing FOPAs, provided phase matching could be realized. This requirement puts stringent limits on the range of frequency shift  $\Omega_s$  between the pump and signal waves for which amplification can occur.

The use of fiber birefringence for phase matching is attractive as birefringence can be adjusted to match  $\Omega_s$  by applying external stress or by bending the fiber. FOPAs with such schemes were demonstrated during the 1980s. In one experiment, a  $1.292\text{-}\mu\text{m}$  signal from a semiconductor laser was amplified by 38 dB as  $\Omega_s$  was tuned by applying external stress to the fiber [60]. In another experiment, a  $1.57\text{-}\mu\text{m}$  signal

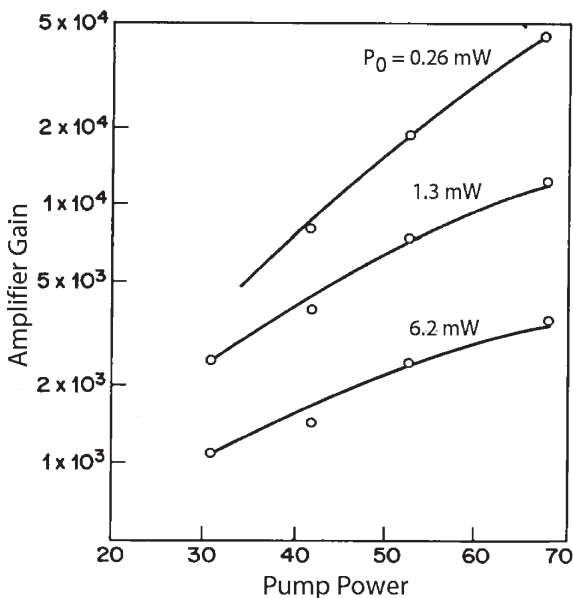


**Figure 10.11** Measured gain  $G_s$  of a parametric amplifier as a function of pump power for three values of the input signal power. (After Ref. [14]; © 1980 IEE.)

from a distributed feedback (DFB) semiconductor laser was amplified by 37 dB using a 1.319- $\mu\text{m}$  pump [61].

The resurgence of interest in FOPAs can be traced back to the work on modulation instability [55] and phase conjugation [70] carried out during the 1990s. It was realized that a broadband FOPA can be designed by choosing the pump wavelength  $\lambda_1$  close to the zero-dispersion wavelength  $\lambda_0$  of the optical fiber. In one implementation of this idea [63], a DFB semiconductor laser operating near  $\lambda_p \approx 1.54 \mu\text{m}$  was used for pumping, while a tunable external-cavity semiconductor laser provided the signal. The length of the dispersion-shifted fiber (with  $\lambda_0 = 1.5393$ ) used for parametric amplification was 200 m. The FOPA bandwidth changed considerably as pump wavelength was varied in the vicinity of  $\lambda_0$  and was the largest when pump wavelength was detuned such that  $\lambda_p - \lambda_0 = 0.8 \text{ nm}$ . Further research revealed that the use of dispersion management, dual-wavelength pumping, and highly nonlinear fibers (see Chapter 11) can provide >40-dB signal gain over a relatively large bandwidth [64–69]. Because of the fast nonlinear response of optical fibers, such FOPAs are useful for a variety of signal processing applications [67].

#### 10.4.2 Gain Spectrum and Its Bandwidth

The most important property of any optical amplifier—and FOPAs are no exception—is the bandwidth over which the amplifier can provide a relatively uniform gain. Typically, FOPAs are pumped using one or two CW lasers acting as pumps. In the

case of dual pumps, the FWM process is governed by Eqs (10.2.1–10.2.4), and a complete description of parametric amplification requires a numerical solution.

Considerable physical insight is gained by employing the approximate analytic solution given in Eqs (10.2.17) and (10.2.18) and obtained under the assumption that the pumps are not depleted much. The constants  $a_3$ ,  $b_3$ ,  $a_4$ , and  $b_4$  in these equations are determined from the boundary conditions. If we assume that both signal and idler waves are launched at  $z = 0$ , we find that the constants  $a_3$  and  $b_3$  satisfy

$$a_3 + b_3 = B_3(0), \quad g(a_3 - b_3) = (i\kappa/2)(a_3 + b_3) + 2i\gamma A_1(0)A_2(0)B_4^*(0). \quad (10.4.1)$$

Solving these equations, we obtain

$$a_3 = \frac{1}{2}(1 + i\kappa/2g)B_3(0) + iC_0B_4^*(0), \quad b_3 = \frac{1}{2}(1 - i\kappa/2g)B_3(0) - iC_0B_4^*(0), \quad (10.4.2)$$

where  $C_0 = (\gamma/g)A_1(0)A_2(0)$ . A similar method can be used to find the constants  $a_4$  and  $b_4$ . Using these values in Eqs (10.2.17) and (10.2.18), the signal and idler fields at a distance  $z$  are given by

$$B_3(z) = \{B_3(0)[\cosh(gz) + (i\kappa/2g)\sinh(gz)] + iC_0B_4^*(0)\sinh(gz)\}e^{-i\kappa z/2}, \quad (10.4.3)$$

$$B_4^*(z) = \{B_4^*(0)[\cosh(gz) - (i\kappa/2g)\sinh(gz)] - iC_0B_3(0)\sinh(gz)\}e^{i\kappa z/2}. \quad (10.4.4)$$

The preceding general solution simplifies considerably when only the signal is launched at  $z = 0$  (together with the pumps), a practical situation for most FOPAs. Setting  $B_4^*(0) = 0$  in Eq. (10.4.3), the signal power  $P_3 = |B_3|^2$  grows with  $z$  as [12]

$$P_3(z) = P_3(0)[1 + (1 + \kappa^2/4g^2)\sinh^2(gz)], \quad (10.4.5)$$

where the parametric gain  $g$  is given in Eq. (10.2.19). The idler power  $P_4 = |B_4|^2$  can be found from Eq. (10.4.4) in the same way. It can also be obtained by noting from Eqs (10.2.13) and (10.2.14) that  $d(P_3 - P_4)/dz = 0$ , or  $P_4(z) = P_3(z) - P_3(0)$ . Using this relation, we obtain

$$P_4(z) = P_3(0)(1 + \kappa^2/4g^2)\sinh^2(gz). \quad (10.4.6)$$

Equation (10.4.6) shows that the idler wave is generated almost immediately after the input signal is launched into the fiber. Its power increases as  $z^2$  initially, but both the signal and idler grow exponentially after a distance such that  $gz > 1$ . As the idler is amplified together with the signal all along the fiber, it can build up to nearly the same level as the signal at the FOPA output. In practical terms, the same FWM process can be used to amplify a weak signal *and* to generate a new wave simultaneously at the idler frequency. The idler wave mimics all features of the input signal except that its phase is reversed (or conjugated). Among other things, such phase conjugation can be used for dispersion compensation and wavelength conversion in a WDM system [53].

The amplification factor for the signal is obtained from Eq. (10.4.5) and can be written using Eq. (10.2.19) as

$$G_s = P_3(L)/P_3(0) = 1 + (\gamma P_0 r/g)^2 \sinh^2(gL). \quad (10.4.7)$$

The parameter  $r$  given in Eq. (10.2.20) equals 1 when a single pump beam is used for parametric amplification. The parametric gain  $g$  in Eq. (10.2.19) varies with the signal frequency  $\omega_3$  because of its dependence on the phase mismatch  $\kappa \equiv \Delta k + \gamma(P_1 + P_2)$ . Here,  $\Delta k$  is the linear phase mismatch given in Eq. (10.1.8). It depends not only on  $\omega_3$  but also on the pump frequencies and the dispersive properties of the fiber used to make the FOPA. Thus, the bandwidth of a FOPA can be controlled by tailoring the fiber dispersion and choosing the pump frequencies suitably.

The gain expression (10.4.7) should be compared with Eq. (8.2.4) obtained for a Raman amplifier. The main difference is that the parametric gain depends on the phase mismatch  $\kappa$  and can become quite small if phase matching is not achieved. In the limit  $\kappa \gg \gamma P_0 r$ , Eqs (10.2.19) and (10.4.7) yield

$$G_s \approx 1 + (\gamma P_0 r L)^2 \frac{\sin^2(\kappa L/2)}{(\kappa L/2)^2}. \quad (10.4.8)$$

The signal gain is relatively small and increases with pump power as  $P_0^2$  if phase mismatch is relatively large. On the other hand, if phase matching is perfect ( $\kappa = 0$ ) and  $gL \gg 1$ , the amplifier gain increases exponentially with  $P_0$  as

$$G_s \approx \frac{1}{4} \exp(2\gamma P_0 r L). \quad (10.4.9)$$

The amplifier bandwidth  $\Delta\Omega_A$  is determined from Eq. (10.4.7). It is usually defined as the range of  $\omega_3$  over which  $G_s(\omega_3)$  exceeds 50% of its peak value and depends on many factors such as fiber length  $L$ , pump power  $P_0$ , and the pumping configuration used for the FOPA. The gain peak occurs at a signal frequency for which  $\kappa = 0$  and the phase-matching condition is perfectly satisfied. In the case of a single pump,  $\kappa$  equals  $\Delta k + 2\gamma P_0$  with  $\Delta k \approx \beta_2 \Omega_s^2$ , where  $\Omega_s = |\omega_1 - \omega_3|$  is the detuning given in Eq. (10.3.9). Thus, the gain peak occurs at  $\Omega_s = (2\gamma P_0 / |\beta_2|)^{1/2}$ .

In the case of long fibers, the gain bandwidth  $\Delta\Omega_A$  is set by the fiber length itself and corresponds to a maximum phase mismatch  $\kappa_m = 2\pi/L$  because  $G_s$  is reduced roughly by a factor of 2 for this value of  $\kappa$ . Using  $\kappa_m = \beta_2(\Omega_s + \Delta\Omega_A)^2 + 2\gamma P_0$  with  $\Delta\Omega_A \ll \Omega_s$ , we obtain [12]

$$\Delta\Omega_A = \frac{\pi}{|\beta_2|\Omega_s L} = \frac{\pi}{L}(2\gamma P_0 |\beta_2|)^{-1/2}. \quad (10.4.10)$$

For relatively short fibers, the nonlinear effects themselves limit the FOPA bandwidth. As seen from Figure 10.1, the parametric gain vanishes when  $\kappa_m = 2\gamma P_0$ . Using this value, the FOPA bandwidth is approximated given by

$$\Delta\Omega_A \approx \frac{\gamma P_0}{|\beta_2|\Omega_s} \equiv \left( \frac{\gamma P_0}{2|\beta_2|} \right)^{1/2}. \quad (10.4.11)$$

As a rough estimate, the bandwidth is only 160GHz for a FOPA designed using a dispersion shifted fiber such that  $\gamma = 2 \text{ W}^{-1}/\text{km}$  and  $\beta_2 = -1 \text{ ps}^2/\text{km}$  at the pump wavelength, and the FOPA is pumped with 1W of CW power. Equation (10.4.11) shows that at a given pump power, it can only be increased considerably by reducing  $|\beta_2|$  and increasing  $\gamma$ . This is the approach adopted in modern FOPAs that are designed using highly nonlinear fibers with  $\gamma > 10 \text{ W}^{-1}/\text{km}$  and choosing the pump wavelength close to the zero-dispersion wavelength of the fiber so that  $|\beta_2|$  is reduced. However, as  $\beta_2$  is reduced below  $0.1 \text{ ps}^2/\text{km}$ , one must consider the impact of higher-order dispersive effects. It turns out that the FOPA bandwidth can be increased to beyond 5THz, for both single- and dual-pump FOPAs, by suitably optimizing the pump wavelengths. In the following discussion, we consider these two pump configurations separately.

### 10.4.3 Single-Pump Configuration

In this configuration, the pump wavelength is chosen close to the zero-dispersion wavelength of the fiber to minimize the wave-vector mismatch governed by  $\kappa$ . In the limit  $\beta_2$  approaches zero, higher-order dispersion terms become important in the expansion of  $\beta(\omega)$ . If we expand  $\Delta k$  in Eq. (10.1.9) in a Taylor series around the pump frequency  $\omega_1$ , we obtain [63]

$$\Delta k(\omega_3) = 2 \sum_{m=1}^{\infty} \frac{\beta_{2m}}{(2m)!} (\omega_3 - \omega_1)^{2m}, \quad (10.4.12)$$

where the dispersion parameters are evaluated at the pump wavelength. This equation is a generalization of Eq. (10.3.6) and shows that only even-order dispersion parameters contribute to the linear phase mismatch. Clearly,  $\Delta k$  is dominated by  $\beta_2$  when signal wavelength is close to the pump wavelength, but higher-order dispersion parameters become important when the signal deviates far from it. The FOPA bandwidth depends on the spectral range over which  $\Delta k$  is negative but large enough to balance the nonlinear phase mismatch of  $2\gamma P_0$ . In practice, the bandwidth can be enhanced by choosing the pump wavelength such that  $\beta_2$  is slightly negative but  $\beta_4$  is positive.

The quantities  $\beta_2$  and  $\beta_4$  can be related to the dispersion parameters, calculated at the zero-dispersion frequency  $\omega_0$  of the fiber and defined as  $\beta_{m0} = (d^m \beta / d\omega^m)_{\omega=\omega_0}$ , by expanding  $\beta(\omega)$  in a Taylor series around  $\omega_0$ . If we keep terms up to fourth-order in this expansion, we obtain

$$\beta_2 \approx \beta_{30}(\omega_1 - \omega_0) + \frac{1}{2}\beta_{40}(\omega_1 - \omega_0)^2, \quad \beta_4 \approx \beta_{40}. \quad (10.4.13)$$

Depending on the values of the fiber parameters  $\beta_{30}$  and  $\beta_{40}$ , we can choose the pump frequency  $\omega_1$  such that  $\beta_2$  and  $\beta_4$  have opposite signs. More specifically, as both  $\beta_{30}$  and  $\beta_{40}$  are positive for most silica fibers, one should choose  $\omega_1 < \omega_0$ . The FOPA bandwidth can exceed 5THz under such operating conditions [63].

As an example, consider a FOPA designed using a 2.5-km-long fiber with its zero-dispersion wavelength at 1550 nm such that  $\beta_{30} = 0.1 \text{ ps}^3/\text{km}$  and  $\beta_{40} = 10^{-4} \text{ ps}^4/\text{km}$ . The FOPA is pumped with 0.5 W of power, resulting in a nonlinear length of 1 km when  $\gamma = 2 \text{ W}^{-1}/\text{km}$ . Figure 10.12a shows the gain spectra for several values of pump detuning  $\Delta\lambda_p = \lambda_1 - \lambda_0$ . The dotted curve shows the case  $\Delta\lambda_p = 0$  for which pump wavelength coincides with the zero-dispersion wavelength exactly. The peak gain in this case is about 8 dB, and the gain bandwidth is limited to 40 nm. When the pump is detuned by  $-0.1 \text{ nm}$  such that it experiences normal GVD, gain bandwidth is reduced to below 20 nm. In contrast, both the peak gain and the bandwidth are enhanced when the pump is detuned toward the anomalous-GVD side. In this region, the gain spectrum is sensitive to the exact value of  $\Delta\lambda_p$ . The best situation from a practical standpoint occurs for  $\Delta\lambda_p = 0.106 \text{ nm}$  because the gain is nearly constant over a wide spectral region.

An interesting feature of Figure 10.12a is that the maximum gain occurs when the signal is detuned relatively far from the pump wavelength. This feature is related to the nonlinear contribution to total phase mismatch  $\kappa$ . The linear part of phase mismatch is negative for  $\Delta\lambda_p > 0$  and its magnitude depends on the signal wavelength. In a certain range of signal wavelengths, it is fully compensated by the nonlinear phase mismatch to yield  $\kappa = 0$ . When phase matching is perfect, FOPA gain increases exponentially with the fiber length, as indicated in Eq. (10.4.9), resulting in an off-center gain peak in Figure 10.12a.

From a practical standpoint, one wants to maximize both the peak gain and the gain bandwidth at a given pump power  $P_0$ . Since the peak gain in Eq. (10.4.9) scales exponentially with  $\gamma P_0 L$ , it can be increased by increasing the fiber length  $L$ . However, from Eq. (10.4.10) gain bandwidth scales inversely with  $L$  when  $L \gg L_{NL}$ . The only solution is to use a fiber as short as possible. Of course, shortening of fiber length

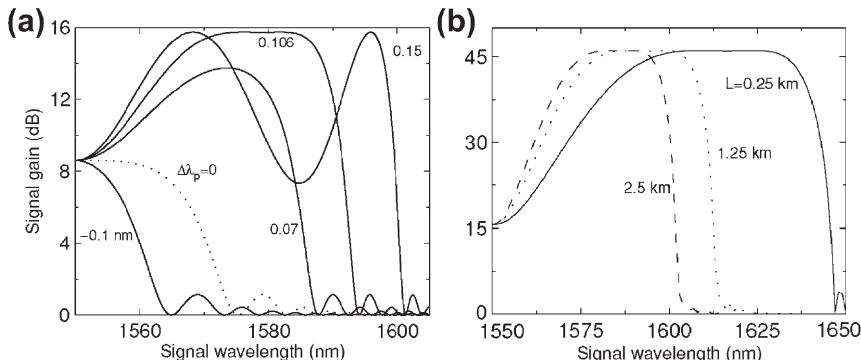


**Figure 10.12** (a) Gain spectra of a single-pump FOPA for several values of pump detuning  $\Delta\lambda_p$  from the zero-dispersion wavelength. (b) Gain spectra for three different fiber lengths assuming  $\gamma P_0 L = 6$  in each case. The pump wavelength is optimized in each case, and only half of the gain spectrum is shown because of its symmetric nature.

must be accompanied with a corresponding increase in the value of  $\gamma P_0$  to maintain the same amount of gain. This behavior is illustrated in Figure 10.12b where the gain bandwidth increases considerably when large values of  $\gamma P_0$  are combined with shorter fiber lengths such that  $\gamma P_0 L = 6$  remains fixed. The solid curve obtained for a 250-m-long FOPA exhibits a 30-nm-wide region on each side of the pump wavelength over which the gain is nearly flat. The nonlinear parameter  $\gamma$  can be increased by reducing the effective mode area. Such highly nonlinear fibers (see Chapter 11) with  $\gamma > 10 \text{ W}^{-1}/\text{km}$  are used to make modern FOPAs. A 200-nm gain bandwidth was realized as early as 2001 by using a 20-m-long fiber with  $\gamma = 18 \text{ W}^{-1}/\text{km}$  [71]. The required pump power ( $\sim 10 \text{ W}$ ) was large enough that the signal was also amplified by SRS when its wavelength exceeded the pump wavelength.

Another scheme for enhancing the bandwidth of FOPAs manages fiber dispersion along the fiber either through periodic dispersion compensation [65] or by using multiple fiber sections with different dispersive properties [72]. Figure 10.13 shows the gain spectra at several pump-power levels for such a single-pump FOPA [73]. At a pump power of 31.8 dBm (about 1.5 W) at 1563 nm, the FOPA provided a peak gain of 39 dB. The 500-m-long FOPA was designed by cascading three fiber sections with zero-dispersion wavelengths at 1556.8, 1560.3, 1561.2 nm. Each fiber section had  $\gamma$  close to  $11 \text{ W}^{-1}/\text{km}$  and a dispersion slope around  $0.03 \text{ ps/nm}^2/\text{km}$ . Such devices can be used to amplify multiple WDM channels simultaneously [74].

As discussed earlier, FOPAs can act as wavelength converters because the idler wave generated internally contains the same information as the signal launched at the input end but at a different wavelength [75]. As early as 1998, peak conversion efficiency of 28 dB was realized over a 40-nm bandwidth using a pulsed pump source [64]. More recently, transparent wavelength conversion over a 24-nm bandwidth (the entire pump tuning range) was realized using a single-pump FOPA made with just 115 m of a highly nonlinear fiber [76].

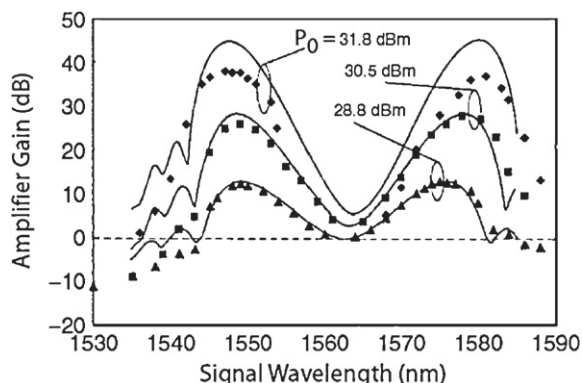


**Figure 10.13** Measured signal gain as a function of signal wavelength at several pump powers. Solid curves show the theoretical prediction. (After Ref. [73]; © 2001 IEEE.)

The performance of FOPAs is affected by several factors that must be considered during the design of such devices [77–86]. For example, although FOPAs benefit from an ultrafast nonlinear response of silica, they also suffer from it because fluctuations in the pump power are transferred to the signal and idler fields almost instantaneously. Indeed, noise in FOPAs is often dominated by the transfer of pump-power fluctuations to the amplified signal [77–80]. Moreover, as the pump beam is typically amplified using one or two erbium-doped fiber amplifiers (EDFAs) before it is launched inside the FOPA, spontaneous emission added by EDFAs can degrade the FOPA performance considerably. In practice, an optical filter is used to block such noise. Another source of noise is spontaneous Raman scattering that occurs whenever the signal or idler falls within the Raman-gain bandwidth [84]. In spite of these factors, noise figures of 4.2 dB for an FOPA with 27.2-dB gain [81] and of 3.7 dB with a 17-dB gain [82] were realized in two 2002 experiments. Such noise levels are close to the fundamental quantum limit of 3 dB for an ideal amplifier.

Another factor that affects FOPAs is the onset of stimulated Brillouin scattering (SBS). As was seen in Section 9.2.2, the SBS threshold is around 5 mW for long fibers ( $> 10$  km) and increases to near 50 mW for fiber lengths of 1 km or so. Since FOPAs require pump power levels approaching 1 W, a suitable technique is needed that raises the threshold of SBS and suppresses it over the FOPA length. The techniques used in practice (1) control the temperature distribution along the fiber length [76] or (2) modulate the pump phase either at several fixed frequencies [73], or over a broad frequency range using a pseudorandom bit pattern [83]. The pump-phase modulation technique suppresses SBS by broadening the pump spectrum. In practice, the FOPA gain is affected to some extent when pump phase is modulated because the phase-mismatch parameter  $\kappa$  depends on the phase of the pump [87]. Moreover, dispersive effects within the fiber convert pump-phase modulation into amplitude modulation of the pump. As a result, the SNR of both the signal and the idler is reduced because of undesirable power fluctuations [88]. Pump-phase modulation also leads to the broadening of the idler spectrum, making it twice as broad as the pump spectrum. Such broadening of the idler is of concern when FOPAs are used as wavelength converters. As seen later, it can be avoided in dual-pump FOPAs.

An important issue associated with single-pump FOPAs is that their gain spectrum is far from being uniform over its entire bandwidth (see Figure 10.12). The reason is that it is hard to maintain the phase-matching condition over a wide bandwidth in a single-pump FOPA. Since the linear contribution  $\Delta k \rightarrow 0$  when signal wavelength approaches the pump wavelength,  $\kappa \approx 2\gamma P_0$  in the pump vicinity. This value of  $\kappa$  is quite large and results in only a linear growth of the signal ( $G = 1 + \gamma P_0 L$ ). As a result, the gain spectrum exhibits a dip in the vicinity of the pump wavelength. Although amplification over a range as wide as 200 nm is possible [71], the gain spectrum remains highly nonuniform, and the usable bandwidth is limited to a much smaller region of the gain spectrum. This problem can be solved to some extent by manipulating fiber dispersion [72]. Theoretically, a fairly flat gain spectrum is possible by using several fiber sections of suitable lengths and properly selecting dispersive properties of these fiber sections [89]. However, such a scheme is difficult

to implement in practice because dispersive properties of fibers are rarely known with sufficient precision. A practical solution is to make use of the dual-pump configuration discussed next.

#### 10.4.4 Dual-Pump Configuration

Dual-pump FOPAs use the nondegenerate FWM process and employ two pumps at different wavelengths [90–95]. With a proper choice of the pump wavelengths, they can provide a relatively uniform gain over a wider bandwidth than that is possible with a single pump. The parametric gain in the dual-pump case is given by Eq. (10.2.19). Using  $r$  from Eq. (10.2.20), it can be written as

$$g(\omega_3) = [4\gamma^2 P_1 P_2 - \kappa^2(\omega_3)/4]^{1/2}, \quad (10.4.14)$$

where  $\kappa = \Delta k + \gamma(P_1 + P_2)$  and  $P_1$  and  $P_2$  are the input pump powers, assumed to remain undepleted. The amplification factor is related to  $g$  as indicated in Eq. (10.4.7) and is given by

$$G_s = P_3(L)/P_3(0) = 1 + (2\gamma/g)^2 P_1 P_2 \sinh^2(gL). \quad (10.4.15)$$

Similar to the single-pump case, the gain spectrum is affected by the frequency dependence of the linear phase mismatch  $\Delta k$ . If we introduce  $\omega_c = (\omega_1 + \omega_2)/2$  together with  $\omega_d = (\omega_1 - \omega_2)/2$ , and expand  $\Delta k$  around  $\omega_c$ , we obtain [92]:

$$\Delta k(\omega_3) = 2 \sum_{m=1}^{\infty} \frac{\beta_{2m}^c}{(2m)!} \left[ (\omega_3 - \omega_c)^{2m} - \omega_d^{2m} \right], \quad (10.4.16)$$

where the superscript  $c$  indicates that dispersion parameters are evaluated at the frequency  $\omega_c$ . This equation differs from Eq. (10.4.12) by the  $\omega_d$  term, which contributes only when two pumps are used. The main advantage of dual-pump FOPAs over single-pump FOPAs is that the  $\omega_d$  term can be used to control the phase mismatch. By properly choosing the pump wavelengths, it is possible to use this term for compensating the nonlinear phase mismatch  $\gamma(P_1 + P_2)$  such that the total phase mismatch  $\kappa$  is maintained close to zero over a wide spectral range.

The most commonly used configuration for dual-pump FOPAs employs a relatively large wavelength difference between the two pumps. At the same time, the center frequency  $\omega_c$  is set close to the zero-dispersion frequency  $\omega_0$  of the fiber so that the linear phase mismatch in Eq. (10.4.16) is constant over a broad range of  $\omega_3$ . To achieve a fairly wide phase-matching range, the two pump wavelengths should be located on the opposite sides of the zero-dispersion wavelength in a symmetrical fashion [93]. With this arrangement,  $\kappa$  can be reduced to nearly zero over a wide wavelength range, resulting in a gain spectrum that is nearly flat over this entire range.

The preceding discussion assumes that only the nondegenerate FWM process,  $\omega_1 + \omega_2 \rightarrow \omega_3 + \omega_4$ , contributes to the parametric gain. In reality, the situation is much more complicated for dual-pump FOPAs because the degenerate FWM process associated with each pump occurs simultaneously. In fact, it turns out that the

combination of degenerate and nondegenerate FWM processes can create up to eight other idler fields, in addition to the one at the frequency  $\omega_4$ . Only four among these idlers, say, at frequencies  $\omega_5$ ,  $\omega_6$ ,  $\omega_7$ , and  $\omega_8$ , are important for describing the gain spectrum of a dual-pump FOPA. These four idlers are generated through the following FWM processes:

$$\omega_1 + \omega_1 \rightarrow \omega_3 + \omega_5, \quad \omega_2 + \omega_2 \rightarrow \omega_3 + \omega_6, \quad (10.4.17)$$

$$\omega_1 + \omega_3 \rightarrow \omega_2 + \omega_7, \quad \omega_2 + \omega_3 \rightarrow \omega_1 + \omega_8. \quad (10.4.18)$$

The last two FWM processes are due to Bragg scattering [93] from a dynamic index grating created by beating of the signal with one of the pumps. They have attracted attention because they can transfer signal power to an idler wave, whose wavelength can be far from the signal, without adding additional noise [96–98]. In addition to the preceding processes, the energy conservation required for FWM is also satisfied by several other combinations of the eight frequencies involved.

A complete description of dual-pump FOPAs becomes quite complicated [93] if one were to include all underlying FWM processes. Fortunately, the phase-matching conditions associated with these processes are quite different. When the two pumps are located symmetrically far from the zero-dispersion wavelength of the fiber, the FWM processes indicated in Eqs (10.4.17) and (10.4.18) can only occur when the signal is in the vicinity of one of the pumps. For this reason, they leave unaffected the central flat part of the FOPA gain spectrum resulting from the process  $\omega_1 + \omega_2 \rightarrow \omega_3 + \omega_4$ . Figure 10.14 compares the FOPA gain spectrum

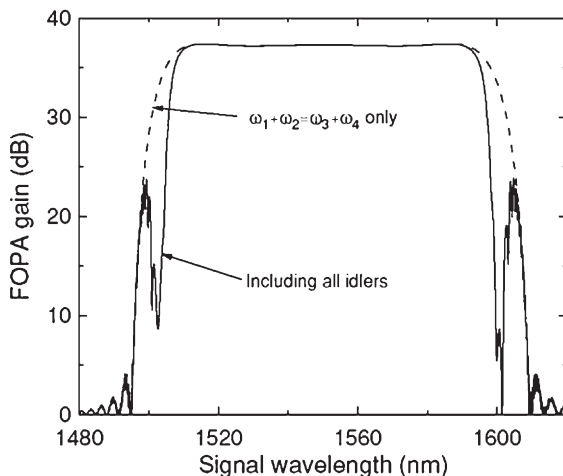


**Figure 10.14** Gain spectrum of a dual-pump FOPA when all five idlers are included (solid curve). The dashed spectrum is obtained when only a single idler, generated through the dominant nondegenerate FWM process, is included in the model.

calculated numerically using all five idlers (solid curve) with that obtained using this sole nondegenerate FWM process. Other FWM processes only affect the edges of gain spectrum and reduce the gain bandwidth by 10–20%. The FOPA parameters used in this calculation were  $L = 0.5$  km,  $\gamma = 10 \text{ W}^{-1}/\text{km}$ ,  $P_1 = P_2 = 0.5$  W,  $\beta_{30} = 0.1 \text{ ps}^3/\text{km}$ ,  $\beta_{40} = 10^{-4} \text{ ps}^4/\text{km}$ ,  $\lambda_1 = 1502.6$  nm,  $\lambda_2 = 1600.6$  nm, and  $\lambda_0 = 1550$  nm.

Dual-pump FOPAs provide several degrees of freedom that make it possible to realize a flat gain spectrum using just a single piece of fiber. A 2002 experiment employed a 2.5-km-long highly nonlinear fiber having its zero-dispersion wavelength at 1585 nm with  $\gamma = 10 \text{ W}^{-1}/\text{km}$  [95]. It also used two pumps with their wavelengths at 1569 and 1599.8 nm. Such a FOPA exhibited a gain of 20 dB over 20-nm bandwidth when pump powers were 220 and 107 mW at these two wavelengths, respectively. The gain could be increased to 40 dB by increasing pump powers to 380 and 178 mW. It was necessary to launch more power at the shorter wavelength because of the Raman-induced power transfer between the two pumps within the same fiber used to amplify the signal through FWM. A bandwidth of close to 40 nm was realized for a dual-pump FOPA in a 2003 experiment [99]. Figure 10.15 shows the experimental data together with a theoretical fit. In this experiment, two pumps were launched with powers of 600 mW at 1559 nm and 200 mW at 1610 nm. The 1-km-long highly nonlinear fiber had its zero-dispersion wavelength at 1583.5 nm with  $\beta_{30} = 0.055 \text{ ps}^3/\text{km}$ ,  $\beta_{40} = 2.35 \times 10^{-4} \text{ ps}^4/\text{km}$ , and  $\gamma = 17 \text{ W}^{-1}/\text{km}$ . The theoretical model included the effects of SRS to account for the Raman-induced power transfer among the pump, signal, and idler fields.

The dual-pump configuration offers several other advantages over the single-pump one, in addition to providing a relatively flat gain over a wide bandwidth. As the pump wavelengths are located at the two edges of the gain spectrum, pump blocking is not necessary when signal wavelength lies in the central flat portion of the gain

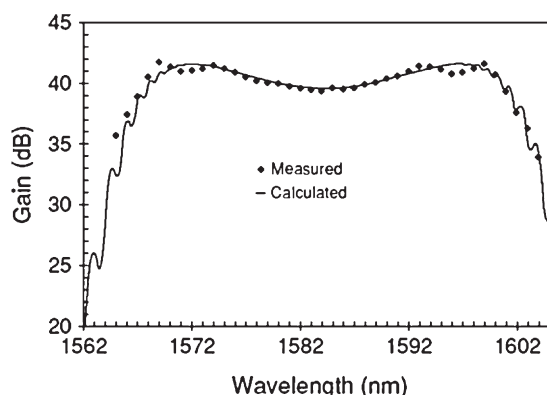


Figure 10.15 Measured (diamonds) and calculated (solid) gain spectra as a function of signal wavelength for a dual-pump FOPA. (After Ref. [99]; © 2003 IEE.)

spectrum. Also, the required power for each pump to realize a certain value of gain is reduced by 50% compared with the single-pump case when both pumps are launched with equal powers. In practice, the shorter-wavelength pump requires more power to offset the impact of Raman-induced power transfer between the two pumps, but its power still remains well below the level of single-pump FOPAs.

An additional advantage of dual-pump FOPAs is related to their use as wavelength converters. Although phase modulation of the pumps is still required to suppress SBS, spectral broadening of the idler is no longer a problem because the phases of two pumps can be manipulated such that a specific idler used for wavelength conversion is not broadened. For example, if the idler frequency  $\omega_4 \equiv \omega_1 + \omega_2 - \omega_3$  is used for wavelength conversion, the two pumps should be modulated out of phase so that the sum  $\phi_1(t) + \phi_2(t) = 0$  at all times [100]. In the case of binary phase modulation, the two bit streams differ in their phases by  $\pi$  to satisfy this condition [101]. In contrast, if the idler at the frequency  $\omega_7$  or  $\omega_8$  is used [see Eq. (10.4.18)], the two pumps should be modulated in phase [102].

Another advantage of the dual-pump configuration is that the state of polarization (SOP) of the two pumps can be controlled to mitigate the dependence of the parametric gain on the signal SOP. This problem affects all FOPAs because the FWM process itself is strongly polarization-dependent. In the case of single-pump FOPAs, a polarization-diversity loop is sometimes employed. In the case of dual-pump FOPAs, the problem can be solved simply by using orthogonally polarized pumps. The polarization effects are considered in more detail in Section 10.5.

Dual-pump FOPAs also suffer from several shortcomings. As already mentioned, wavelength difference between the two pumps often falls within the bandwidth of the Raman-gain spectrum. If the two pumps cannot maintain equal power levels along the fiber because of Raman-induced power transfer, the FWM efficiency is reduced, even though the total pump power remains constant. In practice, the power of the high-frequency pump is chosen to be larger than that of the low-frequency pump at the input end of the fiber. Although Raman-induced power transfer reduces the FOPA gain, it does not affect the shape of the gain spectrum because phase matching depends on the total power of the two pumps, which is conserved as long as the two pumps are not depleted significantly. As in single-pump FOPAs, modulation of pump phases, required for SBS suppression, reduces the signal SNR even for dual-pump FOPAs, if fiber dispersion converts phase modulation into amplitude modulation of the pump [88]. If the two pumps are amplified before launching them into the FOPA, noise added during their amplification also lowers the signal SNR [103].

A major limitation of all FOPAs results from the fact that a realistic fiber is far from having a perfect cylindrical core. In practice, the core shape and size may vary along the fiber length in a random fashion during the manufacturing process. Such imperfections produce random variations in the zero-dispersion wavelength of the fiber along its length. Since the phase-matching condition depends on this wavelength, and the parametric gain is extremely sensitive to dispersion parameters of the fiber, even small changes in the zero-dispersion wavelength ( $<0.1$  nm) produce large changes in the gain spectrum [104]. In general, the standard deviation  $\sigma_\lambda$  of such

fluctuations is a small fraction (<0.1%) of the mean value of  $\lambda_0$  (around 1550 nm). If the correlation length  $l_c$  of zero-dispersion wavelength fluctuations are much smaller than the fiber length used for FOPAs, the first- and second-order moments of  $\delta\lambda_0$  are given by

$$\langle \delta\lambda_0 \rangle = 0, \quad \langle \delta\lambda_0(z)\delta\lambda_0(z') \rangle = D_\lambda^2 \delta(z - z'), \quad (10.4.19)$$

where  $D_\lambda = \sigma_\lambda \sqrt{l_c}$ .

Equations (10.2.13) and (10.2.14) governing the growth of signal and idler fields along the fiber length remain valid in the presence of dispersion fluctuations, but the phase-mismatch parameter  $\kappa(z)$  appearing in these equations becomes a random function of  $z$ . It turns out that the average value of the FOPA gain,  $G_{av} = \langle P_3(L) \rangle / P_3(0)$  can be found analytically [105]. However, the resulting spectrum does not correspond to the spectrum expected for a specific FOPA as it represents an ensemble average. In practice, the gain spectrum will vary over a wide range for an ensemble of FOPAs that are identical in all respects except for uncontrollable dispersion fluctuations. Figure 10.16a shows the individual gain spectra obtained numerically for 100 realizations by solving the stochastic Eqs (10.2.13) and (10.2.14). The FOPA parameters are identical to those used for Figure 10.14. Dispersion fluctuations are included by treating  $\delta\lambda_0$  as a Gaussian random variable that satisfies Eq. (10.4.19) with  $\sigma_\lambda = 1$  nm and  $l_c = 5$  m. Clearly, amplified signal can fluctuate over a wide range for different members of the ensemble even when the RMS value  $\sigma_\lambda$  of fluctuations is only 1 nm.

The important question is how one can design FOPAs that can tolerate zero-dispersion wavelength variations  $\sim 1$  nm. The answer turns out to be that the wavelength separation between the two pumps should be reduced to 50 nm or less.

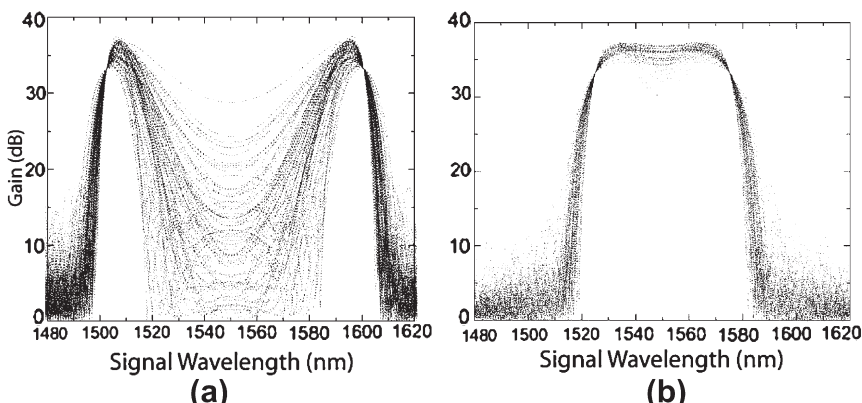


**Figure 10.16** Numerically simulated gain spectra for a dual-pump FOPA for 100 different realizations of dispersion fluctuations along the fiber ( $\sigma_\lambda = 1$  nm and  $l_c = 5$  m) when pump spacing is (a) 98 nm or (b) 50 nm. (After Ref. [105]; © 2004 IEEE.)

Of course, the whole gain spectrum is then narrower, and the FOPA bandwidth is significantly reduced. However, this reduced-bandwidth gain spectrum is much more tolerant of dispersion fluctuations. This is evident in [Figure 10.16b](#) obtained under identical conditions except that the pump wavelengths of 1525.12 and 1575.12 nm are separated by 50 nm rather than 98 nm. Of course, the value of optimum pump separation depends on the level of fluctuations and is reduced further if  $\sigma_\lambda$  is  $> 1$  nm. The important point to note is that zero-dispersion wavelength fluctuations limit the usable bandwidth of a FOPA in practice.

#### 10.4.5 Effects of Pump Depletion

So far, the pumps are assumed to remain undepleted. The inclusion of pump depletion requires a numerical solution [106] of Eqs (10.2.1–10.2.4); an analytic solution in terms of the elliptic functions is also possible under specific conditions [27]. It turns out that the power may even be transferred back to the pumps when phase matching is not perfect. Whether the signal and idler waves are amplified or attenuated depends on the relative phase  $\theta$  defined as

$$\theta = \phi_1 + \phi_2 - \phi_3 - \phi_4, \quad (10.4.20)$$

where  $\phi_j$  is the phase of the amplitude  $A_j$  for  $j = 1\text{--}4$ .

We can use Eqs (10.2.13) and (10.2.14) to find an equation for  $\theta$ . Using  $B_j = \sqrt{P_j} e^{j\phi_j}$ , we obtain the following two equations:

$$\frac{dP_3}{dz} = \frac{dP_4}{dz} = -4\gamma\sqrt{P_1 P_2 P_3 P_4} \sin \theta, \quad (10.4.21)$$

$$\frac{d\theta}{dz} = \kappa + 2\gamma\sqrt{P_1 P_2} \frac{(P_3 + P_4)}{\sqrt{P_3 P_4}} \cos \theta. \quad (10.4.22)$$

Equation (10.4.21) shows clearly that the growth of the signal and idler waves is determined by the angle  $\theta$ . Maximum amplification occurs for  $\theta = -\pi/2$ . If an idler wave is not launched at the input end, the idler grows from noise and its phase is set such that the requirement  $\theta = -\pi/2$  is satisfied automatically near the front end of a FOPA. If  $\kappa = 0$  initially (perfect phase matching), Eq. (10.4.22) shows that  $\theta$  will remain frozen at its initial value of  $-\pi/2$ . However, if  $\kappa \neq 0$ ,  $\theta$  will change along the fiber as dictated by Eq. (10.4.22).

When pump powers do not remain constant because of pump depletion, the phase mismatch  $\kappa$  changes along the fiber length, even if  $\theta = -\pi/2$  at the input end. As soon as  $\theta$  becomes positive and lies in the range 0 to  $\pi/2$ , both the signal and idler waves experience deamplification, as evident from Eq. (10.4.21). This behavior is shown in [Figure 10.17](#) where the evolution of the relative phase  $\theta$ , the idler power  $P_4$ , and the pump power  $P_1$  is shown along the fiber for an input pump power of 70 W, after assuming  $\kappa = 0$ ,  $P_1 = P_2$ , and  $\theta = -\pi/2$  at the input end. Two cases are shown:  $P_3(0) = P_4(0) = 0.1 \mu\text{W}$  (solid lines) and  $P_3(0) = 6 \text{ mW}$  with  $P_4(0) = 0.1 \mu\text{W}$

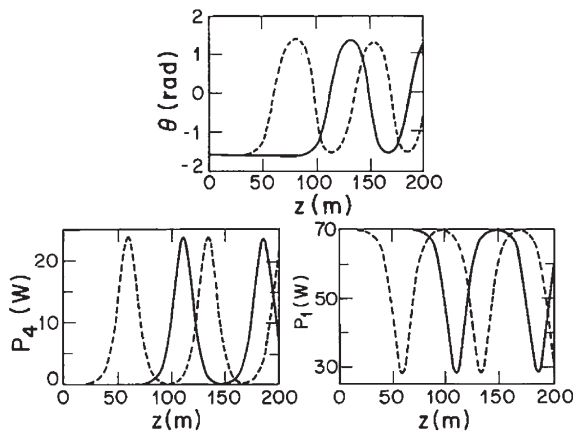


**Figure 10.17** Evolution of relative phase  $\theta$ , idler power  $P_4$ , and pump power  $P_1$  along the fiber length when  $\kappa=0$ ,  $P_1=P_2=70$  W,  $P_4=0.1$   $\mu$ W, and  $\theta=\pi/2$ . Input signal power  $P_3=0.1$   $\mu$ W for solid curves and 6 mW for dashed curves. (After Ref. [106]; © 1987 IEEE.)

(dashed lines). The second case corresponds to a parametric amplifier; both waves grow from noise in the former case. In both cases, the signal and idler waves amplify and deamplify periodically. This behavior can be understood by noting that pump depletion changes the relative phase  $\theta$  from its initial value of  $-\pi/2$ . The main point is that a parametric amplifier requires careful control of the fiber length even in the case of perfect phase matching.

The preceding discussion is based on the CW theory of FWM. In the case of short pump and signal pulses, two effects can reduce parametric interaction among the four waves participating in FWM. First, the pump spectrum is broadened through SPM as the pump propagates through the fiber. If the spectral width of the pump exceeds the amplifier bandwidth, the parametric gain would decrease, similar to the case of Brillouin gain discussed in Section 9.1. Second, the group-velocity mismatch among the four pulses forces them to separate from each other. Both of these effects reduce the effective length over which FWM can occur. If such walk-off effects are negligible together with the GVD effects, then the CW theory can be extended to the pulsed case, and an analytic solution can be obtained in terms of the elliptic functions [107]. The results show that, even in the case of CW pumps, the signal pulse is distorted during its amplification, and the idler pulse is far from being a phase conjugate of the input signal.

## 10.5 POLARIZATION EFFECTS

The scalar theory of Section 10.2 is based on the assumption that all optical fields are linearly polarized initially and maintain their SOP during propagation inside the fiber. In practice, the SOP of the input pumps can be chosen, but the SOP of the input

signal is often arbitrary. The FWM process is highly polarization-dependent because it requires conservation of angular momenta among the four interacting photons. As a result, the gain spectrum of a FOPA depends on the relative SOPs of the input signal and pumps and can change over a wide range depending on them. This section focuses on such polarization effects.

It was shown as early as 1993 that the polarization-independent operation of single-pump FOPAs can be realized by employing a polarization-diversity loop, but the focus was on wavelength conversion [108]. This technique was used in a 2002 experiment to construct an FOPA whose gain was independent of the signal SOP to within 1 dB [109]. In this scheme, the input pump beam is split by a polarizing beam splitter into its orthogonally polarized components such that they have equal powers and counterpropagate inside the loop containing the nonlinear fiber. The signal is also split by this beam splitter into its orthogonally polarized components. Each of these components is amplified inside the loop by the copolarized pump component. The two components of the amplified signal are then recombined by the same polarizing beam splitter after one round trip.

The dual-pump configuration of an FOPA provides an additional degree of freedom that can be used to realize polarization-independent operation without a polarization-diversity loop [46]. It was shown in 1993 that, if the two pumps are launched with linear but orthogonal SOPs, the FWM process can be made nearly independent of the signal SOP [90]. This configuration is often used for dual-pump FOPAs, even though its use reduces the signal and idler gains by a large factor because of a reduced FWM efficiency. One may ask if the efficiency of the underlying FWM process can be improved by choosing pump SOPs such that they are orthogonal but not linear [110]. To answer this question, it is necessary to develop a vector theory of FWM in which the input SOPs of the two pumps and that of the signal are arbitrary [111].

### 10.5.1 Vector Theory of Four-Wave Mixing

A complete description of dual-pump FOPAs should include degenerate as well as nondegenerate FWM processes. However, as discussed earlier, when two pumps are located symmetrically around but relatively far from the zero-dispersion wavelength of the fiber, the FOPA gain spectrum exhibits a central flat region having its origin in the single nondegenerate FWM process ( $\omega_1 + \omega_2 \rightarrow \omega_3 + \omega_4$ ). As the flat portion of the gain spectrum is used in practice, we may focus only on this nondegenerate process in the following analysis. As before, we neglect pump depletion assuming that pump powers are much larger than the signal and idler powers.

In general, one should consider the general form of the nonlinear polarization given in Eq. (8.5.1) so that the Raman contribution is properly included. To simplify the following discussion, we ignore the Raman effects and assume that the nonlinear polarization is given by Eq. (10.1.1). The tensor  $\chi^{(3)}$  in this equation has the form of Eq. (6.1.2) and can be written as

$$\chi_{ijkl}^{(3)} = \frac{1}{3} \chi_{xxx}^{(3)} (\delta_{ij}\delta_{kl} + \delta_{ik}\delta_{jl} + \delta_{il}\delta_{jk}). \quad (10.5.1)$$

In the case of nondegenerate FWM, the total electric field and the nonlinear polarization can be decomposed as

$$\mathbf{E} = \operatorname{Re} \left[ \sum_{j=1}^4 \mathbf{E}_j \exp(-i\omega_j t) \right], \quad \mathbf{P}_{\text{NL}} = \operatorname{Re} \left[ \sum_{j=1}^4 \mathbf{P}_j \exp(-i\omega_j t) \right], \quad (10.5.2)$$

where  $\mathbf{E}_j$  is the slowly varying amplitude at the frequency  $\omega_j$ .

We now follow the procedure outlined in Section 8.5.1 and substitute Eq. (10.5.2) in Eq. (10.1.1). Collecting the terms oscillating at  $\omega_1$  and  $\omega_2$ , the nonlinear polarization at the pump frequencies is found to be

$$\begin{aligned} \mathbf{P}_j(\omega_j) = & \frac{\epsilon_0}{4} \chi_{xxxx}^{(3)} \left[ (\mathbf{E}_j \cdot \mathbf{E}_j) \mathbf{E}_j^* + 2(\mathbf{E}_j^* \cdot \mathbf{E}_j) \mathbf{E}_j + 2(\mathbf{E}_m \cdot \mathbf{E}_m) \mathbf{E}_j \right. \\ & \left. + 2(\mathbf{E}_m \cdot \mathbf{E}_j) \mathbf{E}_m^* + 2(\mathbf{E}_m^* \cdot \mathbf{E}_j) \mathbf{E}_m \right], \end{aligned} \quad (10.5.3)$$

where  $j, m = 1$  or  $2$  with  $j \neq m$ . Using the same process, the nonlinear polarization at the signal and idler frequencies is found to be

$$\begin{aligned} \mathbf{P}_j(\omega_j) = & \frac{\epsilon_0}{2} \chi_{xxxx}^{(3)} \left[ (\mathbf{E}_1^* \cdot \mathbf{E}_1) \mathbf{E}_j + (\mathbf{E}_1 \cdot \mathbf{E}_j) \mathbf{E}_1^* + (\mathbf{E}_1^* \cdot \mathbf{E}_j) \mathbf{E}_1 \right. \\ & + (\mathbf{E}_2^* \cdot \mathbf{E}_2) \mathbf{E}_j + (\mathbf{E}_2 \cdot \mathbf{E}_j) \mathbf{E}_2^* + (\mathbf{E}_2^* \cdot \mathbf{E}_j) \mathbf{E}_2 \\ & \left. + (\mathbf{E}_m^* \cdot \mathbf{E}_1) \mathbf{E}_2 + (\mathbf{E}_m^* \cdot \mathbf{E}_2) \mathbf{E}_1 + (\mathbf{E}_1 \cdot \mathbf{E}_2) \mathbf{E}_m^* \right], \end{aligned} \quad (10.5.4)$$

where  $j, m = 3$  or  $4$  with  $j \neq m$ . In Eqs (10.5.3) and (10.5.4), the SPM and XPM effects induced by the two pumps are included but those induced by the signal and idler waves are neglected because of their relatively low power levels.

To account for the polarization changes, we represent each field in terms of its Jones vector  $|A_j(z)\rangle$  and use

$$\mathbf{E}_j(\mathbf{r}) = F_j(x, y) |A_j(z)\rangle \exp(i\beta_j z), \quad (10.5.5)$$

where  $F_j(x, y)$  represents the fiber-mode profile and  $\beta_j$  is the propagation constant for the field at frequency  $\omega_j$ . As in Section 10.2.1, we assume that mode profiles are nearly the same for the four fields. This approximation amounts to using the same effective mode area for the four waves.

Using Eqs (10.5.3–10.5.5) in the wave equation (2.3.1) and following the procedure of Section 2.3.1, the Jones vectors of the four fields are found to satisfy the following set of four equations [111]:

$$\frac{d|A_1\rangle}{dz} = \frac{2iy}{3} \left( \langle A_1|A_1\rangle + \langle A_2|A_2\rangle + \frac{1}{2} |A_1^*\rangle\langle A_1^*| + |A_2\rangle\langle A_2| + |A_2^*\rangle\langle A_2^*| \right) |A_1\rangle, \quad (10.5.6)$$

$$\frac{d|A_2\rangle}{dz} = \frac{2iy}{3} \left( \langle A_1|A_1\rangle + \langle A_2|A_2\rangle + \frac{1}{2} |A_2^*\rangle\langle A_2^*| + |A_1\rangle\langle A_1| + |A_1^*\rangle\langle A_1^*| \right) |A_2\rangle, \quad (10.5.7)$$

$$\begin{aligned}\frac{d|A_3\rangle}{dz} = & \frac{2i\gamma}{3} (\langle A_1|A_1\rangle + |A_1\rangle\langle A_1| + |A_1^*\rangle\langle A_1^*| \\ & + \langle A_2|A_2\rangle + |A_2\rangle\langle A_2| + |A_2^*\rangle\langle A_2^*|) |A_3\rangle \\ & + \frac{2i\gamma}{3} (|A_2\rangle\langle A_1^*| + |A_1\rangle\langle A_2^*| + \langle A_1^*|A_2\rangle) |A_4^*\rangle e^{-i\Delta kz},\end{aligned}\quad (10.5.8)$$

$$\begin{aligned}\frac{d|A_4\rangle}{dz} = & \frac{2i\gamma}{3} (\langle A_1|A_1\rangle + |A_1\rangle\langle A_1| + |A_1^*\rangle\langle A_1^*| \\ & + \langle A_2|A_2\rangle + |A_2\rangle\langle A_2| + |A_2^*\rangle\langle A_2^*|) |A_4\rangle \\ & + \frac{2i\gamma}{3} (|A_2\rangle\langle A_1^*| + |A_1\rangle\langle A_2^*| + \langle A_1^*|A_2\rangle) |A_3^*\rangle e^{-i\Delta kz}.\end{aligned}\quad (10.5.9)$$

In the case of a single-pump configuration, only the first pump equation should be retained because  $|A_2\rangle = 0$ . Also, one should replace  $|A_2\rangle$  with  $|A_1\rangle$  and  $2\gamma$  with  $\gamma$  in the signal and idler equations.

### 10.5.2 Polarization Dependence of Parametric Gain

The vector FWM equations, Eqs (10.5.6–10.5.9), describe FWM in the general case in which the two pumps and the signal are launched into an optical fiber with arbitrary SOPs. Their complexity requires a numerical approach in general. To investigate the relationship between the FWM efficiency and pump SOPs, we ignore the SPM and XPM terms temporarily and focus on the selection rules that govern the creation of idler photons. The SPM and XPM terms affect only the phase-matching condition and their impact is considered later in this section.

Physically, the polarization dependence of FWM stems from the requirement of angular momentum conservation among the four interacting photons in an isotropic medium. This requirement can be described most simply in a basis in which  $\uparrow$  and  $\downarrow$  denote the left and right circular polarization states and represent photons with an intrinsic angular momentum (spin) of  $+\hbar$  and  $-\hbar$ , respectively [112]. To describe FWM among arbitrarily polarized optical fields, we decompose the Jones vector of each field as

$$|A_j\rangle = \mathcal{U}_j|\uparrow\rangle + \mathcal{D}_j|\downarrow\rangle,\quad (10.5.10)$$

where  $\mathcal{U}_j$  and  $\mathcal{D}_j$  represent the field amplitudes in the spin-up and spin-down states, respectively, for the  $j$ th wave ( $j=1-4$ ). Using this expansion, it follows from Eq. (10.5.9) that the creation of idler photons in the two orthogonal states is governed by the following two equations (assuming perfect phase matching):

$$\frac{d\mathcal{U}_4}{dz} = \frac{4i\gamma}{3} [\mathcal{U}_1\mathcal{U}_2\mathcal{U}_3^* + (\mathcal{U}_1\mathcal{D}_2 + \mathcal{D}_1\mathcal{U}_2)\mathcal{D}_3^*],\quad (10.5.11)$$

$$\frac{d\mathcal{D}_4}{dz} = \frac{4i\gamma}{3} [\mathcal{D}_1\mathcal{D}_2\mathcal{D}_3^* + (\mathcal{U}_1\mathcal{D}_2 + \mathcal{D}_1\mathcal{U}_2)\mathcal{U}_3^*].\quad (10.5.12)$$

The same equations hold for the creation of signal photons if we exchange the subscripts 3 and 4.

The three terms on the right side of Eqs (10.5.11) and (10.5.12) show how different combinations of pump and signal photons produce idler photons and lead to the following selection rules for the FWM process. The first term in these equations corresponds to the case in which both pumps and the signal are copolarized and produce the idler with the same SOP. Physically, if both pump photons are in the  $\uparrow$  state with a total angular momentum of  $2\hbar$ , the signal and idler photons must also be in the same state to conserve the angular momentum. The last two terms in Eq. (10.5.11) correspond to the case in which two pump photons are orthogonally polarized such that their total angular momentum is zero. To conserve this value, the signal and idlers must also be orthogonally polarized. As a result, a signal photon in the state  $\uparrow_3$  can only couple to an idler photon with state  $\downarrow_4$  (and vice versa). This leads to two possible combinations,  $\uparrow_3 + \downarrow_4$  and  $\downarrow_3 + \uparrow_4$ , both of which are equally probable.

A pump with an arbitrary SOP consists of photons in both the  $\uparrow$  and  $\downarrow$  states with different amplitudes and phases. All six terms in Eqs (10.5.11) and (10.5.12) contribute to FWM in this case. The polarization dependence of signal gain is a consequence of the fact that FWM can occur through different paths, and one must add probability amplitudes of these paths, as dictated by quantum mechanics. Such an addition can lead to constructive or destructive interference. For example, if the two pumps are right-circularly polarized, no FWM can occur for a signal that is left-circularly polarized (and vice versa).

In the case of single-pump configuration, the two pump photons have the same SOP as they are indistinguishable. If the pump is circularly polarized, it follows from Eqs (10.5.11) and (10.5.12) that only the first term can produce idler photons. In the case of a linearly polarized pump, all terms can produce idler photons as long as the selection rules are satisfied. However, it is easy to conclude that the signal gain for a single-pump FOPA is always polarization-dependent. Physically speaking, it is impossible to balance the FWM efficiency experienced by the  $\uparrow$  and  $\downarrow$  components of the signal, unless a polarization-diversity loop is employed.

Often, one is interested in a FOPA configuration that yields the same signal gain, irrespective of the SOP of the input signal. Equations (10.5.11) and (10.5.12) show that this situation can be realized by two orthogonally polarized pumps. More specifically, if the two pumps are right- and left-circularly polarized, the terms containing  $\mathcal{U}_1\mathcal{U}_2$  and  $\mathcal{D}_1\mathcal{D}_2$  vanish, and the FWM process becomes polarization-independent. If the two pumps are linearly polarized with orthogonal SOPs, it turns out that  $\mathcal{U}_1\mathcal{D}_2 + \mathcal{D}_1\mathcal{U}_2 = 0$ . The remaining two paths have the same efficiency, making the FWM process polarization-independent. However, the gain is reduced considerably for this configuration, a feature we discuss next.

To study how the parametric gain depends on pump SOPs, we solve Eqs (10.5.6–10.5.9) for two pumps that are elliptically polarized with orthogonal SOPs. Noting that these equations are invariant under rotations in the  $x$ - $y$  plane,

we choose the  $x$  and  $y$  axes along the principal axes of the SOP ellipse associated with the pump at frequency  $\omega_1$ . If we ignore the SPM and XPM terms in Eqs (10.5.6) and (10.5.7), the Jones vectors of the two pumps do not change with propagation, and

$$|A_1(z)\rangle = \sqrt{P_1} \begin{pmatrix} \cos \theta \\ i \sin \theta \end{pmatrix}, \quad |A_2(z)\rangle = \sqrt{P_2} \begin{pmatrix} i \sin \theta \\ \cos \theta \end{pmatrix}, \quad (10.5.13)$$

where  $P_1$  and  $P_2$  are the input powers and  $\theta$  is the angle characterizing the ellipticity.

Using Eq. (10.5.13) in Eqs (10.5.8) and (10.5.9), and still ignoring the SPM and XPM terms, the signal and idler are found to evolve as

$$\frac{d|A_3\rangle}{dz} = \frac{2i\gamma}{3} \sqrt{P_1 P_2} e^{-i\Delta kz} (\cos 2\theta \sigma_2 + 2i \sin 2\theta \sigma_0) |A_4^*\rangle, \quad (10.5.14)$$

$$\frac{d|A_4\rangle}{dz} = \frac{2i\gamma}{3} \sqrt{P_1 P_2} e^{-i\Delta kz} (\cos 2\theta \sigma_2 + 2i \sin 2\theta \sigma_0) |A_3^*\rangle, \quad (10.5.15)$$

where  $\sigma_0$  is a unit matrix and the Pauli matrix  $\sigma_2$  is defined in Eq. (6.6.8). These equations show that the FWM process depends on the pump ellipticity  $\theta$ .

In spite of their vector nature, Eqs (10.5.14) and (10.5.15) can be solved by diagonalizing the constant matrix  $\cos 2\theta \sigma_2 + 2i \sin 2\theta \sigma_0$  and provide the following expression for the signal field when  $A_4(0) = 0$  initially:

$$|A_3(z)\rangle = |A_3(0)\rangle [\cosh(gz) + i(\Delta k/2g) \sinh(gz)] \exp(iK_e z), \quad (10.5.16)$$

where  $K_e$  is related to  $\Delta k$  and the parametric gain  $g$  is given by

$$g(\theta) = [(2\gamma/3)^2 P_1 P_2 (1 + 3 \sin^2 2\theta) - (\Delta k/2)^2]^{1/2}. \quad (10.5.17)$$

This equation should be compared with Eq. (10.2.19), where  $g$  is given for the case in which two pumps are copolarized linearly.

An important conclusion can be drawn from Eq. (10.5.16). Because the signal is amplified by the same factor for any SOP in the absence of the SPM and XPM effects, the nondegenerate FWM process is polarization independent for any two orthogonally polarized pumps. However, the FWM efficiency depends on the exact state of pump polarizations through the  $\theta$  dependence of the parametric gain in Eq. (10.5.17). Figure 10.18 shows the  $\theta$  dependence of  $g(\theta)$ , after normalizing it with  $g_m = 4\gamma\sqrt{P_1 P_2}/3$ , for two values of phase mismatch. The parametric gain is maximum for  $\theta = 45^\circ$  (circularly polarized pumps), but becomes minimum when  $\theta = 0^\circ$ , a value that corresponds to linearly polarized pumps. This behavior can be understood from Eq. (10.5.8) by noting that the overall FWM efficiency is dictated by the last term containing  $\langle A_1^* | A_2 \rangle$ . This quantity is at its maximum when the pumps are circularly polarized but vanishes when they are linearly polarized.

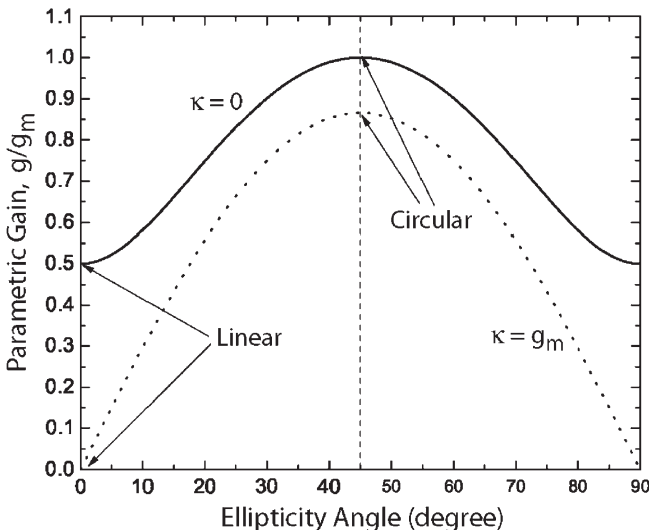


**Figure 10.18** Parametric gain as a function of the ellipticity angle for  $\kappa=0$  (solid curve) and  $\kappa \neq 0$  (dashed curve) when the two pumps are elliptically polarized with orthogonal SOPs.

### 10.5.3 Linearly and Circularly Polarized Pumps

In this subsection we include the SPM and XPM effects induced by the two pumps. The situation changes considerably because both SPM and XPM can change the SOP of an optical field, if they produce phase shifts that are different for the two components of the Jones vector, a phenomenon known as *nonlinear polarization rotation*. In particular, they can make the pump SOPs nonorthogonal even if they were orthogonal initially at  $z = 0$ .

To study such polarization changes, it is useful to write Eqs (10.5.6) and (10.5.7) in the Stokes space after introducing the Stokes vectors of the two pumps as

$$\mathbf{S}_1 = \langle A_1 | \boldsymbol{\sigma} | A_1 \rangle, \quad \mathbf{S}_2 = \langle A_2 | \boldsymbol{\sigma} | A_2 \rangle, \quad (10.5.18)$$

where  $\boldsymbol{\sigma} = \sigma_1 \hat{e}_1 + \sigma_2 \hat{e}_2 + \sigma_3 \hat{e}_3$  is the Pauli spin vector in the Stoke space. Recall that a Stokes vector moves on the surface of the Poincaré sphere; it lies in the equatorial plane for linearly polarized light and points toward a pole for circularly polarized light. In the convention adopted here, the north pole corresponds to left-circular polarization. Recall also that orthogonally polarized pumps are represented by two Stokes vectors that point in opposite directions on the Poincaré sphere.

By differentiating  $\mathbf{S}_1$  and  $\mathbf{S}_2$  and using Eqs (10.5.6) and (10.5.7), one can show that the Stokes vectors for the two pumps satisfy

$$\frac{d\mathbf{S}_1}{dz} = \frac{2\gamma}{3} [(S_{13} + 2S_{23})\hat{e}_3 - 2\mathbf{S}_2] \times \mathbf{S}_1, \quad (10.5.19)$$

$$\frac{d\mathbf{S}_2}{dz} = \frac{2\gamma}{3} [(S_{23} + 2S_{13})\hat{\mathbf{e}}_3 - 2\mathbf{S}_1] \times \mathbf{S}_2, \quad (10.5.20)$$

where  $S_{j3}$  is the third component of  $\mathbf{S}_j$  (along the  $\hat{\mathbf{e}}_3$  direction). This equation shows that the SPM rotates the Stokes vector along the vertical direction. In contrast, the two XPM terms combine such that the XPM rotates the Stokes vector along a vector that lies in the equatorial plane. Equations (10.5.19) and (10.5.20) can be solved numerically to study how the pump SOPs change with propagation inside the fiber [111]. The results show that the two pumps launched with orthogonal SOPs maintain their initial orthogonality only when they are linearly or circularly polarized at  $z = 0$ . This can also be inferred from Eqs (10.5.19) and (10.5.20) directly. When the pumps are linearly polarized,  $S_{13} = S_{23} = 0$ ; when they are circularly polarized,  $\hat{\mathbf{e}}_3 \times \mathbf{S}_j = 0$ . In both cases, the derivative  $d\mathbf{S}_j/dz$  vanishes for  $j = 1$  and 2, ensuring that the pumps remain orthogonally polarized.

We use the same technique to see how the Stokes vector of the signal and idler are affected by the XPM induced by the two pumps. It turns out that, if the two pumps remain orthogonally polarized along the fiber, the SOPs of the signal and idler are not affected by them. In physical terms, even though each pump rotates the signal's Stokes vector on the Poincaré sphere, rotations induced by two equal-power pumps cancel each other when pumps are orthogonally polarized. Thus, only the linear and circular SOPs for the orthogonally polarized pumps can provide polarization-independent gain. In these two specific pumping configurations, the vector problem reduces to a scalar problem and can be solved analytically.

The analytic solution of the signal and idler equations, obtained by solving Eqs (10.5.8) and (10.5.9), provides the following expressions for the signal gain:

$$G_s \equiv \frac{\langle A_3(L)|A_3(L) \rangle}{\langle A_3(0)|A_3(0) \rangle} = 1 + \left(1 + \frac{\kappa^2}{4g^2}\right) \sinh^2(gL), \quad (10.5.21)$$

where  $\kappa$  and  $g$  are defined as

$$\kappa = \Delta k + r_\kappa \gamma (P_1 + P_2), \quad g = [(r_g \gamma)^2 P_1 P_2 - (\kappa/2)^2]^{1/2}. \quad (10.5.22)$$

The constants  $r_\kappa$  and  $r_g$  depend on whether the two pumps are linearly or circularly polarized. For linearly polarized pumps,  $r_\kappa = 1$  and  $r_g = 2/3$ . When the pumps are circularly polarized,  $r_\kappa = 2/3$  and  $r_g = 4/3$ .

Equation (10.5.21) should be compared with Eq. (10.4.5), obtained in the scalar case in which the two pumps are linearly copolarized and generate the signal and idler that are polarized linearly in the same direction. Effectively,  $r_\kappa = 1$  and  $r_g = 2$  in this case. When the signal is orthogonally polarized with respect to linearly copolarized pumps, one finds that  $r_\kappa = 5/3$  and  $r_g = 2/3$ . Such changes in  $r_\kappa$  and  $r_g$  for different pumping configurations indicate that FWM efficiency can change considerably depending on the SOPs of the pump at the input end.

Figure 10.19 shows the gain spectra for several pumping schemes by focusing on a 500-m-long dual-pump FOPA and using parameter values  $\gamma = 10 \text{ W}^{-1}/\text{km}$ ,

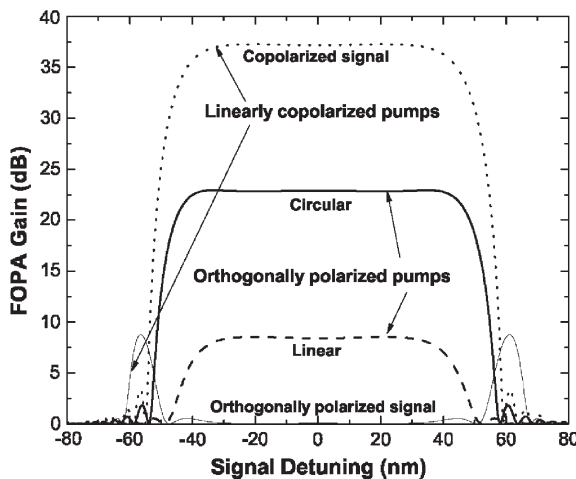


**Figure 10.19** Gain spectra for four different pumping schemes for a dual-pump FOPA pumped with 0.5 W at 1535 and 1628 nm. (After Ref. [111]; © 2004 OSA.)

$\lambda_0 = 1580$  nm,  $\beta_{30} = 0.04$  ps<sup>3</sup>/km, and  $\beta_{40} = 1.0 \times 10^{-4}$  ps<sup>4</sup>/km. The pump wavelengths (1535 and 1628 nm) and powers ( $P_1 = P_2 = 0.5$  W) are chosen such that the FOPA provides a fairly flat gain of 37 dB over a wide wavelength range when the two pumps as well as the signal are linearly copolarized (dotted curve). Of course, this gain is highly polarization-dependent. When the signal is polarized orthogonal to the copolarized pumps, the gain is reduced to almost zero in the central part (thin solid curve). When orthogonal linearly polarized pumps are used, the gain spectrum is still wide and flat (dashed curve), but the gain is relatively small (around 8.5 dB). However, as shown by the solid curve, the FOPA gain can be increased from 8.5 to 23 dB if the two pumps are left- and right-circularly polarized. Although the preceding discussion focuses on signal amplification, the same behavior is expected when the FOPA is used as a wavelength converter because the idler power  $P_4$  is related to signal power  $P_3$  as  $P_4(L) = P_3(L) - P_3(0)$ .

#### 10.5.4 Effect of Residual Fiber Birefringence

As discussed in Section 6.6, most fibers exhibit residual birefringence that varies randomly along fiber length and may also fluctuate with time. Such birefringence fluctuations induce PMD and randomize the SOP of any optical field propagating through the fiber. Random changes in the SOPs of the four waves affect the conservation of angular momentum during the FWM process and thus degrade the performance of FOPAs [113]. Such PMD effects have been observed for both single- and dual-pump devices [67]. The vector theory of FWM can be used to understand the experimental data if it is extended to include the residual birefringence of fibers.

The extension adds an additional term  $[b_0 + b_1(\omega_j - \omega_r)\sigma_1] |A_j\rangle$  for  $j=1-4$  to the right side of Eqs (10.5.6–10.5.9) that converts these equations into a set of four coupled stochastic equations [114]. Here,  $\omega_r$  is a reference frequency, and it is practical to choose  $\omega_r = \omega_1$  and adopt a reference pump in which the SOP of one of the pumps is not affected by birefringence fluctuations. Random variables  $b_0$  and  $b_1$  affect FWM through two different mechanisms. First,  $b_0$  rotates the SOPs of all four fields on the Poincaré sphere in the same direction, and thus reduces the average gain roughly by the same amount over the entire gain bandwidth. Second,  $b_1$  causes the SOPs of the pumps, signal and idler to drift from each other at a rate that depends on their frequency difference  $\Omega$ . The length scale over which such a PMD-induced drift occurs is governed by the diffusion length  $L_{\text{diff}} = 3(D_p\Omega)^{-2}$ , where  $D_p$  is the PMD parameter of the fiber.

Similar to the case of dispersion fluctuations, one can use the stochastic equations to simulate the FOPA gain spectra numerically for different realizations of the birefringence distribution along the fiber. The average gain at any signal wavelength can be calculated by performing an ensemble average over a large number of realizations. In the case of a single-pump FOPA, the average can be performed analytically [115]. The analytical as well as numerical results show that random fluctuations of birefringence reduce the FOPA gain, on average, and distort the gain spectrum such that its flatness is compromised. A similar behavior is expected for dual-pump FOPAs.

As an example, Figure 10.20a shows the impact of PMD on the average gain spectrum of a dual-pump FOPA for three values of  $D_p$  with the same parameter values used for Figure 10.14. More specifically, the 0.5-km-long FOPA is pumped

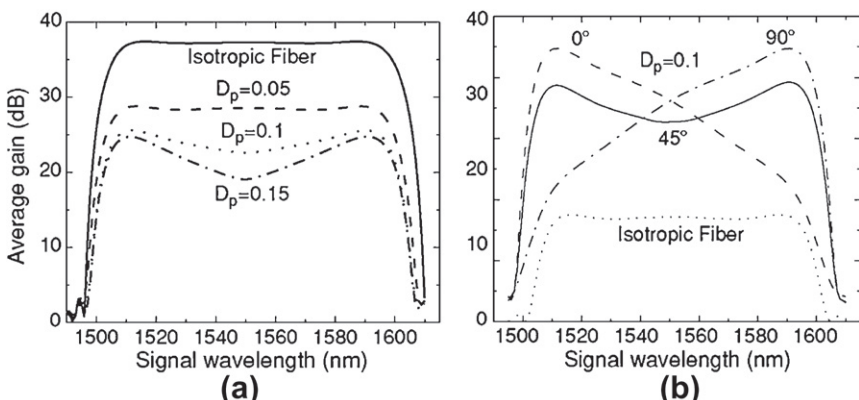


**Figure 10.20** (a) Average gain spectrum for a dual-pump FOPA for three values of  $D_p$ ; (b) average gain spectrum for three initially linear SOPs of the signal when  $D_p = 0.1 \text{ ps}/\sqrt{\text{km}}$ . In both cases, the isotropic case is also shown. (After Ref. [114]; © 2004 IEEE.)

with 0.5 W of power at two wavelengths of 1520.6 and 1600.6 nm, and both pumps and signal are copolarized initially. The average gain at any signal wavelength is obtained by averaging over 50 different realizations of birefringence distribution along the fiber length. The ideal case of isotropic fiber is also shown for comparison. Similar to the case of single-pump FOPA, the effect of  $b_0$  is to reduce the nonlinear parameter  $\gamma$  by a factor of 8/9 [116]. For small values of  $D_p$ , a lower value of  $\gamma$  reduces the peak gain, but the spectrum maintains its flat nature in the central region. However, for  $D_p > 0.1 \text{ ps}/\sqrt{\text{km}}$ , a central dip occurs, as seen in Figure 10.20a. The reason behind the dip formation is as follows. When the signal frequency is close to one of the pumps, that pump provides the dominant contribution. However, as signal frequency moves toward the center, neither of the two pumps remains oriented parallel to the signal, and the gain is reduced.

An important question is how PMD affects the independence of the FOPA gain on the signal SOP when the two pumps are orthogonally polarized (either linearly or circularly). As noted earlier, optical fields with different frequencies change their SOPs at different rates in the presence of PMD. As a result of this frequency dependence, the two pumps will not remain orthogonally polarized and would produce gain that depends on the signal SOP to some extent. Indeed, such a behavior has been observed for a dual-pump FOPA [67]. Figure 10.20b shows the average gain spectra for three different signal SOPs for a specific value of  $D_p = 0.1 \text{ ps}/\sqrt{\text{km}}$ . The two pumps are launched with SOPs that are linear and orthogonal to each other. The signal is also linearly polarized with its SOP inclined at an angle of 0, 45, or 90° from that of the shorter-wavelength pump. The gain spectrum expected in the absence of PMD is also shown as a dotted curve.

Two features of Figure 10.20b are noteworthy. First, at signal wavelengths close to the pump, gain can change by as much as 12 dB as signal SOP is varied; variations are much smaller in the central region. The reason for this behavior can be understood as follows. If the signal has its wavelength close to that of a pump, their relative orientation does not change much along the fiber. As a result, it experiences the highest or smallest gain depending on whether it is initially polarized parallel or orthogonal to the that pump. Second, the PMD effects enhance the gain considerably compared with the case of an isotropic fiber with no birefringence. The reason is understood by recalling from Figure 10.19 that the FWM efficiency is the smallest when the pumps are orthogonally polarized. However, because of the PMD, pump SOPs do not remain orthogonal along the fiber, and may even become parallel occasionally; this results in a higher gain at all signal wavelengths.

PMD effects can be made negligible for FOPAs designed with a relatively short length ( $\sim 100$  m) of low-PMD fibers and pumped at wavelengths spaced apart by  $< 50$  nm. Under such conditions, the diffusion length  $L_{\text{diff}}$  exceeds 1 km for  $D_p < 0.1 \text{ ps}/\sqrt{\text{km}}$ , and the SOPs of all waves maintain their relative orientation over the FOPA length, even though they rotate randomly over the Poincaré sphere because of random birefringence changes. Such rotations reduce the effective value of the nonlinear parameter  $\gamma$  by a factor of 8/9. This feature simplifies the vector

treatment of FWM considerably as the problem becomes deterministic in nature [117]. A simple approach starts with the averaged NLS equation (known as the Manakov equation) for the total field and uses Eq. (6.6.14) to obtain the following set of four deterministic equations for the Jones vectors associated with the pumps, signal, and idler fields:

$$\frac{d|A_1\rangle}{dz} = \frac{8i\gamma}{9} (\langle A_1|A_1\rangle + \langle A_2|A_2\rangle + |A_2\rangle\langle A_2|) |A_1\rangle, \quad (10.5.23)$$

$$\frac{d|A_2\rangle}{dz} = \frac{8i\gamma}{9} (\langle A_1|A_1\rangle + \langle A_2|A_2\rangle + |A_1\rangle\langle A_1|) |A_2\rangle, \quad (10.5.24)$$

$$\begin{aligned} \frac{d|A_3\rangle}{dz} &= \frac{8i\gamma}{9} \left( \sum_{j=1}^2 (\langle A_j|A_j\rangle + |A_j\rangle\langle A_j|) \right) |A_3\rangle \\ &\quad + \frac{8i\gamma}{9} (|A_2\rangle\langle A_1^*| + |A_1\rangle\langle A_2^*|) |A_4^*\rangle e^{-i\Delta kz}, \end{aligned} \quad (10.5.25)$$

$$\begin{aligned} \frac{d|A_4\rangle}{dz} &= \frac{8i\gamma}{9} \left( \sum_{j=1}^2 (\langle A_j|A_j\rangle + |A_j\rangle\langle A_j|) \right) |A_4\rangle \\ &\quad + \frac{8i\gamma}{9} (|A_2\rangle\langle A_1^*| + |A_1\rangle\langle A_2^*|) |A_3^*\rangle e^{-i\Delta kz}. \end{aligned} \quad (10.5.26)$$

The two pump equations can be solved analytically if the pumps are assumed to remain undepleted. The SPM and XPM terms in the remaining two equations can be eliminated by introducing new Jones vectors  $|B_3\rangle$  and  $|B_4\rangle$  with a transformation similar to that given in Eq. (10.2.12) for the scalar case. These new Jones vectors are found to satisfy

$$\frac{d|B_3\rangle}{dz} = \frac{8i\gamma}{9} (|A_2\rangle\langle A_1^*| + |A_1\rangle\langle A_2^*|) |B_4^*\rangle e^{-ikz}, \quad (10.5.27)$$

$$\frac{d|B_4^*\rangle}{dz} = -\frac{8i\gamma}{9} (|A_2\rangle\langle A_1^*| + |A_1\rangle\langle A_2^*|) |B_3\rangle e^{ikz}. \quad (10.5.28)$$

These two equations generalize Eqs (10.2.13) and (10.2.14) to the vector case. They can be solved for arbitrary SOPs of the two pumps and the signal because their relative orientation does not change along the fiber. The signal amplification factor for a dual-pump FOPA is found to be

$$G_s = \frac{1}{2} [(G_+ + G_-) + (G_+ - G_-) \cos(\theta_s)], \quad (10.5.29)$$

where  $\theta_s$  is the input angle between the signal Stokes vector and the vector pointing along  $\hat{p}_1 + \hat{p}_2$  (on the Poincaré sphere). Here  $\hat{p}_1$  and  $\hat{p}_2$  are input Stokes vectors for the two pumps. The two gains are defined as

$$G_{\pm} = |\cosh(g_{\pm}L) + (ik/2g_{\pm}) \sinh(g_{\pm}L)|^2, \quad (10.5.30)$$

$$g_{\pm}^2 = (8\gamma/9)^2 P_1 P_2 [1 \pm \cos(\theta_p/2)]^2 - (\kappa/2)^2, \quad (10.5.31)$$

where  $\theta_p$  is the input angle between  $\hat{p}_1$  and  $\hat{p}_2$ .

Equation (10.5.29) provides the amplification factor of a dual-pump FOPA for arbitrary input SOPs of the two pumps. Consider the perfect phase-matched case by setting  $\kappa = 0$ . When the pumps are copolarized ( $\theta_p = 0$ ),  $g_- = 0$  and  $G_- = 1$ , while  $G_+ = \cosh^2(g_+L)$ . It follows from Eq. (10.5.29), that  $G_s$  varies with the signal SOP in the range of 1 to  $G_+$ , the minimum value of 1 occurring when the signal is polarized orthogonal to the pumps. This SOP dependence of the signal gain can be avoided by launching orthogonally polarized pumps ( $\theta_p = \pi$ ). In this case,  $G_+ = G_-$ , and  $G_s$  becomes independent of  $\theta_s$ , i.e., it does not change with the signal SOP. Of course, the value of  $G_s$  is reduced considerably because  $g_+$  is smaller by a factor of 2. For example, if the signal is amplified by 40 dB when all fields are copolarized, it is amplified by only 20 dB when the pumps are orthogonally polarized.

## 10.6 APPLICATIONS OF FOUR-WAVE MIXING

FWM in optical fibers can be both harmful and beneficial depending on the application. It can induce crosstalk in WDM communication systems and limit the performance of such systems. The FWM-induced crosstalk can be avoided in practice through dispersion management, a technique in which the dispersion of each fiber section is made large enough that the FWM process is not phase matched throughout the link length [53]. At the same time, FWM is useful for a variety of applications [118]. As already mentioned, FOPAs can be employed for signal amplification, phase conjugation, and wavelength conversion. In addition to these, FWM can be useful for applications such as optical sampling, channel demultiplexing, pulse generation, and high-speed optical switching [66]. It can also be used for reducing quantum noise through squeezing and for generating quantum-correlated photon pairs. This section focuses on a few such applications.

### 10.6.1 Parametric Oscillators

Perhaps, the simplest application of the parametric gain is to use it for making a laser by placing the fiber inside an optical cavity and pumping it with a single pump source. Since no signal beam is launched, the signal and idler waves are created initially from noise through spontaneous modulation instability (or FWM) at frequencies dictated by the phase-matching condition; the two are subsequently amplified

through stimulated FWM. As a result, the laser emits the signal and idler beams simultaneously at frequencies that are located symmetrically on opposite sides of the pump frequency. Such lasers are called *parametric oscillators*; the term four-photon laser is also sometimes used. They were made soon after FWM was realized inside an optical fiber. As early as 1980, a parametric oscillator pumped at 1.06  $\mu\text{m}$  exhibited a conversion efficiency of 25% [119]. In a 1987 experiment [120], a parametric oscillator emitted 1.15- $\mu\text{m}$  pulses of about 65-ps duration when it was pumped with 100-ps pulses obtained from a mode-locked, Q-switched, Nd:YAG laser. Synchronous pumping was realized by adjusting the cavity length such that each laser pulse overlapped with the next pump pulse after one round trip.

A new kind of parametric oscillator, called the modulation-instability laser can be made by pumping optical fibers in the anomalous-dispersion region. As seen in Section 10.3.2, modulation instability can be interpreted in terms of a FWM process that is phase-matched by the SPM. Such a laser was first made in 1988 by pumping a fiber-ring cavity (length  $\sim$ 100 m) synchronously with a mode-locked color-center laser (pulse width  $\sim$ 10 ps) operating in the 1.5- $\mu\text{m}$  wavelength region [121]. For a 250-m ring, the laser reached threshold at a peak pump power of 13.5 W. Such a laser generated the signal and idler bands with a frequency shift of about 2 THz, a value in agreement with the theory of Section 5.1. The use of vector modulation instability (see Section 6.4) makes it possible to operate a parametric oscillator in the visible region [122].

A modulation-instability laser is different from a conventional parametric oscillator in the sense that it can convert a CW pump into a train of short optical pulses (rather than generating a tunable CW signal). This objective was realized in 1999 by pumping a 115-m-long ring cavity with a CW laser (a DFB fiber laser). The SBS process was suppressed by modulating the pump phase. The laser reached threshold at a pump power of about 80 mW and emitted a pulse train at the 58-GHz repetition rate when pumped beyond its threshold [123]. The spectrum exhibited multiple peaks, separated by 58 GHz, that were generated through a cascaded FWM process.

A parametric oscillator, tunable over a 40-nm range centered at the pump wavelength of 1539 nm, was realized in a 1999 experiment [124]. This laser employed a nonlinear Sagnac interferometer (with a loop length of 105 m) as a FOPA that was pumped by using 7.7-ps mode-locked pulses from a color-center laser operating at 1539 nm. Such an interferometer separates pump light from the signal and idler waves while amplifying both of them. In effect, it acts as a mirror of a Fabry–Perot cavity with internal gain. A grating at the other end of the cavity separates the idler and signal waves so that the Fabry–Perot cavity is resonant for the signal only. This grating is also used for tuning laser wavelength. The laser emitted 1.7-ps pulses at the 100-MHz repetition rate of the pump laser.

After 2001, the use of highly nonlinear fibers became common for making parametric oscillators [125–131]. Such devices can operate continuously with a narrow line width, or they can be forced to emit a train of short pulses by pumping them with a suitable pulsed source [130]. The use of FWM is essential for realizing fiber-optic parametric oscillators that emit femtosecond pulses and are tunable over

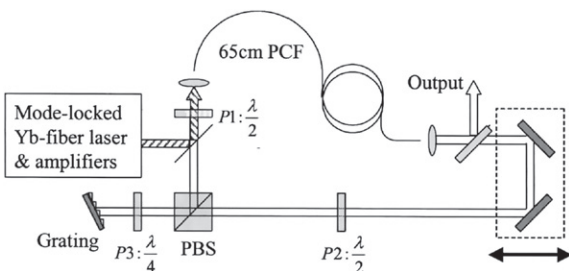


**Figure 10.21** Schematic of the ring cavity used for a parametric oscillator tunable over 200 nm. PCF and PBS stand for photonic-crystal fiber and polarizing beam splitter, respectively; P1, P2, and P3 represent three achromatic wave plates. (After Ref. [131]; © 2005 OSA.)

a wide wavelength range. A tuning range of more than 200 nm was realized in 2005 by employing a ring cavity shown in Figure 10.21 and containing a 65-cm-long photonic crystal fiber [131]. Section 12.3.4 provides more details on such tunable lasers.

## 10.6.2 Ultrafast Signal Processing

The ultrafast nature of the FWM process in optical fibers stems from the electronic nature of fiber nonlinearity. As a result, rapid variations in the input power of the signal or the pumps are transferred to the FOPA output almost instantaneously. It is this feature that converts FOPAs into signal-processing devices capable of responding at picosecond timescales. Moreover, all FOPAs generate one or more idler waves that mimic the launched signal but have a different wavelength. From a practical perspective, these idlers represent a replica of the signal (except for a phase reversal) and thus can serve as a wavelength-converted signal.

When FOPAs are used as a wavelength converter in optical communication systems, one or two CW pump beams are injected together with the signal such that the idler wave is created at the desired wavelength [132]. As the idler is generated through FWM only when the pumps and signal are present simultaneously, it appears in the form of a pulse train consisting of the same sequence of “1” and “0” bits as the signal. In effect, FWM transfers the signal data to the idler at a new wavelength with perfect fidelity. It can even improve the signal quality by reducing the noise level [133–135]. The reason is related to the nonlinear power-transfer characteristics of FOPAs. Figure 10.22a shows the measured output powers at the FOPA output as the input power of the signal is varied over a 30-dB range [135]. The temporal profile of the input signal (a) is compared with the output signal (b) and two idlers (c and d). The idler (d) exhibits much less noise for both 1 and 0 bits and can serve as a regenerated signal. Clearly, FWM may prove useful for all-optical regeneration of channels in WDM systems.

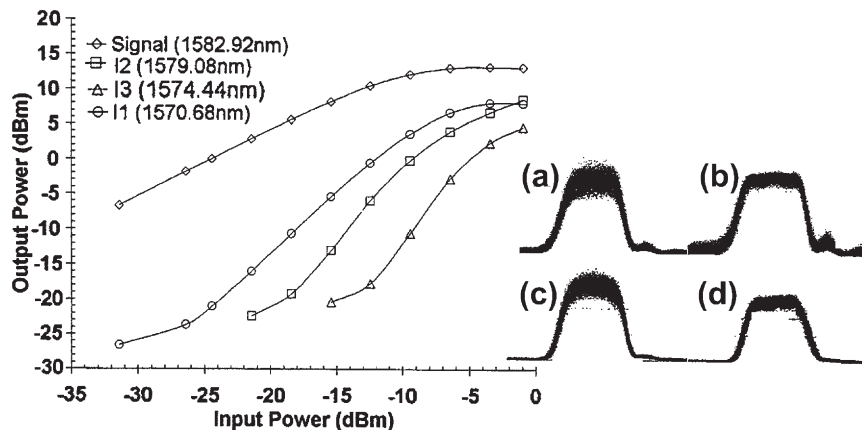


Figure 10.22 Measured output powers in the signal and three idlers as a function of input signal power for a dual-pump FOPA. Temporal profiles are shown for the input signal (a), output signal (b), and two idlers. (After Ref. [135]; © 2003 IEEE.)

Another application employs FWM for demultiplexing a time-division-multiplexed (TDM) signal [136]. In a TDM signal, bits from different channels are packed together such that the bits belonging to a specific channel are separated by  $N$  bits, if  $N$  channels are multiplexed together in the time domain. A specific channel can be demultiplexed if the pump is in the form of an optical pulse train at the bit rate of an individual channel (referred to as an optical clock). Physically, the idler wave is generated only when the pump and signal overlap in the time domain and is thus a replica of the bit pattern associated with a single channel. The FWM process was used for time-domain demultiplexing as early as 1991 [137]. In a 1996 experiment, 10-Gb/s channels were demultiplexed from a 500-Gb/s TDM signal using clock pulses of 1-ps duration [138]. This scheme can also amplify the demultiplexed channel inside the same fiber [139]. The same scheme can be used for all-optical sampling of signal pulses [140]. The basic idea is to employ pump pulses shorter than the signal pulse so that the idler power provides a sample of the signal in the time window associated with the pump pulse. By 2005, subpicosecond temporal resolution over more than 60-nm bandwidth had been realized with the use of FWM [141].

An interesting application uses FWM to convert a CW signal into a pulse train at high repetition rates through pump modulation [66]. The pump is modulated sinusoidally at the desired repetition rate before it is launched into the fiber where FWM occurs. Because of the exponential dependence of the signal gain on the pump power, the signal is amplified mostly in the central part of each modulation cycle and is thus in the form of a pulse train. By 2005, a 40-GHz train of short pulses (width about

2 ps) generated with this technique was used for information transmission at bit rates of up to 160 Gb/s [142].

An important feature of FWM is that a FOPA can be used as an optical gate that opens for a short duration controlled by the pump. This feature has been used for optical switching at bit rates as high as 40 Gb/s [143]. The basic idea is similar to that used for time-domain demultiplexing. In the case of a dual-pump FOPA, one pump remains CW but the other is turned on only for time intervals during which the optical gate should remain open. Because the idler wave is generated when both pumps overlap with the signal, it contains temporal slices of the signal whose duration is dictated by the second pump. As all idlers (as well as the signal) at the FOPA output contain only these temporal slices, a single pump can be used for multicasting the selected signal information at multiple wavelengths. This approach was used in a 2005 experiment to select either individual bits or a packet of bits (packet switching) from a 40-Gb/s signal [143].

### 10.6.3 Quantum Correlation and Noise Squeezing

The simultaneous generation of the signal and idler photons during the FWM process indicates that each photon pair is correlated in the quantum sense. This correlation has found a number of applications, including the reduction of quantum noise through a phenomenon called squeezing [144–146]. Squeezing refers to the process of generating the special states of an electromagnetic field for which noise fluctuations, in some frequency range, are reduced below the quantum-noise level. An accurate description of squeezing in optical fibers requires a quantum-mechanical approach in which the signal and idler amplitudes  $B_3$  and  $B_4$  are replaced by corresponding annihilation operators.

From a physical standpoint, squeezing can be understood as the deamplification of signal and idler waves for certain values of the relative phase between the two [62]. Spontaneous emission at the signal and idler frequencies generates photons with random phases. FWM increases or decreases the number of specific signal-idler photon pairs depending on their relative phases. A phase-sensitive (homodyne or heterodyne) detection scheme shows noise reduced below the quantum-noise level when the phase of the local oscillator is adjusted to match the relative phase corresponding to the photon pair whose number was reduced as a result of FWM.

The observation of squeezing in optical fibers is hindered by the competing processes such as spontaneous and stimulated Brillouin scattering. A particularly important noise process turned out to be Brillouin scattering caused by guided acoustic waves [147]. If noise generated by this phenomenon exceeds the reduction expected from FWM, squeezing is washed out. Several techniques have been developed to reduce the impact of this noise source [146]. A simple method consists of immersing the fiber in a liquid-helium bath. Indeed, a 12.5% reduction in the quantum-noise level was observed in a 1986 experiment in which a 647-nm CW

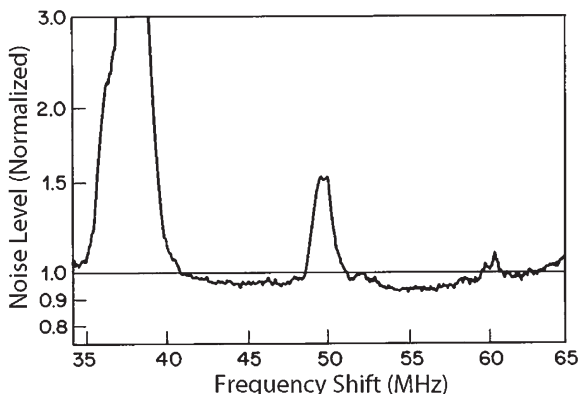


**Figure 10.23** Noise spectrum under minimum-noise conditions. Horizontal line shows the quantum-noise level. Reduced noise of around 45 and 55 MHz is a manifestation of squeezing in optical fibers occurring as a result of FWM. (After Ref. [148]; © 1986 American Physical Society.)

pump beam was propagated through a 114-m-long fiber [148]. Figure 10.23 shows the observed noise spectrum when the local oscillator phase is set to record the minimum noise (two large peaks are due to guided acoustic waves). Squeezing occurs in the spectral bands located around 45 and 55 MHz. During the 1990s several other types of squeezing were realized [146].

Much attention has focused in recent years on optical sources that emit single photons or entangled photon pairs because of applications of such sources for quantum cryptography and quantum computing [149–159]. The nonlinear process of FWM occurring inside optical fibers provides a simple way to generate quantum-correlated photon pairs within a single spatial mode. In this application, only a pump beam is launched into the fiber, and the spontaneous FWM process is employed to generate the correlated photon pairs at different frequencies satisfying the FWM condition  $\omega_3 + \omega_4 = 2\omega_1$ , where  $\omega_1$  is the pump frequency. If it is desirable to have a source that emits correlated photon pairs at the same frequency, a dual-pump configuration is used in which the nondegenerate FWM process produces the signal and idler photons at the same frequency such that  $\omega_3 = \omega_4 = \frac{1}{2}(\omega_1 + \omega_2)$ .

It was observed in several experiments that the quality of the photon-pair source is severely deteriorated by spontaneous Raman scattering that accompanies the spontaneous FWM process inevitably and cannot be avoided in practice [150–155]. In the single-pump configuration, Raman scattering is relatively weak if the pump-signal detuning is relatively small (<1 THz). However, this approach limits available bandwidth of photon pairs to the vicinity of the pump wavelength. In an alternative approach, signal and idler photons are shifted from the pump frequency so that they lie beyond the dominant Raman peak located around 13 THz. Indeed, frequency

shifts as large as 30 THz have been realized by matching the FWM process appropriately [154]. However, spontaneous Raman scattering still remains a limiting factor because of the possibility of cascaded Raman scattering in which the first-order Stokes shifted from the pump by about 13.2 THz can act as a pump and produce the second-order Stokes shifted by 26.4 THz, and so on.

In one 2005 experiment [152], a few-meter-long highly nonlinear fiber was pumped with Q-switched pulses at 1047 nm. The FWM condition could be satisfied for the signal and idler photons far from the pump wavelength because pump pulses propagated in the normal-dispersion region of the fiber. Figure 10.24 shows the optical spectrum at the fiber output showing multiple peaks generated through FWM. The signal and idler peaks located at 834 and 1404 nm correspond to correlated photon pairs used in the experiment. The quality of such a photon-pair source was found to be affected by the fifth-order Raman scattering peak located near 1400 nm. In spite of such complications, FWM inside optical fibers is often used to produce photon-pair sources with high brightness [159].

#### 10.6.4 Phase-Sensitive Amplification

The noise-squeezing idea can be employed for making phase-sensitive amplifiers whose gain depends on the phase of input signal [160–167]. Such FOPAs can amplify a signal with noise figures below the 3-dB limit imposed on phase-insensitive amplifiers. Moreover, they can be used to reduce the noise of phase-modulated telecommunication channels. However, their use requires the presence of both the signal and the idler fields at the input end with their relative phases locked to a fixed value. In the case of a dual-pump configuration, an idler is not needed at the input end when the signal frequency lies exactly at the center of two pump frequencies [162].

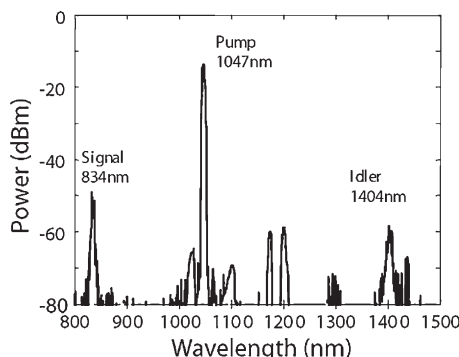


**Figure 10.24** Output spectrum observed when a highly nonlinear fiber is pumped with Q-switched pulses at 1047 nm. (After Ref. [152]; © 2005 OSA.)

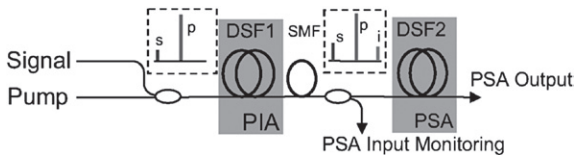


**Figure 10.25 Schematic of a phase-sensitive amplifier (PSA) in which the idler is created using a phase-insensitive amplifier (PIA). DSF and SMF stand for dispersion-shifted and single-mode fibers, respectively. (After Ref. [163]; © 2005 OSA.)**

However, such a degenerate configuration has limited bandwidth and is not useful for WDM applications.

The phase sensitivity of FOPAs can be understood from Eq. (10.4.21) of Section 10.4.5 indicating how the signal gain depends on the phase combination of four waves defined as  $\theta = \phi_1 + \phi_2 - \phi_3 - \phi_4$ . Depending on the value of  $\theta$ , the signal may be amplified or deamplified. The phase sensitivity of FOPAs is also evident from the solution given in Eqs (10.4.3) and (10.4.4) in the general case when both the signal and idler fields are present at the input end. This solution shows clearly that the FOPA response becomes phase insensitive when no idler is present initially.

The realization of a phase-sensitive FOPA requires not only that both the signal and idler be injected into the FOPA (in addition to one or two pumps) but also that the relative phases of all waves be locked to a common reference so that the phase combination  $\theta$  maintains its input value. In one approach, an electro-optic modulator is used to produce phase locking. However, this approach is limited by the modulator bandwidth and restricts the wavelength difference between the pump and the signal to under 1 nm. The alternative is to create the idler first by using a conventional phase-insensitive FOPA whose output is then fed into the phase-sensitive FOPA [163]. Phase locking is automatic in this case, but one must ensure that a suitable mechanism exists for changing  $\theta$ . This scheme, first used in 2005 and shown schematically in Figure 10.25, employed a single-mode fiber to change  $\theta$  through wavelength-dependent phase shifts. By 2008, it was used to amplify three CW signals of different wavelengths simultaneously in a phase-sensitive manner [164].

An important application of phase-sensitive FOPAs is for reducing noise in phase-modulated channels through signal regeneration. A 2006 numerical study showed excellent regenerative performance at a 40-Gb/s bit rate [162]. Multiple Experiments have confirmed that phase-sensitive FOPAs can be used for this purpose [165]. In a 2010 experiment, phase-sensitive amplification of a 40-Gb/s signal (in the DPSK format) was realized over a bandwidth exceeding 20 nm [166]. By 2011, such FOPAs provided broadband amplification with nearly 6 dB improvement in the noise figure over fiber links making use of erbium-doped fiber amplifiers [167].

---

## PROBLEMS

- 10.1** Find an expression for  $P_3$ , similar to that given in Eq. (10.1.4) for  $P_4$ , by using Eqs (10.1.1–10.1.3).
- 10.2** A single CW pump beam is used to produce the signal and idler waves. Starting from Eq. (10.1.1) derive the three nonlinear equations, similar to those in Eqs (10.2.1–10.2.4), governing this FWM process.
- 10.3** Solve the set of three equations obtained in Problem 10.2 assuming that the pump beam remains undepleted. Find the parametric gain for the signal and idler waves as a function of the pump power and the phase mismatch  $\Delta k$ .
- 10.4** Explain how the nonlinear effects can be used to satisfy the phase-matching condition for FWM to occur inside a single-mode fiber. What should be the pump power when the pump and signal wavelengths are 1.50 and 1.51  $\mu\text{m}$ , respectively? Assume  $\gamma = 5 \text{ W}^{-1}/\text{km}$  and  $\beta_2 = -2 \text{ ps}^2/\text{km}$  at the pump wavelength.
- 10.5** Spontaneous FWM is observed to occur in a birefringent fiber when a 1.55- $\mu\text{m}$  pump beam is launched such that it is polarized at  $40^\circ$  from the slow axis. What are the wavelengths and polarization directions the signal and the idler generated through FWM assuming  $\delta n = 2 \times 10^{-4}$  and  $\beta_2 = -2 \text{ ps}^2/\text{km}$ ?
- 10.6** Starting from Eqs (10.2.13) and (10.2.14), derive expressions for the signal and idler powers for a single-pump FOPA of length  $L$ . You can assume that no idler power is launched initially.
- 10.7** A 1-km-long parametric amplifier is pumped at 1552 nm with a single laser. Assume fiber has its zero-dispersion wavelength at 1550 nm with  $\gamma = 5 \text{ W}^{-1}/\text{km}$ ,  $\beta_3 = 0.05 \text{ ps}^3/\text{km}$  and  $\beta_4 = 1.0 \times 10^{-4} \text{ ps}^4/\text{km}$ . Include the fourth-order term in the phase-mismatch term and plot the signal gain as a function of pump-signal detuning for pump powers of 0.4, 0.6, and 0.8 W.
- 10.8** Explain how a dual-pump FOPA can be designed to provide a nearly uniform gain over a wide bandwidth.
- 10.9** Show that the linear phase mismatch can indeed be written in the form of Eq. (10.4.16) for a dual-pump FOPA.
- 10.10** How can you use FWM for wavelength conversion in WDM systems? Starting from Eq. (10.4.4), derive an expression for the conversion efficiency of a dual-pump FOPA.
- 10.11** Derive Eqs (10.5.3) and (10.5.4) after substituting Eq. (10.5.2) in Eq. (10.1.1).
- 10.12** Use Eqs (10.5.3–10.5.5) to derive the set of four equations given as Eqs (10.5.6–10.5.9).
- 10.13** Use Eqs (10.5.11) and (10.5.12) to prove that the FWM process is independent of the signal polarization when the two pumps are orthogonally polarized. Identify the terms that contribute to the signal gain when the pumps are linearly polarized.
- 10.14** Prove that the solution of Eqs (10.5.14) and (10.5.15) is given by Eq. (10.5.16) with  $g(\theta)$  given in Eq. (10.5.17).

- 10.15** Show that Eqs (10.5.27) and (10.5.28) lead to the signal gain  $G_s$  given in Eq. (10.5.29).
- 10.16** Starting from Eq. (10.4.3), find an expression for the signal power  $P_3 = |B_3|^2$  at the end of an amplifier of length  $L$  as a function of  $\theta = \phi_1 + \phi_2 - \phi_3 - \phi_4$ . Calculate the maximum and minimum values of the phase-sensitive amplification factor when the idler power equals the signal power at the input end.

## REFERENCES

- [1] J. A. Armstrong, N. Bloembergen, J. Ducuing, and P. S. Pershan, *Phys. Rev.* **127**, 1918 (1962).
- [2] Y. R. Shen, *The Principles of Nonlinear Optics* (Wiley, 1984).
- [3] M. Schubert and B. Wilhelmi, *Nonlinear Optics and Quantum Electronics* (Wiley, 1986).
- [4] P. N. Butcher and D. Cotter, *Elements of Nonlinear Optics* (Cambridge University Press, 1990).
- [5] R. W. Boyd, *Nonlinear Optics*, 3rd ed. (Academic Press, 2008).
- [6] R. H. Stolen, J. E. Bjorkholm, and A. Ashkin, *Appl. Phys. Lett.* **24**, 308 (1974).
- [7] R. H. Stolen, *IEEE J. Quantum Electron.* **11**, 100 (1975).
- [8] K. O. Hill, D. C. Johnson, B. S. Kawasaki, and R. I. MacDonald, *J. Appl. Phys.* **49**, 5098 (1978).
- [9] A. Säisy, J. Botineau, A. A. Azéma, and F. Gires, *Appl. Opt.* **19**, 1639 (1980).
- [10] K. O. Hill, D. C. Johnson, and B. S. Kawasaki, *Appl. Opt.* **20**, 1075 (1981).
- [11] C. Lin and M. A. Bösch, *Appl. Phys. Lett.* **38**, 479 (1981).
- [12] R. H. Stolen and J. E. Bjorkholm, *IEEE J. Quantum Electron.* **18**, 1062 (1982).
- [13] C. Lin, *J. Opt. Commun.* **4**, 2 (1983).
- [14] K. Washio, K. Inoue, and S. Kishida, *Electron. Lett.* **16**, 658 (1980).
- [15] C. Lin, W. A. Reed, A. D. Pearson, and H. T. Shang, *Opt. Lett.* **6**, 493 (1981).
- [16] C. Lin, W. A. Reed, A. D. Pearson, H. T. Shang, and P. F. Glodis, *Electron. Lett.* **18**, 87 (1982).
- [17] R. H. Stolen, M. A. Bösch, and C. Lin, *Opt. Lett.* **6**, 213 (1981).
- [18] K. Kitayama, S. Seikai, and N. Uchida, *Appl. Phys. Lett.* **41**, 322 (1982).
- [19] K. Kitayama and M. Ohashi, *Appl. Phys. Lett.* **41**, 619 (1982).
- [20] R. K. Jain and K. Stenersen, *Appl. Phys. B* **35**, 49 (1984).
- [21] K. Stenersen and R. K. Jain, *Opt. Commun.* **51**, 121 (1984).
- [22] M. Ohashi, K. Kitayama, N. Shibata, and S. Seikai, *Opt. Lett.* **10**, 77 (1985).
- [23] N. Shibata, M. Ohashi, K. Kitayama, and S. Seikai, *Opt. Lett.* **10**, 154 (1985).
- [24] H. G. Park, J. D. Park, and S. S. Lee, *Appl. Opt.* **26**, 2974 (1987).
- [25] N. Shibata, R. P. Braun, and R. G. Waarts, *IEEE J. Quantum Electron.* **23**, 1205 (1987).
- [26] P. L. Baldeck and R. R. Alfano, *J. Lightwave Technol.* **5**, 1712 (1987).
- [27] Y. Chen and A. W. Snyder, *Opt. Lett.* **14**, 87 (1989).
- [28] Y. Chen, *J. Opt. Soc. Am. B* **6**, 1986 (1989); *J. Opt. Soc. Am. B* **7**, 43 (1990).
- [29] J. K. Chee and J. M. Liu, *IEEE J. Quantum Electron.* **26**, 541 (1990).
- [30] E. A. Golovchenko, P. V. Mamyshev, A. N. Pilipetskii, and E. M. Dianov, *IEEE J. Quantum Electron.* **26**, 1815 (1990); *J. Opt. Soc. Am. B* **8**, 1626 (1991).

- [31] P. N. Morgan and J. M. Liu, *IEEE J. Quantum Electron.* **27**, 1011 (1991).
- [32] G. Cappellini and S. Trillo, *Phys. Rev. A* **44**, 7509 (1991).
- [33] S. Trillo and S. Wabnitz, *J. Opt. Soc. Am. B* **9**, 1061 (1992).
- [34] E. A. Golovchenko and A. N. Pilipetskii, *J. Opt. Soc. Am. B* **11**, 92 (1994).
- [35] P. Tchofo Dinda, G. Millot, and P. Louis, *J. Opt. Soc. Am. B* **17**, 1730 (2000).
- [36] G. Millot, P. Tchofo Dinda, E. Seve, and S. Wabnitz, *Opt. Fiber Technol.* **7**, 170 (2001).
- [37] Y. Inoue, *J. Phys. Soc. Jpn.* **39**, 1092 (1975).
- [38] D. J. Kaup, A. Reiman, and A. Bers, *Rev. Mod. Phys.* **51**, 275 (1979).
- [39] L. M. Kovachev and V. N. Serkin, *Sov. J. Quantum Electron.* **19**, 1211 (1989).
- [40] C. J. McKinstry, G. G. Luther, and S. H. Batha, *J. Opt. Soc. Am. B* **7**, 340 (1990).
- [41] A. A. Zabolotskii, *Sov. Phys. JETP* **70**, 71 (1990).
- [42] D. Liu and H. G. Winful, *Opt. Lett.* **16**, 67 (1991).
- [43] I. M. Uzunov, *Opt. Quantum Electron.* **24**, 1491 (1992).
- [44] S. Wabnitz and J. M. Soto-Crespo, *Opt. Lett.* **23**, 265 (1998).
- [45] J. Botineau and R. H. Stolen, *J. Opt. Soc. Am.* **72**, 1592 (1982).
- [46] K. Inoue, K. Nakanishi, K. Oda, and H. Toba, *J. Lightwave Technol.* **12**, 423 (1994).
- [47] F. Forghieri, R. W. Tkach, and A. R. Chraplyvy, *J. Lightwave Technol.* **15**, 889 (1995).
- [48] W. Zeiler, F. Di Pasquale, P. Bayvel, and J. E. Midwinter, *J. Lightwave Technol.* **17**, 1933 (1996).
- [49] M. Nakajima, M. Ohashi, K. Shiraki, T. Horiguchi, K. Kurokawa, and Y. Miyajima, *J. Lightwave Technol.* **17**, 1814 (1999).
- [50] M. Eiselt, *J. Lightwave Technol.* **17**, 2261 (1999).
- [51] K.-D. Chang, G.-C. Yang, and W. C. Kwong, *J. Lightwave Technol.* **18**, 2113 (2000).
- [52] S. Betti, M. Giacconi, and M. Nardini, *IEEE Photon. Technol. Lett.* **14**, 1079 (2003).
- [53] G. P. Agrawal, *Lightwave Technology: Telecommunication Systems* (Wiley, 2005).
- [54] Z. Su, X. Zhu, and W. Sibbett, *J. Opt. Soc. Am. B* **10**, 1053 (1993).
- [55] M. Yu, C. J. McKinstry, and G. P. Agrawal, *Phys. Rev. E* **52**, 1072 (1995).
- [56] F. Biancalana, D. V. Skryabin, and P. St. J. Russell, *Phys. Rev. E* **68**, 046003 (2003).
- [57] J. D. Harvey, R. Leonhardt, S. Coen, et al., *Opt. Lett.* **28**, 2225 (2003).
- [58] W. J. Wadsworth, N. Joly, J. C. Knight, et al., *Opt. Express* **12**, 299 (2004).
- [59] G. K. L. Wong, A. Y. H. Chen, S. G. Murdoch, et al., *J. Opt. Soc. Am. B* **22**, 2505 (2005).
- [60] M. Ohashi, K. Kitayama, Y. Ishida, and N. Uchida, *Appl. Phys. Lett.* **41**, 1111 (1982).
- [61] J. P. Pocholle, J. Raffy, M. Papuchon, and E. Desurvire, *Opt. Eng.* **24**, 600 (1985).
- [62] I. Bar-Joseph, A. A. Friesem, R. G. Waarts, and H. H. Yaffe, *Opt. Lett.* **11**, 534 (1986).
- [63] M. E. Marhic, N. Kagi, T. K. Chiang, and L. G. Kazovsky, *Opt. Lett.* **21**, 573 (1996).
- [64] G. A. Nowak, Y. Hao, T. J. Xia, M. N. Islam, and D. Nolan, *Opt. Lett.* **23**, 936 (1998).
- [65] M. E. Marhic, F. S. Yang, M. C. Ho, and L. G. Kazovsky, *J. Lightwave Technol.* **17**, 210 (1999).
- [66] J. Hansryd, P. A. Andrekson, M. Westlund, J. Li, and P. O. Hedekvist, *IEEE J. Sel. Topics Quantum Electron.* **8**, 506 (2002).
- [67] S. Radic and C. J. McKinstry, *Opt. Fiber Technol.* **9**, 7 (2003).
- [68] F. Yaman, Q. Lin, and G. P. Agrawal, in *Guided-Wave Optical Components and Devices*, B. P. Pal, Ed. (Academic Press, 2005), Chap. 7.
- [69] M. E. Marhic, *Fiber Optical Parametric Amplifiers, Oscillators and Related Devices* (Cambridge University Press, 2007).
- [70] S. Watanabe and M. Shirasaki, *J. Lightwave Technol.* **14**, 243 (1996).
- [71] M. Ho, K. Uesaka, M. Marhic, Y. Akasaka, and L. G. Kazovsky, *J. Lightwave Technol.* **19**, 977 (2001).

- [72] K. Inoue, *Opt. Lett.* **19**, 1189 (1994).
- [73] J. Hansryd and P. A. Andrekson, *IEEE Photon. Technol. Lett.* **13**, 194 (2001).
- [74] T. Torounidis, H. Sunnerud, P. O. Hedekvist, and P. A. Andrekson, *IEEE Photon. Technol. Lett.* **15**, 1061 (2003).
- [75] M. N. Islam and Ö. Boyraz, *IEEE J. Sel. Topics Quantum Electron.* **8**, 527 (2002).
- [76] M. Westlund, J. Hansryd, P. A. Andrekson, and S. N. Knudsen, *Electron. Lett.* **38**, 85 (2002).
- [77] X. Zhang and B. F. Jorgensen, *Opt. Fiber Technol.* **3**, 28 (1997).
- [78] P. O. Hedekvist and P. A. Andrekson, *J. Lightwave Technol.* **17**, 74 (1999).
- [79] P. Kylemark, P. O. Hedekvist, H. Sunnerud, M. Karlsson, and P. A. Andrekson, *J. Lightwave Technol.* **22**, 409 (2004).
- [80] A. Durécu-Legrand, C. Simonneau, D. Bayart, A. Mussot, T. Sylvestre, E. Lantz, and H. Maillotte, *IEEE Photon. Technol. Lett.* **17**, 1178 (2005).
- [81] J. L. Blows and S. E. French, *Opt. Lett.* **27**, 491 (2002).
- [82] P. L. Voss, R. Tang, and P. Kumar, *Opt. Lett.* **28**, 549 (2003).
- [83] K. K. Y. Wong, K. Shimizu, M. E. Marhic, K. Uesaka, G. Kalogerakis, and L. G. Kazovsky, *Opt. Lett.* **28**, 692 (2003).
- [84] R. Tang, P. L. Voss, J. Lasri, P. Devgan, and P. Kumar, *Opt. Lett.* **29**, 2372 (2004).
- [85] P. Kylemark, M. Karlsson, T. Torounidis, and P. A. Andrekson, *J. Lightwave Technol.* **25**, 612 (2007).
- [86] S. Moro, A. Peric, N. Alic, B. Stossel, and S. Radic, *Opt. Express* **18**, 21449 (2010).
- [87] A. Mussot, A. Durécu-Legrand, E. Lantz, C. Simonneau, D. Bayart, H. Maillotte, and T. Sylvestre, *IEEE Photon. Technol. Lett.* **16**, 1289 (2004).
- [88] F. Yaman, Q. Lin, S. Radic, and G. P. Agrawal, *IEEE Photon. Technol. Lett.* **17**, 2053 (2005).
- [89] L. Provino, A. Mussot, E. Lantz, T. Sylvestre, and H. Maillotte, *J. Opt. Soc. Am. B* **20**, 1532 (2003).
- [90] R. M. Jopson and R. E. Tench, *Electron. Lett.* **29**, 2216 (1993).
- [91] K. Inoue, *J. Lightwave Technol.* **12**, 1916 (1994).
- [92] M. E. Marhic, Y. Park, F. S. Yang, and L. G. Kazovsky, *Opt. Lett.* **21**, 1354 (1996).
- [93] C. J. McKinstrie, S. Radic, and A. R. Chraplyvy, *IEEE J. Sel. Topics Quantum Electron.* **8**, 538 (2002); *Opt. Lett.* **27**, 1138 (2002).
- [94] K. K. Y. Wong, M. E. Marhic, K. Uesaka, and L. G. Kazovsky, *IEEE Photon. Technol. Lett.* **14**, 911 (2002).
- [95] S. Radic, C. J. McKinstrie, , A. R. Chraplyvy, et al., *IEEE Photon. Technol. Lett.* **14**, 1406 (2002).
- [96] C. McKinstrie, J. Harvey, S. Radic, and M. Raymer, *Opt. Express* **13**, 9131 (2005).
- [97] D. Méchin, R. Provo, J. D. Harvey, and C. J. McKinstrie, *Opt. Express* **14**, 8995 (2006).
- [98] R. Provo, S. Murdoch, J. D. Harvey, and D. Méchin, *Opt. Lett.* **35**, 3730 (2010).
- [99] S. Radic, C. J. McKinstrie, R. M. Jopson, J. C. Centanni, Q. Lin, and G. P. Agrawal, *Electron. Lett.* **39**, 838 (2003).
- [100] M. Ho, M. E. Marhic, K. Y. K. Wong, and L. G. Kazovsky, *J. Lightwave Technol.* **20**, 469 (2002).
- [101] T. Tanemura and K. Kikuchi, *IEEE Photon. Technol. Lett.* **15**, 1573 (2003).
- [102] S. Radic, C. J. McKinstrie, , R. M. Jopson, et al., *IEEE Photon. Technol. Lett.* **15**, 673 (2003).
- [103] F. Yaman, Q. Lin, G. P. Agrawal, and S. Radic, *Opt. Lett.* **30**, 1048 (2005).
- [104] M. Karlsson, *J. Opt. Soc. Am. B* **15**, 2269 (1998).

- [105] F. Yaman, Q. Lin, S. Radic, and G. P. Agrawal, *IEEE Photon. Technol. Lett.* **16**, 1292 (2004).
- [106] A. Vatarescu, *J. Lightwave Technol.* **5**, 1652 (1987).
- [107] X. Xiao, P. Shum, E. S. Nazemosadat, and C. Yang, *IEEE Photon. Technol. Lett.* **20**, 1231 (2008); *IEEE Photon. Technol. Lett.* **21**, 483 (2009).
- [108] T. Hasegawa, K. Inoue, and K. Oda, *IEEE Photon. Technol. Lett.* **5**, 947 (1993).
- [109] K. K. Y. Wong, M. E. Marhic, K. Uesaka, and L. G. Kazovsky, *IEEE Photon. Technol. Lett.* **14**, 1506 (2002).
- [110] M. E. Marhic, K. K. Y. Wong, and L. G. Kazovsky, *Electron. Lett.* **39**, 350 (2003).
- [111] Q. Lin and G. P. Agrawal, *J. Opt. Soc. Am. B* **21**, 1216 (2004).
- [112] L. Mandel and E. Wolf, *Optical Coherence and Quantum Optics* (Cambridge University Press, 1995), Chap. 10.
- [113] P. O. Hedekvist, M. Karlsson, and P. A. Andrekson, *IEEE Photon. Technol. Lett.* **8**, 776 (1996).
- [114] F. Yaman, Q. Lin, and G. P. Agrawal, *IEEE Photon. Technol. Lett.* **16**, 431 (2004).
- [115] Q. Lin and G. P. Agrawal, *Opt. Lett.* **29**, 1114 (2004).
- [116] P. K. A. Wai and C. R. Menyuk, *J. Lightwave Technol.* **14**, 148 (1996).
- [117] C. J. McKinstrie, H. Kogelnik, R. M. Jopson, S. Radic, and A. V. Kannev, *Opt. Express* **12**, 2033 (2004).
- [118] G. P. Agrawal, *Applications of Nonlinear Fiber Optics*, 2nd ed. (Academic Press, 2008).
- [119] K. O. Hill, B. S. Kawasaki, Y. Fujii, and D. C. Johnson, *Appl. Phys. Lett.* **36**, 888 (1980).
- [120] W. Margulis and U. Österberg, *Opt. Lett.* **12**, 519 (1987).
- [121] M. Nakazawa, K. Suzuki, and H. A. Haus, *Phys. Rev. A* **38**, 5193 (1988).
- [122] J. E. Rothenberg, *Electron. Lett.* **28**, 479 (1992); *IEEE J. Quantum Electron.* **30**, 1463 (1994).
- [123] S. Coen, M. Haelterman, , P. Emplit, et al., *J. Opt. Soc. Am. B* **15**, 2283 (1998); *J. Opt. B* **1**, 36 (1999).
- [124] D. K. Serkland and P. Kumar, *Opt. Lett.* **24**, 92 (1999).
- [125] M. E. Marhic, K. K. Y. Wong, L. G. Kazovsky, and T. E. Tsai, *Opt. Lett.* **27**, 1439 (2002).
- [126] J. E. Sharping, M. Fiorentino, P. Kumar, and R. S. Windeler, *Opt. Lett.* **27**, 1675 (2002).
- [127] S. Saito, M. Kishi, and M. Tsuchiya, *Electron. Lett.* **39**, 86 (2003).
- [128] J. Lasri, P. Devgan, R. Y. Tang, J. E. Sharping, and P. Kumar, *IEEE Photon. Technol. Lett.* **15**, 1058 (2003).
- [129] C. J. S. de Matos, J. R. Taylor, and K. P. Hansen, *Opt. Lett.* **29**, 983 (2004).
- [130] P. S. Devgan, J. Lasri, R. Tang, V. S. Grigoryan, W. L. Kath, and P. Kumar, *Opt. Lett.* **30**, 528 (2005).
- [131] Y. Deng, Q. Lin, F. Lu, G. P. Agrawal, and W. H. Knox, *Opt. Lett.* **30**, 1234 (2005).
- [132] T. Tanemura, C. S. Goh, K. Kikuchi, and S. Y. Set, *IEEE Photon. Technol. Lett.* **16**, 551 (2004).
- [133] E. Ciaramella and S. Trillo, *IEEE Photon. Technol. Lett.* **12**, 849 (2000).
- [134] K. Inoue, *IEEE Photon. Technol. Lett.* **13**, 338 (2001).
- [135] S. Radic, C. J. McKinstrie, R. M. Jopson, J. C. Centanni, and A. R. Chraplyvy, *IEEE Photon. Technol. Lett.* **15**, 957 (2003).
- [136] G. P. Agrawal, *Fiber-Optic Communication Systems*, 4th ed. (Wiley, 2010).
- [137] P. A. Andrekson, N. A. Olsson, J. R. Simpson, T. Tanbun-Ek, R. A. Logan, and M. Haner, *Electron. Lett.* **27**, 922 (1991).

- [138] T. Morioka, H. Takara, S. Kawanishi, T. Kitoh, and M. Saruwatari, *Electron. Lett.* **32**, 832 (1996).
- [139] P. O. Hedekvist, M. Karlsson, and P. A. Andrekson, *J. Lightwave Technol.* **15**, 2051 (1997).
- [140] P. A. Andrekson, *Electron. Lett.* **27**, 1440 (1991).
- [141] M. Westlund, P. A. Andrekson, H. Sunnerud, J. Hansryd, and J. Li, *J. Lightwave Technol.* **23**, 2012 (2005).
- [142] T. Torounidis, M. Westlund, H. Sunnerud, B. E. Olsson, and P. A. Andrekson, *IEEE Photon. Technol. Lett.* **17**, 312 (2005).
- [143] Q. Lin, R. Jiang, C. F. Marki, C. J. McKinstrie, R. Jopson, J. Ford, G. P. Agrawal, and S. Radic, *IEEE Photon. Technol. Lett.* **17**, 2736 (2005).
- [144] D. F. Walls and G. J. Milburn, *Quantum Optics* (Springer, 1994).
- [145] M. O. Scully and M. S. Zubairy, *Quantum Optics* (Cambridge University Press, 1997).
- [146] A. Sizmann and G. Leuchs, in *Progress in Optics*, Vol. 39, E. Wolf, Ed. (Elsevier, 1999), Chap. 5.
- [147] M. D. Levenson, R. M. Shelby, A. Aspect, M. Reid, and D. F. Walls, *Phys. Rev. A* **32**, 1550 (1985).
- [148] R. M. Shelby, M. D. Levenson, S. H. Perlmutter, R. G. DeVoe, and D. F. Walls, *Phys. Rev. Lett.* **57**, 691 (1986).
- [149] N. Gisin, G. Ribordy, W. Tittel, and H. Zbinden, *Rev. Mod. Phys.* **74**, 145 (2002).
- [150] M. Fiorentino, P. L. Voss, J. E. Sharping, and P. Kumar, *IEEE Photon. Technol. Lett.* **14**, 983 (2002).
- [151] X. Li, J. Chen, P. Voss, J. Sharping, and P. Kumar, *Opt. Express* **12**, 3737 (2004).
- [152] J. G. Rarity, J. Fulconis, J. Duligall, W. J. Wadsworth, and P. St. J. Russell, *Opt. Express* **13**, 534 (2005).
- [153] J. Fan, A. Dogariu, and L. J. Wang, *Opt. Lett.* **30**, 1530 (2005).
- [154] J. Fan and A. Migdall, *Opt. Lett.* **30**, 3368 (2005).
- [155] J. Fulconis, O. Alibart, W. J. Wadsworth, P. St. J. Russell, and J. G. Rarity, *Opt. Express* **13**, 7572 (2005).
- [156] H. Takesue and K. Inoue, *Opt. Express* **13**, 7832 (2005).
- [157] Q. Lin, F. Yaman, and G. P. Agrawal, *Opt. Lett.* **31**, 1286 (2006).
- [158] J. Fulconis, O. Alibart, J. L. O'Brien, W. J. Wadsworth, and J. G. Rarity, *Phys. Rev. Lett.* **99**, 120501 (2007).
- [159] J. Fan, A. Migdall, J. Chen, and E. A. Goldschmidt, *IEEE J. Sel. Topics Quantum Electron.* **15**, 1724 (2009).
- [160] H. A. Haus and J. A. Mullen, *Phys. Rev.* **128**, 2407 (1962).
- [161] C. J. McKinstrie and S. Radic, *Opt. Express* **12**, 4973 (2004).
- [162] A. Bogris and D. Syvridis, *IEEE Photon. Technol. Lett.* **18**, 2144 (2006).
- [163] R. Tang, J. Lasri, P. S. Devgan, V. Grigoryan, P. Kumar, and M. Vasilyev, *Opt. Express* **13**, 10483 (2005).
- [164] R. Tang, P. S. Devgan, V. S. Grigoryan, P. Kumar, and M. Vasilyev, *Opt. Express* **16**, 9046 (2008).
- [165] K. Croussore and G. F. Li, *IEEE J. Sel. Topics Quantum Electron.* **14**, 648 (2008).
- [166] J. Kakande, F. Parmigiani, M. Ibsen, P. Petropoulos, and D. J. Richardson, *IEEE Photon. Technol. Lett.* **22**, 1781 (2010).
- [167] Z. Tong, C. Lundström, , P. A. Andrekson, et al., *Nature Photonics* **5**, 430 (2011).

# Highly Nonlinear Fibers

# 11

As seen in the preceding chapters of this book, three major nonlinear effects occurring inside optical fibers—self-phase modulation (SPM), cross-phase modulation (XPM), four-wave mixing (FWM)—are governed by a single nonlinear parameter  $\gamma$ , defined first in Eq. (2.3.30). For most optical fibers  $\gamma$  has values of  $\sim 1 \text{ W}^{-1}/\text{km}$ . It was realized during the 1990s that this value is too small for optical fibers to be useful as a nonlinear medium for applications requiring short lengths. To solve this problem, several new kinds of fibers with  $\gamma > 10 \text{ W}^{-1}/\text{km}$  have been developed, and they are collectively referred to as *highly nonlinear fibers* (HNLFs). This chapter deals with the properties of such fibers. The techniques used to measure the nonlinear parameter are described first in Section 11.1. Sections 11.2–11.5 then focus on four kinds of fibers that have been developed to enhance the nonlinear effects. In each case, dispersive properties of the fibers are also described because they play an important role whenever highly nonlinear fibers are used for practical applications. It will be seen in Chapters 12 and 13 that the combination of unusual dispersive properties and a high value of  $\gamma$  leads to a variety of novel nonlinear effects. Section 11.6 discusses how the design of HNLFs can modify the effective value of the nonlinear parameter in the case of narrow-core fibers.

---

## 11.1 NONLINEAR PARAMETER

The nonlinear parameter  $\gamma$ , defined in Eq. (2.3.30), can be written as  $\gamma = 2\pi n_2/(\lambda A_{\text{eff}})$ , where  $\lambda$  is the wavelength of light and  $A_{\text{eff}}$  is the effective mode area given in Eq. (2.3.31). This area depends on the fiber design, and it can be reduced with a proper design to enhance  $\gamma$ . On the other hand, the nonlinear-index coefficient  $n_2$  is a material parameter related to the third-order susceptibility, as indicated in Eq. (2.3.13). This parameter is fixed for each glass material. Thus, the only practical approach for enhancing  $\gamma$  for silica-based optical fibers is to reduce the effective mode area  $A_{\text{eff}}$ . The use of non-silica glasses provides an alternative approach to designing highly nonlinear fibers. Before focusing on the design of such fibers, it is important to discuss the techniques used to determine  $n_2$  experimentally. Accurate measurements of both  $\gamma$  and  $A_{\text{eff}}$  are necessary for this purpose.

### 11.1.1 Units and Values of $n_2$

Before proceeding, it is important to clarify the units used to express the numerical values of  $n_2$  [1]. The nonlinear part of the refractive index in Eq. (2.3.12) is expressed as  $\delta n_{\text{NL}} = \bar{n}_2 |E|^2$ . In the standard metric system, the electric field  $E$  has units of V/m. As  $\delta n_{\text{NL}}$  is dimensionless, the units of  $\bar{n}_2$  are m<sup>2</sup>/V<sup>2</sup>. In practice, it is more convenient to write the nonlinear index in the form  $\delta n_{\text{NL}} = n_2 I$ , where  $I$  is the intensity of the optical field related to  $E$  as

$$I = \frac{1}{2} \epsilon_0 c n |E|^2. \quad (11.1.1)$$

Here  $\epsilon_0$  is the vacuum permittivity ( $\epsilon_0 = 8.8542 \times 10^{-12}$  F/m),  $c$  is the velocity of light in the vacuum ( $c = 2.998 \times 10^8$  m/s), and  $n$  is the linear part of the refractive index ( $n \approx 1.45$  for silica fibers). The parameter  $n_2$  is related to  $\bar{n}_2$  as indicated in Eq. (2.3.30):

$$n_2 = 2\bar{n}_2 / (\epsilon_0 c n). \quad (11.1.2)$$

Since  $\delta n_{\text{NL}} = n_2 I$  is dimensionless,  $n_2$  has units of m<sup>2</sup>/W.

Extensive measurements of  $n_2$  were first carried out during the 1970s for several kinds of bulk glasses [2–7]. In the case of fused silica glass, a value of  $n_2 = 2.73 \times 10^{-20}$  m<sup>2</sup>/W was measured (with an accuracy of  $\pm 10\%$ ) at a wavelength of 1.06 μm [4]. A compilation of the measurements made at wavelengths ranging from 248 to 1550 nm indicates that the nonlinear-index coefficient  $n_2$  for fused silica exhibits chromatic dispersion such that its value decreases at longer wavelengths [8]. However,  $n_2$  varies slowly with the wavelength in the wavelength region extending from 800 to 1600 nm and its value decreases by 5% or so over this wavelength range.

The earliest measurements of  $n_2$  for silica fibers [9] were carried out in 1978 using SPM-induced spectral broadening of 90-ps optical pulses, obtained from an argon-ion laser operating at near 515 nm. The estimated value of  $3.2 \times 10^{-20}$  m<sup>2</sup>/W from this experiment was used almost exclusively in many studies of the nonlinear effects in optical fibers, even though the measured value of  $\gamma$  depends on several factors. The wavelength region near 1550 nm became relevant for nonlinear fiber optics with the advent of fiber-optic communication systems. The measured value of  $n_2 = 3.2 \times 10^{-20}$  m<sup>2</sup>/W at 515 nm should not be used near 1550 nm as  $n_2$  is reduced by at least 10% because of its frequency dependence.

The growing importance of the nonlinear effects in optical fibers revived interest in the measurements of  $\gamma$  during the 1990s, especially because fiber manufacturers are often required to specify the numerical value of  $\gamma$  for their fibers [10]. Several different experimental techniques have been developed to measure  $n_2$  and applied to different types of fibers [11–20]. They make use of one of the nonlinear effects discussed in earlier chapters. In fact, all of the three major nonlinear effects—SPM, XPM, and FWM—have been used for this purpose. All techniques measure  $\gamma$  and deduce  $n_2$  from it. Table 11.1 summarizes the results obtained in several experiments

**Table 11.1** Measured values of  $n_2$  for different fibers

Method used	$\lambda$ ( $\mu\text{m}$ )	Fiber type	Measured $n_2$ ( $10^{-20} \text{ m}^2/\text{W}$ )	Experimental conditions
SPM	1.319	Silica core	2.36	110-ps pulses [13]
	1.319	DSF	2.62	110-ps pulses [13]
	1.548	DSF	2.31	34-ps pulses [14]
	1.550	DSF	2.50	5-ps pulses [17]
	1.550	Standard	2.20	50-GHz modulation [18]
	1.550	DSF	2.32	50-GHz modulation [18]
	1.550	DCF	2.57	50-GHz modulation [18]
XPM	1.550	Silica core	2.48	7.4-MHz modulation [15]
	1.550	Standard	2.63	7.4-MHz modulation [15]
	1.550	DSF	2.98	7.4-MHz modulation [15]
	1.550	DCF	3.95	7.4-MHz modulation [15]
	1.548	Standard	2.73	10-MHz modulation [19]
	1.548	Standard	2.23	2.3-GHz modulation [19]
FWM	1.555	DSF	2.25	Two CW lasers [12]
	1.553	DSF	2.35	10-ns pulses [16]

using standard, dispersion-shifted fibers (DSFs), or dispersion-compensating fibers (DCFs) in the wavelength regime near 1550 nm. Measured values are found to vary in the range of  $2.2 - 3.9 \times 10^{-20} \text{ m}^2/\text{W}$ . The uncertainty in  $n_2$  values depends, not only on the measurement errors associated with  $\gamma$ , but also on how accurately one can estimate the effective mode area  $A_{\text{eff}}$  from the mode-field diameter. In the remainder of this section, we discuss various measurement techniques and indicate why they may yield different values of  $n_2$  even at the same wavelength.

### 11.1.2 SPM-Based Techniques

The SPM technique makes use of the broadening of the pulse spectrum (see Section 4.1) and was first used in 1978 [9]. As seen from Eq. (4.1.17), this technique actually measures the maximum value of the nonlinear phase shift,  $\phi_{\text{max}}$ , a dimensionless quantity that is related to  $\gamma$  linearly through Eq. (4.1.17). Once  $\gamma$  has been determined,  $n_2$  is estimated from it using the relation  $n_2 = \lambda A_{\text{eff}} \gamma / (2\pi)$ . The accuracy of such measurements depends on how well one can characterize input pulses because SPM-induced spectral broadening is quite sensitive to the shape of optical pulses used in the experiment.

In spite of the uncertainties involved, the SPM technique is often used in practice [20]. In a set of measurements performed in 1994, mode-locked pulses of 110-ps duration

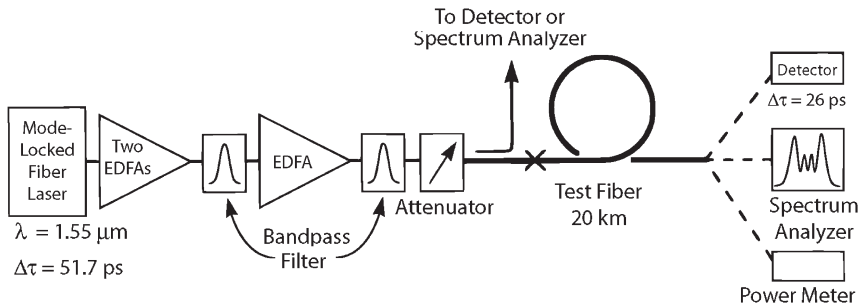


**Figure 11.1** Experimental setup for measuring  $n_2$  using SPM-induced spectral broadening.  
(After Ref. [20]; © 1998 IEEE.)

were obtained from a Nd:YAG laser operating at  $1.319 \mu\text{m}$  [13]. Pulses were broadened spectrally inside the test fiber, and their spectrum measured using a scanning Fabry–Perot interferometer. The input power was adjusted such that the measured spectrum corresponds to one of the shapes shown in Figure 4.2 such that  $\phi_{\max}$  is a multiple of  $\pi/2$ . The effective mode area was calculated from the measured refractive-index profiles of the fiber and used to deduce the value of  $n_2$ . For a silica-core fiber (no dopants inside the core), the measured value of  $n_2$  was  $2.36 \times 10^{-20} \text{ m}^2/\text{W}$  with an uncertainty of about 5%. The measured  $n_2$  values were larger for DSFs (average value  $2.62 \times 10^{-20} \text{ m}^2/\text{W}$ ) because of the contribution of dopants. As discussed in Section 6.6.3, these values are lower by a factor of 8/9 compared with bulk measurements because the fiber used did not maintain the linear state of polarization of launched pulses during their transmission.

The same technique was used in 1998 to measure  $n_2$  of relatively long dispersion-shifted fibers near  $1.55 \mu\text{m}$  [20]. Figure 11.1 shows the experimental setup schematically. A mode-locked fiber laser provided 51.7-ps pulses that were first amplified and filtered and then launched into a 20-km-long test fiber. It was necessary to account for changes in the width and peak power of pulses along the fiber because of its long length. The dispersive and modal characteristics of the test fiber were quantified through separate measurements to ensure accuracy. The NLS equation was then solved to fit the measured spectra and to deduce the values of  $\gamma$  and  $n_2$ . The measured value  $n_2 = 2.45 \times 10^{-20} \text{ m}^2/\text{W}$  is smaller in the  $1.55 \mu\text{m}$  wavelength region compared with its values measured near  $1.3 \mu\text{m}$ . A reduction of about 2% is expected from the frequency dependence of  $n_2$ . The remaining change may be related to different amounts of dopants or measurement errors.

In place of deducing the SPM-induced phase shift from spectral broadening, a related technique deduces it from spectral changes occurring when the light from two lasers operating at slightly different wavelengths is transmitted through the fiber. Such an approach does not require short optical pulses, and measurements can be performed with CW lasers. In a 1996 experiment [18], two CW semiconductor lasers (both DFB type) were used and their wavelength difference (0.3–0.5 nm) was

stabilized by controlling the laser temperature. The optical signal entering the fiber oscillates sinusoidally at the beat frequency ( $\sim 50$  GHz) because of the optical interference and its amplitude is given by

$$E_{\text{in}}(t) = \text{Re}[A_1 \exp(-i\omega_1 t) + A_2 \exp(-i\omega_2 t)] = \text{Re}[A_1 \cos(\Delta\omega t) \exp(-i\omega_{\text{av}} t)], \quad (11.1.3)$$

where  $\Delta\omega = \omega_1 - \omega_2$  is the beat frequency,  $\omega_{\text{av}} = \frac{1}{2}(\omega_1 + \omega_2)$  is the average frequency, and the two fields are assumed to have the same power ( $|A_1| = |A_2|$ ).

When such a signal propagates inside the fiber, the SPM-induced phase shift is also time dependent. Similar to the discussion in Section 4.1.1, if we neglect the effects of fiber dispersion, total optical field at the fiber output is given by

$$E_{\text{out}}(t) = \text{Re}\{A_1 \cos(\Delta\omega t) \exp(-i\omega_{\text{av}} t) \exp[i\phi_{\text{max}} \cos^2(\Delta\omega t)]\}, \quad (11.1.4)$$

where  $\phi_{\text{max}} = 2\gamma P_{\text{av}} L_{\text{eff}}$  and  $P_{\text{av}}$  is the average power of the launched signal. It is easy to see by taking the Fourier transform of Eq. (11.1.4) that the optical spectrum at the fiber output exhibits peaks at multiples of the beat frequency because of the SPM-induced phase shift. The ratio of the peak powers depends only on  $\phi_{\text{max}}$  and can be used to deduce the value of  $n_2$ . In particular, this power ratio for the central and first sideband is given by [18]

$$\frac{P_0}{P_1} = \frac{J_0^2(\phi_{\text{max}}/2) + J_1^2(\phi_{\text{max}}/2)}{J_1^2(\phi_{\text{max}}/2) + J_2^2(\phi_{\text{max}}/2)}. \quad (11.1.5)$$

This equation provides  $\phi_{\text{max}}$  from a simple measurement of the power ratio, which can be used to determine  $\gamma$  and  $n_2$ . For standard telecommunication fibers, the value of  $n_2$  was found to be  $2.2 \times 10^{-20} \text{ m}^2/\text{W}$ . This technique was also used to measure  $n_2$  for several DSFs and DCFs with different amounts of dopants (see Table 11.1). The main limitation of this technique is that it cannot be used for long fibers for which dispersive effects become important. In fact, the fiber length and laser powers should be properly optimized for a given fiber to ensure accurate results [21].

The SPM-induced phase shift can also be measured with an interferometric technique. In one experiment, the test fiber was placed inside a fiber loop that acted as a Sagnac interferometer [17]. Mode-locked pulses of  $\approx 5$ -ps width were launched into the loop such that pulses acquired a large SPM-induced phase shift in one direction (say, clockwise). In the other direction, a 99:1 coupler was used to reduce the peak power so that the pulses acquired mostly a linear phase shift. An autocorrelator at the loop output was used to deduce the nonlinear phase shift and to obtain  $n_2$  from it. A CW laser can also be used with a Sagnac interferometer [22]. Its use simplifies the technique and avoids the uncertainties caused by the dispersive effects. Figure 11.2 shows the experimental setup schematically. The interferometer is unbalanced by using a fiber coupler that launches unequal amounts of laser power in the counter-propagating direction, and the transmitted power is measured for low and high values of the input power. The transmissivity of such a Sagnac interferometer changes at high power levels because of the SPM-induced phase shift and thus provides a way to

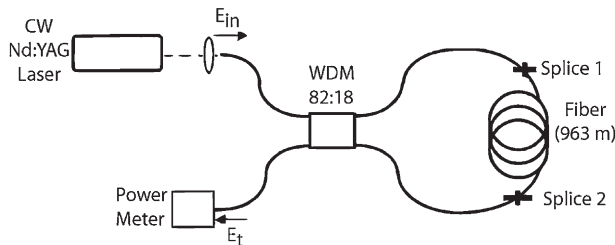


**Figure 11.2** Experimental setup for measuring  $n_2$  using a Sagnac interferometer and a CW laser. (After Ref. [22]; © 1998 OSA.)

measure it. The measured value of  $n_2$  was  $3.1 \times 10^{-20} \text{ m}^2/\text{W}$  at 1064 nm for a fiber whose core was doped with 20% (by mol) of germania.

A self-aligned Mach–Zehnder interferometer (MZI) has also been used for measuring  $n_2$  [23]. In this scheme, pulses pass through a MZI twice after being reflected by a Faraday mirror. The path lengths in that the two arms of MZI are different enough that the two pulses are separated by more than their widths at the MZI output and thus do not interfere. They pass through the fiber twice and accumulate the SPM-induced nonlinear phase shift. After a complete round trip, a single pulse has three different delays as it may pass twice through the long arm, twice through the short arm, or once through long and short arms. In the last case, the power at the detector depends on the phase relationship between the interfering signals and can be used to measure the nonlinear phase shift. Such an interferometer is called self-aligned because the path lengths of the two interfering signals are automatically matched.

### 11.1.3 XPM-Based Technique

The XPM-induced phase shift was used as early as 1987 to measure  $n_2$  [11]. A 1995 experiment employed a pump–probe configuration in which the pump and probe signals were obtained from CW sources [15]. Figure 11.3 shows the experimental setup schematically. When the pump light was modulated at a low frequency ( $<10 \text{ MHz}$ ), the probe spectrum developed FM sidebands because of the XPM-induced phase shift.

The theory behind the formation of the FM sidebands is similar to that discussed earlier in the SPM case when two CW lasers were used. The main difference is that one of the lasers acts as the pump and its intensity is changed in a periodic fashion using a modulator. As a result, the phase shift induced on the probe through XPM beam becomes time dependent. If we again neglect the dispersive effects, the probe field at the fiber output can be written as

$$E_2(t) = \text{Re}\{A_2 \exp(-i\omega_2 t) \exp[i b \phi_{\max} \cos^2(2\pi f_m t)]\}, \quad (11.1.6)$$

where  $\phi_{\max} = 2\gamma P_0 L_{\text{eff}}$ ,  $f_m$  is the modulation frequency,  $P_0$  is the peak power of the pump beam, and the parameter  $b$  is defined in Eq. (6.2.11). If we calculate the probe spectrum by taking the Fourier transform of Eq. (11.1.6), the spectrum is found to

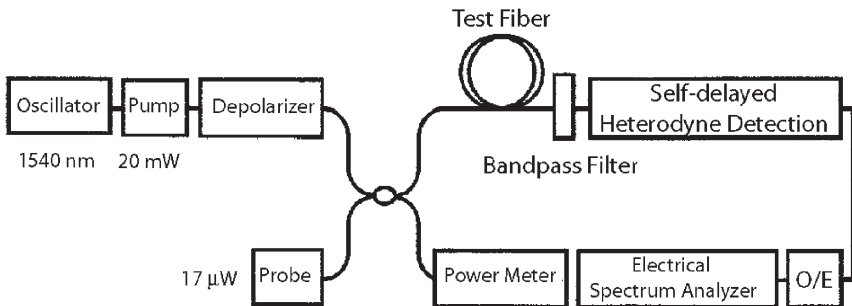


**Figure 11.3** Pump–probe configuration for measuring  $n_2$  using a technique based on the XPM-induced phase shift. (After Ref. [15]; © 1995 OSA.)

exhibit peaks at multiples of  $f_m$  because of the XPM-induced phase shift. As before, the power ratio of two neighboring peaks depends on  $\phi_{\max}$  and can be used to deduce the value of  $n_2$ .

As discussed in Section 6.2.2, the XPM-induced phase shift depends on the relative states of polarizations associated with the pump and probe beams through the parameter  $b$ . If the state of polarization is not maintained inside the test fiber for the two beams, one must make sure that the measured value is not affected by such polarization effects. In practice, pump light is depolarized before it enters the fiber [15]. Under such conditions, the relative polarization between the pump and probe varies randomly, and the measured value of nonlinear phase shift corresponds to  $b = 2/3$ . In the experimental setup shown in Figure 11.2, two CW beams differing in their wavelengths by about 10 nm acted as the probe and the pump. The pump intensity was modulated at a relatively low frequency of 7.36 MHz. XPM inside the fiber converted pump-intensity modulations into phase modulations for the probe. A self-delayed heterodyne technique was used to measure the nonlinear phase shift as a function of pump power. A Sagnac interferometer can also be used to measure the XPM-induced phase shift and to deduce  $n_2$  from it [24].

The values of  $n_2$  obtained with the XPM technique for several kinds of fibers are listed in Table 11.1. They are consistently larger than those obtained with the SPM-based short-pulse technique. The explanation for this discrepancy is related to the electrostrictive contribution to  $n_2$  that occurs for pulse widths  $> 1$  ns (or modulation frequencies  $< 1$  GHz). This issue is discussed later in this section.

#### 11.1.4 FWM-Based Technique

The nonlinear phenomenon of FWM can also be used to estimate  $n_2$ . As discussed in Chapter 10, FWM produces sidebands whose amplitudes and frequencies depend on the nonlinear parameter  $\gamma$ . When two CW beams at frequencies  $\omega_1$  and  $\omega_2$  are launched into the fiber simultaneously, the spectrum at the fiber output develops two dominant sidebands at frequencies  $2\omega_1 - \omega_2$  and  $2\omega_2 - \omega_1$  when the phase-matching

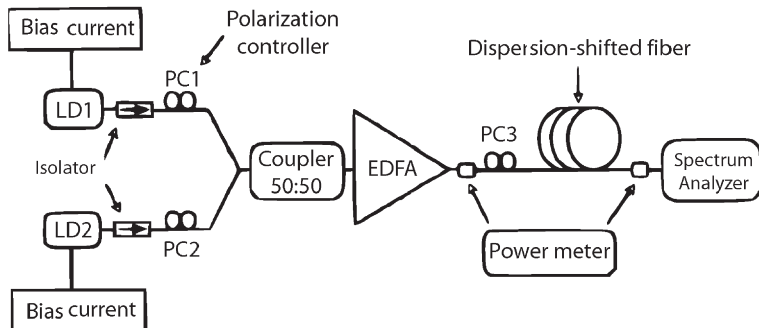


**Figure 11.4** Experimental setup for measuring  $n_2$  using a technique based on FWM-induced sidebands. (After Ref. [12]; © 1993 IEEE.)

condition is approximately satisfied. The power levels of these sidebands depend on the pump powers together with the nonlinear parameter  $\gamma$ .

In a 1993 experiment, the CW output of two DFB lasers, operating near  $1.55\text{ }\mu\text{m}$  with a wavelength separation of  $0.8\text{ nm}$ , was amplified by using a fiber amplifier and then injected into a  $12.5\text{-km-long DSF}$  [12]. Figure 11.4 shows the experimental setup schematically. To suppress the onset of SBS, the line widths of two lasers were increased to beyond  $500\text{ MHz}$  by modulating the laser bias currents. The test fiber had a relatively small dispersion of  $0.063\text{ ps}/(\text{nm km})$  near  $1.55\text{ }\mu\text{m}$  to ensure phase matching. The effective mode area of the fiber was estimated to be  $50\text{ }\mu\text{m}^2$  from its  $8\text{ }\mu\text{m}$  spot size. The powers in the FWM sidebands were measured and used to estimate a value of  $n_2 = 2.25 \times 10^{-20}\text{ m}^2/\text{W}$  for the test fiber.

The modulation instability can be thought of as a special case of FWM (see Section 10.3.2). The main difference is that only a single pump beam is needed at the fiber input. As discussed in Section 5.1, two spectral sidebands centered at the frequencies  $\omega_0 \pm \Omega$  appear at the fiber output, where  $\omega_0$  is the pump frequency. The frequency shift  $\Omega$  as well as the sideband amplitudes depend on the nonlinear parameter  $\gamma$  and thus can be used to deduce the value of  $n_2$ . In a 1995 experiment [16], a DFB laser operating at  $1.553\text{ }\mu\text{m}$  was modulated externally to produce  $25\text{-ns pulses}$  at a repetition rate of  $4\text{ MHz}$ . Such pulses were amplified using two cascaded fiber amplifiers and then launched into a  $10.1\text{ km}$  of DSF. Spontaneous-emission noise added by the amplifiers provided a seed for the modulation instability. As a result, the optical spectrum at the fiber output exhibited two well-developed sidebands, similar to those seen in Figure 5.2. The amplitude of these sidebands changed with the peak power of pulses and was used to deduce a value  $n_2 = 2.35 \times 10^{-20}\text{ m}^2/\text{W}$  for the test fiber.

### 11.1.5 Variations in $n_2$ Values

As seen in Table 11.1, the measured values of  $n_2$  for silica fibers vary in a relatively wide range extending from  $2.23$  to  $3.95 \times 10^{-20}\text{ m}^2/\text{W}$ , depending on the fiber

type and the technique used. To understand the reason behind such a large range of variations in  $n_2$  values, one should first note that the core and the cladding of silica fibers are doped with other materials (such as  $\text{GeO}_2$  and fluorine) to ensure that their refractive indices differ by a small amount (typically  $<1\%$ ). These dopants affect the measured value of  $n_2$  enough that it is expected to be different for various DSFs made with different amounts of dopants inside the fiber core. Several studies have quantified changes in  $n_2$  expected because of dopants used in the core and cladding of a silica fiber [25–27].

Figure 11.5 shows how  $n_2$  varies for fibers fabricated with different amounts of dopants [27]. The doping level is quantified through the relative index difference  $\Delta = (n_1^2 - n_0^2)/2n_1^2$ , where  $n_0$  is the refractive index of pure silica and  $n_1$  is its value when the fiber core is doped  $\text{GeO}_2$  (solid line) or the cladding is doped with fluorine. These values are estimated using an empirical relation first proposed in 1978 [28]. As shown by the straight lines in Figure 11.5,  $n_2$  varies almost linearly with  $\Delta$  such that it increases for fibers whose core is doped with  $\text{GeO}_2$  and decreases for fibers whose cladding is doped with fluorine. The experimental data obtained for several fibers with different doping levels agree with this linear dependence on  $\Delta$ . Based on this linear dependence,  $n_2$  is expected to exceed  $3.5 \times 10^{-20} \text{ m}^2/\text{W}$  for a fiber whose core is doped with  $\text{GeO}_2$  such that  $\Delta = 0.02$ . This is the case in practice for DCFs that are designed with high doping levels to shift their zero-dispersion wavelength (ZDWL) beyond  $1.6 \mu\text{m}$ . Indeed, the measured values of  $n_2$  are close to  $4 \times 10^{-20} \text{ m}^2/\text{W}$  for the DCFs [25].

The dopant dependence of  $n_2$  does not explain fully the spread in  $n_2$  seen in Table 11.1. It turns out that the length of the fiber used in the experiment also affects the

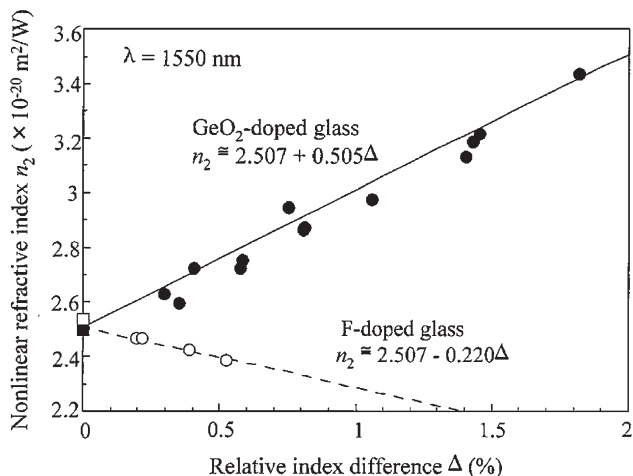


Figure 11.5 Values of  $n_2$  as a function of the relative index difference  $\Delta$  when fiber core is doped with  $\text{GeO}_2$  (filled circles) or cladding is doped with fluorine (empty circles). Straight lines show a linear fit to the data. (After Ref. [27]; © 2002 IEEE.)

measurements. The reason is related to the fact that most optical fibers do not maintain the state of polarization during the propagation of light. If the polarization state changes randomly along the fiber length, one measures an average value of  $\gamma$  that is reduced by a factor of 8/9 (see Section 6.6.3), compared with the value expected for bulk samples that maintain the linear polarization of the incident light [29]. If the standard relation  $\gamma = 2\pi n_2/(\lambda A_{\text{eff}})$  is used to deduce  $n_2$ , the resulting value would be smaller by a factor of 8/9. Of course, one can account for the polarization effects by simply multiplying this value by 9/8.

The measured value of  $n_2$  is also affected by the width of optical pulses used during the experiment. It turns out that the  $n_2$  value is considerably larger under CW or quasi-CW conditions in which pulse width exceeds 10 ns. The reason is that two other mechanisms, related to molecular motion (Raman scattering) and excitation of acoustic waves through electrostriction (Brillouin scattering), also contribute to  $n_2$ . However, their relative contributions depend on whether the pulse width is longer or shorter than the response time associated with the corresponding process. For this reason, one should be careful when comparing measurements made using different pulse widths.

The Raman contribution to the nonlinear susceptibility has been discussed in Section 2.3.2. The first and second terms in Eq. (2.3.38) represent the electronic (Kerr) and the nuclear (Raman) contributions, respectively. When pulse width is much larger than the duration of the Raman response function  $h_R(t)$ , we can treat  $h_R(t)$  as a delta function, and the electrons and nuclei contribute to  $n_2$  fully. This is the case in practice for pulses with widths  $>1$  ps. In contrast, the Raman contribution nearly vanishes when pulse width is  $<50$  fs, and  $n_2$  value is reduced by a factor of  $1 - f_R \approx 0.82$  for such ultrashort pulses. As the shortest pulse width for the data given in Table 11.1 is about 5 ps, the Raman contribution is fully included in all cases. In a 2005 experiment [30], the electronic and Raman contributions were measured simultaneously. The measured value of the electronic part was  $1.81 \times 10^{-20} \text{ m}^2/\text{W}$  (accuracy  $\pm 5\%$ ) for a fiber whose core was made of pure silica. This value confirms that the Raman contribution is indeed in the range 18–20%. A more detailed treatment of the Raman susceptibility shows that the strength of the Raman contribution depends on the dopant concentration within the fiber core [31].

The electrostrictive contribution to nonlinear index  $n_2$  has its origin in the excitation of acoustic waves when light propagates through a fiber [32–34]. We can estimate its magnitude from the theory of Section 9.4.1. An acoustic wave creates density variations whose dynamics are governed by Eq. (9.4.1). A change in glass density by  $\rho'$  changes the dielectric constant of the medium by a small amount  $\Delta\epsilon = (d\epsilon/d\rho)\rho'$ . Noting that  $\epsilon = n^2$ , the change in refractive index is found to be

$$\Delta n(t) = \frac{\Delta\epsilon}{2n} = \frac{\gamma_e}{2n\rho_0} \rho'(t) = \frac{\gamma_e}{2n\rho_0} \int_0^t R_a(t-t') |E(t')|^2 dt', \quad (11.1.7)$$

where  $\gamma_e = \rho_0(d\epsilon/d\rho)$  is the electrostrictive constant introduced in Section 9.1,  $\rho_0$  is the steady-state value of material density, and  $R_a(t)$  is the acoustic response

function obtained by solving Eq. (9.4.1). Using  $E(t) = [E_0 f_p(t)]^{1/2} \exp(-i\omega_0 t)$ , where  $E_0$  is the peak value and  $f_p(t)$  governs the pulse shape, the final result can be written as [32]

$$\Delta n(t) = n_2^A I_0 \int_0^t h_a(t-t') |f_p(t')|^2 dt', \quad (11.1.8)$$

where  $n_2^A = \gamma_e^2 / (8c\rho_0 n^2 v_A^2)$ ,  $I_0$  is the peak intensity of the pulse, and  $h_a(t)$  is the normalized form of the acoustic response function  $R_a(t)$ . Using  $\gamma_e = 1.5$ ,  $\rho_0 = 2210 \text{ kg/m}^3$ ,  $v_A = 5.96 \text{ km/s}$ , and  $n = 1.45$ , we find  $n_2^A = 0.56 \times 10^{-20} \text{ m}^2/\text{W}$ . This value is about 25% of  $n_2 = 2.2 \times 10^{-20} \text{ m}^2/\text{W}$ , the value expected for silica-core fibers. Under CW or quasi-CW (pulse widths > 100 ns),  $h_a(t)$  can be replaced with a delta function. The acoustic contribution then attains its maximum value, and the total  $n_2$  is close to  $2.76 \times 10^{-20} \text{ m}^2/\text{W}$ .

It is clear from the preceding discussion that the largest value of  $n_2$  is expected for measurements performed using CW beams or long optical pulses. The XPM technique has been used to study the frequency dependence of the electrostrictive contribution by changing the pump-modulation frequency from 10 MHz to 3 GHz [34]. As seen in Table 11.1, the measured value is  $2.73 \times 10^{-20} \text{ m}^2/\text{W}$  at 10 MHz (pulse width 100 ns) but is reduced to  $2.23 \times 10^{-20} \text{ m}^2/\text{W}$  when the modulation frequency is increased to 2.3 GHz (pulse width < 1 ns). The electrostrictive contribution should be kept in mind when comparing the data from different experiments.

What nominal value of  $n_2$  should be used for estimating the nonlinear parameter  $\gamma$  used in this book? An appropriate recommendation for fibers whose core is made of pure silica is  $n_2 = 2.75 \times 10^{-20} \text{ m}^2/\text{W}$  for pulses wider than 10 ns, but this value should be reduced to  $2.2 \times 10^{-20} \text{ m}^2/\text{W}$  for pulse widths ranging from 1 ps to 1 ns [35–38]. For femtosecond pulses, the Raman contribution is smaller, as discussed in Section 2.3, and  $n_2$  may become as small as  $1.8 \times 10^{-20} \text{ m}^2/\text{W}$ . The  $n_2$  value is higher for fibers whose cores are doped with  $\text{GeO}_2$  and increases by an amount  $\approx 0.5\Delta$ , where  $\Delta$  is the relative core-cladding index difference (%). For standard fibers with  $\Delta = 0.3\%$ , the  $n_2$  value is expected to increase by 0.15 and is thus close to  $2.9 \times 10^{-20} \text{ m}^2/\text{W}$  under quasi-CW conditions.

A natural question one may ask is how the nonlinear effects can be enhanced inside an optical fiber. One can increase  $n_2$  by doping the core but this increase is limited in practice to a factor of 2 or so. A much more dramatic enhancement is possible by controlling the effective mode area. This parameter is used to enhance the value of the nonlinear parameter in highly nonlinear fibers. We turn to the design of such fibers in the following sections.

## 11.2 FIBERS WITH SILICA CLADDING

A simple way to enhance the value of the nonlinear parameter  $\gamma$  consists of reducing the core diameter of a silica fiber, while also controlling its refractive-index profile, because  $A_{\text{eff}}$  depends on both the core size and the doping levels that determine how

tightly the mode is confined to the core [39]. For example, dispersion-shifted fibers, with a core diameter of  $6\text{ }\mu\text{m}$  or so, have  $A_{\text{eff}}$  close to  $50\text{ }\mu\text{m}^2$  compared with the standard fibers for which  $A_{\text{eff}} \approx 75\text{ }\mu\text{m}^2$ . The situation is even more favorable for dispersion-compensating fibers in which  $A_{\text{eff}}$  is close to  $20\text{ }\mu\text{m}^2$ , and  $\gamma$  is enhanced by a factor of 4 compared with its value for standard fibers. Even though such fibers were originally developed for controlling fiber dispersion, they were used during the 1990s for generating supercontinuum and making Raman amplifiers because of the enhanced nonlinear effects inside them [40–43].

The same approach has been used to develop new kinds of highly nonlinear fibers with controlled dispersive properties [44–47]. Included among such fibers are the *dispersion-decreasing* fibers, in which the magnitude of dispersion parameter  $D$  decreases along the length of fiber [44], and the *dispersion-flattened* fibers in which the slope of the dispersion parameter  $D$  is reduced to values as small as  $0.0002\text{ ps/km nm}^2$  [45]. As early as 1999, dispersion-shifted fibers with  $\gamma$  close to  $20\text{ W}^{-1}/\text{km}$  were fabricated [39] by controlling the doping levels within the core and the cladding such that the optical mode was confined so tightly to the core that  $A_{\text{eff}}$  was only  $10.7\text{ }\mu\text{m}^2$ . Moreover, the dispersion could be flattened over a wavelength range  $>100\text{ nm}$  by adopting the depressed-cladding design shown in Figure 11.6a. In this design, the refractive index is reduced to below that of silica within an inner-cladding region surrounding the core by doping it with fluorine. The diameter of inner cladding plays an important role and it can be used to control the dispersive properties of the fiber. Figure 11.6b shows the calculated dispersion spectrum  $D(\lambda)$  for several dispersion-flattened fibers with different values of the inner-cladding radius  $b$  while maintaining  $a/b = 0.58$ , where  $a$  is the core radius. Even though  $\gamma$  at a wavelength of  $1.55\text{ }\mu\text{m}$  was only near  $3.2\text{ W}^{-1}/\text{km}$  for such fibers, their low losses ( $0.22\text{ dB/km}$ ), relatively flat dispersion, and long lengths (1 km or more) still made them suitable for nonlinear applications.

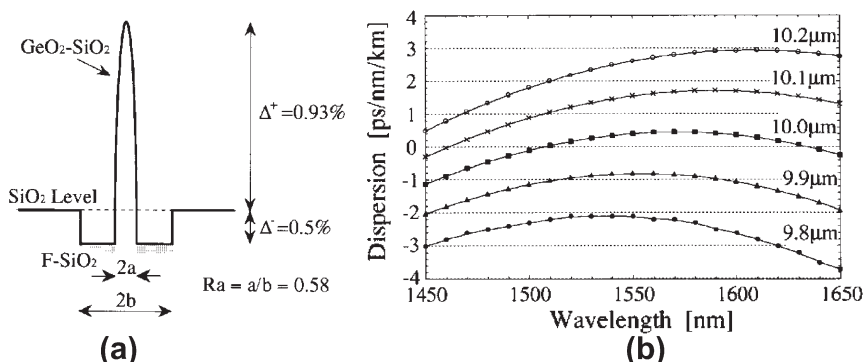


**Figure 11.6** (a) Refractive-index profile for a dispersion-flattened fiber with the depressed-cladding design; (b) calculated dispersion as a function of wavelength for several values of the inner-cladding diameter. (After Ref. [39]; © 1999 IEEE.)

The values of the nonlinear parameter  $\gamma$  for most highly nonlinear fibers with silica-based core and cladding are in the range of  $10\text{--}20 \text{ W}^{-1}/\text{km}$  [45]. It is difficult to increase  $\gamma$  much beyond this range because one cannot reduce the core diameter to lower and lower values without loss of the mode confinement. The reason is easy to understand from the  $V$  parameter given in Eq. (1.2.2). If we approximate  $n_1^2 - n_c^2$  by  $2n_1^2\Delta$ , where  $\Delta = (n_1 - n_c)/n_1 \ll 1$  is the relative index step at the core-cladding interface, we can write the  $V$  parameter as

$$V = (2\pi a n_1/\lambda) \sqrt{2\Delta}, \quad (11.2.1)$$

where  $n_1$  is the core index,  $n_c$  is the cladding index, and  $\lambda$  is the wavelength of light launched into the fiber. For a single-mode fiber  $V < 2.405$  is required. As  $a$  is reduced,  $V$  decreases, and the optical mode is confined less and less as it extends farther into the cladding. One can maintain  $V$  at its original value if  $\Delta$  is increased while reducing  $a$  such that  $a^2\Delta$  keeps the same value.

The mode-confinement issue can be made more explicit if we use the definition of the effective mode area given in Eq. (2.3.31) to calculate the nonlinear parameter  $\gamma$  [48]. As discussed in Section 2.3.1,  $A_{\text{eff}}$  equals  $\pi w^2$  when the mode profile  $F(x, y)$  is approximated with a Gaussian function of width  $w$ , as indicated in Eq. (2.2.14). Since the mode radius  $w$  can be related to  $V$  as  $w = a/\sqrt{\ln V}$  [49], the nonlinear parameter  $\gamma$  becomes

$$\gamma(V) = \frac{2n_2 \ln V}{\lambda a^2} = (4\pi n_1)^2 (n_2 \Delta / \lambda^3) \frac{\ln V}{V^2}, \quad (11.2.2)$$

where Eq. (11.2.1) was used to eliminate the core radius. If we maximize  $\gamma$  by setting  $d\gamma/dV = 0$ , we find that the maximum value occurs for a specific value of  $V$  given by  $V = \sqrt{e} \approx 1.65$ . When core diameter is reduced such that  $V < 1.65$ , the optical mode spreads farther into the cladding, resulting in smaller values of  $\gamma$ . Typically  $\Delta < 0.005$  for optical fibers. Even if we use  $\Delta = 0.05$ , a relatively large value, the core diameter  $2a \approx 0.7V\lambda$  from Eq. (11.2.1), indicating that the optimum value of the core diameter is close to  $1.8 \mu\text{m}$  at wavelengths near  $1.55 \mu\text{m}$ . From Eq. (11.2.2), the maximum value of  $\gamma$  is about  $21 \text{ W}^{-1}/\text{km}$  for highly nonlinear fibers with a silica cladding.

## 11.3 TAPERED FIBERS WITH AIR CLADDING

A simple approach for reducing the core diameter to below  $2 \mu\text{m}$ , while maintaining the confinement of the optical mode to the fiber core, consists of replacing the cladding material with air. Since  $n_2 \approx 1$  for an air cladding, the index step at the core-cladding interface is about 0.45 for silica-core fibers ( $\Delta = 0.31$ ). Such a large index step keeps the mode confined to the core even when the core diameter is close to  $1 \mu\text{m}$ .

It is not easy to make narrow-core fibers with air cladding. A technique, used as early as 1993 to enhance the self-phase modulation effects [50], tapers down the

silica cladding of a standard fiber from a diameter of 125  $\mu\text{m}$  to 2  $\mu\text{m}$  or so [51–56]. Tapering of optical fibers was first carried out during the 1970s for making fiber couplers by heating and stretching the fiber [57]. Heating can be accomplished with a flame torch, but a CO<sub>2</sub> laser has also been used in recent years [58–61]. As the laser light is absorbed, the heat generated softens the fiber. Suitable weights attached to the two fiber ends provide the force that pulls the fiber and reduces its diameter. The fiber diameter is monitored continuously during the stretching process, and the laser is turned off when the desired diameter has been reached. The end result is a fiber whose cladding diameter narrows down from 125  $\mu\text{m}$  to about 2  $\mu\text{m}$  in two transition regions that surround a central region of 20–30 cm length. As an example, Figure 11.7 shows microphotographs of (a) the fiber before tapering, (b) the transition region, and (c) the central region with a narrow core [54]. It should be stressed that the core of the original fiber becomes so thin in the central region that it is unable to confine the incident light. The cladding of the original fiber acts as a core and confines light, with the surrounding air acting as a cladding.

The important question is: how large is the nonlinear parameter  $\gamma$  in the central thin region of a tapered fiber? The standard definition of  $\gamma$  given in Eq. (2.3.29) cannot be used because  $n_2$  is not the same in the core and the cladding. Rather, as indicated in Eq. (2.3.20),  $\gamma$  should be defined as

$$\gamma = \frac{2\pi}{\lambda} \frac{\iint_{-\infty}^{\infty} n_2(x, y)|F(x, y)|^4 dx dy}{(\iint_{-\infty}^{\infty} |F(x, y)|^2 dx dy)^2}. \quad (11.3.1)$$

The integrals can be performed analytically if we approximate the mode profile with a Gaussian shape given in Eq. (2.2.14) and use  $F(x, y) = \exp(-\rho^2/w^2)$ , where  $\rho$  is the radial coordinate and  $w$  is the mode-field radius. If we assume for simplicity that  $n_2 = 0$  for air, we obtain [48]

$$\gamma = \frac{2n_2}{\lambda w^2} [1 - \exp(-4a^2/w^2)] = \frac{2n_2}{\lambda a^2} \ln V \left(1 - \frac{1}{V^4}\right), \quad (11.3.2)$$

where we used the relation  $a/w \approx \sqrt{\ln V}$  [49].

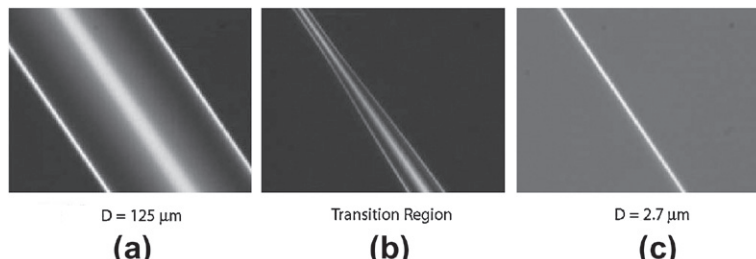


**Figure 11.7** Microphotographs of (a) the original single-mode fiber, (b) the transition region, and (c) the central region with a narrow core. (After Ref. [54]; © 2004 OSA.)

At this point, it is important to remember that the  $V$  parameter itself depends on the core radius as  $V = (2\pi a/\lambda)(n_1^2 - 1)^{1/2}$ , where we used  $n_c = 1$  for the refractive index of air cladding. As an example, for a tapered fiber with  $2\text{-}\mu\text{m}$  core diameter ( $a = 1\text{ }\mu\text{m}$ ),  $V \approx 7$  at a wavelength near  $1\text{ }\mu\text{m}$  if we use  $n_1 = 1.45$  for the refractive indices of silica core. For these values  $\gamma$  is nearly  $100\text{ W}^{-1}/\text{km}$  from Eq. (11.3.2). Clearly, a tapered fiber with a  $2\text{ }\mu\text{m}$  diameter is a highly nonlinear fiber as  $\gamma$  is enhanced for it by a factor of 50 compared with standard fibers. Such large values of  $\gamma$  are a direct consequence of the strong mode confinement resulting from air cladding. The effective mode area of a  $2\text{ }\mu\text{m}$  diameter tapered fiber is only about  $1.6\text{ }\mu\text{m}^2$  if we use  $A_{\text{eff}} = \pi w^2 = \pi a^2 / \ln V$ . It is also important to note that such a fiber supports multiple modes since its  $V$  parameter does not satisfy the single-mode condition  $V < 2.405$ .

The nonlinear parameter  $\gamma$  can be enhanced even further for tapered fibers by reducing their core diameter to below  $2\text{ }\mu\text{m}$ . Moreover, if the fiber is designed such that  $V < 2.405$ , it would support a single mode. It is evident from Eq. (11.3.2) that  $\gamma$  can be maximized for a specific value of  $V$ . For this purpose, we first express  $a$  in terms of  $V$  in Eq. (11.3.2) and obtain

$$\gamma(V) = \left(8\pi^2 n_2 / \lambda^3\right) \left(n_1^2 - 1\right) \frac{\ln V}{V^2} \left(1 - \frac{1}{V^4}\right), \quad (11.3.3)$$

where we used  $n_2 = 1$  for the air cladding. By setting  $d\gamma/dV$  equals 0,  $\gamma$  is found to become maximum for  $V \approx 1.85$  [48], and the maximum value is about  $370\text{ W}^{-1}/\text{km}$  if we use  $n_1 = 1.45$  and  $\lambda = 1\text{ }\mu\text{m}$ .

Dispersive properties of tapered fibers are also quite different than those of conventional fibers and depend strongly on their core diameter. They can be studied by solving the eigenvalue equation (2.2.8) numerically for specific values of the radius  $a$  and the refractive index  $n_1(\omega)$  of the tapered core with  $n_2 = 1$  for the cladding. The dispersion of the silica material can be included by employing the Sellmeier equation (1.2.6). The solution of Eq. (2.2.8) for  $m = 1$  provides the propagation constant  $\beta(\omega)$ , or the effective refractive index of the fundamental fiber mode, as a function of  $\omega$ . The  $m$ th-order dispersion parameter can then be calculated using  $\beta_m = (d^m \beta / d\omega^m)_{\omega=\omega_0}$ , where  $\omega_0$  is the carrier frequency of the optical pulse launched into the fiber.

Figure 11.8 shows the wavelength dependence of the second- and the third-order dispersion parameters,  $\beta_2$  and  $\beta_3$ , calculated numerically with this approach for several values of the core diameter  $d \equiv 2a$  of a tapered fiber. The main point to note is that the ZDWL of the fiber shifts toward visible wavelengths as the core diameter is reduced to below  $3\text{ }\mu\text{m}$ . This feature is of practical significance because it allows the dispersion to become anomalous at wavelengths near  $800\text{ nm}$ , where Ti:sapphire lasers provide intense ultrashort pulses routinely. As a result, optical solitons can form inside tapered fibers at such wavelengths. Figure 11.8b shows that  $\beta_3$  is also enhanced for tapered fibers. This feature suggests that higher-order dispersive effects become more important for such fibers.

One may ask how narrow the core of a tapered fiber can be made and how the properties of such fibers change when the core diameter is reduced to below  $1\text{ }\mu\text{m}$ . There has been considerable practical interest in such nanoscale fibers in recent years,

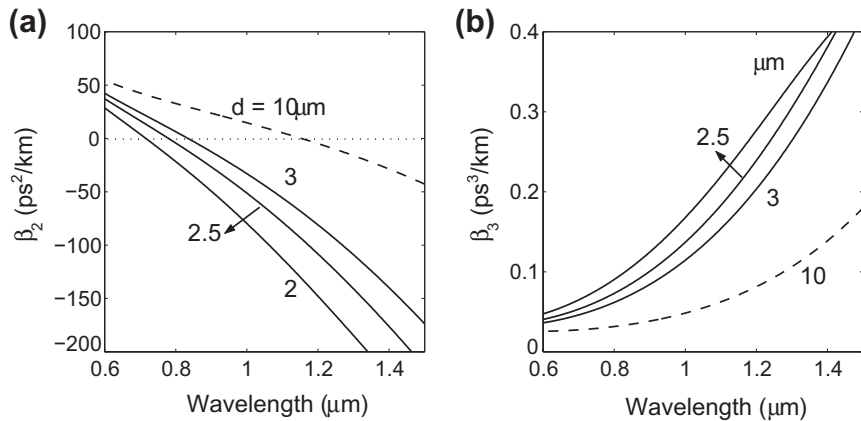


**Figure 11.8** (a) Second- and (b) third-order dispersion parameters as a function of wavelength  $\lambda$  for several values of the core diameter  $d$  for a tapered fiber with a silica core and air cladding.

and their modal, nonlinear, and dispersive properties have been studied in detail [62–66]. It turns out that the nonlinear parameter  $\gamma$  peaks when the core diameter is about 75% of the wavelength of light transmitted through such a fiber. Figure 11.9 shows (a) the dimensionless quantity  $\gamma \lambda^3/n_2$  as a function of wavelength and (b) the dispersion parameter  $D(\lambda)$  for several values of the core diameter  $d = 2a$  using  $n_1 = 1.45$  for the silica core [65]. These curves are obtained numerically without employing the Gaussian approximation for the mode profile. The mean-field diameter (MFD) of the optical mode, shown by a dashed line, attains its minimum value of  $0.816\lambda$  when the core diameter is  $0.74\lambda$ . At that point, the nonlinear parameter  $\gamma$  attains its maximum

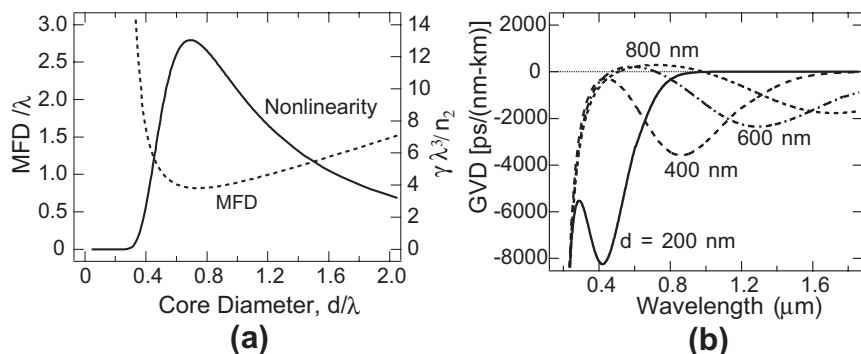


**Figure 11.9** (a) The quantity  $\gamma \lambda^3/n_2$  and (b) GVD parameter  $D(\lambda)$  for several values of the core diameter  $d$  for a tapered fiber with a silica core ( $n_1 = 1.45$ ) and air cladding. The mean-field diameter (MFD) is also shown by a dashed line. (After Ref. [65]; © 2004 OSA.)

value. This value scales with wavelength as  $\lambda^{-3}$  and is close to  $662 \text{ W}^{-1}/\text{km}$  at  $\lambda = 0.8 \mu\text{m}$  if we use  $n_2 = 2.6 \times 10^{-20} \text{ m}^2/\text{W}$ .

The dispersive properties of a tapered fiber are quite sensitive to its core size. As seen in Figure 11.9b, the wavelength dependence of this parameter displays qualitatively different features as the core diameter is varied from 200 to 800 nm. A standard single-mode fiber has a core diameter of about  $8 \mu\text{m}$  before tapering such that  $D(\lambda) = 0$  at a wavelength near  $1.3 \mu\text{m}$ . Such a fiber exhibits normal GVD [ $D(\lambda) < 0$ ] at wavelengths shorter than the ZDWL. As seen in Figure 11.8, this wavelength becomes shorter for a tapered fiber and occurs near 800 nm when the core diameter is close to  $2.5 \mu\text{m}$ . With a further decrease in the core diameter, the fiber develops two ZDWLs. This behavior is apparent in Figure 11.9b for  $d = 800 \text{ nm}$ . The GVD for such a fiber is anomalous in a wavelength window covering nearly the entire visible region, but it switches to being normal outside of it. This window shrinks for fibers with  $d = 600 \text{ nm}$  and disappears altogether when  $d = 400 \text{ nm}$ . The main point to note is that the dispersive properties of a tapered fiber are quite sensitive to the core size and can be tailored by changing the core diameter.

Dispersion of tapered fibers is also affected by the air that surrounds a narrow core. Thus, it is possible to tailor the dispersion of such fibers to some extent by immersing them in fluids such as water. In one set of experiments [66], heavy water ( $\text{D}_2\text{O}$ ) was used in place of water ( $\text{H}_2\text{O}$ ) because the absorption peak occurring near 1440 nm for water is shifted toward 1980 nm for heavy water. Figure 11.10 shows changes in the dispersion spectra occurring when a tapered fiber with  $2.5\text{-}\mu\text{m}$  core diameter is immersed in heavy water. Not only does the ZDWL of the fiber shift toward the red side but the dispersion becomes nearly constant over a broad wavelength range extending from 1 to  $1.6 \mu\text{m}$ . Such dispersion modifications may be desirable if the fiber is pumped using a laser operating near  $1.06$  or  $1.3 \mu\text{m}$ . Many other organic liquids, such as pentane and hexane, can be employed for dispersion tailoring [67]. A chain of tapered fibers immersed in different fluids may also be useful for some applications.

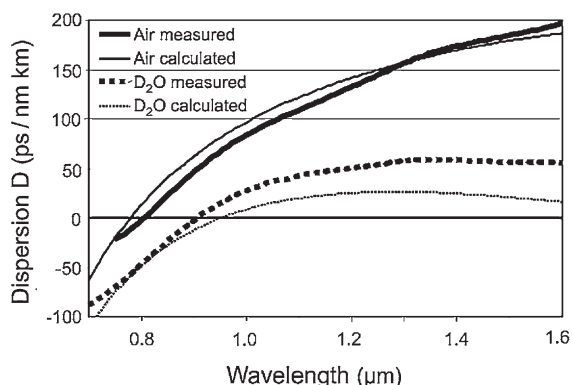


**Figure 11.10** Measured and calculated dispersion spectra for a tapered fiber with  $2.5 \mu\text{m}$  waist immersed in air and heavy water. (After Ref. [66]; © 2005 OSA.)

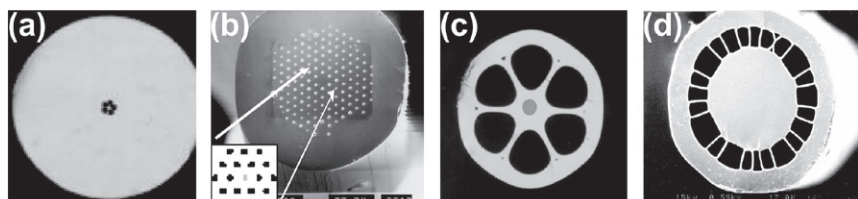
## 11.4 MICROSTRUCTURED FIBERS

Narrow-core tapered fibers with an air cladding suffer from a practical problem. They are fragile, are hard to handle, and are rarely much longer than 30 cm. This problem has been solved to a large extent with the development of microstructured fibers in which a narrow silica core is surrounded by a silica cladding with embedded air holes [68–75]. Such fibers are also known as “holey” fibers. For historical reasons, a subset of them is also referred to as the *photonic crystal fibers* (PCFs). In fact, PCFs were developed first in 1996 in the form of a photonic-crystal cladding with a periodic array of air holes [68]. It was realized later that the periodic nature of air holes is not critical for silica-core fibers as long as the cladding has multiple air holes that effectively reduce its refractive index below that of the silica core [69–74]. In this case, light is guided by the total internal reflection, and the air holes serve to reduce the effective refractive index of the cladding region.

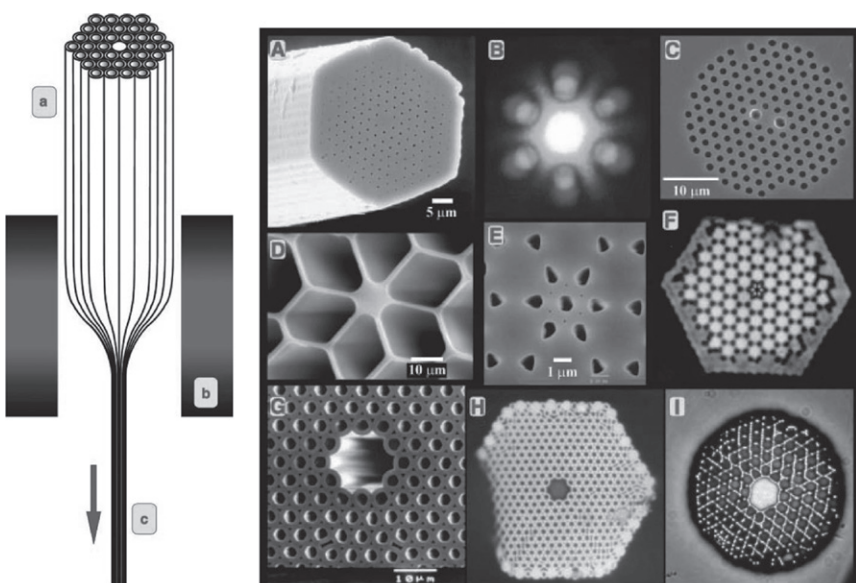
### 11.4.1 Design and Fabrication

Figure 11.11 shows four designs of microstructured fibers [71]. In design (a), the narrow silica core is surrounded by a single ring of air holes, resulting in a high refractive-index step. The rest of the cladding is made of silica. In design (b), the narrow silica core is surrounded by multiple rings of periodic air holes, resulting in a PCF structure. In design (c), air holes surrounding the narrow silica core are so large in size that the core is mostly surrounded by air. This design is sometimes referred to as the “grapefruit” structure because of its appearance. In design (d), the core is surrounded by a ring of mostly air. The integrity of the structure is maintained by narrow silica bridges that connect the core with the rest of the cladding. In all designs, the size of air holes varies from structure to structure and can change from  $<1\text{ }\mu\text{m}$  to several micrometers.

A common technique for fabricating microstructured fibers consists of first making a preform by stacking multiple capillary tubes of pure silica (diameter about 1 mm) in a hexagonal pattern around a solid silica rod [68]. The preform is then drawn into a fiber form using a standard fiber-drawing apparatus, shown schematically in Figure 11.12. A polymer coating is added on the outside to protect the



**Figure 11.11** Scanning electron micrographs of four types of microstructured fibers. (After Ref. [71]; © 2001 OSA.)



**Figure 11.12** Left: Schematic of the drawing apparatus used for making microstructured fibers showing (a) the preform, (b) furnace, and (c) drawn fiber. Right: SEM images of several PCFs (scale indicated) together with a few optical near-field images. (After Ref. [73]; © 2003 AAAS; reprinted with permission.)

resulting fiber. When viewed under a scanning electron microscope (SEM), such a fiber shows a two-dimensional pattern of air holes around the central region acting as a core. Figure 11.12 shows the SEM images of several PCFs together with a few optical near-field images. A hollow-core fiber can be made with the same technique by removing the central silica rod at the preform stage (see the SEM image G). In contrast with the tapered fibers of Section 11.3, the length of a microstructured fiber can be quite long (it can exceed 1 km) while maintaining uniform properties all across it. Such fibers are as easy to handle as conventional fibers because of a polymer coating added on top of the cladding. They can also be spliced to other kinds of fibers, although splice losses typically exceed 1 dB unless special precautions are taken.

Another technique used for fabricating microstructured fibers is known as the *extrusion technique*. In this approach, the preform is produced by extruding material selectively from a solid glass rod of 1–2 cm diameter. More specifically, the molten glass rod is forced through a die containing the required pattern of holes. This technique allows one to draw fibers directly from any bulk material, whether crystalline or amorphous, and it is often used in practice with polymers or compound glasses. The structured preform with the desired pattern of holes is reduced in scale using a fiber-drawing tower in two steps. First, the outside diameter is reduced by a factor of 10 or so. The resulting “cane” is inserted into a glass tube whose size is then further reduced by a factor of more than 100.

A shortcoming of all microstructured fibers is that they exhibit much higher losses compared with those of conventional fibers [76]. Typically, losses exceed 1000 dB/km when the core diameter is reduced to enhance the nonlinear parameter  $\gamma$ . The origin of such losses is related to the nature of mode confinement in such fibers. More specifically, both the core and the cladding are made of silica, and the mode confinement to the core is produced by air holes that are present in the cladding. Both the number and the size of air holes affect how the optical mode is guided inside such a waveguide. With a proper design, losses can be reduced to below 1 dB/km, if core diameter is made relatively large ( $>5\text{ }\mu\text{m}$ ), but only at the expense of a reduced value of the nonlinear parameter [77]. In essence, a trade-off must be made between confinement losses and  $\gamma$  values. High values of  $\gamma$  require a narrow core and thus suffer from larger losses.

### 11.4.2 Modal and Dispersive Properties

It is not easy to analyze the modal and dispersive properties of microstructured fibers or PCFs because the refractive index of the cladding is far from being homogeneous in such fibers. A numerical approach based on plane-wave expansion, the multipole method, expansion using localized functions, or the finite-element method is often used to solve Maxwell's equations with a realistic device geometry [78–85]. The objective in all cases is to find the propagation constant  $\beta(\omega)$  and the effective mode area for various modes supported by such a fiber.

In the case of a PCF with a periodic arrays of holes, such as the structures shown in Figure 11.12, it turns out that the effective mode area  $A_{\text{eff}}$  is nearly independent of the number of hole rings, even though confinement losses  $\alpha_c$  depend strongly on this number [84]. These two parameters also depend on the ratios  $d/\Lambda$  and  $\lambda/\Lambda$ , where  $d$  is the air-hole diameter,  $\Lambda$  is the hole-to-hole spacing, and  $\lambda$  is the wavelength of light. Figure 11.13 shows  $A_{\text{eff}}/\Lambda^2$  as a function of these two ratios for a fiber with 10 hole rings. The dashed curves show the ratio  $\pi w^2/\Lambda^2$ , where  $w$  is the RMS value of the mode radius. Although  $A_{\text{eff}}$  nearly equals  $\pi w^2$  when  $d/\Lambda$  is close to 1, this relation does not hold for  $d < \Lambda/2$ . The important point to note is that  $A_{\text{eff}} \sim \Lambda^2$  over a wide range of fiber parameters. It is thus possible to realize  $A_{\text{eff}} \sim 1\text{ }\mu\text{m}^2$  with a proper design. The nonlinear parameter for such fibers exceeds  $40\text{ W}^{-1}/\text{km}$ .

The number of modes supported by a PCF also depends on the two ratios  $d/\Lambda$  and  $\lambda/\Lambda$  [82]. The concept of an effective cladding index,  $n_{\text{eci}}$ , is quite useful in this context as it represents the extent to which the air holes reduce the refractive index of silica in the cladding region. Figure 11.14a shows how  $n_{\text{eci}}$  depends on the ratios  $d/\Lambda$  and  $\lambda/\Lambda$ . As one would expect, larger and closely spaced air holes reduce  $n_{\text{eci}}$  considerably, resulting in a tighter mode confinement. One can even introduce an effective  $V$  parameter using

$$V_{\text{eff}} = (2\pi/\lambda)a_e \left( n_1^2 - n_{\text{eci}}^2 \right)^{1/2}, \quad (11.4.1)$$

where the effective core radius of the PCF is defined as  $a_e = \Lambda/\sqrt{3}$  [85]. With this choice of  $a_e$ , the single-mode condition  $V_{\text{eff}} = 2.405$  coincides with that of standard

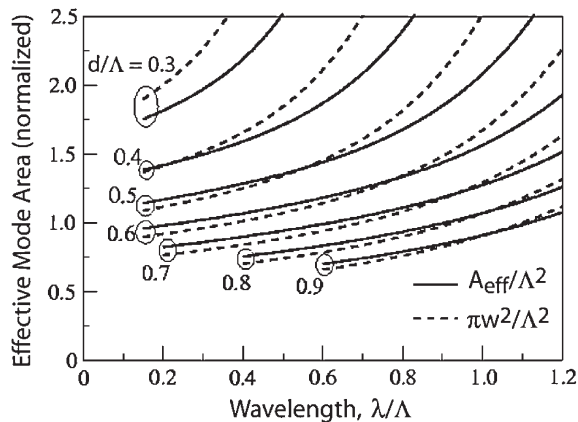


**Figure 11.13** Normalized  $A_{\text{eff}}$  as a function of  $\lambda/\Lambda$  for several values of the ratio  $d/\Lambda$ . The dashed curves show, for comparison, the ratio  $\pi w^2/\Lambda^2$ . (After Ref. [84]; © 2003 OSA.)

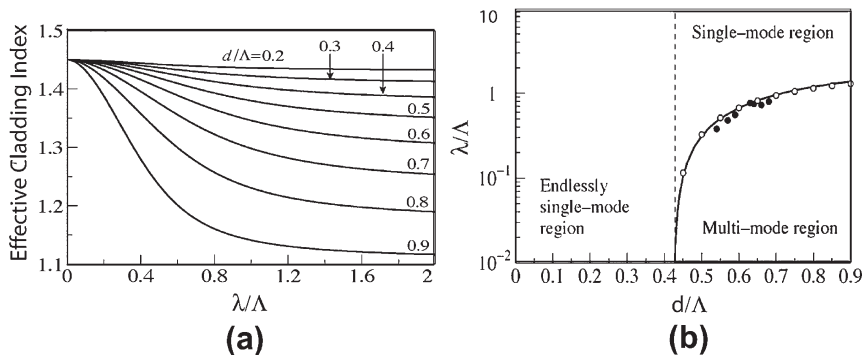


**Figure 11.14** (a) Effective cladding index of a PCF plotted as a function of  $\lambda/\Lambda$  for values of  $d/\Lambda$  in the range of 0.2–0.9. (b) Three operational regimes of a PCF. The solid curve corresponds to the condition  $V_{\text{eff}}=2.405$ . The empty and filled circles show the numerical and experimental data, respectively. (After Ref. [85]; © 2005 IEEE.)

fibers. The solid curve in Figure 11.14b shows this condition in the parameter space of the ratios  $d/\Lambda$  and  $\lambda/\Lambda$ . As seen there, a PCF may support multiple modes for relatively large-size air holes. However, the PCF supports only the fundamental mode at all wavelengths if  $d/\Lambda$  is reduced to below 0.45; such a fiber is referred to as the *endlessly single-mode fiber* [68]. For larger values of  $d/\Lambda$ , the PCF supports higher-order modes if  $\lambda/\Lambda$  is less than a critical value.

The dispersive properties of PCFs are also very sensitive to the same two parameters, namely the air-hole diameter  $d$  and the hole-to-hole spacing  $\Lambda$ . Figure 11.15 shows the wavelength dependence of the dispersion parameter  $D$  as a function of the

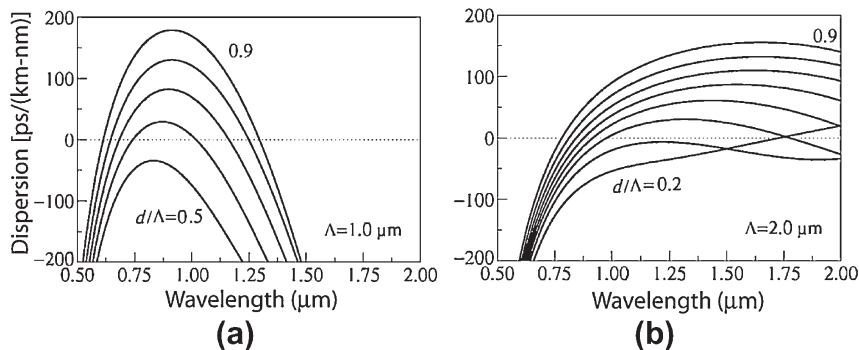


Figure 11.15 Variation of dispersion  $D$  with wavelength  $\lambda$  for PCFs designed with different values of  $d/\Lambda$  when  $\Lambda = 1$  and  $2 \mu\text{m}$ . (After Ref. [85]; © 2005 IEEE.)

ratio  $d/\Lambda$  for  $\Lambda = 1$  and  $2 \mu\text{m}$  [85]. Notice how much GVD changes even with relatively small variations in  $d$  and  $\Lambda$ . This feature indicates that microstructured fibers allow much more tailoring of dispersion compared with that possible for tapered fibers. The ZDWL of such fibers can be varied over a wide range extending from  $0.5$  to  $1.5 \mu\text{m}$  with changes in  $d$  and  $\Lambda$ . A remarkable feature of Figure 11.15 is that such fibers can exhibit two ZDWLs, one falling in the visible region and the other beyond  $1 \mu\text{m}$ , such that GVD is anomalous in the spectral region between them. It will be seen later that this feature can be exploited for observing a variety of novel nonlinear effects.

The tapering technique discussed in Section 11.3 has been employed for reducing the core diameter of PCFs [86–88]. The main advantage is that both the dispersive and nonlinear properties of a PCF can be altered with tapering, provided care is taken to ensure that air holes within the cladding do not collapse. In practice, the core size as well as the diameter of air holes can be reduced by a factor of 2 or so without collapsing the air holes. Even such small changes modify the characteristics of most microstructured fibers significantly because their dispersion is extremely sensitive to the size and spacing of air holes.

### 11.4.3 Hollow-Core Photonic Crystal Fibers

The waveguiding in solid-core PCFs, containing a periodic two-dimensional array of air holes in their cladding, is often through the traditional mechanism of total internal reflection. The periodic nature of the air holes becomes important in the so-called *photonic-bandgap* fibers in which an optical mode is confined to the core through periodic variations of the refractive index within the cladding. In the case of a hollow-core fiber, mode guiding is generally through the photonic bandgap because of the absence of total internal reflection inside the hollow core. Such photonic-bandgap fibers were first realized in 1999 [89], and they have continued to attract attention since then [90–92].

Why are the hollow-core PCFs useful? One possibility is to use them for transporting high optical powers, as all nonlinear effects are likely to be much weaker owing to the presence of air inside the core ( $n_2$  smaller by a factor of 1000 compared with that of silica). However, most such fibers exhibit relatively high losses ( $\sim 1$  dB/m) compared to conventional silica fibers that depend on many design factors, including the shape and size of air holes. Figure 11.16 shows the measured loss spectrum of a hollow-core PCF whose cladding was designed in the form of a kagome lattice [93]. Such a lattice consists of interlaced triangles such that each crossing has four nearest neighbors. In the case of PCFs, the use of a kagome lattice results in a cladding filled mostly with air such that the network of silica struts occupies <20% of the space.

In recent years the use of the kagome lattice has reduced losses of hollow-core PCFs by a factor of 1000 to near 1 dB/km [94]. These fibers employ a relatively large hollow core (diameter 20  $\mu\text{m}$  or more) and increase the pitch of the kagome lattice to beyond 10  $\mu\text{m}$ . Because such a PCF consists of mostly air, the nonlinear effects are reduced dramatically inside them. Narrower-core PCFs exhibit higher losses but they are still useful for applications such as pulse compression that make use of their dispersive properties [91].

Current applications of hollow-core PCFs turn them into a highly nonlinear medium by replacing air inside the core with a suitable gas or liquid. As early as 2002, when air was replaced with hydrogen in such a fiber, stimulated Raman scattering was observed at pulse energies that indicated that the Raman threshold was more than 100 times lower than that of silica fibers [93]. Since then, a variety of fluids have been used for enhancing various nonlinear effects [95–101]. The

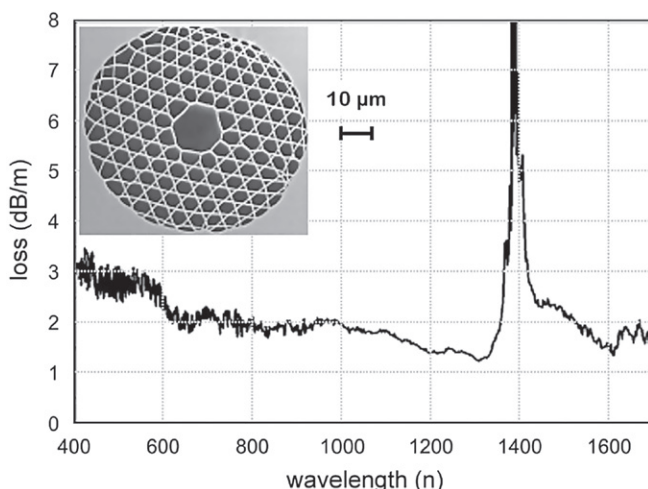


**Figure 11.16** Measured loss versus wavelength for a hollow-core PCF made with kagome-type cladding shown in the inset. The peak near 1400 nm is due to residual water contents. (After Ref. [75]; © 2006 IEEE.)

main point to stress is that the fluid inside the core of such a PCF provides high nonlinearity, whereas its periodic cladding guides the light over long lengths and also helps to control the dispersive effects. It should be stressed that it is not easy to fill the core of a PCF with a fluid. The reader is referred to a 2011 review for details [91].

#### 11.4.4 Bragg Fibers

PCFs designed with a two-dimensional pattern of air holes in their cladding region suffer from scattering losses at multiple air–glass interfaces, especially when the hole size is reduced to below the wavelength of light launched into them. Another kind of PCFs, known as *Bragg fibers*, have been developed that do not suffer from this problem because of their all-solid nature. Such fibers require two glasses with a relatively large difference in their refractive indices. They are used to form a cladding in the form of concentric solid rings, with alternating layers of each glass, to create a one-dimensional periodic structure in the radial direction. Although the design of such Bragg fibers was proposed in the 1970s [102], their development took off only after the year 2000. Since then, several types of Bragg fibers have been developed using a variety of materials [103–109].

Figure 11.17 shows an example of a Bragg fiber together with variations in the refractive index along its radial direction [105]. It is designed with a large central silica core surrounded with multiple rings whose refractive indices take values  $n_1$  and  $n_2$  alternatively. The central ring, in general, can have a different refractive index and may even contain air, resulting in a hollow-core Bragg fiber. The right side of Figure 11.17 shows calculated losses as a function of wavelength of a Bragg fiber whose 125- $\mu\text{m}$  silica core is surrounded with seven rings using  $n_1 = 1.45$  and  $n_2 = 2.05$ . Although

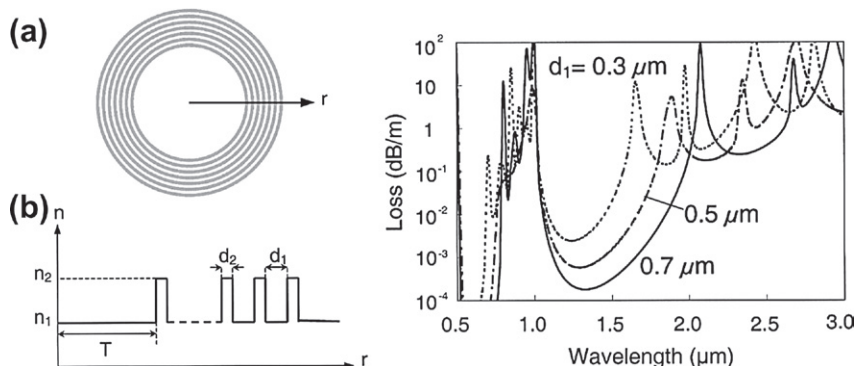


**Figure 11.17** (a) Cross section and (b) radial refractive-index variations of a Bragg fiber. Calculated losses versus wavelength of a fiber whose 125- $\mu\text{m}$  silica core is surrounded with seven rings;  $n_1 = 1.45$ ,  $n_2 = 2.05$ ,  $d_2 = 0.35 \mu\text{m}$ , and  $d_1$  varies from 0.3 to 0.7  $\mu\text{m}$ . (After Ref. [105]; © 2004 OSA.)

losses depend considerably on relative thicknesses of various layers, with a proper design, they can be reduced to below 1 dB/km in the spectral region near 1.5  $\mu\text{m}$ .

Several Bragg fibers have been developed using different kinds of materials. In all cases, light is confined to the low-index central core (often containing air) because of the periodic nature of concentric surrounding rings that act as a Bragg mirror and reflect most of the light back into the core. Although such a structure is superficially similar to a hollow metallic waveguide, the periodic nature of the cladding also leads to the formation of photonic bandgaps [103]. Alternating polymer and chalcogenide-glass cladding layers were used in 2002 to make a Bragg fiber capable of transmitting light at wavelengths near 10  $\mu\text{m}$  [104]. The design shown in Figure 11.17 was employed in 2004 by using alternating layers made of silicon and silica [105]. In an all-silica design of such a fiber, all cladding layers employed silica as the base material but their refractive index was changed by doping them with different materials. Such an approach results in a relatively small index contrast ( $<0.001$ ) between the neighboring cladding layers [106].

In another all-silica design, the hollow core of a Bragg fiber was surrounded with cladding layers containing silica and air in an alternating fashion [107]. The “air rings” were connected to the neighboring silica rings through nanoscale support bridges. A similar design employed the polymethyl methacrylate (PMMA) polymer in place of silica [108]. In a later design, two different polymers (PMMA and polystyrene) were used to make the alternating cladding rings [109]. It turns out that three air rings are sufficient to provide mode confinement in such fibers. Note, however, that optical modes supported by a Bragg fiber fall in the category of the leaky modes and suffer invariably from confinement losses [110].

Bragg fibers are continuing to attract attention. Although their main use appears to be for transmitting light within their core, they have also been used for sensing applications [111]. Nonlinear effects in Bragg fibers have also been studied. Large spectral broadening inside an all-silica Bragg fiber was observed in a 2009 experiment by launching 120-fs pulses at a wavelength of 1067 nm [112]. It was also found numerically that a tapered Bragg fiber can transform a Gaussian pulse into a parabolic shape if the normal dispersion provided by the fiber decreases along its length [113].

## 11.5 NON-SILICA FIBERS

Because of a relatively low value of  $n_2$  of silica fibers, several other kinds of glasses with larger nonlinearities have been used to make optical fibers [114–128]. These include materials such as lead silicates, chalcogenides, tellurite oxide, and bismuth oxide. This section reviews the progress made in realizing large values of the nonlinear parameter  $\gamma$ .

It is well known that the nonlinear-index coefficient  $n_2$  of different glasses scales with the linear refractive index  $n$  of the material because both depend on the density of the material; an empirical relation between the two was first proposed in 1978 [28].

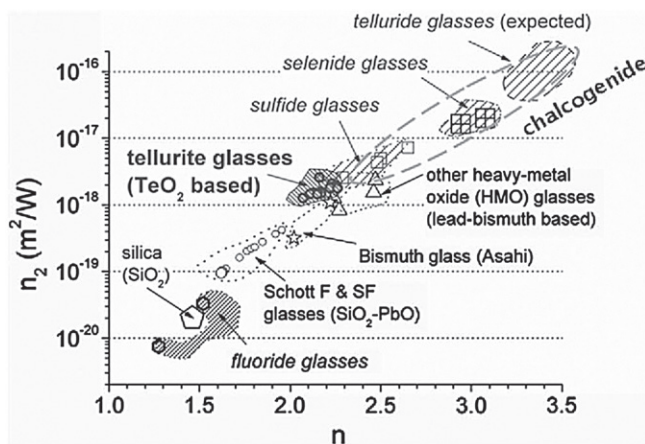


**Figure 11.18** Nonlinear-index coefficient  $n_2$  versus linear refractive index  $n$  for a wide variety of optical glasses. Symbols F and SF stand for flint and lead-silicate glasses. (After Ref. [127]; © 2010 Elsevier.)

Figure 11.18 shows this relationship for a wide variety of glasses [127]. As seen there,  $n_2$  can vary by a factor of 1000 or more depending on the glass material and its composition. Silica glasses with a refractive index of 1.45 fall on the lower end of this range. The largest value of  $n_2$  occurs for chalcogenide glasses whose refractive index is close to 3.0.

### 11.5.1 Lead-Silicate Fibers

Lead-silicate glasses are silica glasses in which a fraction of silicon atoms have been replaced with lead, resulting in a network of PbO and SiO<sub>2</sub> molecules. The addition of lead increases the refractive index of such glasses in the range of 1.55–1.85, depending on the lead content. Such glasses have been commercialized by the Schott AG (a German company) and are known by their company codes [129]. For example, SF6 and SF11 glasses have the refractive indices near 1.75 (at 1550 nm) because of their relatively large lead content. Since the SF57 glass has even a larger refractive index (close to 1.80 at 1550 nm), it is used often to make optical fibers.

Lead-silicate fibers attracted attention in the late 1980s, and  $n_2$  was measured to have a value of  $2 \times 10^{-19} \text{ m}^2/\text{W}$  at a wavelength of 1064 nm for a lead-silicate fiber with  $n = 1.774$  inside its core [114]. Since the SF57 glass has a value of nearly double that, it has been used in recent years for fabricating several types of microstructured fibers [123–127]. The extrusion technique can be used for this purpose because of a relatively low softening temperature (about 520 °C) of this glass. The value of  $\gamma$  depends on the fiber design and can be enhanced using narrow cores. A value of  $640 \text{ W}^{-1}/\text{km}$  was observed in 2003 for a holey fiber with  $A_{\text{eff}} = 2.6 \mu\text{m}^2$  and a 1.7-μm core diameter [123]. The nonlinear parameter  $\gamma$  was estimated from the

measurements of the SPM-induced nonlinear phase shift. Figure 11.19a shows the measured data for a 37-cm-long fiber as a function of input power. The wavelength dependence of the dispersion parameter  $D$  is shown in Figure 11.19b for two fibers with different core diameters. As seen there, the dispersion characteristics of such fibers are similar to those of silica fibers. Even though the ZDWL of SF57 glass is near  $2\text{ }\mu\text{m}$  in the bulk form, it shifts to below  $1.3\text{ }\mu\text{m}$  when fiber's core diameter is reduced to below  $2\text{ }\mu\text{m}$ .

The extrusion technique allows fabrication of holey fibers whose cladding region consists of mostly air. Figure 11.20a shows the scanning electron microscope (SEM) images of the cross section of a fiber whose core diameter is close to  $950\text{ nm}$  [125]. Because of a relatively large index difference between the core and the cladding, the optical mode is confined tightly to the core. Figure 11.20a shows the measured mode

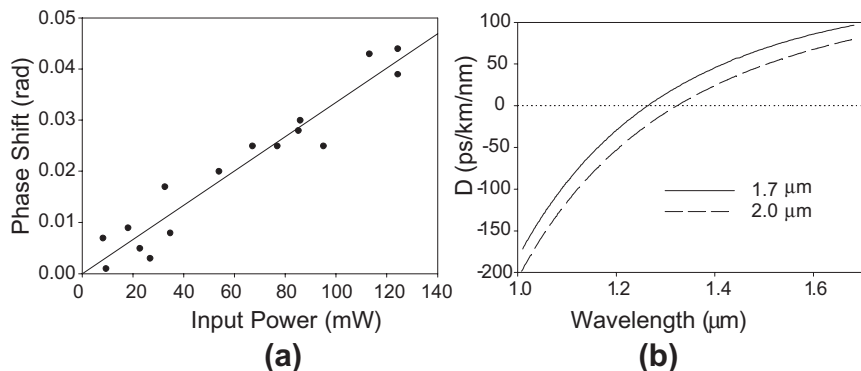


Figure 11.19 (a) SPM-induced nonlinear phase shift measured as a function of input power (circles). The solid line shows the linear fit to the data. (b) Dispersion parameter  $D$  as a function of wavelength for two values of core diameter. (After Ref. [123]; © 2003 OSA.)

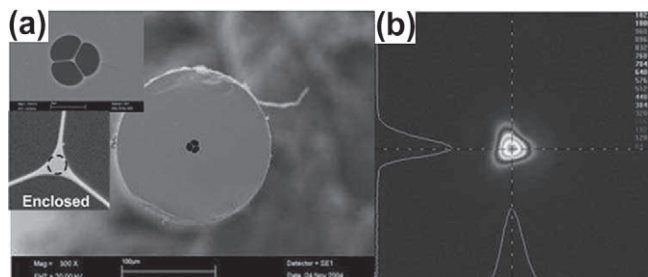
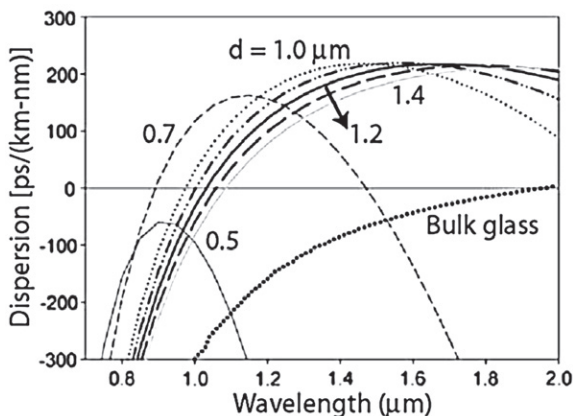


Figure 11.20 (a) SEM image of the cross section of a holey fiber fabricated with the extrusion technique. The insets show details of the core and cladding regions. The dashed circle represents the core with a  $950\text{ nm}$  diameter. (b) Measured mode profiles together with the constant-intensity contours in the transverse plane. (After Ref. [125]; © 2006 IEEE.)

profiles together with the constant-intensity contours in the transverse plane. Such narrow-core holey fibers can exhibit values of the nonlinear parameter in excess of  $1000 \text{ W}^{-1}/\text{km}$  when the effective mode area  $A_{\text{eff}}$  is  $\sim 1 \mu\text{m}^2$  because the material parameter  $n_2$  is larger by a factor of 15 compared with its value for silica. A value as high as  $\gamma = 6000 \text{ W}^{-1}/\text{km}$  has been predicted for a core diameter of 500 nm.

Dispersion characteristics of such holey fibers also change considerably with the core diameter and require a numerical approach such as a finite-element method [125]. Figure 11.21a shows the dispersion parameter  $D$  as a function of wavelength for core diameters ranging from 0.5 to 1.4  $\mu\text{m}$ . The material dispersion of SF57 bulk glass is also shown for comparison. The contribution of waveguide dispersion shifts the ZDWL from 2  $\mu\text{m}$  to close to 1  $\mu\text{m}$ . It also dramatically affects the shape of the dispersion curve when the core diameter is reduced to below 1  $\mu\text{m}$ . More specifically, a roughly parabolic shape develops such that GVD is anomalous in a spectral window between the two ZDWLs. Similar to the case of tapered fibers, this window disappears when the core diameter of a microstructured or holey fiber is reduced to below 600 nm.

PCF designs with multiple rows of air holes outside a central core have also been used for making lead-silicate fibers [127]. However, such fibers suffer from scattering losses at multiple air–glass interfaces, especially when the hole size is reduced to below the wavelength of light launched into them. As discussed in Section 11.4.4, Bragg fibers do not suffer from this problem because of their all-solid nature. Such fibers require two glasses with a relatively high refractive-index contrast to create a one-dimensional periodic structure. A low-loss Bragg fiber was fabricated in 2009 using two lead-silicate glasses with refractive indices of 1.53 (Schott LLF1) and 1.76 (Schott SF6) at wavelengths near 1550 nm [126]. The nonlinear parameter had a value of  $\gamma = 120 \text{ W}^{-1}/\text{km}$  for this fiber with a loss of only 0.8 dB/m, both at the 1550 nm wavelength.



**Figure 11.21** Dispersion parameter  $D$  as a function of wavelength for lead-silicate fibers with core diameters ranging from 0.5 to 1.4  $\mu\text{m}$ . The dispersion curve for SF57 bulk glass is provided for comparison. (After Ref. [125]; © 2006 IEEE.)

### 11.5.2 Chalcogenide Fibers

Chalcogenide fibers have attracted attention since the early 1990s because  $n_2$  can be larger for them by a factor of 1000 or more, compared with its value for silica fibers, depending on the fiber composition [117–122]. Chalcogenide fibers make use of glasses whose composition includes elements from group 16 in the periodic table such as sulfur, selenium, and tellurium (S, Se, and Te). Early experiments made use of  $\text{As}_2\text{S}_3$  glass, but  $\text{As}_2\text{Se}_3$  glass became the material of choice by 2000 because of its higher refractive index. In a 2000 experiment, the measured value of  $n_2$  for this material was found to be 500 times larger than that of silica [120]. By 2004, an optical fiber fabricated with higher-purity material exhibited an enhancement in  $n_2$  by a factor of about 1000 at wavelengths near 1550 nm [121]. The nonlinear parameter  $\gamma$  is thus relatively large for chalcogenide fibers.

The 85-cm-long fiber used in the 2004 experiment had a 7- $\mu\text{m}$  core diameter with an effective mode area of about  $40 \mu\text{m}^2$ . Figure 11.22 shows the SPM-broadened spectrum of 3.2-ps pulses at three peak power levels together with the measured Raman-gain spectrum for the same fiber when pumped at 1550 nm. The observed spectral broadening is consistent with a value of  $\gamma = 2450 \text{ W}^{-1}/\text{km}$ . Using  $A_{\text{eff}} = 40 \mu\text{m}^2$ ,  $n_2$  is deduced to be  $2.4 \times 10^{-17} \text{ m}^2/\text{W}$ , a value about 1000 times larger than that of silica. At the same time, the Raman gain  $g_R$  for this material is about  $5.1 \times 10^{-11} \text{ m/W}$  at pump wavelengths near 1.55  $\mu\text{m}$ , a value nearly 800 times larger than that of silica fibers.

Because of their highly nonlinear nature, chalcogenide fibers have attracted considerable attention for applications related to nonlinear fiber optics, in spite of their relatively high losses. Their use for making fiber gratings and nonlinear switches can reduce the required power considerably [118]. The values of  $\gamma$  can be further enhanced by reducing the core diameter and adopting a microstructure for the cladding with air holes

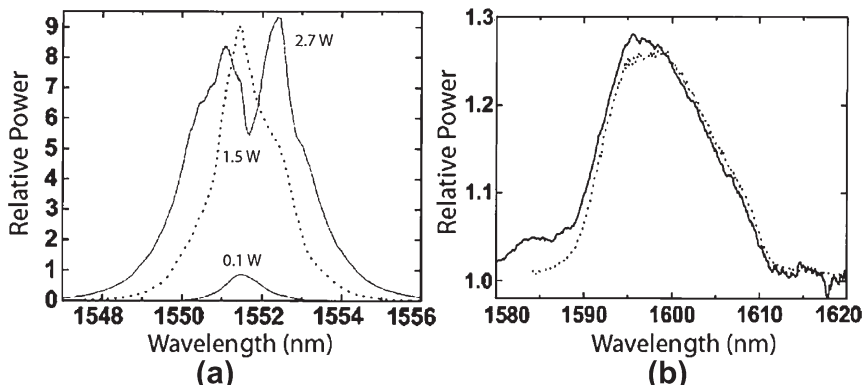


Figure 11.22 (a) SPM-broadened spectrum of 3.2-ps pulses at peak power levels of 0.1, 1.5, and 2.7 W. (b) Measured Raman-gain spectrum of the same fiber when pumped at 1540 nm; dotted curve shows the bulk case. (After Ref. [121]; © 2004 OSA.)

[80]. By 2010, such fibers exhibited losses as low as 0.35 dB/m fiber near 1550 nm while maintaining values of  $\gamma > 2000 \text{ W}^{-1}/\text{km}$  and exhibiting strong nonlinear effects [128].

### 11.5.3 Bismuth-Oxide Fibers

Third-order nonlinearities of bismuth-oxide ( $\text{Bi}_2\text{O}_3$ ) glasses were measured in 1996 and were found to be relatively large compared with silica glasses [130]. An optical fiber made in 2002 with such glasses exhibited a loss of 0.8 dB/m together with a value of  $64.2 \text{ W}^{-1}/\text{km}$  for the nonlinear parameter  $\gamma$  [131]. Bismuth-oxide fibers attracted considerable attention soon after that and were employed to make a variety of nonlinear devices [132–138]. By 2004, such fibers exhibited values of  $\gamma > 1000 \text{ W}^{-1}/\text{km}$  at a wavelength near  $1.55 \mu\text{m}$  when their core diameter was reduced to below  $2 \mu\text{m}$ . Figure 11.23a shows the cross section of a fiber whose narrow core (diameter  $2.1 \mu\text{m}$ ) is almost completely surrounded with large air holes. The effective mode area of this fiber was estimated to be only  $3.1 \mu\text{m}^2$ .

The nonlinear parameter  $\gamma$  was estimated for three fibers with different core sizes from the measurements of the SPM-induced nonlinear phase shifts as a function of the input power. Figure 11.23a shows the measured values together with the prediction of a model in which the core is taken to be completely surrounded with air. The  $\gamma$  values range from 460 to  $1100 \text{ W}^{-1}/\text{km}$ , the largest value occurring for the fiber with a core diameter of  $2.1 \mu\text{m}$ . The theoretical model predicts that values of  $\gamma$  close to  $2000 \text{ W}^{-1}/\text{km}$  are possible with a further reduction in the core size.

Bismuth-oxide fibers have been used in a variety of applications relevant for telecommunication systems. Because of their relatively high losses ( $\sim 1 \text{ dB/m}$ ), their fiber length is typically  $< 2 \text{ m}$ . In a 2005 experiment, only 1 m length of a highly nonlinear fiber was needed to make a FWM-based wavelength converter capable of operating at 80 Gb/s [133]. Because of their highly nonlinear nature, bismuth-oxide fibers

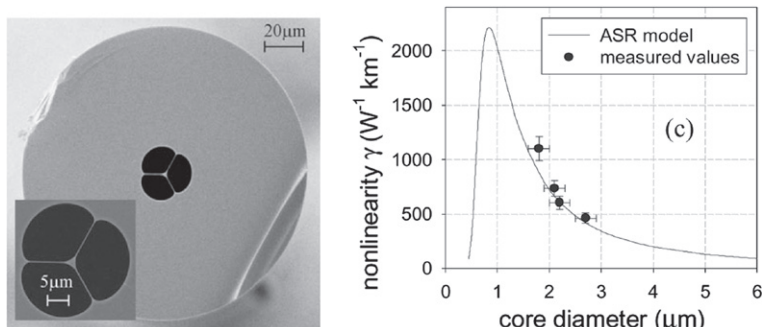


Figure 11.23 (a) Cross section of a holey bismuth-oxide fiber; inset shows an enlarged view. (b) Measured values of  $\gamma$  for three such fibers together with the prediction of the air-suspended-rod (ASR) model. (After Ref. [132]; © 2004 OSA.)

are often used for supercontinuum generation [134], a process discussed in Chapter 13. Other applications include parametric amplification, add-drop-multiplexing, tunable pulse delays, and all-optical signal regeneration [135–137]. Bismuth-oxide fibers have also been used to make optical amplifiers and lasers after doping them with rare-earth elements such as erbium and ytterbium. A Bragg grating can also be fabricated inside such fibers. Such a grating was recently used for realizing nonlinear optical switching [138].

In another class of optical fibers,  $\text{TeO}_2$  glass is used in place of  $\text{BiO}_2$  glass. Tellurite glasses offer a value of  $n_2$  nearly 10 times larger than that of silica [115]. At the same time, the peak Raman gain for them is up to 30 times larger when compared with silica glass [139]. In a 2003 experiment, tellurite glass with the composition of 5%  $\text{Na}_2\text{CO}_3$ , 20%  $\text{ZnO}$ , and 75%  $\text{TeO}_2$  was used to fabricate a microstructured fiber [140]. The fiber drawn using this glass had a core diameter of  $7 \mu\text{m}$ . As the core was suspended by 100-nm-thick strands, it was surrounded mostly by air, resulting in a strong confinement of the optical mode and an effective mode area of only  $21.2 \mu\text{m}^2$ . The estimated value of  $\gamma$  was  $48 \text{ W}^{-1}/\text{km}$  for this fiber. In another tellurite fiber,  $A_{\text{eff}}$  was reduced to near  $2.6 \mu\text{m}^2$ , and the value of  $\gamma$  was measured to be  $580 \text{ W}^{-1}/\text{km}$  at a wavelength near  $1050 \text{ nm}$  [124]. Tellurite glasses are continuing to attract attention for their nonlinear applications, and they have been used to fabricate microstructured fibers with a core diameter as small as 400 nm [141].

## 11.6 PULSE PROPAGATION IN NARROW-CORE FIBERS

The core diameter in HNLFs is often reduced to near or below  $1 \mu\text{m}$  to enhance the nonlinear effects in such fibers. Since the core size under such conditions become comparable to or shorter than the optical wavelength, the longitudinal component of the electric field is not negligible in such fibers, and one must consider the vectorial nature of optical modes. It turns out that the nonlinear parameter  $\gamma$  is enhanced, compared to its value expected from scalar theory when the vector nature of the electromagnetic field is fully included [142–146]. In this section we revisit the theory of Section 2.3 to discuss pulse propagation in HNLFs.

### 11.6.1 Vectorial Theory

As was done in Section 2.2, we assume that Maxwell's equations have been solved in the frequency domain for a specific HNLF to obtain both the electric and magnetic field vectors associated with each optical mode in the form

$$\tilde{\mathbf{E}}_m(\mathbf{r}, \omega) = \mathbf{e}_m(x, y, \omega) \exp[i\beta_m(\omega)z], \quad \tilde{\mathbf{H}}_m(\mathbf{r}, \omega) = \mathbf{h}_m(x, y, \omega) \exp[i\beta_m(\omega)z], \quad (11.6.1)$$

where  $\beta_m(\omega)$  is the propagation constant for the  $m$ th mode. When an optical pulse propagates inside such a fiber, its electric field  $\tilde{\mathbf{E}}(\mathbf{r}, \omega)$  can be expanded in terms of these modes as (see Section 2.3.4)

$$\tilde{\mathbf{E}}(\mathbf{r}, \omega) = \sum_m \mathbf{F}_m(x, y, \omega) \tilde{A}_m(z, \omega) \exp[i\beta_m(\omega)z], \quad (11.6.2)$$

where  $\mathbf{F}_m = \mathbf{e}_m / \sqrt{N_m}$  and  $N_m$  is related to the spectral power obtained using the Poynting vector in the form [143]

$$N_m(\omega) = \frac{1}{2} \left| \iint [\mathbf{e}_m(x, y, \omega) \times \mathbf{h}_m^*(x, y, \omega)] \cdot \hat{z} dx dy \right|. \quad (11.6.3)$$

Here  $\hat{z}$  is the unit vector along the direction of propagation.

The magnetic field is expanded in a similar fashion using the same amplitude  $\tilde{A}_m(z, \omega)$ . The nonlinear polarization is then used to obtain a time-domain differential equation for  $A_m(z, t)$ , as was done in Section 2.3.4. Since details are available in several publications [142–146], only final results are summarized here. In the Kerr limit, one can use the form of the nonlinear polarization given in Eq. (2.3.6). Focusing on the fundamental fiber mode, we ignore the mode subscript  $m$  and find that  $A(z, t)$  still satisfies the standard NLS equation given in Eq. (2.3.28), but the nonlinear parameter  $\gamma$  is modified. It can be written in the form  $\gamma = \omega_0 n_2^{\text{eff}} / (c A_{\text{eff}})$  with the following definitions for  $n_2^{\text{eff}}$  and  $A_{\text{eff}}$  [143]:

$$n_2^{\text{eff}} = \frac{\epsilon_0 \omega_0 \iint n_2(x, y) n^2(x, y) [2|\mathbf{e}(x, y)|^4 + |\mathbf{e}^2(x, y)|^2] dx dy}{(3\mu_0 c) \left| \iint [\mathbf{e}(x, y) \times \mathbf{h}^*(x, y)] \cdot \hat{z} dx dy \right|^2}, \quad (11.6.4)$$

$$A_{\text{eff}} = \frac{\left| \iint [\mathbf{e}(x, y) \times \mathbf{h}^*(x, y)] \cdot \hat{z} dx dy \right|^2}{\iint |[\mathbf{e}(x, y) \times \mathbf{h}^*(x, y)] \cdot \hat{z}|^2 dx dy}, \quad (11.6.5)$$

where the fields associated with the optical mode are calculated at the fixed carrier frequency  $\omega_0$  of the pulse, and this dependence is not shown to simplify the notation.

The effective mode area  $A_{\text{eff}}$  is defined similar to its definition in Eq. (2.3.31), except for including the vectorial nature of the optical field. Using the relations between the electric and magnetic fields dictated by Maxwell's equations, Eq. (11.6.5) can be written in terms of the electric field alone as

$$A_{\text{eff}} = \frac{\left| \iint [\beta |\mathbf{e}_t(x, y)|^2 + i\mathbf{e}_t(x, y) \cdot \nabla_t e_z(x, y)] dx dy \right|^2}{\iint |\beta |\mathbf{e}_t(x, y)|^2 + i\mathbf{e}_t(x, y) \cdot \nabla_t e_z(x, y)|^2 dx dy}, \quad (11.6.6)$$

where  $e_z$  is the longitudinal component and  $\mathbf{e}_t$  is the transverse part of the electric field. In the limit of negligible  $e_z$ ,  $A_{\text{eff}}$  reduces to its definition in Eq. (2.3.28). However, its value changes for HNLFs with core diameters below 1  $\mu\text{m}$  depending on the relative importance of  $e_z$ . The effective value of  $n_2$  calculated from Eq. (11.6.4) is also affected by the fiber geometry. This expression can be used for hollow or gas-filled fiber cores as well by using suitable values of  $n$  and  $n_2$  inside the core region while evaluating the integral.

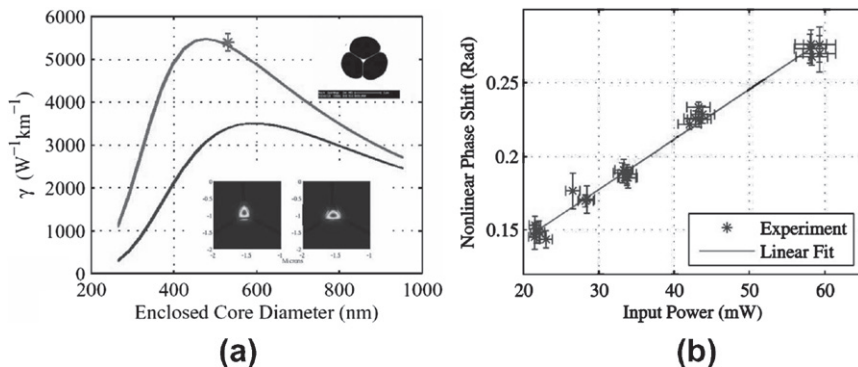


**Figure 11.24** (a)  $\gamma$  as a function of core diameter for a  $\text{BiO}_2$  fiber (whose design is shown in the top inset) calculated with the vector (gray curve) and scalar (black curve) theories. Bottom insets show the near-field images of the fundamental mode for orthogonal polarizations. (b) Nonlinear phase shifts measured as a function of input power for a  $\text{BiO}_2$  fiber with 530-nm core diameter. The data were used to deduce the  $\gamma$  value marked in part (a). (After Ref. [145]; © 2009 IEEE.)

Figure 11.24a shows the calculated values of  $\gamma$  as a function of the core diameter of a HNLF, whose  $\text{BiO}_2$  core is surrounded mostly with air (see top inset), using the vector (gray curve) and scalar (black curve) theories [145]. Such a fiber was fabricated with a core diameter of 530 nm and its  $\gamma$  parameter was estimated by measuring the nonlinear phase shift  $\phi_{\text{NL}}$  as a function of the launched power  $P_0$ . Figure 11.24b shows the data and the linear fit expected from  $\phi_{\text{NL}} = \gamma P_0 L_{\text{eff}}$ . The measured value of  $5200 \text{ W}^{-1}/\text{km}$  is marked in Figure 11.24a and is in agreement with the vector theory but deviates considerably from the prediction of the scalar theory. In general, the vectorial effects can enhance  $\gamma$  by up to 70% and should be included for HNLFs with core diameters below 1  $\mu\text{m}$ .

The vectorial method can be extended to include the Raman contribution to the nonlinear polarization [144]. The analysis shows that the Raman gain is also affected by the vector nature of the optical modes in narrow-core HNLFs. The extended analysis is useful if such fibers are employed for Raman amplification or other applications where stimulated Raman scattering plays a role.

## 11.6.2 Frequency-Dependent Mode Profiles

In the preceding description, the mode profile  $\mathbf{e}_m(x, y, \omega)$  was assumed not to change significantly over the pulse bandwidth from its value at the carrier frequency  $\omega_0$ . This assumption becomes questionable when the pulse spectrum broadens considerably during propagation or shifts toward longer wavelengths because of intrapulse Raman scattering, both of which can occur readily when femtosecond pulses are propagated inside narrow-core PCFs. It has been found recently that a new kind of nonlinearity, called the geometrical nonlinearity, becomes important under such conditions [147].

If the mode profiles change considerably with the frequency  $\omega$ , we need to expand the electric field  $\mathbf{e}_m(x, y, \omega)$  in a Taylor series around the carrier frequency  $\omega_0$  as

$$\mathbf{e}_m(x, y, \omega) = \sum_{n=0}^{\infty} \frac{1}{n!} \left( \frac{\omega - \omega_0}{\omega_0} \right)^n \mathbf{f}_m^{(n)}(x, y), \quad (11.6.7)$$

where  $\mathbf{f}_m^{(n)} = \omega_0^n (\partial^n \mathbf{e}_m / \partial \omega^n)$  is evaluated at  $\omega = \omega_0$ . It is evident from Eq. (2.3.51) with  $\mathbf{F}_m = \mathbf{e}_m / \sqrt{N_m}$  that such an expansion considerably complicates the resulting time-domain equation for the mode amplitude  $A_m(z, t)$ . Even if we restrict the analysis to a single mode of the fiber and ignore the subscript  $m$ , the generalized NLS equation (2.3.36) has an infinite number of nonlinear terms of the form [147]

$$\frac{\partial A}{\partial z} - i \sum_{n=1}^{\infty} \frac{i^n \beta_n}{n!} \frac{\partial^n A}{\partial t^n} = i \sum_{mnpq} \gamma^{mnpq} \left( 1 + \frac{i \partial_t}{\omega_0} \right) \left( \frac{i \partial_t}{\omega_0} \right)^m \phi^{npq}(z, t), \quad (11.6.8)$$

where we have neglected the loss terms for simplicity and used

$$\phi^{npq}(z, t) = \omega_0^{-(n+p+q)} [(i \partial_t)^n A(z, t)] (R(t) \otimes \{[(i \partial_t)^p A(z, t)][(-i \partial_t)^q A^*(z, t)]\}). \quad (11.6.9)$$

Here, the symbol  $\otimes$  denotes convolution and  $\partial_t$  stands for a partial time derivative.

The nonlinear coefficients  $\gamma^{mnpq}$  depend on the field derivatives  $\mathbf{f}^{(n)}(x, y)$ . When the nonlinear response is in the form in Eq. (2.3.32),  $\gamma^{mnpq}$  is defined as [147]

$$\begin{aligned} \gamma^{mnpq} = & \frac{\omega_0}{8cN^2} \iint dx dy \frac{\chi_{xxxx}^{(3)}(x, y)}{m!n!p!q!} \\ & \times \left( [\mathbf{f}^{(m)} \cdot \mathbf{f}^{(n)}][\mathbf{f}^{(p)} \cdot \mathbf{f}^{(q)}] + [\mathbf{f}^{(m)} \cdot \mathbf{f}^{(p)}][\mathbf{f}^{(n)} \cdot \mathbf{f}^{(q)}] \right. \\ & \left. + [\mathbf{f}^{(m)} \cdot \mathbf{f}^{(q)}][\mathbf{f}^{(n)} \cdot \mathbf{f}^{(p)}] \right). \end{aligned} \quad (11.6.10)$$

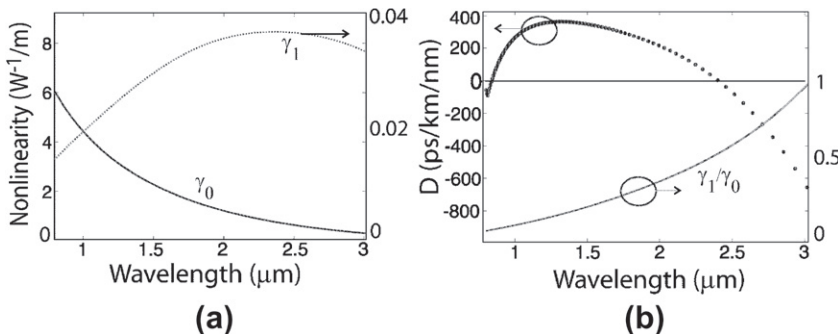


**Figure 11.25** (a) Calculated values of  $\gamma_0$  and  $\gamma_1$  as a function of wavelength for a PCF designed with a dispersion profile shown in part (b), where the ratio  $\gamma_1/\gamma_0$  is also plotted. (After Ref. [147]; © 2010 American Physical Society.)

The single nonlinear parameter  $\gamma$  appearing in Eq. (2.3.36) corresponds to  $\gamma^{0000}$ . Values of  $m, n, p$ , and  $q$  larger than zero in the sum in Eq. (11.6.8) take into account the frequency dependence of the mode profile to successively higher orders. It is easy to see from Eq. (11.6.10) that  $\gamma^{mnpq}$  satisfy symmetry relations that reduce the number of independent nonlinear coefficients considerably. If we restrict ourselves to first-order corrections, a single higher-order parameter  $\gamma_1 = \gamma^{1000} = \gamma^{0100} = \gamma^{0010} = \gamma^{0001}$  is required.

Figure 11.25a shows the calculated values of  $\gamma_0$  and  $\gamma_1$  as a function of wavelength for a PCF designed with a dispersion profile shown in part (b). At wavelengths near  $1\text{ }\mu\text{m}$ , the ratio  $\gamma_1/\gamma_0$  is relatively small, indicating that higher-order nonlinear terms in Eq. (11.6.8) play a minor role. However, at wavelengths  $>2\text{ }\mu\text{m}$ , this ratio exceeds 0.25. As a result,  $\gamma_1$  term contributes significantly to the nonlinear evolution at such wavelengths. Numerical simulations reveal that it can considerably reduce the Raman-induced frequency shift, among other things [147]. The main point to note is that the frequency dependence of the mode profile may become important in practice, depending on the fiber design.

## PROBLEMS

- 11.1** The refractive index of an optical fiber is specified as  $n = n_0 + n_2 I$ , where  $n_0 = 1.45$ ,  $n_2 = 2.7 \times 10^{-20}\text{ m}^2/\text{W}$ , and  $I$  is the optical intensity. If it is written in terms of the electric field as  $n = n_0 + n_2^E |E|^2$ , find the magnitude of  $n_2^E$ .
- 11.2** Light from two CW lasers differing in their wavelengths by a small amount  $\Delta\lambda$  is transmitted through a fiber of length  $L$ . Derive an expression for the optical spectrum at the fiber output after including the effects of SPM-induced phase shift. Assume equal input powers for the two lasers and neglect fiber loss and dispersion for simplicity.
- 11.3** Explain how the optical spectrum obtained in the preceding problem can be used to estimate the nonlinear parameter  $\gamma$ . Also, derive the expression for the power ratio given in Eq. (11.1.5).
- 11.4** Discuss how the nonlinear phenomenon of XPM can be used to deduce  $\gamma$  for an optical fiber. Why is it important to depolarize the pump light when a pump–probe configuration is employed?
- 11.5** The measured values of  $\gamma$  are found to be smaller by about 20% when pulses shorter than 1 ns are employed. Explain the physical process responsible for this reduction. What would happen if femtosecond pulses are employed for measuring  $\gamma$ ?
- 11.6** Explain why large values of  $\gamma$  cannot be realized by reducing the core diameter of a fiber designed with silica cladding to below  $1\text{ }\mu\text{m}$ . Using  $A_{\text{eff}} = \pi w^2$  with  $w = a/\sqrt{\ln V}$ , prove that the maximum value of  $\gamma$  occurs when the  $V = \sqrt{e}$ , where  $V$  parameter of the fiber is defined as in Eq. (11.2.1).

- 11.7** Solve the eigenvalue equation (2.2.8) given in Section 2.2.1 for a tapered fiber with air cladding using  $n_1 = 1.45$ ,  $n_2 = 1$ , and  $a = 1 \mu\text{m}$  and plot  $\beta(\omega)$  in the wavelength range of  $0.4\text{--}2 \mu\text{m}$ . Also plot second and third-order dispersion parameters,  $\beta_2$  and  $\beta_3$ , over this range and find the zero-dispersion wavelength of this fiber.
- 11.8** Repeat the preceding problem for tapered fibers with diameters  $<1 \mu\text{m}$  and generate the dispersion curves given in Figure 11.9b.
- 11.9** Derive an expression for  $\gamma$  in tapered fibers in terms of the V parameter using a Gaussian mode profile of the form  $\exp(-\rho^2/w^2)$  with  $w = a/\sqrt{\ln V}$ , where  $a$  is the core radius. Prove that  $\gamma$  is maximum when fiber is designed such that  $V \approx 1.85$ .
- 11.10** Explain the mode-confinement mechanism in microstructured fibers in two cases in which the central core is made of silica or contains air. How is the light confined in the second case when the cladding contains a periodic array of air holes?

## REFERENCES

- [1] P. N. Butcher and D. N. Cotter, *The Elements of Nonlinear Optics* (Cambridge University Press, 1990), Appendix 5.
- [2] A. Owyong, R. W. Hellwarth, and N. George, *Phys. Rev. B* **5**, 628 (1972).
- [3] A. Owyong, *IEEE J. Quantum Electron.* **9**, 1064 (1973).
- [4] D. Milam and M. J. Weber, *J. Appl. Phys.* **47**, 2497 (1976).
- [5] M. J. Weber, D. Milam, and W. L. Smith, *Opt. Eng.* **17**, 463 (1978).
- [6] R. Adair, L. I. Chase, and S. A. Payne, *J. Opt. Soc. Am. B* **4**, 875 (1987).
- [7] M. Asobe, K. Suzuki, T. Kanamori, and K. Kubodera, *Appl. Phys. Lett.* **60**, 1153 (1992).
- [8] D. Milam, *Appl. Opt.* **37**, 546 (1998).
- [9] R. H. Stolen and C. Lin, *Phys. Rev. A* **17**, 1448 (1978).
- [10] G. P. Agrawal, in *Properties of Glass and Rare-Earth Doped Glasses for Optical Fibers*, D. Hewak, Ed. (INSPEC, IEE, London, 1998), pp. 17–21.
- [11] M. Monerie and Y. Durteste, *Electron. Lett.* **23**, 961 (1987).
- [12] L. Prigent and J. P. Hamaide, *IEEE Photon. Technol. Lett.* **5**, 1092 (1993).
- [13] K. S. Kim, R. H. Stolen, W. A. Reed, and K. W. Quoi, *Opt. Lett.* **19**, 257 (1994).
- [14] Y. Namihira, A. Miyata, and N. Tanahashi, *Electron. Lett.* **30**, 1171 (1994).
- [15] T. Kato, Y. Suetsugu, M. Takagi, E. Sasaoka, and M. Nishimura, *Opt. Lett.* **20**, 988 (1995).
- [16] M. Artiglia, E. Ciaramella, and B. Sordo, *Electron. Lett.* **31**, 1012 (1995).
- [17] M. Artiglia, R. Caponi, F. Cisternino, C. Naddeo, and D. Roccato, *Opt. Fiber Technol.* **2**, 75 (1996).
- [18] A. Boskovic, S. V. Chernikov, J. R. Taylor, L. Gruner-Nielsen, and O. A. Levring, *Opt. Lett.* **21**, 1966 (1996).
- [19] A. Fellegara, M. Artiglia, S. B. Andereasen, A. Melloni, F. P. Espunes, and M. Martinelli, *Electron. Lett.* **33**, 1168 (1997).
- [20] R. H. Stolen, W. A. Reed, K. S. Kim, and G. T. Harvey, *J. Lightwave Technol.* **16**, 1006 (1998).

- [21] T. Omae, K. Nakajima, and M. Ohashi, *IEEE Photon. Technol. Lett.* **13**, 571 (2001).
- [22] D. Monzón-Hernández, A. N. Starodumov, Yu. O. Barmenkov, I. Torres-Gómez, and F. Mendoza-Santoyo, *Opt. Lett.* **23**, 1274 (1998).
- [23] C. Vinegoni, M. Wegumuller, and N. Gisin, *Electron. Lett.* **36**, 886 (2000).
- [24] K. Li, Z. Xiong, G. D. Peng, and P. L. Chu, *Opt. Commun.* **136**, 223 (1997).
- [25] T. Kato, Y. Suetsugu, and M. Nishimura, *Opt. Lett.* **20**, 2279 (1995).
- [26] A. Wada, S. Okude, T. Sakai, and R. Yamauchi, *Electron. Commun. Jpn., Part I* **79**, 12 (1996).
- [27] K. Nakajima and M. Ohashi, *IEEE Photon. Technol. Lett.* **14**, 492 (2002).
- [28] N. L. Boling, A. J. Glass, and A. Owyoung, *IEEE J. Quantum Electron.* **14**, 601 (1978).
- [29] S. V. Chernikov and J. R. Taylor, *Opt. Lett.* **21**, 1559 (1996).
- [30] F. A. Oguama, H. Garcia, and A. M. Johnson, *J. Opt. Soc. Am. B* **22**, 426 (2005).
- [31] A. Martínez-Rios, A. N. Starodumov, Y. O. Barmenkov, V. N. Filippov, and I. Torres-Gómez, *J. Opt. Soc. Am. B* **18**, 794 (2001).
- [32] E. L. Buckland and R. W. Boyd, *Opt. Lett.* **21**, 1117 (1996).
- [33] E. L. Buckland and R. W. Boyd, *Opt. Lett.* **22**, 676 (1997).
- [34] A. Fellegara, A. Melloni, and M. Martinelli, *Opt. Lett.* **22**, 1615 (1997).
- [35] A. Melloni, M. Martinelli, and A. Fellegara, *Fiber Integ. Opt.* **18**, 1 (1999).
- [36] C. Mazzali, D. F. Grosz, and H. L. Fragnito, *IEEE Photon. Technol. Lett.* **11**, 251 (1999).
- [37] A. Fellegara, A. Melloni, and P. Sacchetto, *Opt. Commun.* **162**, 333 (1999).
- [38] S. Smolorz, F. Wise, and N. F. Borrelli, *Opt. Lett.* **24**, 1103 (1999).
- [39] T. Okuno, M. Onishi, T. Kashiwada, S. Ishikawa, and M. Nishimura, *IEEE J. Sel. Topics Quantum Electron.* **5**, 1385 (1999).
- [40] T. Morioka, S. Kawanishi, K. Mori, and M. Saruwatari, *Electron. Lett.* **30**, 790 (1994).
- [41] T. Okuno, M. Onishi, and M. Nishimura, *IEEE Photon. Technol. Lett.* **34**, 72 (1998).
- [42] P. B. Hansen, G. Jacobovitz-Veselka, L. Gruner-Nielsen, and A. J. Stentz, *Electron. Lett.* **34**, 1136 (1998).
- [43] Y. Emori, Y. Akasaka, and S. Namiki, *Electron. Lett.* **34**, 2145 (1998).
- [44] K. Mori, H. Takara, and S. Kawanishi, *J. Opt. Soc. Am. B* **18**, 1780 (2001).
- [45] T. Okuno, M. Hirano, T. Kato, M. Shigematsu, and M. Onishi, *Electron. Lett.* **39**, 972 (2003).
- [46] J. W. Nicholson, A. K. Abeeluck, C. Headley, M. F. Yan, and C. G. Jørgensen, *Appl. Phys. B* **77**, 211 (2003).
- [47] K.-W. Chung and S. Yin, *Microwave Opt. Technol. Lett.* **40**, 153 (2004).
- [48] A. Zheltikov, *J. Opt. Soc. Am. B* **22**, 1100 (2005).
- [49] A. W. Snyder and J. D. Love, *Optical Waveguide Theory* (Kluwer Academic, 1983).
- [50] P. Dumais, F. Gonthier, S. Lacroix, J. Bures, A. Villeneuve, P. G. J. Wigley, and G. I. Stegeman, *Opt. Lett.* **18**, 1996 (1993).
- [51] T. A. Birks, W. J. Wadsworth, and P. St. J. Russell, *Opt. Lett.* **25**, 1415 (2000).
- [52] J. M. Harbold, F. O. Ilday, F. W. Wise, T. A. Birks, W. J. Wadsworth, and Z. Chen, *Opt. Lett.* **27**, 1558 (2000).
- [53] J. Teipel, K. Franke, D. Türke, F. Warken, D. Meiser, M. Leuschner, and H. Giessen, *Appl. Phys. B* **77**, 245 (2003).
- [54] F. Lu and W. H. Knox, *Opt. Express* **12**, 347 (2004).
- [55] M. A. Foster and A. L. Gaeta, *Opt. Express* **12**, 3137 (2004).
- [56] G. Brambilla, *J. Opt.* **12**, 043011 (2010).
- [57] D. C. Johnson, B. S. Kawasaki, and K. O. Hill, *Fiber Integ. Opt.* **3**, 263 (1980).

- [58] H. Yokota, E. Sugai, and Y. Sasaki, *Opt. Rev.* **4**, 104 (1997).
- [59] T. E. Dimmick, G. Kakarantzas, T. A. Birks, and P. St. J. Russell, *Appl. Opt.* **38**, 6845 (1999).
- [60] G. Kakarantzas, T. E. Dimmick, T. A. Birks, R. Le Roux, and P. St. J. Russell, *Opt. Lett.* **26**, 1137 (2001).
- [61] L. C. Özcan, V. Tréanton, F. Guay, and R. Kashyap, *IEEE Photon. Technol. Lett.* **19**, 657 (2007).
- [62] L. M. Tong, R. R. Gattass, J. B. Ashcom, S. L. He, J. Y. Lou, M. Y. Shen, I. Maxwell, and E. Mazur, *Nature* **426**, 816 (2003).
- [63] L. M. Tong, J. Y. Lou, and E. Mazur, *Opt. Express* **12**, 1025 (2004).
- [64] S. Leon-Saval, T. Birks, W. Wadsworth, P. St. J. Russell, and M. Mason, *Opt. Express* **12**, 2864 (2004).
- [65] M. A. Foster, K. D. Moll, and A. L. Gaeta, *Opt. Express* **12**, 2880 (2004).
- [66] C. M. B. Cordeiro, W. J. Wadsworth, T. A. Birks, and P. St. J. Russell, *Opt. Lett.* **30**, 1980 (2005).
- [67] R. Zhang, J. Teipel, X. Zhang, D. Nau, and H. Giessen, *Opt. Express* **12**, 1700 (2004).
- [68] J. C. Knight, T. A. Birks, P. St. J. Russell, and D. M. Atkin, *Opt. Lett.* **21**, 1547 (1996).
- [69] N. G. R. Broderick, T. M. Monro, P. J. Bennett, and D. J. Richardson, *Opt. Lett.* **24**, 1395 (1999).
- [70] J. Broeng, D. Mogilevtsev, S. B. Barkou, and A. Bjarklev, *Opt. Fiber Technol.* **5**, 305 (1999).
- [71] B. J. Eggleton, C. Kerbage, P. S. Westbrook, R. S. Windeler, and A. Hale, *Opt. Express* **9**, 698 (2001).
- [72] T. P. White, R. C. McPhedran, C. M. de Sterke, L. C. Botten, and M. J. Steel, *Opt. Lett.* **26**, 1660 (2001).
- [73] P. St. J. Russell, *Science* **299**, 358 (2003).
- [74] J. K. Ranka and A. L. Gaeta, in *Nonlinear Photonic Crystals*, R. E. Slusher and B. J. Eggleton, Eds. (Springer, New York, 2003).
- [75] P. St. J. Russell, *J. Lightwave Technol.* **24**, 4729 (2006).
- [76] V. Finazzi, T. M. Monro, and D. J. Richardson, *J. Opt. Soc. Am. B* **20**, 1427 (2003).
- [77] K. Nakajima, J. Zhou, K. Tajima, K. Kurokawa, C. Fukai, and I. Sankawa, *J. Lightwave Technol.* **17**, 7 (2005).
- [78] D. Mogilevtsev, T. A. Birks, and P. St. J. Russell, *Opt. Lett.* **23**, 1662 (1998).
- [79] A. Ferrando, E. Silvestre, J. J. Miret, P. Andrés, and M. V. Andrés, *Opt. Lett.* **24**, 276 (1999).
- [80] T. M. Monro, D. J. Richardson, N. G. R. Broderick, and P. J. Bennett, *J. Lightwave Technol.* **18**, 50 (2000).
- [81] F. Brechet, J. Marcou, D. Pagnoux, and P. Roy, *Opt. Fiber Technol.* **6**, 181 (2000).
- [82] N. A. Mortensen, *Opt. Express* **10**, 341 (2002).
- [83] Z. Zhu and T. G. Brown, *Opt. Express* **8**, 547 (2001); *Opt. Commun.* **206**, 333 (2002).
- [84] M. Koshiba and K. Saitoh, *Opt. Express* **11**, 1746 (2003).
- [85] K. Saitoh and M. Koshiba, *J. Lightwave Technol.* **23**, 3580 (2005).
- [86] E. C. Mägi, P. Steinurzel, and B. J. Eggleton, *Opt. Express* **12**, 776 (2004).
- [87] H. C. Nguyen, B. T. Kuhlmeij, E. C. Mägi, et al., *Appl. Phys. B* **81**, 377 (2005).
- [88] W. J. Wadsworth, A. Witkowska, S. G. Leon-Saval, and T. A. Birks, *Opt. Express* **13**, 6541 (2005).
- [89] R. F. Cregan, B. J. Mangan, J. C. Knight, et al., *Science* **285**, 1537 (1999).
- [90] A. R. Bhagwat and A. L. Gaeta, *Opt. Express* **16**, 5035 (2008).

- [91] F. Benabid and P. J. Roberts, *J. Mod. Opt.* **58**, 87 (2011).
- [92] J. C. Travers, W. Chang, J. Nold, N. Y. Joly, and P. St. J. Russell, *J. Opt. Soc. Am. B* **28**, A11 (2011).
- [93] F. Benabid, J. C. Knight, G. Antonopoulos, and P. St. J. Russell, *Science* **298**, 399 (2002).
- [94] F. Couny, F. Benabid, and P. S. Light, *Opt. Lett.* **31**, 3574 (2006).
- [95] F. Benabid, F. Couny, J. C. Knight, T. A. Birks, and P. St. J. Russell, *Nature* **434**, 488 (2005).
- [96] S. Yiou, P. Delaye, , A. Rouvie, et al., *Opt. Express* **13**, 4786 (2005).
- [97] C. R. Rosberg, F. H. Bennet, , D. N. Neshev, et al., *Opt. Express* **15**, 12145 (2007).
- [98] S. Lebrun, P. Delaye, R. Frey, and G. Roosen, *Opt. Lett.* **32**, 337 (2007).
- [99] F. Couny and F. Benabid, *J. Opt. A* **11**, 103002 (2009).
- [100] J. Bethge, A. Husakou, , F. Mitschke, et al., *Opt. Express* **18**, 6230 (2010).
- [101] M. C. Huy, A. Baron, S. Lebtun, R. Frey, and P. Delaye, *J. Opt. Soc. Am. B* **27**, 1886 (2010).
- [102] P. Yeh, A. Yariv, and E. Marom, *J. Opt. Soc. Am.* **68**, 1196 (1978).
- [103] S. G. Johnson, M. Ibanescu, , M. Skorobogatiy, et al., *Opt. Express* **9**, 748 (2001).
- [104] B. Temelkuran, S. D. Hart, G. Benoit, J. D. Joannopoulos, and Y. Fink, *Nature* **420**, 650 (2002).
- [105] T. Katagiri, Y. Matsuura, and M. Miyagi, *Opt. Lett.* **29**, 557 (2004).
- [106] S. Février, R. Jamier, J.-M. Blondy, et al., *Opt. Express* **14**, 562 (2006).
- [107] G. Vienne, Y. Xu, C. Jakobsen, et al., *Opt. Express* **12**, 3500 (2004).
- [108] A. Argyros, M. A. van Eijkelenborg, M. C. J. Large, and I. M. Bassett, *Opt. Lett.* **31**, 172 (2006).
- [109] A. Dupuis, N. Guo, B. Gauvreau, et al., *Opt. Lett.* **32**, 2882 (2007).
- [110] K. J. Rowland, S. Afshar V., and T. M. Monro, *J. Lightwave Technol.* **26**, 43 (2008).
- [111] M. S. Ferreira, J. M. Baptista, P. Roy, et al., *Opt. Lett.* **36**, 993 (2011).
- [112] H. T. Bookey, S. Dasgupta, N. Bezwada, et al., *Opt. Express* **17**, 17130 (2009).
- [113] B. Nagaraju, R. K. Varshney, G. P. Agrawal, and B. P. Pal, *Opt. Commun.* **283**, 2525 (2010).
- [114] M. A. Newhouse, D. L. Weidman, and D. W. Hall, *Opt. Lett.* **15**, 1185 (1990).
- [115] J. S. Wang, E. M. Vogel, and E. Snitzer, *Opt. Mat.* **3**, 187 (1994).
- [116] I. Kang, T. D. Krauss, F. W. Wise, B. G. Aitken, and N. F. Borrelli, *J. Opt. Soc. Am. B* **12**, 2053 (1995).
- [117] M. Asobe, T. Kanamori, and K. Kubodera, *IEEE J. Quantum Electron.* **29**, 2325 (1993).
- [118] M. Asobe, *Opt. Fiber Technol.* **3**, 142 (1997).
- [119] T. Cardinal, K. A. Richardson, H. Shim, et al., *J. Non-Cryst. Solids* **256**, 353 (1999).
- [120] G. Lenz, J. Zimmermann, T. Katsufuji, et al., *Opt. Lett.* **25**, 254 (2000).
- [121] R. E. Slusher, G. Lenz, J. Hodelin, J. Sanghera, L. B. Shaw, and I. D. Aggarwal, *J. Opt. Soc. Am. B* **21**, 1146 (2004).
- [122] L. B. Fu, M. Rochette, V. G. Ta'eed, D. J. Moss, and B. J. Eggleton, *Opt. Express* **13**, 7637 (2005).
- [123] P. Petropoulos, H. Ebendorff-Heidepriem, V. Finazzi, et al., *Opt. Express* **11**, 3568 (2003).
- [124] X. Feng, A. K. Mairaj, D. W. Hewak, and T. M. Monro, *J. Lightwave Technol.* **23**, 2046 (2005).
- [125] J. Y. Y. Leong, P. Petropoulos, J. H. V. Price, et al., *J. Lightwave Technol.* **24**, 183 (2006).

- [126] X. Feng, F. Poletti, A. Camerlingo, et al., *Opt. Express* **17**, 20249 (2009).
- [127] X. Feng, F. Poletti, A. Camerlingo, et al., *Opt. Fiber Technol.* **16**, 378 (2010).
- [128] M. El-Amraoui, J. Fatome, J. C. Jules, et al., *Opt. Express* **18**, 45478 (2010).
- [129] Schott Optical Glass Catalogue; <http://www.schott.com>.
- [130] N. Sugimoto, H. Kanbara, S. Fujiwara, K. Tanaka, and K. Hirao, *Opt. Lett.* **21**, 1637 (1996); *J. Opt. Soc. Am. B* **16**, 1904 (1999).
- [131] K. Kikuchi, K. Taira, and N. Sugimoto, *Electron. Lett.* **38**, 166 (2002).
- [132] H. Ebendorff-Heidepriem, P. Petropoulos, S. Asimakis, et al., *Opt. Express* **12**, 5082 (2004).
- [133] J. H. Lee, K. Kikuchi, T. Nagashima, T. Hasegawa, S. Ohara, and N. Sugimoto, *Opt. Express* **13**, 3144 (2005); *Opt. Express* **13**, 6864 (2005).
- [134] J. T. Gopinath, H. M. Shen, H. Sotobayashi, E. P. Ippen, T. Hasegawa, T. Nagashima, and N. Sugimoto, *J. Lightwave Technol.* **23**, 3591 (2005).
- [135] J. H. Lee, T. Nagashima, T. Hasegawa, S. Ohara, N. Sugimoto, and K. Kikuchi, *J. Lightwave Technol.* **24**, 22 (2006).
- [136] F. Parmigiani, S. Asimakis, N. Sugimoto, F. Koizumi, P. Petropoulos, and D. J. Richardson, *Opt. Express* **14**, 5038 (2006).
- [137] M. P. Fok and C. Shu, *IEEE J. Sel. Topics Quantum Electron.* **14**, 587 (2008).
- [138] I. V. Kabakova, D. Grobnić, S. Mihailov, et al., *Opt. Express* **11**, 5868 (2011).
- [139] R. Stegeman, L. Jankovic, H. Kim, et al., *Opt. Lett.* **28**, 1126 (2003).
- [140] V. V. R. K. Kumar, A. K. George, J. C. Knight, and P. St. J. Russell, *Opt. Express* **11**, 2641 (2003).
- [141] M. Liao, X. Yan, Z. Duan, T. Suzuki, and Y. Ohishi, *J. Lightwave Technol.* **29**, 1018 (2011).
- [142] F. Poletti and P. Horak, *J. Opt. Soc. Am. B* **25**, 1645 (2008).
- [143] S. Afshar V. and T. M. Monro, *Opt. Express* **17**, 2298 (2009).
- [144] M. D. Turner, S. Afshar V., and T. M. Monro, *Opt. Express* **17**, 11565 (2009).
- [145] T. M. Monro, H. Ebendorff-Heidepriem, W. Q. Zhang, and S. Afshar V., *IEEE J. Quantum Electron.* **45**, 1357 (2009).
- [146] B. A. Daniel and G. P. Agrawal, *J. Opt. Soc. Am. B* **27**, 956 (2010).
- [147] F. Biancalana, T. X. Tran, S. Stark, M. A. Schmidt, and P. St. J. Russell, *Phys. Rev. Lett.* **105**, 093904 (2010).

# Novel Nonlinear Phenomena

# 12

The development of highly nonlinear fibers discussed in Chapter 11 has led to the observation of novel nonlinear effects such as the generation of extremely broad optical spectra (supercontinuum generation) and large Raman-induced frequency shifts that allow wavelength tuning of mode-locked lasers. These nonlinear phenomena are finding a multitude of new applications for optical fibers in fields as diverse as high-precision metrology and optical coherence tomography. This chapter focuses on several such nonlinear effects, while Chapter 13 is devoted to supercontinuum generation. We revisit in Sections 12.1 and 12.2 the topics of soliton fission and intrapulse Raman scattering, discussed earlier in Section 5.5. It turns out that these phenomena play an important role when femtosecond pulses propagate inside highly nonlinear fibers. Section 12.3 considers how dispersion tailoring in such fibers can be used to enhance the four-wave-mixing (FWM) process for practical applications. Sections 12.4 and 12.5, devoted to the topic of harmonic generation in optical fibers, focus on the second and third harmonics, respectively.

---

## 12.1 SOLITON FISSION AND DISPERSIVE WAVES

As discussed in Section 5.5, several higher-order effects perturb solitons as they propagate inside a fiber. What happens to a soliton because of such perturbations depends on its order, quantified by the parameter  $N$  and defined first in Eq. (4.2.3). In terms of the dispersion and nonlinear lengths,  $L_D = T_0^2/|\beta_2|$  and  $L_{NL} = 1/(\gamma P_0)$ ,  $N^2$  represents their ratio and is given by

$$N^2 = \frac{L_D}{L_{NL}} = \frac{\gamma P_0 T_0^2}{|\beta_2|}, \quad (12.1.1)$$

where  $T_0$  is the width and  $P_0$  is the peak power of input pulses. When  $N$  exceeds 1.5, an optical pulse propagates as a second- or higher-order soliton that undergoes a fission process when perturbed by the third- or higher-order dispersion. Although soliton fission was predicted and observed in the 1980s [1–5], it was only after the advent of highly nonlinear fibers in the late 1990s that it began to play a much more important role in the evolution of femtosecond pulses in such fibers.

### 12.1.1 Fission of Second- and Higher-Order Solitons

When the inverse scattering method of Section 5.2.1 is used to solve the ideal NLS equation (5.2.2) with an integer value of  $N$ , the solution given in Eq. (5.2.8) consists of a superposition of  $N$  fundamental solitons that evolve as one entity in a periodic fashion. For a non-integer value of  $N$ , the soliton order is the integer closest to  $N$ . The inverse scattering method shows that the widths and peak powers of the individual fundamental solitons are related to the width  $T_0$  and peak power  $P_0$  of input pulses as [3]

$$T_k = \frac{T_0}{2N + 1 - 2k}, \quad P_k = \frac{(2N + 1 - 2k)^2}{N^2} P_0, \quad (12.1.2)$$

where  $k$  varies from 1 to  $N$ . A high-order soliton can remain intact only if all of its constituent fundamental solitons travel with the same group velocity.

As seen in Section 5.5, several higher-order dispersive and nonlinear effects become important for a femtosecond optical pulse, and they perturb this pulse continuously as it propagates down the fiber. Eventually these perturbations break up the pulse propagating as a high-order soliton into its constituent fundamental solitons, a phenomenon called soliton fission. As an example, Figure 12.1 shows the temporal and spectral evolutions of a third-order soliton ( $N = 3$ ) over a distance of  $1.5L_D$  by solving the generalized NLS Equation (5.5.8) numerically. Only perturbations induced by the third-order dispersion (TOD) are included by setting  $\delta_3 = 0.01$ ,  $s = 0$  and  $\tau_R = 0$  in this equation. A clear evidence of soliton fission is seen in the spectral evolution, where we see a sudden emergence of a new spectral peak at a distance of about  $z = 0.4L_D$  on the high-frequency (blue) side of the pulse spectrum and the formation of spectral fringes at distances longer than that. Temporal fringes are also apparent in Figure 12.1b.

The origin of temporal and spectral fringes seen in Figure 12.1 lies in the interference of coherent optical fields. Just as two spectrally separated coherent fields interfere and produce temporal modulation, two temporally separated optical pulses produce spectral modulation. As the three fundamental solitons move at slightly different speeds because of TOD, they separate from each other, and this separation results in the spectral fringes seen in Figure 12.1b. Mathematically, the spectrum of two identical optical pulses whose peaks are shifted by  $t_s$  is obtained by taking the Fourier transform of  $A(t) + A(t - t_s)$ . The spectral power is then given by  $P(\omega) = 2|\tilde{A}(\omega)|^2[1 + \cos(\omega t_s)]$ , where  $\tilde{A}(\omega)$  is the Fourier transformation of  $A(t)$ . Clearly, the spectrum is modulated at a frequency  $1/t_s$ . The situation is more complicated in the case of Figure 12.1 because three pulses with different peak amplitudes are involved, but the origin remains the same.

The temporal evolution in Figure 12.1a also has a clear evidence of soliton fission. It shows that a part of the pulse energy leaves the central region in the form of a dispersive wave that travels slower than the three solitons in the central region and spreads rapidly in size. The generation of this dispersive wave is discussed later in this section. Another noteworthy feature is that the central region, where three

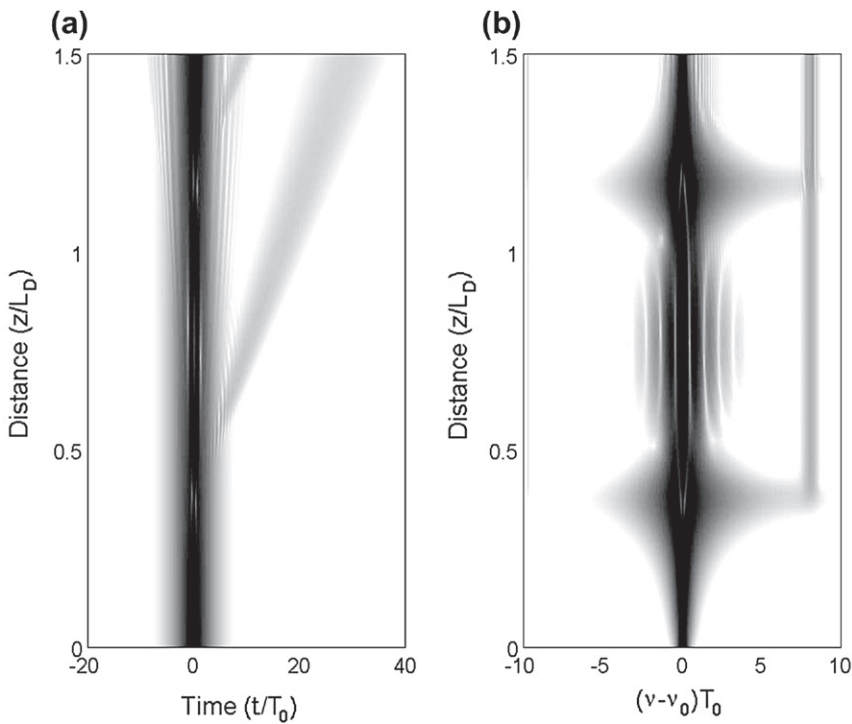


**Figure 12.1** (a) Temporal and (b) spectral evolutions of a third-order soliton ( $N=3$ ) over a distance  $z=1.5L_D$  when it is perturbed by the TOD alone ( $\delta_3=0.01$ ,  $s=0$  and  $\tau_R=0$ ). A decibel scale over 70dB range is used such that a darker shade represents a more intense region.

fundamental solitons propagate after the fission process, itself becomes broader and exhibits temporal fringes. This behavior can also be understood by recalling that three solitons broaden as they loose energy and separate from each other (but not enough to be clearly visible).

The fission of high-order solitons was observed in a 1987 experiment by recording spectra of 830-fs input pulses of different peak powers at the output of a 1-km-long fiber [4]. Figure 12.2a shows these spectra at three peak-power levels together with the input pulse spectrum. The fission process occurs in all three cases at different distances within the fiber and creates multiple fundamental solitons, representing pulses of different widths and peak powers. The spectrum of each pulse shifts toward longer wavelengths because of intrapulse Raman scattering, the shortest pulse exhibiting the largest shift. At the highest peak power of 530W, one can see three distinct peaks in Figure 12.2a on the long-wavelength (red) side that correspond to three fundamental solitons. The shortest soliton has shifted by nearly 200 nm because of intrapulse Raman scattering.

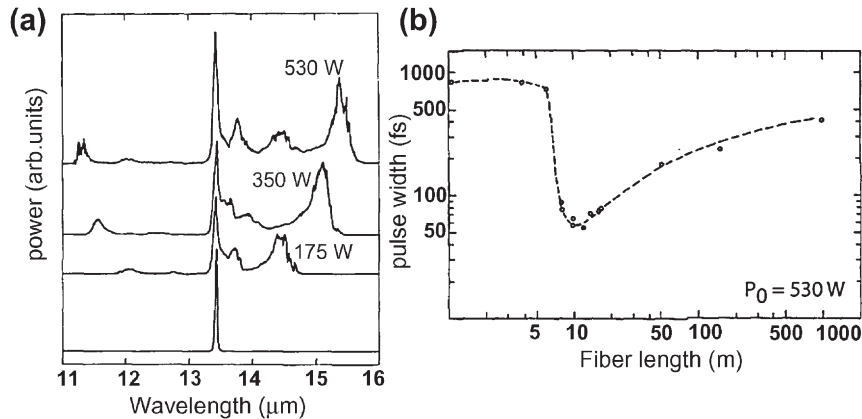


**Figure 12.2** (a) Measured optical spectra at the output of a 1 km-long fiber for three values of the peak power  $P_0$  of 830-fs input pulses. Initial pulse spectrum is also shown for comparison. (b) Measured pulse widths as a function of fiber length for  $P_0 = 530 \text{ W}$ . Note a sudden change in width after soliton fission. (After Ref. [4]; © 1987 IEEE.)

A clear-cut evidence of fission was provided by measuring width of the pulse associated with the rightmost spectral peak in Figure 12.2a. As seen in part (b), autocorrelation measurements for fibers of different lengths show a sudden reduction in the pulse width, from 830 fs to near 50 fs, at a distance where soliton fission occurs (about 7 m at the input peak power of 530 W). Such a reduction in pulse width is predicted by Eq. (12.1.2) if the soliton order  $N$  for the input pulse exceeds 10. This is indeed the case if we use Eq. (12.1.1) with  $T_0 = 0.5 \text{ ps}$  and  $P_0 = 530 \text{ W}$  together with the typical values of  $\gamma$  and  $\beta_2$  for the standard fiber used in the experiment. Notice that the width of the shortest pulse increases with propagation. The reason is that the GVD parameter  $\beta_2$  in Eq. (12.1.1) itself depends on wavelength and increases as the soliton spectrum shifts toward longer wavelengths. As a result, the pulse width must increase to maintain  $N = 1$  for the soliton.

High-order solitons are perturbed by several effects inside optical fibers, including TOD, self-steepening, and intrapulse Raman scattering (see Section 5.5). One may ask which process plays a dominant role in initiating the soliton fission. The answer depends on the relative magnitudes of the three parameters,  $\delta_3$ ,  $s$ , and  $\tau_R$ , appearing in the normalized NLS equation (5.5.8) and defined in Eq. (5.5.9). All three parameters scale inversely with the pulse width and become larger for shorter pulses. The self-steepening parameter  $s$  is the smallest in practice, and it is unlikely to dominate the fission process. The TOD parameter  $\delta_3$  should exceed a critical value before it can initiate soliton fission. This critical value is 0.022 for  $N = 2$ , reduces to 0.006 for  $N = 3$ , and decreases further with increasing  $N$  [2]. Clearly,  $\delta_3$  can become relatively large for femtosecond pulses launched close to the ZDWL of the fiber. The Raman parameter  $\tau_R$  takes a value of 0.03 for 100-fs pulses if we use  $T_R = 3 \text{ fs}$ . Numerical simulation show that a value of  $\tau_R$  as small as 0.001 can lead to the fission of a higher-order soliton [5]. The reason is that intrapulse Raman scattering shifts the

spectrum of constituent fundamental solitons by different amounts, forcing them to travel at different speeds. As mentioned earlier, such speed changes would break a second or higher-order soliton into its constituents.

### 12.1.2 Generation of Dispersive Waves

The pulse spectra in Figure 12.2a show clearly the fission of a high-order soliton and the resulting Raman-induced spectral shifts of constituent fundamental solitons. Somewhat surprising is the appearance of one or more small-amplitude peaks on the anti-Stokes side of the input pulse spectrum. Such a peak was initially interpreted as a kind of FWM between the Stokes and anti-Stokes waves [4], but its frequency does not satisfy the FWM condition. Indeed, it was found numerically in 1986 that a spectral peak on the short-wavelength side can form even when the Raman effects are neglected and only TOD is included as a perturbation to solitons [2]. Such a blue-shifted peak is also seen in Figure 12.1, where we also see its evidence in the time domain in the form of a dispersive wave. Since the TOD cannot be avoided for femtosecond pulses, it generally plays an important role whenever short optical pulses are transmitted through a fiber.

The important question is what physical process creates spectral components on the short-wavelength side of the pulse spectrum. It turned out that any fundamental soliton ( $N = 1$ ) sheds a part of its energy to a dispersive wave at a specific frequency when it is perturbed by the third- or higher-order dispersion. This frequency is determined by a phase-matching condition that is quite different than that associated with a FWM process. Dispersive waves are linear waves that can propagate in any dispersive medium. However, their amplitude remains negligible until an appropriate phase-matching condition is satisfied.

Generation of dispersive waves through perturbation of solitons by TOD attracted considerable attention soon after this phenomenon was identified numerically [6–17]. Such radiation is also known as the Cherenkov radiation [11] or as the *non-solitonic radiation* (NSR). It is emitted at a frequency at which phase velocity of the dispersive wave matches that of the soliton. The frequency shift between the soliton and the dispersive wave is the temporal analog of the angle at which the Cherenkov radiation is emitted by charged particles in a bulk medium.

The frequency of the dispersive wave that grows because of radiation emitted by the perturbed soliton can be obtained by a simple phase-matching argument requiring that the dispersive wave propagate with the same phase velocity as that of the soliton [11]. Recall that the phase of an optical wave at frequency  $\omega$  changes as  $\phi = \beta(\omega)z - \omega t$ . If  $\omega$  and  $\omega_s$  are frequencies of the dispersive wave and of the soliton, respectively, the two phases at a distance  $z$  after a delay  $t = z/v_g$  are given by [13]

$$\phi(\omega) = \beta(\omega)z - \omega(z/v_g), \quad (12.1.3)$$

$$\phi(\omega_s) = \beta(\omega_s)z - \omega_s(z/v_g) + \frac{1}{2}\gamma P_s z, \quad (12.1.4)$$

where  $v_g$  is the group velocity of the soliton. The last term in Eq. (12.1.4) is due to the nonlinear phase shift occurring only for solitons. Its origin is related to the phase

factor  $\exp(iz/2L_D)$  appearing in Eq. (5.2.16), where  $L_D = L_{NL} = (\gamma P_s)^{-1}$ . The two phases are equal when the following phase-matching condition is satisfied

$$\beta(\omega) = \beta(\omega_s) + \beta_1(\omega - \omega_s) + \frac{1}{2}\gamma P_s \equiv \eta(\omega), \quad (12.1.5)$$

where we used the relation  $v_g = 1/\beta_1$ . Solutions of this equation determine the frequency  $\omega$  of one or more dispersive waves generated because of soliton perturbation.

A graphical way to visualize the phase-matching condition is to plot the left and right sides of Eq. (12.1.5) for a fiber with known dispersion relation  $\beta(\omega)$ . Figure 12.3 illustrates two cases with different forms of  $\beta(\omega)$ , showing that dispersive waves can be generated both in the (a) anomalous- and (b) normal-GVD regions of an optical fiber [14]. The frequency dependence of the GVD parameter  $\beta_2$ , shown by the dashed parabolic curve, is based on the expansion of  $\beta(\omega)$  in a Taylor series around a reference frequency and retaining terms of up to the fourth order. The dotted line represents soliton dispersion  $\eta(\omega)$ , and its intersection with the solid curve determines the radiation frequency  $\omega_r$ . It is clear from Figure 12.3 that the form of  $\beta(\omega)$  plays an important role in determining  $\omega_r$ . In some cases, more than one dispersive waves can also be generated.

Analytic solutions of the phase-matching condition (12.1.5) are possible for a few specific forms of the dispersion relation [11]. If we expand  $\beta(\omega)$  in a Taylor series around the soliton frequency  $\omega_s$  and retain terms up to fourth order in the frequency shift  $\Omega = \omega - \omega_s$ , Eq. (12.1.5) leads to the following fourth-order polynomial:

$$\beta_2\Omega^2 + \frac{\beta_3}{3}\Omega^3 + \frac{\beta_4}{12}\Omega^4 - \gamma P_s = 0. \quad (12.1.6)$$

Note that  $P_s$  is the peak power of a fundamental soliton formed after the fission process (and not that of the input pulse). Similarly, the dispersion parameters appearing

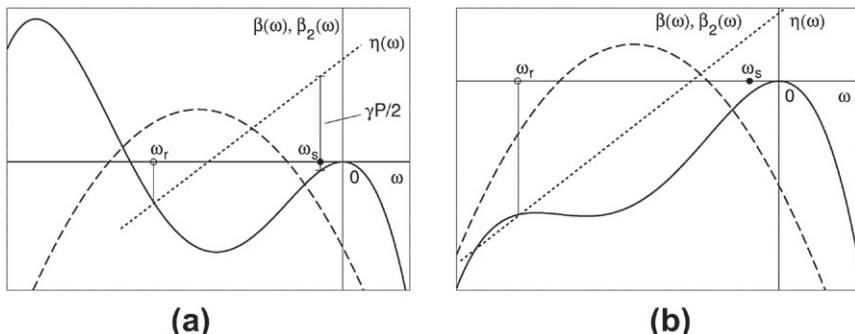


**Figure 12.3** Graphical solution of the phase-matching condition when the radiation frequency  $\omega_r$  lies in the (a) normal and (b) anomalous-GVD regions of the fiber. The solid, dashed, and dotted lines show  $\beta(\omega)$ ,  $\beta_2(\omega)$ , and  $\eta(\omega)$ , respectively. (After Ref. [14]; © 2007 American Physical Society.)

in Eq. (12.1.6) are at the soliton central frequency  $\omega_s$ . If this frequency changes because of intrapulse Raman scattering, the frequency of dispersive waves would also change. Only real solutions of the polynomial in Eq. (12.1.6) have a physical meaning.

As an example, consider the simplest case in which the fourth-order dispersion is negligible and we can set  $\beta_4 = 0$ . The resulting cubic polynomial provides the following approximate solution [11]

$$\Omega \approx -\frac{3\beta_2}{\beta_3} + \frac{\gamma P_s \beta_3}{3\beta_2^2}. \quad (12.1.7)$$

For solitons propagating in the anomalous-dispersion region such that  $\beta_2 < 0$  and  $\beta_3 > 0$ , the frequency shift of the dispersive wave is positive. As a result, the NSR is emitted at a higher frequency (or a shorter wavelength) than that of the soliton. This was the case for the numerical results shown in Figure 12.1. Indeed, the frequency of NSR in this figure agrees well with the prediction of Eq. (12.1.7). The situation changes in fibers with  $\beta_3 < 0$  for which the NSR can be emitted at wavelengths longer than that of the soliton. It is important to stress that predictions of Eq. (12.1.7) are only approximate if the fourth and higher-order dispersive terms in Eq. (12.1.6) are not negligible.

As a second example, consider the special case in which  $\beta_3$  can be set to zero in Eq. (12.1.6) so that the soliton is perturbed by the fourth-order dispersion alone. In this situation, two dispersive waves are generated simultaneously, shifted from the soliton frequency by

$$\Omega_{\pm} \approx \pm(-12\beta_2/\beta_4)^{1/2}, \quad (12.1.8)$$

where we neglected the  $\gamma$  term as it is relatively small in practice. For solitons propagating in the anomalous-dispersion region of a fiber such that  $\beta_2 < 0$  and  $\beta_4 > 0$ , both solutions are real and have opposite signs, indicating that NSR occurs on both sides of the soliton frequency. However, if  $\beta_4 < 0$  for this fiber, both solutions become imaginary, and no dispersive waves are produced.

One can verify the preceding predictions by solving the underlying generalized NLS equation numerically. If we use the normalized form of this equation given in Eq. (5.5.8) and retain only the dispersive perturbation by setting  $s = \tau_R = 0$ , it takes the form

$$i\frac{\partial u}{\partial \xi} + \frac{1}{2}\frac{\partial^2 u}{\partial \tau^2} + |u|^2 u = i\delta_3 \frac{\partial^3 u}{\partial \tau^3} - \delta_4 \frac{\partial^4 u}{\partial \tau^3}, \quad (12.1.9)$$

where the last term representing fourth-order dispersion has been added, and the two normalized dispersion parameters are defined as

$$\delta_3 = \frac{\beta_3}{6|\beta_2|T_0}, \quad \delta_4 = \frac{\beta_4}{24|\beta_2|T_0^2}. \quad (12.1.10)$$

In terms of these two parameters, the polynomial in Eq. (12.1.6) can be written in the following normalized form [17]:

$$\delta_4 f^4 + \delta_3 f^2 - \frac{1}{2} f^2 = \frac{1}{2}(2N - 1)^2, \quad (12.1.11)$$

where  $f = \Omega T_0$  and  $P_s$  in Eq. (12.1.7) was replaced with  $P_1$  in Eq. (12.1.2), assuming that dominant contribution to dispersive waves comes from the shortest soliton formed after the fission process.

Figure 12.4 shows the temporal and spectral evolutions of a third-order soliton ( $N = 3$ ) over a distance of  $3L_D/2$  by solving Eq. (12.1.9) numerically with  $\delta_3 = 0$  and  $\delta_4 = 0.0005$ . This figure should be compared with Figure 12.1 obtained by solving the same equation with  $\delta_3 = 0.01$  and  $\delta_4 = 0$ . Similar to the case of TOD, fourth-order dispersion also leads to the soliton fission at a distance near  $\xi = 0.3$ . However, in contrast with the TOD case, we see a sudden emergence of two new spectral peaks after the fission on both the blue and red sides of the original pulse spectrum. The frequencies of these peaks agree with the prediction of Eq. (12.1.10). Indeed, if we neglect the last term and set  $\delta_3 = 0$  in this equation, the solution is given by  $f = \pm(2\delta_4)^{-1/2}$ , resulting in  $f/2\pi = \pm 5.03$ , in good agreement with the results in Figure 12.4b. Temporal

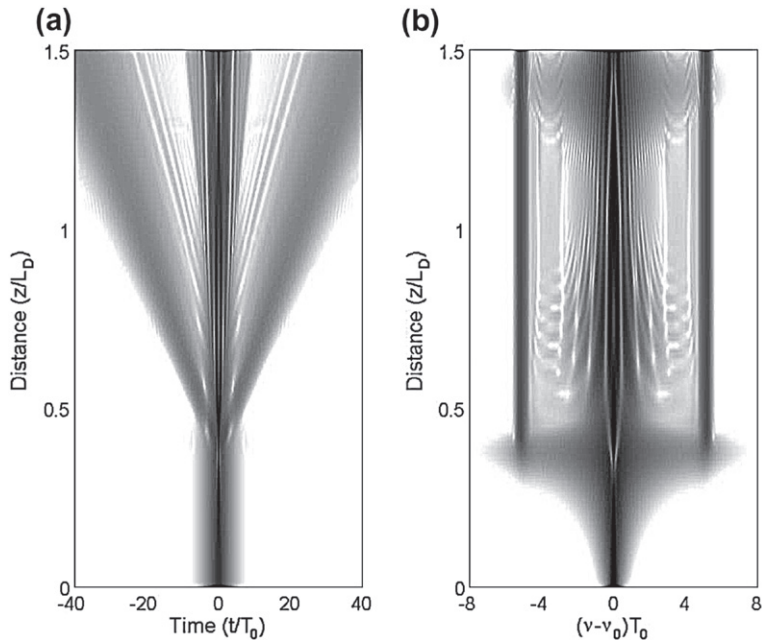


**Figure 12.4** (a) Temporal and (b) spectral evolutions of a third-order soliton ( $N = 3$ ) over a distance  $z = 1.5L_D$  when it is perturbed by the fourth-order dispersion alone ( $\delta_4 = 0.0005$ ). A decibel scale over 70 dB range is used such that a darker shade represents a more intense region.

evolution in Figure 12.4a shows that two dispersive waves are generated simultaneously, one propagating faster and the other traveling slower than the input pulse. We also observe the formation of temporal and spectral fringes at distances  $z > 0.5L_D$ . These can be understood to result from an interference among the three fundamental solitons and two dispersive wave propagating at different speeds with different phase shifts.

The preceding discussion clearly shows that the generation of dispersive waves during soliton fission is sensitive to minute details of the dispersion relation  $\beta(\omega)$  of the fiber, and it may be necessary in some situations to include dispersion terms even higher than the fourth order. A numerical approach with multiple higher-order dispersion terms shows that all odd-order terms generate a single NSR peak on the blue or the red side of the carrier frequency of the pulse, depending on the sign of the corresponding dispersion parameter [16]. In contrast, even-order dispersion terms with positive signs always create two NSR peaks on opposite sides of the carrier frequency. In general, the frequencies as well as the amplitudes of the NSR peaks depend not only on the magnitudes of various dispersion parameters of the fiber but also on higher-order nonlinear effects discussed in the following section.

An important question is how much pulse energy is transferred to dispersive waves during soliton fission. Although several approximate analytic approaches have been used for this purpose [6–11], an accurate answer requires numerical solutions of the generalized NLS equation [15]. Figure 12.5 shows peak power of the NSR spectral band (relative to input peak power) as a function of  $\delta_3$  when a second-order soliton undergoes fission. The gray curve shows the case when Eq. (12.1.9) is solved with  $\delta_4 = 0$  and predicts that the NSR peak power can exceed 1% of the input peak power for  $\delta_3 > 0.02$ . Since higher-order nonlinear effects can also modify the fission process, the black curve is obtained by solving Eq. (2.3.36). One sees clearly that, for any value of  $\delta_3$ , the inclusion of intrapulse Raman scattering lowers the amplitude of the NSR peak. The next section provides more details on the impact of intrapulse Raman scattering on femtosecond pulses.

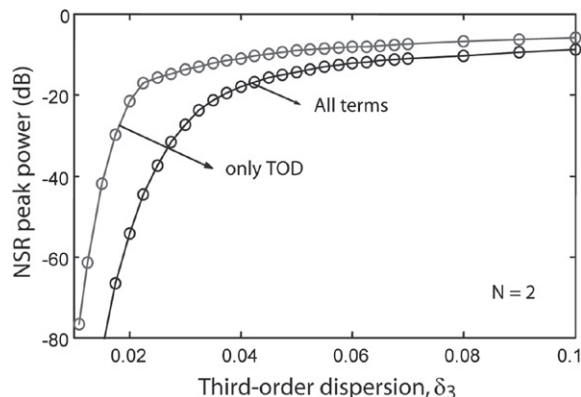


**Figure 12.5** NSR peak power (relative to input peak power) as a function of  $\delta_3$  when a second-order soliton undergoes fission. (After Ref. [15]; © 2009 American Physical Society.)

## 12.2 INTRAPULSE RAMAN SCATTERING

As discussed in Section 5.5.4, the spectrum of an ultrashort pulse shifts toward longer wavelengths because of intrapulse Raman scattering. Such a shift was first noticed around 1985 in the context of solitons and was called the soliton self-frequency shift [18–20]. The term Raman-induced frequency shift (RIFS) was used in Section 4.4.3 because a spectral shift can occur even in the normal-GVD regime of an optical fiber where solitons are not formed [21]. With the advent of highly nonlinear fibers, it was discovered that the RIFS of solitons can become quite large in such fibers and that it can be used for providing a tunable source of femtosecond pulses. Later experiments revealed that it can also be suppressed under certain conditions. This section focuses on such novel aspects of intrapulse Raman scattering.

### 12.2.1 Enhanced RIFS Through Soliton Fission

In a 1986 experiment, 560-fs optical pulses were propagated as fundamental solitons in a 0.4-km-long fiber and their spectrum was found to shift by up to 8 THz [19]. It was discovered soon after that the fission of higher-order solitons generates a much larger RIFS [4]. This is clearly evident in Figure 12.2a where the shortest soliton created after the fission exhibits a shift of more than 20 THz after 1 km of propagation inside a fiber. A soliton whose wavelength shifts continuously during propagation is sometimes referred to as the Raman soliton. Although the properties of Raman solitons attracted some attention during the 1990s [22–27], it was only after 1999 that the RIFS was observed and studied in microstructured and other narrow-core fibers [28–43].

The generalized NLS equation (5.5.8) of Section 5.5 can be used for studying RIFS in microstructured fibers if it is modified to add the effects of fourth-order dispersion. Neglecting the self-steepening term ( $s = 0$ ), it takes the form

$$i \frac{\partial u}{\partial \xi} + \frac{1}{2} \frac{\partial^2 u}{\partial \tau^2} + |u|^2 u = i \delta_3 \frac{\partial^3 u}{\partial \tau^3} - \delta_4 \frac{\partial^4 u}{\partial \tau^3} + \tau_R u \frac{\partial |u|^2}{\partial \tau}, \quad (12.2.1)$$

where  $\tau_R = T_R/T_0$  is a dimensionless parameter and  $T_R \approx 3$  fs, as defined in Eq. (2.3.43). As an example, Figure 12.6 shows the temporal and spectral evolutions of a third-order soliton ( $N = 3$ ) over a distance of  $3L_D/2$  by solving Eq. (12.2.1) numerically with  $\delta_3 = 0.01$ ,  $\delta_4 = 0$ , and  $\tau_R = 0.04$ . This figure should be compared with Figure 12.1, obtained by solving the same equation with  $\tau_R = 0$  so that the Raman effects are absent. A comparison of two figures shows how intrapulse Raman scattering affects the pulse evolution. A dispersive wave is still generated on the blue side of the input spectrum but its amplitude is much smaller for  $\tau_R = 0.04$ , in agreement with the results in Figure 12.5. More importantly, we observe in Figure 12.6a that the shortest soliton created after the fission process separates from the main part of the pulse and its trajectory bends continuously toward the right side. Physically, this can happen if it travels slower and slower as it propagates down the fiber. This

deacceleration of the soliton is produced by the RIFS that continuously shifts the spectrum of the shortest soliton toward the red side. Such a spectral shift is indeed seen in Figure 12.6b. Notice also how the spectrum oscillates along the fiber length just after the fission of the third-order soliton occurs near  $\xi = 0.3$ . As before, temporal and spectral fringes in Figure 12.6 result from interference of multiple optical fields.

The important issue from a practical standpoint is how the RIFS depends on the input parameters associated with the optical pulse and the fiber used. The theory of Section 5.5.4 can be employed to study how RIFS scales with these parameters. In general, one should employ Eq. (5.5.17) when an input pulse with a power profile,  $P(t) = P_0 \operatorname{sech}^2(t/T_0)$ , is launched into a fiber such that it propagates as a fundamental soliton. In the case of negligible fiber losses and frequency chirp, pulse width remains nearly unchanged, and we can employ Eq. (5.5.18). If we introduce  $\Delta\nu_R = \Omega_p/(2\pi)$ , the RIFS grows linearly along the fiber at a rate

$$\frac{d\Delta\nu_R}{dz} = -\frac{4T_R|\beta_2|}{15\pi T_0^4} = -\frac{4T_R(\gamma P_0)^2}{15\pi|\beta_2|}, \quad (12.2.2)$$

where we used the soliton condition in Eq. (12.1.1). The preceding equation shows that the RIFS produces a spectral shift toward lower frequencies (a red shift), and

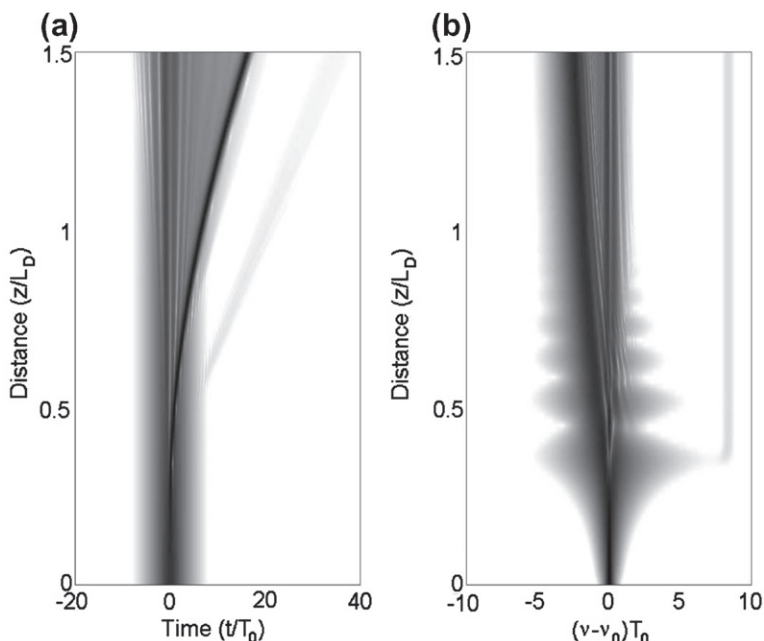


**Figure 12.6** (a) Temporal and (b) spectral evolutions of a third-order soliton ( $N = 3$ ) over a distance of  $1.5L_D$  when  $\delta_3 = 0.01$ ,  $\delta_4 = 0$ , and  $\tau_R = 0.04$ . A decibel scale over 70 dB range is used such that a darker shade represents a more intense region.

it scales with the width as  $T_0^{-4}$ , or quadratically with the product  $\gamma P_0$ . Such a quadratic dependence of  $\Delta\nu_R$  on the soliton peak power was seen in the original 1986 experiment [19].

It follows from Eq. (12.2.2) that the RIFS can be made large by propagating shorter pulses with higher peak powers inside highly nonlinear fibers. Using the definition of the nonlinear length,  $L_{NL} = (\gamma P_0)^{-1}$ , the RIFS is found to scale as  $L_{NL}^{-2}$ . As an example, if we use a highly nonlinear fiber with  $\beta_2 = -30 \text{ ps}^2/\text{km}$  and  $\gamma = 100 \text{ W}^{-1}/\text{km}$ ,  $L_{NL} = 10 \text{ cm}$  for 100-fs (FWHM) input pulses with  $P_0 = 100 \text{ W}$ , and the pulse spectrum shifts inside the fiber at a rate of about 1 THz/m. Under such conditions, it will shift by 50 THz over a 50-m-long fiber, provided that  $N = 1$  can be maintained over this distance.

Eq. (12.2.2) does not apply to the propagation of high-order solitons. However, it can be used to estimate RIFS of fundamental solitons after the fission process provided we replace  $T_0$  and  $P_0$  with the values given in Eq. (12.1.2). Even then, it provides only a rough estimate of the RIFS because its derivation is based on the approximate form of the generalized NLS equation given in Eq. (2.3.34). Moreover, its use requires a numerical value of the parameter  $T_R$ . As indicated in Eq. (2.3.43), this parameter depends on the slope of the Raman-gain spectrum at origin. The dashed line in Figure 12.7 shows that such a linear approximation deviates considerably from the actual shape of the Raman-gain spectrum, especially for short pulses with a relatively wide spectrum [43]. As a result, it overestimates the rate of RIFS in silica fibers for pulses shorter than 200 fs or so, and the actual Raman-gain spectrum should be used for predicting the RIFS. An alternative is to use the modified form of the Raman response function given in Eq. (2.3.41). Its predictions agree well with the results obtained using the actual Raman-gain spectrum [39]. The use of Eq. (2.3.40) should be avoided because it overestimates considerably the RIFS of pulses shorter than 100 fs.

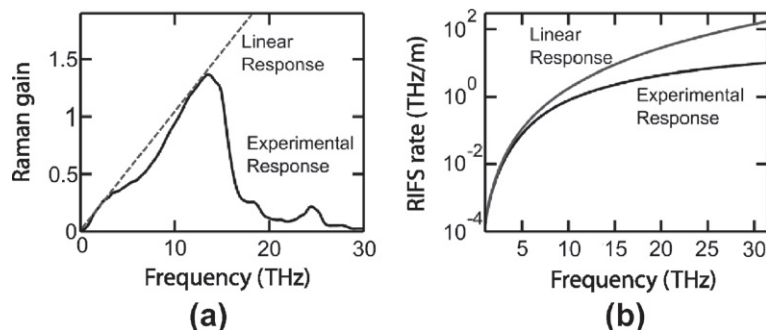


**Figure 12.7** (a) Raman-gain spectrum (solid curve) and its linear approximation (gray line). (b) Rate of RIFS ( $d\Delta\nu_R/dz$ ) experienced by a fundamental soliton as a function of the pulse bandwidth in the two cases. (After Ref. [43]; © 2010 OSA.)

Relatively large RIFS were realized in a 2001 experiment in which 200-fs pulses at an input wavelength of 1300 nm were launched into a 15-cm-long fiber, tapered down to a 3- $\mu\text{m}$  core diameter [31]. Figure 12.8 shows the experimentally measured output spectrum and the autocorrelation trace, together with numerical predictions of the generalized NLS equation (2.3.34). The parameters used for simulations corresponded to the experiment and were  $L_{\text{NL}} = 0.6 \text{ cm}$ ,  $L_D = 20 \text{ cm}$ , and  $T_R = 3 \text{ fs}$ . The effects of third-order dispersion were included using  $L'_D = 25 \text{ m}$ . In this experiment, a spectral shift of 45 THz occurs over a 15-cm length, resulting in a rate of 3 THz/cm, a value much larger than that expected from Eq. (12.2.2) or Figure 12.7. This discrepancy can be resolved by noting that the soliton order  $N$  exceeded 1 under the experimental conditions, and the input pulse propagates initially as a higher-order soliton inside the fiber.

The qualitative features of Figure 12.8 can be understood from the soliton-fission scenario discussed in Section 12.1. Recall that soliton fission breaks a higher-order soliton into multiple fundamental solitons whose widths and peak powers are related to  $N$  as indicated in Eq. (12.1.2). When  $N = 2.1$ , two fundamental solitons created through the fission process have widths of  $T_0/3.2$  and  $T_0/1.2$ . The narrower soliton exhibits a much larger RIFS compared with the broader one because of the  $T_0^{-4}$  dependence seen in Eq. (12.2.2). For the  $N = 2.1$  example, the enhancement factor for the narrower soliton is about 105. Figure 12.8 agrees with this scenario as the Raman soliton, whose spectrum has been shifted by 250 nm, has a width of 62 fs,

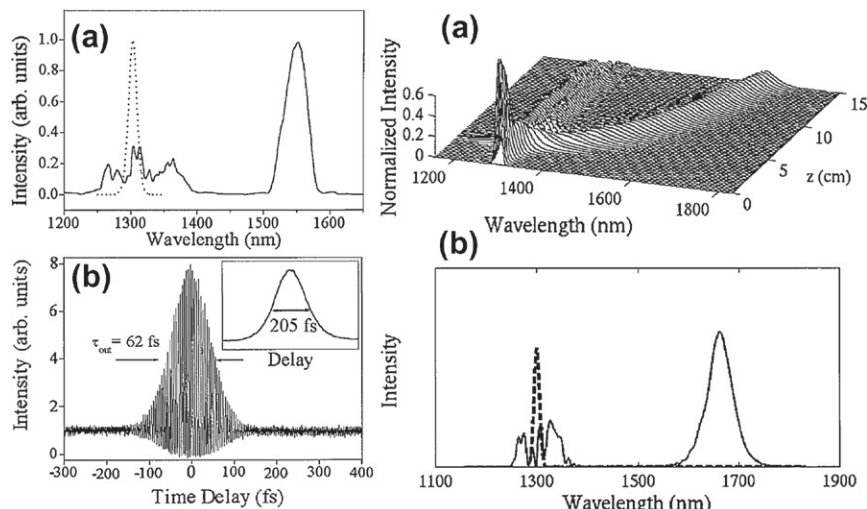


**Figure 12.8** Left panel: measured (a) spectrum and (b) autocorrelation trace of the Raman soliton at the output of a tapered fiber. Right panel: numerically simulated (a) evolution of pulse spectrum and (b) output spectrum. Dashed curves show the input spectrum. (After Ref. [31]; © 2001 OSA.)

about 3.3 times smaller than the input pulse width of 205 fs. Numerical simulations reveal that fission occurs within 2 cm of propagation inside the tapered fiber. The spectrum of the ultrashort soliton shifts rapidly toward the red side, as dictated by Eq. (12.2.2). After 15 cm, the spectrum has shifted to near 1550 nm. This predicted behavior agrees with the experimental data qualitatively.

### 12.2.2 Cross-correlation Technique

Figure 12.8 shows evidence of soliton fission through the observed pulse spectrum at the fiber output together with a separate autocorrelation measurement of the pulse width in the time domain. As seen in Figure 12.6, the shortest soliton separates from other solitons because its speed is reduced more and more as its spectrum shifts toward longer wavelengths. To observe the temporal and spectral features simultaneously, an extension of the technique based on frequency-resolved optical gating (FROG), discussed in Section 3.3.4, is used in practice. It is referred to as the X-FROG technique [44] and it consists of performing a cross-correlation of the output pulse and a narrow reference pulse (with an adjustable relative delay) inside a nonlinear crystal through second-harmonic or sum-frequency generation. More precisely, one records a series of optical spectra at the crystal output with different delays between the two pulses. Mathematically, the cross-correlation is given by

$$S(\tau, \omega) = \left| \int_{-\infty}^{\infty} A(L, t) A_{\text{ref}}(t - \tau) \exp(i\omega t) dt \right|^2, \quad (12.2.3)$$

where  $A(L, t)$  is the pulse amplitude at the end of a fiber of length  $L$  and  $A_{\text{ref}}(t - \tau)$  is the amplitude of the reference pulse delayed by an adjustable amount  $\tau$ . In practice, rather than employing another source of femtosecond pulses, the same laser is used to provide both the input and reference pulses by splitting the laser power into two parts.

In a different approach, the output spectrum was filtered to extract the Raman soliton, which was then used as a reference pulse for performing cross-correlation [53]. In this experiment, 110-fs pulses from a fiber laser operating at 1556 nm were launched into a polarization-maintaining fiber exhibiting a dispersion of only  $-0.1 \text{ ps}^2/\text{km}$  at the laser wavelength. The output was divided into two beams, one of which was passed through a low-pass filter (with its cutoff wavelength at 1600 nm) and a delay line before reaching the KTP crystal. The spectrum of the sum-frequency signal was recorded using a monochromator for a range of delay times.

Figure 12.9 shows the X-FROG traces and optical spectra of output pulses for fiber lengths of 10 m and 180 m, when 110-fs pulses at a 48-MHz repetition rate are launched with 24-mW average power. In the case of a 10-m-long fiber (left panel), the Raman soliton is shifted to near 1650 nm and is delayed by about 3 ps, compared with the residual part of the input pulse located near 1550 nm. This delay is due to a change in the group velocity that accompanies any spectral shift. The most interesting feature is the appearance of NSR near 1440 nm in the normal-GVD regime of the

fiber. In the case of a 180-m-long fiber (right panel), the Raman soliton has shifted even more, and its spectrum is located close to 1700 nm. It is also delayed by about 200 ps from the residual input pulse (not shown in Figure 12.9). The radiation in the normal-GVD regime now appears near 1370 nm and is spread temporally over a 4-ps-wide window.

The group velocity of the NSR may not necessarily coincide with that of the Raman soliton. However, Figure 12.9 reveals that the two overlap temporally for both the short and long fibers. This overlap is related to the phenomenon of soliton trapping, discussed earlier in Section 6.5.2 in the context of a birefringent fiber. As soon as the NSR and Raman soliton, propagating at different speeds, approach each other, they interact through XPM. This interaction modifies the spectrum of the NSR such that the two begin to move at the same speed. In other words, the Raman soliton traps the NSR and drags it along. Such trapping was observed in a 2002 experiment in which the NSR and the soliton were first separated using low- and high-pass optical filters, and then launched into a 170-m-long highly nonlinear fiber [54]. As the

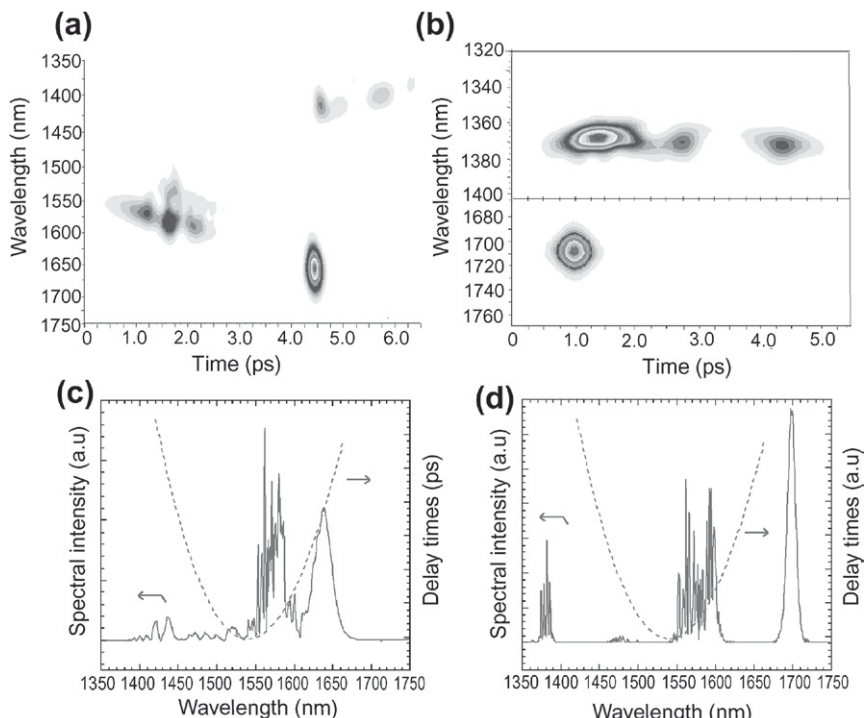


**Figure 12.9** X-FROG traces (top row) and optical spectra (bottom row) for fiber lengths of 10 m (left column) and 180 m (right column). Dashed curves show the delay time as a function of the wavelength. (After Ref. [53]; © 2001 OSA.)

soliton spectrum shifted through the RIFS, the NSR spectrum also shifted with it such that they moved at the same speed. This trapping mechanism has also been used for ultrafast optical switching [55].

### 12.2.3 Wavelength Tuning through RIFS

An important application of RIFS consists of tuning the wavelength of a model-locked laser by sending femtosecond optical pulses through a highly nonlinear fiber. The wavelength tuning results from the fact that the RIFS in Eq. (12.2.2) depends on several fibers parameters ( $\beta_2$ ,  $\gamma$ , and  $z$ ) and the peak power  $P_0$  of input pulses. In addition, the fiber's dispersion parameter  $\beta_2$  depends on the laser wavelength that can be varied if the pulse source itself is tunable. In this way, RIFS can be used for tuning the wavelength of a model-locked laser toward longer wavelengths over a wide range.

A 60-cm-long photonic crystal fiber (PCF) having its zero-dispersion wavelength (ZDWL) at 690 nm was used in a 2002 experiment [34]. Figure 12.10 shows the experimentally measured output spectra at several average power levels when 70-fs pulses with a 48-MHz repetition rate at a wavelength of 782 nm were launched into this fiber. After the input power exceeds a value large enough to ensure  $N > 1$ , a Raman soliton is generated, and its wavelength shifts continuously through the RIFS inside the fiber. The total shift at the output of fiber becomes larger as the input power is increased. The spectral profile follows a nearly “sech” shape, and its width of 18 nm remains almost constant. As much as 70% of input energy appears in the form of a Raman soliton. Note the appearance of a second Raman soliton when the input power is 3.6 mW. This is expected when the soliton order exceeds 2 for the input pulse. Larger wavelength shifts can be realized by optimizing the fiber and pulse parameters.

Although the tuning range of RIFS was initially limited to near 100 nm [28–30], the RIFS technique was soon employed to produce widely tunable sources of femtosecond pulses [45–52]. As early as 2001, a 220-m-long polarization-maintaining

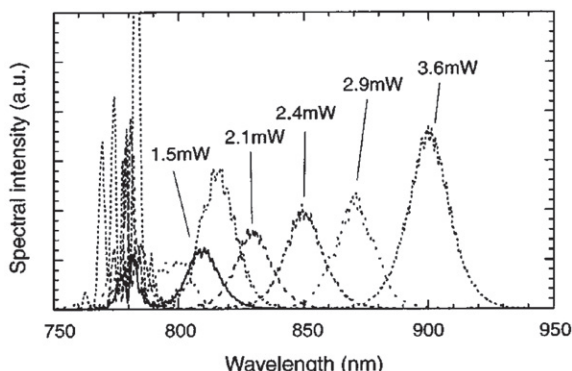


**Figure 12.10** Output spectra for several input average powers when 70-fs pulses were launched into a 60-cm-long photonic crystal fiber. (After Ref. [34]; © 2002 IEEE.)

fiber (core diameter  $5.8\text{ }\mu\text{m}$ ) was used to tune the wavelength of 110-fs pulses from 1560 to 2030 nm [45]. Clearly, much shorter lengths will be required if microstructured fibers with narrow core diameters were used for shifting the pulse wavelength. Moreover, since the ZDWL of such fibers shifts toward shorter wavelengths, they can be used with other mode-locked lasers operating near or below  $1\text{ }\mu\text{m}$ . In a 2002 experiment, a 4.7-m-long holey fiber with a core diameter of  $<2.5\text{ }\mu\text{m}$  was doped with ytterbium and used to amplify  $1.06\text{-}\mu\text{m}$  femtosecond pulses [46]. As pulses were amplified, their wavelength shifted toward longer wavelengths because of the RIFS. As a result, output wavelength could be tuned from 1060 to 1330 nm by varying the launched power. By 2005, an all-fiber source of femtosecond pulses, tunable from 1030 to 1330 nm, was realized by launching 2-ps pulses from a Yb-doped fiber laser into a 1.5-m-long microstructured fiber with a  $2\text{-}\mu\text{m}$  core diameter [47].

A much larger tuning range was realized in a 2006 experiment in which a 10-m-long PCF was employed for changing the wavelength of 66-fs pulses from its initial value of  $1.05\text{-}\mu\text{m}$  [48]. The PCF with a core diameter of  $2.8\text{ }\mu\text{m}$  had  $\gamma = 23\text{ W}^{-1}/\text{km}$  and exhibited anomalous dispersion with  $\beta_2 = -14.6\text{ ps}^2/\text{km}$  at the input wavelength of  $1.05\text{-}\mu\text{m}$ . Figure 12.11 shows the experimentally measured spectra at the PCF

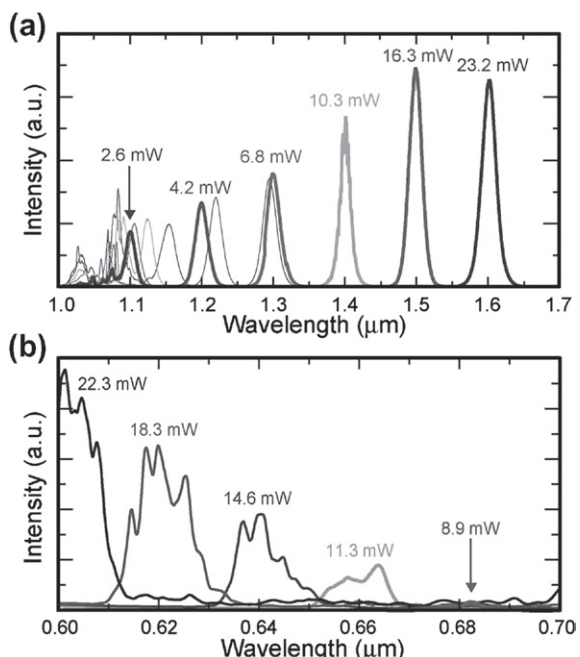


Figure 12.11 Output spectra for several input average powers on the (a) long and (b) short-wavelength sides of input wavelength when 66-fs pulses were launched into a 10-m-long PCF. Power values indicate the total power at output end of the PCF. (After Ref. [48]; © 2006 IEEE.)

output for several average output powers on the (a) long and (b) short-wavelength sides of input wavelength. The output wavelength could be tuned from 1050 to 1700 nm by changing the input power. Once the input power was large enough to excite a higher-order soliton, multiple peaks were observed. At the same time, as expected, some pulse energy appeared at shorter wavelengths in the form of dispersive waves. The tuning range of RIFS was extended to 910 nm in a 2008 experiment by launching 65-fs pulses (obtained from a model-locked laser operating at 1245 nm) into a PCF that was only 70-cm-long and had its ZDWL at 975 nm [51]. It exhibited anomalous dispersion with  $|\beta_2| = 32 \text{ ps}^2/\text{km}$  at 1245 nm, a value that increased continuously as the pulse wavelength shifted from 1245 to 2160 nm. Because of increasing dispersion, pulse width increased as the wavelength shifted into the infrared. The important point is that the use of RIFS can provide a source of femtosecond pulses whose wavelength can be tuned by more than 900 nm.

#### 12.2.4 Effects of Birefringence

Propagation of ultrashort pulses in a birefringent fiber leads to novel nonlinear effects when a linearly polarized input pulse is launched at an angle  $\theta$  from the slow axis such that it excites the two orthogonally polarized modes of the fiber simultaneously [56–59]. If the pulses in these two modes do not have the same peak powers, the order parameter  $N$  will be different for them. As a result, their fission would create orthogonally polarized Raman solitons of different widths, and their spectra would shift at different rates throughout the fiber. Thus, a single optical pulse should produce two Raman solitons of different wavelengths at the output end of a nonlinear fiber.

This is indeed what was observed in a 1999 experiment [56]. Figure 12.12a shows the optical spectra recorded for two input launch angles from the slow axis of a 100-m-long polarization-maintaining fiber with a birefringence of  $7 \times 10^{-4}$ . In this

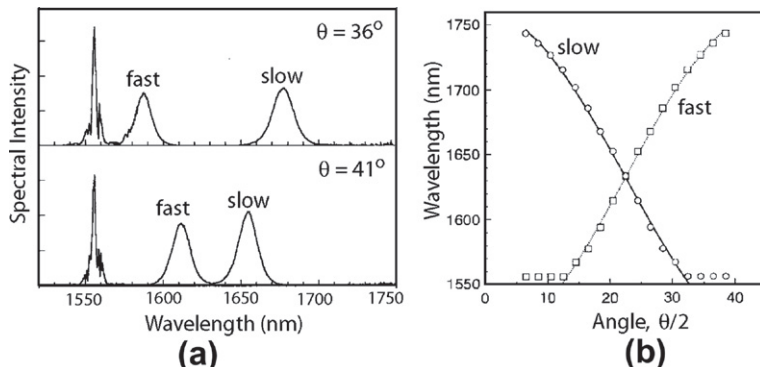


**Figure 12.12** (a) Optical spectra at the output of a 110-m-long fiber for two values of  $\theta$  showing formation of two orthogonally polarized Raman solitons. (b) Measured wavelengths of two solitons plotted as a function of  $\theta/2$ . (After Ref. [56]; © 1999 IEEE.)

experiment, 180-fs pulses were launched at a wavelength of 1556 nm with an average power of 11.2 mW at the 48-MHz repetition rate. Only a single Raman soliton was observed along the slow axis for  $\theta < 24^\circ$  because the power in the mode polarized along the fast axis was too small to form a fundamental soliton. When  $\theta = 36^\circ$ , two Raman solitons are formed, but the one along the fast axis is shifted much less than the other one because of its lower peak power. The two solitons spectra move closer as  $\theta$  is increased further, and they overlap perfectly when  $\theta = 45^\circ$ . This is what one would expect intuitively. Figure 12.12b shows the wavelengths of two Raman solitons as a function of  $\theta/2$ . The two Raman solitons travel at different speeds within the fiber and become separated by more than 320 ps, as the large fiber birefringence results in a group delay of  $>3$  ps/m. For  $\theta > 66^\circ$ , the Raman soliton forms only along the fast axis because the input power along the slow axis becomes too small to form a soliton.

An interesting feature of such a dual-wavelength pulse pair was discovered in a 2002 experiment in which a fiber with reduced birefringence was employed [57]. It was found that the more-intense pulse can trap the other one, if the two overlap temporally when they are formed and interact through XPM. After this trapping occurs, the pair move together at a common group velocity. Figure 12.13a shows the X-FROG spectrogram of trapped pulses at the output of a 140-m-long fiber exhibiting a birefringence of  $3 \times 10^{-4}$ . In this experiment, 110-fs pulses at a 48-MHz repetition rate were launched at a wavelength near to 1550 nm and were polarized such that a larger part of pulse energy was polarized in the mode along the slow axis of the fiber. As seen in Figure 12.13a, the spectrum of the Raman soliton for this mode is centered near 1684 nm. The other mode should have shifted less because of its lower power, but its spectrum was actually located near 1704 nm. Such a large spectral shift was attributed to the trapping of the lower-energy pulse by the soliton. Figure 12.13b shows the measured wavelengths of the two components for three fiber lengths.

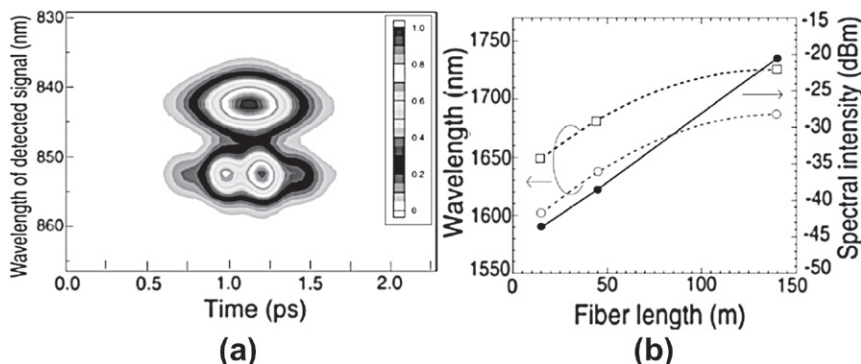


Figure 12.13 (a) X-FROG spectrogram of trapped pulses at the output of a 140-m-long fiber. (b) Measured wavelengths of slow (circles) and fast (squares) polarization components for three different fiber lengths. Filled circles show power of the fast component at the central wavelength. (After Ref. [57]; © 2002 OSA.)

Clearly, once trapping occurs, the two pulses move together and their wavelengths are shifted by the same amount.

An unexpected feature of [Figure 12.13b](#) is that the power in the trapped pulse polarized along the fast axis increases exponentially along the fiber length. This is due to amplification of the trapped pulse by the soliton polarized along the slow axis through the Raman gain. The soliton acts as a pump and amplifies the trapped pulse located 20 nm away on the Stokes side. Even though the Raman gain is not very large for an orthogonally polarized pump, numerical simulations based on two coupled generalized NLS equations show that it can still amplify the trapped pulse enough that the peak power of the amplified pulse becomes comparable to that of the soliton [57]. Such a trapping mechanism can be used for ultrafast optical switching by selectively dragging one pulse from a pulse train [58].

The preceding approach can be used to create more than two Raman solitons. The basic idea consists of creating multiple pulses with different peak powers from a single pump pulse. For example, if the pulse is first passed through a high-birefringence fiber of short length and large core diameter so that nonlinear effects are negligible inside it, the pulse will split into two orthogonally polarized pulses with a temporal spacing set by the birefringence of this fiber. If these two pulses are then launched into a highly nonlinear birefringent fiber whose principal axes are oriented at an angle to the first fiber, each pulse would create two Raman solitons, resulting in the formation of four solitons at four different wavelengths. Time-domain multiplexing or polarization-mode dispersion inside a fiber can be used to make multiple copies of one pulse with different amplitudes, each of which then creates a Raman soliton at a different wavelength in the same highly nonlinear fiber [59].

### 12.2.5 Suppression of Raman-Induced Frequency Shifts

One may ask whether the RIFS of solitons can be reduced, or even suppressed, under some conditions. The question attracted attention soon after this phenomenon was discovered, and several techniques have been proposed in response [60–66]. Bandwidth-limited amplification of solitons for RIFS suppression was suggested in 1988 [60] and verified in a 1989 experiment [61]. Other possibilities include the use of cross-phase modulation [62], frequency-dependent gain [63], or an optical resonator [64]. More recently, the unusual properties of PCFs [65] and photonic bandgap fibers [66] have been utilized for this purpose. In this section we focus on the use of PCFs.

As seen in [Figure 12.3](#), the GVD parameter  $\beta_2$  of any fiber has a parabolic shape when fourth-order dispersion is included. Depending on their design,  $\beta_2$  in some microstructured fibers vanishes at two wavelengths, one lying in the visible region and the other located in the infrared region. The dispersion slope, governed by the TOD parameter  $\beta_3$ , is positive near the first zero but becomes negative near the second one. This change in the sign of  $\beta_3$  changes the frequency associated with the dispersive wave generated during soliton fission. As seen from Eq. (12.1.7), the frequency shift  $\Omega$  of the NSR becomes negative for solitons propagating in the anomalous-GVD region near the second ZDWL, where both  $\beta_2$  and  $\beta_3$  take negative values. As a

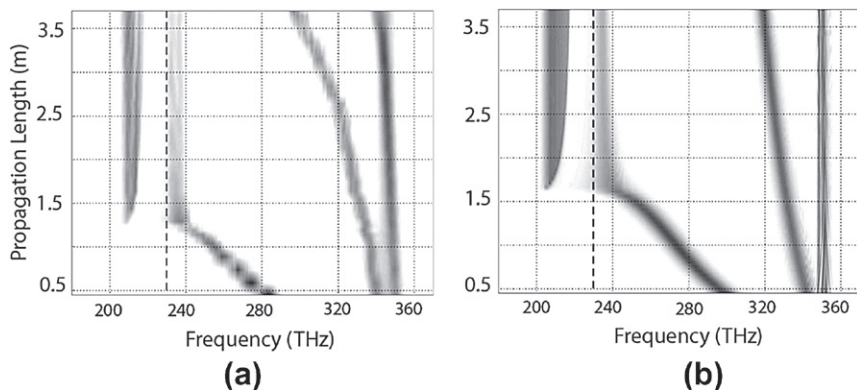


**Figure 12.14** (a) Experimental and (b) numerical spectra plotted as a function of propagation distance when 200-fs pulses are launched with 230-W peak power into a PCF exhibiting two ZDWLs. A darker shade represents a more intense region. A vertical dashed line marks the location of the second frequency where  $\beta_2=0$ . (After Ref. [65]; © 2003 AAAS.)

result, soliton loses its energy to NSR at a wavelength that lies in the infrared region beyond the second ZDWL. It turns out that *spectral recoil* from this NSR suppresses the RIFS as the soliton approaches the second ZDWL [67].

Figure 12.14a shows the spectral evolution of 200-fs pulses, launched with a peak power of 230 W at a wavelength of 860 nm, into a photonic crystal fiber exhibiting  $\beta_2 = 0$  at two wavelengths near 600 and 1300 nm [65]. Under these experimental conditions, the launched pulse forms a fourth-order soliton ( $N = 4$ ) that undergoes fission and creates 4 fundamental solitons. The shortest soliton has a width of only about 28.6 fs and shifts rapidly toward the red side through the RIFS. The spectra of other solitons shifts much less because of their larger widths. The shortest soliton approaches the second  $\beta_2 = 0$  frequency (shown by a vertical dashed line) at a distance of about 1.25 m. As seen in Figure 12.14, its spectrum suddenly stops shifting, a clear indication that the RIFS is suppressed beyond this point. At the same time, a new spectral peak appears on the red side of the second ZDWL. This peak represents the dispersive wave to which the soliton transfers a part of its energy. Its frequency is smaller (and wavelength is larger) than that of the Raman soliton because of a change in the sign of  $\beta_3$ .

The generalized NLS Equation (2.3.36) was used to simulate pulse propagation numerically under experimental conditions [67], and the results are shown in Figure 12.14b. The agreement with the experimental data is excellent, although some quantitative differences are also apparent. The main reason for these differences is related to the use of the approximate form of the Raman response function  $h_R(t)$  given in Eq. (2.3.40). As discussed in Section 2.3.2, this form approximates the Raman-gain spectrum with a single Lorentzian profile. The use of  $h_R(t)$  based on the actual gain spectrum (see Figure 2.2) should provide a better agreement.

The question is why the emission of dispersive waves near the second ZDWL suppresses the RIFS in Figure 12.14. To answer it, we need to understand how the energy lost to the NSR affects the soliton itself [67]. The requirement of energy conservation dictates that a soliton would become slightly wider as it loses energy to NSR, as  $N = 1$  must be maintained. This broadening is relatively small in practice if solitons lose energy slowly. Much more important is the requirement of momentum conservation. It dictates that, as NSR is emitted in the normal-GVD regime, the soliton should “recoil” into the anomalous-GVD regime [11]. This spectral-recoil mechanism is responsible for the suppression of the RIFS in Figure 12.14. Near the first ZDWL, spectral recoil is negligible because the RIFS forces the soliton spectrum to shift away from this wavelength, and the loss of energy decreases as  $\beta_2$  increases. However, the exact opposite occurs near the second ZDWL, where the RIFS moves the soliton closer to it, and the rate of energy loss to NSR increases drastically. The resulting spectral recoil reduces

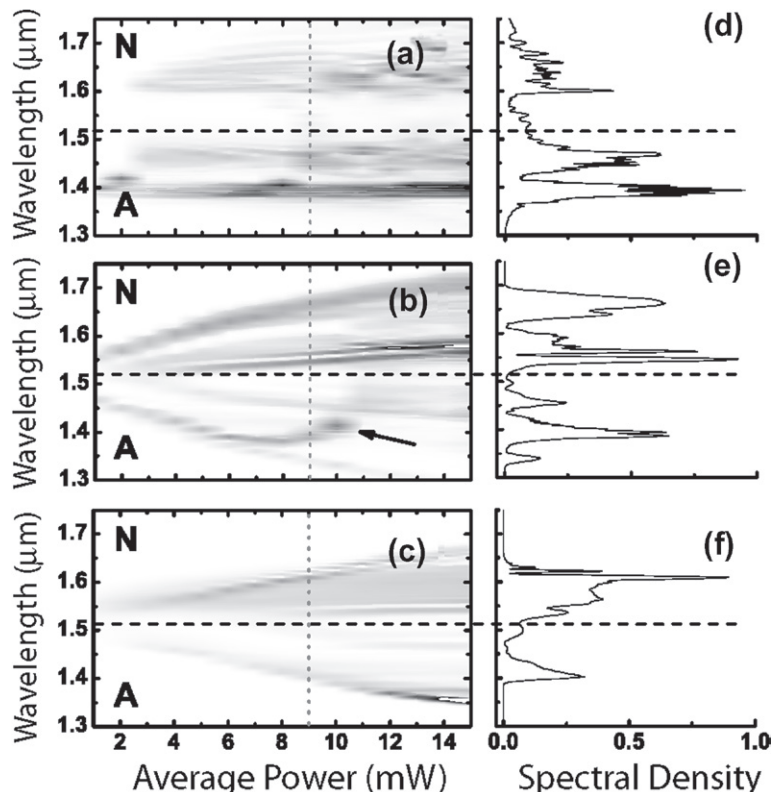


**Figure 12.15** Measured spectra as a function of average input power when 110-fs pulse at wavelengths (a) 1400, (b) 1510, and (c) 1550 nm were launched into a PCF with its second ZDWL near 1510 nm (horizontal dashed line). A darker shading represents a higher power. The right panel shows the spectra at the 9-mW power level. (After Ref. [70]; © 2005 Elsevier.)

the RIFS until a steady state is reached in which spectral recoil is just large enough to nearly cancel the RIFS. The X-FROG technique as well as numerical simulations confirm the preceding physical scenario [68]. The moment method has also been used to study momentum conservation near the second ZDWL [69]. All results confirm that the unusual soliton dynamics near the second ZDWL, in combination with the NSR produced by higher-order dispersive effects, is responsible for the suppression of the RIFS.

The pulse-propagation scenario seen in Figure 12.14 depends on the input wavelength of pulses because it sets the initial values of the dispersion parameters. In one study, 110-fs pulses were launched at wavelengths close to the second ZDWL (around 1510 nm) of a 1-m-long PCF [70]. Figure 12.15 shows the measured spectra at the fiber output as a function of the average input power (at a 80-MHz repetition rate) for three input wavelengths of 1400, 1510, and 1550 nm. In case (a), a Raman soliton is generated through fission, but its spectrum stops shifting beyond 1470 nm because of the RIFS suppression induced by the NSR appearing in the normal-GVD regime lying beyond 1510 nm. In case (b), a part of the pulse lies in the normal-GVD regime, and it disperses without forming a soliton. The remaining part propagates in the anomalous-GVD regime, and its spectrum shifts towards shorter wavelengths with increasing power. At a certain value of the input power, soliton effects begin to dominate, and the spectrum shifts through the RIFS toward longer wavelengths, resulting in the comma-like shape (marked by an arrow). At even higher powers, the RIFS is arrested by the spectral-recoil mechanism. In case (c), the pulse propagates in the normal-GVD regime and mostly experiences SPM-induced spectral broadening. At high powers, the spectrum broadens enough that a part of the pulse energy lies in the anomalous regime and begins to form a soliton.

As discussed in Section 11.4, some microstructured fibers exhibit a photonic bandgap (PBG) such that light can propagate inside the core only if its wavelength falls within this bandgap region. Although a hollow core is often used, PBG fibers can be designed with a solid core. In a 2010 experiment, 270-fs pulses at 1200 nm were launched into such a fiber to study the RIFS phenomenon [66]. Figure 12.16

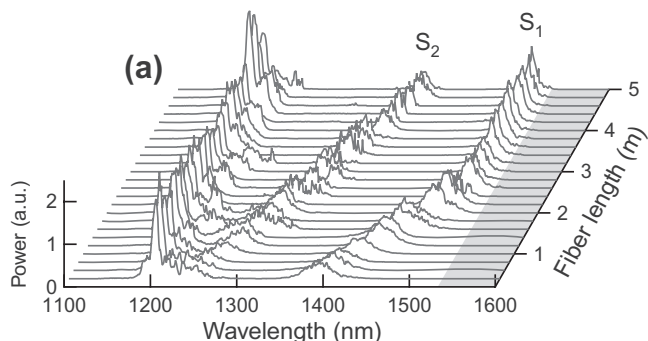


**Figure 12.16** Measured spectra for fiber lengths ranging from 0.4 to 5 m as when 270-fs pulses are launched into a photonic bandgap fiber. The gray shading marks a bandgap edge at 1535 nm. (After Ref. [66]; © 2010 OSA.)

shows the measured output spectra for fiber lengths ranging from 0.4 to 5 m. The fission of high-order solitons occurs within first 10 cm of the fiber, and the spectrum of the two shortest solitons, marked as  $S_1$  and  $S_2$ , shifts rapidly toward longer wavelengths. However, the spectrum of  $S_1$  approaches the PBG edge after 2.5 m of propagation and it stops shifting beyond that distance, with its central wavelength locked at 1510 nm. Clearly, the RIFS is nearly suppressed close to a PBG edge. Numerical results based on the generalized NLS equations confirm these results.

The physical explanation of this type of RIFS reduction is quite different from that used for Figure 12.14, where the soliton approached the ZDWL of a photonic crystal fiber. In the case of a PBG fiber, the parameters  $\beta_2$  and  $\gamma$  change considerably as the PBG edge is reached. Moreover, changes occur such that  $\beta_2$  increases and  $\gamma$  decreases at the same time. As a result, the requirement that the parameter  $N$  in Eq. (12.1.1) remain close to 1 can only be satisfied if the soliton width increases substantially. Since the RIFS rate in Eq. (12.2.2) scales as  $T_s^{-4}$ , where  $T_s$  is the local soliton width, this rate is reduced drastically as the soliton approaches the PBG edge. Indeed, the spectral width of the soliton was measured [66] for the data in Figure 12.16, and it was found to contract by a factor of almost 8. This spectral contraction translates into a temporal broadening factor of 8, and a reduction in the RIFS rate by a factor of more than 4000.

### 12.2.6 Soliton Dynamics Near a Zero-Dispersion Wavelength

It is clear from Figure 12.14 that the evolution of a soliton in the anomalous-dispersion region near a ZDWL of the fiber is affected strongly by the signs of the third- and fourth-order dispersion parameters,  $\delta_3$  and  $\delta_4$ , appearing in Eq. (12.2.1). The moment method has been applied to this equation to study the soliton evolution and the behavior of RIFS near a ZDWL [14]. When  $|\delta_3| \neq 0$ , one finds that RIFS is reduced for  $\delta_3 > 0$  because of an increase in  $|\beta_2|$  and a corresponding increase in the soliton width. In contrast, when  $\delta_3 < 0$ , soliton width decreases, and RIFS rate increases until the soliton wavelength approaches the ZDWL, where the RIFS is nearly suppressed.

As discussed earlier, the use of Eq. (12.2.1) becomes questionable for studying RIFS because it includes the Raman effects approximately through a single parameter  $\tau_R$ . An accurate description requires the use of generalized NLS Equation (2.3.36). In its normalized form, this equation can be written as

$$\begin{aligned} i\frac{\partial u}{\partial \xi} + \frac{1}{2}\frac{\partial^2 u}{\partial \tau^2} + |u|^2 u + \sum_{n=3}^{\infty} i^n \delta_n \frac{\partial^n u}{\partial t^n} &= i \left( 1 + is \frac{\partial}{\partial \tau} \right) \\ &\times \left[ u(\xi, \tau) \int_0^\infty R(\tau') |u(\xi, \tau - \tau')|^2 d\tau' \right], \end{aligned} \quad (12.2.4)$$

where  $s = \gamma_1/\gamma \approx (\omega_0 T_0)^{-1}$  and fiber losses have been neglected. This equation includes dispersion to all orders but the third- and fourth-order parameters,  $\delta_3$  and  $\delta_4$ , play the most critical roles near a ZDWL.

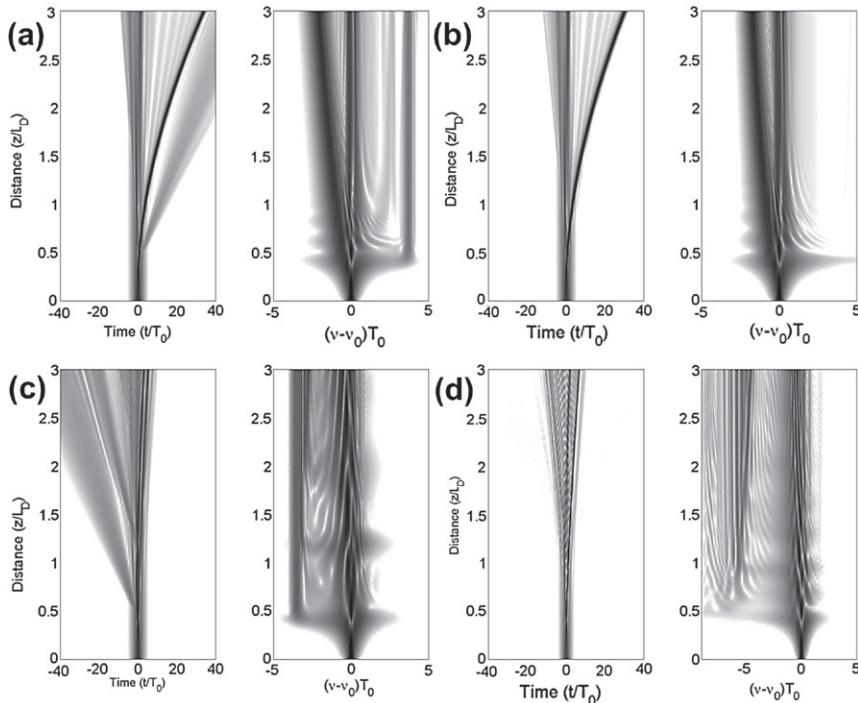


**Figure 12.17 Temporal and spectral evolution of a third-order soliton over a distance  $3L_D$  on a 50-dB intensity scale when (a)  $\delta_3=0.02$  with  $\delta_4=0.0002$ , (b)  $\delta_3=0.02$  with  $\delta_4=-0.0002$ , (c)  $\delta_3=-0.02$  with  $\delta_4=0.0002$ , and (d)  $\delta_3=-0.02$  with  $\delta_4=-0.0002$ .**

It turns out that even relatively small values of  $\delta_4$  affect the fission process considerably. As an example, Figure 12.17 shows the spectral and temporal evolution of a third-order soliton ( $N = 3$ ) in four cases: top and bottom rows correspond to  $\delta_3 = \pm 0.02$ , while  $\delta_4 = \pm 0.0002$  for the left and right columns. Thus, the four cases cover four possible sign combinations of  $\beta_3$  and  $\beta_4$ . It is remarkable how much the evolution of a high-order soliton is affected by small changes in the dispersion characteristics when solitons propagate near a ZDWL of the fiber.

Consider first the case  $\beta_3 > 0$  shown in the top row. When  $\beta_4$  is positive but relatively small, the fission generates a dispersive wave on the blue side (as expected for  $\beta_4 = 0$ ) and the shortest soliton is separated from others as its speed is reduced because of a continuously increasing RIFS. These features are expected from the earlier discussion in this section. However, if the sign of  $\beta_4$  is negative, as seen in part (b), the dispersive wave is totally suppressed. At the same time, the RIFS of the shortest soliton is reduced. Now consider the case  $\beta_3 < 0$  shown in the bottom row of Figure 12.17. Two things occur when  $\beta_4$  is positive and relatively small. First, the dispersive wave, as expected from Eq. (12.1.7), is generated on the red side of

the input spectrum. Second, the RIFS is nearly suppressed, and this suppression is accompanied by a large increase in the amount of NSR in the normal-dispersion region lying beyond the ZDWL of the fiber. As discussed earlier, RIFS suppression is related to spectral recoil induced by the NSR pressure. In the final case shown in part (d), both  $\beta_3$  and  $\beta_4$  are negative. We now see the emergence of two dispersive wave, one on the blue and one on the red side together with some RIFS. Note also considerable spectral changes resulting from optical interference.

A new phenomenon can occur when both  $\beta_3$  and  $\beta_4$  are negative for a fiber [14]. In this case, the frequency dependence of  $\beta_2$  exhibits an inverted parabola shown schematically in Figure 12.4. If this parabola crosses the frequency axis, two ZDWLs exist such that the spectral region between them exhibits normal dispersion and is surrounded on both sides with regions exhibiting anomalous dispersion. When a soliton, undergoing RIFS, approaches one of the ZDWLs, it may tunnel across the entire normal-dispersion band and transfer most of its energy to a new soliton in the second anomalous-dispersion region. This phenomenon, called *soliton spectral tunneling*, was first predicted in 1993 [71]. With the advent of microstructured fibers, it attracted attention again in the context of a PCF with sub-wavelength air holes [72].

A more systematic numerical study has revealed that soliton spectral tunneling may be difficult to observe experimentally because of an extreme sensitivity of this phenomenon to the cladding-design parameters such as the diameter and spacing of air holes [73]. As an example, Figure 12.18 shows numerical simulations for two

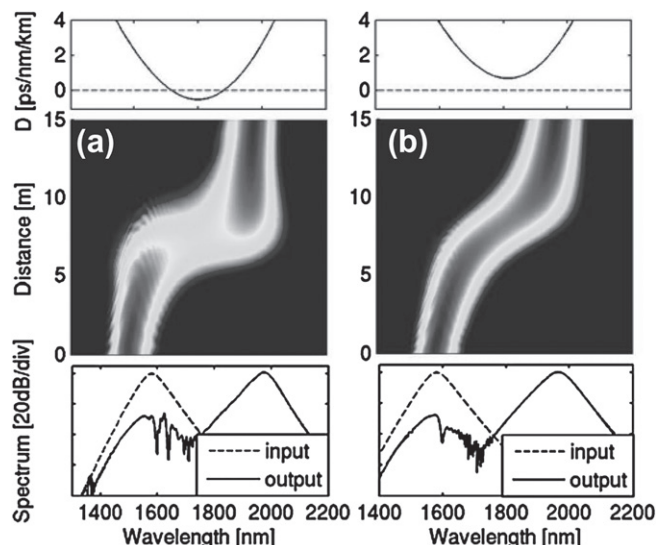


**Figure 12.18** Nonlinear propagation of a 50-fs pulse over 15 m for two nearly identical holey fibers. The top row shows  $D(\lambda)$ , the middle row shows spectral evolution, and the bottom row compares the input and output pulse spectra. Soliton spectral tunneling occurs in case (a) but not in case (b). (After Ref. [73]; © 2008 IEEE.)

holey fibers that are identical in all respects (core diameter  $1.8\text{ }\mu\text{m}$ ) except for a difference of 1% in the air-hole diameter. As seen there, this minor difference changes fiber dispersion such that two ZDWLs exist for one fiber but not for the other. As a result, soliton spectral tunneling occurs in case (a), but not in case (b). However, the spectral evolution of a 50-fs pulse over 15 m appears similar for both fibers, with nearly identical spectra at the fiber output. Since no normal-dispersion region exists for the situation in part (b), it may be difficult in practice to pin-point the spectral-tunneling phenomenon.

### 12.2.7 Multipeak Raman Solitons

The results shown in Figure 12.17 correspond to an input pulse with a peak power  $P_0$  such that the pulse propagates initially as a third-order soliton  $N = 3$ . It was noticed in a 2007 experiment that pulses launched with larger peak powers exhibit a new phenomenon in which two Raman solitons created after the fission process may come close to each other and form a bound pair under ceratin conditions [74]. Such bound states were first discovered in 1996 [75] and have been studied further in recent years after their experimental observation [74–78].

Figure 12.19 shows the experimental spectra recorded over distances of up to 45 cm when a 110-fs pulse was launched into a PCF with 8.5-kW peak power ( $N \approx 12$ ). One sees clearly that two rightmost Raman solitons form a bound pair and their spectra shift together. Part B shows that this bound state continues to hold over distances as long as 15 m even though peak amplitudes decrease considerably because of internal losses. Numerical simulations based on Eq. (12.2.4) reveal that the formation of such a bound pair is very sensitive to the precise value of the input peak power.

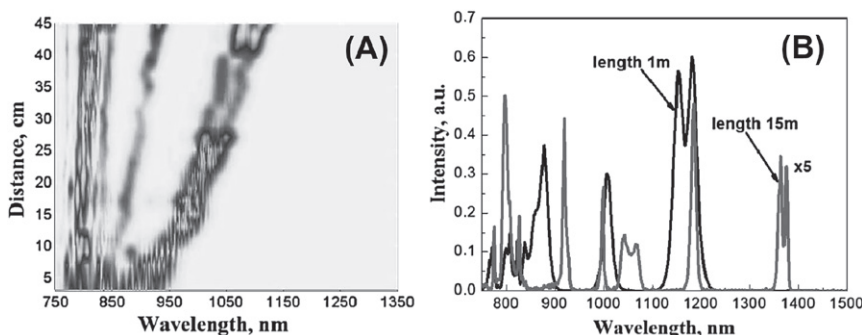


**Figure 12.19** (A) Experimental spectra over 45 cm of a PCF for a 110-fs pulse launched with 8.5-kW peak power. (B) Output spectra for two PCFs of 1 m (black) and 15 m (gray) lengths. (After Ref. [74]; © 2007 OSA.)

To understand the underlying physics, it is best to focus on a much simpler theoretical model given in Eq. (5.5.19) and reproduced here,

$$i \frac{\partial u}{\partial \xi} + \frac{1}{2} \frac{\partial^2 u}{\partial \tau^2} + |u|^2 u = \tau_R u \frac{\partial |u|^2}{\partial \tau}. \quad (12.2.5)$$

This equation includes only the second-order dispersion, ignoring higher-order dispersion completely, and the Raman effect is included through a dimensionless parameter  $\tau_R$ . In spite of these limitations, it is useful to study the propagation of individual fundamental solitons created after the fission of a higher-order soliton.

As mentioned in Section 5.5.4, Eq. (12.2.5) was solved approximately in 1990 using the following transformation [79]:

$$u(\xi, \tau) = f(\eta) \exp[i\xi(q + b\tau - b^2\xi^2/3)], \quad (12.2.6)$$

where  $\eta = \tau - b\xi^2/2$  is a new temporal variable in a reference frame moving with the soliton. The parameter  $b$  depends on  $q$  and  $\tau_R$  as  $b = 32\tau_R q^2/15$ . Using the preceding form of  $u(\xi, \tau)$  in Eq. (12.2.5),  $f(\eta)$  is found to satisfy the following second-order differential equation:

$$\frac{1}{2} \frac{d^2 f}{d\eta^2} = (q + b\eta) f - |f|^2 f + \tau_R f \frac{d|f|^2}{d\eta}. \quad (12.2.7)$$

Solutions of this equation with appropriate boundary conditions determine the eigenvalue  $q$  together with the pulse shape  $f(\eta)$ . An approximate analytic solution in the form of a single Raman soliton with  $q = \frac{1}{2}$  was first obtained in Ref. [79] and its functional form is given in Eq. (5.5.21). It was discovered numerically in 1996 that Eq. (12.2.7) also has solutions in the form of two Raman solitons of different amplitudes that form a pair [75] and move as one unit. More recently, it has been found that multiple Raman solitons of differing amplitudes can also form a multipeak bound state [78].

Figure 12.20 shows the temporal profiles of four solutions of Eq. (12.2.5) obtained numerically using  $\tau_R = 0.1$ . The single-peak solution in part (a) corresponds to a Raman soliton whose spectrum as well as temporal position shifts continually with  $\xi$  (see Figure 12.17). The two-peak solution in part (b) corresponds to a soliton pair that has been observed in experiments (see Figure 12.19). The most noteworthy feature of Figure 12.20 is that amplitudes of multiple peaks decrease with a constant ratio  $r$ . The origin of this feature is related to the term  $b\eta$  in the eigenvalue Eq. (12.2.7). If we ignore the last two nonlinear terms, this equation represents effectively the motion of a unit-mass particle of energy  $q$  in a gravity-like potential  $U(\eta) = b\eta$ , the parameter  $b$  playing the role of gravity [80]. This potential is shown by a dashed line in Figure 12.20 and is the reason why peak amplitudes should decrease with a constant ratio  $r$  that depends on the value of  $q$ . Another consequence of this potential is that all solutions in Figure 12.20 exhibit an oscillatory structure on the leading edge of the pulse (not seen on a linear scale because of its relatively low amplitude). The reason

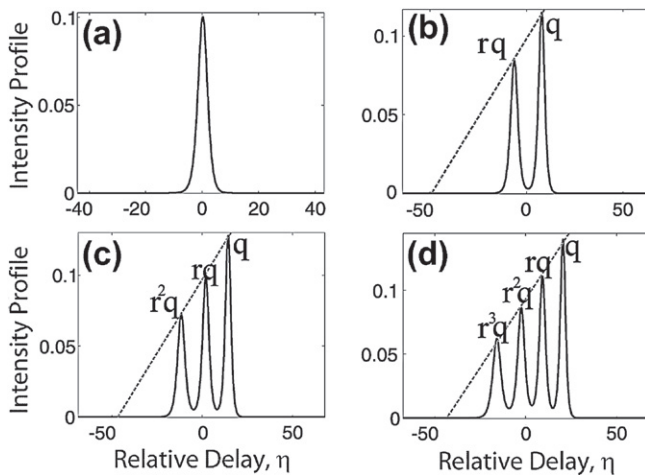


**Figure 12.20** Temporal profiles of four solutions obtained numerically using  $\tau_R = 0.1$ . The dashed line shows the gravity-like potential that enforces a constant ratio  $r$  between successive peaks. (After Ref. [78]; © 2010 OSA.)

is easily understood from Eq. (12.2.7), whose solution is in the form of an Airy function near the leading edge of the pulse where the last two nonlinear terms are negligible [75].

An important issue is related to the stability of the multipeak intensity profiles seen in Figure 12.20. Stability can be tested by solving Eq. (12.2.5) numerically over long distances with the input corresponding to a specific multipeak intensity profile. The results are shown in Figure 12.21 for the two-, three-, and four-peak structures of Figure 12.20. As seen there, even though they are not absolutely stable, a multipeak Raman soliton can propagate over hundreds of dispersion lengths before the bound state is destroyed.

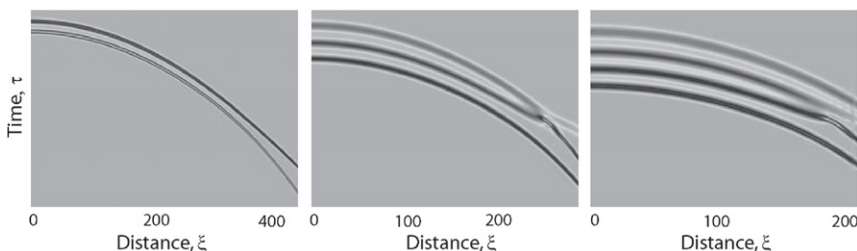


**Figure 12.21** Temporal evolution of multipeak Raman solitons over hundreds of dispersion lengths. (After Ref. [78]; © 2010 OSA.)

## 12.3 FOUR-WAVE MIXING

The phenomenon of FWM has been discussed extensively in Chapter 10. The unusual dispersive properties of highly nonlinear fibers affect the FWM process through the phase-matching condition. For example, as already mentioned in Section 10.3.3, the inclusion of higher-order dispersive effects offers the possibility of phase matching even when the pump wavelength lies in the normal-GVD regime. In this section, we focus on such features of FWM in more detail.

Highly nonlinear fibers were used for FWM soon after their development [81–88]. In a 2001 experiment, a single-pump configuration was employed to amplify signals by 13 dB over a 30-nm bandwidth with a pump peak power of only 6 W using a 6.1-m-long microstructured fiber [81]. A 2.1-m section of such a fiber was used in a 2002 experiment to realize a fiber-optic parametric oscillator that was tunable over 40 nm [83]. The threshold for this laser was reached when pump pulses had a peak power of 34.4 W. In another experiment, a 100-m-long highly nonlinear fiber was pumped continuously at 1565 nm [84], and two fiber gratings were used to form a cavity. Such a parametric oscillator reached threshold at a pump power of 240 mW and was tunable over a 80-nm bandwidth. In these experiments, the pump wavelength lay in the anomalous-GVD regime of the fiber, and the signal and idler frequencies were set by Eq. (5.1.9) of Section 5.1.

### 12.3.1 Role of Fourth-Order Dispersion

Considerable attention has been paid to understanding the FWM phenomenon in microstructured fibers [89–95]. As discussed in Section 10.3.3, higher-order dispersive effects often become important and should be included for highly nonlinear fibers. It was found there that all even-order dispersion terms affect the phase-matching condition, and fourth-order dispersion plays an important part in setting the signal and idler frequencies. If dispersion to all orders is included, the phase-matching condition in Eq. (10.3.10) becomes

$$\sum_{m=2,4,\dots}^{\infty} \frac{\beta_m(\omega_p)}{m!} \Omega_s^m + 2\gamma P_0 = 0, \quad (12.3.1)$$

where  $\Omega_s = \omega_s - \omega_p$  is the shift of the signal frequency from the pump frequency  $\omega_p$ . The idler frequency follows from the FWM condition  $\omega_i = 2\omega_p - \omega_s$ . In the anomalous-GVD regime ( $\beta_2 < 0$ ), the  $m = 2$  term dominates, and the frequency shift is given by  $\Omega_s = (2\gamma P_0 / |\beta_2|)^{1/2}$ . In the normal-GVD regime such that  $\beta_4 < 0$ ,  $\Omega_s$  is given by Eq. (10.3.11). However, if both  $\beta_2$  and  $\beta_4$  are positive, the signal and idler frequencies are determined by still higher-order dispersive terms in Eq. (12.3.1).

It is important to stress that dispersion parameters change with the pump frequency, and one must use the actual dispersion curve to find them, if the objective is to study how signal and idler frequencies alter with small changes in the pump wavelength. Figure 12.22a shows how the second-order dispersion parameter  $D$  changes,

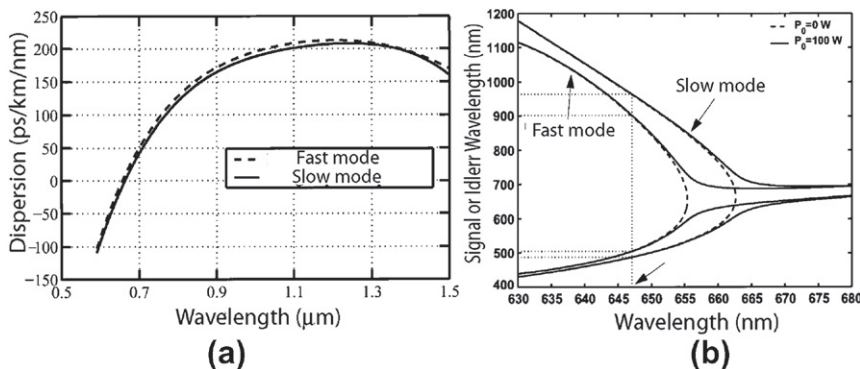


**Figure 12.22** (a) Second-order dispersion parameter measured as a function of the wavelength for a photonic crystal fiber with light polarized along the slow (solid line) and fast (dashed line) axes. (b) Phase-matching curves as a function of the pump wavelength at a low power (dashed curve) and at 100-W power level. Dotted lines mark the predicted signal and idler wavelengths at a pump wavelength of 647 nm. (After Ref. [85]; © 2003 OSA.)

with the wavelength, for a slightly birefringent photonic crystal fiber [85]. These measurements were used to deduce  $\beta_2$  and  $\beta_4$ , and then to determine the signal and idler wavelengths as a function of pump wavelength  $\lambda_p$  from Eq. (12.3.1) for an input power level of 100W (solid curves). The signal and idler wavelengths are different for light polarized along the slow and fast axes because of birefringence (dotted lines). The dashed curves show the low-power case.

When the pump wavelength  $\lambda_p$  exceeds the ZDWL  $\lambda_0$ , the pump travels in the anomalous-GVD regime, and the signal and idler wavelengths are relatively close to the pump wavelength. In contrast, they differ by several hundred nanometers in the normal-GVD regime ( $\lambda_p < \lambda_0$ ), and fourth-order dispersion is required for phase matching. This type of highly nondegenerate FWM was observed by launching 70-ps pump pulses at 647 nm, with peak powers of up to 1 kW, inside a 1-m-long fiber placed inside the cavity of a parametric oscillator. The recorded optical spectra in Figure 12.23 show the generation of the signal and idler waves that are seeded through spontaneous modulation instability [85]. Their wavelengths change with pump polarization because of fiber birefringence.

### 12.3.2 Role of Fiber Birefringence

As seen in Figure 12.23 and discussed in Section 6.4, fiber birefringence considerably affects the FWM process that is behind the phenomenon of modulation instability. Moreover, it can also lead to the so-called polarization instability. As one would expect, both instabilities change considerably for highly nonlinear fibers with unusual dispersion characteristics. In one study, dispersion terms up to the 12th order were included for calculating the instability gain, while carrying out a linear stability

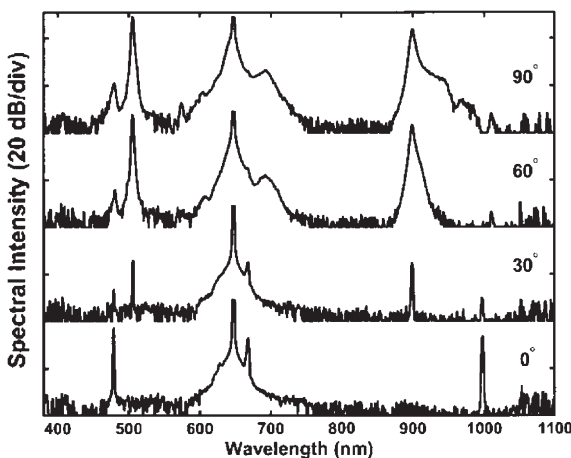


**Figure 12.23** Output spectra recorded for four values of the pump polarization angle from the slow axis of a photonic crystal fiber that was pumped at 647 nm using 70-ps pulses with 160-W peak power. (After Ref. [85]; © 2003 OSA.)

analysis of the coupled NLS equations for the two orthogonally polarized modes [92]. The two cases of low and high birefringence were studied for a narrow-core tapered fiber with two ZDWLs, and new instability bands were found to occur.

In a 2004 experiment, a 20-m-long PCF with a relatively low birefringence was used to study the FWM process by launching into it CW light from a Ti:sapphire laser tunable from 650 to 830 nm [86]. This fiber exhibited two ZDWLs near 755 and 1235 nm that were different for the two orthogonally polarized modes. The first set of these occurred near 755 and 785 nm for the fast and slow modes, respectively. Multiple semiconductor lasers operating at 975, 1064, 1312, and 1493 nm were employed to seed the FWM process. Figure 12.24 shows the phase-matched wavelengths (square data points) measured as a function of pump wavelength when the pump and seed fields were polarized along one of the principal axes of the fiber. The solid curve is based on the average dispersion values, as it was not possible to characterize the dispersion separately for the fast and slow modes. Even though a quantitative agreement is not expected, the qualitative behavior agrees well with the predictions of a scalar theory.

The birefringence of a 4-m-long microstructured fiber, used in another experiment, was characterized carefully before observing the vector modulation instability [82]. Figure 12.25(a) shows the measured optical spectra when nanosecond pulses with 90-W peak power at a wavelength of 624.5 nm were launched into the fiber such that the two orthogonally polarized modes were equally excited. Under such conditions, the two sidebands at the signal and idler wavelengths should be orthogonally polarized, a feature verified experimentally. Moreover, the predicted frequency shift of 3.85 THz at which the instability gain peaked in Figure 12.25b agreed well with

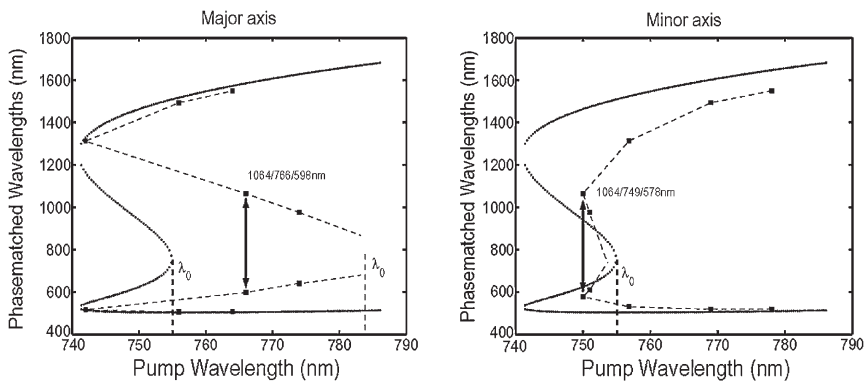


**Figure 12.24** Measured phase-matched wavelengths (dashed lines) as a function of pump wavelength for a birefringent photonic crystal fiber when pump light is polarized along the major or minor axis of the fiber. The solid curves show the theoretical prediction based on the average dispersion. (After Ref. [86]; © 2004 OSA.)

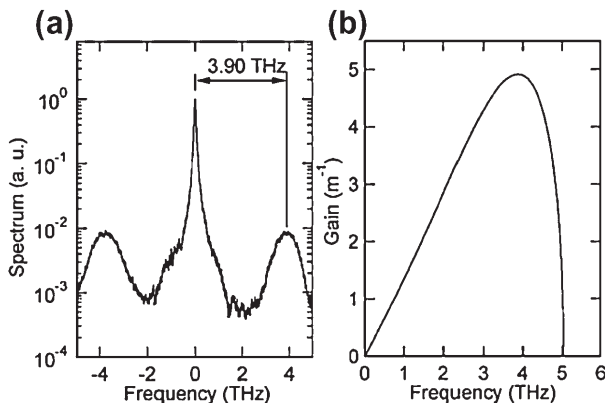


**Figure 12.25** (a) Measured output spectra showing FWM-induced sidebands for a 624.5-nm quasi-CW pump, linearly polarized at  $45^\circ$  from the slow axis of a 4-m-long microstructured fiber. (b) Theoretical gain curve calculated using actual fiber parameters. (After Ref. [82]; © 2002 OSA.)

the measured value of 3.9 THz. Such a large frequency shift of sidebands at relatively low pump powers was possible because of a relatively large value of the nonlinear parameter (resulting from an effective mode area of only  $1.7 \mu\text{m}^2$ ) and a relatively large birefringence ( $\sim 10^{-4}$ ) associated with the microstructured fiber used in the experiment.

As discussed in Section 10.6.3, FWM in highly nonlinear fibers provides a simple way to generate correlated photon pairs useful for applications related to quantum

cryptography and quantum computing. However, the quality of such a photon-pair source is severely deteriorated by spontaneous Raman scattering if the signal and idler are copolarized with the pump. This problem can be solved to a large extent by using a configuration in which the signal and idler photons are polarized orthogonally to the pump [94]. The reason is that the Raman gain almost vanishes for an orthogonally polarized pump, whereas the FWM efficiency is only reduced by a factor of 1/3 in an isotropic fiber with no birefringence. In an FWM process that is phase-matched through fiber birefringence, it is possible to reduce the impact of Raman gain without sacrificing the FWM efficiency much.

As mentioned earlier, microstructured fibers often exhibit two ZDWLs. FWM in such fibers has been studied and it leads to interesting new features [86]. Equation (12.3.1) can still be used to calculate the signal and idler wavelengths that satisfy the phase-matching condition, provided that the actual dispersion curve of the fiber is used to find the dispersion parameters at each pump wavelength. Figure 12.26 shows the phase-matched wavelengths for a PCF with a 1.8- $\mu\text{m}$  core diameter for a CW pump whose wavelength is varied by 20 nm near the first ZDWL. The launched pump power is assumed to be 1 kW. The measured wavelength dependence of  $\beta_2$  for this fiber is also shown;  $\beta_2$  vanishes at wavelengths of 755 and 1235 nm.

A novel feature of such fibers is that two sets of wavelengths can be phase-matched simultaneously at a fixed pump wavelength. For example, when the pump light travels in the normal-GVD regime close to the first ZDWL near 755 nm, the four wavelengths fall in a range extending from 500 to 1500 nm. The longest wavelength generated through the FWM process is more than 600 nm away from the pump wavelength in this specific case. Even larger wavelength shifts can occur for pump wavelengths near 900 nm. This type of multiwave generation was first predicted in a 1989 study [96] and was also found in 1995 to occur in dispersion-flattened fibers with two ZDWLs [97].

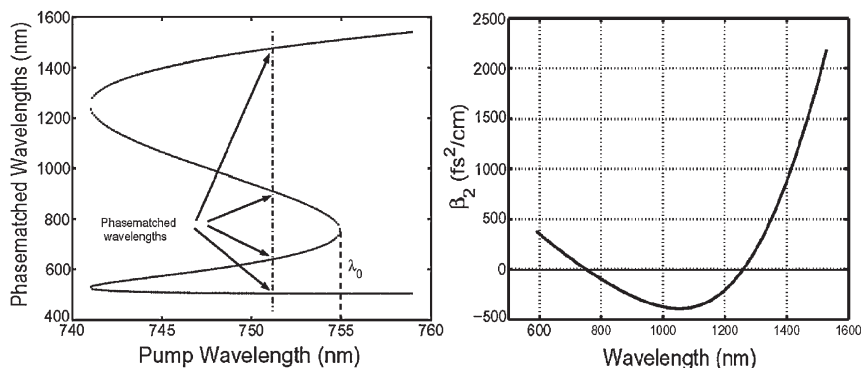


**Figure 12.26 Phase-matching curves as a function of the pump wavelength for a PCF whose dispersion curve, shown on the right, exhibits two ZDWLs near 755 and 1235 nm.**

Arrows mark the four wavelengths phase-matched simultaneously when  $\lambda_p = 752 \text{ nm}$ .

(After Ref. [86]; © 2004 OSA.)

### 12.3.3 Parametric Amplifiers and Wavelength Converters

As already discussed in Section 10.4, FWM can be used to make a parametric amplifier that can also be used as a wavelength converter (because of an idler wave that is automatically generated). The use of PCFs or other microstructured fibers reduces the required fiber length (because of a larger  $\gamma$ ), which in turn increases the bandwidth of such amplifiers and wavelength converters. For this reason, these kinds of fibers are routinely used for making such devices [98–105].

Polarization-insensitive wavelength conversion was realized in a 2005 experiment [98] by using a 64-m-long PCF designed with a relatively low value of third-order dispersion near 15,550 nm. The idler wavelength could be tuned from 1535 to 1575 nm with a conversion efficiency of  $-16$  dB at a pump power of about 300 mW. Wavelength conversion was nearly insensitive to the polarization state of the input signal because of the use of a polarization-diversity scheme. In another 2005 experiment [99], a 1–7-m-long microstructured fiber was employed to amplify an optical signal by a factor of 1000. This experiment employed 3.5-ps pump pulses with a peak power close to 3.6 W. A relatively wide gain bandwidth of 100 nm with a uniform gain of 11 dB was realized in a 2007 experiment [102]. A length of only 1 m was needed in one experiment to realize wavelength conversion from 1530 to 1570 nm [103]. This was possible because the microstructured fiber used in this experiment was made with bismuth-oxide glass. As a result, the nonlinear parameter  $\gamma$  had a relatively large value of  $580 \text{ W}^{-1}/\text{km}$  for an effective mode area of  $3.2 \mu\text{m}^2$ .

Recently a 100-m-log PCF was used to realize parametric amplification and wavelength conversion in the wavelength range of 1040–1090 nm [105]. The amplifier was pumped at 1064 nm using 450-ps pulses from a Q-switched Nd:YAG laser. Figure 12.27 shows the amplification factor for a 1081-nm signal as a function of peak pump power. The signal could be amplified by up to a factor of 40 dB because the

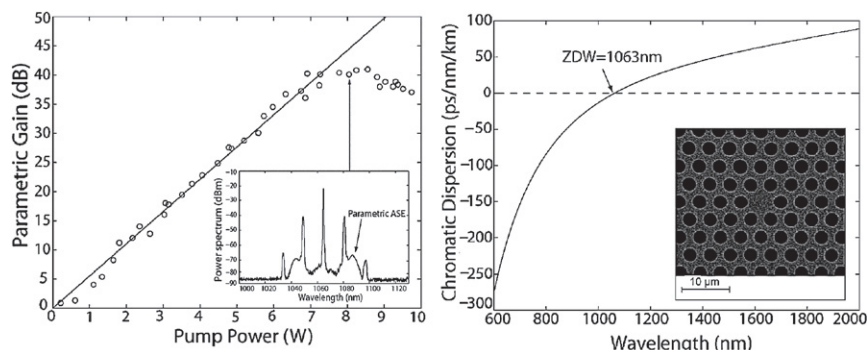


**Figure 12.27** Amplification factor of a 1081-nm signal as a function of peak pump power when the 100-m-long PCF was pumped at 1064 nm using 450-ps pulses. The inset shows the measured optical spectrum at a pump power marked by an arrow. The design and dispersion of the PCF are shown on the right. (After Ref. [105]; © 2009 American Institute of Physics).

zero-dispersion wavelength of this PCF was near 1063 nm, as seen in Figure 12.27. The resulting relatively small value of  $\beta_2 = -0.21 \text{ ps}^2/\text{km}$  at the pump wavelength allowed phase matching for the FWM process. The amplifier bandwidth was limited to about 50 nm because the pump propagates in the anomalous-GVD regime of the fiber. It can be increased to close to 100 nm by employing shorter PCFs [100]. As apparent in Figure 12.22, a much larger bandwidth is possible when the pump wavelength lies in the normal-GVD region and the fiber is designed to have a negative value of the fourth-order dispersion. Such fibers have been used to make tunable parametric oscillators, a topic we turned to next.

#### 12.3.4 Tunable Fiber-Optic Parametric Oscillators

An important application of FWM in microstructured fibers is for realizing widely tunable lasers known as fiber-optic parametric oscillators [106–114]. In some cases, FWM in the normal-GVD regime of a highly nonlinear fiber was used to enhance the tuning range of parametric oscillators. In a 2005 experiment, pulses shorter than 0.5 ps and tunable over a 200-nm range were obtained using a ring cavity containing 65 cm of a PCF [106]. The laser was pumped synchronously using 1.3-ps pulses from a mode-locked ytterbium fiber laser capable of delivering up to 260 mW of average power. Figure 12.28a shows how the signal and idler wavelengths change when the pump wavelength is varied over a relatively narrow range of 25 nm. These curves are obtained using the phase-matching condition in Eq. (12.3.1), retaining only two terms in the sum, and employing the specific values of  $\beta_2$  and  $\beta_4$  for the PCF used in the experiment. The parametric oscillator is, in principle, tunable over 300 nm by changing the pump wavelength over a 20-nm range. In practice, the walk-off effects, resulting from the group-velocity mismatch, limited the tuning range to

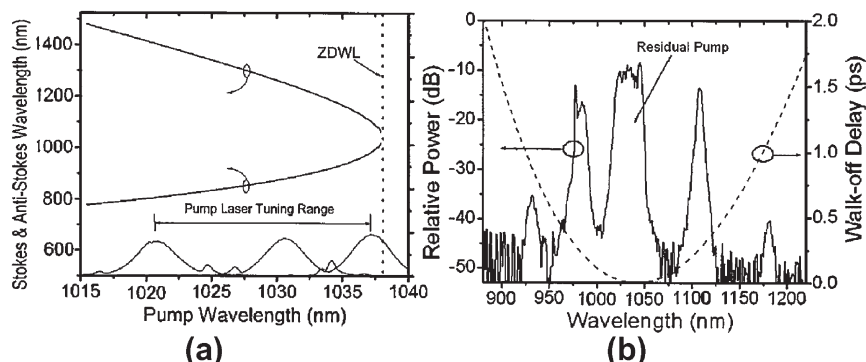


**Figure 12.28** (a) Phase-matching curves as a function of pump wavelength for a PCF having its ZDWL at 1038 nm. Tuning curve of the pump laser is also shown. (b) Walk-off delay (dashed curve) as a function of pump wavelength and a typical output spectrum showing the signal and idler bands on opposite sides of the pump. (After Ref. [106]; © 2005 OSA.)

around 200 nm. The dashed curve in Figure 12.28b shows that the walk off between the pump and laser pulses exceeds 1 ps for a 150-nm detuning.

The extent of temporal walk off between the pump and laser pulses can be reduced either by using shorter fibers or by employing longer pump pulses, and both help in increasing the tuning range of fiber-optic parametric oscillators. In a 2007 experiment, tuning range was enhanced considerably (covering one octave) when length of the microstructured fiber was reduced to 3 cm [107]. In contrast, another 2007 experiment employed a 40-m-long fiber but avoided the walk-off problem by using much longer 4-ns pump pulses [108]. Tuning over a very wide range was realized in 2008 by using a 1.3-m-long PCF with a butt-coupled mirror at both ends, thus forming a Fabry–Perot cavity [109]. The PCF exhibited normal GVD at wavelengths  $\lambda < 725$  nm. The pump pulses were 8 ps wide but their wavelength was tunable from 705 to 725 nm. Figure 12.29a shows that the laser frequency can be shifted from 23 to 164 THz on both sides of the pump frequency for the PCF used in the experiment. As a result, the signal (Stokes) and idler (anti-Stokes) wavelengths could be tuned over a broad range by simply changing the pump wavelength from 705 to 725 nm. The relative walk off for the three pulse pairs is shown in Figure 12.29b. As it exceeds the width of pump pulses for frequency shifts  $> 60$  THz, the output power is reduced considerably for large frequency shifts. The use of 100-ps pulses from a pump operating near 1550 nm has produced lasers whose wavelength can be tuned over a wide range extending from 1320 to 1820 nm [111].

Recent work on tunable parametric oscillators has followed several distinct directions [112–115]. Continuous-wave (CW) pumping was used in 2009 to realize a CW laser tunable over 240 nm [112]. The FWM process was affected considerably by the Raman gain in this experiment. In the other extreme limit, wavelength-tunable pulses shorter than 100 fs were produced in a 2010 experiment by pumping with 400-fs pump pulses at wavelengths near 1030 nm [113]. The length of the PCFs used

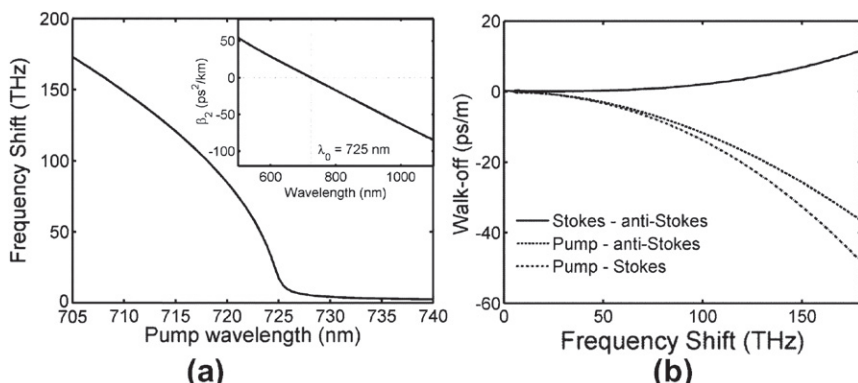


**Figure 12.29** (a) Phase-matching curve as a function of pump wavelength for a 1.3-m-long PCF fiber having its ZDWL at 725 nm; inset shows  $\beta_2(\lambda)$  for this PCF. (b) Temporal walk off for three pulse pairs as a function of frequency shift. (After Ref. [109]; © 2008 OSA.)

in this experiment varied from 2 to 6 cm. The duration of Stokes pulses was only 48 fs for a 2.7-cm-long PCF. In contrast, the duration of anti-Stokes pulses was close to 200 fs. In a 2011 experiment, the objective was to obtain high output powers, and the average power exceeded 1.9 W over a wide wavelength range extending from 1350 to 1790 nm [114]. In another approach, a PCF was heated up to 500 °C to tune the oscillator [115].

## 12.4 SECOND-HARMONIC GENERATION

Second-harmonic generation (SHG) is a common nonlinear phenomenon used to generate light in the visible and ultraviolet regions. Strictly speaking, SHG should not occur in silica fibers because the inversion symmetry exhibited by SiO<sub>2</sub> molecules forbids all nonlinear effects resulting from the second-order susceptibility  $\chi^{(2)}$ . However, several early experiments showed that some second harmonic was generated when intense 1.06-μm pump pulses from a Nd:YAG laser were propagated through optical fibers [116–118]. Conversion efficiencies ~0.1% were observed both for the sum-frequency and the second-harmonic processes. Such high efficiencies are unexpected, but several mechanisms can provide an effective  $\chi^{(2)}$  for these processes to occur; the most important ones among them are surface nonlinearities at the core-cladding interface and nonlinearities resulting from quadrupole and magnetic dipole moments. Detailed calculations show that such nonlinearities should give rise to a maximum conversion efficiency  $\sim 10^{-5}$  [119]. Thus, some other mechanism is responsible for SHG in silica fibers.

A clue to the origin of such a mechanism came when it was discovered in 1986 that the second-harmonic power grew considerably when fibers were exposed to pump radiation for several hours. In one experiment [120], the SHG power grew almost exponentially with time and began to saturate after 10 h, when 100-ps pump pulses with an average power of 125 mW were propagated through a 1-m-long fiber. The 0.53-μm pulses at the fiber output had a width of about 55 ps and were intense enough to pump a dye laser. The maximum conversion efficiency was about 3%. This experiment led to extensive research on SHG in optical fibers [121–139]. It turned out that some optical properties of fibers are modified permanently when they are exposed to intense radiation of certain wavelengths. Dopants such as germanium and phosphorus that increase the core index enhance this photosensitivity. In a 1987 experiment, a fiber with Ge-doped core could be prepared for SHG in about 20 min when pumped with 100-ps pump pulses at 647.1 nm with a peak power of only 720 W [125]. In another development, it was found that a fiber could be prepared in only a few minutes provided that a weak second-harmonic signal was launched with the pump pulses [122]. The same fiber could not be prepared even after 12 h without the seeding beam.

### 12.4.1 Physical Mechanisms

Several physical mechanisms were proposed in 1987 to explain SHG in optical fibers [121–124]. They all relied on a periodic ordering of some entity, such as color centers

or defects, along the fiber in such a way that a phase-matching condition was automatically satisfied. In one model, ordering occurs through a third-order nonlinear process in which the pump and the second-harmonic light (internally generated or externally applied) mix together to create a static or dc polarization (at zero frequency) given by [122]

$$P_{dc} = (3\epsilon_0/4)\text{Re}[\chi^{(3)}E_p^*E_p^*E_{SH} \exp(i\Delta k_p z)], \quad (12.4.1)$$

where  $E_p$  is the pump field at the frequency  $\omega_p$ ,  $E_{SH}$  is the second-harmonic seed field at  $2\omega_p$ , and the wave-vector mismatch  $\Delta k_p$  is given by

$$\Delta k_p = [n(2\omega_p) - 2n(\omega_p)]\omega_p/c. \quad (12.4.2)$$

The polarization  $P_{dc}$  induces a dc electric field  $E_{dc}$  whose polarity changes periodically along the fiber with the phase-matching period  $2\pi/\Delta k_p$  ( $\sim 30\text{ }\mu\text{m}$  for a  $1.06\text{-}\mu\text{m}$  pump). This electric field redistributes electric charges and creates a periodic array of dipoles. The physical entity participating in the dipole formation could be defects, traps, or color centers. The main point is that such a redistribution of charges breaks the inversion symmetry and is also periodic with the right periodicity required for phase matching. In effect, the fiber has organized itself to produce second-harmonic light such that the dipoles respond to the optical field with an effective value of  $\chi^{(2)}$ . In the simplest case,  $\chi^{(2)}$  is proportional to  $P_{dc}$  such that

$$\chi^{(2)} \equiv \alpha_{SH} P_{dc} = (3\alpha_{SH}/4)\epsilon_0\chi^{(3)}|E_p|^2|E_{SH}|\cos(\Delta k_p z + \phi_p), \quad (12.4.3)$$

where  $\alpha_{SH}$  is a constant whose magnitude depends on the microscopic process responsible for  $\chi^{(2)}$  and  $\phi_p$  is a phase shift that depends on the initial phases of the pump and the second-harmonic seed. Because of the periodic nature of  $\chi^{(2)}$ , the preparation process is said to create a  $\chi^{(2)}$  grating.

This simple model in which a dc electric field  $E_{dc}$  is generated through a  $\chi^{(3)}$  process suffers from a major drawback [129]. Under typical experimental conditions, Eq. (12.4.1) leads to  $E_{dc} \sim 1\text{ V/cm}$  for pump powers  $\sim 1\text{ kW}$  and second-harmonic seed powers  $\sim 10\text{ W}$ , if we use  $\chi^{(3)} \approx 10^{-22}\text{ (m/V)}^2$ . This value is too small to orient defects and generate a  $\chi^{(2)}$  grating.

Several alternative mechanisms have been proposed to solve this discrepancy. In one model [133] a charge-delocalization process enhances  $\chi^{(3)}$  by several orders of magnitudes, resulting in a corresponding enhancement in  $E_{dc}$ . In another model [134], free electrons are generated through the photoionization of defects, and a strong electric field ( $E_{dc} \sim 10^5\text{ V/cm}$ ) is created through a coherent photovoltaic effect. In a third model [135], ionization occurs through multiple multiphoton processes (involving four pump photons, two second-harmonic photons, or two pump photons and one second-harmonic photon). In this model, the  $\chi^{(2)}$  grating is created through quantum-interference effects that cause the electron-injection process to depend on the relative phase between the pump and second-harmonic fields. Such a charge-transport model is in qualitative agreement with most of the observed features.

Conversion efficiencies realized in practice are limited to  $\sim 1\%$  [120]. The second-harmonic power grows exponentially during initial stages of the preparation process but then saturates. One possibility is that the light created through SHG interferes with formation of the  $\chi^{(2)}$  grating because it is out of phase with the original grating [122]. If this is the case, it should be possible to erase the grating by sending just the second harmonic through the fiber without the pump. Indeed, such an erasure has been observed [126]. The erasing rate depends on the second-harmonic power launched into the fiber. In one experiment [127], conversion efficiency decreased from its initial value by a factor of 10 in about five minutes at an average power level of about 2 mW. The decay was not exponential, but followed a time dependence of the form  $(1 + Ct)^{-1}$ , where  $C$  is a constant. Furthermore, erasure was reversible, that is, the fiber could be re-prepared to recover its original conversion efficiency. These observations are consistent with the model in which the  $\chi^{(2)}$  grating is formed by the ordering of charged entities such as color centers, defects, or traps.

### 12.4.2 Thermal Poling and Quasi-Phase Matching

Because of a limited conversion efficiency associated with photosensitive fibers, the technique of quasi-phase matching has been used to make fibers suitable for SHG. This technique was proposed in 1962 [140] but has been developed only during the 1990s, mostly for electro-optic materials such as LiNbO<sub>3</sub>. It was used for optical fibers as early as 1989 and was referred to as electric field-induced SHG [141]. The basic idea is quite simple. Rather than inducing an internal dc electric field optically, the dc field is applied externally, resulting in an effective  $\chi^{(2)}$ . However, a constant value of  $\chi^{(2)}$  along the fiber length is not very useful in practice because of the large phase mismatch governed by  $\Delta k_p$  in Eq. (12.4.2).

The technique of quasi-phase matching enhances the SHG efficiency by reversing the sign of  $\chi^{(2)}$  along the sample periodically [142]. When this technique is applied to optical fibers, one needs to reverse the polarity of the electric field periodically along the fiber length. The period should be chosen such that the sign of  $\chi^{(2)}$  is reversed before the SHG power reverts back to the pump, i.e., its numerical value should be  $2\pi/\Delta k_p$ . Quasi-phase matching is commonly used in combination with thermal poling, a technique that can produce relatively large values of  $\chi^{(2)}$  of a permanent nature in silica glasses and fibers [143–146]. Although thermal poling has been used since 1991, the exact physical mechanism responsible for producing  $\chi^{(2)}$  remains controversial [147–152]. Recent measurements of  $\chi^{(2)}$  symmetry provide convincing evidence that  $\chi^{(2)}$  originates from a  $\chi^{(3)}$  process such that the effective value of  $\chi^{(2)}$  is given by  $\chi_{ijk}^{(2)} = 3\chi_{ijkl}^{(3)}E_l^{\text{dc}}$ , where  $E_l^{\text{dc}}$  is the dc electric field along the  $l$  direction induced through thermal poling [153].

Thermal poling requires that a large dc electric field be applied across the fiber core, at an elevated temperature in the range of 250–300°, for a duration ranging anywhere from 10 min to several hours. If one wants to establish a constant value of  $\chi^{(2)}$  across the entire fiber length, electrodes can be inserted through two holes within the cladding of a fiber. The positive electrode should pass quite close to the fiber core because formation of a negatively charged layer close to this electrode

plays an important role in the charge migration and ionization process thought to be responsible for inducing  $\chi^{(2)}$  [146].

The technique of quasi-phase matching requires reversal of the polarity of the electric field periodically along fiber length during the thermal-poling process. To make such periodically poled silica fibers, the cladding on one side of the fiber is etched away to produce a D-shaped fiber. The flat surface of the fiber should be quite close to the core,  $5\text{ }\mu\text{m}$  being a typical distance [154]. A patterned aluminum contact is fabricated on the flat surface using a standard lithographic technique. The required period is close to  $56.5\text{ }\mu\text{m}$  for a pump wavelength of  $1.54\text{ }\mu\text{m}$ . Thermal poling of the fiber then produces a  $\chi^{(2)}$  grating with the same period.

In a 1999 experiment, such a quasi-phase-matched fiber (length 7.5 cm) was pumped by using 2-ns pulses with peak powers of up to 30 kW at a wavelength of  $1.532\text{ }\mu\text{m}$  [154]. Second-harmonic light at 766 nm was generated with an average efficiency of up to 21%. Figure 12.30 shows both the average SHG power and the conversion efficiency as a function of the average power of the pump beam. This experiment showed that quasi-phase-matched thermal poling represents a potentially useful technique for SHG in optical fibers. The main drawback of quasi-phase matching is that the period of  $\chi^{(2)}$  grating depends on the pump wavelength and should be matched precisely. A mismatch of even 1 nm in the pump wavelength can reduce the efficiency by 50%. The technique of thermal poling was applied to microstructured fibers soon after they became available [155]. Their modal properties offer the possibility of SHG over a much broader range of pump wavelengths [156]. However, conversion efficiencies realized were relatively small.

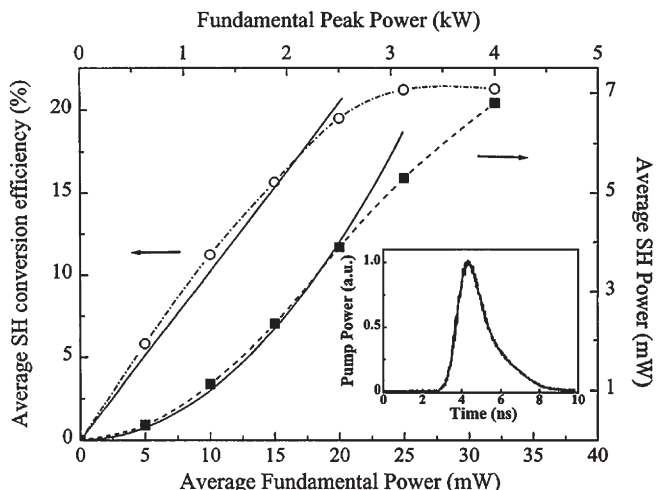
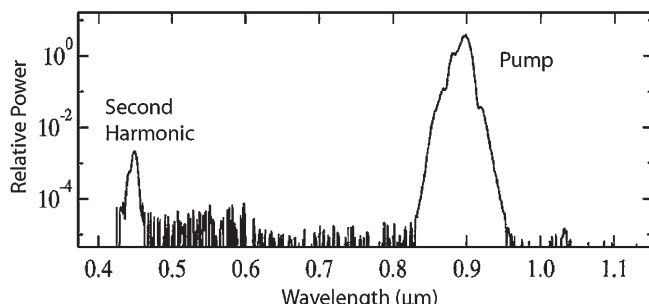


Figure 12.30 Average conversion efficiency and SHG power as a function of the average pump power when 2-ns pulses at a 4-kHz repetition rate are launched into a thermally poled fiber. Solid lines represent linear and quadratic fits expected from theory. The inset shows the shape of pump pulses. (After Ref. [154]; © 1999 OSA.)

Several techniques have been proposed in recent years for improving the SHG process in optical fibers [157–160]. In one approach, the wavelength of the pump laser could be tuned over 45 nm through mechanical compression of the  $\chi^{(2)}$  grating [157]. In a 2009 experiment, up to 236 mW of second-harmonic power was produced, with an average conversion efficiency of about 15%, using a longer (32-cm) periodically poled silica fiber [158]. The  $\chi^{(2)}$  grating was chirped in a 2010 experiment through aperiodic poling [159]. As a result, the pump wavelength could be varied over a 50 nm range when the grating period ( $66.5 \mu\text{m}$  at one end) was increased linearly by  $1.5 \mu\text{m}$  over 10-cm length of the fiber. Unfortunately, the SHG efficiency decreased so rapidly with the magnitude of the chirp that this technique may not be practical. Twisting of a birefringent periodically poled fiber allows a new form of phase matching that does not occur in untwisted fibers [160]. In particular, enhanced SHG can occur in such fibers through type-II phase matching.

In a 2000 experiment, a spectral peak close to the second-harmonic wavelength was observed, without thermal poling and quasi-phase matching, in a 10-cm-long microstructured fiber [161]. Figure 12.31 shows the spectrum measured at the output of such a fiber when 100-fs pulses at 895 nm with 250-W peak power were launched into it. The SHG peak was polarized orthogonally to the pump pulse, suggesting that fiber birefringence played an important role in this experiment. A 60-cm-long microstructured fiber was pumped with 50-fs pulses (at 800 nm) in a 2008 experiment, and a blue light near 400 nm was generated with up to 15% efficiency [162]. The physical mechanism behind this blue peak was believed to be a FWM process (rather than SHG) of the form  $2\omega_p = \omega_s + \omega_i$ , where  $\omega_p$  is the pump frequency,  $\omega_s$  is the blue-peak frequency, and the frequency  $\omega_i$  of the idler corresponds to a terahertz wave. It is known that such a process can become phase-matched in optical fibers [163].

SHG was observed in 2005 in a two-mode microstructured fiber [164]. Its efficiency was only a few percent, but it was sufficient to generate an ultrawide supercontinuum extending from 350 to 1750 nm when 600-ps pulses, with a 6-kW peak power at a wavelength of 1060 nm, were launched into a 2-m-long fiber. Such a wide bandwidth was attributed to the onset of SHG-induced modulation instability. The



**Figure 12.31** Spectrum at the output of a 10-cm-long microstructured fiber when 100-fs pulses at 1064 nm are launched into it with 250 W peak power. (After Ref. [161]; © 2000 OSA.)

origin of SHG in this experiment may be related to surface nonlinearities resulting from the presence of a large number of air holes within the cladding. The FWM process involving terahertz waves might have also played a role.

In the case of modal phase matching, the fundamental and second-harmonic waves propagate in different modes of the fiber. This technique has been analyzed in the context of tapered multimode fibers, and it was found that relatively high conversion efficiencies are possible with a proper taper design over a pump bandwidth that can exceed 10 nm [165]. In a different approach, self-poling of a Ge-doped fiber, using Q-switched pulses at 1064 nm with peak power close to 19 kW, was efficient enough to create an intense second-harmonic pulse, which in turn produced a wide-band spectrum in the visible region through a cascaded Raman process that generated up to nine Stokes bands [166]. FWM also played a significant role in this experiment because the 20-m-long fiber supported multiple modes in the visible region.

Another mechanism that can lead to SHG in fibers with an ultranarrow core (the so-called silica nanowires) is the nonlinear response of surface dipoles [167–169]. However, the SHG process in such fibers is strongly affected by the extent of surface uniformity, and high conversion efficiencies are yet to be realized.

### 12.4.3 SHG Theory

One can follow a standard procedure [140] to study SHG from  $\chi^{(2)}$  given by Eq. (12.4.3). Assume that a pump wave at the frequency  $\omega_1$  is incident on such a prepared fiber. The frequency  $\omega_1$  can be different from the frequency  $\omega_p$  of the pump used to prepare the fiber. The pump field  $A_p$  and the second-harmonic field  $A_h$  then satisfy a set of two coupled amplitude equations having the form [121]

$$\frac{dA_p}{dz} = i\gamma_p(|A_p|^2 + 2|A_h|^2)A_p + \frac{i}{2}\gamma_{SH}^* A_h A_p^* \exp(-ikz), \quad (12.4.4)$$

$$\frac{dA_h}{dz} = i\gamma_h(|A_h|^2 + 2|A_p|^2)A_h + i\gamma_{SH} A_p^2 \exp(ikz), \quad (12.4.5)$$

where  $\gamma_p$  and  $\gamma_h$  are defined similarly to Eq. (2.3.28),

$$\gamma_{SH} = (3\omega_1/4n_1c)\epsilon_0^2\alpha_{SH} f_{112}\chi^{(3)}|E_p|^2|E_{SH}|, \quad (12.4.6)$$

$f_{112}$  is an overlap integral (see Section 10.2),  $\kappa = \Delta k_p - \Delta k$ , and  $\Delta k$  is given by Eq. (12.4.2) after replacing  $\omega_p$  with  $\omega_1$ . The parameter  $\kappa$  is the residual wave-vector mismatch occurring when  $\omega_1 \neq \omega_p$ . The terms proportional to  $\gamma_p$  and  $\gamma_h$  are due to SPM and XPM and must be included in general.

Equations (12.4.4) and (12.4.5) can be solved using the procedure of Section 10.2. If we assume that the pump remains undepleted ( $|A_h|^2 \ll |A_p|^2$ ), Eq. (12.4.4) has the solution  $A_p(z) = \sqrt{P_p} \exp(i\gamma_p P_p z)$ , where  $P_p$  is the incident pump power. Introducing  $A_h = B_h \exp(2i\gamma_p P_p z)$  in Eq. (12.4.5), we obtain

$$\frac{dB_h}{dz} = i\gamma_{SH} P_p \exp(ikz) + 2i(\gamma_h - \gamma_p)P_p B_h. \quad (12.4.7)$$

Equation (12.4.7) is readily solved to obtain the second-harmonic power as

$$P_h(L) = |B_h(L)|^2 = |\gamma_{\text{SH}} P_p L|^2 \frac{\sin^2(\kappa' L/2)}{(\kappa' L/2)^2}, \quad (12.4.8)$$

where  $\kappa' = \kappa - 2(\gamma_h - \gamma_p)P_p$ . Physically, SPM and XPM modify  $\kappa$  as they contribute to the phase-matching condition.

The approximation that the pump remains undepleted begins to break down for conversion efficiencies  $>1\%$ . It turns out that Eqs (12.4.4) and (12.4.5) can be solved analytically even when the pump is allowed to deplete. The solution in the form of elliptic functions was first obtained in 1962 [140]. The periodic nature of the elliptic functions implies that the power flows back to the pump after the SHG power attains its maximum value. The analysis also predicts the existence of a parametric mixing instability induced by SPM and XPM [138]. The instability manifests as a doubling of the spatial period associated with the frequency-conversion process. As pump depletion is negligible in most experimental situations, such effects are difficult to observe in optical fibers.

The derivation of Eq. (12.4.8) assumes that the  $\chi^{(2)}$  grating is created coherently all along the fiber. This would be the case if the pump used during the preparation process were a CW beam of narrow spectral width. In practice, mode-locked pulses of duration  $\sim 100\text{ ps}$  are used. The use of such short pulses affects grating formation in two ways. First, a group-velocity mismatch between the pump and second-harmonic pulses leads to their separation within a few walk-off lengths  $L_w$ . If we use  $T_0 \approx 80\text{ ps}$  and  $|d_{12}| \approx 80\text{ ps/m}$  in Eq. (1.2.14), the values appropriate for  $1.06\text{-}\mu\text{m}$  experiments,  $L_w \approx 1\text{ m}$ . Thus, the  $\chi^{(2)}$  grating stops to form within a distance  $\sim 1\text{ m}$  for pump pulses of  $100\text{ ps}$  duration. Second, SPM-induced spectral broadening reduces the coherence length  $L_{\text{coh}}$  over which the  $\chi^{(2)}$  grating can generate the second harmonic coherently.

It turns out that  $L_{\text{coh}}$  sets the ultimate limit because  $L_{\text{coh}} < L_w$  under typical experimental conditions. This can be seen by noting that each pump frequency creates its own grating with a slightly different period  $2\pi/\Delta k_p$ , where  $\Delta k_p$  is given by Eq. (12.4.2). Mathematically, Eq. (12.4.1) for  $P_{\text{dc}}$  should be integrated over the pump-spectral range to include the contribution of each grating. Assuming Gaussian spectra for both pump and second-harmonic waves, the effective dc polarization becomes [128]

$$P_{\text{dc}}^{\text{eff}} = P_{\text{dc}} \exp[-(z/L_{\text{coh}})^2], \quad L_{\text{coh}} = 2/|d_{12}\delta\omega_p|, \quad (12.4.9)$$

where  $d_{12}$  is defined in Eq. (1.2.13) and  $\delta\omega_p$  is the spectral half-width (at  $1/e$  point). For  $|d_{12}| = 80\text{ ps/m}$  and  $10\text{-GHz}$  spectral width (FWHM),  $L_{\text{coh}} \approx 60\text{ cm}$ .

In most experiments performed with  $1.06\text{-}\mu\text{m}$  pump pulses, the spectral width at the fiber input is  $\sim 10\text{ GHz}$ . However, SPM broadens the pump spectrum as the pump pulse travels down the fiber [see Eqs (4.1.6) and (4.1.11)]. This broadening reduces the coherence length considerably, and  $L_{\text{coh}} \sim 10\text{ cm}$  is expected. Equation (12.4.8) should be modified if  $L_{\text{coh}} < L$ . In a simple approximation [121],  $L$  is replaced by  $L_{\text{coh}}$  in Eq. (12.4.8). This amounts to assuming that  $P_{\text{dc}}^{\text{eff}} = P_{\text{dc}}$  for

$z \leq L_{\text{coh}}$  and zero for  $z > L_{\text{coh}}$ . One can improve over this approximation using Eq. (12.4.9). Its use requires that  $\gamma_{\text{SH}}$  in Eq. (12.4.7) be multiplied by the exponential factor  $\exp[-(z/L_{\text{coh}})^2]$ . If  $L_{\text{coh}} \ll L$ , Eq. (12.4.7) can be integrated with the result [128]

$$P_2(k) = (\pi/4)|\gamma_{\text{SH}} P_p L_{\text{coh}}|^2 \exp\left(-\frac{1}{2}\kappa^2 L_{\text{coh}}^2\right). \quad (12.4.10)$$

This expression is also approximate as it is based on Eqs (12.4.4) and (12.4.5) that are valid only under quasi-CW conditions. For short pump pulses, the GVD effects can be included in Eqs (12.4.4) and (12.4.5) by replacing the spatial derivatives by a sum of partial derivatives as indicated in Eq. (10.2.23).

## 12.5 THIRD-HARMONIC GENERATION

In contrast with the SHG, third harmonic of incident light should be created readily inside silica fibers, if the corresponding phase-matching condition is satisfied, because it originates from the same third-order nonlinear process that leads to FWM and other nonlinear effects. Indeed, third-harmonic generation (THG) has been observed in several experiments, although efficiency is typically low because phase matching is difficult to realize in standard single-mode fibers [170–176]. In a 1993 experiment, the doping level of germania was found to affect the THG process [172]. The presence of other dopants such as erbium or nitrogen also helps, and efficiencies as high as  $2 \times 10^{-4}$  were realized by 1997.

### 12.5.1 THG in Highly Nonlinear Fibers

It turns out that phase matching is much easier to accomplish in highly nonlinear fibers. In a 2000 experiment the THG light appeared in a higher-order mode of a 50-cm-long microstructured fiber when 1-kW pulses at 1064 nm were launched into it [161]. A PCF was used for THG in a 2001 study [177]. Since then, this nonlinear process has attracted considerable attention [178–190].

To understand why THG is easier to observe in microstructured fibers, consider first why it is difficult to realize phase matching in standard silica fibers. For a quasi-CW pump launched at the frequency  $\omega$ , the phase-matching condition takes the form

$$\Delta\beta \equiv \beta(3\omega) - 3\beta(\omega) = (3\omega/c)[\bar{n}(3\omega) - \bar{n}(\omega)] = 0, \quad (12.5.1)$$

where  $\beta(\omega) \equiv \bar{n}(\omega)\omega/c$  is the propagation constant and  $\bar{n}(\omega)$  is the effective mode index. The values of  $\bar{n}$  at  $\omega$  and  $3\omega$  differ enough for the fundamental mode that the THG process cannot be phase-matched in single-mode fibers. However, if the fiber supports multiple modes at the third-harmonic wavelength,  $\bar{n}(3\omega)$  may match nearly  $\bar{n}(\omega)$  when the third harmonic propagates in a specific higher-order mode. However, this can only occur if the difference,  $\bar{n}(3\omega) - \bar{n}(\omega)$ , is less than the core-cladding index difference, a quantity that rarely exceeds 0.01 for most standard fibers.

As seen in Figure 1.4, the refractive index of pure silica increases by more than 0.01 at the third-harmonic wavelength, falling in the range of 300–500 nm in most experiments. Since no bound modes can have its effective index less than that of the cladding, phase matching cannot be realized for fibers in which the core-cladding index difference is 0.01 or less. If this index difference is enhanced by increasing the doping level of germania within the core, THG can become phase-matched, as observed in a 1993 experiment [172]. THG can also be realized through the Cherenkov-type phase matching in which the third harmonic propagates in a leaky mode of the fiber [173]. However, a microstructured fiber with air holes in its cladding provides the best environment for THG because the effective core-cladding index difference can exceed 0.1, especially in fibers with large air holes. Indeed, it was observed easily in a 2000 experiment performed with a 50-cm-long microstructured fiber [161]. As expected, the third harmonic appeared in a higher-order mode of the fiber.

In the case of ultrashort pulses, the THG process is affected by other nonlinear effects occurring simultaneously within the same fiber. Figure 12.32a shows the spectrum of third harmonic at the output of a 95-cm-long photonic crystal fiber when 170-fs pulses at 1550 nm (with 45 mW average power at a 80-MHz repetition rate) were launched into it [177]. The 517-nm peak is expected as this wavelength corresponds to the third harmonic of the 1550-nm pump. The origin of the second broad peak near 571 nm becomes clear from the output pump spectrum shown in Figure 12.32b, where the 1700-nm peak corresponds to the Raman soliton formed through the RIFS of the pump pulse. The 571-nm peak is generated by this Raman soliton. It is broader than the 517-nm peak because the spectrum of Raman soliton shifts continuously inside the fiber. The observed far-field pattern (with six bright lobes around a central dark spot) indicated clearly that the third harmonic was generated in a specific higher-order mode for which the phase-matching condition was satisfied. In general, the THG spectrum produced by femtosecond pump pulses is

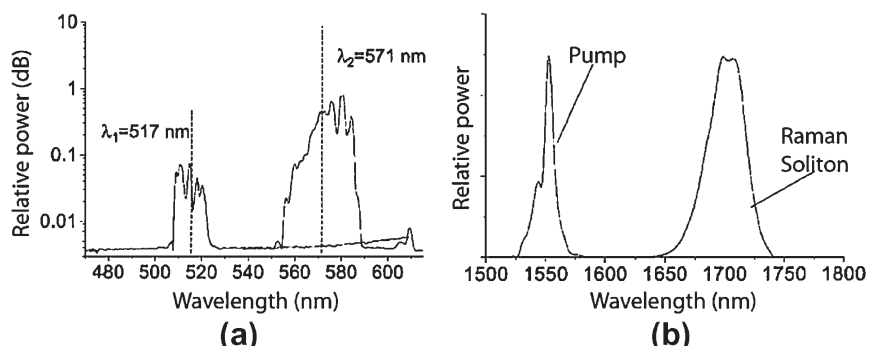


**Figure 12.32** Measured optical spectra near (a) third harmonic and (b) pump wavelengths when 170-fs pulses were launched into a 95-cm-long fiber. (After Ref. [177]; © 2001 OSA.)

asymmetric and exhibits considerable structure [183]. The formation of Raman solitons with continuously shifting spectra helps considerably in generating a third harmonic in a higher-order guided mode of the same fiber [185].

### 12.5.2 Effects of Group-Velocity Mismatch

In the case of short pump pulses with a broad spectrum, phase matching of the THG process is more complicated because the effects of group-velocity mismatch cannot be ignored. Physically speaking, the generated THG pulse width is comparable to the pump pulse, but the two move at different speeds through the fiber. The THG pulse can grow coherently only if it overlaps with the pump pulse. In fact, the spectrum of the third harmonic may not be located exactly at  $3\omega_p$  for a pump pulse whose spectrum is centered at  $\omega_p$  because of the effects of group-velocity mismatch.

To understand this feature, we should expand  $\beta(\omega)$  appearing in Eq. (12.5.1) in a Taylor series around  $\omega_p$ . A similar expansion should be carried out for  $\beta(3\omega)$ . If we retain terms only up to first order in this expansion, we find that [183]

$$\Delta\beta = \Delta\beta_0 + \Delta\beta_1\Omega, \quad (12.5.2)$$

where  $\Omega = 3(\omega - \omega_p)$  is the frequency shift of third harmonic and

$$\Delta\beta_0 = \beta(3\omega_p) - 3\beta(\omega_p), \quad \Delta\beta_1 = v_{gh}^{-1} - v_{gp}^{-1}. \quad (12.5.3)$$

The quantities  $v_{gj}$  and  $\beta_{2j}$  represent the group velocity and its dispersion at the frequency  $\omega_j$  with  $j = p$  for the pump and  $j = h$  for the third harmonic. Clearly, the condition  $\Delta\beta = 0$  is satisfied when the third harmonic is shifted from  $3\omega_p$  by an amount  $\Omega = -(\Delta\beta_0/\Delta\beta_1)$ . This shift depends on the group-velocity mismatch and can be positive or negative depending on the fiber mode for which phase matching occurs. Equation (12.5.2) does not include the contribution of SPM and XPM. This nonlinear contribution to the phase mismatch also affects the exact value of the frequency shift  $\Omega$ .

It is possible for the THG spectrum to exhibit several distinct peaks, if the phase-matching condition in Eq. (12.5.2) is satisfied for several different values of  $\Omega$  such that each peak corresponds to THG in a different fiber mode [183]. This feature was observed in a 2006 experiment in which 60-fs pulses at a wavelength of 1240 nm were launched into a 8-cm-long microstructured fiber with 4- $\mu\text{m}$  core diameter [184]. Figure 12.33 shows the spectrum of third harmonic at the fiber output for pulses with 0.5 nJ energy. The peak located near 420 nm is shifted from the third harmonic of 1240 nm at 413.3 nm by more than 6 nm. Moreover, several other peaks occur that are shifted by as much as 60 nm from this wavelength. A theoretical model predicts that three higher-order modes, EH<sub>14</sub>, TE<sub>04</sub>, and EH<sub>52</sub>, provide phase matching for spectral peaks located near 370, 420, and 440 nm, respectively.

The simple theory developed earlier for SHG can be extended for the case of THG, with only minor changes, when the pump pulses are relatively broad. However,

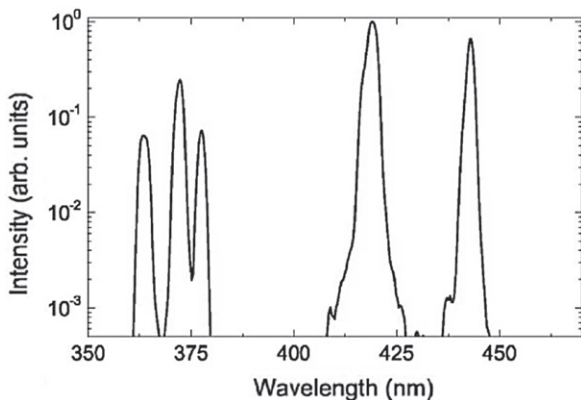


**Figure 12.33** Measured third-harmonic spectrum when 60-fs pulses at 1240 nm with 0.5 nJ energy were launched into a 8-cm-long fiber. (After Ref. [184]; © 2006 American Physical Society.)

one must include the dispersive effects in the case of short pump pulses by changing  $dA/dz$  as indicated in Eq. (10.2.23). The resulting set of equations can be written as

$$\frac{\partial A_p}{\partial z} + \frac{1}{v_{gp}} \frac{\partial A_p}{\partial t} + \frac{i\beta_{2p}}{2} \frac{\partial^2 A_p}{\partial t^2} = i\gamma_p(|A_p|^2 + 2|A_h|^2)A_p + \frac{i}{3}\gamma_{TH}^* A_h A_p^{*2} e^{i\Delta\beta_0 z}, \quad (12.5.4)$$

$$\frac{\partial A_h}{\partial z} + \frac{1}{v_{gh}} \frac{\partial A_h}{\partial t} + \frac{i\beta_{2h}}{2} \frac{\partial^2 A_h}{\partial t^2} = i\gamma_h(|A_h|^2 + 2|A_p|^2)A_h + i\gamma_{TH} A_p^3 e^{-i\Delta\beta_0 z}, \quad (12.5.5)$$

where  $\gamma_j$  is the nonlinear parameter, as defined in Eq. (2.3.29),  $\beta_{2j}$  is the GVD parameter, and  $j=p$  or  $h$  for the pump and its third harmonic, respectively. The THG growth is governed by  $\gamma_{TH}$ .

The preceding set of two equations should be solved numerically in general. An analytic solution is possible if we neglect GVD, pump depletion, and the SPM and XPM terms. If we set  $T = t - z/v_{gp}$  and work in a reference frame moving with the pump pulse, Eq. (12.5.5) is reduced to

$$\frac{\partial A_h}{\partial z} + \Delta\beta_1 \frac{\partial A_h}{\partial T} = i\gamma_{TH} A_p^3(T) e^{-i\Delta\beta_0 z}, \quad (12.5.6)$$

where  $A_p(T)$  is the amplitude of pump pulse at the input end at  $z = 0$ . This equation can easily be solved in the frequency domain to obtain the following expression for the third-harmonic power [183]:

$$|A_h(z, \Omega)|^2 = |\gamma_{TH}|^2 \frac{\sin^2[(\Delta\beta_0 + \Delta\beta_1\Omega)z/2]}{(\Delta\beta_0 + \Delta\beta_1\Omega)^2} \times \left| \iint_{-\infty}^{\infty} A_p(\Omega - \Omega_1) A_p(\Omega_1 - \Omega_2) A_p(\Omega_2) d\Omega_1 d\Omega_2 \right|^2. \quad (12.5.7)$$

Clearly, the maximum growth of third harmonic occurs for a value  $\Omega = -(\Delta\beta_0/\Delta\beta_1)$ , the same value predicted by Eq. (12.5.2). The solution (12.5.7) is useful for calculating the spectrum of THG pulses for a given pump-pulse spectrum.

### 12.5.3 Effects of Fiber Birefringence

As we have seen earlier in the context of FWM, the birefringence of an optical fiber affects the phase-matching condition; the same is expected for THG. In essence, birefringence doubles the number of modes supported by a fiber by forcing the two orthogonal polarized components of each mode to have slightly different mode indices. As a result, the third-harmonic mode for which the phase-matching condition in Eq. (12.5.2) is satisfied may be different depending on whether the pump is polarized along the slow or fast axis.

This behavior was observed in a 2003 experiment in which 170-fs pulses at 1550 nm were launched into a 20-cm-long fiber with a slightly elliptical core [180]. Figure 12.34 shows the spectrum of third harmonic at the fiber output as a function of average input power when pump pulse propagates either along the slow or along the fast axis. The THG process creates a spectral band near 514 nm in both cases. However, another spectral band centered at 534 nm is also created when the average power exceeds 16 mW and the pump pulse is launched along the fast axis. At high enough input powers, only this second band appears. Of course, both spectral bands are present simultaneously when both polarization modes are excited by pump pulses. Similar to the case shown in Figure 12.32, the 534-nm band is due to THG from the Raman soliton.

A detailed study of the birefringence was carried out in 2003 using birefringent microstructured fibers with core diameters ranging from 1.5 to 4  $\mu\text{m}$  [181]. An optical parametric oscillator, providing 100-fs pulses with a 82-MHz repetition rate at

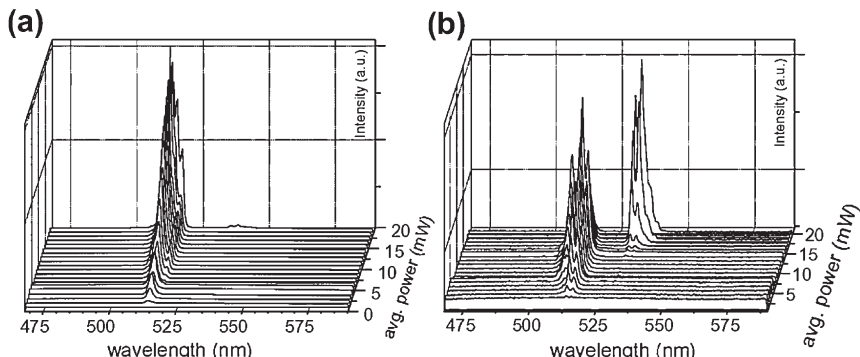


**Figure 12.34** Measured THG spectra when 170-fs pulses at 1550 nm are launched along the (a) slow or (b) fast axis of a 20-cm-long microstructured fiber. (After Ref. [180]; © 2003 OSA.)

wavelengths tunable from 1450 to 1650 nm, was employed as a pump source, and the average input power was varied in the range of 5–80 mW. For a 6-cm-long fiber with  $2.5\text{ }\mu\text{m}$  core diameter, the THG spectra exhibited peaks near 510 and 550 nm, but the peak wavelengths shifted by 5 nm or so when pump pulses were polarized along the two principal axes. Each peak appeared as a doublet whose relative heights varied with the average power launched into the fiber. As in Figure 12.34, the longer-wavelength THG peak results from the Raman soliton that separates from the main pump pulse after a short distance into the fiber as a result of a large RIFS. The observed far-field patterns associated with the THG peaks were complex with eight lobes around a central dark spot and corresponded to a fiber mode whose order was relatively high ( $>20$ ). A theoretical model predicted the observed patterns quite well. For a fiber with  $1.5\text{-}\mu\text{m}$  core diameter, the mode order for which THG was phase-matched was as high as 48.

Recently, the efficiency of SHG and THG was found to increase considerably when 400-fs pulses at 1550 nm were launched inside 30-cm-long tellurite microstructured fibers [188]. The nonlinear parameter  $\gamma$  exceeded  $1000\text{ W}^{-1}/\text{km}$  for such fibers when core diameter was close to  $2.5\text{ }\mu\text{m}$ . This feature generated an ultrawide supercontinuum that extended from 470 to 2400 nm. The next chapter focuses on the topic of supercontinuum generation in detail.

## PROBLEMS

- 12.1** A short pulse with 100 W peak power propagates as a fundamental soliton inside a 10-m-long highly nonlinear fiber with  $\gamma = 100\text{ W}^{-1}/\text{km}$  and  $\beta_2 = -10\text{ ps}^2/\text{km}$ . Calculate the pulse width (FWHM) and the dispersion and nonlinear lengths.
- 12.2** A fourth-order soliton with 150-fs width (FWHM) undergoes fission inside a 10-m-long fiber with  $\gamma = 100\text{ W}^{-1}/\text{km}$  and  $\beta_2 = -10\text{ ps}^2/\text{km}$ . Calculate the widths, peak powers, and Raman-induced spectral shifts for the four fundamental solitons created.
- 12.3** What is meant by the Cherenkov radiation in the context of optical fibers? Under what conditions is this radiation emitted by a soliton? Derive an expression for the radiation frequency assuming that solitons are perturbed only by the third-order dispersion.
- 12.4** Use Eq. (12.1.11) and plot the frequencies of the two dispersive waves for a third-order soliton as a function of  $\delta_4$  for  $\delta_3 = -0.01, 0,$  and  $0.01$ . Estimate these frequencies when a 100-fs (FWHM) input pulse is launched and  $\delta_4 = 0.001$  for the fiber.
- 12.5** Extend the MATLAB code given in Appendix B for solving Eq. (12.1.9) and reproduce the plots given in Figures 12.1 and 12.4.
- 12.6** Extend the MATLAB code for the preceding problem to include the Raman term in Eq. (12.2.1) and reproduce the plot given in Figure 12.6.

- 12.7** Explain why the spectrum of an ultrashort pulse propagating as a soliton shifts toward longer wavelengths. Do you expect this shift to occur if the pulse were to propagate in the normal-dispersion regime of the fiber? Discuss the logic behind your answer.
- 12.8** Explain the FROG technique and sketch a typical experimental setup used for it. How would you extend this technique to make use of cross-correlation in place of autocorrelation?
- 12.9** Discuss why the Raman-induced frequency shift of a soliton is suppressed in a microstructured fiber exhibiting two zero-dispersion wavelengths when the soliton spectrum approaches the second wavelength.
- 12.10** Derive the phase-matching condition given in Eq. (12.3.1). Consider the terms up to fourth-order dispersion and calculate the frequency shift in THz when  $\beta_2 = 5 \text{ ps}^2/\text{km}$ ,  $\beta_4 = -1 \times 10^{-4} \text{ ps}^4/\text{km}$ , and  $L_{\text{NL}} = 1 \text{ cm}$ .
- 12.11** Discuss how a microstructured fiber can be used inside the cavity of a fiber-optic parametric oscillator to extend the tuning range of such lasers. What is the main factor that limits the tuning range when such a laser is pumped with short optical pulses?
- 12.12** Explain how thermal poling can be used to generate second a harmonic inside in an optical fiber. Describe the physical mechanism involved in detail.
- 12.13** Why is it difficult to realize phase matching for generating a third harmonic inside standard optical fibers with a core-cladding index difference of 0.01 or less? How is this problem solved in microstructured fibers?

## REFERENCES

- [1] E. A. Golovchenko, E. M. Dianov, A. M. Prokhorov, and V. N. Serkin, *JETP Lett.* **42**, 87 (1985).
- [2] P. K. A. Wai, C. R. Menyuk, Y. C. Lee, and H. H. Chen, *Opt. Lett.* **11**, 464 (1986).
- [3] Y. Kodama and A. Hasegawa, *IEEE J. Quantum Electron.* **23**, 510 (1987).
- [4] P. Beaud, W. Hodel, B. Zysset, and H. P. Weber, *IEEE J. Quantum Electron.* **23**, 1938 (1987).
- [5] K. Tai, A. Hasegawa, and N. Bekki, *Opt. Lett.* **13**, 392 (1988).
- [6] P. K. A. Wai, H. H. Chen, and Y. C. Lee, *Phys. Rev. A* **41**, 426 (1990).
- [7] J. P. Gordon, *J. Opt. Soc. Am. B* **9**, 81 (1992).
- [8] J. N. Elgin, *Phys. Rev. A* **47**, 4331 (1993).
- [9] V. I. Karpman, *Phys. Rev. E* **47**, 2073 (1993).
- [10] Y. Kodama, M. Romagnoli, S. Wabnitz, and M. Midrio, *Opt. Lett.* **19**, 165 (1994).
- [11] N. Akhmediev and M. Karlsson, *Phys. Rev. A* **51**, 2602 (1995).
- [12] J. N. Elgin, T. Brabec, and S. M. J. Kelly, *Opt. Commun.* **114**, 321 (1995).
- [13] A. V. Husakou and J. Herrmann, *Phys. Rev. Lett.* **87**, 203901 (2001).
- [14] E. N. Tsoy and C. M. de Sterke, *Phys. Rev. A* **76**, 043804 (2007).
- [15] S. Roy, S. K. Bhadra, and G. P. Agrawal, *Phys. Rev. A* **79**, 023824 (2009).
- [16] S. Roy, S. K. Bhadra, and G. P. Agrawal, *Opt. Lett.* **34**, 2072 (2009).
- [17] S. Roy, S. K. Bhadra, and G. P. Agrawal, *Opt. Commun.* **282**, 3798 (2009).

- [18] E. M. Dianov, A. Y. Karasik, P. V. Mamyshev, et al., *JETP Lett.* **41**, 294 (1985).
- [19] F. M. Mitschke and L. F. Mollenauer, *Opt. Lett.* **11**, 659 (1986).
- [20] J. P. Gordon, *Opt. Lett.* **11**, 6662 (1986).
- [21] J. Santhanam and G. P. Agrawal, *Opt. Commun.* **222**, 413 (2003).
- [22] G. P. Agrawal, *Opt. Lett.* **16**, 226 (1991).
- [23] D. J. Richardson, V. V. Afanasjev, A. B. Grudinin, and D. N. Payne, *Opt. Lett.* **17**, 1596 (1992).
- [24] J. K. Lucek and K. J. Blow, *Phys. Rev. A* **45**, 666 (1992).
- [25] T. Sugawa, K. Kurokawa, H. Kubota, and M. Nakazawa, *Electron. Lett.* **30**, 1963 (1994).
- [26] C. Hedaley and G. P. Agrawal, *J. Opt. Soc. Am. B* **13**, 2170 (1996).
- [27] M. Golles, I. M. Uzunov, and F. Lederer, *Phys. Lett. A* **231**, 195 (1997).
- [28] N. Nishizawa and T. Goto, *IEEE Photon. Technol. Lett.* **11**, 325 (1999).
- [29] M. E. Fermann, A. Galvanauskas, M. L. Stock, K. K. Wong, D. Harter, and L. Goldberg, *Opt. Lett.* **24**, 1428 (1999).
- [30] T. Hori, N. Nishizawa, H. Nagai, M. Yoshida, and T. Goto, *IEEE Photon. Technol. Lett.* **13**, 13 (2001).
- [31] X. Liu, C. Xu, W. H. Knox, J. K. Chandalia, B. J. Eggleton, S. G. Kosinski, and R. S. Windeler, *Opt. Lett.* **26**, 358 (2001).
- [32] R. Washburn, S. E. Ralph, P. A. Lacourt, J. M. Dudley, W. T. Rhodes, R. S. Windeler, and S. Coen, *Electron. Lett.* **37**, 1510 (2001).
- [33] D. T. Reid, I. G. Cormack, W. J. Wadsworth, J. C. Knight, and P. St. J. Russell, *J. Mod. Opt.* **49**, 757 (2002).
- [34] N. Nishizawa, Y. Ito, and T. Goto, *IEEE Photon. Technol. Lett.* **14**, 986 (2002).
- [35] D. A. Chestnut and J. R. Taylor, *Opt. Lett.* **28**, 2512 (2003).
- [36] A. Efimov, A. J. Taylor, F. G. Omenetto, and E. Vanin, *Opt. Lett.* **29**, 271 (2004).
- [37] K. S. Abedin and F. Kubota, *IEEE J. Sel. Topics Quantum Electron.* **10**, 1203 (2004).
- [38] M. G. Banaee and J. F. Young, *J. Opt. Soc. Am. B* **23**, 1484 (2006).
- [39] Q. Lin and G. P. Agrawal, *Opt. Lett.* **31**, 3086 (2006).
- [40] J. H. Lee, J. van Howe, C. Xu, and X. Liu, *IEEE J. Sel. Topics Quantum Electron.* **14**, 713 (2008).
- [41] Z. Chen, A. J. Taylor, and A. Efimov, *J. Opt. Soc. Am. B* **27**, 1022 (2010).
- [42] R. Pant, A. C. Judge, E. C. Magi, B. T. Kuhlmeij, C. M. de Sterke, and B. J. Eggleton, *J. Opt. Soc. Am. B* **27**, 1894 (2010).
- [43] M. Erkintalo, G. Genty, B. Wetzel, and J. M. Dudley, *Opt. Express* **18**, 25449 (2010).
- [44] S. Linden, J. Kuhl, and H. Giessen, *Opt. Lett.* **24**, 569 (1999).
- [45] N. Nishizawa and T. Goto, *IEEE J. Sel. Topics Quantum Electron.* **7**, 518 (2001).
- [46] J. H. V. Price, K. Furusawa, T. M. Monro, L. Lefort, and D. J. Richardson, *J. Opt. Soc. Am. B* **19**, 1286 (2002).
- [47] H. Lim, J. Buckley, A. Chong, and F. W. Wise, *Electron. Lett.* **40**, 1523 (2005).
- [48] J. Takayanagi, T. Sugiura, M. Yoshida, and N. Nishizawa, *IEEE Photon. Technol. Lett.* **18**, 2284 (2006).
- [49] A. V. Andrianov, S. V. Muraviov, A. V. Kim, and A. A. Sysoliatin, *JETP Lett.* **85**, 364 (2007).
- [50] S. Kivistö, T. Hakulinen, M. Guina, and O. G. Okhotnikov, *IEEE Photon. Technol. Lett.* **19**, 934 (2007).
- [51] M.-C. Chan, S.-H. Chia, T.-M. Liu, et al., *IEEE Photon. Technol. Lett.* **20**, 900 (2008).
- [52] K. Wang and C. Xu, *Opt. Lett.* **36**, 842 (2011).

- [53] N. Nishizawa and T. Goto, *Opt. Express* **8**, 328 (2001).
- [54] N. Nishizawa and T. Goto, *Opt. Lett.* **27**, 152 (2002); *Opt. Express* **10**, 1151 (2002).
- [55] N. Nishizawa and T. Goto, *Opt. Express* **11**, 359 (2003).
- [56] N. Nishizawa, R. Okamura, and T. Goto, *IEEE Photon. Technol. Lett.* **11**, 421 (1999).
- [57] N. Nishizawa and T. Goto, *Opt. Express* **10**, 256 (2002).
- [58] N. Nishizawa, Y. Ukai, and T. Goto, *Opt. Express* **13**, 8128 (2005).
- [59] M. Kato, *J. Lightwave Technol.* **24**, 805 (2006).
- [60] K. J. Blow, N. J. Doran, and D. Wood, *J. Opt. Soc. Am. B* **5**, 1301 (1988).
- [61] A. S. Gouveia-Neto, A. S. L. Gomes, and J. R. Taylor, *Opt. Lett.* **14**, 514 (1989).
- [62] D. Schadt and B. Jaskorzynska, *J. Opt. Soc. Am. B* **5**, 2374 (1988).
- [63] M. Ding and K. Kikuchi, *IEEE Photon. Technol. Lett.* **4**, 497 (1992).
- [64] M. Ding and K. Kikuchi, *IEEE Photon. Technol. Lett.* **4**, 927 (1992).
- [65] D. V. Skryabin, F. Luan, J. C. Knight, and P. St. J. Russell, *Science* **301**, 1705 (2003).
- [66] O. Vanvincq, A. Kudlinski, A. Bétourné, Y. Quiquempois, and G. Bouwmans, *J. Opt. Soc. Am. B* **27**, 2328 (2010).
- [67] F. Biancalana, D. V. Skryabin, and A. V. Yulin, *Phys. Rev. E* **70**, 016615 (2004).
- [68] A. Efimov, A. J. Taylor, , F. G. Omenetto, et al., *Opt. Express* **12**, 6498 (2004).
- [69] E. N. Tsoy and C. M. de Sterke, *J. Opt. Soc. Am. B* **23**, 2425 (2006).
- [70] N. Y. Joly, F. G. Omenetto, A. Efimov, A. J. Taylor, J. C. Knight, and P. St. J. Russell, *Opt. Commun.* **248**, 281 (2005).
- [71] V. N. Serkin, V. A. Vysloukh, and J. R. Taylo, *Electron. Lett.* **29**, 12 (1992).
- [72] B. Kibler, P.-A. Lacourt, F. Courvoisier, and J. M. Dudley, *Electron. Lett.* **43**, 967 (2007).
- [73] F. Poletti, P. Horak, and D. J. Richardson, *IEEE Photon. Technol. Lett.* **20**, 1414 (2008).
- [74] A. Podlipensky, P. Szarniak, N. Y. Joly, C. G. Poulton, and P. St. J. Russell, *Opt. Express* **15**, 1653 (2007).
- [75] N. Akhmediev, W. Królikowski, and A. J. Lowery, *Opt. Commun.* **131**, 260 (1996).
- [76] A. Podlipensky, P. Szarniak, N. Y. Joly, and P. St. J. Russell, *J. Opt. Soc. Am. B* **25**, 2049 (2008).
- [77] A. Hause and F. Mitschke, *Phys. Rev. A* **80**, 063824 (2009); *Phys. Rev. A* **82**, 043838 (2010).
- [78] T. X. Tran, A. Podlipensky, P. St. J. Russell, and F. Biancalana, *J. Opt. Soc. Am. B* **27**, 1785 (2010).
- [79] L. Gagnon and P. A. Bélanger, *Opt. Lett.* **9**, 466 (1990).
- [80] A. V. Gorbach and D. V. Skryabin, *Phys. Rev. A* **76**, 063824 (2007).
- [81] J. E. Sharping, M. Fiorentino, A. Coker, P. Kumar, and R. S. Windeler, *Opt. Lett.* **26**, 1048 (2001).
- [82] G. Millot, A. Sauter, J. M. Dudley, L. Provino, and R. S. Windeler, *Opt. Lett.* **27**, 695 (2002).
- [83] J. E. Sharping, M. Fiorentino, P. Kumar, and R. S. Windeler, *Opt. Lett.* **27**, 1675 (2002).
- [84] M. E. Marhic, K. K. Y. Wong, L. G. Kazovsky, and T. E. Tsai, *Opt. Lett.* **27**, 1439 (2002).
- [85] J. D. Harvey, R. Leonhardt, S. Coen, et al., *Opt. Lett.* **28**, 2225 (2003).
- [86] T. V. Andersen, K. M. Hilligse, C. K. Nielsen, et al., *Opt. Express* **12**, 4113 (2004).
- [87] W. Wadsworth, N. Joly, J. Knight, T. Birks, F. Biancalana, and P. Russell, *Opt. Express* **12**, 299 (2004).
- [88] D. Amans, E. Brainis, M. Haelterman, and P. Emplit, *Opt. Lett.* **30**, 1051 (2005).
- [89] W. H. Reeves, D. V. Skryabin, F. Biancalana, et al., *Nature* **424**, 511 (2003).

- [90] F. Biancalana, D. V. Skryabin, and P. St. J. Russell, *Phys. Rev. E* **68**, 046603 (2003).
- [91] A. V. Husakoua and J. Herrmann, *Appl. Phys. Lett.* **83**, 3867 (2003).
- [92] F. Biancalana and D. V. Skryabin, *J. Opt. A* **6**, 301 (2004).
- [93] A. V. Yulin, D. V. Skryabin, and P. St. J. Russell, *Opt. Lett.* **29**, 2411 (2004).
- [94] Q. Lin, F. Yaman, and G. P. Agrawal, *Opt. Lett.* **31**, 1286 (2006).
- [95] J. D. Harvey, S. G. Murdoch, S. Coen, R. Leonhardt, and D. mechini, *Opt. Quantum Electron.* **39**, 1103 (2007).
- [96] R. A. Sammut and S. J. Garth, *J. Opt. Soc. Am. B* **6**, 1732 (1989).
- [97] M. Yu, C. J. McKinstrie, and G. P. Agrawal, *Phys. Rev. E* **52**, 1072 (1995).
- [98] K. K. Chow, C. Shu, C. L. Lin, and A. Bjarklev, *IEEE Photon. Technol. Lett.* **17**, 624 (2005).
- [99] J. Fan, A. Dogariu, and L. J. Wang, *Appl. Phys. B* **81**, 801 (2005).
- [100] A. Zhang and M. S. Demokan, *Opt. Lett.* **30**, 2375 (2005).
- [101] S. Asimakis, P. Petropoulos, F. Poletti, et al., *Opt. Express* **15**, 596 (2006).
- [102] T. Torounidis and P. Andrekson, *IEEE Photon. Technol. Lett.* **19**, 650 (2007).
- [103] K. K. Chow, K. Kikuchi, T. Nagashima, T. Hasegawa, S. Ohara, and N. Sugimoto, *Opt. Express* **15**, 15418 (2007).
- [104] M. E. Marhic, *Fiber Optical Parametric Amplifiers, Oscillators and Related Devices* (Cambridge University Press, 2007).
- [105] T. Sylvestre, A. Kudlinski, A. Mussot, J.-F.Gleyze, A. Jolly, and H. Maillotte, *Appl. Phys. Lett.* **94**, 111104 (2009).
- [106] Y. Deng, Q. Lin, F. Lu, G. P. Agrawal, and W. H. Knox, *Opt. Lett.* **30**, 1234 (2005).
- [107] J. E. Sharping, M. A. Foster, A. L. Gaeta, J. Lasri, O. Lyngnes, and K. Vogel, *Opt. Express* **15**, 1474 (2007).
- [108] G. K. L. Wong, S. G. Murdoch, R. Leonhardt, J. D. Harvey, and V. Marie, *Opt. Express* **15**, 2947 (2007).
- [109] Y. Q. Xu, S. G. Murdoch, R. Leonhardt, and J. D. Harvey, *Opt. Lett.* **33**, 1351 (2008).
- [110] J. E. Sharping, *J. Lightwave Technol.* **26**, 2184 (2008).
- [111] Y. Zhou, K. K. Y. Cheung, S. Yang, P. C. Chui, and K. K. Y. Wong, *Opt. Lett.* **34**, 989 (2009); *IEEE Photon. Technol. Lett.* **22**, 1756 (2010).
- [112] Y. Q. Xu, S. G. Murdoch, R. Leonhardt, and J. D. Harvey, *J. Opt. Soc. Am. B* **26**, 1351 (2009).
- [113] C. Gu, H. Wei, S. Chen, W. Tong, and J. E. Sharping, *Opt. Lett.* **35**, 3516 (2010).
- [114] Y. Q. Xu, K. F. Mak, and S. G. Murdoch, *Opt. Lett.* **36**, 1966 (2011).
- [115] A. Kudlinski, A. Mussot, R. Habert, and T. Sylvestre, *IEEE J. Quantum Electron.* **47**, 1514 (2011).
- [116] Y. Fujii, B. S. Kawasaki, K. O. Hill, and D. C. Johnson, *Opt. Lett.* **5**, 48 (1980).
- [117] Y. Sasaki and Y. Ohmori, *Appl. Phys. Lett.* **39**, 466 (1981); *J. Opt. Commun.* **4**, 83 (1983).
- [118] Y. Ohmori and Y. Sasaki, *IEEE J. Quantum Electron.* **18**, 758 (1982).
- [119] R. W. Terhune and D. A. Weinberger, *J. Opt. Soc. Am. B* **4**, 661 (1987).
- [120] U. Österberg and W. Margulis, *Opt. Lett.* **11**, 516 (1986); *Opt. Lett.* **12**, 57 (1987).
- [121] M. C. Farries, P. S. J. Russel, M. E. Fermann, and D. N. Payne, *Electron. Lett.* **23**, 322 (1987).
- [122] R. H. Stolen and H. W. K. Tom, *Opt. Lett.* **12**, 585 (1987).
- [123] J. M. Gabriagues and H. Février, *Opt. Lett.* **12**, 720 (1987).
- [124] N. B. Baranova and B. Y. Zeldovitch, *JETP Lett.* **45**, 12 (1987).
- [125] B. Valk, E. M. Kim, and M. M. Salour, *Appl. Phys. Lett.* **51**, 722 (1987).

- [126] A. Krotkus and W. Margulis, *Appl. Phys. Lett.* **52**, 1942 (1988).
- [127] F. Ouellette, K. O. Hill, and D. C. Johnson, *Opt. Lett.* **13**, 515 (1988).
- [128] H. W. K. Tom, R. H. Stolen, G. D. Aumiller, and W. Pleibel, *Opt. Lett.* **13**, 512 (1988).
- [129] M.-V. Bergot, M. C. Farries, M. E. Fermann, L. Li, L. J. Poyntz-Wright, P. St. J. Russell, and A. Smithson, *Opt. Lett.* **13**, 592 (1988).
- [130] T. E. Tsai, M. A. Saifi, E. J. Friebel, D. L. Griscom, and U. Österberg, *Opt. Lett.* **14**, 1023 (1989).
- [131] E. V. Anoikin, E. M. Dianov, P. G. Kazansky, and D. Yu. Stepanov, *Opt. Lett.* **15**, 834 (1990).
- [132] Y. E. Kapitzky and B. Ya. Zeldovich, *Opt. Commun.* **78**, 227 (1990).
- [133] N. M. Lawandy, *Opt. Commun.* **74**, 180 (1989); *Phys. Rev. Lett.* **65**, 1745 (1990).
- [134] E. M. Dianov, P. G. Kazansky, and D. Y. Stepanov, *Sov. Lightwave Commun.* **1**, 247 (1991); *Proc. SPIE* **1516**, 81 (1991).
- [135] D. Z. Anderson, V. Mizrahi, and J. E. Sipe, *Opt. Lett.* **16**, 796 (1991).
- [136] D. M. Krol and J. R. Simpson, *Opt. Lett.* **16**, 1650 (1991).
- [137] V. Dominic and J. Feinberg, *Opt. Lett.* **17**, 1761 (1992); *Opt. Lett.* **18**, 784 (1993).
- [138] R. I. MacDonald and N. M. Lawandy, *Opt. Lett.* **18**, 595 (1993).
- [139] P. G. Kazansky, A. Kamal, and P. St. J. Russel, *Opt. Lett.* **18**, 693 (1993); *Opt. Lett.* **18**, 1141 (1993); *Opt. Lett.* **19**, 701 (1994).
- [140] J. A. Armstrong, N. Bloembergen, J. Ducuing, and P. S. Pershan, *Phys. Rev.* **127**, 1918 (1962).
- [141] R. Kashyap, *J. Opt. Soc. Am. B* **6**, 313 (1989); *Appl. Phys. Lett.* **58**, 1233 (1991).
- [142] L. E. Myers and W. R. Bosenberg, *IEEE J. Quantum Electron.* **33**, 1663 (1997).
- [143] R. A. Myers, N. Mukherjee, and S. R. J. Brueck, *Opt. Lett.* **16**, 1732 (1991).
- [144] A. Okada, K. Ishii, K. Mito, and K. Sasaki, *Appl. Phys. Lett.* **60**, 2853 (1992).
- [145] N. Mukherjee, R. A. Myers, and S. R. J. Brueck, *J. Opt. Soc. Am. B* **11**, 665 (1994).
- [146] P. G. Kazansky and P. St. J. Russell, *Opt. Commun.* **110**, 611 (1994).
- [147] A. L. Calvez, E. Freysz, and A. Ducasse, *Opt. Lett.* **22**, 1547 (1997).
- [148] P. G. Kazansky, P. St. J. Russell, and H. Takabe, *J. Lightwave Technol.* **15**, 1484 (1997).
- [149] V. Pruneri, F. Samoggia, G. Bonfrate, P. G. Kazansky, and G. M. Yang, *Appl. Phys. Lett.* **74**, 2423 (1999).
- [150] M. Janos, W. Xu, D. Wong, H. Inglis, and S. Fleming, *J. Lightwave Technol.* **17**, 1039 (1999).
- [151] C. Corbari, P. G. Kazansky, S. A. Slattery, and D. N. Nikogosyan, *Appl. Phys. Lett.* **86**, 071106 (2005).
- [152] E. Franchina, C. Corbari, P. G. Kazansky, N. Chiodini, A. Lauria, and A. Paleari, *Solid State Commun.* **136**, 300 (2005).
- [153] E. Y. Zhu, L. Qian, L. G. Heit, et al., *Opt. Lett.* **35**, 1530 (2010).
- [154] V. Pruneri, G. Bonfrate, P. G. Kazansky, et al., *Opt. Lett.* **24**, 208 (1999).
- [155] D. Faccio, A. Busacca, W. Belardi, et al., *Electron. Lett.* **37**, 107 (2001).
- [156] T. M. Monro, V. Pruneri, N. G. R. Broderick, D. Faccio, P. G. Kazansky, and D. J. Richardson, *IEEE Photon. Technol. Lett.* **13**, 981 (2001).
- [157] A. Canagasabey, C. Corbari, Z. Zhang, P. G. Kazansky, and M. Ibsen, *Opt. Lett.* **32**, 1863 (2007).
- [158] A. Canagasabey, C. Corbari, A. V. Gladyshev, et al., *Opt. Lett.* **34**, 2483 (2009).
- [159] A. Canagasabey, M. Ibsen, K. Gallo, et al., *Opt. Lett.* **35**, 724 (2010).
- [160] E. Y. Zhu, L. Qian, L. G. Heit, et al., *J. Opt. Soc. Am. B* **27**, 2410 (2010).
- [161] J. K. Ranka, R. S. Windeler, and A. J. Stentz, *Opt. Lett.* **25**, 796 (2000).

- [162] L. Ji, P. Lu, W. Chen, et al., *J. Opt. Soc. Am. B* **25**, 513 (2008).
- [163] K. Suizu and K. Kawase, *Opt. Lett.* **32**, 2990 (2007).
- [164] V. Tombelaine, C. Lesvigne, P. Leproux, L. Grossard, V. Couderc, J.-L. Auguste, and J.-M. Blondy, *Opt. Express* **13**, 7399 (2005).
- [165] S. Richard, *J. Opt. Soc. Am. B* **27**, 1504 (2010).
- [166] V. Couderc, A. Tonello, C. Buy-Lesvigne, P. Leproux, and L. Grossard, *Opt. Lett.* **35**, 145 (2010).
- [167] V. Grubsky and J. Feinberg, *Opt. Commun.* **274**, 447 (2007).
- [168] G. Brambilla, F. Xu, , P. Horak, et al., *Adv. Opt. Photon.* **1**, 107 (2009).
- [169] J. Lægsgaard, *J. Opt. Soc. Am. B* **27**, 1317 (2010).
- [170] J. M. Gabriagues, *Opt. Lett.* **8**, 183 (1983).
- [171] U. Österberg, *Electron. Lett.* **26**, 103 (1990).
- [172] D. L. Nicácio, E. A. Gouveia, N. M. Borges, and A. S. Gouveia-Neto, *Appl. Phys. Lett.* **62**, 2179 (1993).
- [173] J. Thøgersen and J. Mark, *Opt. Commun.* **110**, 435 (1994).
- [174] J. M. Hickmann, E. A. Gouveia, A. S. Gouveia-Neto, D. C. Dini, and S. Celaschi, *Opt. Lett.* **20**, 1692 (1995).
- [175] M. T. de Araujo, M. V. D. Vermelho, J. M. Hickmann, and A. S. Gouveia-Neto, *J. Appl. Phys.* **80**, 4196 (1996).
- [176] I. A. Bufetov, M. V. Grekov, K. M. Golant, E. M. Dianov, and R. R. Khrapko, *Opt. Lett.* **22**, 1394 (1997).
- [177] F. G. Omenetto, A. J. Taylor, M. D. Moores, et al., *Opt. Lett.* **26**, 1158 (2001).
- [178] A. N. Naumov, A. B. Fedotov, A. M. Zheltikov, et al., *J. Opt. Soc. Am. B* **19**, 2183 (2002).
- [179] L. Tartara, I. Cristiani, V. Degiorgioc, F. Carbone, D. Faccio, M. Romagnoli, and W. Belardi, *Opt. Commun.* **215**, 191 (2003).
- [180] F. G. Omenetto, A. Efimov, A. J. Taylor, J. C. Knight, W. J. Wadsworth, and P. St. J. Russell, *Opt. Express* **11**, 61 (2003).
- [181] A. Efimov, A. J. Taylor, F. G. Omenetto, J. C. Knight, W. J. Wadsworth, and P. St. J. Russell, *Opt. Express* **11**, 910 (2003).
- [182] A. Efimov, A. Taylor, F. Omenetto, J. Knight, W. Wadsworth, and P. Russell, *Opt. Express* **11**, 2567 (2003).
- [183] A. M. Zheltikov, *J. Opt. Soc. Am. B* **22**, 2263 (2005); *Phys. Rev. A* **72**, 043812 (2005).
- [184] A. A. Ivanov, D. Lorenc, I. Bugar, et al., *Phys. Rev. E* **73**, 016610 (2006).
- [185] E. E. Serebryannikov, A. B. Fedotov, and A. M. Zheltikov, *J. Opt. Soc. Am. B* **23**, 1975 (2006).
- [186] B. Kibler, R. Fischer, G. Genty, D. N. Neshev, and J. M. Dudley, *Appl. Phys. B* **91**, 349 (2007).
- [187] A. Bétourné, Y. Quiquempois, G. Bouwmans, and M. Douay, *Opt. Express* **16**, 14255 (2008).
- [188] G. Qin, M. Liao, C. Chaudhari, X. Yan, C. Kito, T. Suzuki, and Y. Ohishi, *Opt. Lett.* **35**, 58 (2010).
- [189] K. Tarnowski, B. Kibler, C. Finot, and W. Urbanczyk, *IEEE J. Quantum Electron.* **47**, 622 (2011).
- [190] K. Tarnowski, B. Kibler, and W. Urbanczyk, *J. Opt. Soc. Am. B* **28**, 2075 (2011).

# Supercontinuum Generation

# 13

As we saw in Chapter 12, when optical pulses propagate through a highly nonlinear fiber, their temporal as well as spectral evolution is affected not only by a multitude of nonlinear effects but also by the dispersive properties of this fiber. All nonlinear processes are capable of generating new frequencies within the pulse spectrum. It turns out that, for sufficiently intense pulses, the pulse spectrum becomes so broad that it may extend over a frequency range exceeding 100 THz. Such extreme spectral broadening is referred to as *supercontinuum generation*, a phenomenon first observed around 1970 in solid and gaseous nonlinear media [1–3].

In the context of optical fibers, a supercontinuum was first observed in 1976 using 10-ns pulses from a dye laser [4]. Although this topic attracted some attention during the decades of 1980s and 1990s, it was only after 2000, with the emergence of microstructured and photonic crystal fibers (PCFs), that the use of optical fibers for supercontinuum generation became common; several reviews of the resulting progress have appeared in recent years [5–7]. Since physical mechanisms responsible for creating a supercontinuum depend on the pulse width, we discuss in the first two sections the cases of picosecond and femtosecond pulses separately. Section 13.3 focuses on the physical mechanisms responsible for supercontinuum generation when the femtosecond input pulse is intense enough to excite a relatively high-order soliton. Section 13.4 is devoted to the situation of continuous-wave (CW) pumping. The focus of Section 13.5 is on the polarization effects, and coherence properties of a supercontinuum are discussed in Section 13.6. In the last section we discuss the optical analog of a rogue wave and its relation to a supercontinuum.

## 13.1 PUMPING WITH PICOSECOND PULSES

Supercontinuum generation in optical fibers was first observed in 1976 by launching Q-switched pulses (width  $\sim 10$  ns) from a dye laser into a 20-m-long fiber [4]. The output spectrum spread as much as over 180 nm when the peak power of input pulses exceeded 1 kW. In a 1987 experiment, 25-ps pulses were launched into a 15-m-long fiber supporting four modes at the input wavelength of 532 nm [8]. As

seen in Figure 10.5, the output spectrum extended over 50 nm because of the combined effects of SPM, XPM, SRS, and FWM. Similar features are expected when single-mode fibers are used [9]. Indeed, a 1-km-long single-mode fiber was used in a 1987 experiment [10] in which 830-fs input pulses with 530-W peak power produced a >200-nm-wide spectrum at the output end of the fiber (see Figure 12.2). Similar results were obtained later with longer pulses [11,12].

Starting in 1993, supercontinuum generation in single-mode fibers was used as a practical tool for generating pulse trains at multiple wavelengths simultaneously by launching a single picosecond pulse train at a wavelength near  $1.55\text{ }\mu\text{m}$  [13–25]. Such a device acts as a useful source for WDM systems. In a 1994 experiment [14], 6-ps pulses with a peak power of 3.8 W at a 6.3-GHz repetition rate (obtained by amplifying the output of a gain-switched semiconductor laser operating at 1553 nm) were propagated in the anomalous-dispersion region of a 4.9-km-long fiber ( $|\beta_2| < 0.1\text{ ps}^2/\text{km}$ ). The supercontinuum generated was wide enough (>40 nm) that it could be used to produce 40 WDM channels by filtering the fiber output with an optical filter exhibiting periodic transmission peaks. The resulting 6.3-GHz pulse trains in different channels consisted of nearly transform-limited pulses whose widths varied in the range of 5–12 ps. By 1995, this technique produced a 200-nm-wide supercontinuum, resulting in a 200-channel WDM source [15].

The same technique was used to produce even shorter pulses by enlarging the bandwidth of each transmission peak of the optical filter. In fact, pulse widths could be tuned in the range of 0.37–11.3 ps when an array-waveguide grating filter with a variable bandwidth was used [16]. A supercontinuum source was used in 1997 to demonstrate data transmission at a bit rate of 1.4 Tb/s using seven WDM channels with 600-GHz spacing [17]. In this experiment, time-division multiplexing was used to operate each WDM channel at 200 Gb/s. Individual 10-Gb/s channels were demultiplexed from the 200-Gb/s bit stream through FWM inside a separate fiber designed for this purpose.

### 13.1.1 Nonlinear Mechanisms

One should ask what nonlinear mechanisms are responsible for broadening the spectrum of a picosecond pulse. As was seen in Section 4.1.3, SPM can produce considerable spectral broadening at the fiber output. The spectral broadening factor in Eq. (4.1.12) is given approximately by the maximum SPM-induced phase shift,  $\phi_{\max} = \gamma P_0 L_{\text{eff}}$ , where  $P_0$  is the peak power of the pulse and  $L_{\text{eff}}$  is the effective fiber length. For typical values of the experimental parameters used, this spectral broadening factor is  $\sim 10$ . Since the input spectral width is  $\sim 1\text{ nm}$  for picosecond pulses, SPM alone cannot produce a supercontinuum extending over 100 nm or more.

Another nonlinear mechanism that can generate new wavelengths is SRS. If the input peak power  $P_0$  is large enough, SRS creates a Stokes band on the long-wavelength side, shifted by about 13 THz from the center of the pulse spectrum. Even if the peak power is not large enough to reach the Raman threshold, SRS can amplify the pulse spectrum on the long-wavelength side as soon as SPM broadens it by 5 nm

or more. Clearly, SRS would affect any supercontinuum by enhancing it selectively on the long-wavelength side, and thus making it asymmetric. However, SRS cannot generate any frequency components on the short-wavelength side.

FWM is the nonlinear process that can create sidebands on both sides of the pulse spectrum, provided a phase-matching condition is satisfied, and it is often behind a supercontinuum generated using optical fibers. FWM is also the reason why dispersive properties of the fiber play a critical role in the formation of a supercontinuum. Indeed, because of a large spectral bandwidth associated with any supercontinuum, the GVD parameter  $\beta_2$  cannot be treated as a constant over the entire bandwidth, and its wavelength dependence should be included through higher-order dispersion parameters in any theoretical modeling. Moreover, the process of supercontinuum generation may be improved if dispersion is allowed to change along the fiber length. As early as 1997, numerical simulations showed that the uniformity or flatness of the supercontinuum improved considerably if  $\beta_2$  increased along the fiber length such that the optical pulse experienced anomalous GVD near the front end of the fiber and normal GVD close to the output end [18]. By 1998, a 280-nm-wide supercontinuum could be generated by using a special kind of fiber in which dispersion not only varied along the fiber length but was also remained relatively flat over a 200-nm bandwidth in the wavelength region near  $1.55\text{ }\mu\text{m}$  [19]. Dispersion flattening turned out to be quite important for supercontinuum generation. In a 1998 experiment, a supercontinuum extending over a 325-nm bandwidth (at 20-dB points) could be generated when 3.8-ps pulses were propagated in the normal-dispersion region of a dispersion-flattened fiber [20].

At first sight, it appears surprising that supercontinuum can be produced in a fiber exhibiting normal GVD ( $\beta_2 > 0$ ) along its entire length. However, one should note, that even though  $\beta_3$  is nearly zero for a dispersion-flattened fiber, the fourth-order dispersion governed by  $\beta_4$  plays an important role. As discussed in Section 10.3.3 and seen in Figure 10.9, FWM can be phase-matched even when  $\beta_2 > 0$  provided  $\beta_4 < 0$ , and it generates signal and idler bands that are shifted by  $>10\text{ THz}$ . It is this FWM process that can produce a wideband supercontinuum in the normal-GVD region of an optical fiber. In fact, a 280-nm-wide (at 10-dB points) nearly flat supercontinuum was generated when chirp-free pulses (width 0.5 ps), obtained from a mode-locked fiber laser, were propagated in a dispersion-flattened fiber with a small positive value of  $\beta_2$ . Even when 2.2-ps-wide pulses from a mode-locked semiconductor laser were used, supercontinuum as broad as 140 nm could be generated, provided pulses were initially compressed to make them nearly chirp-free. Figure 13.1 shows the pulse spectra obtained at several power levels when a 1.7-km-long dispersion-flattened fiber with  $\beta_2 = 0.1\text{ ps}^2/\text{km}$  at 1569 nm was used for supercontinuum generation [21]. Input spectrum is also shown as a dashed curve for comparison. The nearly symmetric nature of the spectra indicates that the Raman gain played a relatively minor role in this experiment. The combination of SPM, XPM, and FWM is responsible for most of spectral broadening seen in Figure 13.1. In a 1999 experiment such a supercontinuum spectrum was used to produce 10-GHz pulse trains at 20 different wavelengths, with nearly the same pulse width in each channel [22].

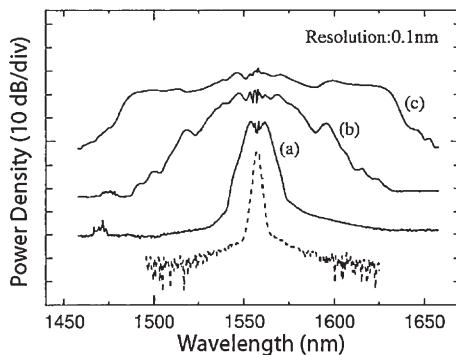


**Figure 13.1** Supercontinuum spectra measured at average power levels of (a) 45 mW, (b) 140 mW, and (c) 210 mW. Dashed curve shows the spectrum of input pulses. (After Ref. [21]; © 1998 IEEE.)

From the standpoint of its application as a multichannel WDM source, the supercontinuum generated in the 1.55- $\mu\text{m}$  spectral region does not have to extend over a very wide range. What is really important is the flatness of the supercontinuum over its bandwidth. A dispersion-flattened fiber (polarization-maintaining kind) was used in a 2001 experiment to produce 150 channels spaced apart by 25 GHz [23]. The total bandwidth of all channels occupied only a 30-nm bandwidth. Of course, the number of channels can be increased to beyond 1000 if the supercontinuum bandwidth were to increase beyond 200 nm. Indeed, it was possible to create a WDM source with 4200 channels spaced apart by only 5 GHz when the supercontinuum bandwidth was close to 200 nm [24]. By 2003, such a WDM source provided 50-GHz-spaced channels over the spectral range extending from 1425 to 1675 nm, thus covering the three main (S, C, and L) telecommunication bands [25].

### 13.1.2 Experimental Progress After 2000

Until the year 2000, most experiments employed long fibers (length  $\sim 1$  km) for generating a supercontinuum. However, highly nonlinear fibers with lengths  $< 10$  m can produce a reasonably wide supercontinuum provided the peak power of the input pulses is increased suitably. In a 2000 experiment [26], a 140-nm wide supercontinuum was created when 1.3-ps pulses were launched into a 4.5-m-long dispersion-shifted fiber with a nominal value of the nonlinear parameter ( $\gamma = 2.3 \text{ W}^{-1}/\text{km}$ ). The supercontinuum bandwidth increased to 250 nm when a 4-m-long fiber with a larger value of  $\gamma$  ( $9.9 \text{ W}^{-1}/\text{km}$ ) was employed. Figure 13.2 shows the supercontinuum spectra measured at the output of these two fibers. As seen there, the power density is higher on the Stokes (long-wavelength) side because of the contribution of the Raman gain but the spectrum is much flatter on the anti-Stokes side. It is important to realize that the spectral power density is plotted on a log scale (in dBm/nm units). This is commonly done in practice because a supercontinuum appears quite nonuniform on a linear scale.

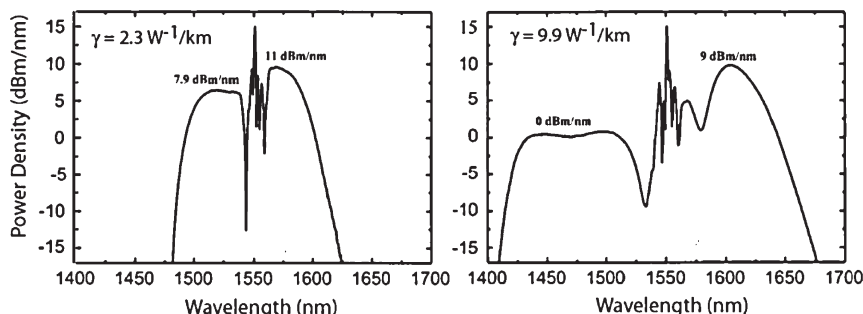


**Figure 13.2** Supercontinuum spectra at the output of two dispersion-shifted fibers having  $\gamma$  of  $2.3 \text{ W}^{-1}/\text{km}$  and  $9.9 \text{ W}^{-1}/\text{km}$  when 1.3-ps input pulses were launched into relatively short fibers.  
(After Ref. [26]; © 2000 IEEE.)

In most preceding studies, a supercontinuum was initiated by launching picosecond pulses at a wavelength close to  $1.5 \mu\text{m}$  to take advantage of the relatively low dispersion of dispersion-shifted fibers. The resulting spectrum at the fiber output covered a wavelength range extending at most from 1300 to 1700 nm, and thus it lay entirely in the infrared region. With the advent of microstructured fibers exhibiting low dispersion close to 700 nm, it became possible to generate a supercontinuum extending over the entire visible area and even extending into the near-infrared region. A systematic study of the process of supercontinuum generation with picosecond pulses was carried out using a PCF whose ZDWL was close to 675 nm [27]. A mode-locked Krypton-ion laser operating at 647.1 nm was used as a source of 60-ps pulses.

Figure 13.3 shows the measured spectra at the output of a 3-m-long fiber at four peak power levels ranging from 100 to 400 W [27]. The nonlinear phase shift  $\gamma P_0 L$  is close

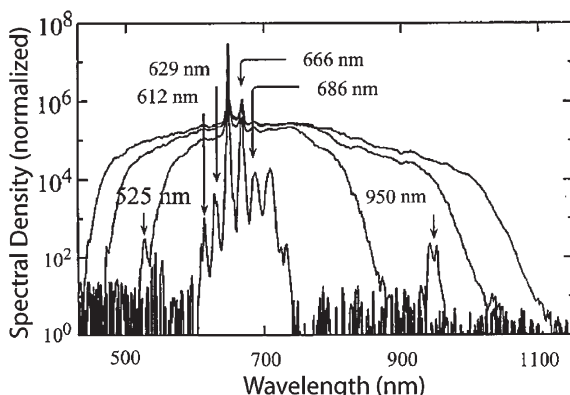


**Figure 13.3** Supercontinuum spectra at the output of a 3-m-long photonic crystal fiber, generated using 60-ps input pulses with peak powers of 100 (the innermost curve), 230, 330, and 400 W. (After Ref. [27]; © 2002 OSA.)

to 180 for  $P_0 = 100$  W and  $L = 3$  m, as the fiber employed had  $\gamma \approx 150$  W<sup>-1</sup>/km. Even at the 100-W level (the innermost curve), SRS affects the SPM-broadened pulse spectrum by producing two Stokes bands located at 666 and 686 nm (through cascaded SRS). The anti-Stokes bands are also created near 612 and 629 nm through a process known as coherent anti-Stokes Raman scattering. The spectrum is relatively narrow at the 100-W level because the pulse is propagating in the normal-dispersion region of the fiber [ $D = -20$  ps/(nm-km)]. At a power level of 230 W, two FWM-induced side bands appear near 525 and 950 nm. As they were found to be orthogonally polarized, phase matching for them appears to be provided by the fiber birefringence.

The important question is what mechanism produces a nearly symmetric broad supercontinuum in Figure 13.3 at power levels above 200 W. The answer turned out to be a combination of SPM, SRS, and FWM. First, SPM broadens the pulse spectrum and SRS extends it on the red side through cascaded SRS. Then, multiple Raman bands act as a pump and generate the Stokes and anti-Stokes bands in a symmetric fashion. One should also note that some Stokes components fall in the anomalous-GVD regime of the fiber and thus they may form solitons. At high pump powers, their peak power becomes large enough that new sidebands are generated through modulation instability. The location of FWM-induced sidebands depends on the pump power such that they are shifted further from the pump as its power increases. Multiple spectral bands also interact with each other through XPM and SRS to produce a nearly flat supercontinuum extending over 500 nm for  $P_0 = 400$  W. Numerical simulations based on the generalized NLS equation also support this scenario [27].

In recent years, picosecond pulses from a Nd:YAG microchip laser or from a Yb-doped fiber laser have been used to produce supercontinuum sources capable of providing high-brightness radiation over an ultrabroad spectral range [28–32]. In a 2005 experiment, 15-ps pulses with peak powers of up to 50 kW (obtained from a fiber laser) were launched into a PCF having its ZDWL near 1040 nm [28]. The resulting supercontinuum extended from 400 to >1700 nm with a spectral density of more than 1 mW/nm. In a 2006 experiment, the PCF was tapered such that its ZDWL decreased continuously along its length [30]. Figure 13.4a shows the

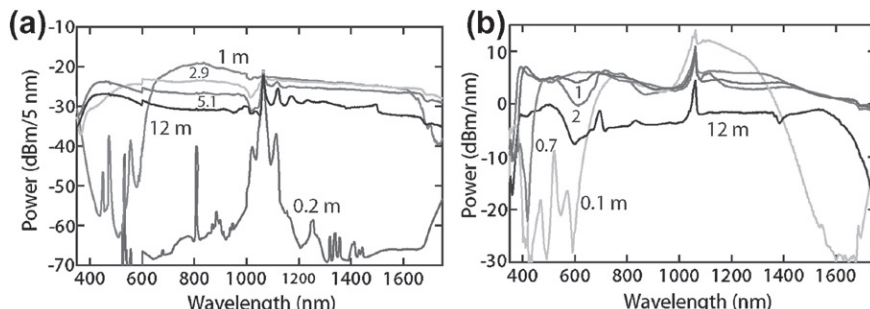


**Figure 13.4** Measured spectra for several PCF lengths when pumped with (a) 600-ps and (b) 4-ps pulses. (After Ref. [30]; © 2006 OSA.)

measured spectra for several taper lengths when the PCF was pumped with 600-ps pulses from a Nd:YAG microchip laser with peak powers of about 15 kW. Figure 13.4b shows similar spectra when 4-ps pulses from a Yb-doped fiber laser with about 50 kW peak power were sent through several tapers of different lengths. In both cases a high-brightness supercontinuum is obtained for PCF lengths of 1 m or more. A 2-m-long PCF was used in a 2010 experiment to obtain an ultrawide supercontinuum (expanding from 0.4 to 2.3  $\mu\text{m}$ ) with a 39 W output power and spectral density of more than 30 mW/nm [32].

## 13.2 PUMPING WITH FEMTOSECOND PULSES

The use of femtosecond pulses became practical with the advent of narrow-core microstructured fibers whose ZDWL lies close to 800 nm, the wavelength region around which tunable Ti:sapphire lasers operate. Starting in 2000, femtosecond pulses from these and other mode-locked lasers were used for supercontinuum generation, and their use has become relatively common in recent years [33–54].

### 13.2.1 Microstructured Silica Fibers

In an early 2000 experiment, 100-fs pulses at 770 nm were launched into a 75-cm-long section of a microstructured fiber exhibiting anomalous dispersion near this wavelength [33]. Figure 13.5 shows the spectrum observed at the fiber output when the peak power of input pulses was about 7 kW. Even for such a short fiber, not only the supercontinuum was extremely broad, extending from 400 to 1600 nm, it was also relatively flat (on a logarithmic power scale) over the entire bandwidth.

Similar features were observed in another 2000 experiment in which a 9-cm-long tapered fiber with 2- $\mu\text{m}$  core diameter was employed [34]. Figure 13.6 shows the output spectra of 100-fs pulses observed at average power levels ranging from

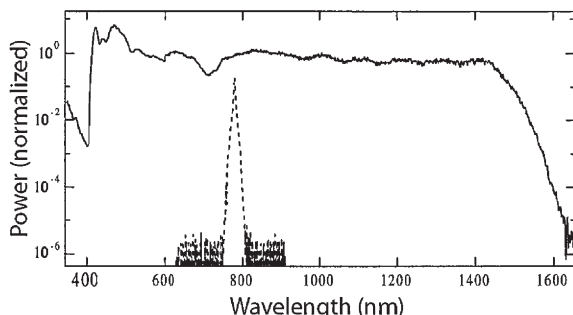


**Figure 13.5** Supercontinuum generated in a 75-cm-long microstructured fiber when 100-fs pulses with 0.8 nJ energy are launched close to the ZDWL near 767 nm. The dashed curve shows for comparison the spectrum of input pulses. (After Ref. [33]; © 2000 OSA.)

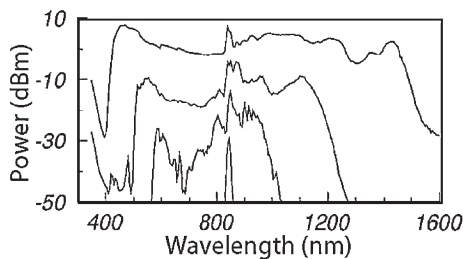


**Figure 13.6** Optical spectra at the output of a 9-cm-long tapered fiber with a 2- $\mu\text{m}$  waist. The average power was 380, 210, and 60 mW (from top to bottom) for the three curves. The input spectrum is also shown for comparison. (After Ref. [34] © 2000 OSA.)

60 to 380 mW. It is important to note that the optical power in Figures 13.1 to 13.6 is plotted on a decibel scale; the spectra would appear much more nonuniform on a linear scale. How should one characterize the spectral width of such a supercontinuum because the concept of a FWHM cannot be applied? A common approach is to employ the 20-dB spectral width, defined as the frequency or wavelength range over which the power level exceeds 1% of the peak value. The 20-dB spectral width exceeds 1000 nm in Figure 13.5, and the supercontinuum extends over two octaves.

It is evident from the superbroad and nearly symmetric nature of the supercontinuum spectra in Figures 13.5 and 13.6 that a different physical mechanism is at play in the case of femtosecond pulses. At high peak power levels and anomalous dispersion used in the experiments, input pulses correspond to a relatively high-order soliton. The order of a soliton is governed by the parameter  $N$ , defined in Eq. (12.1.1) as

$$N^2 = \frac{L_D}{L_{NL}} = \frac{\gamma P_0 T_0^2}{|\beta_2|}, \quad (13.2.1)$$

where  $L_D = T_0^2/|\beta_2|$  is the dispersion length and  $L_{NL} = 1/(\gamma P_0)$  is the nonlinear length. As discussed in Sections 12.1 and 12.2, high-order solitons are perturbed considerably by third-order dispersion and intrapulse Raman scattering and fission into multiple, much narrower, fundamental solitons. It turns out that if  $N$  is relatively large (more than 10), the phenomenon of soliton fission can produce a supercontinuum [35] similar to that seen in Figures 13.5 and 13.6. We discuss such details in the following section and focus here on the experimental results.

The 2000 observation of supercontinua generated using short PCFs led to an explosion of research activity during the years of 2002 and 2003 in this nascent field [36–49]. The choice of the pump wavelength relative to the ZDWL of the fiber was found to be a critical factor for supercontinuum generation [42]. When the input wavelength fell in the normal-GVD region of the fiber, spectral broadening was reduced considerably because higher-order solitons could not form in this situation. Input wavelengths longer than 1000 nm were used in several experiments. A Yb-doped fiber laser producing parabolic-shape pulses was used in one 2002 experiment [43]. In

another 2002 experiment [44], femtosecond pulses at 1260 nm with 750 pJ of energy were launched in the proximity of the second ZDWL of a tapered fiber. The resulting supercontinuum extended from 1000 to 1700 nm.

The initial width of input pulses also plays an important role during supercontinuum formation. Pulses shorter than 20 fs were launched in a 2002 experiment inside cobweb-type PCFs with core diameters ranging from 1 to 4  $\mu\text{m}$  [45]. Since the PCF core was not perfectly circular, the fiber exhibited some birefringence. The spectral widths of observed supercontinua varied considerably with the polarization angle of incident light with respect to the slow axis of the fiber. The output spectra were also found to depend on the extent of frequency chirp on input pulses. The input phase for a linearly chirped pulse varies with time as  $\phi(t) = \phi_0 + ct^2$ . Figure 13.7 shows the output spectra of 18-fs pulses observed at the end of a 4.1-cm-long fiber for several values of  $c$ . The supercontinuum is the widest for unchirped pulses ( $c = 0$ ) with a distinct peak near 500 nm. In another experiment, 200-fs pulses were launched into a 6-m-long PCF (with its ZDWL at 806 nm) at a wavelength of 850 nm [46]. The observed spectra exhibited multiple distinct peaks on the long-wavelength side that corresponded to Raman solitons formed after the fission of a high-order soliton. Pulses shorter than 10 fs pulses were used in a 2003 experiment [47].

Most of these experiments made use of a bulky Ti:sapphire laser as a source of femtosecond pulses. An all-fiber version was realized in 2003 by employing 200-fs pulses from a mode-locked erbium fiber laser [48]. This experiment also used a relatively long silica fiber (up to 600 m length) with a  $\gamma$  of only  $10 \text{ W}^{-1}/\text{km}$ . The observed

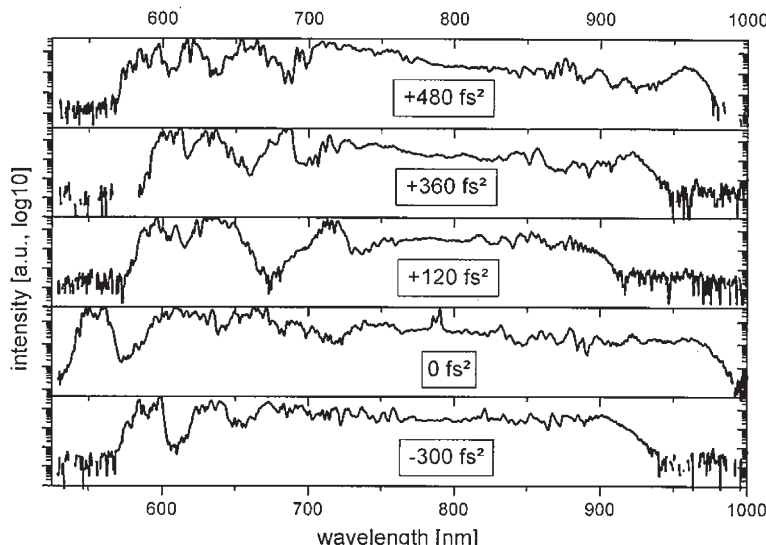


**Figure 13.7** Observed spectra for several input chirp levels at the output of a 4.1-cm-long PCF with a  $2.5\text{-}\mu\text{m}$  core. The average input power was 400 mW. (After Ref. [45] © 2002 OSA.)

supercontinuum was octave spanning as it extended from 1100 to 2200 nm. A much flatter supercontinuum was realized in 2004 by employing a hybrid fiber made of three sections with different dispersive and nonlinear properties [50]. The first section (a 17-cm-long polarization-maintaining fiber) was followed with a 4.5-cm-long second section of dispersion-shifted fiber that was sliced to a 1-m-long third section of a fiber exhibiting normal dispersion at the input wavelength. In this experiment 100-fs pulses at 1560 nm (from a mode-locked erbium fiber laser) were launched. Figure 13.8 shows the output spectra at the end of each fiber section together with the input spectrum. The output supercontinuum extends from 1200 to 2100 nm. A single 5-m-long section of a highly nonlinear, polarization-maintaining fiber was used in a 2005 experiment to produce a supercontinuum extending from 1000 to 2500 nm [52].

Recent work has focused on different aspects of supercontinuum generation. Coherence properties of supercontinuum [38] are important for practical applications and are discussed in a separate section. Extension of the supercontinuum into the blue region of the visible spectrum is also important, and several techniques have been proposed for this purpose. Fibers with nanometer-size cores have also been employed [53]. In a 2010 experiment, a 5-cm-long tapered PCF, having a core diameter near 600 nm and exhibiting two ZDWLs at 509 and 640 nm, was employed for extending the supercontinuum into the blue and ultraviolet regions [54]. Figure 13.9 shows the output spectra observed as the peak power of input pulses (width < 50 fs) was increased from 0.1 to 4 kW. Input wavelength of 640 nm is close to the second ZDWL of the fiber. The soliton order  $N$  is close to 50 at a peak power of 0.2 kW and exceeds 200 at peak powers > 3 kW. The observed supercontinuum at such high peak powers covers the entire visible region and extends further into the infrared and ultraviolet regions.

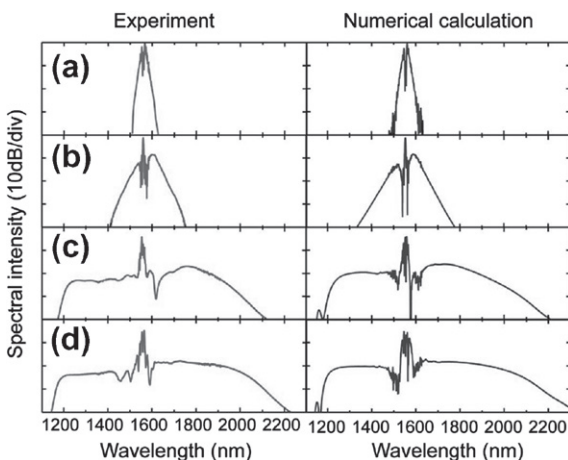


**Figure 13.8** Input spectrum (a) and observed spectra at the end of (b) first, (c) second, and (d) third fiber section. The peak power of 100-fs input pulses was 3.7 kW. Corresponding numerical simulated spectra are also shown. (After Ref. [50] © 2004 OSA.)

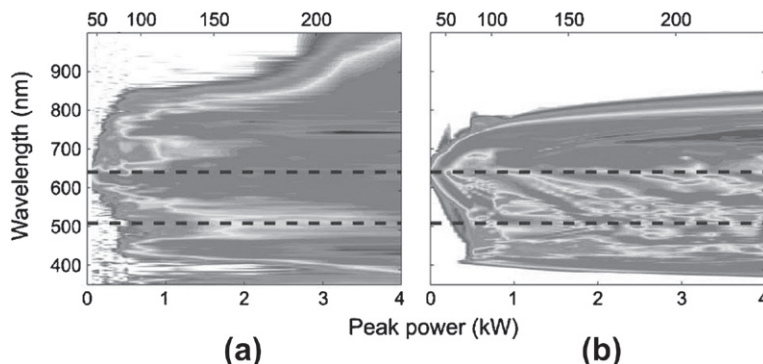


**Figure 13.9** (a) Experimental and (b) numerically simulated spectra as the peak power of input pulses (width <50fs), launched at 640 nm, is increased from 0.1 to 4 kW. Two horizontal dashed lines indicate the ZDWLs of the 5-cm-long tapered PCF. Top scale shows values of the soliton order  $N$ . (After Ref. [54] © 2010 OSA.)

### 13.2.2 Microstructured Nonsilica Fibers

Starting in 2003, nonsilica fibers were used for supercontinuum generation, and it was discovered that they can produce spectra even wider than those generated by silica fibers [55–69]. A 30-cm-long fluoride fiber was pumped in the 2003 experiment with 60-fs pulses at 1560 nm with 210 pJ energy. The resulting supercontinuum extended from 350 to >1750 nm [56]; the measured spectra were limited to under 1750 nm because of a limit set by the optical spectrum analyzer employed. This limit was overcome by 2006 using an infrared HgCdTe detector that could go up to 3000 nm, and it was found that the spectrum extended beyond this limit even for a fiber that was only 0.57 cm long [58].

Figure 13.10 shows a graphical view of the power-dependence of the fission process, similar to that seen in Figure 13.9. In this experiment [58], 110-fs pulses, with a 80-MHz repetition rate at a wavelength of 1550 nm, were launched into a 2.6- $\mu\text{m}$ -core PCF made of lead-silicate glass (Schott SF6), for which  $n_2$  is 10 times larger than that of silica. The experiment was repeated for average launched powers in the range of 1–70 mW. Figure 13.10 shows the recorded spectra over this entire range of input powers as a surface plot. The fiber length is only 0.57 cm in the image (a) and increases to 70 cm for the image (b). In the case of the long fiber, one can clearly see the formation of multiple Raman solitons with different RIFS after the fission process that occurs for  $P_{\text{av}} > 1$  mW; the number of Raman solitons at the output end, of course, depends on the launched power. It is evident from Figure 13.10 that the wavelength of the shortest soliton exceeds 1800 nm for  $P_{\text{av}} > 30$  mW and should reach beyond 3000 nm for  $P_{\text{av}} > 70$  mW. This was indeed observed experimentally using a HgCdTe detector.

The optical spectra in Figure 13.10a were observed for a lead-silicate PCF that was only 0.57 cm long. The fiber length in this case is so much shorter than the dispersion length (about 40 cm) that the fission of a high-order soliton does not occur. A nearly symmetric nature of the optical spectra also indicates that the supercontinuum

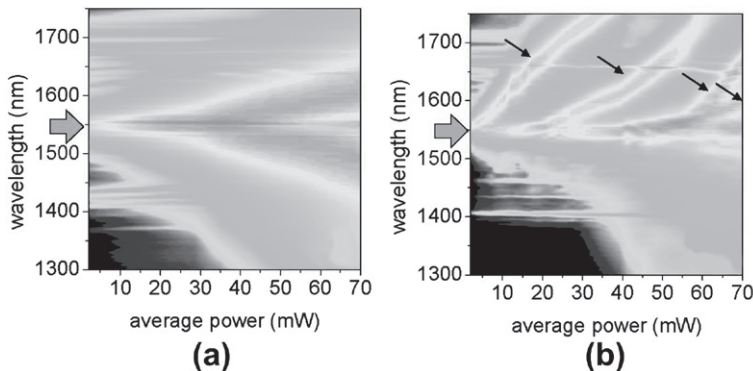


**Figure 13.10 Recorded spectra as a function of average power at the output of a microstructured fiber when 110-fs pulses are propagated over a fiber length of (a) 0.57 and (b) 70 cm. Arrows indicate solitons created after the fission. (After Ref. [58]; © 2006 OSA.)**

extending from 350 to 3000 nm is formed mainly through the SPM process. Although this behavior is not observed for silica fibers, it occurs here because of a much larger value of  $\gamma$  for this non-silica fiber. As we will see later, a supercontinuum created predominantly through SPM is also much more smoother and spectrally coherent compared with the one formed through soliton fission.

It was found in a 2006 experiment that the supercontinuum can be extended to up to 4500 nm by combining a silica fiber (length  $\sim 1$  m) with a few-meters-long fluoride fiber [59]. The upper limit was consistent with the strong absorption exhibited by the fibers at wavelengths beyond 4500 nm. The largest bandwidth was realized in 2009 when a 2-cm-long fluoride fiber was pumped with 180-fs pulses at a wavelength of 1450 nm [68]. Figure 13.11a shows the output spectrum observed at the average power level of 20 mW (peak power about 50 MW). The bandwidth at 10 dB extends from 565 to 5240 nm. The long-wavelength regions for 0.9 and 2-cm-long fibers are compared in part (b). This comparison indicates that virtually the same bandwidth is obtained for the shorter fiber. It is important to realize that soliton fission and related phenomena (intrapulse Raman scattering and emission of dispersive waves) may not be the dominant mechanism behind supercontinuum generation when fiber length is shorter than 1 cm. Because of a much larger value of the nonlinear parameter  $\gamma$ , SPM-induced spectral broadening can itself create an ultrabroad spectrum [58].

Tellurite-glass-based PCFs have also been used for supercontinuum generation. In a 2008 experiment [62], 100-fs pulses with 1.9 nJ energy at a 1550-nm wavelength were transmitted through a 0.8-cm-long PCF. The output spectrum extended from 790 to 4870 nm when measured at the points 20 dB below the peak spectral power. In another 2008 experiment [63], a 9-cm-long microstructured tellurite fiber with a large effective mode area of  $3000 \mu\text{m}^2$  was pumped with 120-fs pulses. Even in this case the observed supercontinuum extended from 900 to 2500 nm. A 6-cm-long hexagonal-core fiber was pumped in a 2009 experiment using 400-fs pulses at 1557 nm [67]. At pulse energies close to 0.6 nJ, the observed supercontinuum extended from visible region to beyond  $2.4 \mu\text{m}$ .

Recently chalcogenide fibers have attracted attention for supercontinuum generation. The Kerr parameter is about 400 times larger for these materials compared with silica. Moreover, the effective mode area can be reduced to below  $0.5 \mu\text{m}^2$  in fibers with core diameters close to  $0.5 \mu\text{m}$ . As a result, the nonlinear parameter  $\gamma$  had a value of  $93.4 \text{ W}^{-1}/\text{m}$  (about 80,000 times larger than that of standard silica fibers) in a 2008 experiment [64]. The 3-cm-long fiber was pumped at 1550 nm using 250-fs pulses. Figure 13.12 shows the output spectra observed for several values of

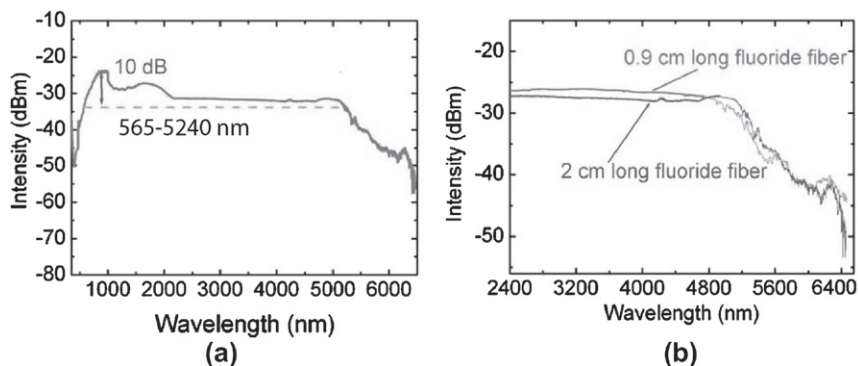


Figure 13.11 (a) Supercontinuum observed at the output end of a 2-cm-long fluoride fiber at 20-mW average power (peak power about 50 MW). Dashed line shows the 10-dB bandwidth. (b) Comparison of the long-wavelength region for 0.9 and 2-cm-long fibers. (After Ref. [68] © 2009 American Institute of Physics.)

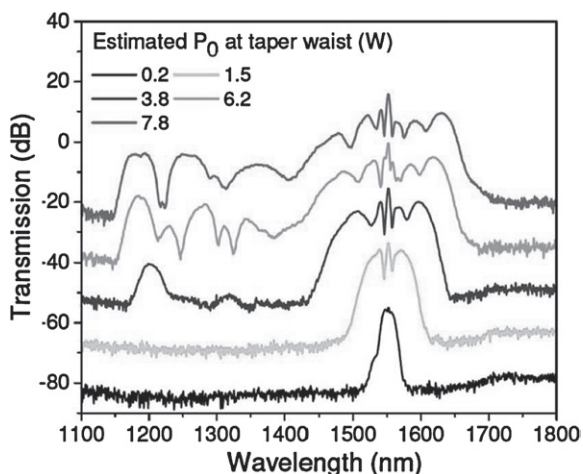


Figure 13.12 Supercontinuum observed at the output of a 3-cm-long chalcogenide fiber for peak powers of 250-fs pulses. The effective mode area of this fiber was only  $0.5 \mu\text{m}^2$  because of a nanoscale core. (After Ref. [64] © 2008 OSA.)

peak powers. Notice that these power levels are much smaller than those used in Figure 13.11 for a fluoride fiber. Nevertheless, the observed supercontinuum extended from 1150 to 1650 nm, a range large enough for practical applications. The shape of observed spectra was consistent with the soliton-fission scenario. In a 2011 experiment, the supercontinuum extended beyond 2000 nm when 250-fs pulses were launched into a 5-cm-long chalcogenide fiber with energies of less than 77 pJ [69].

---

### 13.3 TEMPORAL AND SPECTRAL EVOLUTIONS

In this section we consider in more detail the temporal and spectral evolutions of femtosecond pulses and focus on the physical phenomena that create the supercontinuum at the fiber output. A numerical approach is necessary for this purpose. We discuss first the model based on the generalized NLS equation and then focus on soliton fission, dispersive wave, Raman solitons, and nonlinear interactions among them.

As was seen in Section 5.1, fission of a  $N$ th-order soliton produces  $N$  fundamental solitons whose widths and peak powers follow Eq. (12.1.2). All of these solitons are shorter than the original input pulse, the shortest one being narrower by a factor of  $2N - 1$ . For 100-fs or shorter input pulses propagating with  $N > 5$ , the shortest soliton after fission would have a width below 10 fs and its spectrum would be relatively wide ( $>40$  THz). As we saw in Section 12.2, such short pulses are affected considerably by intrapulse Raman scattering and their spectra shift rapidly toward longer and longer wavelengths with further propagation inside the fiber. For a large value of  $N$ , many new spectral peaks corresponding to multiple solitons of different widths would form on the long-wavelength side of the original pulse spectrum. At the same time ultrashort solitons, created through the fission process and perturbed by third- and higher-order dispersion, would emit nonsolitonic radiation (NSR) in the form of dispersive waves whose wavelengths fall on the short-wavelength side of the input spectrum for  $\beta_3 > 0$ . The only remaining question is why various peaks merge together to form a broadband supercontinuum. As we see later in this section, the nonlinear phenomena of XPM and FWM provide an answer to this question.

#### 13.3.1 Numerical Modeling of Supercontinuum

The supercontinuum generation process can be studied by solving the generalized NLS equation of Section 2.3.2. As it is important to include the dispersive effects and intrapulse Raman scattering as accurately as possible, one should employ Eq. (2.3.36) for modeling supercontinuum generation, after generalizing it further

by adding higher-order dispersion terms. The resulting equation can be written in the form

$$\frac{\partial A}{\partial z} + \frac{1}{2} \left( \alpha + i\alpha_1 \frac{\partial}{\partial t} \right) A - i \sum_{m=2}^M i^m \frac{\beta_m}{m!} \frac{\partial^m A}{\partial t^m} = i \left( \gamma + i\gamma_1 \frac{\partial}{\partial t} \right) \times \left( A(z, t) \int_0^\infty R(t') |A(z, t-t')|^2 dt' \right), \quad (13.3.1)$$

where  $M$  represents the order up to which dispersive effects are included. The  $m = 1$  term has been removed from Eq. (13.3.1) by assuming that  $t$  represents time in a reference frame moving at the group velocity of the input pulse. The  $\alpha_1$  terms should be included because fiber loss may not remain constant over the entire bandwidth of the supercontinuum. Both loss terms can however be neglected for relatively short fibers. The approximation  $\gamma_1 \approx \gamma/\omega_0$  is often employed in practice [see Eq. (2.3.37)] but its use is not always justified [70].

Equation (13.3.1) has proven quite successful in modeling most features of supercontinua observed experimentally by launching ultrashort optical pulses into highly nonlinear fibers [38–42]. The split-step Fourier method discussed in Section 2.4.1 is used often in practice for solving this equation. The choice of  $M$  in the sum appearing in Eq. (13.3.1) is not always obvious. Typically,  $M = 6$  is used for numerical simulations, although values of  $M$  as large as 12 are sometimes employed. In fact, dispersion to all orders can be included numerically if we recall that the dispersive step in the split-step Fourier method is carried out in the spectral domain of the pulse after neglecting all nonlinear terms. In the Fourier domain, the sum in Eq. (13.3.1) can be replaced with

$$\sum_{m=2}^{\infty} \frac{\beta_m}{m!} (\omega - \omega_0)^m \tilde{A} = [\beta(\omega) - \beta(\omega_0) - \beta_1(\omega_0)(\omega - \omega_0)] \tilde{A}, \quad (13.3.2)$$

where  $\tilde{A}(z, \omega)$  is the Fourier transform of  $A(z, t)$  and  $\omega_0$  is the frequency at which the spectrum of the input pulse is centered initially. This approach requires a knowledge of  $\beta(\omega)$  over the whole frequency range of a supercontinuum. As discussed in Section 11.3, in the case of a fiber whose core and cladding have constant refractive indices, one can solve the eigenvalue Eq. (2.2.8) numerically to obtain the propagation constant  $\beta(\omega)$ . This approach is not appropriate for a microstructured fiber designed with air holes within its cladding. As mentioned in Section 11.4, several other numerical techniques can provide  $\beta(\omega)$  for such fibers.

As a relevant example of supercontinuum generation in highly nonlinear fibers, a fiber with a 2.5-μm-diameter silica core, surrounded by air acting as a cladding, was used in one numerical study [38]. The frequency dependence of the propagation constant  $\beta(\omega)$  was found numerically by solving Eq. (2.2.8), dispersion parameters calculated from it through a Taylor-series expansion. The ZDWL for this fiber is near 800 nm. If we assume that 150-fs pulses from a Ti:sapphire laser operating at 850 nm

are used for supercontinuum generation, dispersion parameters at this wavelength are:  $\beta_2 = -12.76 \text{ ps}^2/\text{km}$ ,  $\beta_3 = 8.119 \times 10^{-2} \text{ ps}^3/\text{km}$ ,  $\beta_4 = -1.321 \times 10^{-4} \text{ ps}^4/\text{km}$ ,  $\beta_5 = 3.032 \times 10^{-7} \text{ ps}^5/\text{km}$ ,  $\beta_6 = -4.196 \times 10^{-10} \text{ ps}^6/\text{km}$ , and  $\beta_7 = 2.570 \times 10^{-13} \text{ ps}^7/\text{km}$ . The higher-order terms have a negligible influence on the following results.

The nonlinear effects are included through the terms appearing on the right side of Eq. (13.3.1). The nonlinear parameter  $\gamma$  for the 2.5- $\mu\text{m}$  waist fiber can be estimated from Figure 11.9 and is found to be about  $100 \text{ W}^{-1}/\text{km}$ . The nonlinear response function  $R(t)$  has the form  $R(t) = (1 - f_R)\delta(t) + f_R h_R(t)$  given in Eq. (2.3.38) with  $f_R = 0.18$ . The Raman response function  $h_R(t)$  is sometimes approximated by Eq. (2.3.40). However, the numerical accuracy is improved if the oscillatory trace seen in Figure 2.2 is employed because it takes into account the actual shape of the Raman gain spectrum.

Any implementation of the split-step Fourier method for solving Eq. (13.3.1) requires a careful consideration of the step size  $\Delta z$  along the fiber length and the time resolution  $\Delta t$  used for the temporal window. Because of the use of the FFT algorithm, the size of the spectral window is governed by  $(\Delta t)^{-1}$ . Since this window must be wide enough to capture the entire supercontinuum,  $\Delta t$  should be 3 fs or less if the supercontinuum extends over 300 THz. At the same time, the temporal window should be wide enough that all parts of the pulse remain confined to it over the entire fiber length. Typically, the temporal window should extend over 10 ps even for femtosecond pulses to allow for the Raman-induced changes in the group velocity of the pulse. For this reason, it is often necessary to employ 10,000 points or more in the time and frequency domains for the FFT algorithm. The step size  $\Delta z$  should be a small fraction of the shortest nonlinear length. It can become  $< 10 \mu\text{m}$  under some conditions, thereby requiring  $> 1000$  steps/cm along the fiber length. Clearly, numerical simulations for modeling supercontinuum formation in optical fibers can be time-consuming. However, continuing advances in the computing technology have made it possible to perform such simulations even on a personal computer.

An alternative approach solves Eq. (13.3.1) in the frequency domain, where it reduces to a large set of ordinary differential equations, which can be solved with any finite-difference scheme. This approach allows for an adaptive step size in the  $z$  direction, provides control over numerical accuracy, and can be faster than the split-step Fourier method in some cases. The reader should consult Chapter 3 of Ref. [7] for more details.

Figure 13.13 shows the spectral and temporal evolution of a 150-fs (FWHM) “sech” pulse launched into a 10-cm-long tapered fiber with 10-kW peak power. If we use  $T_0 = 85$  fs and  $P_0 = 10$  kW for the pulse parameters, the dispersion and nonlinear lengths are found to be about 57 cm and 1 mm, respectively, and the soliton order  $N$  is about 24 under such conditions. As seen in Figure 13.13b, the pulse undergoes an initial compression phase, a common feature of any high-order soliton, while its spectrum broadens because of SPM. However, at a distance of 2 cm or so, the soliton undergoes the fission process, mainly because of perturbations caused by the third-order dispersion, and the pulse breaks up into multiple fundamental solitons [35].

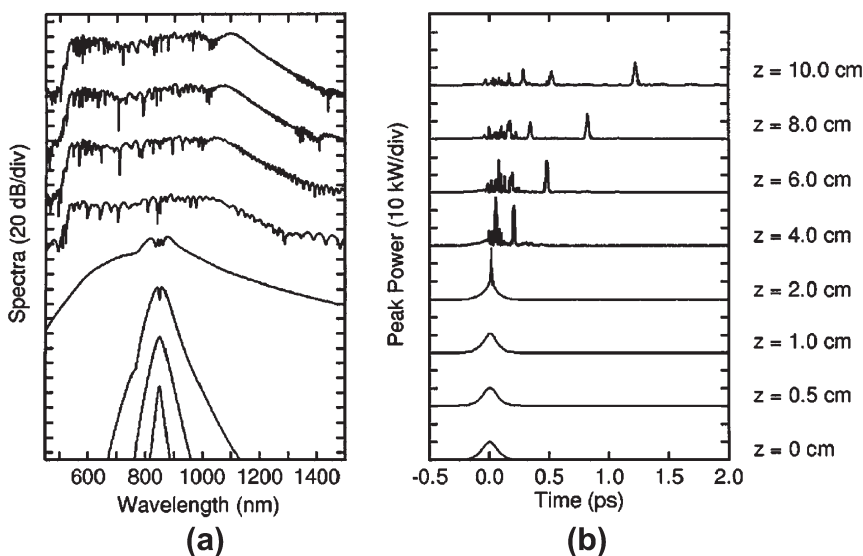


Figure 13.13 (a) Spectral and (b) temporal evolution of a 150-fs pulse launched with 10-kW peak power into a 10-cm-long tapered fiber with 2.5- $\mu\text{m}$  waist. (After Ref. [38]; © 2002 IEEE.)

The spectrum changes qualitatively at a distance of  $z = 4 \text{ cm}$  and acquires a shape that is typical of a supercontinuum.

A clue to this sudden spectral change is provided by the pulse shape at  $z = 4 \text{ cm}$ . It exhibits a narrow spike that has separated from the main pulse. As discussed in Section 12.2, this separation is due to a change in the group velocity of the shortest fundamental soliton, occurring when the spectrum of this soliton shifts toward longer wavelengths (Stokes side) because of intrapulse Raman scattering. As the spectrum of a soliton shifts, its group velocity is reduced (because of GVD), and it separates from the main pulse. Other solitons also experience such a Raman-induced frequency shift (RIFS), but the magnitude is smaller for them because of their larger widths and smaller peak powers. They also eventually separate from the main pulse, as seen in Figure 13.13b at a distance  $z = 10 \text{ cm}$ . Thus, the spectral broadening beyond 900 nm is due to a combination of SPM and RIFS.

In the supercontinuum seen in Figure 13.13, the spectral components are also generated on the short-wavelength (or anti-Stokes) side of the input wavelength. As discussed in Section 12.1, Cherenkov radiation or NSR is responsible for them [71]. Because of third- and higher-order dispersive effects, each Raman soliton loses some of its energy in the form of a dispersive wave. The wavelength of this NSR is governed by the phase-matching condition given in Eq. (12.1.5). For a fiber with  $\beta_3 > 0$ , the phase-matching condition is satisfied for a wavelength that lies below 800 nm.

Since this wavelength is different for different solitons, multiple spectral peaks form in Figure 13.13a in the visible region.

### 13.3.2 Role of Cross-Phase Modulation

Numerical results in Figure 13.13 do not explain physically why various peaks merge together to form a broadband supercontinuum. It turns out that the nonlinear phenomena of XPM and FWM are responsible for this merging. To understand their role, we need to realize that, even though the Raman solitons and dispersive waves have widely separated optical spectra, they may still overlap in the time domain. Any temporal overlapping of a Raman soliton with a dispersive wave results in their mutual interaction through XPM. As we have seen in Section 7.4, such a nonlinear interaction can create new spectral components and broaden the spectrum of dispersive waves in an asymmetric fashion. For this reason, the XPM effects play an important role during supercontinuum formation inside highly nonlinear fibers [75–87].

A simple way to visualize the temporal overlapping of Raman solitons and dispersive waves is to produce a spectrogram through the X-FROG technique discussed in Section 12.2.2. Figure 13.14 shows the temporal and spectral evolutions of a  $N = 6$  soliton over two dispersion lengths together with the spectrogram at  $z = 2L_D$ . A normalized form of Eq. (13.3.1), given in Eq. (12.2.4), was used for these numerical results. Moreover, only the third-order dispersion term was retained so that a single parameter ( $\delta_3 = 0.05$ ) was required. The parabolic dashed curve in part (c) shows changes as a function of frequency in the derivative  $d\beta/d\omega$ , which is inversely related to the group velocity.

Figure 13.14 provides considerable physical insight into the process of supercontinuum generation inside optical fibers. Parts (a) and (b) show clearly how two

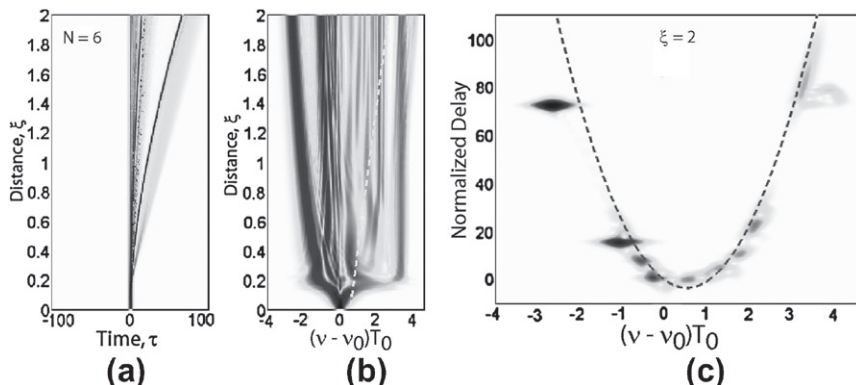


**Figure 13.14** (a) Spectral and (b) temporal evolutions of a pulse launched as a sixth-order soliton over a distance 0 to  $2L_D$ . (c) Corresponding spectrogram at  $z = 2L_D$ . The parabolic dashed curve shows changes in group velocity with frequency.

Raman solitons separate from the main pulse as their spectra shift toward the Stokes side. They also show dispersive waves that spread in time domain but their spectrum lies on the anti-Stokes side. The new feature seen in the spectrogram in part (c) is that the two Raman solitons (dark objects) overlap temporally with two dispersive waves (light objects) and thus interact with them through XPM and FWM. Indeed, one can even see broadening of the spectrum associated with the dispersive wave that overlaps with the shortest Raman soliton, the one whose spectrum shifts the most and is thus delayed the most in the time domain because of a continuing reduction in its speed.

The XPM-induced broadening of spectral peaks within a supercontinuum was clearly observed in a 2002 experiment [42], where the peak power of input pulses was varied over a wide range to change the soliton order associated with the input pulse from  $N < 1$  to  $N > 6$ . Figure 13.15 shows the spectra observed at the output of a 5-m-long microstructured fiber when 100-fs pulses were launched (at 804 nm) and the average launched power was varied from 0.05 to 55 mW. The fiber had its ZDWL at 650 nm such that  $\beta_2 = -57.5 \text{ ps}^2/\text{km}$  at 804 nm, resulting in a dispersion length of 6 cm or so. At power levels of 1 mW or less, the output spectrum exhibits some SPM-induced broadening, but it neither shifts spectrally nor produces any NSR, as the nonlinear effects play a relatively minor role. By the time the average power is  $< 4$  mW, the soliton order  $N$  exceeds 1, and one or more Raman solitons are created through the fission process, and distinct spectral peaks appear on the Stokes side whose number depends on the launched power; three of them are present when  $P_{\text{av}} = 16$  mW. At the same time, each Raman soliton produces an NSR peak in the visible region that corresponds to a different dispersive wave that is phase-matched to that specific soliton. A supercontinuum begins to form for  $P_{\text{av}} > 40$  mW, a power level at which  $N$  exceeds 5 for the input pulse, as various

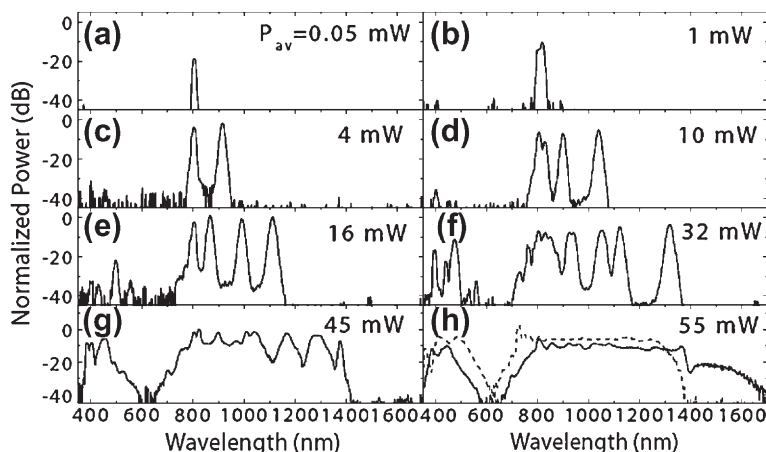


**Figure 13.15** (a) Recorded spectra at the output of a 5-m-long fiber for 8 average power levels of 100-fs input pulses. (After Ref. [42]; © 2002 OSA.)

peaks merge together because of XPM-induced coupling among solitons and dispersive waves. Numerical simulations confirm that NSR peaks in the visible region are not generated if third- and higher-order dispersive effects are not included in the calculation.

The X-FROG technique has also been used in several experiments on supercontinuum generation [72–75]. In one approach, cross-correlation of a spectrally filtered output pulse with a reference pulse (with an adjustable delay) is recorded as a function of filter wavelength through two-photon absorption inside a silicon avalanche photodiode [74]. Mathematically, the intensity cross-correlation is given by

$$S(\tau, \omega_c) = \int_{-\infty}^{\infty} I_f(t, \omega_c) I_{\text{ref}}(t - \tau) dt, \quad (13.3.3)$$

where  $I_{\text{ref}}(t - \tau)$  is the intensity of the reference pulse delayed by  $\tau$ ,  $I_f(t, \omega_c)$  is the intensity of the filtered fiber output,

$$I_f(t, \omega_c) = \left| \int_{-\infty}^{\infty} \tilde{A}(\omega) H_f(\omega - \omega_c) e^{-i\omega t} d\omega \right|^2, \quad (13.3.4)$$

and  $H_f(\omega - \omega_c)$  is the transfer function of the filter centered at the frequency  $\omega_c$ .

Figure 13.16 shows an example of such a spectrogram, created by launching a 100-fs pulse into a 2-m-long dispersion-shifted fiber with 2.5-kW peak power [74]. The fiber parameters at the input wavelength of 1.56 μm were  $\beta_2 = -0.25 \text{ ps}^2/\text{km}$  and  $\gamma = 21 \text{ W}^{-1}/\text{km}$ . The right panel of Figure 13.16 shows the measured spectrum

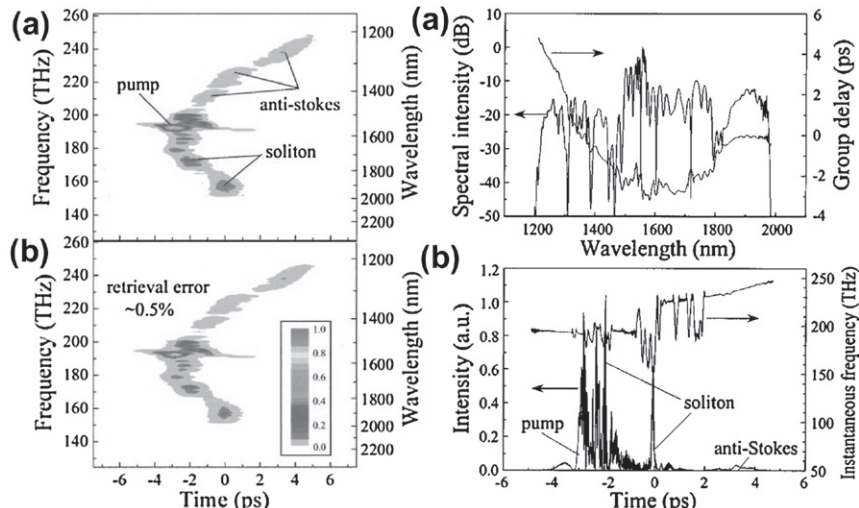


**Figure 13.16** Left: experimental (a) and reconstructed (b) spectrograms at the end of a 2-m-long fiber for 100-fs input pulses with 2.5 kW peak power. Right: (a) measured spectrum and calculated group delay; (b) reconstructed intensity and chirp profiles. (After Ref. [74]; © 2003 OSA.)

and the temporal profile of the output pulse deduced from the X-FROG measurements. The group delay as a function of the wavelength and the chirp across the pulse can also be deduced from the FROG data. As a check on the accuracy of the reconstruction process, a sonogram retrieved from the measured spectral data and the deduced amplitude and phase profiles (using an iterative phase-retrieval algorithm) is also shown for comparison.

Several features are noteworthy in the spectrogram displayed in Figure 13.16. Two solitons with their spectra shifted through RIFS toward the Stokes side are clearly visible. The spectral components on the anti-Stokes side spread much more temporally because dispersive waves associated with them propagate in the normal-GVD regime of the fiber. They represent relatively low-power pulses that are broadened because of GVD. In fact, the nearly parabolic shape of the spectrogram results from a quadratic phase of the form  $\frac{1}{2}\beta_2\omega^2z$  that is added by GVD during propagation inside the fiber. Note also that, in the normal-GVD regime, blue-shifted dispersive waves travel slower compared with the central part of the pulse. As a result, they slow down and begin to overlap with the red-shifted solitons in the time domain. Once this happens, the two interact nonlinearly through XPM and their spectra begin to change. Moreover, the soliton can also trap a dispersive wave, as seen in Figure 13.16. This phenomenon is similar to the soliton trapping discussed in Section 6.5.2 in the context of highly birefringent fibers and is discussed further in the following subsection.

### 13.3.3 XPM-Induced Trapping

The XPM interaction between a Raman soliton and a dispersive wave can also trap that dispersive wave [83–87]. If the dispersive wave travels in the normal-GVD regime, the group-velocity mismatch between this wave and the soliton can be relatively small, depending on their respective wavelengths. If the two overlap temporally, it is possible for a Raman soliton to trap a nearby dispersive wave such that the two move together.

In a 2004 study of the XPM effects on supercontinuum generation, the XPM was found to create another spectral peak whose wavelength was shifted toward the blue side, and the magnitude of shift depended on the input power launched into the fiber [77]. Figure 13.17a shows the observed spectra at the output of a 1.5-m-long microstructured fiber for several values of the average power when 27-fs pulses at 790 nm with a 1-GHz repetition rate were launched into it. This fiber exhibited two ZDWLs at 700 and 1400 nm. The Raman soliton and NSR are visible for  $P_{av} = 53$  mW, and their wavelengths shift in the opposite directions with increasing power. The peak near 1600 nm in the spectrum for  $P_{av} = 118$  mW also represents a dispersive wave. It is created when the Raman soliton approaches the second ZDWL of the fiber, and its spectrum stops shifting because of the RIFS suppression phenomenon discussed in Section 12.2.

Figure 13.17b shows the spectrum for  $P_{av} = 118$  mW on a magnified vertical scale, together with the phase mismatch as a function of wavelength between the

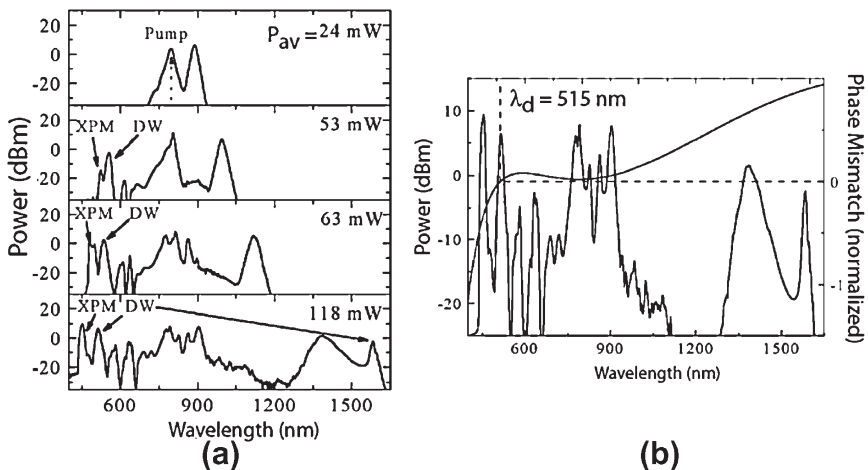


**Figure 13.17** (a) Experimental spectra at several power levels at the output of a 1.5-m-long fiber. (b) Magnified view of the spectrum for  $P_{av} = 118 \text{ mW}$ . Phase mismatch of the dispersive wave is also shown. (After Ref. [77]; © 2004 OSA.)

shortest soliton and its dispersive wave [77]. The phase matching occurs for 515 nm, and the peak located there corresponds to the dispersive wave. The peak on the blue side of this peak, shifted by more than 60 nm due to XPM. Numerical simulations based on the generalized NLS equation reproduce well the observed spectral features qualitatively. They also help in understanding how the second peak is created. The spectrograms at different distances within the fiber reveal that the soliton slows down as its spectrum shifts toward the red and begins to overlap with the dispersive wave; their interaction through XPM creates the blue-shifted peak. However, the two eventually separate from each other because of a mismatch in their group velocities, a feature that indicates that soliton trapping did not occur in this experiment. Note that the second dispersive wave created near 1600 nm travels faster than the soliton. An XPM-induced spectral peak was not generated in this case because the dispersive wave separated rapidly from the soliton.

Since the exact wavelength of the dispersive waves created through NSR depends on the dispersive properties of the fiber employed, the group-velocity mismatch between the soliton and the dispersive wave generated by it depends on the fiber and pulse parameters. Soliton trapping can occur when this mismatch is not too large. It was found in a 2005 numerical study that XPM-coupled soliton pairs, similar to those discussed in Section 7.3, can form under certain conditions in fibers exhibiting two ZDWLs [78]. Figure 13.18 shows the spectrograms for two photonic crystal fibers, with the only difference that the spacing of 1- $\mu\text{m}$ -diameter air holes changes from 1.2 to 1.3  $\mu\text{m}$ .

In the 1.2- $\mu\text{m}$  case shown on left in Figure 13.18, the second ZDWL of the fiber occurs near 1330 nm. When 13-ps pulses with 15-kW peak power are launched into

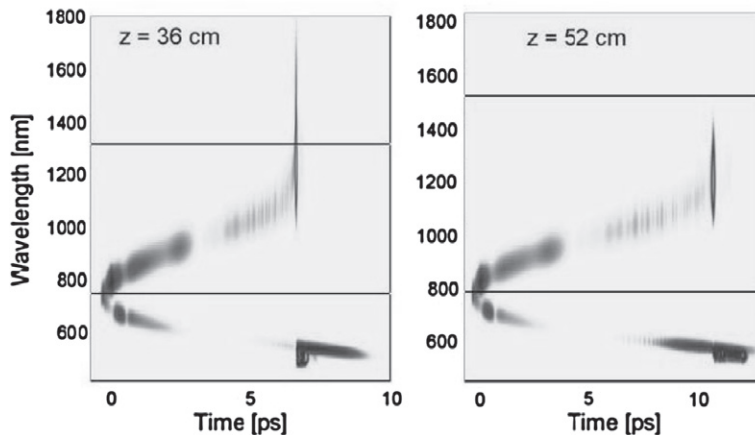


**Figure 13.18** Spectrograms for two PCFs with air-hole spacings of  $1.2 \mu\text{m}$  (left) and  $1.3 \mu\text{m}$  (right) when 13-ps pulses with 15-kW peak power are launched. Two horizontal lines indicate the ZDWLs of each fiber. (After Ref. [78]; © 2005 OSA.)

such a fiber at a wavelength of  $804 \text{ nm}$ , the Raman soliton emits NSR first in the visible region, and then in the infrared region lying beyond  $1330 \text{ nm}$ , as its RIFS is suppressed close to the second ZDWL. The infrared radiation is emitted in large amounts such that its group velocity is close to that of the soliton. As a result, the two form a soliton pair at a distance of  $z = 35 \text{ cm}$  through the XPM-induced coupling between them [78]. This pair moves as one unit for  $z > 35 \text{ cm}$ . The temporal width of the dispersive wave did not change much even at  $z = 60 \text{ cm}$  as this wave was propagating in the anomalous-GVD regime of the fiber. This phenomenon was not observed for the second fiber with a  $1.3\text{-}\mu\text{m}$  hole spacing because its ZDWL lies close to  $1500 \text{ nm}$ .

We can find the condition under which the XPM-induced pairing is possible by noting that the parameter  $\beta_1 \equiv 1/v_g$  for a dispersive wave at the frequency  $\omega_d$  can be written as

$$\beta_1(\omega_d) \approx \beta_1(\omega_s) + \beta_2(\omega_s)\Omega + \frac{1}{2}\beta_3(\omega_s)\Omega^2, \quad (13.3.5)$$

where  $\Omega = \omega_d - \omega_s$  and  $\omega_s$  is the frequency at which soliton spectrum is centered, and we have retained terms only up to third order. Clearly,  $\beta_1(\omega_d) = \beta_1(\omega_s)$  when  $\Omega = -2\beta_2/\beta_3$ . If this condition is satisfied for a fiber, the dispersive wave can be trapped by the soliton, and the two can move together as a pair through the XPM coupling between them.

The XPM effects can also be initiated by launching the main intense pulse into a highly nonlinear fiber together with another pulse at a different wavelength [79–83]. This configuration allows more control, as the second pulse can be delayed or advanced such that the two overlap after some distance inside the fiber. It also

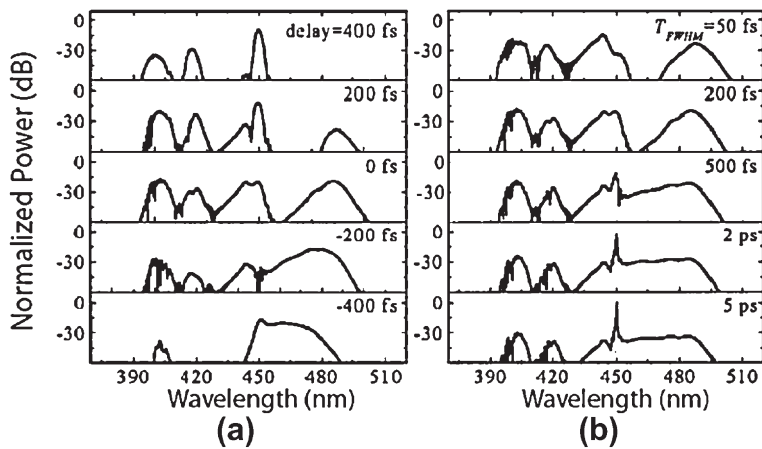


**Figure 13.19** Predicted spectra when 27-ps pulses with 1.7 kW peak power propagate inside a microstructured fiber together with second-harmonic pulses at 450 nm with only 5.6 W peak power: (a) spectra for different initial delay of 200-fs pulses; (b) spectra for different pulse widths launched with no initial delay. (After Ref. [81]; © 2005 OSA.)

permits one to choose the wavelength, width, and energy of the second pulse. In practice, the second pulse is chosen at the second-harmonic wavelength of the main pulse for experimental convenience. The main advantage of using two input pulses is that XPM interaction between the two leads to considerable spectral broadening in the visible region of the generated supercontinuum. The use of XPM for blue-light generation was proposed in a numerical study in which 27-fs pulses at 900 nm with 1.7-kW peak power were propagated inside a microstructured fiber with 200-fs pulses at 450 nm with only 5.6-W peak power [81]. The ZDWL of the fiber was set at 650 nm so that the two pulses propagate with nearly the same group velocity (resulting in enhanced XPM interaction). The width of the second pulse as well as its relative delay was found to affect the visible spectrum. Figure 13.19 shows the predicted spectra in the blue region at the output of a 80-cm-long fiber as a function of (a) initial delay of 200-fs pulses and (b) width of the second-harmonic pulse with zero delay.

In a 2005 experiment, 30-fs pulses at a wavelength of 1028 nm were launched into a 5-m-long microstructured fiber with and without weak second-harmonic pulses [83]. Their relative delay was adjusted using a delay line. The fiber had two ZDWLs located at 770 and 1600 nm. Figure 13.20 compares the output spectra as a function of launched power when pump pulses were propagated (a) alone and (b) with the second-harmonic pulses. When only pump pulses are launched, the supercontinuum is generated through the formation of Raman solitons that shift toward longer wavelengths until their RIFS is suppressed near the second ZDWL at 1600 nm. The NSR emitted by them near 1700 nm is clearly visible. However, the supercontinuum does not extend in the spectral region below 900 nm. When second-harmonic pulses at 514 nm are also

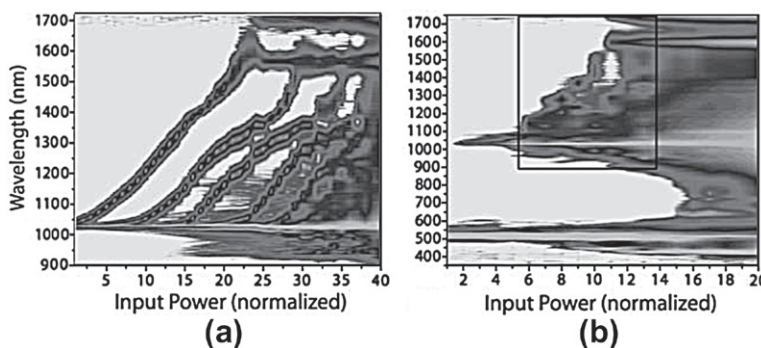


Figure 13.20 Measured spectra as a function of launched power at the output of a 5-m-long fiber when 30-fs input pulses were propagated (a) without and (b) with weak second-harmonic pulses. The black rectangle indicates the region covered in part (a) on the left. (After Ref. [83]; © 2005 OSA.)

launched, the preceding scenario does not change because these pulses are too weak to affect the main pump pulse. However, the XPM-induced phase shift produced by pump pulses chirps the green pulses such that the resulting supercontinuum extends into the visible region and covers a wide range from 350 to 1700 nm. In another experiment, when the power ratio between the pump and second-harmonic pulses was adjusted, it was possible to produce a smooth and nearly flat supercontinuum that covered the entire visible region [79]. Clearly, XPM can be used as a tool to tailor the properties of the generated supercontinuum.

### 13.3.4 Role of Four-Wave Mixing

As discussed earlier, fission of a high-order soliton creates multiple Raman solitons and multiple dispersive waves with distinct spectral peaks that cover a wide wavelength range. Clearly, each Raman soliton can act as a pump and interact with a dispersive wave through FWM to create an idler wave, provided an appropriate phase-matching condition is nearly satisfied. Such a FWM process has been observed experimentally and its theory has also been developed [88–92]. It turns out that two distinct FWM mechanisms exist in the case of supercontinuum generation, and the corresponding phase-matching conditions are given by [91]

$$\beta(\omega_3) + \beta(\omega_4) = \beta_s(\omega_3) + \beta_s(\omega_4), \quad \beta(\omega_3) - \beta(\omega_4) = \beta_s(\omega_3) - \beta_s(\omega_4), \quad (13.3.6)$$

where  $\beta_s(\omega)$  and  $\beta(\omega)$  are the propagation constants associated with a soliton and a dispersive wave, respectively. As seen in Eq. (12.1.5) of Section 12.1, the dispersion relation for a soliton has the form  $\beta_s(\omega) = \beta(\omega_s) + \beta_1(\omega - \omega_s) + \frac{1}{2}\gamma P_s$ , where  $P_s$  is the soliton's peak power. In contrast, the dispersion relation  $\beta(\omega)$  of dispersive waves does not depend on power but contains terms that vary with frequency quadratically and cubically. The idler frequencies  $\omega_4$  corresponds to the solutions of Eq. (13.3.6).

The first phase-matching condition corresponds to traditional FWM in which two pump photons taken from the soliton are converted into the signal and idler photons. In this case, the idler frequency is far from the original dispersive wave as it lies on the opposite side of the input spectrum. In the case of a positive third-order dispersion, such a FWM process creates new frequency components on the Stokes side of the soliton frequency, and it plays an important role in expending the supercontinuum into the infrared side of the input wavelength.

The second phase-matching condition corresponds to a Bragg-scattering-type FWM process in which the beating of a soliton and a dispersive wave creates a moving index grating that produces an idler wave. In this situation, the idler frequency lies close to the original dispersive wave. In the case of a positive third-order dispersion, such a FWM process creates new frequency components on the anti-Stokes side of the dispersive wave and helps to extend the supercontinuum toward the blue side of the input wavelength [90].

Several experiments have shown that both FWM processes take place inside optical fibers. In a 2005 experiment, a CW wave was launched together with an optical pulse propagating as a soliton [89], and it was observed that new spectral components were created as predicted by Eq. (13.3.6). In a 2006 experiment, 200-fs pulses at 800 nm were launched with 6.2-kW peak power inside a 2-m-long PCF with its ZDWL at 820 nm, and the evolution of the output spectrum along its length was observed [91]. Numerical simulations based on Eq. (13.3.1) agreed with the

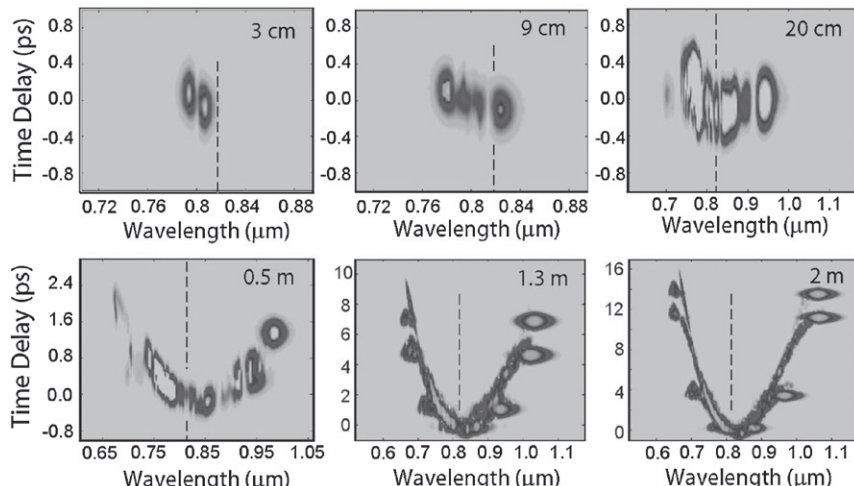


**Figure 13.21** X-FROG spectrograms calculated numerically at six locations within a PCF when 200-fs pulses at 800 nm are launched with 6.2-kW peak power. A dashed vertical line marks the ZDWL of the PCF used. (After Ref. [91]; © 2006 OSA.)

experimental spectra showing the generation of FWM-induced spectral peaks in the visible region.

Figure 13.21 shows six X-FROG spectrograms calculated numerically at six locations within the fiber ranging from 3 cm to 2 m. These spectrograms reveal graphically how the supercontinuum is produced when femtosecond pulses propagate inside the fiber. Only SPM-induced spectral broadening occurs at a distance of 3 cm, and the entire spectrum still lies in the normal-GVD regime of the fiber. The spectrum broadens with further propagation, and at  $z = 9$  cm, one of the spectral lobs lies in the anomalous-GVD range. It propagates as a high-order soliton that undergoes fission. One can see at  $z = 20$  cm, the formation of a Raman soliton together with a dispersive wave near 700 nm. With further propagation, the spectra of Raman solitons shift toward the Stokes side and FWM sets in. At  $z = 50$  cm, we see a clear evidence of FWM band near 650 nm. At a distance of 1.3 m and 2 m, several FWM bands can be seen together with the trapping of dispersive waves by various Raman solitons.

## 13.4 CW OR QUASI-CW PUMPING

The use of picosecond or shorter pulses is not essential for supercontinuum generation. As mentioned earlier, 10-ns pulses were used for this purpose in the original 1976 experiment [4]. In a 2003 experiment, 42-ns pulses from a Q-switched Nd:YAG laser were launched into a 2-m-long microstructured fiber (with a random hole pattern) to produce a wide supercontinuum at 10-kW power levels [94]. Somewhat surprisingly, it turned out that even CW lasers can produce a supercontinuum at sufficiently high power levels. CW lasers were used for this purpose as early as 2003 and, by now, such supercontinuum sources are being used for a variety of applications [93–109]. In this section we first discuss the nonlinear mechanisms behind CW supercontinuum generation and then review the experimental progress. It should be stressed that the following discussion applies also for quasi-CW pumping in which optical pulses of widths  $>1$  ns are employed.

### 13.4.1 Nonlinear Mechanisms

It should come as no surprise that the phenomenon of modulation instability is behind the CW supercontinuum generation [110–114]. As was seen in Section 5.1 that, when a CW beam propagates in the anomalous dispersion region of an optical fiber, the phenomenon of modulation instability can create two sidebands at specific frequencies  $\omega_0 \pm \Omega_{\max}$ , where  $\omega_0$  is the frequency of the CW beam. As seen from Eq. (5.1.9), the frequency shift  $\Omega_{\max}$  depends on the input power  $P_0$ , in addition to the fiber's dispersion and nonlinear parameters, as

$$\Omega_{\max} = \sqrt{\frac{2\gamma P_0}{|\beta_2|}}. \quad (13.4.1)$$

In the case of spontaneous modulation instability, the growth of these sidebands is initiated by intensity fluctuations within the CW beam.

Recall from Section 10.3.3 that modulation instability can be viewed as a FWM process in which the input CW beam acts as the pump and the noise fields associated with the two sidebands act as the signal and the idler waves. The amplitudes of the two sidebands grow initially with distance  $z$  as  $\exp(2z/L_{\text{NL}})$ , where  $L_{\text{NL}} = 1/(\gamma P_0)$  is the nonlinear length. This growth manifests in the time domain as sinusoidal oscillations of the form  $P(z, t) = P_0 + p_m(z) \cos[\Omega_{\text{max}}t + \psi](z)$  with the period  $T_m = 2\pi/\Omega_{\text{max}}$ . The exponential growth continues as long as the fraction of the power in the two sidebands remains a small fraction of the total power (the so-called linear regime).

Once the modulation-instability process enters the nonlinear regime, evolution of the optical field can only be studied by solving the NLS equation (5.1.1) numerically with noise added to the input CW beam. Figure 13.22 shows temporal power variations predicted for a 20W input power at the output of a 50-m-long fiber for several values of the  $\beta_2$  and  $\gamma$  parameters of the fiber. The nonlinear length is 10m for  $\gamma = 5 \text{ W}^{-1}/\text{km}$  and reduces to 1m when  $\gamma$  is increased by a factor of 10. Figure 13.22a shows that the ratio  $L/L_{\text{NL}}$  should exceed 10 or so before significant modulations appear on the pump beam. As the nonlinear length shortens, modulations become sharper and sharper and take the form of a train of short optical pulses.

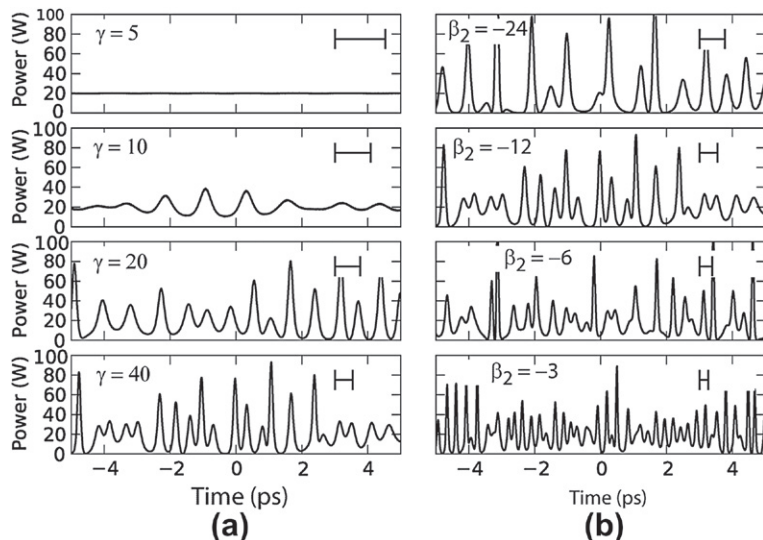


**Figure 13.22** Temporal structures at the output of a 50 m long fiber for a CW input beam with 20 W pump power; (a)  $\gamma$  is varied for  $\beta_2 = -12 \text{ ps}^2/\text{km}$ ; (b)  $\beta_2$  is varied for  $\gamma = 40 \text{ W}^{-1}/\text{km}$ . The bars show the value of  $T_m$ . (After Ref. [114]; © 2010 Cambridge University Press.)

pulses of different widths that propagate as solitons in the anomalous-GVD regime of the fiber.

We can estimate the average width of these solitons using a simple argument [114]. The energy of an optical soliton of peak power  $P_s$  is related to its width  $T_s$  as  $E_s = 2P_s T_s$  (see Section 5.2.2). This energy must equal the energy  $P_0 T_m$  of the CW beam in one modulation period  $T_m$ . However, for a fundamental soliton, we must also have  $L_D = L_{NL}$  or  $P_s T_s^2 = |\beta_2|/\gamma$ . Using  $\Omega_{\max}$  from Eq. (13.4.1), we find the simple relation

$$T_s = \frac{T_m}{\pi^2} = \sqrt{\frac{2|\beta_2|}{\pi^2 \gamma P_0}} = \frac{1}{\pi} \sqrt{2|\beta_2| L_{NL}}. \quad (13.4.2)$$

This equation shows, in agreement with Figure 13.22, that smaller values of  $|\beta_2|$  and larger values of  $\gamma$  help in reducing the width of solitons formed through modulation instability. If modulation instability is induced by launching a weak signal at the sideband frequency, all solitons within the pulse train would have the same width. However, when modulation instability is seeded by noise and is of the spontaneous kind, pulse widths fluctuate in a way seen in Figure 13.22.

The formation of a supercontinuum proceeds as follows. First, modulation instability converts the CW beam into a train of pulses of different widths and peak powers that propagate as fundamental solitons. Since the RIFS depends on the pulse width, different solitons shift their spectra by different amounts toward longer wavelengths. At the same time, blue-shifted radiation is generated in the form of dispersive waves because of perturbations of these solitons by third-order dispersion. As a soliton shifts its spectrum, it also slows down as long as it experiences anomalous GVD. As a result, solitons collide (overlap temporally) with neighboring solitons and dispersive waves and interact with them through XPM and FWM. It turns out that such a collision can transfer energy to the slowing soliton, which reduces its width further (to maintain the condition  $N = 1$ ) and slows it down even more, and its spectrum shifts even further toward longer wavelengths. Multiple soliton collisions eventually produce a supercontinuum that is extended mostly toward the red side of the input wavelength.

It is clear from the preceding description that the noisy nature of an input CW beam plays a critical role since it seeds the process of modulation instability. Even a CW laser beam is only partially coherent because of its finite spectral width resulting from intrinsic phase fluctuations. Any numerical modeling must include such fluctuations [110–112]. Moreover, since an experimental optical spectrum represents a long-time average of the fiber output, one must perform an ensemble average of the numerically simulated spectra. Figure 13.23 shows the temporal and spectral evolution over 500 m of a highly nonlinear fiber with  $\gamma = 10.6 \text{ W}^{-1}/\text{km}$ ,  $\beta_2 = -0.17 \text{ ps}^2/\text{km}$ , and  $\beta_3 = 0.0393 \text{ ps}^3/\text{km}$  at the 1486 nm wavelength of the CW beam launched with 4 W of power [112]. Dark-gray curves represent an ensemble average over 50 light-gray spectra. The NLS equation given in Eq. (13.3.1) was solved numerically to obtain these results. Modulation instability occurs within the first 100 m, and it leads to rapid temporal oscillations as well as two spectral

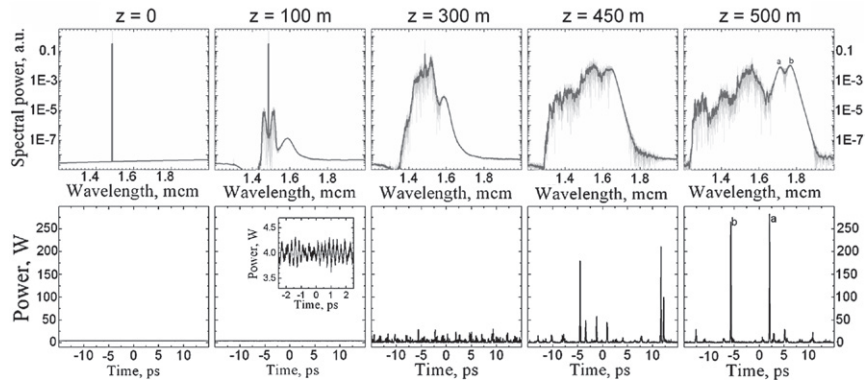


**Figure 13.23 Temporal (bottom) and spectral (top) evolutions over 50 m of fiber when a CW beam is launched with 4 W of power. Dark-gray curves represent an average over 50 light-gray spectra. (After Ref. [112]; © 2005 OSA.)**

sidebands shifted from the central peak by about 3.6 THz. After 300 m of propagation, we see a clear evidence of different solitons of different widths undergoing large red shifts through intrapulse Raman scattering. Two temporal spikes at  $z = 500$  m (marked as a and b) correspond to two solitons whose spectra have shifted the most. Multiple peaks on the blue side of the input wavelength correspond to dispersive waves.

### 13.4.2 Experimental Progress

The two most important ingredients for any recipe of CW supercontinuum are a high-power laser and a highly nonlinear fiber so that the product  $\gamma P_0 L$  exceeds 30 or so, where  $P_0$  is the CW power launched into a fiber of length  $L$ . This condition can be satisfied for a 100-m-long fiber with  $\gamma = 100 \text{ W}^{-1}/\text{km}$  at a pump-power level of a few watts. Such power levels are readily available from modern, high-power, Yb-doped fiber lasers. In the original 2003 experiment, a 100-m-long holey fiber was employed and a Yb-fiber laser was used for CW pumping at 1065 nm [93]. The resulting supercontinuum extended from 1050 to 1380 nm when 8.7 W of CW power was coupled into the fiber.

In a 2004 experiment, three highly nonlinear fibers of lengths 0.5, 1, and 1.5 km were used for supercontinuum generation by launching a CW beam at 1486 nm [98]. The ZDWL of the fibers was  $< 1480$  nm, resulting in anomalous GVD at the pump wavelength. Output spectra were measured for the three fibers at power levels ranging from 0.4 to 4 W. In each case, the output spectrum broadened from 1200 to  $> 1800$  nm when the pump power was close to 4 W. The spectrum was highly asymmetric with much more power on the long-wavelength side. As discussed earlier, this asymmetry

is due to intrapulse Raman scattering that selectively extends the spectrum toward the long-wavelength side.

A 20-m-long PCF with  $\gamma = 43 \text{ W}^{-1}/\text{km}$  was used in a 2008 experiment [103]. It exhibited two ZDWLs located near 810 and 1730 nm. As a result, dispersion was relatively large (65 ps/km/nm) at the pump wavelength of 1070 nm but it decreased for longer wavelengths. Figure 13.24 shows the observed supercontinuum at the fiber output when 44 W of CW power was launched into the fiber. The supercontinuum spans from 1050 to 1680 nm. More importantly, the output power is close to 29 W,

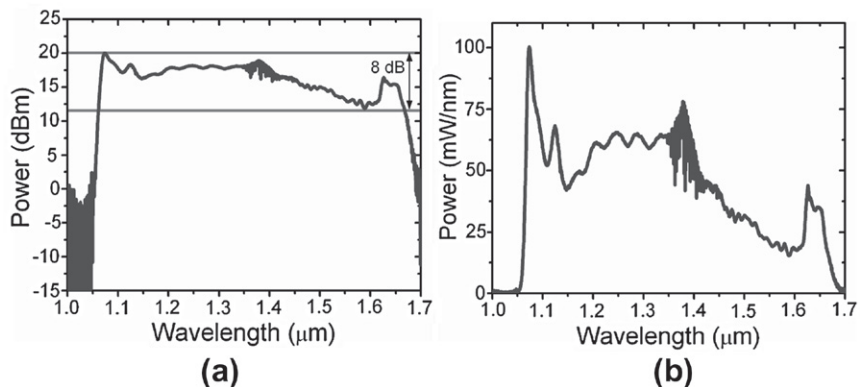


Figure 13.24 Observed supercontinuum on (a) semi-log and (b) linear scales at the fiber output of a 20-m-long PCF when 44 W of CW power at 1070 nm was launched into the fiber. (After Ref. [103]; © 2008 OSA.)

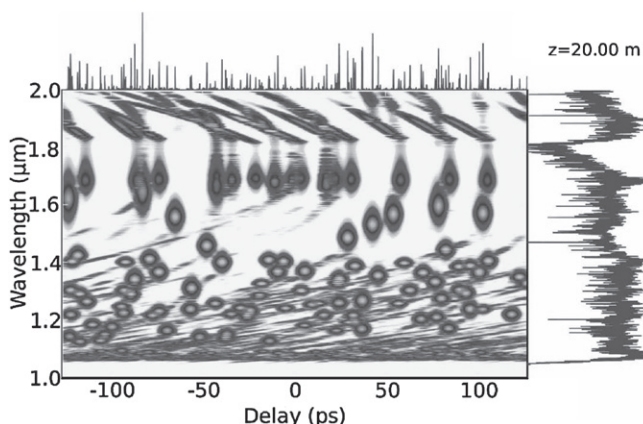


Figure 13.25 X-FROG spectrogram calculated numerically under the conditions of the supercontinuum in Figure 13.24. (After Ref. [103]; © 2008 OSA.)

and the spectral power density exceeds 50 mW/nm up to 1400 nm. These features are useful for applications of such a supercontinuum source for biomedical imaging.

Numerical simulations reproduce most of the experimental features seen in Figure 13.24. More importantly, they shed light onto the physical process of soliton collisions that plays an important role. Figure 13.25 shows the X-FROG spectrogram of a supercontinuum [103]. One sees clearly the formation of solitons (round objects) through modulation instability, together with their different spectral shifts and different speeds (leading to different delays). Collisions among these solitons are also apparent from their temporal overlap. Eventually the spectrum of a short soliton approaches the ZDWL near 1730 nm, where it stops shifting because of the radiation pressure induced by the corresponding dispersive waves (cigar-like objects) emitted at wavelengths longer than 1730 nm. The interaction (collision) of solitons with these dispersive waves generates new spectral components through FWM [108] that can be seen in Figure 13.24 in the wavelength region near 1900 nm.

The formation of the CW supercontinuum in the visible region has also attracted attention [115–119]. This is not easy to do because the most practical source of CW radiation is a high-power Yb-fiber laser emitting light near 1060 nm. When such a laser is used with a suitable PCF having its ZDWL near 1000 nm, the observed supercontinuum rarely extends below 900 nm. In a 2006 experiment, a tapered PCF whose core diameter, and hence the ZDWL, decreased along its length was employed for this purpose [30]. A quasi-CW source (a Nd:YAG microchip laser) emitting nanosecond pulses was used with different taper lengths to produce the optical spectra shown in Figure 13.4a. As seen there, the supercontinuum extended from 350 to 1750 nm with a high spectral density when the taper length exceeded 5 m. The extension of the supercontinuum into the visible region was possible because a monotonically decreasing  $|\beta_2(z)|$  allowed the FWM phase-matching condition to be satisfied for progressively shorter idler wavelengths.

CW pumping near 1060 nm of a constant-diameter PCF can also create spectral components at wavelengths below 900 nm. In a 2008 experiment, a 100-m-long PCF with its ZDWL at 1068 nm was pumped with a 50-W Yb-fiber laser emitting light at 1070 nm, and wavelengths shorter than 900 nm were observed at the fiber output at high power levels [115]. FWM was again behind this extension of the supercontinuum, although visible wavelengths were not produced in this experiment. Much better results were obtained in another 2008 experiment by using two cascaded PCFs such that a 100-m-long section followed another 100-m-long tapered section in which  $|\beta_2|$  decreased with length [116]. When pumped with 12.5 W of power at 1064 nm, the output spectrum contained a broad peak in the green region together with a supercontinuum extending from 700 to 1300 nm.

By 2009, the use of a PCF whose core was both tapered and doped with  $\text{GeO}_2$  created a CW supercontinuum that extended toward wavelengths as short as 450 nm [118]. Figure 13.26 compares the spectra obtained for the uniform-core and tapered-core PCFs whose core was doped with  $\text{GeO}_2$ . In case (a) of a uniform-core PCF, the launched CW power at 1075 nm was 70 W, and the supercontinuum extended from 550 to >1750 nm with a spectral power variation of less than 12 dB. In case (b), a uniform-core section of

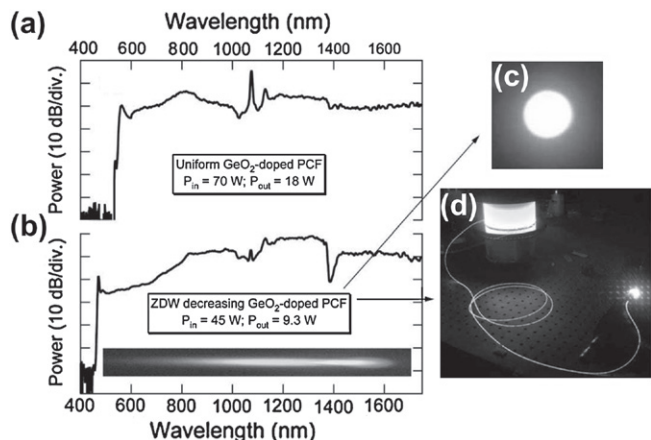


**Figure 13.26** Experimental spectra for a launched power of (a) 70 W in a uniform-core PCF and (b) 45 W in a tapered-core PCF; the inset shows the photograph of output dispersed by a prism. Photographs of (c) the output spot and (d) of the fiber spool are also shown.  
(After Ref. [118]; © 2009 OSA.)

50 m was followed with a 130-m-long PCF section whose outer diameter decreased from 135 to 85  $\mu\text{m}$ . When pumped with 40 W of CW power, the supercontinuum extended from 470 to  $>1750$  nm and thus covered the entire visible region, as is also evident from the white spot in part (c). When a prism was used to disperse the output light, a rainbow-like spectrum was observed, as seen in the inset of Figure 13.26. These results clearly show that an ultrabroad supercontinuum covering both the visible and near-infrared regions can be produced with 1060-nm pumping provided the PCF is suitably designed.

Even the ultraviolet region could be covered in a 2012 experiment in which a supercontinuum extending from 350 to 470 nm was produced by pumping a PCF with Q-switched pulses at 355 nm [120]. This is remarkable since the PCF exhibited large normal dispersion and strong absorption in the ultraviolet region. Physical mechanisms behind supercontinuum generation were found to be multimode FWM and cascaded SRS.

## 13.5 POLARIZATION EFFECTS

The numerical model based on Eq. (13.3.1) assumes that the state of polarization (SOP) of an input pulse is preserved during its propagation inside the fiber. As we have seen in Chapter 6, this assumption is often not valid in practice. In the case of a highly birefringent fiber, the SOP may remain preserved if the input pulse is launched with its polarization oriented along a principal axis of the fiber. However, if it is initially tilted at an angle, the input pulse will split into two orthogonally polarized modes of

the fiber that would begin to separate from each other because of their different group velocities. Even in an ideal isotropic fiber, nonlinear polarization rotation induced by XPM-induced coupling between the two orthogonally polarized fiber modes can affect the process of soliton fission. The important question is how such phenomena affect the generation of a supercontinuum in highly nonlinear fibers [121–129].

### 13.5.1 Birefringent Microstructured Fibers

Microstructured fibers, with a cladding containing multiple air holes, often do not have a circular core. The polarization dependence of a supercontinuum in such fibers has been observed in several experiments [121–123]. In a 2002 experiment, PCFs with a hexagonal symmetry of air holes in their cladding were employed [45]. The birefringence should be relatively weak in these fibers because of a nearly circular core. Nevertheless, it was found that the supercontinuum changed with the input SOP. Moreover, different parts of the supercontinuum exhibited different SOPs, indicating a nonlinear coupling between the two orthogonally polarized pulses within the fiber. Figure 13.27 shows changes in the recorded supercontinuum spectra with  $\pm 30^\circ$  rotations in the SOP of a linearly polarized input pulse, realized by rotating a 41-mm-long fiber with the  $2.5\text{-}\mu\text{m}$  core diameter. In this experiment, 18-fs input pulses from a Ti:sapphire laser operating at 790 nm were launched into the fiber. It is clear from Figure 13.27 that spectral details of a supercontinuum are quite sensitive to the input SOP of the pulse.

In a 2008 experiment, a highly birefringent microstructured fiber with an elliptical core (see Figure 13.28) was employed [128]. Figure 13.28 shows changes in the

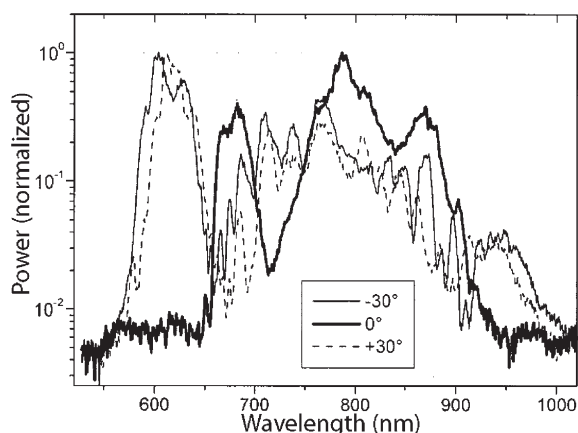


**Figure 13.27** Supercontinuum spectra at the output of a photonic crystal fiber for three different orientations of linearly polarized 18-fs input pulses. (After Ref. [45]; © 2002 OSA.)

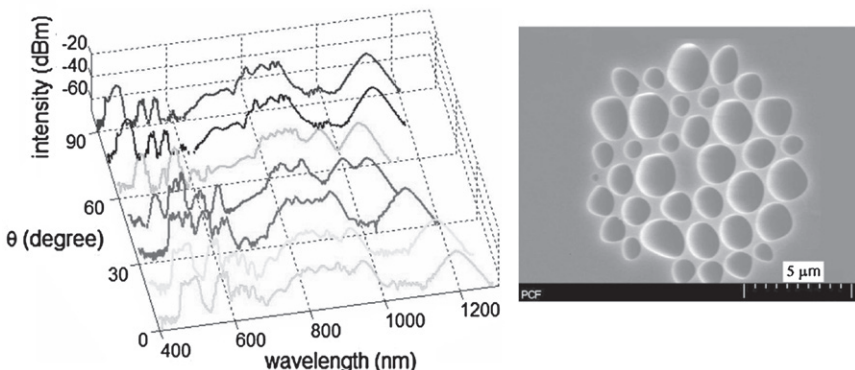


**Figure 13.28** Supercontinuum spectra at the output of a highly birefringent fiber (micrograph on the right) for several different polarization angles. (After Ref. [128]; © 2008 American Physical Society.)

supercontinuum spectra observed as the angle  $\phi$  (that the SOP direction of the input pulse makes from the slow axis) was varied. This experiment launched 15-fs pulses with 300 mW average power at a wavelength of 800 nm into a 12-cm-long fiber with an effective mode area of about  $2 \mu\text{m}^2$ . The ZDWL of the fiber was 683 and 740 nm for light polarized along the fast and slow axes of the fiber, respectively. When light is polarized along these two axes ( $\theta = 0$  or  $90^\circ$ ), only one of the orthogonally polarized modes is excited. Differences observed in the supercontinuum spectra in these two cases are due to different dispersive properties of the fiber experienced by the pulse because of a large birefringence.

For values of  $\theta$  between 0 and  $90^\circ$  in Figure 13.28, both modes are excited with generally different peak powers because pulse energy splits along the slow and fast axes. The two orthogonally polarized pulses travel at different group velocities because of birefringence. However, they separate from each other quickly as the walk-off length is  $< 1$  mm for 15-fs pulses. Since the two pulses cease to interact with each other through XPM after they have separated, the impact of XPM is negligible in the experiment. As a polarizer was not placed before the photodetector, the observed spectrum represents a superposition of two supercontinua generated separately along the two principal axes of the fiber [128]. In general, spectral bandwidth is reduced as  $\theta$  increases from 0 toward  $45^\circ$  because the peak power of the pulse along each direction is reduced compared with the case  $\theta = 0$  case. The shortest bandwidth occurs, as one may expect, for  $\theta = 45^\circ$ .

### 13.5.2 Nearly Isotropic Fibers

The situation is entirely different in nearly isotropic fibers in which the two orthogonally polarized pulses travel with nearly the same group velocities, and thus continue to overlap over most of the fiber length. The XPM-induced coupling between

these pulses then leads to a complex evolution of the SOP, and different parts of the supercontinuum at the fiber output exhibit different SOPs [124]. This nonlinear coupling can also occur in ideal isotropic fibers, with a perfectly circular core exhibiting no birefringence, if the SOP of the input pulse is not linear so that both polarization modes are excited [125]. Its mathematical description requires that we solve two coupled generalized NLS equations of the form Eq. (13.3.1). Using the Jones vector and the Pauli matrices, as defined in earlier chapters, they can be written in a vector form as

$$\begin{aligned} \frac{\partial|A\rangle}{\partial z} + \frac{1}{2} \left( \alpha + i\alpha_1 \frac{\partial}{\partial t} \right) |A\rangle + \sum_{m=2}^M i^{m-1} \frac{\beta_m}{m!} \frac{\partial^m|A\rangle}{\partial t^m} \\ = \frac{i}{2} \left( \Delta\beta + i\Delta\beta_1 \frac{\partial}{\partial t} \right) \sigma_1 |A\rangle + i \left( \gamma + i\gamma_1 \frac{\partial}{\partial t} \right) |Q(z,t)\rangle, \end{aligned} \quad (13.5.1)$$

where  $|Q(z,t)\rangle$  is related to the third-order nonlinear response of the fiber and has the following form if we neglect the anisotropic part of the Raman response:

$$\begin{aligned} |Q(z,t)\rangle = & \frac{2}{3}(1-f_R)[\langle A|A\rangle]|A(z,t)\rangle + \frac{1}{3}(1-f_R)[\langle A^*|A\rangle]|A^*(z,t)\rangle \\ & + f_R|A(z,t)\rangle \int_{-\infty}^t h_R(t-t')\langle A(z,t')|A(z,t')\rangle dt'. \end{aligned} \quad (13.5.2)$$

The birefringence effects are included in Eq. (13.5.1) through the quantities  $\Delta\beta$  and  $\Delta\beta_1$ , where  $\Delta\beta = \beta_{0x} - \beta_{0y}$  is given in Eq. (6.1.13) and  $\Delta\beta_1 = \beta_{1x} - \beta_{1y}$  accounts for the difference in the group velocities of two orthogonally polarized pulses.

Numerical simulations based on Eqs (13.5.1) and (13.5.2) reveal that the SOP of a specific spectral component in a supercontinuum is generally elliptical even when a linearly polarized pulse is launched initially into the fiber. Moreover, it can vary widely for different spectral components. In one study, the ellipticity, defined as

$$e_p(\omega) = \langle \tilde{A}(L,\omega)|\sigma_3|\tilde{A}(L,\omega)\rangle / \langle \tilde{A}(L,\omega)|\tilde{A}(L,\omega)\rangle, \quad (13.5.3)$$

used as a simple measure for SOP variations across the supercontinuum [124]. Here,  $|\tilde{A}(L,\omega)\rangle$  is the spectral amplitude at the end of a fiber of length  $L$ ,  $\sigma_3$  is a Pauli matrix, and  $\langle \tilde{A}(L,\omega)|\tilde{A}(L,\omega)\rangle$  represents the total power density at the frequency  $\omega$ . Figure 13.29 shows, as an example, the temporal and spectral evolutions over 6 cm of a microstructured fiber when 100-fs pulses with 10-kW peak power are launched with a linear SOP oriented at 45° from the slow axis. The fiber has a core diameter of 2.2 μm with  $\beta_2 = -13.5 \text{ ps}^2/\text{km}$ ,  $\gamma = 80 \text{ W}^{-1}/\text{km}$ , and  $\Delta\beta = 1 \times 10^{-5}$ .

Several features of Figure 13.29 are noteworthy. First, even though two orthogonally polarized pulses are identical at  $z = 0$ , they evolve quite differently because the two are coupled linearly as well as nonlinearly. In particular, the XPM-induced coupling between the two leads to a SOP that varies with wavelength across the

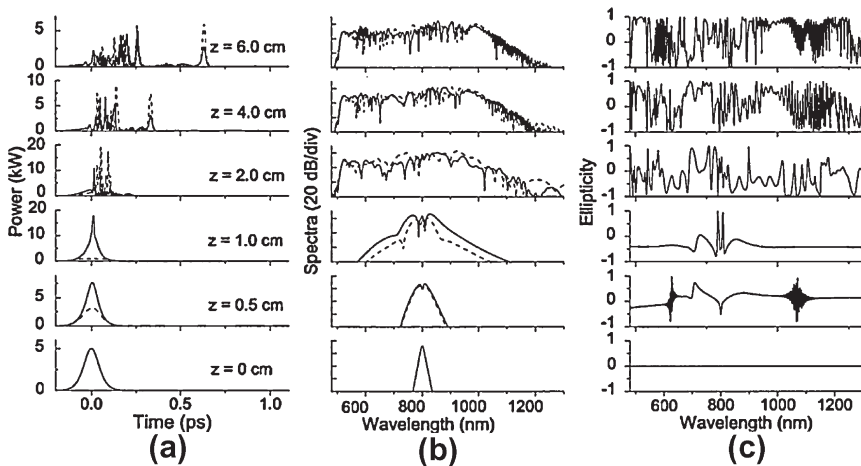


**Figure 13.29** (a) Temporal, (b) spectral, and (c) ellipticity evolution over 6 cm of a fiber when 100-fs input pulses are linearly polarized at  $45^\circ$  from the slow axis of the fiber. Solid and dashed curves represent the  $x$  and  $y$  polarization components. (After Ref. [124]; © 2004 OSA.)

entire supercontinuum in a complicated fashion. If a polarizer were to be placed at the fiber output before the spectrum is recorded, the observed spectral features would change as the polarizer is rotated. This is exactly what is observed experimentally and seen in Figure 13.27. A similar behavior occurs if the initial SOP of the input pulse is changed.

### 13.5.3 Nonlinear Polarization Rotation in Isotropic Fibers

A question one may ask is whether such polarization variations across the supercontinuum are expected to occur in an ideal isotropic fiber with zero birefringence for which both  $\Delta\beta$  and  $\Delta\beta_1$  vanish in Eq. (13.5.1). Clearly, if the SOP of the input pulse is linear initially, no polarization-dependent effects are expected since all directions are equivalent for an isotropic fiber. However, if the input SOP is slightly elliptical, both polarization modes will be excited, and their SOP would evolve in a nonlinear fashion because of the XPM-induced coupling responsible for nonlinear polarization rotation. In a 2004 study, numerical simulations based on Eq. (13.5.1) revealed that different fundamental solitons created through the fission process develop different ellipticities that do not change much as the soliton spectrum shifts along the fiber through the RIFS [125]. In contrast, the SOP of spectral components associated with the NSR evolve continuously along the fiber. At a given distance, the SOP of the pulse varies on the Poincaré sphere in a complicated fashion, both temporally and spectrally. These features indicate that the soliton-fission process is vectorial in nature even in an isotropic fiber.

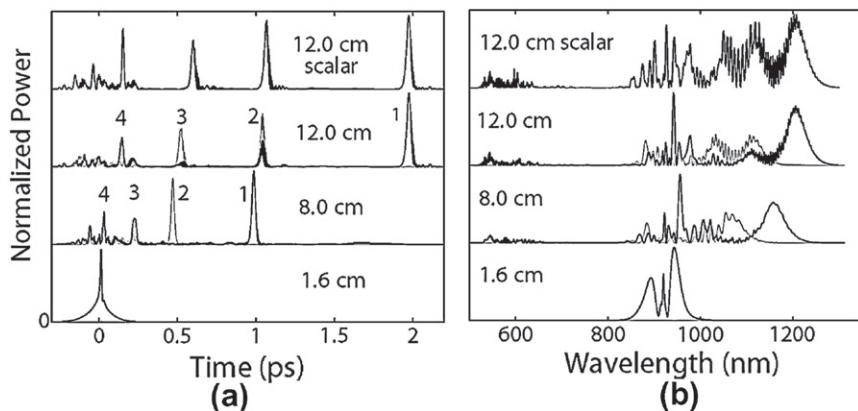


**Figure 13.30** Temporal (a) and spectral (b) patterns at a distance of 1.6, 8, and 12 cm when a 150-fs pulse with  $N \approx 12$  is launched into a tapered fiber. The scalar case at  $z = 12\text{ cm}$  is shown for comparison. Black and gray curves represent the  $x$  and  $y$  polarization components. Note that spectral intensity is plotted on a linear scale. (After Ref. [125]; © 2004 APS.)

As an example, Figure 13.30, shows the temporal and spectral evolution of a 150-fs pulse launched with the soliton order  $N \approx 12$  into a 12-cm-long tapered fiber with an ellipticity angle of  $1.4^\circ$  such that the  $y$ -polarized component of the pulse initially had  $<0.1\%$  of input energy [125]. The pulse remains almost linearly polarized until it begins to breakup near  $z = 1.6\text{ cm}$ . Beyond that distance, the higher-order soliton undergoes fission and breaks into multiple fundamental vector solitons with different SOPs. The SOP of the rightmost soliton (with the maximum RIFS) is close to linear, but the second, third, and fourth solitons have ellipticity angles of  $5.4^\circ$ ,  $15.4^\circ$ , and  $16^\circ$ , respectively. The temporal structure near  $t = 0$  contains the remaining pulse energy and exhibits even more complex polarization features. A comparison of the scalar and vector traces at  $z = 12\text{ cm}$  shows that the vectorial nature of the fission also affects the delay experienced by individual solitons. These results indicate that the use of Eq. (13.5.1) may be essential for interpreting the observed data, depending on the fiber and other experimental conditions.

## 13.6 COHERENCE PROPERTIES

A comparison of the experimental spectra in Figures 13.5 and 13.6 with the numerically simulated spectra in Figure 13.13 reveals that the former are much smoother than the latter ones. This feature is related to the fact that most experiments employ a pulse train at a repetition rate of 80 MHz or so, whereas a single pulse is used for numerical simulations. Any spectral measurement of a supercontinuum represents an average over a large number of pulses. Since most mode-locked lasers exhibit pulse-to-pulse fluctuations, the fine structure seen in Figure 13.13 is washed out during averaging.

From a practical perspective, coherence properties of a supercontinuum are important when such a device is employed as a broadband source of light for medical, metrological, or other applications. For this reason, the coherence issue has attracted considerable attention [130–147]. The first question we should ask is what we mean by the coherence in the context of a supercontinuum. If optical pulses are propagating inside a single-mode fiber with a fixed spatial profile, the output would be spatially coherent. However, its temporal coherence is affected by fluctuations in the energy, width, and arrival time of individual input pulses. As a result, spectral phase is also likely to fluctuate from pulse to pulse across the bandwidth of the supercontinuum.

### 13.6.1 Spectral-Domain Degree of Coherence

A suitable measure of coherence for a supercontinuum is the degree of coherence associated with each spectral component. In the scalar description, it is defined as [38]

$$g_{12}(\omega) = \frac{\langle \tilde{A}_1^*(L, \omega) \tilde{A}_2(L, \omega) \rangle}{[\langle |\tilde{A}_1(L, \omega)|^2 \rangle \langle |\tilde{A}_2(L, \omega)|^2 \rangle]^{1/2}}, \quad (13.6.1)$$

where  $\tilde{A}_1$  and  $\tilde{A}_2$  are the Fourier transforms of two neighboring pulses, and the angle brackets denote an average over the entire ensemble of pulses. Experimentally, the degree of coherence can be measured by interfering two successive pulses in a pulse train incident on the fiber using a Michelson interferometer, and recording the contrast of resulting spectral fringes as a function of wavelength [136]. The ensemble average is performed automatically by the integration time associated with the optical spectrum analyzer.

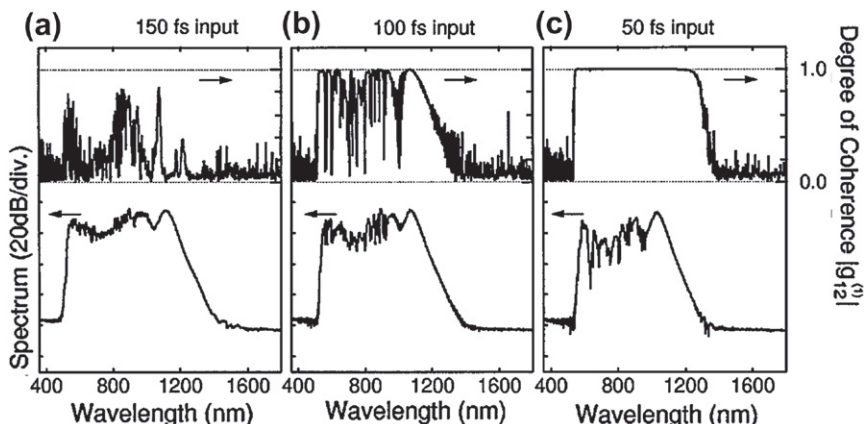


**Figure 13.31** Averaged spectra (bottom traces) and the degree of coherence (top traces) at fiber output when input pulses at 850 nm are launched with 10 kW peak power and their width is varied from 150 to 50 fs. (After Ref. [38]; © 2002 IEEE.)

One can calculate  $g_{12}(\omega)$  numerically by adding quantum noise to the input pulse (one photon per spectral mode) and solving repeatedly Eq. (13.3.1), or Eq. (13.5.1) if polarization effects are important [38]. This approach shows that both the shape and spectrum of output pulses change from pulse to pulse. Moreover,  $g_{12}(\omega)$  varies considerably across the supercontinuum depending on the average value of input pulse parameters. In particular, the degradation of coherence is quite sensitive to the input pulse width. Figure 13.31 shows the averaged output spectra and the degree of coherence  $g_{12}(\omega)$  for three different pulse widths, assuming that the peak power of the input pulse is 10 kW in all cases. Fiber parameters are identical to those used for Figure 13.13. Clearly, the supercontinuum is much less coherent for a 150-fs pulse compared with the 100-fs pulse. More importantly, the coherence is preserved across the entire supercontinuum for 50-fs pulses.

To understand the features seen in Figure 13.31, we note that the soliton order  $N$  scales with pulse width  $T_0$  linearly. Thus,  $N$  is relatively small for the 50-fs pulse. Also, since the dispersion length scales as  $T_0^2$ , it is nine times shorter for the 50-fs pulse (about 63 mm) compared with the 150-fs pulse. The nonlinear length  $L_{NL}$  is about 1 mm in all cases, as the peak power is kept fixed. The main conclusion one can draw is that the soliton-fission process is inherently noisy as it is sensitive to both the amplitude and phase of the input pulse. If  $N$  is small, the pulse splits into a smaller number of solitons and suffers less from noise. In contrast, noise is enhanced if a large number of fundamental solitons are created through the fission. Some support for this observation comes from the fact that, even if Raman effects are ignored by setting  $f_R = 0$  artificially, the coherence is degraded more for wider pulses [38]. Numerical simulations also show that coherence is preserved even for 150-fs pulses when they are propagated in the normal-GVD regime of the fiber where soliton fission does not occur.

Coherence of a supercontinuum has been measured in several experiments [133–137]. In one experiment in which 100-fs pulses were launched into a 6-cm-long tapered fiber, the GVD of the fiber at the wavelength of input pulses was found to play a crucial role [136]. As expected, coherence was high in the normal-GVD regime, as soliton fission did not occur, but the bandwidth of supercontinuum was also limited to 200 nm. Close to the ZDWL (around 820 nm), coherence was nonuniform across the supercontinuum with spectral regions of low and high coherence. In the anomalous-GVD regime, coherence degraded severely at 860 nm, but was relatively high at a wavelength of 920 nm. In this case, the supercontinuum is extended from 500 to 1300 nm with a mean value of  $g_{12} \approx 0.7$  across the entire bandwidth. These results can be understood by noting that an increase in  $\beta_2$  has the same effect as reducing the pulse width since both the soliton order  $N$  and the dispersion length  $L_D$  decrease for larger values of  $\beta_2$ . In general, spectral coherence is improved for smaller values of  $L_D$  because the soliton order  $N$  scales as  $\sqrt{L_D}$  at a given input power.

The noisy nature of a supercontinuum has practical implications. For example, it limits the stability of supercontinuum-based frequency combs useful for metrological applications [138]. It also sets a fundamental limitation on the compression of ultrashort pulses when their spectra are broadened using a highly nonlinear fiber

[139]. Even when a CW laser is used for generating a supercontinuum, the coherence of the CW laser affects the noise at the fiber output. In one experiment, output of a low-coherence semiconductor laser operating at 1480 nm was amplified to 1.6 W before launching it into a 5-km-long highly nonlinear fiber [140]. The relative intensity noise of the resulting supercontinuum was found to be enhanced by more than 15 dB/Hz across a bandwidth > 1 GHz. Temporal traces of the fiber output exhibited power fluctuations that often exceeded 50% of the average power level and had a standard deviation of 35%. Numerical simulations based on Eq. (13.3.1), modified to include spontaneous Raman noise, show that soliton fission plays an important role and leads to enhanced intensity noise [142]. They also show that the smoothness of experimental spectra results from a time averaging taking place during measurements.

In a 2006 study, the impact of the temporal coherence of a CW beam on supercontinua was investigated [143]. Two sources used consisted of an erbium-doped fiber laser operating at 1480 nm and another laser operating below the threshold so that its output consisted of amplified spontaneous emission (ASE). In both cases, the coherence time  $\tau_c$  was adjusted using optical filters before launching the CW beam inside a highly nonlinear fiber. Figure 13.32 shows the measured spectra at the fiber output in the case of the fiber laser at three power levels for four different coherence times ranging from 9 to 205 ps. Notice how the flatness of the supercontinuum at the

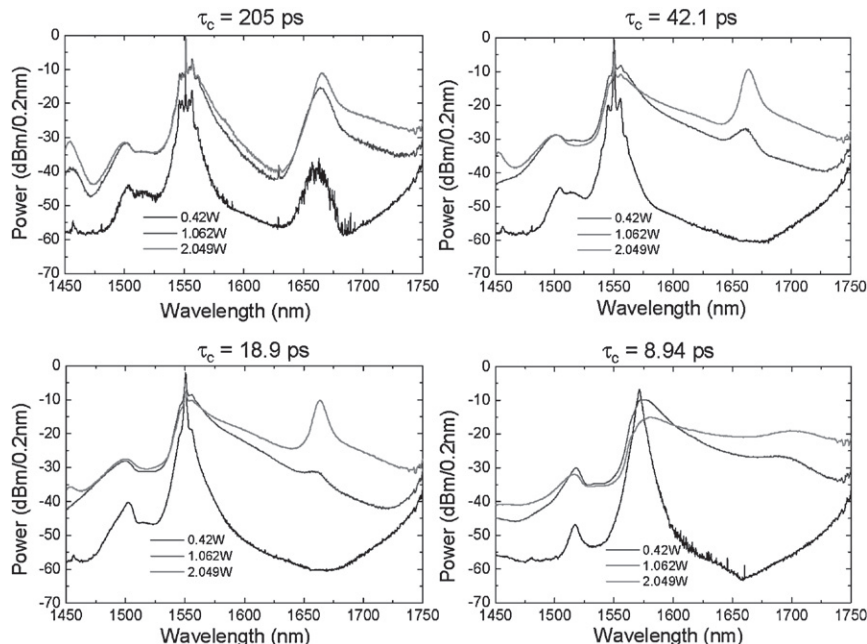


**Figure 13.32** Measured output spectra at three power levels of a CW laser for four different values of  $\tau_c$ , adjusted using optical filters with different bandwidths. (After Ref. [143]; © 2006 OSA.)

input power of 2.05 W improves as the coherence time is reduced to near 9 ps. Even flatter supercontinua were observed in the case of the ASE source when its coherence time was reduced to below 1 ps. It was found in another 2006 study that the best performance may be realized in practice for an optimum value of the coherence time associated with the CW source [145].

### 13.6.2 Techniques for Improving Coherence

It is possible to improve the coherence of a supercontinuum, and several techniques have been proposed for this purpose [148–155]. In an interesting approach, known as dispersion micro-management (DMM), dispersion is made nonuniform across fiber length by tapering the fiber appropriately [149]. In the experiment, supercontinua were generated by launching 100-fs pulses at 920 nm into three different fibers: a 80-cm-long holey fiber (HF), with 2.6- $\mu\text{m}$  core, a 6-cm-long tapered fiber with 2.7- $\mu\text{m}$  core, and a 2.3-cm-long PCF with a 1-cm region where its core diameter decreased from 3.3 to 2.6  $\mu\text{m}$ . Figure 13.33a shows the output spectra for these three fibers. The supercontinuum is much smoother in the case of the DMM fiber whose core diameter decreases along its length. The intensity noise spectra, centered around the repetition rate of mode-locked pulses, shown in Figure 13.33b reveal that the noise floor is also reduced to the background level in the DMM case. When an optical filter, centered at 580 nm and having a 25-nm bandwidth, was used to slice each supercontinuum, the output was in the form of a single peak and did not exhibit any noisy structure.

Several other factors can improve the coherence of a supercontinuum. Suitable chirping of input pulse was found to help in one study [150]. It was found in another study that coherence is also affected by the quality of compressed input pulses when pulse compression is employed to reduce their width [151]. The use of a large-mode-area fiber

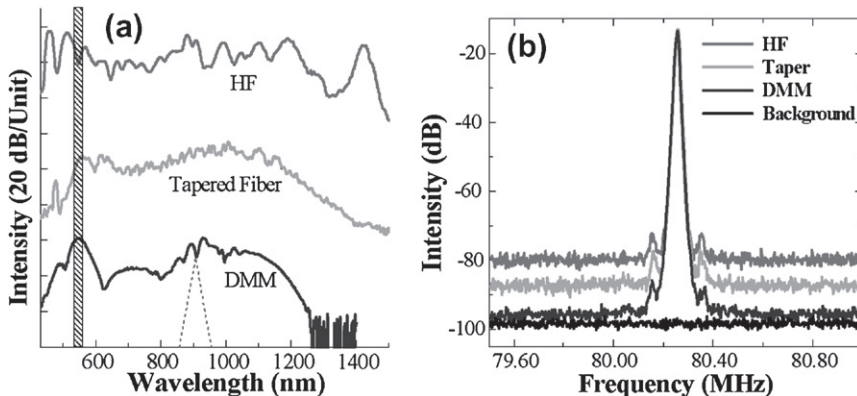


**Figure 13.33** Comparison of (a) output spectra and (b) intensity noise spectra for three types of fibers described in the text. The vertical bar in part (a) shows the portion that was filtered optically. (After Ref. [149]; © 2005 OSA.)

for pulse compression was found to improve the supercontinuum coherence by as much as a 10 dB because of the reduced nonlinear effects inside this fiber. The use of metal-coated hollow-core fiber was suggested in a 2009 study, where the onset of plasma was found to improve the supercontinuum coherence [153]. The use of short femtosecond pulses launched with relatively low values of the soliton order ( $N < 10$ ) also helps [5].

The origin of coherence degradation is generally related to the fission of higher-order solitons, a process that is very sensitive to small variations in the widths and peak powers associated with the input pulses [38]. It follows that the supercontinuum coherence should improve dramatically if input pulses are launched in the normal-GVD regime of a fiber where solitons cannot form. Indeed, this feature was predicted as early as 2005 in a PCF exhibiting two ZDWLs that was tapered along its length to ensure that optical pulses always experienced normal dispersion [148]. However, the resulting supercontinuum was not very broad and its bandwidth was limited to below 400 nm for pulses propagating in the normal-GVD region of a fiber. The problem was solved by 2011, and broadband supercontinua were generated with this approach by using PCFs whose dispersion was suitably tailored.

Two PCFs employed in one 2011 study were designed such that they exhibited normal dispersion over a wavelength region that extended from 400 to beyond 1500 nm [154]. The most important feature of these fibers was that femtosecond pulses launched into them did not spread too much in spite of experiencing normal dispersion inside them. Figure 13.34a shows the broadband spectra observed at the output of a 50-cm-long PCF fabricated with a 2.3- $\mu\text{m}$ -diameter core when it was pumped at a wavelength of 1050 nm with 50-fs pulses of energies ranging from 0.25 to 7.8 nJ. Figure 13.34b

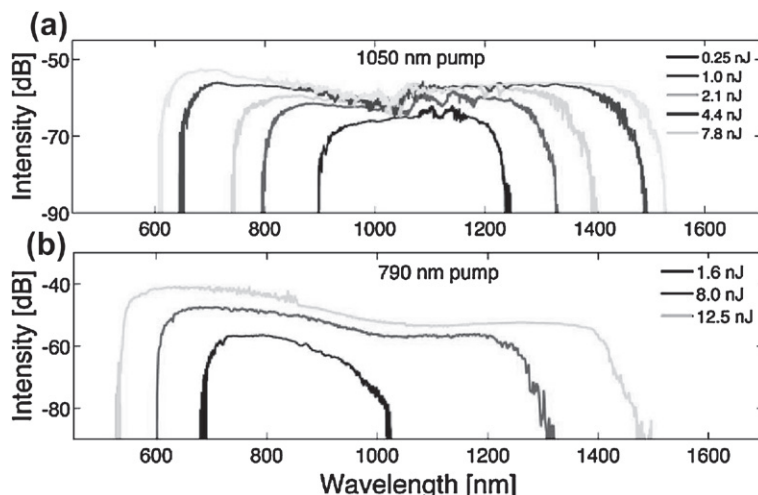


**Figure 13.34** (a) Optical spectra observed at the output of a 50-cm-long PCF when it was pumped at a wavelength of 1050 nm with 50-fs pulses of energies ranging from 0.25 to 7.8 nJ. (b) Output spectra when the same PCF was pumped at 790 nm. (After Ref. [154]; © 2011 OSA.)

shows the output spectra when the same PCF was pumped at 790 nm. In both cases, the supercontinua extend over a bandwidth close to 800 nm at the highest pulse energy and are relatively flat and smooth compared to those formed in the anomalous-GVD region.

A similar PCF design was used in another 2011 study [155]. It exhibited normal dispersion over a wide wavelength region with a minimum occurring near 1064 nm, the wavelength at which 400-fs input pulses were launched. The output spectrum at the end of a 4-cm-long piece of such a fiber exhibited a shape that is typical of SPM (see Figure 4.2). When the fiber was 1 m long, the supercontinuum extended over 800 nm and its shape was relatively flat and smooth. Moreover, the output was compressible to a duration of 26 fs and exhibited a high degree of coherence between its spectral components. Such a coherent supercontinuum is useful for a variety of applications including biomedical imaging.

### 13.6.3 Spectral Incoherent Solitons

As we saw in Section 13.5, the mechanism of supercontinuum generation does not involve soliton fission in the case of CW or quasi-CW pumping. Rather, a multitude of fundamental solitons of different widths are created directly through modulation instability. It is not surprising that the coherence properties of resulting supercontinua would be different than those seen in Figure 13.31. Indeed, recent studies show that incoherence results through a process of thermalization that leads to the formation of a new kind of spectral incoherent soliton [156–161].

Spectral incoherent solitons were discovered in 2008 in a numerical study that solved a simpler version of the generalized NLS Eq. (13.3.1) by including only the  $\beta_2$  dispersion term [156]. Such solitons are different from those of Chapter 5 in the sense that they exhibit confinement only in the spectral domain (and not in the time domain). They are also incoherent in the sense that they represent nonequilibrium stable states of an incoherent field. Their existence requires SRS because a finite nonlinear response time is essential for their formation.

Spectral incoherent solitons were first observed in a 2009 experiment through supercontinuum generation inside a PCF exhibiting two ZDWLs near 1033 and 1209 nm [158]. Figure 13.35 shows these optical spectra observed (a) as a function of fiber length ( $P_0 = 3.5$  kW) and (c) as a function of input peak power  $P_0$  (length 40 m) when the PCF was pumped using Q-switched pulses at 1064 nm. In part (a) we notice that pulse spectrum broadens rapidly on both sides of the input spectrum within the first few meters of the PCF and it stops broadening on the high-frequency side after 5 m or so. In contrast, because of the RIFS, the spectrum keeps broadening on the high-frequency (or Stokes) side, and it develops a distinct peak with a red shift of about 100 THz. This peak, marked by S in parts (b) and (d), represents the formation of a spectral incoherent soliton through thermalization of the optical field. This interpretation is supported by the numerical predictions of Eq. (13.3.1) for the PCF used in the experiment.

It should be stressed that the incoherent regime seen in Figure 13.35 is quite distinct from the coherent regime studied in Section 13.4 even though CW or quasi-CW

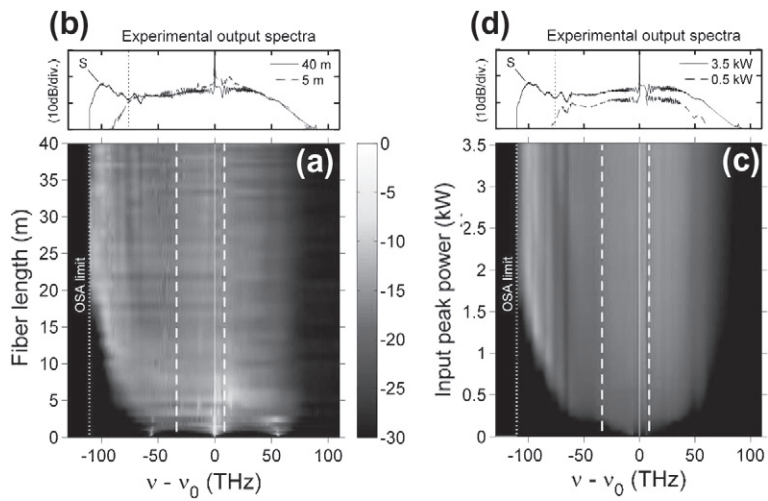


**Figure 13.35** (a) Output spectra (a) as a function of the fiber length ( $P_0 = 3.5$  kW) and (c) as a function of the input peak power  $P_0$  (length 40 m) when a PCF was pumped using Q-switched pulses at 1064 nm; (b) and (d) show selected spectra with S marking a spectral incoherent soliton. Vertical dashed lines show the two ZDWLs of the fiber. (After Ref. [158]; © 2009 OSA.)

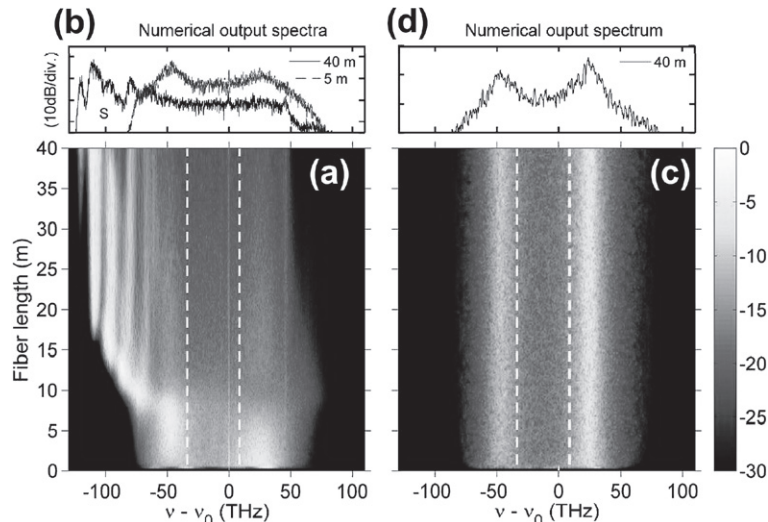


**Figure 13.36** (a) Numerical evolution of a supercontinuum along the fiber length for a 60-ps Gaussian input pulse ( $P_0 = 3.5$  kW) for the same PCF used for Figure 13.35. (b) Spectra at distances of 5 and 40 m; S indicates a spectral incoherent soliton. (c) Same as (a) but without the Raman and self-steepening effects. (d) Two-peak spectrum at a distance of 40 m. Vertical dashed lines show the two ZDWLs of the fiber. (After Ref. [158]; © 2009 OSA.)

pumping is used in both cases. The incoherent regime requires much higher input power levels, resulting in much larger fluctuations in the pulse train generated through the onset of modulation instability. As a result, the optical field exhibits turbulent dynamics in which solitons do not play a significant role [157]. In practice, it also requires fibers with two ZDWLs that are not too far apart. Spectral broadening is then dominated by a thermalization process that produces a symmetric two-peak supercontinuum, shown on the right in Figure 13.36, when Eq. (13.3.1) is solved for a noisy CW beam without including the Raman and self-steepening effects [158]. The inclusion of these two effects results in a much wider, asymmetric supercontinuum, shown on the left in Figure 13.36, for 60-ps Gaussian input pulses. On the low-frequency side, a distinct spectral peak appears that corresponds to a spectral incoherent soliton.

The two-peak spectrum seen in part (c) Figure 13.36 is a specific signature of the thermalization process, as verified using thermodynamic arguments based on the kinetic wave theory [157]. Inclusion of the Raman effect modifies this spectrum considerably by transferring energy from the blue peak to the Raman peak, as seen in part (a). At the same time, a spectral incoherent soliton is generated whose spectrum is not fully separated from the two-peak structure seen in part (b). The experimental results in Figure 13.35b exhibit a similar feature. A more systematic study of spectral incoherent solitons was carried out in 2011, both experimentally and numerically [161]. The experiment employed a 21-m-long PCF exhibiting two ZDWLs near 910 and 1152 nm with  $\beta_2 = -3.5 \text{ ps}^2/\text{km}$  at the 1064-nm pump wavelength. The supercontinuum observed at the end of the fiber at a peak power of 1.32 kW exhibited features similar to those seen in Figure 13.35b except that a 3-peak structure similar to that seen in Figure 13.36b was observed on its low-frequency edge. Such a structure can be interpreted as a “discrete” spectral incoherent soliton consisting of a central peak with two side bands shifted by the Raman shift of about 13 THz [160]. Numerical simulations confirm that such a three-peak spectrum shifts toward the red side during propagation while keeping its internal structure intact. It should be stressed that research on spectral incoherent solitons is still in its infancy and much remains to be done to fully understand the incoherent regime of supercontinuum formation.

---

## 13.7 OPTICAL ROGUE WAVES

The same pulse-to-pulse fluctuations that degrade the coherence of a supercontinuum inside optical fibers have recently been found to give rise to an optical analog of oceanic rogue (or freak) waves—rare but giant water waves that can form in oceans [162–164]. Such waves are characterized by their “L-shaped” statistics, reflecting the fact that most waves have small amplitudes, but waves with very high amplitudes can also form albeit with a relatively small probability. This section focuses on optical rogue waves observed in the context of a supercontinuum.

### 13.7.1 L-Shaped Statistics of Pulse-to-Pulse Fluctuations

The term “optical rogue waves” was coined in 2007 by Solli et al., who found that pulse-to-pulse fluctuations during supercontinuum formation inside optical fibers can give rise to the L-shaped statistics that are a signature of oceanic rogue waves [165]. More precisely, the measured statistics of supercontinua generated with picosecond pulses provided experimental evidence of rare “rogue” output pulses with much higher intensities and much larger Raman-induced spectral shifts compared with most other input pulses. This experiment led to a flurry of activity in the emerging area of optical rogue waves [166–177].

The generalized NLS Eq. (13.3.1), used in this chapter for explaining supercontinuum formation, can produce the L-shaped statistics of optical rogue waves, provided this equation is solved multiple times for a noisy input pulse. Figure 13.37a shows calculated optical spectra when 5-ps Gaussian pulses at a wavelength of 1060 nm are launched into a 20-m-long PCF with its ZDWL at 1055 nm [166]. Dispersion terms up to the tenth order were included using  $\gamma = 15 \text{ W}^{-1}/\text{km}$  for the nonlinear parameter and an average peak power  $P_0 = 100 \text{ W}$ , resulting in a nonlinear length of about 67 cm. As the dispersion length was close to 22 km, the soliton order in these simulations is relatively large ( $N \sim 180$ ). One can see in Figure 13.37a that spectral power at any wavelength can fluctuate by 20 dB (a factor 100) or more even when only quantum noise of the input pulse is included in the frequency domain by adding one photon per frequency bin. Part (b) shows an expanded view of such fluctuations in the long-wavelength region that corresponds to the spectrum of the shortest Raman soliton.

To characterize power fluctuations in this long-wavelength region, the shortest Raman soliton was isolated by filtering the output spectrum so that it only contained wavelengths  $> 1210 \text{ nm}$ . The peak power of the resulting optical pulse was

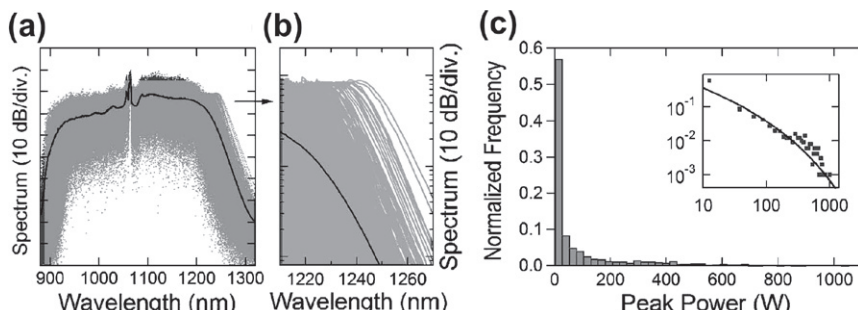


**Figure 13.37** (a) Simulated supercontinua at the end of a 20-m-long fiber for 1000 samples of noisy 5-ps Gaussian pulses (superimposed gray curves); black curve represents the mean spectrum. (b) Expanded view at wavelengths above 1210 nm. (c) Histogram of the peak power (bin size 25 W) of the shortest Raman soliton; the inset plots the same data on a log-log scale. (After Ref. [166]; © 2008 OSA.)

then used to generate the histogram seen in Figure 13.37c using a bin size of 25 W. One can see clearly the L-shape statistics associated with rogue waves; the fraction of high-power Raman solitons is extremely small. In particular, the peak power of the shortest Raman soliton exceeds 1 kW only once out of an ensemble of 1000 pulses. The log–log plot of the same histogram is shown as an inset in Figure 13.37c. The solid line corresponds to a Weibull distribution, used commonly to analyze events associated with large deviations from the mean and the median [178]. The L-shaped statistics of peak-power fluctuations were also observed in two experiments performed with picosecond optical pulses [165,169]. The use of pulses is not a requirement. Optical rogue waves appear even when CW pumping is used to generate a supercontinuum [171], and their origin lies in the spontaneous, or noise-induced, modulation instability.

### 13.7.2 Techniques for Controlling Rogue-Wave Statistics

As large fluctuations of optical rogue waves are undesirable from a practical standpoint, one may ask whether it is possible to control such fluctuations through external means. It was found numerically in a 2008 study that rogue-wave generation could be enhanced considerably when the temporal profile of the input pulse was modulated weakly at terahertz frequencies. It was also found that optical rogue waves can be nearly suppressed by placing multiple optical filters along the fibers whose passbands were shifted from each other appropriately (the so-called sliding-frequency filters).

The active control of optical rogue waves was demonstrated in a 2008 experiment in which picosecond pump pulses were launched into a fiber together with seed pulses at a different wavelength [167]. This technique makes use of the fact that modulation instability is the mechanism that initiates supercontinuum generation in the case of relatively long pulses (see Section 13.4). In the absence of a seed pulse, *spontaneous* modulation instability is initiated by the noise components at the frequencies  $\omega_0 \pm \Omega_{\max}$ , where  $\omega_0$  is the carrier frequency of the pump pulse and  $\Omega_{\max}$  is the frequency given in Eq. (13.4.1) at which the gain of modulation instability becomes maximum. The role of the seed pulse is to provide an input that seeds the process of *induced* modulation instability at its own frequency (and thus avoids noise seeding). In the experiment, 3.7-ps pump pulses at 1550 nm were launched into a 15-m-long highly nonlinear fiber together with seed pulses at 1630 nm. It was necessary to control the relative delay between the pump and probe pulses for a proper seeding of the modulation instability.

The results showed that a supercontinuum could be generated at much lower pump power levels when the seed pulse was present. This is expected from the theory of Section 5.1 and follows from the fact that the amplitude of a seed pulse is pulse larger than a typical noise amplitude. Moreover, since the seed amplitude exhibits much less fluctuations, the resulting supercontinuum is much less noisy and much more coherent. In particular, it does not exhibit extreme low-probability

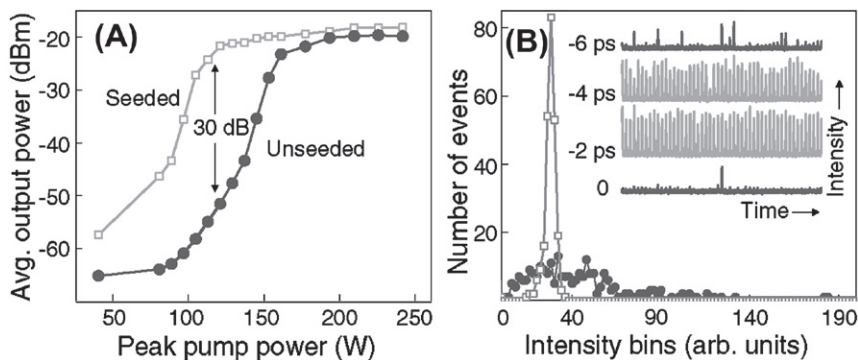


**Figure 13.38** (A) Average output power (within the 10-nm bandwidth of an optical filter centered at 1685 nm) as a function of peak power  $P_0$  of pump pulses with and without a seed pulse. (B) Comparison of rogue-wave statistics in the seeded (rectangles) and unseeded (circles) cases. The insets show the filtered pulse trains for four seed-pulse delays with respect to the pump pulse. (After Ref. [167]; © 2008 American Physical Society.)

events that give rise to optical rogue waves. Figure 13.38 summarizes the experimental results by showing (a) the average power within the 10-nm bandwidth at 1685 nm as a function of peak power  $P_0$  of pump pulses and (b) the comparison of rogue-wave statistics in the seeded ( $P_0 = 130$  W) and unseeded ( $P_0 = 200$  W) cases [167]. The average power of the shortest Raman soliton (most red-shifted part of the supercontinuum) at a given  $P_0$  increases by as much as 30 dB when the seed pulse is present. At the same time, the probability distribution narrows down considerably because of the absence of the rogue-wave events. Interferometric measurements reveal that the supercontinuum becomes much more coherent in the case of external seed pulses. In a 2010 experiment, the pump and seed pulses were obtained from the same optical parametric oscillator, and the resulting supercontinuum exhibited considerable reduction in the amount of seeding-induced noise reduction [176].

Pulse-to-pulse fluctuations in a supercontinuum can also be controlled through a suitable design of the fiber used to produce it. In a 2010 experiment, a significant reduction in power fluctuations was observed for the shortest Raman soliton, whose spectrum is red-shifted the most [177]. This reduction was possible because the experiment employed a solid-core, photonic-bandgap fiber exhibiting a stop band whose one edge was located near 1600 nm. Because of this feature, the red shift of the shortest soliton was nearly halted as it approached the stop-band edge. It turned out that the resulting statistics of peak-power fluctuations was modified such that it changed from an L-shape distribution (expected in the absence of the stop band) to a narrow Gaussian one.

In another 2010 experiment, it was discovered that pulse-to-pulse fluctuations were reduced considerably when the PCF used for supercontinuum generation was tapered suitably along its length [119]. When a 150-m-long PCF with uniform diameter was used with 600-ps pulses at 1064 nm, the statistics of power fluctuations

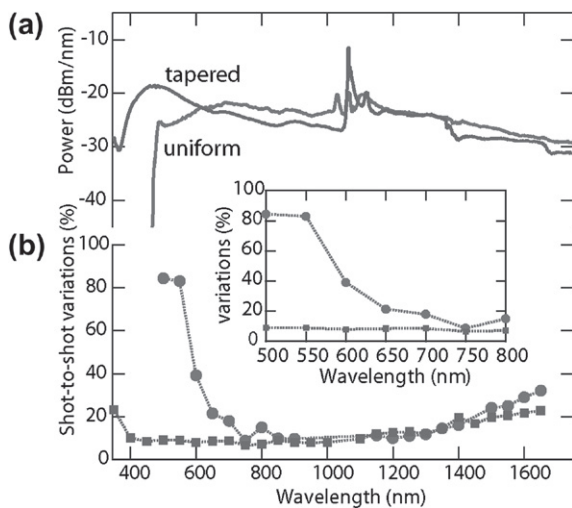


**Figure 13.39** (a) Output spectra and (b) wavelength dependence of shot-to-shot power variations for the uniform and tapered fibers. The inset shows a magnified view of the visible region. (After Ref. [119]; © 2010 OSA.)

was different in different spectral regions of the supercontinuum. In particular, the L-shaped statistics were observed only at its extreme edges located near 650 and 1650 nm. In the case of a PCF consisting of a 8-m-long uniform section, followed with a 7-m-long tapered section where the outer diameter decreased from 160 to 65  $\mu\text{m}$  in a nearly linear fashion, power fluctuations were relatively low ( $\sim 10\%$ ) along the entire bandwidth of the supercontinuum. Figure 13.39 shows (a) the output spectra together with (b) the wavelength dependence of shot-to-shot power variations for the two fibers. These results indicate that the dispersive properties of the fiber affect the statistics of power fluctuations considerably, especially at the two edges of the supercontinuum where  $|\beta_2|$  becomes relatively large in the case of a constant-diameter fiber. Tapering of the PCF allows  $|\beta_2|$  to be adjusted along the fiber length.

### 13.7.3 Modulation Instability Revisited

Optical rogue waves can appear in the context of several other nonlinear processes including Raman amplification [168] and FWM [170]. So, it is natural to ask if there is a common underlying origin of such waves. It appears that any nonlinear mechanism that exhibits optical gain and can transfer power from a pump wave to noise at a frequency within the gain bandwidth may give rise to optical rogue waves. In this subsection we focus on the phenomenon of modulation instability (related to FWM). The recent work of Akhmediev et al. is noteworthy in this context [179–184]. It has led to a connection of optical rogue waves with the periodic and algebraic solutions of the NLS equation.

As discussed in Section 5.1.1, the CW solution of the NLS equation is unstable in the region of anomalous dispersion ( $\beta_2 < 0$ ) because of modulation instability. The analysis in that section was limited to the linear regime in which any periodic modulation of the CW state is amplified exponentially with the gain given in Eq. (5.1.8). Clearly, such a growth cannot continue forever and is eventually limited by the nonlinear effects. It was discovered in 1986 that the NLS equation has a family of periodic solutions that describe this nonlinear regime analytically [185]. Such solutions of the NLS equation (5.1.1) are called *Akhmediev breathers* and can be written in the form [182]

$$A(z, T) = \sqrt{P_0} e^{i\xi} \left[ \frac{(1 - 4a) \cosh(b\xi) + ib \sinh(b\xi) + \sqrt{2a} \cos(\Omega T)}{\sqrt{2a} \cos(\Omega T) - \cosh(b\xi)} \right], \quad (13.7.1)$$

where  $\Omega$  is the modulation frequency,  $\xi = (z - z_c)/L_{\text{NL}}$ , and  $L_{\text{NL}} = 1/(\gamma P_0)$  is the nonlinear length. The parameters  $a$  and  $b$  are defined as

$$a = \frac{1}{2}[1 - (\Omega/\Omega_c)^2], \quad b = \sqrt{8a(1 - 2a)}, \quad (13.7.2)$$

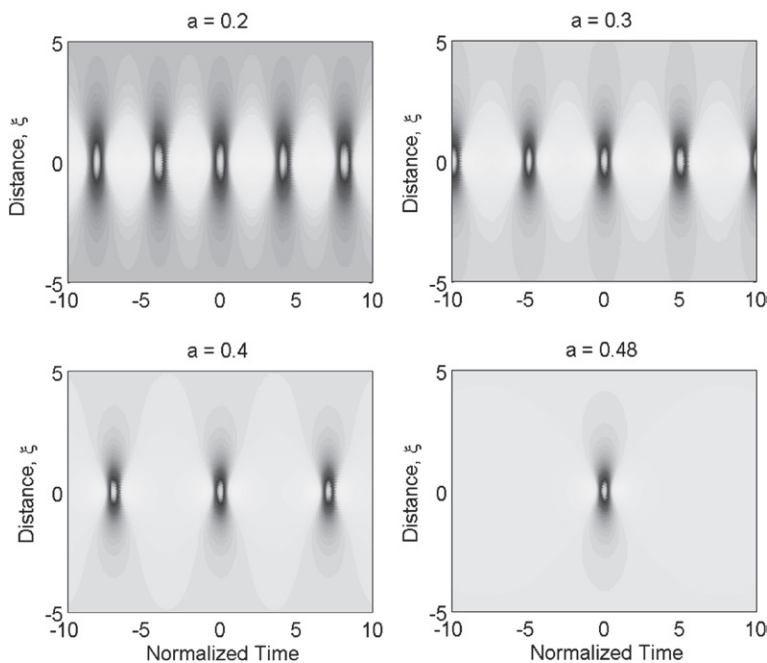


**Figure 13.40** Surface plots of the periodic solution  $|A|^2$  as a function of  $\xi$  and  $\Omega_{\max}T$  for four values of  $a$ . Only a single pulse is within the plotting region for  $a=0.48$ .

where  $\Omega_c$  is the critical modulation frequency given in Eq. (5.1.7). Physically,  $a$  governs the range of modulation frequencies that can experience the modulation-instability gain, and  $b$  is a measure of that gain. Notice that values of  $a$  are limited to the range  $0 < a < \frac{1}{2}$ .

It is easy to see that Eq. (13.7.1) describes a solution  $|A(z, T)|^2$  that is periodic in time, and is also confined spatially in  $z$  such that each pulse peaks at  $z = z_c$ . Figure 13.40 shows such a pulse train by plotting  $|A|^2/P_0$  as a function of  $\xi$  and  $\Omega_{\max}T$  for four values of  $a$ , where  $\Omega_{\max} = \Omega_c/\sqrt{2}$  is the frequency at which the modulation-instability gain becomes maximum. As  $a$  increases toward its limiting value of  $\frac{1}{2}$ , the duration between neighboring pulses increases, and each pulse in the pulse train becomes shorter. As seen in Figure 13.40, only a single pulse appears within the plotting region for  $a = 0.48$  because of a relatively large spacing between two neighboring pulses. In the limit  $a = \frac{1}{2}$ , the pulse train reduces to a single pulse that is localized in both the  $z$  and  $T$  dimensions. This solution was discovered in the 1980s in the form of an algebraic solution of the NLS equation [186] and is known as the *Peregrine soliton*:

$$A(z, T) = \sqrt{P_0} e^{i\xi} \left[ 1 - \frac{4(1 + 2i\xi)}{1 + (\Omega_c T)^2 + 4\xi^2} \right]. \quad (13.7.3)$$

To see how the Peregrine soliton is related to the periodic solution in Eq. (13.7.1), we note from Eq. (13.7.1) that individual pulses in the periodic pulse train are most compressed at  $z = z_c$  for all values of  $a$ . The power,  $P_c(T) = |A(z_c, T)|^2$  at this point is obtained by setting  $\xi = 0$  in this equation, resulting in

$$P_c(T) = P_0 \left[ \frac{(1 - 4a) + \sqrt{2a} \cos(\Omega T)}{1 - \sqrt{2a} \cos(\Omega T)} \right]^2. \quad (13.7.4)$$

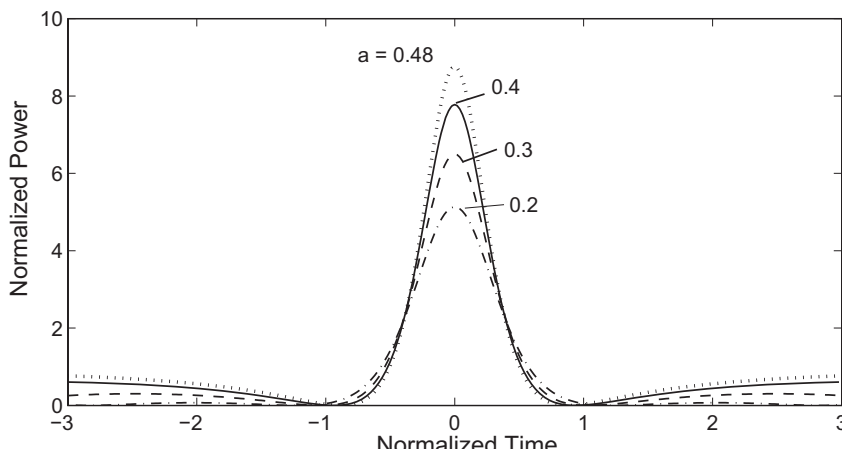


**Figure 13.41** Pulse shapes for the same four values of  $a$  used in Figure 13.40. The dotted curve for  $a=0.48$  is close to the shape of the Peregrine soliton.

[Figure 13.41](#) shows changes in the pulse shape by plotting  $P_c(T)$  for the same four values of  $a$  used in [Figure 13.40](#). The dotted curve for  $a = 0.48$  is almost identical to the shape of the Peregrine soliton obtained using Eq. (13.7.3) with  $\xi = 0$ . This type of pulse shape was observed in a 2010 experiment in which a suitably modulated CW field was transmitted through a 900-m-long highly nonlinear fiber [187]. Because of its connection to Akhmediev breathers and the Peregrine soliton, modulation instability is attracting renewed attention [187–191].

The existence of the Peregrine soliton can be used to understand the origin of optical rogue waves when modulation instability is seeded with noise (the so-called spontaneous modulation instability). As a noise component at any frequency falling within the gain spectrum of modulation instability can be amplified, the parameter  $a$  can take any value in its range  $0 < a < \frac{1}{2}$ . The shortest and most intense pulses are formed when  $a$  is close to  $\frac{1}{2}$ , but the probability of the formation of such pulses is relatively small because the instability gain is reduced considerably as  $a \rightarrow \frac{1}{2}$ . As seen in [Figure 13.41](#), the peak power of the pulse is nearly 9 times of the input CW power in this limit. The width of the shortest Peregrine soliton, occurring at  $\xi = 0$ , can be estimated from Eq. (13.7.4) and is found to be

$$T_s \approx 1/\Omega_c = \frac{1}{2} \sqrt{|\beta_2| L_{NL}}. \quad (13.7.5)$$

As an example, if we use  $\beta_2 = -0.1 \text{ ps}^2/\text{km}$  and  $L_{NL} = 1 \text{ m}$  as typical values,  $T_s = 5 \text{ fs}$ . This value indicates that noise-induced modulation instability converts a CW beam into a random pulse train whose widths can vary over a wide range, with some pulses being shorter than 10 fs. Most of these pulses propagate as fundamental solitons and generate dispersive waves as solitons are perturbed by third-order dispersions. At the same time, their spectra shift toward longer wavelengths, the shortest soliton shifting the most. These two processes broaden the narrow input spectrum by a large factor, and the output spectrum is in the form of a supercontinuum. This reasoning suggests that the supercontinuum formation in the case of CW or quasi-CW pumping does not require the fission of higher-order solitons, the phenomenon that plays an essential role in the case of femtosecond pulses. The experimental work of Dudley et al. [182] also supports this interpretation.

A 2011 study introduced the concept higher-order modulation instability arising from a nonlinear superposition of first-order instabilities [191]. In this analysis, The use of multiple Darboux transformations led to successive splittings of each pulse in a periodic pulse train. The theoretical predictions agreed with the experiment and direct numerical simulations of the standard NLS equation. Third-order dispersion can also influence this process as its role is not negligible [188]. Clearly, modulation instability exhibits much richer dynamics when one goes beyond the linear stability analysis of Section 5.1.

---

## PROBLEMS

- 13.1** Consider a microstructured fiber whose cladding has large air holes. Calculate numerically  $\beta(\omega)$  in the wavelength range of  $0.4\text{--}2\,\mu\text{m}$  using  $n_1 = 1.45$ ,  $n_2 = 1$  and  $2.5\,\mu\text{m}$  for the core diameter. Use a polynomial fit to deduce dispersion parameters up to 8th order and use them to plot the second-, third-, and fourth-order dispersion parameters as a function of wavelength.
- 13.2** Write a computer code for solving Eq. (13.3.1) using  $M = 8$ . Include the nonlinear effects using  $R(t)$  given in Eq. (2.3.38) with  $f_R = 0.18$  but neglect losses. Use this code to study temporal and spectral evolution of a 100-fs pulse launched with 10-kW peak power along a 10-cm-long fiber with a  $2.5\,\mu\text{m}$  core diameter. Use values of dispersion parameters obtained in the preceding problem. You need to produce plots similar to those in Figure 13.14.
- 13.3** Use the code developed for the preceding problem to study the evolution of a 150-fs pulse launched with 10-kW peak power at 850 nm into a 10-cm-long fiber and reproduce plots shown in Figure 13.13. Use values of dispersion parameters given in Section 13.1.
- 13.4** Write a computer code for solving Eq. (13.3.1) in the frequency domain using Eq. (13.3.2) and verify that it provides the same results for the pulse shapes and spectra as in the preceding problem.
- 13.5** Employ Eq. (12.2.3) to calculate the spectrogram of the output field  $A(L, t)$  obtained in the preceding two problems using a 1-ps-wide Gaussian pulse for  $A_{\text{ref}}(t)$ . The spectrogram should appear similar to that in Figure 13.14. Calculate the wavelengths of various solitons and the dispersive wave seen in this spectrogram.
- 13.6** What is meant by XPM-induced trapping of dispersive waves in the context of supercontinuum generation? Do you see any evidence of this phenomenon in the spectrogram obtained in the preceding problem?
- 13.7** Explain why a supercontinuum can be produced even by launching a CW beam into a highly nonlinear fiber. Discuss all nonlinear processes involved in this situation. Does soliton fission play a role in the CW case? Justify your answer.
- 13.8** Read Ref. [103] and reproduce the spectrogram given in Figure 6 of that paper. Explain what is happening to solitons whose wavelength exceeds 1800 nm.
- 13.9** What is meant by the coherence of a supercontinuum? Explain how such coherence is measured experimentally and calculated numerically. How can one improve coherence in practice?
- 13.10** What is an oceanic rogue wave? Explain why this concept can be applied to supercontinuum generation in optical fibers. How can such optical rogue waves be controlled through a suitable fiber design?

---

## REFERENCES

- [1] F. Shimizu, *Phys. Rev. Lett.* **19**, 1097 (1967).
- [2] R. R. Alfano and S. L. Shapiro, *Phys. Rev. Lett.* **24**, 584 (1970).
- [3] R. R. Alfano, Ed., *The Supercontinuum Laser Source*, 2nd ed. (Springer, 2006).
- [4] C. Lin and R. H. Stolen, *Appl. Phys. Lett.* **28**, 216 (1976).
- [5] J. M. Dudley, G. Genty, and S. Coen, *Rev. Mod. Phys.* **78**, 1135 (2006).
- [6] G. Genty, S. Coen, and J. M. Dudley, *J. Opt. Soc. Am. B* **24**, 1771 (2007).
- [7] J. M. Dudley and J. R. Taylor, *Supercontinuum Generation in Optical Fibers* (Cambridge University Press, 2010).
- [8] P. L. Baldeck and R. R. Alfano, *J. Lightwave Technol.* **5**, 1712 (1987).
- [9] B. Gross and J. T. Manassah, *J. Opt. Soc. Am. B* **9**, 1813 (1992).
- [10] P. Beaud, W. Hodel, B. Zysset, and H. P. Weber, *IEEE J. Quantum Electron.* **23**, 1938 (1987).
- [11] M. N. Islam, G. Sucha, I. Bar-Joseph, M. Wegener, J. P. Gordon, and D. S. Chemla, *J. Opt. Soc. Am. B* **6**, 1149 (1989).
- [12] I. Ilev, H. Kumagai, K. Toyoda, and I. Koprinkov, *Appl. Opt.* **35**, 2548 (1996).
- [13] T. Morioka, K. Mori, and M. Saruwatari, *Electron. Lett.* **29**, 862 (1993).
- [14] T. Morioka, K. Mori, S. Kawanishi, and M. Saruwatari, *IEEE Photon. Technol. Lett.* **6**, 365 (1994).
- [15] T. Morioka, K. Uchiyama, S. Kawanishi, S. Suzuki, and M. Saruwatari, *Electron. Lett.* **31**, 1064 (1995).
- [16] T. Morioka, K. Okamoto, M. Ishiiki, and M. Saruwatari, *Electron. Lett.* **32**, 836 (1997).
- [17] S. Kawanishi, H. Takara, K. Uchiyama, I. Shake, O. Kamatani, and H. Takahashi, *Electron. Lett.* **33**, 1716 (1997).
- [18] K. Mori, H. Takara, S. Kawanishi, M. Saruwatari, and T. Morioka, *Electron. Lett.* **33**, 1806 (1997).
- [19] T. Okuno, M. Onishi, and M. Nishimura, *IEEE Photon. Technol. Lett.* **10**, 72 (1998).
- [20] M. Sotobayashi and K. Kitayama, *Electron. Lett.* **34**, 1336 (1998).
- [21] Y. Takushima, F. Futami, and K. Kikuchi, *IEEE Photon. Technol. Lett.* **10**, 1560 (1998).
- [22] Y. Takushima and K. Kikuchi, *IEEE Photon. Technol. Lett.* **11**, 324 (1999).
- [23] E. Yamada, H. Takara, T. Ohara, et al., *Electron. Lett.* **37**, 304 (2001).
- [24] K. Takada, M. Abe, T. Shibata, and T. Okamoto, *Electron. Lett.* **38**, 572 (2002).
- [25] K. Mori, K. Sato, H. Takara, and T. Ohara, *Electron. Lett.* **39**, 544 (2003).
- [26] Ö. Boyraz, J. Kim, M. N. Islam, F. Copfinger, and B. Jalali, *J. Lightwave Technol.* **18**, 2167 (2000).
- [27] S. Coen, A. H. L. Chau, R. Leonhardt, et al., *J. Opt. Soc. Am. B* **19**, 753 (2002).
- [28] A. B. Rulkov, M. Y. Vyatkin, A. B. Rulkov, M. Y. Vyatkin, and V. P. Gapontsev, *Opt. Express* **13**, 377 (2005).
- [29] J. Teipel, D. Türke, H. Giessen, A. Zintl, and B. Braun, *Opt. Express* **13**, 1734 (2005).
- [30] A. Kudlinski, A. K. George, J. C. Knight, et al., *Opt. Express* **14**, 5715 (2006).
- [31] A. Roy, P. Leproux, P. Roy, J.-L. Augste, and V. Couderc, *J. Opt. Soc. Am. B* **24**, 788 (2007).
- [32] K. K. Chen, S. Alam, J. H. V. Price, et al., *Opt. Express* **18**, 5426 (2010).
- [33] J. K. Ranka, R. S. Windeler, and A. J. Stentz, *Opt. Lett.* **25**, 25 (2000).
- [34] T. A. Birks, W. J. Wadsworth, and P. St. J. Russell, *Opt. Lett.* **25**, 1415 (2000).
- [35] A. V. Husakou and J. Herrmann, *Phys. Rev. Lett.* **87**, 203901 (2001).
- [36] J. Herrmann, U. Griebner, and N. Zhavoronkov, *Phys. Rev. Lett.* **88**, 173901 (2002).

- [37] J. M. Dudley, L. Provino, N. Grossard, et al., *J. Opt. Soc. Am. B* **19**, 765 (2002).
- [38] J. M. Dudley and S. Coen, *IEEE J. Sel. Topics Quantum Electron.* **8**, 651 (2002).
- [39] A. V. Husakou and J. Herrmann, *J. Opt. Soc. Am. B* **19**, 2171 (2002).
- [40] A. L. Gaeta, *Opt. Lett.* **27**, 924 (2002).
- [41] B. R. Washburn, S. E. Ralph, and R. S. Windeler, *Opt. Express* **10**, 575 (2002).
- [42] G. Genty, M. Lehtonen, H. Ludvigsen, J. Broeng, and M. Kaivola, *Opt. Express* **10**, 1083 (2002).
- [43] J. H. V. Price, W. Belardi, T. M. Monro, A. Malinowski, A. Piper, and D. J. Richardson, *Opt. Express* **10**, 382 (2002).
- [44] J. M. Harbold, F. Ö. Ilday, F. W. Wise, et al., *Opt. Lett.* **27**, 1558 (2002).
- [45] A. Apolonski, B. Povazay, A. Unterhuber, et al., *J. Opt. Soc. Am. B* **19**, 2165 (2002).
- [46] A. Ortigosa-Blanch, J. C. Knight, and P. St. J. Russell, *J. Opt. Soc. Am. B* **19**, 2567 (2002).
- [47] X. Fang, N. Karasawa, R. Morita, R. S. Windeler, and M. Yamashita, *IEEE Photon. Technol. Lett.* **15**, 233 (2003).
- [48] J. W. Nicholson, M. F. Yan, P. Wisk, et al., *Opt. Lett.* **28**, 643 (2003).
- [49] K. M. Hilligsoe, H. N. Paulsen, J. Thogersen, S. R. Keiding, and J. J. Larsen, *J. Opt. Soc. Am. B* **20**, 1887 (2003).
- [50] T. Hori, J. Takayanagi, N. Nishizawa, and T. Goto, *Opt. Express* **12**, 317 (2004).
- [51] K. Sakamaki, M. Nakao, M. Naganuma, and M. Izutsu, *IEEE J. Sel. Topics Quantum Electron.* **10**, 976 (2004).
- [52] J. Takayanagi, N. Nishizawa, H. Nagai, M. Yoshida, and T. Goto, *IEEE Photon. Technol. Lett.* **17**, 37 (2005).
- [53] R. R. Gattass, G. T. Svacha, L. Tong, and E. Mazur, *Opt. Express* **14**, 9408 (2006).
- [54] S. P. Stark, A. Podlipensky, N. Y. Joly, and P. St. J. Russell, *J. Opt. Soc. Am. B* **27**, 592 (2010).
- [55] J. Y. Y. Leong, P. Petropoulos, J. H. V. Price, et al., *J. Lightwave Technol.* **24**, 183 (2006).
- [56] H. Hundertmark, D. Kracht, D. Wandt, et al., *Opt. Express* **11**, 3196 (2003).
- [57] J. T. Gopinath, H. M. Shen, H. Sotobayashi, et al., *Opt. Express* **12**, 5697 (2004).
- [58] F. G. Omenetto, N. A. Wolchover, M. R. Wehner, et al., *Opt. Express* **14**, 4928 (2006).
- [59] C. Xia, M. Kumar, O. P. Kulkarni, et al., *Opt. Lett.* **31**, 2553 (2006).
- [60] C. Xia, M. Kumar, M. Y. Cheng, et al., *Opt. Express* **15**, 865 (2007).
- [61] J. H. V. Price, T. M. Monro, H. Ebendorff-Heidebreim, et al., *IEEE J. Sel. Topics Quantum Electron.* **13**, 750 (2007).
- [62] P. Domachuk, N. A. Wolchover, M. Cronin-Golomb, et al., *Opt. Express* **16**, 7161 (2008).
- [63] X. Feng, W. H. Loh, J. C. Flanagan, et al., *Opt. Express* **16**, 13651 (2008).
- [64] D. I. Yeom, E. C. Mägi, M. R. E. Lamont, et al., *Opt. Lett.* **33**, 660 (2008).
- [65] C. N. Xia, Z. Xu, M. N. Islam, et al., *IEEE J. Sel. Topics Quantum Electron.* **15**, 422 (2009).
- [66] H. Hundertmark, S. Rammler, T. Wilken, R. Holzwarth, T. W. Hänsch, and P. St. J. Russell, *Opt. Express* **17**, 1919 (2009).
- [67] M. S. Liao, C. Chaudhari, G. S. Qin, et al., *Opt. Express* **17**, 12174 (2009).
- [68] G. Qin, X. Yan, C. Kito, et al., *Appl. Phys. Lett.* **95**, 161103 (2009).
- [69] D. D. Hudson, S. A. Dekker, E. C. Mägi, et al., *Opt. Lett.* **36**, 1122 (2011).
- [70] B. Kibler, J. M. Dudley, and S. Coen, *Appl. Phys. B* **81**, 337 (2005).
- [71] N. Akhmediev and M. Karlsson, *Phys. Rev. A* **51**, 2602 (1995).

- [72] N. Nishizawa and T. Goto, *Opt. Lett.* **27**, 152 (2002); *Opt. Express* **10**, 1151 (2002).
- [73] J. Dudley, X. Gu, L. Xu, et al., *Opt. Express* **10**, 1215 (2002).
- [74] T. Hori, N. Nishizawa, T. Goto, and M. Yoshida, *J. Opt. Soc. Am. B* **20**, 2410 (2003).
- [75] T. Hori, N. Nishizawa, T. Goto, and M. Yoshida, *J. Opt. Soc. Am. B* **21**, 1969 (2004).
- [76] L. Tartara, I. Cristiani, and V. Degiorgio, *Appl. Phys. B* **77**, 307 (2003).
- [77] G. Genty, M. Lehtonen, and H. Ludvigsen, *Opt. Express* **12**, 4614 (2004).
- [78] M. H. Frosz, P. Falk, and O. Bang, *Opt. Express* **13**, 6181 (2005).
- [79] P. A. Champert, V. Couderc, P. Leproux, et al., *Opt. Express* **12**, 4366 (2004).
- [80] S. O. Konorov, A. A. Ivanov, D. A. Akimov, et al., *New J. Phys.* **6**, 182 (2004).
- [81] G. Genty, M. Lehtonen, and H. Ludvigsen, *Opt. Lett.* **30**, 756 (2005).
- [82] C. Cheng, X. Wang, Z. Fang, and B. Shen, *Appl. Phys. B* **80**, 291 (2005).
- [83] T. Schreiber, T. Andersen, D. Schimpf, J. Limpert, and A. Tünnermann, *Opt. Express* **13**, 9556 (2005).
- [84] A. V. Gorbach and D. V. Skryabin, *Phys. Rev. A* **76**, 053803 (2007).
- [85] J. C. Travers and J. R. Taylor, *Opt. Lett.* **34**, 115 (2009).
- [86] A. C. Judge, O. Bang, and C. M. de Sterke, *J. Opt. Soc. Am. B* **27**, 2195 (2010).
- [87] S. Roy, S. K. Bhadra, K. Saitoh, M. Koshiba, and G. P. Agrawal, *Opt. Express* **19**, 10443 (2011).
- [88] A. Efimov, A. J. Taylor, F. G. Omenetto, et al., *Opt. Express* **12**, 6498 (2004).
- [89] A. Efimov, A. V. Yulin, D. V. Skryabin, et al., *Phys. Rev. Lett.* **95**, 213902 (2005).
- [90] D. V. Skryabin and A. V. Yulin, *Phys. Rev. E* **72**, 016619 (2005).
- [91] A. V. Gorbach, D. V. Skryabin, J. M. Stone, and J. C. Knight, *Opt. Express* **14**, 9854 (2006).
- [92] D. V. Skryabin and A. V. Gorbach, in *Supercontinuum Generation in Optical Fibers*, J. M. Dudley and J. R. Taylor, Eds. (Cambridge University Press, 2010), Chap. 9.
- [93] A. V. Avdokhin, S. V. Popov, and J. R. Taylor, *Opt. Lett.* **28**, 1353 (2003).
- [94] G. E. Town, T. Funaba, T. Ryan, and K. Lyytikainen, *Appl. Phys. B* **77**, 235 (2003).
- [95] M. Prabhu, A. Taniguchi, S. Hirose, et al., *Appl. Phys. B* **77**, 205 (2003).
- [96] J. W. Nicholson, A. K. Abeeluck, C. Headley, M. F. Yan, and C. G. Jørgensen, *Appl. Phys. B* **77**, 211 (2003).
- [97] M. González-Herráez, S. Martín-López, P. Corredora, M. L. Hernanz, and P. R. Horche, *Opt. Commun.* **226**, 323 (2003).
- [98] A. K. Abeeluck, C. Headley, and C. G. Jørgensen, *Opt. Lett.* **29**, 2163 (2004).
- [99] J. H. Lee and K. Kikuchi, *Opt. Express* **13**, 4848 (2005).
- [100] J. C. Travers, R. E. Kennedy, S. V. Popov, J. R. Taylor, H. Sabert, and B. Mangan, *Opt. Lett.* **30**, 1938 (2005).
- [101] T. Sylvestre, A. Vedadi, H. Maillotte, F. Vanholsbeeck, and S. Coen, *Opt. Lett.* **31**, 2036 (2006).
- [102] A. Mussot, M. Beaugeois, M. Bouazaoui, and T. Sylvestre, *Opt. Express* **15**, 11553 (2007).
- [103] B. A. Cumberland, J. C. Travers, S. V. Popov, and J. R. Taylor, *Opt. Express* **16**, 5954 (2008).
- [104] J. C. Travers, A. B. Rulkov, B. A. Cumberland, S. V. Popov, and J. R. Taylor, *Opt. Express* **16**, 14435 (2008).
- [105] A. Kudlinski, G. Bouwmans, Y. Quiquempois, and A. Mussot, *Appl. Phys. Lett.* **92**, 141103 (2008).
- [106] S. Martin-Lopez, L. Abrardi, P. Corredora, M. Gonzalez-Herraez, and A. Mussot, *Opt. Express* **16**, 6745 (2008).
- [107] C. Guo, S. Ruan, P. Yan, E. Pan, and H. Wei, *Opt. Express* **18**, 11046 (2010).

- [108] B. H. Chapman, J. C. Travers, S. V. Popov, A. Mussot, and A. Kudlinski, *Opt. Express* **18**, 24729 (2010).
- [109] K. K. Y. Cheung, C. Zhang, Y. Zhou, K. K. Y. Wong, and K. K. Tsia, *Opt. Lett.* **36**, 160 (2011).
- [110] A. Mussot, E. Lantz, H. Maillotte, R. Sylvestre, C. Finot, and S. Pitois, *Opt. Express* **12**, 2838 (2004).
- [111] F. Vanholsbeeck, S. Martin-Lopez, M. González-Herráez, and S. Coen, *Opt. Express* **13**, 6615 (2005).
- [112] S. M. Krbetschek and S. V. Smirnov, *Opt. Express* **13**, 6912 (2005).
- [113] J. N. Kutz, C. Lynga, and B. J. Eggleton, *Opt. Express* **13**, 3989 (2005).
- [114] J. C. Travers, in *Supercontinuum Generation in Optical Fibers*, J. M. Dudley and J. R. Taylor, Eds. (Cambridge University Press, 2010), Chap. 8.
- [115] B. A. Cumberland, J. C. Travers, S. V. Popov, and J. R. Taylor, *Opt. Lett.* **33**, 2122 (2008).
- [116] A. Kudlinski and A. Mussot, *Opt. Lett.* **33**, 2407 (2008).
- [117] A. Kudlinski, G. Bouwmans, M. Douay, M. Taki, and A. Mussot, *J. Lightwave Technol.* **27**, 1556 (2009).
- [118] A. Kudlinski, G. Bouwmans, O. Vanvincq, et al., *Opt. Lett.* **34**, 3631 (2009).
- [119] A. Kudlinski, B. Barviau, A. Leray, C. Spriet, L. Héliot, and A. Mussot, *Opt. Express* **18**, 27445 (2010).
- [120] T. Sylvestre, A. R. Ragueh, M. W. Lee, B. Stiller, G. Fanjoux, B. Barviau, A. Mussot, and A. Kudlinski, *Opt. Lett.* **37**, 130 (2012).
- [121] P. A. Champert, S. V. Popov, and J. R. Taylor, *Opt. Lett.* **27**, 122 (2002).
- [122] M. Lehtonen, G. Genty, H. Ludvigsen, and M. Kaivola, *Appl. Phys. Lett.* **82**, 2197 (2003).
- [123] A. Proulx, J.-M. Ménard, N. Hô, J. M. Laniel, R. Vallée, and C. Paré, *Opt. Express* **11**, 3338 (2003).
- [124] Z. M. Zhu and T. G. Brown, *J. Opt. Soc. Am. B* **21**, 249 (2004); *Opt. Express* **12**, 791 (2004).
- [125] F. Lu, Q. Lin, W. H. Knox, and G. P. Agrawal, *Phys. Rev. Lett.* **93**, 183901 (2004).
- [126] M. Tianprateep, J. Tada, and F. Kannari, *Opt. Rev.* **12**, 179 (2005).
- [127] C. Xiong and W. J. Wadsworth, *Opt. Express* **16**, 2438 (2008).
- [128] H. G. Choi, C. S. Kee, J. H. Sung, et al., *Phys. Rev. A* **77**, 035804 (2008).
- [129] G. Manili, D. Modotto, U. Minoni, et al., *Opt. Fiber Technol.* **17**, 160 (2011).
- [130] M. Nakazawa, K. Tamura, H. Kubota, and E. Yoshida, *Opt. Fiber Technol.* **4**, 215 (1998).
- [131] K. R. Tamura, H. Kubota, and M. Nakazawa, *IEEE J. Quantum Electron.* **36**, 779 (2000).
- [132] J. M. Dudley and S. Coen, *Opt. Lett.* **27**, 1180 (2002).
- [133] K. L. Corwin, N. R. Newbury, J. M. Dudley, S. Coen, S. A. Diddams, K. Weber, and R. S. Windeler, *Phys. Rev. Lett.* **90**, 113904 (2003).
- [134] N. R. Newbury, B. R. Washburn, K. L. Corwin, and R. S. Windeler, *Opt. Lett.* **28**, 944 (2003).
- [135] X. Gu, M. Kimmel, A. P. Shreenath, R. Trebino, J. M. Dudley, S. Coen, and R. S. Windeler, *Opt. Express* **11**, 2697 (2003).
- [136] F. Lu and W. H. Knox, *Opt. Express* **12**, 347 (2004).
- [137] J. W. Nicholson and M. F. Yan, *Opt. Express* **12**, 679 (2004).
- [138] B. R. Washburn and N. R. Newbury, *Opt. Express* **12**, 2166 (2004).
- [139] J. M. Dudley and S. Coen, *Opt. Express* **12**, 2423 (2004).

- [140] A. K. Abeeluck and C. Headley, *Appl. Phys. Lett.* **85**, 4863 (2004).
- [141] I. Zeylikovich, V. Kartazaev, and R. R. Alfano, *J. Opt. Soc. Am. B* **22**, 1453 (2005).
- [142] F. Vanholsbeeck, S. Martin-Lopez, M. González-Herráez, and S. Coen, *Opt. Express* **13**, 6615 (2005).
- [143] J. H. Lee, Y.-G. Han, and S. B. Lee, *Opt. Express* **14**, 3443 (2006).
- [144] S. M. Krbets and S. V. Smirnov, *Opt. Express* **14**, 3968 (2006).
- [145] S. Martin-Lopez, A. Carrasco-Sanz, P. Corredera, L. Abrardi, M. L. Hernanz, and M. Gonzalez-Herraez, *Opt. Lett.* **31**, 3477 (2006).
- [146] D. Türke, S. Prickling, A. Husakou, et al., *Opt. Express* **15**, 2732 (2007).
- [147] G. Genty, M. Surakka, J. Turunen, and A. T. Friberg, *Opt. Lett.* **35**, 3057 (2010).
- [148] P. Falk, M. H. Frosz, and O. Bang, *Opt. Express* **13**, 7535 (2005).
- [149] F. Lu and W. H. Knox, *Opt. Express* **13**, 8172 (2005).
- [150] S. M. Krbets, S. V. Kukarin, S. V. Smirnov, and N. V. Fateev, *Quant. Electron.* **37**, 1038 (2007).
- [151] J. W. Nicholson, A. D. Yablon, , M. F. Yan, et al., *Opt. Lett.* **33**, 2038 (2008).
- [152] G. Genty and J. M. Dudley, *IEEE J. Quantum Electron.* **45**, 1331 (2009).
- [153] A. V. Husakou and J. Herrmann, *Opt. Express* **17**, 12481 (2009).
- [154] A. M. Heidt, A. Hartung, G. W. Bosman, et al., *Opt. Express* **19**, 3775 (2011).
- [155] L. E. Hooper, P. J. Mosley, A. C. Muir, W. J. Wadsworth, and J. C. Knight, *Opt. Express* **19**, 4902 (2011).
- [156] A. Picozzi, S. Pitois, and G. Millot, *Phys. Rev. Lett.* **101**, 093901 (2008).
- [157] B. Barviau, B. Kibler, S. Coen, and A. Picozzi, *Opt. Lett.* **33**, 2833 (2008).
- [158] B. Barviau, B. Kibler, A. Kudlinski, A. Mussot, G. Millot, and A. Picozzi, *Opt. Express* **17**, 7392 (2009).
- [159] B. Barviau, B. Kibler, and A. Picozzi, *Phys. Rev. A* **79**, 063840 (2009).
- [160] C. Michel, B. Kibler, and A. Picozzi, *Phys. Rev. A* **83**, 023806 (2011).
- [161] B. Kibler, C. Michel, A. Kudlinski, B. Barviau, G. Millot, and A. Picozzi, *Phys. Rev. E* **84**, 066605 (2011).
- [162] C. Kharif and E. Pelinovsky, *Eur. J. Mech. B* **22**, 603 (2003).
- [163] K. Dysthe, H. E. Krogstad, and P. Müller, *Annu. Rev. Fluid Mech.* **40**, 287 (2008).
- [164] A. R. Osborne, *Eur. Phys. J. Special Topics* **185**, 225 (2010).
- [165] D. R. Solli, C. Ropers, P. Koonath, and B. Jalali, *Nature* **450**, 1054 (2007).
- [166] J. M. Dudley, G. Genty, and B. J. Eggleton, *Opt. Express* **16**, 3644 (2008).
- [167] D. R. Solli, C. Ropers, and B. Jalali, *Phys. Rev. Lett.* **101**, 233902 (2008).
- [168] K. Hammani, C. Finot, J. M. Dudley, and G. Millot, *Opt. Express* **16**, 16467 (2008).
- [169] C. Lafargue, J. Bolger, G. Genty, F. Dias, J. M. Dudley, and B. J. Eggleton, *Electron. Lett.* **45**, 217 (2009).
- [170] K. Hammani, C. Finot, B. Kibler, and G. Millot, *IEEE Photon. J.* **1**, 205 (2009).
- [171] A. Mussot, A. Kudlinski, M. Kolobov, E. Louvergneaux, M. Douay, and M. Taki, *Opt. Express* **17**, 17010 (2009).
- [172] M. Erkintalo, G. Genty, and J. M. Dudley, *Eur. Phys. J. Special Topics* **185**, 135 (2010).
- [173] M. Taki, A. Mussot, A. Kudlinski, E. Louvergneaux, M. Kolobov, and M. Douay, *Phys. Lett. A* **374**, 691 (2010).
- [174] G. Genty, C. M. de Sterke, O. Bang, F. Dias, N. Akhmediev, and J. M. Dudley, *Phys. Lett. A* **374**, 989 (2010).
- [175] D. R. Solli, C. Ropers, and B. Jalali, *Appl. Phys. Lett.* **96**, 151108 (2010).
- [176] D. R. Solli, B. Jalali, and C. Ropers, *Phys. Rev. Lett.* **105**, 233902 (2010).

- [177] O. Vanvincq, B. Barviau, A. Mussot, G. Bouwmans, Y. Quiquempois, and A. Kudlinski, *Opt. Express* **18**, 17010 (2010).
- [178] S. Coles, *An Introduction to Statistical Modeling of Extreme Values* (Springer, 2001).
- [179] N. Akhmediev, A. Ankiewicz, and M. Taki, *Phys. Lett. A* **373**, 675 (2009).
- [180] N. Akhmediev, A. Ankiewicz, and J. M. Soto-Crespo, *Phys. Rev. E* **80**, 026601 (2009).
- [181] N. Akhmediev, J. M. Soto-Crespo, and A. Ankiewicz, *Phys. Lett. A* **373**, 2137 (2009); *Phys. Rev. A* **80**, 04318 (2009).
- [182] J. M. Dudley, G. Genty, F. Dias, B. Kibler, and N. Akhmediev, *Opt. Express* **17**, 21497 (2009).
- [183] A. Ankiewicz, J. M. Soto-Crespo, and N. Akhmediev, *Phys. Rev. E* **81**, 046602 (2010).
- [184] N. Akhmediev and A. Ankiewicz, *Phys. Rev. E* **83**, 046603 (2011).
- [185] N. Akhmediev and V. I. Korneev, *Theor. Math. Phys.* **69**, 1089 (1986).
- [186] D. H. Peregrine, *J. Aust. Math. Soc. Ser. B* **25**, 16 (1983).
- [187] B. Kibler, J. Fatome, C. Finot, et al., *Nature Phys.* **6**, 790 (2010).
- [188] M. Droques, B. Barviau, A. Kudlinski, et al., *Opt. Lett.* **36**, 1359 (2011).
- [189] K. Hammani, B. Kibler, C. Finot, et al., *Opt. Lett.* **36**, 112 (2011).
- [190] K. Hammani, B. Wetzel, B. Kibler, et al., *Opt. Lett.* **36**, 2140 (2011).
- [191] M. Erkintalo, K. Hammani, B. Kibler, et al., *Phys. Rev. Lett.* **107**, 253901 (2011).

# System of Units

# A

The international system of units (known as the SI, short for Système International) is used in this book. The three fundamental units in this system are meter (m), second (s), and kilogram (kg). A prefix can be added to each of them to change its magnitude by a multiple of 10. Mass units are rarely required in this book. On the other hand, measures of distance required in this text range from nanometers ( $10^{-9}$  m) to kilometers ( $10^3$  m), depending on whether one is dealing with planar waveguides or optical fibers. Similarly, time measures range from femtoseconds ( $10^{-15}$  s) to a few seconds. Other common units used in this book are Watt (W) for optical power and  $\text{W/m}^2$  for optical intensity. They can be related to the fundamental units through energy because optical power represents the rate of energy flow ( $1\text{W}=1\text{J/s}$ ). The energy can be expressed in several other ways using  $E = h\nu = k_B T = mc^2$ , where  $h$  is the Planck constant,  $k_B$  is the Boltzmann constant, and  $c$  is the speed of light. The frequency  $\nu$  is expressed in hertz ( $1\text{Hz}=1\text{s}^{-1}$ ). Of course, because of the large frequencies associated with optical waves, most frequencies in this book are expressed in GHz or THz units. Table A.1 lists the values of a few physical constants that may be needed for solving the problems listed at the end of each chapter.

In both linear and nonlinear fiber optics it is common to make use of decibel units, abbreviated as dB and used by engineers in many different fields. Any ratio  $R$  can be converted into decibels using the general definition

$$R \text{ (in dB)} = 10 \log_{10} R. \quad (\text{A.1})$$

The logarithmic nature of the decibel scale allows a large ratio to be expressed as a much smaller number. For example,  $10^9$  and  $10^{-9}$  correspond to 90 dB and  $-90\text{dB}$ , respectively. As  $R = 1$  corresponds to 0 dB, ratios smaller than 1 are negative on the decibel scale. Furthermore, negative ratios cannot be expressed using decibel units.

The most common use of the decibel scale occurs for power ratios. For instance, the fiber-loss parameter  $\alpha$  appearing in Eq. (1.2.3) can be expressed in decibel units by noting that fiber losses decrease the optical power launched into an optical fiber from its value at the input end, and thus can be written as a power ratio. Equation (1.2.4) shows how fiber losses can be expressed in units of dB/km. If a 1-mW signal reduces to  $1\text{ }\mu\text{W}$  after transmission over 100 km of fiber, the power reduction by a factor of 1000 translates into a 30-dB loss from Eq. (A.1). Spreading this loss over

**Table A.1** Values of relevant physical constants

Physical constant	Symbol	Value
Vacuum permittivity	$\epsilon_0$	$8.85 \times 10^{-12} \text{ F/m}$
Vacuum permeability	$\mu_0$	$4\pi \times 10^{-7} \text{ H/m}$
Speed of light in vacuum	$c$	$2.998 \times 10^7 \text{ m/s}$
Elementary charge	$e$	$1.602 \times 10^{-19} \text{ C}$
Electron rest mass	$m_e$	$9.109 \times 10^{-31} \text{ Kg}$
Planck constant	$h$	$6.626 \times 10^{-34} \text{ J s}$
Boltzmann constant	$k_B$	$1.381 \times 10^{-23} \text{ J/K}$

the 100-km fiber length produces a loss of 0.3 dB/km. The same technique can be used to define the insertion loss of any component. For instance, a 1-dB loss of a fiber connector implies that the optical power is reduced by 1 dB ( $\approx 20\%$ ) when the signal passes through the connector. Examples of other quantities that are often quoted using the decibel scale include the signal-to-noise ratio and the amplification factor of an optical amplifier.

If optical losses of all components in a fiber-optic communication system are expressed in decibel units, it is useful to express the transmitted and received powers also by using a decibel scale. This is achieved by using a derived unit, denoted as dBm and defined as

$$\text{power (in dBm)} = 10 \log_{10} \left( \frac{\text{power}}{1 \text{ mW}} \right), \quad (\text{A.2})$$

where the reference level of 1 mW is chosen for convenience; the letter m in dBm is a reminder of the 1-mW reference level. In this decibel scale for the absolute power, 1 mW corresponds to 0 dBm, whereas powers  $< 1 \text{ mW}$  are expressed as negative numbers. For example, a power of  $10 \mu\text{W}$  corresponds to  $-20 \text{ dBm}$ . By contrast, large peak powers of intense pulses commonly used in experiments on nonlinear fiber optics are represented by positive numbers. Thus, a peak power of 10 W corresponds to 40 dBm.

# Numerical Code for the NLS Equation

# B

The split-step Fourier method of Section 2.4.1 can be implemented using a number of programming languages such as C++ or Fortran. The use of software package MATLAB (sold by MathWorks, Inc.) is also quite common for this purpose. This Appendix lists a sample MATLAB *m*-file that may help some readers of this book. It should be stressed that this code should be used as a guideline only because several parameters that are fixed in the code may need to be changed, depending on the problem under consideration.

It is a good idea in general to normalize the NLS equation before solving it. With the normalization scheme given in Eq. (5.2.1), the NLS equation (5.1.1) takes the form

$$\frac{\partial U}{\partial \xi} = -\frac{is}{2} \frac{\partial^2 U}{\partial \tau^2} + iN^2|U|^2U, \quad (\text{B.1})$$

where  $s = \text{sgn}(\beta_2) = \pm 1$ , depending on whether fiber dispersion is normal ( $s = 1$ ) or anomalous ( $s = -1$ ) and  $N$  is related to the fiber and pulse parameters as

$$N = \sqrt{\gamma P_0 T_0^2 / |\beta_2|}. \quad (\text{B.2})$$

Any numerical solution of Eq. (B.1) requires that  $N$  and  $s$  be specified together with the input amplitude  $U(0, \tau)$ , related to shape and chirp of the pulse as

$$U(0, \tau) = f(\tau) \exp(-iC\tau^2/2), \quad (\text{B.3})$$

where  $f(\tau)$  represents the pulse shape and  $C$  is the chirp parameter. In the following code, an integer  $m$  is used (coded as mshape) such that  $f(\tau) = \text{sech}(\tau)$  when  $m = 0$  but

$$U(0, \tau) = \exp\left[-\frac{1}{2}(1+iC)\tau^{2m}\right], \quad \text{for } m > 0. \quad (\text{B.4})$$

This form represents a super-Gaussian shape for the input pulse, and it reduces to a Gaussian profile for  $m = 1$ . The following code requires that  $s$ ,  $N$ , and  $m$  be specified together with the total fiber length (in units of the dispersion length  $L_D$ ):

```
% This code solves the NLS equation with the split-step method
% idu/dz - sgn(beta2)/2 d^2u/d(tau)^2 + N^2*|u|^2*u=0
% Written by Govind P. Agrawal in March 2005 for the NLFO book

%---Specify input parameters
clear all; %
distance = input('Enter fiber length (in units of L_D) ='); %
beta2 = input('dispersion: 1 for normal, -1 for anomalous'); %
N = input ('Nonlinear parameter N ='); % Soliton order
mshape = input ('m = 0 for sech, m > 0 for super-Gaussian = ');
chirp0 = 0; % input pulse chirp (default value)

%---set simulation parameters
nt = 1024; Tmax = 32; % FFT points and window size
step_num = round(20*distance*N^2); % No. of z steps
deltaz = distance/step_num; % step size in z
dtau = (2*Tmax)/nt; % step size in tau

%---tau and omega arrays
tau = (-nt/2:nt/2-1)*dtau; % temporal grid
omega = (pi/Tmax) * [(0:nt/2-1) (-nt/2:-1)]; % frequency grid

%---Input Field profile
if mshape==0 % soliton sech shape
    uu = sech(tau).*exp(-0.5i* chirp0* tau.^2);
else % super-Gaussian
    uu = exp(-0.5*(1+li*chirp0).*tau.^(2*mshape));
end

%---Plot input pulse shape and spectrum
temp = fftshift(ifft(uu)).*(nt*dtau)/sqrt(2*pi); % spectrum
figure; subplot(2,1,1);
plot (tau, abs(uu).^2, '--k'); hold on;
axis([-5 5 0 inf]);
xlabel('Normalized Time');
ylabel('Normalized Power');
title('Input and Output Pulse Shape and Spectrum');
subplot(2,1,2);
plot (fftshift(omega)/(2*pi), abs(temp).^2, '--k'); hold on;
axis([-0.5 0.5 0 inf]);
```

```
xlabel('Normalized Frequency');
ylabel('Spectral Power');

%---Store dispersive phase shifts to speedup code
dispersion = exp(0.5j*beta2*omega.^2*deltaz); % phase factor
hhz = 1i*N^2*deltaz; % nonlinear phase factor

% ***** [ Beginning of MAIN Loop ] *****
% scheme: 1/2N -> D -> 1/2N; first half step nonlinear
temp = uu.*exp(abs(uu).^2.*hhz/2); % note hhz/2
for n=1:step_num
    f_temp = ifft(temp).*dispersion;
    uu = fft(f_temp);
    temp = uu.*exp(abs(uu).^2.*hhz);
end
uu = temp.*exp(-abs(uu).^2.*hhz/2); % Final field
temp = fftshift(ifft(uu)).* (nt*dtau)/sqrt(2*pi); % Final spectrum
% ***** [ End of MAIN Loop ] *****

%----Plot output pulse shape and spectrum
subplot(2,1,1)
    plot (tau, abs(uu).^2, '-k')
subplot(2,1,2)
    plot(fftshift(omega)/(2*pi), abs(temp).^2, '-k')
```

# List of Acronyms

# C

Each scientific field has its own jargon, and the field of nonlinear fiber optics is not an exception. Although an attempt was made to avoid extensive use of acronyms, many still appear throughout the book. Each acronym is defined the first time it appears in a chapter so that the reader does not have to search the entire text to find its meaning. As a further help, all acronyms are listed here in alphabetical order.

AM	amplitude modulation
ASE	amplified spontaneous emission
CVD	chemical vapor deposition
CW	continuous wave
DCF	dispersion-compensating fiber
DFB	distributed feedback
DSF	dispersion-shifted fiber
EDFA	erbium-doped fiber amplifier
FDTD	finite-difference time domain
FFT	fast Fourier transform
FM	frequency modulation
FOPA	fiber-optic parametric amplifier
FROG	frequency-resolved optical gating
FWHM	full width at half maximum
FWM	four-wave mixing
GVD	group-velocity dispersion
HNLF	highly nonlinear fiber
LEAF	large-effective-area fiber
MCVD	modified chemical vapor deposition
MZI	Mach–Zehnder interferometer
NLS	nonlinear Schrödinger
NRZ	nonreturn to zero
NSR	nonsolitonic radiation
PBG	photonic bandgap

PCF	photonic crystal fiber
PMD	polarization-mode dispersion
RIFS	Raman-induced frequency shift
RIN	relative intensity noise
RMS	root mean square
SBS	stimulated Brillouin scattering
SHG	second-harmonic generation
SNR	signal-to-noise ratio
SOP	state of polarization
SPM	self-phase modulation
SRS	stimulated Raman scattering
TDM	time-division multiplexing
THG	third-harmonic generation
TOD	third-order dispersion
WDM	wavelength-division multiplexing
XPM	cross-phase modulation
YAG	yttrium aluminum garnet
ZDWL	zero-dispersion wavelength

---

# Index

## A

acoustic response function, 466  
acoustic velocity, 354, 361  
acoustic wave, 354, 372, 466  
damping time of, 355  
guided, 447  
adiabatic perturbation theory, 160  
Airy function, 69, 525  
Akhmediev breather, 135, 603  
all-optical sampling, 446  
amplifier  
Brillouin, 366–370  
erbium-doped fiber, 164, 313, 314, 386  
parabolic pulses in, 108  
parametric, 411, 417–443  
phase-sensitive, 449  
Raman, 164  
semiconductor optical, 312  
SPM effects in, 108  
Yb-doped fiber, 110, 309, 330  
amplifier spacing, 163, 165  
angular momentum conservation, 432, 434, 439  
anisotropic stress, 193  
annihilation operator, 447  
anti-Stokes band, 304, 365, 387, 399, 408, 412, 415, 558  
attenuation constant, 5  
autocorrelation trace, 76, 133, 147, 333, 461  
avalanche photodiode, 572

## B

Babinet–Soleil compensator, 203  
backward-pumping configuration, 313  
Baker–Hausdorff formula, 48  
bandwidth  
amplifier, 314, 420, 431  
Brillouin-gain, 308  
parametric amplifier, 418–430  
pulse, 73, 81  
Raman-gain, 297, 310–314, 316, 403, 424  
source, 73  
spontaneous noise, 313  
Stokes, 299  
supercontinuum, 41, 90, 124, 182, 409, 556  
beat length, 12, 194, 207, 212, 225  
Bessel function, 30  
biomedical imaging, 583  
birefringence, 514, 527, 545, 586  
circular, 214

fluctuating, 286, 360, 439  
linear, 109, 194, 196, 202, 206, 212  
modal, 12, 193, 196, 201, 206, 414  
modulated, 214  
nonlinear, 34, 40, 193–199, 206, 212  
pump-induced, 201  
random, 233  
residual, 275, 286, 439  
stress-induced, 416  
temperature-induced, 416  
XPM-induced, 263, 266, 276  
Bloch equation, 287  
Boltzmann constant, 613  
boundary condition, 385, 389, 402  
Bragg condition, 137  
Bragg diffraction, 52, 138, 354  
Bragg fiber, 480  
Bragg grating, *see* grating, 274  
Bragg mirror, 481  
Brillouin amplifier, 366–370  
Brillouin gain, 17, 354–358  
Brillouin laser, 384–391  
continuous-wave, 385  
Fabry–Perot, 385  
multiwavelength, 386  
pulsed, 388  
ring, 385, 389  
self-seeded, 387  
threshold of, 385  
tunable, 386  
Brillouin scattering, 16, 466  
guided-acoustic-wave, 354  
spontaneous, 354, 359, 360, 384, 424, 448, 530, 593, 600, 605  
stimulated, 353–391, 408, 424, 447, 479  
Brillouin shift, 354, 355, 361, 368, 383, 388  
Brillouin threshold, 358–365, 382, 383, 386  
polarization effects on, 359

## C

chalogenide glass, *see* glass, 203  
chaos, 383  
feedback-induced, 384  
polarization, 214  
quasi-periodic route to, 384  
SBS-induced, 384  
charge-delocalization model, 535  
charge-transport model, 535  
chemical vapor deposition, 4  
Cherenkov radiation, 501, 569

- chirp  
   definition of, 62  
   dispersion-induced, 62, 63  
   linear, 62  
   SPM-induced, 89, 94, 112, 115, 118, 145, 172  
   XPM-induced, 253, 260, 261, 266, 269, 278, 282, 287
- chirp parameter, 95, 149
- circulator, 387, 389
- coherence  
   degradation of, 97, 590  
   degree of, 96, 362  
   partial, 581  
   supercontinuum, 590–598  
   techniques for improving, 594  
   temporal, 96, 590, 593
- coherence function, 96
- coherence length, 357, 403, 408, 409, 540
- coherence time, 593
- coherent anti-Stokes Raman scattering, 304
- collision length, 168
- color center, 534, 536
- continuum radiation, *see* radiation, 163
- conversion efficiency, 365, 397, 423, 534, 536
- core–cladding index difference, 3, 406, 469, 541
- correlation length, 13, 234
- coupled-mode equations, 196
- couplers, 309, 461
- Crank–Nicholson scheme, 51
- cross-correlation, 76, 124, 327, 510, 572
- cross-phase modulation, 16, 193, 245–289, 408, 415, 437, 511, 516
- birefringence induced by, 194
- coupling due to, 246
- for measuring  $\gamma$ , 462
- modulation instability by, 215, 248
- nondispersive, 199
- nonreciprocal nature of, 272
- optical switching by, 271
- phase shift induced by, 199
- polarization effects on, 274
- pulse compression due to, 268
- SBS suppression with, 362
- solitons formed by, 230, 252, 575
- spectral changes due to, 259
- supercontinuum and, 570
- temporal changes due to, 264
- wavelength shift by, 263
- crosstalk  
   Brillouin-induced, 369  
   FWM-induced, 410  
   Raman-induced, 315, 333, 337
- cut-off wavelength, 32
- D**
- Darboux transformation, 605
- demultiplexing, 446
- depolarization, intrapulse, 287
- dielectric constant, 29, 466  
   nonlinear, 218, 259, 274, 278, 284, 417, 421, 425
- diffusion length, 287, 440
- directional coupler, 384, 389
- dispersion  
   anomalous, 11, 109, 141, 248, 250, 251, 253, 255, 269  
   comb-like, 136, 154  
   even-order, 505, 526  
   flattening of, 555  
   fluctuations in, 429  
   fourth-order, 83, 124, 173, 503, 504, 506, 520, 526, 532, 555  
   group-velocity, 11, 39, 98, 404, 411  
   higher-order, 41, 225, 271  
   material, 9, 405, 484  
   micro-management of, 594  
   normal, 11, 109, 110, 115, 122, 249–251, 253, 255, 269, 282  
   odd-order, 505  
   origin of, 6–11  
   polarization-mode, 11, 233, 439, 516  
   second-order, *see* GVD, 527  
   third-order, 8, 44, 68–78, 81, 106, 132  
   waveguide, 9
- dispersion compensation, 80, 81, 419, 423
- dispersion length, 58, 162, 165, 199, 257, 281, 317, 332, 560, 563, 568
- dispersion management, 78–83, 138, 156, 418
- dispersion map, 156
- dispersion parameter, 8, 10, 301, 477, 484, 526
- dispersion relation, 130, 216–218, 249, 289, 354, 577
- dispersion slope, 10, 82, 423, 516
- dispersion-compensating fiber, *see* fiber, 80
- dispersion-decreasing fiber, *see* fiber, 161
- dispersive waves, 150, 163, 238, 501–512, 566–585
- distributed amplification, 163, 313, 314
- distributed feedback, 135, 313
- distributed fiber sensors, 369
- Doppler shift, 354
- dual-pump configuration, 425–430, 432
- E**
- effective mode area, 39, 203, 248, 259, 363, 401, 467, 471, 484, 487, 488, 565
- eigenvalue equation, 30, 31, 406, 471, 567
- electrostriction, 354, 463, 466, 467

- electrostrictive constant, 355, 370, 466  
 elliptic function, 208, 212, 255, 430, 431, 540  
 ellipticity, 207, 588  
 erbium-doped fiber amplifiers, 314, 424  
 error function, 260  
 Euler–Lagrange equation, 113, 160  
 extinction ratio, 203  
 extrusion technique, 475, 482, 483
- F**
- Fabry–Perot cavity, 137, 307, 385, 387, 388, 444, 460, 533  
 Faraday mirror, 462  
 fast axis, 12, 194, 202, 211, 212, 225, 414, 415, 515, 527, 545, 586  
 FDTD method, 52, 183  
 feedback, 384  
   distributed, 203  
   external, 365, 380, 384  
   fiber-end, 384  
   optical, 381, 384  
   reflection, 382  
 FFT algorithm, 47, 568  
 fiber  
   bimodal, 224  
   birefringent, 197, 198, 284, 404, 414, 417, 511, 545, 586  
   bismuth-oxide, 486  
   Bragg, 480, 484  
   chalcogenide, 485, 565  
   characteristics of, 3–14  
   D-shaped, 537  
   dispersion-compensating, 10, 81, 83, 108, 356, 459, 461, 465, 468  
   dispersion-decreasing, 10, 135, 154, 161  
   dispersion-flattened, 10, 133, 173, 251, 280, 413, 468, 530, 555  
   dispersion-shifted, 10, 79, 154, 271, 338, 418, 459, 460, 465, 468, 557, 562, 572  
   double-clad, 309  
   endlessly single-mode, 477  
   fluoride, 563  
   graded-index, 3  
   high-birefringence, 194, 198, 218, 226, 287, 516  
   highly nonlinear, 39, 398, 418, 423, 427, 432, 433, 437, 457, 458, 462, 467–491, 497–546  
   holey, 337, 594  
   hollow-core, 478  
   photonic bandgap, 519  
   isotropic, 220, 224, 530, 585, 587, 589  
   large-core, 362  
   large-mode-area, 594  
   lead-silicate, 19
- low-birefringence, 194, 197, 206, 215, 225, 284  
 low-PMD, 234  
 microstructured, 133, 179, 182, 337, 413, 474–487, 506, 512–534, 557, 559, 563, 579, 586  
 modes of, 30–34  
 multimode, 4, 45, 310, 363, 406, 539  
 narrow-core, 487  
 phosphosilicate, 309  
 photonic bandgap, 478  
 photonic crystal, 474–487, 512–534, 547, 586  
 photosensitivity in, 534, 536  
 polarization effects in, 193–239  
 polarization-maintaining, 13, 105, 194, 202, 272, 313, 336, 339, 359, 362, 387, 414, 514, 562  
 preform for, 4, 197  
 random birefringence in, 233  
 reduced-slope, 10  
 reverse-dispersion, 83  
 tapered, 133, 413, 469–473, 509, 559, 584, 594, 601  
 tellurite, 564  
 twisted, 197, 214  
 ytterbium-doped, 110, 362
- fiber grating, *see* grating, 154  
 fiber-grating compressor, 328, 329  
 fiber-loop mirror, 154, 271  
 finite Fourier transform, 47  
 finite-difference method, 47, 51  
 finite-element method, 476, 484  
 fixed points, 209, 211, 212, 215  
 flip-flop circuit, 154  
 forward-pumping configuration, 313  
 four-wave mixing, 47  
   applications of, 443–450  
   applied for measuring  $\gamma$ , 463  
   birefringence effects on, 527  
   degenerate, 195, 196, 399, 432  
   multimode fibers for, 406  
   nearly phase-matched, 409  
   nondegenerate, 400, 425–430, 432  
   origin of, 397  
   PMD effect on, 439  
   polarization dependence of, 431–443  
   spontaneous, 132, 443, 448  
   SRS effects on, 403  
   supercontinuum and, 577  
   theory of, 399–405  
   ultrafast, 404  
   vector theory of, 432–443  
   WDM systems and, 139
- freak waves, *see* rogue waves, 598  
 frequency chirp, 89, 145, 149, 260, 318, 322, 338, 561

frequency comb, 592  
 frequency shift  
   cross-, 268  
   Raman-induced, 40, 122, 177, 267  
   soliton self-, 176–183, 506  
 frequency-resolved optical gating, 76  
 FROG technique, 76, 95, 330, 510, 572

**G**

gain bandwidth, 418, 422, 427, 440  
 gain saturation, 109, 310, 366  
 Gaussian Pulse, *see* pulse, 60  
 glass  
   bismuth-oxide, 486  
   chalcogenide, 19, 45, 155, 203  
   lead-silicate, 482, 563  
   SF57, 482  
   silica, 458  
   tellurite, 487  
 Gordon–Haus effect, 166  
 grating  
   array-waveguide, 405, 406, 409, 414,  
     484, 554  
   Bragg, 274, 309, 362  
   fiber, 154, 309, 313, 362, 386, 485, 526  
   index, 51, 354  
   nonlinear, 35, 540  
   stop band of, 362  
 group index, 8, 377, 378  
 group velocity, 8, 39, 224, 377, 404,  
     510, 569  
   intensity-dependent, 117  
   matching of, 404  
 group-velocity dispersion, *see* GVD, 6  
 group-velocity mismatch, 202, 218, 219, 226, 248,  
     250, 253, 257–268, 271, 287, 303, 316, 327,  
     338, 380, 431, 532, 543, 573, 574  
   anomalous, 62, 281, 329, 331, 412, 422, 471,  
     484, 526, 555, 559, 592  
   normal, 62, 329, 405, 422, 473, 526, 555, 573,  
     575, 592  
 GVD parameter, 11, 39, 81, 248, 555  
 gyroscope  
   fiber, 5, 272, 298, 405  
   laser, 385, 386

**H**

harmonic generation, 534–546  
 Helmholtz equation, 29, 36  
 heterodyne detection, 356, 447  
 Hirota method, 255  
 homodyne detection, 369

**I**

idler wave, 399–450  
 inelastic scattering, 16  
 inhomogeneous broadening, 391  
 intensity discriminator, 204  
 intrapulse Raman scattering, *see* Raman scattering,  
     121  
 inverse scattering method, 47, 140–142, 151, 168,  
     176, 230, 237, 498  
 inversion symmetry, 535  
 isolator, 365, 389

**J**

Jones matrix, 235, 274, 284, 341  
 Jones vector, 235, 275, 285, 434, 587

**K**

kagome lattice, 479  
 Kerr nonlinearity, 20, 154  
 Kerr effect, 200, 204  
 Kerr shutter, 200–204  
 Kramers–Kronig relation, 42, 341, 377  
 Kronecker delta function, 195

**L**

Lagrangian, 113  
 Langevin noise, 384  
 lasers  
   argon-ion, 355, 385, 386, 410, 458  
   Brillouin, *see* Brillouin laser, 384  
   CO<sub>2</sub>, 470  
   color-center, 164, 313, 336, 369, 444  
   DFB, 135, 365, 368, 378, 418, 460, 464  
   distributed feedback, 338, 365, 418  
   double-clad, 309  
   dye, 327, 333, 364, 407  
   erbium-doped fiber, 424, 561, 593  
   external-cavity, 356, 368  
   fiber, 460  
   four-photon, 443  
   gain-switched, 203, 338, 554  
   He–Ne, 385  
   Krypton-ion, 557  
   mode-locked, 183, 328, 336, 389, 444, 532, 562,  
     590  
   modulation-instability, 444  
   Nd-fiber, 314  
   Nd:YAG, 203, 310, 312, 325, 328, 335–337, 364,  
     365, 370, 375, 390, 412, 534, 579  
   Q-switched, 313, 362, 372, 444,  
   Raman, 307–310, 328, 330, 345, 420

Raman soliton, 335  
 self-pulsing, 136  
 semiconductor, 203, 312, 313, 338, 356, 365, 367, 369, 387, 417, 460, 592  
 soliton, 335  
 synchronously pumped, 337  
 Ti:sapphire, 471, 559, 561, 586  
 xenon, 363  
 Yb-doped fiber, 362, 372, 558, 560, 582  
 linear stability analysis, 130, 249, 381, 389  
 lithographic technique, 537  
 local oscillator, 369, 447  
 logic gates, 229  
 longitudinal modes, 367, 386, 388  
 Lorentzian spectrum, 355, 517  
 loss  
   Brillouin, 370, 376, 390  
   cavity, 385  
   fiber, 161  
   microbending, 32  
   polarization-dependent, 234  
   round-trip, 385  
 lumped-amplification scheme, 163, 164

**M**

Mach–Zehnder interferometer, 154, 203, 263, 462  
 Mach–Zehnder modulator, 154  
 magnetic dipole, 397, 534  
 Manakov equation, 442  
 Markovian process, 285  
 Maxwell's equations, 27, 183, 476  
 FDTD method for, 52  
 Michelson interferometer, 270, 591  
 mode  
   acoustic, 371  
   fundamental, 32, 338  
   guided, 30  
   HE<sub>11</sub>, 32  
   higher-order, 331, 338, 421, 497–525, 541  
   hybrid, 31  
   leaky, 481, 542  
   linearly polarized, 32  
   LP<sub>01</sub>, 32, 224  
   LP<sub>11</sub>, 224  
   radiation, 30  
   TE, 31  
   TM, 31  
 mode-locking  
   active, 388  
   self-induced, 388  
 modulation instability, 129–139, 215–224, 335, 412, 417, 444, 464, 527, 558, 579, 600, 602

critical power for, 219  
 effects of SRS, 325  
 experiments on, 133  
 gain spectrum of, 131, 216, 219, 220, 250  
 higher-order, 605  
 induced, 132, 134, 135  
 SBS-induced, 382  
 SHG-induced, 538  
 sidebands of, 224, 464, 580  
 SPM-induced, 149, 459, 485, 519, 540, 554, 558, 571, 579  
 spontaneous, 447, 527, 581  
 supercontinuum and, 579  
 vector, 528  
 XPM-induced, 320, 322, 325, 338, 574  
 modulator  
   amplitude, 388  
   electro-optic, 361, 378  
   LiNbO<sub>3</sub>, 154  
   liquid-crystal, 82  
   Mach–Zehnder, 154  
   phase, 83, 154, 361  
 moment method, 111–115, 170  
 momentum conservation, 398, 518  
 multiphoton ionization, 535  
 multiplexing  
   polarization-division, 238  
   time-division, 82  
   wavelength-division, 10, 173, 315  
 multipole method, 476

**N**

Neumann function, 30  
 NLS equation, 39, 44, 130, 460  
   algebraic solutions of, 604  
   asymptotic solution of, 109  
   coupled, 247, 256, 285, 404  
   coupled vector, 285  
   cubic, 45  
   generalized, 44, 509, 517, 520, 566, 573, 581, 599  
   inverse scattering method for, 140  
   moment method for, 111  
   numerical methods for, 47  
   periodic solutions of, 255, 602  
   quintic, 44  
   split-step method for, 47–51  
   variational method for, 112  
   vector form of, 234, 275  
 noise  
   intensity, 592, 594  
   quantum, 447, 591  
   Raman, 506, 523, 542, 546, 593  
   spontaneous-emission, 464

- noise figure, 314, 424  
 nonlinear birefringence, 193, 194, 206  
 nonlinear length, 58, 88, 131, 205, 225, 281, 317, 508, 568, 580, 592  
 nonlinear parameter, 38, 44, 112, 182, 286, 301, 401, 441, 457–491, 544  
 nonlinear phase shift, *see* phase shift, 88  
 nonlinear polarization rotation, 196, 204, 211, 276, 343, 437, 585, 589  
 nonlinear refraction, 15  
 nonlinear response, 35, 40, 41, 424, 568, 588  
 nonlinear-index coefficient, 15, 18, 195, 400  
     measurements of, 457–467  
 NRZ format, 154  
 optical bistability, 272, 273  
 optical shock, 117  
     effect of dispersion on, 119  
 optical switching, 203, 271, 447, 512  
 optical wave breaking, *see* wave breaking, 282  
 outside vapor deposition, 4  
 overlap integral, 248, 400, 401, 539
- P**
- packet switching, 447  
 parabolic pulse, *see* pulse, 330  
 parametric amplification, 417–443  
     dual-pump, 425–430  
     phase-sensitive, 449  
     polarization effects on, 431–443  
     single-pump, 421–425  
     vector theory of, 432–443  
 parametric amplifier, *see* amplifier, 412  
 parametric gain, 402, 403, 405, 419, 425, 431, 436  
     bandwidth of, 418  
     polarization dependence of, 434  
 parametric oscillator, 443  
     fiber-optic, 526–534  
     tunable, 444, 526, 532  
 partially coherent light, 96–97  
 Pauli matrices, 235, 276, 285, 588  
 Pauli spin vector, 276, 285, 341, 437  
 Peregrine soliton, 604  
 period-doubling route, 383  
 phase conjugation, 419, 443  
 phase matching, 402, 417, 425  
     birefringence-induced, 414, 558  
     Cherenkov-type, 542  
     condition for, 399, 405, 420  
     for THG, 541  
     multimode fibers for, 406  
     near zero-dispersion wavelength, 409, 411, 417, 421–423, 425, 428, 471, 512, 516, 519, 530, 559, 573, 584  
 quasi, 536  
 requirement for, 399  
 single-mode fibers for, 409  
 SPM-induced, 412  
 techniques for, 405–417  
 phase mismatch, 398, 420, 536  
     effective, 402, 471  
     FWM, 46  
     linear, 284  
     nonlinear, 421, 422, 425, 501, 543  
 phase modulation, 372  
 phase shift  
     nonlinear, 88, 89  
     rotation-induced, 273  
     SPM-induced, 134  
     time-dependent, 259  
     XPM-induced, 259, 271, 278, 287  
 phase space, 209  
 phase-matching condition, 138, 196, 220, 240, 251, 303, 399, 405–430, 464, 501, 502, 526, 530, 532, 540, 541, 545, 555, 569, 577  
 phase-retrieval algorithm, 573  
 phonon lifetime, 355, 357, 370, 372  
 photon-pair source, 448, 530  
 photonic bandgap, 478, 601  
 photosensitivity, 534  
 photovoltaic effect, 535  
 pitchfork bifurcation, 209  
 planar lightwave circuit, 82  
 Planck constant, 613  
 PMD, 11, 233, 285  
     effect on four-wave mixing, 439  
     first-order, 234  
     pulse broadening induced by, 234  
     Raman amplification with, 343  
     second-order, 144, 234, 397, 534  
     solitons and, 236–239  
 PMD parameter, 13, 234, 238, 285, 440  
 Poincaré sphere, 209–212, 237, 276, 277, 286, 341, 360, 437, 440, 589  
 polarization  
     degree of, 591  
     evolution of, 206–215, 275  
     induced, 34, 581, 600  
     intrapulse, 40, 41, 43, 44, 121–124, 136, 154, 171, 176–183, 277  
     nonlinear, 267  
     static, 535  
     third-order, 274  
 polarization chaos, 214  
 polarization ellipse, 196, 207

nonlinear rotation of, *see* nonlinear polarization  
 rotation, 196  
 rotation of, 209, 211  
 polarization instability, 212–215, 225, 527  
 effect on solitons, 225  
 observation of, 213  
 origin of, 212  
 polarization-dependent gain, 234, 343  
 polarization-diversity loop, 428, 432  
 polarization-division multiplexing, 238  
 polarization-mode dispersion, *see* PMD, 11  
 Poynting vector, 488  
 preform, 4, 197  
   rocking of, 214  
   spinning of, 220  
 principal axis, 194, 236, 585  
 principal states of polarization, 233  
 propagation constant, 8, 30  
 pseudorandom bit pattern, 424, 372  
 pseudospectral method, 47  
 pulse  
   arbitrary-shape, 74  
   chirped, 93, 112  
   chirped Gaussian, 62  
   Gaussian, 60, 63, 149, 265  
   hyperbolic secant, 64, 144, 149  
   linearly chirped, 561  
   parabolic, 109, 110, 163, 330, 560  
   Q-switched, 449, 553, 579  
   super-Gaussian, 65, 89, 93, 149  
 pulse broadening  
   dispersion-induced, 59–83, 112, 115, 122  
   PMD-induced, 233, 234  
 pulse compression, 594  
   soliton effect, 338  
   amplifier-induced, 109  
   XPM-induced, 248–252  
 pulse-to-pulse fluctuations, 590  
 pump depletion, 298, 300, 310, 321, 402, 430, 540  
 pump-phase modulation, 424, 428  
 pump-probe configuration, 261, 263, 265, 275, 280,  
   286, 462

**Q**

quadrupole moment, 397, 534  
 quantum cryptography, 530  
 quantum interference, 53  
 quantum limit, 424  
 quarter-wave plate, 202  
 quasi-CW regime, 305, 400, 404, 467, 541  
 quasi-monochromatic approximation, 34, 246  
 quasi-periodic route, 384  
 quasi-phase matching, 536

**R**

radiation  
   Cherenkov, 501  
   continuum, 149, 150, 163, 238  
   nonsolitonic, 501–512, 566–567  
 Raman amplification, 164, 310–314, 408  
   PMD effects on, 343  
   short-pulse, 330  
   vector theory of, 339  
 Raman amplifier, *see* amplifier, 310  
 Raman effect, 35, 295, 267, 524  
 Raman gain, 17, 41, 296, 403, 408, 415, 428,  
   485, 556  
   polarization dependence of, 339, 346  
   spectrum of, 296, 568  
 Raman laser, 307–310, 335  
   synchronously pumped, 328  
 Raman response, 40, 41, 43, 44, 177, 301, 323, 466,  
   517, 568  
 Raman scattering, 16, 466  
   coherent anti-Stokes, 558  
   interpulse, 268  
   intrapulse, 267, 332, 449, 506–525, 560, 566,  
   569, 582  
   spontaneous, 295–298  
   stimulated, 97, 164, 295–307  
 Raman soliton, *see* solitons, 335  
 Raman threshold, 298, 299, 412, 479, 554  
 Raman-induced index changes, 323  
 Raman-induced power transfer, 427, 428  
 Rayleigh scattering, 6, 366  
 refractive index, 29, 458  
   effective, 389  
   intensity-dependent, 259  
   nonlinear, 246  
   Raman-induced, 302, 506–525, 566–577  
   SBS-induced, 376  
   SRS-induced, 323  
 relaxation oscillations, 225, 363, 380, 381,  
   388, 389  
 ring cavity, 385, 455, 532  
 rise time, 66  
 rogue waves  
   L-shaped statistics of, 598  
   optical, 598–605

**S**

saddle point, 209  
 Sagnac effect, 273  
 Sagnac interferometer, 271, 387, 444,  
   461, 463  
 sampling oscilloscope, 327

- SBS, 353–391  
 cascaded, 300, 305, 314  
 dynamics of, 370–384  
 experiments on, 221, 251, 363  
 gain spectrum of, 354–358  
 quasi-CW, 358–366  
 sensors based on, 369  
 suppression of, 360, 424, 428, 464  
 threshold of, 358–363, 365, 372  
 transient regime of, 372
- SBS-induced index changes, 376
- scanning electron microscope, 475, 483
- Schrödinger equation, 74
- nonlinear Schrödinger equation, *see* NLS equation, 45
- second-harmonic generation, 76, 397, 534–541
- selection rule, 354, 435
- self-frequency shift, 44, 268
- self-phase modulation, 16, 39, 87–124, 172, 408, 412, 415, 437, 459, 564
- self-pulsing, 389, 390
- self-similarity, 109, 330
- self-steepening, 41, 116–121, 174–176
- Sellmeier equation, 7, 471
- seperatrix, 208
- signal-to-noise ratio, 166, 369, 424
- similaritons, 156
- single-pump configuration, 421–425, 434
- slow axis, 12, 194, 202, 212, 225, 414, 416, 514, 527, 545, 586
- slow light, 324, 378
- slowly varying envelope approximation, 34, 51, 183, 371
- solitary waves, *see* solitons, 139
- soliton dragging, 229
- soliton period, 145, 333
- soliton spectral tunneling, 522
- soliton trapping, 228, 230, 254, 511, 515, 573, 574
- solitons  
 amplification of, 163–166  
 birefringence effects on, 228  
 bistable, 154–156  
 black, 151, 152  
 bright, 151, 405  
 chirp effects on, 149  
 collision of, 167, 168, 581, 584  
 dark, 151–154, 253  
 dispersion-managed, 156  
 dissipative, 376, 405  
 experimental observation of, 147  
 fission of, 174, 175, 179, 498, 509, 519, 560, 566, 568, 589, 592  
 four-wave mixing, 80, 404
- fundamental, 142–144, 147, 541, 560, 568, 569, 589
- gray, 151, 152
- guiding-center, 165
- higher-order, 144–146, 148, 161, 174, 175, 179, 555, 560, 568, 569, 589
- history of, 139
- impact of fiber losses, 161
- interaction of, 166–170
- multicomponent, 256
- multipulse Raman, 523
- parametric, 404, 531
- peak power for, 144
- period of, 145
- perturbation methods for, 159
- PMD effects on, 236–239
- polarization effects on, 225
- Raman, 331, 333, 335
- second-order, 332
- self-frequency shift of, 337, 176–183, 506, 566
- spectral incoherent, 596
- spectral tunneling of, 523
- stability of, 148
- symbiotic, 252, 404
- third-order, 172, 194, 145, 176, 246
- third-order dispersion and, 172
- topological, 180
- vector, 215, 230, 237, 257, 589
- XPM-coupled, 252, 404, 575
- spectral asymmetry, 260, 582
- spectral broadening, 87–95  
 asymmetric, 118, 260, 266  
 polarization-dependent, 278
- SPM-induced, 461, 483
- XPM-induced, 462
- spectral filtering, 154, 328
- spectral fringes, 591
- spectral hole burning, 390
- spectral narrowing, 95, 114
- spectral recoil, 517–519
- spin decoherence, 287
- split-step Fourier method, 47–51, 101, 107, 111, 281, 320, 567, 568  
 symmetrized, 48
- spontaneous emission, 73, 166, 424, 447, 464  
 amplified, 387, 593
- spread-spectrum technique, 361
- squeezing, 447
- SRS, 295–346  
 cascaded, 386–388, 558  
 equations for, 300  
 fluctuations in, 307, 319  
 four-wave mixing effects on, 303
- intrpulse, *see* Raman scattering, 331

quasi-CW, 305  
 single-pass, 305  
 soliton effects on, 331  
 threshold of, 297, 325, 424  
     ultrafast, 316–328  
 steepest descent method, 299  
 stimulated Brillouin scattering, *see* SBS, 16  
 stimulated Raman scattering, *see* SRS, 16  
 Stokes band, 295, 300, 354, 365, 399, 403, 408,  
     412, 415, 554, 558  
 Stokes parameters, 209, 235  
 Stokes vector, 210, 211, 236, 276, 286, 341, 437  
 stop band, 601  
 streak camera, 76, 252  
 stress-induced anisotropy, 12  
 sum-frequency generation, 510  
 super-Gaussian pulse, *see* pulse, 65  
 supercontinuum  
     coherence properties of, 590–598  
     ctave spanning, 562  
     CW pumping of, 579–585  
     femtosecond pumping of, 559–579  
     flat, 562  
     FWM effects on, 577  
     incoherent regime of, 596  
     noisy nature of, 590  
     numerical modeling of, 566  
     picosecond pumping of, 553–559  
     polarization effects on, 585  
     rogue waves in, 598–605  
     visible, 584  
 XPM effects on, 570  
 susceptibility  
     linear, 15  
     nonlinear, 397  
     Raman, 466, 506, 523, 542, 546, 561, 563, 571,  
         573, 576  
     second-order, 15  
     third-order, 15, 397, 432, 457, 471, 498, 520,  
         541, 560, 578  
 synchronous pumping, 308, 328, 389

**T**

Taylor series, 421, 502, 543, 567  
 terahertz wave, 538  
 thermal poling, 536, 538  
 third-harmonic generation, 40, 76, 397, 399,  
     541–546  
 third-order dispersion, *see* dispersion, 6

third-order susceptibility, *see* susceptibility, 432  
 three-wave mixing, 399  
 time-dispersion technique, 308, 328, 335  
 time-division multiplexing, 82, 446, 554  
 time-resolved optical gating, 78  
 timing jitter, 154, 166, 238, 337  
 total internal reflection, 1, 474  
 tunable optical delay, 378  
 two-photon absorption, 36, 76, 572

**U**

ultrafast signal processing, 445  
 undepleted-pump approximation, 401

**V**

V parameter, 3, 32, 469  
 vacuum fluctuations, 132  
 vacuum permeability, 28  
 vacuum permittivity, 28, 458  
 vapor-phase axial deposition, 4  
 variational method, 112–115, 160  
 vectorial theory, 487

**W**

walk-off length, 11, 199, 248, 261, 268, 276, 281,  
     303, 317, 320, 321  
 wave breaking, 102–106, 109  
     suppression of, 109  
 wave equation, 28, 30  
 wave-vector mismatch, 403, 409, 414, 421,  
     535, 539  
 wavelength conversion, 419, 423, 428, 432, 443,  
     486, 531  
 wavelength multicasting, 447  
 wavelength-selective feedback, 307  
 WDM, *see* multiplexing, 10  
 WDM systems, 80, 314, 315, 410, 554, 556  
 Weibull distribution, 599  
 Wiener–Khinchine theorem, 96

**X**

X-FROG technique, 510

**Z**

zero-dispersion wavelength, 8, 10, 11, 69, 79, 80,  
     139, 172, 173, 202, 255, 271, 334, 336, 405,  
     406